SPIE—The International Society for Optical Engineering

Conference Digest

Eighteenth International Conference on Infrared and Millimeter Waves

James R. Birch
Terence J. Parker
Editors

6–10 September 1993
University of Essex
Colchester, United Kingdom

Volume 2104

PROCEEDINGS
SPIE—The International Society for Optical Engineering

Conference Digest

Eighteenth International Conference on Infrared and Millimeter Waves

James R. Birch
Terence J. Parker
Editors

6–10 September 1993
University of Essex
Colchester, United Kingdom

Sponsored and Published by
SPIE—The International Society for Optical Engineering

Volume 2104

Please use the following format to cite material from this book:
Author(s), "Title of paper," in *Eighteenth International Conference on Infrared and Millimeter Waves*, James R. Birch, Terence J. Parker, Editors, Proc. SPIE 2104, page numbers (1993).

Library of Congress Catalog Card No. 93-85656
ISBN 0-8194-1392-5

Published by
SPIE—The International Society for Optical Engineering
P.O. Box 10, Bellingham, Washington 98227-1101 USA
Telephone 206/676-3290 (Pacific Time) • Fax 206/647-1445

Printed in the United States of America.

Eighteenth International Conference on Infrared and Millimeter Waves

6-10 September 1993

FINAL PROGRAM

MON AM	OPENING CEREMONY, PRIZE GIVING AND PLENARY LECTURE 1: M.F. KIMMITT			
	FEL I	DETECTORS AND SOURCES I	GAS LASERS I	SPECTROSCOPY I
MON PM	FEL II	DETECTORS AND SOURCES II	GAS LASERS II	SPECTROSCOPY II
TUES AM	PLENARY LECTURE 2: H.P. GUSH, E.H. WISHNOW AND M. HALPERN			
	WINDOWS FOR HIGH POWER APPLICATIONS	DETECTORS AND SOURCES III	SCATTERING	SPECTROSCOPY III
TUES PM	PLASMA DIAGNOSTICS	DETECTORS AND SOURCES IV	WAVEGUIDES I	SPECTROSCOPY IV
WED AM	PLENARY LECTURE 3: M. THUMM			
	GYROTRON I	QUASI-OPTICAL COMPONENTS I	WAVEGUIDES II	BIOLOGICAL EFFECTS
WED PM	GYROTRON II	QUASI-OPTICAL COMPONENTS II	INSTRUMENTATION I	POST DEADLINE
THURS AM	PLENARY LECTURE 4: D.R. TILLEY			
	GYROTRON III	QUASI-OPTICAL COMPONENTS III	INSTRUMENTATION II	SPECTROSCOPY V
THURS PM	GYROTRON IV	QUASI-OPTICAL COMPONENTS IV	INSTRUMENTATION III	SPECTROSCOPY VI
FRI AM	PLENARY LECTURES 5 & 6: G.E. PECKHAM AND R.A. SUTTIE: B.J. KERRIDGE			
	GYROTRON V	ASTRONOMICAL AND ATMOSPHERIC SYSTEMS JOINT SESSION		SPECTROSCOPY VII

The program listed in this Digest is the final conference program. A number of changes have been made from the preliminary program. Please disregard the preliminary program and use only the program given here.

Morning sessions begin at 0830 hours. Afternoon sessions begin at 1400 hours.

On Monday morning there will be a short opening ceremony at 0830 hours, followed by the presentation of the Kenneth J Button Prize to Professor Jun-ichi Nishizawa. The plenary lecture by Dr M F Kimmitt will then be given. On the other four days the plenary lectures will begin at 0830 hours.

Apart from Monday, Plenary Lectures are allotted 1 hour: 50 minutes for presentation and 10 minutes for questions. *Invited Keynote* papers are allotted 30 minutes: 25 minutes for presentation and 5 minutes for questions. Contributed papers are allotted 15 minutes: 12 minutes for presentation and 3 minutes for questions.

CONFERENCE ORGANISATION:

This Program has been organised through the efforts of the following individuals:

General Chairman: Kenneth J Button
Conference Chairman: Terence J Parker
Program Chairman: James R Birch
Technical Exhibit: Thomas Dumelow
Digest Editors: James R Birch and Terence J Parker
Proceedings (Journal) Editor: Kenneth J Button

LOCAL ORGANISING COMMITTEE:

T J Parker (Essex) (Chairman)
J R Birch (NPL)
T Dumelow (Essex)
M F Kimmitt (Essex)
S R P Smith (Essex)
D R Tilley (Essex)

PROGRAM COMMITTEE:

J R Birch (NPL) (Chairman)
D V Bartlett (JET Joint Undertaking)
M F Kimmitt (Essex)
D H Martin (QMW)
G Mourier (Thomson Tubes Electroniques)
T J Parker (Essex)
J Yarwood (Durham)
G Zhizhin (Troitzk)

PROGRAM COUNCIL FOR THE SERIES

James C Wiltse, Georgia Tech., Atlanta
Michael von Ortenberg, Humboldt University of Berlin
Kenneth J Button, Satellite Beach, Florida
James R Birch (NPL)
Koji Mizuno, Tohoku University, Sendai
Nicholas Fourikis, Defence Science Org., Salisbury
T J Parker, University of Essex, Colchester
David B Rutledge, California Institute of Technology, Pasadena
Richard J Temkin, Massachusetts Institute of Technology, Cambridge
Alexiy Vertiy, Institute of Radiophysics, Kharkov
Liquan He, Southeast University, Nanjing

FOREWARD

The Eighteenth International Conference on Infrared and Millimeter Waves is held from September 6th to September 10th, 1993, at the University of Essex in Colchester, UK. The scope of the Conference covers progress in all areas of infrared and millimeter wave science and technology, and the large number of contributions (more than 300) received from more than 25 countries demonstrates the importance of the field and the need for the Conference.

The Local Organising Committee and the Program Committee would like to take this opportunity to thank all authors whose high quality work has contributed to the success of this Conference.

The organisation of the Conference would not have been possible without the generous sponsorship of the following organisations:

SPIE - The International Society for Optical Engineering

The University of Essex

The Association of British Spectroscopists

European Office of the United States Army

United States Air Force European Office of Aerospace Research and Development

QMC Instruments Ltd

The Optical Group of the Institute of Physics

The generous support of commercial organisations and other institutions which have provided financial support is also gratefully acknowledged, and the names of these organisations are listed elsewhere in the Digest.

We also wish to thank the University of Essex for providing the infrastructure and facilities which were essential for organising this conference.

T J Parker
Chairman of the Local Organising Committee

TECHNICAL EXHIBIT

The Technical Exhibit will be held in Room LTB 4 which is on the Ground Floor of the Lecture Theatre Block to the right of the Foyer. The Technical Exhibit will be held for two full days (Tuesday, September 7th, and Wednesday, September 8th).

We wish to express our thanks to the companies and organisations listed below which have expressed their interest in taking part at the time of going to press.

Thomas Dumelow
Technical Exhibit Manager.

A B Millimetre, Paris, France

Bruker Spectrospin Ltd, Coventry, UK

Cryophysics Ltd, Witney, UK

Diversified Optical Ltd, Ipswich, UK

Edinburgh Instruments Ltd, Edinburgh. UK

Granta Electronics, Cambridge, UK

Graseby-Specac Ltd, Orpington, UK

Instruments SA (UK) Ltd, Stanmore, UK

Infrared Laboratories Inc, Tucson, Arizona, USA

Ontar Corporation, Brookline, Mass., USA

QMC Instruments Ltd, London, UK

Taylor and Francis Ltd, Basingstoke, UK

CONFERENCE PUBLICATIONS

Conference Digest

The Conference Digest for the Eigteenth International Conference again attests to the strength of the field of infrared and millimeter waves.

The Digest is a convenient, timely reference in the field of infrared and millimeter waves. Copies of the Digest may be purchased from SPIE at the address given on the title page. Papers in the Digest may be referred to in journal articles by citing the SPIE Volume Number. Many libraries throughout the world acquire SPIE publications for their collections. For this reason a paper contributed to the Digest represents an important research contribution.

The Digest Editors would especially like to thank Mrs Barbara Hopkins and Mr G D King for their valuable assistance during the preparation of this Digest.

The Proceedings.

Conference delegates are encouraged to submit a full length manuscript for publication in the monthly journal "International Journal of Infrared and Millimeter Waves". Papers published in this journal by conference delegates constitute the proceedings of the conference.

Authors must prepare final manuscripts on camera-ready templates (available from K J Button) to save time and expense. There is no page charge and there is no limit on the length of your manuscript. Your manuscript will be published in about eight weeks (no deadline). Manuscripts may be sent to K J Button at the address below at any time, before or after the Conference. Those who cannot attend the Conference this year are urged to send their manuscript for publication in the Proceedings anyway. We may miss seeing you, but we do not want to miss the chance of learning about your work.

Please send your manuscripts to:

Kenneth J Button
Box 372455
Satellite Beach
Florida 32937-0455
USA

Fax: (407) 777 7293

Nineteenth International Conference on Infrared and Millimeter Waves.

The next conference in this series, the Nineteenth International Conference on Infrared and Millimeter Waves, will be held in Sendai, Japan, from October 17th to 21st, 1994. Professor Jun-ichi Nishizawa of Tohoku University will be the conference chairman. His address is:

Professor Jun-ichi Nishizawa
Research Institute of Electrical Communication
Tohoku University
2-1-1 Katahira
Aoba-ku
Sendai 980
Japan

Kenneth J Button Prize

On the occasion of the 15th International Conference on Infrared and Millimeter Waves a prize was initiated by the Program Council "to be awarded for outstanding contributions to the field of infrared and millimeter waves". It was later agreed, following a suggestion by the chairman of the 1991 conference, to formally name the prize the "Kenneth J Button Prize" in recognition of Professor Kenneth J Button's outstanding contributions to the Infrared and Millimeter Wave Community, both as a scientist and as the initiator and driving force of this series of conferences.

The 1993 prize committee consists of:

K J Button, Satellite Beach, Florida, USA
M von Ortenberg, Humboldt University of Berlin, Berlin, Germany
D H Martin, Queen Mary and Westfield College, London, UK
T J Parker, University of Essex, Colchester, UK
J R Birch, National Physical Laboratory, Teddington, UK
R J Temkin, MIT, Cambridge, Mass, USA
J C Wiltse, Georgia Tech Research Institute, USA
K Mizuno, Tohoku University, Sendai, Japan
K Sakai, Kobe, Japan

The 1993 Kenneth J Button Prize is awarded to Professor Jun-ichi Nishizawa, Tohoku University, Sendai, Japan.

Please note that the Prize will be presented at the opening ceremony on Monday, September 6, 1993, and not as previously announced.

T J Parker
Chairman, 1993 Kenneth J Button Prize Committee.

Kenneth J Button Prize

awarded to

Professor Jun-ichi Nishizawa

The Kenneth J Button Prize for 1993 is awarded to Professor Jun-ichi Nishizawa for outstanding contributions to the field of Infrared and Millimeter Waves. Professor Nishizawa has made major contributions throughout his career, not only by achieving a truly formidable range of outstanding scientific results, but also by stimulating the activity of our community through the organisation of international conferences.

During his career Professor Nishizawa has been credited with many notable inventions. These have included: p-i-n diodes and p-n-i-p (n-p-i-n) transistors in co-operation with p-i-n photo diodes (1950), ion implantation (1950), avalanche photo diodes (1952), semiconductor injection lasers (1957), solid state focusing optical fibres (1964), and the transit time effect negative-resistance diode (1954), including the use of avalanche and tunnel injection (1958), hyper abrupt variable capacitance diodes (1959), semiconductor inductance (1957), the static inductance transistor (SIT) (1950, 1971), etc.. He is currently carrying out research specialising in the development of static induction transistors (to operate at higher frequencies and higher power), the high speed thyristor, the high speed low power dissipation integrated circuit and a growth technique for III-V compound semiconductors. The latter involves a temperature difference method under controlled vapour pressure (TDM-CVP) which gives rise to high efficiency LEDs. He is also researching long life laser diodes based on perfect silicon crystal technology obtained by lattice constant compensation. Professor Nishizawa also originated electro-epitaxy (1955) and photo-epitaxy (1961). He discovered the avalanche effect in semiconductors and explained the backward character of the p-n junction by this effect (1953).

Presentation of the Prize.

The Prize will be presented at the opening ceremony which begins at 08.30 on Monday, September 6, 1993. Please note that this is not as previously announced.

NPL

National Physical Laboratory

MEASUREMENT SERVICES AND RESEARCH FACILITIES AT NEAR-MILLIMETRE AND INFRARED WAVELENGTHS

The National Physical Laboratory is the United Kingdom's centre for measurement standards. In recent years the Division of Electrical Science of NPL has pioneered many measurement techniques and applications at wavelengths from several millimetres to those of the thermal infrared.

It can make available its measurement services, research facilities and general consultancy in this spectral region. The research programme of the Division includes:

- spectroscopic techniques for the characterisation of the optical and dielectric properties of materials, components and devices at temperatures from 4.2 to 1300 K
- radiometric techniques for emissivity studies
- spectroscopic techniques for the determination of hemispherical transmittance and reflectance
- power, frequency and spectral calibrations
- development of thin film NbN and YBCO Josephson junctions as high harmonic mixers, and of other devices for superconducting electronics

Facilities include:

- a range of Fourier transform spectrometers
- high power optically pumped lasers
- large area clean room for thin film production and patterning
- system design, construction and calibration

We can supply thin superconducting films of Nb, NbN and YBCO on various substrates.

If you have a measurement, calibration or application problem, please contact J.R.Birch at the conference or at:

Division of Electrical Science, National Physical Laboratory
Teddington, Middlesex TW11 OLW, UK
Tel: 081 943 6784 Fax: 081 943 6098

FIRL-100 INTEGRATED CO_2/FIR LASER SYSTEM

- Turn-Key compact system 215 x 38cm
- High efficiency dichroic FIR output coupler 40-1000μm
- Hand held controller for ease of system optimisation
- Guaranteed 120mW on 118.8μm
- M^2 of the pump CO_2 section <1.25
- More than 50W cw CO_2 laser output available

EDINBURGH INSTRUMENTS

Edinburgh Instruments Ltd, Riccarton, Currie Edinburgh EH14 4AP Scotland UK Tel 031-449 5844 Telex 72553 EDINST G Fax 031-449 5848

SESSION P

PLENARY LECTURES

SESSION M1

Monday AM | FEL - I | September 6

M1.1 THE ENEA COMPACT MILLIMETRE WAVE FEL (*Invited Keynote*) - A.Doria, G.P.Gallerano, E.Giovenale, M.F.Kimmitt, G.Messina and A.Renieri. ENEA, Area INN, Dipartimento Sviluppo Tecnologie di Punta, P.O. Box 65, 00044 Frascati, (Rome) Italy.

M1.2 STATUS OF THE DESIGN OF THE 200 GHZ FOM-FUSION-FEM - A.G.A.Verhoeven, W.A.Bongers, B.S.Q.Elzendoorn, A.M.van Ingen, P.Manintveld, A. Tulupov, M.J. van der Wiel and W.H. Urbanus, FOM-Instituut voor Plasmafysica, 'Rijnhuizen', Association EURATOM-FOM, P.O. Box 1207, 3430 BE Nieuwegein, The Netherlands; V.L.Bratman, G.G.Denisov, A.V. Savilov and M.Yu. Shmelyov, Institute of Applied Physics, Ulyanova Ulitsa 46, Nizhni Novgorod, Russia, H.-U.Nickel, and M.Thumm, IHE Universität Karlsruhe and ITP Kernforschungszentrum Karlsruhe, Germany; W.Kasparek, J.Pretterebner and D.Wagner, Institut fur Plasmaforschung, Stuttgart University, Germany; C. Shang and M. Caplan, Lawrence Livermore National Laboratory, Livermore, CA, U.S.A.

M1.3 A COMPACT RELATIVISTIC ELECTRON BEAM SOURCE FOR GENERATION OF FAR - INFRARED RADIATION, C.R.Jones and J.M.Dutta. North Carolina Central University, Durham, USA.

M1.4 DESIGN OF A TUNABLE 4-MW FREE ELECTRON MASER FOR HEATING FUSION PLASMAS - M.Caplan, G. Kamin, C.C.Shang and W. Lindquist, Lawrence Livermore National Laboratory, P.O. Box 808, L-637, Livermore, CA 94551, USA.

M1.5 ULTRA-SHORT PULSES OF COHERENT MILLIMETER-WAVE RADIATION FROM A PREBUNCHED FEL - G.P.LeSage, P.G. Davis, S. Fochs, F.V. Hartemann, D.B.McDermott and N.C.Luhmann Jr, Department of Electrical Engineering, University of California, Los Angeles, CA 90024, USA; S.C. Hartman, S. Park, R.S. Zhang and C.Pellegrini, Department of Physics, University of California, Los Angeles, CA 90024, USA.

M1.6 OROFEMITRON - THE NEW TYPE OF SMITH-PURCELL AMPLIFIERS.- Yuri A. Romantsov, Radio Astronomy Institute of Ukrainian Acad. of Sc., Department of Microwave Electronics, Kharkov, 310002, Ukraine.

M1.7 MICROWAVE OSCILLATOR - THE OROTRON WITH THE DC MAGNETIC NONUNIFORMITY - A.Shmat'ko and E. Odarenko, Kharkov State University, Department of Radiophysics, Freedom Square 4, 310077 Kharkov, Ukraine.

M1.8 STUDY AND DEVELOPMENT OF SUB MM RANGE VACUUM SOURCES IN THE INSTITUTE OF RADIOPHYSICS AND ELECTRONICS OF UKRAINIAN ACADEMY OF SCIENCES - V.D. Yeremka, G.Ya.Levin and A.Ya.Usikov, Inst. of Radiophysics and Electronics of Ukrainian Academy of Sciences, 12 Acad. Proskura st., Kharkov, 310085, Ukraine.

SESSION M2

Monday AM	DETECTORS AND SOURCES - I	September 6

M2.1 OPTIMIZATION OF FIR PHOTODETECTORS FOR BOTH LOW - AND HIGH-BACKGROUND OPERATION - S.E.Church, A.G. Murray, M.J.Griffin and P.A.R. Ade, Department of Physics, Queen Mary and Westfield College, Mile End Road, London E1 4NS, UK.

M2.2 BIB PHOTODETECTORS BASED ON ANTIMONY DOPED SILICON - G.Sirmain, S.Pasquier, C.Mény, P. Etiève*, W. Knap, P. Adet*, N. Fabre**, A. Murray***, M. Griffin*** and J. Léotin, Laboratoire de Physique des Solides, SNCMP-INSA, Complexe Scientifique de Rangueil, 31077 Toulouse-Cedex, France; *Tekelec Microwave, 91953 Les Ulis, France; **LAAS, 7 av. du Colonel Roche, 31077 Toulouse-Cedex, France; ***QMW, Mile End Road, London E1 4NS, UK.

M2.3 CHARACTERISTICS AND PERFORMANCE OF Ge:Ga FAR-INFRARED PHOTOCONDUCTORS FOR SPACE APPLICATIONS - N. Hiromoto, M.Fujiwara, T.Itabe, H. Shibai* and H. Okuda*, Communications Research Laboratory, Koganei, Tokyo 184, Japan; *Institute Space Astronaut. Sci., Sagamihara, Kanagawa 229, Japan.

M2.4 EFFECTS OF IONISING RADIATION IN Ge:Ga AND Ge:Be FAR-INFRARED PHOTOCONDUCTORS - M.C.Price, S.E.Church, M.J.Griffin and P.A.R. Ade, Department of Physics, Queen Mary and Westfield College, Mile End Road, London E1 4NS.

M2.5 THE NOISE AND OPTIMUM OPERATING TEMPERATURE OF HIGH T_c SUPERCONDUCTING INFRARED BOLOMETER - Chen Juxin, Shi Baoan, Wu Rujia, Gong Shuxing, Shanghai Inst. of Technical Physics, Shanghai 200083, PRC, Yang Caibing, Cao Xiaoneng, Institute of Electronics, Beijing 100080, PRC, Zhang Yinzi and Li lin, Institute of Physics, Beijing 100080, PRC.

M2.6 EXCITONIC DETECTORS OF INFRARED AND SUBMILLIMETER WAVES - G.K.Vlasov, D.N.Vylegzhanin and E.I.Chizhikova, Center for Program Studies, Russian Academy of Sciences, SU-117810 Moscow, Russia.

M2.7 NEW MICROWAVE DETECTOR - S.Asmontas and A.Suziedelis, Semiconductor Physics Institute, 2600 Vilnius, Lithuania.

M2.8 NEW HOT-CARRIER EFFECTS IN SUBMICRON STRUCTURES FOR INFRARED AND MILLIMETER WAVE RECEIVERS - V.B.Yurchenko, Kharkov Polytechnic Institute, Dept. Materials for Electronics and Solar Cells, 21 Frunze St., Kharkov 310002, Ukraine.

SESSION M3

Monday AM — **GAS LASERS - I** — September 6

M3.1 HIGH POWER TUNABLE 20 atm CO_2-LASERS AND THEIR OPFIRL APPLICATIONS (*Invited Keynote*) - W.Schatz and K.F.Renk, Institut für Angewandte Physik, Universität Regensburg, W-8400 Regensburg, Germany.

M3.2 MEASUREMENT OF POWER AND ENERGY - D.H.Martin, Department of Physics, Queen Mary and Westfield College, Mile End Road, London E1 4NS, UK.

M3.3 FAR INFRARED LASER LINES FROM CH_3OH AND ISOTOPES: A REVIEW - S.C.Zerbetto and E.C.C.Vasconcellos, Instituto de Física, "Gleb Wataghin", Depto. Electrônica Quântica, Universidade Estadual de Campinas - Cx.P.: 6165 13083.970, Campinas, SP, Brazil.

M3.4 NEW FIR LASER LINES FROM OPTICALLY PUMPED C_2H_3F, C_2H_3Cl, C_2H_3CN, $C_2H_2F_2$, C_2H_5F AND CF_2O - P.B. Davies, Yuyan Liu, Zhuan Lui*, Dept. of Chemistry, University of Cambridge, Lensfield Road, Cambridge CB2 1EW, UK; *Permanent Address: Wuhan Institute of Physics, the Chinese Academy of Sciences, Wuhan 430071, P.R. China.

M3.5 IDENTIFICATION OF SUBMILLIMETER CD2O LASER LINES - S.F.Dyubko and S.V.Syrota, Dept. of Quantum Radiophysics, Kharkov State University, Ukraine.

M3.6 A TABLE OF THE ABSORPTION STRONG LINES OF FORMIC ACID WHICH ARE COINCIDED WITH THE FIR LASERS FREQUENCIES - S.F.Dyubko and S.V.Syrota, Dept. of Quantum Radiophysics, Kharkov State University, Ukraine, 310077.

M3.7 TIME DEPENDENT SIMULATION OF OPTICALLY PUMPED FIR LASER FOR ARBITRARY POLARISATION CONFIGURATIONS - V.A.Batanov, A.O.Radkevich and A.L.Telyatnikov, Inst. of Physics and Technology, Krasikova 25A, Moscow, Russia.

M3.8 THEORETICAL RESEARCH AND DISCUSSION OF DYNAMICAL STATES OF OPTICALLY PUMPED SUBMILLIMETER LASER - Luo Liguo[1] Nie Dezhen[1], Chen Jishu[2] and Su Jinwen[3], [1]Department of Optics, Shandong University, Jinan, Shandong, 250100, P.R. China; [2]Department of Physics, Ningbo University, Ningbo, Zhejiang, 315211, P.R. China; [3]National Laboratory for Infrared Physics, Shanghai Institute of Technical Physics, Academia Sinica, Shanghai, 200083, P.R. China.

M3.9 EXPERIMENTAL RESEARCH OF PULSATION AND CHAOS IN OPTICALLY PUMPED SUBMILLIMETER LASER - Luo Liguo[1], Chen Jishu[2] and Su Jinwen[3], [1]Department of Optics, Shandong University, Jinan, Shandong, 250100, P.R. China; [2]Department of Physics, Ningbo University, Ningbo, Zhejiang, 315211, P.R. China; [3]National Laboratory for Infrared Physics, Shanghai Institute of Technical Physics, Academia Sinica., Shanghai, 200083, P.R. China.

SESSION M4

Monday AM	SPECTROSCOPY - I	September 6

M4.1 EXPERIMENTAL STUDIES WITH OPEN RESONATORS ON FREQUENCY DEPENDENT DIELECTRIC LOSS AT MM WAVELENGTHS (*Invited Keynote*) - V.V.Parshin, Applied Physics Institute, Russian Academy of Sciences, 603600, Nizhni Novgorod, Russia, R.Heidinger and G.Link, Kernforschungszentrum, D-7500 Karlsruhe 1, Germany.

M4.2 DIELECTRIC LOSS MEASUREMENTS BETWEEN 25-300 K WITH A HEMISPHERICAL FABRY-PEROT RESONATOR - R.Heidinger and G.Link, Kernforschungszentrum Karlsruhe, Association KfK-Euratom Institut für Materialforschung, Postfach 3640, D-76021 Karlsruhe, F.R.G.

M4.3 MONOCHROMATIC SUBMILLIMETER SPECTROMETRY IN STANDARDS AND MATERIAL CHARACTERISATION - R.Brazis, A.Namajunas, V.Gaidelis, L.Safonova and S.Bumeliene, Semiconductor Physics Institute, A. Gostauto 11, Vilnius 2600, Lithuania.

M4.4 PROPERTIES OF MATERIALS FOR PRACTICAL USE AT THE MM AND SUBMM WAVELENGTHS - V.V.Meriakri and E.E.Chigrai, Institute of Radioengineering and Electronics, Russian Academy of Sciences, Frjazino, Moscow region 141120, Russia.

M4.5 ON THE MEASUREMENT OF THE COMPLEX DIELECTRIC CONSTANT OF THE MEDIUM - Yu Rong and Xingguo Li, Dept. of Electronic Engineering, East China Institute of Technology, Nanjing, P.O. Code 210014, P.R. China.

M4.6 BIREFRINGENCE AND DICHROISM IN MAGNETIC FLUIDS, INDUCED BY MAGNETIC FIELD, IN FREQUENCY RANGE 36GHz-600 GHz - A.V.Semenov and E.A.Vinogradov, Submillimeter-Range Physics Laboratory, General Physics Institute, Russian Academy of Science, 117942 Moscow, Russia.

M4.7 MM-WAVE DIELECTRIC MEASUREMENTS WITH AN ELECTRIC-FIELD CROSS-CORRELATION FOURIER TRANSFORM SPECTROMETER - Ding Hanyi and Zhang Guangzhao, Electronics Dept., Zhongshan University, Guangzhou 510275, P.R. China.

M4.8 TWO-FREQUENCY QUASI-OPTICAL RADIOSPECTROMETER FOR SUBSTANCE INVESTIGATIONS - A.A.Vertiy, I.V Ivanchenko and N.A.Popenko, Institute of Radiophysics and Electronics, Academy of Sciences of the Ukraine, 310085 Kharkov, Ukraine.

M4.9 DIELECTRIC LOSSES IN GASES UNDER IONISING RADIATION - J.Mollá, A.Ibarra and E.R.Hodgson, Inst. Investigación Básica. CIEMAT, Ed. 2. Av. Complutense, 22. E-28040 Madrid, Spain.

SESSION M5

Monday PM	FEL - II	September 6

M5.1 SMITH PURCELL RADIATION IN THE RELATIVISTIC LIMIT (*Invited Keynote*) - J.E. Walsh, Department of Physics and Astronomy, Dartmouth College, 6127 Wilder Laboratory, Hanover, N.H. 03755-3528, USA.

M5.2 THE ANALYSIS OF ELECTROMAGNETIC WAVE AMPLIFICATION IN QUASI-OPTICAL WAVEGUIDE WITH ELECTRON BEAM (SELECTRON) - N.L.Romashin, A.I. Kleev* and V.A. Solntsev**, Institute of Radioengineering and Electronics, Russian Academy of Sciences, Marx av. 18, Moscow 103907, Russia; *P.L.Kapitza Institute for Physical Problems, Russian Academy of Sciences, ul. Kosygina 2, Moscow 117334, Russia; **MIEM, B.Vuzovsky, 3/12, Moscow 109028, Russia.

M5.3 THE INFLUENCE OF e-BEAM PHASE SPACE ON FEL PERFORMANCE - Zili Weng and Yijin Shi, Institute of Atomic Energy, P.O. Box 275(18) 102413 Beijing, P.R. China.

M5.4 NON-LINEAR THEORY OF TWO-STREAM SUPERHETERODYNE FREE ELECTRON LASERS - V.V.Kulish, S.A.Kuleshov and A.V.Lysenko. Sumy Physical-Technology Institute, 2 Rymski-Korsakov St., Sumy 244007, Ukraine.

M5.5 ENTROPYLIKE QUANTITY OF THE EQUILIBRIUM ELECTRONS IN A COLLECTIVE FREE-ELECTRON LASER - Shi-Chang Zhang, Qing-Xiang Liu and Yong Xu, Southwest Jiaotong University, Dept. of Applied Physics, Chengdu, Sichuan 610031, P.R. China.

M5.6 CHERENKOV RADIATION FROM A FINITE EMISSION LENGTH - M.Ikezawa, Institute for Scientific Measurements, Tohoku University, Sendai 980, Japan.

M5.7 OBSERVATION OF COHERENT MILLIMETER WAVE RADIATION FROM AN INTENSE ELECTRON BUNCH FOR BEAM DIAGNOSTICS - Juzo Ohkuma, Shuichi Okuda, Toichi Okada and Kiyomi Sakai*, Radiation Laboratory, The Institute of Scientific and Industrial Research, Osaka University, Mihogaoka, Ibaraki, Osaka 567, Japan; *Communications Research Laboratory, Kansai Advanced Research Center, Iwaoka, Nishiku, Kobe 651-24, Japan.

M5.8 EXPERIMENTAL INVESTIGATIONS OF AN EXTERNAL FEEDBACK SYSTEM FOR WAVELENGTH SELECTION OF HIGH POWER MICROWAVE RADIATION IN A FREE ELECTRON MASER REGIME - V.A.Bogachenkov, V.A.Papadichev, I.V.Sinilschikova and O.A.Smith, P.N.Lebedev Physical Institute, Moscow 117924, Russia.

M5.9 THE MAGNETIC FIELD PROFILE AND e-BEAM TRANSPORT IN THE DOUBLE HELIX LINEARLY POLARIZED WIGGLER - Hu Jianpin, Wang Pingshan, Hu Kesong, Chen Yutao, Southwest Institute of Applied Electronics, P.O. Box 523, No.65, Chengdu, Sichuan, P.R. China.

SESSION M6

Monday PM	DETECTORS AND SOURCES - II	September 6

M6.1 A SUB-MILLIMETRE WAVE SIS RECEIVER - B.N. Ellison+, S.M.X. Claude+, A. Jones+, D.N. Matheson+, L.T. Little* and S.R. Davies*, +Space Science Department, Rutherford Appleton Laboratory, Didcot, Oxon, OX11 OQX; *Electronic Engineering Laboratory, University of Kent at Canterbury, Canterbury, Kent, CT2 7NT, UK.

M6.2 HIGH SPEED HOT-ELECTRON SUPERCONDUCTING BOLOMETER - G.N.Gol'tsman and E.M.Gershenzon, Moscow State Pedagogical University, 1 M. Pirogovskaja Str., Moscow 119435, Russia.

M6.3 PICOSECOND DETECTION OF INFRARED RADIATION WITH $YBa_2Cu_3O_{7-\delta}$ THIN FILMS - M.Danerud*, M. Zorin#, M.Lindgren††, V. Trifonov#, B. Karasik#, E.M. Gershenzon#, G.N. Gol'tsman# and D. Winkler*, *Department of Physics, ††Department of Optoelectronics and Electrical Measurements, Chalmers University of Technology, S-412 96 Göteborg, Sweden; #Department of Physics, Moscow State Pedagogical University, 1 Malaya Pirogovskaja, Moscow 119435, Russia.

M6.4 NORMAL STATE $YBa_2Cu_3O_7$. FILMS: A NEW FAST DETECTOR FOR FAR INFRARED LASER RADIATION - S. Zeuner, P.G. Huggard, K. Goller, H. Lengfellner and W. Prettl, Institut für Angewandte Physik, Universität Regensburg, 93040 Regensburg, Germany.

M6.5 TRANSVERSE MIR FAST RESPONSE IN PbSe FILMS - S.Marchetti and R.Simili, IFAM-CNR, via del giardino 7, 56100 Pisa, Italy.

M6.6 A MINIATURIZED BOLOMETER ARRAY FOR FIR LASER SPECTROSCOPY - P.T.Lang*, K.F.Mast*, K.F. Renk** and W. Schatz**, *MPI für Plasmaphysik, EURATOM Association, W-8046 Garching; **Institut für Angewandte Physik, Universität Regensburg, W-8400 Regensburg, Germany.

M6.7 NANOSECOND RESPONSE TIME DETECTORS FOR MILLIMETRE WAVE FELS - M.F.Kimmitt, A. Doria*, G.P. Gallerano* and E. Giovenale*, Department of Physics, University of Essex, Colchester CO4 3SQ, UK; *Dipartimento Sviluppo Tecnologie di Punta, ENEA, PO Box 65-00044, Frascati, Italy.

M6.8 PHYSICAL GROUNDS OF HIGH-SENSITIVE DETECTION OF IR RADIATION IN THE CRYSTAL AT ROOM TEMPERATURE - G.K.Vlasov, N.A.Dolgikh and E.I.Chizhikova, Center of Program Studies, Russian Academy of Sciences, SU-117810 Moscow, Russia

M6.9 PBZT INFRARED MATERIAL AND DETECTOR - Wu Ping* and Kang Lin**, *Department of Physics, Nanjing Aeronautical Institute, 210016 Nanjing, P.R. China; **Department of Information Physics, Nanjing University, 210008 Nanjing, P.R. China.

SESION M7

Monday PM — **GAS LASERS - II** — September 6

M7.1 A DUAL CHANNEL OPTICALLY PUMPED FIR LASER SYSTEM FOR PLASMA DIAGNOSTICS - B.W.Davis and R.S.Thomas, Edinburgh Instruments Ltd., Riccarton, Edinburgh, EH14 4AP, UK.

M7.2 IMPROVEMENTS OF THE CHARACTERISTICS OF A HIGH-POWER OPTICALLY-PUMPED FAR-INFRARED LASER AND ITS APPLICATION - T.Hori, N.Hiromoto and A. Yamamoto*, Communications Research Laboratory, 4-2-1 Nukui-kita, Koganei, Tokyo 184, Japan; *National Space Development Agency of Japan, 1-29-6 Hammamatsu-cho, Minato-ku, Tokyo 105, Japan.

M7.3 OPFIRL INVESTIGATION OF AMMONIA - W.Schatz and K.F.Renk, Institut für Angewandte Physik, Universität Regensburg, W-8400 Regensburg, Germany.

M7.4 SYNCHRONIZATION EFFECTS IN BROADBAND FIR RAMAN SCATTERING IN NH3 - S.Marchetti and R.Simili, IFAM-CNR, Via del giardino 7, 56100, Pisa, Italy.

M7.5 DENSITY-MATRIX MODELLING OF THREE-PHOTON 1+1+1(UV+IR+UV) RESONANCE IONIZATION OF IRON - A.L.Telyatnikov*, O.R. Jones and H.H.Telle, Physics Department, University College of Swansea, Singleton Park, Swansea SA2 8PP, Wales, UK; *Present address: Institute of Physics and Technology of Russian Academy of Sciences, Krasikova 25A, Moscow, Russia, 117218.

M7.6 TUNING AND SPECTRA FEATURES OF CONTINUOUSLY TUNABLE CH_3F RAMAN LASER - V.A.Batanov, A.O.Radkevich and A.L.Telyatnikov, Institute of Physics and Technology of Russian Academy of Sciences, Krasikova 25A, Moscow, Russia, 117218.

M7.7 NEW APPROACH FOR NUMERICAL SIMULATION OF THE NON-STEADY-STATE INFRARED LASER BEAM STRUCTURE - L.V.Yurchenko, Institute of Radiophysics and Electronics of the Academy of Sciences of Ukraine, 12 Proskura st., Kharkov 310085, Ukraine.

M7.8 OPTIMUM PUMP BEAM PROFILING IN A RAMAN LASER - V.A.Batanov, V.S.Petriv and A.O.Radkevich, Institute of Physics and Technology of the Russian Academy of Sciences, 117218 Moscow, Krasikova 25A, Russia.

M7.9 DEPOLARIZATION OF OUTPUT LASER RADIATION IN HCN LASER - Yu.Ye.Kamenev, Ye.M.Kuleshov, V.P.Radionov and A.A.Filimonova, Institute of Radiophysics and Electronics of Academy of Sciences of Ukraine, 12 Acad. Proscura st., Kharkov 310085, Ukraine.

SESSION M8

Monday PM — **SPECTROSCOPY - II** — September 6

M8.1 FAR INFRARED REFLECTANCE STANDARDS (*Invited Keynote*) - E.A.Nicol and J.R.Birch, National Physical Laboratory, Teddington, Middlesex TW11 OLW, UK.

M8.2 MODELLING OF INTRINSIC MM-WAVE ABSORPTION IN LOW LOSS DIELECTRICS WITH COMPLEX CRYSTAL STRUCTURE - G.Link and R.Heidinger, Kernforschungszentrum Karlsruhe, Association KfK-Euratom Institut für Materialforschung, Postfach 3640, Karlsruhe, F.R.G.

M8.3 TEMPERATURE DEPENDENCE OF THE OPTICAL CONSTANTS OF POLYETHYLENE IN THE REGION OF THE 73 CM^{-1} LATTICE MODE - J.R.Birch and Kong Fan Ping, NPL, Teddington, Middlesex, TW11 OLW, UK.

M8.4 DIRECT DETERMINATION OF THE FAR INFRARED COMPLEX REFRACTIVE INDEX OF InAs AT 300 AND 100 K - A.K.Wan Abdullah, School of Physics, Universiti Sains Malaysia, Malaysia, T.J.Parker, Univ. of Essex, Colchester CO4 3SQ, UK, and C.Patel, Department of Nuclear Physics, Univ. of Oxford, OX1 3RH, UK.

M8.5 A VARIABLE TEMPERATURE DISPERSIVE FOURIER TRANSFORM SPECTROMETER FOR COMPLEX REFLECTION MEASUREMENTS ON OPAQUE SOLIDS - J.R.Birch and P.G.Quincey, NPL, Teddington, Middlesex, TW11 OLW, UK.

M8.6 REFRACTOMETRY OF OIL PRODUCTS IN MILLIMETER AND SUBMILLIMETER RANGE - A.B.Latyshev, D.A.Loukianov and A.V.Semenov, General Physics Institute, Russian Academy of Science, 117942, Moscow, Russia.

M8.7 CHARACTERIZATION OF MATERIALS BY SUBMILLIMETER MULTIBEAM TECHNIQUES - B.P.Gorshunov, G.Gruner, I.V.Fedorov, G.V.Kozlov, I.I. Tkachev and A.A.Volkov, General Physics Institute, Russian Academy of Science, 38 Vavilov str., 11792 Moscow, Russia; B. Holzapfel, G. Saemann-Ischenko, Institute of Physics, University of Erlangen, Erwin-Rommel Strasse, D-8520 Erlangen, Germany.

M8.8 CHARACTERISATION OF MICROWAVE CERAMICS AT SUBMILLIMETRE WAVES - I.V.Fedorov, G.A.Komandin, G.V.Kozlov and A.A. Volkov, General Physics Institute, Russian Academy of Sciences, 38 Vavilov str., 117942 Moscow, Russia; E.A.Nenasheva, "Gyricond" Research Institute, St. Petersburg, Russia and J.Petzelt, Institute of Physics, Na Slovance 2, Prague, Czechia.

M8.9 INFRARED SPECTRA OF WOOL FIBERS γ-IRRADIATED IN MIXTURES OF SOLVENTS - S.M.Rabie, M.A.Moharram* and O.M.Mahmoud*, Middle Eastern Regional Radioisotope Center for the Arab Countries, Cairo, Egypt; *National Research Centre, Cairo, Egypt.

SESSION Tu 1

Tuesday AM	WINDOWS	September 7

Tu1.1 DEVELOPMENT OF BROADBAND VACUUM WINDOWS FOR HIGH-POWER MILLIMETER WAVE SYSTEMS - H.-U.Nickel*, H.Massler and M.Thumm*, Universität Karlsruhe, Institut für Höchstfrequenztechnik und Elektronik, Kaiserstraße 12, D-76131 Karlsruhe, Germany, also *Kernforschungszentrum Karlsruhe, Institute für Technische Physik, P.O. Box 3640, D-7602[illegible] Karlsruhe, Germany.

Tu1.2 THE OPTICAL CONSTANTS, AT ELEVATED TEMPERATURES, OF SOME POTENTIAL WINDOW MATERIALS FOR HIGH POWER AND PLASMA DIAGNOSTIC APPLICATIONS.- J.R.Birch, E.A.Nicol, T.P.Hughes* and D.V.Bartlett*, Division of Electrical Science, National Physical Laboratory, Teddington, Middlesex TW11 OLW, U.K.; *JET Joint Undertaking, Abingdon, Oxon OX14 3EA, UK.

Tu1.3 ANTI-REFLECTION TREATMENTS FOR JET MILLIMETRE WAVE DIAGNOSTIC WINDOWS.- T.P.Hughes, S.D.Richards and D.V. Bartlett, JET Joint Undertaking, Abingdon, Oxon OX14 3EA, UK.

Tu1.4 ELECTRICAL ANALYSIS OF WIDEBAND AND DISTRIBUTED WINDOWS USING TIME-DEPENDENT FIELD CODES - C.C.Shang and M.Caplan, University of California, Lawrence Livermore National Laboratory, Livermore, CA 94551, USA; H.-U. Nickel and M.Thumm, IHE Universität Karlsruhe and ITP Kernforschungszentrum Karlsruhe, Germany.

Tu1.5 ON THE USE OF A HYBRID MODE MIXTURE FOR LOWERING THE THERMAL LOAD PEAK IN CERAMIC WINDOWS FOR MM-WAVE ECRH EXPERIMENTS - F.Billè*, S. Cirant**, L.Manià*, G. Solari** and G.Viciguerra*; *DEEI - Universita di Trieste, Via A. Valerio 10, 34127, Trieste, Italy; **Istituto di Fisica del Plasma - Assoc. EURATOM-ENEA-CNR, Via Bassini 15-20133 Milano, Italy.

Tu1.6 EFFECT OF WINDOW TOLERANCES ON GYROTRON PERFORMANCE - J.Jelonnek and K.Schünemann. Technische Universität Hamburg-Harburg, Germany.

Tu1.7 INCREASE OF GYROTRON WINDOW CARRYING CAPACITY BASED ON OPTIMIZATION OF OUTPUT WAVEBEAM STRUCTURE - V.I.Belousov, G.G.Denisov, V.I.Malygin, D.V.Vinogradov, V.E.Zapevalov and S.A.Malygin*, Institute of Applied Physics, Nizhny Novgorod, Russia; *R&D Institute "Salut", Nizhny Novgorod, Russia.

Tu1.8 NEW WINDOW MATERIALS FOR HIGH POWER GYROTRON - M.N. Afsar and Hua Chi, Department of Electrical Engineering, Tufts University, Medford, Massachusetts 02155 - 5528, U.S.A.

Tu1.9 RADIATION INDUCED REDUCTION OF SILICON LOSS TANGENT - A. Ibarra, J. Mollá and E.R Hodgson, Inst. Investigación Básica, CIEMAT, Ed. 2. Av. Complutense, 22, E-28040 Madrid, Spain.

SESSION Tu 2

Tuesday AM	DETECTORS AND SOURCES - III	September 7

Tu2.1 ULTRALOW BACKGROUND RADIATION FAR INFRARED SPECTROSCOPY BASED ON THE MAGNETICALLY TUNABLE SELECTIVE SOURCES, FILTERS AND DETECTORS (*Invited Keynote*) - W.Knap, D.Dur, C.Chaubet and A.Raymond, Groupe d'Etude des Semiconducteurs, Université Montpellier II (CNRS - URA 357), Place E. Bataillon, 34095 Montpellier Cedex 05, France.

Tu2.2 THE FAR INFRARED p-Ge LASER: TRANSITION IDENTIFICATION AND EVIDENCE FOR STREAMING MOTION - C.R.Pidgeon and B.Murdin, Department of Physics, Heriot-Watt University, Riccarton, Currie, Edinburgh, UK; C.Kremser, K.Unterrainer and E.Gornik, Institut fur Festkorperelectronik, Technische Universitat Wien, A-1040, Austria.

Tu2.3 MODE STRUCTURE AND WAVELENGTH TUNABILITY OF THE p-Ge FAR-INFRARED HOT HOLE LASER - A.V.Muravjov, S.G.Pavlov, V.N.Shastin, Institute of Applied Physics, Russian Academy of Science, Nizhny Novgorod 603600, Russia; E.Bründermann, M.F.Kimmitt* and H.P.Röser, Max-Planck-Institut für Radioastronomie, D-W-5300 Bonn 1, Germany; *Permanent address: University of Essex, Colchester, CO4 3SQ, UK.

Tu2.4 FAR INFRARED RADIATION (FIR) SOURCES BASED ON IMPURITY EMISSION FROM SELECTIVELY DOPED MULTI QUANTUM WELLS (MQW) - D.Dur, W.Knap, C.Chaubet, A.Raymond, P. Vicente, A Dubois, I. Salesse, Groupe d'Etude des Semiconducteurs, Université Montpellier II (CNRS - URA 357), Place E. Bataillon, 34095 Montpellier, Cedex 05, France; B. Etienne, L2M/CNRS, 196 av. Henri Ravera, 92220 Bagneux Cedex, France; C.R. Stanley, M.B.E. Research Group, Department of Electronics and Electrical Engineering, University of Glasgow, Glasgow G12 811, UK.

Tu2.5 DIMINUTIVE AND SUPER DIMINUTIVE SURFACE WAVE MAGNETRONS OF MM RANGE - V.D. Yeremka, G.Ya.Levin, S.N.Terechin and A.Ya.Usikov, Institute of Radiophysics and Electronics, 12 Ac. Proskura st., Kharkov 310085, Ukraine.

Tu2.6 A FAR-INFRARED ACTIVE MEDIUM BASED ON SHALLOW ACCEPTOR STATES IN SEMICONDUCTORS - V.N.Shastin, A.V.Muravjov, E.E.Orlova and S.G.Pavlov, Institute of Applied Physics, Russian Academy of Science, Nizhny Novgorod 603600, Russia.

Tu2.7 A CLASS OF MICROWAVE SYNTHESISERS AND NOISE GENERATORS FOR MICROWAVE SPECTROSCOPY - V.L.Vaks, A.N.Panin, S.J.Pripolsin, F.Neubert, U.Mau, A.V.Smorgonski, V.V.Chodos and A.O.Schulechov. Analytik & Messtechnik GmbH, Chemnitz, Austria.

Tu2.8 TUNABLE FAR INFRARED (TuFIR) SPECTROSCOPY OF TRANSIENT MOLECULES - S.R.Boardman, C.H. Bryant, P.B. Davies and T.J.Sears*, Dept. of Chemistry, University of Cambridge, Lensfield Road, Cambridge CB2 1EW, UK; *Permanent address: Brookhaven National Laboratory, Upton, N.Y., USA, S.E.R.C. Visiting Fellow.

SESSION Tu 3

Tuesday AM	SCATTERING	September 7

Tu3.1 SCATTERING OF GUIDED MODES BY SPHERE IN A QUASI-OPTICAL WAVEGUIDE OF THE CLASS OF 'HOLLOW DIELECTRIC CHANNEL' - V.K.Kiselyev and T.M.Kushta. Inst. Radiophysics and Electronics, Academy of Sciences of Ukraine, 12 Acad. Proskura str., Kharkov, Ukraine.

Tu3.2 SCATTERING OF A DIELECTRIC-SLAB WAVEGUIDE EIGENMODE FROM AN INTERNAL PENETRABLE INHOMOGENEITY - A.G.Yarovoy. Kharkov State University, Department of Radiophysics, 4 Svobody Sq., Kharkov 310077, Ukraine.

Tu3.3 RIGOROUS ANALYSIS OF 3-D DISCONTINUITY PROBLEM IN DIELECTRIC WAVEGUIDE - Xinzhang Wu and Shanjia Xu, Department of Radio and Electronics, University of Science and Technology of China, Hefei, Anhui, 230027, P.R. China.

Tu3.4 ANALYSIS OF SCATTERING OF THE OPEN RESONATOR FIELD FROM THE CAVITY-BACKED APERTURE - O.Belous, V. Veremey A.Fisun and A.Fursov. Institute of Radiophysics and Electronics Ukrainian Academy of Sciences, 12 ac. Proskura st., Kharkov, 310085, Ukraine.

Tu3.5 RESONANT FREQUENCIES AND Q-FACTORS OF A SPHERICAL CAVITY LOADED BY AN ECCENTRIC DIELECTRIC SPHERE - Li-Yang Zhang, Pin Wang and Chang-Hong Liang, Dept. of Electromagnetic Engineering, Xidian University, Shaanxi 710071, P.R. China.

Tu3.6 TM POLARIZED WAVE SCATTERING FROM DIELECTRIC CYLINDER EMBEDDED IN A STRATIFIED MEDIUM.- A.G.Yarovoy and N.P.Zhuck, Kharkov State University, Kharkov 310077, Ukraine.

Tu3.7 VARIATIONAL SOLUTION OF RESONANT CAVITY FILLED WITH ANISOTROPIC PLASMA. - Kai Liu, Wenxun Zhang and Jimin Ying, Department of Radio Engineering, Southeast University, Nanjing 210018, P.R. China.

Tu3.8 OPEN RESONATOR WITH MODE SELECTION FOR MILLIMETER- WAVE DEVICES. - O.I.Belous, A.I.Fisun, A.M.Fursov, A.A.Kirilenko and V.I.Tkachenko, Inst. of Radiophysics and Electronics Ukranian Academy of Science, 12, Acad. Proskura st., Kharkov 310085, Ukraine.

Tu3.9 QUASI-OPTICS EIGENMODES OF THE WAVEGUIDE RESONATOR - A.I.Kleev. P.L.Kapitza Institute for Physical Problems, Russian Academy of Sciences, ul. Kosygina 2, Moscow, 117334, Russia.

SESSION Tu 4

Tuesday AM — **SPECTROSCOPY - III** — September 7

Tu4.1 FIR MULTIPHOTON ABSORPTION AND PHOTON DRAG EFFECTS IN DEGENERATE VALENCE BAND SEMICONDUCTORS - S.D.Ganichev*, E.L.Ivchenko, R. Ya. Rasulov, I.D.Yaroshetskii and B.Ya. Averboukh, A.F.Ioffe Physicotechnical Institute, Russian Academy of Sciences, St.Petersburg 194021, Russia; *Present address: Uni. Regensburg, Institute für Angewandte Physik III, 93040 Regensburg.

Tu4.2 FAR INFRARED MEASUREMENTS ON BAND NONPARABOLICITIES IN DOPED MULTIPLE QUANTUM WELL STRUCTURES - S.K.Kang[1], J.P.Bryant[1], T.Dumelow[1], T.J.Parker[1], C.T. Foxon[2], J.W. Orton[3] and J.J. Harris[4]; [1]Department of Physics, University of Essex, Wivenhoe Park, Colchester CO4 3SQ, UK; [2]Department of Physics, University of Nottingham, University Park, Nottingham NG7 2RD, UK; [3]Department of Electrical and Electronic Engineering, University of Nottingham, University Park, Nottingham NG7 2RD, UK; [4]IRC for Semiconductor Materials, Blackett Laboratory, Imperial College, Prince Consort Road, London SW7 2BZ, UK.

Tu4.3 INVESTIGATION OF THE ELECTRON DISTRIBUTION IN $Cd_xHg_{1-x}Te$ SUPERLATTICES BY FAR INFRARED AND RAMAN SPECTROSCOPY - S.K.Kang[1], T.Dumelow[1], T.J.Parker[1], R.J.York[1], S.R.P.Smith[1], S.N. Ershov[2] and M.I. Vasilevski[2]; [1]Department of Physics, University of Essex, Wivenhoe Park, Colchester CO4 3SQ, UK; [2]Faculty of Physics, Nizhni Novgorod State University, 37 Sverdlova Street, Nizhni Novgorod 603000, Russia.

Tu4.4 THE CONTROL OF GAP WIDTH IN THE LOW-DIMENSIONAL SYSTEMS WITH CDW INSTABILITY - A.I.Dmitriev, G.V. Lashkarev and D.A.Fedorchenko, Institution on Material Problems of Academy of Sciences of Ukraine, Kiev, Ukraine.

Tu4.5 DEFECT AND CLUSTERING MODES OF HgCdMnTe CRYSTALS - Yu.I.Mazur, S.I.Kriven, S.R.Lavorik and G.G.Tarasov, Institute of Semiconductors, Academy of Sciences of Ukraine, Kiev 252028, pr. Nauki 45, Ukraine.

Tu4.6 EXCITONIC LUMINESCENCE OF $Hg_{1-x-y}Cd_xMn_yTe$ CRYSTALS. - J.W.Tomm*, Yu. I. Mazur**, S.I. Kriven**, S.R. Lavorik** and G.G. Tarasov**, *Section of Physics, Humboldt University, Berlin, Germany; **Institute of Semiconductors, Ukr. Acad. Sci., Kiev, Ukraine.

Tu4.7 MID-INFRARED ABSORPTION SPECTRA OF IRON GROUP IMPURITIES IN II-IV SEMICONDUCTORS - M.Castillo, Universidad Nacional Experimental del Táchira, Apto 436, San Cristóbal, Venezuela.

SESSION Tu 5

Tuesday PM	PLASMA DIAGNOSTICS	September 7

Tu5.1 DEVELOPMENT OF REFLECTOMETRY FOR PLASMA DENSITY MEASUREMENTS AT JET - A.E.Costley, JET Joint Undertaking, Abingdon, Oxon OX14 3EA, UK.

Tu5.2 AN ADVANCED RADAR TECHNIQUE FOR ELECTRON DENSITY MEASUREMENTS ON LARGE TOKAMAKS - P.Millot and H. Léveque, Centre d'Etudes et de Recherches de Toulouse (ONERA/CERT), Département d'Etudes et de Recherches en MicroOndes, 2, avenue Edouard Belin, 31400 Toulouse Cedex, France.

Tu5.3 A FOUR-CHANNEL POLARIZING INTERFEROMETER FOR ECE MEASUREMENTS ON FTU TOKAMAK - P.Buratti and M.Zerbini, Associazione EURATOM-ENEA Sulla Fusione, CRE Frascati, CP 65, I-00044 Frascati (Roma), Italy.

Tu5.4 THE RECEIVER SYSTEM OF THE FAST ION AND ALPHA PARTICLE DIAGNOSTIC AT JET - J.Fessey, J.A.Hoekzema and T.P.Hughes, JET Joint Undertaking, Abingdon, Oxon OX14 3EA, UK.

Tu5.5 A PLASMA IMAGING CAMERA WITH A FILLED, 2-DIMENSIONAL FOCAL PLANE ARRAY. - E.L.Moore, G.R.Huguenin, C.T.Hsieh, A.S.Vickery, K.R.Wood and J.E.Kapitzky, Millitech Corporation, P.O. Box 109, South Deerfield Research Park, South Deerfield, Mass. 01373, USA.

Tu5.6 SUPPRESSION OF COHERENCE EFFECTS IN THE MEASUREMENT OF MMWAVE ABSORPTION IN THE JET PLASMA - R.J.Smith, D.V.Bartlett, A.R.Harvey*, J.C.G.Lesurf* and M.Salisbury**, JET Joint Undertaking, Abingdon, Oxon OX14 3EA, UK; *University of St. Andrews, Dept. of Physics and Astronomy, St. Andrews, Scotland; **Imperial College of Science, Technology and Medicine, London, SW7 2BZ, UK.

Tu5.7 A BROADBAND QUASI-OPTICAL COLLECTION SYSTEM FOR THE JET HETERODYNE RADIOMETER.- L.Porte, D.V.Bartlett, A.Rookes* and R.J.Wylde**, JET Joint Undertaking, Abingdon, Oxon OX14 3EA, UK; * Imperial College of Science Technology and Medicine, London, UK; **Thomas Keating Ltd., Billingshurst, West Sussex, UK and Physics Dept., Queen Mary and Westfield College, London E1 4NS, UK.

Tu5.8 SUBMILLIMETER LASER INTERFEROMETER-POLARIMETER FOR PLASMA DIAGNOSTICS - Yu.E.Kamenev, V.K.Kiselev, E.M.Kuleshov, B.N.Knyaz'kov, V.K.Kononenko, P.K.Nesterov and M.S.Yanovsky, Inst. Radiophysics and Electronics, 12 Ac Proscura st., Kharkov, 310085, Ukraine.

Tu5.9 FIRST ELECTRON TEMPERATURE EDGE MEASUREMENTS ON THE ASDEX UPGRADE TOKOMAK USING A HETERODYNE RADIOMETER - N.A.Salmon, Max-Planck-Institut für Plasmaphysik, EURATOM Association, D-8046 Garching, Fed. Rep. Germany.

SESSION Tu 6

Tuesday PM	DETECTORS AND SOURCES - IV	September 7

Tu6.1 HOT-ELECTRON SUPERCONDUCTING MIXERS - E.M.Gershenzon and G.N.Gol'tsman. Moscow State Pedagogical University, 1 M.Pirogovskaja str., Moscow 119435, Russia.

Tu6.2 A COMBINED 3MM AND 1.3MM BANDS SIS RECEIVER FOR THE IRAM INTERFEROMETER - M.Carter, J.Blondel, A.Karpov, F. Mattiocco and B.Lazareff, IRAM, Institut de Radio Astronomy Millimetrique, St.Martin d'Heres, France.

Tu6.3 AND 270 GHZ SIS RECEIVERS DEVELOPMENT FOR ATMOSPHERIC OBSERVATION - S.Ochiai and H.Masuko, Communs. Res. Lab., Tokyo 184, Japan.

Tu6.4 PREPARATION AND MICROWAVE MEASUREMENTS OF STACKED $Nb/(Al/AlO_x/Nb)_n$ SUPERCONDUCTING TUNNEL STRUCTURES - I.P.Nevirkovets and L.P. Strizhko*, Department of Materials Science and Metallurgy, University of Cambridge, Pembroke St, Cambridge CB2 3QZ, UK; *Institute for Radio Astronomy of the Ukrainian Academy of Sciences, Krasnoznamennaja str., 4, 310002 Kharkov, Ukraine.

Tu6.5 PERFORMANCE OF AN SIS RECEIVER OVER 460 GHZ TO 640 GHZ USING SUBMICRON Nb JUNCTIONS WITH INTEGRATED RF TUNING CIRCUITS - P.Febvre*, W.R.McGrath, P.Batelaan, H.G.LeDuc, B. Bumble, M.A.Frerking and J.Hernichel**, Jet Propulsion Laboratory, California Institute of Technology, Pasadena, CA 91109, USA; *Permanent address: DEMIRM-Observatoire de Meudon, 92195 Meudon Cedex, France; **Permanent address: Universität Köln, 5000 Köln 41, Germany.

Tu6.6 HIGH QUALITY NbN-BASED JUNCTIONS FOR 500 GHZ WAVEGUIDE MIXERS - M.G.Blamire, Z.H.Barber, H. van de Stadt*, J.J. Wezelman* and S. Withington**, Department of Materials Science, University of Cambridge, Pembroke St., Cambridge, CB2 3QZ, UK; *SRON, Laboratory for Space Research Groningen, P.B. Box 800, 9700 AV Groningen, The Netherlands; **Cavendish Laboratory, University of Cambridge, Madingley Road, Cambridge, CB3 OHE, UK.

Tu6.7 QUASI-OPTICAL 0.5 THZ SIS RECEIVER WITH TWIN JUNCTION TUNING CIRCUIT - S.W.Jacobsson†, V.Yu Belitsky††, L.V. Filippenko††, S.A. Kovtonjuk††, V.P. Koshelets†† and E.L.Kollberg†, †Department of Microwave Technology, Chalmers University of Technology, S-412 96, Göteborg, Sweden; ††Institute of Radio Engineering and Electronics, Russian Academy of Sciences, Mokhovaja 11, 103907 Moscow, Russia.

Tu6.8 FREQUENCY MEASUREMENT OF SUB-MILLIMETRE WAVELENGTH LASER LINES USING JOSEPHSON JUNCTIONS - M.C.Wicks and J.R.Birch, Division of Electrical Science, National Physical Laboratory, Middlesex, TW11 OLW, UK.

Tu6.9 MILLIMETRE WAVE MIXING WITH YBCO JOSEPHSON JUNCTIONS ON BICRYSTAL SUBSTRATES - P.G.Quincey and M.C.Wicks, Division of Electrical Science, National Physical Laboratory, Middlesex, TW11 OLW, UK.

Tu6.10	METHODS OF FREQUENCY MEASUREMENTS OF MICROWAVE SIGNALS OF MM- AND SUBMM- WAVE BANDS WITH THE USE OF AS JOSEPHSON EFFECT - S.E.Anischenko, S.Y.Larkin and P.V.Khabayev, State Research Center "Fonon", 37 Pobedy Ave., KPI-3240, Kiev, 252056, Ukraine.
Tu6.11	FOR QUESTION OF SUPERCONDUCTIVE WIDE BAND FREQUENCY METER DESIGNING: MAIN METHODICS AND PROBLEMS - G.A.Marusly, V.G.Gurovich, G.A.Zatona and N.V.Pilinsky, State Research Center of Superconductive Radioelectronics, Ave. 50 Years of October, 2b, 252680 Kiev, Ukraine.
Tu6.12	SIS-MIXER DEVELOPMENT AT SRON - J. Mees[a], G. de Lange[a,b], A. Skalare[a,c], C.E. Honingh[a,d], M.M.T.M. Dierichs[a], H. Kuipers[a,b], R.A. Panhuyzen[a], H. van de Stadt[a], Th. de Graauw[a] and T.M. Klapwijk[b], [a]Space Research Organisation Netherlands (SRON), Postbox 800, 9700 AV Groningen, The Netherlands; [b]Dept. of Applied Physics and Materials Science Center, University of Groningen, Nijenborgh 4, 9747 AG Groningen, The Netherlands; [c]Now at: Jet Propulsion Laboratory, California Institute of Technology, CA 91109, USA; [d]Now at: Universität zu Köln, 1 Physikalisches Institut, Zülpicherstr. 77, 5000 Köln 41, Germany.

SESSION Tu 7

Tuesday PM	WAVEGUIDE - I	September 7

Tu7.1 NETWORK ANALYSIS OF THE DISPERSION CHARACTERISTICS FOR THE GROOVE GUIDE WITH ARBITRARY CURVED SHAPES - Xu Shanjia and Zhang Yaojiang, University of Science and Technology of China, Hefei, Anhui, 230027, P.R. China.

Tu7.2 PHASE AND ATTENUATION COEFFICIENTS IN BI-DIELECTRIC ECCENTRIC CIRCULAR TRANSMISSION LINES - Li-Yang Zhang, Pin Wang, Yong-Chang Jiao and Chang-Hong Liang, Dept. of Electromagnetic Engineering, Xidian University, Shaanxi 710071, P.R. China.

Tu7.3 THE CHARACTERISTICS OF THE CLOSED CIRCULAR GROOVE GUIDE - Jun Qian, Yang Hong-Sheng and Lu Zhong-Zuo, Department of Electronic Engineering, National Key Laboratory of Millimeter Waves, Southeast University, Nanjing, 210018, P.R. China.

Tu7.4 THE HIGHER ORDER MODES IN CIRCULAR GROOVE GUIDE - Ma Jianglei, Yang Hong-Sheng and Lu Zhong-Zuo, National Key Lab. of Millimeter Waves, Southeast University, Nanjing, 210018, P.R. China.

Tu7.5 A TRANSITION FROM RECTANGULAR WAVEGUIDE TO CIRCULAR GROOVE GUIDE - Yang Hong-Sheng, Shen Zheng-Kun and Xu Zheng-Rong, National Key Lab. of Millimeter Waves, Southeast University, Nanjing, 210018, P.R. China.

Tu7.6 AN ANALYSIS OF A KIND OF DIELECTRIC WAVEGUIDE - Hong Wu and Jun Qian. Southeast University, Nanjing, 210018, P.R. China.

Tu7.7 TRANSITIONS FOR THE QUASI-OPTICAL WAVEGUIDES - V.K.Kiselyev and T.M.Kushta. Inst. Radiophysics and Electronics, Kharkov, Ukraine.

Tu7.8 FREQUENCY DEPENDENT CHARACTERISTICS OF THICK MICROSTRIP LINES IN LOSSY MULTILAYERED DIELECTRIC MEDIA - J.R.Souza, Center for Telecommunications Studies - CETUC, Pontifical Catholic University of Rio de Janeiro - PUC/Rio, Rua Marquês de São Vicente, 225, 22453 Rio de Janeiro - RJ, Brazil.

Tu7.9 REJECTION FILTER - S.A. Pogarsky and I.I. Saprykin, Microwave Physics Department, State University, Sq. Svobody, 4, 310077, Kharkov, Ukraine.

SESSION Tu 8

Tuesday PM	SPECTROSCOPY - IV	September 7

Tu8.1 OPTICAL CHARACTERISATION OF THIN FILMS USING SURFACE POLARITONS AND SURFACE ELECTROMAGNETIC WAVE MEASUREMENTS (*Invited Keynote*) - E.V.Alieva, L.A.Kuzik, V.A.Yakovlev and G.N.Zhizhin, Institute of Spectroscopy, Academy of Sciences of Russia, Troitzk, Moscow reg. 142092, Russia.

Tu8.2 INFRARED SURFACE WAVE HETERODYNING ON METALS AND SEMICONDUCTORS - V. Valcikauskas, R.Petruskevicius, R.Antanavicius and R.Januskevicius, Institute of Physics, A. Gostauto 12, 2000 Vilnius, Lithuania.

Tu8.3 SURFACE ELECTROMAGNETIC WAVE PROPAGATION ON $NaClO_3$ AND KTP CRYSTALS - E.V.Alieva, L.A.Kuzik and VA.Yakovlev, Institute of Spectroscopy, Academy of Science of Russia, Troitzk, Moscow reg. 142092, Russia.

Tu8.4 INTERFEROMETRIC MEASUREMENTS OF PHASE SHIFT IN THE IR REFLECTION-ABSORPTION SPECTROSCOPY - L.A.Kuzik, A.B.Sushkov, V.A.Yakovlev and G.N.Zhizhin, Institute of Spectroscopy, Academy of Sciences of Russia, Troitzk, Moscow reg. 142092, Russia.

Tu8.5 SPECTROSCOPY OF CONFINED LO PHONONS IN SUPERLATTICES: A PROBE FOR STUDY OF INTERFACIAL DISORDER - M.I.Vasilevskiy, Faculty of Applied Physics and Microelectronics, Nizhni Novgorod State University, 37 Sverdlova str., Nizhni Novgorod 603000, Russia.

Tu8.6 FAR INFRARED SPECTROSCOPY OF PHONONS IN GaInAs/InP SUPERLATTICES - T.S.Sethi[1], J.P. Bryant[2], A.A. Hamilton[2], T. Dumelow[2], W.F. Sherman[1] and T.J. Parker[2]; [1]Department of Physics, King's College London, Strand, London WC2R 2LS, UK; [2]Department of Physics, University of Essex, Wivenhoe Park, Colchester CO4 3SQ, UK.

Tu8.7 QUANTUM SIZE OSCILLATIONS IN OPTICAL AND ELECTRICAL PROPERTIES OF SUPERTHIN Nb AND Cu FILMS - L.A.Kuzik, Y.E.Petrov, V.A.Yakovlev, Institute of Spectroscopy, Academy of Sciences of Russia, Troitzk, Moscow reg 142092, Russia; F.A. Pudonin, P.N. Lebedev Physical Institute, Academy of Sciences of Russia, Moscow, Russia.

Tu8.8 NON-LINEAR DOPPLER SHIFT OF THE PLASMON RESONANCE IN A GRATING-COUPLED DRIFTING 2DEG - R.E.Tyson, R.J.Stuart, H.P.Hughes, J.E.F. Frost, D.A.Ritchie, G.A.C. Jones and C. Shearwood, University of Cambridge, Cavendish Laboratory, Madingley Road, Cambridge CB3 OHE, UK.

Tu8.9 OPTICAL TRANSITIONS IN QUANTUM WIRES WITH AN AXIAL MAGNETIC FIELD - M. Masale, N.C. Constantinou and D.R. Tilley, Dept of Physics, Univ. of Essex, Colchester CO4 3SQ, UK.

Tu8.10 FAR INFRARED AND RAMAN STUDY OF THE EFFECT OF GROWTH ON THE INTERFACES OF ASYMMETRIC GaAs/AlAs SUPERLATTICES - A.Z.Mamun[1], J.P.Bryant[1], T.Dumelow[1], T.J.Parker[1], R.J.York[1], S.R.P.Smith[1], C.T.Foxon[2], J.W.Orton[3] and K.J.Moore[4]; [1]Department of Physics, University of Essex, Colchester, CO4 3SQ, UK; [2]Dept. of Physics, University of Nottingham, Nottingham, NG7 2RD, UK; [3]Dept. of Electrical and Electronic Engineering, University of Nottingham, NG7 2RD, UK; [4]Dept. of Physics, Manchester Metropolitan University, Manchester, M1 5GD, UK.

Tu8.11 SIZE EFFECTS IN VIBRATIONAL POLARITON SPECTRA - E.A. Vinogradov, Institute of Spectroscopy, Russian Academy of Sciences, 142092, Troitsk, Moscow, Russia.

SESSION W1

Wednesday AM | GYROTRON - I | September 8

W1.1 A QUASI-OPTICAL MODE CONVERTER FOR GYROTRONS OPERATING IN HIGH ORDER MODES - M.Blank, K.E.Kreischer and R.J.Temkin, MIT Plasma Fusion Center, Cambridge, MA 01219, USA; E.Giguet, Thomson Tubes Electroniques, 78141, Velizy Villacoublay, France.

W1.2 COMPACT QUASIOPTICAL TE_{22-6} TO TEM_{00} TEM CONVERTER WITH FEED WAVEGUIDE DEFORMATIONS - J. Pretterebner[12], A. Möbius[13], M. Thumm[34], A. Wien[34]; [1]Innovative Microwave Technology Ltd., Heinrich Baumannstrasse 49, W-7000 Stuttgart 1, Germany; [2]Institut für Plasmaforschung, Universität Stuttgart, Pfaffenwaldring 31, W-7000 Stuttgart 80, Germany; [3]Kernforschungszentrum Karlsruhe, Inst. f. Technische Physik, P.O. Box 3640, W-7500, Karlsruhe, Germany; [4]Institut für Höchstfrequenztechnik und Elektronik, Universität Karlsruhe, W-7500 Karlsruhe, Germany.

W1.3 A TRAVELLING-WAVE RESONATOR FOR EXCITING WHISPERING-GALLERY MODES IN AN OVERMODED CIRCULAR WAVEGUIDE - T.A.Hea, R.A.Peebles and R.J.Vernon, Department of Electrical and Computer Engineering, University of Wisconsin, Madison, WI 53706, USA.

W1.4 MODE COUPLING IN OVERMODED, VARYING-RADIUS COAXIAL GYROTRON CAVITIES - D. Wagner, J. Pretterebner, Universität Stuttgart, Institut für Plasmaforschung, 70569 Stuttgart, Germany; M.Thumm, Kernforschungszentrum Karlsruhe, Institut für Technische Physik and Universität Karlsruhe, Institut für Höchstfrequenztechnik und Elektronik, 76021 Karlsruhe, Germany.

W1.5 MODELLING OF MODE PURITY IN HIGH POWER GYROTRONS - S.Y.Cai, T.M.Antonsen and B.Levush, University of Maryland, College Park, MD 20742, USA.

W1.6 MODE PRIMING AN 85 GHZ QUASIOPTICAL GYROKLYSTRON - R.P.Fischer, A.W.Fliflet, W.M.Manheimer, B.Levush* and T.M.Antonsen, Jr.*, Beam Physics Branch, Plasma Physics Division, U.S. Naval Research Laboratory, Washington, D.C. 20375-5000, USA; *Laboratory for Plasma Research, University of Maryland, College Park, MD 20742, U.S.A.

W1.7 ADVANCED COMPLEX CAVITY FOR MULTI-MEGAWATT GYROTRON - K.Xu and M.Thumm*, Kernforschungszentrum Karlsruhe, Institut für Technische Physik, P.O. Box 3640, D-7500 Karlsruhe 1, Germany; *also Universität Karlsruhe, Institut für Höchstfrequenztechnik und Elektronik, D-7500 Karlsruhe 1, Germany.

W1.8 KW SIXTH-HARMONIC GYROFREQUENCY MULTIPLIER - A.J.Balkcum, D.B.McDermott, F.Hartemann and N.C.Luhmann Jr., Dept. of Electrical Engineering, University of California, Los Angeles, CA 90024, USA.

SESSION W 2

Wednesday AM	QUASI-OPTICAL COMPONENTS - I	September 8

W2.1 LOW PASS FILTERS FOR THE FAR INFRARED - C.V. Haynes and P.A.R.Ade, Department of Physics, Queen Mary and Westfield College, Mile End Road, London E1 4NS, UK.

W2.2 REJECTION OF FREQUENCY BANDS OF ELECTROMAGNETIC RADIATION BY QUASI-OPTICAL BRAGG STRUCTURES - A.A.Vertiy, S.P.Gavrilov and I.N.Goltvyanskiy, Institute of Radiophysics and Electronics, Academy of Sciences of Ukraine, 12 acad. Proskura st., Kharkov 310085, Ukraine.

W2.3 PERFORMANCE OF A HIGH T_C SUPERCONDUCTING ULTRA-LOSS MICROWAVE MICROSTRIP FILTER - O.D.Pustylnik, A.A.Dymnikov, I.V.Voinovsky and O.A.Khimenko, SRC "Fonon", 39 Pobedy Av., KPI-3240, Kiev, Ukraine; V.F. Vratskikh, Institute for Thermophysics. Kutateladze 1, Novosibirsk 630090, Russia.

W2.4 FREQUENCY SELECTIVE SURFACES FOR MILLIMETRE AND SUBMILLIMETRE-WAVE QUASI-OPTICAL DEMULTIPLEXING - J.W.Bowen, Department of Physics, Queen Mary and Westfield College, Mile End Road, London E1 4NS, UK; R.Cahill, Systems and Payloads Department, British Aerospace Space Systems Ltd., FPC 320, PO Box 5, Filton, Bristol BS12 7QW, UK, and E.A.Parker, Electronic Engineering Labs, The University of Kent, Canterbury, Kent CT2 7NT, UK.

W2.5 RUGGED FAR INFRARED BANDPASS FILTERS - P.G.Huggard, M.Meyringer, A. Schilz and W.Prettl, Institut für Angewandte Physik, Universität Regensburg, 93040 Regensburg, Germany.

W2.6 QUASI-OPTICAL NARROW-BAND NOTCH FILTERS - G.G.Denisov, S.V. Kuzikov and M.Yu.Shmelyov. Institute of Applied Physics, Russian Academy of Science, 46 Ulyanov Street, 603600 Nizhny Novgorod, Russia.

W2.7 DESIGN OF RIDGED WAVEGUIDE E-PLANE BANDPASS FILTERS IN MILLIMETER WAVE APPLICATIONS - D.Budimir, V.Postoyalko and J.R.Richardson., Microwave and Terahertz Technology Group, Dept. of Electronic and Electrical Engineering, University of Leeds, Leeds LS2 9JT, UK.

W2.8 FILTERS AND WAVEFRONT DIVIDING BEAMSPLITTERS FOR THE NEAR AND MID INFRARED PRODUCED BY MICROMACHINING TECHNIQUES - J.Warren, National Synchrotron Light Source, Brookhaven National Laboratory, Upton, NY 11973, USA; J.B.Heaney, NASA Goddard Space Flight Center, Greenbelt, Maryland 20771, USA, and K.D.Möller, Department of Physics, New Jersey Institute of Technology, Newark, NJ 07102, USA.

SESSION W3

Wednesday AM	WAVEGUIDE - II	September 8

W3.1 A NOVEL TYPE OF WAVEGUIDE-TO-COPLANAR WAVEGUIDE ADAPTER - Gong Ke and Wang Ji, Department of Electronic Engineering, Tsinghua University, Beijing 100084, P.R. China.

W3.2 SIMULTANEOUS CONSIDERATION OF CONDUCTOR THICKNESS AND SEMICONDUCTOR SUBSTRATE IN FIN-LINES - H.C.C.Fernandes, E.A.M.de Souza, A.C.R.de Brito and E.D.Barbosa. Federal University of Rio Grande do Norte, P.O.Box, 1583, Natal, Brazil.

W3.3 CHARACTERISTICS OF MICROSTRIP LINES WITH FINITE METALLIZATION THICKNESS AND TURNING-UP EDGE FOR HIGH POWER TRANSMISSION - Ao Sheng Rong and Zhong Liang Sun. State Key Lab. of Millimeter Waves, Southeast University, Nanjing 210018, PRC.

W3.4 SPECTRUM DYNAMICS OF NON-RADIATING MODES OF SEMI-OPEN TRANSMISSION LINES BASED ON PLANAR WAVEGUIDE JOINTS - A.G.Yushchenko and S.F.Shibalkin, Microwave Devices Lab. of Kharkov State University, Freedom Square 4, Kharkov 310077, Ukraine.

W3.5 TRANSVAR DIRECTIONAL COUPLER FOR MILLIMETER-WAVE APPLICATIONS - Yonghui Shu, Epsilon Lambda Electronics Corporation, 427 Stevens Street, Geneva, IL 60134, USA.

W3.6 GHZ MICROSTRIP LINE SP4T PIN DIODE SWITCH - Yonghui Shu, Epsilon Lambda Electronics Corporation, 427 Stevens Street, Geneva, IL 60174, USA.

W3.7 MODAL ANALYSIS OF MICROSTRIP AND FINLINE STEP DISCONTINUITIES FOR MICROWAVE AND MILLIMETER-WAVE INTEGRATED-CIRCUITS APPLICATIONS - C. Nguyen and K.M. Rahman, Department of Electrical Engineering, Texas A&M University, College Station, Texas 77843-3128, U.S.A.

W3.8 RECENT DEVELOPMENT OF MICROSTRIP BAND-PASS FILTERS FOR MICROWAVE AND MILLIMETER-WAVE INTEGRATED CIRCUITS - C. Nguyen, Department of Electrical Engineering, Texas A&M University, College Station, Texas 77843-3128, U.S.A.

SESSION W4

Wednesday AM | **BIOLOGICAL EFFECTS** | September 8

W4.1 MILLIMETRE WAVES AND QUANTUM MEDICINES (*Invited Keynote*) - P.Sit'ko, Scientific Research Center on Physics of the Alive and Microwave Resonance Therapy, Kiev, 252033, Ukraine.

W4.2 INFRARED SPECTRA OF URINE FROM CANCEROUS BLADDERS - M.A.Moharram, A.Higazi* and A.A.Moharram,* Spectroscopy Department, Physics Division, National Research Centre, Cairo, Egypt, *Faculty of Medicine, Cairo University.

W4.3 DRO-AUTODYNE SPECTROMETER FOR INVESTIGATION OF INTERACTION OF MILLIMETER ELECTROMAGNETIC WAVES WITH BIOLOGICAL OBJECTS - G.P.Ermak and Ye.B.Senkevich, Inst. of Radiophysics and Electronics of the Ukrainian Academy of Sciences, 12 Ac. Proskura st., Kharkov, 310085, Ukraine.

W4.4 INFRARED SPECTROSCOPY DETECTION OF MILLIMETRE-WAVE EFFECT UPON BIOMOLECULES - G.S.Litvinov, L.I. Berezhinsky, G.I. Dovbeshko, M.P. Lisitsa and L.I. Matseiko, Scientific Research Center "Vidhuk", Volodymyrska 61-b, Kiev 252033, Ukraine.

W4.5 TREATMENT OF CARDIOVASCULAR DISEASES BY MEANS OF WIDE-BAND COHERENT SIGNAL OF MM RADIO WAVE RANGE - V.D.Yeremka, A.A.Kuznetsov, V.V.Smorodin, A.I.Fisun, A.M.Fursov, L.P.Himenko and P.L.Himenko, Inst. of Radiophysics and Electronics of Ukrainian Academy of Sciences, 12, Acad. Proskura st., Kharkov 310085, Ukraine.

W4.6 REARRANGEMENTS IN POLARISED VIBRATIONAL SPECTRA OF GLYCINE-CONTAINING CRYSTALS UNDER MILLIMETER WAVE ACTION - G.I.Dovbeshko, L.I.Berezhinsky, G.S.Litvinov and V.V.Obukhovsky, Scientific Research Centre on Physics of the Alive and Microwave Resonance Therapy, Kiev, Ukraine.

W4.7 THE COMBINED EFFECT OF HIGH TEMPERATURE AND MICROWAVE FIELDS ON WINTER WHEAT SEEDS - V.G.Shakhbazov, A.A. Shmatko and Al. A.Shmatiko, Kharkov State University, Department of Genetics and Cytology, 4 Nezavisimosti Square, Kharkov, Ukraine.

W4.8 PECULIARITIES OF THE FAR INFRARED SPECTRA OF AMINOACIDS, BIOPOLYMERS AND CELLS - G.S.Litvinov and G.I.Dovbeshko, Scientific Research Center "Vidhuk", Volodymyrska 61-b, Kiev, 252033 Ukraine.

W4.9 THE INFLUENCE OF MICROWAVE FIELDS ON ELECTROKINETIC PROPERTIES OF CELLULAR NUCLEI OF HUMAN BUCCAL EPITHELIUM - V.G.Shakhbazov and Al.A.Shmatiko, Kharkov State University, Department of Genetics and Cytology, 4 Nezavisimosti Square, Kharkov, Ukraine.

SESSION W 5

Wednesday PM	GYROTRON - II	September 8

W5.1 OPTIMUM OPERATION OF GYROTWISTRONS - P.E.Latham and G.S.Nusinovich. University of Maryland, College Park, MD, USA.

W5.2 UNIVERSALLY SCALED EQUATIONS FOR GYROTRON AND CARM AMPLIFIERS - B.W.J.McNeil, G.R.M.Robb and A.D.R.Phelps, Dept. of Physics and Applied Physics, University of Strathclyde, Glasgow, G4 ONG, UK.

W5.3 EXPERIMENTS OF 3RD AND 10TH CYCLOTRON HARMONIC PENIOTRON OSCILLATORS - K.Yckoo, T.Ishihara, H. Tadano, K.Sagae, H.Shimawaki, N.Sato and S.Ono, Research Institute of Electrical Communication, Tohoku University, Sendai 980, Japan.

W5.4 RELATIVISTIC PENIOMAGNETRON OF MM AND SUB MM RADIO WAVE RANGE - V.D.Yeremka, V.A.Zhurakhovskiy and L.P.Mospan, Institute of Radiophysics and Electronics of Ukrainian Academy of Sciences, 12, Acad. Proskura st., Kharkov, 310085, Ukraine.

W5.5 TWO-STAGE 35 GHZ GYRO-PENIOTRON AMPLIFIER EXPERIMENT - G.S.Park[§], C.M.Armstrong, A.K.Ganguly, R.H.Kyser[¶] and J.L. Hirshfield[§], Naval Research Laboratory, Code 6840, Washington, DC 20375, USA; [§]Omega-P, Inc., New Haven, CT 06520; [¶]B-K Systems, Inc., Rockville, MD 30850.

W5.6 EXPERIMENTAL STUDY OF A RELATIVISTIC PENIOTRON - S.Musyoki, K.Sakamoto, A.Watanabe and M. Shiho, Japan Atomic Energy Research Institute, Naka Fusion Research Establishment, Naka-machi, Naka-gun, Ibaraki 311-01, Japan; K.Yokoo, N.Sato and S. Ono, Research Institute of Electrical Communication, Tohoku University, Sendai 980, Japan; S.Kawasaki and M.Takahashi, Faculty of Science, Saitama University, 255 Shimookubo, Urawa-shi, Saitama-ken 388, Japan; H.Ishizuka, Fukuoka Institute of Technology, Higashi-ku, Fukuoka, Japan.

W5.7 PENIOMAGNETRON WITH QUASIOPTICAL TWO-MIRRORS RESONATOR - V.D.Yeremka, Institute of Radiophysics and Electronics of Ukrainian Academy of Sciences, 12, Acad. Proskur st., Kharkov, 310085, Ukraine

W5.8 THEORY OF REFLECTION-TYPE GYRO-TWT AND GYRO-BWO - A.P. Chetverikov, Saratov University, Physical Department, Astrahanskaya, 83, Saratov 410071, Russia.

W5.9 COMPARATIVE ANALYSIS OF OSCILLATIONS IN BACKWARD WAVE OSCILLATORS - A.P. Chetverikov, Saratov University, Physical Department, Astrahanskaya, 83, Saratov 410071, Russia.

SESSION W6

Wednesday PM — **QUASI-OPTICAL COMPONENTS - II** — September 8

W6.1 INFRARED POLARIZERS MADE OF ANODIC ALUMINA FILMS - M.Saito, T.Kano, T.Seki and M.Miyagi, Tohoku University, Department of Electrical Communications, Sendai 980, Japan.

W6.2 REFLECTION TYPE ISOLATOR FOR SUBMILLIMETER WAVES - V.K.Kononenko and E.M.Kuleshov, Inst. of Radiophysics and Electronics, Academy of Sciences of Ukraine, 12 Acad. Proscura st., Kharkov, 310085, Ukraine.

W6.3 HIGH PERFORMANCE QUASI-OPTICAL FARADAY ROTATORS - G.M.Smith†, M.Webb* and J.C.G.Lesurf†, †University of St.Andrews, Dept. of Physics and Astronomy, Fife, KY16 9SS, UK, *DSTO, SRL, Salisbury, Australia, formerly at St. Andrews.

W6.4 MODULATION CHARACTERISTICS OF INJECTION HETEROLASERS COMPRISING CHARGE CARRIERS HEATED BY EXTERNAL MW ELECTRIC FIELD IN VIEW OF ELECTRON-ELECTRON AND ELECTRON-HOLE INTERACTIONS AS WELL AS HIGHER FIELD TRANSPORT - T.Yu.Bagaeva, I.I.Filatov, V.B.Gorfinkel, S.A. Gurevich* and T.I.Solodkaya, Saratov Branch of IRE Russian Academy of Science, 410019 Saratov, Russia, *A.F. Ioffe Institute of Russian Academy of Science, St. Petersburg, Russia.

W6.5 ABOUT USE OF THE INDUCED ANTIFERROMAGNETIC ORDERING EFFECT IN SHF DEVICES - V.N.Polupanov, V.K.Kiselev and V.N.Seleznev*, Inst. of Radiophysics and Electronics, Academy of Sciences of Ukraine, 12, Acad. Proscura st., Kharkov 310085, Ukraine, *State University of Simferopol', 4, Yaltinskaya st., Simferopol', 333036, Krimea, Ukraine.

W6.6 TRANSVERSE RESONANCES IN OVERSIZED WAVEGUIDES - D.Wagner, J.Pretterebner, Universität Stuttgart, Institut für Plasmaforschung, 70569 Stuttgart, Germany; M. Thumm, Kernforschungszentrum Karlsruhe, Institut für Technische Physik and Universität Karlsruhe, Institut für Höchstfrequenztechnik und Elektronik, 76021 Karlsruhe, Germany.

SESSION W7

Wednesday PM	INSTRUMENTATION - I	September 8

W7.1 WAVEFRONT DIVIDING RING-INTERFEROMETERS FOR THE FAR INFRARED - K.D.Möller, K.Chin and C. Qiu, Department of Physics, New Jersey Institute of Technology, Newark, NJ 07102, USA, P.Bruelemans and P.Janssen, Dept. of Physics, Katholieke Universiteit, Leuven, Belgium.

W7.2 HIGH RESOLUTION FAR INFRARED FOURIER SPECTROMETER USING A BUFFERED ADC - A.K.Wan Abdullah, M.Roslan and W.A.Kamil*, School of Physics, *School of Chemical Sciences, Universiti Sains Malaysia, 11800 Penang, Malaysia.

W7.3 A HIGH RESOLUTION, HIGH SPEED DATA ACQUISITION SYSTEM BASED ON AN IBM-PC 486, FOR CONTROL OF A FOURIER TRANSFORM SPECTROMETER - Z.B.Maricic+, L.P.Ellison+, B.Gowland* and G.A.Gledhill,+ +Dept. of Physics, *Computer Centre, Royal Holloway, University of London, Egham Hill, Egham, Surrey, TW20 OEX, UK.

W7.4 CHARACTERIZATION OF CH-PLASMAS WITH CSR BASED MICROWAVE SPECTROMETERS - F.Wolf, F.Neubert, T.Hessel and V.L.Vaks, Analytik & Meβtechnik GmbH Chemnitz, Stollberger Str. 4a, D-09119 Chemnitz, Germany.

W7.5 A Nb OPEN RESONATOR FOR MILLIMETER WAVE SURFACE RESISTANCE MEASUREMENTS OF SUPERCONDUCTIVE THIN FILMS - B.Komiyama and H.Shimakage, Communications Research Laboratory, Iwaoka Kobe 674, Japan.

W7.6 A NEW METHOD FOR COMPLEX SPECTRAL MEASUREMENTS IN MILLIMETER AND SUBMILLIMETER FREQUENCY RANGE - A.B.Latyshev, D.A.Loukianov and A.V.Semenov, General Physics Institute, Russian Academy of Science, 38 Vavilov St, 117942 Moscow, Russia.

W7.7 HIGH MICROWAVE PULSE POWER MEASUREMENT IN A FREE SPACE - M.Dagys, Z.Kancleris, R.Simniskis, Semiconductor Physics Institute, Gostauto 11, Vilnius 2600, Lithuania, and M.Bäckström, U.Thibblinn and B.Wahlgren, SAAB Military Aircraft, Linkoping S-581 88, Sweden.

W7.8 THE MILLIMETER WAVES POWER TRANSDUCER - K.Repsas, R.Vaskevicius, and V.Orsevskis, Semiconductor Physics Institute, 2600 Vilnius, Gostauto 11, Lithuania.

W7.9 FOURIER TRANSFORM INFRARED SPECTROMETER USING DELTA-SIGMA MODULATION FOR HIGH DYNAMIC-RANGE SPECTROMETRY - K. Minami and S. Kawata, Department of Applied Physics, Osaka University, Suita, Osaka 565, Japan.

SESSION W8

Wednesday PM | POST-DEADLINE | September 8

W8.1 NEW FIR LASER ASSIGNMENTS IN THE ν_5, ν_7, and ν_8 EXCITED STATES OF $^{13}CD_3OH$ METHANOL - Li-Hong Xu and R.M. Lees, CEMAID and Physics Department, University of New Brunswick, Fredericton, N.B., Canada E3B 5A3.

W8.2 ASSIGNMENT OF THE FIR AND IR ABSORPTION SPECTRA OF THE METHANOL ISOTOPIC SPECIES - G. Moruzzi[1], F. Strumia[1], R.M. Lees[2], Li-Hong Xu[2], B.P. Winnewisser[3], M. Winnewisser[3] and I. Mukhopadhyay[4]; [1]Dipartimento di Fisica dell'Università di Pisa, Piazza Torricelli 2, I-56126 Pisa; [2]Department of Physics, University of New Brunswick Fredericton, New Brunswick, Canada E3B 5A3; [3]Physikalish-Chemisches Institut der Justus-Liebig - Universität Giessen, Heinrich-Buff-Ring 58, D-W6300 Giessen; [4]Government of India, Department of Atomic Energy, Centre for Advanced Technology, Indore 452013, India.

W8.3 INJECTION SEEDING OF A PULSED FAR INFRARED MOLECULAR GAS LASER - H.P.M. Pellemans, J. Burghoorn*, T.O. Klaassen and W. Th. Wenckebach, Faculty of Applied Physics, Delft University of Technology, The Netherlands; *currently with the Max-Planck-Institut für festkörperforschung, Hochfeld-Magnetlabor, Grenoble, France.

SESSION Th 1

Thursday AM	GYROTRON - III	September 9

Th1.1 COMPARATIVE STUDY OF GYROTRONS BASED ON THERMIONIC AND COLD CATHODES - A.W.Cross, S.N.Spark, K. Ronald, A.D.R.Phelps and W. He, Dept. of Physics and Applied Physics, University of Strathclyde, Glasgow G4 ONG, UK.

Th1.2 RESULTS OF EXPERIMENTS ON PARAMETERS OF ELECTRON GUNS FOR GYROTRONS - B.Piosczyk. Kernforschungszentrum, Karlsruhe, ITP, Postfach 3640, D-7500, Karlruhe 1, Germany.

Th1.3 VACUUM MICROELECTRONIC ARRAY GYROTRON CATHODE EXPERIMENTS - M.Garven, S.N.Spark and A.D.R.Phelps and N. Cade*, Dept. of Physics and Applied Physics, University of Strathclyde, Glasgow G4, ONG, UK; *GEC-Marconi Ltd., Hirst Research Centre, East Lane, Wembley, Middx., HA9 7PP, U.K.

Th1.4 HIGH SPEED DIAGNOSTIC STUDY OF PULSED, COLD CATHODE, GYROTRONS - K.Ronald, S.N.Spark, A.D.R.Phelps and W. He, Dept. of Physics and Applied Physics, University of Strathclyde, Glasgow, G4 ONG, U.K.

Th1.5 NON-ADIABATIC ELECTRON GUNS FOR GYROTRONS - J.J.Barroso, I.P.Spassovsky and C.Stelatti., Instituto Nacional de Pesquisas Espaciais, 12201-970, São José dos Campos, SP - Brazil.

Th1.6 DIOCOTRON INSTABILITY IN THE DRIFT TUBE OF A GYROTRON - R.Schuldt, Nuclear Research Center Karlsruhe, HDI, W 7500, Karlsruhe 1, Germany.

Th1.7 ELECTROSTATIC EFFECTS ON THE QUALITY OF GYROTRON BEAMS - J.L.Vomvoridis, K.Hizanidis, I.Tigelis* and D.I. Frantzeskakis*, Dept of Electrical and Computer Engineering, National Technical University of Athens, Greece; *Department of Physics, University of Athens, Greece.

Th1.8 HZ PRF CARM EXPERIMENT - S.J.Cooke, S.N.Spark, W. He and A.D.R.Phelps, Dept. of Physics and Applied Physics, University of Strathclyde, Glasgow, G4 ONG, UK.

Th1.9 EFFECT OF BEAM GEOMETRIC DEFORMATION ON THE PROPERTIES OF ECRM - Yu Yongjian, University of Electronic Science and Technology, Dept. of Electronic Engineering, Chengdu, P.R. China.

Th1.10 DESIGN AND PERFORMANCE OF 94-GHZ HIGH POWER MULTICAVITY GYROKLYSTRON AMPLIFIER - I.I.Antakov, E.V.Zasypkin and E.V.Sokolov, Institute of Applied Physics, Russian Academy of Sciences, 46 Uljanov st., Nizhni Novgorod, 603600, Russia.

SESSION Th 2

Thursday AM — QUASI-OPTICAL COMPONENTS - III — September 9

Th2.1 ANALYSIS OF A DIODE MOUNTING STRUCTURE OF A SUB-HARMONICALLY PUMPED MILLIMETER-WAVE MIXER - S.D.Vogel, Institute of Applied Physics, Microwave Department, University of Bern, CH-3012, Bern, Switzerland.

Th2.2 TERAHERTZ METAL PIPE WAVEGUIDES - A.S.Treen and N.J. Cronin, School of Physics, University of Bath, Claverton Down, Bath, Avon. BA2 7AY, U.K.

Th2.3 NEW DEVELOPMENTS IN MILLIMETER WAVE BEAM CONTROL ARRAYS - T.Liu, X-H. Qin, F.Wang, L.Sjogren, C.W.Domier and N.C.Luhmann Jr., Dept. of Electrical Engineering, University of California at Los Angeles,, Los Angeles, California, U.S.A. 90024-1594.

Th2.4 DESIGN OF A MILLIMETER WAVE QUASI-OPTICAL OSCILLATOR - J. Bae, M. Akaishi, Y.Aburakawa and K. Mizuno, Research Institute of Electrical Communication, Tohoku University, 2-1-1 Katahira, Aoba-ku, Sendai 980, Japan.

Th2.5 LEAKY WAVE CORRUGATED DIELECTRIC ANTENNA FOR MILLIMETER WAVE APPLICATIONS - S.C.Shrivastava and A.K.Tiwari, Maulana Azad College of Technology, Bhopal - 462-007, India.

Th2.6 OPTIMIZATION OF COUPLING BETWEEN HE_{11}-WAVEGUIDE MODE AND GAUSSIAN BEAM - T.Graubner, W.Kasparek and H.Kumric, Institut für Plasmaforschung, Universität Stuttgart, Pfaffenwaldring 31, D-7000 Stuttgart 80, Germany.

Th2.7 SLOTLINE SURFACE-WAVE LEAKAGE AND SLOT ANTENNA PERFORMANCE - C.Letrou and V.Popescu. Institut National des Télécommunications, 91011 Evry, France.

Th2.8 MICROSTRIP RESONATOR USING HIGH-Tc SUPERCONDUCTING THIN FILM ON SAPPHIRE SUBSTRATES - O.D.Pustylnik, A.A.Dymnikov, I.V.Volnovsky and O.A.Khymenko, SRC "Fonon", 39 Pobedy Ave., KPI-3240, Kiev, Ukraine; V.F. Vratskikh, Institute for Thermophysics, Kutateladze 1, Novosibirsk 630090, Russia.

Th2.9 MICROWAVE SYSTEMS BASED ON THE EFFECT OF IMAGE MULTIPLICATION IN OVERSIZED WAVEGUIDES - G.G.Denisov, D.A.Lukovnikov and M.Yu.Shmelyov, Institute of Applied Physics, Russian Academy of Science, 46 Ulyanov Street, 603600 Nizhny Novgorod, Russia.

SESSION Th 3

Thursday AM	INSTRUMENTATION - II	September 9

Th3.1 TRANSMISSION-REFLECTION MEASUREMENTS FROM 8 GHZ TO THE THZ (*Invited Keynote*) - P.Goy, M.Gross and F. Beck*, AB Millimètre, 52 rue Lhomond, 75005 Paris, France, *Université de Lille 1, I.E.M.N., 59655 Villeneuve d'Ascq Cedex, France.

Th3.2 AN INTERFEROMETER FOR NEAR MILLIMETER WAVE DIELECTRIC STUDIES ON SOLIDS AT ELEVATED TEMPERATURES - J.R.Birch and E.A.Nicol, NPL, Teddington, Middx., TW11 OLW, UK.

Th3.3 WAVEFRONT DIVIDING INTERFEROMETER WITH AND WITHOUT MOVING PARTS - K.D.Möller, Department of Physics, New Jersey Institute of Technology, Newark N.J. 07102, Fairleigh Dickinson University, Teaneck, NJ 07666, USA.

Th3.4 MILLIMETER-WAVE BAND MICROWAVE SIGNAL SPECTRUM MEASUREMENT ON THE BASIS OF THE HILBERT TRANSFORM OF JOSEPHSON JUNCTION FUNCTION RESPONSE - S.Y.Larkin, S.E.Anischenko and V.V. Kamyshin, State Research Center "Fonon", 37, Pobedy Ave., KPI-3240, Kiev 252056, Ukraine.

Th3.5 A NEW METHOD FOR NETWORK ANALYZER CALIBRATION - A.Jöstingmeier*, A.v.Borzyszkowski**, G.Faby*, M.Jenett* and K.Schünemann*, *Technische Universität Hamburg-Harburg, Arbeitsbereich Hochfrequenztechnik, Postfach 90 10 52, D-W-2100 Hamburg 90, Germany, **Universität Hamburg, Institut für Angewandte Mathematik, Edmund-Siemers-Allee 1, D-W-2000 Hamburg 13, Germany.

SESSION Th 4

Thursday AM	SPECTROSCOPY - V	September 9

Th4.1 FAR INFRARED SPECTROSCOPY OF PHONONS AND PLASMONS IN SEMICONDUCTOR SUPERLATTICES *(Invited Keynote)* - T.Dumelow, A.A.Hamilton, T.J.Parker, S.R.P.Smith and D.R.Tilley, University of Essex, Colchester CO4 3SQ, UK.

Th4.2 FAR INFRARED OPTICS OF GaAs/AlAs SUPERLATTICES - A.A.Hamilton, T.Dumelow, T.J.Parker and D.R.Tilley, University of Essex, Colchester CO4 3SQ, UK.

Th4.3 INVESTIGATION OF PHONONS AND PLASMONS IN ALLOYS AND SUPERLATTICES COMPOSED OF InAs AND InSb - S.K.Kang[1], T. Knight[2], Y.B. Li[2], A.G. Norman[2], J.R. Birch[3], T.Dumelow[1], T.J.Parker[1], C.C. Phillips[2] and R.A. Stradling[2]; [1]Department of Physics, University of Essex, Colchester CO4 3SQ, UK; [2]Blackett Laboratory, Imperial College, London SW7 2BZ, UK; [3]National Physical Laboratory, Teddington TW11 OLW, UK.

Th4.4 CHARACTERISATION OF HYDROGENATED SILICON NITRIDE FILMS BY LOW TEMPERATURE FTIR SPECTROSCOPY - M.M.Pradhan and M.Arora, National Physical Laboratory, Dr. K.S. Krishnan Road, New Delhi 110012, India.

Th4.5 REFLECTANCE STUDY OF T.M.O. GLASSES - A.Memon, M.N.Khan, S.Al-Dallal, Department of Physics, University of Bahrain, and D.B.Tanner, Department of Physics, University of Florida, Gainsville, FL, USA.

Th4.6 THEORY OF MULTIPHONON ABSORPTION IN CRYSTALS AT IR AND MM RANGES - B.M.Garin, Institute of Radio Engineering and Electronics of the Russian Academy of Sciences, Vvedensky Square 1, Fryazino, Moscow region 141120, Russia.

Th4.7 A FEL STUDY OF RELAXATION BETWEEN BOUND DONOR STATE IN Si:P - K.K. Geerinck, J.E. Dijkstra, J.N. Hovenier, T.O. Klaassen, W.Th. Wenckebach, Faculty of Applied Physics, University of Technology Delft, The Netherlands; A.F.G. van der Meer and P.W. van Amersfoort, FOM Institute for Plasma Physics Rijnhuizen, Nieuwegein, The Netherlands.

Th4.8 FT-FIR MAGNETO-SPECTROSCOPY ON RESONANT BOUND POLARONS IN n-GaAs - A.J. van der Sluijs, K.K. Geerinck, T.O. Klaassen and W.Th. Wenckebach, Faculty of Applied Physics, Delft University of Technology, The Netherlands.

SESSION Th 5

Thursday PM | GYROTRON - IV | September 9

Th5.1 HIGH FREQUENCY, MEGAWATT GYROTRON EXPERIMENTS AT MIT - K.E.Kreischer, M.Blank, W.C. Guss, S.K.Lee and R.J.Temkin, MIT Plasma Fusion Centre, Cambridge, MA 01219, USA.

Th5.2 DESIGN CONSIDERATIONS FOR A 1 MW CW GYROTRON WITH AN INTERNAL CONVERTER - K.Felch, T.S.Chu, H.Huey, H.Jory, J.Neilson and R.Schumacher, Varian Associates, Inc., 811 Hansen Way, Palo Alto, CA 94304, USA; J.A. Lorbeck and R.J. Vernon, University of Wisconsin - Madison, Dept. of Electrical and Computer Engineering, 1415 Johnson Drive, Madison, WI 53706, USA.

Th5.3 MW/140 GHZ $TE_{10,4}$ GYROTRON WITH BUILT-IN HIGHLY EFFICIENT QUASIOPTICAL CONVERTER - E.Borie, G.Dammertz, G.Gantenbein, M.Kuntze, A.Möbius, H.-U.Nickel*, B.Piosczyk and M.Thumm*, Kernforschungszentrum Karlsruhe GmbH, ITP, Postfach 3640, 76021 Karlsruhe, Germany; *also Universität Karlsruhe, Institut für Höchstfrequenztechnik und Elektronik.

Th5.4 DESIGN OF A 3 MEGAWATT, 140 GHZ GYROTRON BASED ON A $TE_{21,13}$ COAXIAL CAVITY - M.E.Read, G.S.Nusinovich, O.Dumbrajs, H.Q.Dinh, D. Opie and G. Bird, Physical Sciences Inc., Alexandria, VA, 22314, USA; K.E.Kreischer and M.Blank , MIT, Cambridge, MA 02139, USA.

Th5.5 GHZ HARMONIC GYROKLYSTRON - G.P.Scheitrum, T.Bemis, T.A. Hargreaves and L.Higgins, Litton Systems Electronic Devices Division, San Carlos, CA 94070, USA.

Th5.6 DESIGN OF A 100 MW, 17 GHZ SECOND HARMONIC GYROKLYSTRON EXPERIMENT - P.E.Latham, W.Lawson, J.Calame, V.Specht, M.K.E.Lee, Q.Qian, M.Rimlinger and B.Hogan, University of Maryland, College Park, MD, USA.

Th5.7 HIGH POWER OPERATION OF A K-BAND SECOND HARMONIC GYROKLYSTRON - W.Lawson, H.W.Matthews, M.K.E.Lee, B.Hogan, J.P. Calame and J.Cheng, Electrical Engineering Department and Laboratory for Plasma Research, University of Maryland, College Park, MD 20742, USA.

Th5.8 WIDEBAND GYRO-TWT AMPLIFIER EXPERIMENTS - J.J.Choi*, G.S.Park¶, S.Y.Park¶, C.M.Armstrong, A.K. Ganguly, R.Kyser‖ and M.L.Bursanti, Naval Research Laboratory, Code 6840,Washington, DC 20375, USA; *SAIC, McLean, VA 22102; ¶Omega-P, Inc., New Haven, CT 06520; ‖B-K Systems, Inc., Rockville, MD 20850.

Th5.9 GYRO-TWT AMPLIFIERS AT UCLA - K.C.Leou, Q.S.Wang, C.K.Chong, A.J.Balkcum, S.N.Fochs, E.S. Garland, J. Pretterebner[a], A.T. Lin[b], D.B.McDermott, F.Hartemann and N.C.Luhmann Jr., Dept. of Electrical Engineering, University of California, Los Angeles, CA 90024, USA; [a]IMT GmbH, Heinrich-Baumann-Strasse 49, D-7000 Stuttgart 1, Germany; [b]Department of Physics, University of California, Los Angeles, CA90024, USA.

Th5.10 DEVELOPMENT OF MEDIUM POWER, SUBMILLIMETER WAVE GYROTRONS - T. Idehara, T. Tatsukawa, I. Ogawa, Y. Shimizu, S. Makino and K. Ichikawa, Department of Applied Physics, Faculty of Engineering, Fukui University, Fukui 910, Japan.

Th5.11 HARMONIC CONVERTERS FOR MEGAWATT-LEVEL 140 GHZ - RADIATION, A.K. Ganguly, Code 6841, Naval Research Laboratory, Washington, DC 20375; J.L.Hirshfield, Omega-P, Inc., 2008 Yale Station, New Haven, CT 06520; and Physics Dept., Yale Univ., New Haven CT 06511, USA.

SESSION Th 6

Thursday PM — QUASI-OPTICAL COMPONENTS - IV — September 9

Th6.1 IMPEDANCE MATCHING OF MICROSTRIP LINE CIRCUITS BY OPTICALLY TUNABLE STUBS - H.Shimasaki and M.Tsutsumi, Kyoto Institute of Technology, Matsugasaki, Sakyo-ku, Kyoto 606, Japan.

Th6.2 OPTICAL CONTROL OF MILLIMETER WAVES IN THE SILICON WAVEGUIDE - M.Tsutsumi, Kyoto Institute of Technology, Matsugasaki, Kyoto, Japan, and Y.Satomura, Osaka Institute of Technology, Omiya, Osaka, Japan.

Th6.3 QUASI-OPTICAL SWITCHING FOR MM-WAVE CAVITY DUMPING - G.M.Smith, J.C.G.Lesurf, Y.Cui and M.H. Dunn, University of St Andrews, Department of Physics and Astronomy, Fife KY16 9SS, Scotland.

Th6.4 PHASE SHIFT AND LOSS MECHANISM OF OPTICALLY EXCITED E-PLANE ELECTRON-HOLE PLASMA - Ao Sheng Rong and Zhong Liang Sun, State Key Lab. of Millimeter Waves, Department of Radio Engineering, Southeast University, Nanjing 210018, Jiangsu, P.R. China.

Th6.5 MULTIMODE ANALYSIS OF SUBMILLIMETRE-WAVE OPTICAL SYSTEMS - S.Withington, Cavendish Laboratory, Madingley Road, Cambridge, UK, and J.A.Murphy, Maybooth College, Co. Kildare, Ireland.

Th6.6 THE IMPLICATIONS OF PARTIALLY COHERENT SIGNAL BEAMS ON THE PERFORMANCE OF INTERFEROMETRIC SPECTROMETERS IN THE 30-800 GHZ RANGE - J.W.Bowen, Department of Physics, Queen Mary and Westfield College, University of London, London, E1 4NS, UK.

Th6.7 NON-LINEAR TRANSMISSION LINES USING MULTIPLE BARRIER VARACTOR DEVICES - W-M.Zhang, H.Shi, C.W.Domier and N.C.Luhmann Jr., Dept. Electrical Engineering, UCLA, Los Angeles, CA 90024-1594, USA.

Th6.8 MM-WAVE SPATIAL INTERFEROMETRY AS A PASSIVE ALTERNATIVE TO RADAR - J.C.G.Lesurf and M.R.Robertson, Dept. of Physics and Astronomy, University of St.Andrews, Fife, KY16 9SS, Scotland.

Th6.9 A SPECIAL 3-MIRROR QUASI-OPTICAL POWER COMBINING SYSTEM - Xie Wenkai and Liu Shenggang, University of Electronic Science and Technology of China, Chengdu, Sichuan 610054, P.R. China.

Th6.10 OPTIMIZATION CALCULATION OF 3-MIRROR AXISYMMETRIC QUASI-OPTICAL POWER COMBINING - Xie Wenkai, Cheng Zhixun, Liu Senggang, University of Electronic Science and Technology of China, Chengdu, Sichuan 610054, P.R. China.

SESSION Th 7

Thursday PM — **INSTRUMENTATION - III** — September 9

Th7.1 ADVANCES IN MEASUREMENTS WITH AN ALL-ELECTRONIC TERAHERTZ SPECTROSCOPY SYSTEM - D.W.Van Der Weide*, J.S.Bostak, B.A.Auld and D.M.Bloom, Edward L. Ginzton Laboratory, Stanford University, Stanford, CA 94305, USA, *Currently with Max-Planck-Institut für Festkörperforschung, Heisenburgstr. 1, D-7000 Stuttgart 80, Germany.

Th7.2 SOME RECENT APPLICATIONS OF THE FREE ELECTRON LASER (CLIO AND FELIX) IN SEMICONDUCTOR NONLINEAR OPTICS - C.R.Pidgeon, Heriot-Watt University, Riccarton, Currie, Edinburgh, UK.

Th7.3 QUASI-OPTICAL DEVICES FOR SUBMILLIMETER TECHNIQUE - V.B.Anzin, G.A.Komandin, G.V.Kozlov, S.P.Lebedev, A.N. Lipatov and A.A.Volkov, Institute for General Physics, Russian Academy of Sciences, Vavilov str., 38, 117942 Moscow, Russia.

Th7.4 BIAS PULSE MODULATOR FOR A HIGH POWER Kα BAND (26-40 GHZ) IMPATT OSCILLATOR - P.G.Frayne and C.W.T.Nicholls, Royal Holloway College, Egham, TW20 OEX, Surrey, UK.

Th7.5 MICROWAVE SPECTROMETERS FOR THE INVESTIGATION OF FAST PROCESSES IN THE TIME DOMAIN - A.B. Brailovsky, V.V. Khodos, V.L.Vaks, A.N.Panin, S.J.Pripolzin and F.Wolf, Analytik & Meβtechnik GmbH Chemnitz, Stollberger Str. 4a, D-09119 Chemnitz, Germany.

Th7.6 A FREQUENCY-STABILISED MICROWAVE GENERATOR FOR INVESTIGATIONS OF ABSORPTION LINES OF WATER - V.L.Vaks and S.J.Pripolsin, Analytik & Meβtechnik GmbH Chemnitz, Stollberger Str. 4a, D-09119 Chemnitz, Germany.

Th7.7 QUASI-OPTICAL METHOD FOR MOISTURE MEASUREMENTS OF GASES - A.A.Vertiy and S.P.Gavrilov, Inst. Radiophysics and Electronics, Academy of Sciences of Ukraine, 12 Acad. Proskura st., Kharkov 310085, Ukraine.

Th7.8 METHOD AND MEASUREMENT COMPLETE SET FOR NON-DESTRUCTIVE LOCAL PARAMETER MICROWAVE MEASUREMENTS OF MATERIALS - A.A. Zvyagintsev and A.V. Strizhachenko, University, Freedom Sq., 4, 310077, Kharkov, Ukraine.

Th7.9 FREQUENCY STABILIZED MILLIMETER WAVE PULSED IMPATT OSCILLATORS IN AUTO-OSCILLATED AND INJECTION-LOCKED MODES (DESIGNING AND INVESTIGATION) - A.V. Gorbachev, L.V. Kasatkin, V.V. Novozhilov and M.I. Poigina, Research Institute "ORION", Kiev, Ukraine, p.o. 252057.

Th7.10 SOLID-STATE 8-MM WAVE TRANSCEIVER WITH PULSE-TO-PULSE SWITCHING OF OPERATING FREQUENCIES (INVESTIGATION AND DESIGNING) - A.V. Gorbachev, L.V. Kasatkin, V.A. Sackov, I.N. Homenko and I.V. Zverghovsky, Research Institute "ORION", Kiev, Ukraine, p.o. 252057.

SESSION Th 8

Thursday PM	SPECTROSCOPY - VI	September 9

Th8.1 SURFACE LAYERS AND FAR INFRARED SPECTRA OF HIGH-T_c SUPERCONDUCTORS (*Invited Keynote*) - X.Gerbaux, A.Hadni and M.Tazawa*, Laboratoire Infrarouge Lointain, L.M.C.P.I., U.R.A. - C.N.R.S. no.809 B.P.239, F-54506 Vandœuvre-les Nancy Cedex, France; *GIRI, Nagoya, 1, Hirate cho, Nagoya 462, Japan.

Th8.2 MEASUREMENTS ON THE FAR INFRARED LASER TRANSMISSION OF $Y_1Ba_2Cu_3O_{7-\delta}$ THIN FILMS - T.P.O'Brien, M.L.McConnell, P.G.Huggard, Gi. Schneider and W.J.Blau, Physics Department, Trinity College, Dublin, Ireland.

Th8.3 FAR INFRARED ELLIPSOMETRIC STUDY OF HTSC GAP IN AB- AND C-ORIENTED EPITAXIAL YBaCuO FILMS - A.B.Sushkov* and E.A. Tishchenko, P.L. Kapitza Institute for Physical Problems, Russian Academy of Science, Kosygina str. 2, 117973 Moscow, Russia; *Institute of Spectroscopy, Russian Academy of Science, 142092 Troitzk, Moscow region, Russia.

Th8.4 SUBMILLIMETER WAVE ESR OF COPPER-OXIDES - H.Ohta and M.Motokawa, Dept. of Physics, Faculty of Science, Kobe University, Rokkodai, Nada, Kobe 657, Japan.

Th8.5 MILLIMETER WAVES SCANNING - NEW METHODS AND POSSIBILITIES INVESTIGATING THE HIGH TEMPERATURE SUPERCONDUCTORS - M.N.Kotov*, V.F. Masterov**, A.V.Prichodko* and O.V.Smertin*, *Microwave Laboratory, Semiconductor Physics Institute, 11 A. Gostauto str., Vilnius 2600, Lithuania; **Experimental Physics Dept., State Technical University, 29 Politechnitcheskaja str., St. Petersburg, Russia.

Th8.6 LOCAL AND NON-DESTRUCTIVE DIAGNOSTICS OF HIGH-T_c SUPERCONDUCTOR LAYERS BY MILLIMETER WAVES - A.Laurinavičius, F.Anisimovas, A. Deksnys, V.Lisauskas and B.Vengalis, Semiconductor Physics Institute, Gostauto 11, 2600 Vilnius, Lithuania.

SESSION F1

Friday AM	GYROTRON - V	September 10

F1.1	COLLECTIVE MM-WAVE SCATTERING TO MEASURE FAST ION AND ALPHA-PARTICLE DISTRIBUTIONS IN JET (*Invited Keynote*) - J.A.Hoekzema, A.E.Costley, T.P.Hughes, J.A. Fessey, N.P.Hammond, H.Oosterbeek, P.Roberts, A.L.Stevens, P.E. Stott and W. Suverkropp, JET Joint Undertaking, Abingdon, Oxfordshire, OX14 3EA, UK.
F1.2	STATE OF THE ART OF GYROTRON INVESTIGATION IN RUSSIA (*Invited Keynote*) - V.A.Flyagin, A.L.Goldenberg and V.E.Zapevalov, Institute of Applied Physics, Russian Academy of Sciences, 46 Uljanova st, Nizhni Novgorod, 603600, Russia.
F1.3	THE TRANSMISSION LINES AND ANTENNAS OF THE TORE SUPRA ECRH SYSTEM - F.M.A.Smits, G. Berger-by, G. Bon Mardion, J.-J. Capitain, D. Chatain, J.-J. Cordier, J.P. Crenn, L. Doceul, M. Pain, G.-F. Tonon, A. Dubrovin*, P. Garin* and J.M. Krieg*, Association CEA-Euratom sur la Fusion Contrôlée, CEN-Cadarache, F-13108 St.Paul-lez-Durance CEDEX, France; *Thomson Tubes Electroniques, 2, Rue Latécoère, 78141 Vélizy-Villacoublay, France.
F1.4	MM-WAVE TRANSMISSION IN THE FAST ION AND ALPHA-PARTICLE DIAGNOSTIC AT JET - J.A.Hoekzema and N.P.Hammond, JET Joint Undertaking, Abingdon, Oxfordshire, OX14 3EA, UK.
F1.5	OPTIMIZATION OF AN OVERMODED SMOOTH-WALL CIRCULAR WAVEGUIDE SECTION FOR CARRYING STRONG MM-WAVE POWER IN ECRH EXPERIMENTS - F.Billè*, G. Granucci**, L.Manià*, A. Simonetto** and G.Viciguerra*, *DEEI, Università di Trieste, Via A. Valerio 10, 34127, Trieste, Italy; **Istituto di Fisica del Plasma, Associazione EURATOM-ENEA-CNR, Via Bassini 15, 20133, Milano, Italy.
F1.6	RADIATION PATTERNS AND OPTIMIZATION OF BEAM EXCITATION OF HIGHLY OVERMODED CORRUGATED RECTANGULAR WAVEGUIDES - B.C.Brown, J.A.Lorbeck and R.J.Vernon, Department of Electrical and Computer Engineering, The University of Wisconsin - Madison, Wisconsin 53706, USA.
F1.7	CONDITIONING OPTICS FOR ASTIGMATIC GAUSSIAN BEAMS AT 140 GHZ, 0.5 MW - A.Bruschi, S.Ciraut, G.Granucci, A.Simonetto and G.Solari, Istituto di Fisica del Plasma, EURATOM/ENEA/CNR Association, Via Bassini 15, 20133, Milano, Italy.
F1.8	A PROPOSAL FOR A CALORIMETRIC LOAD AT 140 GHZ FOR HIGH POWER HE11 TRANSMISSION LINES - L.Argenti, A.Bruschi, S.Cirant and G.Solari, Istituto di Fisica del Plasma, EUROTOM/ENEA/CNR Association, Via Bassini 15, 20133, Milano, Italy.
F1.9	DIFFRACTION RADIATION OSCILLATORS FOR HIGH-TEMPERATURE PLASMA DIAGNOSTICS AND SPECTROSCOPY - V.P.Shestopalov, B.K.Skrynnik, I.D.Revin and G.P.Ermak, Institute of Radiophysics and Electronics of the Ukrainian Academy of Sciences, 12 Acad. Proskura st., Kharkov, 310085, Ukraine.

SESSION F2

Friday AM — ASTRONOMICAL AND ATMOSPHERIC SYSTEMS — September 10

F2.1 TELESCOPE DESIGN STUDY FOR THE NASA STRATOSPHERIC OBSERVATORY FOR INFRARED ASTRONOMY (SOFIA) - G.W.Sutton, H.M. Martin*, Hans Kärcher** and Kent Pflibsen, Kaman Aerospace Corporation, Optical Development Center, Tucson, AZ 85706, *Steward Observatory Mirror Laboratory, University of Arizona, Tucson, Arizona, **MAN GHH, Gustavsburg, Germany.

F2.2 A 380 GHZ SIS HETERODYNE SPECTROMETER FOR "PRONAOS" (BALLOON BORNE EXPERIMENT FOR SUBMILLIMETER RADIOASTRONOMY) - G.Beaudin,* A.Deschamps,* P. Encrenaz**, P.Febvre*, P. Feautrier**, C. Gac*, M.Gheudin,* B.Léridon,* R.Maoli,* D. Michet*, J.C. Pernot**, C.Robert*, C. Rosolen*, G.Ruffié,* and P. Vola*, *Observatoire de Paris-Meudon, 5 place Jules Janssen, 92195 Meudon, France, **Ecole Normale Supérieure, Laboratoire de Radioastronomie, 24 rue Lhomond, 75005 Paris, France.

F2.3 A COST EFFECTIVE TOTAL POWER RADIOMETER PACKAGE FOR ATMOSPHERIC RESEARCH - B.N.Lyons, W.M.Kelly, D.R.Vizard and U.S.Lidholm, Farran Technology Ltd., Ballincollig, Co.Cork, Ireland.

F2.4 IR DETECTORS FOR SPACEBORNE APPLICATIONS - Y.V.Munro and D.Hickman, Matra Marconi Space UK LTD, Anchorage Road, Portsmouth, UK.

F2.5 QUASI-OPTICAL TRIPLEXING FEED FOR SPACECRAFT RADIOMETER - R.J.Martin and W.J.Hall, BAe Space Systems, Bristol, UK.

F2.6 THE ISO LONG-WAVELENGTH SPECTROMETER - P.E.Clegg, Department of Physics, Queen Mary and Westfield College, London E1 4NS, UK.

F2.7 REFLECTOR AND MIRROR SYSTEMS FOR SUBMILLIMETER AND INFRARED TELESCOPES - AN OVERVIEW OF TECHNOLOGY AND COSTS - Hans J.Kärcher, MAN GHH, Gustavsburg, Germany.

F2.8 A HORIZONTAL ATMOSPHERIC TEMPERATURE SOUNDER BASED ON THE 60 GHZ OXYGEN ABSORPTIONS - R.W.McMillan, Georgia Institute of Technology, Georgia Tech Research Institute, Atlanta, Georgia 30332, USA.

F2.9 A SUBMILLIMETER-WAVE SENSOR FOR TRACE GAS STUDIES IN THE MIDDLE ATMOSPHERE - H. Nett, S. Crewell and K. Künzi, University of Bremen, FB 1, Institute of Remote Sensing, P.O. Box 330440, 2800 Bremen 33, FRG.

F2.10 GROUND-BASED MILLIMETER-WAVE MONITORING OF STRATOSPHERIC OZONE AT ALTITUDES ABOVE 20 KM - A.A. Krasil'nikov, Yu. Yu. Kulikov, and L.I. Fedoseev, Institute of Applied Physics of the Russian Academy of Sciences, 46 Ul'janov Str., Nizhny Novgorod, 603600, Russia.

SESSION F3

Friday AM	SPECTROSCOPY - VII	September 10

F3.1 FAR INFRARED SPIN RESONANCE IN II-VI D.M.S. (*Invited Keynote*) - J.L.Martin*, M.Goiran*, Z. Golacki**, J.Léotin* and S.Askenazy*, *Service des Champs Magnetiques Intenses, INSA, Complexe scientifique de Rangueil, 31077 Toulouse-Cedex, France; **Institute of Physics, Polish Academy of Sciences, 32/46 Al. Lotnikow, 02668 Warsaw, Poland.

F3.2 SUBMILLIMETER SPECTROSCOPY OF THE ELECTRON EXCITATIONS IN RARE-EARTH ORTHOFERRITES (*Invited Keynote*) - G.V.Kozlov, S.P.Lebedev, A.A.Mukhin, A.S.Prokhorov and A.A. Egoyan, General Physics Institute, Russian Academy of Sciences, 38 Vavilov St., Moscow 117942, Russia.

F3.3 PROGRESS IN GERMAN HIGH FIELD MAGNETO SPECTROSCOPY USING IR, FIR, AND MM WAVES: A QUANTUM TRANSITION FROM THE HOCHMAGNETFELDANLAGE IN BRAUNSCHWEIG TO THE HUMBOLDT HIGH MAGNETIC FIELD CENTER IN BERLIN (*Invited Keynote*) - M. von Ortenberg and coworkers, HUMBOLDT Universität zu Berlin and Technische Universität Braunschweig, Germany.

F3.4 ORIGIN OF SATELLITE STRUCTURES OF HIGH FIELD EPR IN $Cd_{1-x}Mn_xTe$ - G.Eilers*, M. von Ortenberg and R. Galazka**, Institut für Halbleiterphysik und Optik, Technische Universität Braunschweig, 3300 Braunschweig, Germany; **Polish Academy of Science, Institute of Physics, Warsaw, Poland.

F3.5 INFRARED REFLECTIVITY OF SEMICONDUCTOR MAGNETOPLASMAS - F. Elmzughi and D.R. Tilley, University of Essex, Colchester CO4 3SQ, UK.

F3.6 INFRARED REFLECTIVITY CALCULATIONS FOR RARE-EARTH METALS - K. Abraha and D.R. Tilley, University of Essex, Colchester CO4 3SQ, UK.

F3.7 HIGH RESOLUTION FTS STUDY OF MAGNETIC COMPOUNDS - M.N.Popova, Institute of Spectroscopy, Russian Academy of Sciences, 142092 Troitzk, Moscow region, Russia.

F3.8 FAR INFRARED STUDIES OF MAGNETIC SYSTEMS - T.Dumelow, D.E.Brown and T.J.Parker, Department of Physics, University of Essex, Colchester CO4 3SQ, UK.

F3.9 FIR-STUDY OF $TbPO_4$ - P.Janssen and P.Bruelemans, Katholieke Universiteit Leuven, Belgium.

F3.10 TIME-RESOLVED FAR INFRARED MAGNETOSPECTROSCOPY OF ULTRA-HIGH MOBILITY n-GaAs LAYERS AND GaAs/AlGaAs MULTI QUANTUM WELLS - R.E.M. de Bekker[+], J.M. Chamberlain*, M.B. Stanaway*, P. Wyder[+], C.R. Stanley** and M. Henini*, [+]MPI/HML, Boite Postale 166X, F-38042 Grenoble Cedex, France; *Physics Department, Nottingham University, Nottingham, NG7 2RD, England; **Department of Electronic & Electrical Engineering, Glasgow University, Glasgow G12 8QQ, Scotland.

F3.11 INFRA-RED CYCLOTRON RESONANCE OF 'CROSSED' BAND GAP SUPERLATTICES AT MAGNETIC FIELDS OF UP TO 150T - D.J. Barnes*#, R.J. Nicholas[+], R.J. Warburton,[+] N.J. Mason,[+] P.J. Walker [+] and N. Miura*, *Institute of Solid State Physics, Roppongi 7-22-1, Tokyo 106, Japan; [+]Physics Dept., Clarendon Laboratory, Parks Road, Oxford OX1 3PU, U.K; #Present address: Physics Dept., Geschwister-Scholl-Platz 1, University of Munich, 8000 Munich 22, Germany.

AUTHOR INDEX

AUTHOR INDEX

AUTHOR INDEX

AUTHOR INDEX

AUTHOR INDEX

AUTHOR INDEX

AUTHOR INDEX

AUTHOR INDEX

AUTHOR INDEX

AUTHOR INDEX

AUTHOR INDEX

AUTHOR INDEX

AUTHOR INDEX

Submillimetre Waves - the Early Years

M.F. Kimmitt,
Department of Physics, University of Essex, Colchester CO4 3SQ,, U.K.

'If I have seen further it is by standing on the shoulders of giants.' Sir Isaac Newton.

It has been rightly pointed out that such has been the expansion of science in the twentieth century that well over 50% of scientists known to history are still alive today. Indeed, in a wondrously mixed metaphor, one present-day researcher has stated that "In the sciences, we are now uniquely privileged to sit side by side with the giants on whose shoulders we stand." And nowhere is that more true than in the field of research covered by this Conference. Those of us whose far-infrared experience reaches back to the 1950s will remember that virtually the only source we had was a mercury arc lamp and the only detector was a Golay. There were no books and just a handful of relevant papers. Even by 1970 the authors of the introductory paper at the Brooklyn Symposium on Submillimeter Waves were writing "It is appropriate to view the submillimeter wave region as a transition region lying between the millimeter wave and infrared portions of the electromagnetic spectrum and possessing as yet no hallmark of its own". That was perhaps a pessimistic summary, as there were nearly sixty papers at that meeting. Now that we have an annual conference - this one with over three hundred papers - I think we can say that what used to be called the 'unexplored region' is being fully explored.

However, there was an early golden age of far infrared and millimetre wave research which began almost exactly one hundred years ago and culminated in the 1920s with the joining of the infrared to what was then called the electric wave spectrum. To mark this centenary it is surely appropriate to highlight some of the achievements of the first workers in our field. The giant figure in the early years was Rubens, working in Berlin. But there were several others of great importance, including Nichols, who worked with Rubens before the turn of the century and in his later years developed millimetre wave sources, and R W Wood, the inventor of the blazed diffraction grating. Wood was one of the great researchers of this century and his book, 'Physical Optics', was the pioneering text on modern optics. He was always quick to give credit to earlier research and points out that the possibility of making gratings that concentrate most of the light into a single order was first suggested by Lord Rayleigh. We, who work at the University of Essex, are proud that Rayleigh was an Essex man and the Rayleigh-Jeans formula for black-body radiation will be much in evidence during the Conference. It is with black-body emission that this talk will begin, for I think it is not sufficiently realised that it was Rubens' work in the long wavelength infrared region which provided the experimental evidence which led Max Planck to derive his radiation law and lay the foundation for quantum theory.

A major problem engaging the attention of physicists during the closing years of the last century was that of the radiation from a black-body. Wien had found a formula which represented the observed data very well for small values of the product of wavelength and absolute temperature. In 1900 Rayleigh suggested from classical considerations that the energy should vary as $T\lambda^{-4}$ (T is absolute temperature and λ is wavelength) but clearly this could not be correct at short wavelengths, as it led to what was called the 'ultraviolet catastrophe'. Later Rayleigh and Jeans came to the exact formula which now bears their names.

It is clear that Rayleigh felt that experimental data was needed for the energy emitted where the product of wavelength and temperature was large. Larmor, a contemporary of Rayleigh, states that Rayleigh asked Rubens to measure the variation of energy at long wavelengths and he, with Kurlbaum, confirmed the $T\lambda^{-4}$ relationship by working out to 51 μm over a temperature range from 85-1173K. Planck, who had for some time been struggling with the Wien formula, learned of this experimental agreement with Rayleigh's prediction, and derived his formula empirically to fit both the short and long wavelength results. He then went on - genius that he was - to look for a physical explanation, and this led to his introduction of quantum oscillators. It seems likely that Planck had already been feeling his way towards quantum theory but there appears to be no doubt that it was after Rubens' precise measurements that he finally went beyond the logic of classical physics for an explanation.

Research which contributed to the development of quantum theory must certainly be the outstanding achievement of early far-infrared experiments, but there were other significant developments which will be discussed in this paper. This talk will not only be about the research but also about the researchers. For example, R W Wood was a great practical joker; he was also instrumental in the downfall of the notorious N-ray research and it was Rubens who persuaded him to expose the delusion that N-rays existed. Nichols was another giant who did much more than infrared research. He was an outstanding experimenter and perhaps his greatest achievement was to measure radiation pressure. He was also brave enough to move from research to be a College President, then go back to research when he found administration not to his liking, and he has the unique honour of writing the very first paper in Physical Review. He died as he had lived. While presenting a paper in 'Joining the Infrared and Electric Wave Spectra' before his peers at the National Academy of Sciences in Washington in 1924 such a long pause occurred in his delivery that the chairman finally walked to the podium, to find that Nichols had died of a heart attack while standing before them, propped up by the dais.

Rocket Measurement of the Submillimeter Cosmic Background Spectrum

H.P. Gush, E.H. Wishnow and M. Halpern
Department of Physics, U.B.C. Vancouver, B.C. Canada,V6T1Z1

Abstract

The spectrum of the cosmic background radiation (CBR) has been measured using a liquid helium cooled spectrometer carried to high altitude by a rocket. The spectrum in the frequency band 2 to 30 cm-1 is very well fitted by a Planck function of temperature T=2.736K. The estimated experimental accuracy of the mean temperature is +/- 17 mK.

Introduction

The cosmic background radiation (CBR), being one of the oldest quantities accessible to measurement, has been recognized as a very important observable in cosmology since its discovery in 1965.[1,2] Substantial experimental effort has been devoted in the past 25 years to investigating the properties of this radiation. The information to be gained is very important to an understanding of the early universe but experimental difficulties have been such that definitive measurements have been obtained only recently.[3,4]

This paper describes the principle of operation and the results of the rocket spectrometer COBRA which was used to make a successful measurement of the CBR spectrum in 1990. Further detail can be found in some other publications.[5,6]

The apparatus

Based on experience gained in earlier attempts to measure the spectrum of the CBR from high altitude,[7-9] a new rocket instrument was developed and tested during the 1980's. The instrument is shown schematically in Fig.1. Radiation from the sky is directed to one

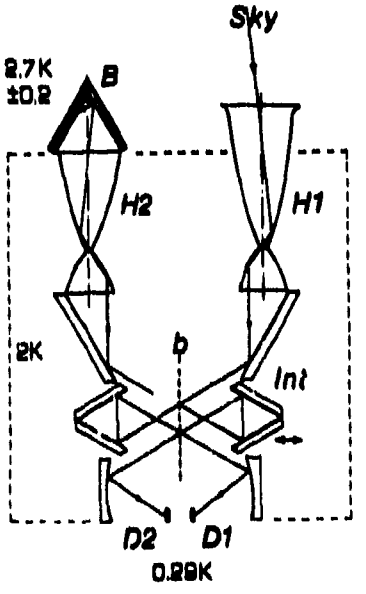

Fig. 1. A diagram showing the principle of the apparatus. **H1** and **H2** are similar horn telescopes of 6^0 field of view. **H1** receives radiation from the sky whereas **H2** is illuminated by a black body simulator **B**. Radiation issuing from the horns enters a two-beam interferometer **Int**, with a beamsplitter at **b**, from whence it emerges to be focussed on two bolometer detectors **D1** and **D2**. As the path difference in the interferometer is changed the signal generated by each detector (interferogram) is proportional to the difference intensity of the sky and the black body. The numbers indicate temperatures of various sections of the spectrometer.

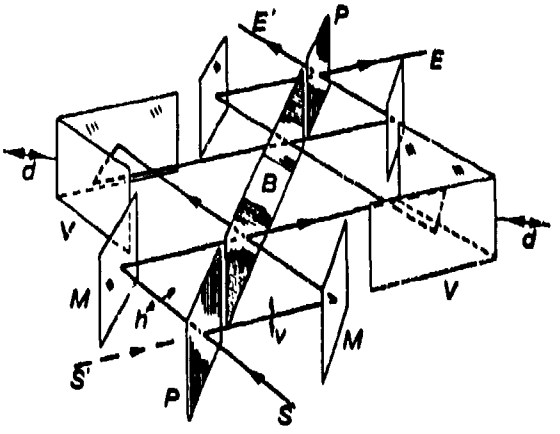

Fig. 2. A schematic diagram of the polarization interferometer. Radiation from a source at S is split by the wire grid polarizer P into vertically and horizontally polarized beams (v and h). Flat mirrors M direct these beams through the interferometer itself, which consists of the oblique wire grid beamsplitter B, and the two dihedral mirror pairs V. Optical delay in the interferometer is varied by simultaneous displacements d of both dihedral pairs as shown. The exit beams, E and E', are formed by directing the interferometer outputs through a vertical analysing polarizer P. The path from the second source at S' entirely overlaps the radiation path shown here, after the input analysing polarizer. The modulated signals at E and E' contain information about the brightness difference between S and S', and are independent of source polarization.

side of a symmetric two-beam interferometer by means of a hyperbolic horn telescope. The second side of the interferometer is illuminated by an identical telescope terminated, however, with a black body simulator whose temperature can be controlled. By moving the pair of dihedral mirrors, a variable path difference is introduced in the interferometer, and the signal given by each detector is an interferogram whose Fourier transform is proportional to the spectrum of the intensity *difference* between the sky and the calibrator. If the sky spectrum is Planckian of the same temperature as the calibrator, there is a null signal. The absolute sensitivity of the instrument is obtained by periodically changing the temperature of the calibrator by steps of 0.2K near 2.7K, the approximate expected temperature of the CBR. This procedure allows one to calculate the sky emission spectrum without achieving a null interferogram and without reference to pre or post flight calibration data.

The interferometer is of the polarizing type, the optical arrangement being shown in Fig.2. It is a modification of an early design used in mid-infrared aeronomy measurements.[10] The principal merit of the design in the present context, apart from uniform frequency response and good efficiency, is that the instrument is highly symmetric. This is important because one would like to obtain truly null interferograms when the sky and the calibrator have the same temperature. This ideal was closely approached.The balance was tested in the laboratory by introducing a variable temperature liquid helium cooled black body over the sky telescope, and setting its temperature equal to the internal calibrator temperature. Small offset interferograms corresponding to temperature shifts of about 50mK were measured which are subtracted from the sky interferograms before calculating final spectra.

Results

Fig. 3 shows a set of interferograms recorded during the flight, as well as the derived sky spectrum. The spectrum is very

well fitted by a Planck curve of temperature 2.736K The error on the temperature is conservatively estimated to be +/-0.017K. Our value for the temperature agrees well with the most recent value evaluated from the COBE satellite data, 2.726+/-0.010K.[11]

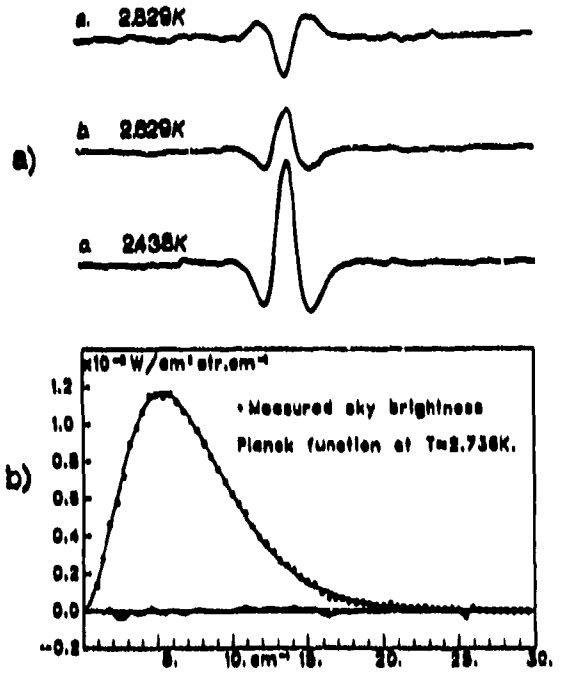

Fig. 3. a) Interferograms obtained late in the flight, shown as detector voltage vs. optical path difference for three different temperatures of the internal black body. The sign inversion between a) and b) indicates that the sky spectrum lies between Planck functions of 2.63K and 2.83K. Approximately one minute of data are shown here.
b) The intensity of the sky as a function of wavenumber derived from the shown interferograms. The smooth curve is a Planck function which fits the data well. The residuals are shown oscillating along the abscissa axis.

The instrument was recovered from the launch and it is currently being refurbished and modified to make CBR anisotropy measurements from balloon altitudes. In this case the internal calibrator is removed. By means of a suitable optical system and telescope the two input channels of the interferometer are focussed on two regions of the sky separated by a few degrees. This will permit the *spectrum* of the observed anisotropy to be measured which will be of help in discriminating against foreground sources.[12]

References

1. R.H. Dicke, P.J.E. Peebles, P.G. Roll and D.T. Wilkinson, Astrophys. J. 142, 414 (1965).
2. A.Z. Penzias and R.W. Wilson, Astrophys. J. 142, 419 1965).
3. H.P. Gush, M. Halpern and E.H. Wishnow, Phys. Rev. Lett. 65, 537 (1990)
4. J.C. Mather, E.S. Cheng, R.E. Eplee, R.B. Isaacman, S.S. Meyer, R.A. Shafer, R. Weiss, E.L. Wright, C.L. Bennett, N.W. Boggess, E. Dwek, S. Gulkis, M.G. Hauser, M. Janssen, T. Kelsall, P.M. Lubin, S.H. Moseley, Jr., T.L. Murdock, R.F. Silverberg, G.F. Smoot, and D.T. Wilkinson, Astrophys. J. Lett. 354, L37 (1990).
5. M. Halpern, H.P. Gush, and E.H. Wishnow in "After The First Three Minutes", AIP Conference Proceedings 222, edited by S.S. Holt, C.L. Bennett, & V. Trimble, p 53, 1991.
6. H.P. Gush and M. Halpern, Rev. Sci. Instrum. 63, 3249 (1992).
7. H. Gush, Can. J. Phys. 52, 554 (1974).
8. H. Gush, Phys. Rev. Lett. 47, 745 (1981).
9. H. Gush in "Gamow Cosmology", edited by F. Melchiorri and R. Ruffini (Italian Physical Society, Bologna, Italy) p260, 1986.
10. R. MacDonald, H.L. Bulja and H.P. Gush, Can. J. Phys. 46, 2575 (1968).
11. J.C. Mather, E.S. Cheng, D.A. Cottingham, R.E. Eplee, Jr., D.J. Fixen, T. Hewagama, R.B. Isaacman, K.A. Jensen, S.S. Meyer, P.D. Noerdlinger, S.M. Read, L.P. Rosen, R.A. Shafer, E.L. Wright, C.L. Bennett, N.W. Boggess, M.G. Hauser, T. Kelsall, S.H. Moseley, Jr., R.F. Silverberg, G.F. Smoot, R. Weiss and D.T. Wilkinson, COBE preprint no. 93-01 (1993).
12. M. Halpern, H.P. Gush, I. Shinkoda, G.S. Tucker and W. Towlson in "Proceedings of the 16th Texas Symposium on Relativistic Astrophysics", edited by C. Akerlof and M. Srednicki, New York Academy of Sciences (1993).

Progress in Development of High Power Gyrotrons

M. Thumm*
Kernforschungszentrum Karlsruhe, Institut für Technische Physik
*also Universität Karlsruhe, Institut für Höchstfrequenztechnik und Elektronik
D-7500 Karlsruhe 1, Germany

1. INTRODUCTION

Gyrotrons are microwave oscillators based on the Electron Cyclotron Maser (ECM) instability. The free energy is the rotational energy of weakly relativistic electrons ($1 < \gamma \leq 1.2$) in a longitudinal magnetic cavity field. A net transfer of energy from the gyrating electrons to the electromagnetic field in the interaction circuit occurs due to the azimuthal phase bunching when the wave frequency is somewhat larger than the relativistic electron cyclotron frequency Ω or its harmonics. Many other types of microwave sources are also based on the ECM instability, such as gyro-klystron, gyro-travelling wave amplifier (gyro-TWA) or gyro-backward wave oscillator (gyro-BWO). Cyclotron maser devices operating in the relativistic Doppler-shifted regime where the axial bunching mechanism can substancially offset the azimuthal bunching are called cyclotron autoresonance maser (CARM).

2. GYROTRONS FOR FUSION PLASMA APPLICATIONS

At present, gyrotron oscillators are mainly used as high power millimeter wave sources for electron cyclotron resonance heating (ECRH) and diagnostics of magnetically confined plasmas in controlled thermonuclear fusion research [1,2]. Long-pulse and CW gyromonotrons utilizing open-ended cylindrical resonators which generate output powers of 100-400 kW per unit, at frequencies between 28 and 84 GHz, have been used very sucessfully for plasma formation, electron cyclotron resonance heating (ECRH) and local current density profile control by noninductive current drive (ECCD) in tokamaks [1] and stellarators [2]. Gyrotron complexes with total power of up to 4 MW are used . The confining toroidal magnetic fields in present day fusion machines are in the range of B_0=1-3.5 Tesla. As experimental devices become larger and operate at higher magnetic fields (B_0=5T) and higher plasma densities (n_{e0}=1-2 · $10^{20}/m^3$) in steady state, present and forthcoming ECH requirements call for gyrotron output powers of at least 1 MW,CW at frequencies ranging from 100-180 GHz. Since efficient ECRH and ECCD needs axisymmetric, narrow, pencil-like mm-wave beams with well defined polarization, single mode emission is necessary in order to generate a TEM_{00} Gaussian beam mode at the plasma torus launching antenna .

Single mode mm-wave gyrotron oscillators capable of high average power, 0.5-1 MW per tube, in long-pulse or CW operation, are currently under development in several scientific and industrial laboratories. The present state of the art at 140 GHz is given in Table I. 140 GHz gyrotrons with output power P_{out} = 0.6 MW, pulse length τ = 2.0 s and efficiency η = 34 % are commercially available. The worldwide first ECRH and ECCD experiments at 140 GHz have been performed in the Stellarator W7-AS [5]. Diagnostic gyrotrons deliver P_{out} = 40 kW with τ = 40 µs at frequencies up to 650 GHz ($\eta \geq 4$ %).

Institution	Mode cavity	Mode output	Power (MW)	Efficiency (%)	Pulse length (s)
KfK, Karlsruhe, PHILIPS, Hamburg	TE_{03}	TE_{03}	0.12	23	0.4
KfK, Karlsruhe	$TE_{10,4}$	$TE_{10,4}$	0.69	29	0.005
SALUT, IAP, Nizhny Novgorod	$TE_{22,6}$	TEM_{00}	0.9 0.5	36 36	0.3 0.55
TORIY, Moscow, IAP, Nizhny Novgorod	$TE_{22,5}$	TEM_{00}	0.97 0.58	34 34	0.3 2.0
VARIAN, Palo Alto	$TE_{02/03}$ $TE_{15,2}$	TE_{03} $TE_{15,2}$	0.1 0.26 0.33 1.04	27 28 28 38	CW 5.0 2.5 0.0005

Table I: Present development status of 140 GHz gyrotron oscillators for fusion plasma EC Wave applications.

With increasing operating frequency, power level and pulse duration a number of problems arise which necessitate significant changes in the gyrotron design approach. The main difficulties encountered in the realization of efficient megawatt CW mm-wave gyrotrons for fusion reactors (120 GHz to 200 GHz) are connected with:

- formation of an electron beam with sufficient orbital energy ($\alpha \geq 1.5$) and small velocity spread (electron gun design)
- propagation of the electron beam, spurious oscillations in the beam tunnel between the electron gun and the interaction cavity, voltage depression (dependent on the ratio of electron beam radius to cavity radius), space charge effects and beam instabilities
- ohmic wall losses in the cavity (cavity heating)
- mode selectivity in a highly overmoded cavity, single mode operation, good mode separation of working mode from competing modes
- unwanted mode conversion in the electrodynamic system of the tube
- thermal loading of the electron beam collector
- heating of the output window, selection of output mode
- enhancement of total system efficiency up to 50-60 %.

Design trade-offs and operating limits are necessary. This paper reports on achievements and problems related to the development of very high power mm-wave gyrotrons for long-pulse or CW operation and describes the microwave technological peculiarities of the different approaches as e.g. conventional gyrotrons with cylindrical cavity (without or with internal mode converter), second harmonic gyrotrons and quasi-optical gyrotrons.

3. GYROTRONS FOR INDUSTRIAL APPLICATIONS

Recently, gyrotron oscillators also are successfully utilized in material processing (e.g. advanced ceramic sintering, surface hardening or dielectric coating of metals and alloys) as well as in plasma chemistry [3]. Such technological applications require gyrotrons with the following parameters: $f \geq 28$ GHz, $P_{out} = 10\text{-}30$ kW, CW, $\eta \geq 30$ %. The use of gyrotrons appears to be of interest if one can realize the relatively simple, low cost device which is easy in service (such as a magnetron). Gyrotrons with low magnetic field (operating at the 2nd harmonic of the electron cyclotron frequency), low anode voltage, high efficiency and long lifetime are under development. The state of the art in this area is also briefly reviewed here.

4. GYRO-DEVICES FOR OTHER APPLICATIONS

The next generation of high-energy physics accelerators and the next frontier in understanding of elementary particles is based on the super collider. For linear electron-positron colliders that will reach center-of-mass energies of about 1 TeV it is the thought that sources at 17 to 35 GHz with $P_{out} = 300$ MW, $\tau = 0.2$ µs and characteristics that will allow approximately 1000 pulses per second will be necessary as drivers [4]. These must be phase-coherent devices, which can be either amplifiers or phase locked oscillators. Such generators are also required for super range resolution radar and atmospheric sensing without coherent-on-receive data processing [6]. Therefore this contribution gives a short overview of the present development status of CARMs gyro-TWAs and gyroklystrons for such purposes as well as of broadband gyro-BWOs for use as drivers for free electron maser (FEM) amplifiers. Very high electron beam quality is required to obtain a high efficiency in these gyro-devices. Dramatic improvement in performance appears to be achievable by tapering of the magnetic field (ramped field) and in the case of the gyro-TWT also of the waveguide radius along the axis of the interaction region to maintain the resonance condition over a wide frequency range. This precise axial contouring is a topic of intensive current study.

5. REFERENCES

[1] R. Prater, J. Fusion Energy, **9** (1990) 19-30.
[2] V. Erckmann, W7II-AS Team, W. Kasparek, G.A. Müller, P.G. Schüller and M. Thumm, Fusion Technology, **17** (1990) 76-85.
[3] Y. Bykov, A.L. Goldenberg, V.A. Flyagin, Matls.Res.Soc.Proc., **169** (1991) 41-42.
[4] V.L. Granatstein, W. Lawson, P.E. Latham, Conf.Digest, 13th Int. Conf. on Infared and Millimeter Waves, Honolulu, Hawaii, SPIE, **1039** (1988) 230-231.
[5] V. Erckmann et al., Proc. Europhysics Topical Conf. on RF Heating and Current Drive of Fusion Devices, Brussels, EC'A, **16E** (1992) 297-300.
[6] W.M. Manheimer, Int. J. Electronics, **72** (1992) 1165-1189.

Far Infrared Spectroscopy of Manufactured Solids

D.R. Tilley

University of Essex, Department of Physics
Wivenhoe Park, Colchester, CO4 3SQ U.K.

Reflection and transmission of electromagnetic radiation is governed by the frequency dependent dielectric permittivity tensor $\overleftrightarrow{\varepsilon}(\omega)$, in some cases with contributions from the magnetic permeability tensor $\overleftrightarrow{\mu}(\omega)$. These are fundamental linear response functions, so the corresponding spectroscopy occupies a central position in the study of solids. Generally speaking, $\overleftrightarrow{\varepsilon}$ and $\overleftrightarrow{\mu}$ are the natural point of contact between theory and experiment.

One of the simplest examples is a cubic ionic solid, for example NaCl or GaAs. In this case the permittivity is a scalar $\varepsilon(\omega)$ taking the well known form

$$\varepsilon(\omega) = \varepsilon_\infty \left(1 + \frac{\omega_L^2 - \omega_T^2}{\omega_T^2 - \omega^2 - i\omega\Gamma} \right) \qquad (1)$$

in which ω_T is the TO frequency and Γ the damping. The normal-incidence reflectivity calculated from (1) has the characteristic reststrahl form so that reflectivity measurements determine the parameters ω_T, ω_L and Γ. In addition to the usual techniques, attenuated total reflection (ATR), which couples directly to surface polaritons, may yield additional information[1]. In complicated cases the complementary technique of Raman spectroscopy may give direct determination of phonon frequencies. Developments of this form of phonon spectroscopy include the study of soft modes and anharmonicities in ferroelectrics.

Recently, the combination of FIR and Raman spectroscopy has been brought to bear on the phonon spectra of semiconductor superlattices[1]. The macroscopic symmetry of these engineered materials is uniaxial, so that $\overleftrightarrow{\varepsilon}(\omega)$ has different in-plane and normal components $\varepsilon_{xx}(\omega)$ and $\varepsilon_{zz}(\omega)$. Since normal-incidence reflectivity is governed by $\varepsilon_{xx}(\omega)$ alone, oblique-incidence and ATR measurements are necessary for a full study. In short-period samples, confined optic phonons of the right parity all contribute to $\overleftrightarrow{\varepsilon}(\omega)$, so that a series of resonances appears in place of the single resonance of (1). A full understanding of these effects calls for detailed theoretical modelling together with the spectroscopic studies.

Excitation of electron-hole pairs across the band gap governs the fundamental absorption edge in semiconductors, although in the usual group IV and III-V materials the frequency is visible or near infrared and therefore outside the scope of this review. The similar phenomenon of the breaking-up of Cooper pairs in a superconductor gives an absorption threshold at photon energy $\hbar\omega = 2\Delta$, where 2Δ is the energy gap. The determination of 2Δ by this means was a major achievement of FIR spectroscopy some 30 years ago[2]. Similar studies in the high-temperature superconductors have proved difficult because the features related to the energy gap appear as only a few percent of background.

From the theoretical point of view, both electron-hole and collective electron effects are contained in the Lindhard function $\Pi(q, \omega)$, for which a general expression may be found from quantum-mechanical linear response theory. Far infrared properties, because of the long wavelength, are governed by the limit $q \to 0$, $\Pi(o, \omega)$. In the simplest case of a free-electron gas the dielectric function derived from $\Pi(o, \omega)$ is the simple plasma expression

$$\varepsilon(\omega) = 1 - \omega_p^2/\omega^2 \qquad (2)$$

in which ω_p is the plasma frequency. Of course, this can be derived by more elementary means. In doped semiconductors ω_p generally lies in the FIR and spectroscopic features depend on the combination of (1) and (2). Again, an important modern application is the study of doped semiconductor superlattices[1].

Considerable theoretical attention, but less experimental work, has been devoted to magnetoplasmas. In the presence of a magnetic field, the scalar (2) is replaced by a gyrotropic tensor; in the plane transverse to the magnetic field

$$\overleftrightarrow{\varepsilon} = \begin{pmatrix} \varepsilon_1 & i\varepsilon_2 \\ -i\varepsilon_2 & \varepsilon_1 \end{pmatrix} \qquad (3)$$

where ε_1 and ε_2 both have poles at the cyclotron resonance frequency $\omega_c = eB/m^*$. One important consequence is that surface-related properties become non-reciprocal, that is, they change when B is reversed[3]. For example, the oblique-incidence reflectivity has this property, $R(\omega,-B) \neq R(\omega,B)$. Although theoretical studies have been pursued, for example, as far as detailed investigation of magnetoplasma superlattices, experimental work is less advanced.

Whilst effects in the visible and near-infrared are governed solely by $\overleftrightarrow{\varepsilon}(\omega)$, with no contribution from $\overleftrightarrow{\mu}(\omega)$[4], magnetic response can play a part in the FIR. In general $\overleftrightarrow{\mu}(\omega)$ should have poles at the appropriate resonance frequencies, which are in the microwave region for ferromagnets but in the FIR for antiferromagnets. Ferromagnets, which are antiferromagnetically coupled but with a net moment, have both a low-frequency ferromagnetic resonance and a higher frequency antiferromagnetic-type resonance. The form of $\overleftrightarrow{\mu}(\omega)$ has been derived for a number of cases[5], including the spiral and cone spin orderings found in some rare earth metals[6]. Here again, the theory has been pursued much further than experiment[3]. The first experimental results[7] of what is planned as a sustained investigation of magnetic systems show the non-reciprocal reflection off the uniaxial antiferromagnet FeF_2 with beautiful clarity.

With the development of powerful crystal growth techniques like molecular-beam epitaxy and continuing advances in lithographic methods, an ever greater variety of manufactured solids and solid-state structures will appear. FIR spectroscopy can and should play a major part in the investigation of these materials. The general principle that one is studying the elementary excitation spectrum via the linear response functions $\overleftrightarrow{\varepsilon}(\omega)$ and $\overleftrightarrow{\mu}(\omega)$ will continue to apply, but the details will show considerable variety.

REFERENCES

1. T.Dumelow, T.J. Parker, S.R.P. Smith and D.R. Tilley, *Surface Science Reports* **17** 151 (1993).
2. D.M. Ginsberg and M. Tinkham, *Phys. Rev.* **118** 990 (1960).
3. R.E. Camley, *Surface Science Reports* **7** 103 (1987).
4. L.D. Landau and E.M. Lifshitz, Electrodynamics of Continuous Media *Pergamon, Oxford* (1960).
5. E.F. Sarmento and D.R. Tilley, Chapter 7 of Electromagnetic Surface Modes ed. A.D. Boardman, *Wiley, New York* (1982).
6. N.S. Almeida and D.R. Tilley, *Phys. Rev. B* **43** 11145 (1991).
7. D. Brown, T. Dumelow and T.J. Parker, *these Proceedings.*

Critical technologies for atmospheric composition measurements by microwave limb sounding

G. E. Peckham and R. A. Suttie

Heriot-Watt University, Edinburgh

Limb sounding technique

Limb sounding radiometers determine the concentrations of atmospheric constituents by measuring thermal emission from the atmospheric limb along a tangent path (fig 1). Microwave limb sounders have the

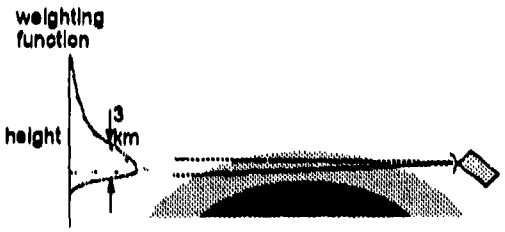

Fig 1 Geometry for limb sounding

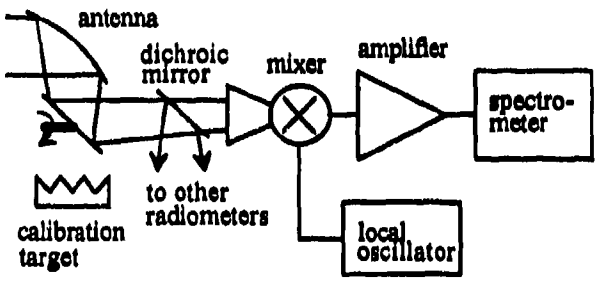

Fig 2. Radiometer components

following properties:

- By viewing the atmospheric limb
  - Species are identified through their spectral signatures contrasted against a cold space background
  - The viewing geometry provides good (~3 km) vertical resolution
  - Vertical profiles are obtained by scanning the antenna in elevation
  - Global maps are produced by a combination of satellite motion and earth rotation
  - Atmospheric pressure is available from measured line widths so that precise platform pointing information is not necessary
  - The long atmospheric path gives sensitivity to species with low abundance
- By using thermal emission
  - Measurements are made continuously during both day and night
  - Reliable in-flight calibration is provided by onboard targets
- At microwave frequencies
  - Thermal emission is relatively insensitive to temperature
  - Aerosols and ice clouds have negligible effect
  - The high spectral resolution of heterodyne receivers allows measurement of individual line shapes so that contaminating lines can be removed

The basic components of a microwave limb-sounding radiometer are shown in figure 2. Radiation from the atmosphere is focused by an antenna onto a mixer where the frequencies are down-converted so that signals can be amplified electronically. The amplifier outputs (possibly after further down-conversion)

are analysed by spectrometers which record the signal power spectrum across selected IF bands. A number of radiometers may be fed from a common antenna and calibration system through a sequence of dichroic or polarising beamsplitters.

Performance requirements

Microwave limb sounders operate at millimetre and sub-millimetre wavelengths. Frequencies range from 60GHz (O_2 emission used by UARS MLS[1] and MAS[2] to sense pressure), through 205 GHz (ClO emission UARS MLS and MAS) to 640GHz (HCl and ClO proposed for EOS MLS, AMAS[3] and MOSES[4]) and 2.5THz (OH proposed for EOS MLS[5]). Throughout the troposphere and stratosphere, lines are pressure broadened. To resolve lines in the upper stratosphere, resolutions of order 1MHz are required, whilst to reliably record a line originating at the tropopause, a bandwidth of order 1GHz is needed. Larger IF bandwidths (up to 20GHz) allow many atmospheric constituents to be measured using a common mixer and local oscillator.

Technologies for millimetre and sub-millimetre wave radiometers

A number of critical technologies needed to build a microwave limb sounding radiometer are identified below. Designs for all these components exist, but further development would improve performance particularly at frequencies of a few hundred gigahertz and above.

- Optics
  - Dichroic beam splitters (allows antenna to be shared by several radiometers)
  - Sideband filters (rejects signals in image sideband)
- Mixer
  - Fundamental pump Schottky diode mixer (best signal to noise if adequate LO power available)
  - Subharmonic pump two-diode mixer (has broader bandwidth and simple LO coupling)
  - Single diode harmonic mixer (can operate up to terahertz frequencies)
  - SIS mixer (low noise, low LO power requirement, must be cooled to ~4K)
- Local Oscillator
  - Gunn (up to ~100GHz), or frequency multiplied Gunn (up to ~1THz)
  - FIR (Far Infrared) laser for terahertz frequencies
- IF amplifiers
  - Based on HEMT transistors for low noise, high bandwidths (good noise performance up to ~20GHz)
- Spectrometers
  - Filter bank
  - Acousto-optic
  - Chirp transform
  - Digital autocorrelator

---

1 Microwave Limb Sounder on Upper Atmosphere Research Satellite.
2 Microwave Atmospheric Sounder on Space Shuttle.
3 Advanced Microwave Atmospheric Sounder (under development).
4 Molecules in Outer Space and in Earth's Stratosphere (under development).
5 Microwave Limb Sounder for Earth Observation System (under development for Chemsat mission).

Radiometer system noise temperatures

The most critical item is the mixer. With no RF amplification (impractical at frequencies greater than ~100GHz), the dominant source of receiver noise is from this device. Mixer noise temperatures are listed in the following table together with the corresponding radiometer noise temperatures after making allowance for pre-mixer losses and IF amplifier noise. These figures are derived from experience with practical devices[6] where these exist, otherwise estimates have been made.

Table 2. Microwave radiometer system noise temperatures

RF frequency (GHz)	100.0		200.0		400.0		600.0		1,800.0		2,500.0	
Pre-mixer loss (dB)	0.5		0.5		0.5		0.5		0.5		0.5	
Mixer noise temperature (single sideband, 10^3K)	0.6	1.2	0.9	1.8	1.5	3.0	2.5	5.0	7.0	14.0	10.0	19.0
	1.0	2.0	1.2	2.5	*2.0*	*4.0*	*3.5*	*7.0*	–	–	–	–
	1.2	2.5	1.5	3.0	*2.5*	*5.0*	*4.0*	*8.0*	–	–	–	–
Mixer conversion loss (dB)	5.5	6.0	7.5	8.0	8.5	9.0	9.5	10.0	11.0	11.5	11.5	12.0
	8.5	9.0	10.5	11.0	*11.5*	*12.0*	*12.5*	*13.0*	–	–	–	–
	9.5	10.0	11.5	12.0	*11.5*	*12.0*	*12.5*	*13.0*	–	–	–	–
Matching loss (dB)	0.5	0.5										
	1.0	1.0	...		...		...		...		...	
	1.0	1.0										
Amplifier noise temperature (K)	25	90										
	30	110	...		...		...		...		...	
	45	170										
System noise temperature (single sideband, 10^3K)	0.9	2.0	1.3	3.0	2.0	4.6	3.2	7.2	8.4	18.0	12.0	24.0
	1.6	4.2	2.1	5.9	*3.2*	*8.5*	*5.1*	*13.0*	–	–	–	–
	2.2	6.1	2.9	8.6	*4.1*	*10.0*	*6.0*	*16.0*	–	–	–	–

Table 3. Key to table 2 entries

		Low (80 K) temperature	High (300 K) temperature
Narrow band IF	2–4 GHz	...	...
Wideband IF	< 12 GHz	...	...
3–18 GHz	> 12 GHz	...	...

Figures in *italic* not yet demonstrated

6 D. N. Matheson, private communication

Potential of millimetre/sub-millimetre heterodyne instruments to sound atmospheric composition

B. J. Kerridge

Rutherford Appleton Laboratory
Chiltern, Didcot, Oxon, OX11 OQX, UK

1. INTRODUCTION

Changes to atmospheric composition are of central importance to stratospheric ozone depletion and to global climate change and specific measurement requirements can be identified, both for investigation of mechanisms and for monitoring. The attributes of heterodyne measurements at millimetre and sub-millimetre wavelengths appear particularly well suited to these requirements, especially for the important lower stratosphere/upper troposphere region, and certain critical molecules can be measured only at these wavelengths. Many of these attributes have already been demonstrated at microwave and millimetre wavelengths by ground-based, aircraft, balloon and most recently space instruments. Technological advances are now providing access to the sub-millimetre region as well.

This paper will describe the advantages of heterodyne measurements for atmospheric composition sounding and, by reference to instruments which are currently in the development or study phase, will illustrate how technical progress in key areas has significantly increased the potential of such measurements for stratospheric ozone research and for climate research.

2. ATTRIBUTES OF MM/SUB-MM HETERODYNE MEASUREMENTS

There are a number of advantages inherent to emission sensing at long wavelengths. Notable among these are insensitivity to aerosol and comparatively low sensitivity to ice and water clouds; attributes which have long been exploited by nadir-viewing satellite sensors to sound surface properties and meteorological variables. The recent successes of the Microwave Limb Sounder (MLS) on the Upper Atmosphere Research Satellite (UARS) and the Millimetre-wave Atmospheric Sounder (MAS) on ATLAS 1 and 2 have in large part been due to their insensitivity to stratospheric aerosol injected by the Mt. Pinatubo eruption in 1991 and to polar stratospheric clouds. It is also well established that the much weaker dependence of Planck function on temperature at long wavelengths means that data inversion is less sensitive to temperature uncertainties and to temperature itself, which is useful for sounding composition in a cold region such as the tropopause when viewing through an intervening warm region.

Less widely recognised, is the advantage of measuring atmospheric emission which is strictly *thermal* in origin. The rotational and fine-structure transitions which give rise to most spectral lines at sub-millimetre and longer wavelengths occur in the ground electronic and vibrational states where populations are governed by collisions and so the *source function* in the equation of radiative transfer can be represented simply by the Planck function evaluated at local kinetic temperature. By contrast, at shorter wavelengths there are many examples of *non-thermal* emissions pumped by radiative or chemical processes which, although interesting in their own right, can significantly complicate data inversion in the stratosphere and above. Under many circumstances, radiative transfer at

sub-millimetre and longer wavelengths is more straightforward to model than for IR emission or solar backscattered radiation in the UV and visible regions.

An important advantage of the heterodyne technique is the comparatively high spectral resolution which can be attained. This allows spectral interference to be minimized and the pressure-broadened lineshape to contribute height information to augment that due to viewing geometry alone. The former is of considerable benefit for sounding the lower stratosphere and upper troposphere where interference can often be a limiting factor. The latter has already been exploited by ground-based instruments to sound the stratosphere and mesosphere from below and will be of great value for satellite sounding of constituents such as O_3, CO, NO, OH, and HO_2 in the lower stratosphere and/or upper troposphere where their abundances are much smaller than at higher altitudes.

In-flight radiometric calibration for longwave emission measurements is inherently accurate and is not expected to degrade significantly with time so, assuming pre-flight characterisation of the antenna and calibration system to be adequate, such measurements should provide a reliable means to monitor critical constituents from space.

3. CAPABILITIES FOR STRATOSPHERIC OZONE RESEARCH

The major objective of current stratospheric ozone research is to explain the larger than predicted depletion in global ozone and the especially significant depletion at northern high latitudes observed during the last decade by ground-based Dobson spectrophotometers and confirmed by TOMS on Nimbus 7. The underlying cause is believed to be anthropogenic emissions of chlorine and to a lesser extent bromine, which eventually give rise to catalytic cycles which destroy ozone in the lower stratosphere.

To further investigate the processes responsible, it will therefore be necessary to observe stratospheric ozone and constituents which are implicated in its destruction, especially in the height range 15 to 25 km. A number of these constituents can now be targetted by millimetre/sub-millimetre instruments including halogens (ClO, HCl, HOCl, BrO, and CH_3Cl), hydrogen oxides (H_2O, OH, HO_2, and H_2O_2) and nitrogen oxides (N_2O, NO, NO_2, and HNO_3).

A number of atmospheric windows exist at millimetre and sub-millimetre wavelengths in which to sound stratospheric composition. With few exceptions (nb. H_2O, O_3, and O_2), the intensities of stratospheric emission lines are weak and reach maximum values in the sub-millimetre region. The inverse dependence of half-power beamwidth on frequency also means that adequate ($\approx$ 1km) vertical resolution for limb-viewing is more readily achieved at shorter than at longer wavelengths. Sub-millimetre limb-viewing is therefore an especially suitable technique with which to sound stratospheric composition.

Three areas of technological advance will be of particular benefit to stratospheric sounding: (i) attainable frequency, (ii) sensitivity and (iii) spectral bandwidth. Examples of new airborne instruments which will seek to exploit these advances for stratospheric ozone research are (i) 2.5 THz receiver to detect OH, HO_2, H_2O_2 and HOCl, (ii) high-sensitivity 500 and 690 GHz receivers to detect ClO and BrO and (iii) 850/950 GHz receiver to detect NO. These instruments are all European

collaborations intended to have their initial flights on the German DLR Falcon during 1995-6. All will exploit the capability of the acousto-optic spectrometer to measure over a bandwidth of ≥1 GHz. The 2.5 THz receiver depends upon technical innovation in two areas: firstly for fabrication of a waveguide mixer of significantly smaller dimensions than has been possible hitherto and secondly for development of a gas laser local oscillator which is sufficiently compact for use on the Falcon. The 500 and 690 GHz receivers will employ superconductor-insulator- superconductor (SIS) mixers in order to attain the high sensitivity needed for measurement of ClO and BrO. For the 850/950 GHz receiver, an SIS mixer will be developed to operate at a higher frequency than has previously been demonstrated.

It is generally accepted that the performance and reliability of heterodyne technology at frequencies below 1 THz has reached the stage at which space-borne instrumentation can be proposed to monitor stratospheric ozone and other critical constituents. For example, the ODIN project proposes to launch a sub-millimetre receiver for joint astronomy/atmospheric science research in 1997. In the longer term, NASA has approved the successor to UARS MLS for flight on the EOS Chemistry platform in 2002 and ESA are engaged in a study of sub-millimetre instrumentation for possible launch on ENVISAT-2 on a similar timescale.

4. CAPABILITIES FOR CLIMATE RESERCH

A major objective of climate research is to understand the full implications of increasing atmospheric concentrations of greenhouse gases and other trace constituents. It has long been appreciated that the direct effect of increasing CO_2, CH_4, N_2O and other pollutants would be to increase the "greenhouse effect". However, global warming has yet to be detected unambiguously in the historical record. Furthermore, a number of complicated feedback mechanisms have been postulated involving physical, chemical and biological processes on land, in the ocean and in the atmosphere, which combine to make the climatic response to greenhouse forcing difficult to model. In addition to monitoring sea-surface temperature, meteorological variables and other indicators of climate change, additional observations will be needed to investigate the mechanisms which control climate.

Atmospheric composition is one of the most critical areas in which new measurements are needed. In particular, since water vapour is the major greenhouse gas, its global, height-resolved distribution in the troposphere plays a central role in climate feedback. The next generation of downward-viewing operational sounders such as the Advanced Microwave Sounding Unit will measure emission from the 183 GHz H_2O line in several spectral intervals up to ± 7 GHz from line centre to derive height-resolved information for numerical weather prediction. This information will also be of value for climate research, especially for the lower troposphere (ie. pressures greater than 300 mb). However, better height resolution is needed in the upper troposphere (ie, pressures less than 300 mb) which is important for greenhouse forcing because temperature contrast with the surface is greatest. Furthermore, the downward viewing IR spectrometric techniques which are under development for operational platforms will have difficulty sounding humidity in this region because their height resolution depends upon temperature lapse rate (which by definition is zero at the tropopause).

An alternative method which has been proposed to sound water vapour and other constituents in the upper troposphere is millimetre limb-sounding, for which the principles have already been established by stratospheric measurements from balloon and satellite platforms. Several advantages of millimetre measurements referred to in § 2 could be applied here to good effect and good height resolution (≤ 1km) should be achievable for an antenna of reasonable size. A number of technical advances now make possible the measurement of a broad spectral region (5-10 GHz) at comparatively high resolution (50-100 MHz) in single side-band mode. This would enable spectral lineshapes of H_2O and several other molecules to be well resolved and spectral baseline to be characterized adequately, which in turn would minimize sensitivity to clouds and the anomalous water vapour continuum.

A proposal is currently in preparation for an airborne broad-band millimetre receiver operating in the 200, 300, 325 and 350 GHz regions. This instrument is intended to demonstrate the feasibility of measuring H_2O, O_3, CO and other gases in the upper troposphere and lower stratosphere and will be accompanied by an ancilliary optical/IR cloud detector. It is envisaged that, if successful, a space-borne version would be proposed, possibly as companion to a sub-millimetre instrument on ENVISAT-2.

THE ENEA COMPACT MILLIMETRE WAVE FEL

A.Doria, G.P.Gallerano, E.Giovenale, M.F.Kimmitt, G.Messina, A.Renieri

ENEA, Area INN, Dipartimento Sviluppo Tecnologie di Punta, P.O. Box 65
00044 Frascati, (Rome) Italy

Introduction

Conventional Free Electron Lasers (FELs) suffer from some drawbacks related to the large size of most electron beam (e-beam) accelerators that implies high costs, system complexity and shielding requirements. In the Far InfraRed (FIR) and Millimetre (MM) wave region the FEL can meet the demand of compactness following several approaches involving the different sub-systems of the device. For example the low e-beam energies required (< 10 MeV) allow the use of small size accelerators like Radio-Frequency (RF) Linacs or Microtrons. The increased performance in terms of gain at wavelengths in the FIR and MM also requires a shorter length of the interaction region, thus allowing the use of short period undulators and small number of periods and resulting in a better efficiency. Following these considerations a compact FEL source in the MM wave range has been realised at ENEA Frascati.

Experimental Set-up

The experimental layout (see Fig.1) has been realised in 1989 [1] as a test facility for compact free electron devices. The facility employs a *5 MeV* microtron as e-beam source powered by a *3 GHz 2.5 MW* magnetron. For the present experiment the energy has been lowered down to *2.3 MeV* in order to operate in the "zero slippage" condition [2]. The microtron delivers electron bunches of *15 ps* duration and *6 A* of peak current spaced by the RF period. This train of pulses is *4* μs long and can be produced at a repetition rate up to *50 Hz*. The e-beam goes through a straight-line transport channel, made up of 3 quadrupoles and two deflecting coils, up to the undulator. The SmCo permanent magnet linear undulator has a period λ_u=*2.5 cm* and is N=*8* periods long; it is capable of producing an on-axis magnetic field of *6.3 kGauss* at a gap of *6.5 mm*. A WR42 waveguide is used inside the undulator gap to confine the radiation and, the small transverse dimensions, introduce new features on the FEL kinematics and dynamics [2]. A Fabry-Perot resonator with a variable length has been realised utilising wire grid polarisers as Electron Transparent Mirrors (ETM) [3]. The radiation is extracted at 90° degrees by means of an ETM mesh and is analysed in a shielded soparated area.

Results and Theoretical Comparison

The presence of the waveguide, that is a spectral dispersive element, inside the undulator alters the radiation generation mechanism [2] introducing new tuning possibilities in addition to those traditional for the FELs. The spontaneous emission band for the waveguide FEL is very broad and for our device has been measured to range from *1.5 mm* to *4.5 mm*; this gives a wide possibility of lasing action provided that a frequency selective element is used. Our laser has two such elements: the first is the optical cavity itself and the second is the presence of the RF harmonics due to the bunched nature of the electron beam [4]. The combination of these two elements together with the gain function gives a measured laser action between *2.1 mm* and *3.5 mm*, obtained by only changing the cavity length [5]. The experimental tuning curve is reported in Fig.2 and reveals the well-known

asymmetric behaviour. The maximum output power is obtained when a higher number of harmonics are sustained in the cavity and this happens at $\lambda \approx 2.6mm$. Moving along the tuning curve the radiation output changes its temporal and spectral characteristics because the optical pulse formation is determined by the harmonics that are simultaneously longitudinal modes of the cavity. The maximum output power delivered by the FEL $\approx 1.5\ kW$ over $4\mu s$.

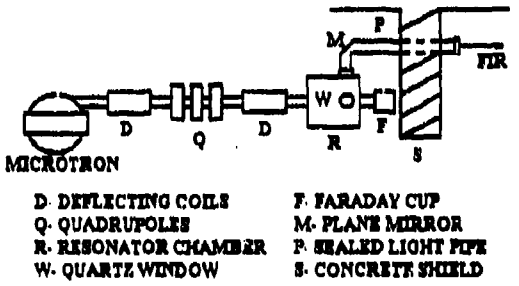

Fig1: FEL experimental layout

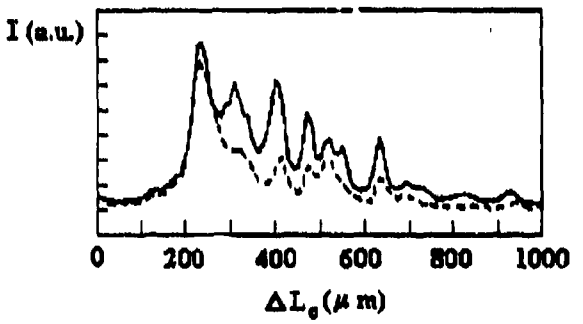

Fig.2: FEL intensity vs. resonator length variation

Developments and Applications

The first improvement that will be done on the layout is the installation of a *15 MW* Klystron, instead of the Magnetron, as RF source for the accelerator. In the new configuration it will be possible to change the time duration of the electron pulse from *2* μs to *12* μs, making possible some studies of FEL physics on the signal built-up.

A new undulator is under construction, it has $N=16$ periods and will be utilised on the same device to extend the operating range in the FIR down to *500* μm. For this experiment the electron energy will be raised again to its maximum value of *5 MeV*.

The ENEA compact FEL has been utilised, and will be in the future, for application in physics. In the present configuration the laser has been utilised for testing fast detectors in the MM wave range (see these Conference proceedings).

In the FIR configuration it will be utilised as a test prototype for a for an experiment of spectroscopy of atomic levels in muonic hydrogen. The experiment will be performed in collaboration with INFN-Trieste (Italy) and PSI-Villigen (Switzerland) [6].

Bibliography

[1] A.Doria, G.P.Gallerano, M.F.Kimmitt, Proceedings of the 16th International Conference on Infrared and Millimeter Waves, SPIE 1576, 548, (1991).

[2] A.Doria, G.P.Gallerano, A.Renieri, Opt. Commun. 80, 417 (1991).

[3] A.Dipace, A.Doria, G.P.Gallerano, M.F.Kimmitt, P.Raimondi, A.Renieri, E.Sabia, IEEE J.Quantum Electron., 27, 2629, (1991).

[4] A.Doria, R.Bartolini, J.Feinstein, G.P.Gallerano, R.H.Pantell, to appear in IEEE J. Quantum Electron., May issue, (1993).

[5] F.Ciocci, R.Bartolini, A.Doria, G.P.Gallerano, E.Giovenale, M.F.Kimmitt, G.Messina, A.Renieri, Phys. Rev. Lett., 70, 928 (1993).

[6] D.Chatellard et al., Proceedings of the Conference on Muonic Atoms and Molecules, edited by L.A. Schaller C.Petitjean, Ascona (CH), (1993).

Status of the design of the 200 GHz FOM-Fusion-FEM

A.G.A. Verhoeven, W.A. Bongers, B.S.Q. Elzendoorn, A.M. van Ingen, P. Manintveld, A. Tulupov, M.J. van der Wiel, W.H. Urbanus.
FOM-Institiuut voor Plasmafysica 'Rijnhuizen', Association EURATOM-FOM
tel: (31)3402-31224, fax: (31)3402-31204, e-mail: verhoeve@rijnh.nl
P.O. Box 1207, 3430 BE Nieuwegein, the Netherlands

V.L. Bratman, G.G. Denisov, A.V. Savilov, M.Yu. Shmelyov.
Institute of Applied Physics, Ulyanova Ulitsa 46, Nizhny Novgorod, Russia

H.-U. Nickel, M. Thumm.
IHE Universität Karlsruhe and ITP Kernforschungszentrum Karlsruhe, Germany

W. Kasparek, J. Pretterebner, D. Wagner.
Institut für Plasmaforschung, Stuttgart University, Germany

C. Shang, M. Caplan
Lawrence Livermore National Laboratory, Livermore, CA, USA

A Free Electron Maser is being designed for ECRH applications on future fusion devices. The FEM will have an output power of 1 MW, a central frequency of 200 GHz and will be adjustable over the complete frequency range of 125 GHz to 250 GHz.
The FEM operates with a thermionic electron gun. Fast tunability is achieved by variation of the voltage of the 2 MeV electrostatic accelerator. The undulator and mmw system are located in a terminal at a voltage of 2 MV, inside a vessel filled with SF_6 at a pressure of 7 bar. After interaction with the mm waves in the undulator, the energy of the electron beam will be recovered by means of a decelerator and a multi-stage depressed collector. The -low emittance- electron beam will be completely straight to minimize current losses to less than 20 mA. This current is to be delivered by the 2 MV dc accelerating voltage power supply. Simulations indicate that the overall efficiency will be over 50 %.
The interaction between the electron beam and the mm waves is simulated using both a 1-D, non-stationary code and a fully 3-D, stationary, amplifier code. Results with both codes will be presented, indicating that -with a beam current of 12 A- an output power of 1 MW can be generated for all required frequencies with a beam energy ranging from 1.3 MeV (for 125 GHz) to 2 MeV (for 250 GHz).

The MMW sytem

The mmw system of the FEM will be an oscillator, consisting of a waveguide amplifier section and a feedback system (see Fig. 1). For the oversized waveguide inside the undulator a rectangular corrugated HE_{11} waveguide is chosen with a cross section of 15x20 mm^2. Behind the undulator the mm waves will be separated from the electron beam by means of a stepped waveguide [1,2]. Here the width of the waveguide changes step-wise. As a result of this step, the initial HE_{11} beam is splitted into two identical off-axis HE_{11} beams at about 1.5 m from the step. At this position two mirrors can be located with a hole in between, large enough to let the electron beam pass without disturbing the mmw beams.

At the mirrors the two mmw beams are reflected with adjustable phases by changing the position of one of the mirrors. This enables a 0-100 % variation of the reflection coefficient: the fraction of the power that goes back through the interaction waveguide to the input side of the undulator. At this position a 100 % reflector is located based on the same principle. The remaining power is evenly divided over two output beams, these can be recombined to make the 1 MW output. Very encouraging low-power measurements on a prototype separation system will be shown.

Tunability is achieved via variation of the width of the waveguide a (after the step), which is given by $a = \sqrt{2\lambda L}$, where L is the length of the electron-beam/mmw splitter: 1.5 m. A system is being designed to move the sidewalls of the splitter in order to optimize the dimension a for all frequencies from $a = 60$ mm for 250 GHz to $a = 85$ mm for 125 GHz. This system enables to vary the frequency over the complete range of 125 to 250 GHz by just changing the accelerator voltage, the splitter width and the reflection coefficient. All this can be controlled remotely.

Detailed simulations, which take the propagation of the mmw beam in the cavity and the interaction with the electron beam into account, show that 99.8 % of the mmw power is in the HE_{11} mode.

Transport of the mm waves from the electron beam/mmw splitter to outside the pressure vessel will be done in the following way. The two mmw output beams (see Fig. 1) are combined to one beam by means of a combiner system: the same system as the splitter mentioned before, but this one working in the reciprocal way. By using a quasi-optical confocal mirror system the single beam is transferred to the insulator tube. This is a tube very similar to the 2 MV accelerator tube. However, to let the mm waves pass from the 2 MV level to earth potential a wider -tapered- bore hole is used for the electric-field steering electrodes.

The vacuum barrier will be a window at the Brewster angle. For the first stage of the project a single disc will be sufficient to withstand 100 ms pulses. For the long pulse experiments novel ideas like a double disc Brewster window are being worked out.

References

[1] *L.A. Rivlin, Laser Focus (1981) p. 82.*

[2] *G.G. Denisov, D.A. Lukovnikov and M. Yu. Shmelyov, this conference.*

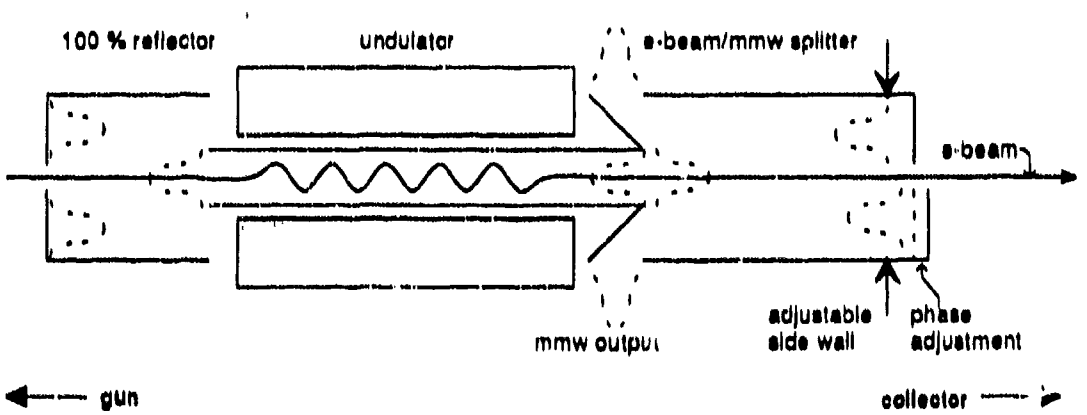

Fig. 1. The mmw system of the FOM-Fusion-FEM

Abstract Submitted
for
the 18th International Conference on Infrared and Millimeter Waves,
September, 6-10, 1993, University of Essex, Colchester, Essex, U.K.

Title: A Compact Relativistic Electron Beam Source for Generation of Far Infrared Radition

C. R. Jones and J. M. Dutta
Department of Physics, North Carolina Central University, Durham, NC U.S.A

A compact electron beam source now in operation at NCCU will be described and the application of this beam for the production of radiation from the microwave to the submillimeter will be reported.

Design of a Tunable 4-MW Free Electron Maser for Heating Fusion Plasmas*

M. Caplan, G. Kamin, C. C. Shang, and W. Lindquist
Lawrence Livermore National Laboratory
P.O. Box 808, L-637
Livermore, California 94551
USA

ABSTRACT

There is an ongoing program at the FOM institute, The Netherlands, to develop a 1-MW, long-pulse, 200-GHz Free Electron Maser (FEM) using a DC accelerator system with depressed collector. We present an extrapolation of this design to more than 4 MW of output microwave power in order to reduce the cost per kW and increase the power per module in a plasma heating system.

Introduction

The FOM Institute for Plasma Physics, The Netherlands, is now constructing a Free Electron Maser (FEM) to be used as a high-frequency tunable microwave source for heating fusion plasmas.[1] This source has been designed to ultimately operate CW at the 1-MW power level over an adjustable tuning range of 150–250 GHz. The design philosophy is to use a high-voltage, DC beam system with depressed collector in order to make the overall wall plug efficiency 40–50%. The high-voltage, 1.75-MV power supply provides only loss current (~ 30 mA) while the 12-A beam current is supplied by the 100–200 kV collector supplies.

A compatible microwave interaction circuit, coupling system and wiggler magnet is shown in Figure 1. The rectangular corrugated circuit operating in HE_{11} mode is very low loss capable of handling multi-megawatts of power CW. The stepped waveguide system allows feedback and output coupling in highly overmoded guide while maintaining mode purity. The two-stage stepped undulator allows for increased electronic efficiency while maintaining high-quality focusing.

There is an interest in extrapolating this design to higher powers in order to reduce the cost/kW and develop a more compact microwave system. The most straight forward extrapolation is to increase the current beyond 12 A to as high as 30 A, keeping as much of the system the same while ensuring the integrity of the beam-focusing system and CW power-handling capability. The cost savings occur because the high-voltage supply costs scale slowly with current.

High-Current Design

It is important to note that the 1.75-MeV beam radius is determined by emittance in the 10 to 30-A range. As the beam current increases, the emittance is also allowed to increase in order to keep the electron charge density from increasing excessively, causing problems due to ionization of background gas. The increase in emittance does not degrade microwave interaction efficiency.

The original focusing system for the low-current design can be used even though the beam radius increases by 40%, the charge density increases by 20%, and the emittance increases by a factor 2. The low-loss corrugated waveguide system can handle up to 5 MW with acceptable wall loading (< 1 kW/cm^2). Further stepping of the waveguide would be required to separate the power into 4 output ports each having corrugated distributed cooled windows capable of handling ~ 1 MW CW power.[2] Table 1 gives the modified 30-A design from the original FOM design. It is still assumed that the depressed collector can recover 90% of the power and dissipate up to 5 MW.

Computer Simulations

The FEM performance was modelled using a fully self-consistent 3D multimode non-wiggle averaged computer code including both AC and DC space charge effects.[3] The beam is modelled as several hundred particles which represent a specified emittance and charge density profile.

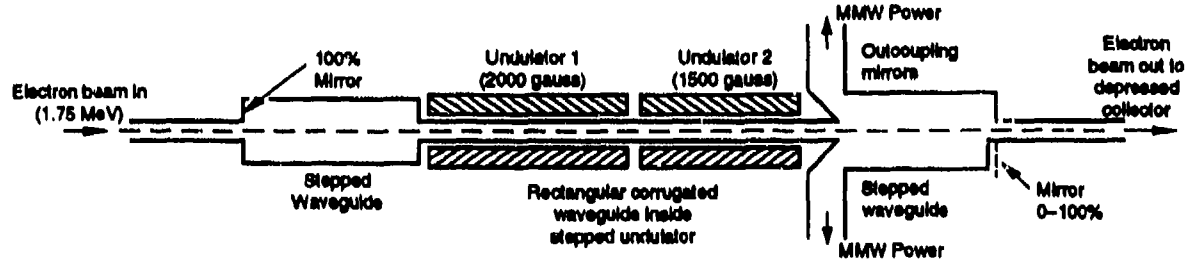

Fig 1. Schematic of MMW cavity of FEM showing step undulator, waveguide, and reflection/outcoupling system.

*This work was performed under the auspices of the U. S. Department of Energy by the Lawrence Livermore National Laboratory, under contract W-7405-Eng-48.

FEM Parameters	FOM Design	Extrapolation of FOM Design to High Power
Net Microwave Output	1.3 Megawatts	4.7 Megawatts
Beam Current	12 amperes	30 amperes
Beam Voltage	1.75 MeV	same
Reflection Coefficient	29%	20%
Beam emittance	50 π mm m rad	90 π mm m rad
Beam radius	0.92 mm	1.28 mm
Overall total length	158 cm	138 cm
No. full periods Section 1	20	17
No full periods Section 2	14	13
Peak wiggler field Section 1	2.0 kG	same
Peak wiggler field Section 2	1.3 kG	1.5 kG
Inter wiggler gap	6.0 cm	6.4 cm
Wiggler period	4 cm	same
Waveguide mode	HE_{11} rectangular	same
Waveguide height	2 cm	same
Waveguide width	1.5 cm	same
Frequency	200 GHz	same
High voltage loss current	< 40 milliamps	<100 milliamps
Depressed collector efficiency	90%	same
Wall plug efficiency	40%	50%

Table 1. Extrapolation of FOM Design to High Power

Figure 2 shows the prediction for steady state microwave power generated as the beam traverses the wiggler. The step-tapered wiggler enhances the power by almost 2.5 times to 4.7 MW. Figure 3 shows the beam cross section upon entering and exiting the wiggler. The

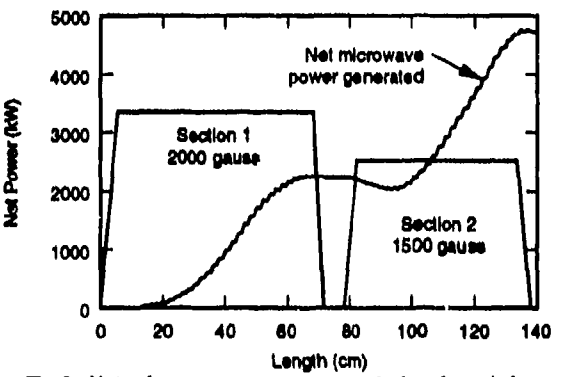

Fig 2. Net microwave power generated *vs* length for extrapolated high power design of Table I.

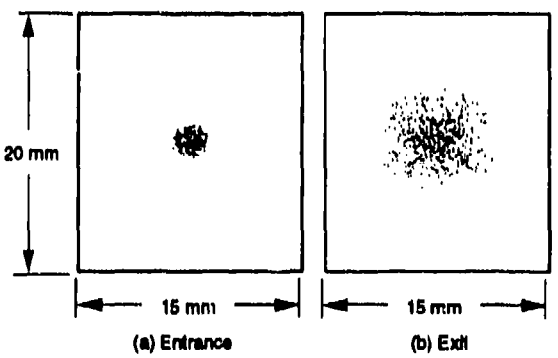

Fig 3. Transverse beam cross-section in rectangular waveguide at (a) entrance to undulator 1 and (b) exit side of undulator 2 after traversing step wiggler interaction region

beam increases by a factor of 2 in size, but is still well confined and centered in the original waveguide structure. The electron energy spread in the beam after the interaction is about 300 keV.

A number of simulations were performed at various currents between 12 and 30 amperes with each case being optimized. The results are shown in Figure 4, which shows how the output power scales with beam current assuming a roughly fixed charge density. The dependency goes faster than linear (~ $I^{1.4}$) because the FEM efficiency increases with current.

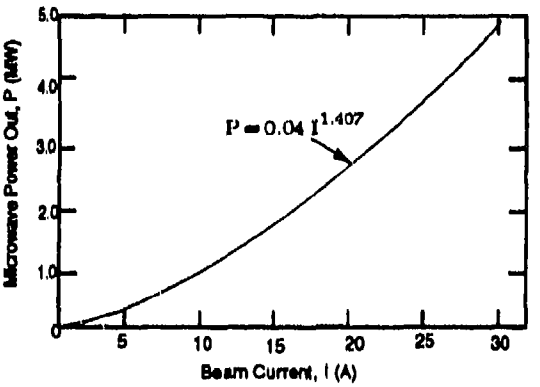

Fig. 4. The dependence of microwave output power on beam current for the configuration of Fig. 1.

Conclusion

The 1-MW FEM now being built at FOM could be upgraded to as much as 4.7 MW by increasing the current from 12 to 30 amperes, still keeping many of the key design parameters constant (voltage, wiggler configuration, microwave waveguide system).

The upgraded design can greatly reduce the cost/kW since power supply costs at fixed voltage increase slowly with current (much less than linear) while output power increases faster than linear with increasing current.

REFERENCES

1. A. G. Verhoeven, *et al.*, "The 1 MW, 200 GHz FOM-FUSION FEM," *Proceedings of Seventeenth International Conference on Infrared and Millimeter Waves*, Pasadena, California, December, 1992.

2. C. C. Shang, *et al.*, "Electrical Analysis of Wideband and Distributed Windows Using Time Dependent Field Codes," *Proceedings of Eighteenth International Infrared and Millimeter Wave Conference*, Essex, England.

3. M. Caplan, "Predicted Performance of a DC Beam Driven FEM Oscillator Designed for Fusion Applications at 200-250 GHz," *Proceedings of 14th International Free Electron Laser Conference*, Kobe, Japan 1992.

Ultra-Short Pulses of Coherent Millimeter-Wave Radiation from a Prebunched FEL*

G. Le Sage, P.G. Davis, S. Fochs, F.V. Hartemann, D.B. McDermott and N.C. Luhmann, Jr.
Department of Electrical Engineering, University of California, Los Angeles, CA. 90024
S.C. Hartman, S. Park, R.S. Zhang and C. Pellegrini
Department of Physics, University of California, Los angeles, CA. 90024

Abstract

A high power (10 MW), ultra-short pulse (10 ps to 1 ns), millimeter-wave (35 GHz to 100 GHz) Free-Electron Laser (FEL) experiment is currently underway at UCLA. The device is energized by a 1½ cell S-band photocathode RF linac which produces electron bunches in the 3-4 MeV energy range, with pulse FWHMs ranging between 3 and 10 ps and charges up to 1 nC. The copper photocathode is driven by a 1 ps HWHM frequency-quadrupled Nd:YAG laser. The electron bunch is transversally accelerated by a 8.4 cm-period, helically polarized wiggler. Because the electron bunch is much shorter than the FEL wavelength, all electrons coherently radiate spontaneously in the free-space limit, where slippage is important. In the TE_{11} grazing limit, where the axial bunch velocity matches the electromagnetic wave group velocity, the device behaves as a superradiant high-gain Compton FEL amplifier, seeded by the coherent spontaneous radiation produced at the wiggler entrance. Since the beam is prebunched, efficiencies are very high. Detailed studies of the temporal, spectral, power and phase characteristics of the radiation produced in both regimes are planned.

1. Introduction

The study of ultra-short, high-power, millimeter-wave and FIR pulses of coherent electromagnetic radiation has numerous applications ranging from chemistry and surface and solid-state physics to the next generation of ultra-wideband radars. A strong effort is currently underway at UCLA to develop high-brightness, ultra-short pulsed electron sources for coherent electromagnetic radiation generation. These new devices are based on high-gradient RF photocathode linacs.

The 1½ cell RF gun operates at 2.856 GHz with a 20 MW SLAC klystron. The strong electric field built up within the half cell, near the photocathode, quickly accelerates the photoelectrons, thereby maintaining a very low beam emittance.

The photocathode is driven by a frequency-quadrupled Nd:YAG laser with 2 ps FWHM and produces a bunch charge ranging from 10 pC to 1 nC. The beam energy obtained at the output of the 1½ cell linac is in the 3-4 MeV range [1].

The electron bunch is subsequently transversally accelerated by a 2 m long, 8.4 cm-period, 3 kG, helically polarized wiggler, as shown in Fig. 1, to produce high-power coherent electromagnetic radiation in the Ka-band. Theoretical calculations show that in the coherent spontaneous radiation limit, where the bunch essentially behaves as an accelerated point charge, peak power levels in excess of 1 MW can be achieved with RF pulse lengths ~ 1 ns. In the waveguide TE_{11} grazing limit, where superradiant high-gain Compton FEL amplification is obtained, the power levels are even higher, in excess of 10 MW, with pulse widths ranging between 10 ps and 100 ps. The waveguide interaction region has a cutoff frequency of 11 GHz.

2. Coherent Spontaneous Radiation(Free-Space Limit)

In this section, we consider the radiation process of a spatially extended charge distribution accelerated in a helically polarized wiggler field. In the 1-D limit, the bunch velocity and charge density fields are given by

$$\underline{\beta}(z,t) = \beta_{//}\hat{z} + \beta_{\perp}[\hat{x}\cos(k_w z) + \hat{y}\sin(k_w z)], \quad (1)$$

$$\rho(z,t) = \frac{q}{\sqrt{\pi}\,\Delta z}\exp\left[-(z-\beta_{//}ct)^2/\Delta z^2\right] \quad (2)$$

Here, $k_w = 2\pi/l_w$ is the wiggler wavenumber, l_w its period, q is the total charge, and Δz is the axial width of the electron bunch. It is easily seen that the continuity equation is satisfied by Eqs. (1) and (2). The transverse velocity is given in terms of the wiggler field B_w by $\beta_{\perp} = eB_w/\gamma_0 m_0 k_w c$, and energy conservation yields

$$\frac{1}{\gamma_0^2} = 1 - \beta_{\perp}^2 - \beta_{//}^2. \quad (3)$$

Following the derivation given by Jackson [2], we can evaluate the distribution of energy radiated on-axis per unit solid angle and per unit frequency for a N_w period long wiggler, with the following result.

$$\frac{d^2I(\theta=0)}{d\omega\,d\Omega} = \frac{\omega^2\beta_{\perp}^2 q^2}{16\pi^4\varepsilon_0 c\Delta z^2}\left|\int_0^{N_w l_w/\beta_{//}c} dt\int_{-\infty}^{+\infty} dz[\hat{x}\cos(k_w z) + \right.$$

$$\left. + \hat{y}\sin(k_w z)]\exp\left[i\omega\left(t-\frac{z}{c}\right) - \frac{(z-\beta_{//}ct)^2}{\Delta z^2}\right]\right|^2 \quad (4)$$

For a point charge ($\Delta z \to 0$), the normalized frequency spectrum is shown in Fig. 2. The main spectral line satisfies the FEL resonance condition $\omega^+(1-\beta_{//}) = k_w\beta_{//}c$, and its width scales as $1/N_w$. The total instantaneous radiated power scales as q^2, and is given by

$$P = \frac{q^2}{6\pi\varepsilon_0 c}\gamma_0^4\beta_{\perp}^2\beta_{//}^2(k_w c)^2. \quad (5)$$

For our wiggler parameters and a 1 nC charge, we find $P = 3.35$ MW and $\omega^+/2\pi = 35$ GHz. The transition between the coherent and incoherent spontaneous radiation regimes can be studied by evaluating the energy density in the main spectral line as a function of the electron bunch axial width. The resulting distribution, shown in Figure 3, is given by

$$\frac{d^2I(\omega=\omega^+)}{d\omega\, d\Omega} = \frac{1}{8\pi\varepsilon_0 c}\frac{q^2 N_w^2 \beta_\perp^2}{(1-\beta_{//})^2}\exp\left[-\frac{2\pi^2}{\beta_{//}^2}\left(\frac{\Delta z}{\lambda}\right)^2\right], \quad (6)$$

where we recover the q^2 and N_w^2 scaling (coherent radiation process) and where λ is the radiation wavelength. As the bunch length to wavelength ratio increases, the radiation process becomes incoherent and the power level decreases dramatically.

3. Superradiant FEL Amplification

In a waveguide, the bunched beam will not slip relative to the wave if the FEL resonance line satisfies the grazing condition, $\beta_g = d\omega/cdk_{//} = \beta_{//}$. If the linear equations of an ideal prebunched FEL [3] are solved for the case of a superradiant TE_{mn} amplifier, the power is found to grow spatially as

$$P(z) = P(0) + 2P^{1/2}(0)|\xi z| + (\xi z)^2, \quad (7)$$

where we have defined

$$\xi = \frac{2\gamma_0 I_b\left(\frac{\Omega_w}{\omega}\right)}{a\beta_{//}^{3/2}\sqrt{\pi\varepsilon_0 c\left(1+\kappa^2\right)}}\frac{1}{\sqrt{1-\chi_{mn}'^{-2}}}\frac{J_m'(\chi_{mn}' r_\perp/a)}{J_m(\chi_{mn}')}, \quad (8)$$

and a is the waveguide radius, $\Omega_w = eB_w/m_0 c$, $\kappa = \Omega_w/k_w c\beta_{//}$ and I_b is the beam current. For our experimental parameters, shown in Table 1, the output power is essentially independent of the input power, and reaches a level of 10 MW at 35 GHz in the TE_{11} mode for I_b =10 A in a length of 25 cm.

Bunch Energy	3-4 MeV
Bunch Charge	10 pC-1 nC
Bunch Width	1-10 ps
Peak Current	10-100 A
Bunch Radius	1-2 mm
Wiggler Period	84 mm
Wiggler Field	3 kG
Number of Periods	20
Frequency	35-100 GHz
Operating Mode	TE_{11}
Waveguide Radius	7.94 mm
TE_{11} Cutoff Frequency	11 GHz
Max. Transverse Velocity	0.3
Max. Quiver Radius	4.1 mm

Table 1 Experimental parameters.

References

[1] "Photocathode driven linac at UCLA for FEL and plasma wakefield acceleration experiments", P. Davis *et al*, Proceedings of the Particle Accelerators Conference, San Francisco, CA. (1991).

[2] *Classical Electrodynamics*, J.D. Jackson, (Wiley and Sons, New York, NY. 1975); Chapter 14.

[3] "Prebunched free-electron laser", D.B. McDermott, K.C. Leou and N.C. Luhmann, Jr., Int. Journal of Electronics **65**, 529 (1988).

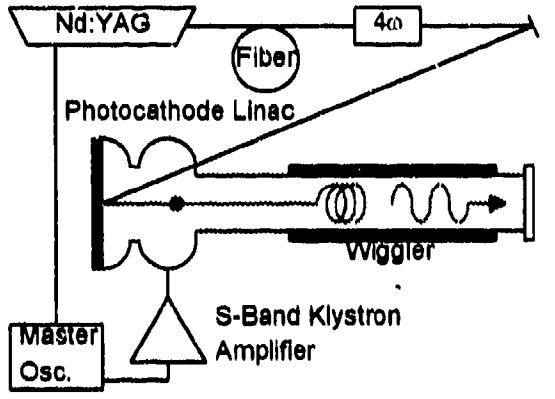

Fig. 1 Overall Experimental Setup.

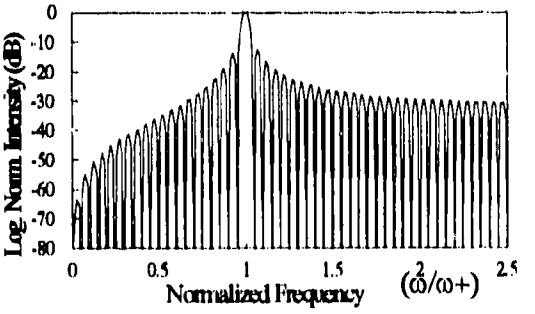

Fig. 2 Normalized on-axis spectrum for a point charge.

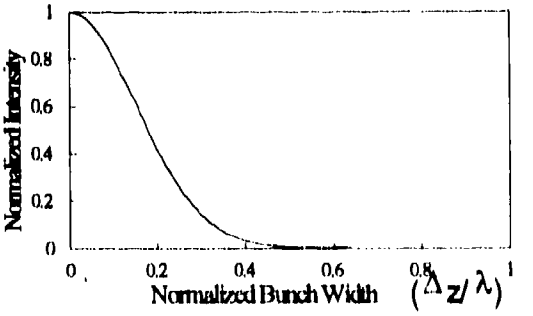

Fig.3 Peak spectral intensity as a function of bunch width.

* Work supported by DOE under Grant DE-FG0-90ER-40565, AFOSR under Grant F49620-92-J-0175 and Rome Laboratory (ATRI) under contract F3062-91-C-0020.

Orofemitron - the new type of Smith-Purcell amplifiers

Yuri A. Romantsov

Radio Astronomy Institute of Ukrainian Acad. of Sc. , Department of Microwave Electronics
Kharkov 310002 , Ukraine

ABSTRACT

The new amplifier of millimeter (MM) and submillimeter (SBMM) wave bands named as **orofemitron**[1] is introduced. The fundamentals of the construction are discussed and the most promising designs are pointed out. On the basis of the theory developed the ultimate output parameters of the **orofemitron** are estimated.

2. INTRODUCTION

Vacuum microelectronics (VM) technology originating in the silicon industry has been shown now great promise for novel microwave electronic devices to be created with the applying of low voltage matrix field- emission electron sources[2] , and among them the new types of MM & SBMM waves amplifiers. One possibility is that the new types of Smith-Purcell devices, named as **orofemitrons**, may be developed by the using of the phenomena of microwave modulation of field emission[1]. This technique of electron current bunching showed its effectiveness both in **femitrons** - klystron-type amplifiers and multipliers of X-band[3] and in MM wave amplifiers with microstrip electrodynamical structure[4]. As for resonance amplifiers based on **orotron**-type electrodynamical systems , such method of electron flow density modulation makes **orofemitron's** construction more workable for practical realization in comparison with multi-resonator Smith-Purcell devices[5,6], whose opto-electronic and electrodynamical systems are essentially complicated through the extension of an interaction space of input section required for effective electron beam bunching by the injected signal. By this means the perspectiveness of the **orofemitron** is stipulated by the use in the same design the most effective in MM & SBMM wave bands electrodynamical system and the phenomena of microwave modulation of field-emission .

3. DESIGN AND THEORY

The essential elements of **orofemitron** construction are the open resonator , which formed by short focus and plane metallic mirrors (the reflecting diffraction grating partially covers the lower mirror), and the special electron gun consisting of microstrip structure with the matrix field emitter , whose current is modulated by the injected signal, and the electrodes for electron beam focusing and accelerating. The electron flow directed by a longitudinal static magnetic field is transmitted within immediate vicinity of the grating. The energy output is provided through a coupling slot in the upper mirror. The input signal power P_{inp} amplification is accounted for by the sharp slope of **Fowler-Nordheim** current-voltage characteristics of the emitter and the effective distributed interaction of electron beam with the open resonator field , as well as due to the shaped electron bunches power increase through additional acceleration by voltage U_a .One of such design is diagrammed by Fig..

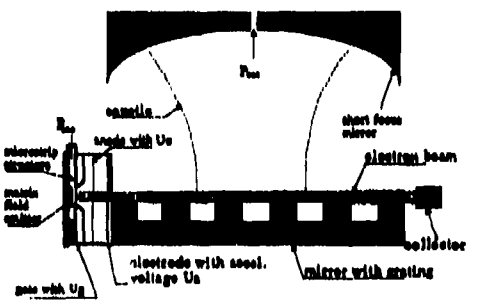

The theory and the estimations of **orofemitron's** output parameters are depend on the original mathematical model of microwave bunching of field emission current and on well-known methods of joint solution of Maxwell's equations & equations of motion for resonant systems with distributed interaction[5,6]. For the low signal amplification mode (input signal voltage U_g << gate voltage U_g) we observe the dependence of maximum power gain factor of **orofemitron**

$$K_{max} \approx [R_{inp} I_0 / U_g] g_0^2 [U_a / U_0] [\lambda \nu_0 / c / R] [J / (1 - J)^2] \approx 20 + 30 \text{ dB}$$

upon: R_{inp} - coupling impedance of the microstrip structure , the relative slope $g_o = (U_g / I_o(U_g))(dI_o / dU_g)$ of the current-voltage characteristic $I_o(U_g)$,accelerating voltage U_g to anode voltage U_o ratio , and the relation $J = I_0/I_{st} < 1$ between beam current I_o and current $I_{st} \sim 1/Q$ of self-excited oscillations of resonator. Here c is the velocity of the light , $v_o(U_g)$ - beam velocity , $R = \sqrt{(\lambda / \pi)\sqrt{d(r-d)}}$ - the radius of the open resonator field spot on the diffraction grating surface,λ - wave length of the input signal. It should be noted that the high Q-factor of the loaded open resonator Q ~ 1000 in MM & SBMM wave bands and high efficiency of distributed beam-field interaction allow to realize the values J ≈ 0.5 + 0.8 with the beam current $I_o \sim 0.1$ A.

In the power amplification mode ($U_g/U_a \sim 0.1 + 0.5$) the considerable efficiency η ~0.1+0.5 may be reached due to the severe bunching of electron beam and also through the optimal conditions for effective interaction of the electron bunches with the resonator field. The results of numerical and analytical investigation of this process[7] showed that the maximum efficiency η_{max} of the **orofemitron** is determined by parameters V_O , R and λ :

$$\eta_{max} \approx [\, \lambda v_o / c / R \,] [\, 1 - 0.25\, (\lambda v_o / c / R) \,]$$

subject to the conditions that

$$v_{ph} \approx v_o / (1 + 3(\lambda v_o / c / R)/8\,) \text{ and } U_g/U_a \sim 0.5,$$

where v_{ph} is the phase velocity of slow space harmonic, a one of the infinite number of harmonics,excited in the vicinity of the grating , which is synchronous with the electron flow , d - the distance between the resonator mirrors is generally taken to be small in comparison with the curvature radius of the upper mirror. It should be noted that for miniature short focus open resonators[8] values of r stood at 3 + 5 λ and d ~ 0.5 r , so $R \le \lambda$. Therefore, the maximum achievable efficiency depends mainly on acceleration voltage U_g . In order to estimate the maximum achievable output power levels (in W), one can use the expression[5,7] in which U_a is pointed in kV

$$P_{max} \cong 0.65(\lambda / R)^2\, U_a^{7/2} [1 - 0.25(\lambda v_o / R / c)].$$

Let us to obtain the estimation of P_{max} and η_{max}, for hemispherical short focus open resonator with r=3.5 λ, d=0.48 r and λ =4.26 mm applied in experiments with miniature orotron[8] . The choice of U_g = 2.4 kV yields the estimations for maximum CW output power and η_{max} as follows : $P_{max} \cong 24$ W and $\eta_{max} \cong 13\%$.

4. CONCLUSION

The latest achievements in the VM technology and miniature open resonators design used for development of the Smith-Purcell devices allow to create compact high stability amplifiers with output power P ≈1+100 W and efficiency η~10 +40% in the MM and SBMM ranges of electromagnetic wave spectrum. Furthermore, the **orofemitron** type construction has attached interest as synchronous generators , multipliers and mixers for the same frequency bands.

5. REFERENCES

1. Yu. A. Romantsov, " Theory and design of a new Smith-Purcell amplifier", Proceedings of International Conf. on MM wave & Far-Infrared Technology, Beijing, August, 1992.

2. Special issue on vacuum microelectr. devices, *IEEE Trans. on Electron. Devices, Vol. 36, n. 11, Part II* ,1989

3. W.P. Dyke, " Field emission, a new practical electron source", *IRE Trs. on Military Elect., Vol. 4*,pp. 38-45,Jan.,1960.

4. H.G. Kosmahl," Wide-Band high-gain small-size distributed amplifier with field-emission triodes for the 10 to 300 GHz frequency range", *IEEE Trans. on Electron. Devices,Vol. 36,n. 11, Part II*, pp.2726-2737,1989

5. D.Vavriv & O.Tretyakov,Theory of the Resonant Amplifiers with distributed interaction, "Naukova Dumka", Kiev,1989.

6. D.Vavriv & Yu. A. Romantsov ," Current status and further progress in the Smith-Purcell amplifiers research", Proc. of 21st. European Microwave Conf., Vol.1 ,pp.824-829 , Stuttgart, Sept., 1991.

7. Yu. A. Romantsov, The investigation of relativistic particles dynamics in resonant systems with distributed interaction, Preprint n.47, Institute of Radio Astronomy, Kharkov, 1990.

8. A.V. Nesterenko .,A.I. Tsvyk ,V.P. Shestopalov, " The miniaturization of the diffraction radiation generators ", *Doklady of USSR Academy of Sci.,Vol. 277,n.1*, pp.84-88,1984.

Microwave oscillator - the orotron with the dc magnetic nonuniformity

Alexander Shmat'ko and Evgeny Odarenko

Kharkov State University, Department of Radiophysics,
Freedom Square 4, 310077, Kharkov, UKRAINE

ABSTRACT

The effect of the profiled focusing magnetic field on the operation of the orotron is studied. The two-dimensional model of the beam-wave interaction is described. The decrease of the starting current and efficiency enhancement are possible for chosen theoretical model.

1. THEORETICAL MODEL

The longitudinal dc magnetic field (MF) is used in the vacuum microwave devices for focusing (TWT, orotron etc.) and beam phasing (magnetron, gyrotron etc.). Effect of the MF space distribution on the output characteristics may be significant. In the present work we consider the starting conditions and nonlinear characteristics of the orotron with localized magnetic nonuniformity (LMN). The modification of the MF space distribution results in distorsion of the electron trajectories and complex beam-wave interaction in the open resonator.

Self-cosistent nonlinear equations and their small-signal approximation are used for the theoretical study. The normalized MF longitudinal component dependence is approximated by the Gauss function in the LMN area

$$B_{\parallel} = 1 + A_N \exp[-((y-y_N)/L_{WN})^2] \qquad (1)$$

where A_N, y_N, W_N - the LMN parameters; y - longitudinal coordinate; L - interaction space length. Combining Eq.(1) and divergence relation (divB=0) yields

$$B_{\perp} = (2A_N/(L_{WN})^2)(y-y_N)(z-z_N)\exp[-((y-y_N)/L_{WN})^2] \qquad (2)$$

where z - transversal coordinate; z_N=const.

The longitudinal dc MF is intense enough so that the ripples of the electron beam boundaries can be neglected. Moreover, we assume LMN to be weak (i.e. $B_{\perp} << B_{\parallel}$).

2. DISCUSSION

Fig.1 illustrated the starting current dependence on the LMN center position. The dotted line gives I_{st} value in the case of uniform MF ($A_N = 0$). The dashed curves correspond to positive values of the parameter A_N. Positive and negative values of A_N indicate accordingly the enhancement and weakening of the MF in LMN area. In both cases the starting current decrease is achieved. Dependently on the A_N sign the LMN should be situated on the opposite grating ends. These results can be explained by transformation of the rf amplitude distribution in the beam frame. It is known that the variation of the amplitude distribution influences on the beam-wave interaction and in this manner the efficiency can be significantly enhanced[2].

Fig.2 shows the maximum electron efficiency η (at values of the initial electron velocity for which the theoretical model has peak efficiency) as function of the parameter y_N for several values of the parameter A_N ($A_N<0$). All dependences are plotted at the fixed beam current. Dashed line gives the η value for usual uniform MF. Curve 1 corresponds to the case when interception of electrons by grating is absent. There is wide area of the y_N values where η is enhanced in comparison with the case when $A_N=0$. When the fraction of the electron beam is striking the grating, the LMN center should be situated on the interaction space end (curve 2 and 3). In this area the majority of the electrons being intercepted are in the region where bunches are located in phase position such that they are extracting energy from the wave. Thus, the interception results in phase selection of the electrons. The decrease of the accelerated electrons amount leads to widening of the initial electron velocity region where oscillations exist and electron efficiency enhancement.

3. CONCLUSIONS

Using the nonuniform focusing MF it is possible improve starting characteristics (starting current decreases) and enhance the efficiency of the orotron. The transformation of the rf amplitude distribution in the beam frame is the main mechanism of the starting current decrease. The enhancement of the electron efficiency is obtained due to phase selection of the electrons..

4. REFERENCES

1.E.N.Odarenko,A.A.Shmat'ko,"The effect of the static magnetic localized nonuniformity on the starting characteristics of the resonant O-type generators", Radiotehnica i Electronica, V.37, N5, pp. 901-909, 1992.

2.M.M.Tarasov,O.A.Tretyakov,A.A.Shmat'ko,"Optimization of the field in O-type electronic resonant generators", Radiotehnica i Electronica, V.33, N1, pp. 141-148, 1988.

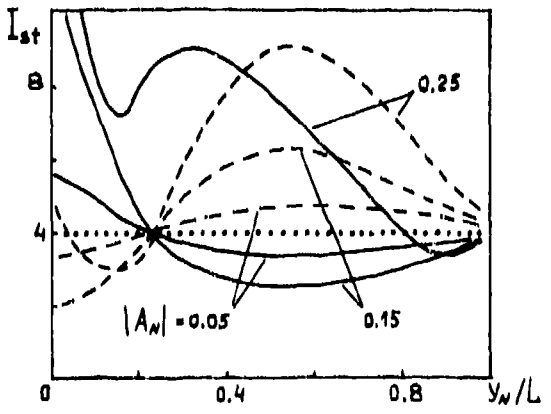

Fig.1. Starting current as a function of the parameter y_N/L.

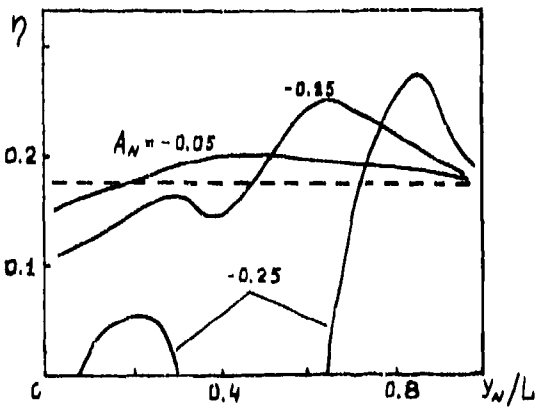

Fig.2. Efficiency vs y_N/L for different values A_N.

Study and development of sub mm range vacuum sources in the Institute of Radiophysics and Electronics of Ukrainian Academy of Sciences

Yeremka V.D., Levin G.Ya., Usikov A.Ya.

Institute of Radiophysics and Electronics of Ukrainian Academy of Sciences
12, Acad.Proskura st., Kharkov, 310085, Ukraine

ABSTRACT

We present the results of development and study of sub mm range vacuum sources, that are carried out in the Institute of Radiophysics and Electronics of Ukrainian Academy of Sciences (IRE).

1.INTRODUCTION

The broadening of fundamental study area in THz region of spectrum is limited by the absence of easy changed small-sized sources in the frequency range from 0.3 to 3.0 THz. In the sixties in IRE the main attention was directed on the development of sub mm wave sources with easy frequency change[1].

2.THE RESULTS OF STUDY AND DEVELOPMENT

2.1.Impulse and continuous clynotrons

Backward wave tubes, namely impulse clynotrons that were the sources of coherent radiation in the frequency range from 0.3 to 0.6 THz with output power of 500-200 W correspondingly were designed. The possibility to increase impulse power of clynotrons by the increasing of operating current owing to the increasing of transversal section of beam area[2] was experimentally confirmed. In according to this the special attention was directed to electrodynamics of slow wave structures (SWSs) and to the possibility of their single-mode excitation by adequate band electron flows. The experimental study of the tubes with SWS of width of $b = 3\lambda$, 6λ and 12λ (where λ is the length of the wave being oscillated) confirmed that at the broadening of SWS width did not decrease and output power of clynotron versus supplied power at different width of SWS. Electrical frequency change range of clynotron autooscillations reaches 20% at λ=1.0mm, 12% at λ=0.5-0.6mm. Characteristic steepness $\Delta f/\Delta U$ reaches 3-7 MHz/V. The dependence of output power at wavelength λ=0.95mm versus angle φ between electron beam and SWS surface, namely clynotron grid (beam thickness Q_0= 0.8mm, SWS length L= 40mm), is shown in Fig.2. One can see the optimum angle is 40% and 60% of beam current hit SWS. When the beam is directed parallel to SWS surface, clynotron does not excited. Characteristic operating regime of impulse clynotrons is excess of operating current over starting one in two times approximately in magnetic field of 0.6-0.7 T (starting magnetic field is 0.2-0.3 T). Fig.3 presents the typical dependence of output power versus the strength of focusing magnetic field from 1.2 to 1.5 THz with output power of several hundreds of Watt.

Fig.4. shows the dependence of output power P/P_{max} (solid lines) of clynotron and its starting current I_{st}/I_{stmin} (dotted lines) versus the angle between operating surface of slow wave structure and the beam in homogeneous and unhomogeneous magnetic field at the operating wavelength λ=0.5 mm. One can see that excitation region by the angle φ is $\Delta\varphi$=7' in homogeneous magnetic field and it is equal to $\Delta\varphi$ = 12' in unhomoheneous one. Operating voltage of devices was 4.0-5.5 kV, operating current was 0.15-0.2 A, strength of magnetic field was 0.8-1.0 T.

2.2. Impulse reflex klystrons[3]

Breadboards of klystrons of sub mm range producing in impulse regime at the wavelengths of 0.95; 0.87 and 0.70 mm the power of 115; 25 and 7 mW correspondingly, were experimentally designed.

2.3. Orotrons - continuous diffraction radiation oscillators (DROs)[4]

Design and study of DROs in the range from 0.3 to 1.0 THz are carried out by Academician V.P.Shestopalov with collaborators. The power of impulse DRO in the frequency range from 300 to 353 GHz is approximately 0.5 W and in the one from 527 to 577 GHz is 0.1 W.

2.4. Peniotrons, orbitrons and orotrons at high harmonics

Different models of such devices are laboratory studied at present time.

3.CONCLUSION

The development of vacuum sources of radio waves in the range from 0.3 to 3.0 THz and corresponding systems and radar detectors are carried out in IRE during 30 years.

4.REFERENCES

1. A.Ya.Usikov, E.A.Kaner, I.D.Truten', G.Ya.Levin, "Electronics and radiophysics of mm and sub mm radio waves", 386 P., "Naukova dumka", Kiev, 1986.

2. G.Ya.Levin, A.I.Borodkin, A.Ya.Kirichenko, A.Ya.Usikov "Clynotron", 200 P., "Naukova dumka", Kiev, 1992.

3. A.Ya.Usikov, V.D.Yeremka, "Development and investigation of mm wave region klystrons in IRE", in 17-th Int. Conf. on IR and MM Waves, Proc. SPIE 1576, PP.442-443.

4. V.P.Shestopalov, "Diffraction electronics", 231 P., "Vyscha shkola", Kharkov, 1976.

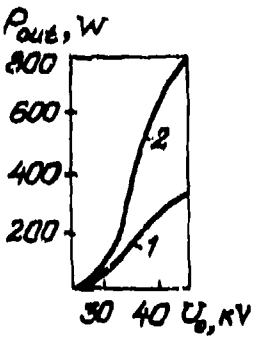

Fig.1. Dependence of output power on operating voltage of impulse clynotrons, the wave: λ=0.8-0.9 mm slow wave structure width 1) b=5 mm, 2) b=10 mm

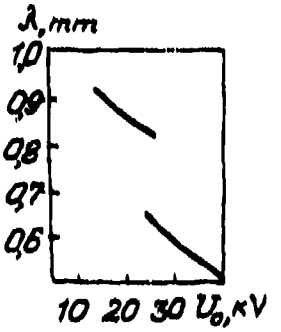

Fig2. Dependence of wavelength on accelerating voltage of two impulse clynotrons

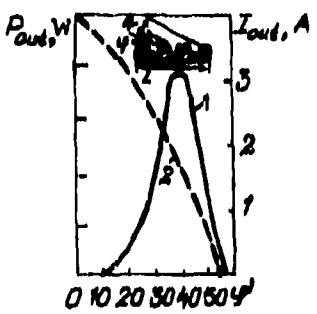

Fig.3. Dependence of the power (1), being generated, and current to the collector (2) of impulse clynotron on beam slope φ

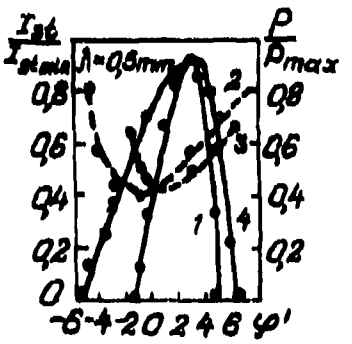

Fig.4. Dependence of the power, being generated and starting current (dotted lines) on the angle φ between the beam and slow wave structure surface

Optimization of FIR photoconductors for both low- and high-background operation.

S.E. Church, A.G. Murray, M.J. Griffin and P.A.R Ade

Department of Physics, Queen Mary and Westfield College,
Mile End Road, London, E1 4NS, UK.

1. INTRODUCTION

Far infrared photoconductors find important applications in astronomy, Earth observation and laboratory spectroscopy. We will review the main performance characteristics of these detectors, and discuss the choice of detector type, readout electronics, operating temperature etc., for a given application. The optimisation of two detector systems, one for low-background space astronomy (the Long Wavelength Spectrometer - LWS - for the Infrared Space Observatory) and one for a high-background aircraft experiment (SAFIRE - Spectroscopy of the Atmosphere using Far Infrared Emission) will be described.

2. LOW-BACKGROUND APPLICATIONS

The LWS uses ten, 1mm^3, doped-Ge photoconductors for low-background spectroscopy over the wavelength range 45-200μm. One Ge:Be detector is used which cuts off at 50μm, the other channels use Ge:Ga. Beyond 120μm, the cutoff wavelength of the Ge:Ga detectors is extended by the application of uniaxial stress to the detector crystals. Examples of the spectral responses of a range of LWS detectors are shown in Fig. 1.

The sensitivity under low-background conditions (as measured by the lowest achievable NEP) is limited by shot noise from the detector dark current and the noise of the first stage cold amplifier. To minimise the latter, integrating amplifiers (IAs) are used (Fig. 2a) in which the detector current charges up the small (7.5pF) input capacitance of the amplifier. The current can then be recovered by measuring the gradient of the integrating ramp. The integrating node is periodically discharged using the reset FET. This circuit has the disadvantage of reducing the bias slightly during an integration but any resulting non-linearity is small and can be corrected for. The dominant noise contribution from IAs is the read-noise which is about 16 e$^-$. The detectors are operated below 4K to reduce the dark current. Excellent NEP values have been measured for the LWS detectors, ranging from 10^{-16} WHz$^{-1/2}$ for Ge:Be to 5×10^{-19} WHz$^{-1/2}$ for stressed Ge:Ga[1]. The performance parameters of the LWS detectors are shown in Table 1a.

3. HIGH-BACKGROUND APPLICATIONS

The rotational transitions of many important atmospheric molecules lie in the FIR spectral region. The SAFIRE instrument will study particular transitions in several narrow-band channels between 30 and 120μm using a fast-scanning Fourier Transform Spectrometer (FTS)[2]. Consequently, the detectors must have fast response as well as good sensitivity. In addition to Ge:Ga and Ge:Be; Ge:Zn, Ge:Sb and Si:Sb-BIB detectors have also been tested to try to maximise the sensitivity in each channel.

Typical SAFIRE backgrounds are estimated to be between 1 and 30nW at the detector. The corresponding detector currents are too large ($> 10^{10}$es^{-1}) to allow the use of IAs. In any case, the noise requirements on the amplifiers are less stringent since photon noise dominates in this regime. Trans-impedance amplifiers (TIAs – see Fig. 2b) offer the advantages of high detector linearity (because the detector bias remains constant) and the high electrical bandwidth required by the FTS. The appropriate measure of detector sensitivity for high-background operation is the detective quantum efficiency (DQE), defined as $(NEP_{BLIP}/NEP_{meas})^2$ where NEP_{BLIP} is the theoretical minimum value from photon fluctuations. The DQE and responsivity values for each detector type[2] are shown in table 1b.

4. REFERENCES

1. Church S.E. et al., in ESA Symposium *Photon Detectors for Space Instrumentation*, p. 205, **ESA SP-356** (1992).

2. Murray, A.G. et al., in ESA Symposium *Photon Detectors for Space Instrumentation*, p. 159, **ESA SP-356** (1992).

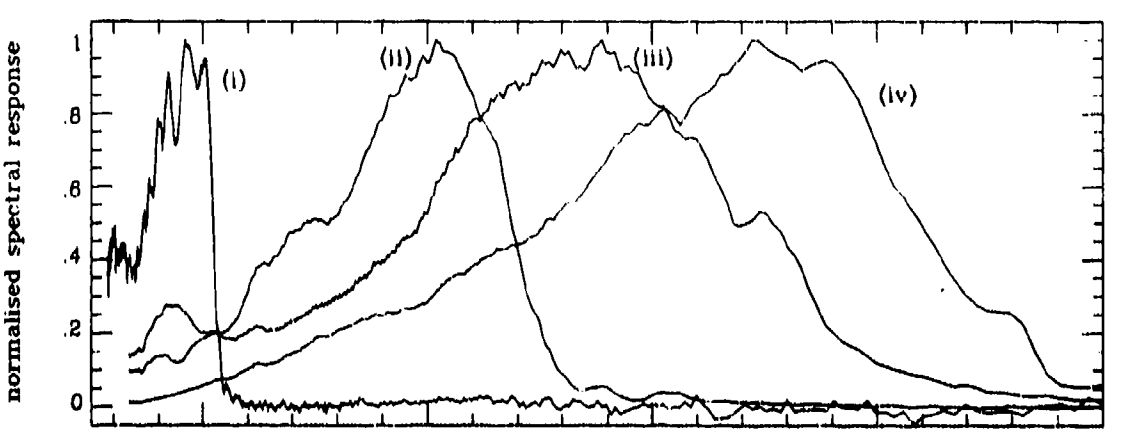

Figure 1: *Spectral response of four LWS detectors (i) Ge:Be, (ii) unstressed Ge:Ga, (iii) lightly stressed Ge:Ga, (iv) highly stressed Ge:Ga.*

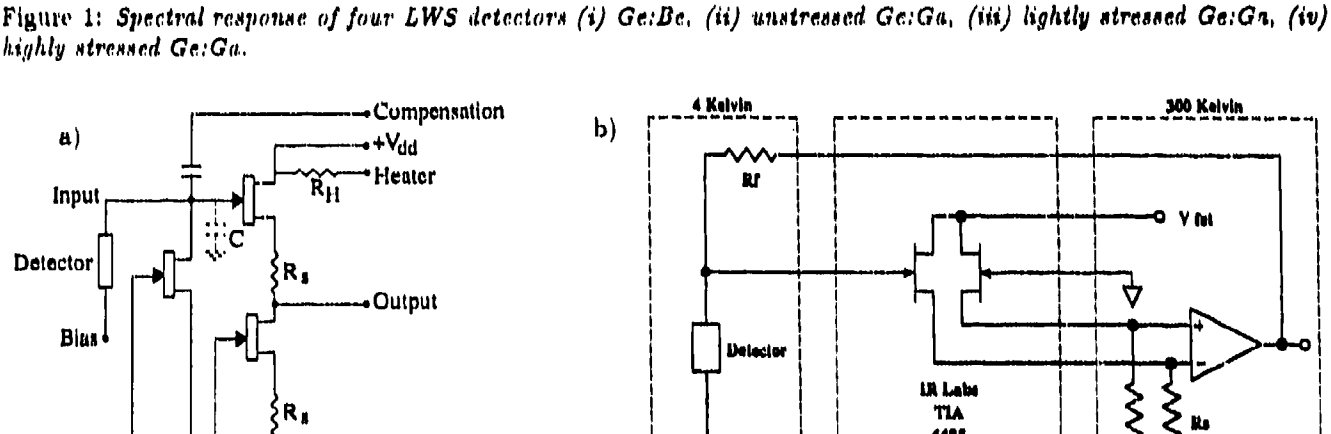

Figure 2: *Schematic of a) The LWS JF4 integrating amplifier b) the SAFIRE Trans-Impedance Amplifier.*

a)

Detector type	λ (μm)	I_{dark} es^{-1}	S (A/W)	NEP ($WHz^{\frac{1}{2}}/10^{-18}$)
Ge:Be	50	234	0.43	0.3
Ge:Ga(u)	85	264	1.0	4.0
Ge:Ga(s)	120	78	8.7	0.5
Ge:Ga(s)	160	430	0.6	0.6

b)

Detector type	λ (μm)	S (A/W)	DQE
Ge:Ga(s)	103	2.5	0.26
Ge:Ga(u)	90	5.6	0.29
Ge:Sb	90	2.8	0.27
Ge:Be	46	2.1	0.17
Ge:Be	31	0.5	0.08
Ge:Zn	31	2.4	0.05
Si:Sb(BIB)	31	0.5	0.12

Table 1: *a) Measured dark currents, I_{dark}, responsivities, S, and NEPs of some LWS detectors. The two Ge:Ga(s) detectors have different stressing levels. b) Measured responsivities, S, and and DQEs of SAFIRE detectors.*

BIB PHOTODETECTORS BASED ON ANTIMONY DOPED SILICON

G. Sirmain, S. Pasquier, C. Mény, P. Etiève°, W. Knap,
P. Adet°, N. Fabre°°, A. Murray°°°, M. Griffin°°°, J. Léotin

Laboratoire de Physique des Solides, SNCMP-INSA
Complexe Scientifique de Rangueil 31077 Toulouse-Cedex (France)
° Tekelec Microwave, 91953 Les Ulis (France)
°° LAAS, 7, av. du Colonel Roche, 31077 Toulouse-Cedex (France)
°°° QMW, Mile End Road London E14NS (Great Britain)

INTRODUCTION

Firstly conceived at Rockwell Science Center by Petroff and Stapelbroek in 1977 (Ref. 1), the Blocked Impurity Band photodetector (BIB) is now recognised to provide significant improvements in comparison with conventional photoconductors. Because they are epitaxially grown, they are easily developed in array configurations having quite uniform pixel response. They are inherently radiation hard due to their small volume. In addition, they have better noise characteristics and they may give some extension of the spectral response towards longer wavelengths. This paper presents some results on BIB photodetectors based on antimony doped silicon, which gave a significant spectral responsivity in the 30 μm wavelength region.

BASIC PHYSICS

Figure 1 presents the doping profile in a BIB device consisting of an n^+inn^+ structure . It can be described as a extrinsic photoconductor which contains between the two ohmic contacts one active photoconductive layer highly doped and one pure blocking layer. Both layers are epitaxially grown on a degenerately doped n^+-type silicon substrate. The blocking layer surface is ion implanted with arsenic to give a transparent thin front electrode for incoming far infrared radiation.

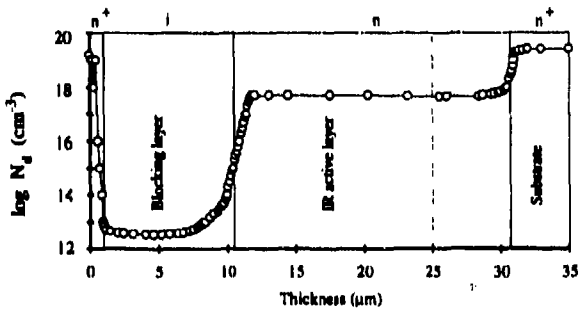

Fig. 1. Doping profile of a BIB device measured by Spreading Resistance with an active layer having 10^{18} cm^{-3} antimony atoms.

The active layer doping level is about two orders of magnitude higher than in a conventional photoconductor. This causes formation of an impurity band exhibiting hopping conductivity (Ref. 2). However, when the n^+-i junction (transparent contact/blocking layer) is positively biased, the electron hopping current cannot enter the pure blocking layer. So, without incoming photons, the i-n junction (blocking layer/active layer) drives no current into the blocking layer since there are no impurity sites for hopping, and also no electrons in the conduction band. Moreover, mobile holes (ionised donors) in the active layer are repelled from the i-n interface, leaving a space charge region of negative ionised acceptors with the thickness W.

When a photon is absorbed in the active region, thus ionising a neutral donor, an electron is generated in the conduction band and a hole in the impurity band. The electron/hole pair will be separated by the electric field and always be collected at the n^+ electrodes since no recombinaison can occur. Conversely, a photon absorbed in the neutral region does not give photocurrent, since the electric field is zero in this region at zero bias current. To increase the quantum efficiency, one needs to extend the active charged region into the entire active layer. However, in order to keep the internal electric field below the breakdown value, the residual acceptor concentration should be kept quite low.

In the following, we report experimental results on one BIB sample doped with 10^{18} cm^{-3} antimony atoms.

ELECTRICAL CHARACTERISATION

The BIB structure can be viewed as a condenser made by the insulating blocking layer and the two n^+ and n layers as electrodes. Indeed, residual acceptor concentration N_a and thickness W can be both determined from capacitance measurements with

$$C(V) = \frac{\varepsilon}{(b + W)} \qquad (1)$$

and

$$W = \sqrt{\frac{2\varepsilon V}{qN_a} + b^2} - b \qquad (2)$$

where b is the blocking layer thickness and ε the semiconductor lattice dielectric permittivity.

C(V) measurements have been realised for different active layer doping levels at 4.2 K and at 1 Hz frequency. The capacitance decreases when a positive bias voltage widens the depletion region according to relations (1) and (2). Figure 2 shows the variation of $1/C^2$ versus bias voltage. The straight line fitting the curve corresponds to a residual acceptor concentration of 4×10^{13} cm^{-3}.

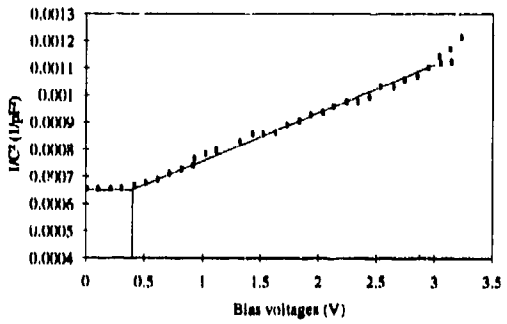

Fig. 2. $1/C^2$ curve versus bias voltage.

At low enough bias voltages, the responsivity can be expressed as

$$S(\nu, V) = \frac{C_0 \sigma(\nu) V}{h\nu} \frac{N_d}{N_a} \qquad (3)$$

where $\sigma(\nu)$ is the absorption cross section at ν frequency and C_0 the capacitance at zero bias voltage (Ref. 3). This indicates that BIB samples having the same N_d/N_a ratio exhibit the same sensitivity at low bias voltages. As a result, their I(V) characteristics under the same background photons flux should be identical. Such a behaviour was actually observed in three samples with an active layer doping ranging from 10^{17} to 10^{18} cm^{-3}.

SPECTRAL RESPONSE

Spectral response measurements were performed using a Fourier Transform Spectrometer at 4 K. Figure 3 shows the spectral responsivity at increasing bias voltages. All curves could be normalised to the same amplitude in the high wavenumber range, far from the cut off.

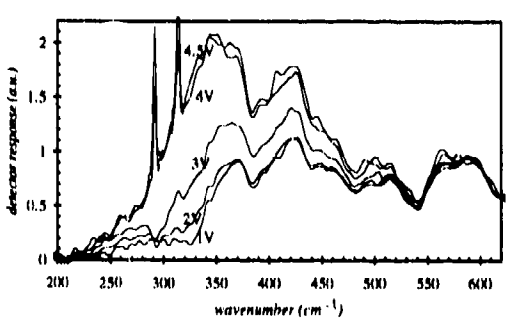

Fig. 3. Responsivity at different bias voltages.

A remarkable feature is a huge enhanced normalised responsivity near the cut off region at high voltages. This enhancement saturates at a bias of 4 V and two narrow peaks rise strongly at photon energies below the impurity binding energy. It turns out that the cut off responsivity at half maximum decreases by 45 cm^{-1}. A similar but smaller effect was observed in bulk Si:Sb photoconductors doped in the range $(1\text{-}8) \times 10^{16}$ cm^{-3} (Ref 4). The value of the cut off wavenumber shift saturates around 14 cm^{-1}. Electric field induced impact ionisation of electrons in the excited impurity states was assumed to cause this effect. The cut off wavenumber shift is larger in our sample which is higher doped, and also experiences higher electric field due to the BIB structure. The two narrow peaks may arise from excited states of isolated impurities statistically scattered among overlapping impurities.

NEP MEASUREMENTS

Responsivity and noise measurements were performed to get the Noise Equivalent Power as a function of bias voltage and at temperatures ranging from 1.8 to 4.2 K. All measurements used a calibrated optical filter centred at 320 cm^{-1}. The modulation frequency was 1 kHz. The photon background power at detector aperture, estimated to 46 nW, gives an ideal background limited noise equivalent power NEP_{BLIP} of 3.8×10^{14} W/$\sqrt{\text{Hz}}$. The optimum measured ratio NEP_{BLIP}/NEP of 0.35 is obtained at 1.8 K (Ref. 3).

CONCLUSION

Blocked impurity band Si:Sb photoconductor was investigated, including epitaxial layers growth, sample processing, electrical and optical characterisations of the device, and final figure of merit measurements.

REFERENCES

1. M.D. Petroff and M.G. Stapelbroek, Blocked impurity band detectors, U.S. Patent, n°4-568-960 , 4 february 1986.

2. B.I. Shklovskii and A.L. Efros, Electronic properties of doped semiconductors, Vol. 45, Springer Series in Solid-State Sciences, edited by M. Cardona, 1984.

3. G. Sirmain, P. Etiève, W. Knap, C. Mény, S. Pasquier, P. Adet, N. Fabre, A. Murray, M. Griffin and J. Léotin, BIB photodetectors based on antimony doped silicon, Proceedings of an ESA symposium on photon detectors for space instrumentation, ESA SP-356, p. 153, december 1992.

4. H.R. and M. Chandrasekhar, K.K. Bajaj and N. Sclar, Electric-field-induced new features in the photoconductivity of extrinsic silicon, Vol. 31, n° 4, Physical Review B, p. 2494, 15 february 1985.

Characteristics and Performance of Ge:Ga Far-Infrared Photoconductors for Space Applications

N.Hiromoto, M.Fujiwara, T.Itabe, H.Shibai*, and H.Okuda*

Communications Research Laboratory, Koganei, Tokyo 184, Japan
*Inst. Space Astronaut. Sci., Sagamihara, Kanagawa 229, Japan

ABSTRACT

Ge:Ga far-infrared photoconductors with dimension of 0.5-mm^3 cube have been fabricated for space astronomical applications. The detectors have excellent detectivity at 2K operation under low photon-background, and also good characteristics such as almost no spike noise, small change in responsivity depending on background-photon influx, almost no hook response, and small amplitude of slow transient response. We have found that reponsivity to chopped infrared light is suppressed at higher bias electric field, while the responsivity to step change in illumination (DC response) increases normally.

1.INTRODUCTION

We have fabricated unstressed Ge:Ga photoconductors as well as a three-element stressed Ge:Ga photoconductor array[1] for the Infrared Telescope in Space (IRTS). The small element has been adopted to decrease cosmic-ray hits to the detectors in the orbit. The characteristics of Ge:Ga wafers and the process for fabrication are the same as the detectors for balloon-borne observations[2]. We have tested eight unstressed detectors at 4K to 2K under low-photon background to examine the characteristics including nonlinear behaviors in response.

2.RESPONSIVITY AND DETECTIVITY

Table 1 summarizes the experimental conditions at 2K including background photon influxes and the performance such as responsivity, Q.E.-photoconductive gain (ηG) product. Please notice that the NEP's in the table are photon-noise limited values at 1.2 V/cm-bias field under the background photon influxes of a few X 10^6 photons/s and include noises of a preamplifier and a feedback resister. The best NEP was better than $1.0\text{X}10^{-17}$, obtained at around 2 V/cm (Fig.1).

3.RESPONSIVITY CHANGE DEPENDING ON BACKGROUND-PHOTON INFLUX

ηG was measured for step-change in illumination and for chopped light at 15 to 210 Hz under background photon influx between $1\text{X}10^6$ and $2\text{X}10^8$ photons/s. The change in ηG was less than a factor of 1.3.

4.SLOW TRANSIENT RESPONSE

The detectors showed the slow transient response to step increase in illumination with a time constant $\tau \sim 10$ sec. The ratio of amplitude of the slow response to the stationary level (DC response) increases from 0.1 to 0.4, according to the bias field, while the time constant decreased from ~15 to ~5 sec.

5.MODERATE FAST-RESPONSE

Figure 2 shows ηG for chopped light at 15 Hz and 7.5Hz as well as for step increase in illumination (indicated as DC) as a function of bias field. The figure displays that the ηG is lower when chopped at

higher frequency and also the ηG is suppressed at higher bias field: This means a time constant restrains the chopped response (moderate fast-response). We found the time constant increases from 0.015 to 0.025 sec between 1.2 and 1.8 V/cm of the bias field.

6.REFERENCES

1.N.Hiromoto, T.Itabe, H.Shibai, H.Matsuhara, T.Nakagawa, and H.Okuda, "Three-Element Stressed Ge:Ga Photoconductor Array for the Infrared Telescope in Space", Appl. Opt., 31(4), 460, 1992.

2.N.Hiromoto, M.Saito, and H. Okuda, "Ge:Ga Far-Infrared Photoconductor with Low Compensation", J. J. Appl. Phys., 29(9), 1739, 1990.

Detector number	5G555-2	5G555-3	5G555-5	5G555-6	5G555-7	5G555-8	5G555-9	5G555-10
Background photon influx(10^6photons/s)	1.5	1.1	1.1	1.5	1.5	2.2	2.2	2.2
Feedback resistor ($10^9\Omega$)	9.0	15.0	15.0	9.0	9.0	9.0	9.0	9.0
Bias voltage (mV)	60	60	60	60	60	60	60	60
Breakdown voltage (mV)	154	127	145	136	168	157.5	173	157.5
Impedance at zero-bias ($10^{12}\Omega$)	5.7	5.0	3.8	9.0	6.0	2.6	3.6	3.6
Impedance at 60mV-bias ($10^{12}\Omega$)	2.1	1.3	2.15	2.1	2.1	0.9	0.96	0.6
Responsivity for 15Hz-chopping (A/W)	2.1	1.9	2.2	2.1	3.0	2.7	2.6	3.3
ηG for chopping at 15Hz	0.027	0.024	0.028	0.027	0.037	0.044	0.048	0.049
NEP for chopping at 15Hz ($10^{-17}W/Hz^{1/2}$)	9.5	8.8	6.7	9.6	6.9	7.5	7.0	6.2
Responsivity for DC signal (A/W)	4.38	10.0	10.6	5.4	5.9	6.8	4.6	8.3
ηG for DC signal	0.055	0.13	0.13	0.068	0.075	0.10	0.074	0.15
NEP for DC signal ($10^{-17}W/Hz^{1/2}$)	4.6	1.4	1.4	3.8	3.6	3.0	4.0	2.4

Table 1. Performance of Ge:Ga photoconductors at 2K.

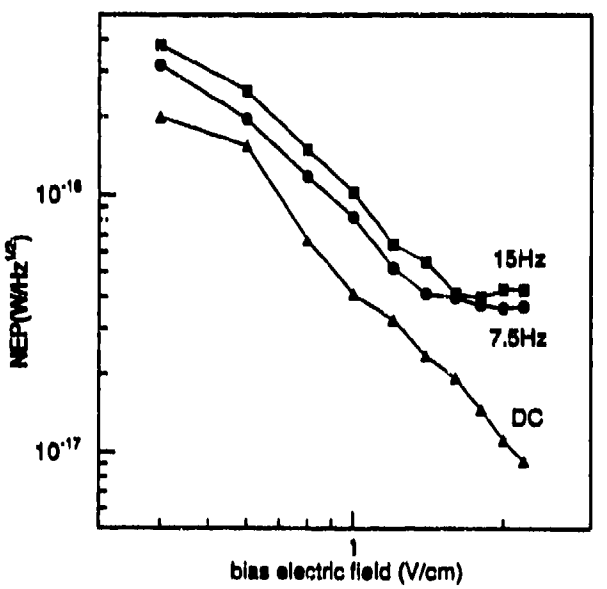

Fig.1.NEP as a function of bias at 2K.

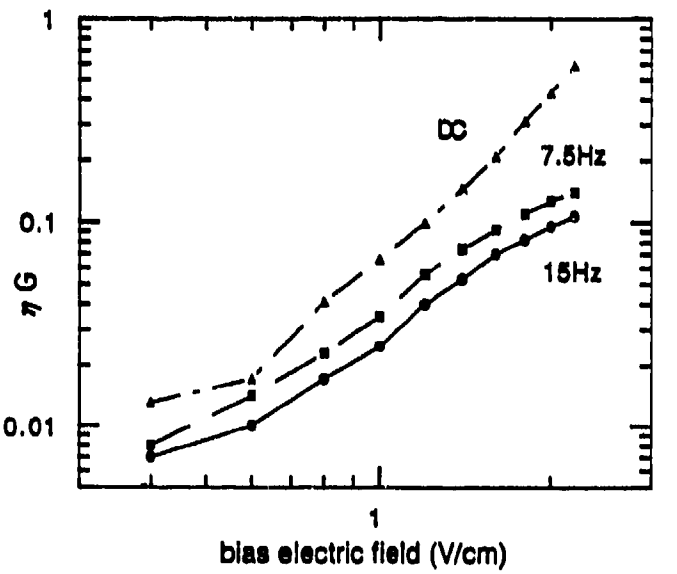

Fig.2. ηG as a function of bias.

Effects of ionising radiation in Ge:Ga and Ge:Be far-infrared photoconductors.

M. C. Price , S. E. Church , M. J. Griffin and P. A. R Ade.

Physics Dept., Queen Mary and Westfield college, Mile End Road, London, E1 4NS.

1. INTRODUCTION

Doped germanium photoconductors cooled to temperatures ~3 K are the most sensitive detectors for wavelengths >30 μm . However under very low far-infrared (FIR) backgrounds ~fW, expected in-flight on the ISO LWS, these detectors can exhibit non-linear behaviour which can severely compromise the overall sensitivity. These non-linear effects can be broadly catagorised into two types.

Non-linear effects due to the interactions of ionising radiation within the detector crystal. This leads to an increase in the responsivity, dark current and noise of the detector. Unless some form of detector annealing is implemented post-irradiation recovery of the detector takes place on time scales $\gtrsim$ 8 hours. Inherent non-linear effects caused by a step change in the illumination level. This can lead to very long settling times $\gtrsim$ 30 seconds.

2. EXPERIMENTAL SETUP

Three different types of doped Ge photoconductor were tested; a Ge:Be detector sensitive to wavelengths up to 55μm , an unstressed Ge:Ga detector with a cutoff wavelength of 100μm and a stressed Ge:Ga detector sensitive to wavelengths up to 185μm . The detectors tested were the Engineering Qualification Model (EQM) ISO LWS detectors and are nominally identical to the flight model detectors to be operated in flight on the LWS. All detectors were tested inside a specially modified HD3 cryostat. Irradiation was performed with an externally mounted 100mCi ^{241}Am 60 keV γ-ray source to simulate the effects of a transit through the Van Allen radiation belts. Post irradiation annealing of the detectors was performed by applying a 'bias boost' across the detector. Bias boosting involves applying an electric field across the crystal greater than the breakdown field of the detector. This should sweep out any trapped carriers and restore the detector characteristics back to their pre-irradiation levels. This was the only method of detector annealing investigated as it will be the only method available on the ISO LWS during flight. Figure 1 shows the very slow dark current recovery of the EQM Ge:Ga(u) detector after irradiation and the effects of applying a bias boost to 'cure' the detector.

3. EXPERIMENTS PERFORMED

To investigate the radiation induced non-linear effects and the inherent non-linear effects two types of test were performed. Irradiation tests to simulate effects of passage through the Van Allen belts. Experiments included:-

1. Effects of applying a bias boost to the detector in the absence of any ionising radiation and subsequent monitoring of detector recovery.
2. The effects of irradiation and the post-irradiation recovery of the detector without any annealing.
3. The effects of irradiation and the recovery of pre-irradiation detector characteristics with application of a bias boost.

Inherent non-linearity tests. This involved measuring the detector response to a step increase in illumination under different bias voltages and infrared flux levels.

4. RESULTS

Our irradiation tests have shown that bias boosting is effective in curing unstressed Ge:Ga detectors on time scales of the order of an hour but is not totally effective in restoring the dark current and responsivity of Ge:Be or stressed Ge:Ga characteristics to better than a factor of 1.5-2 above their pre-irradiation levels of J^{o}_{dark} and S_o. Increasing the length of time the bias boost is applied or increasing the bias boost field strength does not measurably alter the recovery profile. Table 1 tabulates the results obtained for the EQM detectors. The quoted value of settling time is the time taken for the detector to reach a stable state where the dark current and responsivity were not dropping significantly.

Analysis of the inherent non-linearities to a step response in illumination was performed by fitting a phemenonological model using three time constants to the data. It is shown that there are two fast components (with values ~ a few seconds) and a third, much slower, component ($\gtrsim$ a few tens of seconds). Experiments have shown that all three time constants are weak functions of illumination level and the first two time constants are also weakly dependent on bias field. However the third time constant has a strong bias dependence and governs the overall settling time of the detector. Figure 2 illustrates this long settling time for the EQM Ge:Ga(u) detector operating at 3K. Figure 3a shows the dependence of this time constant on bias field and figure 3b illustrates the weak dependence on infrared signal power. Ge:Ga and Ge:Be also show different 'switch-off' characteristics to a step decrease in illumination. The Ge:Be detector has a much longer settling time to a decrease in illumination under the same operating conditions as the Ge:Ga detectors.

	Without Boost			With Boost		
Detector	Ge:Ga(s)	Ge:Ga(u)	Ge:Be	Ge:Ga(s)	Ge:Ga(u)	Ge:Be
Dark Current	$14I^{o}_{dark}$	$20I^{o}_{dark}$	$2I^{o}_{dark}$	$1.5I^{o}_{dark}$	$1I^{o}_{dark}$	$1.5I^{o}_{dark}$
Responsivity	$4S_o$	$\sim 14S_o$	$2S_o$	$2S_o$	$1S_o$	$2S_o$
Settling time	2^h	1.5^h	2^h	1^h	1^h	15^m

Table 1: Tabulated summary of results from experiments performed on the ISO LWS EQM detectors.

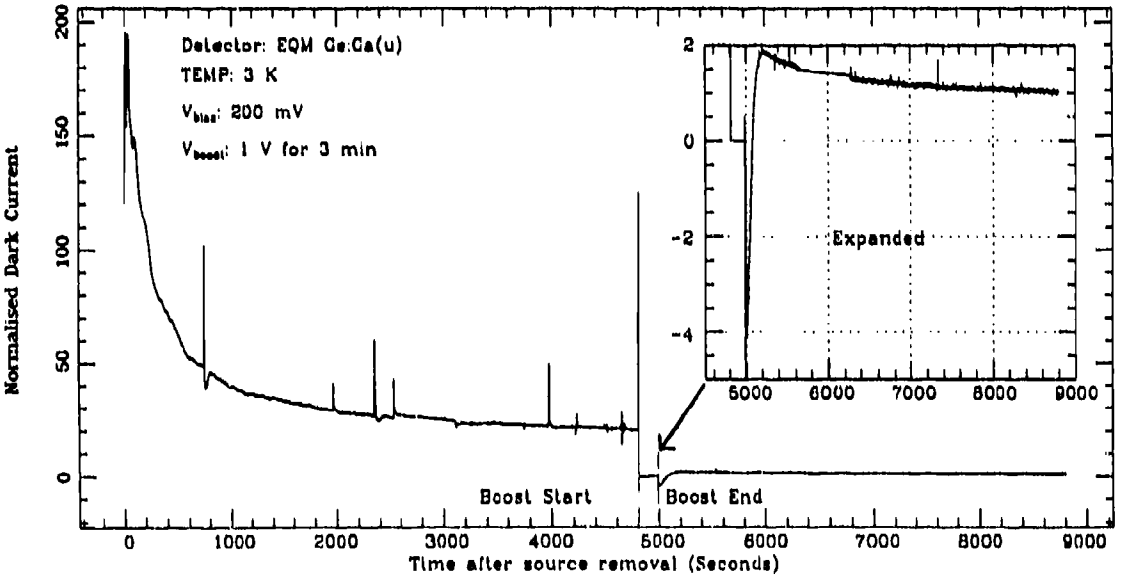

Figure 1: Dark current recovery after irradiation and boost for the EQM Ge:Ga(u) detector.

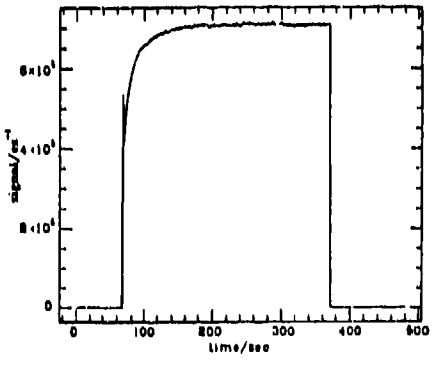

Figure 2: Illustration of inherent detector non-linearities due to a step change in illumination level.

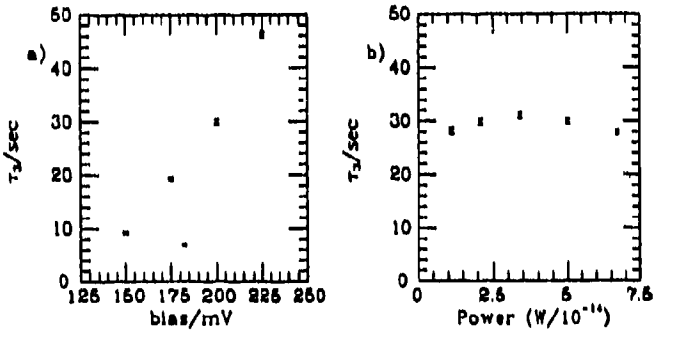

Figure 3: Dependence of slow time constant, τ_3 on bias and infrared signal power.

The Noise and Optimum Operating Temperature of High Tc Superconducting Infrared bolometer

Chen Juxin, Shi baoan, Wu Rujia, Gong Shuxing
Shanghai Institute of Technical Physics,
Academia Sinica, Shanghai 200083

Yang Caibing, Cao Xiaoneng
Institute of Electronics, Academia Sinica, Beijing 100080

Zhang Yinzi, Li lin
Institute of Physics, Academia Sinica,
Beijing 100080

ABSTRACT

The temperature and the bias current dependence of noise as well as the noise spectrum for high Tc superconducting infrared bolometer (HTSIB) have been investigated. The influence of the bolometer structure on device noise has been discussed. The responsibility spectrum and the detectivity D^* spectrum for HTSIB has also been obtained. The optimum operating temperature has been determined,that is between T_{CO}(zero-resistance temperature) and T_{cm}(the temperature at mid transition point). the performances of our HTSIB are $D^*(500,10,1) = 3.7 \times 10^9 cmHz^{1/2}W^{-1}$and noise equivalent power $NEP(500,10,1) = 2.4 \times 10^{-11} WHz^{-1/2}$.

Excitonic detectors of infrared and submillimeter waves

Gennadii K.Vlasov, Dmitrii N.Vylegzhanin, Elena I.Chizhikova

Center for Program Studies, Russian Academy of Sciences
SU-117810 Moscow, Russia

ABSTRACT

The theory of infrared (IR) and submillimeter radiation detection in direct-gap semiconductors based on "quenching" effect of Raman lines due to interaction between free and bound excitons is proposed. The first experiments were performed which shows the possibility to obtain NEP = 10^{-17}-10^{-19} $WHz^{-1/2}$ at helium temperature.

2.INTRODUCTION

We present the theory of infrared radiation detector using optical (contact-less) read out of a response produced by IR-signal in the crystal. Two main mechanisms are considered, both are grounded on the effects of quenching by IR-signal of spectral lines or bands of secondary radiation in direct-gap semiconductor crystal excited by light in the fundumental absorption region. These lines are connected with Raman light scattering (RLS) due to interaction between free and bound excitons and (or) green "edge" radiation (luminescence).

For every of considered mechanisms there is possible to achieve the theoretical quantum limit for sensitivity. The theory is confirmed by the experiments performed at helium temperature on CdS crystals excited by mercury lamp radiation.

3.EXPERIMENT

High quality platelets of CdS crystal, grown from gas phase, were excited at T=4,2 K by Hg-lamp radiation through the filter selecting line λ=365 nm. The spectrum of luminescence contains some lines with intensities, which increase near linearly as the level of UV excitation groves after the filter (λ=365 nm) was taken off. Among these lines there are ones belonging to excitons bounded on neutral acceptors (I_1), or neutral donors (I_2), and ones which are their LO-phonon replicas, and so on. Therewith, the line of above-mentioned RLS reduces its intensity in ≈1400 times,while the wide band of"edge" emission - in 100 times,comparing with the case of excitation through the filter. Because this filter was nontransparent for IR-radiation, this behavior may be interpreted to be connected with IR-quenching. Forapumping sourse for the RLS the stimulated emission on line I_1 was used[1,2]. To detect The middle IR-radiation one must use the crystals with dominating I -line, while to detect the radiation in submillimeter region one must use the crystals with dominating I_2-line. After IR illumination the concentration of neutral impurities that only can capture excitons lowers. Thus the number of scattering centers for RLS decreases causing the quenching of RLS intensity.

4.THEORETICAL LIMIT

Signal-to-noise ratio in output curcuit of photomultiplier is

$$S/N = \left(\frac{P_o e\eta}{\hbar\omega_s}\right)^2 \frac{\hbar\omega_s}{2e^2(P_o+P_b')\Delta\nu} , \qquad (1)$$

where $\hbar\omega_s$ is energy of a photon of secondury visible radiation, e is electron charge, η is quantum yield, $\Delta\nu$ is bandwidth of registrating system, P_b' is power of background radiation in visible region, which may be neglected, and

$$P_o = P_R - \Delta P|\cos \Omega t| - \delta P \qquad (2)$$

where in turn P_R is power of (Stoks)RLS line without IR-illumination, ΔP is amplitude of quenching by IR-signal with power P_s, δP is amplitude of quenching by IR-background with power P_b', Ω is modulation frequency for IR-signal. Assuming narrow-band selection on the frequency Ω, we have

$$\left(S/N\right)_\Omega = \frac{\eta\Delta P}{\hbar\omega_s\Delta\nu} = \beta \frac{\eta}{\hbar\omega_s\Delta\nu} P_s . \qquad (3)$$

Here it was assumed also, that δP, $\Delta P \ll P = P_R - \delta P$.

From (3) it follows, that

$$NEP = \left(\beta \frac{\omega_{ir}}{\omega_s}\right)^{-1} \frac{\hbar\omega_{ir}\Delta\nu}{\eta} , \qquad (4)$$

where ω_{ir} is angular frequency of incoming IR-wave. In the case of IR quenching of RLS line coefficient β is defined by following expression

$$\beta = \frac{k_a \tau \sigma d \Phi P}{S\, 4\pi \hbar\omega_s} , \qquad (5)$$

where k_a is absorption coefficient for IR-photon, corresponding to impurity-band transitions, τ is life-time for electron capture, σ is cross-section of RLS, d is scattering length, Φ is solid angle in which the secondary radiation registration is performed, and S is crystal area. Assuming the following values for these quantities

$k_a = 10^2$ cm^{-1}, $\tau = 10^{-7}$ s, $\sigma = 10^{-12}$ cm^2, $d = 0{,}1$ cm, $\Phi = \pi$, $S = 0{,}1$ cm^2,

$\hbar\omega_s = 10^{19}$ J, $P = 4 \cdot 10^{-3}$ W

we have $\beta=10^{-1}$ and considering $\omega_{ir}/\omega_s=10^{-1}$/, $\eta\simeq1$, finally we obtaine

$$NEP \simeq 10^{-18}\ WHz^{-1/2}. \quad (6)$$

As for heterodyne receivers, in our case the main noise is caused by strong light field (see, e.g.[3]). From th above, the IR background radiation does not restriot NEP value as long as $P_b \ll 10^{-1}$W.

The exoitonio detectors described here may also serve as IR-imagers or TV-photocathodes with high spatial resolution.

7. REFERENCES

1. G.K.Vlasov, D.V.Prokhorov, E.I.Chizhikova, "Raman light scattering due to collisions of Wannier-Mott exoitons with impurities and between them" *Phys.Stat.Sol.(b)*, vol.176, pp.511-519, April 1993.

2. G.K.Vlasov, M.S.Brodin et al., "Antistoks Raman light scattering..." *ZhETF*, v.71, pp.310-318, 1976.

3.A.Yariv. Introduction to Optical Electronics, *2-nd ed.*, *Holt Rinehart & Winston*. New York, Chicago etc.

New microwave detector

Steponas Ašmontas and Algirdas Sužiedėlis

Semiconductor Physics Institute, Vilnius, Lithuania

Point-contact of metal-semiconductor is widely used as a microwave (MW) power detector or harmonic mixer. However, at high frequencies, the application of such contact is problematic due to small size of the waveguide.

We propose a new type of planar detector which operation is based on nonuniform electron heating by MW field. The nonuniformity of electron heating we have achieved using asymmetrically necked thin semiconductor film containing n-n^+ junction.

Vapour-grown of n-n^+-GaAs epitaxy layers and n-Si monocrystal wafers were used for fabrication of the detector. Ohmic contacts to GaAs were made by thermal evaporation of separate Ge/Ni/Au layers with following thermal annealing in inert gas atmosphere. Those contacts to Si were made by thermal phosphor diffusion through the windows created in SiO_2 by photolitography method. As metal contact we used the thermal evaporated and annealed Al/V/Cu sandwich. The asymmetrically necked semiconductor structure was formed by chemical etching in the case of GaAs, and by plasma etching in the case of Si. Then we coated those structures with polyimide film of small permittivity ($\varepsilon < 3$). After thinning-down the semiconductor wafer, the semiconductor material from the ohmic contacts were removed by chemical etching.

When the relaxation of average energy of hot electrons can be neglected, i.e. $(\omega\tau_\varepsilon)^2 << 1$ (ω is angular frequency of MW field, τ_ε is a phenomenological energy relaxation time), a conductivity current exceeds displacement one. In this case the voltage sensitivity of the diode is[1]

$$S = U_d/P = \Delta R/2U \qquad (1)$$

where U_d is the detected signal of diode, P is the MW power which the diode have absorbed, $\Delta R = R_{+U} - R_{-U}$ is the difference of point contact resistance, when reverse and forward dc voltages U are applied.

Solving the current density, heat balance, heat flow density and Poison equations for the electric current, passing through the asymmetrically necked semiconductor structure with n-n^+ junction, we have obtained the difference of resistance of asymmetrically necked diode, when reverse and forward voltages are applied in warm electron region:

$$\Delta R = \frac{4U\rho\mu_0\tan\alpha_1[\tau_\varepsilon(1+s)+\tau_M]}{3hd^2\ln[1+(a/d)\tan\alpha_1]} \qquad (2)$$

where s is the index of power dependence of electron momentum relaxation time on energy, τ_M is Maxwell relaxation time in n-region, ρ,μ_0 is resistivity and electron mobility of n-region semiconductor material respectively, a,d are width of semiconductor structure in the widest and the narrowest part of diode, h is thickness of n-region, α_1 is the angle of n-region widening.

This expression shows that the resistance difference is direct proportional to applied voltage. Experimentally measured dependences of resistance difference of asymmetrically necked semiconductor structures at room (T=295K)

and liquid nitrogen (T=80K) temperatures are in good agreement with those calculated from equation (2). At the liquid nitrogen temperature the relative resistances difference of the diode is greater than that at a room temperature for the same value of applied voltage. It is connected with the higher value of electron mobility and energy relaxation time in n-GaAs and n-Si at the T= 80K in comparison with those at a room temperature.

Placing the diodes in rectangular waveguide the dependence of detected signal on applied MW was measured in wide range of MW frequencies at T=80K and T=295K. When the MW power is small (the electrons are slightly heated by electric field) the value of detected signal is directly proportional to the microwave power. Therefore, those semiconductor structures based on n-GaAs and n-Si may be used as the measurement element of MW power. The volt-power characteristic at a room temperature is linear in wider range of MW power than that at a liquid nitrogen one. This is associated with the fact, that at T= 295K τ_ε depends weakly on the instantaneous value of MW electric field strength E_m, meanwhile, at liquid nitrogen temperature the electron energy relaxation time decreases rapidly with E_m increase. The value of voltage sensitivity measured at MW frequency f=143 GHz is (20÷30)% lower in comparison with that at f=26 GHz. The value of this decrease of voltage sensitivity of our diodes are in good agreement with the theoretical predictions for frequency dependence of voltage sensitivity of small area n-n$^+$ junction diode[2].

REFERENCES

1. S. Ašmontas, L. Vingelis, V. Guoga, A. Olekas, A. Sužiedėlis, "Relationship between voltage sensitivity and I-V characteristics acymmetry of detector with point contact n-n$^+$-junction", Fiz. Tekh. Poluprovodn., Vol.16, No.2, pp. 367-369, February 1982.

2. S. Ašmontas, Electrogradient phenomena in semiconductors, 183 p., Mokslas, Vilnius, 1984. (in russian)

New hot-carrier effects in submicron structures for infrared and millimeter wave receivers

Vladimir B. Yurchenko

Kharkov Polytechnic Institute, Dept. Materials for Electronics and Solar Cells
21 Frunze St., Kharkov, 310002, UKRAINE

1. INTRODUCTION

Advances in technology of submicron semiconductor structures make it possible to develop a great variety of novel non-conventional photoreceivers. Even if considering the classical effects only, one can see that various kinds of the effects could take place in the structures of that scale. The nature of the effect depends on relations between the device active layer thickness a and the main physical lengths which describe the relaxation processes in a semiconductor. For submicron structures, the relations

$$l_i \, , \, l_{ee} \ll a \ll l_\varepsilon \, , \, l_r \qquad (1)$$

or

$$l_i \ll a \ll l_{ee} \, , \, l_\varepsilon \, , \, l_r \qquad (2)$$

are the most typical, l_i, l_{ee}, l_ε, l_r being the lengths of the momentum relaxation, the inter-electron collisions, the carrier energy relaxation, and the carrier recombination, respectively. In both the cases, carrier excitation in a photoreceiver leads to carrier photo-heating and to appearance, if any built-in-field exists, of hot-carrier photovoltage considered as a measured signal. However, the values of the voltage generated in these cases are different. The reason is that in the case (2), unlike (1), essentially non-Maxwellian carrier energy distribution is formed which may result in appearance of a specific additional photovoltage of hot carriers[1].

The aim of this paper was, therefore, to investigate the processes of hot-carrier photovoltage generation under the conditions of non-Maxwellian carrier energy distribution in submicron structures for infrared or millimeter wave photoreceivers.

2. PHYSICAL MODEL AND METHOD OF COMPUTATION

As a simple model of a submicron structure we consider a thin n-type semiconductor layer with nonuniform doping profile $n(x)$ providing the given carrier concentrations at the surfaces $n(0)$ and $n(a)$. We suppose a uniform intraband excitation of the majority carriers due to far infrared, microwave or millimeter wave irradiation. Non-equilibrium carrier distribution function formed under the condition (2) is determined by the steady-state Boltzmann's equation which does not account for electron-electron and electron-phonon energy relaxation processes. The energy relaxation occurs on the layer surfaces where the metal contacts are supposed and the equilibrium distribution functions are taken as the boundary conditions. The carrier excitation is described by the terms which contain the square mean value of the electric field of high-frequency electromagnetic wave, E_0 . Internal electric field in the layer, $E_i(x)$, is determined self-consistently assuming the open-circuit conditions at the contacts. In the case considered, the original Boltzmann's equation was reduced to the nonlinear elliptic partial differential equation for the symmetrical part of the carrier distribution function $f_s(\varepsilon,x)$. The equation obtained was solved numerically

for the cases being of interest, by means of a specially developed method based on the Stone's strongly implicit procedure[2] completed with the self-consistent calculation of the electric field $E_i(x)$. The results for $E_i(x)$, mean carrier energy $\bar{\varepsilon}(x)$ and photovoltage V_c were compared with the data obtained from the energy balance equation which was written and solved analytically for some cases under the conditions (1) providing the carrier temperature approximation.

3. RESULTS AND DISCUSSIONS

The analytical treatments and the computer simulations have been carried out for two kinds of doping profile:

$$n_1(x) = A_1 + B_1 \exp(x/L) \quad , \tag{3}$$

and

$$n_2(x) = A_2 + B_2 \cos(\pi x/a) \quad , \tag{4}$$

assuming the given ratio $n(a)/n(0)=10$. Various momentum scattering mechanisms have been studied including the deformation acoustic (DA) and the charged impurity (CI) scattering. The value $E_0=T/ea$ has been taken as a typical high-frequency electric field which satisfies the condition $|\bar{\varepsilon}(x)-T| \ll T$, T is the lattice temperature and e is the carrier charge. The relative voltages V_a and V_c calculated under the conditions (1) and (2), respectively, are given in the table:

Doping profile n(x):	$n_1(x)$		$n_2(x)$	
Scattering mechanism:	DA	CI	DA	CI
Voltage:				
eV_c/T	0.20	0.06	0.27	0.08
eV_a/T	0.09	0.04	0.13	0.06

The data show that the voltage V_c is generally greater than V_a which is caused by the increase of the values $f_s(\varepsilon,x)$ in high-energy domain under the conditions (2) as compared with Maxwellian function formed under the conditions (1). The voltage grows in the case of DA carrier momentum scattering and the built-in-field localization in the middle of the layer.

4. CONCLUSIONS

An increase of the voltage generated by infrared or millimeter waves in a submicron layer with a built-in-field has been predicted and numerically simulated. The effect is caused by the formation of essentially non-Maxwellian carrier energy distribution function due to the intraband hot-carrier excitation under the conditions (2) . The voltage considered grows in a periodic multi-layer structure because of summing the effects from all the layers.

5. ACKNOWLEDGMENTS

The author wishes to thank Yu. Gurevich for discussions and support of this work.

6. REFERENCES

1. Yu.G.Gurevich and V.B.Yurchenko, "Generation of photovoltage in homogeneous unipolar conductive medium," Solid State Commun., Vol.72, pp.1057-1058, Nov. 1989.

2. R.Hockney and J.Eastwood, Computer simulation using particles, Chap.6, McGraw-Hill, New York, 1981.

HIGH POWER TUNABLE 20 atm CO_2-LASERS AND THEIR OPFIRL APPLICATIONS

W. Schatz and K.F. Renk
Institut für Angewandte Physik, Universität Regensburg
W-8400 Regensburg, Germany

Abstract

We report the development of two 20 atm CO_2-laser systems delivering continously tunable mid-infrared radiation with output powers of 250 mJ and 1 J respectively. Using this radiation for optical pumping a superradiant far-infrared laser we obtain for several molecular gases emission via stimulated Raman scattering in the region from 8 cm^{-1} to 250 cm^{-1}.

High-pressure CO_2-lasers are very convenient for optically pumping a far-infrared (FIR) laser, for their frequency is continuously tunable in the mid-infrared frequency region. Therefore generation of tunable FIR radiation via stimulated Raman scattering is possible and has been demonstrated for several molecular gases as for the methylhalides [1], heavy water [2] and ammonia [3].

The laser we used up to now has been described in detail elsewhere [4]. The resonator consists of a concave germanium output coupler (reflectivity ≈ 0.7; radius ≈ 25 m) and a 150 l/mm grating for frequency tuning; an off-axis Galilean telescope is inserted to expand the beam diameter at the grating surface. Optical access is given to the 20 atm pressure chamber by two NaCl Brewster's angle windows. With this configuration, frequency tuning is possible in steps of 1 GHz over ranges of about 500 GHz, the spectral width of the emitted radiation is about 5 GHz (FWHM). The emitted pulses have a total duration of about 300 ns and a maximum energy of 250 mJ, limited by the damage threshold of the NaCl Brewster windows. With our new laser system this limitation is not valid any longer. Using an intra cavity beam expander (1:2) we are able to obtain 1 J without damages on the NaCl window. To reduce the problems with alignment we used the frequency selective grating also for output coupling purposes; the other end of the pressure chamber is sealed with a high reflecting molybdenium mirror (see figure). The bandwidth of the emitted radiation is about 10 GHz (FWHM) for the grating has only 120 l/mm. In the table the tuning ranges of both lasers have been listed. The CO_2-laser radiation is focussed into the fused quartz waveguide (diameter 7 mm) of the Raman laser. This laser is equipped with a BaF_2 entrance and a TPX (polymeric 4-methyl-1-pencene) output window. Since TPX does not completely absorb the CO_2-laser radiation transmitted through the FIR laser tube, an additional crystalline quartz plate is mounted.

Laser media we investigated so far were the methylhalides ($^{12}CH_3F$, $^{13}CH_3F$, $^{12}CD_3F$, $^{13}CD_3F$, $^{12}CH_3Cl$, $^{12}CH_3Br$, $^{12}CH_3J$), heavy water ($D_2^{16}O$, $D_2^{18}O$) and the ammonia isotopes $^{14}NH_3$, $^{14}NH_2D$,

$^{14}NHD_2$, $^{15}NH_3$ and $^{15}ND_3$. Optical pumping the methylhalides delivered 630 emission lines in the frequency region from 8 cm^{-1} to 71 cm^{-1}, 29 of them could be assigned as overtone transitions ($2\nu_3$) of $^{12}CH_3J$. Using heavy water as laser medium we obtained 93 laser lines in the frequency region from 25 cm^{-1} to 240 cm^{-1} and with ammonia we observed 350 laser lines from 15 cm^{-1} to more than 200 cm^{-1}. The photon conversion coefficients reached values of up to 12% ($^{14}NH_3$ and $^{12}CD_3F$); the maximum observed FIR tuning ranges were 36 GHz ($^{12}CH_3F$), 17 GHz ($D_2^{16}O$) and more than 90 GHz ($^{14}NH_3$).

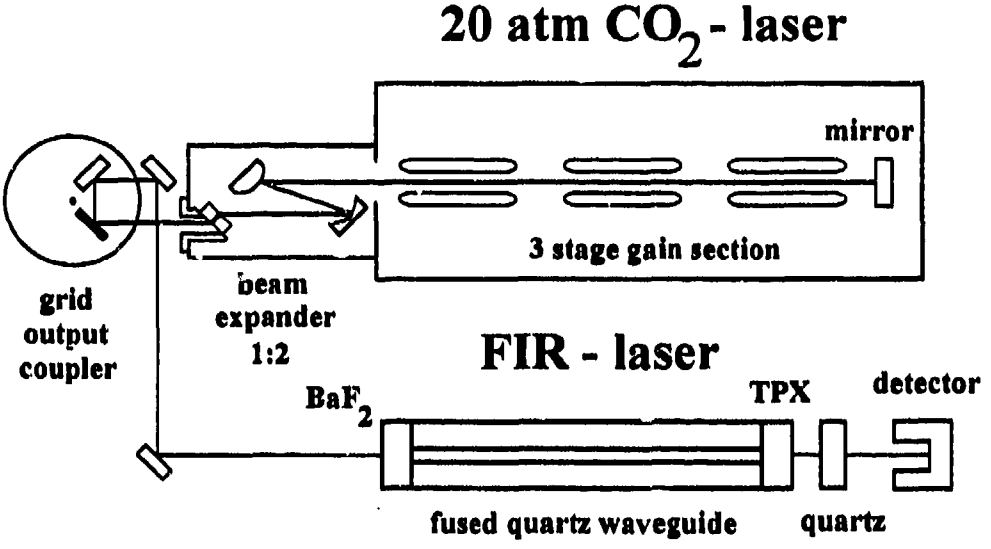

Figure: Experimental setup

branch	80 cm gain region	150 cm gain region
10R	R(6) - R(28)	R(2) - R(40)
10P	P(8) - P(28)	P(4) - P(38)
9R	R(6) - R(30)	R(2) - R(44)
9P	P(10) - P(26)	P(4) - P(38)

Table: Tuning ranges of the two high pressure CO_2-lasers

References

[1] P.T. Lang, *Infrared Phys.* **4**, 237 (1992).
[2] P.T. Lang, W Schatz and K.F. Renk, *Opt. Commun.* **84**, 29 (1991).
[3] W. Schatz and K.F. Renk, *this volume.*
[4] Chong-Yi Wan, U. Werling and K.F. Renk, *J. Appl. Phys.* **57**, 990 (1985).

Measurement of Power and Energy at Teraherts Frequencies

D.H. Martin, G.W. Poulson, Luo Xizhany,
E. Puplett, R. Martin and R.J. Wylde

Laboratory for Millimetre Waves,
Queen Mary and Westfield College,
Mile End Road,
London E1 4NS

As major applications for millimeter and submillimeter electromagnetic waves have developed there has arisen a need for instruments which will allow measurements to be made of the power carried by free-space propagating beams and of the energy carried in short pulses. Such instruments should be calibrated absolutely and re-calibration should be a straightforward matter. This paper will report on the power and energy meters we have developed for the 60-900 GHz range.

Two measurement methods have been developed to cover the two domains:

(i) measurement of powers exceeding 1 μW (with 1s response time) and energies exceeding 1 μJ (in pulses of duration less than 10 ms),

(ii) measurement of powers exceeding 0.1 pW (with 1s response time) and energies exceeding 0.1 pJ in pulses of duration less than 100 ms.

For the first domain we have developed a power meter in which the signal beam passes through a thin metallic film which has the resistance-per-square which maximises the fraction of the signal power absorbed in the film as the beam passes through it. This film on a 1 μm polymeric substrate, lies between a window and a back-reflector, or a second window, to form a narrow-gap airfilled cell. The power absorbed from the signal beam heats the film and this raises the temperature of the air layers in contact with the film which results in an increase in air pressure in the cell. The signal beam is modulated and the consequent variations in pressure in the cell are measured by a miniature pressure-transducer at the periphery of the cell. The film has electrodes along opposite edges so that current can be passed through the film to provide ohmic power which serves to absolutely calibrate the power meter.

The paper will examine the properties of this photo-acoustic detection system which make it a reliable and sensitive absolute power meter. Two versions of the meter will be described, one for precision measurements in the millimetric range and one which operates over a wide-band from millimetric to far infrared frequencies.

The second domain involves much smaller signal power levels and what is required is a means for calibrating absolutely, as a function of frequency, the response of a sensitive detector, e.g. pyro-electric detectors down to 1 nW and cooled photoconductive or bolometric detectors down to 1 pW. This paper will describe how this can be done with a thermal source (black-body cavity) and a two-beam polarising interferometer employed as a band-pass filter which is tuneable over the millimetric and far infrared ranges and whose throughput efficiency throughout that range can be determined with precision.

FAR INFRARED LASER LINES FROM CH_3OH AND ISOTOPES: A REVIEW

S.C. Zerbetto and E.C.C. Vasconcellos
Instituto de Física "Gleb Wataghin", Depto. Eletrônica Quântica
Universidade Estadual de Campinas - Cx.P.: 6165
13083.970, Campinas, SP, Brasil

ABSTRACT

Methyl Alcohol is the most prolific and one of the most efficient molecules for the production of optically pumped FIR laser lines. We present a review of nearly 2000 CO_2 pumped FIR laser wavelengths, and frequencies of about fifteen percent of those, measured in CH_3OH and its isotopes.

1. INTRODUCTION

Chang et al[1] early recognized methanol as a source of strong far infrared (FIR) laser lines. Since then, more than 100 papers were published containing information about new laser emissions. Recently, Moruzzi et al[2] presented a review of 575 lines produced by methanol ($^{12}CH_3OH$). In the present paper, we have extended the review to 10 other isotopic modifications of this molecule.

Optically pumped lasers are today the most important source of coherent radiation in the FIR spectral region, and are increasingly finding wide applications in several fields of physics.

In the present work, the pump source which produced most of the lines is a CO_2 laser. In a few cases isotopic CO_2 lasers were employed. CO_2 sequence band and hot band laser lines were also eventually used for optical pumping. As far as the FIR laser cavity is concerned, a great variety of resonators has been employed. It was noticed that the highest output powers have been achieved in hollow dielectric waveguides. However, Fabry-Perot cavities are widely used as well[3].

2. CH_3OH

The vibrational-rotational structure of CH_3OH is well known[4], and data on its other isotopic species are constantly being improved. The reason for this success is the overlap between the strong absorbing CO-stretch band and the CO_2 laser emission spectrum (specially the 9R and 9P branches). Exchanging H for D to obtain the deuterated species does not alter the situation appreciably, so that the CO-stretch absorption band still coincides with the CO_2 laser spectrum. It is also possible to substitute ^{13}C for ^{12}C and ^{9}O for ^{8}O.

3. RESULTS

In table 1 we present an overview of the results, together with some statistical data. From this table we can see another reason why the methanol analogues are such important molecules for FIR laser generation. Most of the lines have wavelengths that are less than 200 μm, and a significant percentage have short wavelengths (<100μm). It is a well known fact that for other molecules (with the exception of CH_2F_2 and isotopic forms) the situation favors longer wavelengths[5]. This short wavelength region is the most scarce in coherent sources and the most interesting for spectroscopic applications. The increasing investigation of CH_3OH and CH_2F_2 can help to fill in this gap by hopefully making available a new set of pump laser lines.

4. APPLICATIONS

Being practically the only source of coherent radiation in the FIR region, optically pumped lasers find a variety of applications in various fields of physics. Laser Magnetic Resonance (LMR) in the far-infrared is an example: a molecular transition frequency is tuned into coincidence with that of a fixed laser frequency by the application of a variable magnetic field (0-20 kGauss)[6]. Important chemical species were studied by this extremely sensitive technique, such as the OH radical, for example. Current interest is on the involvement of this species in the fundamental steps of chemical reactions[7], specially those occuring in the atmosphere[8]. In fact, the photochemistry of the OH radical controls the rate at which many trace gases are oxidized and removed from the atmosphere. For example, Brown et al[9,10] used CH_3OH laser lines in LMR spectroscopy.

TABLE 1: PERCENTAGES OF LASERS LINES ACCORDING TO WAVELENGTH RANGE

Wavelength range (μm)	Nummber of laser lines (%)
< 100	23.7
100- 200	28.1
200- 300	22.4
300- 400	10.6
400- 500	6.7
500- 600	3.0
600- 700	2.3
700- 800	1.4
800- 900	0.6
900-1000	0.5
> 1000	0.8

5. REFERENCES

(1) T.Y. Chang, T.J. Bridges, E.G. Burkhardt, Appl. Phys. Lett. 17, 249 (1970)
(2) G. Moruzzi, J.C.S. Moraes, F. Strumia, Int. J. IR & MM Waves 13, 1269 (1992)
(3) S. Jacobsson, Infrared Phys. 29, 853 (1989)
(4) J.O Henningsen, "Infrared and Millimiter Waves,"K.J. Button ed., Academic Press, New York (1982)
(5) N.G. Douglas, "Millimiter and Submillimiter Wavelength Lasers," Springer series in Optical Sciences, Springer-Verlag (1989)
(6) K.M. Evenson, Far. Disc. Chem. Soc. 71, 7 (1981)
(7) R. Atkinson, Chem. Rev. 85, 69 (1985)
(8) W. Chameides, D.D. Davis, C & En, Oct 4, , p39-52(1982)
(9) J.M. Brown, J.E. Schubert, K.M. Evenson, H.E. Radford, The Astroph. J. 258, 899 (1982)
(10) J.M. Brown, C.M.L. Kerr, F.D. Wayne, K.M. Evenson, H.E. Radford, J. Mol. Spectrosc. 86, 544 (1981)

New FIR Laser Lines from Optically Pumped C_2H_3F, C_2H_3Cl,C_2H_3CN,$C_2H_2F_2$,C_2H_5F and CF_2O

P.B. Davies, Yuyan Liu, Zhuan Liu*

Department of Chemistry, University of Cambridge
Lensfield Road, Cambridge CB2 1EW, England

*Permanent Address: Wuhan Institute of Physics, the Chinese Academy of Sciences, Wuhan 430071, P.R. China

Over the past two decades, a large number of optically pumped far infrared laser lines have been discovered with a wide variety of lasing gases. Amongst these C_2H_3F, C_2H_3Cl, $C_2H_2F_2$, C_2H_5F, C_2H_3CN and CF_2O are important examples. They give many strong laser lines which are very useful for far infrared laser magnetic resonance(FIR LMR) and tunable far infrared(TuFir) laser spectroscopy. Although these gases have been investigated before, we have nevertheless discovered over 30 new laser lines between 140 μm and 988μm.

The optically pumped FIR laser was originally developed for FIR LMR spectroscopy. The cavity is 1 m long and formed by two concave gold coated mirrors with radii of 1.635m and 1.835m, respectively. The laser gas fills a gold-coated glass tube, 7cm in diameter, located between the cavity mirrors. Pump radiation from a cw CO_2 laser, 60w for the stongest line, enters the cavity through a side wall window and is transversely multiply reflected in the glass tube. The FIR radiation is coupled out through a 2mm hole in the R=1.635m mirror and detected with a Golay cell. In order to eliminate the effect of thermal radiation from FIR laser components, the CO_2 laser beam was chopped instead of the FIR radiation. This apparently facilitated the search for new laser lines. Laser wavelength measurement was achieved using a micrometer, on which the totally reflecting FIR laser mirror is mounted, with an estimated precision of $\pm$0.5μm.

In order to obtain as many FIR laser lines as possible, we carefully investigated every CO_2 pump line on the above gases, changing the laser gas pressure and the tuning of the pump laser. Generally, each laser line has its own optimum gas pressure and optimum CO_2 laser frequency offset. In TableI are listed all the new laser lines obtained, including measured wavelength, CO_2 pump line, optimum pressure and relative intensity.

Of special interest is the case of the 10P22 pump line for C_2H_3F. There appear to be two very close components lasing together. This has been supported by observing LMR spectra of the CF radical. The two components gave slightly different LMR spectra for CF. C_2H_3Cl also shows two closely spaced lines when pumped by 10 R26.

Table I. New optically pumped FIR laser lines

Wavelength(μm)	Pump line	Lasing gas	Intensity	Optimum pressure(mT)
137.0	9R22	C_2H_3F	S	70
140.4	10R34	CF_2O	S	100
141.0	10R42	CF_2O	V.S.	170
152.5	10R30	CF_2O	V.S.	100
184.0	10R34	CF_2O	S	120
218.5	10P36	C_2H_3Cl	S	80
269.0	10R02	C_2H_3F	M	150
285.0	10P36	C_2H_3Cl	S	80
285.0	10P32	C_2H_3F	S	80
325.0	10P12	$C_2H_2F_2$	V.S.	180
352.2	10P22	C_2H_3Cl	S	130
354.0	10P12	$C_2H_2F_2$	M	120
361.0	10R12	C_2H_3CN	W	100
376.8	9R14	C_2H_5F	M	80
403.2	10P24	C_2H_3Cl	M	150
415.3	10P12	C_2H_3CN	W	50
417.5	10P16	C_2H_3Cl	M	150
438.5	9R24	C_2H_5F	W	80
444.5	10P10	C_2H_3F	M	160
447.3	10P14	C_2H_3F	S	80
477.3	10P36	C_2H_3Cl	M	50
503.2	9P18	C_2H_5F	W	45
513.5	10P34	C_2H_3Cl	M	60
534.3	10R04	C_2H_3Cl	M	70
551.0	9P18	C_2H_5F	M	50
572.8	10R18	C_2H_3CN	M	50
574.0	10R14	C_2H_3CN	M	50
606.5	10P42	C_2H_3F	M	45
618.3	10R12	C_2H_3CN	W	25
629.3	10R06	C_2H_3CN	W	20
669.9	10P20	C_2H_3Cl	W	70
777.3	10P22	C_2H_3F	V.S.	80
777.5	10P22	C_2H_3F	S	55
987.8	10R26	C_2H_3Cl	W	45
988.5	10R26	C_2H_3Cl	W	45

V.S.--very strong, S--strong, M--medium, W--weak as related to the known laser lines from the same lasing gas.

Identification of submillimeter CD2O laser lines

S. F. Dyubko, S. V. Syrota

The analysis of the rotational spectrum of CD2O molecule in excited coupling vibrational states ν_4 and ν_6 has been performed. Optically pumped FIR CD2O laser operates using rotational transition of these vibrational states. Many a CD2O laser lines have been assigned. A table of the generation lines frequencies of a CD2O laser was obtained instead of the known tables of wavelengths.

A Table of the Absorption Strong Lines of Formic Acid which are Coincided with the FIR Lasers Frequencies

S. F. Dyubko, S. V. Syrota

Kharkov State University, Department of Quantum Radiophysics, Kharkov, Ukraine, 310077

We revealed many coincidencies of generation lines frequencies of FIR lasers and absorption lines frequencies of strong lines of the rotational spectrum of formic acid molecule. The results are reported in Table 1. We used FIR lasers frequencies which have been reported in N. G. Douglas handbook [1]. And absorption lines frequencies of fomic acid have been obtained when we investigated the rotational spectrum of these molecules in frequency range up to 400 GHz. About 8,000 frequencies of absorption lines of HCOOH, DCOOH, HCOOD, DCOOD, H13COOH, D13COOH, H13COOD, D13COOD, HC18OOH, HCO18OH, DC18OOH, DCO18OH, DC18OOD, DCO18OD in ground state and, particully, in exited vibrational ones were measured. Accuracy of these measurements was ± 20 ÷ 50 kHz. As a result the sets of rotational and centrifugal molecular parameters of Watson's Hamiltonian, I^{st} representation, have been obtained for each species.

Comparing frequencies of lasers and absorption lines frequencies of formic acid we examined only lines with intensity $\gamma > 10^{-4}$ cm^{-1} and frequency shift $|f_0 - f_i| < 2$ MHz.

The results given in Table 1 may be used for following purposes:

- frequency stability of FIR lasers on power nonlinear resonances;
- constract of the gaseous filters for selection of laser radiation;
- masers constract on Q-transitions of formic acid molecules pumped whith a FIR laser;
- the next investigation of the rotational transitions of formic acid using a FIR laser as a radiation source.

Table 1

LASER [1]	LASER FREQUENCY	MICROWAVE	J′	K_a'	K_c'	TRANSITION J″	K_a''	K_c''	INT. cm^{-1}	
CH3Br	283665.4	283666.9	12	4	8	13	4	9	0.013	HCOOD
CD3I	298197.8	298197.3	13	12	1	14	12	2	0.003	D13COOD
DCOOD	300238.6	300238.9	13	3	10	14	3	11	0.011	HC18OOH
13CH2F2	320426.8	320425.9	14	4	11	15	4	12	0.012	HC18OOH
DCOOD	323058.7	323059.7	13	2	11	14	2	12	0.015	HCOOH
DCOOD	384411.2	384412.7	17	3	15	18	3	16	0.020	HCO18OH
DCOOD	393551.5	393552.9	16	2	14	17	2	15	0.027	HCOOD
NH2NH2	408346.7	408345.5	18	5	14	19	5	15	0.023	D13COOD
CH3Br	419061.7	419058.7	18	8	10	19	8	11	0.033	D13COOH
CD3I	449307.5	449304.4	19	14	5	20	14	6	0.004	H13COOH
CHC1F2	450216.4	450217.1	19	7	13	20	7	14	0.016	HCOOH
CH2F2	456139.1	456141.2	20	15	5	21	15	6	0.005	H13COOD
DCOOH	469064.7	469066.2	21	12	9	22	12	10	0.017	D13COOD
CH2CHC1	472507.5	472507.0	20	13	7	21	13	8	0.001	HCOOH
CH2CHC1	472507.8	472507.1	20	9	11	21	9	12	0.011	HCOOH
DCOOD	534109.6	534108.1	23	5	19	24	5	20	0.026	DCOOH
H13COOH	546225.3	546223.4	23	4	19	24	4	20	0.041	D13COOH
NH2NH2	561772.0	561773.0	24	3	22	25	3	23	0.053	HCOOH
CD3Br	565506.1	565506.5	27	0	27	28	0	28	0.046	D13COOH
TRIOX	598192.4	598194.7	27	6	21	28	6	22	0.037	HCO18OH
CH3OH	607431.2	607433.2	26	13	13	27	13	14	0.016	HCOOH
CH2CF2	618417.5	618418.3	28	11	17	29	11	18	0.027	HC18OOH
DCOOH	642578.4	642578.7	30	6	24	31	6	25	0.041	DCOOD
CH2F2	645530.9	645527.9	28	4	24	29	4	25	0.040	D13COOD
CH2F2	672689.5	672691.8	30	17	13	31	17	14	0.006	HCOOD
NH2NH2	687957.4	687959.5	29	4	25	30	4	26	0.052	H13COOH
CD3OH	695691.5	695688.2	31	13	18	32	13	19	0.020	HCOOD
HCOOD	697695.1	697697.5	30	18	13	31	18	14	0.019	HCOOH
CDF3	712130.6	712128.1	31	7	24	32	7	25	0.034	DCOOH
CHC1F2	723522.9	723524.8	32	3	29	33	3	30	0.029	HCO18OH
HCOOH	739161.0	739161.4	33	13	20	34	13	21	0.020	HCOOD
HCOOD	765384.6	765384.5	33	6	27	34	6	28	0.035	D13COOH
CHD2F	798579.5	798577.1	36	8	29	37	8	30	0.024	D13COOD

1. N. G. Douglas Millimetre and Submillimetre Wavelength Lasers. A Handbook of cw Measurements. -Springer-Verlag Berlin ..., 1989, 289 p.

TIME-DEPENDENT SIMULATION OF OPTICALLY PUMPED FIR LASER FOR ARBITRARY POLARIZATION CONFIGURATIONS

V.A.Batanov, A.O.Radkevich and A.L.Telyatnikov

Institute of Physics and Technology of the Russian Academy of Sciences. 117218, Moscow, Krasikova 25A, Russia.

A numerical model of time-dependent simulation of FIR laser is presented. The model expands the previously reported steady-state solution for the arbitrary field polarisation configurations in OPTIRL to the time dependent model. No limitations on the intensities of the interacting fields are imposed.

Theoretical Research and Discussion of Dynamical States of Optically Pumped Submillimeter Laser

Luo Liguo[1], Nie Dezhen[1], Chen Jishu[2] and Su Jinwen[3]

[1] Department of Optics, Shandong University, Jinan, Shandong, 250100, P. R. China.
[2] Department of Physics, Ningbo University, Ningbo, Zhejiang, 315211, P. R. China.
[3] National Laboratory for Infrared Physics, Shanghai Institute of Technical Physics, Academia Sinica. Shanghai, 200083, P. R. China.

I. Introduction.

It is not an amasement that optically pumped submillimeter laser (OPSML) system can show rich dynamical behaviours of bistability and instability, for it may be taken for a combination of passive and active systems. It is one of the most suitable lasers for laser dynamical research.

II. Fundamental Equations

The three-level model is sufficient and effective for us to study dynamical behaviours of the continuous OPSML system. We assume that both the pump laser and the submillimeter laser emit single- mode travelling- wave fields in a homogeneously broadened medium. The interaction between laser and matter can be described with a set of equations derived from the density matrix and Maxwell's equations as follows:

$$\left.\begin{aligned}
&\dot{\alpha} = K_p(\alpha - \alpha_I) + g_p\rho_{13},\\
&\dot{\beta} = -K_s\beta + g_s\rho_{23},\\
&\dot{d}_{13} = -\gamma_{D1}(d_{13} - 1) + 2(\alpha\rho_{31} + \alpha^*\rho_{13}) + \beta\rho_{32} + \beta^*\rho_{23},\\
&\dot{d}_{32} = -\gamma_{D2}d_{32} - (\alpha\rho_{31} + \alpha^*\rho_{13}) - 2(\beta\rho_{32} + \beta^*\rho_{23}),\\
&\dot{\rho}_{13} = -(\gamma_{13} + i\Delta_p)\rho_{13} - (\alpha d_{13} + \beta\rho_{12}),\\
&\dot{\rho}_{23} = -(\gamma + i\Delta_s)\rho_{23} + (\beta d_{32} - \alpha\rho_{21}),\\
&\dot{\rho}_{12} = -[\gamma_{12} + i(\Delta_p - \Delta_s)]\rho_{12} + \alpha\rho_{32} + \beta^*\rho_{13}.
\end{aligned}\right\}$$

where α_I, α, and β are slowly varying envelope amplitudes of the input pump field, the intracavity pump field and the submillimeter field respectively.

The Kp and Ks are respectively the decay rates of the pump field and the submillimeter field. g_p and g_s are the unsaturated absorption coefficient of the pump field and the unsaturated gain coefficient of the submillimeter field, respectively. Other variables and parameters are in the coventional forms of laser theory.

Ⅲ. Results and Discussion

Several results are obtained by studying the fundamental equations.

(1) Analysis of state without submillimeter laser emission.

Linear stability analysis reveals that there are three kinds of unstable regions of state ($\beta=0$, α). The first arises from bistability of the pump laser. It corresponds to the negative slope of $\alpha \sim \alpha_1$ curve. The second is proved to correspond to the cw output of submillimeter laser (β=cw, α) . The third gives pulsation and even chaos output. All of the regions vary much by changing paramenters of K, g and γ.

(2) Bistability of the OPSML system

The system shows bistabilities for both $\alpha \sim \alpha_1$ curve and $\beta \sim \alpha_1$ curve. These curves change dramatically by adjusting K, g and γ.

(3) Pulsation of the OPSML system

With a pulsation expression of β stable pulsation is easily gotten in the OPSML system on resonance. The pulsation frequency grows with the increase of pump intensity. Unstable pulsation and chaos can be obtained around the initial emergence of the pulsation.

(4) Analysis of small-amplitude pump modulation

By studying the effect of small-amplitude pump modulation, we know that the system has two intrinsic frequencies. The higher frequency concides with the pump Rabi frequency. The lower frequency is mainly related to the choice of K, g and γ, which also determine the emergence of the later frequency pulsation. The two frequencies may have relations with the two different chaos in the OPSML system [C. O. Weiss, N. B. Abraham and U. Hubbner Phys. Rev. Lett. 61 (1988) 1587] .

The project is supported by the National Natural Science Foundation of China.

Experimental Research of Pulsation and Chaos in Optically Pumped Submillimeter Laser

Luo Liguo[1], Chen Jishu[2] and Su Jinwen[3]

[1] Department of Optics, Shandong University, Jinan, Shandong, 250100, P. R. China.
[2] Department of Physics, Ningbo University, Ningbo, Zhejiang, 315211, P. R. China.
[3] National Laboratory for Infrared Physics, Shanghai Institute of Technical Physics, Academia Sinica. Shanghai, 200083, P. R. China.

I. Introduction

Laser dynamical behaviours in both passive and active resonators have attracted much attention of many laboratories since 1980's. The research can not only reveal the origin and character of laser dynamics, and give a good example for general nonlinear theory, but also provide theoretical and experimental foundations of practical designing of submillimeter laser with continuous-wave (cw), pulsation and chaos outputs.

II. Experiment and Results

In our experimental setup an 1.5m long gold-coated waveguide submillimeter resonator is pumped by a CO_2 laser with selectable lines. The output mirror of the submillimeter laser can sweep in length direction and it is tiltable in order to adjust the resonator loss. The submillimeter laser is detected with a GaAs Schottky barrier diode. An oscilloscope and a rf spectrum analyzer are used to display the results.

In optically pumped formic acid submillimeter laser, the 9R(20) CO_2 laser line with power of 20W is used as pump laser. The submillimeter laser wavelength is 433μm with its largest output power of 10mW. The submillimeter laser exists within the HCOOH pressure from 5 to 90 mTorr.

While the submillimeter laser output is gotten, stable pulsation is easily obtained on energy resonance. The pulsation behaviour is very stable and exists for quite a long time. The pulsation frequency decreases from 1.5 MHz to 0.4 MHz as the tilting angle grows. The pulsation frequency increases a little with increasing of the HCOOH pressure.

At higher pressure, unstable pulsations are observed. Various styles of unstable pulsations are sensitive to condition changing. The developed chaos is observed and it also exists for quite a long time. From pulsation to chaos, a two-frequency road is observed.

In optically pumped CH_3I submillimeter laser, the 10P(18) CO_2 laser line with power of 45W is used as pump laser. The submillimeter laser wavelength is 447 μm with the largest output power of 10mW and CH_3I gas pressure ranges from 9 mTorr to 70 mTorr. Stable pulsation is also obtained on energy resonance, but it is sensitive to the increases of gas pressure or output mirror loss. The frequency of an unstable pulsation frequency can vary periodically between 0.5 and 1.5 MHz. The two-frequency route into chaos is also clearly observed.

The 10P(20) CO_2 laser line is used to pump CH_2CF_2 submillimeter laser. The submillimeter laser wavelength is 890 μm with output pawer around 1mW. The pulsation is not very stable and unstable pulsation varies much and it is sensitive to condition changing.

From the experiment we are able to conclude that pulsation and chaos, like the cw output, are the commom output states of many optically pumped submillimeter lasers. These behaviours may have potentiality in laser application in the future.

* The project is supported by the National Natural Science Foundation of China

Experimental studies with open resonators on frequency dependent dielectric loss at mm-wavelengths

V. V. Parshin[1)], R. Heidinger[2)], G. Link[2)]

1) Applied Physics Institute
Russian Academy of Sciences
46 Uljanov St.
603600 Nizhny Novogorod
Russia

2) Association KfK-EURATOM
Kernforschungszentrum Karlsruhe
Inst. für Materialforschung I
Postfach 3640
D-7500 Karlsruhe 1
FRG

Open resonators, both of the spherical and hemispherical geometry, have been used in different sizes and configurations to measure the dielectric loss tangent of low loss dielectrics at numerous frequency spots between 15 GHz and 300 GHz. Data were obtained at room temperature for Sapphire, Quartz and High Resistivity Silicon.

Dielectric loss measurements between 25 - 300 K with a hemispherical Fabry-Perot resonator

R. Heidinger, G. Link

Kernforschungszentrum Karlsruhe, Association KfK-Euratom
Institut für Materialforschung, Postfach 3640, D-76021 Karlsruhe, F.R.G.

ABSTRACT

A measurement system based on the analysis of TEM_{00q} modes in a hemispherical Fabry-Pérot resonator around 145 GHz has been optimized to give access to temperatures as low as 25 K and dielectric loss tangents at 10^{-4}. The extended performance which relies on refined data acquisition and conversion methods is shown for special grades of CaF_2 and Sapphire.

1. INTRODUCTION

The design of a reliable output window is a key problem for high power gyrotrons capable of continuous wave (CW) operation in Electron Cyclotron Wave systems (120 - 160 GHz) proposed for next generation nuclear fusion devices[1]. With present window materials[2], the targets set to 1 MW/CW transmitted power per window are only attainable with cryogenical cooling. Intensive experimental efforts to have been devoted recently[3-6] to determine the dielectric loss tangent (tanδ) which is the primary factor for the power handling capability. Even though their results have been regularly discussed, these activities have not yet provided a currently accepted data base for Sapphire, which is the major candidate material. Some difficulties arise from the different frequency ranges chosen, which imply models for scaling to one reference frequency. In addition, the experimental procedures are especially critical in all these studies, as their principles are extended from room temperature, where they were established, to low temperatures. An obvious issue is that dramatic decreases in tanδ may call for a reevaluation of the limits of resolution in the set-up. Much less considered are possible changes in the relevance of the individual experimental factors which may alter the basic rules to convert the primary observed quantities into the desired tanδ values.

2. REFINEMENTS IN THE EXPERIMENTAL SET-UP AND THE DATA CONVERSION

The schematic arrangement of the basic set-up, which is described in detail in Ref.6, has been slightly modified to register the power transmitted through the resonator around the TEM_{00q} modes fully under frequency control. Per measurement cycle, 60 power data are obtained over a frequency range that corresponds to about three times the resonance half-width. This data set is fitted with a Lorentzian-shape based model including a distortion due to signal leakage. As a result, the Q-factors of the resonances are determined to ±2 %. The fully automated data acquisition allowe the replacement of the static temperature variation method, where individual temperature points are generated finding a balance between cryogenical cooling and electrical heating, by the dynamic temperature variation method, where after cooling to a minimum temperature the system is continuously analyzed under " free heating " conditions[4]. Together with the substitution of the aluminum pedestals by copper pedestals for fixing the resonator to the heat exchanger, this method allowed to minimize temperature gradients and to keep the contraction upon cooling reproducible. Consequently the temperature dependence of ε_r' is measured with high accuracy ($\Delta\varepsilon_r'/\varepsilon_r' < 0.01\%$) and the temperature range down to 25 K is attainable with cold He gas.

The loss measurements are based on the Q-factor and the resonant frequency of the empty and loaded resonator (Q_0, f_0 and Q_l, f_l) as primary quantities which together with the size parameters of the resonator and the specimen are converted into the dielectric parameters[7]. The conversion rule for tanδ can be written in the form:

$$\tan\delta = F_F \left(Q_l^{-1} - (Q_0 / F_L)^{-1} \right) \qquad (1)$$

The filling factor F_F takes into account the effective volume taken by the specimen in the resonator. The loading factor F_L describes the rearrangement of electric and magnetic fields at the mirror due to the specimen. As a consequence of this rearrangement, the ohmic losses at the mirrors and thus their contribution in the Q-factors are modified. Standard conversion rules assume that the ohmic losses dominate all other loss terms - except the dielectric loss in the specimen - and that they are equally shared among mirrors of identical materials[8]. In cryogenic set-ups, however, the surface resistivities (R_s) decrease significantly with temperature because the conductivity of mirror materials increases.

The contribution of diffraction at the coupling holes (R_d), which are suitably placed in the spherical mirror, lift the equal share. This effect can be accounted by the redistribution parameter M[8]:

$$M = \frac{R_s}{R_s+R_d} \quad \text{and} \quad F_L^M = \left(\frac{2}{\Delta+1}\right)\left(\frac{M\Delta+1}{M+1}\right)F_L^{ST} \qquad (2)$$

where F_L^{ST} is the standard filling parameter which is strictly valid only for M = 1. The well-known Δ parameter[7] depends on the number of half-wavelengths contained in the specimen (N_λ). For resonant specimens (N_λ integer), F_L^M equals F_L^{ST}.

3. EXEMPLARY MEASUREMENTS

The redistribution parameter M is specific to the resonator design, and it depends particularly on the geometry of the coupling holes (R_d) and on the surface quality of the mirrors (R_s). In our actual set-up, it has been assessed by varying the material and the surface finish of the flat mirror and by comparing the resulting values of Q_0. The Sapphire specimen, that was studied earlier (HEMEX grade from Crystal Systems, USA), has been remeasured using the M(T) data shown in Fig.1. As shown in Fig.2, the scatter in the data is decisively reduced, and still there is agreement within the previously indicated accuracy. Included into Fig.2 are also results obtained for HEMLUX grade Sapphire (Crystal Systems, USA) and optical window grade CaF_2 (Dr.Steeg & Reuter, FRG) from an international intercomparison exercise.

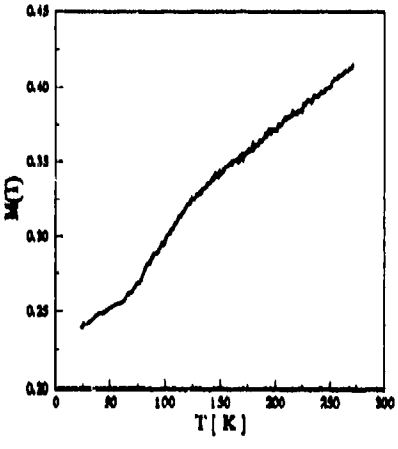

Fig.1 The redistribution parameter M(T) as determined for the present set-up

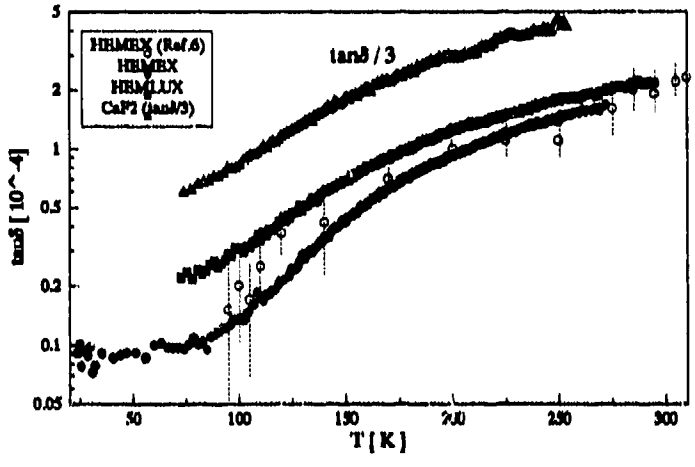

Fig.2 Dielectric loss of Sapphire (HEMEX, HEMLUX grade) and optical window grade CaF_2

4. ACKNOWLEDGEMENT

This work has been performed in the framework of the Nuclear Fusion Project of the KfK and is supported by the European Communities within the European Fusion Technology Programme. The authorsm gratefully acknowledge the useful comments of Dr.A.Lynch and R.N.Clarke of National Physical Laboratory (Teddington, U.K.) concerning the loading factor.

5. REFERENCES

1. L.Rebuffi, Digest 16th. Int. Conf. on Infrared and MM-Waves, Lausanne, SPIE Vol. 1576, pp. 441-4, 1991
2. H.-U.Nickel and R.Heidinger, Proc. 20th Symp. on Electromagnetic Windows, Atlanta, pp. 15-17, 1992
3. M.N.Afsar and H.Chi, Digest 16th. Int. Conf. on Infrared and MM-Waves, Lausanne, SPIE Vol. 1576, pp. 448-9, 1991
4. J.Molla, A.Ibarra, J.Margineda, J.M.Zamarro, A.Hernandez, IEEE Trans. Instr. Meas., accepted for publication.
5. Yu.A.Dryagin and V.V.Parshin, Int.J.IR and MM-Waves, 13(7), pp. 1023-32, 1992
6. R.Heidinger, F.Königer, G.Link, Dig. 15th. Int. Conf. on IR and MM-Waves, Orlando, SPIE Vol. 1514, pp.184-6, 1990
7. R.G.Jones, Proc. IEE, 123 (4), pp. 285-90, 1976
8. R.G.Jones, Electronic Letters, 11(22), pp. 545-7, 1975

Monochromatic submillimeter spectrometry in standards and material characterization

R.Brazis, A.Namajūnas, V.Gaidelis, L.Safonova, and S.Bumelienė

Semiconductor Physics Institute
A.Goštauto 11, Vilnius 2600, Lithuania

ABSTRACT

Backward-wave oscillator (BWO) based tunable monochromatic spectrometer equipped with computer aided control and data processing means is applied for liquid (ethanol, water, mineral oil) and solid (Si, GaAs, YBaCuO) sample characterization in the frequency range above 200 GHz.

SPECTROMETER

BWO exhibiting tunability over an octave in the range above 200 GHz are used as monochromatic sources. Oscillation frequency is tuned by means of computer - aided measuring and control (CAMAC) system with IBM PC AT 386 serving as a control and data acquisition unit. Free-standing wire grid Fabry - Perot cavity and teflon lenses, and the Golay cell detecting system are used to build the quasioptic circuit. Temperature control unit is designed for measuring the solid sample reflectivity when cooling down to liquid nitrogen temperature. Liquid cells equipped with a precise level control unit are used for measuring the refraction index and absorption of liquids at room temperature.

EXPERIMENTAL RESULTS

Ceramics. YBaCuO ceramic plate is employed to study the high frequency response of high T_c superconductors at various temperatures. Together with the sample, the aluminum mirror of the same shape have been placed in the cryostat in order to have the reference value of reflectivity. The results (Fig.1) show pronounced change of reflectivity near T_c. However, reflectivity does not reach unity below T_c exhibiting residual absorption.

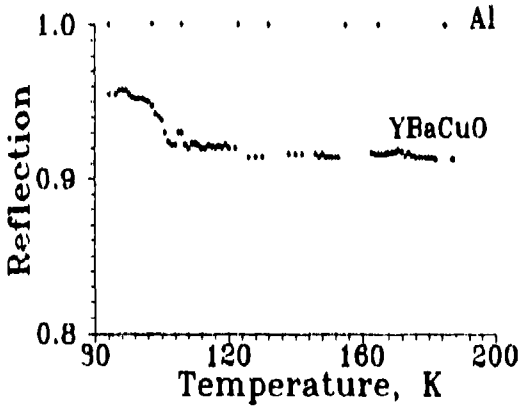

Fig.1. Temperature dependence of reflectivity for YBaCuO ceramics and Al mirror

Single crystals. High resistivity Si crystal plate transmission exhibits resonances (Fig.2) which give the index of refraction. The plate in turn is usable as an etalon for calibrating the frequency vs voltage dependence of BWO.

Metal meshes. GaAs single crystal is used as a substrate for metal mesh produced by means of vacuum deposition and ultraviolet photolitography. The elementary cell of the mesh is square, however, two parallel strips are interrupted. The transmittivity

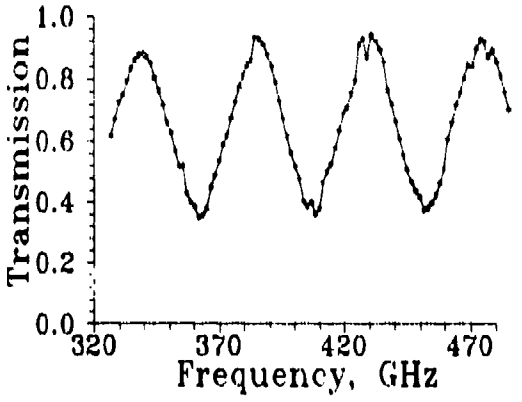

Fig.2. Frequency dependence of transmission for silicon plate (d=1110μ).

of such a structure exhibits substrate Fabry-Perot maxima as well as metal mesh elementary cell resonance minimum at 428 GHz (Fig.3). The transmittivity is dependent on whether the wave electric field oscillates along the interrupted strips (curve 1) or along the solid strips of the mesh (curve 2).

Liquids. Measuring cell is positioned horizontally, and the wave beam passes in vertical direction. Liquid layer thickness is measured by filling control unit, and Fabry-Perot resonances are observed at constant value of wavelength enabling one to measure the index of refraction (Fig.4).

Pure mineral oil is usable in phase tuning whereas water and ethanol are of interest for absorption filters and attenuators.

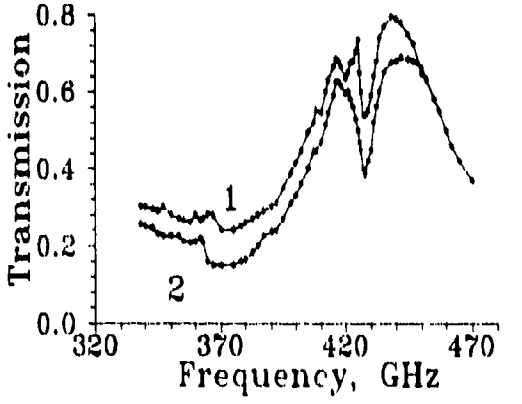

Fig.3. Frequency dependence of transmission through a square metal mesh (elementary cell size d=183μ) on insulating GaAs substrate (thickness D=290μ)

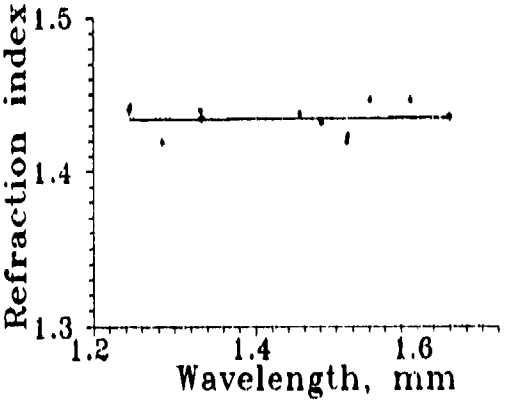

Fig.4. Index of refraction as a function of wavelength for a liquid (mineral oil)

Properties of materials for practical use at the mm and submm wavelengths.

V.V.Meriakri and E.E.Chigrai
Institute of Radioengineering & Electronics
Russian Academy of Sciences,
Frjazino, Moscow region, 141120, Russia.

ABSTRACT

Results of investigations at wavelengths from 6.0 to 0.4 mm ofoptical characteristics (complex refractive index, transmission and reflection coefficients, including anisotropic characteristics) of several dozens of building and common use materials are presented. The quasi optical methods and backward-wave tubes were used for measurements.

1. INTRODUCTION.

Presently, mm waves devices are of great interest for communications and traffic applications as well as effective instruments for nondestructive test of materials, manufactured articles and environment [1]. For all of these problems it is important to know how mm waves propagate in corresponding materials and media. Here we presents some results of mm wave property measurements of building materials, materials for clothes, furniture etc.

2. MEASUREMENT METHODS.

Modules and phases of transmission and reflection coefficient depending on frequency, temperature and water content have been measured using the beam waveguide spectroscopy methods [2].

3. EXPERIMENTAL RESULTS.

The results are summarized in Tables 1 and 2. The measurement errors are about ±(1-2)% for $|t|^2$ and $|r|^2$,and 3-5^{o}for arg(t) arg(r). These values are less than the difference between the corresponding values for the particular examples of the same materials.

In Table 1 n is refractive index, tanδ - loss tangent. Less values of tanδ (see numbers 4,6) are correspond to electrical field perpendicular to wood fibers. Water content in wood less than 7-8%.

Table 1. Building materials, λ=2 mm, T=20^{o}C

N Material	n	tan$\delta \cdot 10^2$
1 Brick	1.8	3.5-4.2
2 Concrete	2.4	5.0-5.5
3 Asphalt (ρ=1.3 g/cm^3)	1.5	8.0
4 Pine-tree wood (ρ=0.5 g/cm^3)	1.4	3.4/2
5 Glass	1.45	5.0
6 Veneer (d=7.6 mm)	1.5	2.6/1.4
7 Marble	1.5	1.0
8 Organic glass	1.6	1.5

In Table 2 clothes material properties are presented. Here d- material thickness n_{eff}-effective refractive index: $n_{eff}=\lambda \cdot arg(t)/2 \cdot \pi \cdot d$.

Table 2. Clothes materials, λ=1.6

N Material	$\lvert t\rvert^2$,%	$\lvert r\rvert^2$,%	$n_{eff}-1$	d,mm
1 Cloths for tents	82-94	$\leq$1	0.2-0.3	0.3-0.5
2 Cl. for coat, wool	77-84	$\leq$3	0.1-0.2	2 - 4
3 Cl. for suit, wool	85-99	$\leq$1	0.20-0.35	0.5-1.0
4 Silk	89-93	$\leq$1	0.28-0.35	0.15-0.25
5 Leathers, natural	79-85	$\leq$8	0.35-0.46	0.9-1.5
6 Leathers, artificial	87-92	$\leq$5	0.22-0.28	0.7-0.8
7 Fur, artificial	75-89	$\leq$3	0.04-0.07	4-12
8 Cl.for shirts	92-95	$\leq$5	0.18-0.23	0.2-0.3

Frequency dependence of n in mm region is weak but tanδ and $\lvert t\rvert^2$ vary considerably as frequency changes. For example tanδ of brick at λ=6.3 mm is only $(0.7-1.5)\cdot 10^{-2}$, tanδ of concrete is $5.3\cdot 10^{-3}$. Transparency of clothes decreases as frequency increases from 99-84% (see Table 2) at 1.6 mm to 76-37% at λ=0.4 mm.

All materials have strong dependence of transparency on moisture. For dry materials $\lvert t\rvert^2$=90-80% in temperature interval T=-40-20^{o}C, for moisture 28% $\lvert t\rvert^2$=80-25% with sharp decay from 65% to 30% near 0^{o}C

4. REFERENCES.

[1]. H.Meinel. Millimeter wave system design and application. Alta Frequenza, vol 58, No 5-6,1989, 441-456.

[2]. V.V.Meriakri, V.N.Apletalin, A.N.Kopnin and others. Submillimeter beam waveguide spectroscopy and its application., in book Problems of modern radio engineering and electronics, Nauka Publishers, Moscow, 198 , pp.197-196.

On the measurement of the complex dielectric constant of the medium

Yu Rong and Xingguo Li
Dept. of Electronic Engineering, East China Institute of Technology
Nanjing, P.O.Code 210014, P.R.China

ABSTRACT

A method of measuring the complex dielectric constant of the medium is proposed in this paper. Unlike the usual method, this method is based on measurement techniques and the numerical calculation. The simplicity and accuracy of this method is shown.

1. Introduction

To measure the dielectric constant in the millimeter wave range, traditional methods such as closed-cavty resonator method, open-cavity resonator technique and open dielectric resonator are becoming more and more improper.

In this paper, a new and accurate method, which is based on measurement techniques and the numerical calculation, is proposed. Fig.1 shows a simplified model of this method. A full height sample rod of radius R_1 is centeredly inserted in an ordinally rectangular waveguide (a × b). The waveguide is assumed to propagate only the dominate TE_{10} mode, while all higher modes are cut off. Excitation by the dominant mode TE_{10} takes place, it is obvious that only TE_{M0} mode are excited. With the measurement techniques, the equivalent network of this discontinuity can then be obtained. So the complex dielectric constant of this medium is readily derived after the inverse problem of the analysis of this discontinuity is treated.

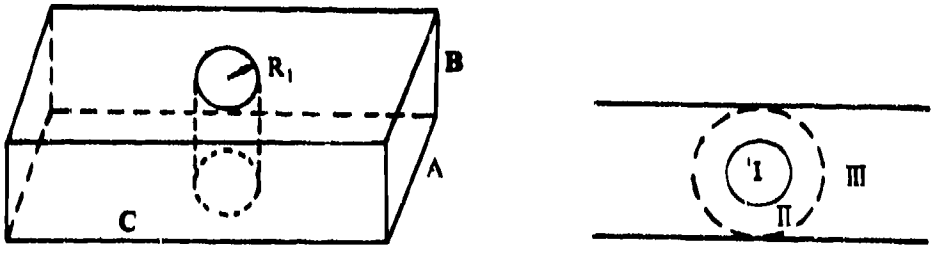

Fig.1 The simplified model

2. FORMULATION

2.1 Analysis

The main steps in analysing problem which is shown in Fig.1 are as follows.

A. Lossless Problem

The system is assumed lossless. In order to facilitate the analysis, the waveguide is divided into three regions: the simple rod , region I, the imaginary region, region II and rectangular waveguide, region III. The field components in each region are expressed by using the mode expansion method. Using the boundary conditions, the equivalent network parameters of Fig.1 can then be obtained. It is readily found that the scattering parameters of this discontinuity can be obtained through the following equations [1] .

$$S_{11} = 0.5(A_1^1 + A_1^2)$$
$$S_{12} = 0.5(A_1^1 - A_1^2) \quad (1)$$

where A_1^1 and A_1^2 are the reflective coefficients A_1 in the characteristic equations under the excitation of the two eigen incident wave pairs, respectively.

B. Lossy problem

It is well known in mathematics that if $\varepsilon''_r \ll \varepsilon'_r$, the following equations can be used.

$$S_{11}(\varepsilon'_r + j\varepsilon''_r) \approx S_{11}(\varepsilon'_r) + \frac{S_{11}(\varepsilon'_r + \Delta\varepsilon'_r) - S_{11}(\varepsilon'_r)}{\Delta\varepsilon'_r} j\varepsilon''_r$$

$$S_{12}(\varepsilon'_r + j\varepsilon''_r) \approx S_{12}(\varepsilon'_r) + \frac{S_{12}(\varepsilon'_r + \Delta\varepsilon'_r) - S_{12}(\varepsilon'_r)}{\Delta\varepsilon'_r} j\varepsilon''_r \quad (2)$$

Using above expression and equation (1), the lossy problem of this discontinuity can then be solved easily. As long as $\varepsilon''_r \ll \varepsilon'_r$ (in fact, it is always true in practice), the results of equation (2) are accurate.

2.2 Optimization

Till now, we have a basis for optimization. Actually, the problem treated here is the inverse problem of the above analysis. Using measurement techniques, we can measure the scattering parameters of the discontinuity as shown in Fig.1. Assumming that its measured scattering matrix is $[S']$, the following objective functional can be constructed.

$$F = |S_{11}(\varepsilon_r) - S'_{11})|^2 + |S_{12}(\varepsilon_r) - S'_{12}|^2 \quad (3)$$

It is obvious that F in above equation will be zero when the unknown value of ε_r approachs the actual value. Therefore, with the POWELL optimization method, the parameter ε_r of the medium can be obtained.

3. NUMERICAL RESULTS

As a measurement method here, the optimization speed of obtaining the numerical solution is much concerned about. So the following work is done. In the part of analysing the discontinuity, the correctness of the calculation method is proved using two principles, i.e., power conservation and the convergence of the numerical solutions. As an example, we found that when K_0a, R_1/a equal 4 and 0.1, respectively, the reflective coefficients of equations (1) are obtained rapidly, where only five modes are considered in the waveguide. This shows that being the inverse problem, the permittivity ε_r of the measured medium can be obtained easily, by way of the POWELL method and equation (3).

4. CONCLUSION

This paper introduces a new method of measuring the permittivity of the medium. To prove the validity of this method, the investigation on this method is made. With the personal computer, we found that it is an effective method of combined measurement.

5. REFERENCES

1. M.E. El-Shandwily, A.A.Kamal, E.A.T. Abdallah, "General field theory treatment of E-plane waveguide junction circuitors--part I : full-height ferrite configuration", IEEE Trans. on MTT, Vol.MTT-25, No.9, pp.784-793, Sept.1977.
2. J.B. Davies, "An analysis of the M-port symmetrical H-plane waveguide junction with central ferrite post", IEEE Trans, MTT, Vol.MTT-10, pp.596-604, June 1962.

Birefringence and dichroism in magnetic fluids, induced by Magnetic field in frequency range 36 GHz - 600 GHz.

Semenov A.V., Vinogradov E.A.

Submillimeter-Range Physics Laboratory, General Physics Institute, Russian Academy of Science, 117942, Moscow, Russia

ABSTRACT

The frequency dependence of complex refraction index and induced anisotropy in magnetite ferrofluid and its components were evaluated from transmission spectra, measured with BWO-spectrometer, using interference model of three-layer cell. The value of birefringence of ferrofluid (dielectric nature, cluster model) is greater, frequency independent and has opposite sign compared to that of ferrite (magnetic nature).

2. INTRODUCTION

The experimental study of the behaviors of complex refractive index and field induced birefringence and dichroism of ferrofluids in wide frequency range covering 40 - 550 GHz was made. Such investigation seems to be important to enhance the understanding of physical phenomena in ferrofluids - a new class of artificial substances of both scientific and applied interest. These substances are colloidal solutions in which ferromagnetic colloidal particles (30-70 Angstrom diameter) are stably dispersed in organic solvent. The particles are covered by monomolecular layer of surfactant to avoid aggregations.

There are many investigations of magnetic field induced anisotropy in visible, IR range. The paper [1] describes similar measurements made by DFT-Spectroscopy methods in frequency range 320 GHz - 700 GHz.

The main advantage of our measurements is the usage of quasioptic monochromatic spectrometer with tunable Backward-Wave-Oscillator (BWO) as a source of a stable and monochromatic CW radiation. The single BWO continuously covers frequency band of about an octave, while with the set of BWO it is possible to get measurements in the range from 8 mm down to 0.3 mm without gaps and with relative resolution greater than 30,000. The reproduceability of spectra is order of0.5%. The wave beam of 50 mm in diameter was shaped by teflon lens, while the similar lens focused the radiation onto the detector window.

The samples of ferrofluid were the colloidal suspensions of single domain particles of magnetite Fe_3O_4 in kerosene at concentrations 10%. The average particles dimension was 9 nm in diameter. The ferrofluids were sealed in the cells of 50 mm diameter between the 2mm-thick melted silica windows. Two cells of thicknesses 12 and 3 mm between windows were used for measurements.

3. METHOD

The transmission spectra for each BWO (in the frequency range 1/2-1/3 octave) were measured. To measure the induced anisotropy the samples were placed between two poles of a magnet (perpendicular configuration, intensity 0.3 T - greater than saturation field). To estimate induced anisotropy ($\hat{n}_o$, $\hat{n}_e$) two transmission spectra were measured in the same frequency range: for ordinary ($\vec{E} \parallel \vec{H}$) and extraordinary ($\vec{E} \perp \vec{H}$) beams.

The complex refractive index was calculated using generalized formula for three-layer cell (window-ferrofluid-window) system to fit the experimental data. The linear term of dispersion of complex refractive index was taken into account. The necessary complex refractive index of silica windows was measured beforehand. The possibility of evaluation of both: imaginary k and real n parts of complex refractive index from transmission spectra only was based on the presence of interference between the windows. The 12mm spacing at low-frequency and 3mm at high-frequency end was chosen for optimum interference.

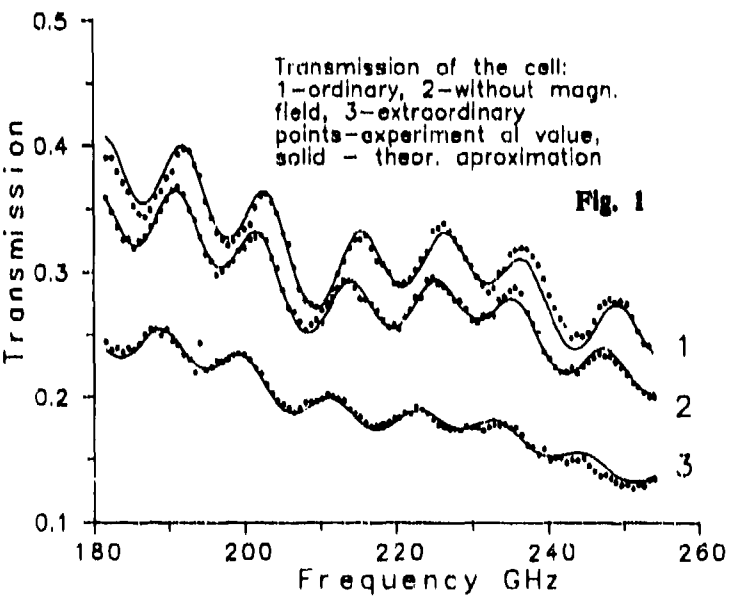

Fig. 1

4. RESULTS

Figure 1 shows a fragment of transmission spectra (dotted curves) fitted as mentioned above (solid curves). These 3 curves are transmission spectra: 1 - ordinary, 2 - without magnetic field, 3 - extraordinary. Good agreement of experimental spectra (points) and fitted theoretical curves (solids) shows that three layer function gives adequate approximation of spectra. One can see the frequency oscillations of transmission spectra. These oscillations have two distinct periods. The longer period (~50 GHz) corresponds to the interference within silica windows only. The shorter (~10 GHz) is due to the interference in the whole cell (window-fluid-window) - the presence of these very oscillations provides the following accuracy of complex refractive index : 0.1% - for n , 2% - for k.

The dependencies of real and imaginary parts of complex refractive index for three configuration (n_o , n , n_e) are shown in the Fig. 2 and Fig.3 correspondingly. The refraction index only slowly falls down (from n=1.795 down to n=1.795) as frequency rises (from f=45GHz up to f=500GHz) without any specific points as it was stated in [1]. Absorption coefficient increases from k=0.029 up to k=0.042 with the increase of frequency. Absorption coefficient for ordinary beam exceeds that for extraordinary one by the factor of 1.4 at the lowest frequency and this coefficient only slightly changes up to the highest frequency.

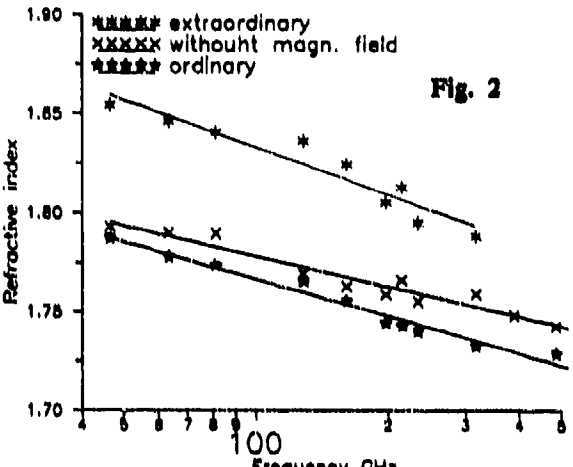

Fig. 2

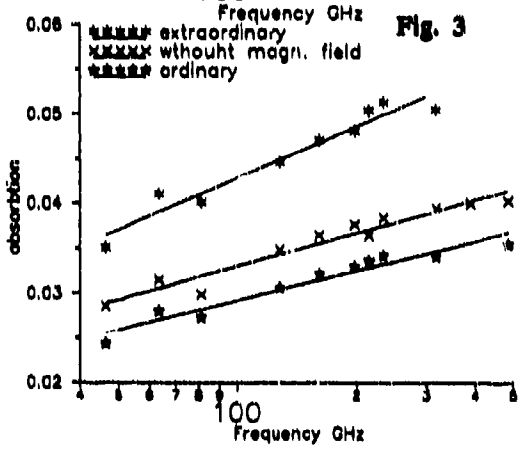

Fig. 3

5. DISCUSSION

Similar measurements for typical VHF ferrite type 1C-4 has shown the opposite sign of induced birefringence and decrease it's value by quadratic low - the normal behavior of magnetic susceptibility.

We attribute the cause of the magnetic birefringence and dichroism of the magnetic fluid to the linear cluster formation of the magnetic colloidal particles in the field direction as [2-3]. These clusters are divided into two classes [2]. One is so small, that can not be observed with optical microscope (1-20 particles) and the other is a macrocluster which is large enough to be observed (5-30 mkm).

Like [3] the magnetic field induced anisotropy for extraordinary ray is about 2 times greater then that for ordinary ray. It can be explained by chain-like cluster model, which predicts this constant difference even from 0.5mkm to dc. The induced anisotropy for extraordinary ray increases as frequency rises. The spacing of the particle chains is less then the wavelength of radiation.

6. SUMMARY

The system of parallel dielectric fibers with non-zero real and imaginary terms of refractive index is likely to be a valid electrodynamic model to describe birefringence and dichroism of ferrofluid. It is very promising, that refraction coefficient is close to that of fused silica and the birefringence and dichroism are high (about 0.05 of absolute value) and are nearly uniform over the whole frequency range.

7. REFERENCES

1. C. A. Bentley, J. P. Llevellyn, J. R. Birch, "Near Millimeter Birefringence and Dichroism in Ferrofluids", *Electronic Letters*, 21, p.313-314, 1985.

2. S. Taketomi at al "Experimental and theoretical investigations on Agglomeration of magnetic particles in magnetic fluid", *Journal of The Physical Society of Japan*, Vol.60, No 5, May 1991, pp. 1689-1707.

3. N. Inaba at al, "Magneto-optical absorption in infrared region for magnetic fluid thin film", *IEEE Transactions on Magnetics*, Vol.25, No.5, September, 1989, pp. 3866 - 3868.

MM-wave dielectric measurements with an electric-field cross-correlation Fourier transform spectrometer*

Ding Hanyi and Zhang Guangzhao

Electronics Dept., Zhongshan University
Guangzhou (510275), P.R.China

ABSTRACT

This paper describes a method for measuring dielectric complex permittivity based on an electric-field cross-correlation Fourier-transform spectrometer. The method is a time-domain one, its principle can be extended over the whole microwave region. The parameters of Teflon, plexiglass and a kind of sand were measured in 8mm-wave region, the accuracy of three or four significant figures of ε_r can be achieved, and the relative accuracy of $\tan\delta$ is only about 10%.

1. THE MEASURING PRINCIPLE

The basic formulae of the electric-field cross-correlation spectrometer is[1]:

$$\begin{cases} \hat{\mathcal{L}}(\omega_0+r\omega_m)= \left[\hat{P}_{sc}(r\omega_m)-i\hat{P}_{sp}(r\omega_m)\right] \Big/ \hat{P}_{bc}(r\omega_m) \\ \hat{\mathcal{L}}(\omega_0-r\omega_m)= \left[\hat{P}^*_{sc}(r\omega_m)-i\hat{P}^*_{sp}(r\omega_m)\right] \Big/ \hat{P}^*_{bc}(r\omega_m) \end{cases} \quad (1 \le r \le N) \qquad (1)$$

1.1. The solid specimen

For a lamellar specimen in the rectangular waveguide (Fig.1), we can derive:

$$\hat{\mathcal{L}} = 4\hat{k}_{g1}\hat{k}_{g2}\exp\left[-i(\hat{k}_{g2}-\hat{k}_{g1})d\right] \Big/ \left[(\hat{k}_{g1}+\hat{k}_{g2})^2-(\hat{k}_{g1}-\hat{k}_{g2})^2\exp(-i2\hat{k}_{g2}d)\right] \qquad (2)$$

Where $\hat{k}_g = \left[(\omega/c)^2\hat{\varepsilon}_r-(\pi/a)^2\right]^{1/2}$, $\hat{\varepsilon}_r = \varepsilon_r(1-i\tan\delta)$.

1.2. The bulk powder specimen

For the case in which two windows are made of the same material (see Fig.2), and using the two-length method, if $d = d_{x1} - d_{x2}$ is small and ε_r not great, an accurate and simple enough approximate formula can be obtained as following:

$$\begin{cases} x = A_1 + [2K\pi - \arctan(\mathcal{L}_i/\mathcal{L}_r)]/A_3 d \\ y = \ln[(\mathcal{L}_r^2+\mathcal{L}_i^2)^{1/2}]/A_3 d \end{cases} \quad (K=\text{integer}) \qquad (3)$$

and

$$\begin{cases} \varepsilon_r = A_4 + x^2 - y^2 \\ \tan\delta = -2xy/\varepsilon_{rx} \end{cases} \qquad \left[\begin{array}{l} A_4 = (c/2af)^2, \quad A_3 = 2\pi f/c \\ A_1 = (1-A_4)^{1/2} \end{array}\right] \qquad (4)$$

Where $\hat{\mathcal{L}} = \mathcal{L}_r + j\mathcal{L}_i = \hat{\mathcal{L}}_1/\hat{\mathcal{L}}_2$ is the ratio of total complex insertion loss (including specimen and two windows) of two different specimen lengths.

* Supported by Foundation of Specialities Opened to Doctorate Study.

2. RESULTS

Table 1 and 2 give results measured and reference values. For the powder specimen, two windows are made of teflon and two lengths of sand are 22.70mm and 19.70mm.

Table 1 Relative permittivity and loss tangent

Specimen	Measuring results		Reference[2, 3]	
	ε_r	tanδ	ε_r	tanδ
Teflon	2.064±.007	$(9\pm1)\times10^{-4}$	2.08	6×10^{-4}
Plexiglass	2.667±.002	$(9\pm1)\times10^{-3}$	$n^2=2.663$	7.8×10^{-3}

Table 2 The dielectric parameter of the shaped sand

Packing density g/cm^3	Relative permittivity	tanδ	Frequency	Ref.
~ 1.47	2.45 ± .03	.02 ± .009	35.1GHz	
2.036	3.155	0.009	11GHz	4
2.224	3.194	0.007		
2.235	3.199	0.008		
2.242	3.223	0.009		

3. CONCLUSION

Although the measurement above is still a primary one, yet the principle has no limitation to be used in other microwave ranges and the method has potentialities to do accurate dielectric measurements.

4. REFERENCES

1. Ding H., Li H. and Zhang G., "An electric-field cross-correlation Fourier transform millimeter wave spectrometer",Int. J. Infrared Millim. Waves,Vol.13, pp.425-432, 1992

2. K.H.Breeden and A.P.Sheppard, "Millimeter and submillimeter wave dielectric measurements with an interference spectrometer", Microwave J., vol.10, pp.59-62, 1967

3. Lin Qing, Master Thesis in Electronics Dept. of Zhongshan Univ., 1989 (in Chinese)

4. H.M.Al-Rizzo and H.T.Al-Hafid, "Measurements of the complex dielectric constant of sand and dust particles at 11GHz", IEEE Trans. Instru. Meas., Vol.37, pp.110-113,1988

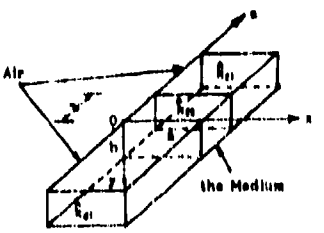

Fig.1 The solid specimen

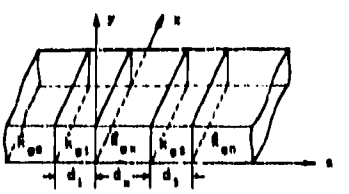

Fig.2 The bulk powder specimen

Two-frequency quasi-optical radiospectrometer for substance investigations

A.A.Vertiy, I.V.Ivanchenko and N.A.Popenko

Institute of Radiophysics and Electronics,
Academy of Sciences of the Ukraine,
Kharkov 310085

ABSTRACT

The quasy-optical two-frequency radiospectrometer was created. The results of the electron-nuclear systems investigation of the dynamic nuclear polarization targets are presented. In particular temperature dependences of the nuclear polarization relaxations were measured. Complex solution of HMBA-Cr^{V} in 1.2-propylene glycol was used as the target substance.

2. RADIOSPECTROMETER DESCRIPTION

In the present paper the quasi-optical two-frequency radiospectrometer is described (frequency of the electron paramagnetic resonance (EPR) F_E =120GHz-150GHz; frequency of the nuclear magnetic resonance (NMR) F_N -200MHz). The radiospectrometer operates in the temperature range 1.7K-4.2K and in the magnetic fields Ho~5T.

A radiophysical block of the spectrometer is a semisymmetrical open resonator (OR). The substance to be investigated is placed into a special dielectric cuvette,fixed at the central part of the plane reflector. In our case a double-diffraction grating (DDG) consists of a silver wire and is used as a NMR contour inside the cuvette, containing the substance. The orientation coils of the DDG are along the H vector of the high frequency OR field. Thus, the high frequency and the radio frequency magnetic fields are all mutually orthogonal, that is necessary for the "ENDOR" experiments. The experimental investigations show that the fundamental and two high modes in such electromagnetic system are excited. The special structure of the fundamental mode represents a slightly deformed TEMooq mode and has the across field size equal to the region, containing the substance. The quality factor $Q=3.2*10^3$. Consequently such complicated electrodynamic system can be considered as a resonance EPR cell [1].

We have used a synchronic detection scheme for the increasing sensitivities of the EPR and NMR contours. Constant magnetic field Ho of the superconducting solenoid was modulated by the periodical signal with the frequency Fo=920Hz.

3. EXPERIMENTAL RESULTS

The HMBA-Cr^{V} complex in propylene glycol was investigated on the radiospectrometer in the "polarized nuclear target" regime. A high nuclear polarization may be received with the help of the "dynamic

nuclear polarization" (DNP) methods [2]. Now it is known that the strong thermal coupling between the "container" of the electronic dipole-dipole spin system and the nuclear Zeeman system in that complex exists [3], i.e. the basic DNP mechanism is "dynamic cooling". Therefore the EPR-line must be saturated by the electromagnetic field of the superhigh frequency (SHF) near of the resonant frequency: F_e=126.6GHz. The magnitude of the constant magnetic field was Ho=4.77T and NMR contour frequency was F_N=192MHz.

The polarization magnitude can be controlled by means of the NMR-signal magnitude at the output of the spectrometer. The high sensitivity of the NMR contour allows to registrate a NMR-signal which is proportional to the equilibrium polarization magnitude Po. In our case Po=1.1*10^{-5}. When maximum polarization P is achieved the SHF electromagnetic field is switched off and we observe a process of the nuclear polarization breakup. In the result the relaxation curves were received (Fig.1).

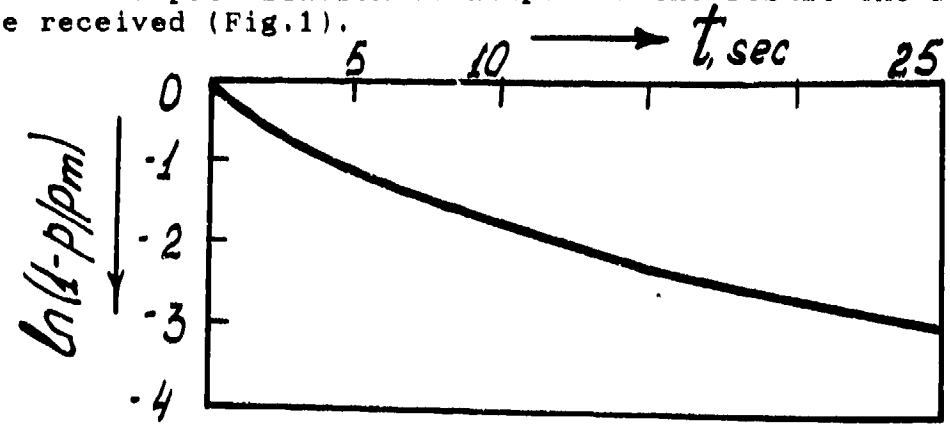

Fig.1

The analysis of these curves P=f(t) shows the unmonoexponential character of such dependences. It is a fact of existence of, at least, two channels of the energy escape from the nuclear system. The breakup times of nuclear polarization were measured in the temperature ranges T=1.7K-4.2K. For example, for T_1=4.2K we have t_1=5sec; for T_2=2.0K we have t_2=25sec.

The described radiospectrometer allows to carry out investigation of paramagnetic substances by means of the "ENDOR" and "NEDOR" methods.

4. REFERENCES

1. Charles P.Poole, "Electron Spin Resonance", Interscience publishers, New York-London-Sydney, 1967.
2. Carson D. Geffries, "Dynamic Nyclear Orientation", Interscience publishers, New York-London-Sydney, 1963.
3. A.A.Vertiy, Yu. Popkov et al, "Investigation of the proton dynamic polarization in ethylene glycol and 1.2-propylene glycol with stable radical CrV", Soviet Physics Doklady, Vol.260, N5, pp. 1093-1095, Oktober 1981.

Dielectric losses in gases under ionizing radiation

J. Mollá, A. Ibarra, E. R. Hodgson
Inst. Investigación Básica. CIEMAT, Ed. 2. Av. Complutense , 22. E-28040-Madrid. Spain.

1. INTRODUCTION

In future fusion reactors as well as in intermediate machines, such as ITER or NET, there will be a new dimension when compared with actual machines, and that is the presence of a high radiation field, both ionizing and displacement. This requires the design and development of radiation resistant systems which may be operated under radiation. In the case of heating systems the measurements of radio frequency window materials has been started only recently to be performed under radiation[1]. These measurements should be made with special attention due to the perturbation induced by the ionization of the filling gases. This effect could also be important in high power heating systems based in pressurized waveguides due to the presence of ionizing radiation[2]. Here the radiation effects on the dielectric properties of different gases at atmospheric pressure are presented.

2. EXPERIMENTAL SET-UP

The measurement system is based on a closed aluminium cylindrical cavity (30 mm diameter, 34 mm long, operating by transmission in TE01n mode) placed at the end of the beam line of a Van de Graaff accelerator. 1.8 MeV electrons enter the resonator through an aluminium window producing up to 3200 Gy/s. The microwave power is coupled through rectangular slots, also used for the gas flow through the cavity.

Dielectric properties of the studied gas are calculated from comparison between the resonant frequency and quality factor of the resonator filled with air and with the gas. The equations which relate the dielectric properties of the gas (ε and tan δ), and the characteristics of the resonance (Q-factor and resonant frequency f_0) are:

$$\frac{\varepsilon}{\varepsilon_0} = \frac{f_0}{f_g} \; ; \qquad \tan\delta = \tan\delta_0 + \frac{1}{Q_g} - \frac{1}{Q_0}$$

where the subscripts o and g mean values with air and gas filling, respectively.

The resonant frequency and quality factor are measured using the procedure described elsewhere[3] and depend on the cavity temperature. During irradiation the cavity warms up, hence the linear expansion and resistivity coefficients of aluminium at room temperature have been used to take into account this temperature increase (maximum 15 ºC).The uncertainties in the measurements of temperature ($\delta T \approx 1$ºC) and quality factor ($\delta Q/Q \approx 50/15000$) give rise to uncertainties of approximately 10^{-4} in permittivity and 3×10^{-7} in loss tangent. The dose rate during irradiation was constant to within ±5%.

3. RESULTS AND DISCUSSION

The dielectric properties of dry air, helium, nitrogen, argon, CO_2, and SF_6 have been measured during irradiation, as a function of dose rate. On irradiation, no change is observed in the permittivity. In the case of loss tangent, the variation with dose rate is for some of the gases quite marked, see figure.

Values without radiation are, in all cases, below the resolution limit. During irradiation, a strong increase of dielectric absorption is found for argon, nitrogen, helium and CO_2, while no effect is detected either for SF_6 or dry air. In those gases in which a radiation effect is observed, the increase in loss tangent is approximately linear although the data are best fitted by a (dose rate)$^{0.8}$ dependence.

The radiation enhances the conductivity of the gases which will depend on their ionization and recombination efficiencies. The increased conductivity increases the microwave absorption given by:

$$\tan\delta = \frac{4\pi\sigma}{\omega\varepsilon_0} = \frac{4\pi ne^2}{m_e \nu_c \omega \varepsilon_0}$$

where n is the free electron density and ν_c the electron collision frequency .

4. REFERENCES

1. G. P. Pells, S. N. Buckley, P. Agnew, A. J. E. Foreman, M. J. Murphy, S. A. B. Staunton-Lambert. "Radiation Effects in Electrically Insulating Ceramics". Harwell Report AERE R 13222 (1988).
2. D. G. Anderson, M. Lisak, P. T. Lewin. "Thermal Lowering of the Threshold for Microwave Breakdown in Air-Filled Waveguides". IEEE Trans. on Microwave Theory and Techniques MTT-35(7) 653-656 (1987)
3. J. Mollá, A. Ibarra, J. Margineda, J. M. Zamarro, A. Hernández. "Dielectric Properties Measurement System at Cryogenic Temperatures and Microwave Frequencies". To be published IEEE Trans. on Instr. and Measurement (August, 1993)

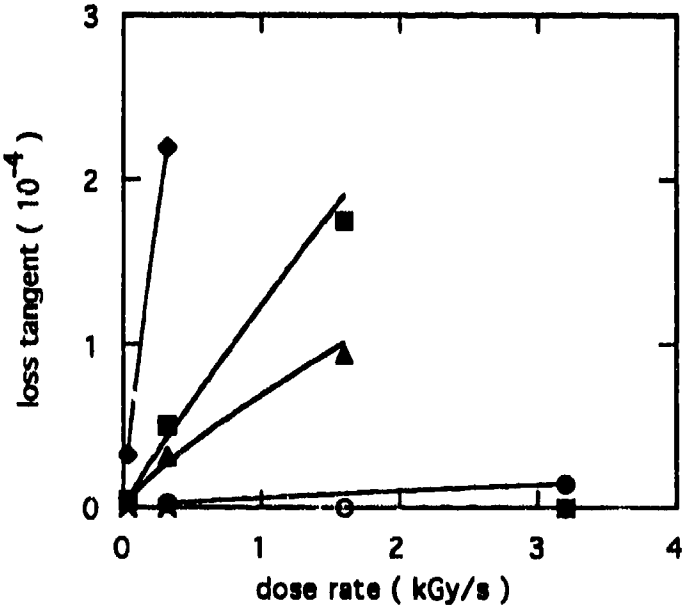

Figure 1. Loss tangent vs dose rate for argon (◆), nitrogen (■), helium (▲) and CO_2 (●) Values for dry air (✕) and SF_6 (○) are lower than 10^{-7}.

DEMONSTRATION OF RESONANTLY ENHANCED DEGENERATE FOUR-WAVE MIXING OF MILLIMETER WAVES IN GAS

N.A. Bogatov, M.S. Gitlin, A.G. Litvak, A.G. Luchinin

Institute of Applied Physics Russian Academy of Sciences,
46 Ulyanov Str., 603600 Nishny Novgorod, Russia

G.S. Nusinovich

Laboratory for Plasma Research, University of Maryland, College Park, Maryland 20742

ABSTRACT

Experimental evidence of millimeter-wave phase conjugation by resonantly enhanced degenerate four-wave mixing (DFWM) is presented for the first time. Nonlinear millimeter-wave interaction was caused by saturation of transition between rotational levels of gaseous carbonyl sulfide (OSC). For radiation with $\lambda \approx 1.64$ mm phase-conjugate reflectivity of about 0.4 % has been observed at the gas temperature 200 K, and under optimal pressure.

2. INTRODUCTION

Recently a considerable interest has arisen for investigation of four-wave mixing of the millimeter and centimeter waves in nonlinear media. This interest is caused by great prospects of using DFWM for phase conjugation[1] (PC) of microwaves on a real time-scale, amplification and generation of electromagnetic waves, control of their spectral and spatio-temporal characteristics, etc., that can become useful applications for radaring, communication, navigation and a number of other fields. We have realised DFWM of millimeter waves for the first time. Gaseous carbonyl sulfide (OSC) was used as a nonlinear medium. Nonlinearity of such medium is caused by power saturation of absorption by the rotational transition of OSC dipole molecules[2]. The advantages of such nonlinear medium are that it is becoming easy to produce, convenient to use, and has a fast response time. This nonlinear medium is most efficient in the short millimeter and submillimeter region, where dipole molecules have strong rotational absorption lines.

3. EXPERIMENTAL SET-UP

The scheme of experimental set-up is given in Fig.1. A gyrotron with pulsed magnetic field[3] was used as a source of powerful millimeter-wave radiation ($\lambda \approx 1.64$ mm). The gyrotron frequency was tuned to the center of the spectral line of the rotational transition $15 \leftarrow 14$ with the accuracy ≈ 10 MHz. For this rotational transition line-center saturation intensity is $I_{sat} \approx 2(PT_0/P_0T)^2$, where I_{sat} is measured in W/cm^2, gas pressure P in Torr, and gas temperature T in K, with $P_0 = 1$ Torr and $T_0 = 300$ K. The gyrotron radiation power at the frequency of this rotational line center was 30 kW. Gyrotron radiation was converted into a quasi-Gaussian beam with a parabolic reflector and a diaphragm $D1$. By aid of plane mirror $M1$ the pump beam f was directed through a quartz window into a metal vacuum chamber (with internal diameter 18 cm and length 30 cm) filled with gaseous OSC. The pump wave intensity I in the center of the beam did not exceed 300 W/cm^2. The back wall of the chamber served as a plane mirror ($M2$) and was used to form the backward pump beam b. The chamber was placed in a thermostat and cooled with dry ice to the temperature ≈ 200 K to increase resonant absorption. The signal beam s was formed by means of beam splitter $S1$ and diaphragm $D2$ and was directed into the chamber at the angle 6 to the pump beam f. At the boundary of the gaseous medium, the ratio of intensities at the maximums of the pump and signal beams was approximately 1.5, and their widths were 7.5 and 6.5cm, respectively. Optical axes of the signal and pump beams were crossed at the surface of mirror $M2$, hence the length of the wave interaction region was approximately equal to the doubled length of the vacuum chamber. Two-pass optical thickness of the gas at the center of the unsaturated rotational line was equal to 2 at $T = 200$ K. The reflected wave c resulting from DFWM in gas, was directed to receiving system R by quartz beam splitter $S2$.

4. RESULTS

If the signal and pump beams were directed into the vacuum chamber simultaneously, then at pressures lower than 30 Torr ($T = 200$ K), movable receiving system R detected phase-conjugate wave c. The fact that the reflected wave

c was produced by DFWM in gas was confirmed, besides the opposite to signal wave direction of its propagation, by disappearance of the wave c when either of the two beams incident at the gas in chamber was blocked by either the signal beam or the pump beam. The dependence of the phase-conjugate reflectivity on gas pressure at the temperature $T = 200$ K was experimentally investigated. The results of these measurements are presented in Fig. 2. The maximal phase-conjugate reflectivity ≈ 0.4 % was observed under gas pressure 7 Torr, when saturation parameter of rotational transition I/I_{sat} was close to 1. Response time of such gaseous media which is determined by the relaxation time of population difference of molecular rotational levels was ~ 10 ns at the gas pressure ~ 10 Torr.

5. REFERENCES

1. *Optical Phase Conjugation*, Ed. by R.A.Fisher, Academic Press, New York, 1983.
2. W.Gordy and R.L.Cook, *Microwave Molecular Spectra*, Wiley, New York, 1984.
3. V.A.Flyagin, A.G.Luchinin and G.S.Nusinovich, "Submillimeter-wave gyrotrons: Theory and experiment," Int. J. Infrared and Millimeter Waves, Vol.4, N4, pp. 629-637, 1983.

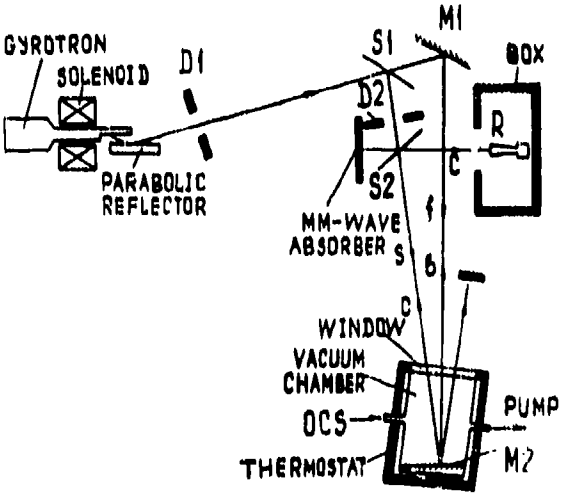

Fig. 1. Experimental set-up

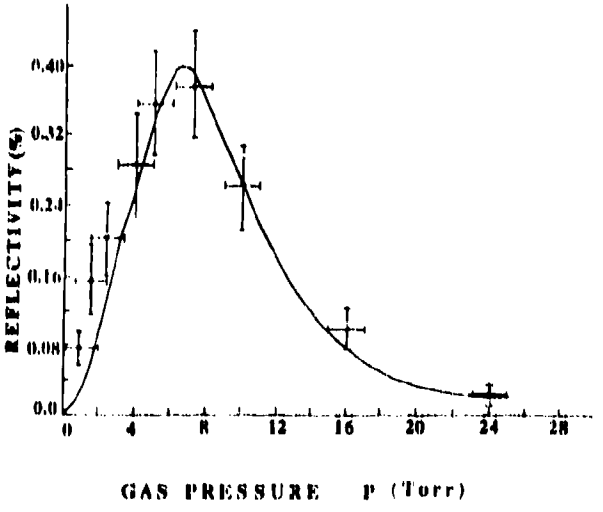

Fig. 2. Dependence of phase-conjugate reflectivity on the gas pressure

PRESSURE BROADENING OF SO_2 BETWEEN 90 K AND 600 K

J. M. Dutta(a), T. M. Goyette (b), F. C. DeLucia (b), and C. R. Jones(a)
(a) Department of Physics
North Carolina Central University, Durham, NC USA
(a) Department of Physics
The Ohio State University, Columbus, Ohio USA

ABSTRACT

The results of recent studies of SO_2 pressure broadened by H_2, He, O_2, and N_2 will be presented. This is part of the variable temperature pressure broadening studies of various molecules between 90 K and 600 K. The 4(2,2)-3(1,3), 13(1,13)-12(0,12), and 26(4,22)-26(3,23) transitions of the ground vibrational state of SO_2 are studied between 236 and 500 K. Measurements at other temperatures are in progress at this time. Results for the temperature dependence of the pressure broadening parameters will be discussed and compared with the results of previous studies on other molecules. Any trend in the 300 K broadening parameters and temperature coefficient as a function of their quantum numbers will be noted.

INTRODUCTION

Pressure broadening data obtained through remote-sensing have long provided information for understanding the transmission properties of radiation through planetary atmospheres, and establishing theoretical model for the upper atmosphere chemistry. The proper understanding and the accurate interpretation of the remote-sensing data requires the collection and compilation of the laboratory-based data. As a part of our investigation on the pressure broadening measurements of various molecules, some preliminary results for the temperature dependence of the pressure broadening parameters of the selected lines of SO_2 will be presented. This is relatively light asymmetric rotor with large dipole moment and b-type transitions. As such, it has many strong transitions throughout the millimeter and sub millimeter spectral region. The hydrogen (H_2), helium (He), oxygen (O_2), and nitrogen (N_2) pressure broadening coefficients of the 4(2,2)-3(1,3), 13(1,13)-12(0,12), and 26(4,22)-26(3,23) rotational lines at 235.151 GHz, 251.199 GHz, and 180.807 GHz respectively, will be discussed. The results for the temperature dependence of the pressure broadening coefficients and cross sections will be compared with our recent studies on other molecules, like, H_2O and HDO [1-3]. The temperature dependencies are over the range from 80 K to 600 K.

EXPERIMENTAL

The broad band spectrometer used in the experiments is described in reference 4. Measurements were taken in two different cells. A quartz equilibrium cell was used for measurements at room and higher temperatures. Low temperature measurements were taken in a collisionally cooled cell [4]. Its temperature is continuously variable from 80 K to 300 K, with the usable upper limit set by the trapping point of the spectroscopic gas. Data were recorded in the 'true line shape' mode in which the frequency of the system is swept by the microprocessor controlled synthesizer at a rate, relative to the bandwidth of the system, so that the line shape is preserved.

RESULTS AND DISCUSSION

At each temperature, line width measurements were made at about 25 different pressures between 0.05 and 1.0 Torr. Because at lower pressures the Doppler width is not negligible compared with the collisional linewidth, a fit to a Voight profile was used to extract the linewidth $\Delta\nu$. The pressure broadening coefficient γ for each temperature was obtained from a least-square fit of the data to the relation

$$\Delta\nu = \gamma P + \Delta\nu_0 \qquad (1)$$

where P is the pressure and $\Delta\nu_0$ is a free parameter. The temperature dependence of pressure broadening coefficients and cross sections are often described by

$$\gamma(T) = \gamma_0(T_0/T)^n \qquad (2)$$

$$\text{and} \quad \sigma(T) = \sigma_0(T_0/T)^m \qquad (3)$$

where σ_0 and γ_0 are the collisional cross section and broadening coefficient at the reference temperature respectively, and n and m are constants. For He as a collision partner data followed Eq.2, both for H_2O and HDO. Except for the lowest temperature measurements (below 150 K) the temperature dependencies of the H_2, O_2, and N_2 pressure broadening parameters for the rotational lines of H_2O and HDO have been shown to be represented by Eqs. 2 and 3. However, low temperature measurements show significant deviation from straight line (Fig. 1). It would be interesting to see if similar trend exist for SO_2 systems. Figure 2 shows if there is any trend that might exist between measured broadening coefficient, γ(300 K) and the rotational quantum numbers, J for the rotational lines of SO_2.

REFERENCES

1. T. M. Goyette, F.C. DeLucia, J. M. Dutta, and C.R. Jones, accepted for publication.
2. J.M. Dutta, C.R. Jones, T.M. Goyette, and F.C. DeLucia, accepted for publication.
3. J.M.Dutta,T.M. Goyette, D.W. Ferguson, F.C. DeLucia, and C.R. Jones, to be published.
4. T.M. Goyette and F.C. DeLucia, J. Mol Spectrosc. 143, 346-358(1990).

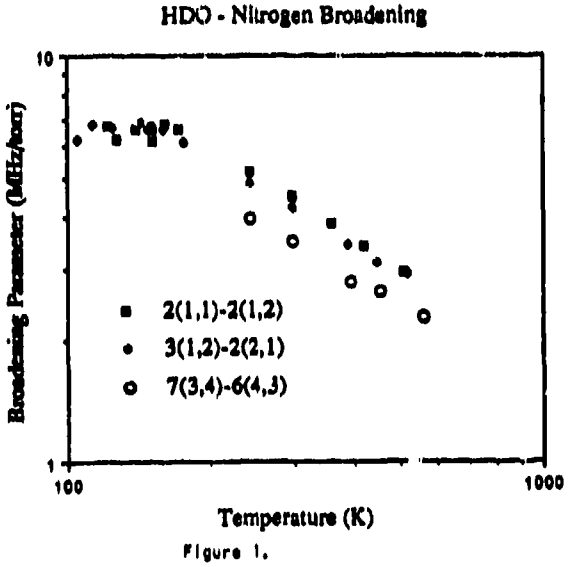

Figure 1.

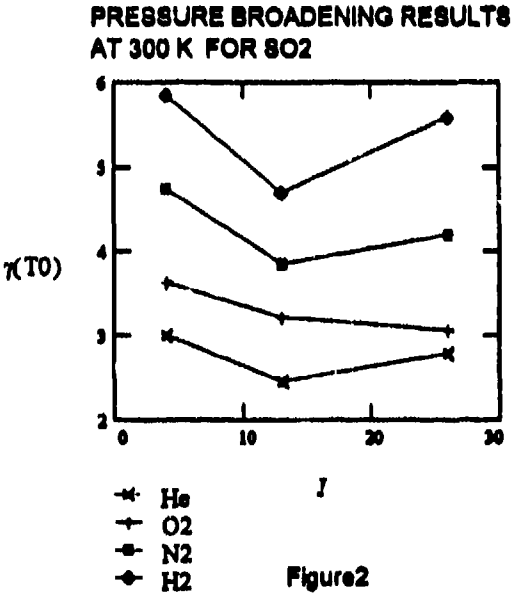

Figure2

Smith Purcell Radiation in the Relativistic Limit

John E. Walsh

Department of Physics & Astronomy, Dartmouth College
6127 Wilder Laboratory, Hanover, N.H. 03755-3528

ABSTRACT

The basic scaling relations governing the production of Smith-Purcell radiation in the relativistic limit are introduced.

Observation of visible radiation produced by an electron beam moving at grazing incidence over a diffraction grating, was reported by Smith and Purcell in 1953. The radiation was generated by the surface current "wake" induced on the grating by the beam electrons. Expressed as a wavenumber $\bar{\nu}(cm^{-1})$, the frequency of the emission, the observation angle θ, the relative velocity of an electron β, and the wavenumber of the grating $\bar{\nu}_g$ ($\bar{\nu}_g = 1/\ell$, ℓ = the grating period) are related by:

$$\bar{\nu} = \frac{\beta \bar{\nu}_g}{1-\beta \cos \theta} \quad . \tag{1}$$

Equation (1) follows from a simple Huygens construction. The energy of the electron beam used by Smith and Purcell in the first experiments was approximately 350 kV and in subsequent investigations by others, beams of still lower energy were employed. The process is also interesting in the relativistic regime and some general expectations and results of recent experiments will be summarized herein.

It is clear from Eq. (1) that $\bar{\nu}$ will be large when either $\bar{\nu}_g$ is made large (small period) or alternatively, when $\cos \theta \rightarrow \beta$ and γ becomes large. In the latter case, near this limiting angle,

$$\bar{\nu} \sim \beta \gamma^2 \bar{\nu}_g \qquad cm^{-1} \tag{2}$$

The wavenumber spectrum is also compressed in this limit, i.e.

$$\bar{\nu}^{-1} \frac{d\bar{\nu}}{d(\cos \theta)} = \frac{\beta \bar{\nu}_g}{(1 - \beta \cos \theta)} \tag{3a}$$

$$\sim \beta \gamma^2 \bar{\nu}_g \quad . \tag{3b}$$

Thus, if the source dimensions are small it might be expected that the brightness of the radiation could increase as well.

In order to explore the relativistic limit, Doucas [2] *et al.* carried out a series of experiments using a 3.6 MeV beam produced by a Van de Graaff accelerator. The grating periods were in the 0.5 - 1 mm range and at relatively high emission angles ($\theta = 90 \pm 30°$) radiation in the far-infrared (FIR) spectral range (350 μm - 2 mm) was detected. At the longer-wavelength end of this range the intensities were as much as 40 times higher than a black body and comparable to the intensity available from an IR beam line on a synchrotron. It follows that grating-coupled radiation sources may have many practical applications.

Realization of the potential implied by Eqs. (3) will require a special set of circumstances. The field above a grating consists of a radiative component and a set of non-radiative space harmonics which are bound to the grating. Resonant coupling occurs with space harmonics whose phase velocity is close to the velocity of the electron beam and hence the strength of the emission will, among other factors, depend on a factor of the general form

$$f_{co}(\bar{\nu}, b, \gamma) = \exp\left[- \frac{4\pi \bar{\nu} b}{\beta\gamma} \right] \quad (4)$$

where b is an effective impact parameter. The impact parameter is approximately equal to one half of the beam thickness in the direction normal to the grating. In the experiments discussed in Reference 2, b ~ 1 - 2 mm and γ was approximately 7, implying $f_{co} \sim 0.1 - 1$.

Equation (4) has interesting consequences in the small angle limit where Eq. (3b) is applicable. Re-expressing the factor in the exponential with the aid of Eq. (1),

$$\frac{4\pi \bar{\nu}}{\beta\gamma} = \frac{\bar{\nu}_g}{\gamma(1 - \beta \cos\theta)} \quad (5a)$$

$$\sim 2\pi \bar{\nu}_g b \gamma \quad (5b)$$

It is clear that in order to realize the potential increase in brightness at shallow angles of emission the scaling constraint

$$4\pi \bar{\nu}_g b \sim 1/\gamma \quad (6)$$

must be observed.

The coupling factor expressed in terms of the emission angle is:

$$f_c(\theta, \gamma, b) = \frac{\sin^2\theta}{(1 - \beta\cos\theta)^3} \times \exp\left[- \frac{4\pi b/\ell}{\gamma(1 - \beta\cos\theta)} \right] \quad (7)$$

which peaks when

$$\pi \bar{\nu}_g b \sim 1/\gamma , \quad (8)$$

The wavelength in this limit scales as:

$$\lambda \sim \pi b/\gamma , \quad (9)$$

a result which comes from the size of the electron's "foot-print" on the grating surface.

Details of the theory and a report on experiments in progress will be presented at the meeting.

ACKNOWLEDGMENT

Support of U.S. Army Research Office DAAL03-91-G-0189 is gratefully acknowledged.

REFERENCES

[1] S. J. Smith and E. M. Purcell, Phys. Rev. 92, 1069 (1953).

[2] G. Doucas, J. H. Mulvey, M. Omori, J. Walsh and M. Kimmitt, Phys.Rev.Lett. 69, 1761 (1992).

The analysis of electromagnetic wave amplification in quasi-optical waveguide with electron beam (SELECTRON)

N.L. Romashin, A.I.Kleev*, V.A. Solntsev**

Institute of Radioengineering and Electronics
Russian Academy of Sciences,
Marx av. 18, Moscow, 103907, Russia

* P.L.Kapitsa Institute for Physical Problems
Russian Academy of Sciences
ul. Kosygina 2, Moscow, 117334, Russia

**MIEM, B. Vusovsky 3/12, Moscow, 109028, Russia.

The problem of designing an amplifier of powerful electromagnetic radiation in millimeter and submillimeter wavelength band is one of the most important problem today. To solve this problem considerable efforts are being made in developing gyro-resonant TWT's as well as O-type electron-wave systems with relativistic beams and oversized electrodynamic structures. In realising such devices a number of difficulties occur. For gyro-resonant TWT it is a necessity to set up more and more powerful magnetic fields while moving into the short-wave band. For relativistic electron-wave systems it is a strong dependence of the output radiation structure on the electron beam parameters and in consequence this dependence is unstable.

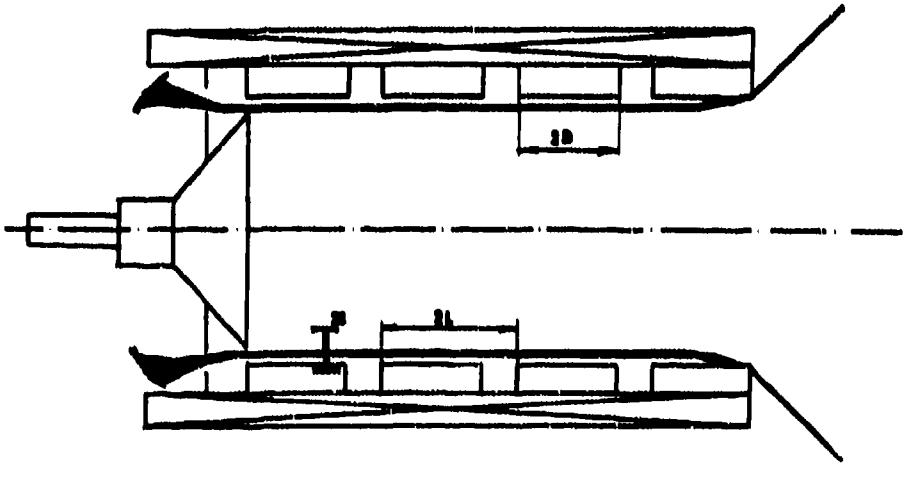

Fig. 1

In refs.[1,2] an electron-wave system (Fig. 1) where the interaction of an electron beam with the open quasi-optical waveguiding line take place has been suggested. It was supposed to realise in this system such regime of interaction with an electron beam which is characterised by the high stability of the output radiation attributed to good selective properties of the open quasi-optical line. The results obtained in papers[1,2] show the possibility of getting good amplification parameters and linear amplification within the

scope of the linear theory assuming the transverse field structure to be fixed (like in the eigenmode of the quasi-optical line).

This paper presents a theoretical analysis of the suggested system taking into account the influence of both the energy exchange with an electron beam and the diffraction effects being characteristic of quasi-optical line on the transverse and longitudinal structures of the field.

To describe the field in this system the excitation theory has been used for waveguide sections in combination with the method based on solution of parabolic equation used to describe the field between the waveguide sections. Thus, a selfconsistent problem has been solved, where a highfrequency current in the electron beam was calculated by solving a differential equation of the second order for current.

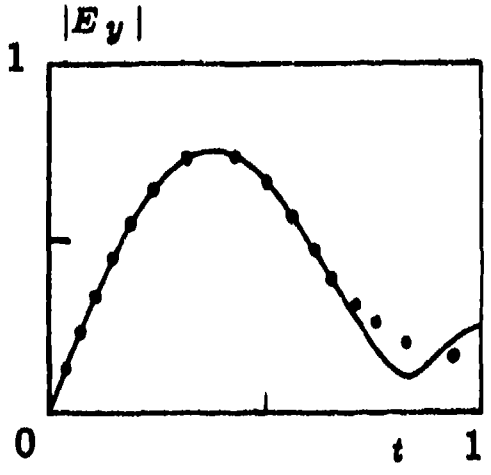

Fig. 2

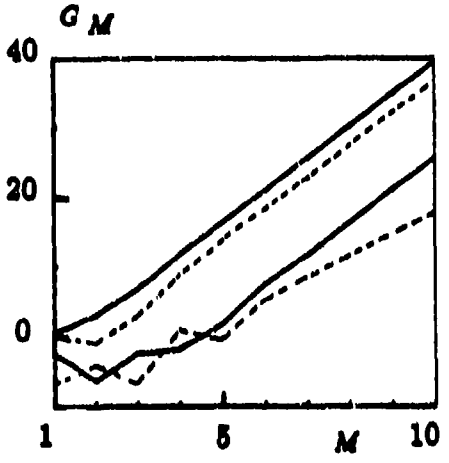

Fig. 3

The results of the numerical simulation of this system has made it possible to detect a number of specific features of the interaction. Namely, under certain conditions the transverse field structure in this system is similar to the structure of one of the eigenmodes of the quasi-optical line. In Fig. 2 the dependence of the transverse normalised field on the radius in the system is shown by the solid line and that one in the quasi-optical line is shown by the dashed line. In Fig. 3 the dependence of the gain coefficient on the number of periods taking into account the unfixed transverse field structure is shown by the solid line and that one assuming the transverse field structure to be fixed in the eigenmode is shown by the dashed line.

The following gain parameters $G = 30$ dB for the length 300 mm have been obtained for an electron beam with voltage 25 kV, current $I = 4$A at the wavelength $\lambda = 3$ mm.

Thus, the results of the theoretical analysis of the amplification allow one to consider the suggested electron-wave system to be a promising amplifier of electromagnetic oscillations in millimeter and submillimeter wavelength band, called selectron.

1.N.L.Romashin, A.I.Kleev and V.A.Solntsev, "Powerful millimeter-wave amplifier with quasi-optical structure", *In Seventeenth International Conference on Infrared and Millimeter Waves*, Richard J.Temkin, Editor, *Proc. SPIE*, Vol. 1929, pp. 328-329, 1992.

2.N.L.Romashin, A.I.Kleev and V.A.Solntsev, "Amplification analysis in the waveguide quasi-optical line with the electron beam", *Radiotekhnika i electronika.*, Vol. 37, pp. 2023-2032, 1992 (in Russian).

The influence of e-beam phase space on FEL performance

Zili Weng and Yijin Shi
Institute of Atomic Energy
P.O.Box 275(18) 102413
Beijing, China

Abstract: A code of 3-D FEL amplifier with single mode was developed on a PC-386. Using this code, the simulation results are: 1.emittance causes the exponential reduction of output power. 2.the geometry of electron phase space has important influence on output power. 3.nonideal incidence of e-beam beyond some region causes the exponential reduction of output power.

Introduction

A 3-D simulation code for FEL is independently developed with the same physical frame as FELEX code of Los Alamos[1]. This code not only takes less amount of calculation but also runs in a PC-386.

As a first example of calculation, we calculated a FEL amplifier with 5m long wiggler[2]. The set of parameters are:electron relativistic factor $\gamma = 100$, energy spread $\delta\gamma / \gamma = 1\%$, normalized emittance(90%) $\varepsilon_N = 0.14$cm-rad, current $I = 2000$A, the length of wiggler $L_w = 5$m, length of wiggler period $\lambda_w = 2.73$cm and intensity $B_w = 3000$G, wavelength of laser $\lambda_s = 10.6\mu$m, input power $P_{in} = 10^6$w, radius of optical beam waist $W_0 = 0.35$cm.

1. Comparion with FRED results[2]

With input power 10^6w and waist redius of e-beam $r_e = 0.3$cm, we got almost the same result as FRED shown in Fig.1 which is two-dimensional code with axial symmetry developed by LLNL. In Fig.1 the solid curve is the results of ours and dot-dash one is FRED's. Since the matched redius of e-beam with $\varepsilon_N = 0.14$cm-rad should be 0.444cm, hereafter we take $r_e = 0.444$cm unless otherwise mentioned.

2.The influence of emittance of e-beam on output power

The Fig.2 shows the output power decline exponentially with increation of emittance. (Here r_e is taken as matched redius with corresponding emittance)

3. The influence of geometry of e-beam phase ellipsoid

3.1 The value of waist redius, r_e

We take $r_e = 0.3, 0.444, 0.55$cm and let the waist of e-beam locating at the entrance of the wiggler with $\varepsilon_N = 0.14$cm-rad, the results are shown in Fig.3 as a function of initial energy γ_0. Obviously, unmatched value of 0.3cm means bad condition of performance.

3.2 The location of waist, L_s

In the fig.4 the output power is a function of location of waist. Since $r_e = 0.444$cm is a matched value, the redius of e-beam envelop keeps nearly a constant along with whole wiggle, the location of waist is a negligible factor on performance. But it is not the case for $r_e = 0.3$cm, as shown in Fig.4, the highest output power of 3.3×10^6w is obtained when the waist is nearly located on the middle of wiggler.

4. Nondeal injection of e-beam

4.1 deviated

We let the e-beam parallel to the wiggler axis but with a displacemant dx(dy) from it at the entrance. The output power is exponentially reduced when dx(dy) / r_e is beyond 0.2 as shown in Fig.5.

4.2 Oblique

In Fig.6, the results are shown in the cases that the center of e-beam obliquely hits against the axis of wiggle at entrance with off-axis angle $d\beta_x(d\beta_y)$ where $\beta_{em} = \varepsilon_N / (\gamma r_e)$.

5. Summary

In terms of the results shown in Fig.2–6, we may say that the initial condition of injected e–beam phase space has important influence on performance of FEL amplifier in the example. We should point out that the wiggler here is not long enough so that the saturated power is not reached as shown in Fig.1. If saturation is reached, the part of conclusion will be changed. Specilly in oscillator configuration, a somewhat different conclusion was drawn[3].

Reference

1. B.D.McWEY Nucl. Instr. and Meth. A250(1986)449
2. E.T.Scharleman J.Appl.Phys. 58(1985)2154
3. Zili Weng and Yijin Shi to be published in the 15th International FEL Conference(1993)

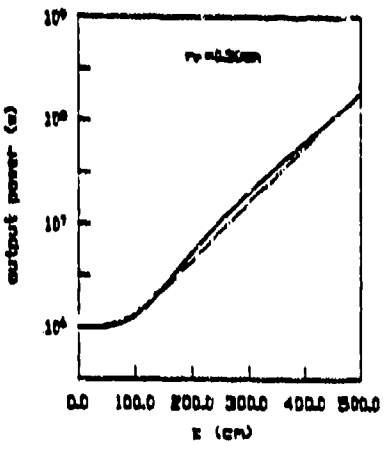

Fig.1

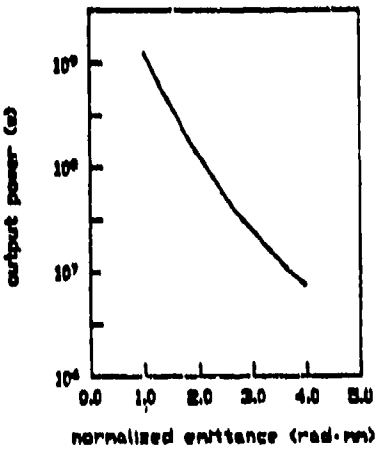

Fig.2

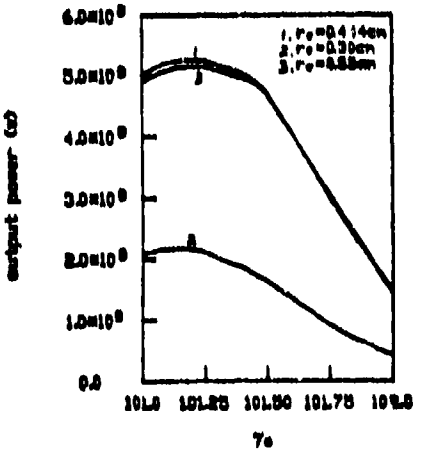

Fig.3

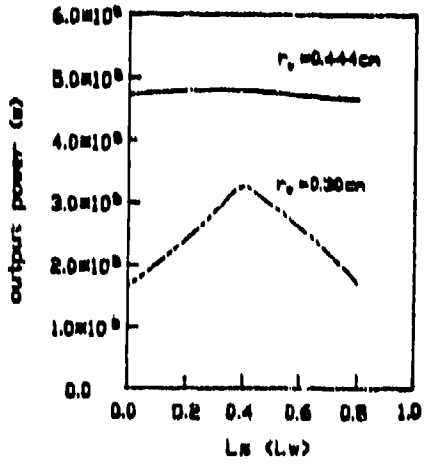

Fig.4

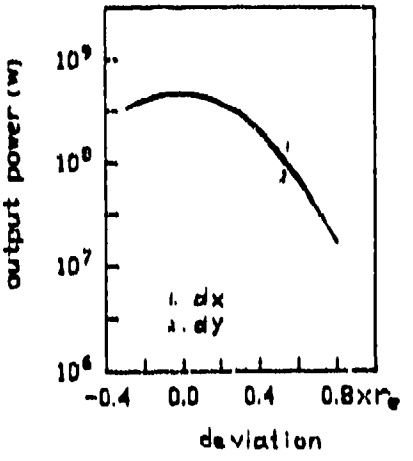

Fig.5

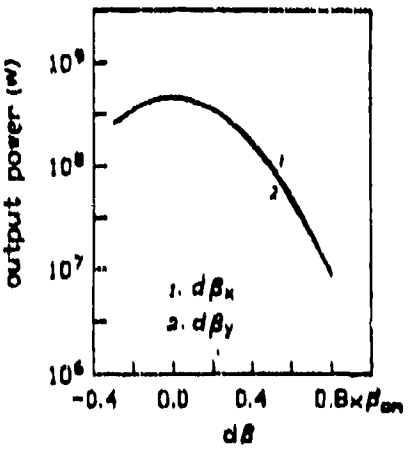

Fig.6

Nonlinear theory of two-stream superheterodyne free electron lasers

V.V.Kulish, S.A.Kuleshov, A.V.Lysenko

Sumy Physical-Technol. Institute
2 Rymski-Korsakov St.,Sumy, 244007, Ukraine

ABSTRACT

A nonlinear self-consistent theory of two-stream electron-wave FEL has been created. The methods of averaged kinetic equation and slowly varying amplitudes was used. A system of nonlinear equation for amplitudes waves and values of generating electric and magnetic fields has been obtained. The analyses of isochronic and non isochronic model has been carried out.

Nonlinear dynamics of processes taking place in two-stream electron-wave superheterodyne free-electron lasers (TEWSFEL) [1] is considered in the paper. Problem statement, method of investigation and system of nonlinear shortened equations for complex wave amplitudes (H-ubitron model) described in paper [2] are used here. Transient processes have been disregarded (the model was assumed to be stationary). Some of the obtained results are illustrated by curves in Figs 1-3. Here ω_p is plasma frequency of partial single-speed beam; ω_1 is signal wave frequency; H_{01} and Λ are the period of the magnetic pumping field, respectively; E_{01} and E_{03} are the initial intensities of the electric fields of the signal and the space charge (SCW), respectively; L is the length of the system; γ_0 is mean (for two partial beams) relativistic factor; K_s is signal amplification factor; η is interaction efficiency; $T = z/L$, z is longitudinal coordinate. Curve 1 in Fig. 1 represents relationship $K_s(T)$ found disregarding the effect of nonlinear generation of longitudinal electric field (ENGLEF) [2]. As one can see, a saturation of amplification (at the chosen numerical parameter) is attained at $T \simeq T_{sat} \simeq 0.65$ at the level $K_s = K_{sat} \simeq 2200$. In region $T > T_{sat}$, like in the case of parametric FEL [2], characteristic oscillation of the curve are observed which are connected with the capture of electrons to buckets. However, we have in the present model also substantial peculiarities. They are three. First, the amplitude of oscillations turns out to be relatively small when compared with the value of K_{sat}. Second, the period of oscillations turns out to be varying with T. The both mentioned peculiarities can be explained by the fact of the strong growth of amplitude of SCW in region $T_{sat} < T < T'_{sat}$ and are caused by the further development here of the mechanism of two-stream instability (see Fig. 2, curve 1, where E_3 is SCW amplitude). And we shall extra point out the noncoincidence which takes place of the wavelengths of saturation of the amplification of electromagnetic signal wave (T) and space-charge wave (T'_{sat}) which are associated with the specific character of mechanisms of the parametric and the two-stream instabilities, respectively. The performed calculation of the gain factor for the equivalent model of parametric FEL (i.e., of the model, where two-speed beam is replaced by the

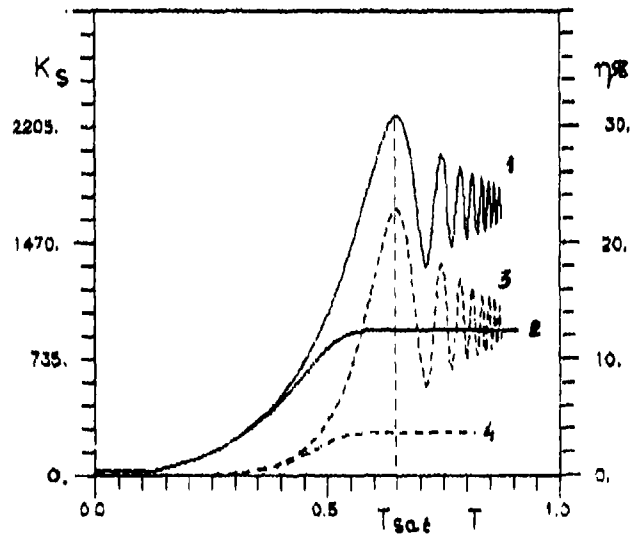

Fig. 1
$\omega_p = 0.8 \cdot 10^{10} s^{-1}$, $\omega_1 = 1.6 \cdot 10^{13} s^{-1}$, $\Lambda = 2mm$, $|H_{02}| = 300$ Gs, $|E_{01}| = 100 V/m$, $|E_{03}| = 1 V/m$, $L = 5m$, $\gamma_0 = 3.04$.

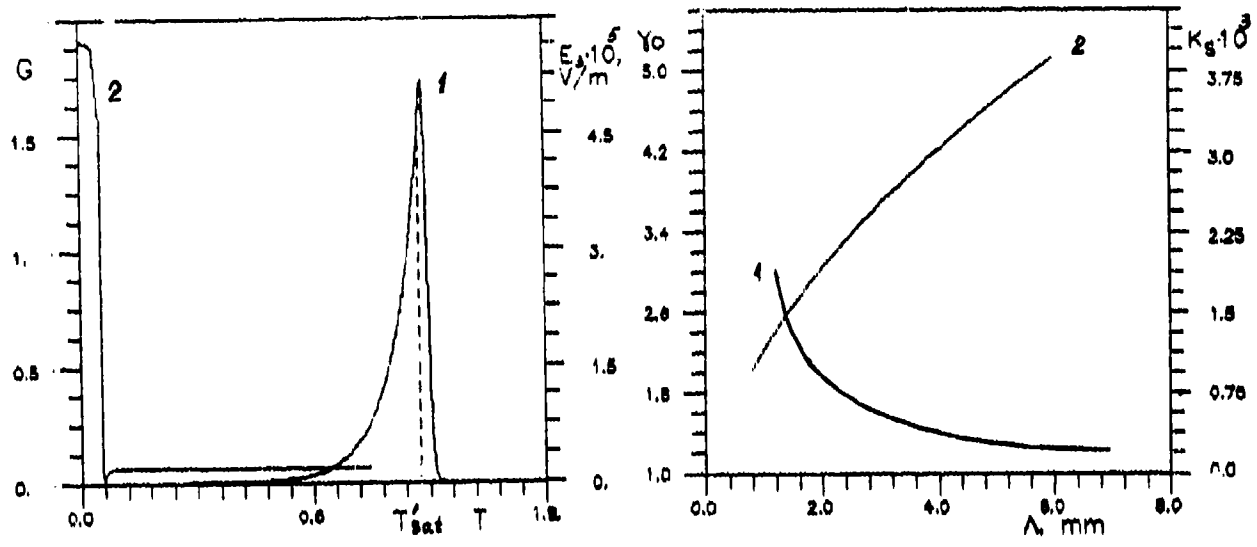

Fig. 2
(See data of Fig. 1).

Fig. 3
(See data of Fig. 1).

single-speed one) gives the value $K_{sat} \sim 1.034$. This is much less than $2.2 \cdot 10^3$ which we have according to Fig. 1 in single stream model. The third of the mentioned peculiarities consists in the character and intensity of the effect of ENGLEF on the mechanism of superheterodyne amplification being studied. As we can see from Fig. 1 (curve 2), the account of this effect results in the decrease of K_{sat} almost by a half and in the suppression of oscillations of electrons in buckets. A conclusion is drawn here from that in two-stream FEL the role of ENGLEF is much more noticeable than in single-stream ones. Qualitatively similar peculiarities take place also for the relations of the interaction efficiency $\eta(T)$ (curves 3 and 4 in Fig.1, respectively).

The conducted analysis has shown the possibility of realization in two-stream FEL of the effect of a self-coordinated change of the interaction regime. As we can see from Fig. 2 (curve 2), the values of the function of regime

$$G(T) = \left| \frac{d^2 E_3}{dT^2} \right| / \left| \Gamma \frac{dE_3}{dT} \right|, \qquad (1)$$

where Γ is low-signal two-stream increment of amplification, vary substantially in the process of interaction ($\Gamma \sim 1$ corresponds to the mixed Compton-regime, $\Gamma \ll 1$ to the Raman regime [1]).

Nonlinear dynamics (curve1)of the effect specific for two-stream FEL of the increase of coefficient K_s (at a fixed signal frequency) with the decreasing pumping period Λ [1] is illustrated in Fig. 3. (Let us recall that the opposite situation is typical for the majority of devices with prolonged interaction). Relation $\gamma_0(\Lambda)$ is also tabulated here which is realised at variation of period Λ (at the fixed value of frequency $\omega_1 = 1.6 \cdot 10^{13} s^{-1}$). Relations $K_s(T)$ at different Λ and the same fixed frequency ω_1 are also presented.

Thus, the performed nonlinear analysis has enabled the main conclusion of the low-signal theory of FEL [1] to be confirmed: two-stream FEL can provide record-breaking levels of amplification in their class of devices.

REFERENCES

1. V.V. Kulish, "Superheterodyne electron-wave free-electron lasers", *The international journal of infrared and millimeter waves*, V.14, N3, March 1993.

2. V.V. Kulish, S.A. Kuleshov and A.V. Lysenko, "Nonlinear self-consistent theory of superheterodyne and parametric free electron lasers", *The international journal of infrared and millimeter waves*, V.14, N3, March 1993.

Entropylike quantity of the equilibrium electrons in a collective free-electron laser

Shi-Chang Zhang, Qing-Xiang Liu, and Yong Xu

Southwest Jiaotong University, Department of Applied Physics, Chengdu, Sichuan 610031, China

ABSTRACT

Numerical computations of the entropylike quantity are given to the equilibrium electrons in a collective free-electron laser. Results show that a reversed guide field may present better beam quality than a positive guide field. The conclusions from the comparison of the entropylike quantities principally coincide with the experimental phenomena observed by the MIT researchers.

1. INTRODUCTION

Recently, a significant phenomenon was reported by the MIT researchers that the effficiency of a collective free-electron laser was raised from 2% upto 27% by a reversed guide field instead of the positive guide field[1]. In our opinion, the efficiency enhancement may result from two parts; the improved quality of the electron beam and an unknown interaction mechanism between the beam and radiation wave. In this paper we examine the first part by analysing the entropylike quantity[2].

2. COMPUTATION OF THE ENTROPYLIKE QUANTITY

The quality of the equilibrium electron beam may be displayed by the divergence of the phase orbits associated with the so-called entropylike quantity[2],

$$k_N(\tau, x, d_0) = \frac{1}{N\tau}\sum_{i=1}^{N} \ln \frac{|d_i|}{|d_0|}, \tag{1}$$

where τ and N are respectively the normalized iteration step and the iteration number, x denotes the phase-point position, $|d_i|$ is the Euclidean norm of the N-th step, and $|d_0|$ is the initial value of $|d_i|$. (Detailed description of the numerical computation can be found in Ref. 2.) In our calculations the 3—D wiggler field, guide field and the dc self-field of the beam are taken into account. The parameters of the MIT experiments[1] are used, i.e., the relativistic energy factor $\gamma = 2.4677$, beam radius $R_b = 0.25$cm, and wiggler wavelenght $\lambda_w = 3.18$cm. We choose $|d_0| = 2.7\times10^{-6}$ and $\tau = 2\times10^{-4}$.

Numerical computations are given to four classes of experiments; (1) Group I; guide field $B_0 = +4060$G, wiggler field $B_w = 630$G, and beam current $I_b = 90$A; (2) Group II; $B_0 = +10900$G, $B_w = 630$G, and $I_b = 300$A; (3) Antiresonance; $B_0 = -7600$G, $B_w = 1470$G, and $I_b = 300$A; (4) Reversed field; $B_0 = -10900$G, $B_w = 1470$G, and $I_b = 300$A. The results are shown in Fig. 1.

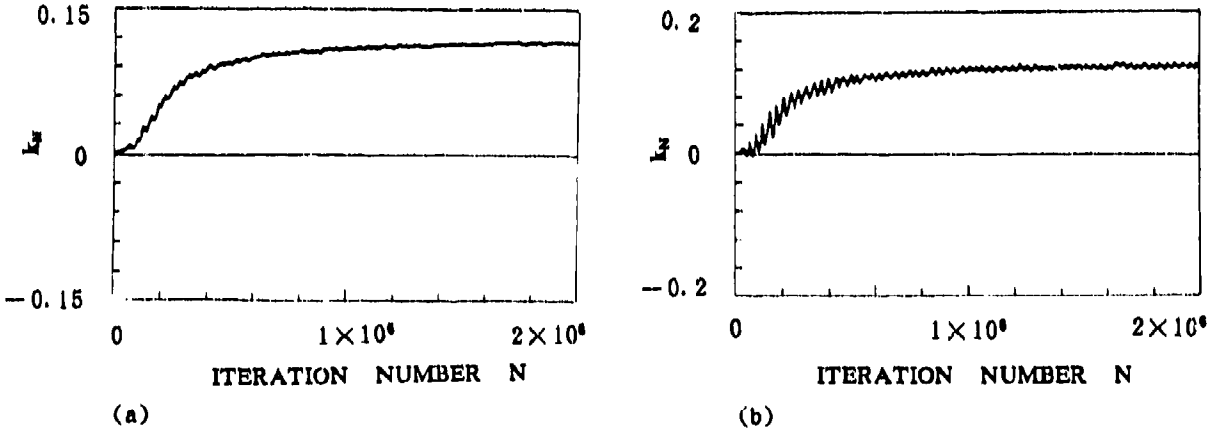

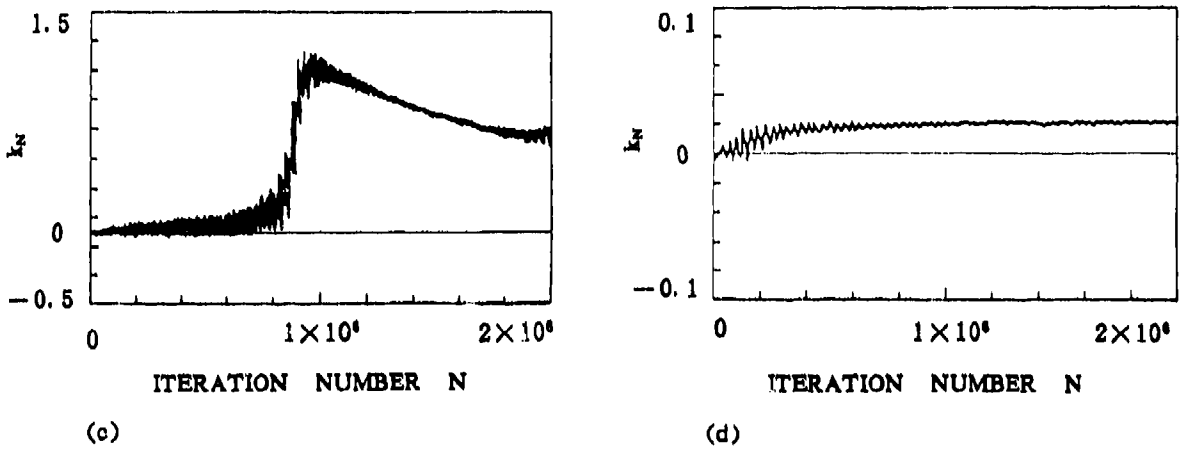

Fig. 1 Entropylike quantity of the equilibrium electrons for (a) Group I ; $B_0 = +4060G, B_w = 630G, I_b = 90A$; (b) Group I ; $B_0 = 10900G, B_w = 630g, I_b = 300A$; (c) Antiresonance, $B_0 = -7600G, B_w = 1470G, I_b = 300A$; (d) Reversed field; $B_0 = -10900G, B_w = 1470G, I_b = 300A$.

3. COMPARISON WITH EXPERIMENTS

Now we table the entropylike quantities and the related output characters of the experiments[1] as follows;

Experiment	Group I	Group I	Antiresonance	Reversed Field
Power(MW)	5.8	4.2	<1.0	81
Efficiency(%)	9	2	<2	27
Entropylike quantity	0.1163	0.1249	0.7297	0.0218

Here we observe that the better output corresponds to the smaller entropylike quantity. This confirms that a proper reversed guide field improves the quality of e-beam. It should be emphasized that the qual'ty at the *antiresonance* in a reversed guide field is spoiled , but still better than the one at resonance in a positive guide field. Conclusions in the present paper coincide with the ones obtained from Poincare surface-of-section maps[3]

4. ACKNOWLEDGMENTS

This project was supported by the NNSFC.

5. REFERENCES

[1] M. E. Conde and G. Bekefi, "Experimental Study of a 33. 3-GH, free-electron laser amplifier with a reversed axial guide magnetic field," Phys. Rev. Lett. , Vol. 67, pp. 3082—3085, 1991.

[2] G. Benettin, L. Galgani, and J. Strelcyn, "Kolmogorov entroy and numerical experiments", Phys. Rev. A, Vol. 14, pp. 2338—2345, 1976.

[3] S. C. Zhang and Y. Xu, "Phase orbits of equilibrium electrons in a free-electron laser with a reversed axial guide magnetic field", SPIE Proc. , Vol. 1929, pp. 64—65, 1992

Cherenkov radiation from a finite emission length

Mikihiko Ikezawa

Institute for Scientific Measurements, Tohoku University
Sendai 980, Japan

ABSTRACT

We have observed Cherenkov radiation from gasses in the millimeter wave and visible regions, which was emitted by electron beams from linear accelerators. The radiation is observed only when a path length of the electrons, or the emission length, is longer than the formation zone.

1. INTRODUCTION

Using electron beams from the linear accelerator, we have been studying coherent synchrotron radiation and coherent transition radiation in the far-infrared and millimeter wave regions.[1-4] When the wavelength is longer than the length of the bunch of the electrons, the intensity of the radiation is enormously enhanced by the coherent effect and excellent sources of IR and MM waves are obtained.

Cherenkov radiation should also be enhanced by the coherent effect. In the long wavelength region, however, the process of Cherenkov radiation has been studied little. Especially the radiation from a finite path length has not been investigated well and the definition of Cherenkov radiation itself seems to be ambiguous.

In the free space, Cherenkov radiation is emitted when the threshold conditions for the refractive index n is fulfilled:

$$\beta n > 1, \qquad (1)$$

where $\beta = v/c$ and v is the velocity of the electron.

Usually the path of the electron is limited by some kind of boundaries such as an exit window of the accelerator or a mirror for the observation of the radiation. Therefore, the path length of the electron is finite and the condition (1) is not sufficient as a criterion for the observation of Cherenkov radiation. Moreover, we usually observe transition radiation from the boundaries together with Cherenkov radiation.

From the analogy of transition radiation,[4,5] the path length, or emission length, L of the electron should fulfill the following condition, as a criterion for the observation of Cherenkov radiation at a wavelength λ:

$$L > Z = \lambda / (n - 1/\beta), \qquad (2)$$

where Z is the formation zone length.

The main purpose of the present experiment is to confirm the additional condition (2). In our experiment, we have carefully considered the contribution of transition radiation. Our experiments have been made by linacs of the Laboratory of Nuclear Science, Tohoku University and of the Research Reactor Institute, Kyoto University. This paper is a review of our recent results.

2. EXPERIMENTAL PROCEDURES

To generate Cherenkov radiation, the electron beam was passed through He or N_2 gas in a chamber as shown in Fig. 1. The refractive index of the gas was changed by changing its pressure. Radiation was reflected by a mirror to a system of grating spectrometer. The emission length L of the electron is limited by an Al foil and the mirror. The energy of the electron from the linacs was 150 MeV or 40 MeV.

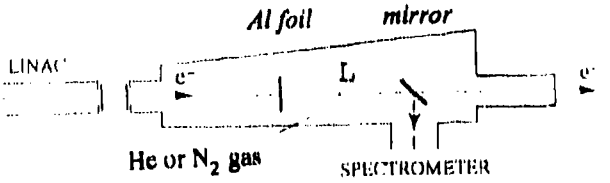

Fig. 1 Radiation chamber.

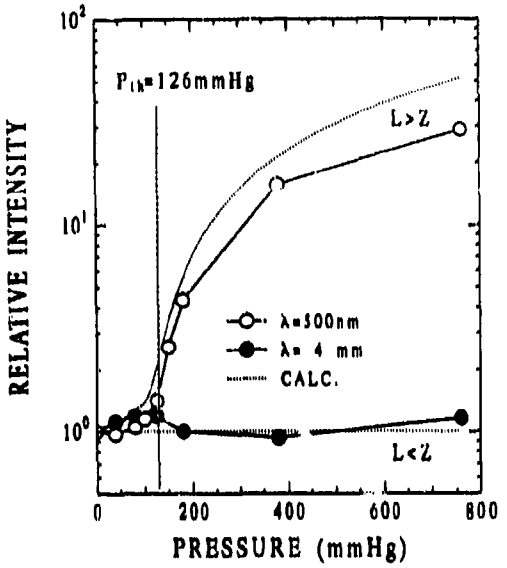

Fig. 2 Radiation from He gas by 150 MeV electron.

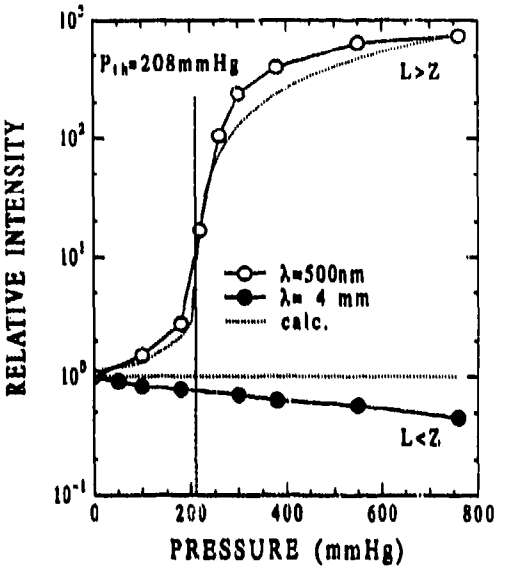

Fig. 3 Radiation from N_2 gas by 40 MeV electron.

3. RESULTS AND DISCUSSION

Cherenkov radiation from the emission length L of 165 mm was observed at wavelengths of 500 nm in the visible region and at 4 mm in the millimeter wave region. The intensity of the radiation changed when the pressure of the gas in the chamber was varied.

The results observed at Tohoku University is shown in Fig. 3. The energy of the electron was 150 MeV and He gas was filled in the chamber. The threshold pressure of Cherenkov radiation in the free space is 126 mmHg. Below the threshold the transition radiation was observed. The lengths of the formation zone at 500 nm and at 4 mm are 17 mm and 140 m, respectively. We can see from Fig. 3 that in the visible region, where the emission length L is longer than the formation zone, the intensity of Cherenkov radiation increased drastically above the threshold pressure of the gas. On the other hand, in the millimeter wave region at 4 mm, where L is much less than Z, the observed intensity remained almost constant of the pressure and Cherenkov radiation was not observed. These results are consistent with the criterion (2).

Similar results were obtained using the linac at Kyoto University. The energy of the electron was 40 MeV and nitrogen gas was filled in the chamber. The threshold pressure was 208 mmHg, and the formation zone at 500 nm and 4 mm were 2 mm and 19 m, respectively. The observed results are shown in Fig. 4 and they are also consistent with the criterion (2).

Rewriting (2), we conclude that a criterion for Cherenkov radiation from a finite emission length L, which is significant particularly in the long wavelength region, is

$$\beta (n - \lambda / L) > 1. \qquad (3)$$

Finally, I would like to emphasize that the results reviewed in this paper were obtained by many collaborators who are the coauthors of refs. 1-4.

4. REFERENCES

1. K.Ishi et al.,"Spectrum of coherent synchrotron radiation in the far-infrared region," Phys. Rev. A **43**, 5597 (1991).

2. Y.Shibata et al., "Observation of interference between coherent synchrotron radiation from periodic bunches," Phys. Rev. A **44**, R3445 (1991).

3. Y.Shibata et al., "Observation of coherent synchrotron, Cherenkov, and wake-field radiation at millimeter wavelengths using an L-band linear accelerator," Phys. Rev. A **44**, R3449 (1991).

4. Y. Shibata et al., "Observation of coherent transition radiation at millimeter and submillimeter wavelengths," Phys. Rev. A **45**, R8340 (1992).

5. U.Happek, A.J.Sievers, and E.Blum, "Observation of coherent transition radiation" Phys. Rev. Lett. **67**, 2962 (1991).

Observation of coherent millimeter-wave radiation from an intense electron bunch for beam diagnostics

Juzo Ohkuma, Shuichi Okuda, Toichi Okada, and Kiyomi Sakai *

Radiation Laboratory, The Institute of Scientific and Industrial Research, Osaka University,
Mihogaoka, Ibaraki, Osaka 567, Japan
* Communications Research Laboratory, Kansai Advanced Research Center
Iwaoka, Nishiku, Kobe 651-24, Japan

Abstract

The measurement conducted in order to develop a precise beam diagnostics based on far-infrared (FIR) transition radiation is described. Coherent transition radiation produced by a high current single bunch of L-band electron linac at Osaka University is observed while the bunch width is tuned. Performance of the beam diagnostics using the spectrometry of FIR radiation from the single bunch is studied.

Introduction

Transition radiation (TR) is produced whenever a high energy electron crosses the boundary between two media with different dielectric constants. The spectrum of TR can range from microwaves to X-rays, depending on the energy of the producing electron, although intensity of the longer wavelength is very weak. On the other hand, TR from a bunch of relativistic electrons is emitted coherently at wavelengths that are comparable to the bunch length which is a few mm in case of a typical electron linac. The intensity of the coherent radiation is proportional to N^2, where N is the number of electrons in the bunch. And the spectrum depends on the distribution of electrons in a bunch[1].

In the pervious study[2], the bunch width analyzed from the experimental spectral distribution well agreed with a theoretically expected value. To confirm the quantitative relationship linking the spectra and the bunch shape, a control system of the bunch length is adopted.

Experimental arrangement

An experimental arrangement for the measurements of beam dynamics and TR is shown in fig.1

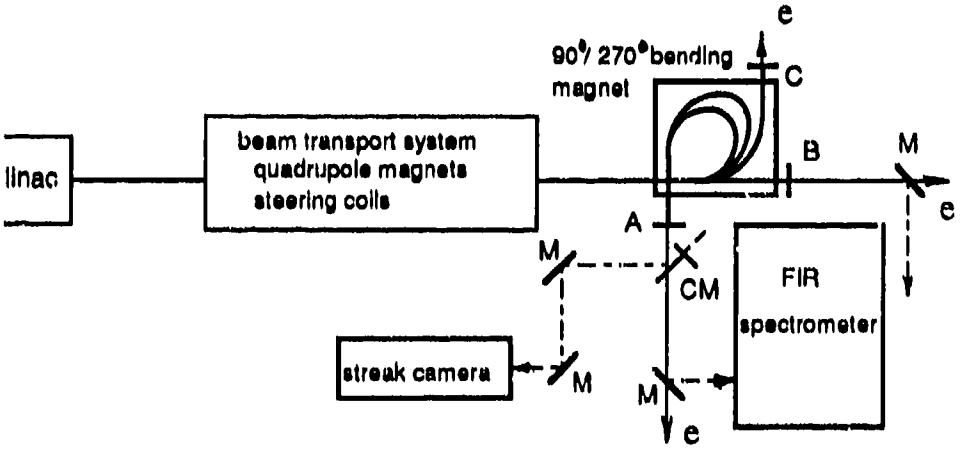

Fig.1. Layout of the beam transport system. (A,B,C: beam exit port; M:mirror; CM: chopping mirror)

The electron beam accelerated with an ordinary electron linac is composed of a train of electron pulses which are bunched to the crest of a microwave field and each bunch width of electrons is very short. On the contrary, for the L-band linac of Osaka University, a single bunch of high current can be generated by means of additional three sub harmonic prebunchers effectively [3]. The single bunch of 30ps with the charge up to 65nC is accelerated to maximum energy of 38MeV and is able to radiate intense coherent millimeter waves [4].

The width of a high current single bunch beam accelerated by the linac is controlled in the range of 20-90 ps by using a 270 ° achromatic magnet and a beam transport system which consist of steering coils and quadruple magnet lens. The bunch length is usually measured with a streak camera system by using visible Cerenkov light generated in air at behind exit windows (Band C) of the linac. Simultaneously, the coherent TR produced at Ti foil of the exit window is measured with a FIR spectrometer.

Some experimental results

Typical energy spectrum of an accelerated single bunch beam of about 30nC and of 30ps (FWHM) which was measured at the port C with the 90° analyzer magnet is shown in fig.2. Its energy spread is 1.4% of FWHM and 10% of the power has energy spread of about 2MeV on both sides of the peak energy 28 MeV. The beam situation was selected considering a tunability of the bunch width, that is bunching or debunching.

The two results shown in fig.3(a) and (b) are chosen to illustrate the bunch width obtained by using a streak camera and to show several aspects of the charge distribution in a bunch. The bunched pulse and debunched one width and the splitted pattern of a single bunch are observed in some cases.

Under the several bunching situations, spectra of the coherent FIR radiation are analyzed and discussed for the significant relation.

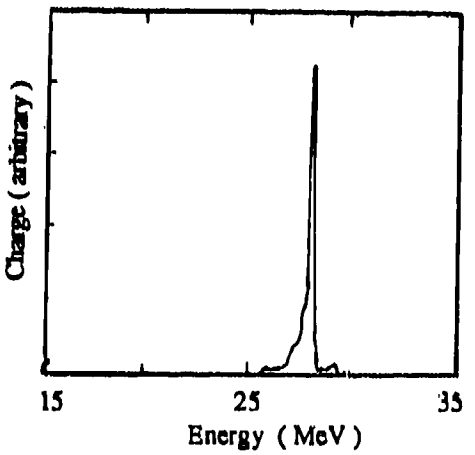

Fig. 2. Tipical Energy spectrum of the single bunch .

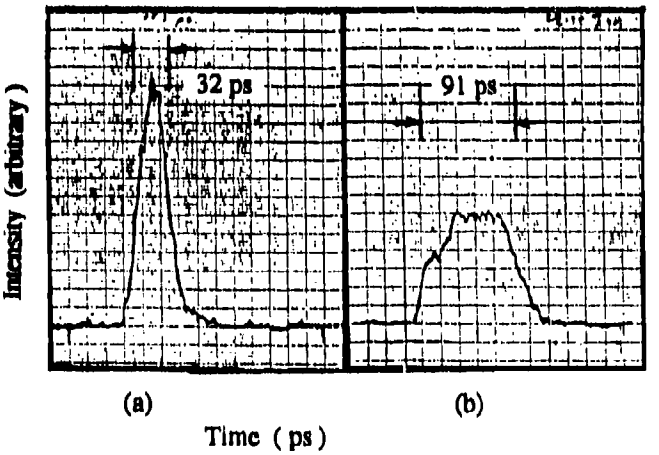

Fig.3. Streak patterns of the single bunch.

Reference :

1. U. Happek, A. J. Sievers and E. B. Blum, Phys. Rev. Lett. 67, 2962 (1991).
2. Y. Shibata, T. Takahashi, T. Kanai, K. Ishi, M. Ikezawa, J. Ohkuma, S. Okuda, and T. Okada, (to be published).
3. M. Kawanishi, K. Hayashi, T. Okada, S. Takamuku, K. Tsumori, S. Takeda, N. Kimura, T. Yamamoto, T. Hori, J. Ohkuma and T. Sawai, Mem. Ins. Sci. Ind. Res.,Osaka Univ. 43, 3 (1986).
4. J. Ohkuma, S. Okuda, and K. Tsumori, Phys. Rev. Lett. 66, 1967 (1991).

EXPERIMENTAL INVESTIGATIONS OF AN EXTERNAL FEEDBACK SYSTEM FOR WAVELENGTH SELECTION OF HIGH-POWER MICROWAVE RADIATION IN A FREE-ELECTRON MASER REGIME.

V.A.Bogachenkov, V.A.Papadichev, I.V.Sinilschikova, O.A.Smith
P.N.Lebedev Physical Institute, Leninsky Prospect 53,
117924 Moscow, Russia

Results of experiments to produce high-power microwave radiation of given wavelength by the tuning of a selective external feedback system are presented. Considered also are the advantages of this system for obtaining a narrower spectral line of radiation in the millimeter and submillimeter wavebands. The generator has a helical undulator and operates in a free-electron maser regime with an electron beam energy of up to 1 MeV and total current of up to 1 kA.

The magentic field profile and e- beam transport in the double helix linearly polarized wiggler

Hu Jianpin, Wang Pingshan, Hu Kesong, Chen Yutao,
Southwest Institute of Applied Electronics
P.O.Box 523, No65, Chengdu, Sichuan, PR China

Abstract: In free electron laser with a long, linear wiggler, the magnetic field at the entrance of wiggler and the external focusing required to keep the electron beam from dispering can determine the character of the electron orbits and seriously influence the FEL gain. To obtain good results in FEL experiments, it is necessary to investigate the linearly polarized wiggler with good magnetic field at the entrance and self-focusing.

In this paper, it is researched in details that the entrance magnetic field and self-focusing at the linearly polarized wiggler produced by double bifilar helix lines. A) The integral formula of the magnetic field on Z axis of the wiggler is derived, the prediction by the formula is good with the experiment, the results show that the field symmetry is better than the bifilar helix wigglers. B) According to Lorentz equation, we have derived the electron trajectory equations with the stable motions and the formula about the threshold transport e- beam current and the wiggler peak field, simlated the orbits of the election at edge in the wiggler, those give us a result that the wiggler has a ability of self-focusing , and can be applied in the linearly polarized FEL experiment.

Key Words: linearly polarized wiggler, magnetic field profile, trajectory of the electron motion, self-focusing

Investigation of EM—FEL With Double Relativistic Electron Beams

Yang Ziqiang, Liang Zheng, Li Jiayin, Zhang Bin, Ma Wenduo,
Wu Jiangqiang, Deng Tiangquang, Chen Xinyu, Hu Shaoxiang,
High Energy Electronic Research Institute
University of Electronic Science and Technology of China
Chengdu 610054, Sichuan P. R. C

Digest

In recent years, a great deal of attention has been focused on the free—electron laser with an electromagnetic wiggler (EM—FEL) due to the potential of shorter wave length operation than the free—electron laser with a magnetostatic wiggler with electron beams of relatively modest energy. In 1983 and 1984, Y. Carmel et al. and G. G. Denisov et al. observed the powerful radiation at millimeter wavelengths with a relativistic backward wave oscillator (BWO) at 3—cm as the electromagnetic wiggler, respectively. In 1985, Bratman et al. reported the general theory on stimulated emission of the powerful relativistic electron beam.

Our experiment has been completed to investigate stimulated Raman millimeter—wave scattering in the presence of a constant axial guide—magnetic field with a high—current relativistic electron beam. The experimental arrangement is shown in Fig. 1. A voltage pulse (70ns, 0.6MeV) is applied to a "cold" field immersed cathode. An annular electron beam is injected axially into the evacuated drift tube and passes through the region of FEL interaction, the electromagnetic pump source and then is captured by the collector.

High powerful microwave is first generated by BWO at 3—cm in the region of EM pump source, then interaction of the same intense relatvistic electron beam with the electromagntic wiggler in the region of FEL interaction stimulates FEL radiation which can be detected by a detector in front of the output window. The FEL output wavelength for an electromagnetic wiggler with a frequency ω_1 is given by

$$\omega_s = \beta_{//} r_{//}^2 cK\{1 + \beta_{//}[1 - (\frac{\omega_{mn}}{Kr_{//}\beta_{//}C})^2]^{1/2}\}$$

where K equals $\frac{\omega_1}{\beta_{//}C}(1+\frac{\beta_{//}}{\beta_{ph}})$.

Here, $\beta_{//} = V_z/C$ (V_z denotes the axial electron—beam velocity), $\gamma_{//} = (1-\beta_{//}^2)^{-1/2}$, C is light velocity, ω_{mn} represents the mode—dependent cutoff frequency of the interaction waveguide, and $\beta_{ph} = V_{ph}/C$, where V_{ph} is the phase velocity of the pump wave. The starting current I for the EM—FEL is governed by

$$I \geq \frac{1.7 \times 10^3 (S/\lambda_1 L)^2 \gamma^4}{Q_c P(GW)}(KA)$$

where S is the area of the transverse cross—section of the interaction region, L the interaction length, λ_1 wavelength of the pump wave, γ the relativistic factor, Q_c the oscillation quality of laser cavity and P the power of the pump wave.

The basic aystem of radiation diagnostic is shown in Fig.2. In this scheme, the parameters of the pump wave drived by BWO is detected by 3－cm dispersive waveguide and the stimulated 3－mm scattering radiation is directly demonstrated by a 3－mm wave detector. The output signal waveforms of the EM－FEL are shown in Fig.3 and Fig.4.

The experimental results are given in Table 1.

Table 1 Experimental results of the EM－FEL developed in UESTC

	designed value	measured value
electron beam voltage	0.6MV	0.6MV
electron beam current	>2KA	3～5KA
wavelength of the pump wave	3.0cm	～3.0cm
mode of the pump wave	TM_{01}	TM_{01}
power of the pump wave	>50MW	～100MW
scattered wavelength of the FEL	～3mm	3～8mm
radiation power of the FEL	>10KW (at 3mm－band)	

Very recently, a new experimental configuration in which EM－pump source is separated from FEL interaction region is presented for optimum characters of the EM－pump source and FEL radiation. The scheme of the new configuration is shown in Fig 5. A vaccum diode is divided into two branches in order to produce double relativistic electron beams by using only one pulse line accelerator. High powerful microwave of pump source is generated by one electron beam excitation the backward wave oscillator and coupled into FEL interaction region. FEL radiation occurs when another electron beam passes the region of FEL interaction and interacts with electromagnetic wiggler. The paramters of the EM－pump source and FEL radiation can be adjusted independently.

Our most recent electron beams transport experiment is performing in this new configuration. Total voltage and each beam current of branches were determined. The waveforms are shown in Fig. 6 and Fig. 7.

References

Y. CARMEL, et al. , Demonstration of a two－stage backward wave oscillaton free－electron laser. Phys. Rev. Latt, Vol. 51, pp. 566－569, 1983.

G. G. DENISOV, et al. , Powerful electromagnetic millimeter wave ocsillations produced by stimulated of microwave radiation by relativistic electron beams. Int. J. Infrared Millimeter waves. Vol. 5, pp. 1389－1403, 1984.

V. L. BRATMAN et al. , Stimulated scattering of waves in microwave generations with high－current relativistic Electron beams, stimulation of two－stage free electron lasers. Int. J. Electron. , Vol. 59, no. 5, pp247－269, 1985.

R. A. KEHS et al. , Free electron laser pumped by a powerful traveling electromagnetic wave, IEEE TRANS. Plasma Sci. Vol. 18, No. 3, pp. 437－446, 1990.

V. L. GRANASTEIN, et al. Realisation of a relativistic Mirron Electromagnetic backscattering from the front of a magnetised relativistic electron beam. Phys. Rev. A, Vol. 14, No. 3, pp. 1194－1201, 1976.

V. L. GRANASTEIN, C. B. WHARTON et al. , 《High－Power Microwave Source》(Artech House, Boston, London) pp. 43.

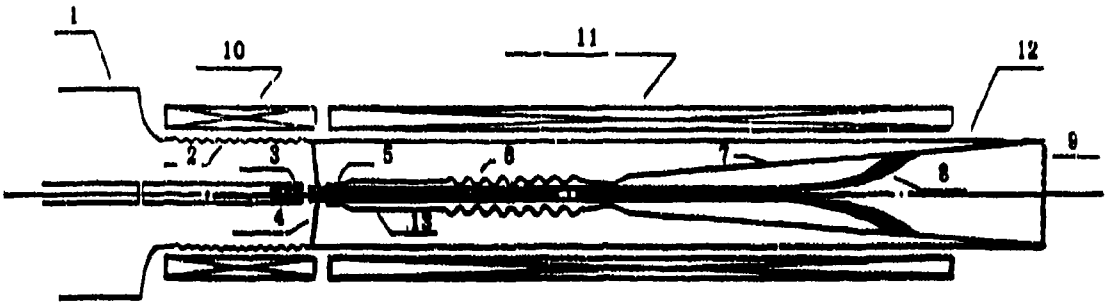

Fig. 1 The basic experimental configuration of the EM—FEL.
1. pulseline accelerator 2. bellow 3. cathode 4. anode 5. wave cut—off region 6. slow—wave struction for BWO 7. output horn 8. relativistic electron beam 9. output window 10. cathode region magnetic—field 11. main magnetic field 12. vaccum cover 13. FEL interaction region

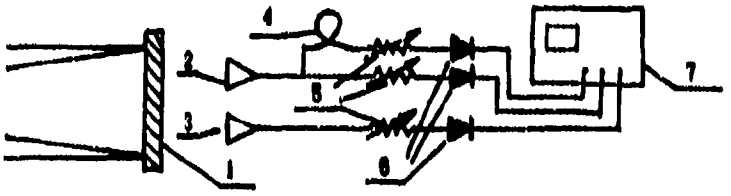

Fig. 2 The basic system of radiation diagnostic
1. output window 2. 3—cm horn 3. 3—mm horn 4. 3—cm dispersive waveguide 5. attenuator 6. detector 7. fast oscilloscope

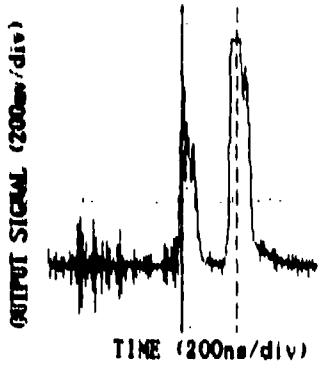

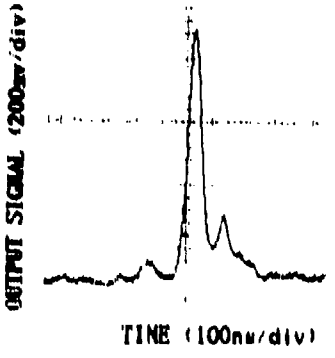

Fig. 3 Waveform of the pump wave out of BWO

Fig. 4 3—mm FEL stimulated scattering signal

Elecrtron beam voltage is 0. 6 MV and axial guide magnetic—field 10KGS

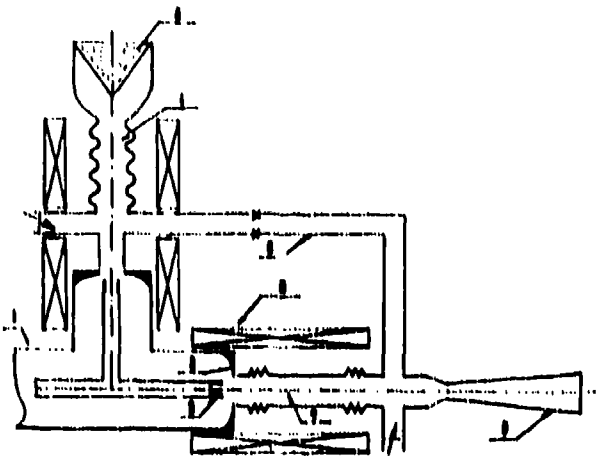

Fig. 5 The scheme of the new experimental configuration.
1. accelerator 2. cathode 3. anode 4. BWO 5. Wave termination of BWO 6. rectangular waveguide 7. FEL interaction region with Bragg reflection resonation 8. magnetic field coil 9. millimeter output horn.

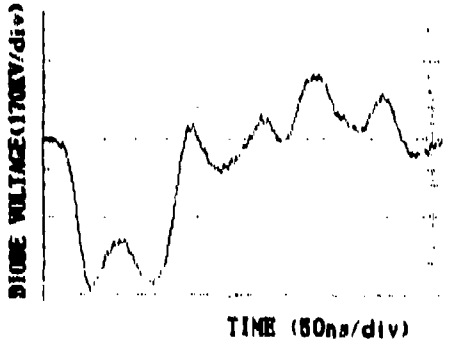

Fig. 6 Waveform of the electron beam voltage

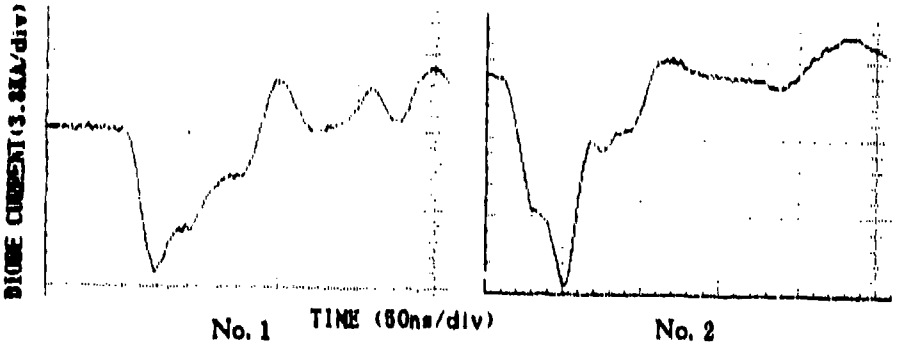

Fig. 7 Waveforms of each beam current of branches.

The design with the stagged loops on the entrance region of the bilifar helied lines wiggler

Hu Jianpin, Hu Kesong, Huang Sunren, Cheng Yutao
Southwest Institute of Applied Electronics
P.O.Box 523, No85, Chengdu, Sichuan, PR China

Abstract: The sharp variation of wiggler entrance region magnetic field in result of lowering the electron beam current quality is able fully to be removed by ulitilization of stagged terminal loops with carefully design, the magnetic field profile without any information generated by this device exactly fits the desirable requirement of adiabatic change of the field amptitute from zero to uniform region value, the axial magnetic field expression of the entrance region and the fabricating technique of the device have been presented in the paper, the experiment measurement results show a good agreement with numerical simulation, and provide a verification for rationality of the design techique. For another possible application, the bifilar helical wiggler with stagged loops will be expected to operate in experiment of variable parameter FEL.

Keywords: bilifar helical wigger, entrance effect, stagged terminal loops, adiabatic variation

Stagged loops linearly polarized wiggler

Hu Jianpin, Cheng Yutao, Hu Shuzhen, Liu Xisan
Southwest Institute of Applied Electronics
P.O.Box 523, No65, Chengdu, Sichuan, PR China

Abstract

In this paper, A new type of linearly polarized wiggler, with the ability that its magenet field amplitude and period can be varied conveniently, has been investigated in details. This device consisted of many loops which seperatedly fix on the drifting tube. Changing the raduis and period, we can obtain the magenetic field profile which we expect. The theory about the magnetic field profile in the device has been derived and stimulted resuts of computer show that it can produce any magnetic profile that we desire by verying loops radius or periods or period and radius togather.

A SUB-MILLIMETRE WAVE SIS RECEIVER

B.N. Ellison+, S.M.X. Claude+, A. Jones+ D.N. Matheson+, L.T. Little* and S.R. Davies*

+Space Science Department, Rutherford Appleton Laboratory
Didcot, Oxon, OX11 0QX

*Electronic Engineering Laboratory, University of Kent at Canterbury
Canterbury, Kent, CT2 7NT

Abstract

A superconducting (SIS) tunnel junction heterodyne receiver has been constructed and tested over the frequency range 450 to 540 GHz. The receiver uses a reduced height waveguide mount and a Pb alloy tunnel junction as the detecting element. Performance measurements made with the receiver installed on the James Clerk Maxwell Telescope, Hawaii, show a noise temperature (DSB) of 165 K at 460 GHz and 220 K at 490 GHz, measured in a 1 GHz instantaneous IF bandwidth centred at 4 GHz. The receiver demonstrates that Pb alloy junctions are sufficiently stable and reliable to allow use at a remote observing site at sub-millimetre wavelengths.

Introduction

Because of their properties of low noise and low local oscillator power requirement, superconductor-insulator-superconductor (SIS) tunnel junctions have become the preferred detecting element used in heterodyne receivers for millimetre and sub-millimetre wavelength astronomy.

In recent years, the millimetre and sub-millimetre receiver building community has favoured the development of SIS junctions with Nb electrodes because of perceived handling difficulties with Pb alloy devices. However, the fabrication of Nb junctions requires expensive equipment beyond the scope of many laboratories. We demonstrate that excellent performance can be obtained from sub-millimetre wave receivers using the relatively cheap Pb alloy technology. The receiver described was developed by the Rutherford Appleton Laboratory (RAL), in collaboration with the University of Kent, and is now in use at the James Clerk Maxwell Telescope (JCMT).

Receiver Description

The receiver was designed to operate over the frequency range 450 to 500 GHz and to be mounted at the Cassegrain focus of the JCMT. An off-axis ellipsoidal mirror, polyethylene lens and corrugated feedhorn couple the signal from the telescope to the SIS mixer. This consists of a single Pb alloy superconducting tunnel junction (Pb In/oxide/Pb Au) mounted across a 1/3 reduced height rectangular waveguide. Junctions (typically 0.5 μm^2 area) were fabricated using the suspended photoresist technique described by Dolan[1]. Two waveguide tuning elements, both of the non-contacting type[2], provide optimum matching conditions tc the junction. An intermediate frequency (IF) impedance matching circuit transforms the output impedance of the mixer to the input impedance of an isolator and low noise amplifier (LNA). Local oscillator power is provided by a Gunn oscillator and quintupling frequency multiplier. The multiplier was developed at RAL and has sufficient power to bias the SIS junction via a simple mylar (3%) beam splitter.

A hybrid liquid helium cryostat is used to cool the mixer and LNA. The typical liquid helium hold time, for a single 4 litre fill at the JCMT, is greater than two weeks.

Results

The receiver noise temperature, derived from a conventional Y factor measurement using hot (296 K) and cold (80 K) blackbody sources, includes all optics losses and is measured in a 1 GHz IF bandwidth centred at 4 GHz. A calibration gas cell was used, during laboratory tests, to confirm that the noise temperatures measured using the broad band sources corresponded to those obtained with a spectroscopic source and to measure the receiver sideband ratio (found to be equal to within 10%). A magnetic field was applied to the junction in order to suppress Josephson tunnelling currents.

Figure 1 shows the measured performance with various junction normal state impedances both in the laboratory and on the telescope. The best performance in the laboratory was obtained with the 65 Ω junction at 490 GHz. Figure 2 shows a typical spectrum obtained with the receiver on the telescope.

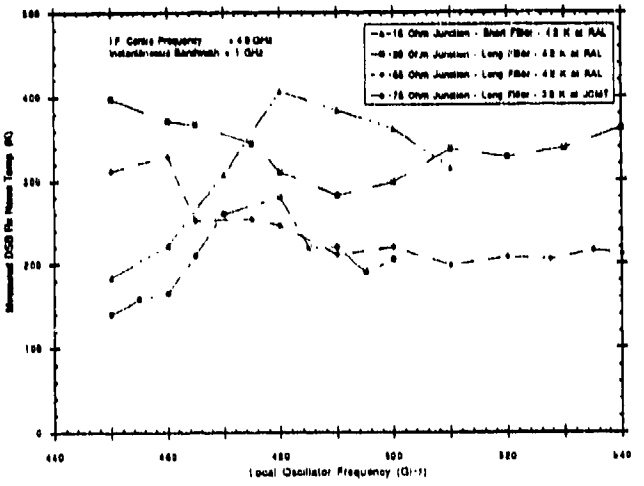

Figure 1. Receiver noise performance

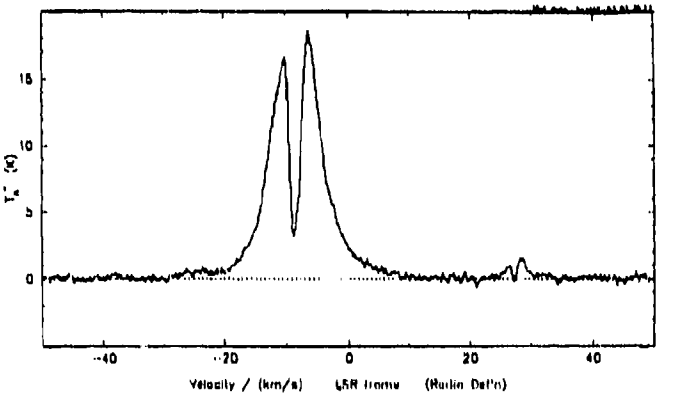

Figure 2. CO J=4-3 (461 GHz) spectrum of Herbig-Haro object 16293-242. Note evidence of self absorption

Conclusions

An SIS tunnel junction receiver designed to operate over the frequency range 450 to 500 GHz has been constructed using Pb alloy superconductors. Results obtained in the laboratory and at the JCMT show it to have a performance across the required RF band similar to equivalent receivers using Nb SIS junctions.

Acknowledgements

The authors are indebted to J. Culver, J. Spencer and D. Wilsher of the Precision Microwave Workshop (RAL) for their contributions towards the development and construction of the receiver. We are also indebted to the staff of the JCMT for their help and support during the commissioning of the receiver.

References

1. Dolan,.G.J., 'Offset masks for lift-off photoprocessing', Appl. Phys. Lett. vol. 31 pp. 337-339, Sept. 1977.

2. Ellison, B.N., Little, L.T., Mann, C.M., and Matheson, D.N., 'Quality and performance of tunable waveguide backshorts', Electronics Letters, Vol. 27 No. 2, 17th Jan. 1991.

High Speed Hot-Electron Superconducting Bolometer

G.N.Gol'tsman, E.M.Gershenzon
Moscow State Pedagogical University
1 M.Pirogovskaja Str., 119435 Moscow, Russia

Physical limitation of response time of a superconducting bolometer as well as the nature of non-equilibrium detection of radiation have been investigated for Al, Nb and NbN thin films in spectral range from submillimeter to near-infrared wavelengths [1,2]. In the case of ideal heat removal from the film with the $\simeq 100$ Å thickness the detection mechanism is an electron heating effect that is not selective to radiation wavelength in a very broad range. The response time of an electron heating bolometer is determined by an electron-phonon interaction time. This time is of about 10 ns, 0.5 ns and 20 ps for Al, Nb, and NbN correspondingly near the critical temperature of the superconducting film. The sensitive area of the bolometer consists of a number of narrow strips (with a width of ~ 1 μm) connected in parallel to contact pads; these pads together with a sapphire substrate and a ground plate represent the microstrip transmission line with an impedance of 50 Ω.

Fig. 1 shows the data obtained by direct measurements of detectivity D^* and τ for different superconducting bolometers. These values were measured at different operating temperatures, nevertheless it does not change the picture in common. The solid line ($D^*\tau^{-1/2} = 4.15 \cdot 10^{15}$ cm/J) lies through across the point representing a one of the best inertial bolometers. Triangles show electron bolometer parameters obtained in the present investigation. These devices have D^* values which have not been reached previosly for fast-response bolometers. Detectivity of the electron heating bolometer is as nigh as $5 \cdot 10^{11}$ $W^{-1}cm \cdot Hz^{1/2}$ for Al, 10^{11} $W^{-1}cm \cdot Hz^{1/2}$ for Nb and 10^{10} $W^{-1}cm \cdot Hz^{1/2}$ for NbN films.

The sensitivity can be enhanced by several orders of magnitude in a microbolometer design. In the case of electron heating bolometer the superconducting strip in the resistive state serve as a resistive load for the infrared or a submillimeter current. In contrast to a conventional microbolometer the noise equivalent power (NEP) of the electron heating one diminishes not only due to a reduction of a sensitive area but because of the decreasing of its thickness also. The principal term in NEP is determined by a electron temperature fluctuation arising from the heat exchenge with phonons. Fig. 2 shows the dependence of NEP on the Nb film thickness; this result is calculated with a using of experimentally measured values of τ and fitted to dimenesions 1×4 μm^2 (asterisks)

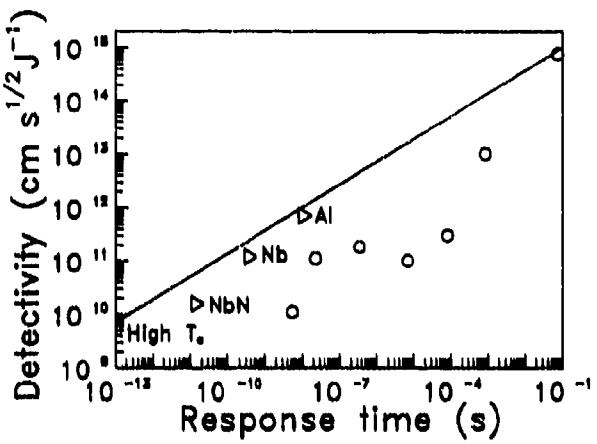

Fig. 1. Relationship between the response time and the detectivity for superconducting bolometers.

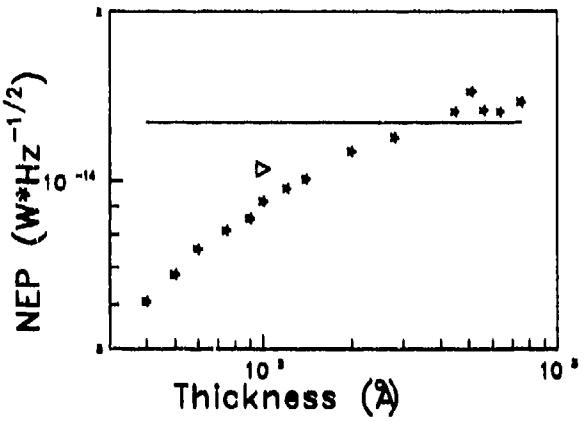

Fig. 2. Dependence of a NEP on the Nb film thickness (see text).

in plane. Triangle in Fig. 2 corresponds to a measured value of NEP reduced to the 4 μm^2 area. Solid line corresponds to an isothermal antena coupled bolometer with the same area [3].

It is clearly visible how the transition from an electron heating regime (NEP $\sim d^{1/2}$) towards isothermal regime (NEP = *const*) occurs. One can conclude that experimental data are quite similar to those which are expected. The fitting of experimental data for Al at 1.6 K and for NbN for 10 K gives values of $1.5 \cdot 10^{-16}$ $W \cdot Hz^{-1/2}$ and $2 \cdot 10^{-14}$ $W \cdot Hz^{-1/2}$ respectively.

The important problem which should be solved to develop a microbolometer is its matching with an antenna. For an ultrathin film the real part of surface resistance is rather large; moreover, the suppression of energy gap in the resistive state leads to an absorptivity which is nearly independent on frequency at submillimeter and far-infrared wavelengths. It means that superconducting strips mentioned above may be considered as a pure resistive load to the antenna. The sheet resistance inherented in thin films (40–80 $\Omega/\Box$) suits well enough for matching to antennas with a 100–200 Ω impedance.

1. E.M.Gershenzon, M.E.Gershenzon, G.N.Gol'tsman, A.M.Lyul'kin, A.D.Semenov, A.V. Sergeev, "On the limiting characteristics of high speed superconducting bolometers", Sov. Tech. Phys. Let., Vol. 15, pp. 118-120, 1989.

2. E.M.Gershenzon, G.N.Gol'tsman, A.D.Semenov, A.V.Sergeev, "Wide band high speed Nb and YBaCuO detectors", IEEE Trans. Mag., Vol. 27, pp. 2836–2840, 1991.

3. J.Mees, M.Nahum, P.L.Richards, "New design for antenna-coupled superconducting bolometers", APL, Vol. 59, pp. 2329–2331, 1991.

Picosecond detection of infrared radiation with $YBa_2Cu_3O_{7-\delta}$ thin films

M. Danerud†, M. Zorin†, M. Lindgren††, V. Trifonov‡, B. Karasik‡,
E. M. Gershenzon‡, G. N. Gol'tsman‡, and D. Winkler†

†Department of Physics, ††Department of Optoelectronics and Electrical Measurements,
Chalmers University of Technology, S-412 96 Göteborg, Sweden
‡Department of Physics, Moscow State Pedagogical University,
1 Malaya Pirogovskaja, Moscow 119435, Russia

ABSTRACT

Picosecond nonequilibrium and slow bolometric responses from a patterned high-T_c superconducting (HTS) film due to infrared radiation were investigated using both modulation and pulse techniques. Measurements at $\lambda = 0.85$ μm and $\lambda = 10.6$ μm have shown a similar behaviour of the response vs modulation frequency f. The responsivity of the HTS film based detector at $f = 0.6$-1 GHz is estimated to be 10^{-2} - 10^{-1} V/W.

1. INTRODUCTION

During the last couple of years the response of HTS thin films to infrared radiation has been intensively studied. One incentive is to investigate potential applications such as high-speed and sensitive detectors for infrared radiation. The pulsed radiation technique, where a transient electrical voltage across the current biased film is measured, provides evidence for at least two types of relaxation processes.[1-3] The first one, of picosecond duration, is attributed to fast relaxation of nonequilibrium excited electron states. This is followed by a second process which is a slow nanosecond (sometimes, microsecond) bolometric decay. Wideband measurements of these phenomena with a high signal-to-noise ratio are difficult because of the poor sensitivity inherent in a wideband pulse registration system. To overcome this problem we have applied a laser modulation technique to study the response of patterned $YBa_2Cu_3O_{7-\delta}$ films in the resistive state created by the transport current at a temperature below T_c. Modulated radiation from both a GaAs laser diode and a CO_2 laser was used. The improvement in sensitivity made it possible to trace all relaxation stages from the frequency dependent response and also to estimate the responsivity of the HTS picosecond infrared detector.

2. EXPERIMENTAL TECHNIQUES AND SAMPLES

Two different experimental setups were used. In one case, the source consisted of a GaAs laser diode with a wavelength $\lambda = 0.85$ μm, whose radiation was modulated by adding an *ac* current with a frequency up to 1 GHz to the *dc* bias. In a second experiment, a CO_2 laser ($\lambda = 10.6$ μm) was modulated by a set of acousto-optical modulators with overlapping bands in the range from 100 kHz to 100 MHz. The modulation depth was 0.2 mW for the laser diode and 0.1 mW for the CO_2 laser. The frequency dependence of the response was recorded by a spectrum analyzer with a resolution bandwidth of 100 Hz. Additional preamplifiers with a noise temperature of about 400 K and 50 dB gain were used to increase the signal-to-noise ratio of the registration system. The frequency dependence obtained at $\lambda = 0.85$ μm was normalized to that of an 18 GHz bandwidth PIN-diode. For the $\lambda = 10.6$ μm radiation, where all output power was modulated, the response from an external powermeter was used as reference.

The 300-800 Å thick $YBa_2Cu_3O_{7-\delta}$ films were deposited either by laser ablation or magnetron sputtering on $LaAlO_3$ and $NdGaO_3$ substrates. The structure consisted of one or a few parallel strips (with a minimum linewidth of 1 μm and the detector area 25 x 25 μm^2), and was prepared by electron beam lithography.[4] All samples demonstrated a linear decrease of the resistance between room temperature and the critical temperature (T_c ~ 87-91 K). The transition width was ~ 1.5-3 K. All detection measurements were carried out at $T = 77$-83 K.

3. RESULTS AND DISCUSSION

The typical data presented in Fig. 1 were obtained at $\lambda = 0.85$ μm for different bias currents (curves 1 and 2 for $NdGaO_3$ substrate, 3 and 4 for $LaAlO_3$ substrate) and at $\lambda = 10.6$ μm (curve 5, $NdGaO_3$ substrate). Similar curves were obtained over a wide range of bias currents corresponding to resistive states from near the superconducting state up to the normal state. The low frequency part of the curves follows the relation f^n. For $NdGaO_3$ (curves 1 and 2), n is approximately 0.6, and for $LaAlO_3$ (curves 3 and 4), $n \approx 0.7$. At $f = 200$-300 MHz the constant slope curve changes to a steeper slope, which eventually ends in a plateau at 0.6–1 GHz. In all cases the amplitude of the signal was proportional to the dU/dT value, where U is the *dc* voltage across the film. For 10.6 μm radiation $n \approx 0.4$.

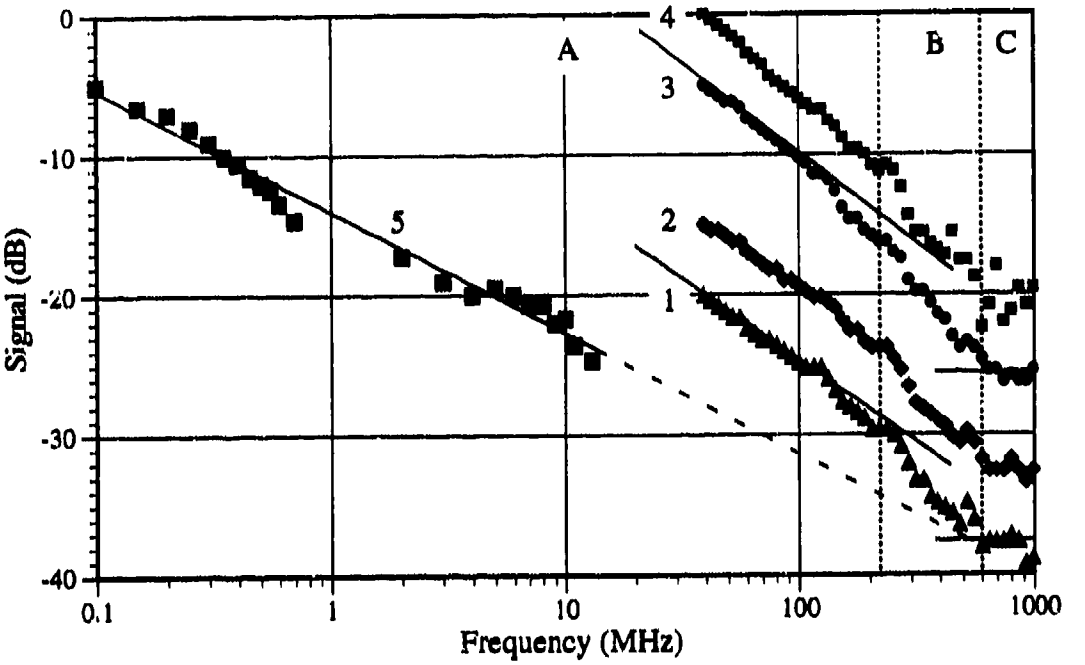

Fig. 1. Frequency response at $\lambda = 0.85$ μm: curves 1 and 2 for $NdGaO_3$ substrate, 3 and 4 for $LaAlO_3$ substrate. Curve 5 shows frequency response at $\lambda = 10.6$ μm. The curves are arbitrarily shifted along the y-axis. Solid lines in region A are fitted according to f^n, where $n \approx 0.6$ for curves 1 and 2, and $n \approx 0.7$ for curves 3 and 4. For curve 5 $n \approx 0.4$. In region C a plateau is reached.

We attribute the origin of the 0.6-1 GHz fast response to the relaxation of excited electron states characterized by a nonequilibrium distribution function. The relaxation rate of the film resistance τ^{-1} is governed by the relaxation rate for the electron subsystem. The τ-value is within the picosecond range.[1] This relaxation process corresponds to the high-frequency plateau in Fig. 1. Additional measurements using a pulsed GaAs laser diode have shown that this time is less than 30 ps. The next stage of relaxation is a transport of nonequilibrium phonons across the film-substrate interface. The presence of a thermal resistance between the film and the substrate is indicated by a steeper part of the frequency dependence in Fig. 1. The last stage of relaxation is the heat diffusion in the substrate following the temporal law $t^{-0.5}$ in the one-dimensional case. This is in agreement with the f^n dependence of the response obtained in our experiment.

Taking into account that the coupling of radiation into the HTS samples has not been optimized we estimate the responsivity for the fast response ($f \approx 0.6$-1 GHz) to be 10^{-2} - 10^{-1} V/W at 0.85 μm. An extrapolation of the frequency dependence of the response at 10.6 μm up to 1 GHz gives a responsivity about 10^{-2} V/W. The results obtained are promising for the development of spectrally broadband picosecond infrared detectors. We intend to continue the study by improving the quality of the samples and by extending the range of available modulation frequencies by mixing of laser radiation.

4. REFERENCES

1. E. M. Gershenzon, G. N. Gol'tsman, I. G. Gogidze, A. D. Semenov, and A. V. Sergeev, "Processes of electron-phonon interaction in thin YBaCuO films", Physica C, Vol. 185-189, pp. 1371-1372, 1991.

2. M. Johnson, "Nonbolometric photoresponse of $YBa_2Cu_3O_{7-\delta}$ films", Appl. Phys. Lett., Vol. 59, pp. 1371-1373, 1991.

3. R. S. Nebosis, R. Sheinke, P. T. Lang, W. Schatz, M. A. Heusinger, K. F. Renk, G. N. Gol'tsman, B. S. Karasik, A. D. Semenov, and E. M. Gershenzon, "Picosecond $YBa_2Cu_3O_{7-\delta}$ detector for far-infrared radiation", J. Appl. Phys., Vol. 72, pp. 5496-5499, 1992.

4. M. Danerud, M. E. Gershenson, Z. Ivanov, D. Winkler, and T. Claeson, "Narrow YBCO microbridges in ultrathin laser deposited thin films", Physica C, Vol. 185-189, pp. 1939-1940, 1991.

Normal state $YBa_2Cu_3O_{7-\delta}$ films: A new fast detector for far infrared laser radiation

S. Zeuner, P. G. Huggard, K. Goller, H. Lengfellner, and W. Prettl,
Institut für Angewandte Physik, Universität Regensburg, 93040 Regensburg, Germany

1. ABSTRACT

Room temperature $YBa_2Cu_3O_{7-\delta}$ films, epitaxially grown on specially cut substrates are shown to be effective detectors of high power far infrared laser pulses. For a 40 nm thick film we have measured a responsivity of $(5 \pm 2) \times 10^{-7}$ V/W, independent of frequency in the range from 20 cm^{-1} to 110 cm^{-1}. The response time is determined by thermal diffusion, giving a 200 MHz bandwidth for this film thickness.

2. INTRODUCTION

A frequent feature of power and energy meters for high power laser pulses is their strong wavelength dependence in the FIR. This may arise from their intrinsic detection mechanism, as for photoconductive and photon drag devices, of from interference effects due to the detector crystal/electrodes as has been observed for pyroelectric elements. This report suggests a new solution to this problem, using a thin film of the high temperature superconductor $YBa_2Cu_3O_{7-\delta}$ at room temperature as the detector element. Such films, when deposited on specially cut substrates, have recently been shown to exhibit a thermoelectric response to UV to FIR radiation [1].

The generation mechanism has been explained by the anisotropy of the thermopower in $YBa_2Cu_3O_{7-\delta}$ [2]. In a microscopic picture, different absolute thermopowers are ascribed to the metallic CuO planes and the more insulating intervening layers. If these planes are tilted by an angle α relative to the film surface (Fig. 1) they form a series connection of atomic scale thermocouples. Heating the film surface, for example by absorption of radiation, established a temperature gradient within the film. Thus a thermoelectric voltage parallel to the film surface is generated and detected as photosignal.

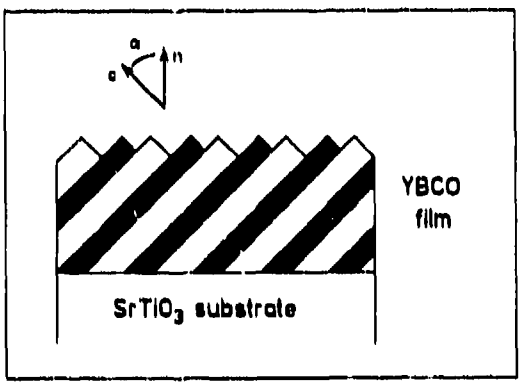

Fig. 1: Formation of a thermopile by CuO layers (black) and intermediate layers (white) in a $YBa_2Cu_3O_{7-\delta}$ film with a c-axis tilt of α to the surface normal n.

3. EXPERIMENTAL

We studied the FIR response of films with different thicknesses. The 1 cm^2 films were grown by laser ablation on $SrTiO_3$ substrates cut with the surface normal at an angle of 10° to the (100) direction. Our radiation source was a TEA CO_2 laser pumped superradiant FIR laser of conventional oversize metal waveguide design. We obtained FIR pulse profiles with a fast intraband photoconductive Ge detector. Figure 2(a) shows the response of a series of $YBa_2Cu_3O_{7-\delta}$ films and the photoconductive detector (bottom trace) to 40 cm^{-1} radiation. From the decay time of 5 ns for the 40 nm film, we estimate the electrical detector bandwidth to be 200 MHz. Using a Gentec ED200 pyroelectric Joulemeter in conjunction with the photoconductive detector, instantanous powers could be calculated at each frequency. The resulting film responsivity of $(5 \pm 2) \times 10^{-7}$ V/W is relatively uniform between 20 cm^{-1} and 110 cm^{-1}: Fig. 2(b). Such a behaviour is to be expected, as the film is much thinner than the radiation absorption depth and neither $YBa_2Cu_3O_{7-\delta}$ nor $SrTiO_3$ have strong absorption features in this spectral region.

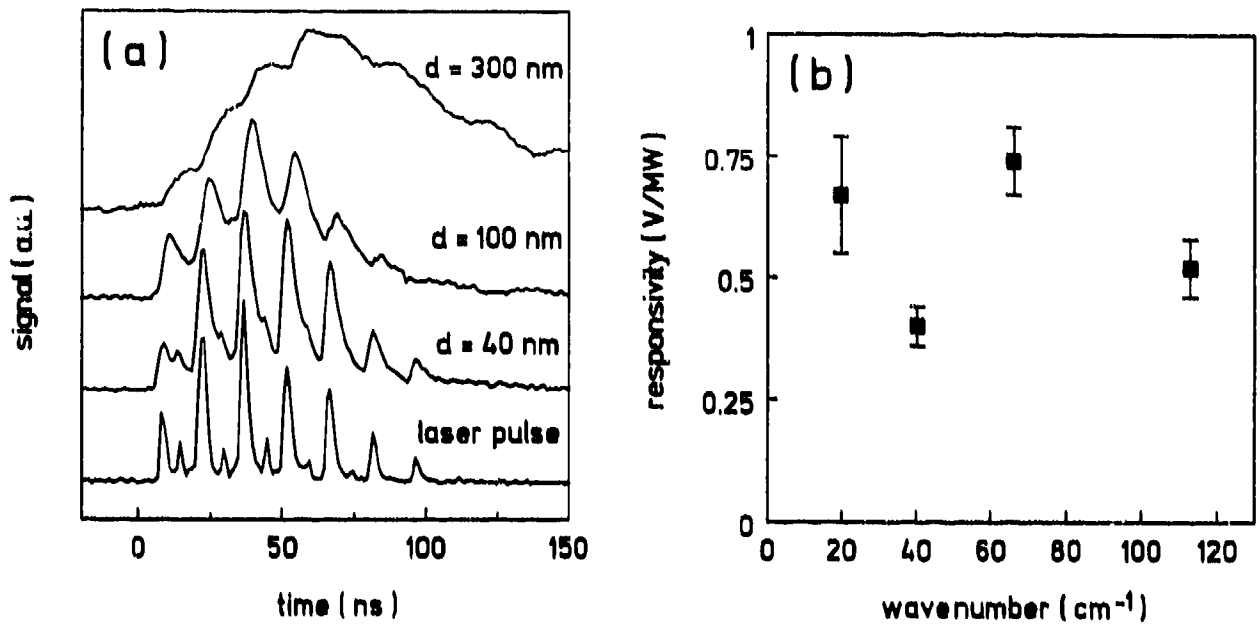

FIG. 2: (a) Response of $YBa_2Cu_3O_{7-\delta}$ films of different thicknesses to a FIR laser pulse at 40 cm^{-1} and (b) the measured responsivity of the 40 nm $YBa_2Cu_3O_{7-\delta}$ film as a function of radiation frequency.

The linearity of the response was checked using calibrated card attenuators. No significant deviations were found over three orders of magnitude down to the noise limit imposed by the amplifier. The detector noise was found to be the same as for a metal film resistor of the same ohmic value. As the film operates without bias current, the NEP is thus determined by the Johnson noise as $3.6 \times 10^{-3}\,W/Hz^{1/2}$.

4. DISCUSSION AND CONCLUSION

A drawback of such films as detectors is their relatively low responsivity. The FIR reflectivity of a 40 nm film at room temperature is about 90 %, and so most of the incident energy is reflected by the film. Considerable improvements might be achieved by use of an absorbing coating on the film surface or incorporating the film into an integrating cavity.

In conclusion, we have shown that epitaxial $YBa_2Cu_3O_{7-\delta}$ films, deposited on specially cut substrates, are effective large area room temperature detectors of FIR laser pulses. The response is relatively uniform at frequencies between 20 cm^{-1} and 110 cm^{-1}. For a 40 nm film we obtained a responsivity of $(5 \pm 2) \times 10^{-7}\,V/W$ with a 200 MHz detector bandwidth and a NEP of $3.6 \times 10^{-3}\,W/Hz^{1/2}$.

5. ACKNOWLEDGEMENTS

S.Z., P.G.H., and W.P. wish to thank the Bayerische Forschungsstiftung FORSUPRA for financial support.

6. REFERENCES

[1] H. Lengfellner, S. Zeuner, W. Prettl, and K.F. Renk, submitted to Phys. Rev. Lett.
[2] H. Lengfellner, G. Kremb, A. Schnellbögl, J. Betz, K.F. Renk, and W. Prettl, Appl. Phys. Lett. **60**, 501 (1992).

Transverse MIR fast response in PbSe films

S. Marchetti . R. Simili
IFAM -CNR ,via del giardino 7, 56100 PISA (ITALY)

ABSTRACT

Anisotropic semiconductor or semimetal films can produce large transverse voltage under lightening. PbSe and PbS films show a room temperature intense sub nsec response (~ V/MW) in the 10μm region due to free carrier photon drag ,but the direct matched response on a 50 Ω impedance is lower (~ 0.1 V/MW for 1cm^2 film) due to the film resistance (> KΩ) . CO_2 700ps mode locked pulses are easily detected in the scope limit .

1.INTRODUCTION

Semimetals and semiconductors with anisotropic band structure can show photon drag response (~ 10^{-12} s) under lightening , due to a different carrier mass. Photon draggging can be also observed by optical pressure on free carriers inside an intraband transition. Generally weak doped semiconductors are used , but in principle also strong doped semiconductors or semimetals can show PD effects. The penetration depth in semimetal or strong doped semiconductors is very small (few μm) so these film detectors are not easy to make . If the film is evaporated on anisotropic mode, a transverse component of this optical pressure can be detected along the film over a large size (~ cm) , giving a large PD transverse signal[1] . This effect has been observed in Sb and Bi both in the MIR and the FIR , but it can be also observed in strong doped PbS and PbSe films as reported here. These semiconductors evaporated with large angle show a large doping maybe due to S (Se) vacancies (> 10^{18} carrier /cm^3) , giving a light absorption, also for λ larger than the interband edge (5 μm). For suitable film depth the light can be completely absorbed in the film . In this way it is possible to detect a very fast MIR signal on large size detectors.

2.EXPERIMENTAL RESULTS AND DISCUSSION

We have evaporated Pbs and PbSe film at typically 40 ^{o} evaporation angle., of few μm thickness and typical 3-30 KΩ /square resistance and a large free carrier concentration. Films with 10-50 KΩ /square show good fast Dember response in the NIR region (1-5 μm)[2]. Light with photon energy lower than the valence-conduction gap shouldn't have Dember response, but a fast response is observed also at 10 and 100μm which we attribute to a PD response. This response is larger in PbSe also if it is affected by a moderate thermoelectric (TE) tail. In fig 1a is reported the response to a fast 1MW/cm^2 10 μm pulse ,emitted by a broadband self mode locked CO_2 laser[3]. The detectors are ~0.5 cm^2 PbS (3KΩ /square) (a) and PbSe (8KΩ /square) (b) films .

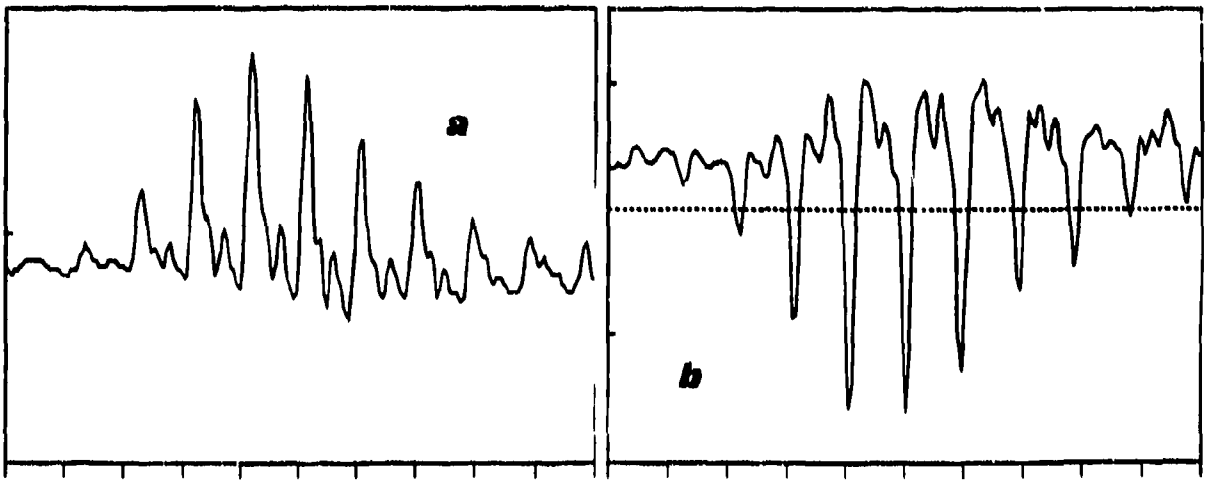

fig 1: PbS response (a) and PbSe response (b) : Xscale = 5ns /div, Yscale=50mV/div

The signal sign is depending on the contact polarity respect the evaporation versus. To obtain the fast response without cable reflections ,the signal is closed on a 50 Ω impedance so that the nominal responsivity is 50-200 times reduces .In spite of this reduction typically 0.2V/MW response can be obtained on a $1cm^2$ area film.
We can see that fast sub-ns spikes can be easily detected in the oscilloscope limit (500MHz bandwidth). The signals strongly depend on the film crystallization . Optical films show a large PD signal while amorphous films show only the TE one . The PbS signal increases with film thickness. Optical films with 3KΩ /square are the thickest ones we can produced . On the contrary PbSe well grown films with 1 KΩ /square can be produced . The thicker films show TE tails depending on the substrate thermal conductivity . The PbS responsivity is in general 3 times lower .
In fig . 2 is reported the response on ~ $0.5cm^2$ PbSe (1KΩ /square, Si substrate)film under $1MW/cm^2$ lightening for front (a) and Back (b) illumination. While the TE tail reverses the sign with thermal gradient inside the film ,the PD sign doesn't change (as observed in Sb and Bi film) showing that it is produced by light deflection inside the transverse microcrystals[1].

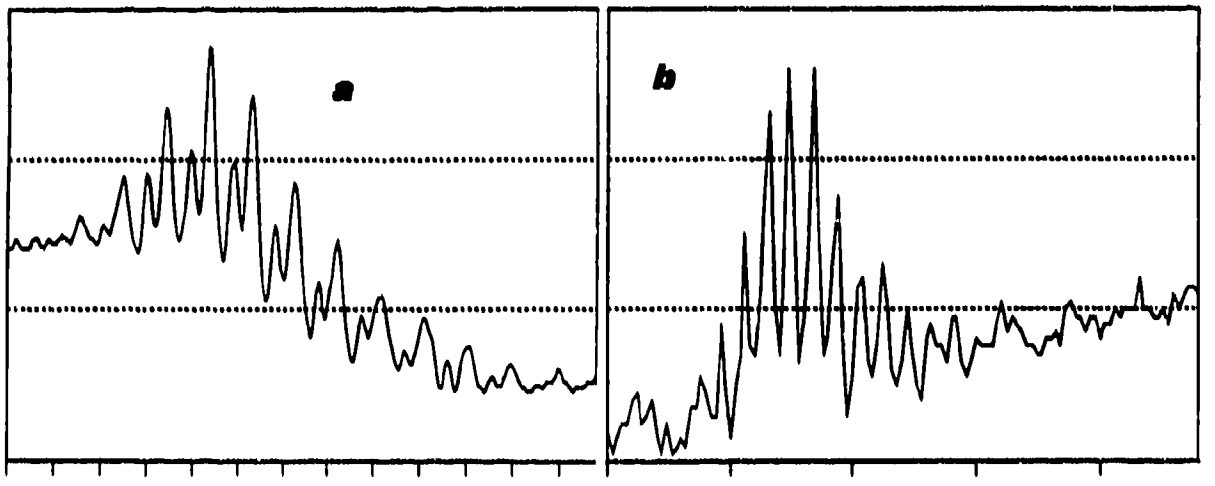

fig2: PbSe on Si response : a)= front (5ns/div , 100mV /div), b)= back illumination (20ns/ div, 20mV /div)

By using a suitable plastic substrate the TE signal can be eliminated. A reduce (~ 0.5 times) PD response has been observed in PbSe also at 100 μm , showing that the 10μm PD signal is influenced by the band edge effect on the carrier mass.Film damage is observed for power densities larger than $4MW/cm^2$

3.CONCLUSION

We have observed fast sub-ns response both in PbS and PbSe anisotropic films in the MIR region (9-11μm) . The PbSe response is larger . A crude 50Ω matched response larger than ~0.5 V/MW on 0.1 cm^2 detector can be observed which is larger than equivalent Ge PD detectors.

4.ACKNOWLEDGEMENTS

This work has been partially supported by the CNR TECNOLOGIE ELETTROOTTICHE Finalized Project

5.REFERENCES

1)S. Marchetti et al. Infrared Phys. 31 , 81 -84 (1991) and references therein
2) S. Marchetti M. Giorgi , C.Lazzeri, V. Palleschi,R. Simili : to appear on Infrared Phys.
3)S.Marchetti , R. Simili: Opt. Comm. 89 , 429-433 (1992)

A MINIATURIZED BOLOMETER ARRAY FOR FIR LASER SPECTROSCOPY

P.T Lang[1], K.F. Mast[1], K.F. Renk[2], and W. Schatz[2]

[1]MPI für Plasmaphysik, EURATOM Association, W-8046 Garching; [2]Inst. für Angewandte Physik, Univ. of Regensburg, W-8400 Regensburg, Germany

ABSTRACT

We report on investigations of the photoresponse induced in a novel, miniaturized low-noise metal resistor film bolometer array when irradiated by laser pulses with wavelengths covering the mid- and far-infrared spectral ranges. Successful operation at room temperature was achieved and almost constant detectivity was found over the whole frequency range investigated (15 - 1100 cm^{-1}). The minimum detectable laser pulse energy was determined to be about 0.6 µJ.

THE BOLOMETER ARRAY

The detector investigated in this study was one detector of a miniaturized low-noise four-channel metal resistor bolometer array module developed for fast bolometric diagnostics of fusion plasma experiments [1]. Figure 1 shows the bolometer detectors installed in the four left channels of the detector array head, whereas the four right channels hide the reference bolometers. The detector basically consists of a thin insulating carrier foil covered on each side with structured gold layers forming identical and independent bolometer bridges. Radiation is detected by means of 4 µm thick gold absorber layers which are blackened in order to reduce their reflectivity. Anodized aluminium cooling plates pressing on 20 µm thick, electrolytically deposited thermal contact layers act as heat sinks. Each bolometer bridge comprises four temperature-dependent gold resistor layers deposited on the rear side of the foil opposite the absorber layers of the measuring and corresponding reference bolometers. A detailed description of the detector, the electronics and the calibration technique can be found in [2].

EXPERIMENTAL

The aim of the experiment was to determine the absolute value of the bolometer's photoresponse signal detectivity and its spectral response characteristics. Thus, photoinduced signals delivered from the bolometer when irradiated with intense pulsed laser radiation covering the frequency range from 15 to 1087 cm^{-1} were measured. The bolometer detectivity was determined by comparing the bolometer photoresponse signal amplitude with that measured when a calibrated reference detector was irradiated with an identical laser pulse. A detailed description of the laser system employed for this study, an electrically pumped high pressure CO_2 laser which, in turn,

pumps a single-pass waveguide molecular gas laser, can be found elsewhere [3]. The CO_2 laser delivers 200 mJ pulses with a length of 250 ns , covering the frequency range around 1000 cm^{-1}. The accessible emission frequencies of the far-infrared laser range from 8 to 240 cm^{-1}; pulse energies of up to 1 mJ within pulse durations of less than 100 ns can be generated.

Results

Sufficiently strong photoinduced signals are obtained from the bolometer over the entire frequency range investigated with the laser system. The bolometer photoresponse signal detectivity obtained from the calibration to reference detectors is shown in figure 2. A detectivity of magnitude 10^4 V/J (at gain G = 2048 of the amplifiers) is valid across the entire frequeny range of this investigation. As in previous experiments, a detectivity of 68.5 V/J at the bridge output, corresponding to $1.4 * 10^5$ V/J at the output of the electronics, was determined for the cases of ohmic heating and irradiation with visible light at atmospheric pressure. This indicates an absorptivity of about 7 % in the mid- and far-infrared spectral ranges. From the voltage noise at the bolometer electronics output, approx. 3 µV, a minimum detectable pulse energy of about 0.6 µJ can be estimated. Thus, the available laser pulse energies of several hundert µJ in the far-IR and of several hundert mJ in the mid-IR exceed this detection limit about 10^3 and 10^6 times, respectively. The detectivity and the noise-equivalent energy of the bolometer detector thus allow the use of this kind of detector for laser spectrocopic methods.

References

[1] K.F. Mast, G. Gadani, P. Gaggini et al., Rev. Sci. Instrum. **63**, 4714 (1992).
[2] K.F. Mast, J.C. Vallet, C. Andelfinger et al., Rev. Sci. Instrum. **62**, 744 (1991).
[3] P.T. Lang, W. Schatz, and K.F. Renk, Optics Comm. **84**, 29 (1991).

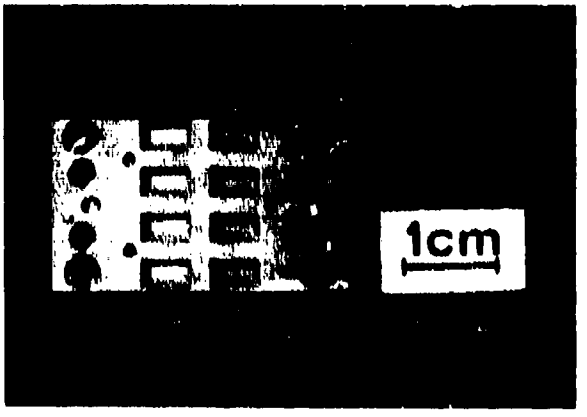

Figure1: Four-channel bolometer detector array; the four left channels of the unit are equipped with measuring bolometers.

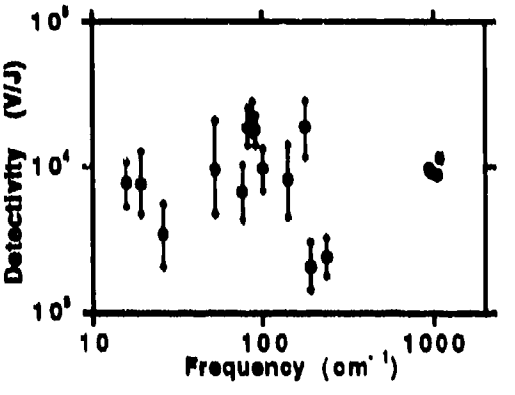

Figure 2: Bolometer detectivity (at a fixed amplification factor of G = 2048) obtained by calibrating with respect to reference detectors.

Nanosecond response time detectors for millimetre wave FELs

M.F. Kimmitt, A. Doria*, G.P. Gallerano* and E. Giovenale*

Department of Physics, University of Essex, Colchester CO4 3SQ,, U.K.
*Dipartimento Sviluppo Tecnologie di Punta, ENEA, P.O. Box 65-00044 Frascati, Italy

The pulse structure of the output of a typical free-electron laser (FEL) is shown in Fig 1. We have recently reported the operation of a compact waveguide FEL for the millimetre-wave region [1] with an average output power of up to 1kW, in a macropulse 4μs long which is repeated at a maximum frequency of 40Hz. The laser is driven by an S band (3GHz) microtron delivering electron pulses of 15ps duration spaced by 330ps and this results in the micropulse structure shown in Fig 1. However, the dispersion of the waveguide and the frequency selectivity of the resonator leads to a micropulse duration of ~100ps. The present output of the FEL is between 2.1 and 2.6mm but a new laser is under construction, designed to extend the wavelength range down to 500μm.

A variety of detectors have been used to study the output of the FEL, including microwave diodes, pyroelectrics, n-InSb electron bolometers operating at 77K, long wavelength response Ge:Ga photoconductors and photon drag detectors. At present the time resolution achieved is 3-4ns, which has allowed study of fast variations in the macropulse, but the eventual aim is to observe the micropulses directly. This will require a very fast display system, such as that used by Renk and his colleagues [2].

With powers available in the 100W to 1kW range the simplest devices to use are microwave diodes, pyroelectrics and photon drag detectors. As the performance of diodes is very well known at long wavelengths, we have confined our studies to the other two detectors. Moderately fast pyroelectric detectors (response time ~100ns) have proved very convenient for observing the macropulse, but results with very fast devices, eg Molectron P5-00, have been disappointing. This is due to a combination of low absorption at millimetre wavelengths, difficulty in focusing sufficient of the FEL output power on to the small area of ~1mm^2 and excess noise from electrical interference.

An optimised 50Ω impedance photon drag detector with 5x5mm cross-section has a responsivity of ~10^{-5} VW^{-1} at 2mm. This is almost identical to a 1mm^2 pyroelectric detector with sub-nanosecond response time at wavelengths where it is 'black'. We have obtained excellent signal to noise using a 30ohm cm n-Ge photon drag detector. It has the added advantage that it is a power-measuring device, as the voltage responsivity can be calculated from the detector dimensions, with the doping, mobility and refractive index of the germanium [3]. As photon drag detectors can be made with response times of <200ns it should be possible to observe features due to the micropulse structure of the FEL output.

Ge:Ga photoconductors have a long-wavelength response well beyond their normal cut-off at ~120μm. This is probably due to an electron bolometer process [4], which should be very fast. However, as typical detector resistances are >10kΩ, nanosecond response times will be difficult to observe. In early experiments we have observed millimetre wavelength response but with excess noise, due to x-rays. These experiments will be continued with a new optical arrangement where the detector will be at an increased distance from the FEL.

The most interesting detector results have been with an InSb electron bolometer operated at 77k. At 4K, the normal operating temperature, the response time is about 500ns, due to slow coupling between the heated electrons and the lattice. At higher temperatures the coupling speed increases and should be much less than 1ns at 77K. However, the present detector has a resistance of 1.5kΩ and the RC time constant is ~20ns As the laser power requires considerable attenuation to prevent detector saturation, we propose using a 50Ω detector to achieve much faster response. An intriguing feature of the 77K results is that at low powers the sign of the detector output is the same as at 4K, but at higher powers the sign reverses. We are investigating this further.

In conclusion, it is worth remarking that the present FEL has proved to be an extremely reliable source of millimetre wave radiation and the pulse structure makes both it, and the new shorter wavelength version, ideal for studying the various new detectors that are now being developed. These include multiquantum wells and devices based on superconductors, both conventional and high Tc, which have been shown to have response times of 100ps or less [2], [5].

References:

1 F. Ciocci, R. Bartolini, A. Doria, G.P. Gallerano, E. Giovenale, M.F. Kimmitt, G. Messina and A. Renieri. Phys. Rev. Lett. **70**, 928 (1993)

2 R.S. Nebosis, R. Steinpe, P.T. Lang, W. Schatz, M.A. Heusinger, K.F. Renk, G.N. Goltsman, B.S. Karasik, A.D. Semenov and E.M. Gershenzon. J. Appl. Phys. **77**, 5496 (1992)

3 A.F. Gibson and M.F. Kimmitt. Infrared and Millimeter Waves (Ed. K.J. Button) Vol. 3, pp182-219, Academic Press, New York (1980)

4 C. Mény, J. Birch and J. Léotin. Proc. 17th Intern. Conf. on Infrared and mm Waves, Pasadena, SPIE vol. 1929, 230 (1992)

5 G.N. Gol'tsman, A.D. Semenov, Y.P. Gousev, M.A. Zorin, I.G. Gogidze, E.M. Gershenzon, P.T. Lang, W.J. Knott and K.F. Renk. Supercond. Sci. Technol. **4**, 453 (1991)

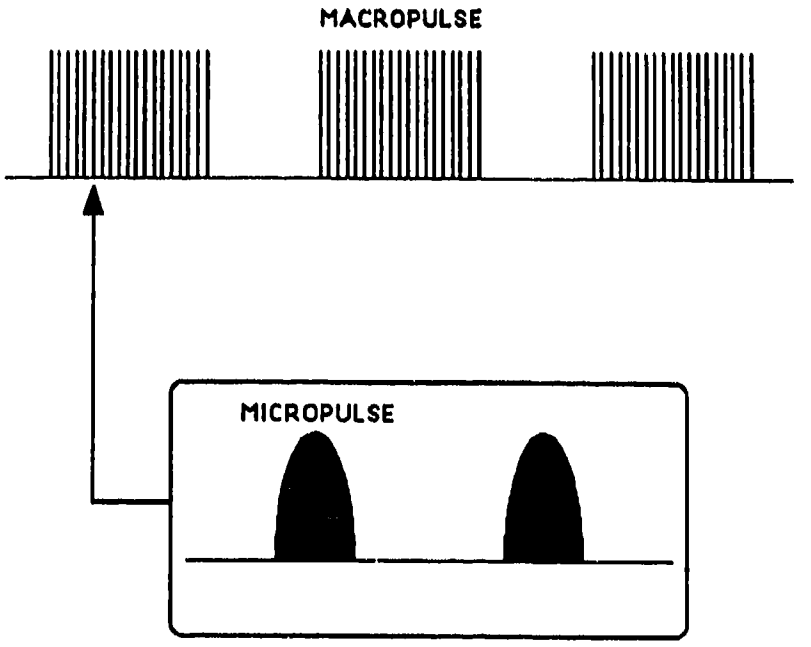

Figure 1

Physical grounds of high-sensitive detection of IR radiation in the crystal at room temperature

Gennadii K.Vlasov, Nickolaii A.Dolgikh, Elena I.Chizhikova

Center of Program Studies, Russian Academy of Sciences
SU-117810 Moscow, Russia

ABSTRACT

The theory of IR-quenching of the visible radiation in the region of relative transparency of CdS crystal at room temperature is proposed. The initial experiments are in well agreement with theory what is likely the first evidence for spherical excitons in impurities to exist. The results obtained indicate that for λ=2-5 mkm NEP < 10^{-12} $WHz^{-1/2}$ can be achievable.

2.INTRODUCTION

At high enough (room) temperatures many physical mechanisms of IR-detection become uneffective as,for instance, photoconductivity at impurity-band transitions in semiconductors.

The aim of this work is to develop new physical ideas which may allow to create the incoherent receiver of IR radiation with the parameters that are essentially better than achieved up-to-date and greatly protected against background radiation.

The effect of probing visible radiation quenching by IR-illumination of CdS volume crystals observed at room temperature can be explained quantitatively only considering the spherical exctons- free (usual)excitons interaction. The spherical excitons may have perceptible cross-sections for different interactions[1], however they were not observed until now.

3.EXPERIMENT

CdS crystals with typical sizes 1x3x4 cm^3 were excited by radiation of mercury lamp DRSh-250, and the spectrum of the radiation transmitted through the crystal was registrated.When the mercury lamp radiation is passed initially through the water filter, the intensities of doublet lines (λ=546 nm and λ = 577 nm) in the spectrum mentioned above are in 1,5-3 times larger than in the case, when the water filter was taken off. Herewith as the measurements show, the ultraviolet part of Hg-lamp emission is attenuated by water filter in $\sim$ 5 times, while the intensity of lines λ = 546 nm and λ= 577 nm decreases in 1,5-2 times.

Thus, we need to understand how the energy absorber being located in the optical path may lead to increasing power of secondary radiation from the crystal. The identifying of this effect may be obtained,by our opinion, with taking into consideration what water cuts off the radiation with λ>1,4 mkm and quartz elements are transparent for λ < 5 mkm. Consequently, the effect is, in fact, the IR-quenching of probe visible radia-tion intensity in the region of the crystal relative transparency, and the wavelength quenching radiation lies in

1,4-5 mkm band.

During initial ≃ 2 minutes after the Hg-lamp was switched on, instead of IR-quenching the opposite effect is observed that agrees well with the know fact that the heating of Hg-lamp quartz walls up to ≃1000K is realized just at this time. At such temperature the maximum of black-body radiation corresponds to $\lambda \simeq 3$ mkm. At $\lambda \simeq 595$ nm the IR-quenching effect changes its sign: the intensity of secondary radiation with $\lambda > \lambda_o = 595$ nm decreases if the water filter was installed.

From the results obtained it follows that IR irradiation with power $P \simeq 10^{-8}$ W leads to changing of absorption coefficient K for probing green radiation by amount of $\Delta K \simeq 0,2$ cm^{-1}. This allows us to estimate the sensitivity (NEP) of IR-detection for given experimental set-up as $\simeq 10^{-12}$ WHz.

4. THEORY

The gist of the mechanisms that explains the experiment is following. A photon of incoming radiation with the energy $\hbar\omega = (E_{ex} - \Delta)$ is absorbed as a result of the process described in the second order of perturbation theory. Here E_{ex} is the energy of ground (n=1) exciton state in the crystal, Δ is the energy deficit. At the first stage the photon disappears and free virtual exciton is created.

At the second stage this exciton fills up its energy deficit due to collision with a spherical exciton localized at manyelectron impurity atom (in our case - the extra Cd atoms). Those spherical excitons, that are able to lose due to collision the energy which is close to their binding energy Ry^*, must be in highly excited states $n, l \gg 1$, where n, l are mean and orbital quantum numbers of spherical exciton.

In the case under consideration

$$Ry^*(Z^*=1) = 381 \text{ cm}^{-1},$$

$$Ry^*(Z^*=2) = 1524 \text{ cm}^{-1},$$

$$Ry^*(Z^*=3) = 3429 \text{ cm}^{-1},$$

where Z^* is effective charge of a hole partipating in the spherical exciton. The value $Z^*=3$ is maximal value of Z^*, which may be obtained due to overcharging of a spherical exciton as a result of photoionization of an impurity atom by IR-radiation.

At T=300 K the position of exciton line in CdS crystal corresponds to $\lambda \simeq 510$ nm and so the maximal energy deficit Δ, which permits the absorption at $\lambda = \lambda_b$, is $\Delta_{max} \simeq 3400$ cm^{-1}. Thus, the creation of spherical excitons with $Z^*=3$ connected with IR-illumination leads to light absorption only when $\Delta < \Delta_{max} \simeq Ry^*(Z^*=3)$.

In this work the theory of spherical excitons creation is deve-

loped (this problem was not considered previously[1] up to end), which shows that such objects come to existence preferentially in highly excited states.The energy of hot electrons needed for coulomb excitation of spherical excitons must be about 10 eV for Cd atom in crystal.

Calculations give that sufficient concentration of such electrons may be obtained by quadrupolar (J=2) photons flow emitted from Hg-lamp at λ=365 nm, which 3-d harmonic generated in the volume of the crystal corresponds just to the excitation energy needed. Spherical excitons in Hg atoms, that can emit the UV photons with J=2, demand for their creation the energy close to 120 eV, what also agrees with our experimental data..

Numerical estimation for the situation discribed above gives the following results:

$$\tau_o \simeq 1{,}2\cdot10^{-7}\,s,\quad N_{sp}(Z^*=3)\simeq 0{,}75\cdot10^{5}\,cm^{-3},\quad n=l\simeq 2\cdot10^{3},\quad \Delta K=0{,}14\ cm^{-1},$$

where τ_o is life-time of a spherical exciton with $n,l\gg1$ relative to transitions to its ground state, N_{sp} is the concentration of spherical excitons. Calculated value of ΔK agrees with the measured one.

5.THEORETICAL LIMIT FOR SENSITIVITY

Likewise as was shown by Vlasov et al.[2] one can obtain

$$NEP = \left(\frac{\hbar\omega\Delta\nu}{\eta}\ \frac{1}{\beta^*}\right)^{1/2},$$

where $\hbar\omega$ is the energy of a visible photon, η is quantum yield, $\Delta\nu$ is the bandwith of registrating system, $\beta^*=\beta/P_{ir}$ ($\beta=\Delta P^{out}/P_{ir}$) is the coefficient of transformation of IR-radiation power into the change of secondary visible radiation power ΔP^{out}.The calculation for conditions of our experiment gives

$$NEP \simeq 3\cdot10^{-19}\ WHz^{-1/2},$$

what is much better than above mentioned estimation based on experimental value of ΔK. In our opinion there are several factors which optimization may lead to essential reduction of experimental estimation of NEP. For instance, one should use much larger solid angle to collect the secondary radiation.

6.REFERENCES

1. G.K.Vlasov, "Spherical excitons in manyelectron atoms", *Intern.J.of Infrared and Millimeter Waves*, vol.12, pp.397-429, April 1991.

2. G.K.Vlasov, D.N.Vylegzhanin, E.I.Chizhikova, "Excitonic detectors of infrared and submillimeter waves:, *Digest of Tech.Papers of 18-th Intern.Conf.on Infrared and Millimeter Waves* (U.K.1993), preceding paper.

PBZT infrared material and detector

Wu Ping[1] and Kang Lin[2]

[1]Department of Physics, Nanjing Aeronautical Institute
Nanjing 210016, China

[2]Department of Information Physics, Nanjing University
Nanjing 210008, China

1. INTRODUCTION

In the development of the pyroelectric infrareal detector, the single crystal pyroelectrics is paid great attention due to its excellent characters in the pyroelectric coefficient η, dielectric constont ε and dielectric loss $\tan\delta$. But the production of the single crystal material needs the complex process, long cycle and great expenses, and it can not withstand the high power radiation. So, its applications are limited, and several polycrystalline pyroelectric materials are studied and developed. PZT (lead zirconate titanate) is a pyroelectric material that can overcome the above weaknesses of the single crystal material and possesses the resistance to heat, damp and oxidation. Heance, its application fileds are very wide.

2. SELECTION AND EXPERIMENT OF PBZT

The stucture of PZT is ABO_3 type. If the Zr to Ti ratio of the material is changed, its phase stucture and characters will be different. The Zr-Ti ratio of a ferroelectrics or pyroelectrics should be selected in earnest according to their applications. From the PZT phase diagrom, we know that there is a coexistent range of F_t (tetragon) and F_R (triangle) nearby the Z_r/T_i being 53/47, that is, the difference of the free energy and the activation energy between F_t and F_R are very little in the range. So a weak electric field may cause the transformation of the phase stucture, the ε and the deformation of PZT are very large, and the internal friction in the course of the electric-domain-wall moving will increase, that is, $\tan\delta$ increases. In accordance with the quality requirements for a pyroelectrics such as high η, low ε and $\tan\delta$, the Z_r-T_i ratio must be far from the range. For pyroelectrics, the Z_r/T_i is generally selected in the range from 90/10 to 94.5/5.5. So, we select the Z_r/T_i as 94/6 and Bi is doped in the ingredinent, the chemical equation is $Pb_xB_{11-x}(Zr_{0.94}Ti_{0.06})O_3$.

The experiment procress is the same as that of . electric ceramics. The PBZT material must be sintered in the PbO atmosphere due to the PbO evaporating. It is polarized in the 120℃ silica oil for 10min at 5KV/mm voltage. The measuring results (T=25℃) show that $\eta = 8.8 \times 10^{-8} c/cm^2 \cdot K$, $\varepsilon = 200$ and $\tan\delta(1KHz) = 2 \times 10^{-3}$.

3. PBZT INFRARED DETECTOR

The PBZT material, crose section being 3mm × 3mm, is polished into a 0.1mm thickness slice. The ∅1.5mm electrodes are evaporated on the two faces of the slice, the front electrode is a blank Ni film that can raises the absorbance for incoming radiation and the back electrode is a Au film. The four corners of the slice are stuck at the four props respectively to be the stucture of the without substrate. The slice is stuck on a quartz glass to be the stucture of the with substrate. The outer casing is sealed with epoxy resin. The S_i is used as the window material. Because of the high resistivity for the PBZT material, it is necessary for the impedance matching of the PBZT and the prepositive amplifier.

On conditions that $T = 500K$ and $f = 10Hz$, the PBZT infrared detectors are measured. The results are $D^* = 5.7 \times 10^8 cmHz^{1/2}/W$ for the without substrate detector and $D^* = 1.2 \times 10^8 cmHz^{1/2}/W$ for the with substrate detector.

4. DISCUSSION

Bi is a kind of the soft additive. The amount of Bi added must be strictly controled ($x \leqslant 0.01$), if not, ε and $\tan\delta$ of the material will increase. Adding just the right amount Bi may compensate the electrons loss of the loseing Pb when sintering, the bulk resistivity of the material will increase, it is favorable for the polarizeing.

Because the without substrate stucture may avoid the harmful influence of the substrate such as the specific heat and thermal conductivity, its detectivi is higher than that of the with substrate.

The PBZT detector can be used in not only the general radiation detecting, but also the powerful radiation measurement such laser. The experiment has shown that there are not the rediation injury and the rift on the absorbing face of the detector after the several watts radiating of the CO_2 laser.

Semi-chaotic pulse effects in self-modulating Gunn oscillators

by D.A.Robertson[α], G.M.Smith[α], J.C.G.Lesurf[α], N.R.Couch[β], M.J.Kearney[β]

Abstract

Self-modulation behaviour has been observed in GaAs Gunn oscillators operating at W-band, leading to nanosecond pulses of relatively high peak power. Pulse repetition rates and pulse-widths can be varied reproducibly as a function of bias and bias termination, and there is evidence for semi-chaotic behaviour in certain regimes.

Introduction

"Bias oscillations" have been known to exist in Gunn diodes operating near threshold for some time and have generally been considered undesirable. Ferrite beads or RC networks are used as close to the cavity as possible to stop them and the devices have usually been operated at higher bias levels to ensure coherent output. Jaskolski & Ishii reported relaxation oscillations, associated with negative resistance at low frequencies, occurring simultaneously with microwave output in GaAs.[1] These relaxation oscillations were shown to be voltage-dependent and circuit-independent. This low frequency negative resistance effect has been exploited to produce u.h.f. Gunn oscillators[2,3] and amplifiers.[4]

Novel Gunn diodes designed and fabricated by GEC-Marconi Ltd., Hirst Research Centre have exhibited an enhanced tendency to such effects. These bias oscillations can correspond to pulsed output of the device itself and can occur for a range of voltages well above threshold. Jaskolski & Ishii have reported similar effects at 10GHz.[1] Here we are reporting large amplitude relaxation oscillations with very fast rise and fall times which can exhibit semi-chaotic behaviour.

Experiment, Results and Discussion

The Gunn oscillator was of a tunable second harmonic design of the type described by Carlström *et al.*[5] A quasi-optical measurement system was used which ensured electrical isolation between source and detector and permitted the use of a free-space ferrite circulator to isolate the oscillator from any signal reflected from the detector. A single Schottky-barrier detector was used to observe the output of the oscillator. The detector signal was then monitored on a spectrum analyser and a fast digital storage oscilloscope (4GSa/s HP54720A). The Gunn oscillator was fed via a bias tee whose r.f. arm was terminated in a 50Ω load to match the cable. The bias voltage was also monitored on the scope.

Typically, the shortest output pulses obtained were of the order of 3.5ns long with a 1.2ns risetime. The pulse repetition rate increased with increasing bias over a wide voltage range (typical repetition period: from 800 to 150ns for bias of 3 to 5V) beyond which the output became cw. The pulse waveform was observed to undergo a number of significant changes as bias was increased. Single, repetitive pulses transformed into bunches of two, three or more pulses separated by longer intervals. At higher bias levels the output re-formed into a continuous pulsetrain, the period of which decreased with bias. At voltages just below the onset of cw operation, the diode produced bursts of pulses separated by relatively long gaps. The inter-burst gap is generally voltage dependent.

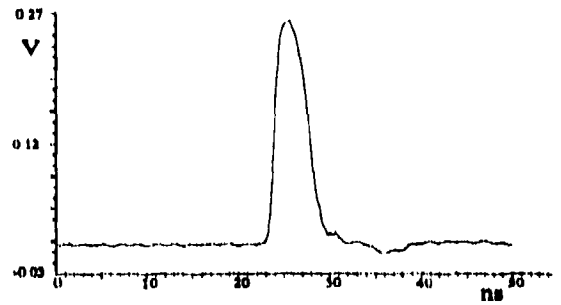

Fig.1 : Typical 3.5ns pulse

Pulse shapes were a function of the termination of the fundamental and second harmonic frequencies, the bias voltage, and the termination of the bias line. Three main effects could be induced: in addition to the short pulses, broad high power rectangular pulses (typically 200 to 800ns wide) were commonly seen, as were rectangular pulses with a larger, sharp spike on the leading edge. Backshort position tended to tune one shape into another, whereas choke position usually caused a jump between narrow spikes and rectangular pulses. There was evidence to suggest a large frequency sweep which caused some of the variations in the exact shape of the pulse. As before, the interpulse period varied with bias and multi-period waveforms were observed.

Fig.2 : An example of broad pulses

Monitoring the Gunn diode bias line showed very large voltage excursions (typically 2.0 to 2.5V)

corresponding to the pulsed output. Typical risetime and pulsewidth values are of the order of 3.2ns and 9.0ns respectively.

It was found that the bias line pulses were largely unaffected by adjustment of the oscillator's cavity length and backshort position, and were principally controlled via the bias voltage.

The output behaviour was dependent on the matching circuit used in the oscillator block. This usually includes a zener diode, to prevent over-biassing, and an RC snubber. The zener undoubtedly plays some role in limiting the magnitude of the bias pulse but it was removed in the interests of simplifying the circuit. The bias tee termination and the 50Ω pad on the scope input both help to match the bias circuit and minmise reflections.

Different bias tee terminations were found to have a marked effect on the output behaviour. Connecting unterminated lengths of cable to the r.f. arm of the bias tee produced bunches of pulses, with more pulses per bunch for longer cables. Terminating the cables removed this effect. Clearly the bias line pulses were being reflected from the open-circuit end of the cable and back to the diode.

Power measurements on the oscillator were made with both a thermal detector (average power) and a fast diode detector (peak power). Just above threshold the peak power could exceed 50mW while the average power amounted to less than 0.5mW. In general, the peak power remains fairly constant with bias, with only a slight drop-off at the upper and lower limits of the bias range, whilst the average power increases with bias voltage.

The periodicity of the waveforms was recorded for increasing bias and the periods between pulses calculated. Plotting period against bias voltage shows the voltage-dependent nature of the pulses and highlights the multi-period effects described above. A clear bifurcation is visible and period-n behaviour is indicated, where n is 2, 3 and possibly 4. The pulses are jittered and this reduces clarity in the bifurcation diagram.

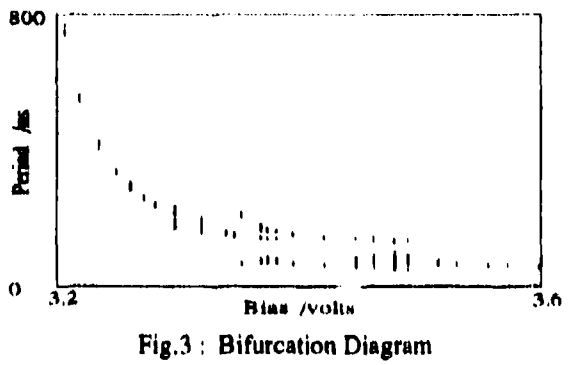

Fig.3 : Bifurcation Diagram

These effects are strongly suggestive of semi-chaotic behaviour. The 'burst' type of output observed at higher voltages suggests a relaxation oscillation, in which the diode suddenly bursts into oscillation for a while and subsequently switches off.

Similar behaviour in Gunn diodes has been described in numerical computer simulations of nonlinear models.[6]

We suggest that the mechanism involved in producing these pulses is similar to that described in Ref. 1. While the diode is oscillating at W-band there is also significant negative resistance at lower frequencies. When suitably biassed, the diode also oscillates at low frequency, modulating the r.f. output. The fast pulses are not subject to the thermal limitations of cw operation, so the peak power is relatively higher (typically 50mW as opposed to 30mW). Further work is needed to understand this self-modulation behaviour in detail, representing as it does a subtle interaction between the diode and its circuit. The effect seems especially pronounced, however, for Gunn diodes which have a strong frequency-bias dependence.

This work was supported in part by the MOD Procurement Executive, sponsored by DRA Malvern and in part by the National Physical Laboratory, Malvern.

REFERENCES

1 JASKOLSKI, S.V. & ISHII, T.K.: 'Simultaneous low-frequency relaxation and high-frequency microwave oscillation of a bulk GaAs c.w. oscillator', *Electronics Letters*, 1967, 3, pp. 12-13

2 CAWSEY, D.: 'V.H.F. and U.H.F. Gunn-effect Oscillators', *Electronics Letters*, 1967, 3, pp. 550-551

3 BRUNT, G.A.: 'Low-frequency negative resistance of X-band Gunn diodes', *Electronics Letters*, 1969, 5, pp.151-153

4 AITCHISON, C.S. *et al*: 'Self-pumped Gunn-effect parametric amplifier', *Electronics Letters*, 1969, 5, pp.36-37

5 CARLSTROM, J.E. *et al*: 'A continuously tunable 65-115GHz Gunn Oscillator', MTT-33, 7, July 1985, pp. 610-619

6 LESURF, J.C.G. & ROBERTSON, M.R.: 'Report on the Feasibilty of "Chaotic" MM-Wave Noise Sources', Report to the NPL, 1992

α Dept. of Physics, St.Andrews University, North Haugh, St. Andrews, Fife, KY16 9SS.

β GEC-Marconi Ltd., Hirst Research Centre, East Lane, Wembley, Middx, HA9 7PP.

Backward wave tube - sources of mm chaotic oscillation

Konstantin A. Lukin, Vladimir A. Rakityansky

Institute of Radiophysics and Electronics of the Academy of Sciences of Ukraine
12 Proskura St., Kharkov, 310085, Ukraine

ABSTRACT

In this paper is considered a new approach to excitation of millimeter noise oscillations with mean power about some watts and using the dynamic properties of backward wave oscillators. A low quality factor oscillator systems of millimeter wave band are used for increase in interaction efficiency and decrease in working current. Autooscillation behaviors of a BWT are studied and a main characteristics of the excited chaotic oscillations are presented.

1. INTRODUCTION

Dynamics of electron-wave oscillator is described by the set of nonlinear integral-differential equations in partial derivatives which have no analytical solutions.[1] Numerical investigation of this equations shows that the increasing of the working-current to starting-current ratio (further is referred as parameter K) causes the change of autooscillation regimes of BWT. Result is a more complicated form of spectral characteristics of the oscillations. At K=30 oscillations become irregular due to chaotic amplitude automodulation. Chaotic automodulation is characterized by a continuous frequency spectrum concentrated not far from the fundamental frequency. Numerical integration of this equations is connected with great difficulties. Besides, millimeter wave band is characterized by a large enough values of the electromagnetic field losses in waveguide structures and large values of the space charge parameter of the high density electron beam and we cannot neglected these factors when we create out numerical simulation. This circumstance makes this problem much more complicated and that is why the experimental research becomes more important.

2. WEAK-RESONANT BWT

Providing of great values of K in millimeter wave band devices is very difficult problem. One of the ways in the solving this problem is the introducing of the reflections at the slow-wave structure ends.[2] Slow-wave structure with low values of reflection factor from its ends we name as weak-resonant oscillatory system. Such system with a large electrical length are used for exciting of the chaotic oscillations with wide and uniform spectrum. The quality factor of the working modes of the system used does not exceed of 40. The system investigated is characterized by two parameters and its dynamic properties are determined by values of parameter K and the complex reflection coefficient R which describes the efficiency of the additional feedback. Experimental results are given for K_4 band BWT.

3. EXPERIMENTAL RESULTS

Weak-resonant BWT's (WBWT's) are the sources with electron retuning of the frequency spectrum of the oscillations generated. At K>3 monochromatic oscillations with continuous electron retuning of the frequency within the band of 12% are

observed. At K>6 the periodic modulation of an oscillation amplitude is developed. The satellite frequencies near the fundamental oscillation spectral line are appeared. It is a peculiarity that automodulation appears in the minimum of the oscillation power for the fundamental oscillation frequency near the boundary of the resonant zone. The frequency of the amplitude modulation can be changed within the band of 140-300MHz by the changing of the accelerating voltage. At K>11 a regular automodulation becomes quasi periodic one with equidistant frequency spectrum. Narrow band chaotic oscillations in WBWT are observed at K=19. Such values of K are less than corresponding values for ordinary BWT. Wide band chaotic oscillations with $\Delta f/f=2-3\%$ (at power level of -10dB) are observed at K=50. Electron retuning of the mean frequency of the chaotic oscillation carrying frequency of the weak-resonant BWT is discrete due to the strong non-uniformity of the interaction efficiency. However, the band of the working frequencies is exceeded by electron retuning due to the narrow interval of the acceleration voltages of the spectrum quantification.

The packaged chaotic (noise) oscillation sources of the millimeter wave band are designed with using weak-resonant BWT. The sources of chaotic signals of middle power level have the following technical specifications

Mean level of the power spectrum density, mW/MHz	5-10
Spectrum Width, MHz	
at power level (-3dB)	300
at power level (-10dB)	800
Electron retuning of the carrying frequency, %	10
Steepness of electron frequency retuning, MHz/V	4-10
Cathode voltage, kV	2-4,5
Cathode current, A	0,1-0,18
Consumption of coolant, l/h	100
Mass of device with rare-earth magneticsystem, kg	9-12

4.CONCLUSION

Application of the weak-resonant BWT's made possible to increase of the interaction efficiency. The results is the decrease of working-current corresponding to the excitation of the millimeter chaotic oscillations. Packaged middle power chaotic oscillators based on the using of WBWT are designed. The developed sources of millimeter wave band allow to design radio systems for solution of many scientific and technic problems. They can be used for design of the sensing or radar systems with high electromagnetic compatibility, correlation and non-coherence reflectometry for precision determination of plasma cut-off layer position and other radio electronic systems in a similar way.

5.REFERENCES

1. B.P.Bezruchko, L.V.Bulgakova, S.P.Kuznecov, D.I.Trubetskov," Experimental and theoretical investigation of BWT chaotic oscillations," Radiotech. and Electr., Vol.28,pp.1136-1142,June 1983,(in Russian).

2. B.P.Efimov, K.A.Lukin, V.A.Rakityansky," About a transformation of the chaotic oscillation spectrum," Journal of technical physics, Vol.58,pp.2398-2400,December 1988,(in Russian).

A Dual Channel Optically Pumped FIR Laser System For Plasma Diagnostics

BW Davis and RS Thomas

Edinburgh Instruments Ltd
Riccarton, Edinburgh EH14 4AP, Scotland, UK

ABSTRACT

A dual output optically pumped FIR laser system for plasma diagnostics has been developed and operated at 184um and 433um. Powers in excess of 300mW per channel have been achieved at 184um with amplitude stabilities of better than +/- 2 %. The two FIR output beams can be tuned to provide intermediate difference frequencies in the range 500kHz to 1.5MHz with stabilities of +/- 10kHz. The system and test results will be presented.

1. INTRODUCTION

The use of optically pumped FIR lasers in dual beam interferometer systems for plasma diagnostics has been well documented (1). This paper describes a commercial system developed for the COMPASS Tokamak in Culham laboratories (2) and for similar applications in Japan. The Edinburgh Instruments PL6 CO_2 and 395 Far Infrared (FIR) lasers form the basis of the described system.

2. LASER SYSTEM

The PL6 grating tuned, flowing gas CO_2 laser operates on up to 90 lines over the 9-11um region with continuous wave (cw) powers in excess of 180 Watts on the strongest lines. This is achieved in a compact configuration using an invar stabilised, folded cavity arrangement. The CO_2 radiation is divided into two beams of near equal power by a ZnSe beamsplitter.

The semi-sealed 395 FIR laser is a dual laser with two independent 1.5 meter long, 36mm diameter dielectric waveguides with plano/plano optics in a common invar stabilised frame. Although the application described only required operation at 184um and 433um the laser system can be operated over the range 40um to 1.22mm. In its standard configuration the laser has integral water cooling of both optics and waveguides to allow efficient pumping with high power cw CO_2 radiation.

The CO_2 input beams are focused through 2.5mm pinholes centrally located in each of the input mirrors. FIR radiation is extracted from specially designed dichroic output mirrors which are mounted on stepper driven micrometer stages. Fine adjustment of the cavity length allows the difference frequency (IF) between the FIR outputs to be tuned over the range 500kHz to 1.5MHz.

3. POWER STABILITY AND STABILISATION

The FIR laser has been operated at 184um (CH_2F_2), with cw FIR powers in excess of 300mW per channel, and 433um (HCOOH) with 50mW per channel. Long term amplitude stability measurements have been made by monitoring both channels with two calibrated thermopile detectors. Stability runs have been performed with, and without, active stabilisation.

An Edinburgh Instruments ALS-1 active stabiliser was used to control the CO_2 laser power to produce near maximum FIR output power. In this, a mylar beamsplitter was used to split off 5% of the FIR power from one channel of the FIR laser. This signal was focused and chopped before being incident onto a pyroelectric detector. The detector output was then fed into the ALS-1 and subsequently the stabiliser controlled the PL6 laser by adjusting its cavity length such that the optimum pumping frequency was maintained.

Measurements over many hours have indicated power stabilities of better than +/- 2%. Thus by actively stabilising the CO_2 laser, and utilising the inherent stability of the FIR laser, hands off operation for many hours can be achieved.

4. FREQUENCY STABILITY

As described, either of the two FIR cavity lengths can be adjusted to provide intermediate difference frequencies (IF) in the range 500kHz to 1.5MHz. The FIR laser outputs were mixed in wavelength optimised corner cube Schottky diode detectors and the detector output was monitored both on an oscilloscope and through a Frequency to Voltage converter in the ALS-1 stabiliser. This enabled stability measurements of the beat signal to be recorded for various IF values.

At an IF of 1MHz, a stability of +/- 10kHz over 60 seconds has been observed at both wavelengths. Similar stabilities have been measured at other frequencies in the 500kHz to 1.5MHz region.

5. CONCLUSIONS

A simple to use CO_2 optically pumped dual FIR laser system has been developed for use in an interferometer system for plasma diagnostic applications in Tokamaks. The system, which has been operated at 184um and 433um, has been shown to have IF stabilities of +/- 10kHz over 60 seconds, with power stabilities of better than +/- 2%.

6. REFERENCES

(1) N.C. Luhmann, Jr., ' Instrumentation and techniques for plasma diagnostics: an overview,' in Infrared and Millimetre Waves, Vol. 2, K.J. Button, Ed. Academic Press, New York, p. 1-65, 1979

(2) T. Edlington and R. Wylde, 'A multichannel interferometer for electron density measurements in COMPASS', Rev.Sci.Instr., Vol. 63(10), p.4968, Oct. 1992.

Improvements in the characteristics of a high-power optically-pumped far-Infrared laser and its application

T. Hori, N. Hiromoto and A. Yamamoto*
Communications Research Laboratory
4-2-1 Nukui-kita, Koganei, Tokyo 184, Japan

*National Space Development Agency of Japan
1-29-6 Hamamatsu-cho, Minato-ku, Tokyo 105, Japan

1.Introduction

Up to now, a high-power optically-pumped far-infrared laser system has been developed[1], and some tasks were left for improving it. Here the results of the improvements in the characteristics are shown, that is, the increase of output power by optimizing output couplers and adding buffer gas, absolute frequency stabilization by harmonic mixing the laser radiation with millimeter wave from a PLL'ed Gunn oscillator. Results of application of this laser will be presented too.

2.Increase of Output Power

First, optimization of output couplers was done. Dichroic mirrors with aluminium patterns and dielectric multilayers on Z-cut substrates were fabricated with photolithographic technique[2]. Four types of mirrors, that is, a center-hole, capacitive mesh, stripes and mixed mesh (patterns to increase gradually the reflectance from the center to the edge) were examined. The center-hole output couplers had much higher output than capacitive mesh ones and the mixed mesh mirrors with adequate parameters had the highest output. The threshold for mesh miorrors, which yield good beam patterrn, were very low. For stripe mirrors, it was very difficult to get strong oscillations.

From a practical aspect of low loss, thinner substrates yielded more power than thicker ones and substrates 1.5mm thick were used. Substrates were made in concave shape (R=4m), to increase the output.

Next, as an input coupler, offset-hole mirror was used instead of a center-hole one. This is not related to the increase of output power, however, it was favorable to reduce feedback without using complicated polarizing optical components and to decrease threshold.

Finally, He gas was added as a buffer. For HCOOH, the increase of output power could be observed as well as CH_3OH[3] and CH_3F[4]. For CH_3I 447μm line, however, the increase was not observed.

The results obtained with these improvements above are summarized in Table I. The output became much larger (over 3-4 times except for CH_3OH 70.5μm) than that obtained before.

3.Frequency Stabilization by Use of Harmonic Mixing

To obtain better frequency stability, absolute frequency stabilization was achieved by harmonic mixing with millimeter wave from a PLL'ed Gunn oscillator. The FIR output power and frequency measured simultaneously, when the stabilization loop was not closed and CO_2 laser frequency was scanned, are shown in Fig.1 (In Fig.1(a), the CO_2 laser power when it was not introduced into FIR cavity, are shown as a reference.). The results show that FIR frequency depends on the pump laser's frequency a little (about 400kHz$_{p-p}$ at 70-80W pumping) through AC dynamic Stark effect. Roughly speaking, FIR frequency fluctuation mainly came from FIR cavity and amplitude fluctuation from CO_2 laser.

The results when personal-computer controlled stabilization loop was closed, are shown in Fig.2. In the figure the obtained frequency stability was ±20kHz for 3kHz resolution bandwidth of the spectrum analyzer.

Table I. Output Power Measurements for CH_3OH, HCOOH and CH_3I lines

Molecule	Wavelength (μm)	Pump Power (W)	Gas Press. (mTorr)	Helium Press. (mTorr)	Output Power (no He)	Output Power (with He)	
CH_3OH	70.5	77	130	(30)	144	(186)	a
CH_3OH	118.8	72	230	(160)	312	(414)	a
CH_3OH	163.0	58	145	(-)	120	(-)	a
CH_3OH	170.6	72	110	(65)	168	(176)	a
HCOOH	393.6	96	160	(25)	134	(144)	b
HCOOH	432.5	98	130	(30)	86	(108)	b
CH_3I	447.1	86	200	(-)	50	(-)	b
HCOOH	513.0	92	135	(40)	84	(98)	b

a: Center-hole,10mmϕ

b: M.Mesh1=capacitive (g1=200μm, 2a1=80μm) $0 \leq r < 7mm$
capacitive (g2=200μm, 2a2=60μm) $7 \leq r < 10mm$
capacitive (g3=200μm, 2a3=20μm) $10 \leq r < 13mm$

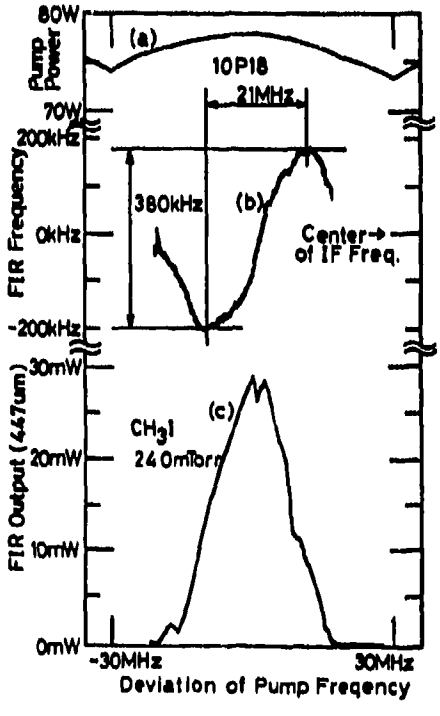

Fig.1 Frequency and output characteristics by scanning pump frequency

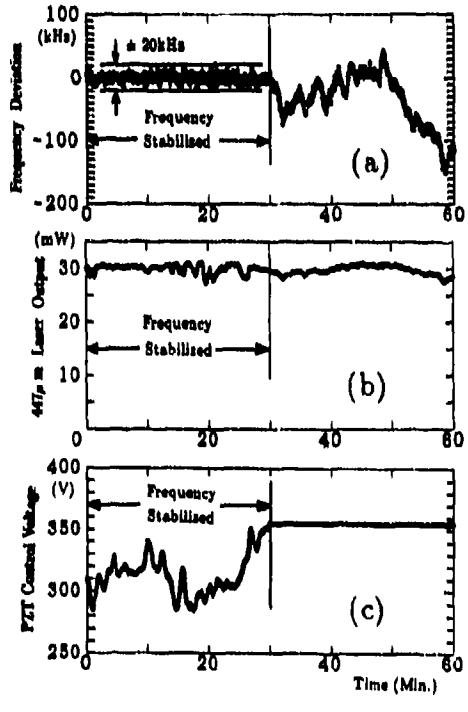

Fig.2 Results of absolute frequency stabilization

References

1) T.Hori and N.Hiromoto, Int.J.IRMMW, p.483, Vol.13,1992.
2) M.S.Durschlag and T.A.DeTemple, Applied Optics, p.1245, Vol.20, 1981.
3) D.K.Mansfield, E.Horlbeck, C.L.Benett and R.Chouinard, Int.J.IRMMW, p.867, Vol.6, 1985.
4) T.Y.Chang and C.Lin, J.Opt.Soc.Am., Vol.66,No.4, p.362, 1976.

OPFIRL INVESTIGATION OF AMMONIA

W. Schatz and K.F. Renk
Institut für Angewandte Physik, Universität Regensburg
W-8400 Regensburg, Germany

Abstract

Using a continuous tunable CO_2-laser system for optical pumping a far-infrared laser we investigated the four ammonia gas isotopes $^{14}NH_3$, $^{15}NH_3$, $^{14}ND_3$ and $^{15}ND_3$. We found laser emission via stimulated Raman scattering at about 300 molecular transitions in the region from 15 cm^{-1} to more than 200 cm^{-1}, about 250 of them observed for the first time. Thereby photon conversion coefficients of up to 12 % and tuning intervals exceeding 3 cm^{-1} have been accieved.

Introduction

Ammonia has been proved to be one of the most powerful laser media used for optical pumping a superradiant far-infrared (FIR) laser. High photon conversion coefficients and the generation of tunable FIR radiation via stimulated Raman scattering over wide tuning intervals have been observed [1]. In this work we report optical pumping of the well investigated isotopes $^{14}NH_3$ and $^{15}NH_3$ but furthermore also deuterated ammonia $^{14}ND_3$ and $^{15}ND_3$ have been pumped for the first time.

Experimental setup

Pump radiation was generated by use of a continuous tunable 20 atm CO_2-laser [2] consisting of two amplifying stages; optical access to the pump volume was obtained by two NaCl Brewster windows. The resonator was built by a concave germanium output coupler (reflectivity $\approx$ 0.7; radius $\approx$ 25 m) and a 150 l/mm grating in Littrow configuration. Frequency tuning is possible in steps of 1 GHz, the spectral width of the emitted radiation is about 5 GHz. The emitted pulses have a total duration of about 300 ns and a maximum energy of 250 mJ, limited by the damage threshold of the NaCl Brewster windows. For wavelength calibration the radiation was directed into a photoacoustic cell containing $^{12}CH_3F$, which has well known absorption lines. The FIR laser consists of a fused quartz waveguide tube (7 mm diameter, 115 cm length). This laser is equipped with a BaF_2 entrance and a TPX (polymeric 4-methyl-1-pencene) output window. Since TPX does not completely absorb the CO_2-laser radiation an additional crystalline quartz plate is mounted. The pulse energies of the emitted FIR radiation were determined by use of a Golay cell, energy calibration was performed with a pyroelectric detector (Molectron P5-01). To measure the FIR frequency we used a scanning Fabry-Perot interferometer consisting of two copper meshes (670 lines/inch) with a stepwidth of 1 μm [3]. To study the transient behavior of the FIR Raman laser, both the pulse shapes of the CO_2 and the FIR laser were detected simultaneously with a pyroelectric detector (Molectron P5-01). Both signals were recorded with a dual channel digital sampling oscilloscope (bandwidth 500 MHz, 1 GSa/s).

Results

At all investigated ammonia isotopes the observed absorption signal coincides with an emission of FIR radiation, therefore the identification with resonant transitions is possible. Because of the high optimum pressure all transitions (except of cascade transitions) were due to stimulated Raman scattering [3]. In the table for all investigated isotopes the number of observed pump frequency regions, the FIR emission lines, the assigned transitions and the number of laser lines observed for the first time is listed. For nearly every FIR emission we measured the frequency, maximum output power, the polarization relative to the pump radiation and the optimum gas pressure. Calculating the photon conversion coefficient we found a maximum value of 12% using $^{14}NH_3$ as laser medium; a similiar value has been observed only for some ν_3R tansitions in methylfluoride. One of the most interesting aim of our investigations was the generation of continuous tunable radiation over a wide spectral region in the FIR. We observed at $^{14}NH_3$ and also at $^{15}NH_3$ tuning ranges of more than 3 cm^{-1}. Due to the nature of stimulated Raman scattering this wide tuning ranges and the corresponding great bandwidth of the FIR radiation can be used to generate ultrashort pulses. Operating the CO_2-laser near threshold results in a pump pulse with strong spiking due to self modelocking; this pulse structure can be transformed to the FIR. We measured minimum pulse durations of less than 800 ps corresponding to the maximum temporal resolution of the data recording system. Therefore we conclude the FIR pulses to be even shorter. An assignment of the FIR emission frequencies using $^{14}ND_3$ laser gas was not possible with the spectroscopic data available for $^{14}ND_3$. As it is well known in literature that a mixture of $^{14}NH_3$ and $^{14}ND_3$ delivers an unexpected high concentration of both $^{14}NH_2D$ and $^{14}NHD_2$ we tried to assign the observed frequencies with the spectroscopic data of this mixture isotopes and found a good coincidence. The assignment of the observed $^{15}ND_3$ laser lines was not possible since the spectroscopic data of the $\nu_4 = 1$ states are not available yet.

Isotope	pump lines	FIR emission	assigned transitions	new laser lines
$^{14}NH_3$	76	72	69	43
$^{14}ND_3$	45	4	–	–
$^{14}NH_2D$	50	50	50	50
$^{14}NHD_2$	22	22	22	22
$^{15}NH_3$	46	49	33	38
$^{15}ND_3$	100	70	–	100

Table: Synopsis on the observed laser lines in ammonia

References

[1] Wen-sen Zhu and J.R. Izatt, *Opt. Commun.* **73**, 141 (1989).
[2] Chong-Yi Wan, U. Werling and K.F. Renk, *J. Appl. Phys.* **57**, 990 (1985).
[3] W. Schatz, P.T. Lang, T. Kass, M.A. Heusinger and K.F. Renk, *Int. J. Infrared Millimeter Waves* **13**, 853 (1992).

Synchronization effects in broadband FIR Raman scattering in NH3

S. Marchetti R. Simili
IFAM-CNR Via del giardino 7, 56100 PISA (ITALY)

ABSTRACT

By using a short pulse broad band (~2 GHz) CO_2 laser around a single well detuned line (15 GHz), it is possible to analyze, with sub-ns resolution ,the dynamics of a broadband FIR Raman scattering

1.INTRODUCTION

The resonant Raman scattering from a long pulse (much larger than the Raman cell transit time T) single mode pump has been extensively analysed[1]. The off resonant Raman component becomes dominant upon the optical pumped emission (OP),after a small time (~ T) specially at larger pressures when the delay of the superfluorescent OP becomes smaller than the pump pulsewidth (T_p). The experimental results are largely affected by cavity effects (window reflections > 10^{-4} have an important role) ,cascade processes, and in some cases four wave mixing (FWM)[2] can be observed .

When a multimode short pulse (T_p comparable with T) pump is used ,the process is drastically modified . In this work we report some interesting results obtained in this configuration . To simplified the experiment a well detuned (D=15GHz) single line system (sR(3,0) NH_3 line) with 90μm emission is used .In general the direct cascade emission is not observed [2]. On the contrary a cascade FIR in the fundamental vibrational level can be observed under strong FWM [2],but generally more than the 80% of the FIR energy is at 90 μm . In broadband multimode Raman scattering with mode-locked pump peaks (~ 0.5ns width) ,the usual equilibrium condition (dephasing time τ much larger than the Raman conversion time) is not satisfied, giving an OP dominance, but in this case the Raman backward and forward degeneration is removed ,and, when we operate in a quasi-cavity condition the OP and FWM thresholds are increased [3].

2.EXPERIMENT AND RESULTS

The broadband CO_2 laser (~200mJ @25ns) and the FIR design has been previously reported [4] .A 2.5m FIR cell (T=8.3ns) is used .The emitted FIR and residual pump pulses are separated by a a Quartz Brewster window and detected by a Sb[5] and PbSe [6] room temperature photon drag (PD) films respectively . While the scope pulse limit (0.7ns) is reached by all the PbSe PD , the Sb films show different response times and responsivities . The faster PD show sometimes 0.7ns FWHM pulses so that we can measure the FIR source spike widths which are generally larger than the corresponding pump spikes. The synchronization is measured to be better than 1ns. As input window ,aligned (AL) or Brewster angle (BW) BaF_2 windows are used .This choice has a large importance on the FIR emission[2]. When the Al configuration is used the Raman threshold is lowered due to Backward gain contribution . A typical single spike Raman FIR (f) emission is reported in fig 1 .

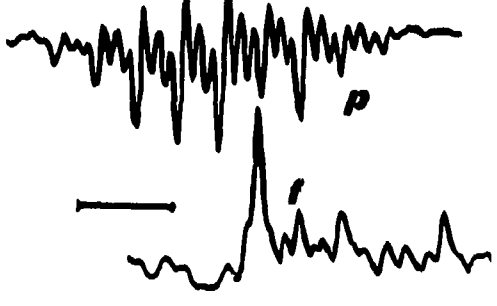

Fig 1: 9P20 FIR emission (f) and the residual pump(p) . Time scale =10ns .(see text)

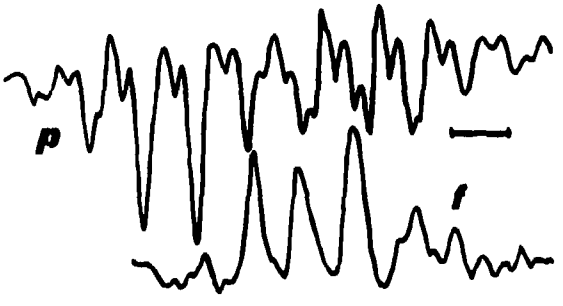

Fig2: 9P20 FIR emission (f) and the residual pump(p) . Time scale =5ns .(see text)

The (p) trace (sign reversed) is the residual pump pulse . The single FIR spike is synchronous with a pump spike depletion. That means a cooperative effect of all the pump modes to the Raman scattering which is foreseen in broad band forward scattering [3]. The FIR spike width is generally larger than the pump one. This fact can be attributed to the backward Raman gain contribution to FIR pulse building-up .Back scattering operates essentially on the strongest CO_2 mode ,so that it leads to a FIR frequency narrowing respect to the pump. This fact is confirmed in fig 2 at a larger pump power when a sequence of FIR synchronous Raman pulses are detected. The widths are ranging from 0.8ns (right) to 3ns (left) showing the active cavity spectral narrowing . Also the Fourier spectrum (FS) of the residual pump pulse are showing that the Raman scattering is producing an hole in the pump spectral distribution. In fig 3a is reported the FS of the pump left part of fig 2 (respect to the FIR onset) .We can see that the mode beatings (~200MHz) are inside the scope bandwidth (~500MHz , dashed line). On the contrary in fig 3b is reported the FS of the residual pump right part coincident with the FIR emission, and we can see that the Raman scattering modifies the pump spectral distribution also for D=15GHz much larger than the pump linewidth L~ 2GHz.

fig3: Fourier spectrum of different p parts of fig 2 (scale=250MHz).(See text)

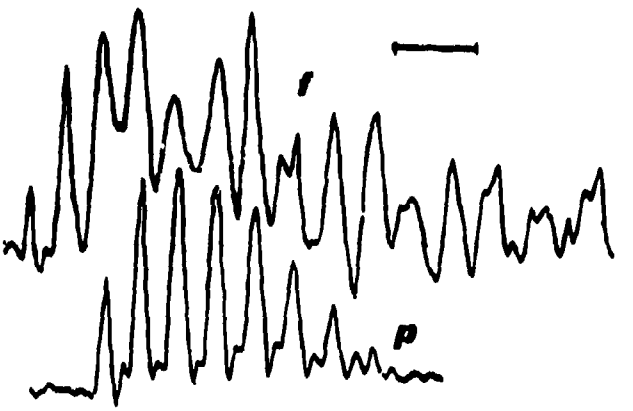

Fig4: 9R 16 FIR emission (f) and residual pump (p). Time scale =10ns . (see text)

The same results can be observed around the nearly coincident 9R16 transition (D=1.3GHz <L) . In fig 4 is reported the emitted FIR (f) and residual pump (p) .We can see than the emission is essentially synchronised (Raman -like) with spike width ranging from 0.7ns (signal beginning) to 3ns at the end. Also the p spikes are modified and enlarged to 2ns, showing the mode filtering due to the resonant absorption . By using a BR configuration the FIR modulation is reduced showing that in a single transit the Raman dominance is reduced. By increasing the pump power density up to the optical breakdown , no FWM MIR emission is observed.

3.ACKNOWLEDGEMENTS

This work has been supported by the CNR TECNOLOGIE ELETTROOTTICHE Finalized Project

4.REFERENCES

1) T.A. De Temple in Infrared MMW 1 , K.J. Button ed. , N. Y. , Academic 1979 pp 129-184
2)M. Bernardini et al : Int . J. Infrared MMW 10,31-41 (1989) and references therein
3) F. Botta : Thesis ,also unpublished
4) S. Marchetti ,R. Simili: a) Opt. Comm 89 ,429-433 b) 17th IMMW conf. ,T3.5, Pasadena ,(1992)
5) S, Marchetti el al : Infrared Phys. 29 , 677-80 (1989) and references therein
6) S. Marchetti, R, Simili : "Transverse MIR fast response in PbSe films ",18th IMMW conf., this issue

DENSITY-MATRIX MODELLING FOR THREE-PHOTON 1+1+1(UV+IR+UV) RESONANCE IONIZATION OF IRON.

A.L.Telyatnikov, O.R.Jones and H.H.Telle*

Department of Physics, University College of Swansea, Singleton Park, SWANSEA, SA2 8PP, Wales, United Kingdom.

**Present address: Institute of Physics and Technology RAN, Krasikova 25A, Moscow, Russia, 117218*

ABSTRACT

A reduced density matrix model for resonant two-colour, three-photon ionization, using a combination of pulsed and cw tunable lasers, is presented. A cw-IR laser is used for the intermediate excitation step. Actual laser and atomic parameters are included, and Doppler broadening is taken into account.

1. INTRODUCTION.

A number of different schemes for RIS/RIMS experiments of iron atoms are found in the literature. The most popular approach is a one-colour two-photon scheme, involving excitation to a resonant state by the first photon, followed by photoionisation by a second photon of the same colour ($\omega_1+\omega_1$). The initial state in the scheme is usually one of the a^5D ground state sublevels, while the intermediate, resonantly excited level belongs to a manifold of states, namely y^5F^o, y^5D^o, z^5G^o, z^3G^o, z^3P^o (Saloman, 1990 and references therein). Two further resonance schemes can be realized, namely two-colour two-photon ($\omega_1+\omega_2$), and one-colour three-photon ($2\omega_1+\omega_1$) processes. The main advantage of two-photon, two-colour RIS/RIMS arises from the fact that the ionisation step can be optimized, which may result in larger ionisation cross-sections, for example ionisation via an autoionising state.

The rich spectrum of iron, and many other elements, makes it feasible to devise further useful schemes which may have, for example, better selectivity, or larger cross-sections for the ionisation step. The one we discuss in this paper could be referred to as $\omega_1+\omega_2+\omega_3$, with an IR diode laser used for the second step. The third photon, ω_3, need not necessarily be different from either ω_1 or ω_2 but could be either of them, depending on the energy level structure. Advantages of this scheme will be that with a diode laser of very narrow banwidth fine details in the excitation can be explored, and possible use can be made of dc field or autoionisation for the ionisation step. However, an obvious problem for the experimental implementation may be the relatively low power provided by standard diode lasers.

The main goal of this paper is to consider the proposed scheme theoretically; the related experiments are just being implemented in this laboratory. The numerical simulation makes use of the density matrix formalism, with the actual laser and atomic parameters included in the calculations.

2. THEORY.

A partial energy level diagram of iron for the 1+1+1 scheme is shown in Fig.1. In particular, the a^5D_4 level is the initial (ground) state, level $y^5P_3^o$ is the first intermediate state, and levels e^5P_3, f^7D_3, e^7P_4, f^5D_4 or e^5D_3 will be those from which ionisation will take place. Several ionisation paths are conceivable: photoionisation, collisional ionisation or the ionisation by a dc electric field. The actual magnitude of the ion signal will depend to a great extent on

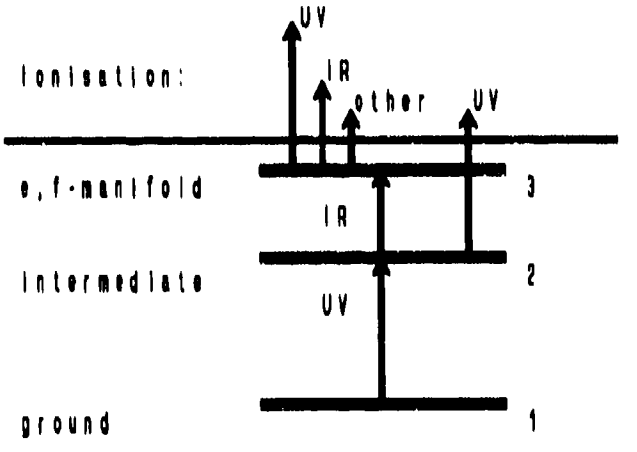

Figure 1. Partial energy level diagram for RIS/RIMS of iron (energy spacing not to scale).

the ionisation method. However, all final results for ion yields will be strongly determined by the excitation of the third level (e-,f- manifold). In the present work we do not consider in detail the actual ionisation processes (photoionisation, field ionisation, etc.).

In addition to the 1+1+1 ionisation routes there will also be ionisation out of the first intermediate state (i.e. $y^1P_1^o$) Since this level is more then half-way to the ionisation limit, E_i, the related signal is associated with one-colour two-photon resonance ionisation which may dominate if the UV radiation field is strong.

We use the density matrix approach for the theoretical description of the system; this incorporates solving the stochastic Liouville equation

$$\frac{\partial \hat{\rho}}{\partial t} = -\frac{i}{\hbar}[\hat{H}\hat{\rho}] - \hat{\Gamma}\hat{\rho} \quad \text{with} \quad \hat{H}=\hat{H}_0+\hat{V}\,, \tag{1}$$

which is modified by including experimental laser and atomic parameters to define the operators V and Γ. These operators represent the interaction of the system with laser fields and its spontaneous decay.

Just a few assumptions are made which, on the other hand, do not grocely affect the generality of the problem formulation. Firstly, the time constants of the decay of corresponding density matrix elements at the frequencies of laser fields are taken to be equal to the coherence time of the laser fields, that is $\tau = 1/\Delta\omega$, where $\Delta\omega$ is the spectral width of the laser radiation field (Agostini *et al*, 1978). Secondly, we neglect collisions, and hence collisional broadening, due to the very low density of the atoms encounted under ordinary operating conditions for RIS/RIMS experiments (10^{11} cm^{-3}). Thirdly, Doppler broadening is taken into accoun' by integrating the ionisation signal over the velocity distribution.

The utilization of pulsed and c ' ' ' ers in the same scheme requires to fully solve the system of time-dependent differential equations (1).

In our approach we consider a system of three descrete energy levels, each of them with degeneracy 2J+1. In this way a variation of excitation conditions of M-substates may be taken into account. The dependence of the dipole transition moment on M leads to a variation in the saturation intensity, and to a variation in the probability of two-photon processes. The laser fields are assumed to be linear polarised, with their polarisation vectors being parallel to each other. This reflects the real situation encountered in the majority of experiments; also it allows us to simplify the modelling to the case of $\Delta M=0$. For the simulation of interaction with non-parallel polarized fields $\Delta M=\pm 1$ transitions have to be added; the related numerical model becomes much more complicated (see e.g. Batanov *et al*, 1992 and references therein).

For solving the Liouville equation (1) for the three level system we use a rotating wave approximation, with the following notations: $\rho_{ii}=P_{ii}$, $\rho_{ij}=P_{ij}e^{i(\omega t+\varphi)}$, $P_{ij}=R_{ij}+I_{ij}$. The system of differential equations can be considered as being the general form of equations similar to those deduced by Murrey *et al*, 1990; they in turn use the results of the quantum-electrodynamic description of resonant laser - atom interaction given by Farrel *et al*, 1988.

In the calculations presented here we limit our consideration to the case of T_1- and T_2-type relaxations. This approach is reasonable, following the investigations of Shore (Shore, 1984) and Vogel and co-workers (Vogel *et al*, 1983). In short, they introduced new relaxation times for the off-diagonal density matrix elements. This follows their finding that phase-jump field fluctuations result only in T_2-type relaxation. Fluctuations of other parameters can lead to the change in relaxation terms for off-diagonal density matrix elements (T_2) as well as for the diagonal (T_1). We take these times as variable parameters in our simulation. While this assumption is often a good approximation it should be pointed out that further investigation of temporal laser characteristics is required if possible pump light fluctuations were to be properly incorporated into the Liouville equation. Accordingly, our system of differential equations is given by

$$\frac{d\vec{Y}(M)}{dt} = \hat{A}(M)\cdot\vec{Y}(M)\,. \tag{2}$$

In this equation one has

$$\vec{Y}^T = (\ P_{11},\ P_{22},\ R_{12},\ I_{12},\ P_{33},\ R_{13},\ I_{13},\ R_{23},\ I_{23}\ ) \tag{3}$$

with I_{ij} and R_{ij} representing the real and imaginary parts of the off-diagonal density matrix elements, P_{ii} being the level populations, and A given by

$$\hat{A} = \begin{bmatrix} 0 & A_{12} & 0 & -2B_p & 0 & 0 & 0 & 0 & 0 \\ 0 & -w_{22} & 0 & 2B_p & A_{23} & 0 & 0 & 0 & -2B_s \\ 0 & 0 & -w_{12} & -x & 0 & 0 & -B_s & 0 & 0 \\ B_p & -B_p & x & -w_{12} & 0 & B_s & 0 & 0 & 0 \\ 0 & 0 & 0 & 0 & -w_{33} & 0 & 0 & 0 & 2B_s \\ 0 & 0 & 0 & -B_s & 0 & -w_{13} & -(x+y) & 0 & B_p \\ 0 & 0 & B_s & 0 & 0 & x+y & -w_{13} & -B_p & 0 \\ 0 & 0 & 0 & 0 & 0 & 0 & B_p & -w_{23} & -y \\ 0 & B_s & 0 & 0 & -B_s & -B_p & 0 & y & -w_{23} \end{bmatrix} \quad (4)$$

where $A_{\alpha\beta}$ are the radiative decay probabilities from substate $|\beta,M\rangle$ to $|\alpha,M\rangle$; x, y are the detunings of the first and second lasers fields from the corresponding resonances; $B_p=E_p\mu_{12}/2\hbar$, $B_s=E_s\mu_{23}/2\hbar$, $w_{22}= 1/\tau_{22}+w_{ion,2}$, $w_{33}= 1/\tau_{33}+w_{ion,3}$, $w_{12}= w_{22}/2+1/\tau_p$, $w_{13}=w_{33}/2$, $w_{23}=(w_{22}+w_{33})/2+1/\tau_s$; τ_p and τ_s are the inverted half-widths of the dye and diode laser lines, respectively.

3. RESULTS AND DISCUSSION.

In our modelling we use the iron spectroscopic data recently published (O'Brian *et al*, 1991). Two results are presented: the position of the ionisation maxima, as a function of UV and IR detunings from the corresponding resonances (so-called "edge curves", which follow the peaks of the three-dimensional spectrum); and the spectrum of level 3 excitation, as a function of IR detuning while the UV is in resonance with the first transition.

First, we consider one of the characteristics of excitation processes - the so called "edge-curves" of the maximum value of P_{33}. For the steady-state solution of (2) it is defined by minimization of the determinant d of the right bottom submatrix of size 4x4 of matrix A (4). The explicit expression for the edge curves is given by:

$$x^*(y) = y\cdot\left(\frac{B_p^2}{y^2+w_{23}^2}-1\right) \quad (5)$$

where x^* and y are the UV and IR detunings from the resonance frequency.

Typical "edge-curves" for different values of M are shown in Figure 2. Each pair of symmetrical curves corresponds to a particular value of M. The actual splitting picture of the edge curves will depend on the type of the transitions - P-, Q- or R-type. The ac Stark splitting, and hence the splitting in Figure

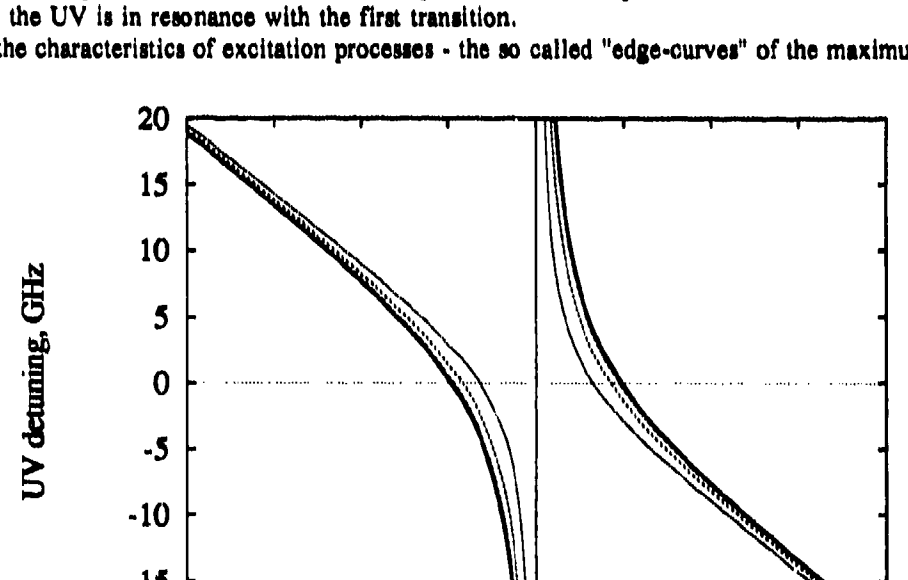

Figure 2. Edge curves for the maximum population of level 3, as a function of laser detunings from the resonances.

2, increases with elevated UV power. On the other hand, Doppler broadening makes this splitting less pronounced.

Figure 3 presents this effect of Doppler broadening, which cannot be avoided in any real experimental set-up, on the resulting population of level 3. There is a distinct difference between co- and counter-propagating laser beams. One can see that the maximum of co-propogating waves takes place when both fields are in resonance, but there is a distinct ac splitting for the counter-propogating waves, as well as a considerably higher maximum value of level excitation. The results presented in Figure 3 were calculated for a rectangular UV pulse. In real experiments, the temporal evolution of the laser pulse is not rectangular. The necessary modifications to take this into acount in our modelling are currently being implemented.

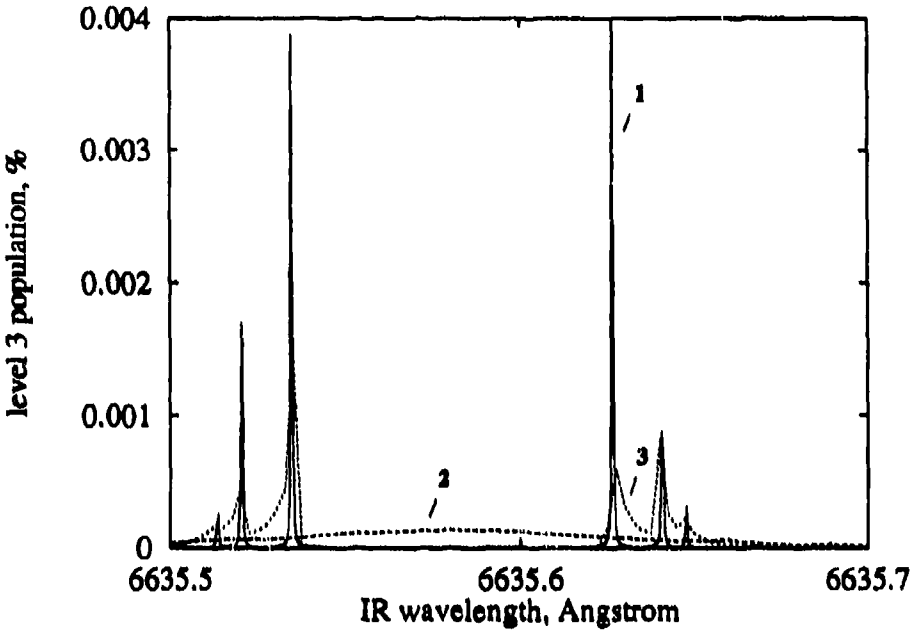

Figure 3. Excited level population spectrum. 1 - no Doppler broadening, 2 - co-, and 3 - counter-propagating UV and IR laser beams. UV-1MW/cm², IR-10mW/cm².

5. ACKNOWLEDGEMENTS.

We gratefully acknowledge the extended spectroscopic data set for iron (O'Brain *et al*, 1991) provided by W.Whaling in machine readable form. The authors also acknowledge the financial support for A.Telyatnikov provided by the Royal Society.

6. LITERATURE.

1. E.B.Saloman. Spectrochimica Acta, 45B, (Data for iron on pp.65-68) (1990).
2. P.Agostini, A.T.Georges, S.E.Wheatley, P.Lambropoulos, M.D.Lenenson. J. Phys .B: At. Mol. Phys., 11, 1733(1978).
3. V.A.Batanov, A.O.Radkevich, A.L.Telyatnikov. Int.J.IR&MM Waves, 13, 1845 (1992).
4. A.J.Murray, W.R.MacGillivray, M.C.Standage. J.Phys.B:At.Mol.Opt.Phys., 23, 3373 (1990).
5. P.M.Farrel, W.R.MacGillivray, M.C.Standage. Phys.Rev.A, 39, 4240 (1988).
6. B.W.Shore. J.Opt.Soc.Am.B, 1, 176 (1984).
7. W.Vogel, D.-G.Welsch. Phys.Rev.A., 28, 1546 (1983).
8. T.R.O'Brian, M.E.Wickliffe, J.E.Lawler, W.Whaling, J.W.Brault. J.Opt.Soc.Am.B., 8, 1185 (1991).

TUNING AND SPECTRA FEATURES OF CONTINUOUSLY TUNABLE CH_3F RAMAN LASER.

V.A.Batanov, A.O.Radkevich, A.L.Telyatnikov

Institute of Physics and Technology of Russian Academy of Sciences, Krasikova 25A, Moscow, Russia, 117218

There are a lot of experimental and theoretical papers concerning the description of spectral and energetic properties of tunable, pulsed, optically pumped FIR lasers, based on the density matrix approach. It was shown /1/ that 3- and 4-level models cannot adequately describe all the processes which take place in the active laser medium.

Previously /1/ we considered in detail the theoretical model based on the 6-level approach. But the results of calculations were confined to the case when only the R absorption branch of CH_3F was pumped. Now we are going to expand the results of the calculations to the case of P- and Q-branches, as well as to four-photon parametric MIR emission. The six level scheme used in this paper and resulting system of equations were described in detail in /1/. The multilevel system includes 3 levels of the ground vibrational state and 3 levels of the exited state with succesive quantum numbers of J-1, J and J+1. The system of equations was solved numerically.

As an example two cases of CH_3F P-branch pumping, for small (J=12) and large (J=35) values of the rotational quantum number J, are presented here.

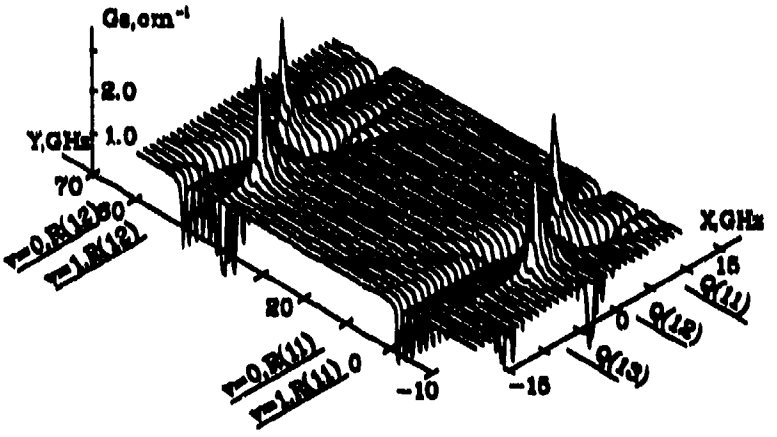

Figure 1. FIR small signal gain spectra for pump tuning in the frequency range Q12-Q13 transitions. (X - pump, Y - FIR offsets. Pump intensity - 10MW/cm², pressure - 20 Torr).

A two-dimensional FIR gain spectrum for J=12 is given in Fig.1. It has essential difference from that in the case of R-branch pumping, presented in /1/, because gain regions are formed only by two Raman processes, which take place at levels 3-5-4 (the corresponding edge are marked A and B) and 3-2-4 (marked C and D). These Raman processes form a double Raman process (DRP). There is a large number of gain depressions in the gain curve, which are caused by the absorption processes, which take place in this scheme. These absorption processes are: strong one-photon absorption at the transitions 2-1 (the valley marked E) and 3-2 (F); weak absorption at the transitions 5-4 and 6-5; four two-photon IR-FIR absorption processes, which correspond to the following groups of levels 2-4-5 (G and H valleys), 1-2-4 (I,J), 3-5-6 (K,L), 2-3-5 (M,N).

In contrast to the case of a weak FIR signal new absorption processes appear which result in the appearance of new valleys in the gain curve due to the increase of the FIR intensity. A numerical simulation of the gain spectrum for the case of strong FIR and pump fields along the DRP gain line was made. The letters A-E in Fig.2a correspond to different

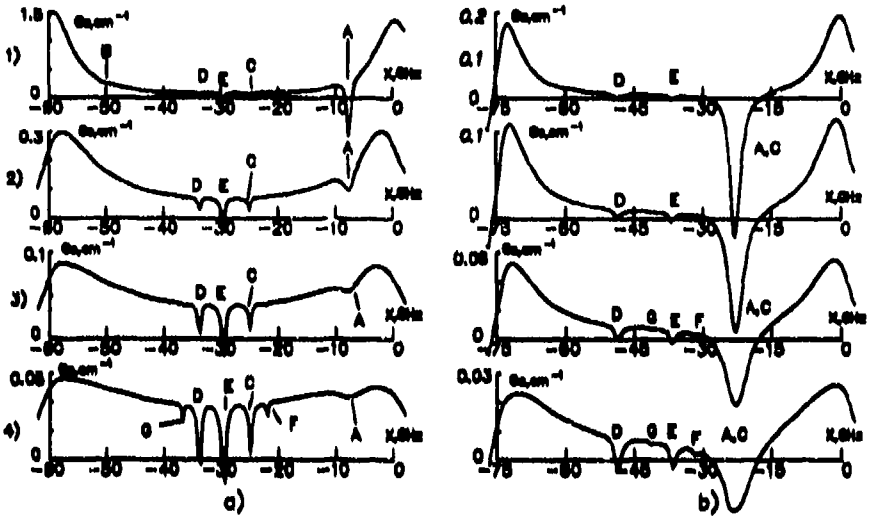

Figure 2. Gain profiles along the tuning curve for the tuning of the pump field in the frequency range of P12-P13(a) and P35-P36 (b) transitions.

absorption processes: A and B - one-photon absorption at the transitions 2-1 and 6-5; C and D - two-photon IR-FIR absorption 6-5-3 and 4-2-1; E - doubled two-photon absorption at the transitions 5-4-2 and 5-3-2.

With the increase of FIR intensity I_f three-photon processes appear, each pair of them corresponding to one dip in the curve in Fig.1. F denotes the absorption maxima, which corresponds to the three-photon absorption processes at the transitions 6-5-3-2 and 6-5-4-2, and G at the transitions 5-4-2-1 and 5-3-2-1. The intensity of these processes grows with the increase of FIR field intensity I_f. Simultaneously with the increase of I_f the role of the ground vibrational two-photon FIR absorption grows. The FIR frequency of this process coincides with the two-photon IR-FIR absorption designated as D.

The spectrum analogous to that in Fig.2a but calculated for CH_3F P-branch pumping of the transition with J=35 is shown in Fig.2b. There is a sharp fall in the gain with the increase of pump detuning from the resonance, and what's more the gain for large detunings, unlike that in Fig.2a, remains smaller than in the resonance case even for high values of I_f. The role of three-photon absorption processes (F and G) is negligible because of the larger difference between the frequency of corresponding FIR transitions. At the same time two-photon absorption remains strong.

The analysis of the above spectra leads to the conclusion that in the case of P-branch pumping the only sufficient three-photon processes are those of absorption, which lead to a smaller gain. Three-photon gain processes do not intersect the gain curve (for small detunings), as took place for R-branch pumping, that is why their effect in case of P-branch pumping is negligible. However, calculations showed that even under moderate pump intensities, of about 10 MW/cm^2, one can obtain continuous tuning of the output FIR emission for pump detunings up to 20-25 GHz (P-branch transitions with J=12-20) with several narrow dips on the tuning curve, and for detunings up to 12-14 GHz (transitions with J=30-35). This can be achieved using cavities with large optical paths (10 metres or more) and by diminishing the active pressure medium.

This is not the case when pumping Q-branch transitions. The spectrum in this case (Fig.1b) is a series of sharp spikes which makes it impossible to obtain FIR generation for pump offsets more than 2-3 GHz.

Numerous calculations were also made for four-photon parametric MIR emission generated under R-branch pumping of CH_3F. These results will also be discussed.

Literature.

1. V.A.Batanov, A.O.Radkevich, A.L.Telyatnikov, A.Yu.Volkov. Int.J. of IR&MM Waves, 11, 31 (1990).

New approach for numerical simulation of the non-steady-state infrared laser beam structure

Lidiya V.Yurchenko

Institute of Radiophysics and Electronics of the Academy of Sciences of Ukraine
12 Proskura St., Kharkov, 310085, UKRAINE

1. INTRODUCTION

Theoretical studying of the laser beam spatial structure evolution is a very difficult problem. The matter is that the complex nonlinear processes of the laser beam generation, propagation and diffraction take place simultaneously. Therefore, the spatial mode analysis used for empty resonators is too complicated in case of real laser systems, especially powerful and non-steady-state ones, since a great number of modes needs to be considered, and the developing processes of the mode interactions and beam structure transformations should be calculated. The direct computer simulation of the process by means of exact numerical solution of both the nonlinear wave equations and the level population kinetic equations is also gloomy because of complexity of the partial differential equations and significant durability of the whole process when compared to the time of a single pass of the light in a resonator. Taking it into account, we have developed a new approach for self-consistent computer simulation of the nonlinear laser beam spatial structure evolution which is applicable for a wide range of real laser systems including various infrared lasers, and which is easy to use in practice.

2. METHOD OF SIMULATION

The approach is based on implication of the Sommerfeld's integral which gives the solution to the linear wave equation in case of spatially restricted monochromatic field propagating in an open resonator[1] . In order to account for nonlinear and non-steady-state processes taking place in an active medium, regular small corrections are made to this field on every pass or some part of the pass of the wave along the resonator. These local corrections are made to both the amplitude and the phase of the wave to describe inhomogeneous amplification and refraction of the wave field in the medium. They are calculated self-consistently depending on both the field and the medium state, and on the external factors such as the given non-uniform pulse pumping. The calculation includes simultaneous solution of the kinetic equations for the quantum level populations $N_j(\rho,t_i)$ which are the functions of the discrete time t_i and the transverse coordinates x,y , or radius-vector ρ in case of the axial symmetry. The computational procedure described is valid under the assumption that all the nonlinearities and inhomogeneities are small and smooth to provide small field transformations on a single pass of the wave in a resonator but to result in a significant effect after many passes during the period of time being of interest.

3. PHYSICAL MODEL

To demonstrate the possibilities of the approach, we have considered the case of a laser system of axial symmetry with optical pulse pumping. In this case, owing to excitation of the active medium through it lateral surface, the main part of the energy pumped into the system would be absorbed either near the surface or near the

axis which depends on the relation between the pumping energy absorption length L and the active medium container radius R . If the refractive index decreases with the temperature increasing, the active medium becomes focusing or defocusing one depending on the condition $L < R$ or $L > R$, respectively. The refractive index variations are usually small and slow, so the field transformations for any pass of the wave in a resonator are also small enough. However, since the changes are taken into account for any moment of time considered, this results in a continuous field restruction during the whole process of the laser beam generation. In case of $L < R$, this leads to significant increase of the field near the axis. If pumping power being large, intensive stimulated generation in the axis region would result in an exhausting of the upper quantum levels and, subsequently, in a rapid fall of the field amplitude on the beam axis. In such a case, a ring-like spatial mode would appear as a result of non-steady-state self-focusing of the field generated in the active medium.

To make the model complete and closed, we have to choose the scheme of the quantum levels, the kinetic equations describing both the transitions between the levels and the field amplification rates, respectively, and the model for the refractive index variations as well. In this work, we have taken a simplified four-level scheme with the working levels E_2 and E_3 , and the pumping levels E_1 and E_4 assuming that the level E_1 is permanently well occupied while the level E_4 is nearly empty. The refractive index variations were supposed proportional to the total pumping energy absorbed in the active medium at the given point ρ by the time t_i .

4. RESULTS

The simulations carried out at the small levels of the pumping power have demonstrated the gradual localization or expansion of the field generated by the laser in the cases of slightly self-focusing or self-defocusing active medium as compared to the standard original mode of the empty resonator.

More interesting phenomena have been observed in the case of the large pumping power. In this case the localization of the field also takes place at the beginning of the process. However, with increasing the field amplitude owing to power stimulated radiation both the population inversion and the field amplification on the axis begin to decrease. As a result, the ring-like field distribution in the beam cross section is forming. The mechanism of the field spatial structure evolution described here is sufficiently universal and it can work in a lot of cases. In the same time, in the case of the defocusing medium this mechanism does not become apparent because of more homogeneous field distribution across the beam.

5. CONCLUSIONS

The approach developed in this work allows to simulate, in a simple and easy way, a wide range of complex nonlinear processes of the laser generation and the beam spatial structure formation under the conditions of non-uniform and non-steady-state laser pumping.

6. REFERENCES

1. S.Solimeno, B.Crosignani, P.DiPorto, Guiding, Diffraction, and Confinement of Optical Radiation, Academic Press, London, 1986.

OPTIMUM PUMP BEAM PROFILING IN A RAMAN LASER.

V.A.Batanov, V.S.Petriv, A.O.Radkevich.

Institute of Physics and Technology of the Russian Academy of Sciences, 117218, Moscow, Krasikova 25A, Russia.

We discuss in the present work the optimisation of the intensity distribution in transverse cross section of the pump beam of a Raman laser. In addition to the selection of optimum initial beam focusing and divergence, it allows increasing the efficiency of frequency conversion in an optically pumped Raman laser. If the maximum on-axis intensity in the pump beam did not change, the largest effect for resonant stimulated Raman scattering is achieved in the beam with uniform amplitude distribution. The hypergaussian beam has a profile which is intermediate in shape between a Gaussian and uniform intensity distribution.

$$I_p = I_{p0} e^{-(r/a)^N}$$

As N increases, the intensity distribution in the central portion of the beam is comparable to that of the uniform distribution.However, sharp amplitude gradients appear on the beam periphery and nonlinear diffraction effects are amplified. When hypergaussian beam is used, two competing processes take place.

In this paper we analyze the influence of diffraction effects on the energy conversion efficiency in the case when the intensity profile of the input pump beam is hypergaussian and the initial wavefront is plane. Below we present the results of the numerical solution of the system of parabolic equations for pump and Stokes beams /1/. The parameters of the beams and the active medium are analogous to the ones in /1/. In the case of narrow input beams (a_p<0.5cm), no noticeable increase in the maximum efficiency is observed for $d_p=\tau(\omega_{31}-\omega_p)>0$ while the maximum efficiency decreases strongly for negative frequency offsets.

When wide pump beams are used, maximum efficiency increases considerably for N=6:8. This effect is especially noticeable when the pump radiation self-focuses for d_p <0.

Fig.1 demonstrates the change in quantum efficiency,

$$\eta = \frac{P_s}{P_p(z=0)} \frac{\omega_p}{\omega_s} \cdot 100\%,$$

against the normalized distance in nonlinear medium (P_γ is the power of radiation). The constant l_p is given by:

$$l_p = \frac{\hbar}{\pi k_p N \Delta_{13}^2 \mu_p^2 \tau}$$

Plots are presented for N=2 and N=6 in the case when d_p=0,±5 and a_p=0.7cm. It can be seen that maximum efficiency in a hypergaussian beam is achieved at the same or larger distances as in the case of a gaussian beam.

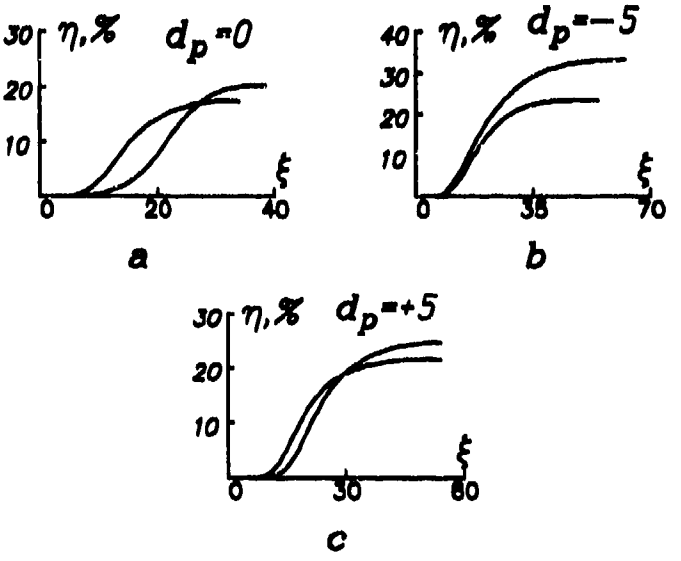

Figure 1. Quantum efficiency η against the distance ξ=1/l_p. All designations from /1/.

Literature.

1. V.A.Batanov, V.S.Petriv, A.O.Radkevich, A.Yu.Volkov. Int. J. of IR & MM Waves. 13. (1992).

DEPOLARIZATION OF OUTPUT LASER RADIATION IN HCN LASER

Yu.Ye.Kamenev, Ye.M.Kuleshov, V.P.Radionov and A.A.Filimonova

Institute of Radiophysics and Electronics of
Academy of Sciences of Ukraine
12 Acad. Proscura st., Kharkov, 310085, Ukraine

ABSTRACT

It is found that in submillimeter HCN-laser with a vent mirror made in the form of a one-dimentional wire grating, the output laser radiation has the elliptical type of polarisation. The ratio of orthogonal components was to 20 dB. In order to draw the comparison, the polarization characteristics of the same laser with a vent mirror in the form of a two-dimentional net with the period of 30 μm are given.

1. INTRODUCTION

Still at the very beginning of the evolutia of quantum electronics, a great attention was given to theoretical and experimental aspects of polarization effects in gas lasers /1/. Lately, the experimental research of the polarization effects in CO_2-lasers has been fulfilled /2/.

It is known that an active medium of HCN-lasers produces the linearly polarized radiation. A resonator with an vent mirror in the form of a one-dimensional wire grating is usually used in order to obtain the laser output with the given direction of a polarization vector. However, we discovered experimentally that an HCN-laser with such resonator does not produce the completely linearly polarized laser radiation.

2. DESIGN OF DEVICE

In the course of the experiments, the DC-pumped HCN-lasers (the wave length is 337 μm) and RF-pumped HCN-lasers (13,5 MHz) were used, the active medium length being 1 m and 1,7 m, correspondently. A plane metal mirror and a wire grating with the period of 30 μm and the wires 8 μm in diameter or a two-dimensional net with the period of 30 μm were used as the resonator mirrors on the one side and the opposite side, correspondently.

3. EXPERIMENTAL RESULTS

Experimentally performed polarization analysis (when a grating is used as a vent mirror of resonator) has shown that the laser radiation has an elliptical polarization, the ratio being 20 dB between the two components, one of which is parallel and the other one is perpendicular to the direction of the grating's wares. The effect of alignment, grating azimuth, change of gases proportions, gas pressure and discharge current on ellipticity of the vent radiation has not been found.

Apparently, a small rotation of polarization vector has taken place in the investigated lasers inside the laser resonator when a signal was passing between the mirror; in so doing the signal comes to a one-dimensional grating with the directi

on of a polarization vector being non-parallel to the grating's wires. As passing through the grating, this signal is decomposed into two orthogonal components which are simultaneously displaced in phase.

According to /2/, the existence of the two orthogonal directions of line polarization is explained by anisotropy of active medium saturation. Such assumption is appropriate when treating the experimental results obtained by us.

The experiments performed with the laser in which a two-dimensional net was used as an vent mirror have shown that there are both the anisotropy of this net and the anisotropy of a discharge tube.

4.CONCLUSION

In conclusion, we shall point out that in order to increase a degree of linear polarization of outgoing laser radiation of the investigated lasers the authors proposed to use a device /3/ in which the resonator is formed by a one-dimensional wire grating and a plane mirror with an additional wire grating having definite parameters mounted in a certain way.

5.REFERENCES

1.W. Van Haeringen, "Polarization Properties of a Single-Mode Operating Gas Laser in a Small Axial Magnetic Field", Phys. Rev.,vol.158,№2,pp.256-272,1967.
2.A.N.Alecseeva,I.I.Kirsanova, "The polarized radiation from a single-mode CO_2-laser with internal mirrors", Kvantovaya Electronica (USSR),vol.17,№2,pp.154-156, 1990.
3.Patent 1289349,USSR, Int.cl.5H01S 3/08. Kamenev Yu.Ye.,Kuleshov Ye.M. "Submillimeter laser".

Far infrared reflectance standards

E.A.Nicol and J.R.Birch

Division of Electrical Science, National Physical Laboratory
Teddington, Middlesex TW11 0LW, UK

ABSTRACT

A method developed for the absolute determination of complex reflectivity is discussed in terms of reflection standards for the 3 to 600 cm^{-1} spectral region. These can be primary standards based on transparent materials such as silicon, or secondary, opaque standards such as thin aluminium films, with or without protective overcoating.

1. INTRODUCTION

In far infrared transmission studies a spectrum is found by comparing spectra obtained with and without the specimen in a spectrometer. This assumes that the transmission spectrum of the local environment is unity, giving an internal calibration of the 100% level of the spectrometer. The situation is different for reflection measurements. Here the specimen is replaced by a reference reflector such as a thin metal film on a glass substrate with an assumed unity reflectance. In order to avoid errors from such approaches, an alternative method was developed to derive the complex reflection spectrum of a transparent solid in an absolute manner[1,2]. It uses dispersive Fourier transform spectroscopy[3] to determin the complex refractive index spectrum of a reasonably transparent and reflecting solid. In the far infrared this can be done with sufficiently high accuracy that the power reflection spectrum of the specimen can be calculated from the complex refractive index with higher accuracy than it can be measured. It can then either be used as a primary reflectance standard, or to calibrate secondary working standards such as aluminium films on glass.

2. EXPERIMENTAL

The reference material must meet several requirements. It should be sufficiently transparent that its complex refraction spectrum can be accurately measured. It should be sufficiently reflecting for its calculated reflectivity to be used in reflection comparisons. It must be capable of being optically worked to a plane parallel form. It must also be homogeneous and mechanically stable. Such requirements are satisfied by pure silicon. The specimen was disc shaped, approximately 40 mm in diameter with a thickness of 2.8 mm. Its complex refractive index was determined at 293K using a polarising wire grid interferometer to cover the spectral region from 5 to 50 cm^{-1}, as shown in figure 1. The spectral variation of the refraction and absorption spectra are typical of free carrier absorption. These spectra had random errors <0.0001 in the refraction spectrum and <0.05 cm^{-1} in the absorption spectrum. Power reflection spectra of the specimen were then calculated from the measurements using standard expressions for the Fresnel single surface case, and for that of an unresolved channel spectrum of a lamella. These are shown in figure 2. The paper will consider systematic errors in such derivations of reflectivity, and look at the question of calibrating secondary standards based on aluminium films on glass substrates.

Acknowledgement: This work was supported under the Optoelectronics Programme of the National Measurement System Policy Unit.

3. REFERENCES

1. J.R.Birch, Infrared Physics 18,613-620,1978.

2. J.R.Birch, IEE Conference Publication 177,220-222,1979.

3. J.R.Birch and T.J.Parker, 'Infrared and Millimeter Waves, Vol.2, Ch.3', Ed. K.J.Button, Academic Press, New York 1979.

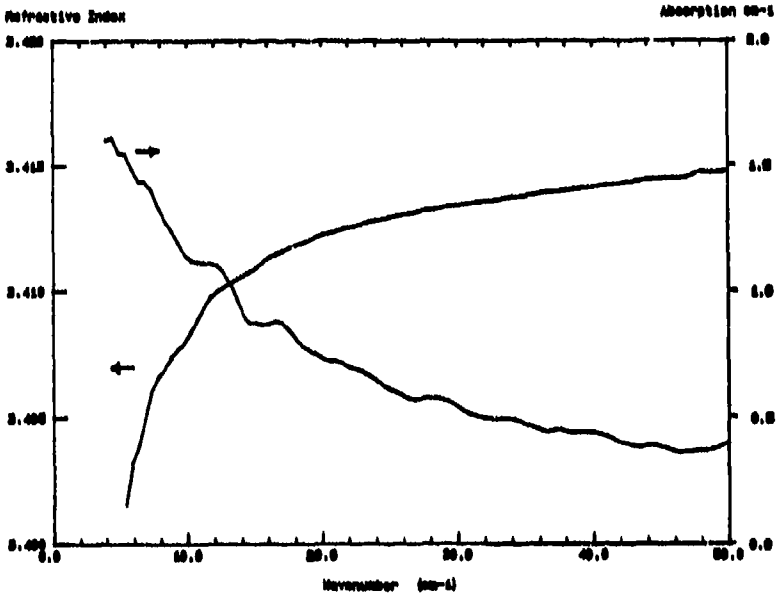

Fig 1. The complex refraction spectrum of the silicon specimen.

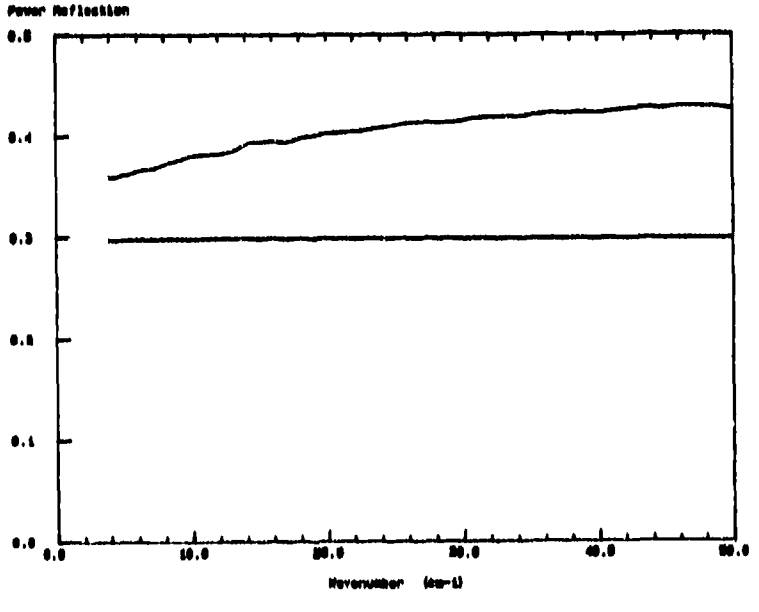

Fig 2. Calculated power reflection spectra of the specimen. The lower curve is the Fresnel spectrum, the upper the lamella with an unresolved channel spectrum.

Modelling of intrinsic mm-wave absorption in low loss dielectrics with complex crystal structure

G. Link, R. Heidinger

Kernforschungszentrum Karlsruhe, Association KfK-Euratom
Institut für Materialforschung, Postfach 3640, D-76021 Karlsruhe, F.R.G.

ABSTRACT

The Sparks-King-Mills model for the intrinsic mm-wave absorption in alkali halides has been generalized and adapted to materials with a more complex structure. The modelling is applied to experimental data for the frequency dependence of tanδ in LiF and CaF_2,and to the temperature dependence of tanδ in Sapphire where the existence of a T^2 regime is assessed.

1. THE CLASSICAL OSCILLATOR MODEL

In the design of cryogenically-cooled windows for high-power gyrotrons, there is a wide-spread use[1,2] of the trial fitting function of Haste et al.[3] to describe the dielectric loss tangent of Sapphire in the ordinary ray (o.r.) below 300 K:

$$\tan\delta = 5.58 \cdot 10^{-11} \cdot f^{0.717} \cdot T^{1.96} \qquad \text{with f [GHz] and T [K]} \qquad (1)$$

Simple scaling laws appear to be also attractive for analyzing the much broader experimental data base that has been generated world-wide since this first fitting. This paper proceeds on the route that was promoted earlier by Thomas et al.[4] to base the pratical fitting functions on the physics to describe data in the Infrared (IR). The starting point is the classical oscillator model proposed for the excitation of Tranverse Optical (TO) phonons by the electromagnetic wave which yields the dielectric function:

$$\varepsilon_r^* = \varepsilon'_{r,\infty} + \Sigma_j \Delta\varepsilon_j \cdot \tilde{\nu}_j^2/(\tilde{\nu}_j^2 - \tilde{\nu}^2 + i\gamma_j\tilde{\nu}) \qquad (2)$$

with $\Delta\varepsilon_j$,$\tilde{\nu}_j$ and γ_j the strength, resonance frequency and the damping constant associated with each excited TO mode, and $\varepsilon'_{r,\infty}$ is the permittivity at optical frequencies. For mm-waves (where $\tilde{\nu} = f/c \ll \tilde{\nu}_j$, c: velocity of light), the various oscillator terms can be summarized by one effective oscillator, and the dieletric loss tangent can be expressed as follows[5]:

$$\tan\delta = ((\varepsilon'_{r,0} - \varepsilon'_{r,\infty})/\varepsilon'_{r,0})\gamma_0\tilde{\nu}/\tilde{\nu}_0^2 \qquad (3)$$

where $\tilde{\nu}_0$ and γ_0 define the effective resonance frequency and damping constant, and $\varepsilon'_{r,0}$ is the permittivity at microwave frequencies. It was shown for dielectric absorption at 300 K, that the proposed linear frequency dependence describes well the experimental data in single crystals (s.c.) of various structures such as Sapphire, Quartz, LiF and CaF_2, evident in most cases[4,5] down to $\tilde{\nu}$ below 10 cm^{-1}. The fit for Sapphire (o.r.) can be expressed by a new fitting function:

$$\tan\delta = 1.58 \cdot 10^{-6} \cdot f \qquad \text{with f [GHz] and T at 300 K} \qquad (4)$$

Its results shows best agreement with those of Eq.1 in the range of 20-30 GHz. The model has its drawbacks if one tries to assess the effective oscillator parameters for mm-wavelengths from the set of oscillator parameters known from IR reflectivity measurements, as the correspondance turns often out to be rather approximative[4,5].

2. THE TWO-PHONON-MODEL

The excitation of TO modes only causes energy dissipation because the excited phonon decays by interaction with other phonons. The quantummechanical treatment of the problem shows that the eigenfrequencies are then shifted and broadened. The damping constant of the classical oscillator model can be generalized[6] by relating it to the frequency and temperature dependent broadening parameter Γ.

$$\gamma_0 \rightarrow \gamma_V = 2(\tilde{\nu}_0/\tilde{\nu})\Gamma(\tilde{\nu}, T) \qquad (5)$$

For alkali halides, it was demonstrated by Sparks et al.[7] that the intrinsic mm-wave absorption can be described on the assumption that the generated virtual TO phonon ($\tilde{\nu}_0$) with a small wavevector ($k_0 \approx 0$) decays into another TO phonon ($\tilde{\nu}_1$) with a wavevector at the Brillouin zone edge ($k_1 = k_{BZ}$) while a second phonon ($\tilde{\nu}_2$) with $k_2 = k_{BZ}$ is absorbed from the transverse acoustical (TA) branch. As the energy gap between the TO and TA branches ($\tilde{\nu}_p = \tilde{\nu}_n - \tilde{\nu}_m$) is larger than the frequency of mm-wave ($\tilde{\nu}$), the process is only allowed energetically if the branches involved are also broadened ($\Delta\tilde{\nu}_n$,$\Delta\tilde{\nu}_m$). For this case, the damping term can be expressed as:

$$\Gamma = \frac{2}{\pi}\Gamma_0\left[\arctan\frac{\tilde{\nu}_0-\tilde{\nu}}{\Delta\tilde{\nu}_{2p}} - \arctan\frac{\tilde{\nu}_0-\tilde{\nu}}{\Delta\tilde{\nu}_{2p}}\right] \qquad \text{where } \Delta\tilde{\nu}_{2p} = \Delta\tilde{\nu}_n + \Delta\tilde{\nu}_m \qquad (6)$$

Further approximations for small numbers of $\tilde{\nu}$ lead to the relation:

$$\gamma_\nu = \frac{4}{\pi}\Gamma_\infty C_A(\Delta\tilde{\nu}_{2p}/\tilde{\nu}_c)\, f(x) \qquad (7)$$

where C_A is a constant to correct for inaccuracies in the expansion of the arctan-terms, Γ_∞ a constant correlated to the lattice anharmonicities[7], and $f(x) = x\cdot e^x\cdot(e^x-1)^{-2}$ and $x = (h\cdot\nu_m\cdot c/k_B\cdot T)$, with h the Planck constant and k_B the Boltzmann constant. At this stage of approximation, the explicit frequency dependence in γ_ν has disappeared and - apart from smaller terms in the phonon parameters - the temperature dependence is given by $f(x)$. So tanδ can be descibed by:

$$\tan\delta = b\cdot(f/c) \qquad \text{with } b = ((\varepsilon'_{r,o}-\varepsilon'_{r,\infty})/\varepsilon'_{r,o})\cdot\gamma_\nu/\tilde{\nu}_o^2 \qquad (8)$$

For special materials with simple structure, such as NaCl, all parameters can be assessed according to Ref.7 (all Γ parameters were defined there as twice of ours). In more complex structures, a variety of different TO branches may contribute. For these general cases, we propose to fix the values of $\tilde{\nu}_o$,$\tilde{\nu}_m$ and $\tilde{\nu}_c$ by selecting a position with two parallel phonon branches (not necessarily at k_{bz}) of correct polarization which give a compromise between minimum values of $\tilde{\nu}_c$ and $\tilde{\nu}_m$. Where $\Delta\tilde{\nu}_{2p}$ and Γ_∞ parameters cannot be found, they may be used as combined or individual fitting parameters. Table 1 exemplifies the modelling of LiF, CaF_2 and Sapphire; the first are treated with no really free parameter and yet reproduce quite well the experimental data of Ref.5. For Sapphire, Γ_∞ is fitted to yield $\tan\delta = 2\cdot10^{-4}$ at 150 GHz.

Table 1. The effective damping constants of LiF, CaF_2 and Sapphire at 300 K calculated with the two-phonon-model (* : $\Delta\nu_{2p}$ fixed to typical values for alkali halides[7])

	$\tilde{\nu}_o$ [cm^{-1}]	$\tilde{\nu}_m$ [cm^{-1}]	$\tilde{\nu}_c$ [cm^{-1}]	$f(x_{300})$	C_A	Γ_∞ [cm^{-1}]	$\Delta\tilde{\nu}_{2p}$ [cm^{-1}]	$\gamma_\nu/\tilde{\nu}_o$	b [cm]
LiF	307	210	90	0.91	0.977	93	20*	0.076	$1.63\cdot10^{-4}$
CaF_2	256	142	42	1.41	0.921	32	20*	0.098	$2.67\cdot10^{-4}$
Sapphire (o.r.)	385	367	65	0.44	0.964	54(fit)	20*	0.023	$0.40\cdot10^{-4}$

3. DESCRIPTION OF THE T^3 REGIME

Often a temperature range is observed experimentally where $\tan\delta\sim T^3$. The two-phonon-model was often disregarded because for $x\ll1$, $f(x)$ is proportional to x^{-1} and therefore predicts $\tan\delta\sim T$. Our analysis, however, shows that the proportionality is no longer obeyed for $x>1$, and an approximation $f(x) = 1.3\cdot x^{-2}$ holds within 15% accuracy in the interval of $1.3 < x < 4$. Therefore in the specially interesting case of Sapphire (ν_m=367 cm^{-1}), the two-phonon model predicts a T^3 law for 130 - 410 K. At lower temperatures, the temperature exponent should continuously increase. Defect related loss, however, can mask this regime with a steep T dependence and can introduce a T^n regime instead. The general fit for *intrinsic loss* in Sapphire is based on Eqs. 3-4 which can be written using the parameters of Tab.1:

$$\tan\delta = 3.0\cdot10^{-6}\cdot f(x_T)\cdot f \qquad \text{with f [GHz]} \qquad (9)$$

which in the T^3 regime reduces to:

$$\tan\delta = 1.48\cdot10^{-11}\cdot f\cdot T^3 \qquad \text{with f [GHz] and T [K]} \qquad (10)$$

4. ACKNOWLEDGEMENT

This work has been performed in the framework of the Nuclear Fusion Project of the KfK and is supported by the European Communities within the European Fusion Technology Programme.

5. REFERENCES

1. T.Yamamoto, K.Yokokura, A.Kasugai, K.Sakamoto, M.Tsuneoka, T.Nagashima, K.Itoh,Y. Saitoh, Digest 17th. Int. Conf. on IR and MM-Waves, Pasadena, SPIE Vol. 1929, pp.460-1, 1992
2. F.V.Hartemann, P.Garin, G.Faillion, G.Mourier, G.Tonon, J.P. Crenn, M. Pain, M. Bon Mardion, Digest 17th. Int. Conf. on IR and MM-Waves, Pasadena, SPIE Vol. 1929, pp.458-9, 1992
3. G.R. Haste, H.D.Kimrey, J.D.Prosise, ORNL-Report TM-9906, Oak Rigde, 1986
4. M.E.Thomas, R.I.Joseph, G.J.Simonis, M.Stead, Digest 13th. Int. Conf. on IR and MM-Waves, Honolulu, SPIE Vol. 1039, pp. 339-341, 1988
5. J.Birch and R.Heidinger, Digest 15th. Int. Conf. on IR and MM-Waves, Orland, SPIE Vol. 1514, pp.464-6, 1990
6. F.Gervais and B.Piriou, J.Phys.C, 7, pp 2374-86, 1974
7. M.Sparks, D.F.King, D.L.Mills, Phys.Rev.B, 26(12), pp6987-7003, 1982

Temperature dependence of the optical constants of polyethylene in the region of the 73 cm^{-1} lattice mode

J.R.Birch and Kong Fan Ping*

Division of Electrical Science, National Physical Laboratory
Teddington, Middlesex TW11 OLW, UK

*Energy and Environment Division, Lawrence Berkeley Laboratory
University of California, Berkeley, CA 94720, USA

ABSTRACT

The results of dispersive Fourier transform spectroscopic studies of the temperature dependence of the optical constants of polyethylene from 30 to 120 cm^{-1} are presented and discussed.

1. INTRODUCTION

In the far infrared polyethylene ($(C_2H_4)_n$) is probably the most widely used material for the construction of low loss transmission optics such as lenses and windows. A consequence of this is that there have been extensive studies of its power transmission properties in this spectral region, including some studies of the spectral variation of its optical constants[1]. If, however, information is required on the temperature dependence of the optical constants, the available data is more sparce. Thus, while there have been a number of studies of the temperature variation of the absorption spectrum, particularly in the 70 to 80 cm^{-1} region of the B_{1u} lattice mode, there is much less information available on the temperature dependence of the refractive index spectrum. The present work was aimed at providing a systematic study of the temperature dependence between 6 and 300 K of the optical constants of a specimen of low density polyethylene (LDPE) in the spectral region from 30 to 120 cm^{-1} which contains the B_{1u} and B_{2u} lattice modes.

2. EXPERIMENTAL

The refraction and absorption spectra of a 9.8 mm thick specimen of LDPE were determined using dispersive Fourier transform spectroscopy[2] (DFTS). This measures the phase shift and attenuation suffered by an electromagnetic wave as it propagates through a specimen. Once these are known, the refraction and absorption spectra of the specimen can be calculated from them without approximation.

The interferometer used in this study was a polarising wire grid interferometer[3]. It was used with a quartz window Golay cell in the spectral region from 30 to 120 cm^{-1}. The specimen was mounted in a variable temperature cryostat which formed part of the fixed mirror arm of the interferometer. Its temperature could be adjusted to any value between 4.2 and 300 K. The specimen could be positioned in or out of the beam in the fixed mirror arm without removing it from the exchange gas volume of the cryostat.

The phase shift and attenuation due to the specimen were measured at seven temperatures, 6, 20, 40, 60, 80, 100 and 293 K. Typically, the temperature was maintained within ±1 K above 60 K, falling to around ±0.3 K at the lower temperatures. All of the measurements were made with a nominal spectral resolution of 2 cm^{-1}.

3. RESULTS

The refraction and absorption spectra of the specimen as determined at each temperature are shown in figure 1. Each represents the average of 4 independent determinations. The reproducibility of these suggested a level of random uncertainty in the refraction spectra of about 0.0001 and about 0.1 cm^{-1} in the absorption spectra. The absorption ordinate scale refers to the 293 K spectrum. The other spectra are offset by a progressive 0.5 cm^{-1} for clarity.

As the thickness of the specimen was only known at 293 K, it was corrected for thermal contraction at each measurement temperature. The effect of this was only seen in the refractive index spectrum, due to the high signal-to-noise of the phase spectrum. The lower signal-to-noise of the attenuation measurements masked such effects. A further correction was necessary to allow for the non-unity refractive index of the helium gas which surrounded the specimen. If ignored, this reduces the derived value of the refractive index from its true value. This can be avoided if the temperature dependence of the refractive index of helium gas is known[4].

Acknowledgement: This work was supported under the Optoelectronics Programme of the National Measurement System Policy Unit.

REFERENCES

1. J.Ashok, P.L.H.Varaprased and J.R.Birch, 'Handbook of Optical Constants of Solids II', Ed. E.D.Palik. Academic Press, Boston 1991.

2. J.R.Birch and T.J.Parker, 'Infrared and Millimeter Waves, Vol.2, Ch.3', Ed. K.J.Button, Academic Press, New York 1979.

3. J.R.Birch and Kong Fan Ping, Infrared Physics 24,309-314,1984.

4. J.R.Birch, Infrared Physics 34,89-93,1993.

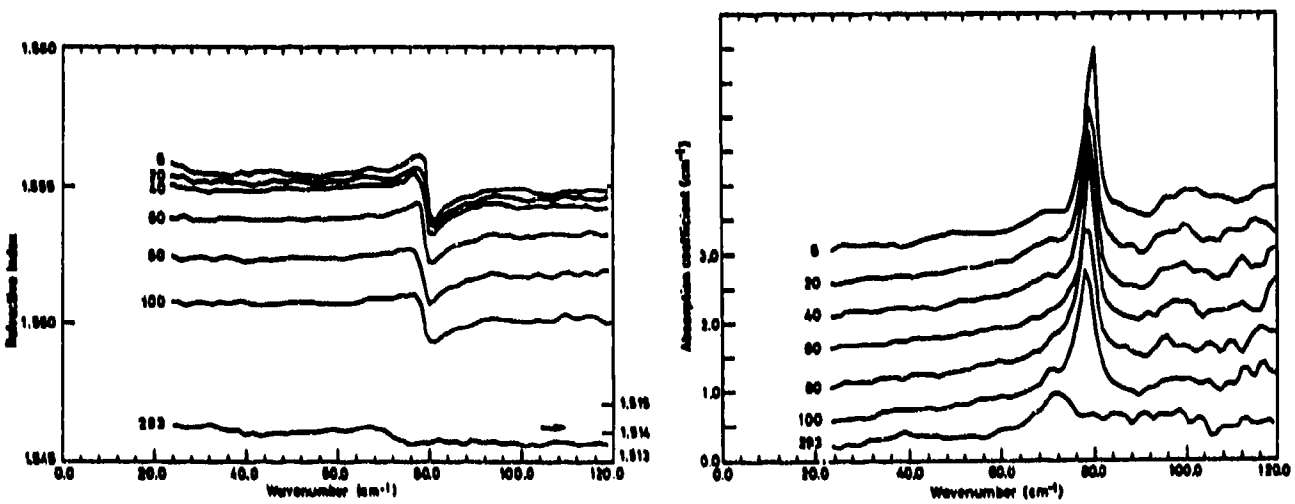

Figure 1. The refractive index and absorption spectra of LDPE

Direct determination of the far infrared complex refractive index of InAs at 300 and 100K

A.K. Wan Abdullah[1], T.J. Parker[2] and C. Patel[3]
[1]School of Physics, Universiti Sains Malaysia, 11800 Penang, Malaysia
[2]Department of Physics, University of Essex, Colchester CO4 3SQ, United Kingdom
[3]Department of Nuclear Physics, University of Oxford, Oxford OX1 3RH, United Kingdom

ABSTRACT

The real and imaginary parts of the far infrared complex refractive index of InAs have been determined at 300 and 100K using the technique of dispersive Fourier transform spectroscopy. Features observed in the spectra have been assigned as phonon combination bands at critical points and used to test the validity of a lattice dynamical model for establishing the phonon dispersion curves in the absence of neutron data.

DISCUSSION

The method of single-pass transmission dispersive Fourier transform spectroscopy (DFTS) is used to obtain directly the amplitude and phase spectra of highly absorbing solids[1]. The instrument that has been developed to obtain the present results on InAs and other binary semiconductors is described elsewhere[2].

In this work, a small crystal of nominally undoped InAs with a surface area of about 1 cm^2 and thickness 500 ± 1.5 μm has been used to obtain the optical constants (n and k) on either side of the reststrahlen band. Measurements of the amplitude and phase spectra at 300 and 100K were first obtained by DFTS and n and k calculated from the Fresnel relations. At 300K the sample was completely opaque below the reststrahlen band, but at 100K a weak transmission signal was detected below the reststrahlen band. The details of this method of measuring the phase change precisely at two different temperatures is described elsewhere[3].

The spectra of n and k are shown in figure 1. The change in thickness of the sample due to thermal contraction[4] was negligible. The real and imaginary parts of the dielectric response function, ε' and ε", respectively, can also be calculated easily from these data, but they are not shown here. The values of n obtained from this work are slightly higher than those reported previously[5] from an analysis of interference fringes measured in transmission[6]. The rise in the value of k at low frequencies is believed to be due to the onset of free carrier absorption. The optical constants in the reststrahlen band measured at room temperature have been reported by several authors[7,8] using the technique of reflection DFTS.

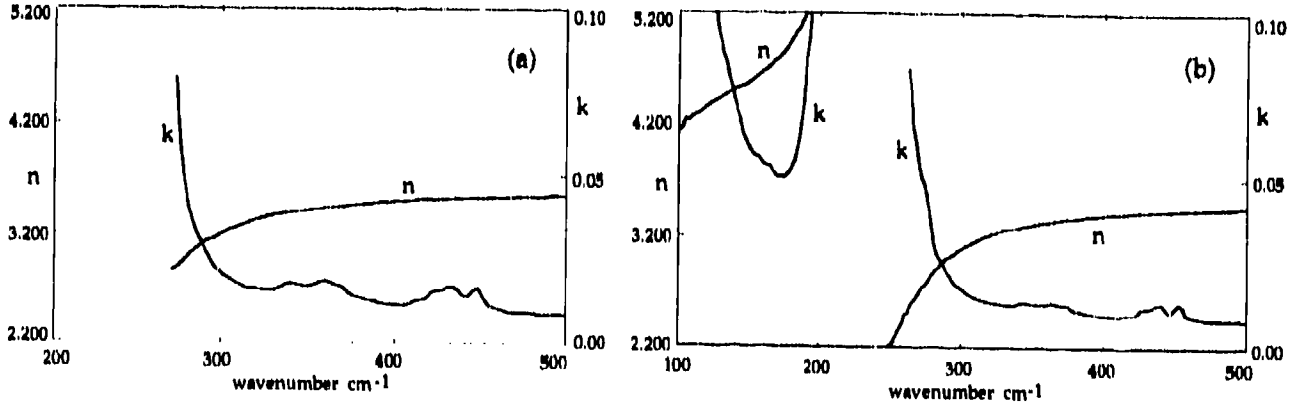

Figure 1: Refractive index n and extinction coefficient k of InAs at (a) 300K and (b) 100K

InAs absorbs neutrons heavily. As a result, very few neutron scattering measurements have been made on this material, and this has greatly inhibited the determination of reliable phonon dispersion curves. Several attempts have been made to establish a complete set of critical point phonon (cpp) frequencies by interpreting the experimentally measured phonon combination bands with the aid of lattice dynamical models[9-13]. However, significant discrepancies exist between the different sets of calculated phonon frequencies.

In the present work the cpp frequencies predicted by an 11-parameter rigid-ion-model (RIM)[13] were used in the assignments of the observed bands. This provides an opportunity to test the validity of the model. The bands have been assigned to two-phonon processes at the critical points Γ, X, L, W and K in the first Brillouin zone, as listed in table 1. It can be seen from the table that in nearly all cases reasonable agreement is found between measured and calculated frequencies.

This work 300K	This work 100K	11-parameter RIM[13]	Infrared[11] 15K	Raman[12] 100K	Assignments
-	108	107.0	-	108	W1 - W5
		109.8			$IIO\Sigma_1 - IA\Sigma_1$
-	115	118.0	-	115	LA(X) - TA(X)
		118.6			$IO\Sigma_1 - IA\Sigma_1$
-	134	134.0	-	-	LO(X) - TA(X)
-	157	158.3	158	160	$IO\Sigma_1 - TA\Sigma_1$
-	166	167.1	165	167	TO(L) - TA(L)
-	175	176.4	178	175	$2IA\Sigma_1$
338	342	341.2	340	343	LO(L) + LA(L)
358	362	358.2	362	363	LO(X) + LA(X)
		359.2			TO(L) + LA(L)
368	373	374.6	373	373	LA(X) + TO(X)
410	415	407.0	413	-	2TO(X)
420	425	422.2	424	425	2TO(L)
430	436	433.0	437	437	2TO(Γ)
445	450	455.3	451	451	LO(Γ) + TO(Γ)

Table 1: List of assignments of the observed bands for InAs

REFERENCES

1. J.R. Birch and T.J. Parker, *"Infrared and Millimeter Waves"*, vol. 2, Ed. K.J. Button, Academic Press, New York, chap. 3, (1979).
2. A.K. Wan Abdullah and T.J. Parker, Infrared Phys., vol. 29, p 799, 1989.
3. A.K. Wan Abdullah and T.J. Parker, Infrared Phys., vol. 29, p 719, 1989.
4. N.N. Sirota and Y.I. Pashintsev, Dokl. Akad. Nauk USSR vol. 127, p 627, 1959.
5. B.O. Seraphin and H.E. Bennet, *"Semiconductors and Semimetals"*, vol. 3, Eds. R.K. Willardson and A.C. Beer, Academic Press, New York, p 499 (1967).
6. O.G. Lorimor and W.G. Spitzer, J. Appl. Phys. vol. 36, p 1841, 1965.
7. J. Gast and L. Genzel, Opt. Comm. vol. 8, p 26, 1973.
8. A. Memon and T.J. Parker, SPIE vol. 289, p 20, 1981.
9. D.L. Stierwalt and R.F. Potter, *"Semiconductors and Semimetals"*, vol. 3, Eds. R.K. Willardson and A.C. Beer, Academic Press, New York, p 71 (1967).
10. D.N. Talwar and B.K. Agrawal, Phys. Stat. Sol. (b) vol 63, p 441, 1974.
11. E.S. Koteles and W.R. Datars, Canad. J. Phys. vol. 54, p 1676, 1976
12. R. Carles Saint-Cricq, J.B. Renucci, M.A. Renucci and A. Zwick, Phys. Rev. B vol. 22, p 4804, 1980.
13. C. Patel, Ph.D thesis, University of London, 1982.

A variable temperature dispersive Fourier transform spectrometer for complex reflection measurements on opaque solids

J.R.Birch and P.G.Quincey

Division of Electrical Science, National Physical Laboratory
Teddington, Middlesex TW11 OLW, UK

ABSTRACT

A switched field-of-view dispersive Fourier transform spectrometer for complex reflection measurements on opaque solids is described. It is for operation in the 30 to 600 cm^{-1} spectral region. The specimen is mounted on the cold stage of a closed cycle refrigerator to allow measurements to be made at any temperature between ambient and 20 K.

1. INTRODUCTION

Dispersive Fourier transform spectroscopy (DFTS)[1-3] is a technique for the determination of the full spectral variation of the optical constants of a material. This is achieved by a measurement of the attenuation and phase shift imposed on an electromagnetic wave by its interaction with a specimen. The complex refractive index spectrum of the specimen can then be calculated from these parameters without approximation. Measurements can be on gases, liquids or solids, and may be in transmission or reflection, as appropriate.

In measurements on opaque solids the Fresnel complex reflection spectrum of the material is determined. This can be done either by a replacement method, in which the specimen physically replaces the fixed mirror of the interferometer, or by a switched field-of-view method. In the latter approach the specimen is the fixed mirror. Its surface is partly aluminised and a screen is used to divide the field-of-view of the interferometer so that either the aluminised or the non-aluminised area of the surface is illuminated. The replacement method is the easiest to implement, but the switched field-of-view method is much better suited to low temperature measurements, and a number of spectrometers for such cryogenic studies have been constructed[4,5]. These have used liquid cryogens in cryostats to operate at fixed temperatures, usually those of liquid nitrogen and helium. The present work describes a DFTS spectrometer for complex reflection measurements that uses a closed cycle refrigerator to achieve any measurement temperature between 20 and 300 K.

2. EXPERIMENTAL

A schematic representation of the interferometer is shown in figure 1. The radiation from a mercury arc lamp was focussed into the interferometer by an off-axis parabolic reflector. A thin film dielectric beamdivider divided the incident beam into two orthogonal beams: one was transmitted from the beamdivider to form a source image at the specimen, the other was reflected to enter the moving mirror arm. This was bent through a right angle by a plane mirror mounted on a vibration generator so that phase modulation could be used. The return radiation from each arm was condensed on to the detector by a further off axis parabolic reflector.

The surface of each specimen was divided into eight sectors of equal area with every other one a vacuum evaporated aluminium film. A four sector mask mounted just before the specimen could be magnetically switched so that either the aluminised or the non-aluminised surface segments were illuminated. The specimen was rigidly connected to the body of the interferometer using PTFE connecting pieces to thermally isolate it from the warm instrument. It was connected to the cold stage of the refrigerator by copper braid to give good thermal contact, while maintaining a non-rigid mechanical contact to isolate it from the vibrations of the compressor cycle of the refrigerator. A Golay cell with a diamond window was used as the detector.

The performance of the interferometer in the spectral region from 50 to 500 cm^{-1} will be described and illustrated with the results of measurements on some YBCO films.

Acknowledgement: This work was supported under the Optoelectronics programme of the National Measurement System Policy Unit.

REFERENCES

1. J.R.Birch and T.J.Parker, 'Infrared and Millimeter Waves, Vol.2, Ch.3', Ed. K.J.Button, Academic Press, New York 1979.

2. J.R.Birch, Mikrochimica Acta III,105,1987.

3. T.J.Parker, Contemporary Physics 31,335,1990.

4. T.J.Parker, R.P.Lowndes and C.L.Mok, Infrared Physics 18,565,1978.

5. P.R.Staal, J.E.Eldridge, P.J.Haas and H.Bless, Infrared Physics 19,625,1979.

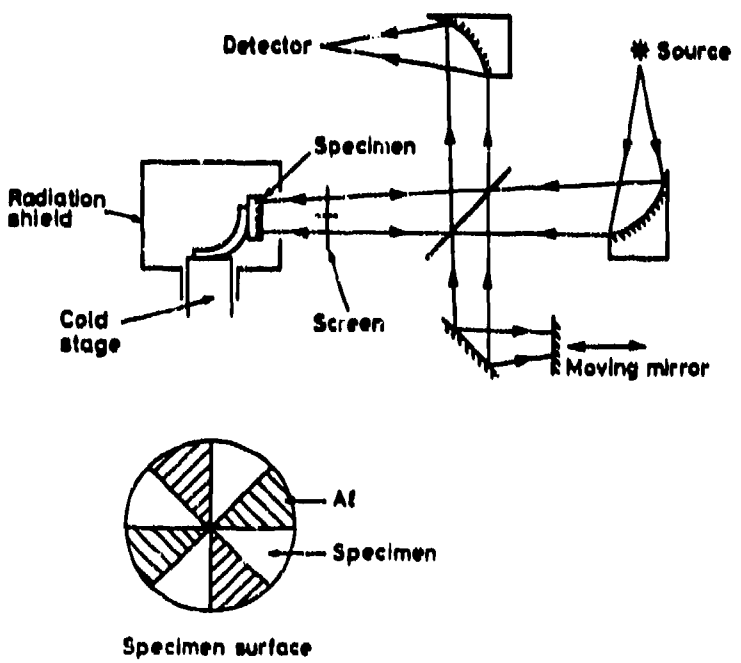

Figure 1. A schematic representation of the interferometer.

Refractometry of oil products in millimeter and submillimeter range

Latyshev A.B., Loukianov D.A., Semenov A.V.

General Physics Institute, Russian Academy of Science, 117942 Moscow, Russia

ABSTRACT

The qualification of different kinds of oil products, either dark (crude oils, adulterated oils, engine oils) or light (gasoline, petrol, kerosene, diesel oil) is shown to be possible. The sensitivity of measurements distinguishes 1/300 between two kinds of russian automobile gasolines with octane numbers 93 and 76 is shown. It can be easily improved to 1/1000 or better.

2. INTRODUCTION

In the latest decades a BWO-Spectroscopy in millimeter and submillimeter band has been actively developing ([1] - [2]). BWO-Spectroscopy implies the technique of measuring frequency dependencies of different parameters of the samples using a tunable monochromatic sources Backward-Wave-Tube-Oscillators (BWO) with electronic frequency sweeping. The BWOs used for spectroscopy can sweep in the range of one octave.

The commonly measured parameter is the sample transmission factor, that is known to be the complex value. Presently there is a series of BWO-spectrometers, measuring not only transmission amplitude, but also its phase spectra. It is noteworthy, that while the amplitude of transmission is mainly influenced by the absorption and refraction indices of sample substance, its phase depends mostly upon the refraction index.

Modern technique of BWO-spectroscopy has the sensitivity of 0.1-0.5 degrees [3]. For instance, at 1mm wavelength and 10mm sample thickness such technique can detect changes of refraction index of the order of 10^{-4}.

Direct measurements of refraction indices with such precision deals with certain problems (however, which can be perfectly solved), particularly the necessity of the knowledge of exact sample geometry with submicron accuracy. The last problem is easy enough if the goal of investigation is to measure not absolute value of refraction index, but its change relative to some reference substance which is similar to those to be investigated. It is relatively easy for liquids. In this case the qualification is limited to the measurements of phase differences of the same cell filled with either reference or investigated liquids.

3. DEMONSTRATION

Our aim was to show attractive features of BWO-spectroscopy like sensitivity to slight refraction index variations, and to demonstrate the applicability of this technique to problems of certain interest to industry.

We have measured transmission phase differences in a series of oil products in the same cell with fluid layer thickness of 10 mm). The measurements where made in 0.9-1.1 mm wavelength range in automatic mode. One sort of russian petrol with octane number 76 was used as reference liquid for all cited below spectra (the choice was arbitrary).

Fig. 1 shows scatter between two phase spectra of the same russian petrol "reference" A-76. It demonstrates the quality of the technique used. It is evident that the reproduceability of phase spectra (and, thus, phase sensitivity) is within 0.5 ^{0} (0.5 degree). The RMS difference of refraction indices (or refraction index sensitivity), calculated from this phase difference is $8\ 10^{-5}$. The absolute value of the refraction index of the petrol A-76 is 1.42.

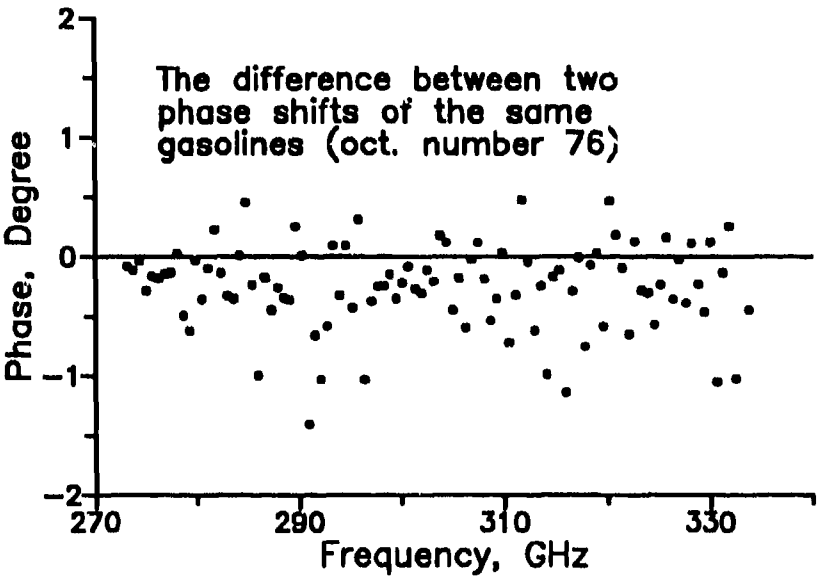

Fig. 1

In Fig. 2 the phase difference between referenced petrol A-76 and a series of Russian oil products are shown. Curve 1 corresponds to petrol AI-93 (Octane number 93). Transmission phase of this petrol exceeds by more then 100 degrees the corresponding phase for reference petrol A-76, and the difference of the refraction index is 0.0366. The difference in refraction indices for these petrols exceeds by 300 times the scatter we had.

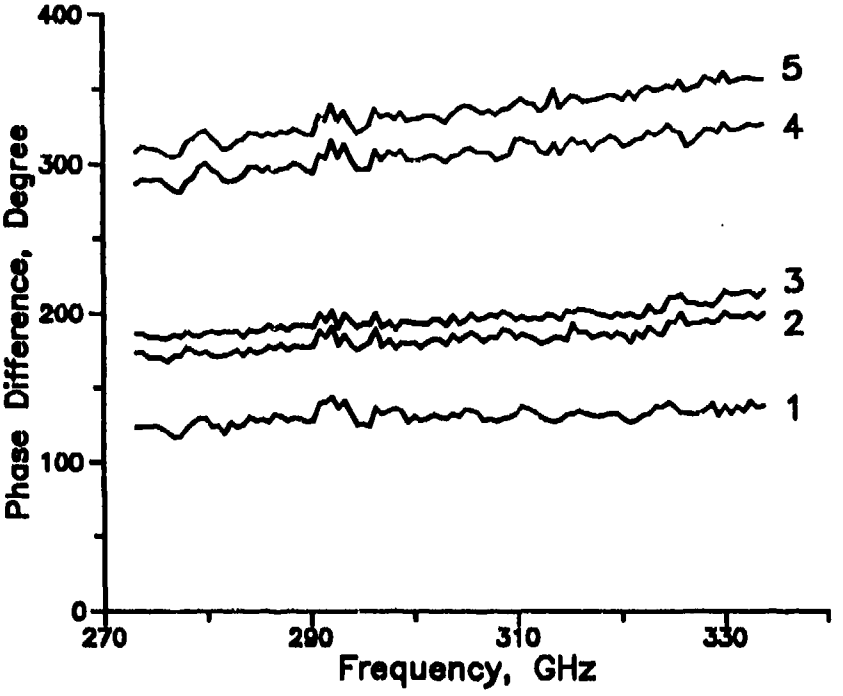

Fig. 2

Curves 2 and 3 in Fig.3 correspond to two varieties of Russian crude oil (relative to the reference petrol A-76). In this case we find it remarkable that our technique can measure light as well as dark (non-transparent in visible range) oil products. Note that difference between two kinds of oil is clear enough to be easy detected by means of BWO-spectroscopy. Relative refraction indices for oils 2 and 3 are 0.0510 and 0.0549 correspondingly.

Curves 4 and 5 on Fig. 2 correspond to the same engine oil (carburator oil M8V1, dark oil product), both new (curve 4) and used in the car engine for 10,000 Km (curve 5). These oil products can be investigated by means of BWO-spectroscopy and can be easily distinguished. The relative refraction indices of these oils referenced to A-76 petrol are 0.0857 and 0.0933.

It should be noted, that all curves in Fig. 2 have a lot of peculiarities, exceeding essentially the sensitivity of the technique used. It is the time to ask which of them reflect the features of investigated liquids and which are the instrumental errors of measuring technique. We can not readily answer this question and this is a subject for further analyses.

4. SUMMARY

The modern technique of millimeter and submillimeter measurements may provide a useful tool for qualitative and even quantitative analysis of different crude oils and oil products as fuels, lubricants, fats, etc. The sensitivity of the measurements can be improved to 10 times or more by simple increasing of cell thickness.

5. REFERENCES

1. N.A. Irisova "Metrica submillimetrovyh woln", Vestnik Academii Nauk SSSR, 1968, T. 10, ctr.63-70. (in Russian).

2. A.A.Volkov, Yo.G.Goncharov, G.V.Kozlov at al., "Dielectric measurements in the submillimeter wave-length region", Infrared Physics, 1985, Vol.25, N1/2, p.369-373.

3. A.B.Latyshev, D.A.Loukianov, I.M.Fedotova, "Method izmereniya phaso-chastotnyh spectrov na quasiopticheskom LOV-spectrometre millimetrovogo i submillimetrovogo diapazonov", Pribory I Tehnika Experimenta, 1990, N1, str.143-144. (in Russian).

CHARACTERIZATION OF MATERIALS BY SUBMILLIMETER MULTIBEAM TECHNIQUES

B.P.Gorshunov, G.Gruner, I.V.Fedorov,
G.V.Kozlov, I.I.Tkachev, A.A.Volkov
Institute for General Physics, Russian Academy of Sciences,
Vavilov str. 38, 117942 Moscow, Russia

B.Holzapfel, G.Saemann-Ischenko
Institute of Physics, University of Erlangen, Erwin-Rommel
Strasse, D-8520 Erlangen, Germany

Use of different multilayer resonance structures in quasioptical submillimeter (SBMM) spectroscopy gives an effective way of increasing the sensitivity of measuring schemes due to multiple interaction of the testing radiation with the sample. We present below three main kinds of interferometric structures used in SBMM quasioptical spectroscopy which allow direct determination of any optical constant of the sample.

1 Investigation of bulk materials.

In this method the measurement of reflectivity of a Fabry-Perot resonator (FPR) with the back mirror represented by the surface of the sample is performed instead measuring reflectivity of the bulk material. We have realized two modifications of this technique. In the first case the front mirror of FPR is a metallic grid. In order to achieve maximum sensitivity in determination of modulus and phase of the reflection coefficient R of the sample, the grid should have its reflectivity as close to R as possible. In the second case the FPR is formed by a plane -parallel transparent plate (dielectric "tester") with its back plane being in (optical) contact with the surface of the sample. The first method was used by us for measurement of the ferroelectric crystals [1] and the second one -- for measurements of the high-temperature superconducting ceramics [2].

2 Investigation of metallic and superconducting films.

An optimum structure for measuring the complex conductivity of such objects is a dielectric Fabry-Perot resonator formed by plane-parallel dielectric plate coated from both sides by investigated films. Experimentally are measured the resonances in the transmissivity spectra of this FPR. We have performed by such technique measurements of the electrodynamic properties of conventional (NbN) and high-temperature ($YBa_2Cu_3O_{7-\delta}$) superconducting films in normal and superconducting phases, which actually for the first time allowed quantitative determination of the real part of the conductivity (absorption) of superconducting films [3] (Fig.1, data for NbN).

3 Investigation of absorbing liquids.

Study of liquids with the help of dielectric tester techinique is especially convenient since in this case there is no problem of providing the optical contact between the sample and the tester. This is done just by putting the liquid on the horizontally situated tester. By using this technique we have studied SBMM dielectric spectra of a number of water solutions.

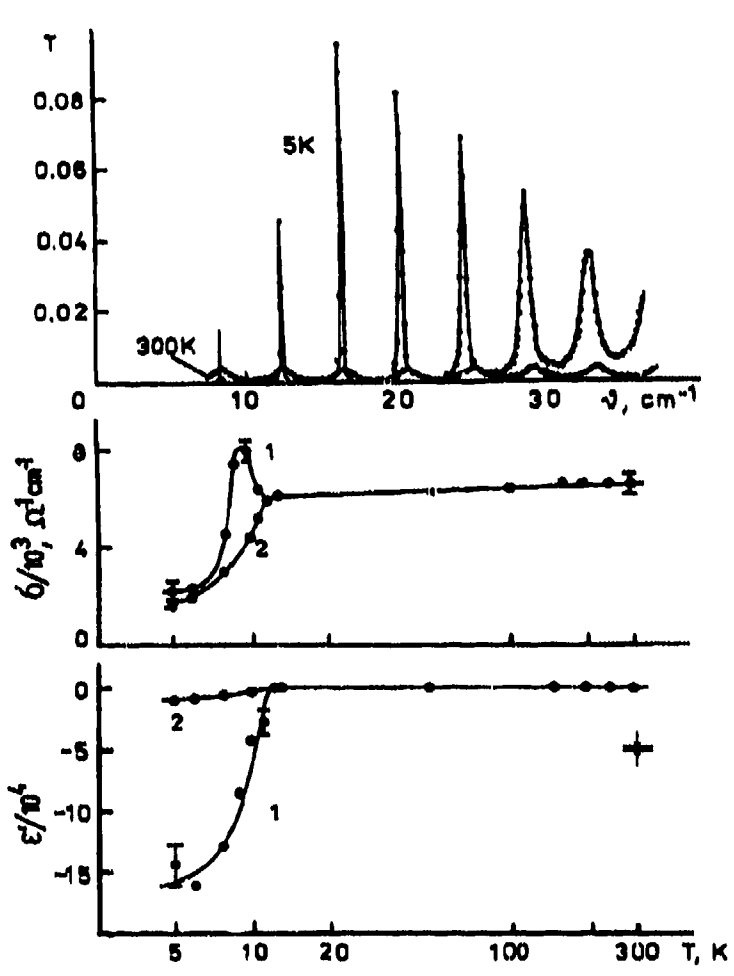

Fig.1 SBMM transmissivity spectra of a FPR formed by two NbN films (540 Å) evaporated onto sapphire substrate, measured in normal and in superconducting state. The lower part shows temperature dependencies of the SBMM conductivity and the dielectric permittivity of NbN films at 8 cm^{-1} (1) and 29 cm^{-1} (2), calculated on the basis of transmissivity spectra.

References

[1] A.A.Volkov, N.A.Irisova, G.V.Kozlov. *Optika i spektroskopia*, 1976, vol.40, N2, p.386-391.

[2] B.P.Gorshunov, Yu.G.Goncharov, G.V.Kozlov, A.M.Prokhorov, A.S.Prokhorov, A.A.Volkov. *Int. J. Modern Physics B*, 1987, vol.1, N3,4, p.867-870.

[3] B.P.Gorshunov, I.V.Fedorov, G.V.Kozlov, A.A.Volkov, A.D.Semenov. To be published in Solid State Communications.

CHARACTERIZATION OF MICROWAVE CERAMICS AT SUBMILLIMETER WAVES

I.V.Fedorov, G.A.Komandin, G.V.Kozlov, A.A.Volkov
Institute for General Physics, Russian Academy of Sciences,
Vavilov str., 38, 117942 Moscow, Russia

E.A.Nenasheva
"Gyricond" Research Institute, St.-Petersburg, Russia

J.Petzelt
Institute of Physics, Na Slovance 2, Prague, Czechia

In this report we discuss the technique for dielectric characterisation of microwave ceramics with the help of submillimeter frequency-tunable monochromatic generators - backward-wave oscillators (BWO). We have developed for frequencies $10^{11} - 10^{12}$ Hz ($\lambda \sim 3 - 0.3$ mm) a technique for fast and precise measurement of the dielectric characteristics ε' and ε'' of transparent ceramic samples. The techinique is aimed at determination of minimal level of losses, connected with the fundamental infrared resonances of the crystal lattice [1, 2]. The measuring procedure consists of recording in optical scheme of the transmissivity spectra of plane-parallel ceramic plates, working as Fabry-Perot interferometers due to their high quality factors. The spectra of ε' and ε'' are determined on the basis of oscillating transmissivity curves using Fresnel formulas (Figs. 1,2).

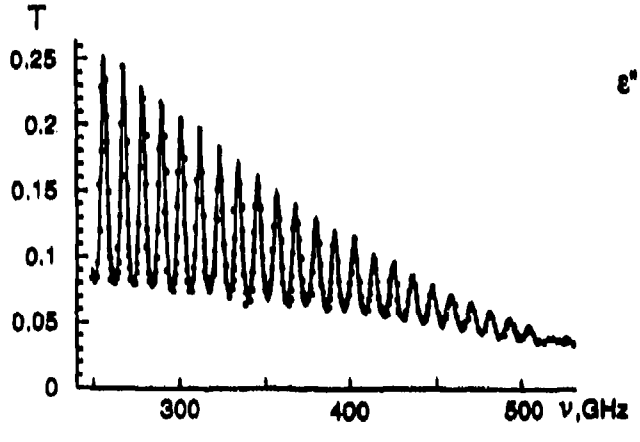

Fig.1 Example of transmissivity spectrum of a plane-parallel barium ceramic plate. Solid line shows theoretical fit givihg ε' and ε'' (see Fig.2).

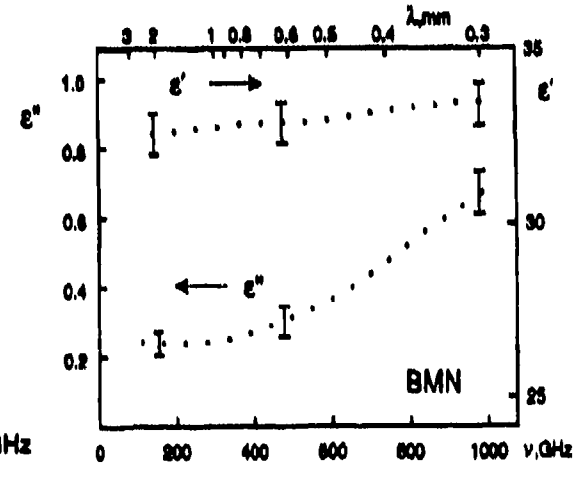

Fig.2 Room temperature $\varepsilon'(\nu)$ and $\varepsilon''(\nu)$ spectra of barium ceramic calculated from transmissivity spectra shown in Fig.1

References

[1] J.Petzelt, R.Zurmühlen, A.Bell, S.Kamba, G.V.Kozlov, A.A.Volkov, N.Setter *Ferroelectrics*, 1992, Vol. 133, pp.205-210.

[2] J.Petzelt, S.Pacesova, J.Fousek, S.Kamba, V.Zelezny, V.Koukal, J.Schwarzbach, B.P.Gorshunov, G.V.Kozlov and A.A.Volkov, *Ferroelectrics*, 1989, Vol.93, p.77

Infrared Spectra Of Wool Fibers γ-Irradiated In Mixtures Of Solvents

S.M.Rabie, M.A.Moharram* and O.M.Mahmoud*

Middle Eastern Regional Radioisotope Center
for the Arab Countries, Cairo, Egypt.
*National Research Center, Cairo, Egypt.

The IR spectra of wool fibers γ-irradiated in mixtures of two organic solvents were recorded. The analysis of the spectra showed that irradiation of wool fibers in the presence of certain mixtures results in the appearance of an absorption band at 1725 cm^{-1} corresponding to the absorption of the carbonyl groups. The intensity of the COO^- band at 1400 cm^{-1} is influenced by the nature of the solvents and the concentration of each solvent in the mixture. This band disappears when the fibers are irradiated in the presence of ethylalcohol and shows the intense absorption when the fibers are irradiated in carbon tetrachloride. The intensities of the absorption bands in the region 1000-1200 cm^{-1} vary also according to the nature of the solvents. Furthermore, the absorbances of the amide I and amide II bands were determined. It was found that the induced changes in the absorbances of these bands depend on the dipole moment of the solvents.

Effect of Organic Solvents on the Frequency of Infra-red Region of the Spectrum

By

M.I. Nasser

Physics Department

National Research Centre

Dokki, Cairo, Egypt.

Due to the Special Importance of the (X-H) bonds, this study was restricted to the (N-H) and the (O-H) bonds of Diphenilamine and α - naphthol respectively.

The frequency of both the (N-H) and the (O-H) groups in the gas phase (ν_g) was experimentally measured, by the author, using a specially designed heated gas cell. It was found that ν_g(N-H)= 3436 cm and ν_g (O-H) = 3658 cm^{-1}. Thus the frequency shift could be precisely determined.

The change in the vibrational frequency of a dipole due to its electrostatic interaction was studied by Kirkwood (1934) The model of a point dipole in a continuous dielectric was used. The relative frequency shift is expressed by the Kerkwood-Bouer-Magat equation :

$$\frac{\Delta \nu}{\nu_g} = C \frac{D - 1}{2D + 1} \qquad \ldots\ldots\ldots\ldots (1)$$

where :

$$\Delta \nu = \nu_g - \nu_s$$

ν_g = vibrational frequency in the gas phase

ν_s = vibrational frequency in solution

D = dielectric constant

C = constant depending on solute model.

according to this equation the plot of $\frac{\Delta\nu}{\nu_g}$ against $\frac{D-1}{D+1}$ should give a straight line passing through the origin.

Later they modifed their equatioin and related the frequency shift to the refractive index of the solvent as follows .1

$$\frac{\Delta\nu}{\nu_g} = C' \frac{n^2-1}{2n^2+1} \quad \text{.....(2)}$$

where :

n = refractive index of the solvent

C' = constant other than C in equation (1)

Josien & Fuson (1954) during their detailed study of the solvent effects on the (N-H) stretching vibrations of pyrole showed that only the frequency shifts in dilute solvents of non-polar solvents fall on the K B M line. In polar solvents the points are shifted twoards highet values of $\Delta\nu$. This shift produced by the polar & aromatic hydrocarbon solvents has been attributed to the hydrogen bonding formation. Such interactions were not taken into consideratioin by the K B M equation.

The author, having designed a specially heated gas cell, was able to determine the frequency in the gas phase. This enabled him to conclude that the frequency shifts do not depend upon the solvent properties only but upon the properties of the solute molecules as well. This finding is in agreement with Bellany's concepts.

Optical properties of lanthanides ions in low vibrational frequency solvents

Andrew Coleman, Harvey Rutt

University of Southampton, Department of Electronics and Computer Science
Highfield, Southampton, Hants, SO9 5NH

Laser action in Neodymium doped inorganic aprotic solvents $POCl_3$ and $SeOCl_2$ has been known for many years, but there has been little work in this field recently. Very little work has been reported on ions other than Nd^{3+}. The ability to readily change the dopant, vary concentrations, add co-dopants etc at low cost is attractive, and using modern laser techniques it is possible that these materials might again be useful. In particular there are a variety of possible solvents which have not been exploited to date which offer the possibility of tailoring the non-radiative rates of the various levels for the particular transition required.

As an initial stage in this program we have prepared solutions of Pr^{3+} and Nd^{3+} in high purity (fibre optic grade) $POCl_3$. All operations were carried out under dry nitrogen. Pure anhydrous neodymium trichloride (99.9%) and praseodymium tribromide (99.9%) were dissolved in a 5:1 molar mixture of $POCl_3$ and $SnCl_4$ by heating and stirring, giving clear lilac and green solutions respectively. The material must be kept slightly warm to avoid crystallization.

The reaction was monitored by Fourier transform infrared spectroscopy. In pure $POCl_3$ a strong band occurs at 1292cm-1, assigned to the P-O stretch. In the solutions an additional band appears at 1209cm-1 (figure 1), which is not present in the solutes. This band is also seen in $POCl_3$ acidified with $ZrCl_4$, and this strongly suggests that it is due to acidified $POCl_3$ species, possibly $PO_2Cl_2^-$. Even in 10cm path spectra no evidence is seen of OH absorption bands, confirming the high purity of the solutions. Infrared spectroscopy is thus an excellent way to monitor purity and investigate the solvation mechanisms.

Fluorescence spectra of the Pr^{3+} solution were excited with the 488nm argon laser line and recorded by photon counting , figure 2. The spectrum is broadly as expected for this ion in an oxide host. The strong fluorescence at ~600nm is $^1D_2$ to $^3H_4$ and shows a ~40uS lifetime.The 640nm fluorescence is $^3P_0$ to $^3F_2$ and shows a short, <5uS lifetime owing to fast non-radiative relaxation to $^1D_2$.

For Nd^{3+} the argon 476nm line was used, and strong fluorescence observed at both~805nm and 860-900nm (figure 3) with essentially identical lifetimes of ~240uS (figure 4). The longer wavelegth band is as expected, from $^4F_{3/2}$ to the ground state, $^4I_{9/2}$, but the long lifetime and strong fluorescence on the ~805nm line, $^4F_{3/2}$-$^4I_{9/2}$, is surprising in view of its proximity to $^4F_{3/2}$.

We shall report systematic studies of the effect of the choice of solvent, Lewis acid and lanthanide ion on the laser potential of these inorganic liquid systems, with a particular view to obtaining laser action in regions of the mid infrared where few lasers are readily available. The authors would particulally like to acknowledge the assistance of Dr W S Brockelsby with the fluorescence measurements.

FIGURE 1

IR Spectra of the Solvent System

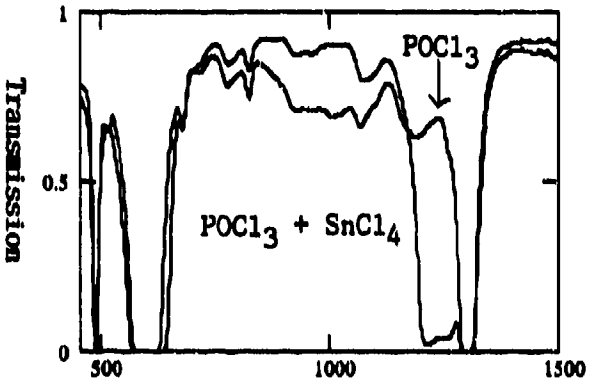

FIGURE 2

Pr^{3+} Fluorescence Spectrum
488nm excitation

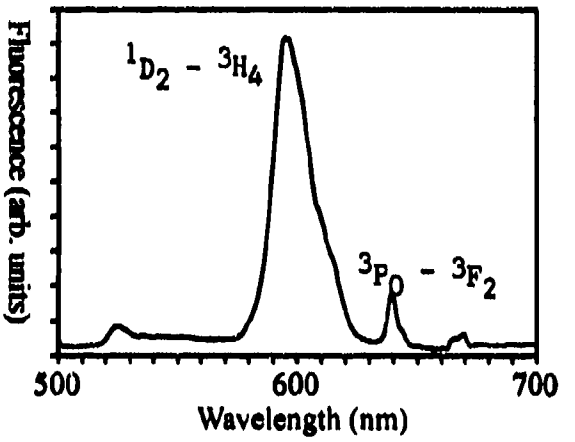

FIGURE 3

Nd^{3+} Fluorescence Spectrum
476nm excitation

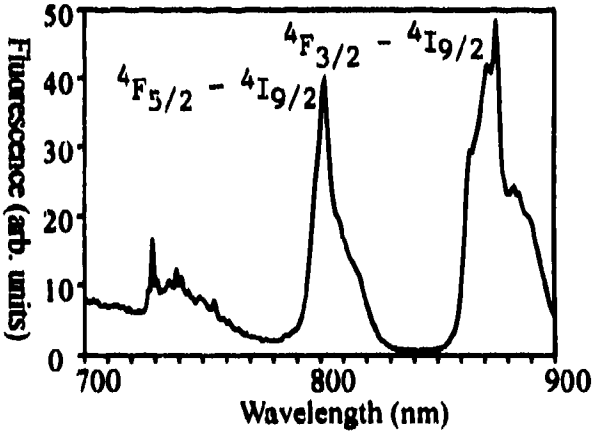

FIGURE 4

Decay of the 805nm and 870 nm
fluorescence

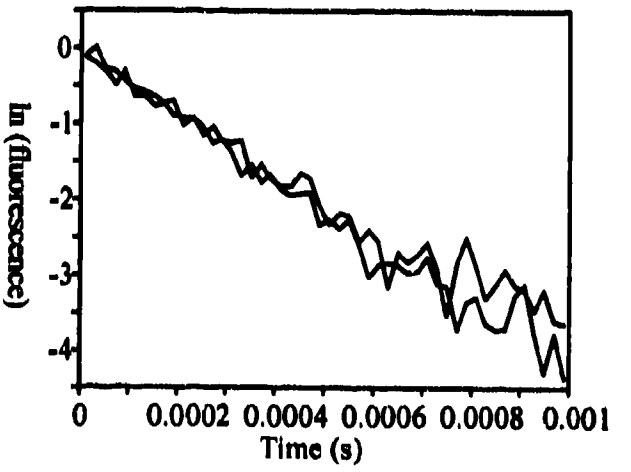

Construction of a nulling bridge-type dispersive interferometric spectrometer in the millimeter wave region

Masanori Hangyo,* Shin-ichi Nakashima,** Yutaka Aoki**, K. Sakai***
*Research Center for Superconducting Materials and Electronics, Osaka University
2-1 Yamadaoka, Suita, Osaka 565, Japan
**Department of Applied Physics, Faculty of Engineering, Osaka University
2-1 Yamadaoka, Suita, Osaka 565, Japan
***Kansai Advanced Research Center, Communication Research Laboratory, M.P.T.
Iwaoka, Kobe-shi, Hyogo 651-24, Japan

ABSTRACT

A nulling bridge-type dispersive interferometric spectrometer has been constructed to measure complex refractive indices of solids in the millimeter wave region. The complex refractive indices of doped Si and GaAs wafers are obtained in the 110 - 170 GHz region and their dispersion is analyzed based on the Drude model. The electrical resistivity estimated from the Drude-model fitting agrees well with that measured by the dc four-point probe method.

1. INTRODUCTION

There has been considerable interest in the spectroscopy in the millimeter and submillimeter wave regions, which lie between the far-infrared and microwave regions. The spectrometers using backward wave oscillators (BWOs) as radiation sources have been developed by several groups.[1-3] These spectrometers have enabled us to obtain complex refractive indices through the measurements of the transmittance and phase shift of the electromagnetic wave after passing through samples. However, these spectrometers are not suitable for opaque samples because of the difficulty in measuring the phase shift of the weak transmitted electromagnetic wave. Further, standing waves formed between sample surfaces and a horn antenna of the radiation source prevent one from measuring the refractive index precisely. Here, we report a newly designed nulling bridge-type interferometric spectrometer, which gives us the reflectivity and the phase shift of the electromagnetic wave reflected by samples. This spectrometer consists of a modified Michelson-type interferometer and avoids the standing wave between the sample surfaces and the horn antenna by the nulling-bridge measurement. Application of the spectrometer to the measurements of the complex refractive indices of relatively highly doped Si and GaAs wafers ($3 \times 10^{14} \sim 7 \times 10^{17}$ cm^{-3}) is demonstrated.

2. PRINCIPLE OF MEASURING COMPLEX REFRACTIVE INDICES

We consider a case in which a electromagnetic wave of a wavelength λ is incident normally on a sample with a complex refractive index $n-i\kappa$ and thickness d. By taking account of the multiple reflections at the sample surfaces, the reflectivity R and phase shift ϕ are expressed as follows,

$$R = \frac{R_0\{(E-1)^2+4E\sin^2 N\}}{(1-R_0E)^2+4R_0E\sin^2(\psi+N)} \quad \text{and} \tag{1}$$

$$\phi = \pi+\psi+\tan^{-1}\frac{E\sin(2N)+R_0E^2\sin(2\psi)-R_0E\sin\{2(\psi+N)\}}{E\cos(2N)-1-R_0E^2\cos(2\psi)+R_0E\cos\{2(\psi+N)\}}, \tag{2}$$

where

$$\sqrt{R_0}\exp(-i\psi) = \frac{1-n+i\kappa}{1+n-i\kappa}, \quad E = \exp(-4\pi\kappa d/\lambda) \text{ and } N = 2\pi nd/\lambda.$$

Since R and ϕ are a function of only n and κ, n and κ are obtained from the measured values of R and ϕ.

3. A NULLING BRIDGE-TYPE INTERFEROMETRIC SPECTROMETER

Figure 1 shows a nulling bridge-type interferometric spectrometer for measuring the reflectivity and phase shift of the electromagnetic wave reflected by the sample. The millimeter wave generated by BWO (Siemens RWO170S) and emitted into a free space from a horn antenna L is focused by a ellipsoidal mirror M_1 with a focal length of 147.6 mm. The vertically polarized millimeter wave passes through a beam splitter BS_1 (wire grid) and is divided by a beam splitter BS_2 into two beams (sample and reference beams) being cross-polarized with each other. The sample beam is reflected by a sample with reflectivity R and accompanying a phase shift ϕ. The reference beam is reflected by a mirror O, which is made of a wire grid. The intensity and phase of the reflected beam are changed by rotating the wire grid (see Fig. 1) and translating O along the optical

path, respectively. The beams reflected by the sample and mirror O are deflected by BS_1 and detected by a pyroelectric detector D. The mirrors M_2, M_3 and M_4 are ellipsoidal mirrors of the same type with M_1. The sample arm (M_2 and the sample), the reference arm (M_3 and O) and BS_2 compose a Michelson-type interferometer. The signal of the detector becomes zero when the waves from the two arms are out of phase with each other and balanced in intensity. R and ϕ can be obtained from the rotation angle of the wire grid and the position of the reference mirror which give zero output. The arrangement of the wire grids is shown schematically in the figure. By inserting a polarizer P, one can avoid the beams reflected from the sample and O to return to a horn antenna when the signal of the detector is zero, and this prevents the undesired influence of the standing wave formed between the sample surfaces and the horn antenna on the measurements.

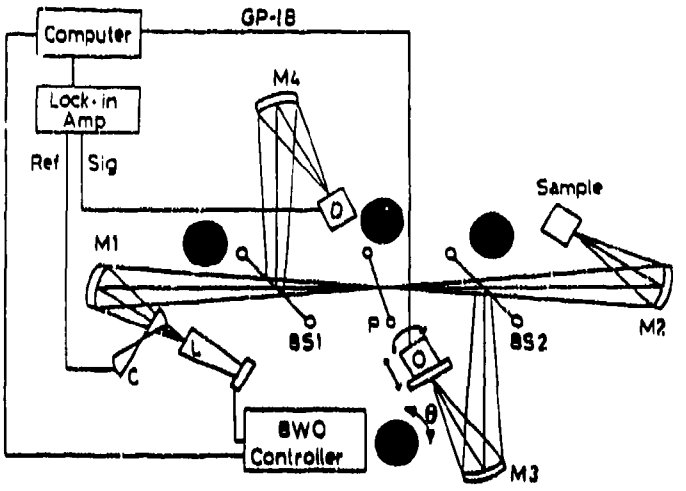

Fig. 1. Scematic diagram of the nulling bridge-type interferometric spectrometer.

4. MEASUREMENTS OF COMPLEX REFRACTIVE INDICES OF SI AND GaAs WAFERS

The complex refractive indices measured for an n-type Si wafer with resistivity 0.13 Ωcm are shown in Fig. 2. It is difficult to measure the complex reflective index of this sample by our Mach-Zehnder type interferometric spectrometer because of the weak intensity of the transmitted wave.[4] The refractive index n is considerably larger than the value of 3.42 of Si wafers with high resistivity (> 100 Ωcm). The solid lines show fitting by the Drude model, in which the density and relaxation time of carriers are taken as parameters. We have measured the complex refractive indices of Si and GaAs wafers with dc resistivity ρ_{dc} of 10^{-3} ~ 10 Ωcm. The resistivity can be obtained from the equation, $\rho_{exp} = m^*/Ne^2\tau$, where N, τ and m^* are the density, relaxation time and effective mass of carriers, respectively, and e is the electronic charge. The agreement between ρ_{dc} and ρ_{exp} is good, which demonstrates the usefulness of the nulling bridge-type interferometric spectrometer for measuring resistivity of semiconductors of 10^{-3} ~ 10 Ωcm. Together with the Mach-Zehnder type interferometric spectrometer,[4] resistivity of semiconductors in the range of 10^{-3} ~ 3×10^3 Ωcm can be measured contactlessly by the millimeter waves.

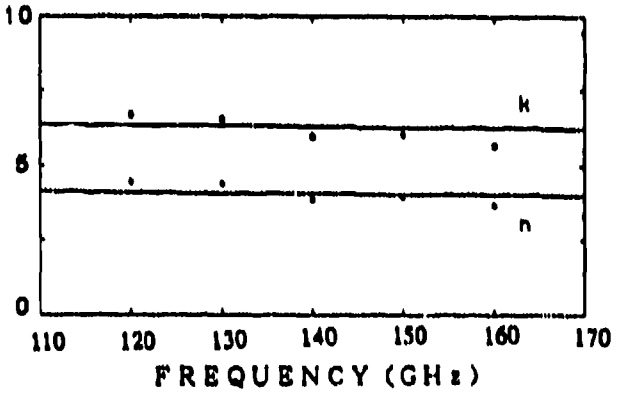

Fig. 2. Complex refractive indices of the Si wafer with the dc resistivity of 0.13 Ωcm.

REFERENCES

1. G.V. Kozlov, A. M. Prokohlov and A. A. Volkov, Problems in Solid-State Physics, Chapter 1, ed. by A. M. Prokholov and A.S. Prokholov, Physics Series, MIR Publishers, Moscow, 1984.

2. L. Genzel, A. Poglitsch and S. Häseler, "A Dispersive Polarizing MM-Wave Interferometer", Int. J. Infrared and Millimeter Waves, vol. 6, pp. 741-750, Aug. 1985.

3. S. Nakashima, T. Hattori, M. Hangyo, A. Yamamoto, K. Sakai, A. Mitsuishi and S. Hashimoto, Oyo Buturi, vol. 59, pp. 1093-1102, Aug. 1990.

4. M. Hangyo, N. Hasegawa, T. Matsuzawa, S. Sonoda, T. Hattori, K. Sakai and S. Nakashima, Conf. Digest of 5th Int. Conf. on Infrared and Millimeter Waves, pp. 271-273, Florida, December 1990.

MILLIMETER WAVE RADAR ABSORBING MATERIALS*

Mohammed N. Afsar and Hua Chi

Tufts University
Department of Electrical Engineering
Medford, Massachusetts 02155 - 5528

ABSTRACT

It was anticipated that ferrimagnetic hexagonal compounds such as $BaFe_{12}O_{19}$, $SrFe_{12}O_{19}$ and $SrAl_2Fe_{10}O_{19}$ have magnetic resonance absorptions at frequencies beyond 30 GHz. We have mixed powder specimens of such materials and deposited in paint form on one surface of a optically polished fused silica glass substrate. The ferromagnetic resonance was then studied as functions of applied external magnetic field intensity, specimen thickness and continuous frequency at millimeter wavelength region. A new dispersive Fourier transform spectrometer was designed and constructed to measure the real and imaginary parts of complex magnetic permeability and real and imaginary parts of complex dielectric permittivity as a continuous function of frequency from about 10 mm wavelength to up to one millimeter wavelength range.

INTRODUCTION

It is necessary to separate out two magnetic parameters from two dielectric parameters either experimentally or by the use of perturbation theory. It is preferable to use the experimental separation at millimeter wavelength region. The experimental separation utilizes the induced ferromagnetic resonance phenomena and the quenching of the magnetic effect at frequencies below the resonance frequency. It is explained here. A spinning electron in a magnetic field has a precessional frequency $\omega_0 = \gamma H$, where γ is the gyromagnetic ratio and H is a vector summation of the d-c magnetic field within the material icluding the field induced by an external magnetic field perpendicular to the material and an a-c microwave magnetic field of frequency ω. The a-c field must be applied at right angle to the d-c field. The power of the a-c field can be much smaller than the d-c field, but the angle if of great concern. The condition of the magnetic resonance is $\omega = 2\pi f = \gamma H$. If the resonance condition is satisfied, we will have the corresponding magnetic resonance by changing the value of the external applied magnetic field intensity. It is important that we have a continuous coverage of frequency from microwave to submillimeter wave range to observe the shifting of the induced resonance line towards higher frequency as the applied magnetic field intensity is increased. With a large value of external applied magnetic field intensity (e.g. 110,000 gauss), the induced resonance line position for a cubic ferrite material will move to about 330 GHz. Below about 270 GHz, the material will be free from any magnetic effect. The use of dispersive Fourier transform technique will then yield continuous data of the real (ε') and imaginary (ε'') parts of complex dielectric permittivity over the frequency range 30 - 270 GHz. The application of dispersive Fourier transform spectroscopy on a magnetic specimen without the influence of external magnetic field yields data in which the real (μ') and imaginary (μ'') parts of complex magnetic permeability contributions are also present together with real (ε') and imaginary (ε'') parts of complex dielectric permittivity. Once one set of data (ε' and ε'') are known, the other set (μ' and μ'') can simply be separated out from combined data. via Maxwell's equations

* This research program is supported by the U.S. Army, Contract Number DAHC90-93-C-0027

INSTRUMENTATION

The use of a larger optics (100mm), doubling of usual mercury lamp source power and a guiding optics enabled us to increase the energy throughput of a Fourier transform spectrometer at 30 GHz. A new indium antimonide detector was fabricated to absorb more energy at millimeter wavelength region. A bridging technique was utilized to translate optical energy to gigahertz region. We have not reported any result with the new detector yet. Results presented in this paper was obtained with a standard indium antimonide detector.

SOME EXPERIMENTAL RESULTS

Figures 1-4 show data as a continuous function of frequency over the frequency range 40 - 210 GHz for a $SrAl_2Fe_{10}O_{19}$ for the real and imaginary parts of complex dielectric permittivity and real and imaginary parts of complex magnetic permeability. Figure 2 suggests that a strong broad-band microwave-millimeter wave dielectric absorption band is present in this material. The imaginary parts of magnetic permeability spectrum shows a magnetic resonance absorption at about 70 GHz and the corresponding dispersion through the resonance band can be seen in the real part of permeability data

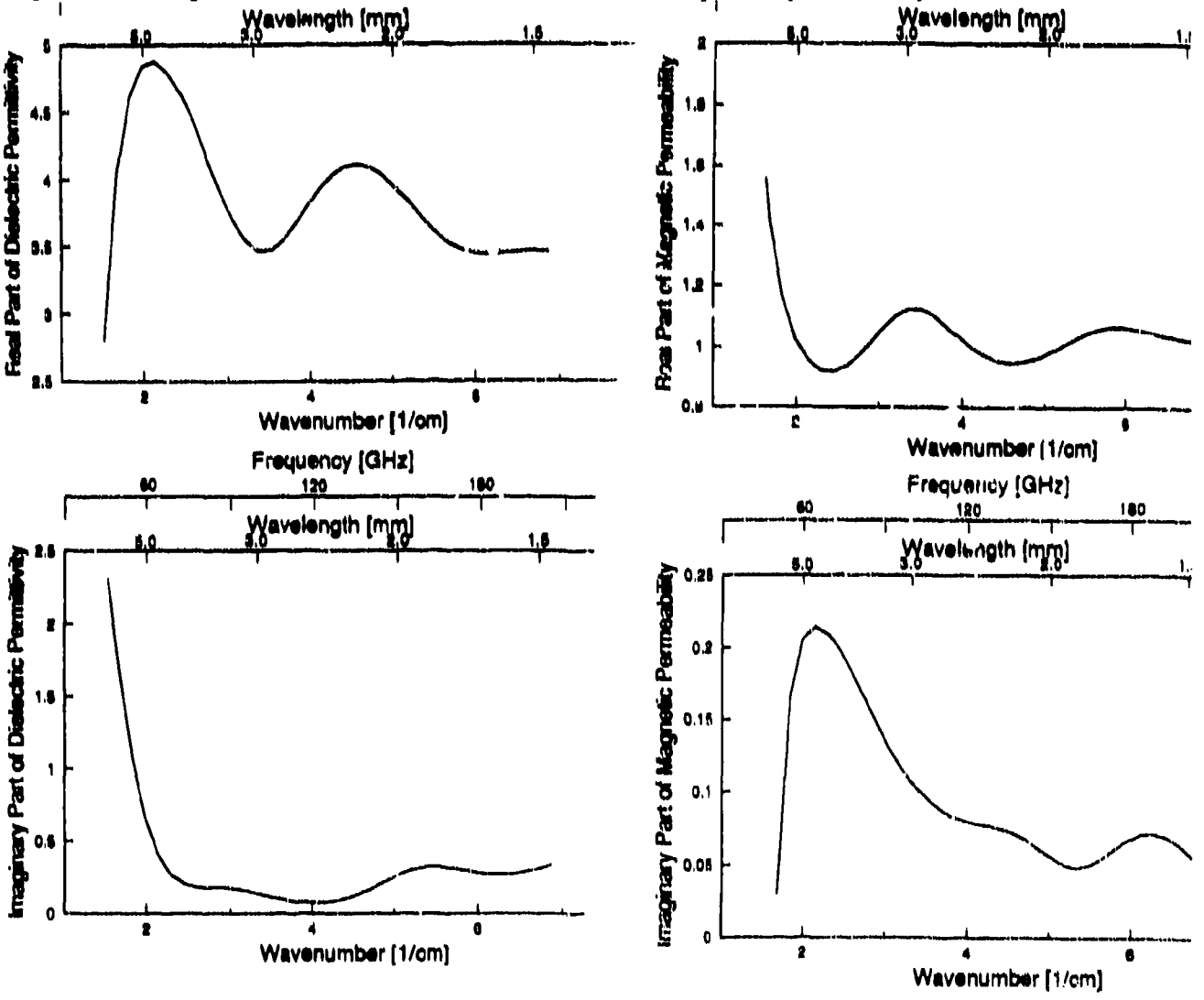

Development of broadband vacuum windows for high-power millimeter wave systems

H.-U. Nickel *, H. Massler, M. Thumm *

Universität Karlsruhe, Institut für Höchstfrequenztechnik und Elektronik
Kaiserstraße 12, D-76131 Karlsruhe, Germany
* also Kernforschungszentrum Karlsruhe, Institut für Technische Physik
P.O. Box 3640, D-76021 Karlsruhe, Germany

ABSTRACT

Frequency agile sources for future electron cyclotron wave (ECW) systems require broadband windows that are suitable for high-power transmission (> 0.5 MW) in the millimeter wave range. While the relative bandwidths of single-disk or double-disk windows used in conventional monofrequent systems are of the order of 1 %, the future systems require for bandwidths of 10 % or even more (e.g. > 60 % for the FOM-Fusion-FEM [1]). A description of the different window types under consideration and first results of a development of suitable windows have been reported in [2]. This paper presents an improved test apparatus as well as our latest experimental and theoretical results about broadband windows.

2. APPARATUS FOR LOW-POWER TESTS

For experimental investigations a test apparatus is required which provides swept frequency measurements of reflection and transmission of a fundamental Gaussian beam (TEM_{00}) on a window under test (WUT). The setup described in [2] has been improved by modifications that substantially increase the dynamic range for reflection measurements. Fig. 1 shows the new setup. It uses the scalar network analyzer (SNA), described in detail in [3], which has been modified to offer a transmission dynamic range of > 70 dB. The SNA has been connected to a Gaussian beam path that includes a quasi-optical directional coupler (QDC) composed of a dielectric beam splitter and a low reflectivity absorber. From source port A of the SNA the generated millimeter wave signal is fed to a scalar feed horn where it is converted to a TEM_{00} beam. This beam is guided via a 1st ellipsoidal metallic mirror, through the QDC (located in the 1st beam waist), and via a 2nd mirror towards a 2nd beam waist where the WUT is located. The portion of the incident beam transmitted by the WUT is matched by mirror 3" to the transmission horn connected to the receiver port B of the SNA. The portion of the incident beam reflected at the WUT reaches mirror 3' via mirror 2 and the coupling path of the QDC. Mirror 3' refocusses the beam towards the reflection horn connected to port B. The selection between transmission and reflection measurements is performed by a waveguide switch at the receiver port. For reflectometry the beam has to be dissipated behind the window by a sufficiently low-reflecting absorber. Since all the horns and mirrors are arranged confocally, the frequency dependence of the size and the location of the beam waists where the WUT and the receiving horns are located is cancelled out (see e.g. [4] for Gaussian beam telescope). Whereas in the previous setup the dynamic range for reflection measurements was limited by the directivity of the waveguide directional coupler to about 25 dB, the QDC now provides a dynamic range of > 60 dB over almost the full frequency range of 117 to 147 GHz (Fig. 2). The high directivity of the QDC is determined by the extremely low reflectivity of the absorber used (Brewster plate made of Macor, $d \approx 10$ mm, backed with absorbing foam).

3. EXPERIMENTS

Fig. 3 shows the results obtained with a window made of polycrystalline (p.c.) Al_2O_3 ceramics ($\varepsilon_r = 9.65$) where both surfaces are corrugated with parallel grooves having almost rectangular cross section. The electric field vector was oriented parallel to the grooves. For numerical calculations [5] it has been assumed that the window is composed of 221 thin dielectric layers (grooves: 2×110, center: 1) each having a homogeneous effective permittivity ε_{reff}. For each layer ε_{reff} has been determined by $\varepsilon_{reff} = (a+(d-a)\varepsilon_r)/d$ with the groove spacing d and the groove width a from the geometry of the real profile.

Figs. 4 and 5 show results obtained from an antireflection coated window designed for a center frequency of 140 GHz. Fig. 4 shows the reflectivity of the pure substrate. Fig. 5 gives the reflectivity of the window assembled with the coatings. Although this type of window already meets most of the bandwidth requirements it is not suitable for high-energy transmission due to its rather large total absorptivity of > 1 %.

4. REFERENCES

1. A.G.A. Verhoeven et al., Status of the design of the 200 GHz FOM-Fusion-FEM, see this conference.
2. H.-U. Nickel, U. Ambrosy, M. Thumm, Dig. 17th Int. Conf. IR&MM Waves, Pasadena, SPIE 1929, pp. 462-463, 1992.
3. T. Geist, G. Hochschild, W. Wiesbeck, Proc. 18th European Microwave Conf., Stockholm, pp. 339-343, 1988.
4. P.F. Goldsmith, Quasi-optical techniques at millimeter and submillimeter wavelengths, in K.J. Button (Ed.), *Infrared and Millimeter Waves*, Vol. 6, Academic Press, New York, pp. 277-343, 1982.
5. H.-U. Nickel, M. Thumm, Dig. 16th Int. Conf. IR&MM Waves, Lausanne, SPIE 1576, pp. 444-445, 1991.

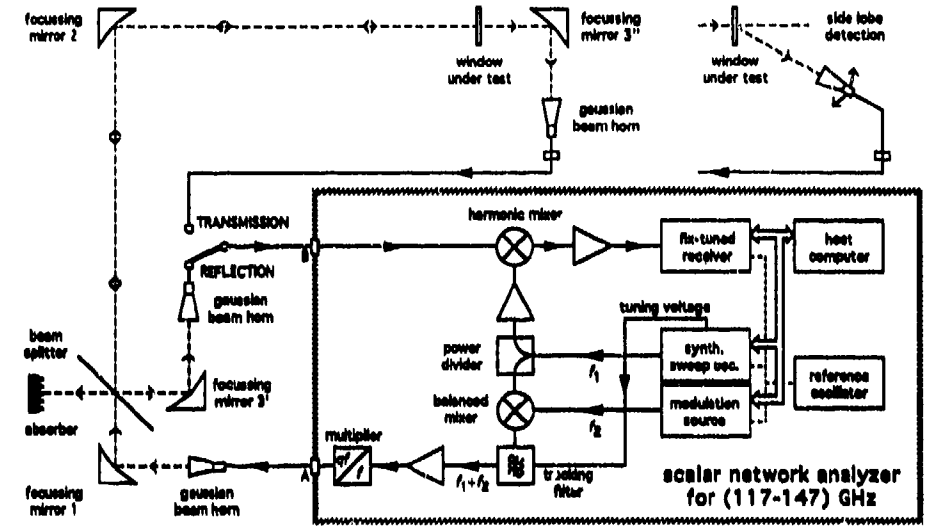

Fig. 1: New apparatus for measuring the frequency dependence of reflection and transmission of a fundamental Gaussian beam (TEM_{00}) in windows.

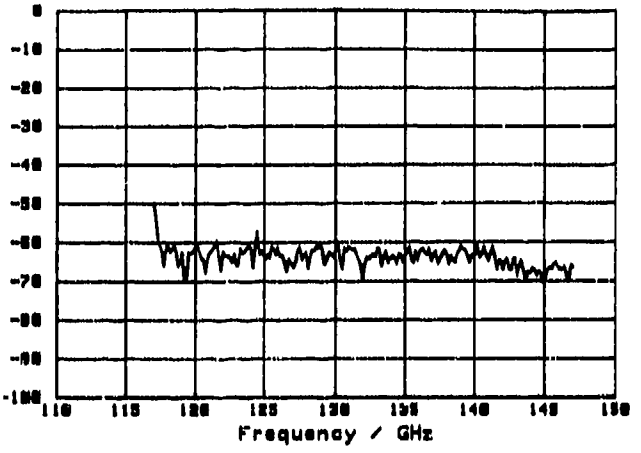

Fig. 2: Minimum detectable reflectivity (in dB) for TEM_{00} achieved with the new apparatus.

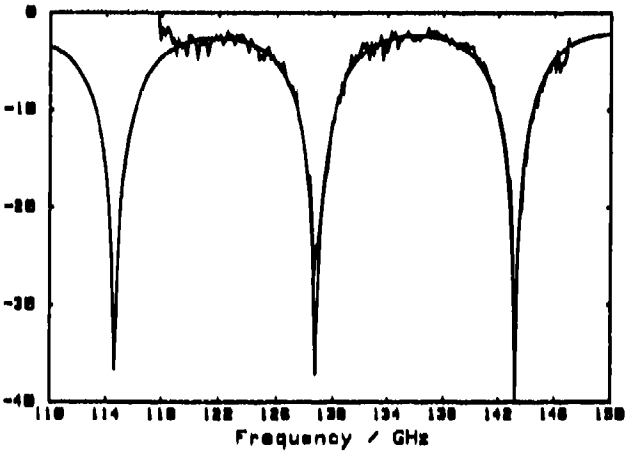

Fig. 3: Measured and calculated reflectivity (in dB) of a p.c. alumina disk. Both surfaces are corrugated with parallel grooves having almost rectangular cross sections (E ∥ grooves).

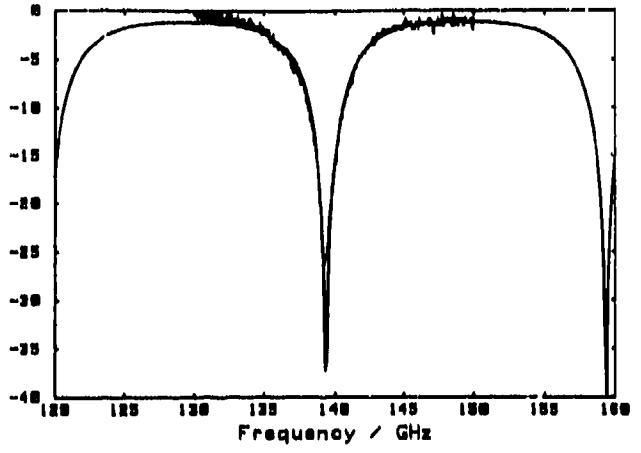

Fig. 4: Measured and calculated reflectivity (in dB) of a pure substrate disk made of D-15 Mg-Ti ceramics from Trans-Tech Inc. (d_S = 1.91 mm and ε_{rS} = 15.5).

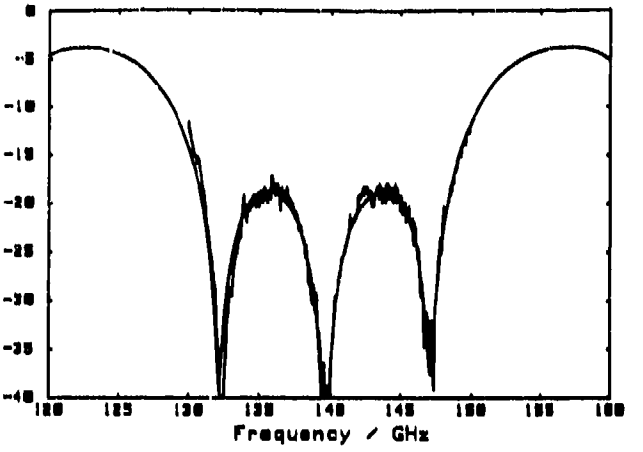

Fig. 5: Measured and calcul. reflectivity (in dB) of a coated window: Substrate as in Fig. 4; Coatings made of fused SiO_2 (Infrasil 1) from Heraeus Inc. (d_C = 0.82 mm and ε_{rC} = 3.81).

The optical constants, at elevated temperatures, of some potential window materials for high power and plasma diagnostic applications

J.R.Birch, E.A.Nicol, T.P.Hughes* and D.V.Bartlett*

Division of Electrical Science, National Physical Laboratory
Teddington, Middlesex TW11 OLW, UK

*JET Joint Undertaking, Abingdon, Oxfordshire OX14 3EA, UK

ABSTRACT

The temperature dependence of the near millimetre wavelength optical constants of some potential window materials for fusion plasma diagnostics, including high power applications, are discussed. The measurements cover the frequency region from 90 to 450 GHz, with specimen temperatures from 20 to 1000 C.

1. INTRODUCTION

At the present time various vacuum windows for use in millimetre wave diagnostics on JET are being replaced or installed. Some of these windows will be double element structures with a vacuum interspace in order to safeguard the integrity of the main torus vacuum, others will be single elements. In either case it will be necessary to optimise several window characteristics, aiming at invariance of transmission with radiation frequency (no rapid changes due to channel fringes), insensitivity of optical performance to temperature over a large range, low reflection losses, visible alignment of the diagnostic system, and the ability to handle high millimetre wave powers and avoid thermal runaway effects.

In order to achieve such optimisation it is necessary to have available quantitative information on the temperature dependence of the spectral variation of the optical constants of potential window materials. As there is little such data available in the literature this paper will present the results of such measurements on a number of materials relevant to some of the JET diagnostics. The general measurement requirements include the following: to cover frequencies from 70 to 250 GHz with a resolution of 30 GHz, to achieve measurement temperatures between 20 and 1000 C both with an absolute accuracy and a uniformity across the window of ±10 C for temperatures <250 C and ±20 C for higher temperatures, to have a measurement geometry in which the radiation passing through the window has a near plane wavefront.

2. EXPERIMENTAL

Measurements were made of the optical constants of a number of materials of interest using the technique of dispersive Fourier transform spectroscopy[1-3]. In this the specimen is placed within one of the two active arms of a two beam interferometer and its complex insertion loss measured. The optical constants can then be calculated without approximation from the insertion loss. The interferometer used for this work was a polarising wire grid instrument with an electrically heated furnace built into the fixed mirror arm.[4]

With this spectrometer measurements could be made over the frequency region from about 90 GHz to 2 THz, although in this work it was only used to 450 GHz. The furnace was such that measurement temperatures from ambient room temperature up to 1100 C could be achieved.

3. RESULTS

Typical measurements of the refraction spectrum of a low water content fused silica (Petrosil) at tempertures between 20 and 1000 C are shown in figure 1. The data were not corrected for thermal expansion from the room temperature thickness. However, calculations based on typical values for the coefficient of linear expansion indicate that the 1000 C spectrum of figure 1 would be 0.0004 too high. The spectra shown were each the average of 6 independent determinations. Their reproducibility was such that the level of random error in the measurements was less than 0.0001, well below the measurement requirement. In the presentation the results of such measurements on both the refraction and absorption spectra of a number of materials will be presented and discussed.

REFERENCES

1. J.R.Birch and T.J.Parker, 'Infrared and Millimeter Waves, Vol.2, Ch.3', Ed. K.J.Button, Academic Press, New York 1979.

2. J.R.Birch, Mikrochimica Acta III, 105, 1987.

3. T.J.Parker, Contempory Physics 31, 335, 1990.

4. E.A.Nicol and J.R.Birch, presented at this conference.

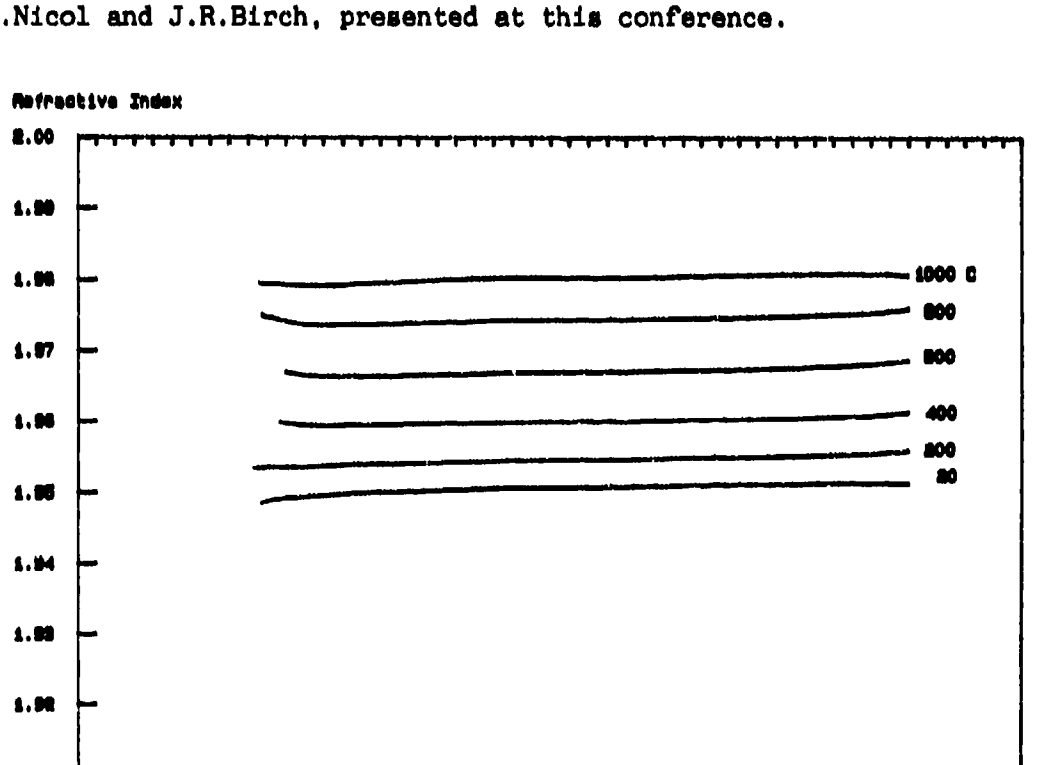

Figure 1. The refraction spectrum of a Petrosil specimen at temperatures from 20 to 1000 C.

ANTI-REFLECTION TREATMENTS FOR JET MILLIMETRE WAVE DIAGNOSTIC WINDOWS

T P Hughes, S D Richards and D V Bartlett
JET Joint Undertaking, Abingdon, Oxfordshire OX14 3EA, UK

This paper discusses low-power windows for millimetre-wave diagnostics on the JET torus. When tritium is used as a fusion fuel in JET repairs will be difficult on the radioactive machine and additional precautions must be taken to avoid vacuum leaks. Double, interpumped vacuum windows will be necessary. Window design is further restricted by the requirement that the bond between the window itself and its supporting ferrule must withstand repeated cycling to a working temperature of about 250° C. The most satisfactory arrangement for low power millimetre waves uses z-cut crystal quartz windows, gold diffusion bonded to stainless steel ferrules, as manufactured by the Special Techniques Group of A E A Technology. Where possible wedged windows are avoided for ease of alignment.

Even with a single window multiple reflections cause the transmission to be significantly frequency dependent. Figure 1(a) shows the calculated intensity transmission spectrum for a 6 mm quartz window, assuming n = 2.1 over the frequency range. With double windows the additional reflections in the multiple etalons cause the transmission to be strongly frequency dependent and create severe problems for the diagnostic systems. Temperature effects are also important. Figure 1(b) shows the intensity transmission spectrum for two 6 mm windows separated by 5 mm.

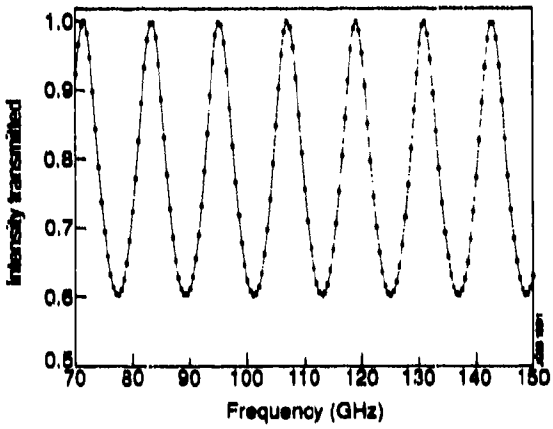

Figure 1(a)

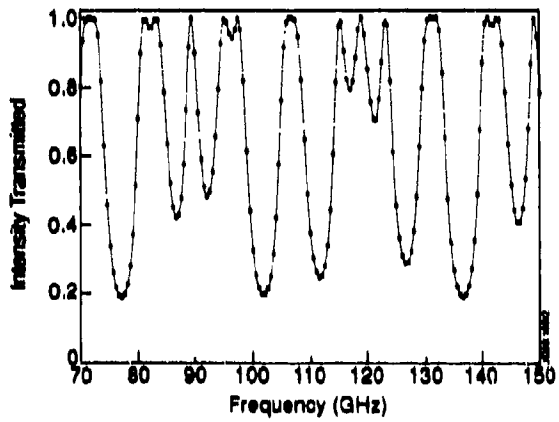

Figure 1(b)

In principle there are several ways to improve the transmission spectrum, but the various millimetre wave diagnostics on JET operate over different frequency ranges, with different resolutions, and must be considered separately. The most generally useful approach would be to treat each of the window surfaces to create a refractive index gradient, such as the "moth eye" structure described by Ma and Robinson [1]. This would, however, weaken a crystalline window substantially and would be unlikely to be acceptable on JET. A possible variant would be to create such a structure on an independent plate of similar refractive index to the crystal quartz and attach it with a thin layer of adhesive.

For the receiver of the alpha particle and fast ion collective scattering diagnostic (J A Hoekzema et al., this conference) the use of quarter wave layers of suitable refractive index would give good results over the 134 to 146 GHz frequency range of interest. The surface facing the torus vacuum will probably have to be left uncoated. Figures 2(a) and (b) show the transmission spectrum for two windows of optical thickness 6 λ at 140 GHz, with $\lambda/4$ layers on all but the first surface, separated by a gap of 2½ λ. The transmission varies by less than $\pm 1\%$ over the frequency range 134 to 146 GHz (Figure 2a), but over the wider range used for ECE diagnostics this solution is unsatisfactory (Figure 2b).

A suitable material for the $\lambda/4$ layer must withstand temperatures up to 250°C and will have the following properties:

1. refractive index near the square root of that of crystal quartz at the working temperature
2. thermal linear expansion coefficient similar to that of crystal quartz
3. low absorption near 140 GHz.

Measurements on possibly suitable plastics are now in progress at NPL (J.R.Birch et al., this conference).

An alternative solution for the collective scattering diagnostic is to tilt one (or both) windows and separate them so that there is no reflection from the second to the first. The two window etalons are now independent and the overall power transmission is the product of the individual transmissions. If one window has a maximum and the other a minimum in transmission at 140 GHz, the result is a smooth transmission spectrum over the range of interest, but at the cost of some polarization dependence and the loss of about half the power. Figure 2(c) shows the calculated result for two quartz windows, thicknesses 6.074 and 6.339 mm inclined at 20° to the beam axis.

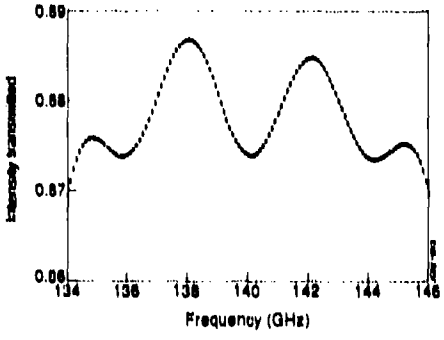

Figure 2(a)

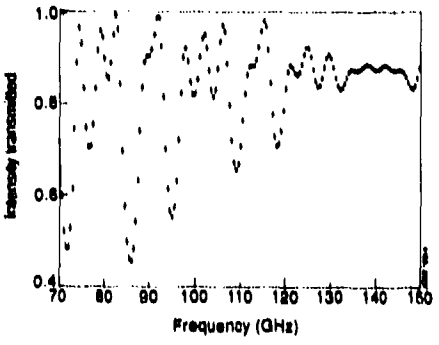

Figure 2(b)

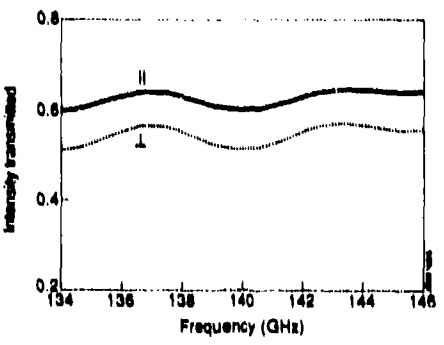

Figure 2(c)

Provided the frequency resolution required is no better than 5 or 10 GHz, it is possible to obtain a flat transmission spectrum over a wide bandwidth, as required for the ECE Michelson interferometer diagnostic, by using very thick windows with a large spacing instead of the usual wedged windows. Figure 3(a) shows the transmission spectrum of two quartz windows 100 mm thick separated by a space of 210 mm (such an assembly might be constructed within a waveguide). Averaging over 5 GHz channel bandwidths removes the fine structure and gives the almost flat spectrum shown in Figure 3(b). There is however a power loss of about 30%.

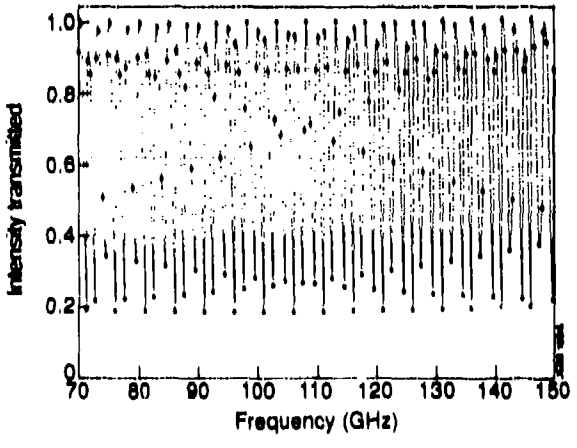

Figure 3(a)

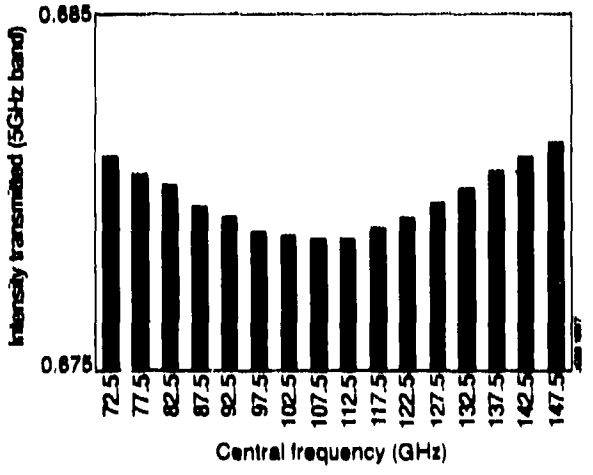

Figure 3(b)

The most difficult problem arises with the ECE heterodyne radiometer, which has high resolution (250 to 500 MHz) over a wide bandwidth (70 to 140 GHz). The development of a moth eye structure seems to be the most promising solution.

Acknowledgements. We are grateful to Dr J R Birch, Dr A E Costley and Dr J A Hoekzema for helpful discussions.

Reference Ma, J Y L and Robinson, L C, Optica Acta 30, 1685 (1983)

Electrical Analysis of Wideband and Distributed Windows Using Time-Dependent Field Codes

C. C. Shang and M. Caplan, University of California,
Lawrence Livermore National Laboratory, Livermore, California, USA

H.-U. Nickel and M. Thumm, IHE Universität Karlsruhe and
ITP Kernforschungszentrum Karlsruhe, Germany

Introduction

Windows, which provide the barrier to maintain the vacuum envelope in a microwave tube, are critical components in high-average-power microwave sources, especially at millimeter wavelengths. As RF power levels approach the 100's of kWs to 1 MW range (CW), the window assembly experiences severe thermal and mechanical stresses. Depending on the source, the bandwidth of the window may be less than 1 GHz for gyrotron oscillators or up to ~20 GHz for the FOM Institute's fast-tunable, free-electron-maser [1]. The bandwidth requirements give rise to a number of window configurations where the common goal is locally distributed heat dissipation. In order to better understand the transmission and RF properties of these microwave structures, we use detailed time-dependent field solvers.

Field Codes

A number of time-dependent field solvers [2] have been developed to examine wakefields in electron and heavy ion accelerators as well as traditional scattering and radiation problems. These algorithms work both on logically regular as well as completely unstructured meshes. The basic algorithm has also been modified to handle both magnetically and electrically dispersive materials. Typically, the numerical solutions are second order accurate and conditionally stable. The practical limitation to application of the codes involves the electrical size of the structure to be modeled. To obtain the proper spectral resolution requires ~10 mesh points per wavelength corresponding to the highest frequency of interest. In practice, large computational problems in 3-D (volumetric) are $10^3\ \lambda^3$ in size.

Application and Results

An ongoing window program at KfK has been aimed at developing high-power, broadband windows [3]. As a start in analyzing wideband windows using general field codes, we examined the corrugations in the concentric grooved window (Figure 1). The groove period is $\lambda/3$ and the groove depth is λ referenced to 140 GHz in free space. We launched a TE_{01} (E parallel to grooves), 140-GHz (±20% in frequency) pulse and obtained 98% transmission in power (Figure 2). Adiabatic theory was inadequate to account for the physics of the match. In fact, the corrugations were found to focus the RF into the bulk dielectric portion of the window. As can be seen in Figure 3, the peak field intensity occurs in the corrugations.

A cropped, adiabatically tapered window with almost triangular corrugations (rectangular symmetry) was fabricated and cold-tested at KfK. The calculational results were obtained by exciting single-frequency, x-directed electric currents, thereby launching waves with E perpendicular to the grooves. A key aspect for maintaining stability of the solution was to place the radiating boundary conditions several wavelengths from the scattering surface of the window. This prevented interaction of the evanescent fields with the numerical radiation boundary condition. For diagnostic purposes, at appropriate transverse slices on the vacuum side of the window, $E \times H$ is computed and summed over the surface directly from the field values. Good qualitative agreement between cold-test reflection data and calculational results can be found in Figure 4. It should be possible to obtain closer

---

Work performed under the auspices of the U.S. Department of Energy by the Lawrence Livermore National Laboratory under Contract W-7405-Eng-48.

correlation to measurements through better geometrical fidelity in the model (e.g., finer, unstructured mesh). However, examination of solution convergence awaits further analysis.

We are currently examining the electrical effects of introducing distributed cooling that are discontinuous material junctions in window structures. The materials include metal cooling strips or dielectric cooling channels. By exploiting the focusing effect of the corrugations, we hope to obtain good transmission characteristics over a wide bandwidth.

Future work will involve coupling the RF calculations for the window assembly to thermal-mechanical codes. A further goal will be to set up the capability of running the EM field codes in pulse mode in order to obtain spectral resolution in the transmission curves proportional to the length of simulation time in only a single run.

ACKNOWLEDGMENTS

Stimulating discussions with Prof. J. Feinstein of Stanford University and Dr. C. Moeller of General Atomics are gratefully acknowledged.

REFERENCES

[1] K. S. Yee, "Numerical Solution of Initial Boundary Value Problems Involving Maxwell's Equations in Isotropic Media," IEEE Trans on APS, AP-14, May 1966, pp. 302-307.

[2] A. G. A. Verhoeven, *et al*, "Status of the Design of the 200 GHz FOM-Fusion-FEM," *Proceedings of the 18th International Conference on IR and MMWs*, Essex, England, 1993.

[3] H.-U. Nickel, H. Massler, and M. Thumm, "Development of Broadband Vacuum Windows for High-power Millimeter Wave Systems," *Proceedings of the 18th International Conference on IR and MMWs*, Essex, England, 1993.

Figure 1.

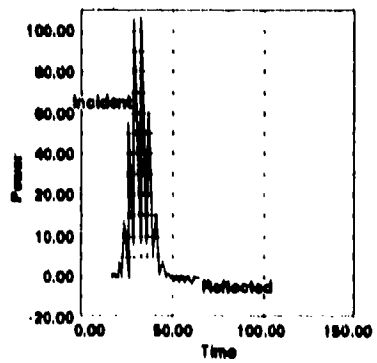

Figure 2.

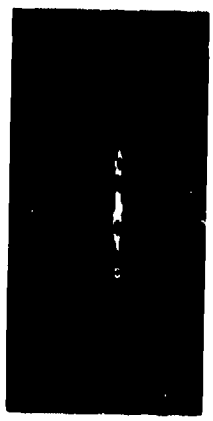

Figure 3.

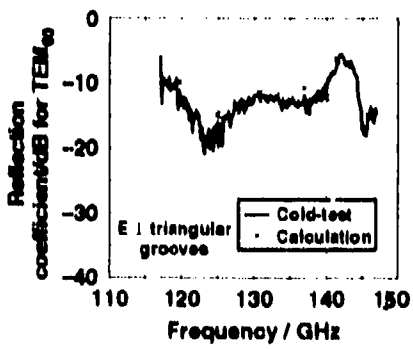

Figure 4a.

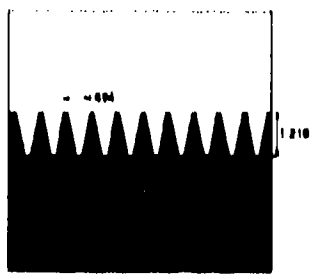

Figure 4b.

On the use of a Hybrid Mode Mixture for Lowering the Thermal Load Peak in Ceramic Windows for MM-Wave ECRH Experiments

F. Billè *, S. Cirant **, L. Manià *, G. Solari **, G. Viciguerra *

(*) DEEI - Università di Trieste - Via A. Valerio 10 - 34127 TRIESTE - Italy
(**) Istituto di Fisica del Plasma - Assoc. EURATOM-ENEA-CNR, Via Bassini 15 -20133 MILANO - Italy

1. Abstract

In mm-wave systems for ECRH using the HE_{11} hybrid mode, the maximum transmitted power is limited by the strongly peaked thermal load in the vacuum barrier window. In this paper we present mode converters at 140 GHz which create a mixture of HE_{1N} hybrid modes in corrugated waveguides. Such a mode mixture yields a more uniform power density than HE_{11} mode in the section where the window is placed, and a Gaussian distribution at the waveguide aperture.

2. Introduction

Corrugated circular waveguides carrying the hybrid HE_{11} mode are generally used in the mm-wave ECRH experiments as high power transmission lines. Besides the good features of low propagation losses, linear constant polarization and Gaussian beam-like radiation pattern, the HE_{11} mode has the disadvantage of having a power density distribution which is highly concentrated around the center of the waveguide cross-section. As a consequence, a highly peaked thermal load heats the central part of the ceramic barrier window. Moreover, it is difficult to remove heat from that region, since the cooling system is located around the periphery of the window. In the next section we will show how a more uniform power density distribution can be achieved by a mixture of hybrid modes, still preserving the fundamental good features of the HE_{11} mode. Reference is made to a system operating at 140 GHz with a standard circular corrugated waveguide with inner radius a=44.45 mm.

3. Hybrid mode mixture.

Let us consider an electric field **E** consisting in a linear superposition of hybrid modes which can propagate inside the corrugated waveguide. The well known expressions of the components of these fields [1] reveal that **E** will preserve the above mentioned HE_{11} features if only the modes of HE_{1k} type will be included in the superposition. Therefore we focus our attention on such fields **E** as given by:

$$\mathbf{E} = a_{11}\mathbf{e}_{11}^{HE} + \sum_{k=2,\,N} a_{1k}\mathbf{e}_{1k}^{HE} \qquad (\mathbf{e}_{1k}^{HE} \text{ is the electric field of the } HE_{1k} \text{ mode}) \qquad (1)$$

Our problem is to search for a set $\{a_{1k}\}$ giving (in a specific section of the waveguide) a peak of **E** significantly lower than that of HE_{11} mode, when **E** and the HE_{11} mode are carrying the same power. Fig. 1 illustrates the behaviour of $|\mathbf{E}|^2$ versus the normalized radial coordinate r/a, for an optimized mixture with N=2 and 3. In particular, a combination of the HE_{11} and HE_{12} modes alone, with coefficients $a_{11} = 1.$ and $a_{12} = -0.305$ allows halving the peak of $|\mathbf{E}|^2$ (noting that the two modes are out of phase); the peak is located at r=0.5a. In a section of the waveguide 0.5 λ_B faway from the window the HE_{11} and HE_{12} modes are in phase (λ_B is the beat -wavelength: for a radius a=44.45 mm, λ_B=2.9 m).In this section the field pattern is very well matched (up to 99.9 %) to a free space Gaussian beam with a waist $w_0 = 0.504$ a.The corresponding radiation patterns are shown in fig. 2.

4. Quasi-optical mode converter.

Fig. 3 shows the geometry of a quasi-optical mode converter which transforms the HE_{11} mode into the HE_{11}-HE_{12} optimum mixture. The mode converter is based on the above-mentioned matching of the HE_{11}-HE_{12} mixture to a free space Gaussian beam with $w_0 = 0.504$ a. Since the waist of the Gaussian beam corresponding to the HE_{11} mode is 0.643 a, a shaped mirror is used to narrow the waist of the reflected Gaussian beam and to focus it over the input section of waveguide B. At a distance of 0.5 λ_B from this

section, the two modes will be out of phase, i.e., in the best condition for crossing the ceramic window; at a distance of 1 λ_B they will be again in phase, that is, in the most suitable phase relationship for radiating.

5. Waveguide mode converter.

The mode conversion from HE_{11} mode to the HE_{1k} modes can be achieved also by a step variation of the waveguide radius, as shown in fig. 4. This discontinuity has been analyzed by a mode-matching technique. In order to avoid the generation of the unwanted modes of EH type, the corrugation depth of the two waveguide should be 0.25 λ. A good conversion on the HE_{12} mode is obtained by a waveguide of radius b=56 mm. In addition to the HE_{12} mode, a great number of modes are excited, but their level is quite small. With this converter the computed field pattern in the waveguide section where the window is placed is as shown in fig. 5. As can be seen, again the peak of the power density is halved with respect to that of the HE_{11} mode alone; the radiation pattern (not shown here) is theoretically matched up to 99.27% to a free space Gaussian beam with w_0 = 0.514 b (28.8 mm).

References

[1] P.J.B.Clarricoats and A.D.Olver: *"Corrugated Horns for Microwave Antennas"*, Peter Peregrinus Ltd.

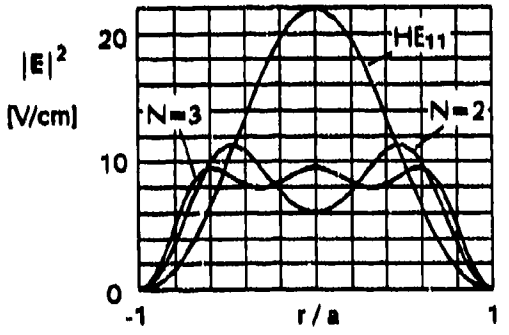

Fig. 1 - Field pattern of HE mode mixture with N=2 and N=3

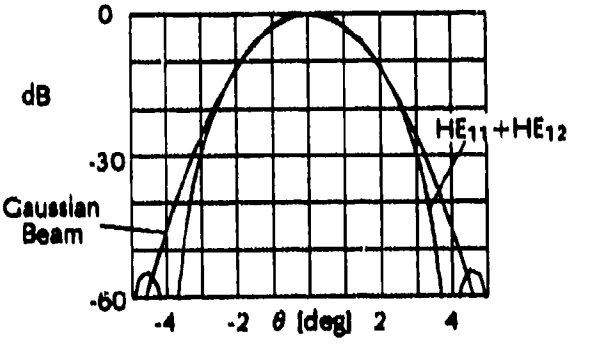

Fig. 2 - Radiation pattern of HE_{11}-HE_{12} mode mixture

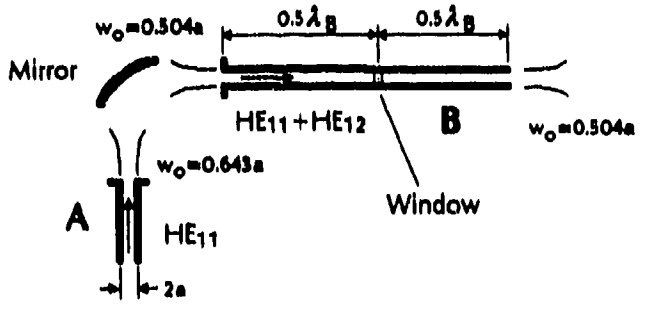

Fig. 3 - Geometry of quasi-optical converter.

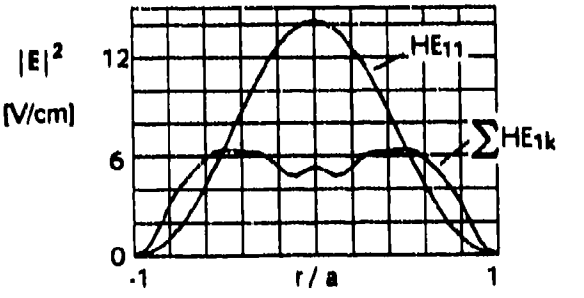

Fig. 5 - Field pattern at the window section.

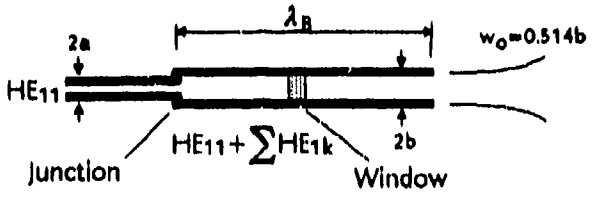

Fig. 4 - Waveguide mode converter

Effect of window tolerances on gyrotron performance

by J. Jelonnek and K. Schünemann

Institut für Hochfrequenztechnik
Technische Universität Hamburg-Harburg
Postfach 90 10 52
D-W-2100 Hamburg 90

Stable large-signal operation of gyrotrons (both of TE_{on}- and TE_{mn}-type) has been analysed with respect to load (window) reflections by applying a network-theoretical approach (which was published at the 16th Conference). Mode conversion from the desired mode has been included. Restrictions to window tolerances have been formulated and compared to measurements.

Increase of Gyrotron Window Carrying Capacity Based on Optimization of Output Wavebeam Structure

V.I. Belousov, G.G. Denisov, V.I. Malygin,
D.V.Vinogradov and V.E.Zapevalov
Institute of Applied Physics, Nizhny Novgorod, Russia

S.A. Malygin
R&D Institute "Salut", Nizhny Novgorod, Russia

One of the main factors, which limit duration of pulses and output powers of gyrotrons operating in the short-wave part of the millimeter wavelength band in the quasi-continuous regime is heating of the gyrotron output window with microwave radiation, which in the long run can lead to its destruction.

Degree of local heating of the window's material depends on local intensity of the microwave field at this point. The most critical are the regions of the maximum intensity of the field. Use of traditional quasi-optical converters and quadratic mirrors within gyrotrons, as a rule, leads to distribution of the field at the gyrotron window with a pronounced maximum at the window center. In order to lower local heating of the window (raise its carrying capacity) it seems rather natural to change the structure of the beam in the window region, having made the maximum of the field distribution lower. The ideal case would be quasi-homogeneous distribution of the field.

Due to design features of the gyrotron (Fig. 1) and quasi-optical character of microwave beam propagation inside the gyrotron, we can achieve the required distribution of the microwave beam field at the gyrotron window by means of synthesis of a special (non-quadratic) profile for the last mirror only (Fig. 2).

We have found a method to obtain the required profiles with sufficient ease.

This method was used in development of the long-pulse 140 GHz gyrotron Use of a specially profiled internal quasi-optic mirror gave more than a two-fold gain in the microwave pulse duration (from 0.5 to 1.1 s for the gyrotron output power 0.5 MW).

Figure 3 shows calculated distributions of field intensities at the gyrotron window. Figure 4 represents experimental distributions of field intensities obtained by means of an IR camera at the window of the gyrotron, whose design scheme included a mirror calculated by means of the said method.

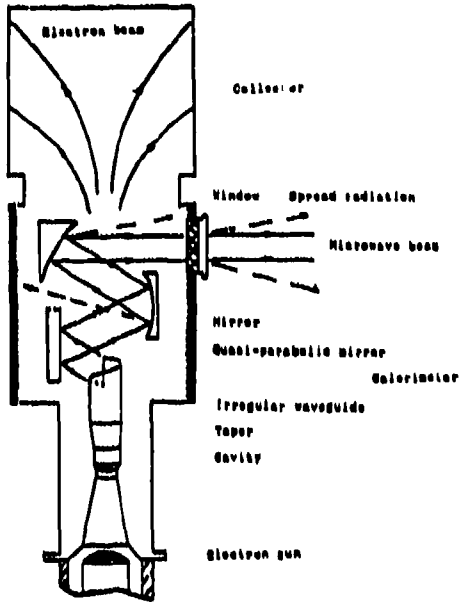

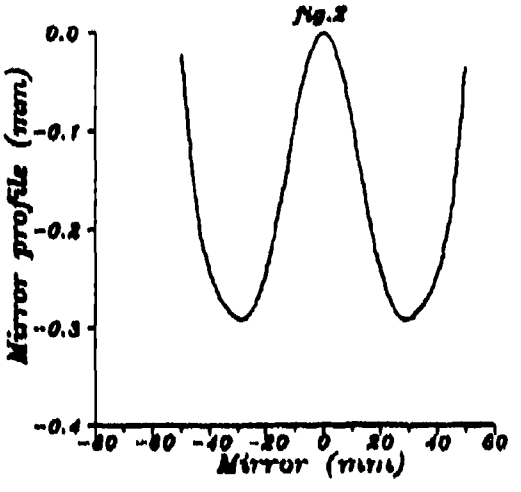

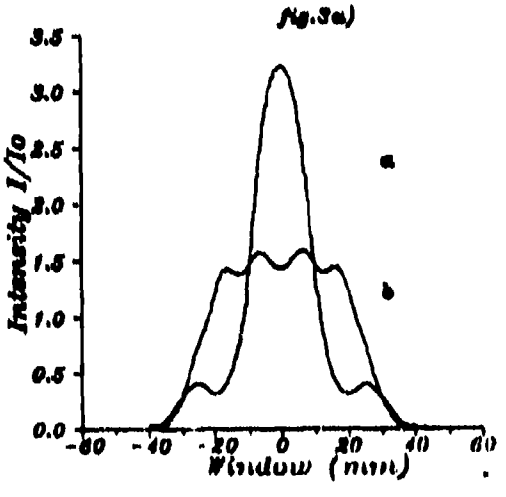

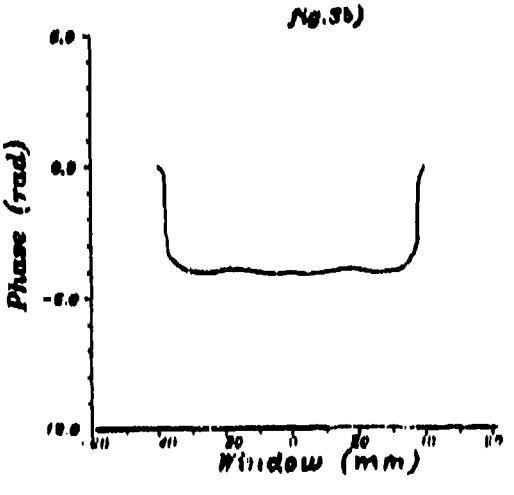

Fig.1. Scheme of the gyrotron output unit.
Fig.2. Example of a calculated mirror profile for gyrotrons under investigation.
Fig.3a. a) Calculated field distribution at the window of a gyrotron with traditional mirrors.
b) Calculated field distribution at the window of a gyrotron using a mirror with special profile
Fig.3b. Calculated field phase distribution at the window of a gyrotron using a mirror with special profile.

NEW WINDOW MATERIALS FOR HIGH POWER GYROTRON*

Mohammed Nurul Afsar and Hua Chi

Department of Electrical Engineering
Tufts University
Medford, Massachusetts 02155 - 5528

ABSTRACT

A single free standing synthetic diamond window seems to have higher absorption coefficient value at millimeter wavelength region at this time although it is claimed that it possesses good mechanical strength and higher thermal conductivity characteristics. It certainly does not rule out the use of diamond film on single crystal high resistivity silicon to improve its mechanical strength and thermal conductivity. One may have to use an appropriate film thickness for a particular wavelength in gyrotron window application. It is also necessary to use an appropriate thickness for the silicon perhaps equivalent to a quaterwavelength in order to avoid the reflection mismatch

INTRODUCTION

The absorption coefficient of most low-absorbing window materials increases with increasing frequency at millimeter wave frequency region.. This is because of the tail of lattice vibration or phonon absorption or various other absorption mechanisms present at submillimeter and far and mid infrared spectral region for solid crystalline and polycrystalline materials. For diamond and single crystal silicon, the monoatomic diamond crystal structure suggests the lattice vibration absorption to appear at frequencies in the infrared region. The entire mid-infrared, far-infrared, submillimeter and millimeter wave region therefore should be free from the tail effect of lattice or phonon absorption bands. An extra high resistivity (11,000 ohm-cm) compensated silicon specimen shows the absence of the microwave and millimeter wave free carrier absorption. However the thermomechanical property of such extra high resistivity silicon is less attractive compare to presently used window material, the single crystal sapphire. One idea to improve its thermo-mechanical properties is to coat the silicon surfaces with synthetic diamond film evaporation. One then expects to see a good room temperature low-absorption loss and mechanically strong window perhaps edge cooled by fluoro-carbon fluid. The cryo-edge-cooling would increase the complexity of a window system although it is expected that the absorption coefficient will decrease with decreasing temperature. At lower temperature a phonon or lattice vibration peak sharpens and the tail effect subsides or reduces significantly. For cryo-edge-cooling one would choose a temperature where the thermal conductivity has its highest value. It is difficult to measure extremely low loss tangent or absorption coefficient value. We have improved the sensitivity of our broadband dispersive Fourier transform spectrometers. We now can measure losses as low as 40 -microradians.

The recent improvement in the synthetic diamond film evaporation technique suggests the possible use of diamond coating over a single crystal high resistivity silicon window material. The use of the diamond film will increase the mechanical strength and thermal conductivity of the sandwich. Figure 1 shows the absorption coefficient spectrum for the 1 mm thick free standing diamond specimen .

* This research program is supported by the U.S. Department of Energy, Office of Fusion Research. Authors acknowledge the loan of a synthetic diamond specimen from Dr. Kevin Gray of Norton Diamond Company

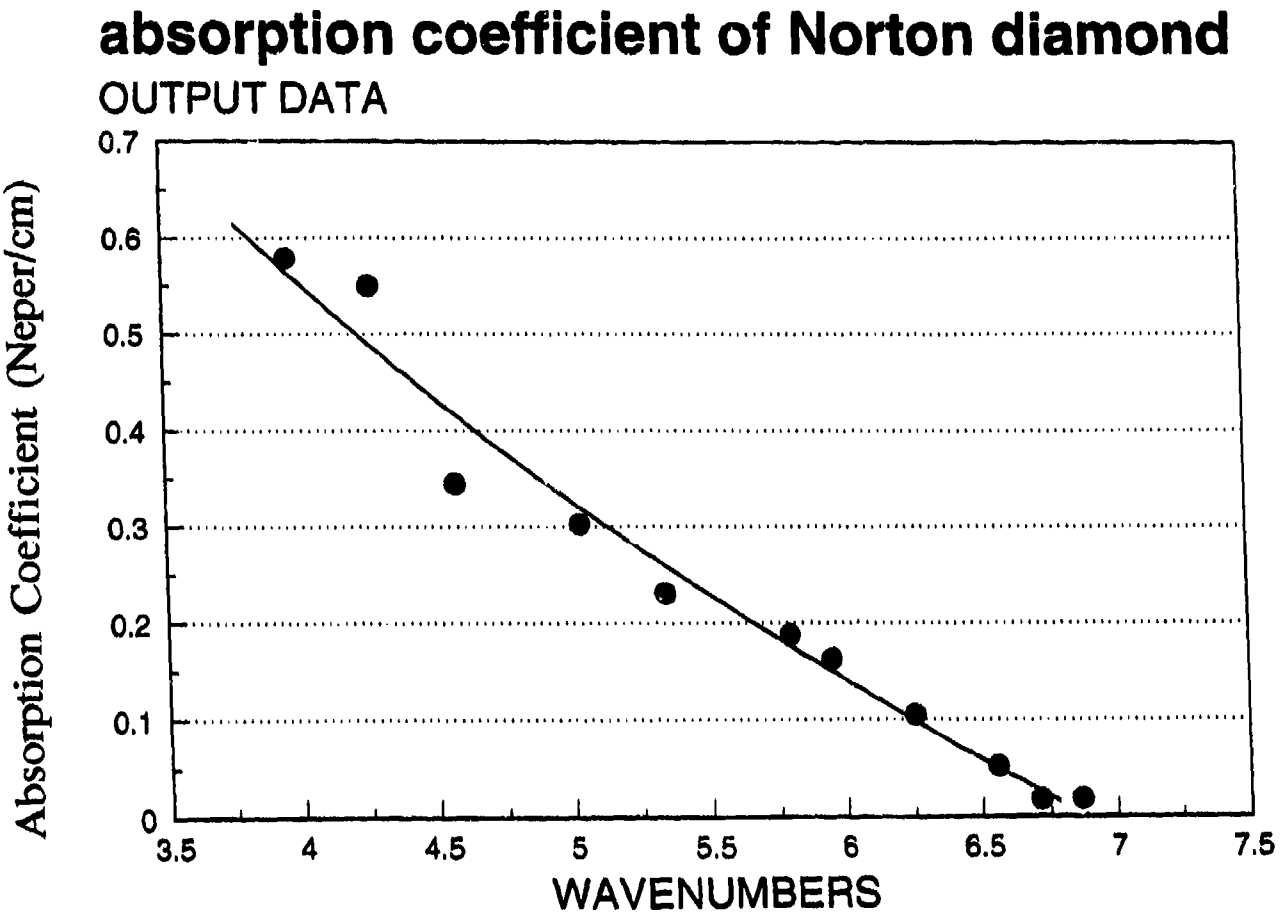

Figure 1 The absorption coefficient spectrum of a free standing diamond specimen manufactured by Norton Diamond Company. The absorption coefficient values were evaluated from directly measured transmittance data over the wavenumber range 4 - 7 cm^{-1}

THE MEASUREMENT

A simpler version of dispersive Fourier transform spectrometer was utilized for this measurement. The thin specimen results in a nominal loss of energy in transmission. It was therefore not possible to evaluate absorption coefficient and refractive index spectra directly. The transmittance spectrum was then measured directly for this thickness of the specimen. The absorption coefficient data were then evaluated at eleven points in the wavenumber (per cm.) region 4 - 7

REFERENCES

[1]. M. N. Afsar, Hua Chi and Xiaohui Li, "Precision Millimeter Wave Complex Refractive Index and Complex Dielectric Permittivity of Pure and Compensated Silicon", presented at the 1990 CPEM, 1990 IEEE Conference on Precision Electromagnetic Measurements, June 11 - 14, 1990, Ottawa, Canada, CPEM'90 Digest, pages 238-239, IEEE Cat.No.90CH2822-5, Library of Congress No.89-82032

Radiation induced reduction of silicon loss tangent

A. Ibarra, J. Mollá, E. R. Hodgson
Inst. Investigación Básica. CIEMAT, Ed. 2. Av. Complutense , 22. E-28040-Madrid. Spain.

1. INTRODUCTION

It is known that the frequency behaviour of the silicon loss tangent shows a ω^{-1} dependence, compared with the general $tan\ \delta \sim \omega$ behaviour for aluminum oxide and other oxides[1]. For this reason, high purity, high resistivity silicon has been proposed to be used in dielectric windows for the high power EC systems[2]. Loss tangent values as low as 10^{-3} and 10^{-4} have been measured at 15 and 145 GHz respectively[1,3]. The main obstacle arises from its high sensitivity to ionizing radiation fields which induce large increases in the loss tangent due to radiation-induced electron-hole pairs[1,4].

In this work the electron irradiation effects on the dielectric properties at 15 GHz of silicon are studied, both after irradiation and under ionizing radiation.

2. RESULTS

High purity, high resistivity monocrystalline silicon, kindly supplied by Dr. Heidinger (KfK), has been electron irradiated at room temperature, using a 2 MeV Van de Graaff accelerator, at different dose rates (between 1 and 50 Gy/s). 30 mm diameter, 3 mm thick samples, polished and chemically etched, have been used. The dielectric properties have been measured during irradiation by using a resonant method, putting the sample inside a closed aluminium cylindrical cavity placed at the end of the beam line of the accelerator. 1.8 MeV electrons enter the resonator through a thin aluminum window.

The loss tangent of as received samples is 7.6×10^{-4}, but under radiation increases strongly as a function of the dose rate (see figure 1) with a linear dependence which is in close agreement with previous results[4]. The proportionality constant, b, between loss tangent increase and the dose rate is a measurement of the sensitivity of silicon to the radiation. It is observed that the value of b decreases with irradiation time (figure 1). The linear dependence between $tan\ \delta$ and dose rate is maintained but the proportionality constant decreases, indicating the decrease of silicon sensitivity to radiation. Such an effect was not observed by R. Heidinger *et al* [4], using low energy X-rays. This difference may be due to the higher energy ionizing spectrum, or possibly to the limited amount of displacement damage in the electron irradiation case.

In figure 2 values of b are represented as a function of dose, indicating a $D^{-0.8}$ dependence. It is also observed that the loss tangent without radiation decreases with total radiation dose (figure 2). After a total dose of 1.8×10^{6} Gy a decrease of a factor of 10, down to 8×10^{-5}, is observed, and with an indication that this value could be further reduced.

These results can be summarized by the expression:

$$tan\ \delta = tan\ \delta_0 + b\,\dot{D}$$

where $tan\ \delta_0$ is the loss tangent without any radiation field, and $\dot{D}$ is the dose rate. Our results indicate that both $tan\ \delta_0$ and b decrease with total irradiation dose.

3. DISCUSSION AND CONCLUSIONS

The loss tangent of silicon both under ionizing radiation and before irradiation, is due to the presence of free charges in the material[3,4]. The measured values are the result of an equilibrium between the number of free charges created (by thermal activation, residual impurities or radiation) and their lifetimes. Within this framework the actual results can be understood assuming that the electron irradiation induces new permanent defects reducing the lifetime of free charges.

Assuming that the frequency dependence observed in the unirradiated samples also holds for the irradiated ones, these results indicate the possibility of obtaining a material with a very low room temperature loss tangent at high frequency (150 GHz) with a low sensitivity to ionizing radiation. This is of great interest for the development of high power EC heating systems.

More work is needed to study the high frequency behaviour of irradiated silicon, to explore the effects of higher irradiation doses and dose rates, as well as the nature of the radiation induced changes and the temperature dependence of loss tangent of irradiated samples.

4. ACKNOWLEDGEMENTS

This work is supported by the European Communities within the European Fusion Technology Programme.

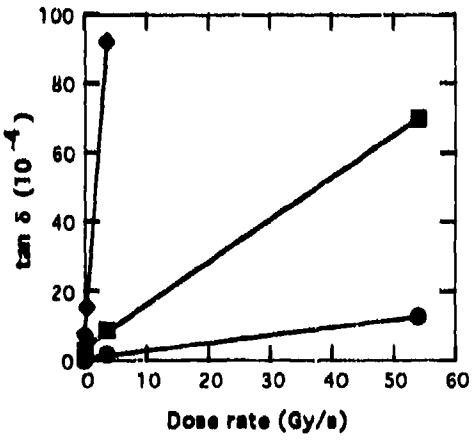

Figure 1: Silicon loss tangent as a function of dose rate for an initially unirradiated sample(◆) after 2.2×10^5 Gy (■) and following 1.8×10^6 Gy (●)

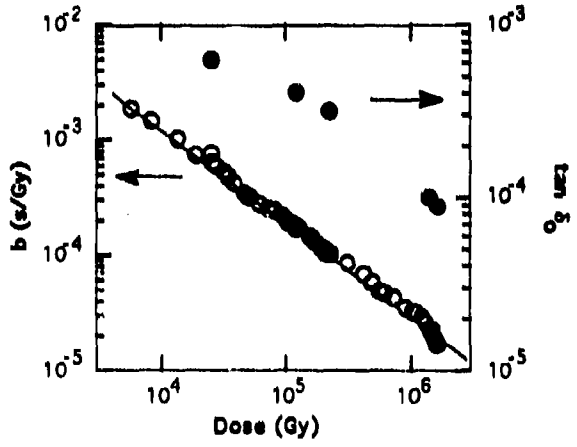

Figure 2: Dose dependence of b (o) and tan δ_0 (●)

5. REFERENCES

1. R. Heidinger, A. Kumlin, "Frequency and temperature dependence of the mm-wave dielectric properties of silicon with high dc resistivity" 15th Int. Conf. on Infrared and Millimeter Waves, R. J. Temkin, ed. SPIE vol. 1514, 274 (1990).
2. M.N. Afsar, H. Chi, X. Li "Window materials for high power gyrotron" *ibid* 544 (1990).
3. R. Heidinger, A. Kumlin, "The impact of extrinsic conductivity on the mm-wave dielectric loss in high resisitivity silicon" *ibid* 450 (1991).
4. R. Heidinger, A. Kumlin, A. Ibarra, J. Mollá "Increased dielectric loss in high resistivity silicon under X-ray irradiation" 16th Int. Conf. on Infrared and Millimeter Waves, M. R. Siegrist, M. Q. Tran, T. M. Tran, editors SPIE vol. 1576, 452 (1991).

Ultralow background radiation far infrared spectroscopy based on the magnetically tunable selective sources, filters and detectors

W.Knap, D.Dur, C.Chaubet, A.Raymond
Groupe d'Etude des Semiconducteurs
Université Montpellier II (CNRS - URA 357)
Place E. Bataillon - 34095 MONTPELLIER Cedex 05, FRANCE

The way how to make spectroscopy in the far infrared by replacing mechanical spectral elements (moving mirrors or gratings) by superconducting solenoids is shown. The magnetic field changes the FIR properties of the semiconductors through the cyclotron resonance or the Zeeman effect allowing to make spectroscopy in the range 35cm^{-1} - 160cm^{-1} with the resolution up to 0.3cm^{-1}. We present the possibilities and limits of the spectroscopy which uses a magnetic field to scan (tune) the characteristic energies of the narrow band spectral elements: sources, filters and detectors. All described below devices work immersed in the liquid helium bath. Therefore spectroscopy based on magnetically tunable narrow band elements provides also ultralow background radiation conditions for measurements.

Sources : transmission spectrometer

We show practical realisation and examples of application of the transmission spectrometer based on the InSb and GaAs cycloton resonance sources (1). The spectrometer can be used in the range from 35 to 200cm^{-1}. Its maximal resolution obtained with the high mobility GaAs heterojunction as the emitter is about 1cm^{-1}. The spectrometer performance is demonstrated by its application to the studies of impurity and free-electron states in two-dimensional systems (Fig. 2).

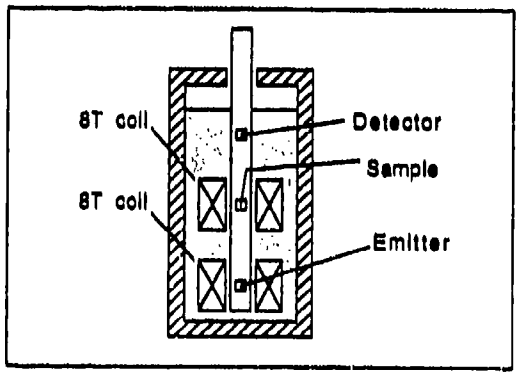

Figure 1: The experimental set up

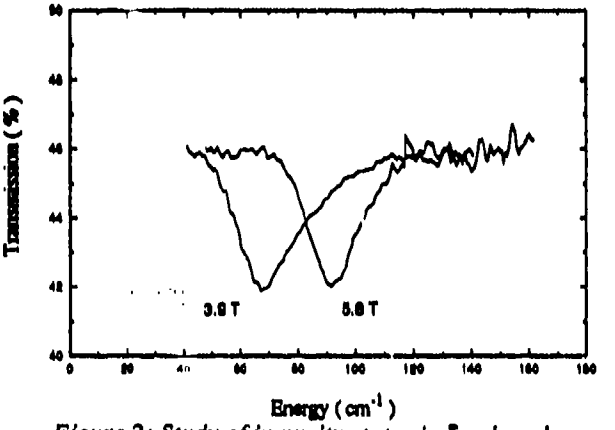

Figure 2: Study of impurity states in δ doped MQW. Transmission spectra versus emitter FIR photon energy are plotted for two magnetic fields.

Detectors : analysis of the emission

By applying th magnetic field to GaAs and InP one can effectively tune the energies of 1s to 2p transitions. In a very high purity material photoconductivity lines due to this transitions are very sharp enabling spectroscopy with a resolution up to 0.3cm^{-1}. We present systematic studies of the detectors sensitivity and noise versus the temperature, electric and magnetic fields (2). We show that the decrease of the performance of these detectors in high magnetic fields is mainly due to appearance of low frequency noise which for strongest fields has a 1/f spectrum. By adjusting the detector temperature we improve the signal to noise ratio and shift the limits of detection possibilities up to 160cm^{-1}. The properties of the detectors are shown by their application to analyse the far infrared emission from GaAs/GaAlAs heterojunctions and multiquantum wells (MQW).(3).

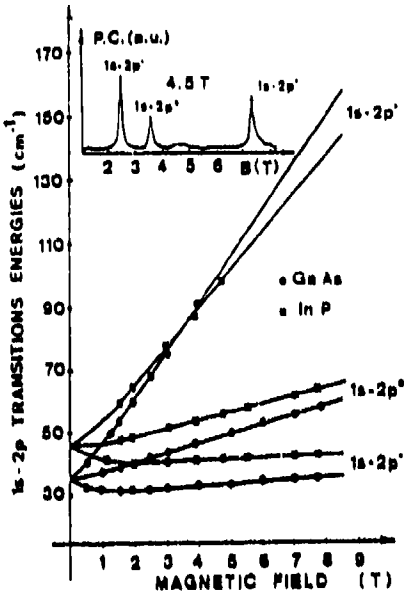

Figure 3:Energies of the 1s-2p(+/0/-) transitions vs magnetic field. Inset shows an example of the photoconductivity spectrum (vs emitter magnetic field) for GaAs detector in a magnetic field of 4.5T. The GaAs cyclotron resonance emitter was used to obtain this spectrum.

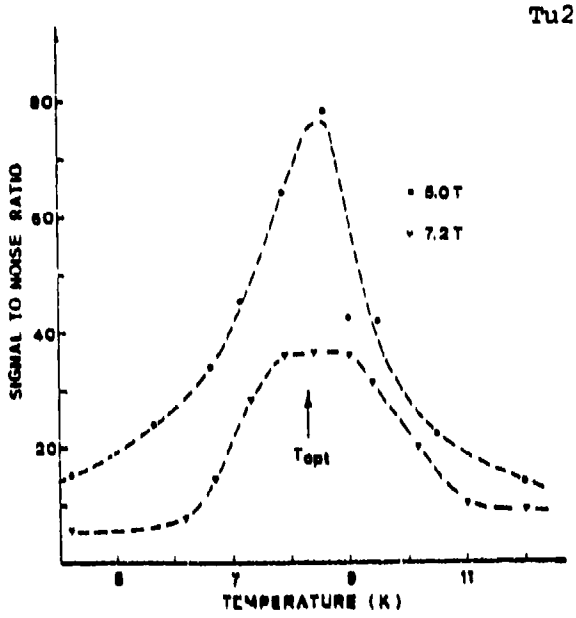

Figure 4: The S/N ratio as function of the temperature for magnetic fields 5T and 7.2T.

Filters : notch filter spectometer

Cyclotron resonance absorption filters can be used to analyse the spectrum of the emission of the far infrared radiation. Emission in this kind of spectrometry is detected by a broadband detector (eg bolometer). The CR filter that is put beetween the emitter and the detector cuts (absorbs) part of the spectrum at the cyclotron energy. Detector signal registered as a function of the magnetic applied to the CR filter contains an information about the spectrum of emitted photons. This technique is an efficient tool for analysis of the FIR emission of solids (4). We show how one can increase the resolution of this technique by use CR filters based on the high mobility heterojunctions. We show how to choose optimal CR filter to make precise and high resolution analysis of the FIR emitted from solids (5) and present examples of analysis of the same emitter with a few different CR filters.

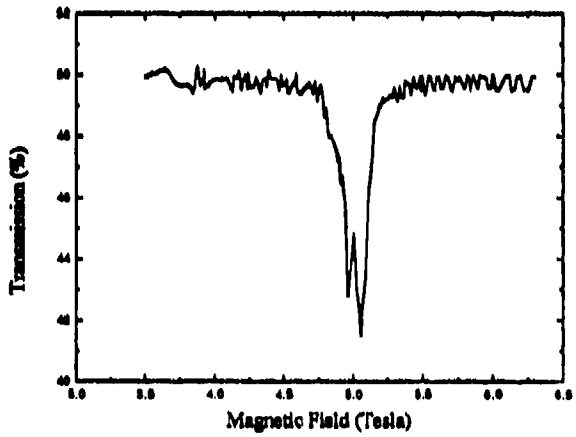

Figure 5: Analyse of the cyclotron resonance from bulk GaAs. A high resolution notch filter is used. The splitting of the CR line due to non -parabolicity effect is observed.

References:

(1) W. Knap, D. Dur, A. Raymond, C. Meny, J. Leotin, S. Huant, and B. Etienne, A far-infrared spectrometer based on cyclotron resonance emission sources, Rev. Sci. Instrum. 63 (6), (1992).

(2) W. Knap, J. Lusakowski, K. Karpierz, B. Orsal, J.L. Robert, Improved performance of magnetically tunable GaAs and InP far-infrared detectors, J. Appl. Physics, 72, (2), (1992).

(3) W. Knap, S. Huant, C. Chaubet and B. Etienne, Magneto-emission from shallow donors in quantum wells, Superlattices and Microstructures, Vol. 8, n° 3, (1990).

(4) M. Helm, P. England, E. Colas, F. De Rosa and S.J. Allen, Intersubband emission from semiconductor superlattices excited by sequential resonant tunneling, Phys. Rev. Lett. 63:74, (1989).

(5) D.Dur et al, Cyclotron resonance notch filter spectrometer, to be published.

The Far Infrared p-Ge Laser : Transition Identification and Evidence for Streaming Motion

C R Pidgeon and B Murdin,
Department of Physics, Heriot Watt University, Edinburgh EH14 4As

C Kremser, K Unterrainer and E Gornik,
Insititut fur Festkorperelektronik, Technische Universitat Wien, A-1040 Wien, Austria.

Crossed electric and magnetic fields applied to p-Ge crystals can lead to stimulated FIR emission between different light hole Landau levels. "Streaming motion" of heavy holes, where they repeatedly accelerate collissionless to the optical phonon energy and scatter back to the origin [1] is thought to be one of the main processes underlying the so-called p-Ge cyclotron resonance (CR) laser. The finite probability for heavy holes to scatter into light hole Landau levels (LL's) leads in this way to an increase of the population of light hole LL's (pumping mechanism). A population inversion between different LL's is built up due to the depopulation of low lying LL's by ionised impurity scattering [2] or due to mixing between light and heavy hole states [3], which, because of streaming motion of the heavy holes, leads to a reduction of the lower LL lifetime.

To date the role of streaming motion in hot hole p-Ge lasers has been inferred only through theoretical considerations [3,4]; in this work we present the first experimental proof of the importance of streaming motion. We have performed magneto-absorption measurements in p-Ge under intense crossed electric and magnetic fields. The broadening of the observed cyclotron transitions and the disappearence of some of these transitions with increasing electric field is attributed to streaming motion. In addition, the observation of the change of a magnetooptical resonance from loss (absorption) to gain with increasing electric field has enabled us to identify directly the high field lasing transition. It is confirmed to be the light hole b-set n=1 to 0 transition in the coupled band model.

The stimulated emission obtained is single line (linewidth of $< 0.2 cm^{-1}$) and linearly tuneable with magnetic field from 25 to 85 cm^{-1}, with an estimated output power of 200 mW in a 1μs pulse.

[1] S. Komiyama, Adv. Phys. 31, 255 (1982);
[2] V A Koslov, L S Masov, I M Nefedorn, M R Zabolotskikh, JETP Lett., 37, 170 (1983);
[3] S A Stoklitskiy, Semicond. Sci. Technol., 7, 610 (1992).
[4] K Unterrainer, C Kremser, E Gornik, C R Pidgeon, Yu. L Ivanov and E e Haller, Phys. Rev. Lett. 64, 2277 (1990); P Pfeffer, W Zawadzki, K Unterrainer, C Kremser, C Wurzer, E Gornik, B Murdin and C R Pidgeon, Phys. Rev. B47, 4522 (1993).

Mode structure and wavelength tunability of the p-Ge far-infrared hot hole laser

A.V. Muravjov, S.G. Pavlov, V.N. Shastin

Institute of Applied Physics, Russian Academy of Science, Nizhny Novgorod 603600, Russia

E. Bründermann, M.F. Kimmitt[1], H.P. Röser

Max-Planck-Institut für Radioastronomie, D-W-5300 Bonn 1, Germany

ABSTRACT

The mode spectrum of the p-Ge far-infrared intersubband transition hot hole laser, with several types of resonator cavity, has been investigated using both grating and Schottky diode spectroscopy. Narrow-band lasing, with continuous wavelength tunability from 75 μm to 110 μm, has been realised due to intracavity frequency selection.

The p-Ge FIR laser in crossed electric and magnetic fields with a nonselective cavity has a very broad emission spectrum of 10-20 μm tunable in the wavelength region 70-120 μm by the applied fields. An intracavity Fabry-Perot (FP) resonator type has been designed for mode selection and the spectrum was measured by grating and Schottky diode spectroscopy (FIG.1) [1,2].

The active p-Ge samples and the configuration of the applied fields were the same as given in ref. [2]. The spherical output mirror and the composite plane back mirror (FIG.4) form the semi-confocal resonator spaced from the polished bulk-end sample by Si. The FP like resonator at the back is coupled with the main resonator by a lamellar grating consisting of evaporated Al-stripes on the Si-spacer surface. The FP resonator gap d can be tuned mechanically.

The laser spectrum (FIG.2a) measured by a grating spectrometer with a Ge:Ga detector shows a narrow spectral line with the wavelength λ smoothly tunable proportional to the gap width d (FIG. 2b). The measured spectrum for $d = 244.5\mu m = 5/2 \times 97.8\mu m$ was close to the grating spectrometer apparatus function (FIG.2a - solid). The real spectrum width can be estimated to 0.02 μm (FIG.2a - dashed) while without selection (d=0) the laser emission has a width of about 20 μm. The videosignal on the Schottky diode with and without selection was the same (200-400 mV) so the intracavity FP selector does *not* change the overall output power but increases the spectral line intensity by 1000. The signal from the diode was then analysed by a spectrum analyzer. In the nonselective case (d=0) only longitudinal modes of the laser resonator were found at the mixing frequency $f_{mix} = c/2L \approx 458$ MHz (L: resonator optical length) with a linewidth of about 1 MHz [2]. So the spectrum consists of a set of very narrow lines with linewidths of about 1 MHz determined only by the laser pulse duration of 3 μs (FIG.2a). For the narrow-band lasing with intracavity selection the mixing signal rises by 15-20 dB. On a fast oscilloscope we can also observe a strong sinusoidal modulation (50-100%) of the videosignal with f_{mix}. The origin of four lines in the mixing spectrum (FIG.3) instead of one line at f_{mix} for the nonselective case and the linewidth will be studied more carefully by a heterodyne mixing experiment.

The shown measurements prove that the output laser power can be concentrated into 2 or 3 longitudinal modes due to the intracavity FP selectivity. We hope by improving the resonator design to operate in single mode.

REFERENCES

[1] H.P. Röser et al., Conf. Digest 15th Conf. IR & MM Waves (1990)
[2] V.N. Shastin et al., Conf. Digest 17th Conf. IR & MM Waves (1992)
[3] A.V. Muravjov et al., Kvantovaya electronika, V. 20, No. 3,p. 182 (1993) (in russian)

[1] Permanent address: University of Essex, Colchester CO4 3SQ, UK

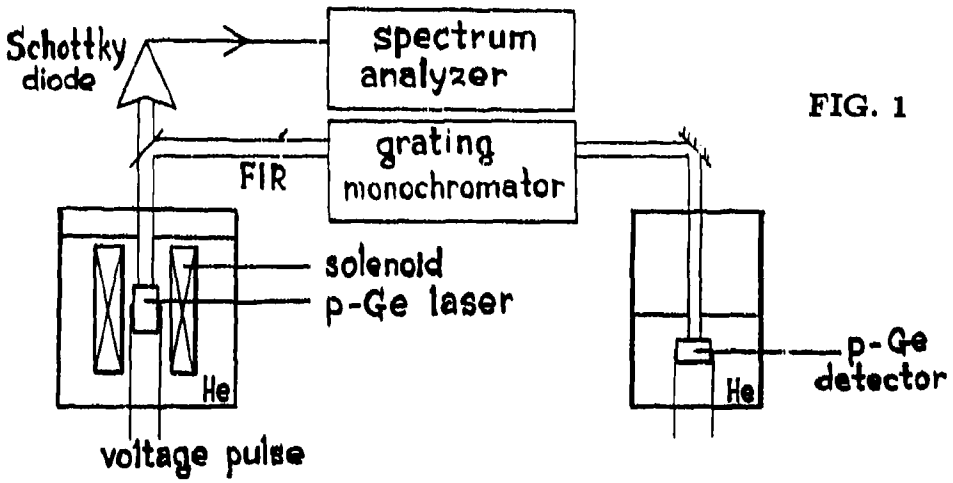

FIG. 1

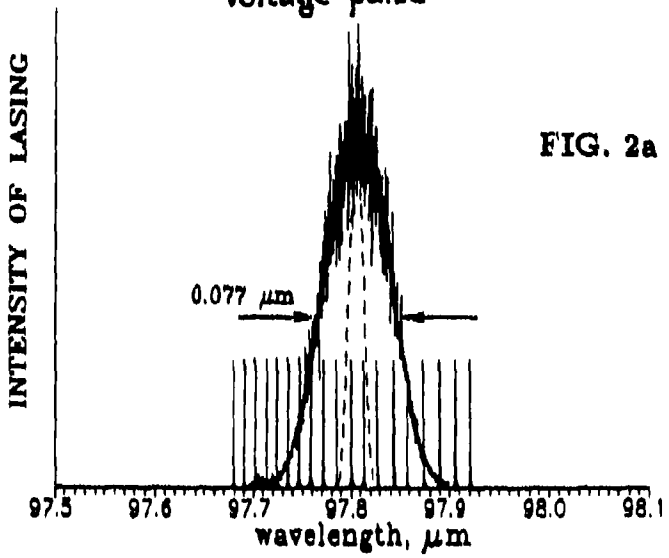

FIG. 2a

FIG. 2b

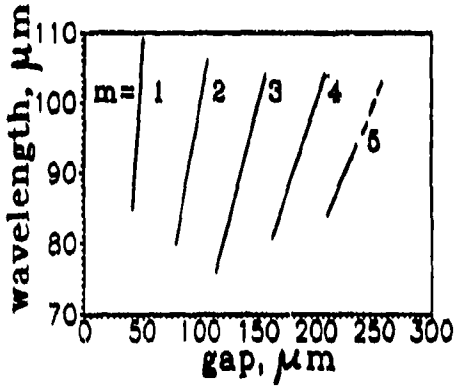

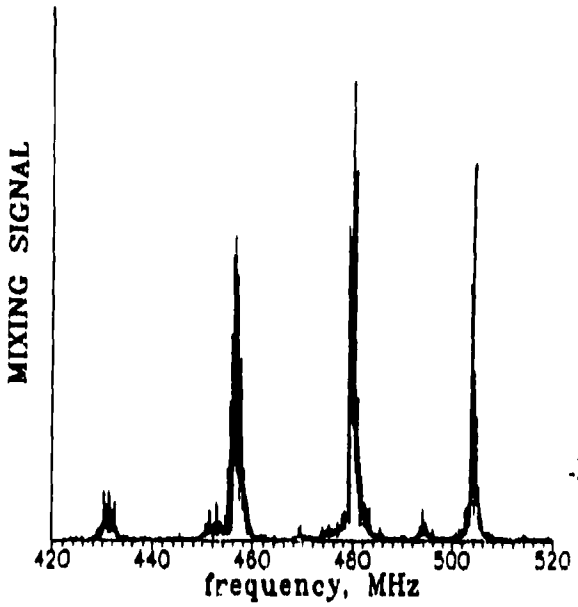

FIG. 3

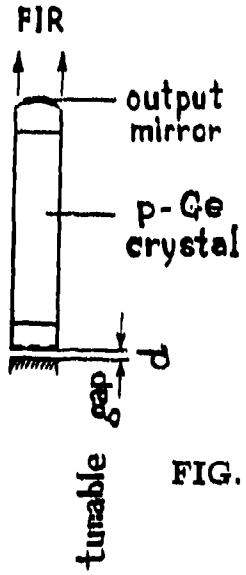

FIG. 4

Far infrared radiation (FIR) sources based on impurity emission from selectively doped multi quantum wells (MQW)

D. Dur, W. Knap, C. Chaubet, A. Raymond, P. Vicente, A. Dubois, I. Salesse
Groupe d'Etude des Semiconducteurs
Université Montpellier II (CNRS - URA 357)
Place E. Bataillon - 34095 MONTPELLIER Cedex 05, FRANCE

B. Etienne
L2M/CNRS, 196, av. Henri Ravera
92220 BAGNEUX Cedex, FRANCE

C.R. Stanley
M.B.E. Research Group
Department of Electronics and Electrical Engineering
University of Glasgow
GLASGOW G.12, 8QQ, U.K.

Emission of FIR due to radiative recombination between shallow impurities states in selectively doped multiquantum wells (MQW) is studied as a function of electric and magnetic fields applied to the structure. It allows to propose the efficient FIR sources for tests of bolometers working in millikelvin temperatures.

The electronic levels of impurities in quantum wells depend on various growth controllable parameters such as the well width and the impurity location.

Recently, efficient emission of far infrared radiation due to 2p → 1s radiative recombination in MQW has been observed. The emission energy was found to depend of the impurity position and to be magnetically tunable[1,2].

In this work, the properties of this new class of FIR emitters is studied. The samples used in this experiment are selectively doped MBE grown GaAs-$Ga_{0.75}Al_{0.25}As$ MQW. Two samples were investigated. Sample A doped only in the middle of the barriers ($N_b = 6.3\ 10^{10}$ cm^{-2} ; 50 periods) and sample B doped in the middle of the barriers and in the middle of the wells ($N_b = 4.\ 10^{10}$ cm^{-2} ; $N_w = 2.\ 10^{10}$ cm^{-2} ; 100 periods). The well and barrier thicknesses are 100 Å and 200 Å respectively. These two samples have been previously studied in FIR transmission experiments and they are therefore well characterised[3,4].

The FIR emission is induced by applying electric pulses to the sample. Indium contacts were alloyed to the samples. The distance between the contacts is 5 millimetres. The time interval between the pulses is choosen to avoid sample heating. The radiation is guided by a copper light pipe to the detector. A GaAs photoconductive detector is used. Its spectral characteristic in zero magnetic field consists mainly of one line due to 1s → 2p transition at energy 4.43 meV (286 μm). FIR emission (registered by this detector) versus magnetic field applied to MQW are shown in figures 1 and 2. The main results are following:

1) There exists a broad band due to impurity emission starting from zero magnetic field which is followed by cyclotron emission.

2) There is an optimal value of the electric field for which impurity emission is maximal. Too high electric fields heat electrons up to the conduction band making that impurity emission decreases and cyclotron resonance increases.

3) Double doping in the centre of the well and in the barrier increases the intensity of impurity emission (in the region of wavelenght 286 μm). A possible explanation is the contribution of shallow donors in the well and/or of D^- states that are formed in such structures[3,4].

4) Maximal output power that can be obtained with this sources was estimated to 1 nW with input power of the order of 10 mW.

FIR sources based on impurity emission from selectively doped MQW were proposed as alternative sources for tests of bolometers working in mK temperatures. They can replace standart black-body sources because of the following advantages:

1) They can be modulated with high frequency.
2) They are selective and the spectral region of the emission can be adjusted by the choice of MQW growth parameters.
3) They need a smaller input power than black-body sources so they do require smaller cooling power to keep the bolometers in mK temperatures.

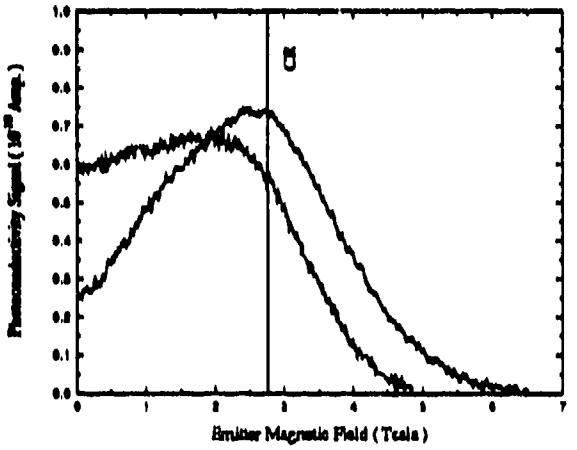

Figure 1: FIR emission for sample B for two different electric fields. For higher electric field impurity emission decreases and cyclotron resonance (CR) emission increases.

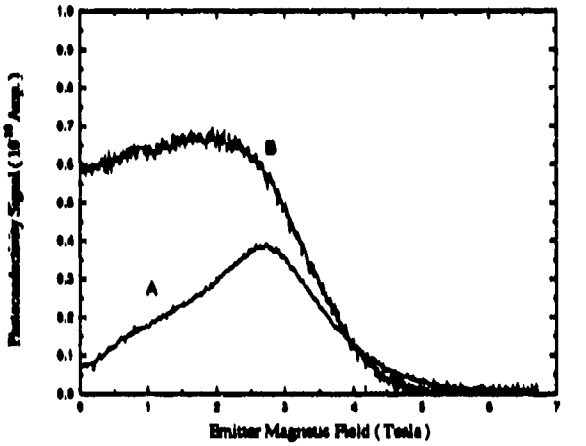

Figure 2: Comparison of the intensities of the FIR emission intensities for samples A and B. Sample B doped in the barrier and in the center of the MQW gives higher impurity emission.

(1) W. Knap, S. Huant, C. Chaubet and B. Etienne, Magneto-emission from Shallow Donors in Quantum Wells, Superlattices and Microstructures, Vol. 8, n° 3, (1990).
(2) M. Helm, P. England, E. Colas, F. De Rosa and S.J. Allen, Intersubband emission from semiconductor superlattices excited by sequential resonant tunnelling, Phys. Rev. Lett. 63:74, (1989).
(3) S. Huant, S.P. Nadja and B. Etienne, Two-Dimensional D^- Centers, Phys. Rev. Lett. 65,1486, (1990)
(4) A. Mandray, S. Huant and B. Etienne, Formation of Stable D^- Centers in Quantum Wells, Europhys. Lett. 20,181, (1992)

Diminutive and super diminutive surface wave magnetrons of mm range

V.D.Yeremka, G.Ya.Levin, S.N.Terechin, A.Ya.Usikov

Institute of Radiophysics and Electronics
12, Ac.Proskura st., Kharkov, 310085, Ukraine

ABSTRACT

The results of design and study of diminutive surface wave magnetrons (SWMs) of mm radio wave range with thermocathode and super diminutive SWMs with heatless cathode are presented.

1.INTRODUCTION

Miniaturization and super-miniaturization of vacuum devices, operating in SHF- and EHF- ranges, clear the new fundamental ways of improvement of radar and measuring equipment, cybernetics devices and communication systems at the realization of fundamental scientific and technical programs of space explore, at the development of inter-satellite communication systems for high orbits etc.

The experience of development of compact continuous and impulse SWMs allowed to carry out their miniaturization.

SWM is one of subclasses of travelling wave magnetrons. The feature of "Kharkov operating regimes" of such magnetrons is the use of interaction of electron flows with one of high space harmonics of HF-field and not with fundamental one as in classical magnetron[1]. If one introduce the generalized parameter $h=H/H_{cr}$ (where H is operating magnetic field, H_{cr} is critical magnetic field), then SWM operates at h approximately equals 1 and classical magnetrons operate at h of approximately 10. SWM has the greater number of resonator of anode block ' periodical structure. This provides the possibility to operate at lesser acccelerating voltages and magnetic fields.

Continuous diminutive SWMs with thermocathode, operating at the frequency of 37 GHz are designed by us (Fig.1). The weight of the device with magnetic system made of samarium and cobalt does not exceed 150 g.

The development of base design of mm range impulse diminutive SWM having the cathode without resistive heat. Anode block of such SWM is periodical structure having 24-36 resonators, that allow the possibility of interaction of electrons with high spatial field harmonics. The cathode of such SWMs has the form of a number of autoemitters (AEs) alternating along the axis and made of Ta and secondary cathode (SC) made of porous tungsten impregnated by barium aluminate, edged autoemitters, activated by barium, provide inertialess excitation of magnetron.

2.RESULTS

Continuous diminutive SWMs with thermocathode at the frequency of 37 GHz provide output power of 0.3-0.7 W at operating voltage of 400-950 V. Output power of diminutive continuous SWMs was 1kW at the operating voltage of 5 kV, pulse duration of 0.3 msec and on-off time ratio of 1000.

The breadboard of super diminutive SWM with AE and SC, synchronized by external signal at the frequency of 37 GHz, produced the power of 1.2 kW at operating voltage of 6 kV, impulse duration of 0.2 msec and on-off time ratio of 2000.

3.CONCLUSION

Diminutive SWMs with thermocathode and super diminutive SWMs with AE and SC can be used in a number of applications side by side with semi-conductor devices because of their ability to operate in wider temperature range at stable frequency. SWMs with AE and SC have instant starting.

4.ACKNOWLEDGEMENTS

This work is supported by the State Fund of Fundamental Research of the Ukraine and by the Committee on Science and Technology of the Ukraine.

5.REFERENCES

1. V.D.Yeremka, G.Ya. Levin, L.P.Mospan et al,"Russian surface millimeter wave magnetrons",in 16-th Int. Conf. on IR & MM Waves, Proc. SPIE 1576, PP.8-9, Lausanne, Switzerland, 1991.

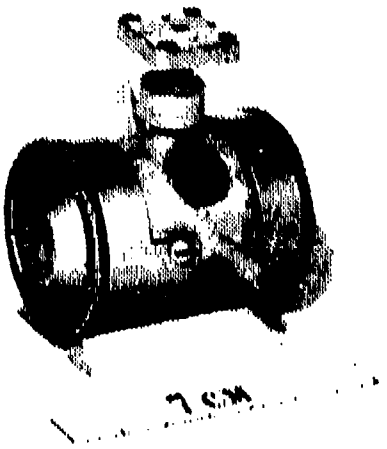

Fig.1. External appearance of diminutive impulse SWS, f~95 GHz

A far infra-red active medium based on shallow acceptor states in semiconductors

V.N. Shastin, A.V. Muravjov, E.E. Orlova, S.G. Pavlov
Institute of Applied Physics, Russian Academy of Science, Nizhny Novgorod 603600, Russia

ABSTRACT

Theoretical proposals concerning far-infrared activity based on shallow acceptor state optical transitions in p-Ge and p-Si semiconductors are discussed. Preliminary experimental investigations will be presented.

Recently it has been pointed out [1,2] that the narrow spectral lines of lasing close to the wellknown lines of shallow impurity absorption (so-called E and C lines) observed in the spectrum of the p-Ge laser on the light-to-heavy hole transitions in crossed electric E and magnetic H fields means an amplification of the ground-to-excited acceptor states optical transitions [1]. Also, the step-wise power saturating level was observed and was supposed to be due to the photoionisation of abnormally highly populated impurity states [3].

We have investigated the processes forming the population of the impurity states using the simple hydrogenical model adjusted to the known parameters of shallow acceptors in Ge. The transition rates for impurity states have been estimated and the mechanisms of the population inversion between the impurity states have been analysed under the conditions of the p-Ge laser (E≈1 kV/cm, H≈7 kOe).

Recombination due to spontaneous optical phonon emission ($t \approx 2 \times 10^{-8}$ sec for the ground state) were found to control the impurity population when the free carrier distribution is heated in crossed electric and magnetic fields while there is no far-infrared lasing. So the abnormally high population (about several percent) of the impurity states despite the high temperature of the holes in the valence band is caused by the fast processes of optical phonon-assisted cooling. The ground state is effectively photoionized ($t \approx 10^{-10}$ sec for a lasing intensity of $I \approx 1$ kW/cm^2) with the development of lasing on light to heavy hole transitions in the wavelength range 100-130μm while photoionisation of excited states is much less effective. Thus heating the free carrier distribution by the electric field will populate the first few excited states inversely if their impact ionisation rate ($t \approx 1.5 \times 10^{-10}$ for the E-line) does not exceed the rate of photoionisation of the ground state and the pumping due to optical phonon emission is even faster than for the ground state. The proposed theoretical model enables us to explain existing experimental results,including the delay dependence of the p-Ge laser pulse on the frequency of the preceding FIR radiation pulse [4].

Optical phonon assisted transitions can be effective in pumping the population inversion on the shallow acceptor states in p-Si by CO_2 laser excitation and this seems to be important for a further development of the FIR semiconductor laser sources.

REFERENCES

[1] S.V. Demihovsky, A.V. Murav'ev, S.G. Pavlov and V.N. Shastin, Semicond. Sci. Technol. 7, B622 (1992)
[2] Yu.A. Mityagin, V.N. Mursin, O.N. Stepanov and S.A. Stoklitsky, Semicond. Sci. Technol. 7, B641 (1992)
[3] F. Keilmann, V.N. Shastin and R. Till, Appl. Phys. Lett. 58, No. 20, p. 2205 (1991)
[4] F. Keilmann (private communication)

A class of microwave-synthesisers and noise-generators for microwave-spectroscopy

Vaks V.L., Panin A.N., Pripolsin S.J., Neubert F., Mau U., Smorgonski A.V., Chodos V.V., Schulechov A.O.

Backward Wave Oscillators (BWO's) are used as the radiation source of the microwave-synthesisers. They work in a frequency-range from 37GHz to 380GHz. They can be used as programmable generators with high accuracy or noise generators. In the first case, a short-time stability of $6*10^{-9}$, a long-time stability of 10^{-8} and a accuracy of frequency of 10^{-8} is reached. The noise generator has a noise-bandwidth of 10GHz with a equivalent noise-temperature of about 10^{10}K.

Tunable Far Infrared (TuFIR) Spectroscopy of Transient Molecules.

S.R. Boardman, C.H.Bryant , P.B.Davies & T.J.Sears*.

Dept. of Chemistry, University of Cambridge, Lensfield Road, Cambridge, CB2 1EW, United Kingdom.

*Permanent address : Brookhaven National Laboratory, Upton, N.Y., USA
S.E.R.C. Visiting Fellow.

ABSTRACT

Tunable Far Infrared (TuFIR) laser sidebands have been generated by non-linear mixing of radiation from a fixed frequency FIR laser and a tunable microwave source. The design of the Cambridge TuFIR spectrometer together with high resolution sub-mm spectroscopic measurements of spectral parameters of stable and transient species will be discussed.

1. Spectroscopic Techniques in the FIR/sub-mm Region - Development of TuFIR.

The region between 1mm and 30 μm is one of the least exploited of the e-m spectrum. It can be loosely defined as the region where microwave based techniques end and where tunable laser sources, namely lead salt diode lasers begin. Harmonic generation in a point contact diode using a klystron source provided the first method of penetrating this region. The subsequent development of optically pumped FIR lasers and the use of non-linear mixing techniques has led to two distinct methods of generating TuFIR radiation.

a) The use of two mid-IR CO_2 lasers producing a difference frequency by mixing on a Metal-Insulator-Metal diode.
b) Sideband generation from mixing a fixed frequency optically pumped FIR laser with tunable microwaves on a GaAs Schottky barrier diode.

The TuFIR spectrometer constructed in Cambridge uses the latter approach.

2. The Cambridge TuFIR Sideband Spectrometer.

A schematic diagram of the spectrometer is shown in Fig.1. An optically pumped FIR laser provides the fixed frequency local oscillator (LO) giving access to 1000's of discrete frequencies in the FIR. A reflex klystron of centre frequency 90 GHz is employed as the tunable microwave source and this provides sidebands of the LO after mixing on a Schottky barrier diode, i.e.

$$\omega_{TuFIR} = \omega_{FIR} \pm \omega_M \qquad (1)$$

The tunability of the TuFIR sideband is determined by the microwave frequency ω_M.

The diplexer, a variant of the Michelson Interferometer, along with a Fabry-Perot Interferometer is used to provide the necessary separation and filtering of the TuFIR sideband from the much more intense FIR carrier which is re-radiated from the mixer.

Fig.1 The TuFIR Sideband Spectrometer.

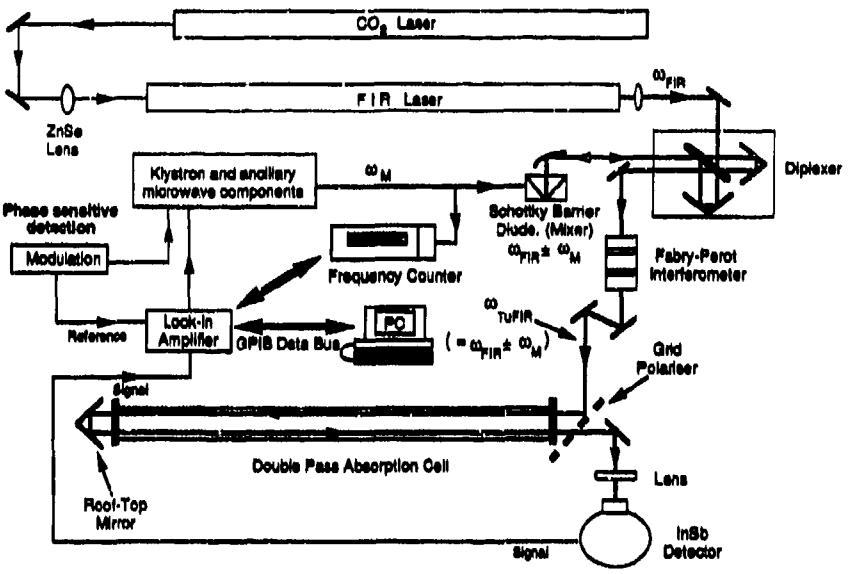

A double pass of the absorption cell is performed using a wire grid polariser and roof-top mirror. The klystron is frequency modulated at 17kHz and the signal recovered via a phase sensitive detector. Computer control facilitates the acquisition of high resolution TuFIR spectra.

3. Results.

After initially testing the sensitivity of the spectrometer on well characterised, pure rotational transitions of NO, work has been carried out on the spectral parameters of several atmospherically important species. To date, rotational transitions and line broadening analysis of ClO, HCl and HO_2 have all been observed. An example of rotational absorption lines in ClO is shown in Fig. 2.

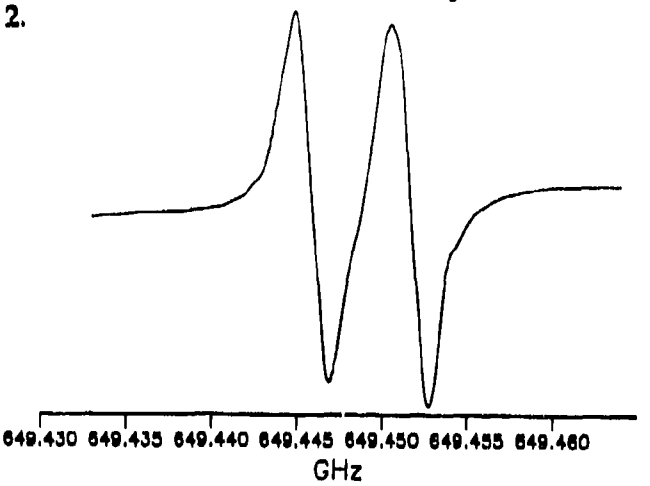

Fig. 2. The TuFIR spectrum of the J = 17.5 - 16.5 transition in ^{35}ClO at 649.445 GHz, pressure broadened by 163mTorr N_2.

Scattering of Guided Modes by Sphere in a Quasi-Optical Waveguide of the Class of "Hollow Dielectric Channel"

V.K. Kiselyev, T.M. Kushta

Institute of Radiophysics and Electronics
Academy of Sciences of Ukraine
12 Acad. Proskura str., Kharkov, Ukraine

ABSTRACT

The scattering of the guided modes due to a conducting sphere in a circular waveguide of the class of "hollow dielectric channel" (DC-waveguide) is investigated theoretically and experimentally. To treat the problem theoretically, the incident guided wave is expanded in terms of the spherical vector wave functions, and scattered fields are obtained by applying the boundary conditions on the surface of object with aid of these expansions. The backscattering of the fundamental mode (EH_{11}) from conducting spheres is investigated experimentally in submm wave range. Measurements are compared with theoretical results.

1. INTRODUCTION

The research of scattering and mode conversion from various objects in waveguides, particularly in DC-waveguide [1,2], is of interest for both the theoretical and practical points of view. In this work we present results of the investigation for the interaction of guided modes with conducting spheres, mounted on centre in the circular DC-waveguide.

2. THEORETICAL ANALYSIS

The theoretical investigation of this problem is conducted in the following way. The electric and magnetic fields of the linearly polarized (EH_{1m}) modes of order zero in $1/Aa$, where $A=2\pi/\lambda$, λ is the wavelength, a is the radius of the interior channel of the DC-waveguide, can be written in the form [1,2]:

$$\mathcal{E}_m = J_0(\alpha_m r)\exp(jh_m z)\mathcal{I}_y, \qquad \mathcal{H}_m = -h_m/(IW)\,J_0(\alpha_m r)\exp(jh_m z)\mathcal{I}_x, \qquad (1)$$

where J_0 is Bessel function, h_m is the propagation constant of the EH_{1m} mode, W is the characteristic impedance of space, $\alpha_m = \sqrt{k^2 - h_m^2}$, $\mathcal{I}_x$ and $\mathcal{I}_y$ represent the unit vectors directed along the positive x and y axes, respectively. The centre of the spherical object of radius b coincides with origines of both the circular-cylindrical coordinates (r,ϕ,z) and spherical coordinates (ρ,θ,ϕ). The incident mode propagates in the positive z direction. Then, the solution of the problem is developed by method similar to those used by Morita and Kumagai [3] to investigate scattering from spherical objects inside an optical fiber. We express EH_{1m} modes, given by (1), in terms of the spherical vector wave functions $\mathcal{M}$ and $\mathcal{N}$. These series expansions, after some manipulations, were derived in the following form:

$$\mathcal{E}_m = \sum_{n=1}^{\infty}(A_{mn}\mathcal{M}_{e1n} + B_{mn}\mathcal{N}_{o1n}), \qquad \mathcal{H}_m = -j/W\sum_{n=1}^{\infty}(A_{mn}\mathcal{N}_{e1n} + B_{mn}\mathcal{M}_{o1n}), \qquad (2)$$

where $A_{mn} = \dfrac{j^{(n)}(2n+1)}{n(n+1)}P_n(\cos\beta_m)$, $\quad B_{mn} = \dfrac{j^{(n-1)}}{n(n+1)}\left((n+1)P_{n-1}(\cos\beta_m) + nP_{n+1}(\cos\beta_m)\right)$,
$\cos\beta_m = h_m/A$, P_n is Legendre polynomial.

The scattered fields are obtained by applying the boundary conditions on the surface of the sphere with aid of expansions, given by (1). In the cross section of the DC-waveguide the scattered fields can be expanded in terms of modes as follows:

$$\mathcal{E}^s=\sum_{n=1}^{\infty} C_{mn}^{\mp}\,\mathcal{E}_n, \qquad \mathcal{H}^s=\sum_{n=1}^{\infty} C_{mn}^{\mp}\,\mathcal{H}_n,$$

where the superscripts - and + represent sets of modes at $z=z_1(<0)$ and $z=z_2(>0)$ respectively, outside the spherical object. Using the Lorentz reciprocity principle and the fact that DC-waveguide is one with boundary conditions of impedance form[1,2], we obtain:

$$C_{mn}^{\mp}=\frac{1}{A^2a^2\cos\beta_m[J_1(u_{0m})]^2}\sum_{l=1}^{\infty}\frac{l^2(l+1)^2}{2l+1}(A_l^m A_l^n a_l+B_l^m B_l^n b_l),$$

where a_l and b_l are well-known Mie coefficient, $J_0(u_{0m})=0$. Notice that we ignore multiple scattering effects between the sphere and boundary of the DC-waveguide since the object is small enough.

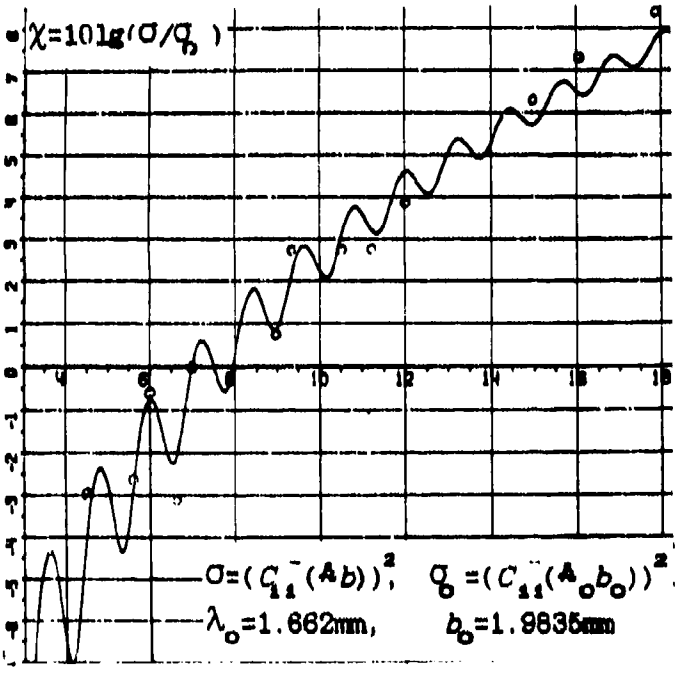

3. EXPERIMENTAL RESULTS

We have chosen 15 conducting spheres of diameter ranging from about 2mm to 12mm. The measurements are conducted in the wavelength range from 1.4mm to 1.6mm. The results of both the calculations and measurements of reflection coefficients of fundamental (EH_{11}) mode from spheres are presented in the figure as a function of Ab. From this figure it can be seen that the agreement between the theoretical and experimental patterns is good (the error is less 1Db).

4. CONCLUSION

Our investigation shows that the similar technique can be applied in analyzing the scattering from other objects inside a DC-waveguide.

5. REFERENCES

1. Yu. N. Kazantzev and O. A. Harlashkin, "Circular waveguides of the class of "hollow dielectric channel" (in Russian), *Radiotechnica i Electronica* Vol.29, №8, pp.1441-1450, 1984.

2. C. Dragone, "High-frequency behavior of waveguides with finite surface impedances," *Bell Syst. Tech. J.*, Vol.60, pp.89-115, January 1981.

3. N. Morita and N. Kumagai, "Scattering and mode conversion of guided modes by a sphe rical object in an optical fiber, "*IEEE Trans. Microwave Theory and* Tech. Vol.MTT-28, pp.137-141, February 1980.

Scattering of a dielectric-slab waveguide eigenmode from an internal penetrable inhomogeneity

Alexander G. Yarovoy

Kharkov State University, Department of Radiophysics
4 Svobody Sq., 310077 Kharkov, Ukraine

ABSTRACT

A numerical technique which may be used to calculate scattering from a homogeneous cylinder with arbitrary smooth cross-section shape inside a dielectric slab waveguide has been developed. By means of surface potentials method the initial diffraction problem is reduced to the system of two integral equations. A new more efficient solution procedure for the latest is proposed. A number of examples for the scattering and mode conversion of guided modes are presented.

1. INTRODUCTION

An analysis of scattering from inhomogeneities inside open waveguides has been of great interest recently in connection with the design of various optical and millimeter-wave components such as filters, grating couplers, and distributed feedback lasers. The unboundedness of a structure causes continuity of the eigenmodes spectrum and presence of radiated waves[1]. That is why the problem is more difficult than that in a closed waveguides. When dimensions of an obstacle in a slab are much smaller then wavelength the asymptotic method can be applied efficiently[2]. For larger obstacles the diffraction problem has been solved for the circular cylinders (only in 2-D case)[3,4] . In this paper a numerical technique has been developed which may be used to calculate scattering from an homogeneous cylinder with an arbitrary smooth cross-section shape inside a dielectric slab waveguide.

2. FORMULATION OF INTEGRAL EQUATIONS AND SOLUTION PROCEDURE

A dielectric slab occupying region $b<z<0$ $(b<0)$ in the three-dimensional space (x,y,z) is considered. A dielectric cylinder is embedded in the slab along x axis. Cross-section S of the cylinder is bounded by an arbitrary smooth curve Σ. Permittivities of the slab and the cylinder are designated as ε_l and ε_c correspondingly. Assume that sources homogeneous along x axis produce the incident TM-polarized electromagnetic field. In view of the geometry and the characteristics of the incident field, this is a two-dimensional problem and the scattered electric field has only an x component. The time factor is assumed to be $\exp(-i\omega t)$. The scattered field outside Σ and total field inside Σ are represented by means of the surface potentials. The kernels of this integral representation are 2D Green's functions of the slab and the homogeneous halfspace with permittivity ε_c correspondingly. Substituting this integral representations in boundary conditions on the curve Σ one may receive a system of two integral equations. The kernel of the first equation has a logarithmic singularity, while the second is the Fredholm type equation of the second kind and the kernels of this equations are bounded continuous functions.

The system obtained has a unique solution in a class of continuous smooth functions, so the surface potentials can be represented by Fourier series. Then utilizing the orthogonality of the functions $\exp(int)$ the initial system of integral equations is reduced to the infinite system of algebraic equations. The latest is the Fredholm's type system of the second kind and can be solved numerically by means of reduction with arbitrary accuracy.

When the values of surface potentials are known the total and scattered field can be calculated using the integral representations. In the far zone of the cylinder in the upper or the lower halfspaces using the asymptotic expression of Green's function, the scattering diagram can be obtained.

3. NUMERICAL EXAMPLES

The lowest order mode is assumed to be incident upon the elliptic cylinder. The equation of the curve Σ we choose as $r(t)=a(\cos(t)y + h\sin(t)z) + b/2z$. We characterize wave scattering outside the slab $b<z<0$ by scattering cross-section $\sigma_r = P_r/P_i$, where P_r is the total power scattered in the upper (lower) halfspace and P_i is the total power transferred by the incident mode along y axis. The scattered field inside the slab is characterized by the total power P_n^+ (P_n^-), which is transferred by the nth mode of the scattered field along y axis in positive (negative) directions, and the mode conversion coefficient $\sigma_n = P_n/P_i$. Fig. 1 shows the cross-sections σ_r (curve 1) and σ_1^+ (2), σ_1^- (3) as functions of frequency. Here $a/|b|=3.0$, $h=0.25$, $\varepsilon_i=2.25$, $\varepsilon_c=1.0$.

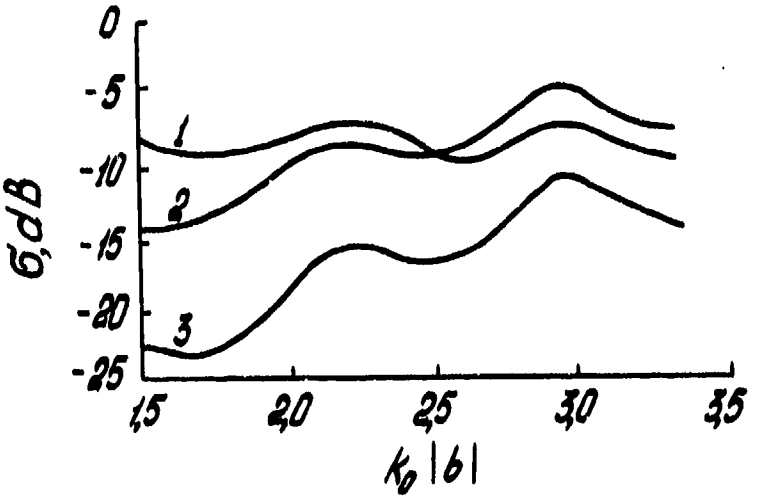

Fig.1. Total scattered power and mode conversion coefficients.

4. CONCLUSION

The scattering and mode conversion of guided modes of the slab waveguide by an arbitrary smooth dielectric cylinder has been analyzed by a numerical method. Some representative numerical examples have been presented. The method proposed may be applied to the open waveguide with complex structure and inhomogeneous obstacles as well.

5. ACKNOWLEDGEMENTS

The author wishes to thank Professor Oleg A. Tretyakov for stimulating discussions and supporting.

6. REFERENCES

1. D. Marcuse, *Theory of Dielectric Optical Waveguides*, Academic Press, New York, 1974.

2. N.K.Uzunoglu and J.G. Fikioris,"Scattering from an inhomogeneity inside a dielectric slab waveguide," *JOSA*, Vol.72, pp.628-637, May 1982.

3. N. Morita," Scattering and mode conversion of guided modes of a slab waveguide by a circular cylinder," *Proc. IEE.*, Vol.127, Pt.H., pp.263-269, May 1980.

4. V.P. Kalinichev and P.N. Vadov,"Numerical investigation of dielectric resonator excitation by dielectric waveguide," *Radiotekhnika i elektronika*, Vol.33, pp.464-472, March 1988 (*in Russian*).

RIGOROUS ANALYSIS OF 3-D DISCONTINUITY PROBLEM IN DIELECTRIC WAVEGUIDE *

Xinzhang Wu and Shanjia Xu
Department of Radio and Electronics
University of Science and Technology of China
Hefei, Anhui, 230027, P.R.China

Abstract

A rigorous analysis of 3-D discontinuity problem in dielectric waveguide is presented by the method which combines the multimode network theory with the rigorous mode matching procedure both in the transverse section and in the longitudinal direction. Good agreement has been found between the numerical results and the experimental data in the literature, and the effectiveness and accuracy of the present method are thus justified.

Summary

Dielectric waveguide has played an important role in millimeter and optical wave integrated circuits. It is necessary to know the scattering characteristics at discontinuities when the integrated circuits are designed. In previous work, a dielectric waveguide 3-D discontinuity problem has for most part been treated by reducing it to an equivalent 2-D model, which may bring errors in accurate circuit design.[1] Although some methods treat the 3-D discontinuity problem directly without using the 2-D model, insufficient approximated field expressions are also introduced in their analysis.[2] In this paper, the scattering characteristics of the 3-D discontinuity problem are investigated by the method which combines the building block approach of multimode network theory with the rigorous mode matching procedure both in the transverse section and in the logitudinal direction. An approximation is introduced to place perfect conducting walls far away from each side of the dielectric block and the dielectric waveguide structure becomes a partially filled dielectric waveguide. In such a way, the model spectrum is discretized to facilitate the analysis, while the essential physics of the scattering process is not affected.

As an example of the 3-D discontinuity problem, Fig.1(a) shows a geometrical configuration of a dielectric image guide (DIG) grating under consideration. Since the structrue is symmetrical in the longitudinal direction, it may be analysed in terms of the symmetrical and anti-symmetrical excitations for which we have the open-circuit (O.C.) and short-circuit (S.C.) bisections respectively, as indicated in Fig.1(b). The scattering properties of each bisection can be investigated through the reflection coefficient of each basic unit. It is proved that the input impedance matrix at $z = z_i^-$ plane looking to the right, is

$$\mathbf{Z}(z_i^-) = \mathbf{Q}_i \mathbf{Z}(z_i^+) \mathbf{Q}_{it}. \tag{1}$$

The reflection coefficient matrix $\mathbf{\Gamma}(z_i^-)$, at the $z = z_i^-$ plane looking to the right, can easily be obtained by

$$\mathbf{\Gamma}(z_i^-) = [\mathbf{Z}(z_i^-) + \mathbf{Z}_{0i}]^{-1}[\mathbf{Z}(z_i^-) - \mathbf{Z}_{0i}]. \tag{2}$$

then, the input impedance matrix at the $z = z_{i-1}^+$ plane looking to the right is determined by

$$\mathbf{Z}(z_{i-1}^+) = \mathbf{Z}_{0i}[\mathbf{I} + \exp(-j\mathbf{k}_{zi}l_i)\mathbf{\Gamma}(z_i^-)\exp(-j\mathbf{k}_{zi}l_i)][\mathbf{I} - \exp(-j\mathbf{k}_{zi}l_i)\mathbf{\Gamma}(z_i^-)\exp(-j\mathbf{k}_{zi}l_i)]^{-1}. \tag{3}$$

*Supported by the National Natural Sciences Foundation of China and the Foundation of State Educational Commission

The reflection coefficient matrix $\mathbf{R}_o$ and $\mathbf{R}_s$ of the step junction corresponding to the O.C. and S.C. bisection can be determined by using eqs.(1)-(3), respectively. The scattering coefficient matrix $\mathbf{R}$ and the transmission coefficient matrix $\mathbf{T}$ of the entire structure are then given by

$$\mathbf{R} = (\mathbf{R}_o + \mathbf{R}_s)/2, \quad \mathbf{T} = (\mathbf{R}_o - \mathbf{R}_s)/2. \tag{4}$$

Fig.2 (a) and (b) show the transmission loss of the E_{11}^y mode versus frequency for two 3-D DIG gratings, respectively. In the figure, the solid lines represent numerical data computed using the present method, whereas the experimental results reported in [1] are indicated by dashed lines, and good agreement is seen over all frequencies; the effectiveness and accuracy of the present method are thus justified.

References

[1] M.Tsuji and H.Shigesawa, 1988 IEEE MTT-S Digest, pp.635-638.

[2] K.Matsumura and Y.Tomabechi, IEEE Trans. on MTT, Vol. MTT-37, pp.414-420, Feb. 1989.

[3] S.T.Peng and A.A.Oliner, IEEE Trans. on MTT, Vol. MTT-29, pp.843-855, Sept. 1981.

[4] Shanjia Xu, S.T.Peng and F.K.Schwering, IEEE Trans. on MTT, Vol. MTT-37, pp.686-690, Apr. 1989.

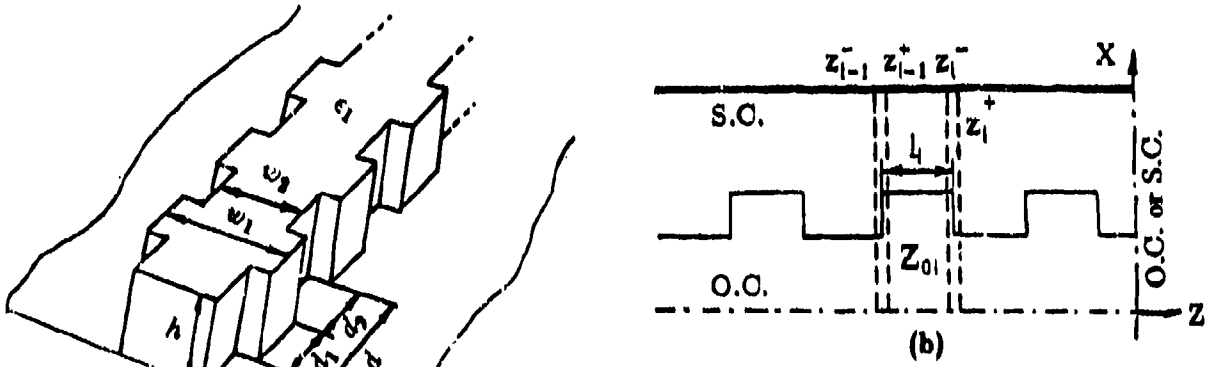

Fig.1 (a) Geometrical configuration of a DIG grating and (b) it bisection with appropriate boundary conditions.

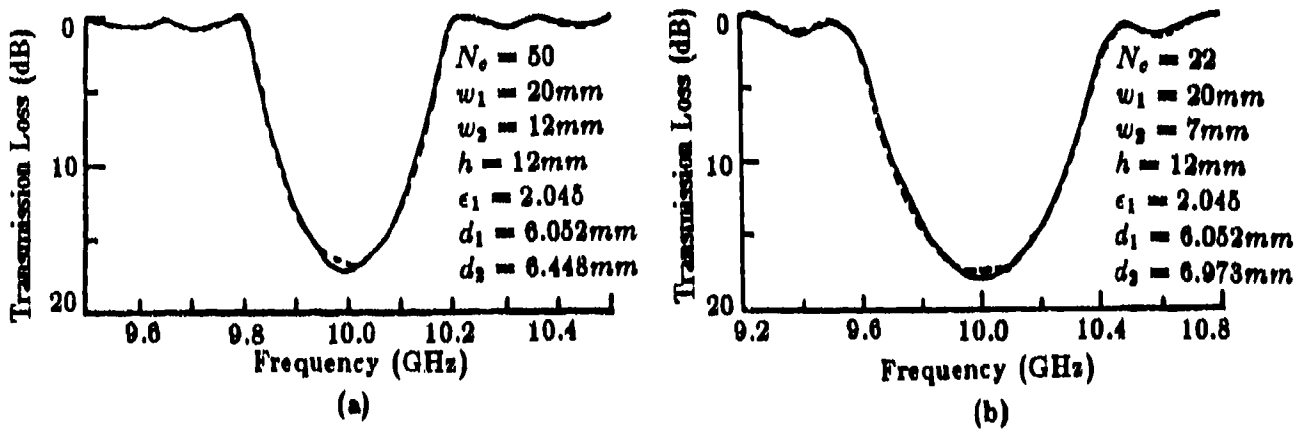

Fig.2 Transmission loss verus frequency for two DIG gratings.

Analysis of scattering of the open resonator field from the cavity-backed aperture

Oleg Belous, Vladimir Veremey, Anatolii Fisun and Anatolii Fursov

Institute of Radiophysics and Electronics Ukrainian Academy of Sciences, 12, ac.Proskura st.,Kharkov,310085, Ukraine

ABSTRACT

Resonance inhomogeneities as cavity-backed apertures are proposed for the mode selection in open resonators. The suggested cavity-backed apertures inhomogeneities is a perfectly conductive circular cylinder with a longitudinal slot. A superposition of two plane waves propagating in opposite directions is considered as an incident field in the theoretical research. It is shown that the slotted cylinder can both be imperceptible for an initial stationary wave field and efficiently scattered it in dependance of the parameters of the cylinder. The experimental results in the 8mm wave band are in good agreement with numerical data. An rotation of the cylinder or its shift from the determined position toward the open resonator mirrors lead to the considerable increasing of the scattered field energy and consequently to decreasing the open resonator Q.

1. An analysis of electromagnetic properties of an Open Resonator (OR) with a perfectly conducting cylindrical inhomogeneity having a resonance cavity is presented. The development of the measuring devices, electrovacuum and solid -state generators of the millimeter waves stimulates interest in the problem of the inhomogeneity effect on the OR characteristics. Inhomogeneities within the quasioptical resonator systems operate as transformers of the OR impedance into the passive or active elements impedances and as effective dissipators of heat produced by from the active structures.

The resonance inhomogeneities as cavity-backed apertures are proposed for the mode selection in open resonators. The suggested cavity-backed apertures inhomogeneities is a thin perfectly conductive circular cylinder with a longitudinal slot.

It was shown experimentally that a superposition of the fields of two plane waves traveling in opposite directions with certain phase shift can serve for a simple model of the quasi-optical OR field near the symmetry axis. This model have been used in the presented theoretical research. The two-dimensional problem of wave diffraction on the perfectly conducting axially slotted cylinder was solved by the method of the Reimann-Hilbert problem.

2. The structure is excited by the plane waves with vector H parallel to the cylinder axis. The initial boundary value problem has been reduced to the N system of dual series equations for Fourier coefficients of the surface current density functions $\{\mu_n\}$ The regularization of the system is the invertion of the matrix operator static part, which correspond to a single element excitation and this invertion has been fulfilled by the method of the Riemann-Hilbert problem.

3. The numerical results for the total flux of Pointing vector for the scattering field (6), divided by 4a are presented. The energy of the scattered field depend upon the frequency and location of the unclosed cylinder in the stationary wave. The phase shift ($\Delta\varphi$) correspond to the position of the cylinder axis with respect to the nodes of the incident field (if $\Delta\varphi$ =0 the axis is in an antinode of the H-field of the stationary wave and if $\Delta\varphi$ = $\pi/2$ the axis is in a node). It was found that the energy of the scattered field can be reduced considerably by the choice of the position of the cylinder in the stationary wave field (Fig.1) or by the rotation of the cylinder (Fig.2).

4. The experiments were carried out in the 27-38GHz band. OR is formed by spherical mirror of curvature radius R=180mm and flat mirror with diameters d=90mm. The distance between the mirrors is 90mm. The resonance volume of the OR is connected with input and output waveguides (with cross-section 7.2*3.4mm) by two coupling slots with cross-section 7.2*0.2mm. The closed circular copper cylinder and the thin circular copper cylinders having longitudinal slot with angular dimensions θ =21.8° and 180° are studied experimentally. The cylindrical inhomogeneities were installed with possibility of displacement and rotation.

The Q-factor of the OR with the inhomogeneities was measured. It was shown that the slotted cylinder with small cross-sectional wavedimensions (less than $\lambda/4$) and with θ =180° is almost imperceptible if the cylinder is located at the definite distances from the flat mirror. The scattered field energy is considerably increased when the cylinder is shifted from the definite position. This result was predicted by the theoretical study of the scattering of a stationary wave field by a circular slotted cylinder.

In the case of the closed circular cylinder or the slotted cylinder (with angular dimensions of the slot 21.8°) within the OR the displacement of the inhomogeneity does not have an substantial influence on the resonator Q. These cylinders efficiently scatter electromagnetic energy and the OR Q is decreased considerably in spite of small cross-sectional wave-dimensions of the inhomogeneities (see Fig 3).

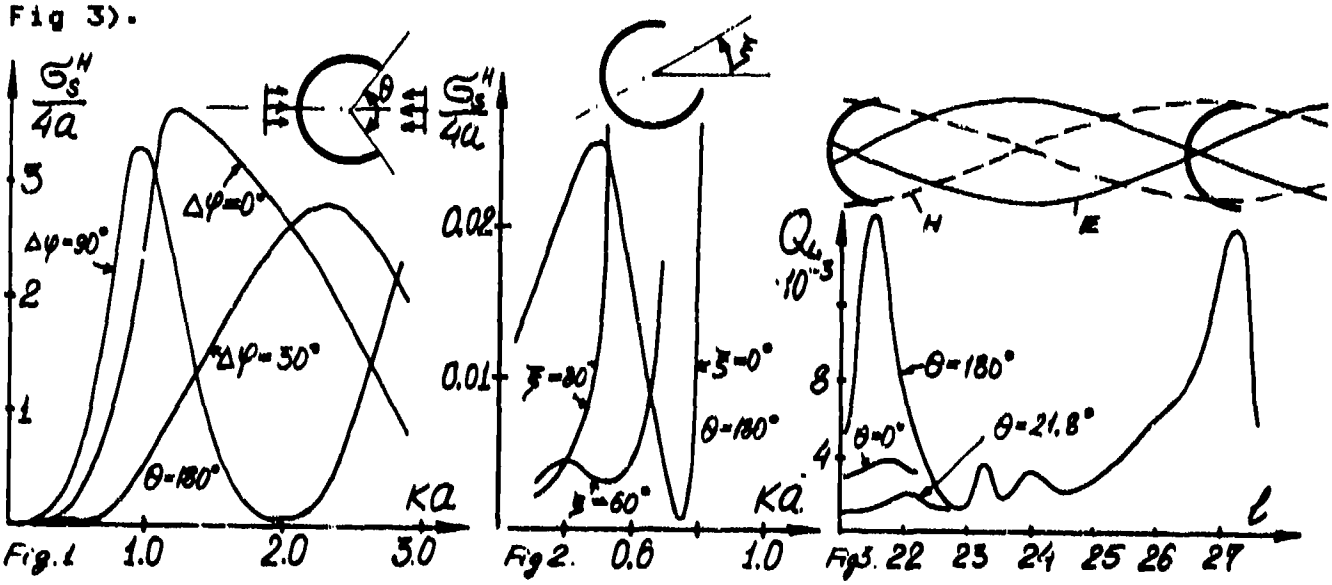

Resonant frequencies and Q-factors of a spherical cavity loaded by an eccentric dielectric sphere

Li-Yang Zhang, Pin Wang, and Chang-Hong Lang
Department of Electromagnetic Engineering
Xidian University, Shaanxi 710071, P. R. China

ABSTRACT

A novel harmonic expansion form is employed for describing the modes in a spherical cavity loaded by an eccentric dielectric sphere. Characteristic equation for complex resonances is obtained. Numerical results for both resonant frequencies and Q-factors showing the stability and efficiency of the method are given.

1. INTRODUCTION

It is believed that determination of the Q-factors of the modes in a dielectric loaded cavity or resonator, as well as the resonant frequencies, play an important role in realistic filter design in microwave circuits, MIC and MMIC. Some methods has been established for calculating resonant frequencies in some special structures recently, e.g. for hybrid modes in cylindric cavity loaded by dielectric rods[1,2] and *TE* and *TM* modes in spherical cavity loaded by an eccentric dielectric sphere[3]. However, conventional method for evaluating Q-factor for a cavity or resonator requires both resonant frequency and field distribution of the concerned mode, especially complicated computations. That subsequently results in awful computational burden in optimal filter design. In this paper, multiple expansion method is developed for determining both resonant frequencies and Q-factors of the structure being composed of two or more nonconcentric dielectric spheres.

2. FORMULATION

Consider the three regions I, II and III in an eccentric spherical configuration shown in Fig.1 filled with arbitrary physical media. The electric field of each mode might be described by the following derivative equation and boundary conditions

$$\nabla \times \nabla \times \mathbf{E}_q(\mathbf{r}) - k_q^2 \mathbf{E}_q(\mathbf{r}_q) = 0, \quad in \ \mathrm{I}, \mathrm{II} \ and \ \mathrm{III} \ (q = 1,2,3), \tag{1}$$

$$\mathbf{r}_1 \times [\mathbf{E}_1(\mathbf{r}) - \mathbf{E}_2(\mathbf{r})] = 0, \quad \mathbf{r}_1 \times \nabla \times [\frac{1}{\mu_1}\mathbf{E}_1(\mathbf{r}) - \frac{1}{\mu_2}\mathbf{E}_2(\mathbf{r})] = 0, \quad on \ S_1, \tag{2}$$

$$\mathbf{r}_2 \times [\mathbf{E}_2(\mathbf{r}) - \mathbf{E}_3(\mathbf{r})] = 0, \quad \mathbf{r}_2 \times \nabla \times [\frac{1}{\mu_2}\mathbf{E}_2(\mathbf{r}) - \frac{1}{\mu_3}\mathbf{E}_3(\mathbf{r})] = 0, \quad on \ S_2, \tag{3}$$

in which $k_q^2 = \omega^2 \varepsilon_q \mu_q$, Let $(r_1, \theta_1, \varphi_1)$ and $(r_2, \theta_2, \varphi_2)$ denote the two spherical coordinates centered at O_1 and O_2, respectively. Notice, the filed in region II can be considered to be generated by the equivalent sources on S_1 and S_2 in free space. Therefore, these fields may exactly be described by multiple expansion involving spherical harmonics in the two spherical coordinates, such as

$$\mathbf{E}_1 = \sum_{n=1}^{\infty} \sum_{m=-n}^{n} (A_{mn}^1 \mathbf{M}_{mn}^{11(1)} + B_{mn}^1 \mathbf{N}_{mn}^{11(1)}), \quad r_1 < a, \tag{4}$$

$$\mathbf{E}_2 = \sum_{n=1}^{\infty} \sum_{m=-n}^{n} (C_{mn}^2 \mathbf{M}_{mn}^{11(3)} + D_{mn}^2 \mathbf{N}_{mn}^{11(3)} + A_{mn}^2 \mathbf{M}_{mn}^{21(1)} + B_{mn}^2 \mathbf{N}_{mn}^{21(1)}), \quad r_1 > a \ and \ r_2 < b, \tag{5}$$

$$\mathbf{E}_3 = \sum_{n=1}^{\infty} \sum_{m=-n}^{n} (C_{mn}^3 \mathbf{M}_{mn}^{22(3)} + D_{mn}^3 \mathbf{N}_{mn}^{22(3)}), \quad r_2 > b. \tag{6}$$

However, in the vicinity of these boundaries, the field in region II may be described by harmonic expansions involving harmonics of a single spherical coordinate, such as

$$\mathbf{E}_2 = \sum_{n=1}^{\infty} \sum_{m=-n}^{n} [a_{mn}^2 (f_n^{ab} \mathbf{M}_{mn}^{21(1)} - g_n^{ab} \mathbf{M}_{mn}^{21(3)}) + b_{mn}^2 (f_n^{ab} \mathbf{N}_{mn}^{21(1)} - g_n^{ab} \mathbf{N}_{mn}^{21(3)})], \quad a + d < r_2 < b, \tag{7}$$

$$\mathbf{E}_2 = \sum_{n=1}^{\infty} \sum_{m=-n}^{n} [c_{mn}^2 (-f_n^{aa} \mathbf{M}_{mn}^{11(1)} + g_n^{aa} \mathbf{M}_{mn}^{11(3)}) + d_{mn}^2 (-f_n^{aa} \mathbf{N}_{mn}^{11(1)} + g_n^{aa} \mathbf{N}_{mn}^{11(3)})], \quad a < r_1 < b - d, \tag{8}$$

where f_n^{ba}, g_n^{ba}, f_n^{aa}, g_n^{aa}, f_n^{bb}, g_n^{bb}, f_n^{ab}, g_n^{ab}, could be determined by using the orthogonality of these

harmonics on S_1 or S_2. Since (7) or (8) represents the identical field described by (5) in the vicinity of the corresponding boundary, compared (7) with (5), as well as (8) with (5), it is found that $A^2_{mn} = a^2_{mn} f^{hb}_n$, $B^2_{mn} = b^2_{mn} f^{hb}_n$, $C^2_{mn} = c^2_{mn} R^{ha}_n$, and $D^2_{mn} = d^2_{mn} R^{ha}_n$. Then considering the above relations and subtracting (8) or (7) from (5), and by employing translational addition theorems for vector spherical harmonics, one gets

$$a^2_{mn} R^{hb}_n + \sum_{\nu=s}^{\infty} (c^2_{m\nu} A^{m\nu}_{mn} R^{ha}_\nu + d^2_{m\nu} B^{m\nu}_{mn} R^{ea}_\nu) = 0, \quad b^2_{mn} R^{eb}_n + \sum_{\nu=s}^{\infty} (d^2_{m\nu} B^{m\nu}_{mn} R^{ha}_\nu + d^2_{m\nu} A^{m\nu}_{mn} R^{ea}_\nu) = 0,$$

$$c^2_{mn} f^{ha}_n + \sum_{\nu=s}^{\infty} (a^2_{m\nu} C^{m\nu}_{mn} f^{hb}_\nu + b^2_{m\nu} D^{m\nu}_{mn} f^{eb}_\nu) = 0, \quad d^2_{mn} f^{ea}_n + \sum_{\nu=s}^{\infty} (a^2_{m\nu} D^{m\nu}_{mn} f^{hb}_\nu + b^2_{m\nu} C^{m\nu}_{mn} f^{eb}_\nu) = 0,$$

$$m = 0, \pm 1, \pm 2, \cdots, s = max(|m|, 1), n \geq s, \tag{9}$$

where $A^{mn}_{m\nu}$, $B^{mn}_{m\nu}$, $C^{mn}_{m\nu}$ and $D^{mn}_{m\nu}$ are the translation coefficients. The characteristic equation for the modes in the structure is consequently obtained by forcing the determinant of the coefficient matrix in (9) to be zero. For a cavity of low loss, Q-factor of the mode may be described by its complex resonance

$$Q_0 = -Re(\omega_0) / 2Im(\omega_0) \ , \ if \ Re(\omega_0) >> Im(\omega_0), \tag{10}$$

3. NUMERICAL RESULTS

It should be pointed out that the media I, II and III may be any homogeneous isotropic medium, e.g. dissipative dielectric or metal of finite conductivity. Suppose medium III get a large but finite conductivity, then the structure means a metallic cavity loaded with an eccentric dielectric sphere. For performing numerical calculation, an adequate truncation number N will be set for the series in (4–6). Consequently (9) gives $4N$ linearly independent equations.

4. CONCLUSIONS

Analysis for both resonances and Q-factors of a spherical cavity loaded by an eccentric dielectric dielectric sphere is initiated in this paper with multiple expansion method. Numerical results are given to show the reliability and efficiency of the formulations.

5. REFERENCES

1. K. A. Zaki and A.Atia, "Modes in dielectric-loaded waveguidesand resonators, " *IEEE Trans. on MTT*, Vol. MTT-31, pp.1039-1044, 1983.

2. M. M. Taheri and D. Mirshekar-Syahkal, " Accurate determination of modes in dielectric-loaded cylindrical cavities using a one-dimensional finite element method, " *IEEE Trans. on MTT*, Vol. MTT.37, pp.1536-1541., 1989.

3. J. D. Kanellopoulos and J. G. Fikioris, " Resonant frequencies in an electromagnetic eccentric spherical cavity, " *Q. Appl. Math.*, Vol. 37, pp. 51-66, 1979.

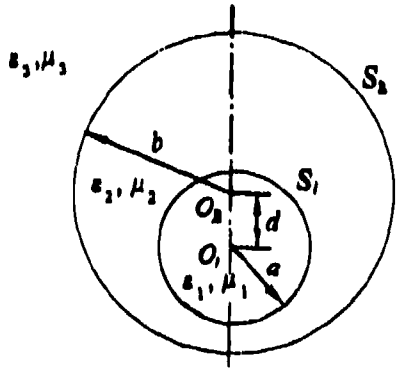

Fig.1 An eccentric spherical cavity

TM-POLARIZED WAVE SCATTERING FROM DIELECTRIC CYLINDER EMBEDDED IN A STRATIFIED MEDIUM

A.G.Yarovoy, and N.P.Zhuck
Department of Radiophysics, Kharkov State University,
4 Svobody Sq., 310077 Kharkov, Ukraine

Abstract- Two-dimensional scattering from an arbitrarily inhomogeneous body buried in a homogeneous layer has been considered using the integral equation formulation over the cross-section of the body and the moment method. The arising system of linear algebraic equations is solved with the aid of conjugate gradient method and one dimensional fast Fourier transform. The solution can be applied to investigate problems connected with microwave and optic design, non-destructive control and remote sensing. Some numerical results are presented.

Variational solution of resonant cavity filled with anisotropic plasma

Kai Liu Wenxun Zhang Jimin Ying

Department of Radio Engineering, Southeast University
Nanjing 210018, P.R.CHINA

ABSTRACT

In this paper, a variational equation for solving electromagnetic field boundary value problem is deduced from Maxwell's equations, it holds the advantage of that the trial functions are not restricted by theboundary condition, and is especially usefull for solving problem with anisotropic medium in an irregular geometry. The resonant characteristics of plasma-filled cavity is analysed by using the Rayleigh-Ritz method, the resonant frequency and Q-value of quasi- TE_{011} and quasi - TE_{111} modes are calculated as the functions of plasma parameters, they have important value of reference in industrial application of plasma.

1.INTRODUCTION

With reference to the electromagnetic field boundary value problem with anisotropic medium, P.S.Epstein[1]had provided rigorous classical analysis which involves tedious tensor deduction, and is valid only for the problems with regular geometry. R.R.Gupta and R.F.Harrington[2] have examined the rectangular cavity filled with anisotropic plasma by using the Methods of Moments(MoM) , and presented several computational curves of the frequency shift and the variation of quality factor(Q) versus the plasma parameters. A.D .Berk first established the variational principles of waveguide and resonant cavity filled with anisotropic medium. A.Konrad[3] deduced a kind of variational equations of rectangular and circular waveguide in detail, but no example was calculated in his paper. In this paper, according to the stationary condition of a functional[4] and by using the Rayleigh-Ritz method, three components of magnetic fields are expanded in the form of polynomial with complex coefficients. In the case of homogeneous medium, the matrix equation will be replaced by several individual algebraic equations which can determine the resonant frequencies of different modes in the cavity without plasma. The coupling between field components, due to presence of plasma, results in that the matrix equation can not be separated, and the resonant frequencies of various modes are changed.

2.STATIONARY FUNCTIONAL FORMULAS

For time-harmonic fields in anisotropic medium, Maxwell's equations are as follows:

$$\nabla \times \bar{E} = -j\omega\bar{\mu}\bar{H}, \qquad \nabla \times \bar{H} = j\omega\bar{\bar{\varepsilon}}\bar{E} + \bar{J}$$

$$\nabla\cdot(\bar{\bar{\varepsilon}}\bar{E}) = 0, \qquad \nabla\cdot(\bar{\mu}\bar{H}) = 0 \tag{1}$$

where $\bar{\mu}$ is the dyadic permeability, $\bar{\bar{\varepsilon}}$ is the dyadic permittivity. Each wave equation corresponding to $\bar{E}$ or $\bar{H}$ can be easily yield. Through the minimal energy-related functional and the Gauss'Divergence Theorem, in a region constituted by plasma without source, the functional related to magnetic field strength is given by

$$F(\bar{H}) = \int_\Omega \nabla \times \bar{H}^* \cdot \bar{\bar{\varepsilon}}^{-1} \cdot \nabla \times \bar{H} d\Omega - \omega^2 \mu \int_\Omega \bar{H}^* \cdot \bar{H} d\Omega \tag{2}$$

This treatment will result in that the trial function is no longer be restricted by the boundary condition.

3.RESONANT CHARACTERISTICS OF PLASMA-FILLED CAVITY

The resonant frequency in a cavity filled with anisotropic plasma will be shifted from that in an empty cavity with the same geometry and the quality factor Q will also be changed, they can be expressed as

$$\Delta(\omega / \omega_0) = Re(-\frac{\omega - \omega_0}{\omega_0}), \qquad \Delta(1/Q) = 2Im(\frac{\omega - \omega_0}{\omega_0}) \tag{3}$$

where ω_0 is resonant frequency of empty cavity. The modes in plasma-filled cavity may not be classified into TE or TM modes related to z-direction. However, they will degenerate to TE or TM modes if the electron density is reduced to zero. Hence, the terminology "quasi-TE" or "quasi-TM" is used to denote these modes, corresponding to their empty cavity designation. As shown in Fig.2, it is evident that the numerical results are good agreement with those computed by using the MoM[2]. In the case of circular cylindrical cavity (Fig.4), when $(\omega_b / \omega) > 1$, the shift $\Delta\omega$ is positive for $(\omega_p / \omega) > 1$; and negative for $(\omega_p / \omega) < 1$.

It seems that an unsuitable combination of D-C magnetic field corresponding to ω_b and the electron density corresponding to ω_p results in those unstable performance of plasma. Hence, they must be chosen carefully in practical applications.

4.REFERENCES

[1] P.S.Epstein," Theory of Wave Propagation in Gyromagnetic Media," *Rev. Modern Physics*, Vol.28, No.1, Jan.,1956.

[2] R.R.Gupta, R.F.Harrington," Cavity Resonate Containing Anisotropic Media," *Appl.Sci.Res.*, Vol.16, pp.46-64,1966.

[3] A.Konrad," Vector Variational Formulation of EM Fields in Anisotropic Media," *IEEE Trans.*, Vol.MTT-24, No.9, Sept.,1976.

[4] Wenxun Zhang, *Engineering Electromagnetism: Functional Method*, Ellis Horwood Ltd.,Chichester, 1990, Ch.3.

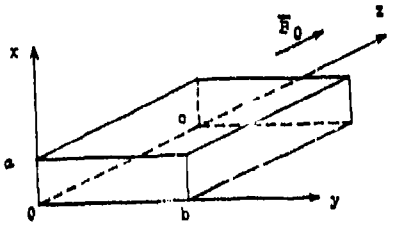

Fig.1 Rectangular cavity with Cartesian coordinates

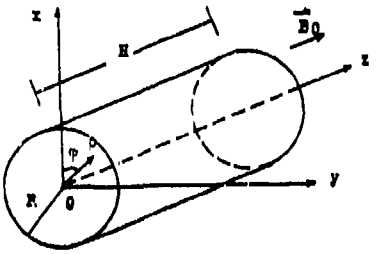

Fig.3 Circular cylindrical cavity with coordinates

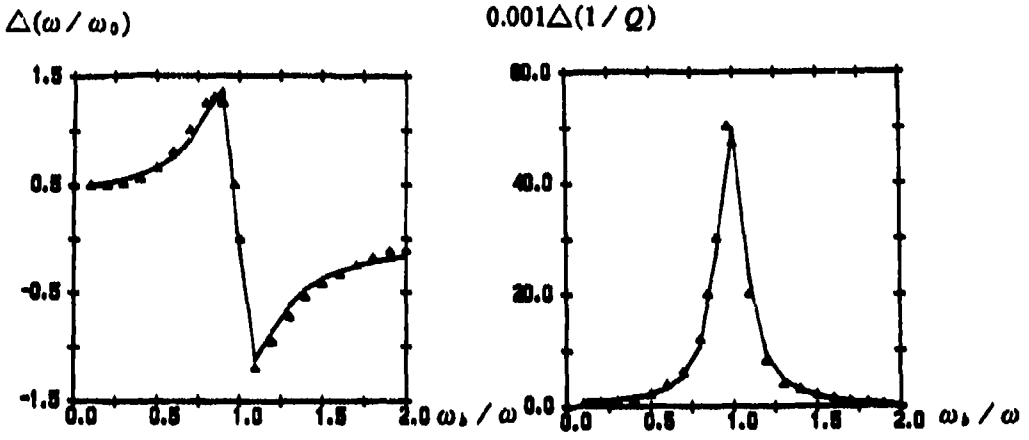

Fig.2 Frequency shift and variation of (1 / Q) vs cyclotron frequency for *quasi* -- TE_{011} mode, $b / a = 2.25, c / a = 3.0, \gamma_e / \omega = \omega_p / \omega = 0.1$

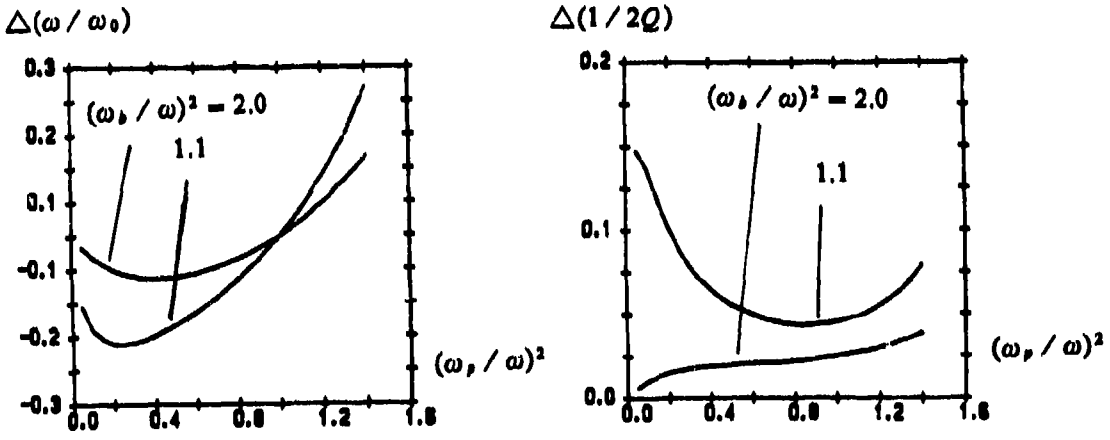

Fig.4 Frequency shift and variation of (1 / Q) for *quasi* – TE_{111} mode in circular cavity, $R / H = 0.5, \gamma_e / \omega = 0.001$.

Open resonator with mode selection for millimeter-wave devices

O.I.Belous, A.I.Fisun, A.M.Fursov, A.A.Kirilenko, V.I.Tkachenko

Institute of Radiophysic and Electronics Ukrainian Academy of Science
12, Acad. Proskura st., Kharkov, 310085, the Ukraine

ABSTRACT

Analysis of the open resonator with a selective elements has been presented. As a selective elements are using a reflection diffraction gratings. The rarefaction of the spectrum depends of the type of the grating. The distribution of the field of the eigenmode was investigate and the domain of application was determine for this results.

1. INTRODUCTION

The first application of the open resonators (ORs) for mm-devices was make for in 1960-1970. The analysis of various types of open resonators has shown, that they possess high Q-quality and dimensions lager of the wave length. However, the rarefaction of the spectrum in OR is insufficient in a number of case. In these paper ORs with echelette or cornerechelette mirrors are investigate [1].

2. SPECTRUM AND FIELD CALCULATION

The real echelette ORs and cornerechelette ORs was represented plane two-dimensional model (see fig.1b,c). The electrodynamics model system (SEM-4) [1] was applied in this research. The approach of the decomposition was used for the precise model of the different electrodynamics structures. The OR was considered as a superposition the number of the waveguide discontinuities with the transmit of the load to the open ends of the waveguides. The know S-matrix of the waveguide discontinuities are using in this calculations (triple waveguide, steps and open ends of the waveguides). The employment of the rapid numerical-analitical algorithm allowed to analyses the spectrum and fields of the open resonator for the characteristic dimensions $\mathfrak{Z}$ =0.5-10, where $\mathfrak{Z} = a/\lambda$, a - interval between a reflectors and λ - wave length.

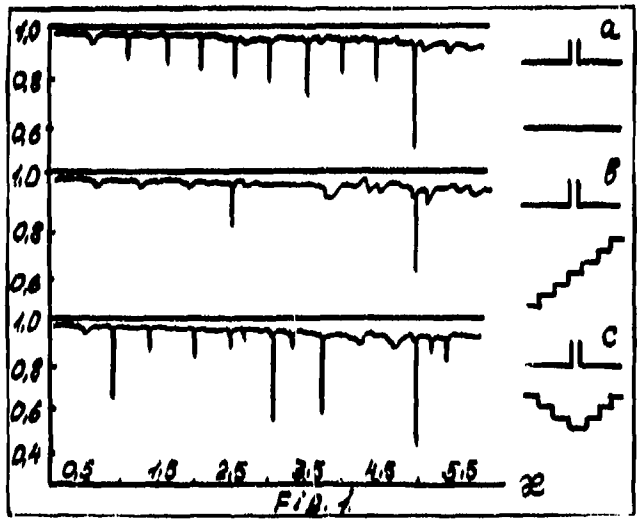

Fig. 1

3. CALCULATION RESULTS

The spectrum of eigenoscillations was calculated as a module of the power reflection coefficient on the section of the exciting waveguide (see fig.1). The curve of the equal values of H-component fields are showed on the fig. 2,3,4 for different numbers $\mathfrak{Z}$. The calculation is

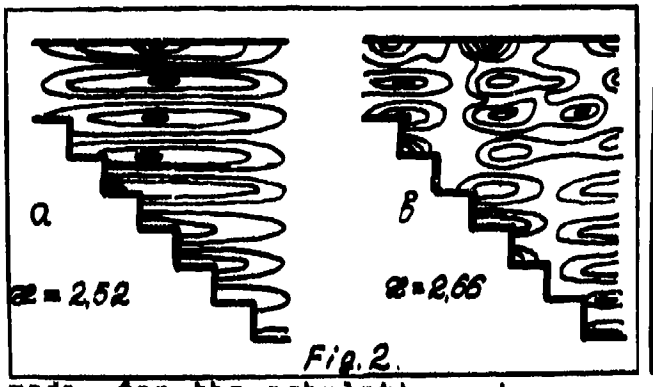

Fig.2.

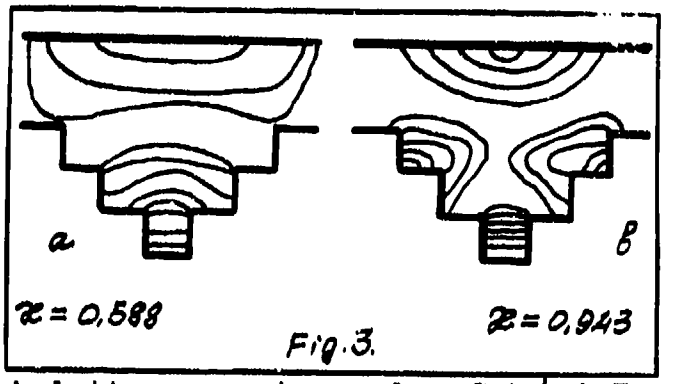

Fig.3.

made for the echelette and cornerechelette resonators for $a/d=0.71$, where d - mirror aperture. The spectrum of the resonator with the smooth reflectors is showed on the fig. 1a for the comparison with another.

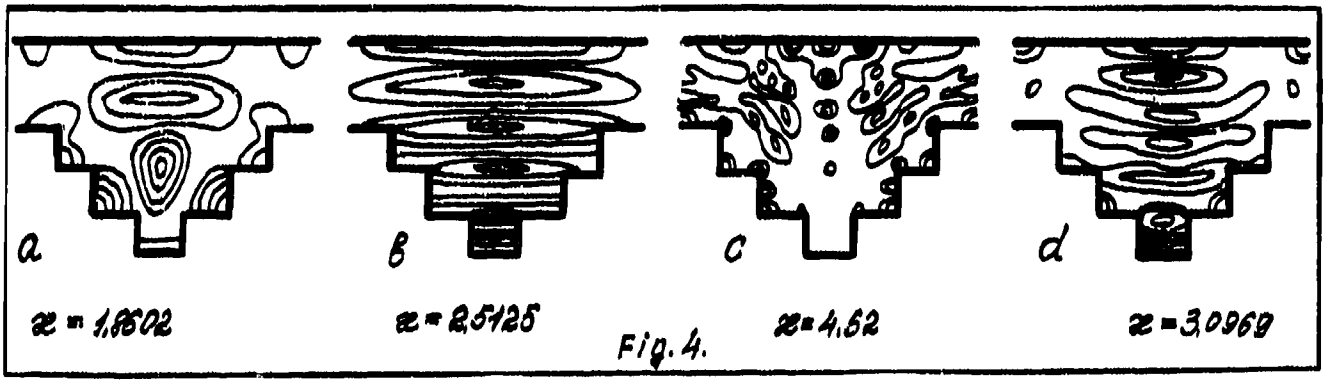

Fig.4.

4. CONCLUSION

4.1. The spectrum of the echelette resonator has at most rarefaction amongst another OR study in these paper. The maximum of the field distribution is moved to the narrow part of resonator. This is well conformed with the experiment [2], and this appearance is explained of the different reflection coefficient from the open ends of resonator.
4.2. The fields of same eigenoscillations have at most intensive of concentration not far from the top of corner in the OR with the cornerechelette mirror (for example æ =0.943, æ =3.0969).
4.3. The H-component field OR distribution is very important parameter for the elaboration of the mm-wave solid-state sources. This distribution shows where the interaction of the nonlinear active elements with the resonator H-component field wile be optimum.

5. REFERENCES

1. Belous O.I., Fisun A.I., Fursov A.M. High-Stability Sphere-Corner-Echelette Open Resonator Gunn-diode and IMPATT-diode Oscillators. The 17th International Conference on Infrared and Millimeter Waves, Pasadena, California, USA, December 14-17, 1992, pp.456-457.
2. Belous O.I., Bulgakov B.M., Fisun A.I., Fursov A.M. Singularities of autocollimation regime in dispersive open resonator with phase-correct mirror (in Russia). Pisma v zhurnal tekhnicheskoi fiziki, v.18, N4, 1992, pp.46-52.

Quasi-optics eigenmodes of the waveguide resonator

A.I.Kleev

P.L.Kapitza Institute for Physical Problems
Russian Academy of Sciences
ul. Kosygina 2, Moscow, 117334, Russia

The quasi-optics eigenmodes of the waveguide resonator for free electron laser (FEL)[1] are considered in this paper. The model of the free electron laser optical system is a waveguide resonator consisting of a uniform waveguide of a $2a$ in diameter and $2D$ in length and mirrors with curvature radii R_1 and R_2 which are placed at distances of L_1 and L_2 from the origin of coordinates (see Fig. 1). We consider the system whose dimensions are much longer than the wavelength λ and a parabolic equation can be used for the description of fields.

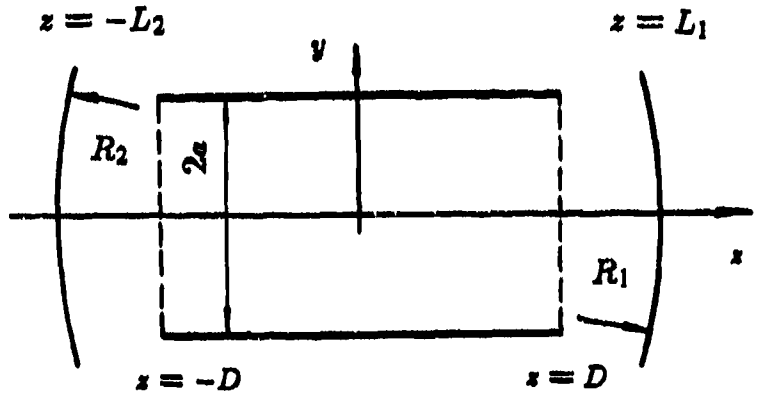

Fig. 1

The electric field in the resonator can be expressed in form of the sum of two waves:

$$\vec{E}_\perp = \vec{E}_\perp^{(1)}(x,y,z)\exp(ikz) - (-1)^q \vec{E}_\perp^{(2)}(x,y,-z)\exp(-ikz),\ \vec{E}_\perp^{(s)} = (E_x^{(s)}, E_y^{(s)}), \tag{1}$$

$s=1,2$, q – integer number. The time factor $\exp(-i\omega t)$ ($\omega = v_c k$, v_c is the vacuum light velocity, $k = 2\pi/\lambda$) is assumed and suppressed throughout the paper. It is convenient to introduce two scalar functions $F_0^{(s)}(t,\theta)$ and $F_2^{(s)}(t,\theta)$

$$\exp(ikL_s)E_y^{(s)} = F_0^{(s)}(t,\theta) + F_2^{(s)}(t,\theta)\exp(-2i\varphi),\ E_x^{(s)} = -iE_y^{(s)},\ t = r/a,\ \theta = z/D. \tag{2}$$

In the waveguide the unknown functions $F_0^{(s)}(t,\theta)$ and $F_2^{(s)}(t,\theta)$ can be expressed in terms of sums

$$F_l^{(s)}(t,\theta) = \sum_{n=0}^{2N-1} b_n^{(s)}(\theta)\gamma_n^{(l)} J_l(g_n t)\exp(-ig_n^2\Delta\theta),\ \Delta = D/2ka^2,\ \gamma_n^{(0)} = 1,\ \gamma_n^{(2)} = -\frac{J_0(g_n)}{J_2(g_n)}. \tag{3}$$

Fields in the system under consideration can be obtained by solving the equation:

$$\mathrm{R}\,\mathrm{b}(1) = \Gamma_m \mathrm{W}\,\mathrm{b}(-1),\ \mathrm{R} = \begin{Vmatrix} 0 & \mathrm{R}_0^{(2)} \\ 0 & \mathrm{R}_2^{(2)} \\ \mathrm{R}_0^{(1)} & 0 \\ \mathrm{R}_2^{(1)} & 0 \end{Vmatrix},\ \mathrm{W} = \begin{Vmatrix} \mathrm{W}_0^{(1)} & 0 \\ \mathrm{W}_2^{(1)} & 0 \\ 0 & \mathrm{W}_0^{(2)} \\ 0 & \mathrm{W}_2^{(2)} \end{Vmatrix}, \tag{4}$$

$$(R_{j,n})_l^{(s)} = \gamma_n^{(l)} \int_0^1 K_l^{(s)}(t_j,t_1) J_l(g_n t_1)\exp(-ig_n^2\Delta)t_1 dt_1,\ (W_{j,n})_l^{(s)} = \gamma_n^{(l)} J_l(g_n t_j)\exp(ig_n^2\Delta)t_1 dt_1,$$

$$\mathrm{b}(\theta) = (b_0^{(1)}(\theta),\ldots,b_{2N-1}^{(1)}(\theta), b_0^{(2)}(\theta),\ldots,b_{2N-1}^{(2)}(\theta)),\ j = 0,1,\ldots,N-1,\ n = 0,1,\ldots,2N-1.$$

We consider an initially monoenergetic highly relativistic electron beam moving in the positive z direction through a periodic circularly polarised wiggler so that the transverse velocity is $v_\perp$ and the longitudinal velocity is $v_\parallel$. The self-consistent system of equations describing the interaction of the electron beam with the field has the form:

$$\frac{db_n(\theta)}{d\theta} = -\frac{\mu}{2\eta p_n} I \exp(-i\Phi_n), \quad \frac{\partial^2 \vartheta(\varphi_0,\theta)}{\partial\theta^2} = -\frac{1}{4\eta^2}\mathrm{Re}\left\{\sum_{n=0}^{2N-1} b_n(\theta)\exp[i(\Phi_n - \varphi_0 - \vartheta(\varphi_0,\theta))]\right\} \tag{5}$$

$$I = \frac{1}{\pi}\int_0^{3\pi} \exp[\varphi_0 + \vartheta(\varphi_0,\theta)]d\varphi_0, \; p_n = N_n/2v_c a^2,$$

where N_n is the norm of the circulary polarised mode of a circular waveguide and

$$\Phi_n = 2(k - g_n^2\Delta/D + k_0 - K_e)D_e = \Phi - 2g_n^2\Delta\eta, \; \mu = \frac{I_0}{I_A}\frac{4kD_e^3}{a^3}\frac{v_\perp^2(v_c^2 - v_\parallel^2)}{v_\parallel^3\gamma_0 v_0}, \tag{6}$$

$$k_e = kv_c/v_\parallel, \; v_0^2 = v_\perp^2 + v_\parallel^2, \; I_A = m_e v_c^3/|e| \approx 17\cdot 10^3 \mathrm{A}$$

here I_0 is a total beam current, e is an electron charge, m_e is its mass, D_e is the ondulator length. On the linear stage, for small gain, when $\mu \ll 1$, the matrix T for conversion of $\mathrm{b}(\theta)$ from the plane $\theta = -1$ to the plane $\theta = 1$ ($\mathrm{b}(1) = \mathrm{Tb}(-1)$) is given by the expression $\mathrm{T} = \mathrm{I} + \mu\mathrm{V}$, where μ is the gain factor for plane wave. When there are two modes with close frequencies in a resonator, the equation defining the eigenfrequencies of the cavity with an electron beam takes the form:

$$(\Gamma_1^{(1)} - \Gamma)(\Gamma_2^{(1)} - \Gamma) = \mu^2\Gamma_1^{(0)}\Gamma_2^{(0)}\frac{(\mathrm{b}_1^{(0)}\cdot\mathrm{Vb}_2^{(0)})^2}{(\mathrm{b}_1^{(0)}\cdot\mathrm{b}_1^{(0)})(\mathrm{b}_2^{(0)}\cdot\mathrm{b}_2^{(0)})}, \tag{7}$$

where $\Gamma_1^{(1)}$ and $\Gamma_2^{(1)}$ are disturbed eigenvalues obtained under the assumption of isolated modes. Calculations have shown that when the condition of "isolation" is broken the proportionality of the gain $\delta = 2(|\Gamma_m| - 1)$ to the total current may not take place. Fig. 2 shows δ versus μ curves calculated for three modes (the curve number represent the number of mode). The investigation carried out showed that new modes of the system are being formed as a result of interaction of resonator field with an electron beam. In the case of modes with close frequencies the influence of the beam results in their coupling. In this case the eigenfunctions hybridisation occurs, i.e. a considerable distortion of eigenmode field. The dependence of the frequency shift on the total current can be nonlinear in this case.

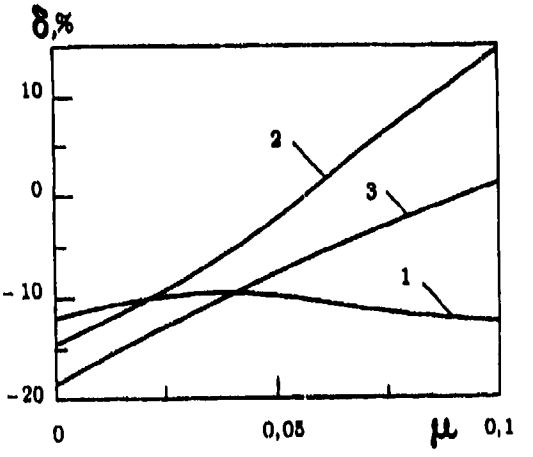

Fig. 2

1. A.Doria, G.P.Gallerano and A.Reniery, "Kinematic and dynamic properties of a waveguide FEL", *Opt. Commun.*, Vol. 80, pp. 417-424, January 1991.

FIR multiphoton absorption and photon drag effects in degenerate valence band semiconductors

S.D. Ganichev*, E.L. Ivchenko, R.Ya. Rasulov, I.D. Yaroshetskii and B.Ya. Averboukh

A.F. Ioffe Physicotechnical Institute, Russian Acad.of the Sciences, St. Petersburg, 194021, Russia

*Alexander von Humboldt Fellow,
Present address: Uni.Regensburg, Institute für Angewandte Physik III, 93040 Regensburg

ABSTRACT

Intraband linear-circular multiphoton dichroism of far infrared absorption in p-Ge has been observed for the first time. Previously this nonlinear optical phenomenon was observed only under the valence-conduction interband electronic transitions induced by IR or visible-range radiation. Experimentally, the dependencies of the optical transmission and the photon drag effect on the FIR radiation (λ = 90 μm) intensity and polarisation have been investigated in p-type Ge crystals. A polarisation dependent sign inversion of the photon drag effect with increasing radiation intensity has been also observed.

2. INTRODUCTION

Experimental investigations of n-photon absorption in crystals are usually made under the conditions that optical transitions with fewer photons are forbidden. Then, many photon transitions of higher order can be ignored in the visible to middle infrared range, as the value of n-photon absorption coefficient $K^{(n)}$ is much higher than the coefficient of (n+1)-photon absorption, $K^{(n+1)}$. This holds up to the light intensities corresponding to the damage threshold of the investigated materials. For the same reason, the main contribution in the case of intraband absorption of light comes from one-photon processes, and many-photon transitions with intermediate virtual states make a negligible contribution.

The appearance of lasers capable of generating high power FIR radiation has revealed new aspects of the interaction of the electromagnetic radiation with solids. In fact, if the calculation of the n-photon absorption coefficient $K^{(n)}$ is limited to the lowest order of perturbation theory for each of these processes, it is found that the ratio $\eta_n = K^{(n)}/K^{(n+1)}$ is proportional to $I\omega^{-3}$ in the case of intraband absorption of light, where I is the intensity of light in a crystal. Thus in the case of FIR radiation of wavelength $\lambda \sim 100$ μ and relatively small intensity I, of the order of 1 MW/cm^2, the parameter η_n is comparable with unity for the first few values of n. A new type of nonlinear absorption of light due to a set of simultaneous n-photon transitions with comparable contributions to the total absorption coefficient has been observed recently for p-type Ge crystals excited by high-power pulses from an optically pumped NH_3 laser (λ = 90.55 μm, $\hbar\omega$ = 13.7 meV)[1].

In the present work the influence of FIR radiation polarisation state on the intra- and (heavy to light holes subbands) multiphoton absorption in p-Ge has been observed and investigated by photon drag effect behaviour.

3. SAMPLES, EXPERIMENTAL TECHNIQUES AND RESULTS

Investigations were carried out on n- and p-type Ge samples with densities 10^{12}-10^{16} cm^{-3} at T = 300 K. The radiation source used was FIR NH_3 laser optically pumped by a TEA CO_2 laser operated at the wavelength λ = 90.5 μm with pulse durations ~ 40 ns. The longitudinal photon drag e.m.f. was investigated. The experimental set up and the typical oscillograms are shown on Fig.1 (a: the excitation pulse , b: p-Ge photoresponse).

It has been shown that the photon-drag current J in p-Ge at T = 300 K changes its polarity with increasing intensity of the incident light *I* (Fig.1b, 2) due to the opposite directions of the one- and two- photon contributions to the photocurrent and the superlinear dependence of two photon current. It has been shown that, at T = 300 K the characteristic intensity I^*, when the inversion takes place, does not depend on the carriers density. The investigation of polarisation dependences has shown that the inversion of the photocurrent induced by circularly polarised radiation (Fig.2, •) occurs at a lower intensity level as compared to the linearly-polarised excitation (Fig.2, x). In n-type Ge, where the absorption is due to the one photon Drude intraband transitions, the inversion of the photon drag effect is absent and the photocurrent depends linearly on the light intensity.

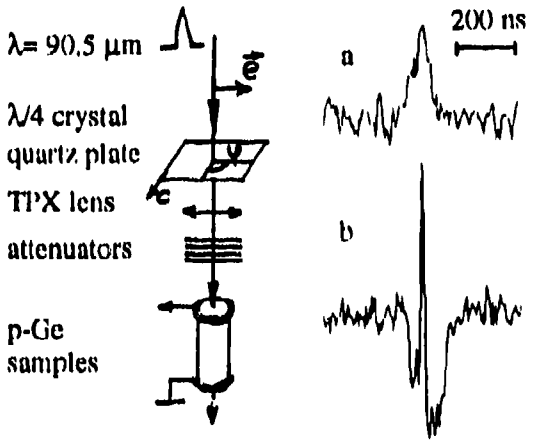

Fig. 1

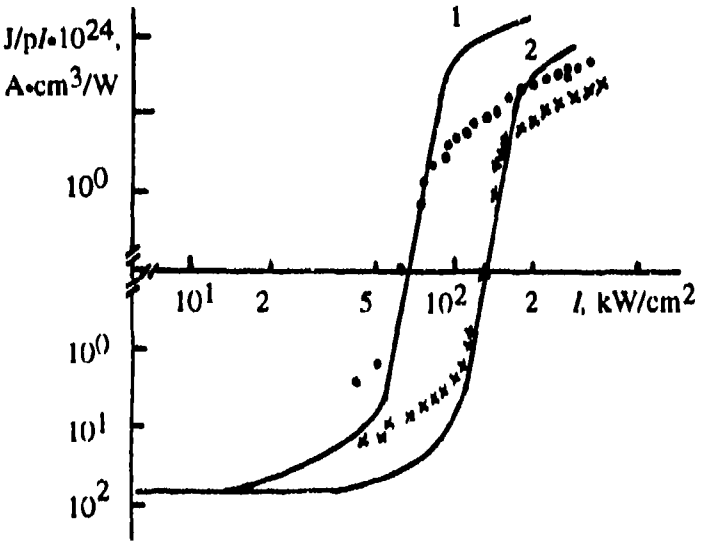

Fig. 2

A theory is developed describing the nonlinear absorption of the intense FIR radiation by direct multiphoton transitions of free carriers between two subbands of a degenerate valence band. The role of the polarisation has been analysed and it has been established that the polarisation dependence of the nonlinear photon drag effect is caused by the two-photons absorption and the resonant saturation of the one-photon absorption. The dependence of the photon drag current $J=J^{(1)}+J^{(2)}$ ($J^{(1)}$, $J^{(2)}$ are one- and -two photons currents) on the light intensity has been calculated for two polarisation. The result is plotted in Fig.2 (curve: 1-circular, 2- linear polarisation). It is seen that experimental results are in the good agreement with the theory, which predicts the stronger two-photon absorption and resonance saturation for the circular polarisation. The role of the light polarisation has been analysed also for the developed nonlinearity regime, when the nonlinearity parameter η_n is about unity and the absorption involves a set of simultaneous n-photon transitions with comparable contributions to the total absorption coefficient.

4. ACKNOWLEDGEMENTS

One of the authors (S.D.G.) thanks the Alexander von Humboldt Foundation for the support of his work.

5. REFERENCES.

1. S.D. Ganichev, E.L. Ivchenko, S.A. Emelyanov, E.Yu. Perlin, A.V. Fedorov, I.D. Yaroshetskii Multiphoton absorption in semiconductors at FIR wavelength, Sov. Phys. JETP, 1986, 64, 4, pp. 729-737

FAR INFRARED MEASUREMENTS ON BAND NONPARABOLICITIES IN DOPED MULTIPLE QUANTUM WELL STRUCTURES

S.K. Kang[1], J.P. Bryant[1], T. Dumelow[1], T.J. Parker[1], C.T. Foxon[2], J.W. Orton[3] and J.J. Harris[4]

1. Department of Physics, University of Essex, Wivenhoe Park, Colchester CO4 3SQ, UK.
2. Department of Physics, University of Nottingham, University Park, Nottingham NG7 2RD, UK.
3. Department of Electrical and Electronic Engineering, University of Nottingham, University Park, Nottingham NG7 2RD, UK.
4. IRC for Semiconductor Materials, Blackett Laboratory, Imperial College, Prince Consort Road, London SW7 2BZ, UK.

The conduction band in quantum well structures splits into subbands due to confinement. This splitting may make simple assumptions on parabolic subband dispersion inappropriate in doped samples. We have used far infrared measurements to investigate this phenomenon.

The far infrared spectra of a series of doped multiple quantum well (MQW) GaAs/AlGaAs structures have been measured by dispersive Fourier transform spectroscopy (DFTS) and oblique incidence reflectivity. In this report we concentrate on DFTS measurements which show only the in-plane superlattice dielectric response.

The plasma frequencies obtained from modelling the DFTS measurements (see figures) were compared with the free carrier concentrations, as determined from Van der Pauw measurements, in order to obtain a value for the plasma frequency for each sample as it relates to the DFTS geometry. It was found that the experimentally obtained values of the in-plane effective masses were considerably higher than the bulk value.

In order to explain this effective mass enhancement it is necessary to consider the energy dispersion of the subbands in a manner that includes the effect of non-parabolicity. The effect of non-parabolicity is significantly greater than in the bulk for two reasons, both relating to the fact that the parabolic band assumption is associated with small wavevector values:

(i) The out-of-plane component k_z of the wavevector essentially depends on well width since k_z is a confinement wavevector. For narrow wells, therefore, k_z becomes large.

(ii) k_x and k_y are large for significant doping levels because the lower subbands are occupied up to a far higher Fermi level than they would be in a bulk sample.

These two factors imply that electrons in a quantum well structure have significantly higher effective masses than they would if they were not confined.

In order to model the plasma effective mass it is useful to consider each electron as having an effective mass m_i^*. For the overall collection of N particles of different masses the plasma frequency ω_p is given by

$$\omega_p^2 = \frac{e^2}{\varepsilon_0 \varepsilon_\infty} \sum_i^N \frac{1}{m_i^*}$$

Thus the equivalent plasma mass can be obtained by averaging the reciprocals of the m_i^* values. The

values of m_i^* are simply taken from the band dispersion, which, for GaAs, has been modelled by Mälcher *et al* [1]. By suitable consideration of the distribution of the n_s electrons in each subband s, an 'effective plasma mass' m_s^*, in the x direction, may be calculated:

$$\frac{n_s}{m_s^*} = \sum_i^s \frac{1}{m_i^*} = \frac{1}{\hbar^2} \int_{-\infty}^{\infty} \int_{-\infty}^{\infty} \frac{\partial^2 E}{\partial k_x^2} F\{E(k_x,k_y)\} \frac{1}{2\pi^2} dk_x dk_y$$

where $F\{E(k_x,k_y)\}$ is the Fermi function representing the thermal distribution of the electrons. In order to calculate the overall effective mass in the wells, the $1/m_s^*$ values are averaged. The effective mass of electrons in the barriers can also be included in the calculation.

Using the above approach, the experimentally measured effective masses could be compared with theoretical values. For the samples investigated, having 100 Å GaAs wells with 400 Å $Al_{0.2}Ga_{0.8}As$ barriers, the measured effective masses were 0·083 for the sample doped to $1{\cdot}4\times10^{12}$ cm^{-2} (measured carrier concentration = $1{\cdot}09\times10^{12}$ cm^{-2}) and 0·092 for the sample doped to $3{\cdot}0\times10^{12}$ cm^{-2} (measured carrier concentration = $2{\cdot}96\times10^{12}$ cm^{-2}). The corresponding effective masses calculated theoretically were 0·061 and 0·069 respectively.

The above results show that far infrared spectroscopy can be used as a measure of band non-parabolicity in quantum well structures, and that the observed extent of this effect is in agreement with theory, using published parameters.

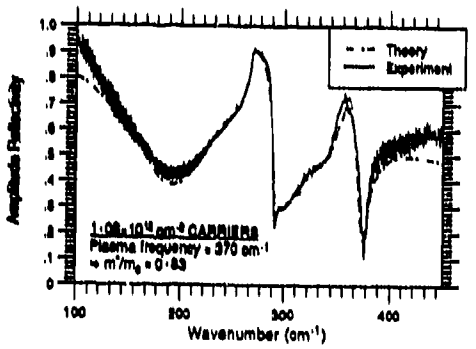

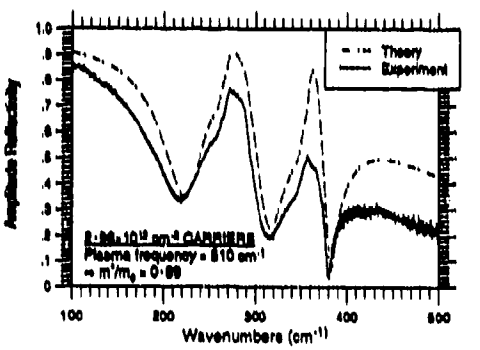

1. F. Mälcher, G. Lommer and U.Rössler, *Superlattices and Microstructures*, 2, 6152 (1986).

INVESTIGATION OF THE ELECTRON DISTRIBUTION IN $Cd_xHg_{1-x}Te$ SUPERLATTICES BY FAR INFRARED AND RAMAN SPECTROSCOPY

S K KANG[1], T DUMELOW[1], T J PARKER[1], R J YORK[1], S R P SMITH[1], S N ERSHOV[2] AND M I VASILEVSKI[2].

[1]Department of Physics, University of Essex, Wivenhoe Park, Colchester, Essex CO4 3SQ, UK.
[2]Faculty of Physics, Nizhni Novgorod State University, 37 Sverdlova Street, Nizhni Novgorod 603000, Russia.

Far infrared spectroscopy may be used in obtaining characterisation information on superlattices containing free carriers; such information complements that obtained by Raman spectroscopy. This study makes use of both infrared and Raman measurements on $Cd_xHg_{1-x}Te$ (CMT) superlattice samples.

In order to interpret plasmon data from superlattices, it is necessary to consider the form of their dielectric functions. In practice, it is sufficient in both infrared and Raman experiments to consider the long wavelength limit resulting in a uniaxial superlattice dielectric tensor. If the superlattice layers are sufficiently thick, each layer retains a dielectric function of the form given by (1). For layer thicknesses d_1 and d_2 and dielectric functions ε_1 and ε_2 respectively, the principal components of the superlattice dielectric tensor are given by [1,2]

$$\varepsilon_{xx} = \varepsilon_{yy} = (\varepsilon_1 d_1 + \varepsilon_2 d_2)/(d_1 + d_2) \quad (1)$$

$$\varepsilon_{zz}^{-1} = (\varepsilon_1^{-1} d_1 + \varepsilon_2^{-1} d_2)/(d_1 + d_2) \quad (2)$$

with the uniaxis z defined normal to the layers. Thus ε_{xx} has poles at the TO frequencies of the superlattice constituents and ε_{zz} has zeroes at the plasma shifted LO frequencies.

We now examine how (1) and (2) may be used in interpreting spectral features obtained using far infrared and Raman techniques, as appropriate for CMT superlattices:

1. Backscattering Raman spectra yield peaks at zeroes in ε_{zz}, i.e. at the plasma shifted LO frequencies of the constituent superlattice layers. For CMT superlattices the penetration depth of Ar^+ laser light is of the order of 300 nm, so that only the top few layers of a thick superlattice are probed.

2. Dispersive Fourier transform spectroscopy (DFTS) and s-polarisation oblique incidence far infrared spectroscopy both probe the polariton modes associated with ε_{xx}. These most obviously yield the TO mode frequencies and an 'average' superlattice plasma frequency sampled over the full width of the superlattice [3].

3. P-polarisation oblique incidence far infrared spectroscopy probes polariton modes associated with both ε_{xx} and ε_{zz}. The resulting spectra are similar to those in s-polarisation but have extra dips at zeroes in ε_{zz} (the plasma shifted LO frequencies of both superlattice constituents) - we describe the resulting dips as Brewster modes. The extra information gained is similar to that obtained from Raman spectroscopy, but in this case the whole superlattice is sampled rather than the top few layers. This is useful in investigating the distribution of free carriers [3].

We illustrate the above principles using room temperature and 77 K oblique incidence reflectivity measurements taken from a $Cd_{0.2}Hg_{0.8}Te/Cd_{0.65}Hg_{0.35}Te$ superlattice, grown on a GaAs substrate by plasma enhanced MOCVD. Phonon frequencies were calculated using a random element isodisplacement (REI) model [5] in the form described by Samson *et al* [6].

The Raman spectrum of the sample agrees well with the modelled LO frequencies; this result is incompatible with the presence of any free carriers within the sampled thickness. However, only the first few layers are probed by Raman, and free carriers may still exist further away from the sample surface. The s-polarisation reflectivity measurements can in fact only be modelled by assuming a significant plasma contribution due to free electrons, although because only ε_{xx} is probed no information on the electron distribution is gained from these spectra. The p-polarisation reflectivity spectrum, however, should show dips at the plasma shifted LO's of both superlattice components. In practice, the damping effects in this sample are rather high, and the only such dips that are well resolved are those due to the barriers. As well as a dip at the plasma-shifted barrier CdTe-like LO frequency (feature 2 in the spectrum), there is also a clear dip at the unshifted frequency (feature 1 in the spectrum). This has been modelled by assuming that the top 0·3 μm of superlattice is depleted of free carriers due to band bending at the surface; this assumption would support the Raman results.

These results show that a combination of far infrared and Raman techniques may be used to gain considerable insight into the electron densities and distributions in CMT superlattices.

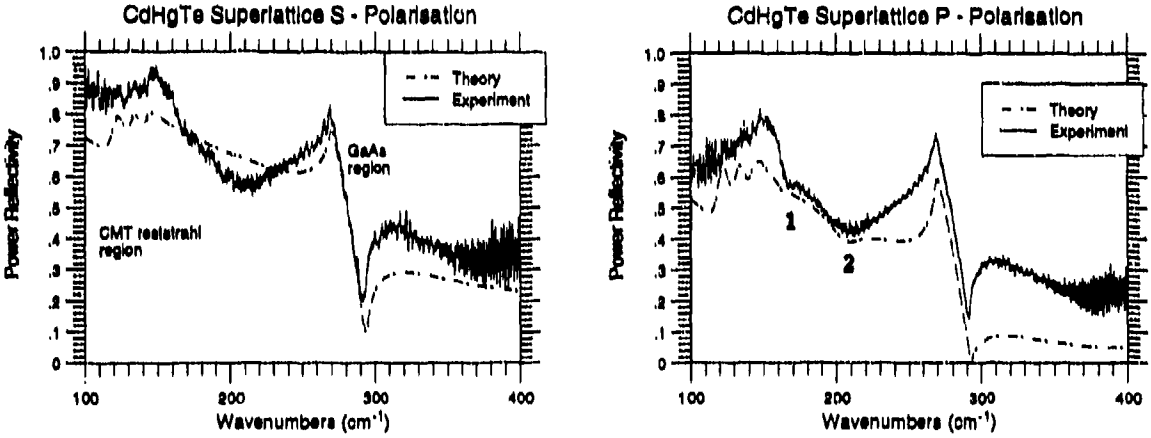

1. V.M. Agranovich and V.E. Kravtsov, *Solid State Commun.* **55**, 85 (1985).
2. N. Raj and D.R. Tilley, *Solid State Commun.* **55**, 373 (1985).
3. T. Dumelow, A.A. Hamilton, T.J. Parker, D.R. Tilley, B. Samson, S.R.P. Smith, R.B. Beall and J.J. Harris, *Superlattices and Microstructures* **4**, 517 (1991).
4. T. Dumelow and D.R. Tilley, *J. Opt. Soc. Amer* **A10**, 633 (1993).
5. I.F. Chang and S.S. Mitra, *Phys. Rev.* **B2**, 1215 (1970).
6. B. Samson, T. Dumelow, A.A. Hamilton, T.J. Parker, S.R.P. Smith, D.R. Tilley, C.T. Foxon, D. Hilton and K.J. Moore, *Phys. Rev.* **B46**, 2375 (1992).
7. S.P. Kozyrev, L.K. Vodopyanov and R. Triboulet, *Solid State Commun.* **45**, 383 (1983).

The control of gap width in the low-dimensional systems with CDW instability

A. I. Dmitriev, G. V. Lashkarev and D. A. Fedorchenko

Institution on Material Problems of Academy of Sciences of Ukraine, Kiev, Ukraine

The earlier studies we had carried on γ- and β-politype crystals of layered semiconductor InSe had shown a series of effects that are the properties of the structures of superlattice (SL) type. It had been found that in the temperature range below 20 - 30 K the electron gas in InSe is two-dimensional and degenerated. At the same temperatures the N-shaped regions of Volt-Ampere characteristics (VAC) of InSe had been observed when the electric current impulses were along the C-axis of crystal (perpendicular to the crystal layers plane).

However, VAC of InSe crystals measured under conditions of I⊥C also have the N-shaped segments although we had not expected any structure of SL type in this direction. This effect and some of the kinetic, galvanomagnetic and optical anomalies which had been observed in the InSe crystals had allowed us to put forward the hypothesis about the existence of the charge density waves (CDW) in InSe at the temperatures below 100 - 150 K. In the " classic " semiconductors the origin of CDW is impossible because of the three-dimensional current carrier gas with its low concentration. However the electron gas in InSe is two-dimensional and degenerated one. Taking into consideration this fact and the hypothesis about the presence of the thin electrons accumulating layers with high carrier concentration in InSe crystals at low temperatures (it had been proposed by series of authors earlier) the CDW existence in this case imagines to be quite possible.

One of the main consequences of CDW existence is the appearance of the gap in the continuum of conduction band of InSe crystal near the Fermi level at the temperature below 100 - 150 K. As the result the longitudinal specific resistance of the crystal in the direction of layers plane increases sharply. In such a state pure InSe crystal having the longitudinal specific resistance about 100 Om·cm at room temperature, becomes the insulator practically. The gap width has been calculated from the data of temperature behaviour of longitudinal specific resistance (which have been measured under conditions of small currents through the InSe crystals) to be in range 10 - 20 meV at the temperatures below 20 K. With the temperature increased, the gap has decreased and disappeared finally at temperature 80 - 120 K. When the impurities of Pb, Sn or In have been introduced into InSe crystal all the effects connected with CDW instability have weakened down to

the complete disappearance when the concentration of impurities has been high enough; we suppose that it has been connected with the influence of non-periodical potential of the impurity ions.

The electric field (current through the sample) was detected to affect strongly on the gap that can be used for the effective control of the gap width by the electric field lower than 100 V/cm. We have observed the reducing of the gap width (from the data of the temperature behaviour of longitudinal specific resistance) from 12 meV to 4 meV with the current through the sample increased to 1 mA. The results obtained have confirmed by the data of the optical investigations.

In the course of measuring of InSe samples with low concentration of Sn and In impurities the photoeffect was detected at temperature 4.3 K and in the energy range of radiation less than 10 meV. The InSe samples were rayed by exiting laser with two fixed significances of the wavelength. The photoeffect value was found to depend strongly on electric current through the crystal. When the value of the electric current throw the sample was small enough the photoeffect was not observed at the wavelength of 337 μm but it appeared at some threshold current U_{th1} that was various for different samples. Then the photoeffect value increased sharply with the electric current throw the sample increased. The further increase of current led to the saturation of the photoeffect and then to its slow decrease. When the current throw the sample reached some the second threshold value U_{th2} the photoeffect disappeared abruptly.

We guess that the observed photoeffect is the consequence of the direct optical transitions of the electrons through the CDW-induced gap in the conductive band of the InSe crystal. According to data of our measurements the initial gap width (without the current throw the crystal) for the tested samples is about 10 - 15 meV, i.e., much more than the exiting laser quant energy. Thus under the condition of small current throw the crystal the existence of photoeffect is impossible. With the current increases to the U_{th1} value the gap width decreases to be the comparable with the quant energy and the photoeffect is observed. The second threshold current existence is likely to be connected with the destruction of CDW by strong electric current. The present effects can be used for the creating the long-wave optoelectronic devices controlled by electric current.

At the wavelength of 195μm the same effects were detected but U_{th1} was essentially less; some of samples under such conditions had the photoeffect without the current ($U_{th1}=0$). To our regret, we had not the possibility to observe the photoeffect on pure InSe samples because of much great value of CDW gap.

DEFECT AND CLUSTERING MODES OF HgCdMnTe CRYSTALS.

Mazur Yu.I., Kriven S.I., Lavorik S.R., Tarasov G.G.

Institute of semiconductors, Academy of Scinces of Ukraine
Kiev 252028, pr. Nauki 45, Ukraine

ABSTRACT

Modes content for quaternary semiconducting narrow-gap alloyes is examined for the case of HgCdMnTe single crystal. FIR-reflection spectra are presented for low manganese concentration (Mn is of 0.015, Cd is of 0.33) and identification of different impurity-induced vibrational states is performed for different contents of cadmium and manganese.

1. INTRODUCTION

FIR spectra allow to trace the peculiarities of lattice dynamics, perturbed by defects of different physical nature and by change of short- or long-range interaction, under content variation. This problem grows strongly in the case of quaternary compounds, based on ternary narrow-gap semiconductors, because the order of impurity embeding into different sublattices can be changed technologically in random way. Therefore, different manifestations of defect modes is possible at the same conditions of crystal growth. Due to their frequencies can fall into the ranges of low phonon density and close to the frequencies which are the eigen-values of dynamic matrix for perfect crystal a substantial modification of spectral distribution should be found both for lattice modes and for defect ones. Here we present the data on FIR reflection of HgCdMnTe and arguments to explain the spectral features starting from position that defect and clustering modes are available. Some evidence is obtained to support the version on improvement of structural ordering of ternary compound matrix, induced by low manganese concentration.

2. EXPERIMENTAL RESULTS AND DISCUSSION

$Hg_{1-x-y}Cd_xMn_yTe$ crystals of different compositions were synthesized by modified Bridgman technique at temperature gradient of 35 K/cm. All crystals were of p-type and free carrier concentrations were varied from $n=5\cdot10^{15}$ cm^{-3} to $n=5\cdot10^{17}$ cm^{-3} at room temperature. Reflection measurements in spectral range 30-600 cm^{-1} were carried out with IFS-113v at temperatures $5K<T<300$ K. The experimental error was of 1-2 cm^{-1} over all spectral range under consideration. Fig.1 presents $Hg_{0.655}Cd_{0.33}Mn_{0.015}Te$ reflection spectra measured at various temperatures.

To interpret the experimental data Kramers-Kronig transformation of reflection spectra was performed. Investigation in detail of fine structure of complex succeptibility for $Hg_{1-x-y}Cd_xMn_yTe$ allows to distinguish three spectral ranges of particular interest. Below long-wave limit of restrahlen rays range ($\nu\sim120$ cm^{-1}) a number of modes were identified ascribing to defect and impurity-induced acoustic lattice

modes of HgCdTe compound. Longitudinal and transverse optical modes of HgTe and CdTe sublattices are localized in spectral range 120 cm^{-1} < ν <160 cm^{-1}. Here the clustering mode is singled at ν =132-135 cm^{-1}. Above the short-wave limit of LO-TO splittings range for HgCdTe we have detected the manganese localized mode for low Mn content and a number of modes which were labeled as surface defect modes. Possessing the data for the set of $Hg_{1-x-y}Cd_xMn_yTe$ samples of fixed cadmium content (x=0.1) and varing manganese one (from y=0 to y=0.15) we have calculated the LO-TO spectrum transformation to detect a mode behaviour at y variation. A modified model of isodisplacements, developed specially for quaternary narrow-gap crystals, gives a good fitting for the frequencies measured and proves a three-mode behaviour of phonon spectrum transformation (Fig.2).

The non-interacting oscillators fitting of reflection spectra shows a different modes which are actual in the case under consideration. Table gives their frequencies (ν), band-widths (γ) and oscillator strengths (S) $Hg_{0.655}Cd_{0.33}Mn_{0.015}Te$ crystal at 100 K.

Table.

ν (cm^{-1})	104	112	123	136.5	149.5	154	172	178	180
S	0.15	0.12	3.9	0.13	0.36	0.25	0.05	0.09	0.1
γ (cm^{-1})	6	10	7.1	5.8	6.8	6.8	5.2	5	7.2

Modes at ν=95 cm^{-1} and ν=190 cm^{-1} are detected at higher Mn-concentrations. At low temperature they were calculated by Green's technique and were found coinciding with experimental ones within 2 cm^{-1} error. It should be noted a relative narrowing of clustering mode at temperature increase. Spectral distribution in spectral range 90 cm^{-1} < ν <110 cm^{-1} can be satisfactory described only with hybridization of wave functions for gap and compound lattice phonon states taking into account. Comparison of our results with the data for HgCdTe show an obvious improvement of optical quality of HgCdTe structure at presence of low manganese concentration.

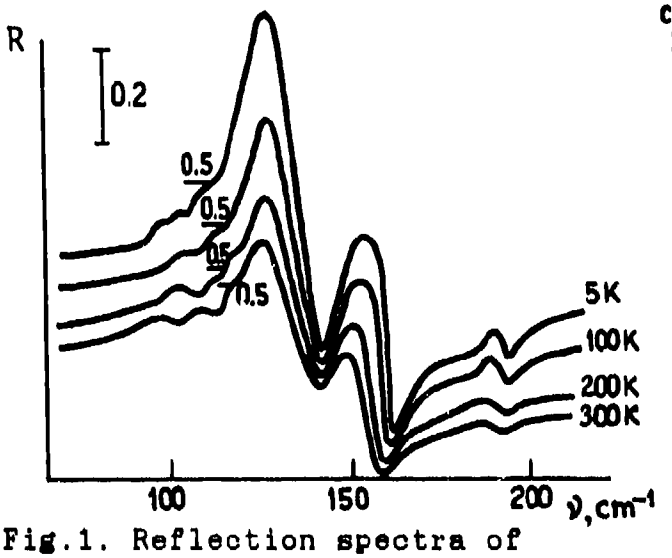

Fig.1. Reflection spectra of $Hg_{0.655}Cd_{0.33}Mn_{0.015}Te$ at different temperatures.

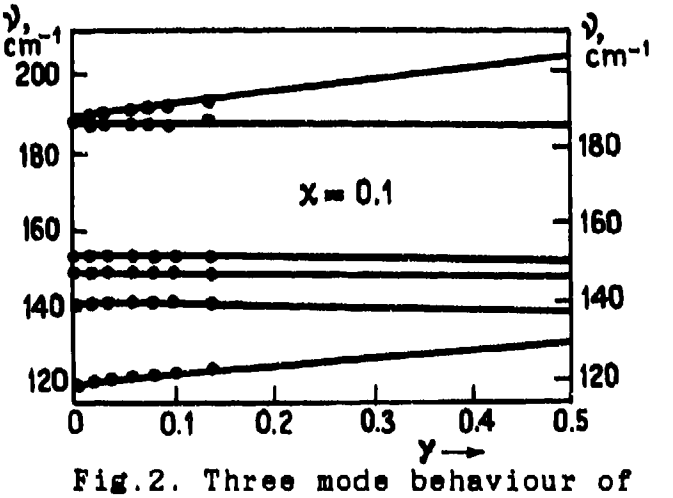

Fig.2. Three mode behaviour of phonon spectrum transformation of $Hg_{1-x-y}Cd_xMn_yTe$: points-experiment; solid curves-the dependencies, calculated for the model of isodisplacements.

EXCITONIC LUMINESCENCE OF $Hg_{1-x-y}Cd_xMn_yTe$ CRYSTALS.

J.W. Tomm (a), Yu.I. Mazur (b), S.I. Kriven (b), S.R. Lavorik (b), G.G.Tarasov (b)

(a) Section of Physics, Humboldt University, Berlin, Germany
(b) Institute of Semiconductors, Ukr. Acad. Sci., Kiev, Ukraine

ABSTRACT

Photoluminescence in excitonic range of spectrum is detected for HgCdMnTe crystals (Cd=0.33, Mn=0.015) for the first time. Luminescence features are well pronounced and strongly effected by intensity of pumping at low temperature.

INTRODUCTION

Luminescent properties of narrow-gap semiconductors based on A_2B_6 compounds are strongly influenced by their chemical content, different defects and structural perfectness. Under increase of Cd or Mn content the energy gap of HgTe becomes open and, starting from x=0.5 for $Hg_{1-x}Cd_xTe$ alloys or y=0.2 for $Hg_{1-y}Mn_yTe$, the problems with photoluminescence detection do not encounter. However at x and y decrease the nonradiative recombination prevails and the luminescent gain becomes too noisy and of small magnitude. In this case the role of structural perfectness grows substantially and should be overcome by technological improvements. One of means is doping of $Hg_{1-x}Cd_xTe$ of low x value by manganese ions. Our data on FIR reflection, transmission, as well as, Raman measurements have showed effects caused by manganese ions in vibrational spectra. Manganese presence prevents, as to our mind, the producing of clusters with excessive Te and assists the growth of structure perfectness. Higher crystal quality smoothens the rigid restrictions for photoluminescence observation. Present data on IR luminescence in quaternary $Hg_{1-x-y}Cd_xMn_yTe$ crystal confirms this conclusion.

EXPERIMENTAL RESULTS

Single crystals of $Hg_{1-x-y}Cd_xMn_yTe$ were synthesized by modified Bridgman procedure. They were of n-type with the free carrier concentration varing from $n=1\cdot10^{15}$ cm^{-3} to $n=5\cdot10^{17}$ cm^{-3} at room temperature. Photoluminescence in $Hg_{0.655}Cd_{0.33}Mn_{0.015}Te$ was excited by Nd: IAG laser at T=10 K. Fig.1 presents the photoluminescence spectra measured for CW-pumping.

The feature at $\hbar\omega$ =329.5 meV is of small width (less 6 meV) and accompained by broad long-energy peak. At pulse excitation this spectral distribution is reproduced at low level of pumping with subsequent asymmetric broading of luminescence peak at pumping increase. Ratio R of peak magnitudes at $\hbar\omega$ =312 meV (I_A) and at $\hbar\omega$=329.5 meV (I_B) ($R=I_B/I_A$) grows monotonously from 1.2 at pumping P_{exc} = 2mW/cm^2 (CW-regime) to values of a few tenths at pulse pumping P_{exc} =100 kW/cm^2. Peak A position does not practically shifts at pumping, but peak B po-

sition follows the intensity icrease. Magnitude of peak B grows superlinearly with angular coefficient close to 2 for the case of CW-excitation at pumping increase up to 3 W. Then this coefficient decreases to value of <1 at further pumping growth. The half-width of peak B (FWHM) has a non-monotonous character at increase of pumping. Its behaviour is presented by Fig.2. As can be seen from Fig.2 at low level of pulse excitation FWHM increases, however at P_{exc} >1 kW/cm^2 the FWHM value substantially decreases and reaches the values less than initial ones.

DISCUSSIONS

Analyzing the tendency of IR-photoluminescence manifestion in ternary HgCdTe crystal we find that quaternary compounds give new possibilities for its observation in those ranges of cadmium content where photoluminescence of HgCdTe is difficult for explanation. In these ranges (0.3<x<0.45) the change of luminescence mechanisms takes place and the contributions of zone-to-zone transitions and excitonic transitions can not be differed surely. Besides a substantial narrowing of luminescence peaks in HgCdMnTe we obtain a good possibility to investigate their manifestation at various experimental conditions. As to physical nature of A, B peaks we conclude that peak B could be refered to bound exciton in HgCdMnTe. Peak A can be ascribed to phonon replica due to its energy position in respect of peak B. However the pumping behaviour of peak magnitude gives some grounds to guess that it is the manifestation of acceptor states. Modification of line-shape for B peak at sufficiently high intensities of excitation (>100 kW/cm^2) shows that zone-to-zone transitions can be developed simultaneously with excitonic ones. Narrowing of luminescence peak B gives some evidence for stimulated processes.

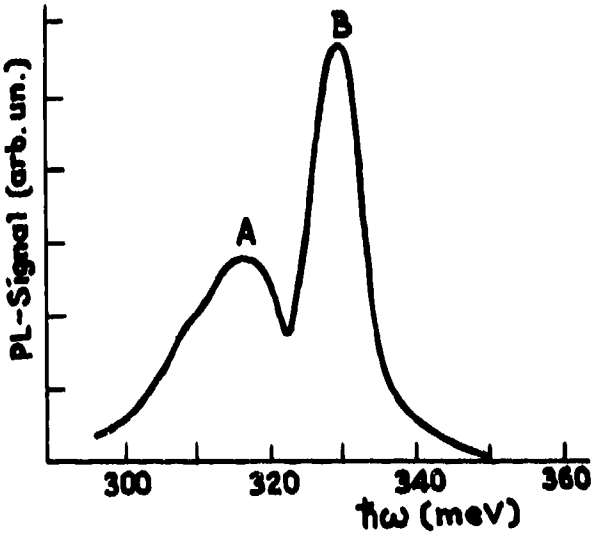

Fig.1. Luminescence spectrum of $Hg_{0.65}Cd_{0.33}Mn_{0.015}Te$ at T=10 K and CW-excitation of 0.8 W/cm^2.

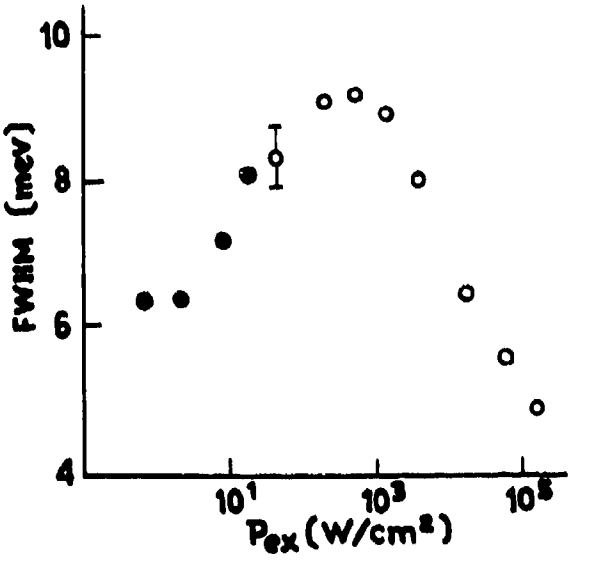

Fig.2. Intensity dependent FWHM of peak B at T=10 K (● - CW-, o - PW-excitation).

Mid-infrared absorption spectra of iron group impurities in II - VI semiconductors

Mireya Castillo
Universidad Nacional del Táchira
Aptdo.436. San Cristóbal-Venezuela

ABSTRACT

The mid-infrared absorption spectra of substitutional 3-d transition metal ions, (V, Cr, Mn, Fe) in II-VI semiconductors Zn(Se, Te) and Cd Se (Te) have been studied by Fourier-Transform Infrared FT-IR spectroscopy. A defect molecule approach is found to provide an adequate description of the observed features.

2. INTRODUCTION

A new theoretical description of transition metals (TM) multiplet in II-VI semiconductors have been used. It is based on a defect-molecule approach with renormalized parameter which has been sucessfully proven for the vacancy in silicon[1]. In this work the structure of the absorption spectra of iron group impurities will be analyzed within the framework of this improved method. In order to confirm the validity of the defect molecule in the prediction of both the defect-ionization energy and the internal transition a systematic study of the energy levels in semiconductor as the metal vary and the trends for a given transition metal as the host vary has been achieved by means of FT-IR (Fourier Transform-Infrared) spectroscopy in which all the expected transitions has been identified, The good agreement with the experimental data gives the opportunity of test the aplicability of this model to the strongly covalent systems such as TM impurities in II-VI semiconductors.

3. EXPERIMENTAL DETAILS

All crystals for FT-IR spectral analysis were grown by the chemical vapour transport (CVT) method and kindly provided by Dr. W. Giriat of Instituto Venezolano de Investigaciones Cientfficas IVIC-Venezuela. The experimental techniques of crystal growth have been described elsewhere[2]. The IR spectra were recorded with a Perkin-Elmer FT-IR PE 1725X Fourier Transform spectrometer equipped with a DTGS internal detector in the transmission mode at room temperature with a resolution of 4 cm^{-1} using a microcell fitted with KBr lenses. Several hundreds events were averaged to minimize the noise level. Measurements were performed after cleaning the sample surface with CCl_2H_2.

4. RESULTS AND INTERPRETATION OF THE SPECTRA

Iron in CdSe and CdTe. An analysis of the position and shape of the main features of the spectra of Fe in CdSe (Fig.1) and CdTe on the basis of the defect molecule approach reveals that the band labeled E centered at 2944 cm^{-1} equivalent to 0.37 e.V.is in good agreement with the corresponding calculated value for the transition $^5E \rightarrow {}^5T_2$ as predicted by the model and the sub-bands should be connected with vibrational structure, the origin of the peak at 1045 cm^{-1}(0.13 eV) in CdIe.Fe and its absence in CdSeFe clearly suggest what this band is related to the CdTe lattice then, the observed frecuency was compared with the predicted ionization energy for a single acceptor for the impurity (Fe) yielding a closer agreement. The fine structure of band D suggests the coupling of one or more of phonon modes of CdSe and local mode due to Fe impurity.

Manganese in ZnS(Te) and Cd(SeTe). The neutral Mn^{+2} has the $^6A_1$ ground state separated from the first excited state by an energy[2] of about 2.5 eV. Consequently, in the mid-infrared region only the absorption inside shallow impurity levels and the phonon coupling are expected. The starting DMS system for these experiments was ZnSMn 0.50. The spectrum reveals two outstanding features a weak broad band rising at about 1700

cm^{-1} this band comprises a doublet at 2.812 and 2937cm^{-1} and the next structure towards lower energy presents a set of peaks 1531,1453,1390,1281,,1125,1062 and 890 cm^{-1} and an additionally phonon features. For ZnTeMn,CdMnTe and CdMnS the spectra are similar therefore, here only the behaviour of the donor will be described. While for CdSe,CdTe and ZnTe the predicted energy level of donor[2] are in reasonable agreement with the experimental data the model fails to predict the energy ionization of Mn in ZnS. The results confirm the prediction that within a class of compounds the binding energy of each impurity is nearly constant. The main results is, that the defect molecule approach is unable to given an unified picture of Mn^{+2} Ions into the DMS. However as a consecuence of the complicated patterns of the spectra it is obvious that none of the existing theories is able to explain all the results.

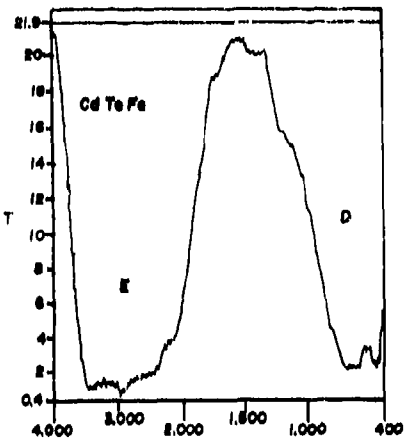

Fig.1

Chromium in ZnSe. For ZnSeCr the spectra exhibit three principal group of bands at room temperature, a broad band centered at 3113 cm^{-1}(0.38 eV) a relatively narrow band, at 1637 cm^{-1}(0.20 eV) and a pattern of sharp bands that appears to be repeated periodically at intervals of approximately 58 cm^{-1} and becomes less distinct toward the low energy side. A comparison of the spectra with the usual energy scheme of a Cr impurity gives no satisfactory agreement with previous works on ZnSe:Cr. However, recently[3] a comparable emission band near 4400 cm^{-1} for the case of CdS:Cr and near 4200 cm^{-1} with CdSe:Cr have been identified as the internal $^5E \rightarrow {}^5T_2$ transition of $Cr^{+2}(d^4)$ Ions. Then, the absorption band in the region 3000-3500 centered at 3113 can be related with the transition $^5E \rightarrow {}^5T_2$ transition of the Cr centre.The structure of this band shows lines with sequence similar to those observed in the lower energy side. The lines are repetition of an interval of 208 cm^{-1} therefore, such effect must be connected with the coupling of phonon to a parent electronic transition.

Vanadium in ZnSe. The spectra for ZnSe:V^{2+} obtained comprises a broad band with a width of $\Delta\nu$506 cm^{-1} with a maximum at about 3401 cm^{-1}(0.42 eV) a narrow weak absorption at 2894 cm^{-1} (0.36 eV) and a pattern of lines between 947 cm^{-1} and 1757 cm^{-1} with a peak at 1076 cm^{-1} (0.13 eV) the next structure in the spectrum between 400-800 cm^{-1} has four main components at 494,603,643 and 683 cm^{-1}. An analysis of the energy level position of the main features of the spectrum on the basis of the defect molecule approach reveals that the band centered at 3401 cm^{-1} is in excellent agreement, with the corresponding predicted value for the transition $^4T_1 - {}^4A_2$ and the peak centered at 1076 cm^{-1}(0.13 eV) is related with the transition $^4T_1 - {}^4T_2$. The additional weak absorption at 2894 cm^{-1} equivalent to 0.36 eV, was compared with the energy given in the literature[1] for the double donor level for the impurity (V) in ZnSe of 0.43 eV (3500 cm^{-1}) yielding in closser agreement. All the remaining structure can be attributed to the absorption involving the coupling of one o more of mode phonons of ZnSe as well as impurity local modes. No doubt, the trasmission spectra ZnSe can be accurately interpreted by the defect molecule approach.

5. REFERENCES

1. Z.Tian and X.Shen. "Defect-molecule model calculations of 3d,transition metal Ions in II-VI semiconductors," J.Appl.Phys.66(6) pp.2414-2419, 1989.
2. J.K. Furdyna "Diluted Magnetic Semiconductors," J. App. Phys.64(4)pp.R29-R63, 1988.
3. G.Goetz, A.Krost and H.J.Schultz "Cr^{+2} (d^4) Infrared emission in CdS and CdSe," J.Cryst.Growth 101(1) pp. 414-419 (1990).

Third order nonlinearities in semiconductors at FIR wavelengths.

P. G. Huggard, K. Goller and W. Prettl,
Institut für Angewandte Physik, Universität Regensburg, 93040 Regensburg, Germany,

W. Bier,
Institut für Mikrostrukturtechnik, Kernforschungszentrum Karlsruhe, 7500 Karlsruhe 1, Germany.

1. Abstract.

The power dependence of third harmonic generation from p-Si at an incident frequency of 40 cm^{-1} has been investigated, using an alternative design of waveguide high pass filter. Significant deviations from the expected cube dependence of harmonic energy on incident energy were observed. at 300 K and 4.2 K.

2. Introduction.

To date, far infrared (FIR) harmonic frequency generation by nonlinear optical processes has, with one notable exception [1, 2] received little attention. Apart from the requirement of high power pulsed lasers, the effective separation of harmonic from fundamental radiation by high contrast filters was a severe prerequisite. However this was achieved by the development of high-pass waveguide filters, consisting of an array of circular holes in a metal sheet [3]. These have enabled the detection of second and third harmonic radiation, generated from fundamental radiation with frequencies between 20 cm^{-1} and 60 cm^{-1}, in such materials as $LiTaO_3$, GaAs, Si and Ge. [1]. Relatively high conversion energy efficiencies, up to 10^{-3} for frequency tripling, were measured here with corresponding second and third order susceptibility magnitudes as high as 10^{-8} mV^{-1} and 10^{-12} m^2V^{-2} respectively.
We have further investigated a small part of this work, namely third harmonic generation arising from free carriers in a Si sample. Our approach was for the most part identical to that described in the above references, except that we developed a different type of high contrast filter, based on rectangular waveguides. In addition we studied the effect of cooling the sample, and found significant harmonic generation even at the lowest temperatures achievable (4.2 K).

3. Experimental.

Our radiation source was a TEA CO_2 laser pumped super-radiant FIR laser of conventional oversize metal waveguide design. Operating on the 9R branch pumped Raman lines of CH_3F, milliJoule FIR energies, with 50 ns pulse durations, were obtained from pump pulses of several Joules. The FIR radiation was focused by an off axis parabolic mirror onto the sample. This was a p-Si wafer, with matt surfaces, attached to the cold finger of an cryostat with TPX windows. The carrier density at

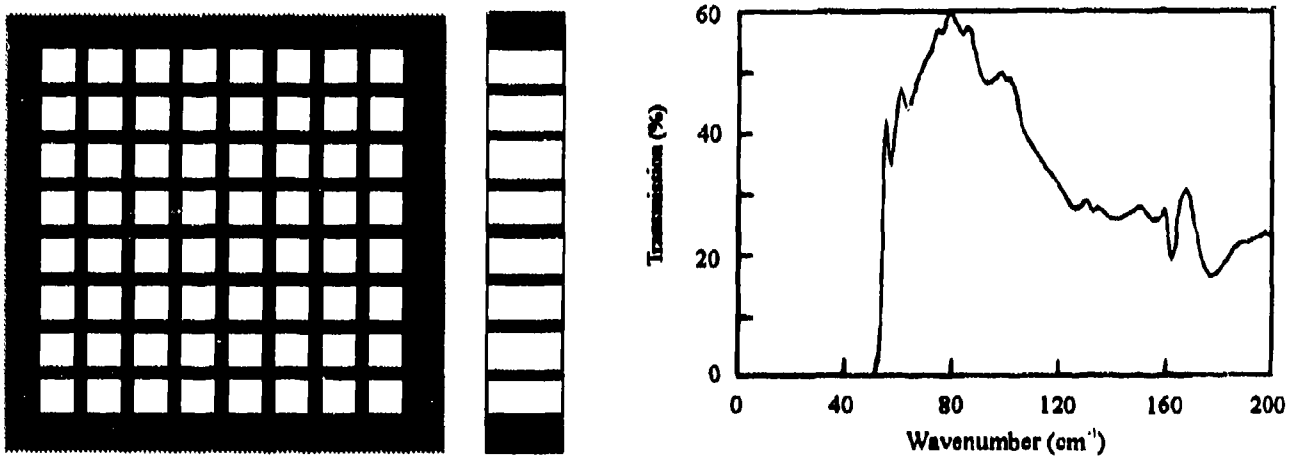

Fig. 1. Schematic drawing of a rectangular waveguide filter with measured transmission spectrum. Note the sharp decrease in transmission below 53 cm^{-1}, arising from the onset of waveguide cut-off.

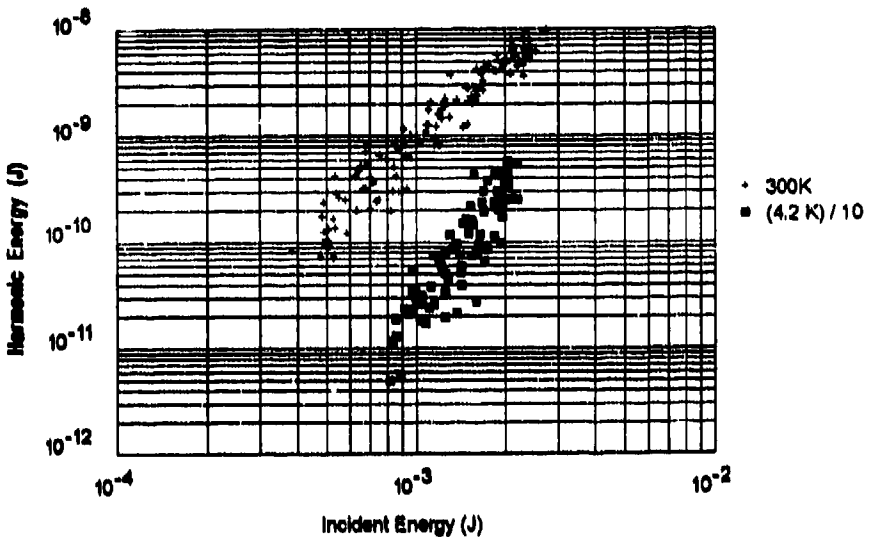

Fig. 2: Measured relationship between fundamental and third harmonic energies for a p-Si wafer at a frequency of 40 cm^{-1} at temperatures of 300 K and 4.2 K. Each point represents an individual laser pulse. Harmonic energies measured with the sample at 4.2 K have been divided by 10.

300 K was $2x10^{-15}$ cm^{-3}, with a corresponding conductivity of $6x10^{-2}$ $\Omega^{-1}cm^{-1}$. Any harmonic radiation was detected by a liquid helium cooled photoconductive epitaxial GaAs detector. The separation of the harmonic radiation was achieved by a filter of the type shown in Fig. 1. This was manufactured by diamond machining grooves into thin copper sheets and then welding a stack of such sheets together. Two such filters were used before the GaAs detector, one just before the detector condensing cone and the second on the liquid nitrogen cold shield of the cryostat. The measured transmission spectrum of a 270 μm thick filter is shown in Fig 1. This had hole dimensions of 92 μm x 69 μm, a wall thickness of 30 μm with a total area of about 1 cm^2. The cut-off frequency for this filter was measured as 53 cm^{-1}, in good agreement with that of the lowest order (0,1) mode of a rectangular guide of these dimensions, 54 cm^{-1}. The transmission drops again for frequencies greater than 100 cm^{-1} due to the onset of diffraction.

4. Results and Discussion.

With an input frequency of 40 cm-1, third harmonic radiation was generated with efficiencies of up to $2x10^{-6}$ at 4.2 K, and twice this value at room temperature: Fig. 2. Using a Drude model to calculate the linear optical constants of the sample, we obtained a value of $|\chi^{(3)}| \sim 10^{-15}$ m^2V^{-2} at 300 K for an input energy of 2 mJ. This value is in good agreement with the previously measured susceptibility of p-Si at room temperature [1]. The third harmonic energy, $E_{3\omega}$, was found to depend on the input energy, E_ω, as $E_{3\omega} = (E_\omega)^n$, where n was different from the expected value of 3. At 300 K the data were best fitted to a value of n = 2.5, which increased to n = 3.6 at 4.2 K. These values indicate that a saturation of the nonlinear susceptibility is occurring at room temperature, while the opposite process occurs at 4.2 K.

5. Acknowledgements.

P. G. H. and W. P. wish to thank the Bayerische Forschungsstiftung FORSUPRA for financial support.

6. References.

1. A. Mayer and F. Keilmann, "Far-infrared nonlinear optics: I. $\chi^{(2)}$ near ionic resonance. II. $\chi^{(3)}$ contributions from the dynamics of free carriers in semiconductors", Phys Rev. B 33, pp. 6954-6968, 1986.
2. F. Keilmann, "Nonlinear far-infrared spectroscopy of solids", Infrared Phys. 31, pp 373-380, 1991.
3. F. Keilmann, "Infrared high-pass filter with high contrast", Int. J. Infrared and Millimeter Waves 2, pp 259-272, 1981.

Analysis of PbTe, $Pb_{1-x}Sn_xTe$ Thin Layers and Multi-Layer PbTe-Pb^a Quantum-Well Structures Obtained by Laser-Pulse Epitaxy Method

A.G.Alexanian, and A.M.Khachatrian
Institute of RadioPhysics & Electronics, Armenian AcSci,
Ashtarack-2, 378410, Armenia, C.I.S.

Using the laser epitaxy method [1] PbTe, $Pb_{1-x}Sn_xTe$ thin layers were obtained from elements Pb, Sn, and Te, as well as periodic structures consisting of a single-crystal PbTe and amorphous Pb^a, grown on Polycor, mica, and BaF_2. Film structure dependence and technological parameters such as temperature, substrates, laser power, target to substrates distance, energy state of erosion plasma were determined. Results of spectral and electrophysical analysis of grown layers are presented. Absorption edge (AE) for PbTe layer, 1μm, thick, at 100K was equal to 5μm, and for $Pb_{1-x}Sn_xTe$ it was 7μm, which corresponds to AE of bulk samples. For the periodic structure PbTe-Pb^a (20 periods, 120Å each: 70+50Å) the AE is shifted towards shorter wavelengths (1,5μm), which corresponds to shift due to size quantization in the PbTe layer with Δ^{cv}=0.6eV (Fig.1). Electrophysical analysis has shown

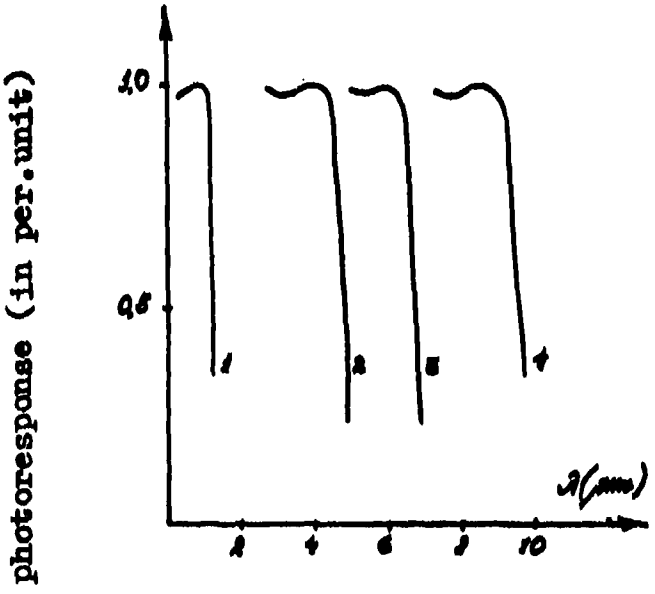

Fig.1

1. PbTe-Pb^a
2. PbTe
3. $Pb_{0.88}Sn_{0.12}Te$
4. $Pb_{0.78}Sn_{0.22}Te$

that the type of grown layers, as well as the free carriers concentration may be varied by changing the proportion of substances evaporated during one laser pulse. Various composition n- and p-type Pb and $Pb_{1-x}Sn_xTe$ layers with carrier concentration in the range ($1.8\cdot10^{12}$ to 10^{20})cm^{-3} at a temperature 100K were

obtained. We have developed the technology of multi-layer structures. Temperature dependence of PbTe, $Pb_{0.88}Sn_{0.12}Te$ layers resistivity and that of PbTe-Pb^a have purely exponential character in the temperature range 100° to 300°K (Fig.2). Resistivity

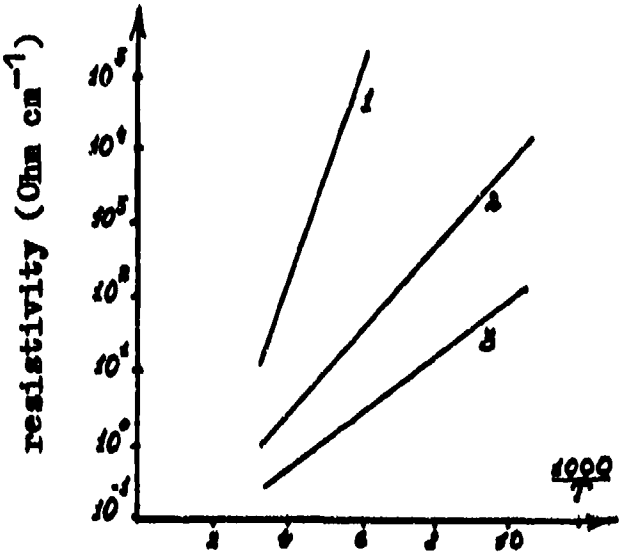

Fig.2
1. PbTe-Pb^a
2. PbTe
3. $Pb_{0.88}Sn_{0.12}Te$

varied by 10^4, 10^3, and 10^5 times while the respective AE was 0.23, 0.15, and 0.83eV. The analyzed layers, where the free carrier concentration is equal to intrinsic carrier concentration, reveal a high sensitivity. In those structures the long-term relaxation which exists in samples obtained by other methods is absent.

A.G. Alexanian, R.K. Kazarian, and L.A. Matevossian. Manufacturing of Super-Thin Semiconductor Films and Varizone Structures by Laser Deposition. Electronnaja Promyshlennost, 1982, 1, 55-58.

DEVELOPMENT OF REFLECTOMETRY FOR PLASMA DENSITY MEASUREMENTS AT JET

A E Costley

JET Joint Undertaking, Abingdon, Oxon, OX14 3EA, UK

1. INTRODUCTION

Although the basic physics of millimetre wave reflectometry has been known for many years, it is only recently that reliable measurements have been obtained with the technique in applications on tokamak plasmas. This is primarily because for these plasmas the electron density is a rapidly fluctuating parameter and these fluctuations generate broad-band 'noise' in the measurement systems. Also, several important experimental requirements were not originally realised. Recently, special techniques and hardware for processing the signals have been developed, and appropriate care taken in designing and implementing the measurement systems. As a result, reliable measurements are now being obtained routinely and are being used extensively in plasma physics studies.

Reflectometry has the potential to provide measurements of the spatial dependence of the electron density, ie. the electron density profile, during quasi-stationary periods of the plasma. It can also provide measurements of the movement of specific density layers during fast phenomena, ie. density transients. In principle, information on the broad band density fluctuations can also be obtained.

Extensive use is made of reflectometry at JET where substantial systems have been developed. In this paper, we discuss the principles of the technique and describe the instrumentation on JET. Results demonstrating the performance of the reflectometers are presented.

2. PRINCIPLES OF REFLECTOMETRY

Millimetre wave radiation is directed at the plasma along the gradient of the electron density and reflected at the layer where the electron density equals a critical value ($n_e = n_c(\omega)$) at which the plasma refractive index has fallen to zero. Usually the launched radiation has its electric vector parallel to the magnetic field (o-mode) and in this case the reflection occurs when the source frequency $\omega = \omega_p = (n_e e^2/\epsilon_0 m_e)^{1/2}$ where ω_p is the plasma frequency. Phase changes in the reflected radiation are measured by mixing it with a reference beam in a detector. The frequency of the source is swept and the corresponding change of phase (ϕ) measured. Different frequencies are reflected at different density layers with higher frequencies being reflected at higher densities which are located towards the centre of the plasma. $d\phi/d\omega$ is determined at each frequency in the range of interest and the spatial profile of the electron density ($n_e(R)$) is determined by an inversion technique [1].

Alternatively, the source frequency can be held constant and movements of a single density layer determined by measuring $\phi(t)$. By combining data from two or more reflectometers it is in principle possible to determine the spatial extent and movement of the density perturbations which generate the broad-band fluctuations in the reflectometer signals. The data are analysed using correlation techniques and the method is known as Correlation Reflectometry [2].

3. IMPLEMENTATION AT JET

The main reflectometer on JET is a multichannel system. The outputs from twelve Gunn oscillators operating in the range $18 < f < 80$ GHz are multiplexed into an oversized (WG 12A) waveguide (figure 1). A combiner employing band branching/channel filtering systems was developed specifically for this purpose [3]. The waveguide has a length of 25 m and employs reduced height E-plane bends to minimise mode conversion. The radiation is launched and received using separate antennas mounted in the JET vacuum vessel. The separation of the reflected signals is effected with a second band branching/channel filtering system, and the signals are detected using sensitive heterodyne receivers. The data acquisition includes automatic fringe counting electronics to give ϕ.

The system can operate in both the swept frequency and fixed frequency modes. In the swept mode, the frequency of each source is swept over a narrow range, typically 100 MHz, in a time of $\lesssim 3$ ms. $d\phi/d\omega$ is determined by interpolation at all frequencies in the measured range and $n_e(R)$ obtained by inverting the data. A typical result is shown

in figure 2. In the fixed frequency mode, fractions of a fringe can be measured and so very small movements, typically < 1 mm, in the positions of the density layers can be determined with recording bandwidths up to 100 kHz.

Two types of correlation reflectometer have also been constructed. In one case, radiation from four Gunn oscillators at 75.5, 75.6, 76.15 and 77.75 GHz is multiplexed into one waveguide and the reflected radiation is detected

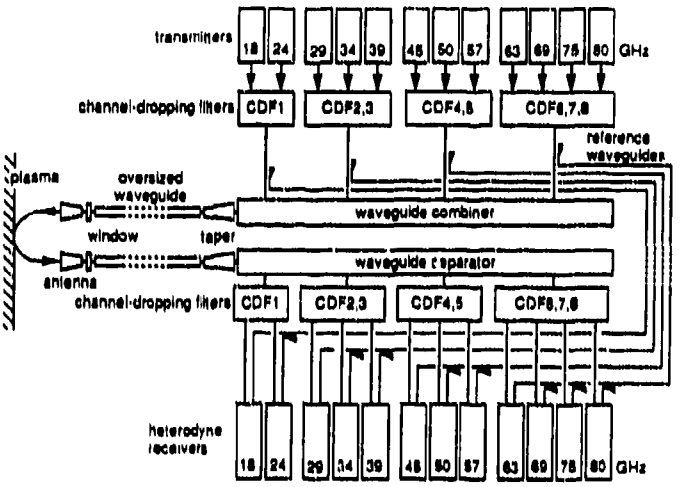

Figure 1. Schematic of the JET multichannel reflectometer system

by a broad-band heterodyne receiver. The different channels are separated by filtering at the IF stage. The fluctuating signals are recorded with a wide bandwidth (100 kHz) and the size of the density perturbations in the direction of the plasma radius is determined by a correlation analysis. In the second case, two reflectometers operating at the same frequency but probing the plasma at different toroidal locations are used to determine the toroidal motion of the perturbations.

The next phase of JET is aimed at improving the control of impurities and plasma exhaust by using a pumped divertor mounted inside the JET vacuum vessel. New diagnostic systems are being prepared for measuring the parameters of the plasma in the divertor region. In particular, a novel 'comb' reflectometer is being prepared. In this device radiation at several fixed frequencies is launched at the plasma along the same line of sight and the highest frequency in reflection is determined by observing both the amplitude of the transmitted beams and the level of fluctuations on the reflected beam. The peak density in the line of sight is therefore estimated. In addition, a swept frequency reflectometer for measuring the density profile in the extreme edge of the plasma (scrape-off-layer) in the mid-plane is being constructed. Possibilities exist for even more advanced systems utilising pulsed radar or pulse compression techniques and these are under consideration.

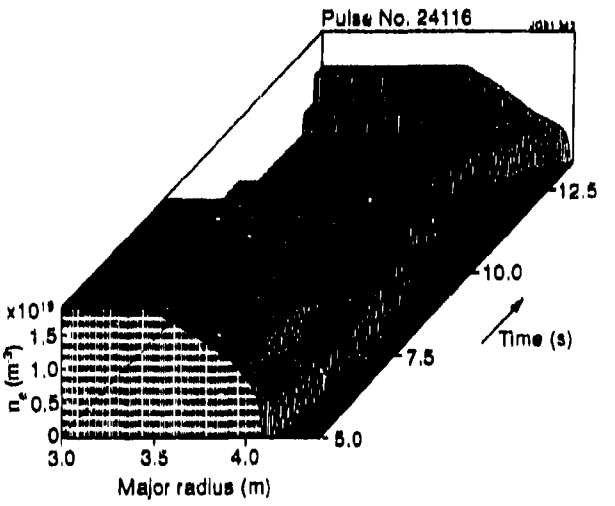

Figure 2: Typical measured electron density profiles.

1. I H Hutchinson, 'Principles of Plasma Diagnostics', 125-128 Cambridge University Press (1987).
2. A E Costley, P Cripwell, R Prentice and A C C Sips, Rev. Sci. Instrum. 61 (10), 2823-2838 (1990).
3. M Medeiros and N Williams, Conf. Digest Twelfth International Conference on Infrared and Millimetre Waves, IEEE Catalog No.87CH2490-1 (1987).

AN ADVANCED RADAR TECHNIQUE FOR ELECTRON DENSITY MEASUREMENTS ON LARGE TOKAMAKS

P.Millot, H.Lévêque
Centre d'Etudes et de Recherches de Toulouse (ONERA/CERT)
Département d'Etudes et de Recherches en MicroOndes
2, avenue Edouard Belin
31400 TOULOUSE Cedex FRANCE

Abstract:

A new way to measure the electron density profile by microwave reflectometry is studied. The idea is to use a pulse compression millimeter waves radar. The technique is discussed and laboratory measurements and simulations are presented.

1. Introduction

The radar technique, although very common in ionospheric studies to measure plasma electron density has never been used on tokamaks for electron density profile measurements by microwave reflectometry. This is due to the very short time-of-flight to be measured (some ns related to plasma geometry).

We propose in this paper to discuss a new idea: a pulse compression radar for plasma reflectometry. Recently, pulsed radar with ultra-short pulses has been proposed [1], but the detection problem due to the very fast acquisition system can not be easily overcomed. Pulse compression, with a space resolution independant of pulse duration T, does not present this drawback [2]. More, the time T can be chosen low enough (some μs), in order that plasma density fluctuations do not hamper the measurements.

2. A millimeter wave pulse compression radar:

According to radar theory, one needs a frequency bandwidth B to achieve a given resolution R. (We recall that the resolution is the ability to separate two reflections). About 20 cm of resolution is enough in most cases to separate spurious reflections (like antennas, vacuum windows...), leading to B of about 1 GHz. The bandwidth B can be obtained in many ways, the easiest is LFM (Linear Frequency Modulation) or "chirp". We can use as waveform generator a direct frequency synthetiser (DFS) for high level performance. The LFM is composed of a number N of CW frequency steps. N is fixed by the range to be measured (20 steps of 50 MHz give a 3m range). The long pulse duration T is equal to N times the commutation time t_c of the synthetiser. At the output of a quadrature detector (I/Q) the signal is sampled at 10 MHz for example, then minimum t_c is 100 ns and T=2 μs.

Since DFS are usually commercially available in centimeter waves, upconversion is necessary to emit in millimeter waves.Quadrature detection is made in centimeter waves (fig 1) after downconversion and low noise amplification.

With the set of data (amplitude,phase) for each frequency step, pulse compression is performed numerically by complex signal processing (correlation process or inverse FFT).

Since the frequency synthetiser is very precise, it is possible to calibrate the microwave system in amplitude and phase versus frequency. This can improve the measurement in particular when a long and complex transmission line is used. One can also remove echos that are always present like vacuum window by direct substraction between two sets of data.

Another improvement could be pulsed instead of CW operation to achieve range gating in cases of long transmission line.

Owning to the versatility of DFS, many different waveforms other than LFM can be investigated.

3. Application to plasma reflectometry:

Oversized waveguides are most often necessary to carry the waves to the tokamak. If these guides are enough oversized, phase dispersivity does not distort the pulses.

In plasma reflectometry, one needs the knowledge of the function $\tau(F)$, where τ represents the group delay for each frequency. One can cover the whole frequency band in broadband operation like in Tore Supra [3], or use a set of discrete frequencies like in JET [4]. The second solution leads to a large number of pulse compression radars. But a chirp of 1 GHz is obviously faster than a chirp of 10 or 20 GHz. Nevertheless, the radar technique is an upgrade solution in both cases.

4. Numerical simulations:

Numerical simulations have been made for the reflection of a chirp of center frequency F with a bandwidth B on a realistic plasma. The assumption that the time delay corresponding to the maximum of the reflected pulse is equal to the group delay $\tau(F)$ has been verified for B varying from .5 to 2 GHz. We have also seen that there is a negligible error on the result of Abel inversion except for cases where the profile is very flat.

5. Laboratory measurements:

A mock-up of a radar reflectometer has been built in the laboratory in Ka and W band (fig 2). Oversized waveguide WG16 excited by linear tapers is used, as well as 8 mitre bends. The arrangement is bistatic (2 antennas making a small angle) and a piece of quartz simulates the vacuum window. Data are taken directly from the S_{12} measurement of a Wiltron vectorial analyser and processed by FFT. Figure 3 shows a rough result of this time domain analysis at 76 GHz with a small rugged mirror (area: 30 cm^2) at 1 m. One recognizes easily the pulse reflected on the mirror(2) and the one reflected on the window(1). Nevertheless, spurious pulses can be seen after the mirror one. They can be explained as the effect of waves partially reflected inside the transmission line and delayed by back and forth comings. A calibration process has been performed using the reflection on a corner cube. In this case, spurious pulses are 20 dB decreased. When the mirror is drawn back of some tens cm, the difference of distance can be estimated with a precision of 1 mm.

6. Conclusion:

A new type of reflectometer using pulse compression has been presented. Obtained results are the following ones:

- pulse compression radar suitability for density profile measurements
- the possibility to work with oversized transmission lines
- efficiency of calibration process

We expect in fast operation a time measurement of some µs (with a 10 MHz acquisition),

In conclusion, we think that pulse compression radar is an advanced solution for plasma reflectometry, with excellent time and space resolution. It is especially well suited for large tokamaks where long transmission lines and complex microwave set-up are used.

The authors are indebted to L.Laurent, C.Laviron and M.Paume from CEA/DRFC for lending the waveguides and other components

References:

[1] C.A.J. Hugenholtz, S.H. Heijen Rev.Sci.Inst. 62 (1991) p.1100-1101

[2] C.E.Cook and M.Bernfeld : Radar Signals, Electrical Science Series. Academic Press Inc. (1967)

[3] P.Millot, F.Mourgues, M.Paume 14th Int.Conf.Int.Millim.Waves Würzburg (1989) p.532-534

[4] A.E.Costley et al. Course and Workshop on Basic & Advanced Diag. Tech. for Fusion Plasmas Varenna (1986) EUR10797EN Vol II 379

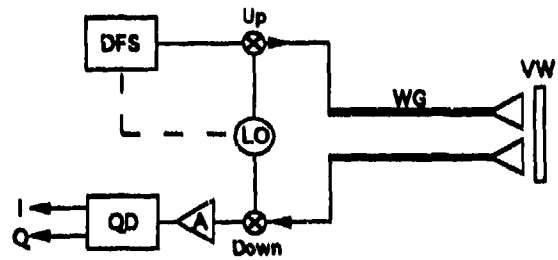

Figure 1 :
Schematic of a pulse compression radar (homodyne)

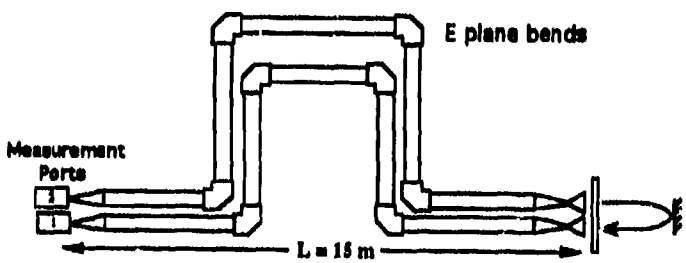

Figure 2 :
Mock-up of reflectometer for laboratory

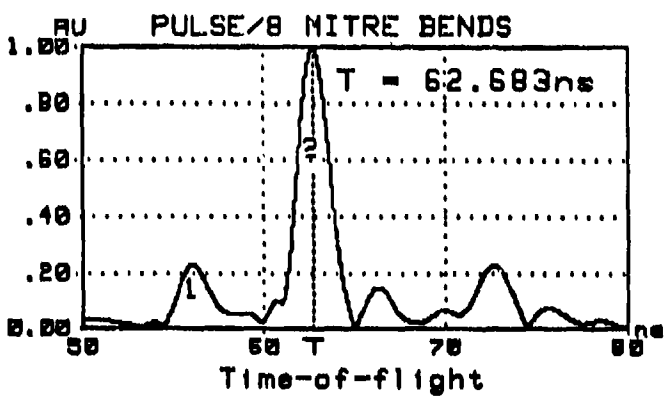

Figure 3 :
- Pulse reflected by the mirror

A FOUR-CHANNEL POLARIZING INTERFEROMETER FOR ECE MEASUREMENTS ON FTU TOKAMAK

P. Buratti, M. Zerbini

Associazione EURATOM-ENEA Sulla Fusione, CRE Frascati, CP 65
I-00044 Frascati (Roma) ITALY

ABSTRACT

Fourier Transform Spectrometers (FTS) are very useful for ECE measurements since they can be absolutely calibrated by standard blackbody sources, so that independent electron temperature measurements can be obtained. The simultaneous use of several Spectrometers is often required, either to analyse two dimensional configurations or to study the spatial distribution of suprathermal electrons.

The path difference in conventional FTS is scanned by translating a plane mirror; an alternative scheme is based on the rotation of a screw shaped reflector; this makes possible the development of multichannel instruments with a single, very fast scanning device.

1. THE FOURIER TRANSFORM SPECTROMETER

ECE measurements are routinely performed on FTU tokamak (major radius 93.5 cm; minor radius 30 cm; toroidal magnetic field up to 8 T) by means of a prototype FTS [1], in which a rotating screw shaped reflector is used to scan the path difference between the arms of the interferometer from 0 to 4 cm, with a duty cycle better than 90%, and a minimum scan time of 1.2 ms.

In this paper we describe a new version of the FTS, in which the size of the screw-shaped reflector has been increased, both in order to increase the étendue and to serve four interferometric channels. The radius of the reflector is 15 cm and the size of the reflecting annulus is 3 cm. The maximum path difference is 4 cm and the scan time is 5 ms. The FTS (fig. 1) receives collimated radiation from an 8x8 cm square section light pipe; radiation is focused onto the screw shaped reflector by a paraboloid with a focal length f_1=33 cm. A field lens with f=33 cm is placed near the reflector; it is crossed twice, so that its effective focal lenght is f/2= 16.5 cm, and it images the FTS input aperture onto the output one. The same arrangement is used for the reference mirror.

The étendue obtained with this optical arangement is about 0.3 cm^2sr, so that there is no reduction with respect to the one of standard InSb detectors. Diffraction effects are negligible at the maximum wavelength for which spectral information is required, i.e. λ=2 mm.

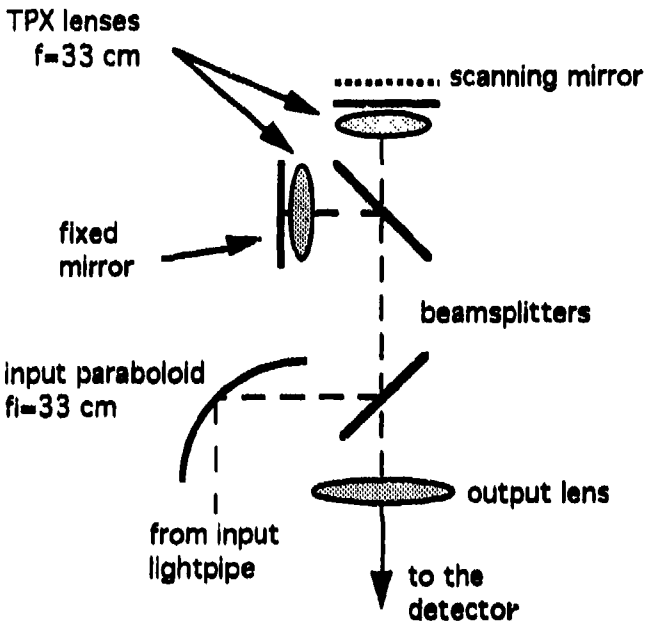

Fig. 1: channel optical arrangement

2. CONCLUSIONS

A novel four-channel Polarizing Fourier Transform Spectrometer has been developed. A single rotating screw shaped reflector is used to scan the path difference between the arms of each interferometer from 0 to 4 cm. The duty cycle is better than 90%; the scan time is 5 ms; the étendue of each channel is 0.3 cm^2sr.

REFERENCES

[1] P. Buratti, O. Tudisco, M. Zerbini, "An ECE diagnostic for electron temperature profiles measurement on FTU tokamak", Diagnostics for Contemporary Fusion Experiments, SIF, 787-793, Varenna (1991).

THE RECEIVER SYSTEM OF THE FAST ION AND ALPHA PARTICLE DIAGNOSTIC AT JET

J.A. Fessey, J.A. Hoekzema, T.P. Hughes

JET Joint Undertaking, Abingdon, Oxfordshire, OX14 3EA, UK.

1. INTRODUCTION

A 140GHz collective Thomson scattering diagnostic is presently being built to study the distribution of fast ions and alpha-particles within the JET plasma. A technical overview[1] and description of the mm-wave transmission system[2] are presented in other contributions to this conference. This paper will discuss the design of the multi-channel super heterodyne receiver and dedicated data acquisition system. 140GHz radiation from a gyrotron (250kW average, 5s pulse duration) is injected into the plasma where it is scattered by the shielding electrons moving with each ion. The receiver is designed to measure the spectral power density of the scattered radiation (10^{-19}- 10^{-16}W/Hz) against an electron cyclotron background emission of much higher magnitude (10^{-16}W/Hz). This is achieved by amplitude modulating the probing beam and synchronous detection of the scattered signal. Refraction of the beams within the plasma can be important at high densities and the position of the scattering volume will therefore change as the plasma evolves. A system of 'slave' receivers is being developed to track this movement and to control the trajectory of the main receiver beam by adjusting the orientation of the antenna.

2. THE MAIN SUPER HETERODYNE RECEIVER

The input to the main receiver is from a quasi-optical polarizer[3] which couples the $HE_{1,1}$ mode of the main transmission waveguide to the $TE_{1,0}$ mode of the receiver. A notch filter placed before the mixer rejects stray light coupled into the receiver waveguide. A conventional balanced mixer with integral pre-amp and separate power amplifier down-converts the 140±6 GHz signal to 12±6 GHz. The bandwidths of the 32 channels are proportional to their displacement from the central frequency, the narrowest being only 20MHz, which is less than the expected gyrotron frequency drift. The central spectral region is therefore down-converted again, using a local oscillator (LO) which is derived from the frequency difference between the first LO and the gyrotron. This is necessary because the width of each channel is proportional to its displacement from the central frequency. The closest channel to the central frequency has a width of only 20MHz, less than the expected gyrotron frequency drift. The frequency discrimination is performed by 32 bandpass filters followed by Schottky diode detectors. The diode signal is amplified and filtered prior to being recorded with a Real Time Signal Averager (RTSA).

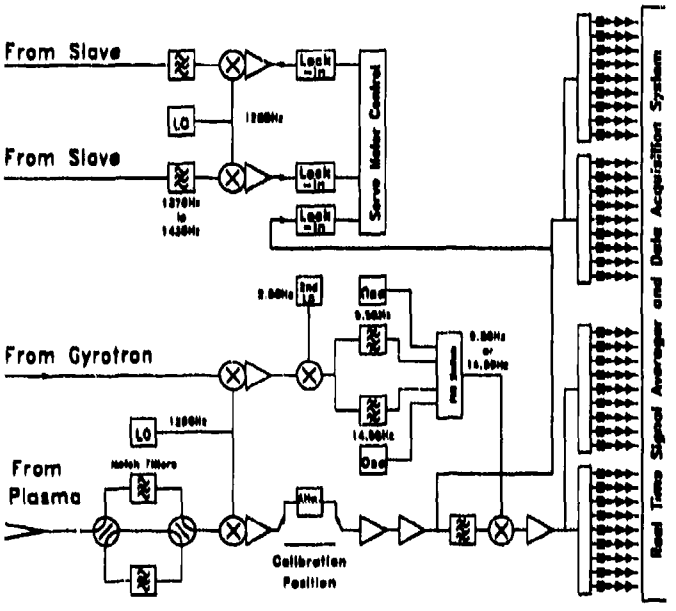

Fig 1. Schematic of the receiver

2.1. First heterodyne stage

The first mixer and integral 23dB pre-amp is biased with a 1mA DC current source and a frequency doubled 64GHz Gunn oscillator. The measured (dsb) noise temperature of the receiver is between 0.5eV and 0.8eV, close to the mixer, which translates to approximately 80eV (ssb) at the plasma antenna. Following amplification and attenuation the signal is divided three-ways, two ways are fed to 8-way power dividers and bandpass filters and the third way is fed to the second heterodyne stage. The attenuator is necessary during plasma measurements to avoid saturation of the amplifiers but is removed during calibration procedures when the full gain is required. An identical receiver, using the same local oscillator, is used to downconvert a sample of the gyrotron power. This nominal 12GHz signal (140GHz gyrotron - 128GHz LO + gyrotron drift -

LO drift) is 'up converted' to either 9.5 or 14.5GHz and used as the LO in the second heterodyne stage in order to compensate for the frequency drift of the gyrotron and first LO[4].

2.2. Second heterodyne stage

The central portion of the spectrum, from 138.9GHz to 140.2GHz, is down converted in a second mixer to the frequency band 2.3 to 3.6GHz. There are two reasons for this second conversion stage. Firstly, it facilitates the manufacture of the bandpass filters and secondly it allows compensation for frequency drift in the gyrotron and first LO. After amplification the signal is divided two ways and fed to two 8-way power dividers and sixteen bandpass filters.

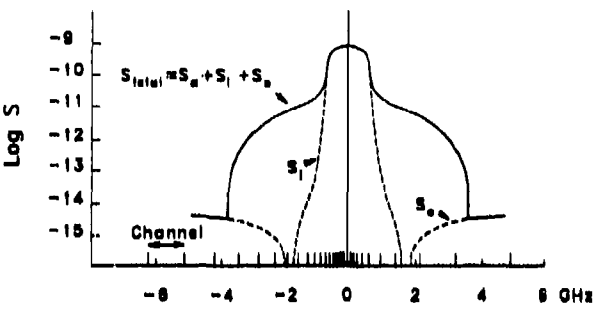

Fig. 2 Spectral distribution of channels

2.3. Video stage

The filtered signals are attenuated and detected with unbiased Schottky diodes. The attenuation is necessary to equalise the power onto each diode, avoiding non-linearities due to saturation, or operation close to the diode noise floor. Conventional low noise video amplifiers with switchable gain and bandwidth are used to condition the signals prior to recording the data with a Real Time Signal Averager.

2.4. Real time signal averager

To recover the scattered signal from the plasma noise the gyrotron signal is amplitude modulated and synchronous detection is employed. A data acquisition system has been designed and built to sample the scattered signal at up to 5 mega-samples per second and perform coherent addition of the signal in real time. This VME based system includes 128k words of 23 bit data memory per channel and a flexible timing system to control the sample rate, summation depth etc. In standard operation it is expected that 10-100 pulses will be added during 1ms to give a single pulse waveform, characterised by 20 points. Further pulse addition will then be done in software to obtain a sufficient S/N ratio (typically 100ns time resolution for fast α-particle measurements).

3. RECEIVER ANTENNA CONTROL

To track the movement of the scattering volume as the plasma evolves, the direction of the receiver antenna will be controlled by a real time feedback system that utilises signals from two slave antennas adjacent to the main antenna plus a signal from the main receiver. The slave receiver front end is identical to that of the main receiver with two balanced mixers and a single 128GHz LO. A notch filter is used to remove the stray light and a 6GHz wide (RF) bandpass filter defines the central portion of the scattered signal that is received. This will allow a time resolution of approximately 1ms.

The signal processing for the feedback signals consists of three lock-in amplifiers feeding VME based analogue to digital converters. The control algorithm will be implemented in the VME processor which will have control of the antenna servo motors.

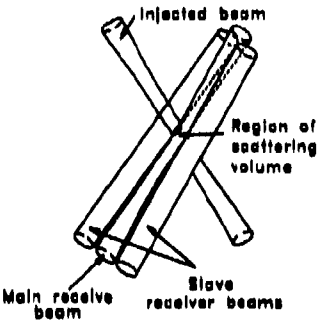

Fig.3 Beam Trajectories

REFERENCES

[1]J.A. Hoekzema et.al., "Collective mm-wave scattering to measure the fast ion and α-particle distributions in JET," this conference.
[2]J.A. Hoekzema et. al., "mm-wave transmission in the fast ion and alpha-particle diagnostic at JET," this conference.
[3]A.R. Harvey, "A quasi-optical universal polarizer," IJIMW,Vol. 14, No. 1, 1993.
[4]J.L. Doane,"Broadband superheterodyne tracking circuit for millimetre wave measurements," Rev.Sci.Inst. 51(3), Mar.1980

A PLASMA IMAGING CAMERA WITH A FILLED, 2-DIMENSIONAL FOCAL PLANE ARRAY

E.L. Moore, G.R. Huguenin, C.T. Hsieh, A.S. Vickery, K.R. Wood, J.E. Kapitzky

Millitech Corporation, P.O. Box 109, South Deerfield Research Park, South Deerfield, MA, 01373, U.S.A.

Summary

A 140 GHz filled two-dimensional focal plane camera which images phase and temperature fluctuations can provide information unobtainable from more conventional plasma diagnostics systems. The instrument was designed to give both spatial and temporal resolution necessary to identify plasma modes which fluctuate over periods of 10's to hundreds of microseconds with scale lengths of centimeters. Filled two dimensional measurements will form 2-D thermal and 3-D reflectometer images of small turbulent modes which are thought to be responsible for plasma energy transport.

The camera consists of a 4 x 16 vertical element continuous width slot antenna focal plane array (fpa) with subharmonically pumped mixers, a phase locked 70 GHz local oscillator, and a 140 GHz transmitter. The 70 GHz oscillator signal is reflected toward the fpa elements by a quasioptical band rejection filter. Each of the 64 channels has a 2 GHz bandwidth radiometric channel and 500 kHz I and Q channels for phase measurements. All of the electronics associated with each block of 8 fpa elements are on 2 printed circuit cards. One motherboard provides video multiplexing, address generation, a coaxial cable driver, and voltage regulators. The backend comprising the I/Q detectors, 30 MHz reference distribution, 500 KHz filter/amplifiers, and d.c. power sources are separated from the fpa by a 9.14 m coaxial ribbon cable.

Figure 1 illustrates the operation of the camera as a reflectometer. The transmitter beam propagates unfocused through a hole in the lens center and illuminates an area 24 cm in diameter at a distance of 2 m from the lens. The power received by each fpa element is focused by the zoned, aplanatic lens to a 1 - 2 cm spot size at the half power width. The 64 pixels are adjacent at the half power level, giving an image spanning about 6 x 24 cm. The camera performance is summarized in Table 1.

Acknowledgments

We gratefully acknowledge helpful suggestions from P.C. Efthimion. This program was supported in part by the U.S. Department of Energy under the SBIR program, contract number DE-AC02-88ER80616.002.

Table I

Specifications	
Transmitter Frequency	139.89 GHz
Transmitter Power	21 mW
3 dB Pixel Size	1 - 2 cm
Array Size	16 Vertical X 4 Horizontal
Focal Surface	24 cm Diameter
Polarization	Linear Vertical
I/Q and Radiometric Video Outputs	64 I, 64 Q, and R
I/Q Video Level	± 500 mV into 1 k Ω
I/Q Phase Accuracy	± 5 Degrees
I/Q Dynamic Range	> 20 dB
R Video Bandpass	0 - 100 kHz

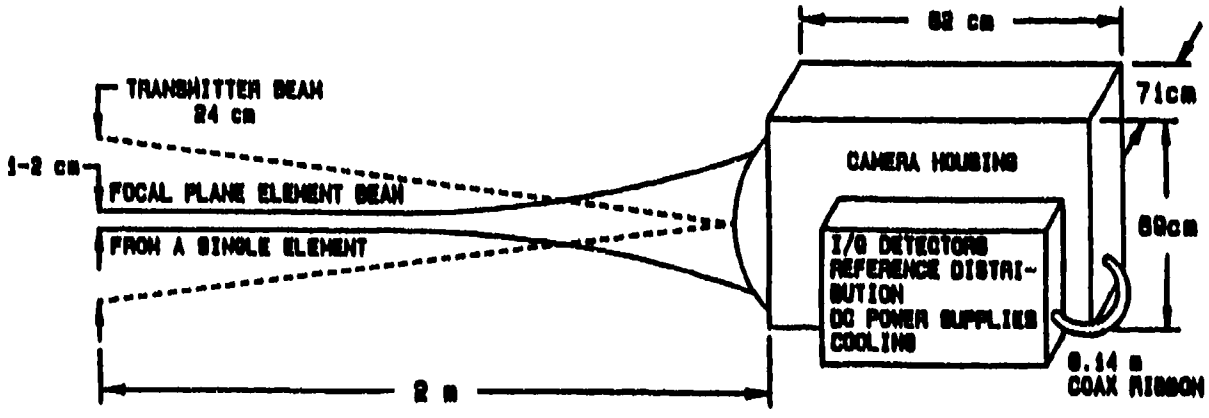

Camera Operating as a Reflectometer
Figure 1

SUPPRESSION OF COHERENCE EFFECTS IN THE MEASUREMENT OF MMWAVE ABSORPTION IN THE JET PLASMA

R J Smith, D V Bartlett, A R Harvey*, J C G Lesurf*, M W Salisbury**

JET Joint Undertaking, Abingdon Oxon OX14 3EA, UK
**University of St Andrews, Dept. of Physics and Astronomy, St Andrews, Scotland*
***Imperial College of Science, Technology and Medicine, London, SW7 2BZ, UK*

1. INTRODUCTION

The pumped divertor[1] is a major upgrade for the JET tokamak. Its purpose is to control the influx of impurities into the plasma and minimize the heat loading on the target tiles. The plasma parameters in the divertor region, low electron temperature, T_e, (10-100 eV) and high electron density, n_e, (~10^{20} m^{-3}) are very different from those of the bulk plasma. Electron cyclotron emission (ECE) cannot be used to measure local T_e because of the resulting low optical depth, τ. However low τ makes the measurement of electron cyclotron absorption (ECA) feasible[2][3]. The absorption is directly related to the local n_eT_e product.

The technique chosen to make this measurement must overcome a variety of problems: high background ECE from the bulk plasma, poor access for antennas, a 50 metre distance from the instrument to the plasma and coherence effects from the microwave source. Moreover, the instrument must be tunable over a 35 GHz bandwidth, which for a given plasma discharge is fixed somewhere in the range 120 to 240 GHz depending on the magnetic field value.

2. DIAGNOSTIC TECHNIQUE

The requirements of covering two waveguide bands (WR6 and WR4) and overcoming the significant losses in the system (~45 dB) have led to a design based on two BWO sources. Each BWO can cover an entire waveguide band, has an output power >10 mW and can be rapidly tuned (< 1ms, full band). However the high temporal coherence of such a source can produce standing waves and trapped modes in the oversized waveguides used to transmit the radiation to and from the plasma. This can result in significant time and frequency dependence of the transmissivity of the system.

2.1 SUPPRESSION OF COHERENCE EFFECTS

Waveguide discontinuities, such as oversized E- and H- plane bends, tapers, antennas and windows, are the cause of the standing waves. The discontinuities can reflect or mode convert some fraction of the radiation, forming resonant cavities which result in a strongly frequency dependent transmission.

Trapped mode resonances, in which power is converted into higher order waveguide modes which are trapped and strongly absorbed in the cavity, can produce particularly severe effects. Small mechanical movements can shift these resonances significantly which would introduce spurious (non-ECA) absorption into the measurement.

We are developing a swept frequency interferometer technique for suppressing these coherence effects. The method relies on a very linear sweep of the source frequency which generates a constant beat frequency at the detector by interference between radiation from a fixed reference arm and that from the plasma arm. The beat frequency, f_{IF}, is given by

$$f_{IF} = \frac{df}{dt} \cdot \frac{\Delta L}{c} \qquad (1)$$

where ΔL is the difference in length between the plasma arm and the reference arm.

Any radiation that is reflected between two discontinuities in the plasma arm will have taken a longer path length to the detector and will generate a displaced beat frequency when it beats with the reference arm (a ghost beat). By making the reference arm shorter than the plasma arm, all ghost beats will be displaced to frequencies above f_{IF}. The frequency separation of the ghosts from f_{IF} is given by

$$f_{ghost} - f_{IF} = \frac{df}{dt} \cdot \frac{2\delta L - \Delta L}{c} \qquad (2)$$

where δL is the effective distance between the two discontinuities. Assuming a sweep rate of 30 GHz/ms and ΔL of 1m, f_{IF} is 100 kHz. By separating bends, tapers and windows with at least 1 m (δL>1m) of straight waveguide, the ghost beats will

lie at least 100 kHz above f_{IF}. They can then be eliminated from the detected signal by filtering. Furthermore, the trapped mode resonances are suppressed, because the rapid frequency sweeping prevents the phase matching required for resonance.

The transmission can be obtained by ratioing the detected signals measured with plasma (during the discharge) and without plasma (before the discharge).

2.2 THE PROTOTYPE INSTRUMENT

Initial experiments have been aimed at proving the principles of the technique. A test instrument has been made with a 10 m oversized (S-band) waveguide arm and a quasi-optical reference arm. A varactor tuned Gunn diode source has been linearised over a 1 ms sweep from 86 to 92 GHz. To generate large standing waves, a cavity circuit was added to the waveguide arm using an in-waveguide beamsplitter. The beat signal with the cavity installed is shown in Fig 1. The power spectra of the beat signals, I(f), with and without the cavity arm is shown in Figs 2 and 3. A 25 kHz top hat filter was applied in the frequency domain, as shown, and the time traces were reconstructed from the filtered spectra. Fig 4 shows the ratio of the modulation envelopes of the two filtered time traces. The modulation, around the expected value of 1, evident in Fig 4, is because the filtering process has not yet been optimized.

3. CONCLUSION

The swept frequency interferometer technique has been successfully implemented on a prototype instrument for the ECA diagnostic. On the basis of these results, the actual instrument is now being designed. This design and further results will presented at the conference.

The authors wish to thank Dr. Richard Wylde for many informative discussions and for contributions to the design of the quasi-optical reference arm used in this work.

(1) Huguet et al., 14th Symposium on Fusion Engineering(San Diego,1991)
(2) D V Bartlett, A E Costley, R Prentice, 15 Int. Conference on Infrared and Millimetre Waves,Orlando,Fl,USA, 1990.
(3) R J Smith, D V Bartlett, A E Costley, S Richards, Proc. of the 8th Joint Workshop on ECE and ECRH, IPP III/186, (Gut Ising, Germany, 1992) IPP Report IPPIII/186(1993).

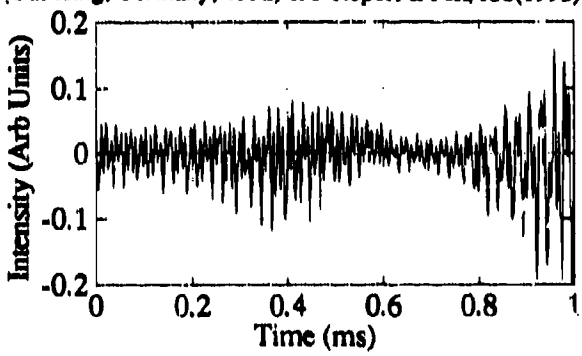

Figure 1: Time trace of the beat signal

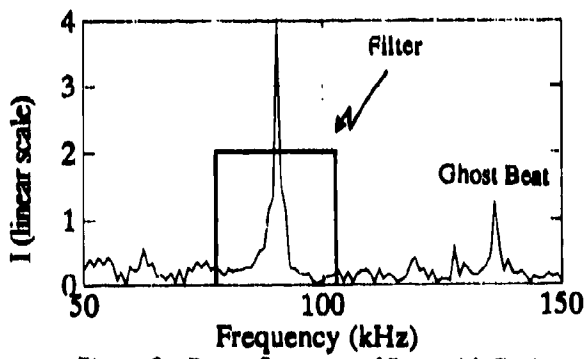

Figure 2: Power Spectrum of Beat with Cavity.

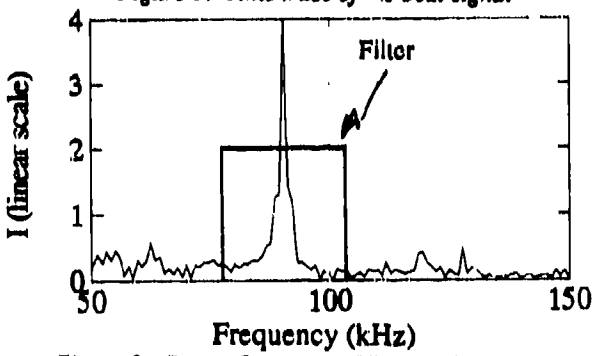

Figure 3: Power Spectrum of Beat without Cavity.

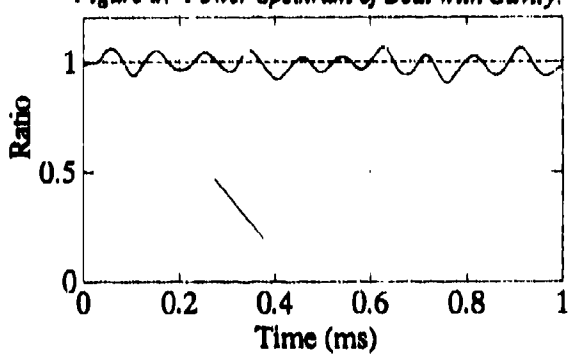

Figure 4: Ratio of the modulation envelopes of the reconstructed time signals

A BROADBAND QUASI-OPTICAL COLLECTION SYSTEM FOR THE JET HETERODYNE RADIOMETER

L Porte, DV Bartlett, A Rookes*, RJ Wylde**

JET Joint Undertaking, Abingdon, Oxon OX14 3EA, England
*Imperial College of Science Technology and Medicine, London, England
**Thomas Keating Ltd, Billingshurst, West Sussex, England and
Physics Dept, Queen Mary and Westfield College, London E1 4NS

A multi-channel, fixed frequency heterodyne radiometer, operating inthe radiation frequency range 73GHz to 127GHz, is used for electroncyclotron emission measurements on the JET tokamak (1). In a tokamak,the spatial variation of the magnetic field in the plasma provides the means by which spatially resolved measurements of theeission can be made (2). To obtain well localised measurements, it isnecessary to minimise the volume over which the measured emission is averaged. The spatial resolution along the line of sight is determined by the spectral resolution of the radiometer which, in the case of the JET radiometer, is 500 MHz. This corresponds to a spatial resolution of ≈20.mm. The spatial resolution transverse to the line of sight is determined by the antenna pattern of the collection system. At present a waveguide system is used and this has a spot size of ≈20 mm at the plasma centre. A quasi-optical system which will be used to improve this is under construction and is described in this paper.

The quasi-optical system has been designed to satisfy certain criteria. It must operate over a wide bandwidth; the bandwidth of the radiometer has been increased to cover 73GHz to 139GHz. It must transmit two orthogonal, linear polarisations with minimal cross-polar scattering because the radiometer measures the intensity of both polarisations independently. The double vacuum window through which the plasma is viewed has a diameter of ≈65mm which means that the beam radius, at the vacuum window, has to be ≈16.mm. In addition, the beam has to couple efficiently to oversized waveguide which is used to transport the radiation along a tortuous path, ≈40m long to the radiometer.

Figure 1 shows schematically the quasi-optical collection system. Radiation from the plasma is reflected by the two off-axis mirrors and, after passing through the vacuum window, arrives at the first aperture of a 'back-to-back' corrugated horn (3). After traversing the horn,the radiation, in a fundamental Gaussian beam, is coupled into oversized waveguide.

The 'back-to-back' horn is formed by two corrugated tapers connected by a short section of corrugated circular guide. The fundamental Gaussian component of the incident field excites the HE11 mode which propagates down the horn structure. The short circular guide, acting as a mode filter, ensures that only the HE11 mode can propagate through the horn and defines the antenna pattern of both the receive and transmit ends. As the back-to-back horn is axially symmetric it transmits orthogonal polarisations of the incident field identically. The antenna pattern of such a horn has been measured and satisfactorily approximates a fundamental Gaussian beam. Side lobes in the antenna pattern were not observed above the noise floor of the measurement which was 24dB below the power in the central peak. Cross-polar mode conversion was also not detectable at this level.

To meet the requirement of a small waist at the vacuum window, the 'back-to-back' horn is mounted directly behind the window and the collection mirrors in the vacuum vessel. The mirrors are limited in size by adjacent components. The smallest waist that can be produced in the plasma is 40mm, at a distance of 2.5m from the paraboloidal collection mirror.The cross-polar power loss and the higher order mode loss for each mirror has been reduced as far as possible. The combined power loss due to these effects is estimated to be less than -24dB for each mirror.

The quartz discs, which form the vacuum window, are tilted to reduce channel fringing in each window and in the gap between them. They are tilted at equal and opposite angles so that the beam remains on axis after traversing the window. Residual channel fringing will occur in each window and may cause the

transmission of the double vacuum window to be strongly frequency dependent. Methods are being explored to reduce this effect (see Hughes et al this conference).

Two different ways of coupling the quasi-optical beam into the oversized waveguide are being examined. The first is to illuminate the mouth of the waveguide directly from the scalar feed. Coupling in this case (4) may be poor, ~0.6, but it can be applied with minimal technical problems in this situation. The second technique is to focus the beam to form a waist at the mouth of the guide using a third mirror (5) as shown in Figure 1. Coupling should be higher in this case, ≥0.9, across the whole bandwidth. However, limited access may prevent the use of this arrangement.

Experiments are in progress to determine the best method for coupling the beam to the oversized waveguide and to verify the performance of the system as a whole.

REFERENCES

(1) DV Bartlett et al, 'The JET Heterodyne Radiometer and Investigations of Fast Phenomena', Proceedings of the 8th International Workshop on ECE and ECRH, 1992.
(2) F Engelmann and M Curatolo, 'Cyclotron Radiation from a Rarefied Inhomogeneous Magnetoplasma', Nuclear Fusion, 13, pp497-507, 1973.
(3) RJ Wylde, 'Millimetre-wave Gaussian beam-mode optics and corrugatedfeed horns', Proc IEE, Part H, 131, pp258-262 (1984)
(4) WB Joyce and BC DeLoach, 'Alignment of Gaussian Beams', Applied Optics, Vol 23(23), pp4187-4196, 1984
(5) W Kasparek, private communication, January 1993

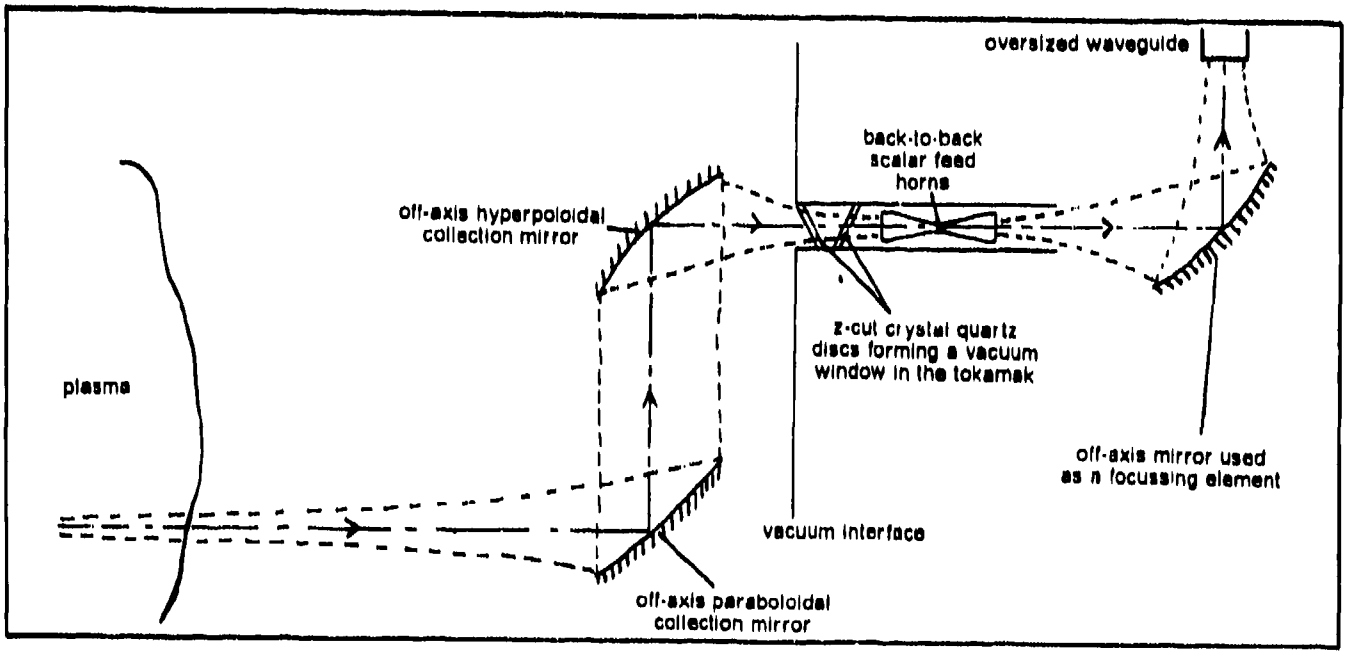

Figure 1: The Collection System for the JET Electron Cyclotron Emission Radiometer

SUBMILLIMETER LASER INTERFEROMETER-POLARIMETER FOR PLASMA DIAGNOSTICS

Kamenev Yu.E., Kiselev V.K., Kuleshov E.M., Knyaz'kov B.N., Kononenko V.K., Nesterov P.K., Yanovsky M.S.

Institute of Radiophysics and Electronics of
the Academy of Sciences of Ukraine
12 Acad. Proscura st., Kharkov, 310085, Ukraine

ABSTRACT

The results are presented of the investigation of the homodyne laser interferometer-polarimeter λ=195 μm made on the quasioptical element basis and designed for the synchronous determination of the electronic density n_e and the magnetic field B_p of the thermonuclear plasma on "TOKAMAK".

1. INTRODUCTION

The determination of the mean electron density n_e and the poloidal magnetic field B_p is of great importance for the investigation of the high temperature thermonuclear plasma. The mw interferometers are widely used for the determination n_e, and the determination B_p may be carried out by the measurement of the poloidal field inducing Faraday rotation in the Tokamak plasma, the polarimeter combining with the interferometer. It is expedient to use a submillimeter laser radiation in the large plasma machine when the electron density is 10^{14} cm^{-3} and the plasma diameter is more than 1000 mm.

2. TECHNICAL FEATURES OF THE DEVICE

We have developed the homodyne interferometer-polarimeter λ=195 μm using the Doppler shifting with the cylindrical rotating grating providing frequency shift about 106 kHz. The experimental model is created on the basis of the hollow circular dielectric waveguide Ø 20 mm and quasioptical devices and its tests are carried out with using the DCN laser and liquid helium cooled detectors (InSb). Faraday rotation angle ψ is measured by the signal level U reflected from the analysing wire grating. The wire grating is mounted orthogonally to the initial polarization of the wave. To reduce influence of radiation ellipticity the analysing and polarizating gratings are mounted directly near at the plasma chamber. Faraday rotation is imitated by the stepped calibrator with the stepping motor operated by a computer. The mean losses in the waveguide are about 1,0 dB/m. The detectors had NEP $4{,}6\times10^{-10}$ W/Hz in heterodyne operation. The actual antennas and the fused quartz windows of the T-15 Tokamak were used in the tests. Window thickness was 1,55 mm, and its diameter was 23 mm.

3. RESULTS AND DISCUSSION

Influence of antennas on ellipticity factor of the output radiation from the plasma chamber was investigated. The losses between flanges of chamber are 24 dB and ellipticity factor is -11,1 dB, when the antennas are attached to the flanges with the windows (free space is 1400 mm). When there are no antennas, the losses are 27,1 dB and the ellipticity factor is -28,5 dB (free space is 4500 mm). To estimate influence of the antennas on the measurement results, polarization characteristics $\bar{U} = f(\psi)$ (where $\bar{U} = U/U_{min}$) were read in heterodyne operation. Polarization characteristics are presented in Fig.1 (U_N - noise level, curve 1 - the antennas are present, curve 2 - the antennas are absent).

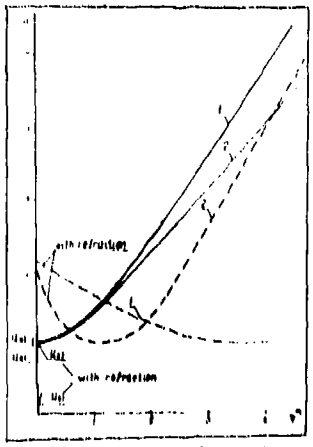

Fig.1 Polarization characteristics

Plasma influence on probing beam is known to be similar to the scattering lens. The maximal refraction angle is 0,5° when λ=195 μm and $n_e = 2 \times 10^{14}$ cm^{-3}. Polarization characteristics read when modeling the refraction by the teflon prism are represented by the dotted line in Fig.1. The radiation ellipticity resulted in the appearing of the signal reflected from the analysing grating when ψ=0°, which exceeds the noise level of the detector. This resulted in the nonlinear dependence of initial part of the polarization characteristic. The linear part of the characteristic can be used by introducing some initial polarization change (about 2°-3°) and taking it for the initial reading, if the radiation has a small ellipticity. This leads, however, to some decreasing of S/N ratio. Accessory probing radiation polarization change is observed by refraction, which increases when the antennas are present. Curve 1' (with the antennas) and curve 2' (without the antennas) on Fig.1 illustrates this effect.

Thus we can draw a conclusion, that it is expedient to refuse from similar antennas to improve characteristics of the interferometer-polarimeter.

The system is calibrated in the absence of the plasma by rotating the polarization grating and detecting the amplifier output as a function of the rotation angle. The grating is turned every 300 ms. The rotation step is (1 ± 0,1)°. The corresponding oscillogram is shown in Fig.2 when there are no antennas and the windows are present. It can be seen that noise level was by far less then the step, the lock-in amplifier using. Its time constant is 10 ms. Due to it, the polarization resolution is not worse than 0,1° when power of laser is 5 mW and the total length of the measuring channel is about 7000 mm.

Fig.2 The calibration

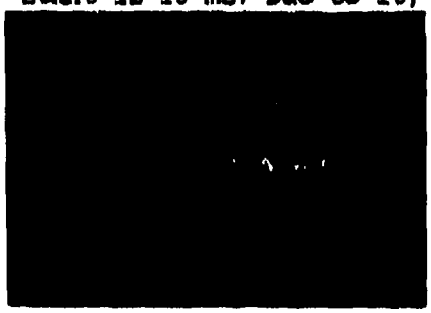

Fig.3 The phase noise

Simultaneously with polarization measurements the device measures the phase shift of the probing radiation with respect to the reference channel radiation. The phase noise oscillogram, when the plasma is absent, is presented in Fig.3. It shows that the value of the phase noise total amplitude is about 15°. It corresponds to the plasma electronic density $n_e = 3,4 \times 10^{14}$ cm^{-3}. Thus, the density response threshold is 0,2% from the expected plasma density. The phase difference measurement error is ±4°.

4. CONCLUSIONS

The results of the investigation of the developed submillimeter interferometer-polarimeter λ=195 μm demonstrated its efficiency and possibility to achieve the polarization resolution not worse than 0,1° and the density response threshold $3,4 \times 10^{14}$ cm^{-3}.

5. REFERENCES

1. H. Soltwish, "Current distribution measurement in a tokamak by FIR polarimetry," *Rev. Sci. Instrum.*, Vol.57, № 8, pp. 1939-1944, 1986.

First electron temperature edge measurements on the ASDEX Upgrade tokamak using a heterodyne radiometer

N.A. Salmon

Max-Planck-Institut für Plasmaphysik, EURATOM Association,
D-8046 Garching, Fed. Rep. of Germany

Abstract

The design of a multi-channel heterodyne radiometer used to determine the electron temperature in the edge region of the ASDEX Upgrade (AUG) tokamak plasma by measuring the microwave electron cyclotron emission (ECE) is described. A novel feature of the system is the use of both side-bands of a heterodyne mixer to maximise the available radiation bandwidth. Calibration, first plasma measurements and their interpretation are discussed.

1. Instrument design

A heterodyne radiometer has been designed specifically to measure the 2nd harmonic e-mode ECE from the low field mid-plane edge region ($0.7 < r/a < 1.$) of the AUG plasma. The AUG project has been designed to study the edge region of the tokamak plasma under conditions similar to those in an envisaged fusion reactor[1]. A heterodyne radiometer is ideal for such a purpose as it can provide continuous temperature measurements with microsecond time resolution at several different spatial locations with a radial resolution of 1 to 2 cm[2]. This is necessary to study fast phenomena and to resolve steep gradients which exist at edge regions of the plasma.

Cyclotron radiation from the plasma is imaged onto the end of a 25 mm diameter waveguide by a TPX lens of 27 cm diameter and 1.0 m focal length. Directly in front of the waveguide entrance is a wire grid (wire dia. 100 μm and spacing 215 μm) linear polariser that selects the e-mode. The waveguide is then tapered up to the transmission waveguide size of 50 mm. The transmission waveguide in which the imaging system excites the linear polarised TE_{11} mode is 25 m long, has 5 E-plane bends and 3 H-plane bends. The combined waveguide and imaging antenna system has a measured transmission of 7.0% (@80 GHz) to 3.5% (@190 GHz)[3]. The measured spot size dia. is 5 cm in the centre of the plasma and 7 cm at the plasma edge.

At the entrance of the receiver the radiation is tapered down from 50 mm to 25 mm. With AUG central magnetic fields ranging from 1.0 to 3.8 T the radiometer needs to be sensitive over the band 44 to 187 GHz. To span this frequency range a system with 5 mixers was chosen. Selection of the appropriate mixer is made by a series of five pairs of oversized (25 mm dia.) waveguide switches. Signals from each pair of switches are tapered down to fundamental waveguide using optimal parabolic tapers and then mode converted to the TE_{10} mode. At the end of each pair of mode converters are two waveguide filters: one transmitting only the lower and the other the upper side band of the mixer (figure 1). The appropriate filter is selected by a rotary waveguide switch located directly in front of the mixer.

Signals from the appropriate mixer are directed into a single IF section by the use of a 5 input / 1 output multi-position coaxial switch. Here the signals are amplified and split into several channels. A bank of power dividers and GaAs FET IF amplifiers responding over the range 3 to 12.5 GHz divide the IF section into several channels. The signals enter an array of band-pass filters with centre frequencies spaced equally across the IF bandwidth before entering the array of Si Schottky barrier detectors. As the radial gradient of the cyclotron frequency in the plasma is a function of the central magnetic field, in order to achieve a given spatial resolution two arrays of band-pass filters are used. For measurements at lower magnetic fields (<2 T) an array of 32 300 MHz wide band-pass filters equally spaced across the frequency range can be used. For measurements at the higher magnetic fields an array of 16 600 MHz filters are used. This enables 15 cm at the plasma edge to be covered with a radial resolution of 1 to 2 cm at all magnetic fields.

Signals output from the detectors enter a 16 channel video stage. A single channel consists of a pre-amp (of gain $\times 100$) followed by a low-pass filter (with cut-off frequency variable from 1 kHz to 150 kHz) and a main amplifier (of gain variable from unity to $\times 10^3$). Signals output from the main amplifier are transmitted a distance of 50 m to the data acquisition system by an optical pulse FM transmission line. A CAMAC data acquisition system with 2 ADCs is used to collect data with a sample frequency of up to 250 kHz (per ADC). The instrumental noise from the system is dominated by the pre-amp and corresponds to a minimum detectable temperature variation of ~8 eV in a 100 kHz video bandwidth. However, during plasma temperature measurements the dominant noise is due to the thermal photon fluctuations[2]. Using a 100 kHz video bandwidth these fluctuations limit the signal to noise ratio to 55 (for the 300 MHz IF filters) and 80 (for the 600 MHz filters).

2. Calibration

The system can be calibrated by measuring the thermal emission from large area microwave absorbers at the temperature of liquid nitrogen and at room temperature. During calibration these are placed in the image plane of a dummy antenna system. Alternatively the instrument can be calibrated against the calibrated AUG ECE Michelson interferometer using the plasma as a radiation source[4]. These calibration methods are discussed more fully in reference[2].

3. Measurements and interpretation

First measurements of the temperature at the edge of the plasma have been made on detached divertor plasmas. Detached in this case refers to plasmas in which at least 30 % of the total power input to the plasma is radiated in the divertor region. Measurements from two channels of the radiometer during this phase are shown in figure 2. The detachment of the plasma is initiated by an increase in the density. CCD camera measurements in the visible part of the spectrum indicate that the plasma detachment occurs between 1.2 and 1.4 s. During this phase of the discharge the temperature falls. However, this fall could partially be due to the power balancing caused by the rising density. A significant observation is that the temperature in the mid-plane does not fall rapidly when the plasma becomes detached. This is in agreement with the classical heat flow ($q_{\parallel} \sim T^{5/2}\nabla T$) along the field lines from the last closed flux surface into the divertor.

Later in this discharge, after 1.4 s, the local electron density rises above the e-mode cut-off density ($5.1 \times 10^{19} m^3$) and the emission cannot propagate directly out of the plasma. In this case the intensity of radiation is greatly reduced and no longer directly proportional to the electron temperature. The signals show that when entering the cut-off phase the level of fluctuations on the signals increases. It is also observed that during the cut-off phase the level of fluctuations on the outer most channel (at the 75 % flux surface) is very large (50 %). As it is known that very little of the cyclotron emission fluctuations can be attributed to temperature fluctuations (as they are known to be small) it must be concluded that the fluctuations are due to density variations close to the critical density. As these measurement are local measurements in the plasma they could be useful when combined with data from other diagnostics, such as density reflectometry, in the study of fluctuations.

4. Conclusions and further developments

A heterodyne radiometer has been used to measure the temperature in the edge region of the ASDEX Upgrade plasma. A useful improvement to the system would be to replace the simple oversized waveguide reflection switches with beam splitters and to have two or more IF channels. This would enable more than one mixer to be operated simultaneously and hence allow temperature measurements to be made in the plasma edge region and the centre at the same time. When rapidly sampling ($\sim 10\mu s$) data on all channels of the radiometer for more than ~500 ms large amounts of data are generated. This situation may be improved by using a transputer based data acquisition system that selects only useful data for permanent storage[5]. This diagnostic should also be a useful instrument with which to study heat waves stimulated by electron cyclotron resonance heating[6].

5. References

[1] Gruber. O., et al, 'Physics Background of the ASDEX Upgrade Project', Journal of Nuclear Materials, 121, pp. 407-414, (1984).
[2] Salmon, N.A., Ph.D Thesis, University of London, (1990).
[3] Salmon, N.A. 'The ASDEX Upgrade ECE Michelson Interferometer', IPP Internal Report, Garching, (1993), to be published.
[4] Salmon, N.A. and Eberhagen A., 'First Electron Temperature Profile and Electron Cyclotron Emission Measurements from the ASDEX Upgrade'. Proc. 19th EPS Conference, Innsbruck, June, (1992).
[5] Zilker M., Private communication, Garching, (1993).
[6] Leuterer, F., et al, 'A 140 GHz/2 MW ECRH System for ASDEX Upgrade', Internal Report, ASDEX Upgrade ECRH Group, Garching and IPF-ECRH Group, Stuttgart, January (1993).

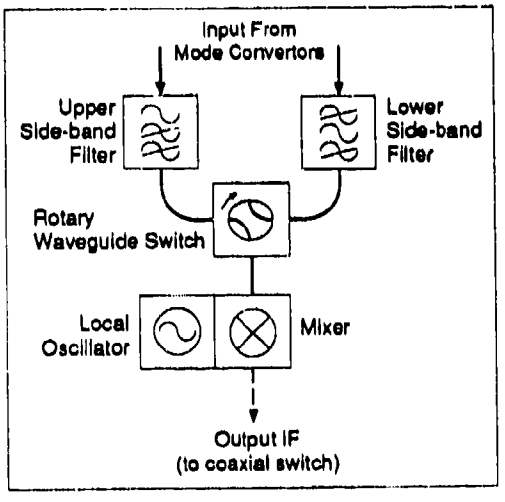

Figure1: Heterodyne Mixer Side-band Selection Module

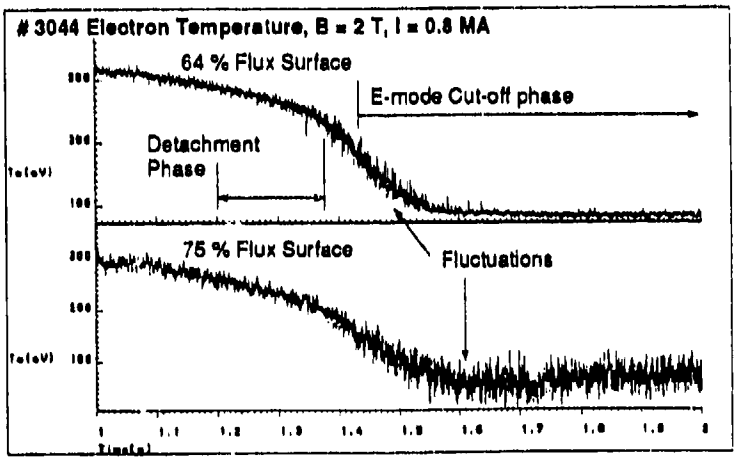

Figure 2: Electron temperatures measured during the divertor detachment and e-mode cut-off phase.

Hot-Electron Superconducting Mixers

E.M.Gershenzon, G.N.Gol'tsman
Moscow State Pedagogical University
1 M.Pirogovskaja Str., 119435 Moscow, Russia

The creation of low noise heterodyne receivers for frequencies above 1 THz is in the urgent need for radio astronomy, laser spectroscopy, plasma diagnostic, etc. In this paper we discuss the nonlinear effect related to hot electrons in superconductors, and their potential use in low noise submilimeter wave mixer. We also discuss results achieved so far as well as possible future developments.

Recently we have shown that in thin ($\sim 100\AA$) and narrow ($\sim 1\mu$m) superconducting strips nonlinearities are present near a transition temperature T_c due to the hot-electron effect. This nonlinearity monitors itself both in conventional and in high-T_c superconductors [1,2]. As radiation is absorbed, the superconductivity is being suppressed, and the quasiparticle concentration increases causing a change in V-I characteristic. When the current flowing through the superconducting strip exceeds its critical value, the strip's state becomes resistive. The nature of the resistive state is attributed to varios physical mechanisms such as (i) phase slip centers which apper at $T \approx T_c$, (ii) flow of magnetic flux vortices at $T < T_c$, and (iii) heated normal condition domains.

An energy relaxation flow within the device is illustrated in Fig. 1. A necessary condition is that there should be a strong electron-electron (Coulomb) interaction to rapid transfer the absorbed energy to all electrons (the typical time constant of electron-electron interaction time τ_{el-el} is of order of $10^{-12} - 10^{-11}$ s for $T_0 \simeq T_c$. It is also required that the energy transfer from electrons to phonons is comparatively slow i.e. the electron-phonon interaction time $\tau_{el-ph} \gg \tau_{el-el}$ (the bottleneck of the process). On the other hand, the time of the detection process should be short enough to allow intermediate frequency (IF) up to several GHz, therefore it is necessary to have $\tau_{el-ph} < 10^{-10}$ s.

The time constants can be affected by a propper choice of the dimensions of the superconducting strip. The excess electron energy must first escape to the phonons in the superconducting strip (the time constant τ_{el-ph} is of order of $3 \cdot 10^{-10}$ s for Nb, 10^{-11} s for NbN and 10^{-12} s for YBCO at $T \simeq T_c$, and then from the phonons in the film to the substrate (time constant τ_{es}). So it is required that non-equilibrium phonons should escape from the film before they could be scattered by electrons (time constant τ_{ph-el}). The τ_{es} time is affected by dimensions of the superconducting strip $\tau_{es} \sim d$ (d is the thickness of the superconducting film). In order to avoid a reverse flow of non-equilibrium phonons from the substrate to the film a width of the strip should be smaller than 1 μm.

Results of IF band neasurements at 150 GHz show that IF bandwidth for Nb mixer can approach 500 MHz, while for the NbN mixer it should yield 10 GHz and for YBaCuO $\simeq$ 100 GHz. Conversion losses of Nb mixer gotten experimentally are presented in [3]. Measurements show a total conversion loss of the receiver from 7.5 to 11 dB. Taking into account the input mismatch

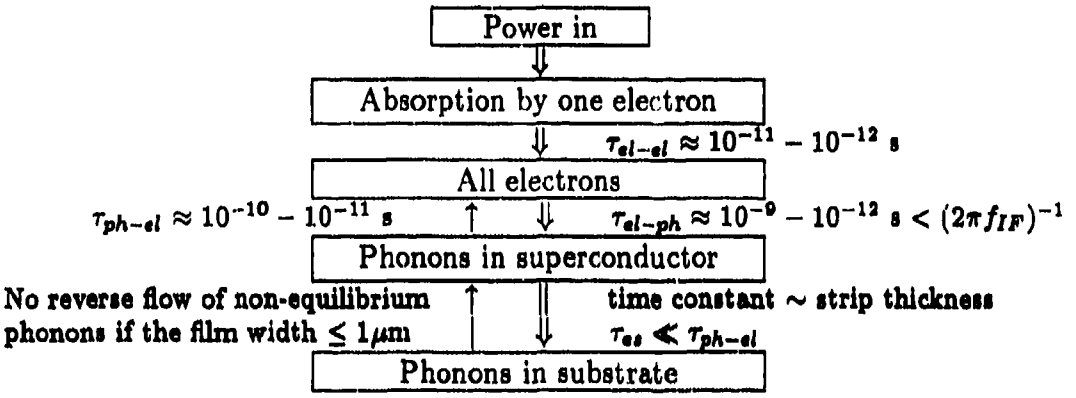

Fig. 1. Shematic diagram showing various energy relaxation mechanisms in superconducting hot-electron devices.

loss, one can estimate that an intrinsic loss of the mixing element is about 1 dB. Since non-equilibrium phenomena in thin films can cause a negative effective resistance, the positive conversion gain is also possible for this mixer. Up to now the noise of the hot electron mixer has not been experimentally established. Measurements indicate only that the noise temperature of the mixer is rather low.

Since the number of static defects in ultrathin films is large, the momentum relaxation time τ_m if of order of $10^{-13} - 10^{-14}$ s, and the film is capable to absorb a power at any radiation frequency from microwave to infrared waves where $\omega\tau_m = 1$. Furthermore, in such "durty" films there is no parasitic elements like intergrain junction capacities or an inductance related to the electron inertia, that is greatly facilitate the design of submillimeter wave mixers.

The resistance of mixing element can be adjusted to 20 - 300 Ω by choosing a length of the strip; therefore the coupling with a waveguide or a planar antenna can be easly done. For such a strip the optimum local oscilator power is of order of 10^{-6} W for Nb, 10^{-4} W for NbN and 10^{-3} W for YBaCuO. If a large dynamic range is required, several strips can be connected in parallel in order to get a larger volume of mixing element. So, the hot-electron mixer promises to be an alternative device for achieving low noise temperatures in the submillimeter and the far-infrared ranges.

1. E.M.Gershenzon, M.E.Gershenzon, G.N.Gol'tsman, A.M.Lyul'kin, A.D.Semenov, A.V. Sergeev, "Electron-phonon interaction in ultrathin Nb films", Sov. Phys. JETP, Vol. 70, pp. 505-513 (1990).

2. E.M.Gershenzon, G.N.Gol'tsman, A.D.Semenov, A.V.Sergeev, "Mechanism of picosecond response of granular YBaCuO films to electromagnetic radiation", Sol. St. Com., Vol. 76, pp. 493-495 (1990).

3. E.M.Gershenzon, G.N.Gol'tsman, Yu.P.Gusev, A.I.Elant'ev, A.D.Semenov, "Electromagnetic radiation mixer based on electron heating in resistive state of superconductive Nb and YBaCuO", IEEE Trans. Mag., Vol. 27, pp. 1317-1321 (1991).

A Combined 3mm and 1.3mm Bands SIS Receiver for the IRAM Interferometer

M.Carter,J.Blondel,A.Karpov,F.Mattiocco,B.Lazareff
IRAM, Institut de Radio Astronomie Millimetrique

The IRAM, Institut de Radio Astronomie Millimetrique, interferometer at the Plateau de Bure has been successfully working for a number of years in the 80-115GHz band with SIS receivers. It was decided to increase the frequency range on the four antennas and their efficiencies by simultaneously covering the 1.3mm frequency band 200-270GHz and the 3mm band,80-115GHz. To do this a different construction of the receiver was required since the size and optical arrangement of the receiver cabin did not allow a parallel cryostats to be mounted.

The new receiver is based on the Infrared Laboratories hybrid cryostat , which has an 8 inch 4K cold plate, and 15 and 77K shields cooled by a CTI 350 refrigerator and 2 output ports. It was decided to simplify the optics as much as possible, but at the same time seek to reduce the hot optic loss to a minimum.

The SIS junctions are made on a quartz substrate , which is suspended across a reduced height waveguide of a copper mixer block,ref 1. The waveguide dimensions for the 3mm mixer has also been reduced in width to improve the mixer performance at 115GHz, which is the important CO12-1 astronomical line. Both waveguide blocks have reduced -height to normal guide transformers fitted into the blocks. The junctions used are made at IRAM,and are made by a trilayer technique of Nb/Aloxide/Nb in an array of two, with a niobium low pass filter fabricated at the same time on the quartz substrate, ref 2. The 1.3mm junctions have integrated tuning in parallel to reduce the junction capacitance,ref 3. The local oscillator is fed on to the mixers by means of side wall couplers, which are mounted directly on to the mixer in the cold. The couplers have an insertion loss of >0.2dB, a coupling of 18-22 dB and an isolation > 40dB. The LO enters into the waveguide in both cases in stainless steel waveguide WR10, which is overmoded for the 1.3mm case. The signal enters onto the mixer by means of a cold corrugated horn/ lens combination. The IF is at a centre frequency of 1.5 GHz with a bandwidth of 500MHz. There are two HEMT amplifiers mounted onto the 15K stage of the cryostat.

The measured noise temperature of the IF is about 6K. The receiver noise temperature, tested using the standard Y-factor technique and using T(hot) as 295K and T(cold) as 77K, liquid nitrogen. The IF bandwidth for these measurements was always 500MHz. The noise temperature for the receivers, plotted against local oscillator frequency can be seen in figures 1 and 2. In the 3mm band between the frequencies of 86GHz ,SiO, and 115GHz CO12-1, the noise temperature DSB is of the order of 40-50K, whilst the SSB noise temperature is about 60K with about 10dB of rejection of the upper sideband. T(receiver) for the 1.3slowly in temperature. The SSB results like 3mm case show noise temperatures about 30% higher across most of the band.

The receivers have been automated so that they can be completely computer controled remotely. This has included the use of an A.G.C. loop on the local oscillator power to stabalize the fluctuations and drifts, ref 4. The normal phase lock loop is still employed.

The schedule for completion of these systems will be to have the first system delivered on to the telescope for the end of 1993, and then have the four antennas working simultaneosly in the 1.3mm and 3mm bands by the end of 1994.

1 R.Blundell,M.Carter,K.H.Gundlach, A low Noise SIS Receiver Copvering the Frequency Range 215-250GHz, Int.J.IR andMM Waves Vol9 pp361-370 Apr.88

2 T.Lehnert,C.Grassl,K.H.Gundlach,J.Blondel, Nb-Al oxide-Nb Junctions for 3mm SIS Receivers; Supercond. Sci. Technol. 4,1991 419-422.

3 A.Karpov,M.Carter,B.Lazareff, M.Voss, D.Billon-Pierron, K.H.Gundlach. Wide Band Fixed Tuned and Tuneable SIS Mixers for 230GHz and 345GHz Receivers Fourth International Symposium on Space TeraHertz Technology

4 J.Lamb private communication

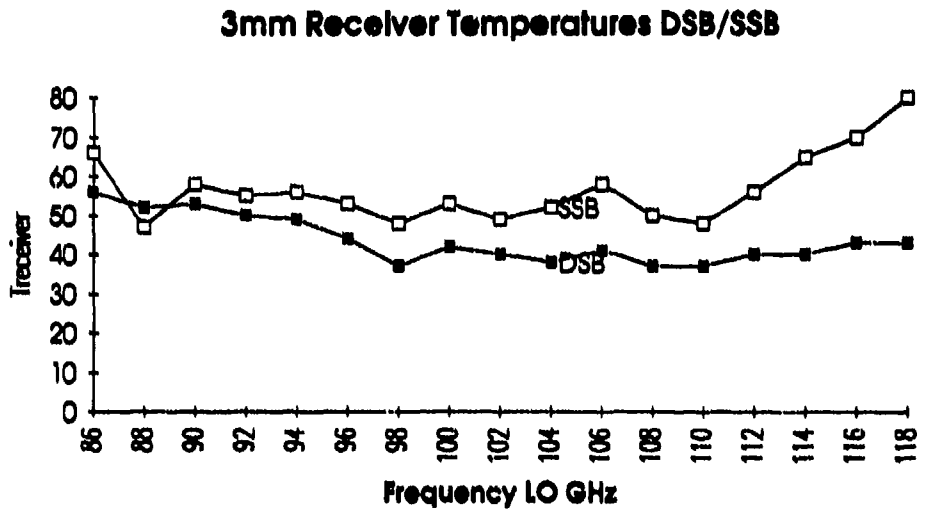

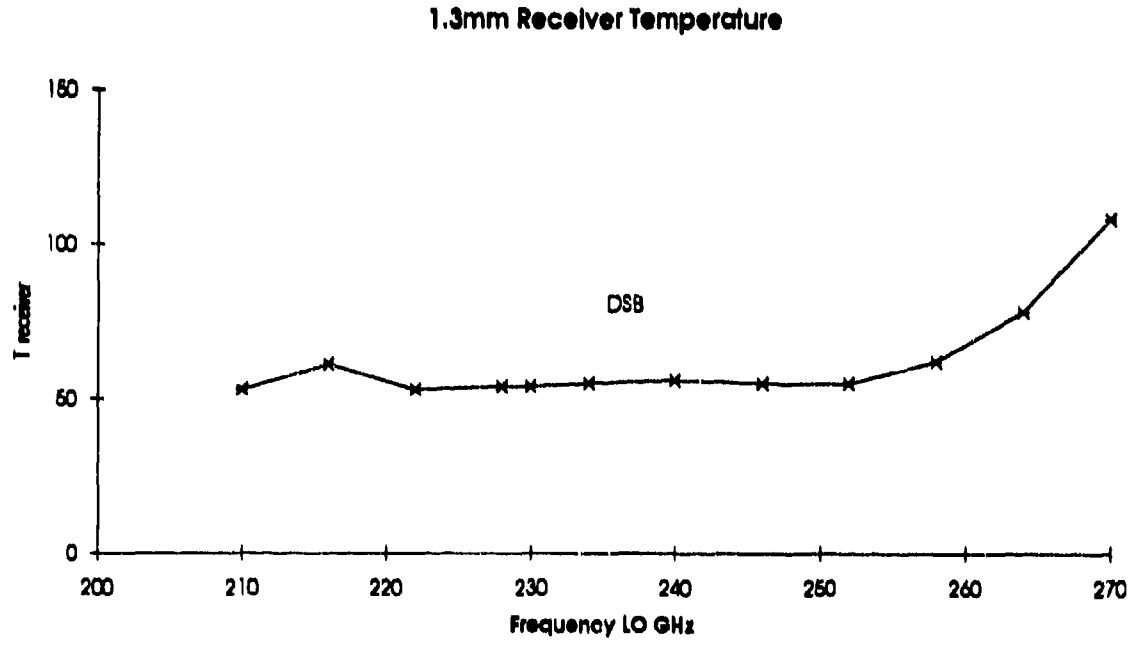

200 and 270 GHz SIS Receivers Development for Atmospheric Observation

S. Ochiai and H. Masuko
Communications Research Laboratory
4-2-1 Nukui-Kita, Koganei, Tokyo 184 Japan

Superconducting mixers have been developed for observations of atmospheric minor constituents such as ClO and ozone at Communications Research Laboratory. This paper describes the work at development of 200 and 270 GHz SIS mixers.

Nb/AlOx/Nb junctions were fabricated at Nobeyama Radio Observatory. The base Nb layer 200 nm, the Al (AlOx) insulation layer, and the counter Nb electrode 150 nm are sputtered. The area outside of a junction defined by etching of the counter electrode is insulated by anodized Nb layer and sputtered SiO_2. After sputtering thick SiO_2 layer on the whole wafer, a contact hole is made by etching. The thickness of the wiring Nb layer is 500 nm. The junctions are formed on the 250 μm thick fused quartz substrate. After the process of the junction fabrication, the quartz substrate is shaved from the back side until 150 μm thickness.

Each junction for 270 GHz mixer has an area of about 1 μm^2. The normal resistance of the six junctions series array is around 70 Ω.

The mixer block has a reduced waveguide (1.2 $\times$ 0.1 mm for 200 GHz and 0.98 $\times$ 0.1 mm for 270 GHz). The waveguide has two tuners in addition to a fixed backshort cavity. This configuration can allow to realize the lower embedding impedance, and less sensitive to the position of the tuners.

The SIS mixers are cooled in a closed cycle He refrigerator. The LO is optically injected through a Fabry Perot interferometer. The 5 - 7 GHz IF is fed to a HEMT amplifier cooled at 15 K.

We have started a preliminary measurement of the noise temperature of the SIS receivers, and comparing with calculated DSB receiver noise temperature assuming 3-port model. We continue to improve the performance of the SIS mixers now.

We intend that the receivers shall be utilized for atmospheric monitor from next winter.

Acknowledgement

We wish to thank Dr. J. Inatani, Dr. T. Noguchi, Dr. K. Sunada, and Mr. A. Sakamoto at Nobeyama for their assistance with designing the receivers and fabrication of SIS junctions. We also wish to thank Dr. Y. Irimajiri and Ms. N. Onozeki for their collaboration.

Preparation and microwave measurements of stacked $Nb/(Al/AlO_x/Nb)_n$ superconducting tunnel structures

I. P. Nevirkovets, and L. P. Strizhko*

Department of Materials Science and Metallurgy, University of Cambridge, Pembroke Street, Cambridge CB2 3QZ, UK; permanent address: Institute of Metal Physics of the Ukrainian Academy of Sciences, Vernadsky Str., 36, 252142 Kiev, Ukraine

*Institute for Radio Astronomy of the Ukrainian Academy of Sciences, Krasnoznamennaja Str., 4, 310002 Kharkov, Ukraine

ABSTRACT

The I-V characteristics of stacked $Nb/(Al/AlO_x/Nb)_n$ superconducting tunnel structures with n=3 and n=6 were measured under microwave irradiation of 45 and 136 GHz. The classical responce of the structures was observed over a wide range of input RF power at 45 GHz. Photon-assisted steps in the I-V characteristics were observed at 136 GHz. The widths of the steps correspond to the response from only 2 and 4 junctions in 3- and 6-barrier structures, respectively.

1. INTRODUCTION

A multilayered approach to SIS receiver design seems to improve the device performance by increasing saturation power and dynamic range, by reducing the capacitance, and by eliminating the inductance problem associated with conventional planar series arrays of SIS junctions. So far, stacked arrays consisting of two junctions have been prepared and tested[1,2]. Recently, it has been shown that it is possible to fabricate vertically stacked arrays $Nb/(Al/AlO_x/Nb)_n$, with n up to 10, with good homogeneity of barriers throughout the stack[3]. The present contribution describes the preliminary results of the microwave measurements of these structures in conjunction with their possible mixer applications.

2. EXPERIMENTAL PROCEDURE

We have fabricated $Nb/(Al/AlO_x/Nb)_n$ tunnel structures with n=3 and n=6 by the sputtering deposition route described elsewhere[3]. The junctions areas were $8x8\ \mu m^2$. In the 3-junction stack, the barriers were spaced by 70 nm Nb layers, while in the 6-junction stack the thicknesses of the inner layers were 30 nm. The bottom and uppermost Nb layers in both types of structures had thicknesses of approximately 120 nm. The structures were inserted into a broad-band RF section weakly coupled with a wave guide and exposed to RF radiation of ν=45 GHz and 136 GHz. The quasiparticle I-V characteristics corresponding to various RF power levels were measured in liquid helium at T=4.2 K.

3. RESULTS AND DISCUSSION

Measurements at ν=45 GHz showed essentially classical responce from both types of structures with photon-assisted tunneling steps slightly pronounced only at high applied microwave signals. This might be due to the fact that the onset of the current step at $V=n\times 2\Delta/e$ was not sharp enough over the range $n\times h\nu/e$.

Fig.1 shows a set of I-V characteristics obtained from a structure with n=6. For this structure, assuming that the particular junctions are connected in series, the photon-assisted steps should have spacing $n\times h\nu/e$=3.38 mV, which is considerably larger than the smearing of the nonlinearity of the quasiparticle current step at $V=n\times 2\Delta/e$. In fact, we observed the classical behaviour at weak input LO power (9 dB curve), and gradual growth of the 1st photon-assisted step at higher power levels. The width of the 1st step increased with power, which is seen from calculated dI/dV curves shown in the inset of Fig.1. At 0 and 1 dB attenuation level, the 2nd and 4th steps appear. As follows from dI/dV curves, the voltage positions of the steps are separated by δV=2.3 mV, which is considerably less than the expected theoretical value, and corresponds to the response of only 4 junctions rather than 6.

Similar results were obtained with n=3 structures. The corresponding I-V characteristics are shown in Fig.2. In this case the width of the phonon-assisted step is δV=1.13 mV instead of the expected value of 1.70 mV. We measured experimental values of δV from observed gap voltages for corresponding I-V curves. As follows from the δV obtained, in the case of n=3 only 2 junctions from the stack contribute to photon-assisted tunnelling.

The main result of our experiments which has to be explained is why not all of the junctions composing the stack participate in photon-assisted tunnelling. As we can see from Fig.1,2, a considerable suppression of the energy gap in superconducting Nb films takes place in our structures because of heating and nonequilibrium effects. The unperturbed value of the energy gap in Nb films is 1.35 mV, so that for a 3-barrier structure the total gap voltage should be $3x2\Delta/e$=8.1 mV, while the measured value at T=4.2 K is 6.7 mV. However, this value gives evidence that no superconducting layer becomes normal in

experimental conditions. Our previous experiments with stacked tunnel junctions showed that good phonon coupling exists between the thin superconducting layers composing the stack, so that they are driven homogeneously under phonon injection[4]. Thus, it seems to be unlikely that heating and nonequilibrium effects could eliminate exactly one junction in a 3-barrier stack (or 2 junctions in a 6-barrier stack) from participation in photon-assisted tunnelling.

A possible cause of the observed behaviour could be the intrinsic RF properties of multibarrier structures. The tunnel barriers in our structures are spaced by Nb layers of thickness $d<2\lambda_L$, where λ_L is London penetration depth. Hence, the junctions composing the structure are inductively coupled, and this, in principle, could allow the applied RF power to be transferred from one junction to another resulting in its nonuniform distribution across the stack. The possibility of RF power transfer from one stripline to another in the system consisting of two weakly coupled striplines is shown in Ref. 5. Whether this could occur in the system of weakly coupled lumped elements is the subject of further investigation.

4. ACKNOWLEDGEMENTS

I.P.Nevirkovets was supported by the Deutsche Akademische Austauschdienst in part of device fabrication. The authors acknowledge Prof. C. Heiden, Dr. H.Kohlstedt, Dr. A.V.Ustinov, and Dr. M.Blamire for helpful discussions.

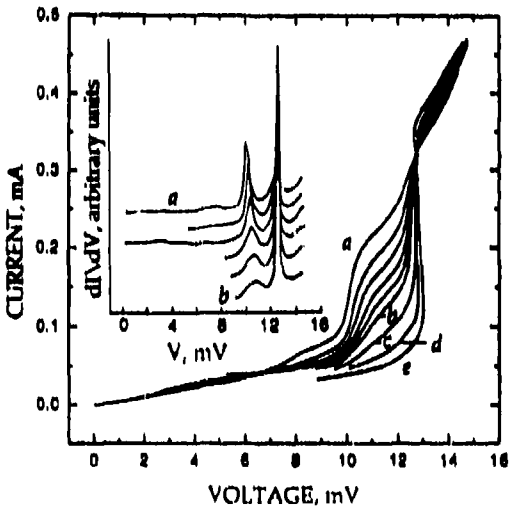

Fig.1. I-V curves for the structure with n=6 at 136 GHz. Curves from *a* to *b* are for attenuations of LO power from 0 to 5 dB with 1 dB increments, *c* and *d* are for 7 and 9 dB, and *e* is unmodulated characteristic. The inset shows derivatives for the curves from *a* to *b*.

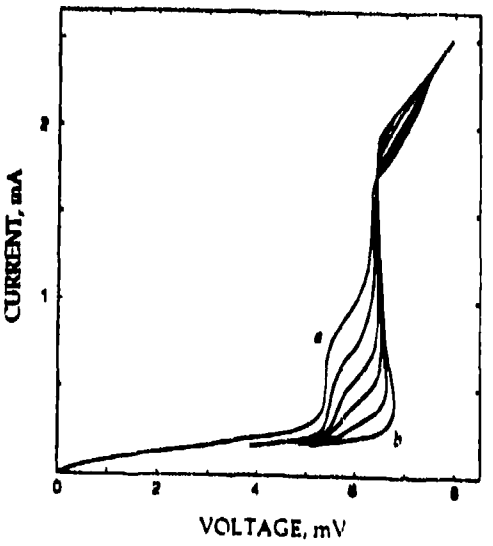

Fig. 2. I-V curves for the structure with n=3 at 136 GHz. Curves from *a* to *b* are measured at attenuations of 0, 2, 4, 7, 9, and ∞ dB.

5. REFERENCES

1. S. A. Kovtonyuk, V. Yu. Belitsky, O. V. Kaplunenko, M. A. Tarasov, S. W. Jacobsson, C-O. Lindstrom, and E. L. Kollberg, "Vertically integrated SIS array for mm wave mixers", *Proceedings 1992 URSI International Symposium on Signals, Systems, and Electronics ISSSE'92*, pp.93-95, Sept. 1992.

2. K. H. Gundlach, T. Lehnert, D. Billon-Perron, M. Voss and P. Pasturel, "Preparation and properties of Nb/Al SIS and SIN junctions for millimeter and submillimeter radioastronomical receivers", *Proceedings of an ESA Symposium on Photon detectors for Space Instrumentation*, pp.313-316, Nov. 1992.

3. I. P. Nevirkovets, H. Kohlstedt, and C. Heiden, "Properties of multilayered Nb-based tunnel structures prepared with the whole-wafer process", *Cryogenics*, Vol.32, ICEC Supplement Proc. of the 14th Int. Cryogenic Engineering Conference & Int. Cryogenic Materials Conference, Kiev, June 1992, pp. 583-586, 1992.

4. I. P. Nevirkovets, "Possible application of series arrays of vertically stacked tunnel junctions as low temperature detectors", presented at 3rd Int. Supercond. Electronic Conf., 25-27 June 1991, Glasgow (unpublished).

5. K. Yoshida, K. Kudo, Md. S. Hossain, and K. Enpuku, "Kinetic-inductance coupling scheme for superconducting stripline system and its device applications", *IEEE Trans. on Mag.*, Vol. 27, pp.2692-2695, June 1991.

Performance of an SIS receiver over 460 GHz to 640 GHz using submicron Nb junctions with integrated RF tuning circuits

P. Febvre[1], W.R. McGrath, P. Batelaan, H.G. LeDuc, B. Bumble, M.A. Frerking, J. Hernichel[2]

Jet Propulsion Laboratory, California Institute of Technology, Pasadena, CA 91109
1. Permanent address: DEMIRM-Observatoire de Meudon, 92195 Meudon Cedex, France
2. Permanent address: Universität Köln, 5000 Köln 41, Germany

I. INTRODUCTION

The most sensitive heterodyne receivers used for millimeter wave and submillimeter wave radioastronomy employ superconductor-insulator-superconductor (SIS) tunnel junctions as the nonlinear mixing element. Good performance has recently been reported for SIS junctions used in planar mixer circuits and waveguide mixers from about 300 GHz to 500 GHz. We have developed a submillimeter wave SIS heterodyne receiver for observing important rotational transitions of molecules in the interstellar medium near 550 GHz and 630 GHz. This receiver is based on a waveguide mixer with an adjustable backshort and E-plane tuner [1]. The mixer uses a high current density, 0.25 μm^2 Nb-AlO_X-Nb tunnel junction defined by electron beam lithography [2]. The capacitance of the junction is compensated with an integrated RF superconductive microstrip tuning circuit. The receiver performance has been measured over the frequency range 460 GHz to 640 GHz. DSB receiver noise temperatures as low as 200 ± 17 K at 540 GHz and 362 ± 33 K at 626 GHz have been obtained. In addition, negative differential resistance has been observed in the DC I-V curve at frequencies around 491 GHz. These results indicate that the superconductive Nb microstrip transmission lines used in the tuning circuits are low-loss and perform well up to at least 90% of the superconductor energy gap frequency.

II. SIS JUNCTIONS WITH INTEGRATED TUNING CIRCUITS

The integrated RF tuning circuit that resonates the junction capacitance is a parallel microstrip line terminated in a radial stub as shown in Figure 1. This circuit has been designed for center frequencies near both 550 and 630 GHz. The radial stub is used to provide an RF short over a broad bandwidth. The stub dimensions were designed using an effective dielectric constant, which accounts for the penetration of the magnetic field into the superconductor. The short is then transformed to an inductance by an appropriate section of microstrip line to compensate the capacitance of the junction. These circuits have been designed to resonate the junction capacitance based on a specific capacitance of 85 $fF/\mu m^2$. In addition a series microstrip transformer circuit has been designed to resonate junction capacitances ranging from 60 $fF/\mu m^2$ to 100 $fF/\mu m^2$, and is discussed elsewhere [3].

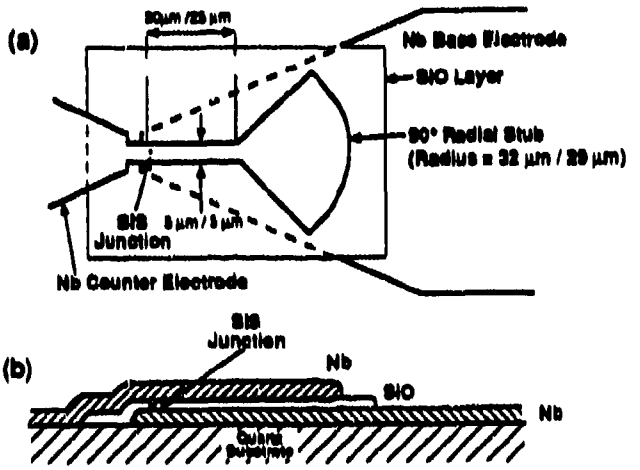

Figure 1: SIS tunnel junction with an integrated parallel microstrip tuning circuit. (a) Top view showing transmission line dimensions for 550 GHz/630 GHz. (b) Cross section view showing film topology

III. RECEIVER DESIGN AND MEASUREMENT TECHNIQUES

The SIS tunnel junction, integrated tuning circuit and low-pass RF filter are fabricated on a quartz substrate which is installed into the waveguide mixer mount and wire bonded to the 50 Ω IF output connector. This mixer has an adjustable backshort and E-plane tuner [1] and the radiation is coupled into the waveguide mount by a dual mode conical horn.

The local oscillator (LO) source consists of two whisker-contacted Schottky varactor frequency multipliers (x2x3) [4] driven by a Gunn oscillator. The signal and LO are combined in a folded Fabry-Perot diplexer and injected into the cryostat through a differentially-pumped window. An off-axis elliptical mirror reflects the combined radiation into the mixer which is installed on the 4 K stage of the cryostat. The 1.4 GHz IF output of the mixer is transformed to the 50 Ω input impedance of the low noise HEMT amplifier by a microstrip transformer. The bandwidth for noise measurements is 300 MHz. A superconducting magnet is used to suppress unwanted Josephson interference.

The total receiver noise temperature is determined by the Y-factor method using hot (295 K) and cold (82 K) loads. The reference plane for these measurements is the input of the diplexer. The radiation power from the loads has been calculated using the full Planck expression.

IV. RESULTS AND DISCUSSION

The receiver performance has been measured over an LO frequency range from 460 GHz to 640 GHz. One SIS junction with no RF integrated tuning circuit and two junctions with integrated circuits have been measured. Figure 2 shows the DSB receiver noise temperature as a function of the LO frequency. Junction A used a tuning circuit designed to resonate the junction capacitance at 550 GHz, while the tuning circuit with junction B has been optimized for 630 GHz. For each data point in Figure 2, the waveguide backshort and E-plane tuner, LO level, and DC bias voltage were optimized. The best performance at 540 GHz was for junction A (R_N = 63 Ω) which gave T_R = 200 K (Y-factor = 1.78). The receiver performance was very good with this junction, yielding $T_R \leq 300$ K over the frequency range from 463 GHz to 549 GHz. The only exception was a few points near 490 GHz, where the noise increased due to the appearance of negative differential resistance (this is discussed in more detail below). Above 600 GHz the noise temperature increases rapidly with the frequency because the tuning circuit does not compensate completely the junction capacitance in this frequency range. The receiver performed well up to 635 GHz with junction B (R_N = 73 Ω) and gave a noise temperature of 362 K at 626 GHz. The noise temperature of this junction increases in the range 460-490 GHz which may due to an undesirable resonance of the low-pass RF filter due to the substrate being narrower than appropriate [1].

Junction 0 which has no tuning circuit has also been measured from 460 to 630 GHz. One can clearly see in Figure 2 that the high capacitance of the SIS junction is not completely compensated by the mechanical tuning backshorts. The DSB receiver noise temperature is 850-1150 K from 470 to 550 GHz. Under 470 and above 600 GHz the noise increases which may be due to the limitations of the mixer mount range of RF matching impedances.

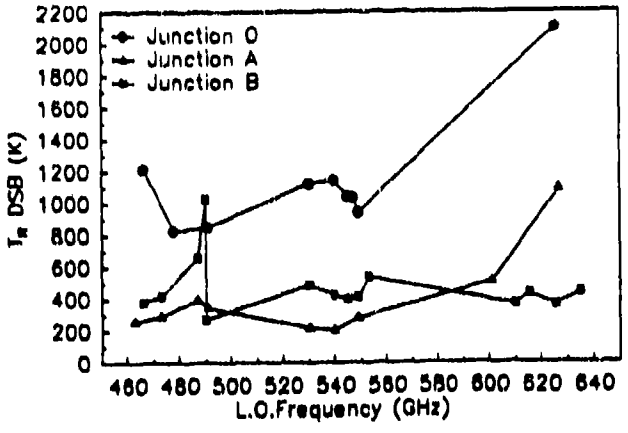

Figure 2: Receiver noise temperature as a function of the LO frequency for 3 different SIS junctions.

A DC negative differential resistance has been observed on the 1st photon step at LO frequencies of 487 GHz and 491 GHz with junction A. This is a quantum mechanical effect which is not predicted by classical theory. When the mixer is biased in the negative resistance region, the IF output power is very high and unstable, probably due to low frequency oscillations. As a result, the receiver is unstable and noisier at these frequencies. As seen in Figure 2, the receiver noise is higher by 100 K - 200 K in this region.

V. CONCLUSION

A receiver for radioastronomy applications in the range 460-640 GHz has been demonstrated. The best results are a DSB receiver temperature as low as 200 K at 540 GHz and 362 K at 626 GHz. The optics have been designed to work in the 500-600 GHz RF frequency range. Nevertheless, this receiver was tested at lower and higher frequencies to determine the behavior of the integrated tuning circuits. In addition, we have begun measuring the performance of this receiver using a series array of two junctions made by optical lithography techniques [5]. A noise temperature T_R (DSB) = 330 K has so far been achieved at 491 GHz. This work is in progress and will be reported later.

ACKNOWLEDGEMENTS

We wish to acknowledge the fabrication of the array junctions by P. Feautrier. This work was supported in part by the Jet Propulsion Laboratory, California Institute of Technology, under contract to the National Aeronautics and Space Administration and the Innovative Science and Technology Office of the Strategic Defense Initiative Organization. Pascal Febvre has been partly sponsored by Matra Marconi Space, Toulouse, France and the DEMIRM (Département de Radioastronomie Millimétrique), Observatoire de Meudon, France.

REFERENCES

[1] W.R. McGrath, K. Jacobs, J. Stern, H.G. LeDuc, R.E. Miller, M.A. Frerking, Proceedings of the 1st Int'l Symposium on Space Terahertz Technology, pp. 409-433, Ann Arbor, MI, March 5-6, 1990.

[2] H.G. LeDuc, B. Bumble, S.R. Cypher, A.J. Judas, J.A. Stern, Proceedings of the 3rd Int'l Symposium on Space Terahertz Technology, pp. 408-418, Ann Arbor, MI, March 24-26, 1992.

[3] P. Febvre, W.R. McGrath, P. Batelaan, H.G. LeDuc, B. Bumble, M.A. Frerking, J. Hemichel, Digest of the IEEE MTT-S International Microwave Symposium, Atlanta, June 14-18, 1993

[4] Made by Radiometer Physics, Meckenheim, Germany

[5] P. Feautrier, M. Hanus and P. Febvre, Supercond. Sci. Technol., vol. 5, pp. 564-568, 1992.

High quality NbN-based junctions for 500GHz waveguide mixers

M.G. Blamire, Z.H. Barber, H. van de Stadt*, J.J. Wezelman* and S. Withington†

Department of Materials Science, University of Cambridge, Pembroke Street, Cambridge, CB2 3QZ, UK
*SRON, Laboratory for Space Research Groningen, P.O.Box 800, 9700 AV Groningen, The Netherlands
†Cavendish Laboratory, University of Cambridge, Madingley Road, Cambridge, CB3 0HE, UK

ABSTRACT

NbN-based tunnel junctions using a thermally oxidised Al layer as the tunnel barrier have been fabricated for 350 GHz and 500 GHz testing. Choke structures containing two junctions in series have been tested in waveguide mixer blocks with E-plane tuners. Receiver noise temperatures obtained have been compared with equivalent Nb-based devices.

1. INTRODUCTION

For many years NbN has been seen as a promising candidate material for the fabrication of superconductor/insulator/superconductor (SIS) junctions for high frequency devices. For quasiparticle mm-wave mixers in particular, NbN has the advantages of high energy gap (Δ) and operating temperature, combined with the high reliability and robustness of Nb-based devices. Niobium carbo-nitride, of imprecise composition, but described by the generic formula NbCN shares these attributes with NbN and has a higher critical temperature (T_c) and Δ (17K and 3.1meV respectively). Despite these desirable attributes a very low noise NbN-based mixer device has yet to be fabricated. Although this stems in part from the greater difficulty, compared with Nb, of depositing the superconductor with high T_c, the main problem lies with the formation of a high quality barrier on a NbN base layer. The short (3nm) coherence length (ξ) of cold-deposited NbN prohibits the use of an artificial tunnel barrier formed by the thermal oxidation of a metal overlayer because of the drastic reduction in the tunneling gap caused by the proximity of any residual metal layer. Even using epitaxial NbN and NbCN, which have a generally higher ξ of ~7nm[1,2], makes the incorporation of a proximity barrier structure difficult. The alternative use of directly deposited barrier materials such as MgO is generally even more difficult because of the great likelihood of barrier defects. Work at JPL has demonstrated reasonable quality NbN junctions with MgO barriers[3], and these have been tested as mixers at frequencies up to 500GHz. However, it has been found that the noise figures obtained with these devices have always been considerably higher than the equivalent all-Nb device[4], leading to the suggestion that NbN/NbCN devices have intrinsic problems at high frequencies which are independent of the quality of the junction itself.

As part of an ESA programme for THz mixer development[5] we have been developing NbN devices for mixer applications. Recently we showed that high quality device structures of the form NbCN/Al/AlO_x/Al/Nb could be fabricated using high quality epitaxial NbCN base layers[2]. Although such structures still show a considerable reduction in the NbCN gap (to the order of 2meV) this still represents an improvement over the equivalent all-Nb device and provides a means of assessing NbCN as a high frequency material. These devices have been pumped at frequencies up to 490GHz and in this paper we report preliminary receiver noise temperatures obtained at 350GHz.

2. DEVICE FABRICATION AND MEASUREMENT

NbCN/Al/AlO_x/Al/Nb structures were deposited onto silica substrates in a UHV magnetron sputter deposition system without breaking vacuum. The NbCN base electrode, formed by reactive sputtering, was grown at a substrate temperature of approximately 820°C. The substrates were then allowed to cool (to room temperature, or below) before depositing a layer of pure Al. Oxygen was introduced for barrier oxidation, followed by a pumping stage before deposition of a Nb counterelectrode. Devices were processed from these wafers using a self-aligned lift-off process similar to that described elsewhere.[2] The complete structure was first reactively ion etched using a $SiCl_4$ plasma to define the filter structures, contact pads and anodisation links. The second process stage defines and insulates the junctions: a photoresist mesa is patterned to define the junction area, followed by a CF_4 barrel etch, anodisation to ~18V and r.f. sputter deposition of SiO_2. The junction areas are exposed by the lift-off of the resist mesas. The metallisation is performed by a Nb deposition and lift-off process. The 490GHz design also allowed the deposition of Pd contact pads. Completed chips were diced and lapped to 120μm x 70μm x 3mm and mounted in the i.f. channel of mixer blocks for the appropriate frequency.

A typical d.c. current vs voltage curve for two junctions in series is shown in Fig. 1(a). Whilst the sub-gap leakage is low, the gap edge is strongly curved above an abrupt change in slope at $V=\Delta_{min}/e$. This form is characteristic of a short coherence length proximity structure. In the same figure are pumped curves showing the photon steps above and below the gap. Since these steps are dominated by the discontinuity at $V=\Delta_{min}/e$, the step shape is also relatively sharp. We have

shown elsewhere that the tunneling density of states in the NbCN/Al electrode is BCS like but with a reduced peak height and a broader spread which extends up to the bulk NbCN gap of 3.1meV.[6] The pumped curves have been compared with the Tien-Gordon model, showing that data and theory agree very well. This suggests that current theories for mixer operation should be applicable to these devices. There is, however, some evidence of heating at the gap edge which is likely to be due to a non-equilibtium effect, rather than to direct thermal heating. At this time the 490GHz receiver was not set up to make noise measurements, and so 350GHz receiver noise temperatures were measured - see Fig. 2(a). 350GHz devices showed a strong series resistance due to the absence of Pd contact pads, but this could be electronically suppressed. Receiver noise temperatures were obtained between 320 and 380GHz with the dual tuner mixer block re-tuned at each measurement frequency. Fig. 2(b) shows the noise performance as a function of frequency.

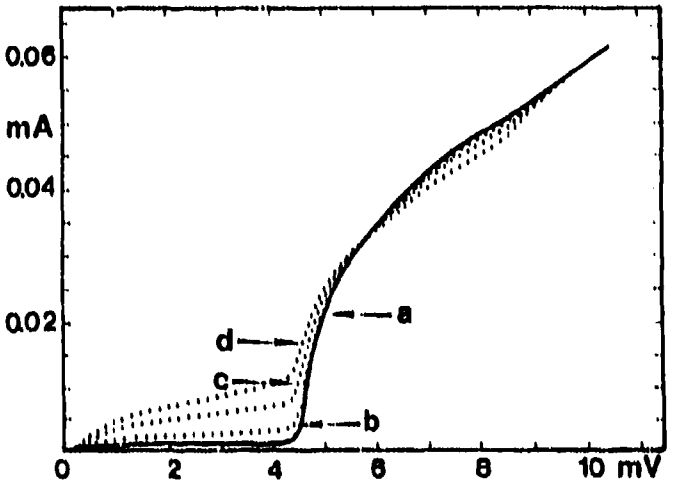

Fig.1. I vs V plots for double junction NbCN/Al/AlO_x/Nb mixer structure, (a) unpumped, (b-d) pumped at 505GHz.

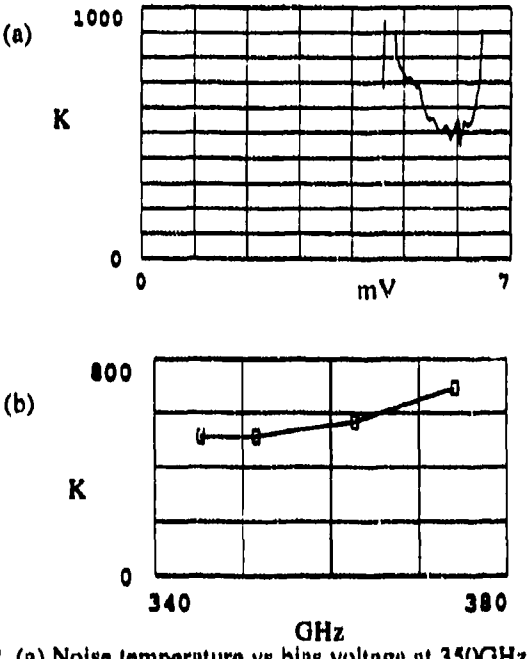

Fig. 2. (a) Noise temperature vs bias voltage at 350GHz for double junction NbCN/Al/AlO_x/Nb device
(b) Optimum noise temperature vs frequency.

4. DISCUSSION

These preliminary results indicate that high quality mixing should be possible with NbN proximity junction structures. Although the noise temperature is significantly higher than for the best Nb devices,[7] the values compare well with measurements of NbN mixers at lower frequencies,[4] and the presence of a large resistance in series with our junctions undoubtedly adds to the total noise figure. We have estimated that the true mixer noise may be as low as 200K, although this cannot be confirmed until further measurements are made on junctions without the contact resistance.

5. REFERENCES

1. A. Shoji, S. Kiryu and S. Kohjiro, "Superconducting properties and normal-state resistivity of single-crystal NbN films prepared by a reactive rf-magnetron sputtering method," *Appl. Phys. Lett.*, Vol. 60, pp. 1624-1627, 1992.
2. Z.H. Barber, M.G. Blamire, R.E. Somekh and J.E. Evetts, "Fabrication and Characterization of all-refractory NbCN/Al/AlO_x/Al/Nb junctions," *IEEE. Trans. Supercon.* (in press).
3. H.G. LeDuc, A. Judas, S.R. Cypher, B. Bumble, B.D. Hunt and J.A. Stern, "Submicron area NbN/MgO/NbN tunnel junctions for SIS mixer applications," *IEEE Trans. Magn.*, Vol. 25, pp. 3192-3195, 1991.
4. W.R. McGrath, J.A. Stern, H.H.S. Javadi, S.R. Cypher, B.D. Hunt and H.G. LeDuc, "Performance of NbN superconductive tunnel junctions as SIS mixers at 205 GHz," *IEEE Trans. Magn.*, Vol. 27, pp. 2650-263, 1991.
5. European Space Agency, Contract No. 7898/88.NL/PB
6. M.G. Blamire, "Deconvolution of tunnelling density of states from superconductor-insulator-superconductor current vs voltage data," *Physica C* (in press).
7. C.E. Honingh, G. de Lange, M.M.T.M. Dierichs, H.H.A. Schaeffer, Th. de Graauw and T.M. Klapwijk, *IEEE Trans. MTT* (in press).

Quasi-optical 0.5 THz SIS receiver with twin junction tuning circuit

S.W. Jacobsson‡, V.Yu. Belitsky†, L.V. Filippenko†, S.A. Kovtonjuk†, V.P. Koshelets†, and E.L. Kollberg‡.

‡ Department of Microwave Technology, Chalmers University of Technology, S-412 96 Göteborg, Sweden.

† Institute of Radio Engineering and Electronics, Russia Academy of Sciences, Mokhovaja 11, 103907, Moscow, Russia.

ABSTRACT

A quasi optical SIS mixer for the frequency band 400-550 GHz has been designed and successfully tested in a laboratory receiver setup. The intrinsic SIS junction capacitance was tuned out by a novel pair (twin) SIS junction compensation circuit. The 4 μm² area Nb-AlO_x-Nb junctions, with $\omega R_n C$ product as high as 7.4 at 500 GHz, were patterned by optical lithography and integrated with a equiangular spiral antenna to give broadband SIS mixer operation. The receiver demonstrated flat response within the tuning range of the available LO source (440 - 520 GHz) with DSB noise temperatures below 300 K over the entire band and with the best receiver noise temperature below 250 K DSB at 453 GHz (measured at 3.5 K physical temperature). No mechanical tuning was employed in the SIS mixer. These noise temperatures include all losses and was measured at an IF center frequency of 1.5 GHz.

1. Introduction

Recent progress in high sensitivity radiometers for spectroscopy, plasma diagnostics and radio astronomy at millimeter and submillimeter wavelengths is strongly linked to the development of low noise superconducting tunnel junction (SIS) mixers. Receivers using SIS mixers demonstrate the best noise performance at millimeter and submillimeter wavelengths. To obtain optimum mixer performance is it necessary to tune out the intrinsic capacitance of the SIS junctions. Consequently, a variety of lumped and distributed circuits for single and arrayed SIS junctions have been developed to tune out the junction capacitance and to obtain broadband SIS mixer operation. Here, we have chosen to investigate a novel type of tuning circuit previously reported in[1]. In this particular design are two identical (twin) SIS junctions connected by a microstrip line impedance converter so that conjugated impedance of the first junction cancel the reactance of the second. The tuning circuitry is symmetrical, meaning that the same DC bias, signal and LO driving levels are available to both junctions.

2. SIS mixer structure.

The quasi-optical SIS mixer used an equiangular spiral antenna designed to cover 250 - 800 GHz. The mixer chip was mounted onto the flat side of an extended hyperhemispherical lens[2]. Figure 1 shows the twin SIS junction capacitance compensation circuit: i.e. two identical junctions are connected in parallel via microstrip impedance conjugator. This tuned structure is then connected to the antenna via a microstrip impedance transformer to provide proper matching to the antenna impedance and to obtain broadband operation[3]. In the modelling of the structure it was assumed all superconducting microstrip lines were lossless and dispersion free. These assumptions are judged by the fact that all microstrip lines lengths are short and that the frequency of operation is still far enough from the Nb-AlO_x-Nb junction gap frequency (≈ 730 GHz). For these particular junctions was the specific capacitance estimated to 94 fF/μm² and, thus, the total junction capacitance for a 4 μm² area junction was ~0.38 pF. The junction capacitance dominates over the quantum susceptance and the latter was neglected in all calculations. The circuit was modelled assuming the following SIS junction parameters: R_n=6Ω (normal resistance), A=4 μm² (junction area), R_l=60Ω (leakage resistance), V_g=2.9 mV (gap voltage), δV_g= 0.29 mV ("gap width"). The centre frequency of 480 GHz for the mixer was chosen to coincide with the available frequency band of the LO source (440 - 520 GHz).

A superconductive loop composed of the two SIS junctions, the base and the counter electrodes of the microstrip impedance conjugator forms a squid-like topology with optimum sensitivity to a magnetic field in the plane of the substrate. Therefore, the twin compensation circuit together with relatively large area SIS junctions make it easy to suppress Josephson effects. Small permanent magnets were integrated in the mixer mount and a pair of external superconductive coils were used for fine tuning of the magnetic field. This arrangement was found quite adequate for complete suppression of the Josephson effects.

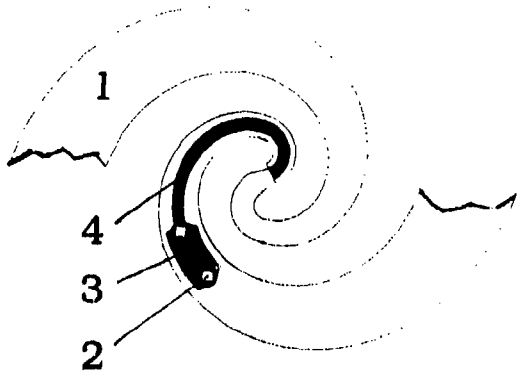

Fig. 1 The antenna aper area in magnification:
1- Spiral antenna arm (metal)
2- SIS junction, area 4 μm^2, patterned by optical lithography.
3 - microstrip twin SIS junction compensation circuit - impedance conjugator, length 12 μm,
4 - microstrip impedance transformer, length 56 μm.

Measurements

The LO signal beam (BWO tunable between 440-520 GHz) and the signal beams were diplexed via either a 12.5 μm or 50 μm thick Mylar beamsplitter. The thicker beamsplitter was used towards the end of LO tuning range to increase the pump power. The input window (at room temperature) on the cryostat was covered by a 1 mm thick Teflon vacuum window (Ø30 mm) followed by a 0.75 mm thick Fluorogold filter. The latter is mounted on the inner radiation shield (approximately at LHe-temperature). The measured receiver noise temperatures are shown in figure 2.

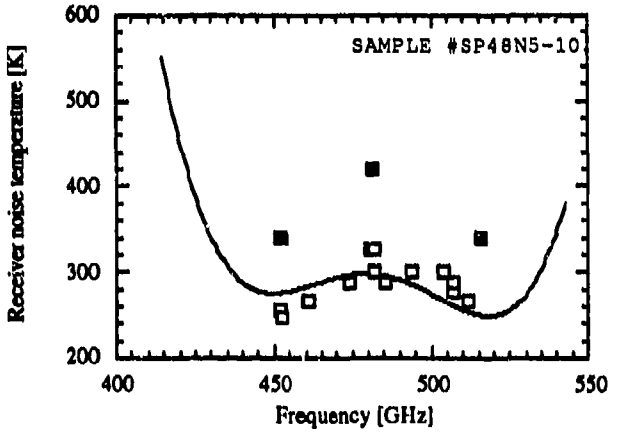

Figure 2 Measured, at 3.5 K, receiver noise temperatures including all losses vs. LO frequency: (□) 12.5 μm and (■) 50 μm Mylar beamsplitter. Solid line: calculated power coupling normalised to measured receiver noise temperature at 480 GHz. The receiver noise temperature was measured using conventional y-factor technique (T_{hot}= 295 K, T_{cold}= 80 K). Cooling the SIS mixer to 3.5 K dramatically improved the receiver performance. The noise temperatures decreased approximately 50 K when the physical temperature was decreased from 4.2 K to 3.5 K..

Conclusions

A new approach to broad band SIS mixer operation using the twin type tuning circuit was successfully applied to a 500 GHz SIS quasi-optical receiver. The SIS receiver noise temperatures were below 300 K DSB was measured across the investigated frequency band with the best noise temperature 246 K DSB at 453 GHz. These noise temperatures include all receiver were was measured at an IF centre frequency of 1.5 GHz. Good agreement between the calculated and measured receiver performance was achieved. The particular twin-matching structure together with relatively large area SIS junctions made easy to suppress Josephson effects

Acknowledgements

This work has been supported by grants form the European Space Agency (ESA) under contracts 7898/88/NL/PB and AOP/WK/314957, Royal Swedish Academy of Sciences, Russia Academy of Sciences, Ministry of Science and the High School of Russia as well as The Swedish Board for Space Activities and The Swedish National Board of Industrial and Technical Development.

References

1 V.Yu. Belitsky, M.A. Tarasov, "SIS junction reactance complete compensation", *IEEE Trans. on Magn.*, vol. MAG-25, 1991.
2 V.Yu. Belitsky *et al.*, "MM Waves Detection Using Integrated Structure with SIS Junction, Stripline Transformer and Spiral Antenna". Extended Abstracts of ISEC-89, pp 179-182, TOKYO, 1989.
3 T.G. Büttgenbach, *et al.*, "A Fixed Tuned Broadband Matching Structure for Submillimeter SIS Receivers", *IEEE Trans. on Appl. Supercond.*, vol. 2, No. 3, pp. 165 -175, 1992.

Frequency measurement of sub-millimetre wavelength laser lines using Josephson junctions

M.C.Wicks and J.R.Birch

Division of Electrical Science, National Physical Laboratory,
Teddington, Middlesex, TW11 0LW, UK

Abstract

Thin film Josephson junctions have been used as harmonic mixers to measure the frequency of submillimetre wavelength laser lines. The highest frequency measured so far is 3.1THz. The need to measure frequencies in this spectral region arises from the measurement standards requirement to relate optical and near optical frequency standards, used for frequency and length measurement, to microwave primary frequency standards. Information on submillimetre wave frequencies is also important to spectroscopists and other workers in what is likely to be an increasingly exploited part of the electromagnetic spectrum.

Introduction

Josephson junctions are particularly useful for frequency measurement applications in the submillimetre region of the EM spectrum because of their ability to generate significant levels of very high order harmonics of signals applied to them. This enables direct comparisons to be made between laser lines and harmonics of microwave signals of accurately known frequency.

The Josephson junctions used for the measurements reported here are thin film niobium nitride devices. The high superconducting energy gap of NbN, 5.5meV compared to 2.7meV for niobium, implies a potential maximum operating frequency of at least 10THz, as Nb point contact mixers have been used at upto 4.25THz. Point contact mixers, although having excellent high frequency performance, are fragile, temperamental and cannot be thermally cycled. In contrast NbN thin film devices are mechanically and electrically stable. The devices used in these experiments have been thermally cycled many times without any changes occurring in their electrical characteristics. This paper describes the devices used, the frequency measurement experiments and methods used to improve the coupling of laser radiation into the Josephson mixer.

Experimental

The devices used were fabricated using the "whole wafer" process developed at ETL, Japan [1]. NbN/MgO/NbN trilayers were deposited in a single vacuum cycle by RF sputtering. The trilayers were then patterned using optical photolithography and reactive ion etching to form the tunnel junctions. The junctions used for the measurements reported here had areas of 4-6μm^2 and normal state resistances of 4-7Ω. The low junction impedance means that incoming free-space radiation will be poorly coupled into the junction, thus reducing the efficency of the mixers described here compared to optimised devices. Two techniques to improve coupling into the junction are being investigated, first the fabrication of thin film antennas and matching structures on the mixer chip and secondly the use of external resonant optical coupling.

The junction used as the mixer was mounted in a vacuum insulated liquid helium cryostat. Cooling was by conduction through the cryostat's cold plate and the junction temperature was about 7K. A copper collecting cone was placed in front of the junction to simplify optical alignment and to improve coupling of radiation into the junction. A tunable backshort, adjusted from outside the cryostat, was placed behind the junction to optimise coupling for various laser wavelengths.

The input signals to the mixer, consisting of the output of an optically pumped far infrared laser and the output of a microwave synthesiser, used as the local oscillator, were combined outside the cryostat by a wire grid and rooftop mirror diplexer. This combined signal then entered the cryostat through a polyethylene window. The intermediate frequency signal of 15-50MHz was coupled out of the cryostat *via* a matching transformer and stainless steel transmission line. The IF signal was amplified and fed to a spectrum analyser and frequency counter. Local oscillator frequencies in the range 18-40GHz were used and the frequency of the LO and the timebase of the frequency counter used to measure the beat frequency were locked to a rubidium frequency standard.

Results

The frequencies of various laser lines have been measured. The highest frequency measured so far was of the 96.5μm line in methanol, a frequency of 3.1THz. The IF signal to noise ratio for this measurement was only 3-5db (100kHz bandwidth) but at lower frequencies, below 2.5THz, the signal to noise ratio was consistently about 10db.

The deterioration in performance at the highest frequency is probably due to increased parasitic losses and poor coupling efficency rather than a fundamental limitation in the performance of NbN devices. Results of attempting to improve the high frequency performance, using the techniques mentioned previously, will be presented at the conference.

Acknolwedgement

This work was supported under the National Measurement System Policy Unit Optoelectronics Programme.

[1] A.Shoji et al, "Niobium nitride Josephson tunnel junctions with magnesium oxide barriers", Appl Phys Lett, Vol. 46, No. 11, pp. 1098-1100, 1985.

Millimetre wave mixing with YBCO Josephson junctions on bicrystal substrates

P.G.Quincey and M.C.Wicks

Division of Electrical Science, National Physical Laboratory,
Teddington, Middlesex, TW11 0LW, U.K.

ABSTRACT

The intrinsic high frequency limit for superconducting mixers is set by the energy gap, which scales roughly as T_c. The arrival of High T_c materials brings the possibility of raising this limit by a substantial factor, perhaps to over 30 THz. This paper describes ongoing experiments with Josephson junctions made from YBCO on bicrystal substrates of $SrTiO_3$ and $NdGaO_3$, exploring their high frequency response and their performance as high harmonic mixers.

1. INTRODUCTION

The National Physical Laboratory has a long-standing interest in high harmonic mixers, which can directly compare the frequency of one narrow band source with the harmonic of another. They are necessary for frequency metrology, relating measurements of, say, optical frequencies with standard frequencies in the microwave region, and for broader metrological uses where measurements of frequency are necessary for precise measurements of length and voltage. Josephson mixers (based on superconductors) have the ability to operate with frequencies differing by a factor of several hundred, and have been used for frequency metrology up to frequencies of about 4 THz. The intrinsic high frequency limit is determined by the energy gap of the superconductor used, a parameter which is approximately proportional to the critical temperature of the material. Superconductors such as $YBa_2Cu_3O_7$ (YBCO), with T_c at 92 K, therefore offer a potentially much extended range compared with traditional superconductors such as niobium (T_c 9 K).

2. DEVICE FABRICATION

The short coherence length of high temperature superconductors makes it very difficult to fabricate a well controlled tunneling barrier of the kind used with low temperature superconductors. Fortunately, a simple grain boundary can act as a suitable barrier, the problem now being to control the formation of an isolated grain boundary in a thin film. Devices were made using the bicrystal substrate route[1], where the junction is formed at a grain boundary created by depositing an epitaxial thin film onto a substrate which itself contains a single, well-defined grain boundary. Bicrystal substrates of both $SrTiO_3$ and $NdGaO_3$ were made in-house from pieces of single crystal fused with heat and pressure[2]. Thin films of YBCO were deposited by DC sputtering from a cylindrical YBCO target.

A simple junction was defined by patterning a track 200 μm by 5 μm across the bicrystal boundary. This was achieved using photolithography and wet etching in dilute orthophosphoric acid. Finally, four contacts were attached to evaporated silver pads.

3. RESULTS

For a Josephson junction to act as a mixer at a given frequency it is a prerequisite that a voltage step in the current-voltage characteristic of the device should be seen when it is illuminated at that frequency. The voltage and frequency are related by the expression $2eV = h\nu$, or $V = 2.07\ \mu V/GHz$. Before any mixing experiments, therefore, it is useful to explore the junctions' response to microwave illumination.

Preliminary work used $SrTiO_3$ bicrystal substrates, although their very high dielectric constant and absorption make them unsuitable for ultimate use in high frequency mixing. An early device[2] which did not show Josephson behaviour at 77 K, and had a low I_CR_N product (the relevant figure of merit) at 4.2 K of 440 μV, nevertheless showed voltage steps up to the equivalent of 2.5 THz, when illuminated with a powerful source at 11.8 GHz.

More recent work with $NdGaO_3$ substrates, which have much better dielectric properties, has led to junctions with an I_CR_N product of 470 μV at 77 K, rising to 4.4 mV at 4.2 K. Exploration of their high frequency response is in progress and will be reported at the conference.

4. ACKNOWLEDGEMENT

This work was supported under the National Measurement System Policy Unit Optoelectronics Programme.

5. REFERENCES

1. D.Dimos, P.Chaudhari and J.Mannhart, "Superconducting transport properties of grain boundaries in $YBa_2Cu_3O_7$ bicrystals," *Physical Review B*, Vol.41, pp. 4038-4049, March 1990.
2. P.G.Quincey, M.Stewart, M.C.Wicks and J.R.Birch, "High frequency response from $YBa_2Cu_3O_7$ Josephson devices on $SrTiO_3$ bicrystal substrates," *NPL Report DES 118*, March 1992.

Methods of frequence measurements of microwave signals of MM- and SubMM- wave bands with the use of AS Josephson effect

S.E.Anischenko, S.Y.Larkin, P.V.Khabayev

State Research Center "Fonon"
37, Pobedy Ave.,KPI-3240, Kiev, 252056, Ukraine

ABSTRACT

The paper is concerned with the methods of frequency measurement in millimeter- and submillimeter- wave bands using AC Josephson effect. The main results obtained for the niobium Josephson junctions and bridges made of HTSC, have been presented.

1. INTRODUCTION

The frequencymeters being manufactured nowadays differentiate one from another by intention, accuracy, principle of operation, covered frequency range, measurement automation and others. There are several methods being used for frequency measurements in millimeter and submilimeter wave bands. The measurement process in some of them may be automaticly controled. This may be applied to the following methods: filtering; heterodining with an electronic count; heterodining with the supplimentary frequency-swept oscillator and electronic count and some others. The principle of operation of all these methods bases on the radio wave propagation and the spectrum transfer. As a result some disadvantages inherent to these methods can be marked: operating within the limited frequency range; necessity in relatively high input signal levels required for mixing process; a priory information on the frequency range of the tested signal sourse . Some new methods with the use of surface acoustic wave devices have been developed lately. There are some advantages over the traditional methods of the frequency measurements when using the Josephson junctions as a measurement sensor.

2. THEORY

There is the AC Josephson effect which supposes existence of the alternating supercurrent I_s in any system that consists of two superconductors with weak link by applying the voltage across the junction. By the theory of the superconductivity I_s is determinated by the equation[2]:

$$I_s = I_c \sin(2\pi(2eU/h)t) \qquad (1)$$

where U is the voltage across the junction, 2e is the charge of Cooper pair; h is the Plank constant; I_c is the critical current. According to Eq.(1) the frequency of the oscillation (Josephson frequency) is directly proportional to the voltage across the junction:

$$\omega_J = 2eU/h \qquad (2)$$

When irradiating a Josephson junction with an external microwave signal one

can observe some peculiarities on it's current-voltage curve (CVC), the so-called "Shapiro steps"[3]. Thus, the voltage ΔU in the region of "Shapiro steps" is related to the frequency of the signal irradiating the junction by the following equation

$$\omega_c = 2e\ \Delta U/h \qquad (3)$$

In case of irradiating the junction by the monochromatic microwave signal its frequency can be measured indirectly by measuring the value ΔU.

It is necessary to mark the following advantages of using the Josephson junctions for frequency measurements:

-broad bandwidth: the use of the Josephson junction for frequency measurements in the shortest part of RF wave band is conditioned by the order of the value 2e/h. The cutoff frequency when using the AC Josephson effect is determined by the relaxation time of the superconductivity order parameter that corresponds to the frequency about 7500 GHz;

-sensitivity: the fundamental limit is determined by the same parameters that determine the sensitivity of the Josephson detector which in millimeter and submillimeter wave bands reaches the value of 10^{-15} W /√Hz;

-plainness of the methodological approaches: measured frequency of the microwave signal is linearly equated with a value of the measured dc voltage at the Josephson junction that gives a wide possibility for automation of the measurement process. It should be pointed out that because of existance of such unique frequency properties of the Josephson junction there is no necessity of using special heterodyning in different frequency ranges. There is no need in a priori information on the approximate frequency range before starting the measurement process. The frequency measurements in the broad band may be carried out having one functional microwave unit.

3. METHOD

Several methodological approaches to the frequency measurements using the AC Josephson effect were investigated.

One of the main methodological approaches to the frequency measurement using the Josephson junctions lies in the application of a voltage source with linearly increasing amplitude as a bias, due to the fact that CVC of irradiated junction has a stepwise form. At certain moments of time $t_0, t_1, t_2 \ldots$ the output unit registrates the jumps of current I_{out} (Fig.1) . The time interval $\Delta T = t_2 - t_1$ and the step voltage U_c are bound by the device constant $K = dU/dt$. A frequency of the microwave signal in this case may be found as:

$$\omega = (2e * K * \Delta T)/h \qquad (4)$$

The second method is based on the implementation of the current source with discretely linear-increasing amplitude of the signal $I(t_n)$ for biasing the working point of the junction on CVC (Fig. 2). The discrete voltage originating across the junction $U(t_N)$ is stored by the output unit and at the end of every measurement cycle it is compared with the voltage value $U(t_{N-1})$ obtained in N-1 cycle:

$$\Delta U = U(t_N) - U(t_{N-1}) \quad (5)$$

It is seen from Fig.2 that at the moment (t_3, t_4) the difference is $\Delta U=0$. As this measuring cycle corresponds to the "Shapiro step" on CVC the frequency ω of the tested signal is obtained as:

$$\omega = U(t_N) * 2e/h \quad (6)$$

There is also an approach when two parallely connected (by bias circuits) Josephson junctions are used as a measuring element. The linearly increasing amplitude voltage source U(t) provides bias of their working points. One of the junctions is irradiated by the comparison signal with a frequency ω_g of the standard oscillator to create a grid of the reference voltages on its CVC. The microwave signal for investigation its frequency irradiates the second junction. The "Shapiro steps" form marks on its CVC (Fig.3). The output unit carries out counting of the reference current pulses, corresponding to the grid of reference voltages, within the time interval Δt between the mark-pulses (the so-called gate). the desired frequency can be represented as:

$$\omega = N * \omega_g \quad (7)$$

4. EXPERIMENTAL RESULTS

Basing on the second method a prototype of the frequencymeter with the following main parameters was designed:

-measured frequency band: 40 - 500 GHz;

minimum input power level: 10^{-8} W over the whole band;

-accuracy: measurement error by order 10^{-5} relative units.

-operating temperature range - 4.2...55K;

-time of one frequency measurement: not long than 0.1 s.

5. REFERENCES

1. L.I.Kats, S.F.Klimenko, V.V.Purtov. The methods providing automation of the frequency measurement process in microwave band.-Moscow, CSRI "Electronics", 1979 (in Russian).

2. W.Buckel. Supraleitung.Grundlagen und Anwendungen. Physik Verlag GmbH, Weinheim/Bergstr. 1972.

3. K.K.Likharev, B.T.Ulrich. Josephson contact systems. Moscow State University Publishing House, 1978

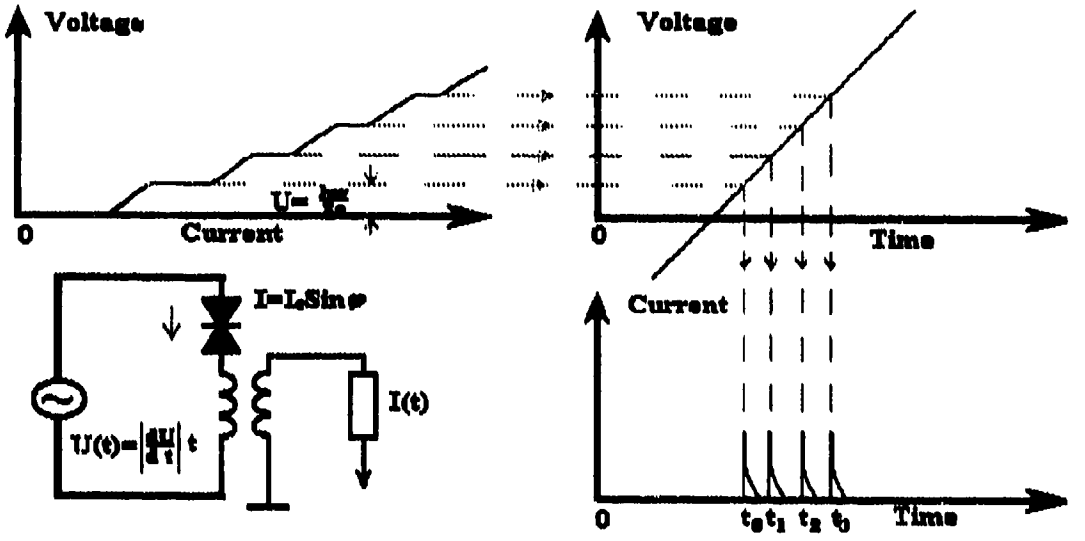

Fig.1.

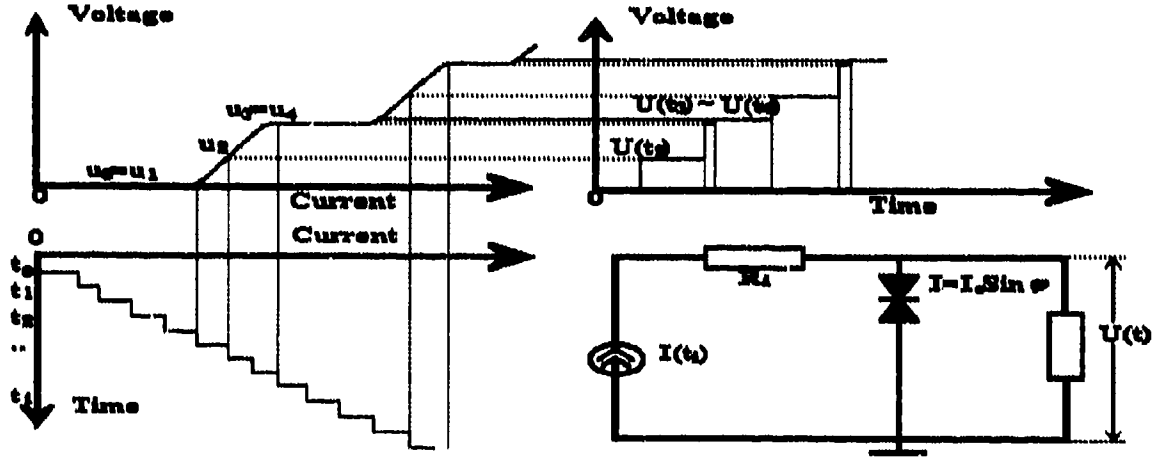

Fig.2.

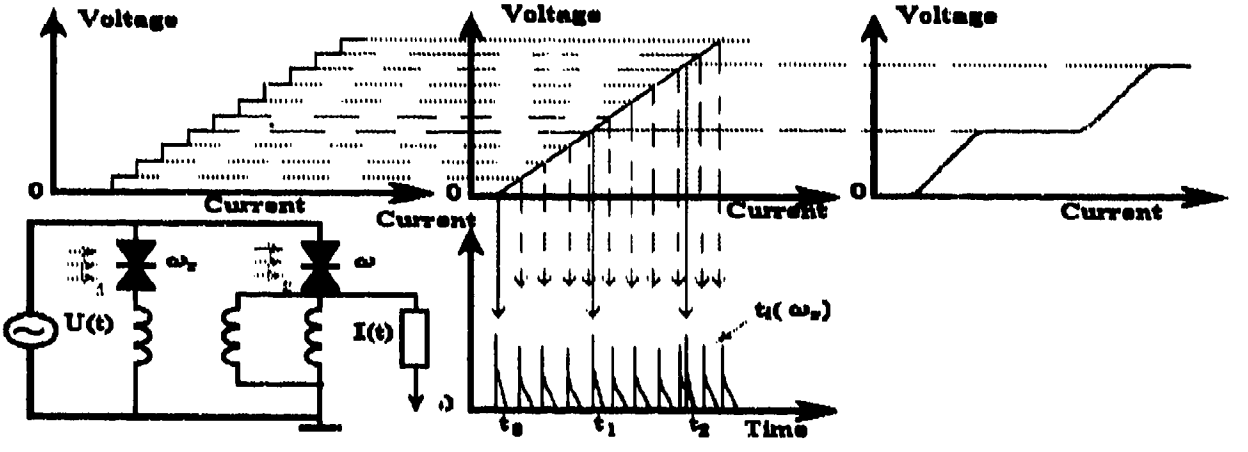

Fig.3.

For question of Superconductive Wide-band Frequencymeter Designing. Main methodics and problems.

Marusiy G.A.,Gurovich V.G.,Zatona G.A.,Pilinsky N.V.

As mentioned in [1] , frequency mesurement in millimeter and submillimeter electromagnetic wave bands seems is not very simple , because special precision mechanical and quazyoptical devices needs for.Moreover, that is difficult to get acceptable and equal accurancy in frequency measurement for both signals in millimeter and submillimeter band by this way.One of ways to fight this difficulties is designing of Wide-band frequencymeter using Josephson Junctions as sensor element.

In our message for Conference we should try to discuss the problems and ideas appeared with designing of superconductive wide-band frequencymeter.In accordance with that , we had determined and considered two ,seemed main for us ,ways of frequency measurement by control of its above frequencymeter was designed.

The first way of this, is measuring method based on consideration of Volt-Amper Characteristic (VAC) of Josephson Junction.This method supports by scientific fact , that on cooled Josephson Junction's VAC , special steps named as "Shapiro Steps", was appears at once ,as this junction influences by high frequency signal ,as that shown on Fig.1.On this figure Curve 1 presents VAC with high frequency signal influence and Curve 2 without its.In that case, determination of signal frequency is very simple.You only need to determine voltage U of corresponding step and made simple calcuations.Frequency of signal depend on strong direct relation from this U, as that shown at expression [1].K is fundamental physical constant calculated from expression [2].

$$F = \frac{2eU}{h} \qquad [1]$$

$$K = \frac{2e}{h} \qquad [2]$$

We must notify, that this method most proper to use for low-temeperature Josephson Junction patterns, because determination of above mentioned "steps" staye more difficult with increasing Junction's pattern temperature.Except this, "steps" shape depends on power of influencing signal, that leads to designing of special devices for signal 's power controlling.

The second way of frequency measuring free of this demerits, because it doesn't links with "steps" determination and consideration.This method based on consideration of Josephson Junction's response which appears with influencing of modulated high frequency signal on it.We must notify , that this method works good for both lowpower and highpower signals.Josephson Junction's reeponse in that case looks like that's shown on Fig.2.

Method of frequency determination quite clear to understand from this figure.K in that case is fundamental physical constant,as that mentioned above.Main problem for this method is choosing of modulation method and increasing of modulation frequency for increasing accurancy and rate of measuring.

We had designed hardware and software for both method examination and got next results :

- Measuring frequency band : 30 - 1000 Ghz;
- Frequencymeter sensitivity : 10E-7 W;

Frequencymeter's hardware consists of high-sensitive Josephson's signal's amplifier and special controller based on Intel 8080 microprocessor which performs scanning of VAC or Josephson's response and calculations required.Frequencymeter's software placed in memory of special controller and supports all parts of mesuring process.Except this, above software allows to connect frequencymeter with IBM PC through both serial or parallel comunication ports.For this purposes special software for IBM PC have been designed.In configuration with IBM PC ,our frequencymeter will be work as powerfull automatic workplace for scientific researching of Josephson Junction's properties.

---

[1] Denisov A.G. et al,
Frequency measurement in millimeter and submillimeter electromagnetic wave bands using Josephson Junctions,
Progress in HTSC - vol.28,
2 nd World Congress on Superconductivity, Houston, Texas 10-13 September 1990,
Editor Calvin G. Burnham, Publishion World Scientific.

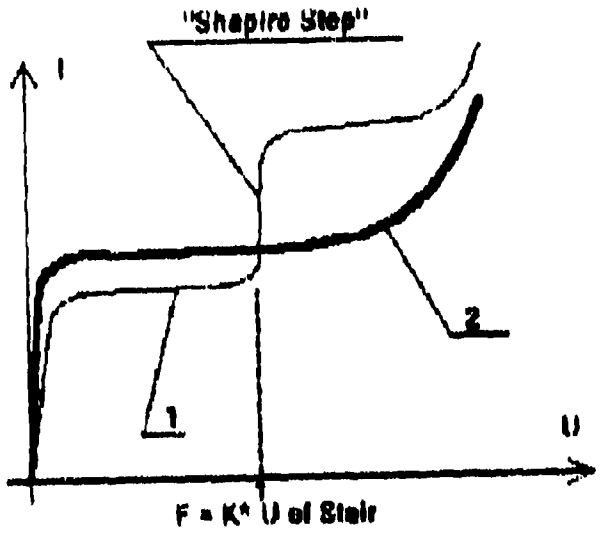

Fig.1

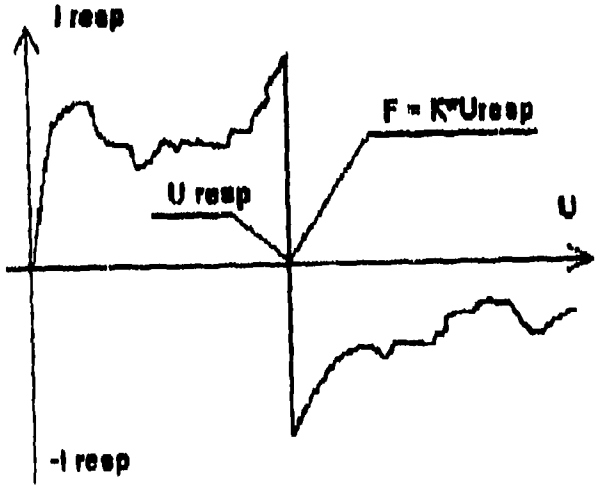

Fig.2

SIS-mixer development at SRON

J. Mees[a], G. de Lange[a,b], A. Skalare[a,c], C.E. Honingh[a,d], M.M.T.M. Dierichs[a], H. Kuipers[a,b], R.A. Panhuyzen[a], H. van de Stadt[a], Th. de Graauw[a], T.M. Klapwijk[b]

a) Space Research Organisation Netherlands (SRON), Postbox 800, 9700 AV Groningen, The Netherlands
b) Dept. of Applied Physics and Materials Science Center, University of Groningen, Nijenborgh 4, 9747 AG Groningen, The Netherlands
c) Now at: Jet Propulsion Laboratory, California Institute of Technology, CA 91109, USA
d) Now at: Universität zu Köln, 1. Physikalisches Institut, Zülpicherstr. 77, 5000 Köln 41, Germany

Abstract

Since several years waveguide and planar antenna SIS-mixers for space applications are developed at SRON in order of ESA. Recent results show excellent mixer performance up to frequencies above the superconducting gap of Nb. Goal is the development of a 1THz-mixer. Best results show a receiver noise temperature of T_{DSB}=400K at 720GHz in case of the waveguide mixer and T_{DSB}=200K at 490GHz for the double dipole planar antenna mixer. We will present the status in the development of SIS-junctions, integrated tuning network, mixers and mounts.

Introduction

SIS-tunnel junctions are highly sensitive detection elements for heterodyne receivers in the mm- and submm-range. They were first used at lower frequencies only. Since then, the frequency range of SIS-mixer receivers could be highly increased - up to the superconducting gap frequency of Nb and even above [1,2]. This is due to great improvements in the precision engineering and to the successful development of local oscillators for higher frequencies.

Another important issue - especially for the quasioptical mixers - is the development of various sorts of integrated tuning networks out of superconducting microstrips. These networks have the purpose to improve the rf-coupling from the SIS-junction to the waveguide or planar antenna. At SRON we have designed and fabricated several kinds of integrated tuning networks in different frequency regimes. The Nb tunnel junctions are fabricated with a Selective Niobium Over-Etch Process (SNOEP) [1]. We studied the frequency response of both types of mixers by means of a Fourier transform spectrometer (FTS) of the Michelson type. Video response could be obtained of both types of mixers up to 700GHz and above. Quasiparticle heterodyne response of the waveguide mixer was measured up to 830GHz. The quasiparticle heterodyne response of different types of junctions was verified by line measurements with gas cells. These results are so encouraging that we belief that efficient mixing with SIS-tunnel junctions may be possible up to 2 times the gap frequency $f_{gap}=eV_g/h$.

Planar Double Dipole Antenna Mixers

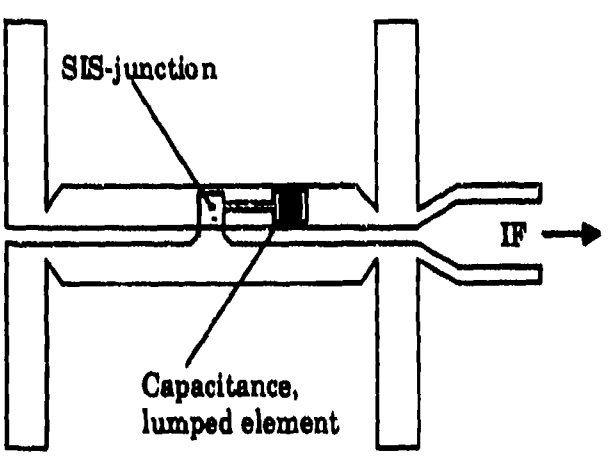

Planar double dipole antennas, consisting out of two halfwave dipoles, are well suited for the construction of sensitive broad band heterodyne SIS-receivers. The double dipole antennas are mounted in a sandwich out of SiO_2 on the back side of an hyperhemisperical lens. A reflecting surface is glued down on the lens in a distance of quarterlambda wavelength to the junction. This prevents losses on the back side. Scaled model measurements show a broadband response of about 1 octave bandwidth. Antenna measurements with integrated bismuth-bolometers yield low side lobes and a non-astigmatic beam [2]. The frequency response of the integrated tuning network was studied in the range of 100-1100GHz with a FTS. Resonances could be obtained up to 550GHz. Lumped element circuits show a more broadband response than than open-ended stubs. We measured a bandwidth (3dB-level) of about 50GHz (10%) at 500GHz. We were able to obtain sensitive video response up to 800GHz even without suitable resonance circuits. Previously published

results [3,4] with small area Nb-tunnel junctions including simple tuning structures have shown an excellent mixing performance at frequencies up to 500 GHz. Best results give a receiver noise temperature of T_{DSB}=200K at 490GHz. We are currently investigating devices with antennas and tuning structures up to 700GHz and above made out of Nb or gold.

Waveguide Mixers

Waveguide mixers at SRON were first developed for 345GHz, later at 500GHz, with one and two tuning elements, described in [5]. These mixers show an excellent performance over the whole frequency band of the waveguide. The tuned bandwidth of the 500GHz receiver is 435-490GHz with a receiver noise temperature T_{DSB} below 140K [6]. At 460GHz the receiver noise temperature, including losses of beamsplitter windows and HDP-lens has a minimum of 116K. Making use of integrated tuning elements the fixed tuned bandwidth can be made very broad. Therefore newer designs of mixerblocks will contain only a single backshort tuner. This has the advantage of simplified fabrication.

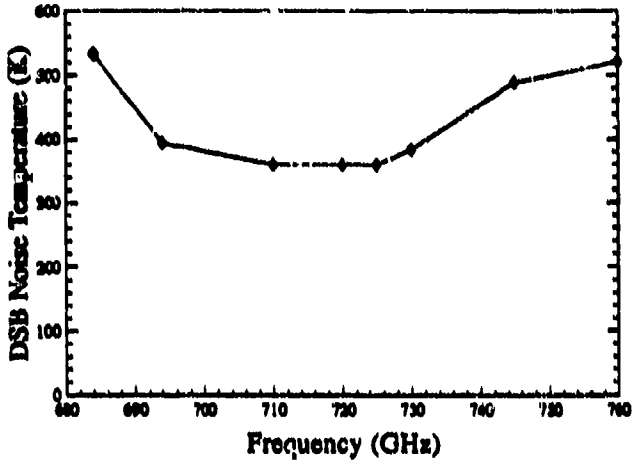

A scaled version of this idea has been realised in a 750GHz mixer block. Novel designs for the integrated tuning network are developed and will be presented. First measurements with a FTS show broadband response from about 500 to 750GHz. The bandwidth varies with the type of network and agrees with predictions from theoretical considerations. Heterodyne response could be obtained up to 830GHz. Y-factor measurements show a double sideband receiver noise temperature of 3000K (1500K corr.) at 830GHz. This is far above of the resonance frequency (720GHz) of the tuning network. Best noise temperatures were obtained at 720GHz with T_{DSB}=400K (360K corr.). This values include all losses and are not corrected for the beamsplitter losses. The corrected values are in brackets. Heterodyne experiments from 680GHz to 750GHz (upper Fig.) were limited by the frequency range of the carcinotron (and frequency doubler) that was used as a local oscillator.

Acknowledgements

This work was supported by the European Space Agency under contract No. 7898/88/NL/PB(SC), the Stichting Technische Wetenschappen and the Stichting voor Fundamenteel Onderzoek der Materie. We acknowledge the assistance of H. Golstein, H. Schaeffer and J. Wezelman in the preparation of the experiments and for helpful discussions.

References

[1] M.M.T.M. Dierichs, R.A. Panhuyzen, C.E. Honingh, M.J. de Boer, T.M. Klapwijk, Appl. Phys. Lett. 62, 774 (1993)

[2] A. Skalare, H. van de Stadt, Th. de Graauw, R.A. Panhuyzen, and M.M.T.M. Dierichs, 3. International Symposium Space TeraHertz Technology (1992)

[3] A. Skalare, M.M.T.M. Dierichs, J. Mees, H. van de Stadt, R.A. Panhuyzen, Th. de Graauw, T.M. Klapwijk, 4. International Symposium Space TeraHertz Technology (1993)

[4] J. Mees, A. Skalare, M.M.T.M. Dierichs, H. van de Stadt, R.A. Panhuyzen, Th. de Graauw, T.M. Klapwijk, E. Armandillo, 4. International Symposium Space TeraHertz Technology (1993)

[5] C.E. Honingh, G. de Lange, M.M.T.M Dierichs, H.H.A. Schaeffer, Th. de Graauw, T.M. Klapwijk, Submitted to IEEE Trans. MTT., Mini Special Issue on Space Terahertz Technology (March 1993).

[6] G. de Lange, C.E. Honingh, M.M.T.M. Dierichs, H.H.A. Schaeffer, H. Kuipers, R.A. Panhuyzen, T.M. Klapwijk, H. van de Stadt, M.W.M. de Graauw, E. Armandillo, 4. International Symposium Space TeraHertz Technology (1993)

NETWORK ANALYSIS OF THE DISPERSION CHARACTERISTICS FOR THE GROOVE GUIDE WITH ARBITRARY CURVED SHAPES *

Xu Shanjia, Zhang Yaojiang
Department of Radio and Electronics
University of Science and Technology of China
Hefei, Anhui, 230027, P.R.China

ABSTRACT

The dispersion characteristics of different single and asymmetrical double groove guide with arbitrary groove shapes are analyzed by a method which combines staircase approximation with microwave network method. Comparing with other method , the present method is not only accurate but also very simple. Therefore, it is particularly suitable for the CAD of the groove guide circuits. The accuracy and effectiveness of the method are verified by the experimental data and the results obtained by other methods.

SUMMARY

Mode-matching, conformal mapping and finite element method are the main approaches to study single or double groove guides with different shapes[1]-[4]. However, the complexities in analyzing curved groove guide or the relatively long calculation time restrict their extensive applications in CAD of groove guide circuits. A.Oliner presented an equivalent transverse network to analyze rectangular groove guide and very accurate results are obtained[5]. In this paper, the staircase approximation is appled to discretize the curved groove guide into multilayer rectangular groove structures in geometry, the equivalent circuit of the step given by A.Oliner is adopted and the transverse resonant technique is used to analyze the dispersion characteristics of curved groove guide. Comparing with other method, present method is simple but accurate in calculation, thus is very suitable for CAD of groove guide circuits.

Table 1. gives the comparisons of cutoff wavelength of different groove guides between the results calculated by finite element method and those obtained by present method. The agreement is good, thus the effectiveness of the method is verified. Fig.1 gives the coupling characteristics of three 3dB groove guide couplers. It shows that the symmetrical groove guide coupler has very narrow bandwidth (curve (1)) whereas the asymmetrical one provides broadband smooth coupling (curve (2))[6]. Curve (3) implies that with the same groove width, groove depth and plane separation , asymmetry made by groove shapes can also provide broadband smooth coupling characteristics. V-shape groove guide has been paid more attentions due to its relatively lower loss comparing with that of rectangular one[4]. Present method gives a possible choice to design the excitation structures of V-shape groove guide using the 0dB V-shape-rectangular groove guide coupler.

*Supported by the National Science Foundation of China

Table 1. The comparisons of cutoff wavelength of different groove guides between the results calculated by finite element method and those obtained by network method

groove shape	$\lambda_c(mm)$		$\frlambda_{c1} - \lambda_{c2}\frac{}{\lambda_{c1}}$ %
	finite element[4] λ_{c1}	network method λ_{c2}	
rectangular	25.6536	25.8877	0.91
V-shape	21.7861	21.6458	0.64
parabolic	22.6241	22.8764	1.12
elliptic	23.3878	23.6219	1.10

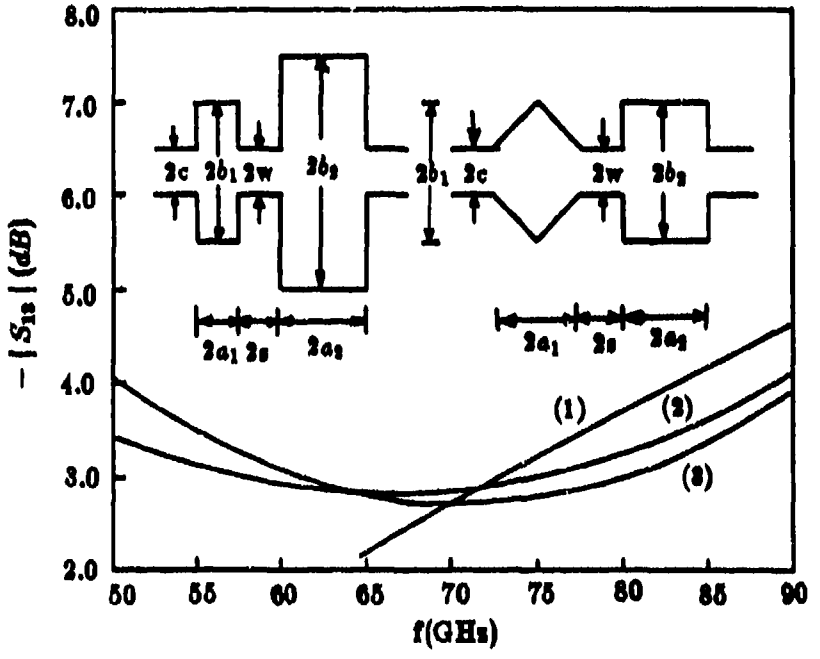

Fig.1 Coupling characteristics of 3dB rectanglar and V-shape-rectangular groove guide couplers (1) $2a_1 = 2a_2 = 4.0$, $2b_1 = 2b_2 = 8.8$, 2c=2w=5.0, 2s=3.0, L=273.0 (2) $2a_1 = 2a_2 = 3.5$, $2b_1 = 8.0$, $2b_2 = 10.0$, 2c=2w=5.0, 2s=0.1, L=70.0 (3) $2a_1 = 2a_2 = 4.0$, $2b_1 = 2b_2 = 8.0$, 2c=2w=5.0, 2s=0.1, L=70.0 (unit: mm)

References

[1] Xu Shanjia and Yin Lujun, J.IR MM Waves, 12(1991), pp.611-628.

[2] Yang Hongsheng, etl, J.IR MM Waves, 12(1991), pp. 535-541.

[3] Yat Man Choi, 1987 IEEE MTT-S, pp.165-167.

[4] Xu Shanjia and Zhang Yaojiang, Proc. of 17th Conf. on IR MM Waves, 1992

[5] Arthun A.Oliner, Paolo Lampariello, IEEE Trans. MTT-33, pp. 755-764, Sept. 1985.

[6] Xu Shanjia and Yin Lujun, Journ. of IR & MM Waves (Chinese), Vol.11, No.6, pp. 430-434, 1992.

Phase and attenuation coefficients in bi-dielectric eccentric circular transmission lines

Li-Yang Zhang, Pin Wang, Yong-Chang Jiao, and Chang-Hong Liang
Department of Electromagnetic Engineering
Xidian University, Shaanxi 710071, P. R. China

ABSTRACT

In this paper, an analysis of complex propagation coefficients in bi-dielectric eccentric transmission lines is initiated. It is convenient to evaluate attenuation coefficients, as well as phase coefficients, with the formulations, especially when the loss caused by material should be taken into account.

1. INTRODUCTION

The cross-sectional configuration of a bi-dielectric circular transmission line, e.g. an optical fiber, is a concentric annulus , of which the inner and outer circular rod are frequently considered to be two dielectrics of different permittivity. Although characteristics of propagating modes in it have been made very clear nowadays[1,2], their variations with the shape perturbations caused in manufacture procedure, to best of the author's knowledge, are hardly known. Another interesting problem is how to determine the attenuation coefficients when the material get a loss. In this paper, a general model for bi-dielectric circular transmission line is dealt with. As shown in Fig.1, the cross section of the transmission line is presumed to be an eccentric annulus, of arbitrary relative dimensions, containing different kinds of arbitrary physical mediums. Compared with the analysis of cutoff wavenumber for eccentric Goubau line performed by J. A. Roumeliotis *et al*[3], both phase coefficients and attenuation coefficients of the modes in the structure are considered here.

2. FORMULATIONS

In the structure shown in Fig.1, each propagating mode can be described by multiple expansions, i.e.

$$E_{1z}^{eo} = \sum_{p=0}^{\infty} a_p^1 \Psi_{pe}^{11(1)} \exp(-j\beta z); \quad H_{1z}^{eo} = \sigma \sum_{p=0}^{\infty} c_p^1 \Psi_{pe}^{11(1)} \exp(-j\beta z), \quad \rho_1 < a, \tag{1a}$$

$$E_{2z}^{eo} = \sum_{p=0}^{\infty} (b_p^2 \Psi_{pe}^{12(3)} + a_p^2 \Psi_{pe}^{22(1)}) \exp(-j\beta z);$$

$$H_{2z}^{eo} = \sigma \sum_{p=0}^{\infty} (d_p^2 \Psi_{pe}^{12(3)} + c_p^2 \Psi_{pe}^{22(1)}) \exp(-j\beta z), \quad \rho_1 > a \cap \rho_2 < b, \tag{1b}$$

$$E_{3z}^{eo} = \sum_{p=0}^{\infty} b_p^3 \Psi_{pe}^{11(3)} \exp(-j\beta z); \quad H_{3z}^{eo} = \sigma \sum_{p=0}^{\infty} d_p^3 \Psi_{pe}^{11(3)} \exp(-j\beta z), \quad \rho_2 > b, \tag{1c}$$

in which, $\sigma = 1(-1)$ for even (odd) modes, $a_p^1, c_p^1, a_p^2, b_p^2, c_p^2, d_p^2, b_p^3$ and d_p^3 are unknown expansion coefficients. The cylindric harmonics are defined as

$$\Psi_{pe}^{l,(k)} = Z_p^{(k)}(k_j^l \rho_l) \cos(p\theta), \qquad \Psi_{po}^{l,(k)} = Z_p^{(k)}(k_j^l \rho_l) \sin(p\theta),$$

in which

$$Z_p^{(1)}(x) = J_p(x), \; Z_p^{(3)}(x) = H_p^{(2)}(x), \; k_j^l = \pm\sqrt{k_j^2 - \beta^2}, \; Im(k_3^l) \leqslant 0,$$

with the superscripts l, j and k standing for coordinates, medium and the type of the harmonics. The boundary conditions for the mode can be written as

$$\hat{\rho}_1 \times \mathbf{E}_1^{eo} = \hat{\rho}_1 \times \mathbf{E}_2^{eo}; \quad \hat{\rho}_1 \times \mathbf{H}_1^{eo} = \hat{\rho}_1 \times \mathbf{H}_2^{eo}, \; \rho_1 = a, \tag{2}$$

$$\hat{\rho}_2 \times \mathbf{E}_2^{eo} = \hat{\rho}_2 \times \mathbf{E}_3^{eo}; \quad \hat{\rho}_2 \times \mathbf{H}_2^{eo} = \hat{\rho}_2 \times \mathbf{H}_3^{eo}, \; \rho_2 = b. \tag{3}$$

However, in the vicinity of the boundaries, the field in medium II may be depicted by employing harmonics in a single coordinate, i.e.

$$E_{2z}^{eo} = \sum_{p=0}^{\infty} \left\{ \begin{bmatrix} e_p^{11} & e_p^{12} \end{bmatrix} \Psi_{pe}^{12(1)} + \begin{bmatrix} e_p^{21} & e_p^{22} \end{bmatrix} \Psi_{pe}^{12(3)} \right\} \begin{bmatrix} a_p^1 & c_p^1 \end{bmatrix}^T \exp(-j\beta z),$$

$$H_{2z}^{eo} = \sigma \sum_{p=0}^{\infty} \left\{ \begin{bmatrix} f_p^{11} & f_p^{12} \end{bmatrix} \Psi_{pe}^{12(1)} + \begin{bmatrix} f_p^{21} & f_p^{22} \end{bmatrix} \Psi_{pe}^{12(3)} \right\} \begin{bmatrix} a_p^1 & c_p^1 \end{bmatrix}^T \exp(-j\beta z), \; a < \rho_1 < b - d, \tag{4}$$

$$E_{2z}^{oe} = \sum_{p=0}^{\infty}\left\{\left[R_p^{11}\ R_p^{12}\right]\Psi_{pee}^{22(1)} + \left[R_p^{2}\ R_p^{22}\right]\Psi_{pee}^{22(3)}\right\}\left[b_p^{3}\ d_p^{3}\right]^T exp(-j\beta z),$$

$$H_{2z}^{oe} = \sigma\sum_{p=0}^{\infty}\left\{\left[h_p^{11}\ h_p^{12}\right]\Psi_{pee}^{22(1)} + \left[h_p^{21}\ h_p^{22}\right]\Psi_{pee}^{22(3)}\right\}\left[b_p^{3}\ d_p^{3}\right]^T exp(-j\beta z),\ a+d<\rho_2<b, \qquad (5)$$

in which, $e_p^{11}, e_p^{12}, e_p^{21}, e_p^{22}, f_p^{11}, f_p^{12}, f_p^{21}, f_p^{22}, R_p^{11}, R_p^{12}, R_p^{21}, R_p^{22}, h_p^{11}, h_p^{12}, h_p^{21}$ and h_p^{22}, may be determined by the boundary conditions at $\rho_1 = a$ or $\rho_2 = b$. Subtracting (4) or (5) from (1), then employing Graf's addition theorem for Bessel functions, we get a set of coupled linear equations

$$\frac{2}{\varepsilon_p}\left[e_p^{11}\ e_p^{12}\right]\left[a_p^{1}\ c_p^{1}\right]^T - \sum_{q=0}^{\infty}\left[R_q^{11}\ R_q^{12}\right]\left[b_q^{3}\ d_q^{3}\right]^T\left[J_{p-q}(k_2'd) + \sigma(-1)^q J_{p+q}(k_2'd)\right] = 0,$$

$$\frac{2}{\varepsilon_p}\left[f_p^{11}\ f_p^{12}\right]\left[a_p^{1}\ c_p^{1}\right]^T - \sum_{q=0}^{\infty}\left[h_q^{11}\ h_q^{12}\right]\left[b_q^{3}\ d_q^{3}\right]^T\left[J_{p-q}(k_2'd) - \sigma(-1)^q J_{p+q}(k_2'd)\right] = 0,$$

$$\frac{2}{\varepsilon_p}\left[R_p^{21}\ R_p^{22}\right]\left[b_p^{3}\ d_p^{3}\right]^T - \sum_{q=0}^{\infty}\left[e_q^{21}\ e_q^{22}\right]\left[a_q^{1}\ c_q^{1}\right]^T\left[J_{q-p}(k_2'd) + \sigma(-1)^p J_{p+q}(k_2'd)\right] = 0,$$

$$\frac{2}{\varepsilon_p}\left[h_p^{21}\ h_p^{22}\right]\left[b_p^{3}\ d_p^{3}\right]^T - \sum_{q=0}^{\infty}\left[f_q^{21}\ f_q^{22}\right]\left[a_q^{1}\ c_q^{1}\right]^T\left[J_{q-p}(k_2'd) - \sigma(-1)^p J_{p+q}(k_2'd)\right] = 0,$$

$$p = 0,1,2\cdots, \qquad (6)$$

The characteristic equation for the complex propagation coefficient β may be obtained by forcing the determinant of the coefficient matrix in (6) to be zero. An attenuation coefficient may be specified in dB

$$\alpha = -20log(e)Im(\beta). \qquad (7)$$

Notice, (8) gives $4N+2$ linearly independent equations for both even and odd modes. Nevertheless, there are only $4N+2$ expansion coefficients that need determining.

3.CONCLUSION

A rigorous analysis of complex propagation coefficients in bi-dielectric eccentric transmission lines is given in this paper.

4.REFERENCES

1. P. J. B. Clarricoats, "Propagation along unbounded and bounded dielectric rods—Part 2: Propagation along a dielectric rod contained in a circular waveguide," *Proc. Inst. Elec. Eng.*, Vol.108, Pt.C, pp.177, 1961.

2. K. A. Zaki and A. E. Atia, "Modes in dielectric-loaded waveguides and resonators," *IEEE Trans. on MTT*, Vol.MTT-31, pp. 1039-1045, 1983.

3. J. A. Roumeliotis and J. G. Fikioris, "Cutoff wavenumbers and the field of surface wave modes of an eccentric circular Goubau waveguide," *J. Franklin Int.*, Vol.309, no.5, pp.309-325, 1980.

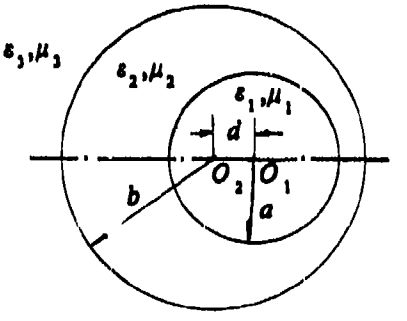

Fig.1 An eccentric bi-dielectric circular transmission line

The Characteristics of the Closed Circular Groove Guide*

Jun Qian, Yang Hong-Sheng, and Lu Zhong-Zuo

Department of Electronic Engineering
National Key Laboratory of Millimeter Waves
Southeast University, Nanjing, 210018, P.R. China

ABSTRACT

The dispersion characteristic is studied in this paper, when the circular-groove guide is closed at the ends by metal. The theoretical curves are given with the eigen-weighted boundary integral equation method.

INTRODUCTION

The circular-groove guide, one kind of the groove guides, is with low loss, low dispersion, simple configuration, large dimension and large power capacity, especially is easy to transform from gyrotron, it has prospects to be used at millimeter and submillimeter waveband[1].

For manufacturing components with the circular-groove guide, and transmitting large power, the closed circular-groove guide should be studied.

When the parallel plate regions are sufficiently long, it does not matter if they remain open or are closed off at the ends[2]. However, these regions are always finite, and we hope they as small as possible. So this is practical problem for using the circular-groove guide.

THEORETICAL BASIS

The cross section of the groove guide is shown in Fig. 1. Only a quarter is considered. Because the TE mode is the dominant mode, we are interested in it.

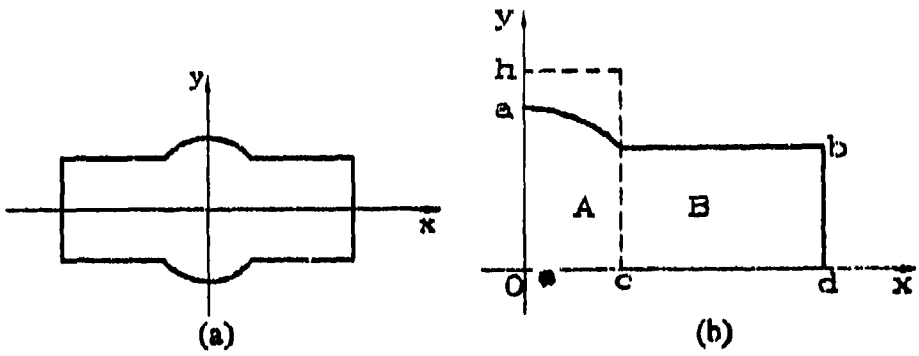

Fig. 1 The cross section of the circular-groove guide.

* The Project Supported by National Natural Science Foundation of P.R. China.

This paper uses the eigen-weighted boundary integral equation method (EWBIEM)[3][4][5].
The boundary integral equation is:

$$\oint_{\Gamma}(\phi\frac{\partial\omega_{\mu}}{\partial n}-\omega_{\mu}\frac{\partial\phi}{\partial n})d\Gamma=0 \tag{1}$$

where Γ is the boundary of the cross section of the groove guide.

ω_{μ} satisfies the Helmholtz Equation and the regular practical or fictitious (dashed line) boundary conditions.

RESULTS

Some numerical results are obtained with EWBIEM. In Fig. 2 (a), the values of $k_c a$ are shown when d/a=*3.0* and d/a=*1.0*. When b/a is near to *0*, $k_c a$ is near to *1.841* (the value of the circular waveguide), and when b/a is near to *1.0*, $k_c a$ is near to $\pi/2$ (the value of the rectangular waveguide). For small b/a, $k_c a$ approaches *1.841*, when d/a=*1.0* (the closed plates are near to the groove).

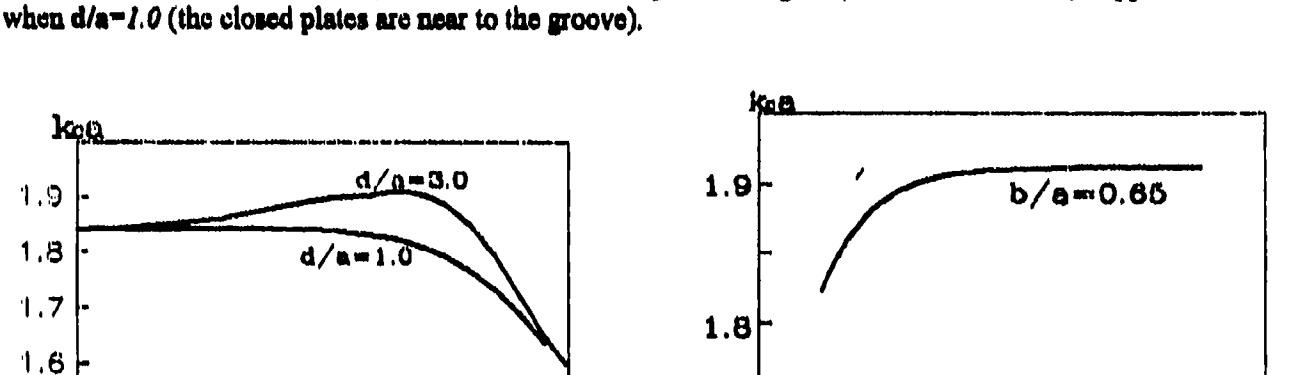

Fig. 2 The cutoff wavenumbers kc

In Fig. 2 (b), we can find that $k_c a$ approaches the value of the open circular-groove guide (*1.911*[5]) when d/a>*2.0*. If we put absorbed material inside of the closed plates, when d/a is greater than *2.0*, we can say the closed circular-groove guide is similar to the open one.

REFERENCES

[1] Yang Hong-sheng, Ma Jianglei, Lu Zhong-zuo, "THE CHARACTISIC EQUATION AND SOLUTION OF CIRCULAR-GROOVE GUIDE", Int. J. of Inf. and MmW, Jun. 1991.
[2]A. A. Oliner and P. Lampariello, "The Dominant Mode Properties of Open Groove Guide: An Improved Solution", IEEE Trans. on MTT, vol. MTT-33, pp. 755-763, Sept. 1985.
[3] Wenxun Zhang, ENGINEERING ELECTROMAGNETISM: FUNCTIONAL METHODS Ellis Horwood Ltd., UK, 1991, pp.142-144.
[4] Lei Zhu, Wenxun Zhang, "THE EIGEN-WEIGHTED BIEM FOR SOLVING ARBITRARY CROSS-SECTION WAVEGUIDES", 1988 IEEE AP-S Int. Symp., pp.589-592.
[5] Jun Qian, Yang Hong-Sheng, Wenxun Zhang, Lu Zhong-Zuo, "ANALYTIC METHOD OF ARBITRARY CROSS SECTION OPEN GROOVE GUIDE", Int. J. of Inf. and MmW, Feb,1993.

THE HIGHER–ORDER MODES IN CIRCULAR GROOVE GUIDE①

Ma Jianglei Yang Hong–sheng Lu Zhong–zuo
National Key Laboratory of Millimeter Waves,
Southeast University, Nanjing, 210018
P. R. China

ABSTRACT

In this paper, the higher–order modes, including TE mode and TM mode, are discussed. By cnalysing the field configurations of these modes, the characteristic equations have been derived.

INTRODUCTION

Circular groove guide is a new type of groove guide we presented in 1989. Its structure is shown in Fig.(1). Up to present, our discussions about circular groove guide are restricted to lowest mode. This is dominant mode and is of most important. In circular groove guide, there are two types of modes, i.e., TE mode and TM mode. In order to find out the condition of single mode operation in circular groove guide, the mode distribution must be understood. In this paper, the field configurations of TE mode and TM mode of different order are discussed and the general expressions of characteristic equations for these two types of modes are derived.

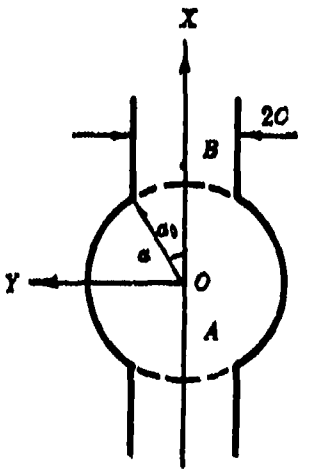

Fig.(1) The structure of circular groove guide

THEORETICAL ANALYSIS

To distinguish different modes, we use symbols TE^r_{pn} and TM^r_{pn} to represent TE mode and TM mode of different order, where p, r, n are integers. Superscript r is the order of mode in y direction in parallel plate region, and subscripts p and n represent the order of azimuthal mode and radial mode respectively in circular groove region. These modes are divided into odd mode and even mode further depending on whether p is odd or even. Among these modes, TE^1_{11} mode is the dominant mode in circular groove guide while the modes corresponding to $p>1$, $n>1$ or $r>1$ are all higher–order modes. Because the field configuration as well as the boundary condition of TE mode and TM mode are different, we will discuss them separately.

①The Project Supported by National Natural Science Founcation of P.R.China

1. TE mode

After proper mathematical derivation, the characteristic equation of TE^{r}_{pn} mode can be obtained. It reads

$$\frac{uJ'_p(u)}{J_p(u)} = \frac{8aA_1(p,r)[rMA_2(p,r) - V(r)A_1(p,r)]}{\pi c} \tag{1}$$

where $u = k_c a$, $V(r) = k_{xr} a$, $M = \frac{\pi a}{2c}$, and the other parameters are defined as

$$A_1(p,r) = \int_0^{\alpha_0} \sin p\alpha \sin(rM\sin\alpha)\cos\alpha d\alpha; \quad A_2(p,r) = \int_0^{\alpha_0} \cos(rM\sin\alpha)\sin p\alpha \sin\alpha d\alpha$$

2. TM mode

Let: $E_1(p,r) = \int_0^{\alpha_0} \cos(rM\sin\alpha)\cos p\alpha d\alpha$

$$E_2(r_1,r_2) = \int_0^{\alpha_0} \sin(r_1 M\sin\alpha)\cos(r_2 M\sin\alpha)\sin\alpha\cos\alpha d\alpha$$

$$E_3(r_1,r_2) = \int_0^{\alpha_0} \cos(r_1 M\sin\alpha)\cos(r_2 M\sin\alpha)\cos^2\alpha d\alpha$$

$$E_4(p,r) = \int_0^{\alpha_0} \cos(rM\sin\alpha)\cos p\alpha\cos\alpha d\alpha$$

Then, we can derive the characteristic equation of TM^{r}_{pn} mode.

$$\frac{uJ'_p(u)}{J_p(u)} = -\frac{\pi[rME_2(r,r) + V(r)E_3(r,r)]}{4E_1(p,r)E_4(p,r)} \tag{2}$$

The relationship of u with V(r) is given by following expression.

$$u^2 = (rM)^2 - V^2(r) \tag{3}$$

DISCUSSION

We have derived the general expressions of characteristic equations for TE^{r}_{pn} mode and TM^{r}_{pn} mode. From the n–order solution of these equations, the cutoff wavenumbers of TE^{r}_{pn} and TM^{r}_{pn} modes can be gotten when definite p and r are taken.

If we take p = r = 1, the equation (1) is the characteristic equation of TE^{1}_{1n} mode which we have discussed and solved. From the lowest–order solution of the equation, the cutoff wavenumber of dominant mode in circular groove guide is known.

Besides, it can be proved that when the plate spacing 2c trends to zero, the equations (1) and (2) degenerate to those for TE_{pn} mode and TM_{pn} mode in circular waveguide separately. Therefore, circular waveguide can be regarded as the limit situation of circular groove guide.

Our work presented above provides us the possibility to study the characteristic of higher–order mode in circular groove guide further.

A Transition from rectangular waveguide to circular groove guide*

Yang Hong-Sheng, Shen Zheng-Kun, Xu Zheng-Rong
Department of Electronic Engineering
National Key Laboratory of Millimeter Waves
Southeast University,Nanjing,210018,P.R.China

ABSTRACT

A transition between rectangular waveguide and circular groove guide is described. The composite transition consists of two sections. It is theoretically designed to provide both mode matching as well as low reflection coefficient. The performance of the transition is plotted.

2.INTRODUCTION

Circular groove guide is a new type of millimeter and submillimeter waveguide. It can operate as a low-loss, low-dispersion, single-mode, wide frequency band, large dimension and high power transmission waveguide[1,2].Recently there is no waveguide measurement system and also no source based on circular groove guide. Therefore a transducer from rectangular waveguide to circular groove guide is needed.

This paper describes a new type of transducer from TE_{01}^{m} main mode to TE_{11}^{0} main mode. Theoretical analysis and design methods of the transducer are given.

3.THEORETICAL ANALYSIS

Two steps of transition are proposed by authors. The first part transforms the TE_{01}^{m} main mode of rectangular waveguide into TE_{11}^{e} main mode of circular waveguide. Analysis and design methods for this kind of transducer are developed by several other authors. Extant transducer is commercially available. The second part transforms the TE_{11}^{e} mode into TE_{11}^{0} main mode of circular groove guide as shown in Fig.1. Therefore we pay more attention to the second part of the transducer.

We assume that the transducer is primarily excited by only main mode, and that it has a much large amplitude than all other modes. We can derive a nonlinear differential equation in reflection coefficient.

$$\frac{d\Gamma}{dx} - 2j\beta\Gamma + \frac{1}{2}(1-\Gamma^2)\frac{d\ln(Z)}{dx} = 0 \tag{1}$$

where Z and β are the characteristic impedance and the propagation constant of the gradually varying circular groove guide. They are expressed as follows

$$Z = \frac{4\omega\mu}{\beta\pi}\cdot\frac{\left[\frac{H_1}{B_1}\int_0^a \frac{1}{k_c^2}\cdot\frac{J_1^2(k_c\rho)}{\rho}d\rho + \frac{k_{yr}}{k_{xr}}\right]^2}{\left\{\int_0^a \left(\frac{H_1}{B_1}\right)^2 \frac{1}{k_c^2}\left[J_1'^2(k_c\rho)\rho + \frac{J_1^2(k_c\rho)}{k_c^2\rho}\right]d\rho + \frac{1}{2}\left(\frac{k_{xr}}{k_{yr}} + \frac{k_{yr}}{k_{xr}}\right)\right\}} \tag{2}$$

For $|\Gamma^2| \ll 1$,a solution of the differential equation(1) is given by

$$\Gamma = \frac{1}{2}\int_0^L e^{-2j\int_0^x \beta dx}\cdot\frac{d(\ln Z)}{dx}dx \tag{3}$$

where L is the length of the second part of the transducer.

The Γ can be represented by

---

* The Project Supported by National Natural Science Foundation of P.R. China.

$$\Gamma = \sum_{n} \frac{1}{2} \cdot \frac{Z_{n+1} - Z_n}{Z_n} \cdot e^{-j\sum_{m=1}^{n} 2\beta(x_m)(x_{m+1}-x_m)} \tag{4}$$

When the frequency band and the magnitude of the reflection coefficient are specified, the dimensions of the transducer can be found on computer.

4.DESIGN OF TRANSDUCER

Suppose that the frequency band is Ku band and the reflection coefficient at the input of the second part is less than 0.1,then three physical dimensions of the transducer, diameter 2a,spacing 2c and the length L will be determined. According to the design method of circular groove guide[2], the cross section size of the transducer at output was calculated to be of inside diameter 14.9mm and spacing 9.685mm. For ease of machining and economy linearly tapered transducer is adopted which is shown in Fig.1. According to the calculation, when L=151.63mm,the reflection coefficient Γ is less than 0.1.The result of calculation are shown in Fig.2.

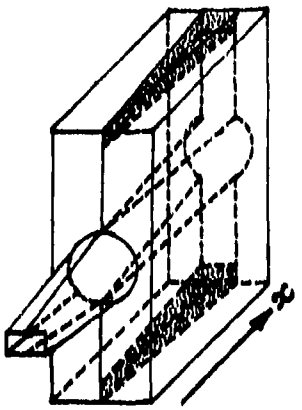

Fig.1 $TE_{01}^{\square}$ — TE_{11}^{ϕ} transducer

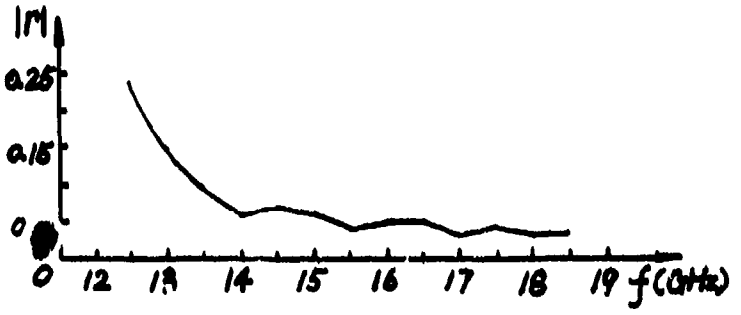

Fig.2 Reflection coefficient versus frequency

5.DISCUSSION

The design of transducer from $TE_{01}^{\square}$ to TE_{11}^{ϕ} may have several methods. The way described here is one of those methods, which has obvious physical idea and ease of machining. A near-optimum design method should be developed from which the length L' is still less than L, and the same performances are kept as before. But the contour of the transducer is nonlinearly tapered along the distance x. It is obvious that the difficulties of machining are increased.

6.REFERENCES

1.Yang Hong-Sheng, Ma Jiang-Lei, Lu Zhong-Zuo, "A new type of groove guide" Proceedings of ISRAMT'89.pp.239-240

2.Yang Hong-Sheng, Ma Jiang-Lei, Lu Zhong-Zuo, "The characteristic equation and solution of circular groove guide" Int. Journal of Infrared and Millimeter Waves,Vol.12,No.5,pp.535-541,1991

AN ANALYSIS OF A KIND OF DIELECTRIC WAVEGUIDE

Hong Wu, Jun Qian

Department of Electronic Engineering
Southeast University, Nanjing, 210018,
P.R. China

ABSTRACT

A general programme, based on the Effective Dielectric Constant method combined with the transverse resonance technique, is presented here for analysing dielectric waveguides. Dispersion curves are also presented for a kind of waveguide with new configuration.

Transitions for the Quasi-Optical Waveguides

V. K. Kiselyev, T. M. Kushta

Institute of Radiophysics and Electronics
Academy of Sciences of Ukraine
12 Acad. Proskura str., Kharkov, Ukraine

Abstract

The aim of this work is to recieve expressions, required for design of transitions between quasi-optical waveguides of the class of "hollow dielectric channel" (DC-waveguide), in particular, between DC-waveguides of same type, having different sizes of cross-section. Parameter $\varepsilon_{\perp\prime}$, characterising type of boundary of DC-waveguides, is introduced to receive mentioned formulae. Proposed way allows to recieve in analytical form the expressions for relative amplitudes of unwanted waves, arising in the result of scattering of fundamental mode by finite waveguide part of varied section, being used as quasi-optical transition. Received formulae allow to calculate transitions with different forms and to study the possibility of optimization of transitions by minimum of the losses at the transformation of fundamental mode into unwanted ones. Circular and rectangular tapered transitions with different type of boundary structures are considered as specific examples.

Frequency-dependent characteristics of thick microstrip lines in lossy multilayered dielectric media

J. R. Souza

Center for Telecommunication Studies - CETUC
Pontifical Catholic University of Rio de Janeiro - PUC/Rio
Rua Marquês de São Vicente, 225
22453 Rio de Janeiro - RJ, Brazil

ABSTRACT

The Spectral Domain Approach (SDA) is used for a rigorous full-wave analysis of thick microstrip lines embedded in lossy multilayered dielectric media. The effects of the conductor thickness on the propagation constant and characteristic impedance are investigated.

1. INTRODUCTION

Microstrip lines in multilayered dielectrics are of interest for monolithic microwave and millimetre wave integrated circuits. The design of such circuits requires accurate modelling of the transmission line characteristics, which should include effects of the strip thickness and material losses. The SDA solution developed for microstrip lines in multilayered substrate configuration[1] is now extended to accommodate strips of finite thickness.

2. FORMULATION

The microstrip line to be considered is shown in Fig. 1. The lossy dielectric layers of the substrate are represented by the relative dielectric constant (ε_r) and conductivity (σ). The shielding and the strip are assumed to be loss free. The hybrid field is described by a superposition of TE_y and TM_y modes, which are represented by vector potentials $\vec{\psi}^h$ and $\vec{\psi}^e$, respectively:

$$\vec{\psi}^{h,e} = \vec{a}_y \, \varphi^{h,e}(x,y) \cdot \exp(-j\beta z) \qquad (1)$$

In the substrate layers and in the air-layer above the strip, all the potentials and field components are Fourier transformed in the x-direction. As shielded microstrip lines are considered, a discrete Fourier Transform is used. The transform and its inverse are define, respectively as:

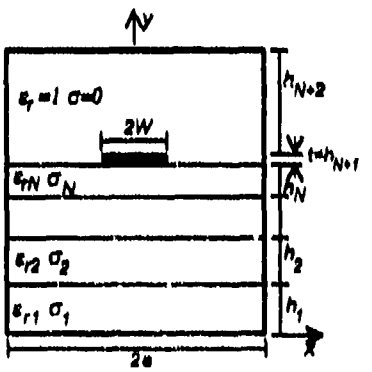

Fig. 1: Thick microstrip line on lossy, multilayered dielectric substrate.

$$\tilde{\varphi}(\alpha_n, y) = \int_{-a}^{a} \varphi(x,y) \cdot e^{j\alpha_n x} dx \,, \quad \varphi(x,y) = \frac{1}{2a} \sum_{n=-\infty}^{\infty} \tilde{\varphi}(\alpha_n, y) e^{-j\alpha_n} \qquad (2)$$

where the parameter α_n is chosen so that the boundary conditions at the side walls are satisfied. For the fundamental mode, $\alpha_n = (2n \pm 1)/2a$.

Next, the formulation developed in reference 1 is used to obtain a relation between the Fourier Transform of the x- and z- components of the magnetic and electric fields at $y=y_N$ and at $y=y_N+t$, where $y_N=h_1+h_2+\ldots+h_N$.

In the air-layer besides the thick strip ($y_N<y<y_N+t$), the vector potentials are written as:

$$\vec{\psi}^{h,e}(x,y,z) = \vec{a}_y \frac{1}{g} \cdot \sum_{k=0}^{\infty} \hat{\varphi}_k^{h,e}(y) \exp(-j\beta z) \qquad (3)$$

where $2g=a-W$, and $\hat{\varphi}_k^{h,e}(y)$ are sine and cosine transforms given, for $x>0$, by:

$$\hat{\varphi}^{e}_{k}(y)=\int_{W}^{a}\varphi^{e}(x,y)\sin[\xi_k(a-x)]dx \quad , \quad \hat{\varphi}^{h}_{k}(y)=\int_{W}^{a}\varphi^{h}(x,y)\cos[\xi_k(a-x)]dx \quad , \quad \xi_k=k\pi/2a, \tag{4}$$

For x<0, the transforms are deduced by symmetry. The potentials are then written in terms of the transformed x- and z- components of the electric field at $y=y_N^+$ and at $y=y_N+t^-$. A relation between the transformed x- and z-components of the magnetic and electric fields at $y=y_N^+$ and at $y=y_N+t^-$ is then obtained. At this point, all the boundary conditions have been enforced, with the exception of those at $y=y_N$ and at $y=y_N+t$.

Let E_{Up}, H_{Up}, E_{Lp}, H_{Lp} represent the p-component (p=x, z) of the electric and magnetic field at $y=y_N+t$ and at $y=y_N$, respectively. For W<x<a the boundary conditions require that:

$$E^{+}_{Up}(x)=E^{-}_{Up}(x) \quad , \quad H^{+}_{Up}(x)=H^{-}_{Up}(x) \quad , \quad E^{+}_{Lp}(x)=E^{-}_{Lp}(x) \quad , \quad H^{+}_{Lp}(x)=H^{-}_{Lp}(x) \quad (p=x,z) \tag{5}$$

The electric field components E_{Up}, E_{Lp} are expanded in terms of suitable basis functions, and their continuity along the apertures at $y=y_N$ and at $y=y_N+t$ is automatically satisfied. Let, then:

$$E_{Up}(x)=\sum_{q=1}^{M_p}A_{pq}f_{qp}(x) \quad , \quad E_{Lp}(x)=\sum_{q=1}^{M_p}B_{pq}f_{qp}(x) \quad (p=x,z) \tag{6}$$

where A_{pq} and B_{pq} are still unknown coefficients; the set $f_{pq}(x)$ represents the chosen basis functions. Next, the equations for the continuity of the magnetic field components are modified as, for example:

$$H^{+}_{Ux}(x)=H^{-}_{Ux}(x) \quad \Rightarrow \quad \int_{W}^{a}H^{+}_{Ux}(x)f^{*}_{zq}(x)dx=\int_{W}^{a}H^{-}_{Ux}(x)f^{*}_{zq}(x)dx \quad \Rightarrow \quad \frac{1}{4a}\sum_{n=-\infty}^{\infty}\tilde{H}^{+}_{Ux}\,\tilde{f}^{*}_{zq}=\frac{1}{a}\sum_{k=0}^{\infty}\hat{H}^{-}_{Ux}\,\hat{f}^{*}_{zq} \tag{7}$$

As the transformed magnetic field components were written in terms of the transformed electric field components, a homogeneous system of equations is obtained, in terms of the unknown propagation constant β and expansion coefficients A_{pq} and B_{pq}. The usual steps of the SDA are followed, and the unknown parameters are determined. A three-layer structure was used to test the solution, with the following data: 2W=30μm, 2a=6mm, $h_1=h_3=5$mm, $h_2=20\mu$m, $h_3=200\mu$m, $\varepsilon_{r1}=1$, $\sigma_1=0$, $\varepsilon_{r2}=1$, $\sigma_2=1.77\times10^7$moh/m, $\varepsilon_{r3}=12.9$, $tg\delta_3=3.0\times10^{-4}$, where tgδ represents the loss tangent. This structure simulates the single layer microstrip with lossy ground plane considered in reference 2. Fig. 2 shows the variation of the square root of the effective dielectric constant as a function of frequency, for different values of the strip thickness t. The characteristic impedance (Z_c) was calculated according to the voltage - transmitted power definition. The power is calculated as indicated in reference 1. The variation of the real part of Z_c with frequency is shown in Fig. 3. It was observed that these values are, in average, less than 2Ω greater than those reported in reference 2 for the voltage-current definition.

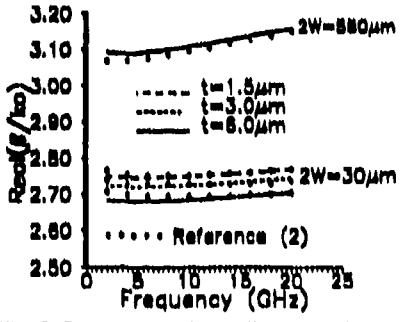

Fig. 2: Square root of the effective dielectric constant versus frequency.

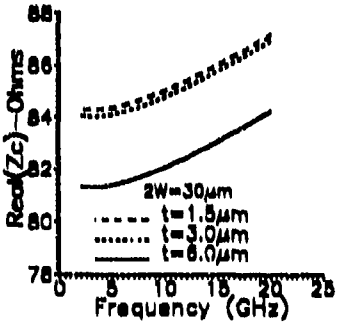

Fig. 3: Real part of the characteristic impedance versus frequency.

3. REFERENCES

1. J. R. Souza, "Spectral Domain Analysis of Printed Transmission Lines in Multilayered Substrate and Superstrate Configuration", *Proc. 8th Annual Review of Progress in Applied Computational Electromagnetics*, pp 290-297, Monterey, CA, U.S.A., March 1992.

2. W. Heinrich, "Full-Wave Analysis of Conductor Losses on MMIC Transmission Lines", *IEEE Trans. on MTT*, Vol. MTT-38, pp 1468-1472, October 1990.

Rejection filter

S.A.Pogarsky, I.I.Saprykin
Microwave Phisics Department, State University,
Sq. Svobody, 4, 310077, Kharkov, Ukraine

ABSTRACT

At present,several methods for millimeter frequency band suppression are known [1]. The essential defects of these methods lie, as we think, in complicated construction, high attenuation level in key-in region, unprofitable correlation between controlling sizes and other element's sizes. This makes impossible to regulate gain frequency characteristic. Moreover, respective devices have unprofitable weight-size parameters. Discribing filter has two important advantages, namely higher attenuation level and a simple construction as compierd with previosly known one. This has been achived by using a combinaton of two transmission lines: an insulated image duide (IIG) and microstrip.

1. SUPPESSION THEORY

The 8-millimeter band rejection filter (or simply filter below) is shown at Fig.1, where 1- metallic screen; 2-insulating dielectric; 3-dielectric wave guide; 4-microstrip resonators.

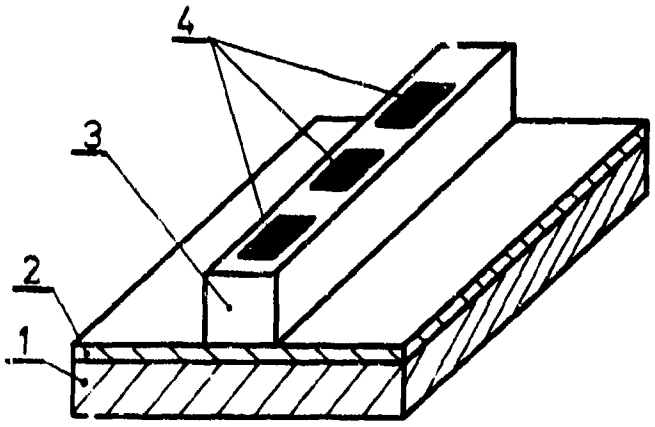

Fig.1

Suppose there exists a signal of complex spectrum at the filter's input in case there were no supplementary conductors within the cross section, electromagnetic energy would have passed through a dielectric rod without essential attenuation. The insertion of supplementary conductors of certain size enables one to take away the energy from the dielectric waveguide due to resonance effect in microstrip resonators. This leads to rejection of the input complex spectrum. The value and level of rejection depends on the total number of resonators and their arrangement while central frequency of the stop-band are defined by size of conductors, the dielectric rod, insulating dielectric and permitivity of the latter.

Phisical explanation of the suppression effect is as follows. The IIG dielectric rod maintains two eigenmodes of E^x_{11} and E^y_{11} types. If the discontinuities in the line dielectric rod-insulating dielectric - metallic screen were absent, the injected electromagnetic energy would pass to the output without attenuation and amplitude oscillations. Conversely, the discontinuities such as metallized plots when inserted in the line show significant influence in the propagation of electromagnetic oscillations. Theoretically, both eigenmodes mentioned above may interact with these discontinuities. However, since the vertical component of the electrical field vector approaches zero and due to the fact

that the ratio between resonator's size and λ_g approaches zero as well, the above mentioned resonators interact with E_{11}^y wave only.

Resonance phenomena occurring in the structure lead to an effective frequency rejection in the frequency range employed if the microstrip resonator's length is proportional to $\lambda_g/2$ where λ_g characterized the microstrip resonator made of a metallic screen, insulating dielectric and the dielectric rod. Moreover, the metallic spot's width has significant influence on the microstrip resonator's energy factor while the length of the microstrip resonator essentially determines the resonant frequency. To form the necessary frequency characteristic, the total number of resonators should be properly chosen.

Exact evaluation of parameter for the filter necessitates application of regorous diffraction theory. Fortunately, for practical purposes the following approximate method has proven to be quite satisfactory. The width w of microstrip should be taken to provide the characteristic impedance of the latter of 50 Ohm. Then the length of the resonant plot is evaluated as:

$$l_i \approx n\,\lambda_g/2 + 4(w-h)/\sqrt{\varepsilon_e}, \qquad (1)$$

where λ_g is a wavelength in the auxiliary microstrip whose width of a current carring conductor is w; ε_e is the effective permitivity of the dielectric rod. Distance between conductors is found to be:

$$s_i \approx 0.8\,l_i(1+w\sqrt{\varepsilon_e}/l_i). \qquad (2)$$

2. EXPERIMENT

It has been asteblished experimentally, that the value of the resonant frequency is independent of resonant condutors' width and under the fixed thicknesses of the dielectric rod and insulating dielectric is determined by the length of the resonator.

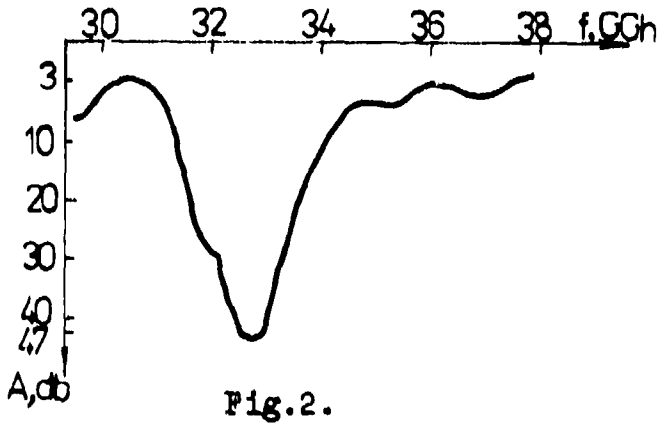

Fig.2.

Fig.2 shows experimental results for a 3-element rejection filter which employs the alumina rod with ε_e=9,6 and sizes 2x2mm with admission ±0,01mm. As insulated dielectric chemically treated teflon is used, with ε_e=2,02, thickness 0,1±0,01mm. Dimensions of the resonators are as followes: s_1=2,3±0,01 mm, s_2=2,25±0,01mm, s_3=2,3±0,01mm. The distances between resonators are l_{12}=3,6±0,01mm, l_{23}=3,2±0,01mm. The filter provides rejrotion level -30dB over the 5,2% stop-bend centered at f_0=32,45 GGh. Maximum rejection level is -47 dB. The filter needs no regulation at all if its sizes are chosen with the accuracy given above.

3. REFERENCES

1. Hoffman R.K. Integrierte Microwellenschatungen. Springer-Verlag, Berlin, Heidelberg, New York, Tokio, 1983.

OPTICAL CHARACTERIZATION OF THIN FILMS USING SURFACE POLARITONS AND SURFACE ELECTROMAGNETIC WAVES MEASUREMENTS

E.V.Alieva, L.A.Kuzik, V.A.Yakovlev, G.N.Zhizhin

Institute of Spectroscopy, Academy of Sciences of Russia,
Troitzk, Moscow reg., 142092, Russia

Reflectivity and transmittance measurements are extensively using for thin film studies. However for extremely thin films their sensitivity is not enough to obtain good spectra and to derive film dielectric function. The new facilities are promised by the application of surface polaritons (SP) and surface electromagnetic waves (SEW) for optical studies of dielectric, semiconductor and metal surfaces and for spectroscopy of thin films on them [1]. The surface polaritons and plasmons being localized exactly on the surface (with the maximum of electric field on it) are extremely sensitive to the presence of thin films being the monolayers or submonolayers.

For SEW excitation various techniques can be applied. Last years aperture excitation of IR SEW [2] was extensively used. Calculations of electromagnetic wave diffraction on the slit above the surface under study [3] gave us the possibility to develop SEW phase spectroscopy using interferometric measurements. This technique permits to measure real as well as imaginary part of SEW wavevector and determine complex dielectric function of the sample [4].

In the Table 1 the results of such measurements in 10μm spectral region are given for several metals. The value $n_e=k_x/\omega c$ (effective refractive index of SEW) was obtained by interferometric measurements, the SEW propagation length L was determined by two prism technique [1]. Using these two measured values we have calculated free electron parameters for the metals under study (ν_p is a plasma frequency and ν_τ is a collision frequency) and reflectivity R_{calc} at normal incidence. The latter value is compared with the result of direct reflectivity measurement by multiple (21) reflection technique R_{exp}.

Table 1.

	$(n_e-1)\cdot10^4$	L,cm	ν_p,cm^{-1}	ν_τ,cm^{-1}	R_{calc}%	R_{exp}%
Cu	1.22±.05	2.0 ±.1	67000±1300	370±30	98.92±.08	98.8±.1
Ag	0.96±.03	2.5 ±.1	68000±1000	330±20	99.0 ±.07	99.1±.1
Au1	0.90±.03	2.65±.1	70200±1200	330±20	99.07±.07	99.0±.1
Au2	0.93±.06	1.7 ±.15	70000±2000	560±50	98.5 ±.2	98.6±.1
Cr	2.65±.1	0.41±.02	43500±500	780±50	96.7 ±.1	96.8±.1
Co	3.4 ±.1	0.34±.01	36160±600	700±40	96.4 ±.2	96.5±.1

In these experiments n_e and L were measured using different techniques but actually both values can be drawn from interferometric measurements. It was demonstrated in the studies of SEW on the materials with small propagation length. High T_c superconductors (ceramics, single crystals and films of $YBa_2Cu_3O_{7-\delta}$) were studied using SEW phase spectroscopy [5,6]. Free carrier parameters were obtained at room temperature. It was shown that the concentration of free carriers is temperature independent.

Dielectric surfaces were extensively studied using SP as well as SEW spectroscopy. Spectra of transition layers created by ion implantation of crystalline quartz and fused silica were studied [7,8]. Optical constants of ultrathin metal films on quartz were obtained [9,10].

As the propagation length of surface plasmons on good conducting metals is several cm they are especially applicable for monolayers spectroscopy. The high sensitivity of SEW spectroscopy was demonstrated by the experiments performed with the lasers as radiation sources. The SEWs were used for studies of metals oxidation and of metal-dielectric phase transition in thin VO_2 layers on vanadium. Optical constants and their temperature behavior including histeresis were studied.

The spectral range of lasers available is restricted. That prevents to study many interesting systems by SEW technique. Use of the thermal broad-band source of IR radiation and Fourier-transform IR spectrometers needs very sensitive detectors. The broad-band FTIR SEW spectroscopy is developing now [11,12]. New possibilities can offer with the use of the synchrotron radiation in SEW spectroscopy.

REFERENCES

1. Surface Polaritons, ed.V.M.Agranovich and D.L.Mills, (North-Holland Publ.Co,1982).
2. S.F.Parker, M.A.Chesters and V.A.Yakovlev, Opt.Commun.,55(1985)1.
3. G.N.Zhizhin, S.A.Kiselev, L.A.Kuzik and V.A.Yakovlev, Computer Optics, 2(1990)167.
4. V.I.Silin, S.A.Voronov, V.A.Yakovlev and G.N.Zhizhin, Int.J. of Infrared and Millimeter Waves,10(1989)101.
5. G.N.Zhizhin, A.F.Goncharov, S.A.Kiselev, L.A.Kuzik and V.A.Yakovlev, Physics Lett.A,133(1988)163.
6. E.V.Alieva, G.N.Zhizhin, L.A.Kuzik, E.V.Pechen', E.I.Firsov and V.A.Yakovlev, Sov.Phys.JETP,70(1990)315.
7. G.N.Zhizhin, K.T.Antonova and V.A.Yakovlev,Int.J. of Optoelectronics, 5(1990)439.
8. S.A.Voronov, G.N.Zhizhin, G.Schirmer and V.A.Yakovlev, Opt. and Spectr., 67(1989)375.
9. E.V.Alieva, E.I.Firsov, L.A.Kuzik and V.A.Yakovlev, Physics Lett.A, 152(1991)89.
10. G.N.Zhizhin, L.A.Kuzik, V.N.Spiridonov, V.A.Yakovlev, P.Grosse and B.Heinz, in Proc. of the 8-th Int. Conf. on Fourier Transform Spectroscopy, Lubeck-Travemunde,1991.
11. G.N.Zhizhin and V.A.Yakovlev, Physics Reports,194(1990)281.
12. G.N.Zhizhin, A.A.Sigarev and V.A.Yakovlev, J. of Molecular Liquids, 53(1992)1.

Infrared surface wave heterodyning on metals and semiconductors

V.Vaičikauskas, R.Petruškevičius, R.Antanavičius, R.Januškevičius

Institute of Physics, A.Goštauto 12, 2000Vilnius, Lithuania

Surface electromagnetic waves (SEW) due to their unique field distribution (field maximum occurs at the two adjacent media interface) is a highly sensitive instrument for studying both metal surfaces and thin films on them. The experimentally measurable parameters in SEW experiments are the SEW propagation distance L ($L=1/4\pi\nu n''_{ef}$) and the real part of SEW refraction index n'_{ef} ($\tilde{n}_{ef}=\left(\frac{\varepsilon_1\varepsilon_2}{\varepsilon_1+\varepsilon_2}\right)^{1/2}$). For metals in middle and far infrared region γ, $\nu\ll\omega_p$ (ν_p, γ - plasmon frequency and damping constant) n'_{ef} is directly determined by plasma frequency. Therefore, the difference between the light line $k_o=\omega/c$ and the surface polariton dispersion curve $k_{sp}=\omega/c\tilde{n}_{ef}$ is insignificant and in such circumstances the measurement of n'_{ef} is problematic. Usually it is measured by scanning interference pattern of bulk radiation with SEW launched on the sample edge [1]. In the FIR region SEW propagation distance on metals is too large (a few meters) and transparent films are sputtered on a metal surface with the purpose to press SEW field to the surface [2]. For SEW phase spectroscopy in doped semiconductors additional is film not requires [3]. Another method, proposed in [4], is based on SEW heterodyning and was realized on gold and copper at CO_2 -laser frequencies.

In the present work FIR SEW heterodyning on stainless steel overcoted with Ge film ($d=0.6\mu m$) as well as on semiconductors n-GaAs(Te) was carried out firstly. Optically pumped cw CH_3OH-laser operating at frequencies 85, 103 and 142 cm^{-1} was used as a radiation source. Unlike the conventional method, the bulk radiation modulated by frequency $\Delta\nu\ll\omega$ is directed along the sample surface perpendicular to two gratings, placed at $l=1cm$ distance. The scattered by wire gratings (30 and 100μm period) SEW and bulk radiation are collinear and signal beatings at frequency $\Delta\nu$ on two detectors, placed under sample have been registered. The phase difference $\Delta\varphi$ between signals can be expressed as $\Delta\varphi=(k'_{sp}-k_o)l$, where $k_o=2\pi\nu$ and surface polariton wavevector $k_{sp}=\frac{\nu}{c}\Re n_{ef}$.

For doped semiconductors A^3B^5 the Drude electron distribution as well as phonon one must be included in ε_2. In the case of degenerate semiconductors plasma frequency ν_p approaches the longitudinal optical phonon frequency ν_{LO} and as a result of plasma-phonon interaction two branches of surface polaritons appear. The lower one is plasmon type in the small wavevectors region. That means the complex SEW refraction index $\tilde{n}$ is determined by electron plasma. Neglecting phonon distribution into ε_2 the expression of n'_{ef} was received:

$$n'_{ef}-1=\left[\left(\frac{\nu}{\nu_p}\right)^4-\left(\frac{\nu}{\nu_p}\right)^2+\frac{\nu^2\nu^2}{\nu_p^4}\right]\Big/\left[\left(\frac{\nu}{\nu_p}\right)^2-1+\frac{\nu^2\nu^2}{\nu_p^4}\right]. \qquad (1)$$

From SEW experiments ν_p value was obtained at three different electron concentrations and quite good agreement with IR reflectance data taking into account plasma - phonon interaction and nonparabolity of conduction band was achieved (Table 1). Plasmon

Table 1. The experimental values of plasma frequency in n-GaAs(Te)(in cm^{-1}) and steel obtained by IR reflectance and SEW (ν=103cm^{-1}) methods (conventional and heterodyne).

Material	N,cm^{-3}	ν_p(IR)	ν_p(conv)	ν_p(het)	γ,cm^{-1}	L,mm
GaAs	7.0×10^{17}	275	272	270	47	3.3
	1.4×10^{18}	510	506	503	61	5.9
	3.3×10^{18}	570	576	572	71	9.1
Steel+Ge	-	-	28000	27500	400	38.0

damping constant γ was calculated from measured SEW propagation distance L. The combined amplitude and phase SEW experiments allowed us to get ν_p and γ for stainless steel, too.

1. V.I.Silin., S.A.Voronov, V.A.Yakovlev and G.N.Zhizhin. Int. J. IR and MM Waves. Vol.10, No 1, pp.101 - 119, 1989.

2. Z.Schlesinger, B.C.Webb and A.J.Sievers. Sol. St. Comm. Vol.39, pp.1035 - 1039, 1981.

3. V.Vaičikauskas. SPIE. Vol 1723, pp.181 - 187, 1991.

4. M.N.Libenson, V.S.Makin and V.V.Trubaev. SPIE. Vol.1440, pp.354-356, 1990.

SURFACE ELECTROMAGNETIC WAVE PROPAGATION ON NACLO$_3$ AND KTP CRYSTALS

E.V.Alieva, L.A.Kuzik and V.A.Yakovlev

Institute of Spectroscopy, Academy of Science of Russia
Troitzk, Moscow reg., 142092, Russia

Sodium chlorate - $NaClO_3$ and potassium titanil phosphate - $KTiOPO_4$ (KTP) single crystals were studied in the mid infrared (IR) using IR reflectivity, surface polariton (SP) dispersion and surface electromagnetic wave (SEW) measurements.

IR reflectivity spectra were measured using Fourier transform spectrometer DA3-36 (BOMEM). From these spectra complex dielectric function was calculated using Lorenz oscillators fit (dispersion analysis DA) and Kramers-Kronig method. SP dispersion and SEW complex effective refractive index were calculated too. For both crystals in the region of CO_2 laser operation SP exist and SEW have measurable propagation length. SP spectra were studied by attenuated total reflection technique using "Michelson-110" (BOMEM) Fourier transform spectrometer.

SEW propagation measurements were made using tunable CO_2 laser.The radiation of the CO_2 laser was focused onto the slit between the sample being investigated and the screen placed at a distance of the order of the wavelength from the sample. A part of radiation is transformed into a SEW which propagates along the surface and converts into a bulk wave at the edge of the sample. This wave interferes with the bulk wave diffracted at the exciting aperture. The interference pattern is recorded by a pyroelectric detector which is uniformly moving along the arc with the slit as center. The angular positions of the extrema φ_m of the order of m/2 are determined by

$$1-\cos\varphi_m = 1-n_e+\frac{m+\Delta}{2a\nu}$$

where m is even for maxima and odd for minima, Δ is the phase shift between the SEW and the bulk wave on the exciting aperture, a is the distance that SEW have run along the surface. The modulation depth of the interference pattern depends on the SEW absorption. So SEW propagation length L can be evaluated using the relationship

$$a/L = 2\ln\frac{\sqrt{I_{max}}+\sqrt{I_{min}}}{\sqrt{I_{max}}-\sqrt{I_{min}}}+A$$

where the intensities I_{max} and I_{min} are determined by the envelopes of maxima and minima, respectively for the appropriate angle value, A is determined by the efficiency of the SEW excitation and at the distances a much less then the distance to the detector is independent of a.

The interference patterns obtained for different laser frequencies at the same distance between excitation point and the sample edge are shown in Fig.1.

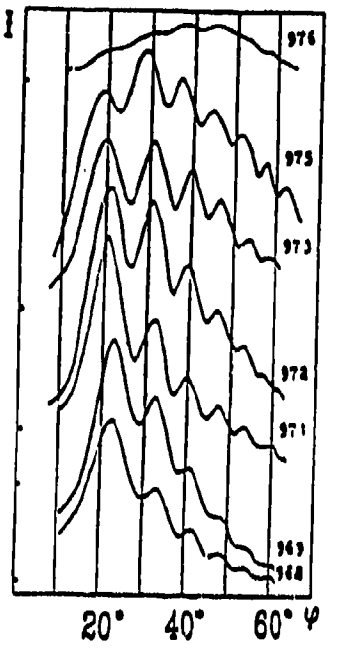

Fig. 1. Interferograms for $NaClO_3$ crystal in 10.3μm region.

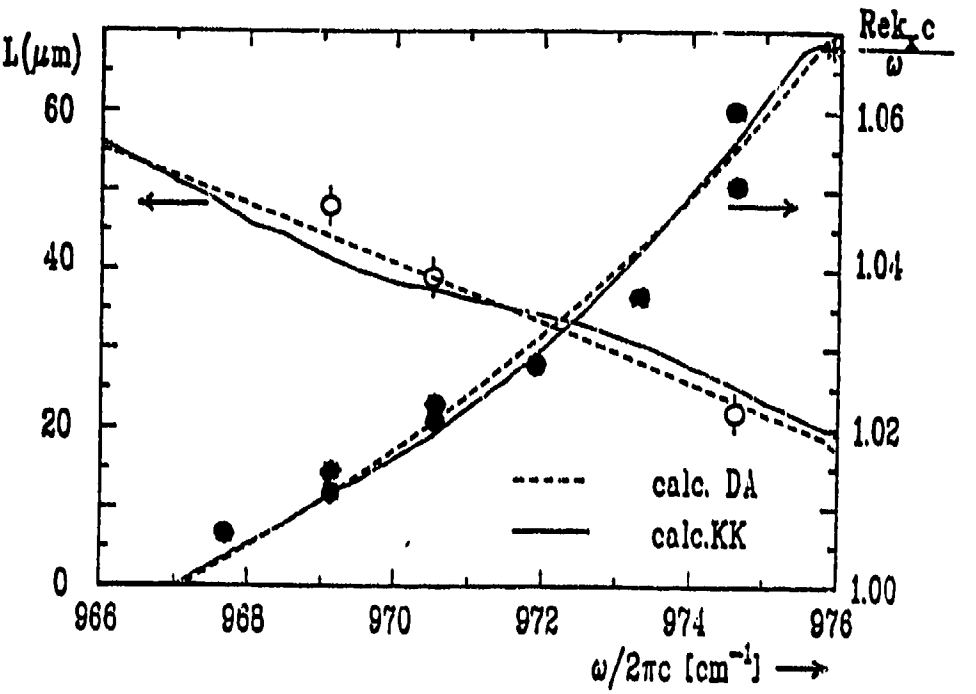

Fig. 2. SEW effective refractive index (closed circles) and propagation length (open circles) on $NaClO_3$-air interface.

The maximal value of SEW propagation length is 50μm at 967cm^{-1}. Experimental points for SEW effective refractive index and propagation length are in a good agreement with calculated using complex dielectric function obtained from reflectivity using DA (dashed lines) and Kramers-Kronig (full lines) methods (see Fig. 2).

For anisotropic KTP crystal SP and SEW measurements are more complicated and time consuming, because this crystal is biaxial and the SP characteristics along each of dielectric function principal axes depend also on the orientation of other axes. We have made SP and SEW measurements on the ab plane along a and b axes. A remarkable anisotropy of SEW propagation could be observed at 9.5μm and 10.3μm CO_2 laser regions.

The authors would like to express their gratitude to Prof. G.Mattei and Prof. M.Pagannone (Istituto di Metodologie Avanzate Inorganiche, CNR, Italy) and to Prof. V.A.Sychugov (Institute of General Physics, Academy of Sciences of Russia) for samples presentation and fruitful discussion of results.

INTERFEROMETRIC MEASUREMENTS OF PHASE SHIFT IN THE IR REFLECTION-ABSORPTION SPECTROSCOPY

L.A.Kuzik, A.B.Sushkov, V.A.Yakovlev and G.N.Zhizhin

Institute of Spectroscopy, Academy of Sciences of Russia
Troitzk, Moscow reg., 142092 Russia

Infrared reflection-absorption spectroscopy (IRRAS) [1] is widely used to study surfaces. In this technique the reflectivity of p-polarized radiation or its ratio to the reflectivity in s-polarization is measured at grazing incidence. However the only measured value is not enough to determine optical constants without using any model for frequency dependence of the dielectric function of the material under study.

In the spectroscopy of surface electromagnetic waves (SEW) such problem is solving using interferometric measurements [2]. Although for well conducting metals SEW spectroscopy is more sensitive [3] but for metals with low conductivity this advantage is disappeared [4]. So to study various metals in optimal conditions it seems to be very useful to combine both techniques in one unit and to switch them according with sample under study. Such combining is possible using aperture excitation of SEW [3,5]. In this case at small coupling gap between the screen and the metal surface SEW excitation takes place but for larger gaps the efficiency of SEW excitation is small [6] and we have only IRRAS signal.

The measurements were made using Fourier-transform infrared spectrometer "Michelson-110" (BOMEM) with liquid nitrogen cooling MCT detector. The scheme of experiment is shown in fig.1. IR radiation fall on the slit between the sample surface and the screen. The slit width z_1 is several tenths of mm. The field distribution in the plane of the output slit can be presented as a sum of fields of two beams. One of them propagates from the input slit near the surface, another one is reflected from the surface at grazing incidence. Output slit placed on the distance z_2 from the surface plane is focused on the detector. So for each point z of the input slit the phase shift Δ between two beams on output slit takes place according to equation

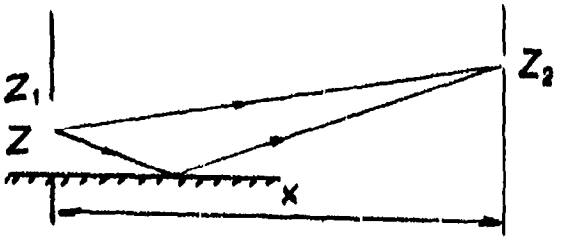

Fig.1. The scheme of the experiment.

$$\Delta = \sqrt{(z+z_2)^2+x^2} - \sqrt{(z-z_2)^2+x^2} - \delta$$

where δ is the phase shift at the reflection from the sample. Thus we can expect an interference between these two beams that should be different for s- and p- polarized radiation because δ is different for s- and p-polarizations. That can give us the possibility to measure phase shift between p- and s-polarized radiation after reflection (the same value is measured in ellipsometry). Such two beam interference takes place in the geometry close to "Lloyd's mirror".

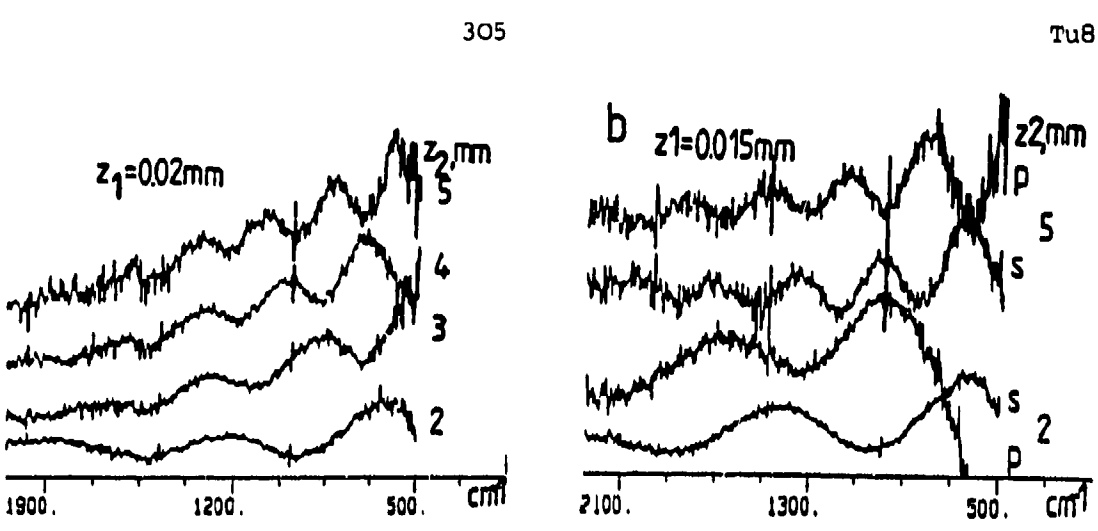

Fig.2. Interference patterns in the spectra a) s-polarization for different positions of output slit and b) p- and s-polarizations for two positions of output slit.

In the experimental spectra obtained in the geometry described above interference is easy observable. The spectral interference patterns are shown in fig.2 for different positions of output slit and for two polarizations. The higher is z the less is the distance between extrema. The shift between p- and s-polarizations is close to a half of the wavelength for small angles of incidence and decreases for grazing incidence. The interference extrema positions in the spectra at the different angles of incidence for s- and p-polarization as functions of interference order are approximately linear. But the phase shift δ_n for s- polarizations does not coincide with calculated one. It seems to be due to the averaging of interfering beams from different points of the input slit. To take it into account we have calculated field distribution in the diffracted on the input slit wave for p- and s- polarizations in similar way as it was made in [7]. This calculations have shown that actually phase shifts are averaging on the slit but they can be drawn from the analysis of interferograms.

REFERENCES

1. R.G.Greenler, J.Vac.Sci.Technol.,12(1982)1410.
2. V.I.Silin, S.A.Voronov, V.A.Yakovlev and G.N.Zhizhin, Int.J. of Infrared and Millimeter Waves,10(1989)101.
3. G.N.Zhizhin and V.A.Yakovlev, Physics Reports,194(1990)281.
4. A.F.Vasilev, N.Yu.Gushanskaya, G.N.Zhizhin, A.A.Sigarev and V.A.Yakovlev, Opt.Spectrosc.,69(1990)364.
5. S.F.Parker, M.A.Chesters and V.A.Yakovlev, Opt.Commun.,55(1985)1.
6. G.N.Zhizhin,S.F.Parker, M.A.Chesters and V.A.Yakovlev, Opt.Spectrosc., 65(1988)223.
7. G.N.Zhizhin, S.A.Kiselev, L.A.Kuzik and V.A.Yakovlev, Computer Optics, 2(1990)167.

Spectroscopy of confined LO phonons in superlattices: a probe for study of interfacial disorder

M.I.Vasilevskiy

Faculty of Applied Physics and Microelectronics,
Nizhni Novgorod State University
37 Sverdlova str., Nizhni Novgorod, 603000 Russia

Spectroscopy of light scattering on LO phonons confined in short-periodicical superlattices (SL) is known to be sensitive to a small-scale structure existing on the interfaces [1]. Recently [2], we have developed a 1D lattice dynamics model providing both mode shifts and the shape of the lines due to broadening of the interfaces. Simple results were obtained for two cases:
(i) if the alloy of constituent materials exhibits explicit two-mode behaviour (for instance, (AlGa)As), the modes of both (AlAs-like and GaAs-like) optical subbands move downwards with respect to the ideal SL;
(ii) if the alloy displays an intermediate type of optical behaviour (but the confinement still exists), the modes of the two subbands move towards each other, as was observed experimentally in ref. [3] for the GaAs/InAs SL.

However, in the case (i) this model predicts a monotonous increase of the shift with mode number, in contradiction with experimental data [1]. The model involves an ensemble of linear chains, each with either Ga or Al atoms in appropriate sites, and the confinement is even stronger for higher mode numbers. In reality, such phonons (of lower frequency) can propagate in the alloy.

Here we suggest a scheme of improvement of the model [2] taking this fact into account. Instead of a virtual-crystal approximation *in plane* implied in [2], we treat each cation plane as a bulk alloy sample of a given composition. Thus, a basic formula for the average Green function

$$Sp\langle G\rangle = \sum_z f(z)\,Sp\bar{G}(n-2z)$$

is still valid (z is the 'push-out' length [2] calculated separately for the GaAs and AlAs layers, f - a partition function for this random variable, and $\bar{G}$ corresponds to GaAs-like or AlAs-like phonons confined in the ideal SL with (n-2z) monolayers while the actual number of monolayers of GaAs or AlAs respectively is n). However, now z is frequency-dependent and defined according to $w=w^{max}(x(z))$, where w^{max} is the maximum frequency of the corresponding LO subband in the alloy of the composition x. More precisely, it corresponds to the appropriate peak of the zone center spectral density of states. This can be either taken from the experiment or calculated. In the latter case possible effects of composition correlations *in plane* can be taken into account (see, for example, [4]).

Figs.1 and 2 show how the shift of the modes and the shape of the line (i.e broadenig of the confined LO modes) depend on average composition distribution near the interfaces. Here we used just a simple linear interpolation for the $w^{max}(x)$ function, and did not consider any *inter-plane* composition correlation. The latter should change f(z) from the Gaussian, thus affecting the shape of the line.

In conclusion, the improved 1D model has been very fruitful in demonstrating the essential features of the SL phonon modes, and it is suitable for analysing the effects of non-random composition distribution near the interfaces due to specific features of a techique used for SL fabrication.

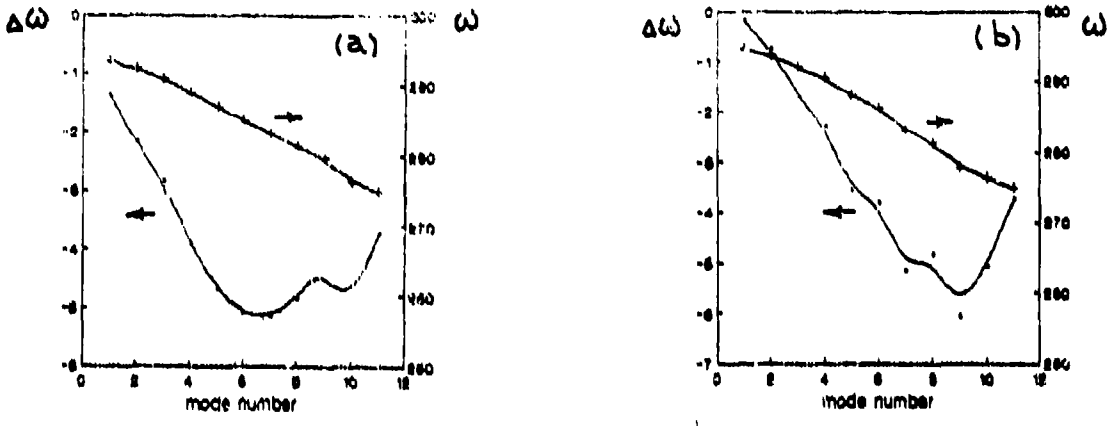

Fig.1. LO phonon frequency and the mode shift (solid line) vs mode number for the GaAs-like subband (a- *erfc*, b- linear composition profile)

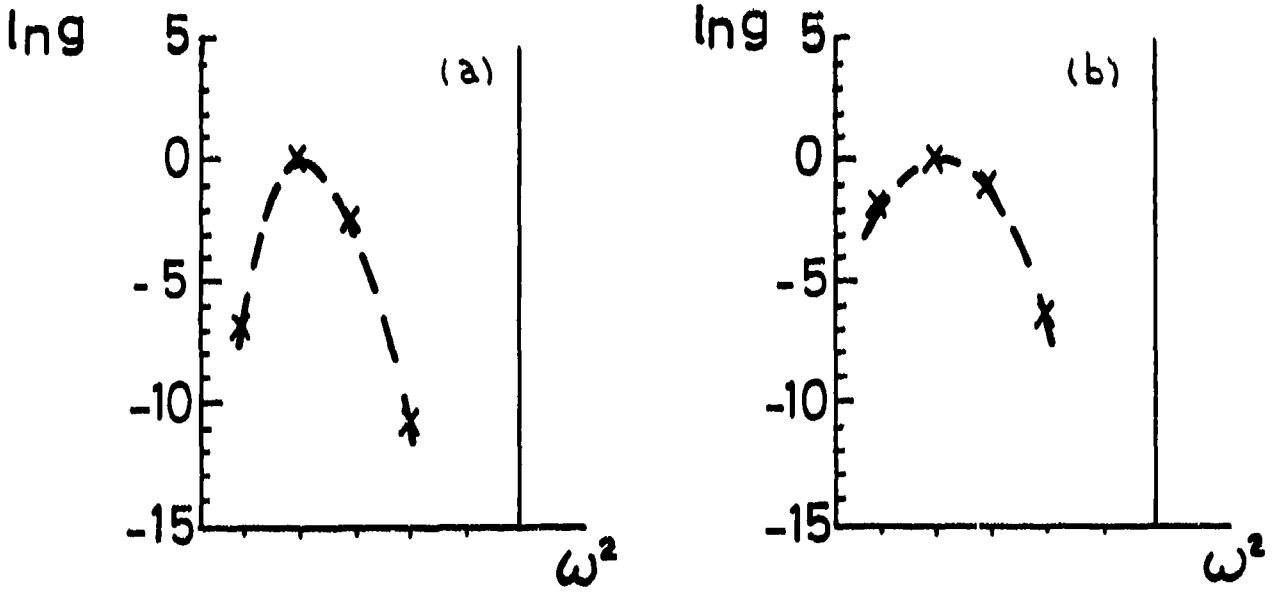

Fig.2. The phonon density of states for the LO_3 GaAs mode for *erfc* (a) and linear (b) composition profile. δ-like peaks correspond to the ideal SL.

References

1. D.Gammon et al., Phys. Rev. Lett. 67, 1547 (1991).
2. M.I.Vasilevskiy, J. Phys.: Condens. Matter 4, 4509 (1992).
3. V.A.Gaisler et al., Zhurn. Eksp. Teor. Fiz. 98, 1081 (1990).
4. O.V.Baranova and M.I.Vasilevskiy, J. Phys.: Condens. Matter 4, 9299 (1992).

FAR INFRARED SPECTROSCOPY OF PHONONS IN GaInAs/InP SUPERLATTICES

T.S. Sethi[1], J P. Bryant[2], A.A. Hamilton[2], T. Durnelow[2], W.F. Sherman[1] and T.J. Parker[2]

1. Department of Physics, King's College London, Strand, London WC2R 2LS, UK.
2. Department of Physics, University of Essex, Wivenhoe Park, Colchester CO4 3SQ, UK.

Far infrared spectroscopy is a technique increasingly used to study phonons in superlattices. Such phonon investigations are potentially useful for studying interface roughness[1], which affects the phonon spectrum by two mechanisms:

(i) The extent of phonon confinement within individual superlattice layers is governed by the layers' effective thicknesses. These thicknesses are, in turn, affected by the width of the interfaces, i.e. the interface roughness. Since confinement shifts the phonon frequencies from their bulk values, the spectral features are shifted to an extent dependent on interface quality.

(ii) Layers having nominal single crystal structure may behave as alloys due to the intermixing of atoms from different layer types. The observed phonon frequencies in this case thus become the relevant alloy frequencies.

Superlattice phonons for a superlattice with interface roughness can be modelled using, for instance, the random element isodisplacement (REI) model of Samson *et al*[1], and both the above mechanisms contribute to the resultant resonant phonon frequencies. Most studies of such phenomena have concentrated on GaAs/AlAs superlattices; in these the first mechanism dominates the behaviour of the GaAs-like modes and the second mechanism dominates the behaviour of the AlAs-like modes. The $Al_xGa_{1-x}As$ alloy that produces the AlAs-like mode has two-mode phonon behaviour. In this paper we examine far infrared results from a GaInAs/InP superlattice. In particular, we observe the effect of alloying on the InP-like mode, noting that an $In_xGa_{1-x}P$ alloy has single-mode phonon behaviour[2].

The sample consisted of 20 periods of 17 Å $Ga_{0.47}In_{0.53}As$/InP and 17 Å InP, grown on an InP substrate with buffer layer by molecular beam epitaxy (MBE). Infrared reflectivity measurements were performed at 77 K with the output beam of a laser controlled Michelson interferometer incident on the sample at an angle of 60°. A polariser was placed in front of the Golay detector.

Both s- and p-polarisation spectra are shown in the figure. The large increase in reflectivity in the region 300-350 cm^{-1} is within the reststrahlen region of InP, and this is the most dominant feature because InP is the substrate material as well as the one of the superlattice components. We concentrate on features in this region because they dominate the spectrum. It should be noted that the presence of the substrate reststrahl can actually enhance features of interest.

Comparison of the two figures shows that there is no significant feature in the p-polarisation spectrum that does not appear in the s-polarisation spectrum. This contrasts with the case when strong confinement occurs. In the latter case sharp dips occur at confined LO frequencies in p-polarisation but are absent in s-polarisation[1]. In the case considered here, however, confinement effects appear to be so small and the

superlattice so thin that no confined LO feature can be resolved. This interpretation is consistent with the small dispersion present in the InP phonon dispersion curve.

Because confinement effects are small we have modelled the dielectric response of the superlattice in terms of a bulk slab model in which each layer is considered as an isotropic bulk. In the long wavelength limit the resulting dielectric functions may be averaged to give a uniaxial dielectric tensor with principal components

$$\varepsilon_{xx} = \varepsilon_{yy} = (\varepsilon_1 d_1 + \varepsilon_2 d_2)/(d_1 + d_2)$$

$$\varepsilon_{zz}^{-1} = (\varepsilon_1^{-1} d_1 + \varepsilon_2^{-1} d_2)/(d_1 + d_2)$$

where ε_1 and ε_2 are the dielectric functions of the two superlattice layers of thickness d_1 and d_2 respectively. z is taken as the growth direction.

In order to model the dip at ~ 335 cm^{-1} in both spectra it is necessary to assume that some Ga atoms have migrated from the $Ga_{0.47}In_{0.53}As$ layers to the InP layers. Thus we consider the superlattice as $Ga_{0.37}In_{0.63}As/Ga_{0.1}In_{0.9}P$ (the migration of P or As is not considered because it does not lead to such pronounced features). The main effect of alloying a small amount of Ga into the InP layers is to introduce an extra oscillator at 336 cm^{-1}. Such a mode is consistent with that observed in $Ga_{1-x}In_xAs$ by Lucovsky *et al*[2]. The dip at ~ 335 cm^{-1} therefore corresponds to this mode, and there is good agreement between theory and experiment using this interpretation. The main observable effect in the $Ga_{0.37}In_{0.63}As$ layer spectrum is a small shift (~ 5 cm^{-1}) in the InAs-like TO frequency.

In summary, we have shown that a sharp feature in the far infrared spectrum can be directly related to superlattice quality in the GaInAs/InP superlattice system grown on an InP substrate. This feature shows up within the reststrahl region of the InP, and is due to Ga impurities in InP.

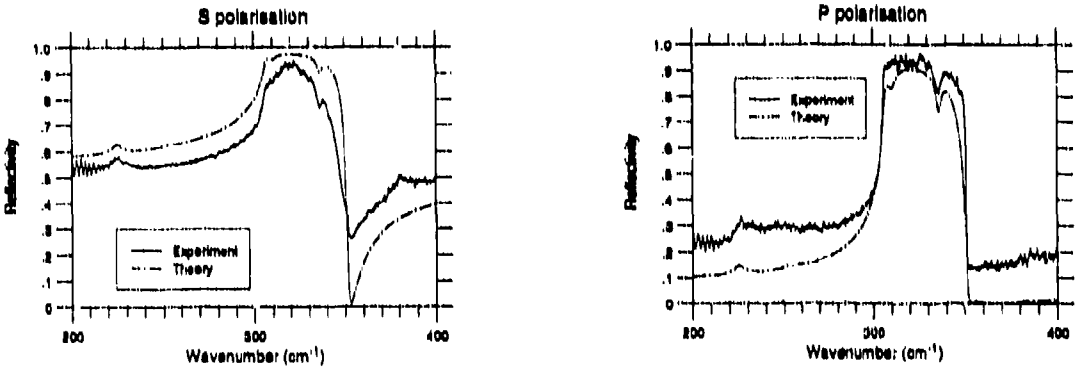

1. B. Samson, T. Dumelow, A.A. Hamilton, T.J. Parker, S.R.P. Smith, D.R. Tilley, C.T. Foxon, D. Hilton and K.J. Moore, Phys. Rev. B46, 2375 (1992).
2. G. Lucovsky, M.H. Brodsky, M.F. Chen, R.C. Chicotka and A.T. Ward, Phys. Rev. B4, 1945 (1971).

QUANTUM SIZE OSCILLATIONS IN OPTICAL AND ELECTRIC PROPERTIES OF SUPERTHIN NB AND CU FILMS

L.A.Kuzik, Y.E.Petrov, V.A.Yakovlev

Institute of Spectroscopy, Academy of Sciences of Russia, Troitzk, Moscow reg., 142092 Russia

F.A.Pudonin

P.N.Lebedev Physical Institute, Academy of Sciences of Russia, Moscow, Russia

Optical properties and DC conductivity of superthin niobium (1Å-100Å) and copper films on crystalline α-quartz and silicon have been studied. The metal films were prepared by radio frequency sputtering. Such films show metallic behavior even for the thickness of a few Å. All measurements were made on air. To avoid oxidation the metal films were coated immediately after deposition by 40Å thick protective silicon film.

We have used reflection and transmittance infrared spectroscopy to study these films. Infrared spectra were obtained using Fourier-transform spectrometer in the region 400-5000cm^{-1}. Imaginary part of dielectric function of the film was estimated from these spectra using approximate formulae valid for very thin films.

In the thickness dependence of $Im\epsilon$ of Nb film deposited on silicon as well as on quartz oscillations with a period ≈6Å exhibit. In [1] we had reported the observation of one maximum in the $Im\epsilon$ at the film thickness 6Å. In [2] we have measured Nb films with thicknesses 1.5-27Å on quartz and could observe four maxima separated by 6Å. For Nb films on silicon such oscillations are exhibiting up to the thickness 70Å.

Direct current resistivity was measured for Nb samples on quartz substrates using the four point technique. All films thicker than 6Å exhibit metallic conductivity and ohmic voltage to current dependence. DC conductivity oscillates with 6Å period too.

Using the Drude model we have calculated the plasma frequency and frequency of electron collisions from DC and optical measurements. Both these values oscillates with the same period as the conductivity.

The same nonmonotonous thickness dependencies can be observed in surface polariton [3] and surface electromagnetic wave [4] measurements of Nb films on quartz substrates. Temperature measurements of reflectivity and DC resistance have shown that the period as well as the relative amplitude of oscillations are practically temperature independent [5].

Thus the oscillations with a period of several Å were found on the film thickness dependence of optical and electric

characteristics. These oscillations exhibits the same period for various sets of samples made of the same metal in slightly different conditions. This period was found to be different for different metals. For niobium films the period was ≈6Å, for copper films it was ≈2Å. For both metals we could observe at least a dozen of periods on the thickness. So conductivity at the infrared frequencies and DC one are periodic functions of the film thickness with a period 6Å. This value is of the order of Fermi wavelength of conduction electron for this metals. The dependence of the optical and electric properties on the geometrical dimensions comparable with the electron Fermi wavelength can be attributed to the presence of the quantum size effects.

The theory of the quantum size effect in electric conductivity for semimetals was given by Sandomirskii in [6]. From this theory follows that DC conductivity is a periodic function of the film thickness with the period equal to a half of the electron Fermi wavelength. This conclusion was confirmed by experimental studies of bismuth [7]. antimony and tin [8] films. The oscillation period for these materials was dozens or hundreds Å. It becomes possible to observe the oscillations in such metals as Nb or Cu with several Å period only due to the use of radio frequency sputtering with precise film thickness control. For metals this effect was first observed in a set of different samples but not on one specially prepared sample as in [8], the period being constant for different sets of samples.

According to the Sandomirskii theory we can explain the similarity of the oscillations at different temperatures by the fact that the distance between the energy levels in a quantum well near the Fermi energy for a Nb film of the thickness under study is of the order of eV. That is much higher than kT. Thus the Sandomirskii theory gives a qualitative description of our results.

REFERENCES

1. E.V.Alieva,E.I.Firsov,L.A.Kuzik,V.A.Yakovlev and F.A.Pudonin, Physics Letters, A152,(1991)89.
2. L.A.Kuzik,Yu.Ye.Petrov,V.A.Yakovlev,G.N.Zhizhin and F.A.Pudonin, Physics Letters, A171,(1991)418.
3. G.N.Zhizhin,L.A.Kuzik,V.N.Spiridonov,V.A.Yakovlev,P.Grosse and E.Heinz, in Proc. of the 8-th Int. Conf. on Fourier Transform Spectroscopy, (Lubeck-Travemunde,1991).
4. E.V.Alieva,F.A.Pudonin and V.A.Yakovlev, (to be published).
5. L.A.Kuzik,Yu.Ye.Petrov,V.A.Yakovlev,G.N.Zhizhin, F.A.Pudonin, P.Grosse and V.Offermann, (to be published).
6. V.B.Sandomirskii, Sov.Phys.JETP,25(1967)101.
7. Y.F.Ogrin,V.N.Lutskii, JETP Letters,3(1966)71.
8. Y.F.Komnik,E.N.Buchstab, JETP Letters,6(1967)58;ibid.8(1968)4.

NON-LINEAR DOPPLER SHIFT OF THE PLASMON RESONANCE IN A GRATING-COUPLED DRIFTING 2DEG

R E Tyson, R J Stuart, H P Hughes, J E F Frost, D A Ritchie, G A C Jones and C Shearwood

University of Cambridge, Cavendish Laboratory, Madingley Road, Cambridge CB3 0HE, U.K.

Experimental and computational investigations of the plasmon resonances of a two dimensional electron gas (2DEG) in the far-infrared have been performed. The object was to study the effects of laterally drifting the 2DEG, that is giving the electrons a net velocity in the plane of the charge sheet. The simplest description of the effect of drifting the 2DEG is in terms of a Doppler shift in the plasmon frequency . For the case of the plasmon wavevector k_x and the drift velocity v_d being parallel, there are two plasmon modes (travelling up and down stream with respect to the drift) and their Doppler shifted plasmon frequencies are (ω_0 being the plasmon frequency in a stationary 2DEG):

$$\omega_\pm = \omega_0 \pm k_x v_d \qquad (1)$$

The situation is complicated by the need to use a coupling structure, such as an overlaid metal grating close to the 2DEG, to match the frequency and wavelength of the plasmon to that of the electromagnetic radiation. The periodicity of a grating overlaid on the structure causes the dispersion relation to become zone-folded and gaps open at the Brillouin zone boundary and at the zone centre, Figure 1. Therefore at zero drift velocity there exist two first order plasmon modes. The in-plane electric field profiles of these two modes are standing waves which are either symmetric (and hence radiative) or antisymmetric (and hence non-radiative) about the centre of a grating finger, assuming a symmetric grating profile.

The scattering matrix method [1] has been extensively used to model the electromagnetic response of stratified systems including gratings and 2DEGs. It is a full electromagnetic field calculation which implicitly takes into account the screening effects of the grating. Calculation of the plasmon frequency as a function of drift velocity shows that there is a splitting at zero drift velocity caused by periodic grating gate screening, and that the plasmon frequency shift is not linear with drift velocity, again because of the grating screening. The calculated plasmon frequencies of the 2DEG with a grating coupler do approach the linear Doppler shift of Equation (1) at sufficiently high drift velocity, shown in Figure 2.

Computing the transmission of the sample structure for varying drift velocity shows that with increasing drift velocity the initially non-radiative (upper) mode begins to couple, and the coupling strength of the lower mode decreases. This can be understood in terms of the oscillating 2DEG number density profiles at these resonant frequencies, which become travelling waves when the 2DEG is drifted, rather than standing waves under the grating for a stationary 2DEG; the travelling character of the upper mode means that it no longer has a symmetry incompatible with the incident radiation, and can thus couple.

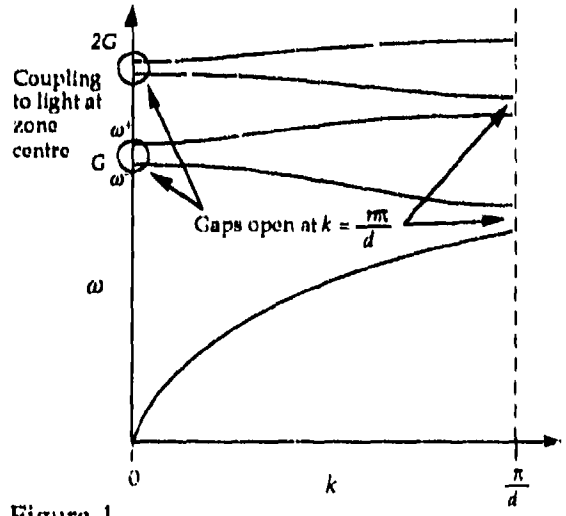

Figure 1.

The samples investigated here were fabricated from MBE-grown, high mobility, AlGaAs/GaAs heterostructure wafer. The grating periods used were 1.0 μm and 0.75 μm. Transmission spectra were obtained of the samples cooled to 10 K using an infra-red Fourier transform spectrometer and a liquid helium cooled silicon bolometric detector. The plasmon spectra taken at a series of drift currents were fitted with a Lorentzian oscillator line-shape to obtain values for the parameters: plasmon frequency, peak height and width. The far-infrared spectra show a downward shift of the plasmon resonance as the drift current is increased; this shift is also non-linear with increasing sheet current density, Figure 3. No splitting of the plasmon is seen, indicating that, at the drift velocities achieved here, coupling to the non-radiative upper mode is still very weak. A larger absolute shift in frequency is measured for the smaller grating period sample, as expected since it has a larger k_x, but the shift for both periods is greater than that predicted by the scattering matrix model. We propose that the additional shift arises from a decrease in the sheet charge density of the 2DEG, N_S, with drift current. The apparent decrease in N_S is approximately linear with current and it is also very similar for the two grating period samples which suggests that the reduction is a consistent electrical effect independent of the grating. At the largest currents passed through the samples the decrease in N_S is only about 3%.

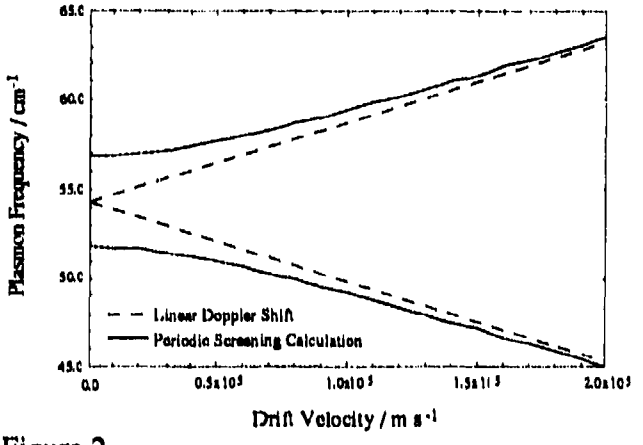

Figure 2.

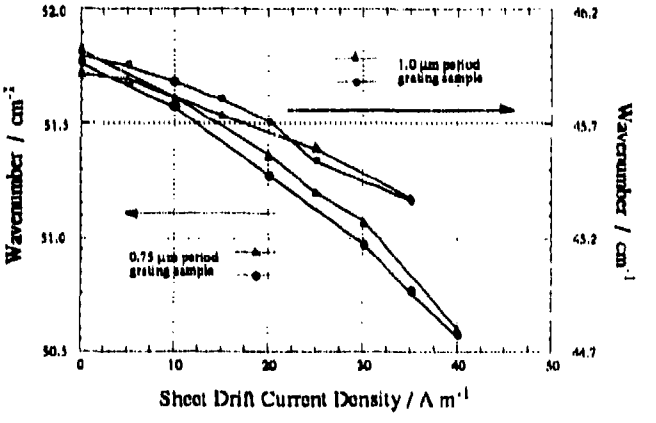

Figure 3.

The width of the plasmon line shape and DC resistance measurements on the 2DEG both show a similar fall in the mobility with applied electric field. This increase in the scattering with electric field results in two problems experimentally. Firstly, the shorter scattering time means that the plasmon amplitude is smaller at a given drift field, which implies that it is more difficult to observe. Secondly, in order to produce high drift velocities the ohmic heating of the sample becomes excessive. The applied electric fields are relatively small (< 5 kVm^{-1}), so the average electron energy is much lower than that needed for intervalley and real space scattering. But the electron energies achieved at the drift fields used here are sufficiently great to cause scattering by the emission of polar optical phonons. A second mechanism which may increase the scattering is the promotion of the electrons to the second 2DEG subband which has a lower mobility and will lower the overall mobility of the electron gas. This again will occur at electric fields of the order of 1 kVm^{-1}. This promotion of the electrons to a higher energy subband may also be responsible for the apparent decrease in number density of the electron gas, since the higher effective mass of the second subband means that those electrons will not participate in the original first order plasmon resonance oscillation.

Work is in progress to observe the plasmon resonance at higher drift velocity, possibly with coupling to the upper mode, using a pulsed electric field to reduce the sample heating.

[1] Ager C D and Hughes H P, *Phys Rev B* **44**, 13452 (1991)

Optical transitions in quantum wires with an axial magnetic field

M.Masale, N.C.Constantinou and D.R. Tilley
Department of Physics, University of Essex.
Colchester, CO4 3SQ U.K.

ABSTRACT

An exact one-electron calculation of the subband energy levels of a cylindrical quantum wire with an axial magnetic field is outlined. Oscillator strengths are obtained for optical transitions between the ground state and first two excited states as a function of the applied magnetic field.

1. SUBBAND SPECTRUM

Recent advances in semiconductor fabrication techniques [1] have made it possible to produce cylindrical quantum wires with diameters on the nanometer scale. For this reason, there has been a renewed interest in the quantum mechanics of particles confined to such wires. The exact solution of the effective-mass Schrodinger equation for a solid cylinder with an axial magnetic field (B) is given in terms of the confluent hypergeometric function [2] (CHF) assuming an infinite square well. We concentrate here on this system although the extension to a hollow cylinder has been recently discussed[3]. The wavefunction in cylindrical co-ordinates (ρ,ϕ,z) is given by [2]

$$\Psi(\rho,\phi,z) = A\, e^{im\phi}\, e^{ikz}\, exp(\zeta/2)\, \zeta^{|m|/2}\, M(a_{mn},b,\zeta) \qquad b=|m|+1,\ m=0,\pm1,\pm2,\pm3,.. \tag{1}$$

where $M(a_{mn},b,\zeta)$ is the CHF, $\zeta=\rho^2/2a_c^2$ with a_c the magnetic length ($a_c^2=\hbar/eB$), k is the axial wavevector and a_{mn} is the nth zero of the CHF obtained from the boundary condition $\Psi(R,\phi,z)=0$, viz.

$$M(a_{mn},b,R^2/2a_c^2)=0 \qquad and \qquad E_{mn}(B) = \hbar\omega_c\left(-a_{mn} + \frac{1}{2}(b+m)\right) \tag{2}$$

with ω_c ($=eB/\mu$) the cyclotron frequency, μ the effective mass, and $E_{mn}(B)$ the subband energy. Figure 1 illustrates the subband energy levels for a cylinder of radius 300Å with parameters appropriate for the GaAs/AlGaAs system. It is seen that for non-zero B the doubly degenerate states ($m\neq0$) are Zeeman split. For small B the splitting is proportional to mB, whilst for larger B the confinement is due to B rather than the potential. In particular, there is a *minimum* in the $m<0$ curves which is intimately linked to the number of flux quanta within the cyclotron radius [2]. The energy level splittings are typically a few meV and are therefore amenable to far infra-red spectroscopy. It is noted here that for a hollow cylinder [3] the ground state is *not* in general the $m=0$ state in striking contrast to the solid cylinder.

2. OSCILLATOR STRENGTHS

We now briefly consider optical absorption between these magnetic subbands. For reasons of symmetry the configuration with clear-cut selection rules will be those of circularly polarised light incident along the cylinder axis. The electric field is $\mathbf{E}=E_0[\cos(\omega t),\pm\sin(\omega t),0]$ in right (+) and left hand (-) polarised light. The interaction potential in the dipole approximation is $W_\pm = \rho eE_0\cos(\omega t\mp\phi)$. Standard analysis then shows that for absorption $m\rightarrow m\pm1$ and stimulated emission $m\rightarrow m\mp1$. The above interaction Hamiltonian together with the *exact* eigenfunctions (eqn.1) provide the basis for a full description of optical absorption. Here we consider the oscillator strength between the ground state ($m=0,n=1$) and the first two excited states ($\pm1,1$). In general the oscillator strength between an initial state (m,n) and a final state (m',n') may be defined as [4]

$$f = \frac{2m_e(E_{m'n'} - E_{mn})}{\hbar^2}\,|\langle\rho\rangle|^2 \tag{4}$$

where $e\langle\rho\rangle$ is the dipole matrix element and m_e is the free-electron mass. Figure 2 illustrates the oscillator strengths for transitions between (0,1) and ($\pm1,1$) as a function of B for the system depicted in figure 1. It is seen that the strengths are equal for B=0 (as they should be), but as B increases the oscillator strength for the $(0,1)\rightarrow(-1,1)$ transition decreases whilst that for the $(0,1)\rightarrow(1,1)$ transition increases initially although for large B it is independent of the field

($\approx 4m_e/\mu$).The insert to figure 2 illustrates the variation of the energy difference ΔE with field for these two transitions. It is hoped that this work will stimulate experimental investigations of intersubband transitions in these novel quasi-one dimensional systems.

3. REFERENCES

1.R.J.Tonucci, B.L.Justus, A.J.Campillo and C.E.Ford, Science **258** 783 (1992).
2.N.C.Constantinou, M.Masale and D.R.Tilley, J.Phys.: Condens. Matter **4** 4499 (1992).
3.M.Masale, N.C.Constantinou and D.R.Tilley, Phys.Rev. **B46** 15432 (1992)
4.D.Ahn and S.L.Chuang, Phys.Rev. **B35** 4149 (1987).

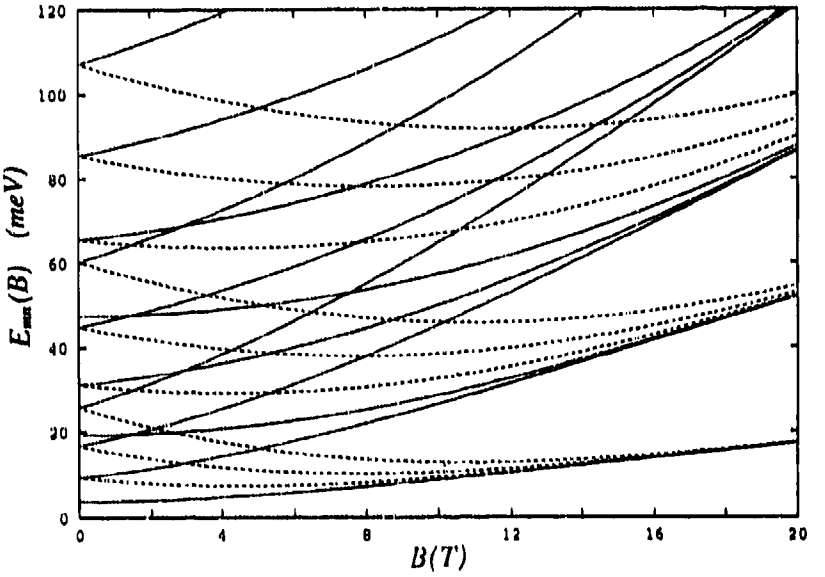

Figure 1.
The subband energy levels for R=300Å as a function of B (full curves m≥0 dashed curves m<0).

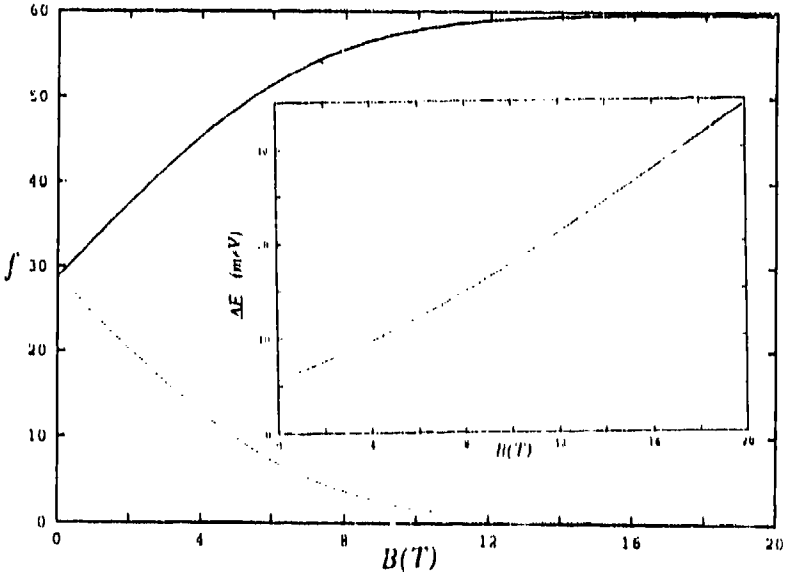

Figure 2.
The oscillator strength as a function of B. The full curve corresponds to the (0,1)→(1,1) transition and the dashed curve to the (0,1)→(-1,1) transition. The insert depicts the energy differences between these two transitions.

Far infrared and Raman study of the effect of growth on the interfaces of asymmetric GaAs/AlAs superlattices.

A Z Mamun[1], J P Bryant[1], T Dumelow[1], T J Parker[1], R J York[1]
S R P Smith[1], C T Foxon[2], J W Orton[3] and K J Moore[4]

1. Department of Physics, University of Essex, Colchester, CO4 3SQ, UK.
2. Dept. of Physics, University of Nottingham, Nottingham, NG7 2RD, UK.
3. Dept. of Electrical and Electronic Engineering, University of Nottingham, NG7 2RD, UK.
4. Dept. of Physics, Manchester Metropolitan University, Manchester, M1 5GD, UK.

Abstract

Phonon confinement in a selection of asymmetric 4-layer GaAs/AlAs superlattice structures grown by molecular beam epitaxy has been studied by polarised far infrared oblique incidence and attenuated total reflection (ATR) spectroscopy and Raman spectroscopy. The results enable measurements to be made of the interface broadening parameters W_i of each interface i. The interface roughness parameter W of a layer of average thickness n monolayers is described by the expression $W^2 = \alpha n n_s/(\alpha n + n_s)$, with $\alpha = 1$ and $n_s = 2$ and 5 for GaAs and AlAs repectively.

I. Introduction

Optic phonons confined in the z direction within a superlattice layer of thickness L have confinement wavevector $k_m = m\pi/L$, and are observable by far infrared and Raman scattering at a frequency $\omega_m = \omega(k_m)$, where $\omega(\mathbf{q})$ is the frequency of bulk phonons with wavevector $\mathbf{q}$. The effective thickness L of a layer depends on the effective width W of the interfaces between the layers in the superlattice. W is determined by the growth process, and depends on the degree of alloying, due to diffusion of adatoms (Ga or Al), and roughness caused by terracing during growth. Thus, measurement of frequencies ω_m can provide information about the effective width W of the interfaces and provides a means of characterising the growth process. The aim of this work has been to measure the effective interface width parameters W, and to provide a model that describes how W depends on the growth conditions of each layer.

The model used to determine the interface roughness of the samples, a one-dimensional linear chain model incorporating alloying, is described by Samson *et al.*[1]. It requires a specification of the average superlattice unit cell composition profile , for which we have used a simple model that attempts to emulate the growth process. The essential feature of the model is the prescription used in describing the interface width parameters W. When a layer of average thickness n monolayers is grown, we assume that the resulting surface, which becomes the interface between this layer and the next, has a width parameter of the empirical form

$$W^2 = \frac{\alpha n n_s}{\alpha n + n_s}, \qquad (1)$$

in which W approaches a saturation limit $\sqrt{n_s}$ when n is large, and the simple statistical limit $\sqrt{\alpha n}$ when n is small. The composition profile, i.e. the fraction P_j of Ga atoms occupying each group III plane j in the superlattice unit cell, is then constructed by assuming that the average composition profile at an interface nominally at $z = 0$ is assumed to have the error function shape $erfc(z/W)/2$.

II. Experimental Measurements and Analysis

The samples studied were grown by molecular beam epitaxy (MBE) on [001] GaAs substrate at 630°C. All the samples had a unit cell of $(AlAs)_{n1}(GaAs)_{n2}(AlAs)_{n3}(GaAs)_{n4}$, where $\sum n_i = 18$. This unit cell was

repeated 400 times to make a complete superlattice with a thickness of approximately 2 μm. The unit cell for all nine samples is given in figure 1, with the direction of growth going from left to right. The frequencies ω_m of the LO(m) (m=1) phonons from the GaAs well s in the samples have been measured by Raman scattering in backscattering $z(x,y)\bar{z}$ configuration at a temperature of 80 K, and by polarised far infrared oblique incidence and attenuated total reflection (ATR) spectroscopy[2].

The construction of the $(AlAs)_{n1}(GaAs)_{n2}(AlAs)_{n3}(GaAs)_{n4}$ superlattices studied here are shown in the figure, and the experimentally measured frequencies (in cm^{-1}) of the GaAs-like LO phonon modes ω_m with $m = 1$ are shown on the right. The samples studied all have a period of 18 monolayers (apart from A, which has half the period, since $n_1 = n_3$ and $n_2 = n_4$). Samples A,B,C and D all have GaAs layers with $n_2 = n_4 = 3$, separated by different widths of AlAs layers. Apart from sample A, they show two distinct GaAs-like phonon modes ω_1 corresponding to the two different GaAs layers, the frequencies of which would be essentially identical if the interfaces were ideally perfect. The pairs of samples F1,F2 and G1,G2 with GaAs layer widths of 2 and 4 monolayers are identical but grown in reverse directions; the frequencies change very markedly when the growth direction is reversed.

A very satisfactory theoretical description of the mode frequencies in all 9 samples can be obtained using the model of Samson *et al* [1] with composition parameters determined by the procedure outlined above and with the interface widths determined through equation (1) with the values $\alpha = 1.0 \pm .1$, $n_s(GaAs) = 2.0 \pm .5$, $n_s(AlAs) = 5.0 \pm .5$. In each superlattice schematic in the figure, the calculated Ga composition profile is indicated by solid lines and the idealised profile by dashed lines, and the number above each interface indicates the roughness parameter W in monolayer units. We conclude from the analysis that equation (1) gives a good description of the dependence of the interface width on the layer thickness.

The authors would like to thank the UK Science and Engineering Research Council for financial assistance with this project.

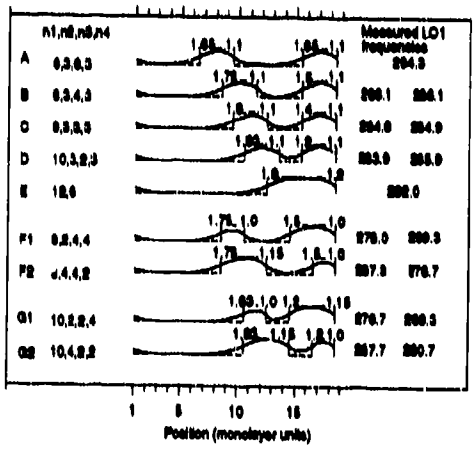

Figure. Layer thicknesses n_i, interface parameters W and gallium concentrations P_j for each of the nine samples studied. The dotted lines indicate the P_j values for idealised sharp interfaces, whilst the solid lines are the model results The number above each interface is the calculated roughness parameter W associated with that interface.

III. References

[1] B. Samson, T. Dumelow, A.A. Hamilton, T.J. Parker, S.R.P. Smith, D.R. Tilley, C.T. Foxon, D. Hilton and K.J. Moore, Phys. Rev. **B46** (1992) 2375.
[2] T. Dumelow, T.J. Parker, S.R.P. Smith and D.R. Tilley, Surface Science Reports, **17** (1993) 151.

Size effects in vibrational polariton spectra

E.A.Vinogradov
Institute of spectroscopy, Russian Academy of Sciences
142092, Troitsk, Moscow, Russia

1. Introduction

As a rule surface polaritons of dielectric or semiconductor crystals and surface plasmon - polaritons of metals are considered as nonradiative excitations because their wave vectors q are large than wave vector of light in a vacuum k_0 [1]. The existence of radiative surface polaritons and the possibility of their experimental detection by the spectra of thermal radiation of samples was investigated in [1-3].

Nonradiative surface polaritons with $q > k_0$, generated by thermal motion of surface atoms and electrons of crystals (or metal), can be converted into light by means of an ATR prism brought to the crystal surface [1,3,4]. Excitation of surface polaritons using an ATR prism over a crystal leads to the light absorption (and emission) by nonradiative surface polaritons. Thus, the ATR prism placed near the surface of a metal turn the nonradiative surface plasma states of the metal - vacuum interface with $q > k_0$ into light absorbing (radiative) states. The presence of a prism near the metal surface leads to a perturbation of surface plasmon-polaritons and, as a result, to a considerable change in the dispersion law [1,3]. With a very thick and zero gap between ATR prism and a crystal (or a metal) surface the interface polaritons remain nonradiative, i.e. these polaritons can not absorb light [3]. When the gap is finite, perturbation of the surface polariton occurs and this leads not only to a change in its dispersion law but also to the appearance of radiative modes (of the Fabry - Perot type) in the gap between the prism and the crystal surface [1,3].

The same conversion of nonradiative surface plasmon of a metal take place when the metal covered by a dielectric film with an optical thickness more than the wavelength of metal plasmon-polariton [2,3]. In this case the dielectric film can consider as a "cavity" and the electromagnetic field of plasmon-polariton of the metal as a "cavity modes". These cavity modes can interact with dipole active excitations in the film. Such resonance interaction are discussed in this report.

2. Theoretical background

The spectra of light absorption (A) and thermal radiation (E) by polaritons of a structure "ATR prism - gap - semiconductor film - metal" are well described by the formula [3]:

$$A = E = 1 - \left| \frac{(\delta_1 - \delta_2)M + (\delta_1 + \delta_2)N}{(\delta_1 + \delta_2)M + (\delta_1 - \delta_2)N} \right|^2 \qquad (1)$$

where $M = (\delta_2 + \delta_3)(\delta_3 + \delta_4) + (\delta_2 - \delta_3)(\delta_3 - \delta_4)exp(-2\kappa_3 l\omega/c)$;
$N = [(\delta_2 - \delta_3)(\delta_3 + \delta_4) + (\delta_2 + \delta_3)(\delta_3 - \delta_4)exp(-2\kappa_3 l\omega/c)]exp(-2\kappa_2 d\omega/c)$;
$\delta_j = \epsilon_j/\kappa_j$ for p-polarized light; $\delta_j = \kappa_j$ for s-polarized light; $\kappa_j = \sqrt{\epsilon_1 sin^2\phi - \epsilon_j}$; j=1,2,3,4. Here ϵ_1 is the dielectric function of the semi-cylinder material (ATR prism), ϵ_2 is the dielectric function of the gap, $\epsilon_3(\omega)$ and $\epsilon_4(\omega)$ are the dielectric functions of the film and the substrate, respectively; l and d are the thicknesses of the gap and the dielectric (semiconductor) film, and ϕ is the radiation angle (inside the medium with ϵ_1).

3. Light absorption by radiative polaritons.

It was shown [1-3] that the interaction of light with two interface vibrational modes of a structure "vacuum - thin film - metal" leads to the appearance of absorption (radiation) peaks at the frequencies of these modes. One of them is located at frequency ω_{TO} and another at frequency ω_{LO}. When we have an ATR prism near the film on metal substrate or dielectric (semiconductor) slab on the metal, it is evident that in the gap and in the film, as in the Fabry - Perot interferometer, radiative interference modes will exist.

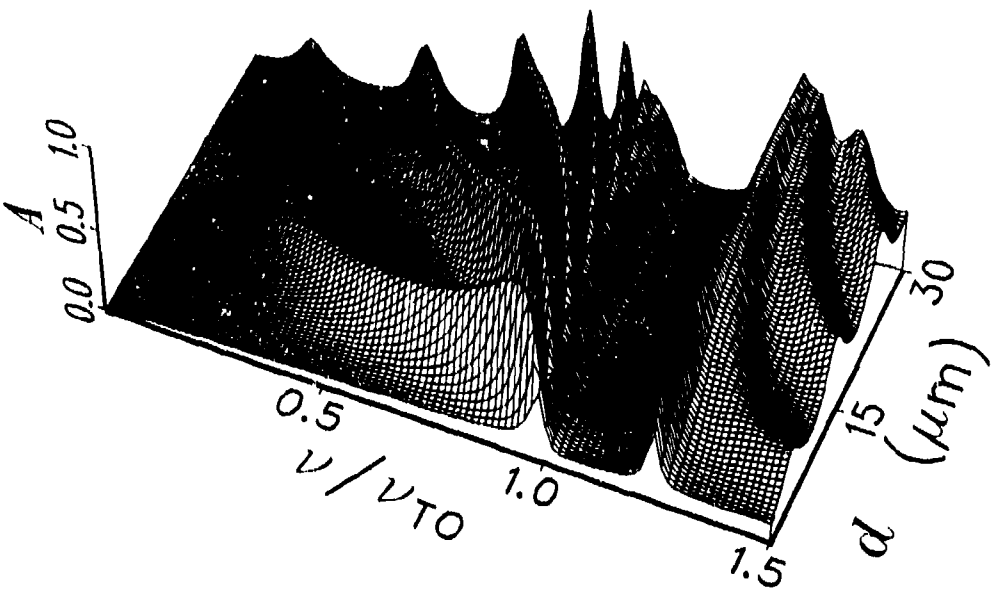

Fig.1 Calculated p-polarized absorption spectra of structure " $ZnSe$ film – Cr substrate" with different thicknesses of the film. The calculated spectra are in a good agreement with experimental results [1-3].

As an example in Fig.1 shown that a set of radiative polariton branches appear to in the frequency regions $\nu < \nu_{TO} = 200\,cm^{-1}$ and $\nu > \nu_{LO} = 250\,cm^{-1}$. The number of these branches is determined only by the thickness and the dielectric function of the film [3]. These "modes", i.e. radiative polaritons, are "tied" to the metal surface and they should be considered as electromagnetic eigenstates of our structure. These "modes" was observed early in experiments [2,3].

It should be noted that the intensities of these additional bands in the spectrum in Fig.1 at the frequency $\nu \ll \nu_{TO}$ and $\nu \gg \nu_{LO}$ are determined, primarily, by the frequency of electron collisions in the metal plasma, i.e. by the quantity $Im[\epsilon_M(\omega)]$. $\epsilon_M(\omega) = 1 - \omega_p^2/(\omega^2 - i\gamma_p\omega)$, where ω_p and γ_p is the plasma frequency and the frequency of electron collision in metal plasma respectively. ($\omega_p = 50000\,cm^{-1}$, $\gamma_p = 5000\,cm^{-1}$.)

There are resonance enhancement in absorption spectra when radiative polaritons (Fabry-Perot modes of the gap or the film) of the structure cross the interface vibrational states of the film on the metal substrate at the frequencies $\omega_1 \approx \omega_{TO}$ and $\omega_2 \approx \omega_{LO}$ and an local vibrations of impurity atoms in the film. The frequencies of the interfaces modes ω_1 and ω_2 and local vibrations of impurity atoms do not depend from wave vector in radiative region, i.e. at $q < k_0$ [1-3].

4. References

[1]. *Surface Polaritons. Electromagnetic Waves at Surfaces and Interfaces*, Ed. by V.M.Agranovich and D.L.Mills, North-Holland, chapters: 1,3,4-7,12,14, 1982.

[2].E.A.Vinogradov. Vibrational Polaritons in Thin Semiconducting Films on Metal Surfaces. *Proceed. 8th Intern Confer. on Fourier Spectroscopy*, Lubeck - Travemuende, Germany, 1991, **SPIE, vol. 1575**, p.151–160, 1992.

[3]. E.A.Vinogradov. *Physics Reports*, v.217, No.4, p.159 - 223, 1992.

A quasi-optical mode converter for gyrotrons operating in high order modes

M. Blank, K.E. Kreischer, R.J. Temkin

MIT Plasma Fusion Center
Cambridge, MA 01219 USA

E. Giguet

Thomson Tubes Electroniques
78141 Velizy Villacoublay France

ABSTRACT

A quasi-optical mode converter has been designed to transform to the $TE_{22,6}$ cylindrical waveguide mode at 110 GHz to a Gaussian beam in free space. The converter consists of an irregular cylindrical waveguide section followed by a step-cut launching aperture and several focussing reflectors. The irregular waveguide section, which is designed using coupled mode theory, is used to bunch the radiation into Gaussian bundles prior to the launch. The reflectors that follow are designed with Gaussian optics. A rigorous diffraction theory has been developed to analyze the converter system. The converter will be built and tested, and results will be compared to the diffraction theory.

2. CONVERTER DESIGN

The quasi-optical mode converter consists of an irregular waveguide section, or pre-bunching section, followed by a step-cut launching aperture and several focussing reflectors. The purpose of the pre-bunching section is to obtain a mode mix in the launching waveguide such that the field intensity on the wall, or wall currents, are Gaussian in profile.[1,2,3]

A Gaussian profile of the field intensity on the waveguide wall can be achieved by pumping power from the main mode, TE_{mp}, to two satellite modes, the $TX_{m_i p_i}$ and the $TX_{m_j p_j}$. The symbol TX indicates that the satellite mode can be either TE or TM. A helicoidal converter, described by Eq. (1), is used to obtain this type of mode conversion.[2]

$$r(\varphi, z) = r_{mean}[1 + \varepsilon_1(z)\cos(\beta_1 z - l_1\varphi) + \varepsilon_2(z)\cos(\beta_2 z - l_2\varphi)], \tag{1}$$

where $\beta_1 \approx \pm(\beta_0 - \beta_i), l_1 = \pm(m_0 - m_i), \beta_2 \approx \pm(\beta_0 - \beta_j), l_2 = \pm(m_0 - m_j)$. The subscript 0 corresponds to the main mode, and the subscripts i and j refer to the first and second satellite modes, respectively. Coupled mode theory is used to analyse the operation of the helicoidal converter.

For the $TE_{22,6}$ converter under consideration, r_{mean} is 6% larger than the cutoff radius, and the two satellite modes are the $TE_{19,7}$ and the $TE_{23,6}$. The other modes that couple to the $TE_{22,6}$ through the wall deformations are also taken into account. The resulting Gaussian wall current pattern (Fig. 1) has a peak to valley ratio of approximately 40. Launching of the radiation is achieved by cutting the wall around a Gaussian bunch, where wall current is at a minimum. The Stratton-Chu diffraction theory was used to analyze the launch of the radiation from the pre-bunching converter. Figure 2 shows the near field radiation pattern at the approximate position of the first reflector, as predicted by the Stratton-Chu formula. The diffraction theory was also used to predict the expansion of the beam. This theoretical expansion was compared to the expansion of a fundamental Gaussian beam (Figs. 3 and 4) and good agreement was obtained.

Because the pre-bunching launcher radiates a Gaussian beam, the focussing reflectors in the converter system were designed using Gaussian optics. The diffraction theory can be used to theoretically propagate the radiation launched from the irregular waveguide through the mirror system and predict the final output beam.

3. REFERENCES

1. G.G. Denisov *et al.*, '110 GHz gyrotron with built-in high-efficiency converter,' *Int. J. Electronics*, Vol. 72, nos. 5 and 6, pp. 1079-1091, 1992.

2. A. Möbius and J. Pretterebner, 'Conditions to achieve stable propagation of a Gaussian-like mode mixture in a deformed waveguide,' *17th International Conference on Infrared and Millimeter Waves, Conference Digest*, pp. 34-35, 1992.

3. G.G. Denisov, M.I. Petelin, and D.V. Vinogradov, 'Effective conversion of high waveguide modes to eigenwaves of open mirror lines,' *17th International Conference on Infrared and Millimeter Waves, Conference Digest*, pp. 124-125, 1992.

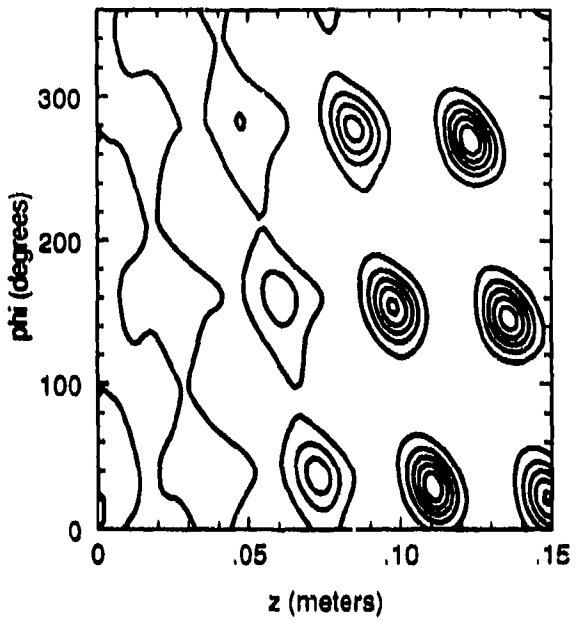

Figure 1. $|H_z|^2$ on the wall of the $TE_{22,6}$ helicoidal converter.

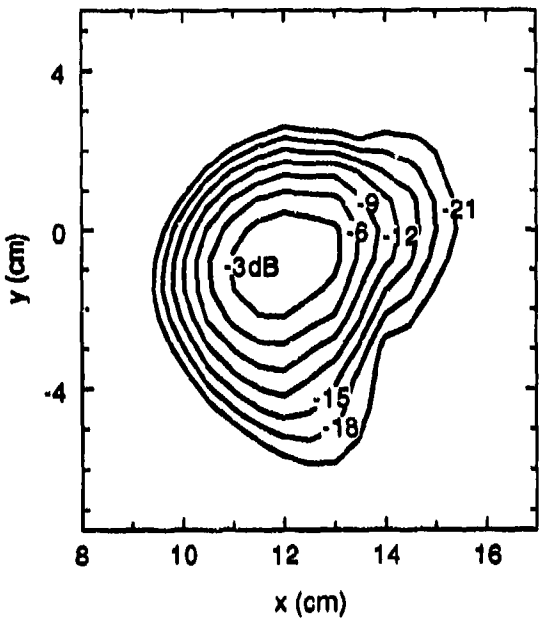

Figure 2. Stratton-Chu theory prediction of the launched radiation ($|E_y|^2$) at z = 4.5 cm, the approximate position of the first reflector. Lines of constant power are shown in dB.

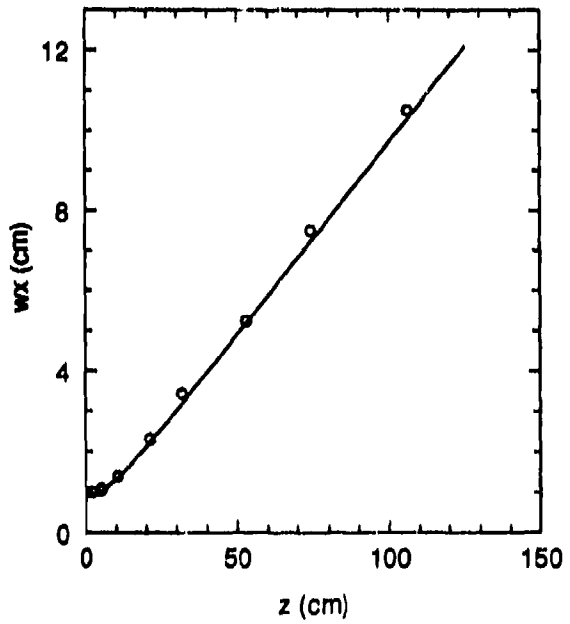

Figure 3. Horizontal beam radius expansion. The circles indicate prediction by Stratton-Chu theory and the solid line is the expansion for a fundamental Gaussian beam with a waist of 0.9 cm.

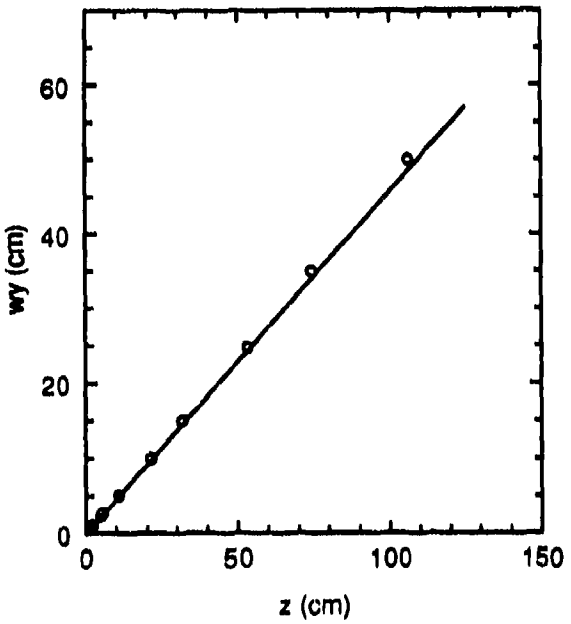

Figure 4. Vertical beam radius expansion. The circles indicate prediction by Stratton-Chu theory and the solid line is the expansion for a fundamental Gaussian with a waist of 0.19 cm.

Compact quasioptical $TE_{22,-6}$ to TEM_{00} converter with feed waveguide deformations

J. Pretterebner[1,2], A. Möbius[1,3], M. Thumm[3,4], A. Wien [3,4]

[1] Innovative Microwave Technology Ltd., Heinrich Baumannstraße 49, W-7000 Stuttgart 1, Germany
[2] Institut für Plasmaforschung, Universität Stuttgart, Pfaffenwaldring 31, W-7000 Stuttgart 80, Germany
[3] Kernforschungszentrum Karlsruhe, Inst. f. Technische Physik, P. O. Box 3640, W-7500 Karlsruhe, Germany
[4] Institut für Höchstfrequenztechnik und Elektronik, Universität Karlsruhe, W-7500 Karlsruhe, Germany

ABSTRACT

Helically cut antennas with feed waveguide deformations together with two or three matching mirrors are used for the efficient conversion of high order helically propagating gyrotron cavity output modes into a free space fundamental Gaussian beam. The aim of this work is to optimize the shape of the deformations such that the antenna is reasonably short and the conversion efficiency ($TE_{22,-6}$ to TEM_{00}) remains high.

2. INTRODUCTION

Helically cut quasi-optical mode converters [1] are used in modern high power gyrotrons [2] to convert the rotating high order cavity volume mode into a linearly polarized fundamental Gaussian beam. Such a mode converter consists of a helically cut aperture antenna serving as a launcher, and two or more reflectors. Especially for converters integrated into the vacuum system of the tube, conversion efficiencies close to unity are required since trapped RF energy jeopardizes the stable operation regime and may lead to heating of the tube structure. To achieve high conversion efficiencies launching an appropriate mode mixture has been suggested in several papers. [3], [4]. However, for gyrotrons operating with high order modes the mode converter necessary to achieve the mixture either is that long that it will be difficult to intergrate it into the vacuum system or it needs to be operated very close to cutoff. Thus, in this paper we come back to the type of feed waveguide deformations proposed in [5]. Since this design has been performed by means of geometrical optics, which can lead to unexpected results, [6], it must be checked by diffraction theory.

In this paper we describe the theory we have derived. We compare the lengths of the converters operating on different principles and apply this theory for the design of the converter system for a $TE_{22,-6}$ mode at 140 GHz.

3. LENGTH OF THE CONVERTERS OF DIFFERENT PRINCIPLES

The overall length of the converter section and the launcher for a TE_{mn} mode (eigenvalue X'_{mn}, wave propagation vectors $k_{\|}$, $k_{\perp}$ can be calculated as

$$L_{tot} = 2\left(\pi + \cos^{-1}\left(\frac{m}{X'_{mn}}\right)\right)\frac{k_{\|}}{k_{\perp}} R_w \frac{\sqrt{1-\frac{m^2}{X'^2_{mn}}}}{\cos^{-1}\frac{m}{X'_{mn}}}$$

Hence, it increases first linearly later with the square of the waveguide radius R_w. The length of rippled wall mode converters also have a similar behaviour, but are generally longer.

4. DESIGN OF THE $TE_{22,-6}$ CONVERTER

The entire mode converter system has to fit into the space between the uptaper behind the gyrotron resonator and the collector which has its location determined by electron beam trajectories in the DC magnetic field. This determines the overall axial space of our converter to 330 mm The launcher radius has been chosen such that the pitch angle of the operating mode $TE_{22,-6}$ is the about 50°. This leads to a launcher length of 87 mm and a feed waveguide deformation section of 120 mm. The mirror system comprising three mirrors have to fit into the remaining space.

5. ANALYSIS OF THE LAUNCHER DEFORMATIONS

The feed waveguide deformations calculated by means of geometrical optics have to be investigated using diffraction theory. In our model we separate the calculation in axial and azimuthal direction and solve Huygens integrals on sufaces depending on two dimensions. In this approach we assume the field radiating from a single causting and calculated the field on the waveguide surface by means of Hankel's functions. Then we twice

calculate the reflected field from the deformed waveguide mirror surfaces and obtain the radiation field of the launcher.

6. NUMERICAL ANALYSIS OF THE LAUNCHER BY FINITE INTEGRATION TECHNIQUE

Since the principles of geometrical optics and the assumption of unperturbed fields on the aperture are not exact, numerical methods have to be used taking into account reflection and diffraction caused by the cut. Discretization of the geometry shows that the number of gridpoints increases with the square of the waveguide radius so it is advantageous to investigate the radiation behavior of the helically cut aperture antenna closer to cutoff in order to reduce the computational effort. A commercial code [7] based on the finite integration technique which solves Maxwell's equations in time domain was applied to the three dimensional problem of an undeformed launcher excited by waveguide modes. The program simulates free space radiation with absorbing boundary conditions, waveguide excitation can be modelled and backscattering can be analyzed, after some modifications of the computer code, especially for the possibility to handle a mode mixture of rotating high order modes.
First test calculations (parameters: $f = 140\,GHz$, $R_w = 8.9\,mm$, rotating $TE_{10-4} \rightarrow \alpha = 70°$ pitch angle) showed that the tangential field distribution on the aperture ($0 \le x \le R_w$, $y = 0$, $0 \le z \le 2\pi R_w / \tan\alpha$) distinguishes from the usually assumed constant amplitudes in axial direction. In Fig.1 one can see a decay of the amplitudes to the end of the cut and backwards travelling waves due to power reflection. Both effects are expected to be negligible for increasing waveguide radius which has to be verified by further computations, also including the proper mode mixtures proposed in [4] .

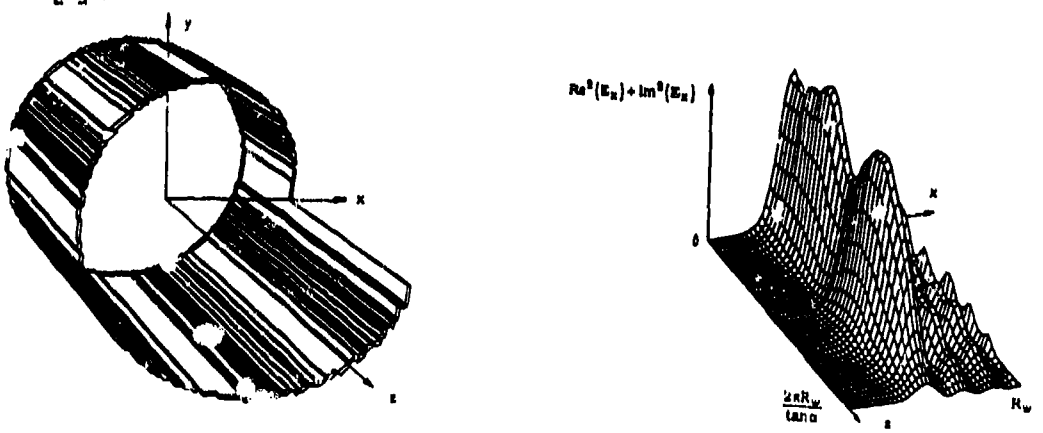

Fig.1: Model of the simulated launcher and coordinate system (left) and square of the tangential electric field amplitude on the aperture (right).

7. ACKNOWLEDGMENT

The work was performed in the frame of the Nuclear Fusion Project of the Kernforschungszentrum Karlsruhe.

8. REFERENCES

[1] VLASOV, S.N., ZAGRYADSKAYA, L.I., and PETELIN, M.I , "Transformation of a Whispering Gallery Mode, Propagating in a Circular Waveguide, into a Beam of Waves". Radio Eng., Electron Phys., 20 , pp 14 - 17, 1975.

[2] DENISOV, G.G., KUFTIN, A.N., MALYGIN, V.I., VENEDIKTOV, N.P., VINOGRADOV, D.V., and ZAPEVALOV, V.E., "110 Ghz gyrotron with a built-in high efficiency converter",. Int. J. of Electronics, 72 1079 - 1092, 1992.

[3] VINOGRADOV, D.V., DENISOV, G.G., PETELIN, M.I., "Highly efficient conversion of high order waveguide modes into the modes of a mirror transmission line", Proc. of X school-seminar on wave diffraction and propagation. Moscow, pp 96 - 128, in Russian, 7-15, February 1993.

[4] PRETTEREBNER, J., MÖBIUS, A. and THUMM, M., "Improvement of Quasi-Optical Mode Converters by Launching an Appropriate Mixture of Modes", Conf. Digest IRMM, SPIE Vol 1929, pp 41 - 42, 1992.

[5] MÖBIUS, A., PRETTEREBNER, J., "Avoidance of Edge Diffraction Effects by Feed Waveguide Deformation" Conf. Digest IRMM, SPIE Vol 1576, pp 531 - 532, 1991.

[6] MÖBIUS, A., and PRETTEREBNER, J., "On the Validity of Geometric - Optical Mode Converter Design", Conf. Digest IRMM, SPIE Vol 1929, pp 46 - 47, 1992.

[7] BARTS, T. et al., "Maxwell's Grid Equations", Frequenz 44 pp 9-15, 1990

A Traveling-Wave Resonator for Exciting Whispering-Gallery Modes in an Overmoded Circular Waveguide

Theodore A. Hea, Robb A. Peebles, and Ronald J. Vernon

Department of Electrical and Computer Engineering
University of Wisconsin, Madison, WI 53706

Introduction

Several gyrotrons currently under development have cavities that operate in rotating TE_{mn} modes with very high azimuthal indices m such as a rotating $TE_{15,2}$ or $TE_{22,2}$ circular waveguide mode. If n $\ll$ m as well, these modes are sometimes called whispering gallery modes. It is desirable to be able to produce these modes at low power from the TE_{10} mode in standard dominant-mode rectangular waveguide so that components to be used within or in conjunction with these gyrotrons can be more easily tested. Recently we discussed the principles of operation of a device which can be used to generate such high azimuthal index modes using an azimuthal array of apertures in the circular waveguide [1]. Other methods of generating WG modes have also been developed. One uses a helical multifoil [2], and another uses a cylindrical input cavity within a coaxial cavity [3]. The azimuthal aperture array method has the possible advantage that more than one different WG mode with the same azimuthal index, m, could be generated with the same device. Also, both senses of rotation and any degree of rotation, including a stationary mode, can be produced with one device for possible testing purposes.

Description of the Azimuthal Aperture Array Mode Generator

In the azimuthal aperture array mode generator, the apertures are excited by a dominant-mode rectangular waveguide which is, in effect, wrapped around the circular waveguide, as shown in Figs. 1 and 2. For simple synchronous operation, the number of wavelengths in this azimuthal rectangular waveguide should be equal to the azimuthal index of the desired mode in the circular waveguide. In order to excite a purely rotating mode in the circular waveguide, a pure traveling wave must be established in the azimuthal rectangular waveguide. The mode with the desired radial index n is selected by forming a cavity in the circular waveguide between a movable short circuit and a partially transmitting screen as shown in Fig. 1. The coupling is strongest to the mode with the highest radial index (for the desired m-index) that can propagate in the cavity. Thus, it is advantageous to make the circular waveguide cavity radius a little smaller than the cutoff radius for the mode with the next highest radial index. It is also desirable to have the amplitude of the traveling wave in the azimuthal rectangular waveguide as nearly constant as possible along the length of this waveguide. To do this it is necessary to keep the coupling through the apertures relatively low. Thus, in order to keep the efficiency of the device as high as possible, it is desirable for the azimuthal rectangular waveguide to act as a traveling wave resonator to increase the amplitude of the traveling wave.

The usual traveling wave resonator design, shown in Fig. 3, uses a directional coupler to excite the resonant ring. Here the degree to which the wave in the ring is purely a traveling wave depends upon a high directivity in the directional coupler. The coupling of the input power to the ring is optimum (total) when the coupling factor k is equal to the attenuation factor in the ring [4]. Neither the directivity of the directional coupler nor the coupling factor are easily adjustable after fabrication. A alternate method of

producing a pure traveling wave uses two tees with a short circuit in one as shown in Figs. 1 and 4. This paper will discuss the analysis of this type of traveling-wave resonator.

Acknowledgement

This work was supported under U.S. Dept. of Energy Contract DE-FG02-85ER52122.

References

[1] R. A. Peebles M. Kasraian, and R. J. Vernon, "Whispering-Gallery Mode Generation by Means of an Azimuthal Array of Apertures," 17th Int. Conf. on Infrared and Millimeter Waves, Pasadena CA, 1992, Digest pp. 112-113.

[2] M. Thumm and A. Jacobs, "In-waveguide TE_{01} to Whispering-Gallery Mode Conversion Using Periodic Wall Perturbations," *Conf. Digest 13th Int. Conf. Infrared and Millimeter Waves*, Honolulu, Hawaii, pp. 465-466, 1988.

[3] C. Moeller, "A Coupled Cavity Whispering-Gallery Mode Transducer," *Conf. Digest 17th Int. Conf. Infrared and Millimeter Waves*, Pasadena, California, (this digest), 1992.

[4] Helmut Golde, "Theory and Measurements of Q in Resonant Ring Circuits" IRE Trans. vol. MTT-8, pp.560-564: Sept. 1960.

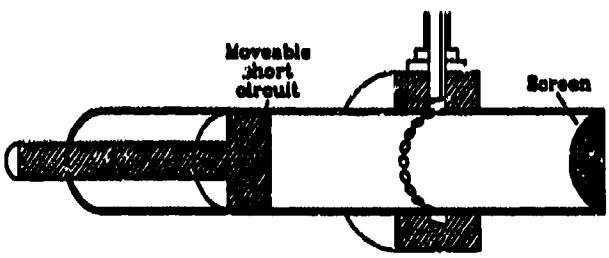

Fig. 1. A cut-away view of the mode generator.

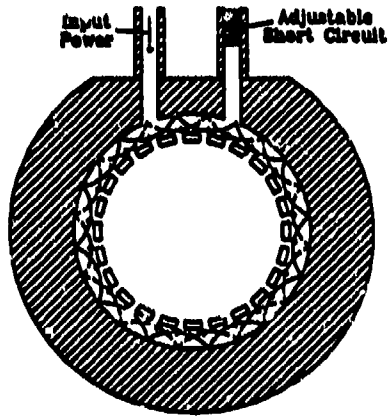

Fig. 2. Side view of mode generator showing field coupling through the apertures.

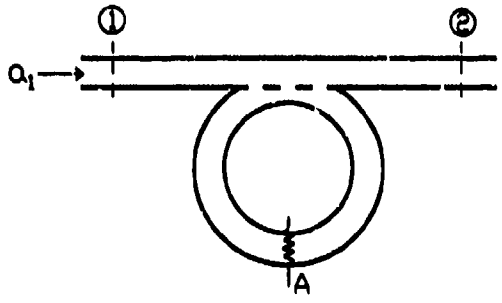

Fig. 3. A conventional traveling wave resonator.

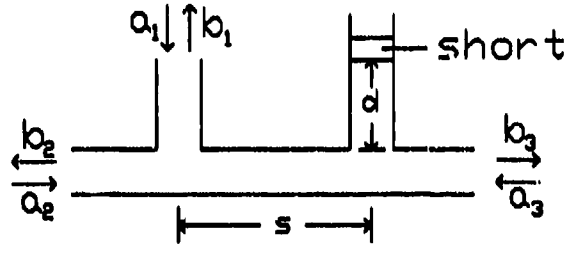

Fig. 4. Two waveguide tees connected to produce a traveling wave in a ring.

MODE COUPLING IN OVERMODED, VARYING RADIUS COAXIAL GYROTRON CAVITIES

D. Wagner, J. Pretterebner
Universität Stuttgart, Institut für Plasmaforschung,
70569 Stuttgart, Germany

M. Thumm
Kernforschungszentrum Karlsruhe, Institut für Technische Physik and
Universität Karlsruhe, Institut für Höchstfrequenztechnik und Elektronik,
76021 Karlsruhe, Germany

ABSTRACT

Circular coaxial structures have been analyzed using a Scattering Matrix Code (SM-Code). The mathematical formulation is given in [1]. The SM-Code includes ohmic losses and avoids the relative convergence problem [2]. This gives the possibility to use a large number of diameter steps in order to analyze long ($L \gg \lambda$) oversized continuous waveguide structures like coaxial gyrotron cavities. Standard cavities with abrupt junctions, improved cavities with rounded contours and cavities including a conical inner conductor have been analyzed.

INTRODUCTION

Oversized resonators suffer the problem of quasi degenerated modes with nearly equal eigenvalues. One possible way to separate the eigenvalues for a fixed outer diameter is to use a coaxial cavity [3]. The eigenvalues of the circular waveguide are increased if the inner conductor overlaps the caustic region. This effect shifts several eigenmodes into the cutoff region and reduces the number of possible resonances (mode competition). Additional the transversal field structure of coaxial eigenmodes depends on the inner to outer conductor diameter ratio and complicates the numerical description [4]. The same mathematical formalism has been used for resonators with circular [5] and rectangular [6] cross section. A gaining medium (electron beam) with a Gaussian amplification profile in the resonator has been assumed. A resonator geometry for the $TE_{21,13}$-mode at 140 GHz including the gain profile is shown in Fig.1. The frequency region where the resonance occurs can be determined by feeding the cavity with a pure $TE_{21,13}$-mode from the output side corresponding to the dip shown in Fig.2. The exact resonance frequency, the gain factor and the quality factor are calculated by solving the eigenvalue problem. Rounded cavities have been modeled using a large number of diameter variations (e.g. 200 unit cells). Due to the radial symmetry of the coaxial cavity only waveguide modes with the same radial index have to be taken into account. This means that the TEM-mode can not be excited by symmetrical diameter steps if the radial index is larger than zero.

NUMERICAL RESULTS

The discrete structure (unit cell with a step in diameter) is described by the wave phenomena of an incident and a reflected wave which is equivalent to a second order difference equation. The numerical integration of the difference equations leads to the Overall Scattering Matrix. The eigenvalue equation is solved using this Overall Scattering Matrix. This gives the resonance frequency, the gain factor and the quality factor of the cavity. Unphysical singularities in the propagation constants will cause convergence problems and can be avoided using a modified Schaffelt-Bayer-formula [7].
A 140 GHz gyrotron cavity oscillating in the $TE_{21,13}$-mode is examined. Adiabatic transitions (rounded) show higher mode purities compared to standard cavities [8]. Table 1 gives the numerical results for the cutoff and the output tapers with a pure $TE_{21,13}$-mode excitation and for the complete resonators (standard cavity and rounded cavity).

mode	abrupt junctions				rounded junctions				standard cavity		rounded cavity	
	cutoff taper		output taper		cutoff taper		output taper					
	backward	forward	backward	forward	backward	forward	backward	forward	backward	forward	backward	forward
$TE_{21,11}$	0.095	0.091	0.027	0.154	0.005	0.001	0.001	0.106	0.149	0.246	0.004	0.142
$TE_{21,12}$	0.499	0.446	0.079	0.777	0.086	0.107	0.000	0.341	0.590	0.452	0.054	0.243
$TE_{21,13}$	0.000	97.231	17.039	80.860	0.000	98.118	12.113	86.428	0.000	98.061	0.000	99.272
$TE_{21,14}$	0.000	0.000	0.000	0.179	0.000	0.000	0.000	0.153	0.000	0.210	0.000	0.173

Table 1: Modal power in [%] in the main modes by feeding cutoff and output taper with a pure $TE_{21,13}$-mode and for the standard and rounded cavities at resonance (ohmic losses are included).

SUMMARY

Oversized coaxial gyrotron cavities have been analyzed. High output mode purity has been obtained using rounded transitions. The SM-Code can describe the resonant cavity including the output taper. The high numerical stability of the SM-Code enables to model continuous structures described by a large number of diameter steps for rectangular, circular and coaxial cross sections.

REFERENCES

[1]P.E.Latham et.al., IEEE Trans. Microwave Theory Techn., 40, 1992, 1973-1977.
[2]A.S.Ilyinsky et.al., Propagation, Scattering and Dissipation of Electromagnetic Waves, IEE Electromagnetic Waves Series 36, Peter Peregrinus Ltd., 1993.
[3]S.N.Vlasov et.al., Radio Eng. and Electron. Phys., 21, 1976, 96-102.
[4]J.Kong, Electromagnetic Theory, 2nd Edition, John Wiley and Sons, 1990.
[5]D.Wagner et.al., 17th Int.Conf. on Infrared and Millimeter Waves, Pasadena, 1992, Proc., SPIE, Vol.1929, 36-37.
[6]D.Wagner et.al., Proc., 2nd Workshop on FEM-mmWaves, 1992, Rijnhuizen, Nieuwegein, The Netherlands.
[7]W.Schaffelt, H.Bayer, A.E.Ü., 1956, Band 10, Heft 3, 89-97.
[8]G.I.Zarudneva et.al., Radiofizika, Vol.31, No.3, 1988, 343-346.

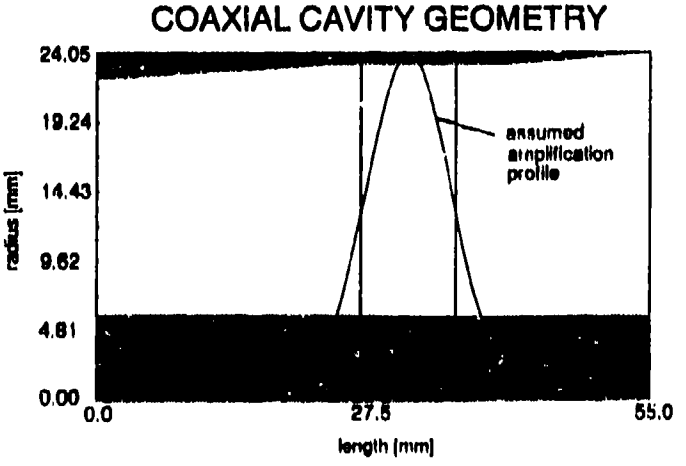

Fig1. Resonator geometry including assumed gain profile

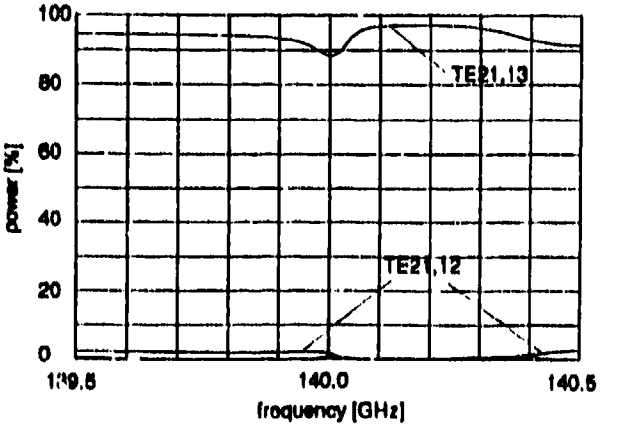

Fig2. Reflection of the cavity excited from the output side

Modeling of Mode Purity in High Power Gyrotron Oscillators*

S. Y. Cai, T. M. Antonsen, Jr., and B. Levush
Laboratory for Plasma Research
University of Maryland, College Park MD 20742, USA

Spurious mode generation at the same frequency of the operational mode in a high power gyrotron can significantly reduce the power handling capability and the stability of a gyrotron oscillator because these mode are usually not matched at the output window and thus have high absorption and reflection rates.

In this paper we study two possible mechanisms for parasitic mode generation in a high power gyrotron oscillator. One is the mode transformation caused by the waveguide inhomogeneity. The other is the gyroklystron effect. The first mechanism is relatively well understood. The power transformed from the operational mode into neighboring modes depends mainly on the gradient of the waveguide radius and the power contained in the operational mode[1]. For a given tube, the percentage of power transformed into a parasitic mode should not depend sensitively on the applied axial magnetic field.

The gyroklystron effect on the other hand relies on a resonant condition,

$$\frac{\omega - \Omega(z)}{V_z} = k_z(z), \qquad (1)$$

where z is the axial coordinate pointing in the same direction as the electron beam travels, ω is the microwave frequency, $\Omega(z) = eB(z)/\gamma mc$ is the relativistic electron cyclotron frequency, $B(z)$ is the DC axial magnetic field, V_z is the axial velocity of the electron beam, and $k_z(z)$ is the axial wavenumber of a waveguide mode. For different waveguide modes, the resonant condition (1) is satisfied at a different location z. The operational mode usually satisfies the relation in a streight section of the cavity, where the main interaction takes place. After the main interaction, the electron beam is bunched in phase. When the bunched beam travels downstream and reaches a point where another mode satisfies the resonant condition the bunched beam can excite this mode. This effect is refered to as the gyroklystron effect. In this case, because the resonant condition involves the axial magnetic field $B(z)$, the level of parasitic mode excitation is expected to depend sensitively on the magnetic field.

To study the spurious mode generation due to the mode transformation and the gyroklystron effects, we have developed a computer code, which solves a set of single frequency time-dependent gyrotron equations self-consistently. This code can include an arbitrary number of TE and TM modes and can account for mode transformations. It can also include reflection for selected modes at the output boundary[2].

The computer code is used to simulate a recent experiment performed at General Atomic (GA) on a Varian built $TE_{18,2}$ mode 110 GHz 500kW CW gyromonotron[3]. The experiment observed excitations of spurious modes with power as high as 10% of the operational mode. The power in these parasitic modes was found to be sensitively dependent on the axial magnetic field. Our simulations are performed with beam parameters of 80 kV beam voltage, 22 amperes beam current and 1.5 velocity ratio. The first set of simulations were done with an uniform magnetic field. The output power of some selected modes are plotted in Fig. 1 as functions of the axial magnetic field. It shows that the power in $TE_{15,3}$ and $TM_{18,3}$ is about 1% of the total power and is sensitive to the magnetic field. The next step we took was to use the actual magnetic field tapering measured in the experiments. The simulation results are plotted in Fig. 2. Here the tapering in the magnetic field reduces the maximum

output power in all modes. We have also performed simulations in which we turned off the coupling between the parasitic modes and the electron beam. The output power obtained of such simulations are very close to that shown in Fig. 2. Therefore in this case the parasitic modes are mainly generated through the mode transformation mechanism. This result is consistent with the fact that, as shown in Fig. 2, the power in the parasitic modes are not sensitive to the magnetic field. Fig. 3 shows the results of our third study where 100% reflection was included for all parasitic modes at the output boundary. In this case, the power of the parasitic modes plotted is not the output power but the power that oscillates inside the tube. It is shown in Fig. 3 that the power in $TE_{15,3}$ can reach more than 10% of the total output power and is very sensitive to the axial magnetic field.

Based on the simulation results described above, we conclude that mode transformation and gyroklystron effects can excite parasitic modes to unacceptable levels in high power gyrotron oscillators. However, these two effects can not fully explain the experimental observations made at GA because the only case in our simulations where the power in a parasitic mode exceeds 10% of the total power is when the output section has unreasonably high reflection for this mode. Therefore, other effects may also have contributed to the generation of parasitic modes in the GA experiment.

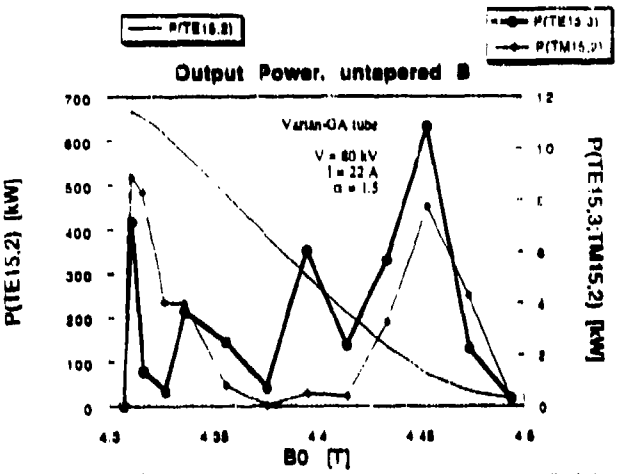

Figure 1: Output power versus magnetic field with untapered B.

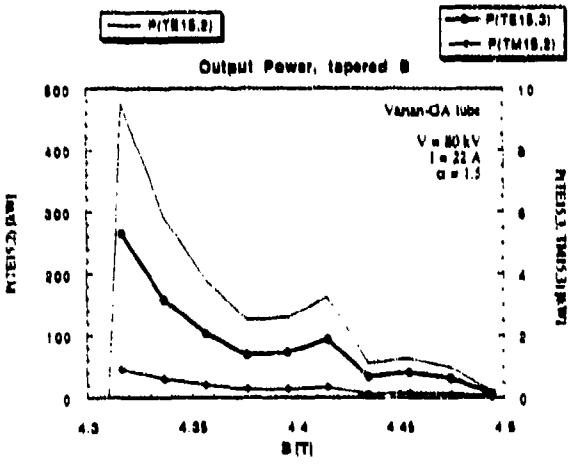

Figure 2: Output power versus magnetic field with tapered B.

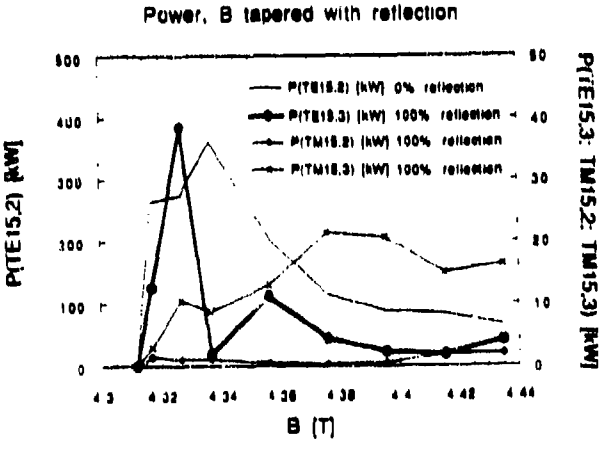

Figure 3: Output power versus magnetic field with tapered B and 100% reflection for parasitic modes.

References

1. S. Y. Cai, T. M. Antonsen, Jr., G. Saraph and B. Levush, *Int. J. Electronics*, **72**, pp759-777(1992).

2. T. M. Antonsen, Jr., S. Y. Cai, and G. S. Nusinovich, *Phys. Fluids*, **B4**, pp4131-4139(1992).

3. C. P. Moeller, US/Russia Gyrotron Workshop, San Diego, CA, January 7-8, 1992.

* Work supported by USDOE.

Mode Priming an 85 GHz Quasioptical Gyroklystron

R. P. Fischer, A. W. Fliflet, W. M. Manheimer, B. Levush†, and T.M. Antonsen, Jr.†
Beam Physics Branch
Plasma Physics Division
U.S. Naval Research Laboratory
Washington, D.C. 20375-5000 U.S.A.

†Laboratory for Plasma Research
University of Maryland,College Park, MD 20742 U.S.A.

ABSTRACT

The quasioptical gyrotron (QOG) is under development at the Naval Research Laboratory as a tunable, high power source of millimeter-wave radiation[1]. A recent gyroklystron experiment has demonstrated operation as an amplifier, a free-running oscillator, a mode-primed oscillator, and a phase-locked oscillator. Two mode selection techniques, alpha priming and mode priming, have been shown to increase the frequency detuning and efficiency of the operating mode in the gyroklystron. These two effects are also observed in the time-dependent, multimode computer simulations, where it is shown that the gyroklystron is operating in the hard excitation region of parameter space.

EXPERIMENTAL SET-UP

The gyroklystron consists of a pair of quasioptical resonators separated by a 10 cm drift region. The output resonator comprises a pair of 5.5 cm-diameter mirrors with a radius of curvature of 38.7 cm and a quality factor $Q \approx 37000$. The mirror separation is varied from 20-28 cm using micrometers mounted outside the magnet dewar so that the frequency is continuously tunable. The resonator axis is tilted by 2° relative to the plane perpendicular to the axis of the electron beam. Tilting the resonator axis allows each electron to interact with both even and odd longitudinal modes in the output resonator, which increases the efficiency and region of stable, single-mode operation[2]. The prebunching resonator is formed by a pair of 3.1 cm-diameter mirrors with a centered hole in each mirror for input and output coupling of the 1.5 kW extended interaction oscillator (EIO) signal. The low quality factor ($Q = 2000$) of the prebuncher is required to prevent oscillations in the input resonator. Typical gyroklystron operating parameters are 70 kV beam voltage, 5 A beam current, and a measured pitch angle ($\alpha = v_\perp/v_\parallel$) of 1.9.

Comparison with theory is made using a computer code which includes the effects of the annular electron beam, even and odd longitudinal resonator modes, the tilted output resonator, the finite rise of the beam voltage and electron perpendicular velocity, and space charge as the electrons traverse the output resonator. At present, the code does not account for energy spread, velocity spread, or second harmonic radiation. Mode priming is simulated by prebunching the electron gyrophases according to $\theta = \theta_0 + q\cos\theta_0$ for 2 μsec during the rise of the voltage pulse. A bunching parameter $q = 2$ is used for the simulations presented in this paper. Alpha priming is modelled by allowing the perpendicular velocity of the electrons to rise 0.25 μsec faster than the voltage in the simulations.

EXPERIMENTAL RESULTS

A plot of measured and calculated efficiency versus normalized frequency detuning is given in Figure 1(a) for mode priming by prebunching the beam for a current of 4.5 A. The normalized frequency detuning, or transit angle, is related to the more familiar gyrotron parameters via $\delta = \frac{1}{2}\mu\Delta$. Measured values of α rise linearly from 1.4-1.9 over this range of detunings, where the gyroklystron operates in a stable, single mode. The simulation uses pitch angles from 1.3-1.6, since higher values result in multimode output states in the code. Mode priming allows for higher detuning and higher efficiency than can be obtained with the free-running oscillator. If the detuning is increased past $\delta = 4.0$, mode competition occurs between the desired 85.5 GHz mode and lower frequency modes. Above $\delta = 3.0$, the gyroklystron is operating in the hard excitation regime where the beam current is lower than the start current of the operating mode ($I < I_{st}$). The peak gyrotron efficiency is usually contained in the hard excitation region.

A similar plot of efficiency as a function of frequency detuning is shown in Figure 1(b) for the case of alpha priming. The resistive divider circuit which powers the mod anode of the electron gun is adjusted so that α rises 0.1 μsec more rapidly during the rise of the voltage pulse. This tends to excite a longitudinal mode earlier in time at slightly lower voltage. The overall effect of alpha priming is very similar to mode priming: higher frequency detuning

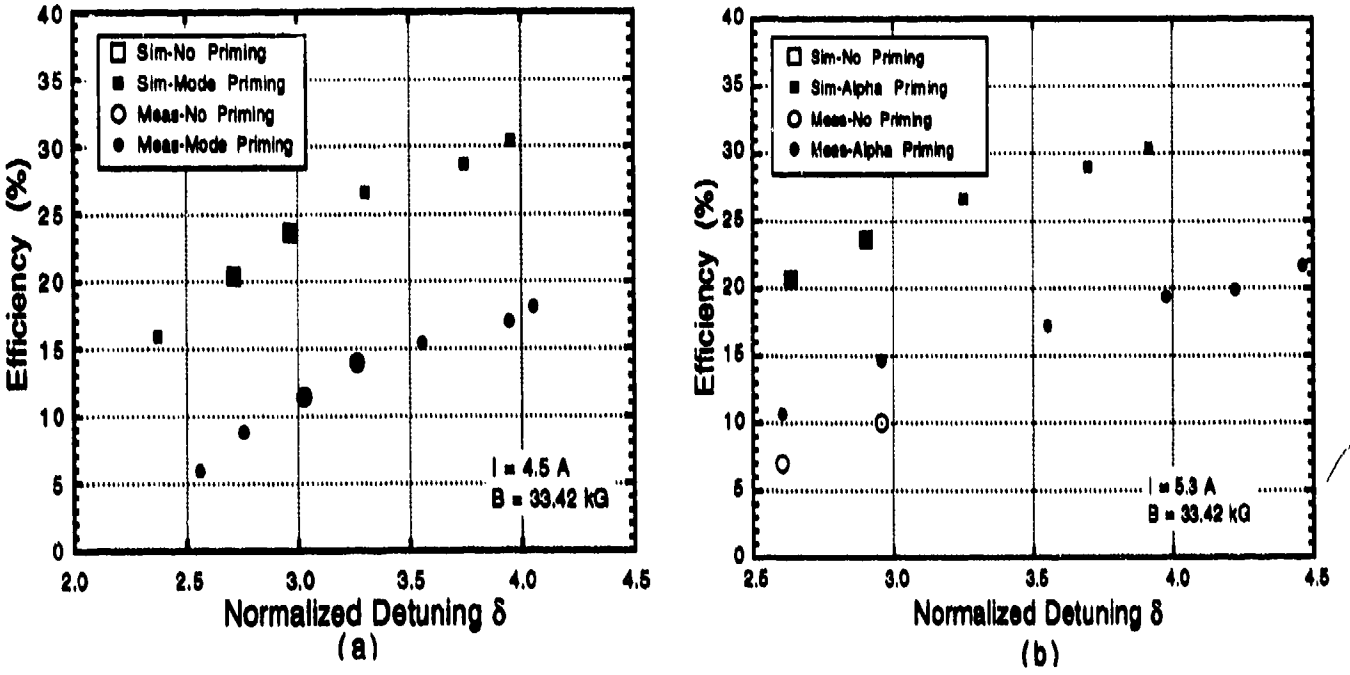

Figure 1: Efficiency versus normalized frequency detuning δ for (a) mode priming and (b) alpha priming.

and higher efficiencies are obtained compared to gyroklystron operation with no priming. Alpha priming does not require prebunching the electron beam, so that this technique should be useful in single-cavity oscillator experiments. A maximum detuning of $\delta = 4.4$ is obtained in the experiment, which corresponds to a measured efficiency of 20% and an electronic efficiency of 22%, which accounts for ohmic losses in the output resonator. Measured efficiencies are still somewhat lower than the simulations, but it is unlikely that this is due to insufficient frequency detuning. Refinements to the code, including velocity spread and energy spread of the electron beam, may provide insight to the differences between theory and experiment.

ACKNOWLEDGEMENT

This work was supported by the Office of Fusion Energy of the U.S. Department of Energy and by the Office of Naval Research.

REFERENCES

[1] T.A. Hargreaves, A.W. Fliflet, R.P. Fischer, M.L. Barsanti, W.M. Manheimer, B. Levush, and T.M. Antonsen, Jr, "Tilted resonator experiments on a quasioptical gyrotron," *Int. J. Elec.*, vol. 72, nos. 5 and 6, pp. 807-825, 1992.

[2] T.M. Antonsen, Jr, B. Levush, and W.M. Manheimer, "Stable single mode operation of a quasioptical gyrotron," *Phys. Fluids B*, vol. 2, no. 2, p. 419, 1990.

Advanced Complex Cavity for Multi-Megawatt Gyrotron

K. Xu, M. Thumm*
Kernforschungszentrum Karlsruhe, Institut für Technische Physik
*also Universität Karlsruhe, Institut für Höchstfrequenztechnik und Elektronik
D-7500 Karlsruhe 1, Germany

1. ABSTRACT

The complex cavity is very attractive because of its excellent ability of mode selection and the simplicity of the structural configuration (hollow waveguide with different diameters). However the very strong requirement posed on the manufacturing accuracy makes the complex cavity fading from the front stage of gyrotron research. In this paper, a novel modification, which overcomes this problem without sacrificing the ability of mode discrimination of the complex cavity, is proposed. This advanced complex cavity has a simple structure and fits the existing manufacturing technologies. Therefore, it is suitable for multi-megawatt gyrotrons.

2. THE ADVANCED COMPLEX CAVITY

In order to overcome the problem of mode competition in high power gyrotrons, several approaches, such as the complex cavity [1-3], the coaxial cavity [4], the two-section cavity [5] and the quasi-optical Fabry-Perot cavity [6,7] are investigated in different laboratories around the world. From the theoretical point of view, the ordinary complex cavitiy is very attractive because of its excellent ability of mode discrimination, which is resulted from its specific structural configuration. A complex cavity is composed of two segments of different radii as shown in the Fig. 1a (we call the smaller one the first segment and the larger one the second segment, which is the main interaction segment of the gyrotron). The resonant modes in these two segments have the same azimuthal mode indexes but different radial mode indexes, i.e. the $TE_{m,n}$ mode in the second segment and the $TE_{m,n-k}$ mode in the first segment. The radii of the two segments are chosen so that the operating $TE_{m,n}$ mode and its most dangerous competing modes are excluded in the first segment, because they are beyond cutoff. The structure of the $TE_{m,n-k}$ mode in the first segment fits to the structure of the $TE_{m,n}$ mode in the second segment in the corresponding cylindric area. The electrons interact with the $TE_{m,n-k}$ mode in the same way as if they were interacting with the $TE_{m,n}$ mode, because the two modes appear to be the same along the electron pathway. When the electrons enter the second segment, they have already been bunched by the $TE_{m,n-k}$-mode and continue to interact with the $TE_{m,n}$ mode. In other words, the operating $TE_{m,n}$ mode has a substitute mode working on behalf of it in the first segment, but the competing modes do not. This is the basic idea of how a complex cavity can effectively suppress the competing modes in high power gyrotrons. It is obvious that the resonant frequencies of the operating $TE_{m,n}$ mode and its partner, the $TE_{m,n-k}$ mode, should be equal to each other to ensure the tight coupling between them. Otherwise, the complex cavity would not work. Unfortunately, even a smallest manufacturing tolerance of the cavity radii may cause a considerable frequency mismatch and severely affect the gyrotron performance. The resonant condition of the complex cavity is determined by

$$2k_z \cdot L_2 + \phi_1 + \phi_2 = 2\pi \qquad (1)$$

where k_z is the longitudinal wave number, L_2 is the effective field profile length in the main segment, ϕ_1 and ϕ_2 are the phase jumps at the cross sections z_2 and z_3 respectively. In the case of a gyrotron cavity ϕ_1, ϕ_2 and L_2 can be regarded as constants. In order to keep the resonant condition k_z must be kept constant. That means if there is any manufacturing error, the frequency (ω) must shift to offset the effect caused by the change of R. For example, in the case of a 140 GHz gyrotron using the $TE_{22,6}$ mode, the cavity radius is 15.56 mm. If the manufacturing error is 0.01 mm, the corresponding frequency shift is about the half width of the resonant curve of a cavity of Q=1500 (Fig. 1b). Obviously it is not a good situation, that a complex cavity operates with such a frequency mismatch. In order to overcome this problem, small tapers are introduced into an ordinary complex cavity as shown in Fig. 2a. The operating $TE_{m,n}$ mode in the second segment is bounced back and force between the cutoff cross section z_2 and the joint section z_3 to form the resonance. the resonant condition of this modified cavity now becomes

$$2\int_{z_2}^{z_3} k_z \cdot dl + \phi_1 + \phi_2 = 2\pi \qquad (2)$$

The important factor is that the effective cavity length L_2 is no longer fixed, because z_2 is not fixed. Suppose the radius R_2 is slightly larger than that it should be ($\Delta R>0$), because of the manufacturing uncertainty. The resonant frequency will shift lower, resulting in a shifting of the position of the cutoff cross section, z_2, to the larger cavity radius (i.e. towards the z_3 in Fig. 2a). The cavity length L_2 becomes shorter. This in turn tends to increase the resonant frequency. Since the two effects on the resonant frequency go in opposite directions (one tends to decrease, another tends to increase the frequency), they offset each other (if $\Delta R<0$ the two effects also offset each other). The modified complex cavity is rendered less sensitive to a change of the cavity radius. The same strategy can be used again in the first segment of the complex cavity, as shown in Fig. 2a. With this double modifications, the tolerance of the frequency to the ΔR can be improved further. Now take the same case of the above mentioned $TE_{22,6}$ mode gyrotron with a modified complex cavity. Suppose only the second segment is modified with an insertion of a 0.3 degree taper and the cavity quality factor is also 1500. The frequency shift corresponding to $\Delta R=0.01$ mm is reduced to about half of the frequency shift of a ordinary complex cavity as shown in the Fig. 2b. If the first segment is also modified, the frequency shift should be even smaller.

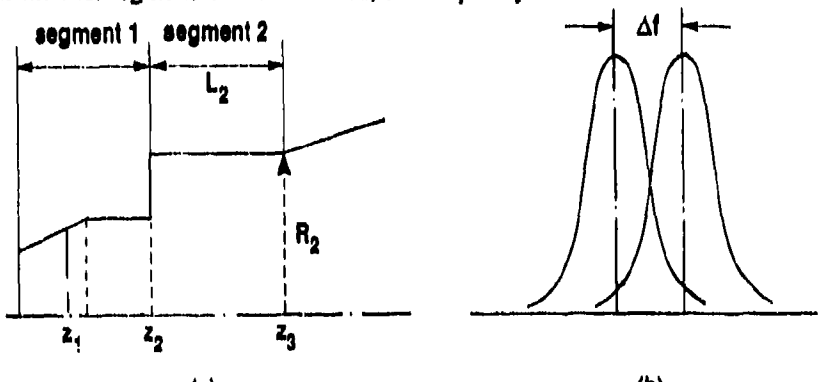

Fig. 1: Ordinary complex cavity with frequency mismatch

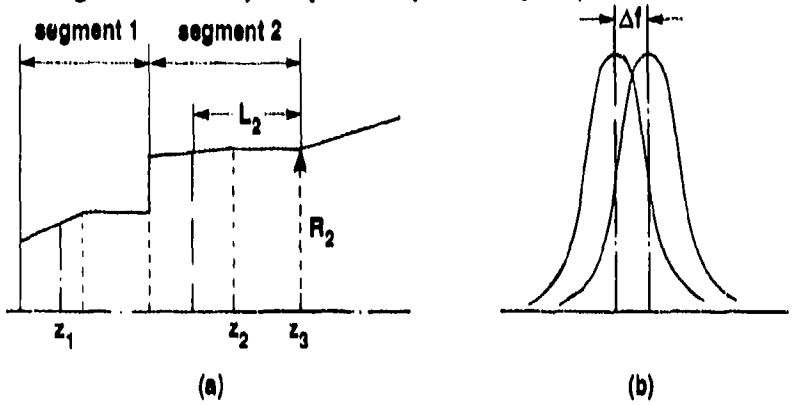

Fig. 2: Advanced complex cavity (only segment 2 is modified) with reduced frequency mismatch

3. REFERENCES

[1] V.G. Pavel'ev, S.E. Tsimring, V.E. Zapevalov, Int. J. Electronics, **63** (1987) 379-391.

[2] A.W. Fliflet, R.C. Lee, M.E. Read, Int. J. Electronics, **65** (1988) 273-283.

[3] O. Dumbrajs, E. Borie, Int. J. Electronics, **65** (1988) 285-295.

[4] G.G. Denisov, V.A. Flyagin, A.L. Goldenberg, V.I. Khizhnyak, A.N. Kuftin, V.I. Malygin, A.B. Pavelyev, A.V. Pylin, V.E. Zapevalov, Conf. Digest 16th Int. Conf. on Infrared and Millimeter Waves, Lausanne, SPIE, **1576** (1991) 632-635.

[5] K.Y. Xu, K.E. Kreischer, W.C. Guss, T.L. Grimm, R.J. Temkin, Conf. Digest 15th Int. Conf. on Infrared and Millimeter Waves, Orlando, SPIE, **1514** (1990) 324-326.

[6] A.W. Fliflet, T.A. Hargreaves, R.P. Fischer, W.M. Manheimer, P. Sprangle, J. Fusion Energy, **9** (1990) 31-58.

[7] S. Alberti, M.Q. Tran, J.P. Hogge, T.M. Tran, A. Bondeson, P. Muggli, A. Perrenoud, B. Jödicke, H.G. Mathews, Phys. Fluids, **B2** (1990) 1654-1661.

150 kW Sixth-Harmonic Gyrofrequency Multiplier

A.J. Balkcum, D.B. McDermott, F. Hartemann and N.C. Luhmann, Jr.
Department of Electrical Engineering, University of California, Los Angeles, CA 90024

ABSTRACT

The design is presented of a 150 kW, 17.4 GHz., sixth-harmonic gyro-multiplier, which is under construction, and will be driven by a 300 keV, 1.7 A prebunched axis-encircling electron beam produced in a 1 MW, 2.9 GHz gyroresonant rf accelerator.

1. THEORY

An exciting new high power millimeter and sub-millimeter wave source is under further development at UCLA. A gyrofrequency multiplier exploits the bunched nature of the rotating spiral-shaped electron beam which emerges from a gyroresonant rf accelerator. The gyrofrequency multiplier emits at a harmonic of the accelerator and electron cyclotron frequencies making it possible to operate with reduced magnetic fields and to multiply the frequency of existing microwave and millimeter wave high power sources. A proof-of-principle experiment at the third-harmonic without magnetic tapering generated 7 kW at 28 GHz with 13% efficiency.[1]

In the input TE_{111} accelerator cavity of a gyrofrequency multiplier (see Fig. 1), low frequency microwaves tuned to the cyclotron frequency accelerate and bunch initially low energy electrons to form an axis-encircling beam rotating at the accelerator's frequency.[2,3] If the resonant frequency of the output cavity's TE_{nmq} mode is equal to the nth harmonic of the accelerator, then the angular velocity of the wave matches that of the helical beam and each electron enters the interaction cavity at the same optimal decelerating phase. By properly tapering the magnetic field so that the harmonic cyclotron resonance condition, $\omega_{nmq} = n\Omega_c + k_z v_z$, is satisfied, the electrons will continue to lose energy throughout the cavity. In the limit of an infinitesimally thin electron beam, all electrons follow the same trajectory and the conversion efficiency of the electron beam's energy into the high frequency wave can exceed 50%.[4]

2. DESIGN

Using a nonlinear particle-tracing simulation code[5], a sixth-harmonic TE_{612} gyro-multiplier has been designed to yield 32% efficiency. Figure 2 shows the interrelation between the device's beam power, conversion efficiency and harmonic output power for a 16% linear magnetic downtaper. The depletion of the total and transverse beam energy over the length of the interaction cavity is depicted in Fig. 3. By lengthening the cavity, the required beam power to achieve optimum efficiency can be reduced, as shown in Fig. 4 for a nonlinear magnetic field taper which satisfies the gyroresonance condition.

An experiment to produce 150 kW at 17.4 GHz with the design parameters listed in Table I is currently under construction at UCLA. The TE_{111} mode gyroresonant rf accelerator will be driven by a 1 MW, 2.9 GHz klystron which will produce an axis-encircling beam with the characteristics shown in Fig. 5. The magnetic field will be tuned to satisfy the gyroresonance condition in both the accelerator and multiplier cavities.

In a future experiment using an available 20 MW, 8.5 GHz klystron, a higher frequency multiplier will emit in the 85 to 170 GHz region with power levels of approximately 2 MW.

This work has been supported by ARO under Contract DAAH04-93-G-0084 and Rome Laboratory (ATRI) under Contract F30602-91-C-0020.

1. C.S. Kou, D.B. McDermott, N.C. Luhmann, Jr., and K.R. Chu, *IEEE Trans. on Plasma Science* **18**, 343 (1990).
2. H.R. Jory and A.W. Trivelpiece, *J. Appl. Phys.* **39**, 3053 (1968).
3. D.B. McDermott, D.S. Furuno and N.C. Luhmann, Jr., *J. Appl. Phys.* **58**, 4501 (1985).
4. A.K. Ganguly and J.L. Hirshfield, *Phys. Rev. Lett.* 70, 291 (1993).
5. K.R. Chu, M.E. Read and A.K. Ganguly, *IEEE Trans. on Microwave Thy. and Tech.* **28**, 318 (1980).

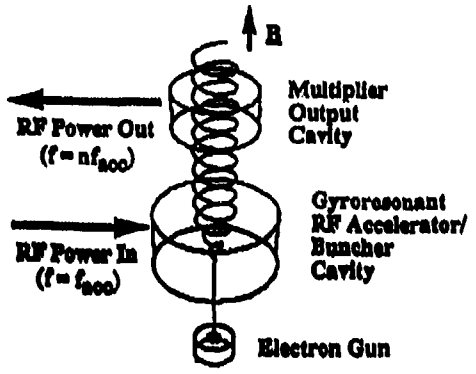

Fig. 1. Schematic of gyrofrequency multiplier.

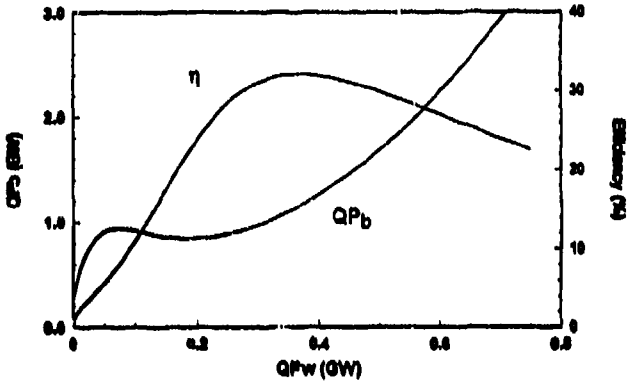

Fig. 2. Dependence of efficiency and beam power (times cavity Q) on wave power (times cavity Q) in gyro-multiplier cavity for the parameters listed in Table I.

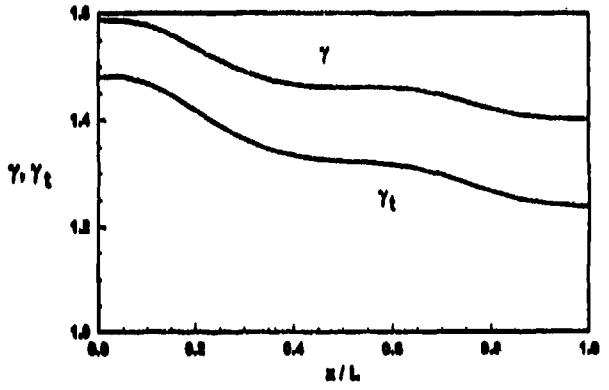

Fig. 3. Spatial dependence of total and transverse electron energies during optimum interaction in Fig. 2 for QP_b = 1 GW where $\gamma_t = [1 - (v_t/c)^2]^{-1/2}$.

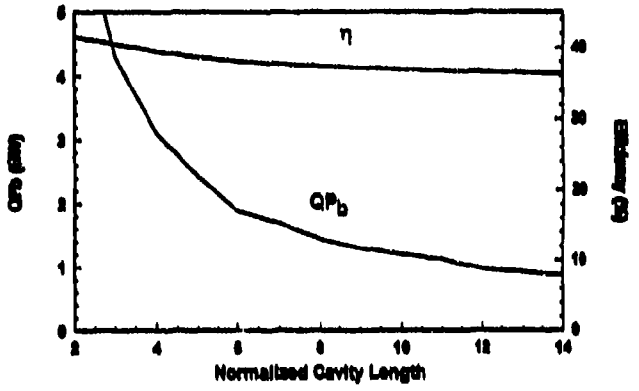

Fig. 4. Dependence of optimum efficiency and beam power (times cavity Q) on cavity length for a magnetic field taper that preserves gyroresonance (TE_{612} mode).

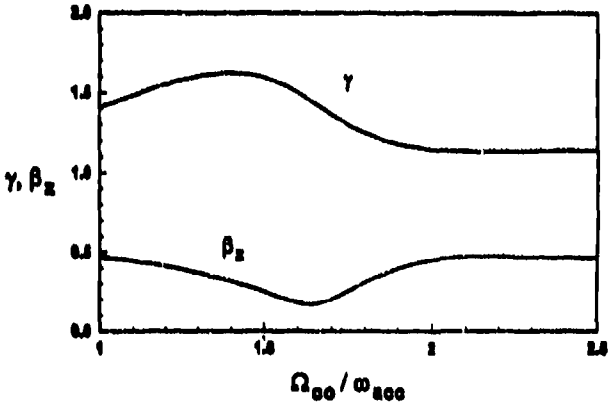

Fig. 5. Dependence of output electron energy and axial velocity on the rest mass electron cyclotron frequency to accelerator frequency ratio (V_{in} = 68 keV, P_{in} = 750 kW, Q = 400).

Table I. Design Parameters for Sixth-Harmonic Gyrofrequency Multiplier

Harmonic	6
Frequency	17.4 GHz
Beam voltage	300 keV
Beam current	1.67 A
α (= v_t/v_z)	3.0
Guiding-center radius	0.0 cm
Guiding-center spread	0.2 cm
Larmor radius	1.3 cm
Cavity radius	2.1 cm
Cavity length	8.4 cm
Cavity Q	2000
Magnetic Field	1.56 kG
Magnetic linear downtaper	16%
Output power	150 kW
Efficiency	32%

THEORETICAL AND EXPERIMENTAL INVESTIGATION OF X-BAND TWO-CAVITY GYROKLYSTRON

I.I.Antakov, M.A Moiseev, E.V.Sokolov and E.V.Zasypkin

Institute of Applied Physics, Russian Academy of Science
46 Uljanov St., 603600, Nizhny Novgorod, Russia

ABSTRACT

Using self-consistent field theory the interaction of electron flow with HF fields in the cavities of a gyroklystron has been analized. As a result, optimal parameters of the output cavity corresponding to the maximum efficiency have been found. Experimental study of the dependencies of efficiency on Q-factor and length of the output cavity has been carried out.

2. THEORY AND NUMERICAL SIMULATIONS

In the framework of our ordinary assumptions (a weakly - relativistic mono-velocity electron beam interacts with a TE-mode of a cavity at the fundamental cyclotron frequency, RF space charge effects are negligibly small) the interaction of the electron beam with the RF field in the output cavity is characterized by the orbital efficiency $\eta_\perp$ which is equal to the ratio of energy extracted by the HF field from electrons to their initial oscillatory energy. The orbital efficiency is found by virtue of nuserical integration of electron motion equation [1] in the cavities and drift region with corresponding initial conditions [2]. Calculated dependencies of the optimal $\eta_\perp$ for a gyroklystron with sinusoidal axial distribution of HF field in the cavities on a normalized beam parameter $I_2 = 1{,}5\pi Q_2 I_0 \lambda\ (1+g^2)G\ /\ L_2 V_0^2 g^4$ and normalized cavity length $\mu_2 = \pi(\beta_\perp^2/\beta_\parallel)\ (L_2/\lambda)$ are presented in Fig.1. Here I_0 and V_0 are beam current and voltage, L_2 and Q_2 are the lenght and Q-factor of the output cavity, g is the beam pitch-factor, G is the coupling coefficient of electron flow with HF field of the cavity, λ is the operating wavelength. As can be seen in the figure, the maximum orbital efficiency equals to 0.72 at following values of normalized parameters

$$I_2 = I_{2st}^{min}\ ,\quad \mu_2 \simeq 4.5\ . \qquad (1)$$

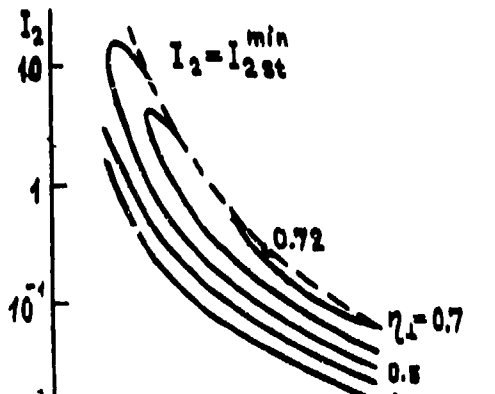

Fig.1. Orbital effciency contours vs parameters I_2 and μ_2

Here I_{2st}^{min} is a starting parameter I_2 minimized by the cyclotron resonanse

mistuning $\Delta=2(\omega-\omega_H)/\beta_\perp^2\omega$. The total efficiency is $\eta = (1- Q_2/ Q_{2ohm})g^2 (1+g^2)^{-1} \eta_\perp$, where Q_{2ohm} is the ohmic Q-factor. If the beam parameters I_0, V_0, g and coupling coefficient G are known, one can find from (1) the optimal values of Q-factor and length of the output cavity.

3. EXPERIMENTAL RESULTS

To check the above theory and interpret the performance characteristics of gyroklystrons the experimental two cavity pulsed tube operating in the TE_{011} mode at X-band was examined. The electron flow was produced by a diode magnetron-injection gun with beam voltage 16 kV and current up to 3 A. The parameters of the first cavity were fixed ($Q_1=250$, $L_1=1.1\lambda$) while the parameters of the output cavity were varied in the wide range - $150 \leq Q_2 \leq 1700$, $1.1 \leq L_2 \leq 2.4$. Fig.2 and 3 show the measured total efficiency η as functions of beam current at various Q_2 and L_2, as well as corresponding theoretical curves predicted by the above theory. The theoretical and experimental curves are in qualitative agreement , it confirms the validity of this theory.

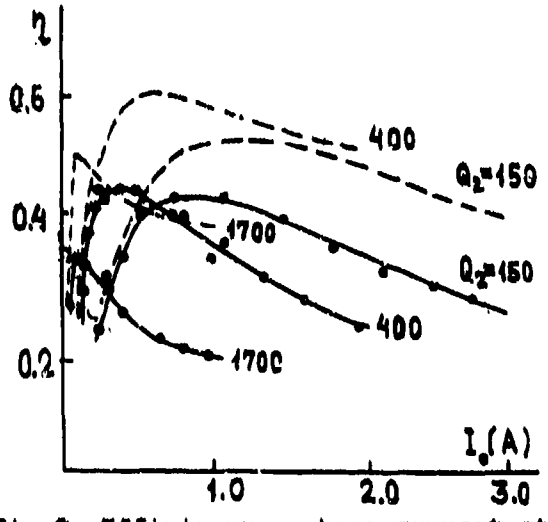

Fig.2. Efficiency vs beam current at various Q_2 (solid lines-experiment, dashed lines - simulation)

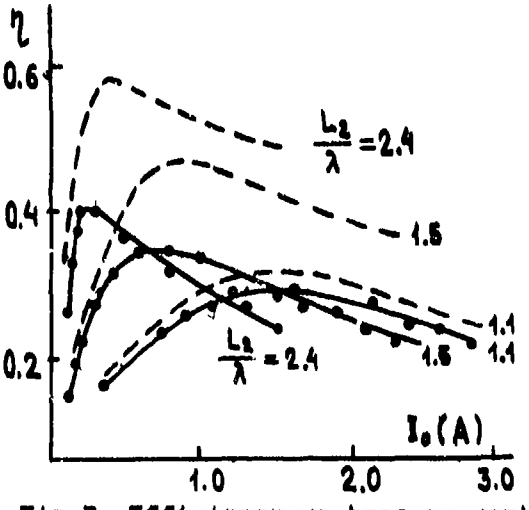

Fig.3. Efficiency vs beam current at various L_2 (solid lines- experiment, dashed lines - simulation)

4. REFERENCES

1. V.A.Flyagin, A.V.Gaponov, M.I.Petelin , and V.K.Yulpatov, "The gyrotron" IEEE Trans. on MTT, Vol.MTT-25, pp.514-520, June 1977.

2. A.V.Gaponov, A.L.Goldenberg, V.K.Yulpatov, "Cyclotron resonance maser with two cavities (CRM - klystron)," Abstracts of the Vth All-Union Conference on Microwave Electronics, Saratov University, p.20, 1966 (in Russian).

35-GHz RADAR GYROKLYSTRONS

I.I. Antakov, E.V. Zasypkin, E.V. Sokolov, and V.K. Yulpatov

Institute of Applied Physics, Russian Academy of Science
46 Uljanov St., 603600, Nizhny Novgorod, Russia

A.P. Keyer, V.S. Musatov, and V.E. Myasnikov

R & D Company " Torry ", 117393, Moscow, Russia

ABSTRACT

Two versions of powerful pulsed gyroklystrons were elaborated for radar systems with specific requirements for their power, gain and bandwidth. The first tube had two cavities in the TE_{021} mode. It yields 750 kW of output power with efficiency 24%, gain 20 dB, and bandwidth 0,6% . The second multicavity gyroklystron in the TE_{011} mode yields output power between 150 and 250 kW with efficiency up to 48%, gain up to 40 db and bandwidth up to 1,5% . The pulse width of the tubes is 100 μs.

INTRODUCTION

The possibility of creation of cyclotron resonance maser (CRM) amplifier of klystron type (multicavity gyrotrons or, according to the terms established in the end of th 70s, gyroklystrons) attracted a great attention in 1966 [1] just after first successful experiments with CRM-monotrons (gyrotrons). In 1967 efficiency of the klystron mechanism of electron bunching in CRMs was demonstrated. Electron efficiency about 70% was achieved in the experiments with a physical model of a gyroklystron operating in the fundamental TE-mode at X - band.

The initial experiments with gyrotrons and gyroklystrons were planned in the short-wave part of X-band. However, well-known advantages of the mechanism of stimulated cyclotron radiation of helical electron flows over the mechanisms of induced Cherenkov and transition radiation used in the "classical" electron devices of the O-type [2] gave a hope for obtaining a high power levels and efficiencies also in the millimeter and submillimeter wavelength regions. This circumstance was reflected in the first inventions connected with gyroklystrons [3] filed as patent applications in 1967.

EXPERIMENTS

Up to the middle of the 70s the characteristics of gyroklystrons were studied at a relatively low levels of the output power at X-band and K-band [4] Results of these studies are in agreement with the notion that a gyroklystron having the characteristics suitable for practical applications can compete by

the level of its output power with an ordinary high-power klystron and TWA of the O-type in the middle part of X-band and becomes more and more advantageous as the operating frequency grows. In that period a great experience of developing gyroklystron modifications was accumulated and gave grounds for formulation of the problem of creating a gyroklystron amplifier operated at Ka-band with output power close to the power of gyrotrons. The efforts in solving this problem were strongly stimulated by the fact that designers of radars became interested in the amplifiers of Ka-band with the output pulse power of several hundreds kilowatts.

Theoretical and experimental investigations performed before the middle of the 80s resulted in creation of powerful pulsed gyroklystrons operated in Ka-band. Basic parameters and characteristics of two versions of gyroklystrons are given in the table .

TABLE

Cavity mode	Number of cavities	Operating frequency	Beam voltage	Output power	Efficiency	Gain	Bandwidth
TE_{02k}	2	35 GHz	75 kV	750 kW	24%	20dB	200 MHz
				350 kW	32%	19dB	180 MHz
TE_{01k}	3,4	35 GHz	55 kV	250 kW	35%	40dB	500 MHz
				160 kW	48%	42dB	320 MHz

In the table the upper half-line of the output characteristics corresponds to the regime of maximum power, the lower one to the regime of maximum efficiency. All the results were obtained at pulse duration about 100 μs. Note that along with the high level of the output powers the half-power bandwidths of these devices excess essentially those achieved in gyroklystrons earlier.

REFERENCES

1. A.V. Gaponov, A.L. Golderberg, V.K. Yulpatov, "Cyclotron resonance maser with two cavities (CRM-klystron)," Abstracts of the Vth All-Union Conference on Microwave Electronics, Saratov University, p.20, 1966 (in Russian).

2. A.V. Gaponov, M.I. Petelin, V.K. Yulpatov, "Induced radiation of excited classic oscillator and its use for high frequency electronics," Radiophisics and Quantum Electronics, Vol. 10, pp.794-812, 1967.

3. A.V. Gaponov, A.L. Goldenberg, G.N. Rapoport, V.K. Yulpatov. Multi-cavity cyclotron resonance maser. Authors Certificate 273001 (USSR). Filed 16.06.67, publ. 15.03.75; I.I. Antakov, A.V. Gaponov, V.A.Gintsburg, A.L. Goldenberg, M.I. Petelin, V.K. Yulpatov. Amplifier of electromagnetic oscillations in the centimeter, millimeter and submillimeter wavelength band: Authors Certificate 302050 (USSR). Filed 16.06.67, publ. 5.11.75.

4. I.I. Antakov, L.A. Aksenova, E.V. Zasypkin, M.A. Moiseev, L.G. Popov, E.V. Sokolov, V.K. Yulpatov," Multi-cavity phase-locked gyrotrons for low-hybrid heating in toroidal plasmas," "Strong Microwaves in Plasmas" Suzdal, Sept. 1990, Proc. Int. Workshop, Nizhny Novgorod, Vol.2, pp.773-778.

Low pass filters for the Far Infrared.

C.V.Haynes and P.A.R.Ade

Physics Department, Queen Mary and Westfield College, Mile End Road, London, E1 4NS

1. INTRODUCTION

We discuss here the use of far infrared multi-layer low pass mesh filters to thermally reject unwanted heat from the intermediate temperature radiation shields of liquid helium cryostats used to cool FIR and submillimetre detectors. This unwanted thermal background increases both the photon noise of the detector and the helium boil-off from the cryostat. Ideally the detector should be filtered to only those wavelengths that are required with all others being reflected, not absorbed, by this filter. Conventionally, the solution has been to use a filter based on high frequency radiation absorption or scattering for this purpose. However, absorption filters are limited in diameter due to warming, with consequent re-emission problems, while scatter filters exhibit a trade-off between low forward scattering and a shallow cut-off edge slope. Here, we present a new form of multilayer low pass mesh filter which is both mechanically rugged and maintains its performance for all temperatures between 1 and 300K. These filters function by reflecting all unwanted high frequency power thus reducing the tendency for the filter to heat up. This property combined with the inherent low emissivity of metal mesh filters reduces the parasitic thermal loading of the cold stage and hence gives enhanced cryogen lifetime (or lower closed cycle cooler operational temperatures).

2. DESIGN and MANUFACTURE

A conventional metal mesh filter consist of a series of meshes with air/vacuum gaps effected by annular metal shims. The individual mesh patterns are generated photolithographically in copper on a thin polyester film substrate (typically 1.5 μm thick mylar). Master plates are produced by electron beam lithography of chrome on glass. The disadvantages of these types of filter are twofold. First, they must be assembled individually using rigid and therefore bulky annular mounting rings and secondly they are very sensitive to mechanical or chemical (solvent) damage. The new filters use the substrate thickness itself to control the required inter-grid spacing. We have made filters using either polyethylene or polypropylene as the substrate. Since nominal thicknesses only are available from the manufacturers we have devised a method of stretching the films to obtain the correct thickness before the mesh pattern is applied. Once all the meshes have been processed the final assembly of meshes is hot pressed in a vacuum oven to produce a slice of filter material. This slice is rugged, flexible and can be cut with a circular punch to make filters of the required diameter. We are now routinely making filters with usable apertures up to 90 mm diameter.

3. RESULTS

The transmission of a 200 cm^{-1} edge filter is shown in Figure 1. Results of other filters will be presented along with the measured increase in cryogen hold time for dewars which use these filters on intermediate radiation shields in comparison with those which use both the standard absorption or scatter type filters.

Figure 1

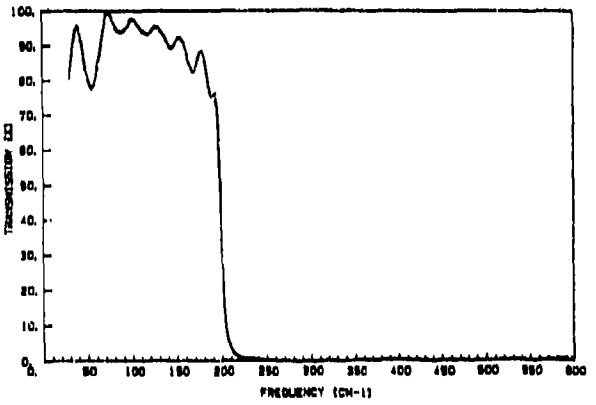

Rejection of frequency bands of electromagnetic radiation by quasi-optical Bragg structures

Vertiy A.A., Gavrilov S.P.and I.N.Goltvyanskiy

Institute of Rdiophysics and Electronics,
Academy of Sciences of Ukraine,
12 acad. Proskura st., Kharkov
310085 Ukraine
Phone (0572) 448-467
Fax (0572) 441-105

ABSTRACT

The paper contains the results of investigation of quasi-optical rejection filter. The filter is created on the base of multilayer dielctric periodical structure. We give the equations allowing to calculate the parameters of the periodical structure at given filter characteristics. These given parameters are: relative reflection band ($\Delta\lambda/\lambda_0$) and the transient constant T/T_0 within limits of this band.

It is shown that in the case of normal incident of electromagnetic wave on the filter the shape of its frequency characteristics in the attenuation band is nearly rectangular.

Amplitude and frequency characteristics of the filter are mearsured in millimeter wave range.

2. INVESTIGATION RESULTS

In millimeter wave region the dielectric multilayer structures are widely used in different UHF devices. Investigation of quasi-optical multilayer structures using minimum number of materials is of particular interest. It is very convenient to calculate these layer structures using simple formulars. The most suitable for these purposes are periodical multulayer structures of Bragg type.

The purpose of the present paper is a calculation and experimental investigation of such periodical structures in millimeter wave region, namely, quasi-optical rejection filter.

The filter is consisted of a set of square polystyrene plates with thickness of $a \simeq 0{,}45\,\lambda_0$ ($\lambda_0 = 4mm$). The plates are separated by air gaps with thickness b. The relation of b/a is equal to 1.1. The filter aperture is $2A \simeq 15\,\lambda_0$, the number N of periods per filter length is equal to 16. Frequency transfer characteristics of this complicated system are investigated in 8-mm and 4-mm frequency ranges. Horns were employed as transmitting and receiving antennas. In the case of a normal incicdent of electromagnetic wave on the filter the reflecting band (rejection) has nearly rectangular shape. Relative reflective bands $\Delta\lambda/\lambda_0$ of the periodical structure considered may be found from the following equation

$$\Delta\lambda/\lambda_0 = (1/\pi m)\left[(n_2 - n_1)/(n_2 + n_1)\right], \quad m = 1,2,\ldots, \quad (1)$$

where n is a refractory index of a dielectric layer with thickness b; n is a regractory index of a dielectric layer with thickness a.

Taking into account the equation (1) and from the measurements we conclude that at $\nu_0 = c/\lambda_0 =$ 28GHz or 56GHz $\Delta\nu/\nu_0$ is 0,2 or 0,1; correspondingly.

Transfer factor in the rejection band may be calculated from the following expression

$$J/J_0 = \exp[-2N\ln(n_2/n_1)] \quad . \quad (2)$$

For the structure investigated the measured value of this relation is less then -30dB.

The thicknesses of the dielectric layers are obtained from the following system of equations

$$2\pi/\lambda_0(n_2a+n_1b)=2\pi m, \quad (3)$$
$$2\pi/\lambda_0(n_2a-n_1b)=\pi(2n+1), \quad (4)$$

where m=1,2..., n=0,1,2.... Value of m is calculated from (1), and n should be chosen near to m (m>n). Fig.1 shows dependences of transfer coefficient T on frequency for Bragg structure at parameter values: $\lambda_0 \approx 5.22$ mm; $a/\lambda_0 \approx 0.34$; $b/\lambda_0 \approx 0.38$; $n_1 = 1$; $n_2 = 1.59$. Curve 1 corresponds to absence of the filter; curve 2 is a measured dependence; curve 3 is a calculated one; $J/J_1 \approx 10^{-2}$; $\Delta\lambda/\lambda_0 \approx 10^{-2}$.

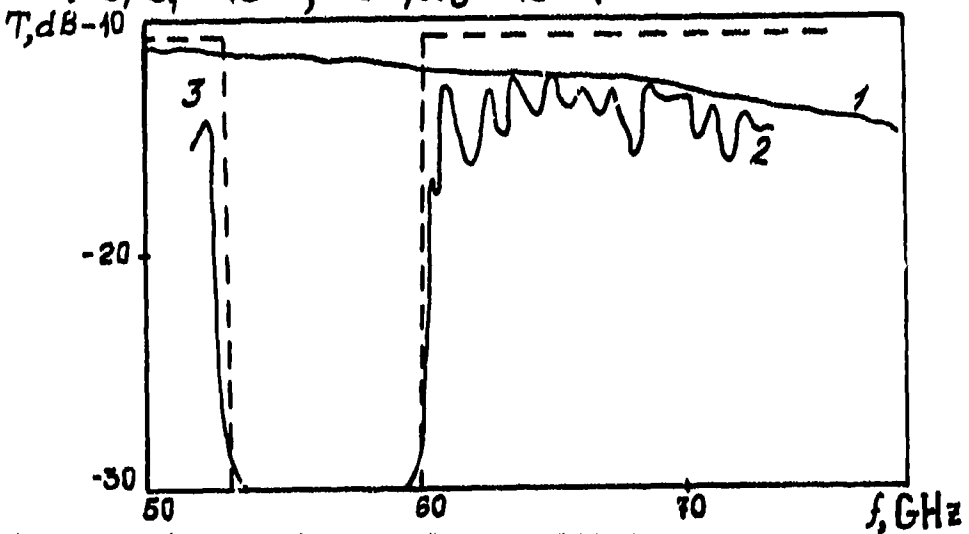

Fig.1. Dependence of transfer coefficient T on frequency at normal incident.

3. CONCLUSION

Thus, the investigation carried out showed that the prospectiveness of application of Bragg type structures as quasi-optical rejection filters.

These filters have a simple construction, inexpensive and have good optical characteristics. Calculation and synthesis of such layer systems may be carried out using simple calculations.

Performance of a high Tc superconducting ultra-loss microwave microstrip filter

O.D.Pustylnik, A.A.Dymnikov, I.V.Voinovsky, O.A.Khimenko

SRC "Fonon", 39, Pobedy Ave., KPI-3240, Kiev, Ukraine

V.F.Vratskikh

Institute for Themophysics, Kutateladze 1, Novosibirsk

630090, Russia

ABSTRACT

High-quality oriented thin films of $YBa_2Cu_3O_y$ having transition been made temperature > 89 K and critical current densities (at 77 K) > 10^6 A/cm^2 by pulsed laser deposition on ($\bar{1}012$) non-buffered sapphire substrates. The microwave surface resistance (Rs) has been measured between 10 K and 300 K at 135 GHz by a copper cavity end-wall-replacement technique. Microwave devices fabricated from films on non-buffered sapphire have included an K-Band modified three-pole Chebyschev filter having an insertion loss of 1,2 dB at 60 K. The HTS filter was designed to be a 5 % bandwidth. Our filters out perform similar copper microstrip filters, indicating that practical levels of HTS performance have been achieved.

1. INTRODUCTION

Numerous paper to date have demonstrated the applicability of thin films of the oxide-based high temperature superconductors to passive microwave circuits. Cavity studies, conductivity measurements and patterned resonator studies have all demonstrated that high quality epitaxial films of these superconductors can have surface resistances significantly lower than normal metals typically used in microwave application. Epitaxial Y-Ba-Cu-O (123) films of high quality have been grown on substrates such as $SrTiO_3$, MgO, YSZ and $LaAlO_3$ by various deposition techniques. It is known, however, that each of these substrates represent some kind of compromise [1]. From practical point of view, the substrate like sapphire is the most desirable material for 123 films because of the low microwave loss, high mechanical strength, high thermal conductivity, high Debye temperature, good surface chemistry and low cost. Epitaxial Y-Ba-Cu-O films on sapphire with good critical, transport and RF properties were demonstrated by Vratskikh et al[2] . In this paper, we report the result of measurement HTS microwave filters in K frequency band. From high Q data and microstrip geometry, we can directly analyze the surface resistance and conductor losses of the patterned $YBa_2Cu_3O_y$ films. Our

patterned filters obtained Rs < 0,35 mOhm after fabrication. These results show that the film degradation was very minimal since unprocessed films have Rs of 0,25 mOhm. Copper microstrip filters of identical geometries were fabricated and measured for comparison. HTS microwave components were clearly superior to normal metal counterparts. Manufacturing patterned $YBa_2Cu_3O_y$ films with quality performance at 135 GHz is important in demonstration the immediate applicability of HTS microwave integrated circuit technology. Microstrip filters produced with $YBa_2Cu_3O_y$ films on non-buffered sapphire achieve a level of insertion loss the cannot be met with normal metal.

2.FILM PREPARATION

Our deposition system will be described in details elsewhere. Briefly, 123 targets were ablated by many-mode Nd:YAG laser. The pulse energy was 300 mJ, the pulse duration 20 ns,the average beam energy density 4 J/cm^2.The distance of the target and the substrate was 6 cm and the screen was placed between target and substrate in order to protect the film surface from droplets. At a pulse repetition rate of 10 Hz the average growth rate was 0,3 nm/s. The oxygen pressure was 0,6 Torr and the substrate temperature, measured with accuracy 5 ^oC, was 755-770 ^oC. There latively high oxygen pressure is necessary to produce large clusters and to reduce in such way the chemical activity of Ba on the substrate surface. The elevated substrate temperature is required for surface mobility of large clusters.

3.FILM CHARACTERIZATION

The x-ray diffraction pattern of our films contains only (00L) sharp peaks showing, that the film is highly oriented with the c-axis perpendicular to the substrate. The FWHM of the [005] rocking curve was in the range of 1.3-2.5^o Some general parameters of samples, used for microwave measurements and device fabrication are represented in Table 1.

Table 1 General parameters of samples.

Sample	Tc (R=0), K	T, K	Jc, A/cm^2	R300/R100	Thickness, nm	Rs, mchm at 34 GHz
A	90	0.25	> 10^6 * at 77K	3,5	150	0.25 at 60 K
B	89.3	0.3	> 10^6 * at 77K	3,3	150	0.3 at 55 K

* dc - transport measurements.

4. DEVICE FABRICATION

The 123 film was patterned with photolithographic technique and etched with dilute phosphoric acid. The film on sapphire was coated with 0.7 micron FP-383 positive photoresist. The photoresist was then baked in 90 ^{o}C oven for 15 min and after wards was exposed 42 s using a 1:1 contact printer using UF lamp. Then 1:1 diluted developer was used to develop the photoresist for about 10 s in a < 100 ^{o}C over for 30 min stabilized the resist for optimized line width control during the 123 wet etch in a diluted solution phosphoric acid. After this etch, the photoresist was stripped in acetone.

5. MICROWAVE MEASUREMENTS

The measurements of the temperature dependence of microwave surface resistance were carried out at 135 GHz using a method of a cylindrical copper host cavity. The cavity was excited in the TE_{011} mode. In detail this method was reported in work[3]. Moreover, the temperature dependence of Rs was calculated from the measurements of the unloaded quality factor Qo of the cavity. Temperature variation between 12 and 150 K was provided by warming the cavity in vacuum in using microcryogenic system. The temperature was measured with a semiconductor resistor with an absolute accuracy of + 0.1 K. Fig.1 shows Rs vs T for our two films (sample A,B in Table 1) measured at 135 GHz. For comparison at the same figure by solid line is plotted the temperature dependence of the surface resistance of the copper cavity walls. Thickness of films were about 150 nm. The low residual resistance film A, taking into account that the film thickness was lower than penetration depth of magnetic field, shows that the film is of high quality. The calculated value of Rs at 31 GHz using quadratic frequency dependence of Rs is represented in Table 1.

The demonstration device chosen was a 3-pole microstrip parallel-coupled-line Chebyschev bandpass filter on non-buffered sapphire. Two filters were of fo=34 GHz made on different quality films on a designed center frequency with a bandwidth of 1500 MHz. The filters were arranged to fit on 12x7,5x0,25 mm^3 sapphire substrates and mounted on copper plate-refrigerator with two waveguide-microstrip connectors.

The transmission coefficient (S_{21}) versus frequency was measured employing an P2-65 network analyzer with transmission calibration at any temperature on a HTS microstrip line. A typical plot from the network analyzer of 123 bandpass filter A is shown on Figure 2.

6 MEASUREMENT RESULTS

The centre frequency of HTS filter A versus temperature date clearly showed kinetic inductance effects. Figure 3 shows the plot of centre frequency as a function of temperature. The plot shows the rapid shift in frequency near Tc

where most of the transformation of normal electrons into superconducting electrons occur. The shift in frequency in self is directly caused by the kinetic inductance of the superconduction electrons. Figure 4 shows the temperature dependence of the insertion loss for the filter A. The insertion loss of Y-Ba-Cu-O filter was about 1,2 dB at the temperature of 60 K compared to the insertion loss of copper filter, which was greater than 2,5 dB. $YBa_2Cu_3O_y$ filters insertion losses began increasing at about 70 K. The bandwidth of $YBa_2Cu_3O_y$ filters was about 1500 MHz with the return loss for filter better than 14 dB.

7. CONCLUSION

We have successfully used $YBa_2Cu_3O_y$ films on non-buffered sapphire to fabricate microstrip filters in K frequency band. These microwave circuits yield high microwave performances than were superior to the same circuits using normal metals. The $YBa_2Cu_3O_y$ filters had a 1,2 dB insertion loss which was much lower than the copper filter one. We achieved surface resistances of less than 250 mOhm at 34 GHz for our patterned $YBa_2Cu_3O_y$ films. The higher level of performance of HTS microstrip filters allows us to apply high-Tc superconductivity to integrated circuit technology.

Research is supported by the State Program of Ukraine "The High Temperature Superconductivity"

8. REFERENCES

1. Char,K. et al, "Properties of epitaxial Y-Ba-Cu-O thin films sapphire", Appl. Phys.Lett., 56 , pp. 595-598, 1990.

2. Pustylnik,O.,et al,"The millimeter wave surface resistance measurements of Y-Ba-Cu-O films epitaxially grown on non-buffered sapphire substrates", Cryogenics , 32, pp.620-623, 1992 .

3. Kessler,J.R.and Gering,J.M., "Use of a Fabry-Perot resonator for the measurement of the surface resistance of high Tc superconductors at mm wave frequencies," Int.J. IR and MM waves, 11 , pp. 151-164, 1990.

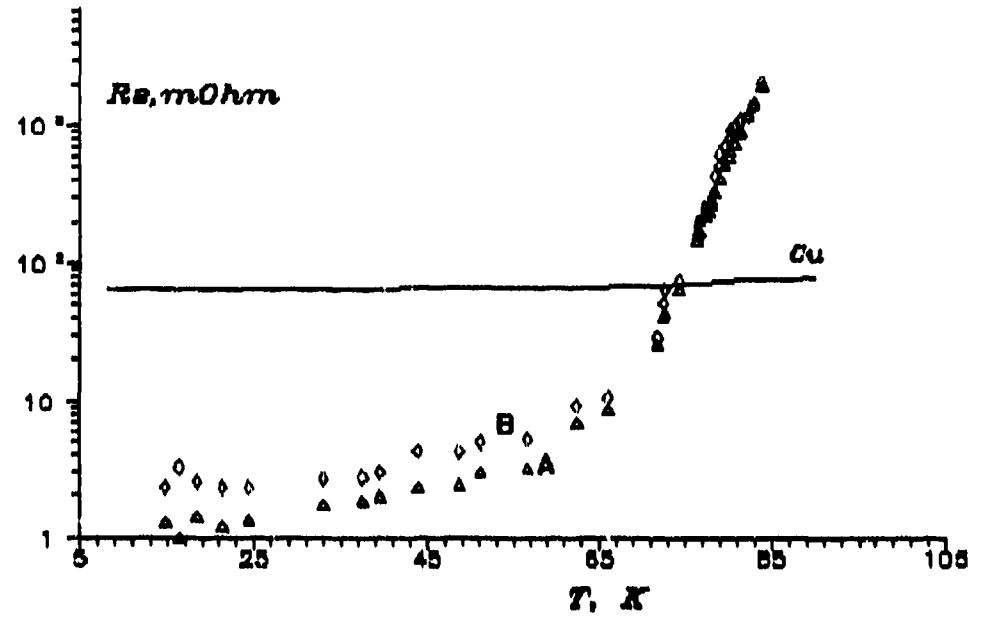

Fig.1. Temperature dependense of surface resistance for samples A,B at 135 GHz.

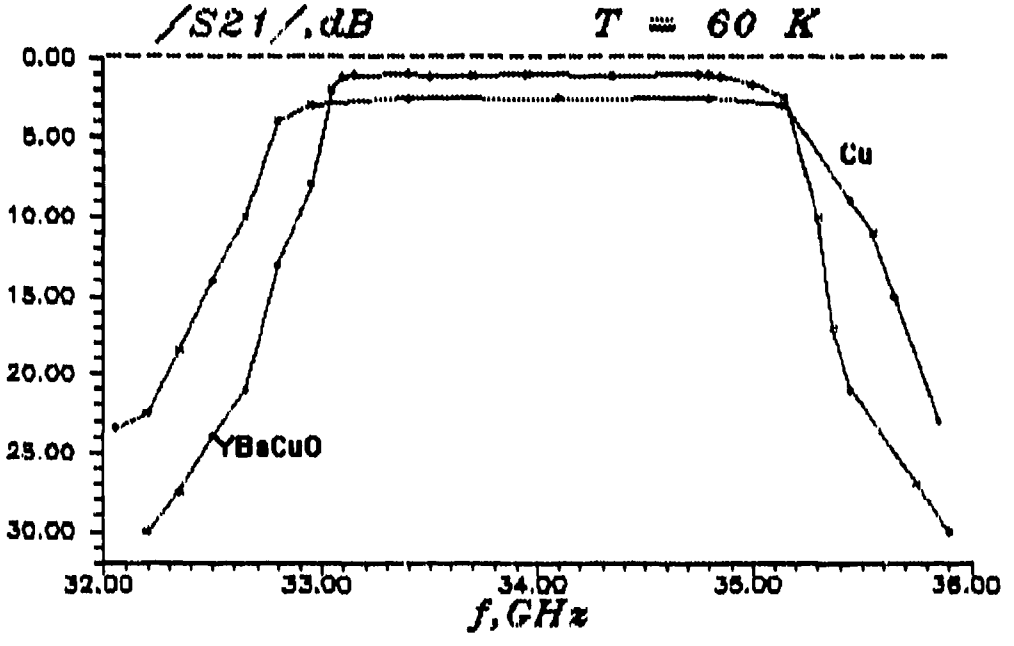

Fig.2. Transmission versus frequency for YBaCuO and Cu filters.

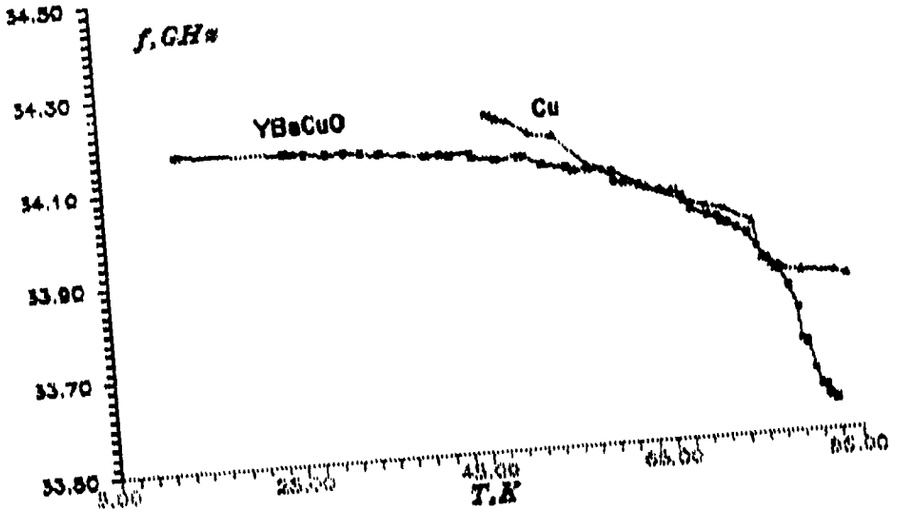

Fig.3. Temperature dependence of the centre frequency for YBaCuO and Cu filters.

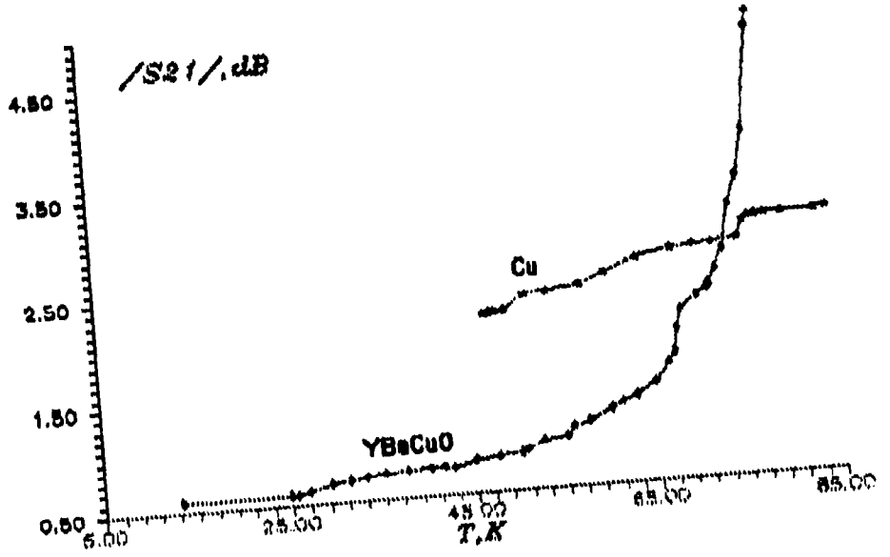

Fig.4. Temperature depence of the insention loss for YBaCuO and Cu filters.

Frequency selective surfaces for millimetre and submillimetre-wave quasi-optical demultiplexing

J W Bowen
Department of Physics, Queen Mary and Westfield College, University of London

R Cahill
Systems and Payloads Department, British Aerospace Space Systems Ltd.

E A Parker
Electronic Engineering Laboratories, The University of Kent

1. INTRODUCTION

There is currently much interest in the development of satellite-borne millimetre and submillimetre-wave radiometers for meteorological and remote sensing applications. Such radiometers typically operate over a number of frequency bands even though they usually only have a single receiving antenna and hence a single incoming beam. Consequently it is necessary to have components that demultiplex the frequency bands. This demultiplexing is usually carried out quasi-optically to take advantage of both the wide bandwidths and low losses afforded by such techniques.

The demultiplexing components are frequency selective surfaces (FSSs), or dichroics, which transmit well over one band of frequencies while reflecting strongly over another. To achieve demultiplexing FSSs have to be used at oblique incidence and this presents special problems in their design and characterisation.

Here we present wide-band millimetre and submillimetre-wave transmission measurements that compare the performance of drilled plate and printed element frequency selective surfaces at non-normal incidence angles. The quasi-optical measurement technique is described emphasising those aspects of particular importance for this type of component. Agreement between the measurements and numerical simulation techniques is demonstrated.

2. DRILLED PLATE FSS

The drilled plate FSS (Fig. 1(a)) consists of a metal disc drilled to form a hexagonal array of circular waveguides. The FSS is characterised by the diameter of the waveguides, the centre-to-centre spacing of the waveguides and the plate thickness, all of which determine its electromagnetic performance. The extent of the array is chosen so that truncation of the beam is negligible.

The FSS acts as a high pass filter; the lowest frequency transmitted being governed by the TE_{11} mode cut-off frequency of the holes and by resonant coupling to the hole array. Below this frequency the FSS will reflect strongly. The transmission above the cut-off frequency will, however, not be flat. In particular, when the frequency at which the onset of diffraction by the hole array into orders additional to zero-order occurs, the power transmitted into the on-going beam will be reduced. The lost power is diffracted out of the system. Standing wave effects within the plate further modify the transmission spectrum.

A modal expansion technique was used to design the FSS. This is a vector formulation which assumes that the FSS is infinite in extent and is illuminated by a plane wave.

3. PRINTED ELEMENT FSS

The printed element FSS consists of an array of conductive elements supported on a dielectric substrate. The frequency response is determined by the element type, size and periodicity, the lattice geometry and the electrical properties of the backing material. Low pass, high pass and passband filter characteristics can be generated by suitable positioning of the transmission and reflection bands. The latter is generated at resonance where the amplitude of the current modes induced in the elements is large.

The pattern of the double square FSS (shown in Fig. 1(b)) was produced photolithographically from 2 μm thick aluminium sputtered onto one face of a fused silica substrate with a thickness of half a wavelength at 150 GHz. The filter was designed using a modal expansion technique similar to the one mentioned above.

4. MEASUREMENT TECHNIQUE

The transmission response of the FSSs was measured using a Martin-Puplett interferometric spectrometer (quasi-optical autocorrelator). A spectrum with continuous frequency coverage over an 80–800 GHz range can be measured with a single sweep of a moving reflector. The spectral resolution was 1.5 GHz.

The modal calculations assume that the incident beam is a plane wave. However, a beam of finite width cannot be described by a single plane wave: it is a superposition of an angular spectrum of plane waves. Such a beam will therefore sample the plane wave properties of a FSS over a range of incidence angles centred on the angle of incidence of the optic axis of the beam. In the measurement beam the amplitudes of the plane wave components have fallen to -10 dB at ±4°. The same angular spectrum applies throughout the beam (the changing form of the field with propagation is solely due to interference between the plane waves) and therefore the measured transmission response is independent of the longitudinal location of the FSS in the beam (except for frequencies above the upper edge of the drilled plate FSS pass band where some of the power diffracted into higher orders may be diffracted out of the spectrometer and not detected). Moreover, when the drilled plate FSS is used at oblique incidence the transmitted beam will be laterally displaced with respect to the incident beam. Care must be taken to correctly take account of this shift, both in alignment of the radiometer system and while measuring the FSS transmission response.

5. MEASUREMENT RESULTS

Fig.s 2 and 3 show the measured transmission response of drilled plate and printed element FSSs over the range 80–200 GHz. at 22° TM incidence. The triangles show the calculated transmission coefficient.

Measurements over a range of angles of incidence show that drilled plate FSS transmission deteriorates rapidly as the angle of incidence is increased towards 30°. In contrast the transmission response of the printed element FSS, was measured to be relatively insensitive to incident angle up to 45°. Although the drilled plate FSS has a much sharper transition between the transmission and reflection bands the relatively shallow incidence angles at which it may be used places tight constraints on the design of quasi-optical demultiplexing systems. Moreover the manufacture of this type of FSS becomes increasingly difficult as frequencies are increased into the submillimetre-wave range.

Fig. 4 shows the measured and calculated transmission response of a double layer *single* square loop printed element FSS at normal incidence over 100–800 GHz. Note the excellent agreement between the design predictions and measurements. The filter remains usable at 45° incidence.

6. ACKNOWLEDGEMENTS

We thank A C de C Lima of the University of Kent for running some of the software and Dr I M Sturland of the Materials Science Department, BAe Sowerby Research Centre for fabricating the printed FSS devices.

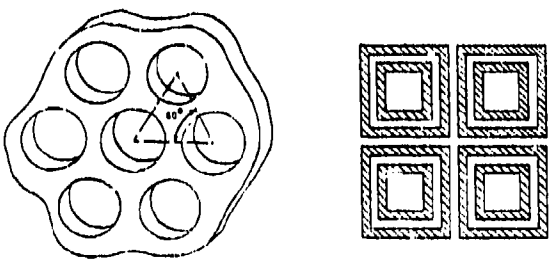

Fig. 1. (a) Drilled plate FSS, (b) Double Square FSS.

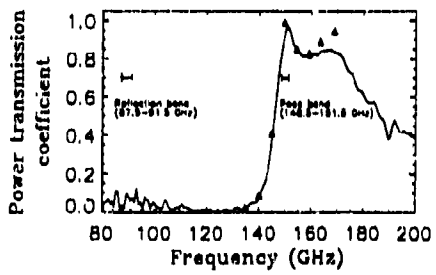

Fig. 2. Drilled plate FSS, 22° TM incidence.

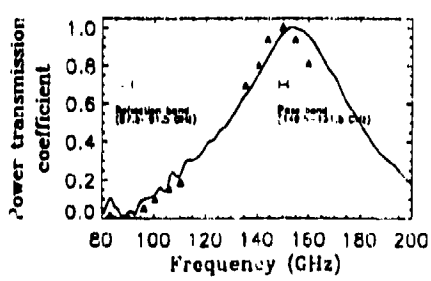

Fig. 3. Double square FSS, 22° TM incidence.

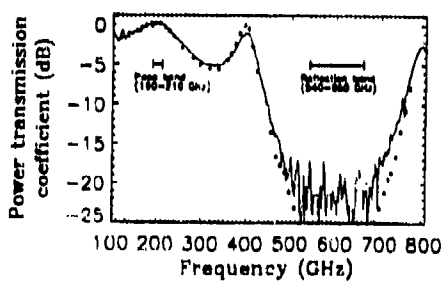

Fig. 4. Double layer single square FSS, normal incidence.

Rugged far infrared bandpass filters.

P. G. Huggard, M. Meyringer, A. Schilz and W. Prettl,

Institut für Angewandte Physik, Universität Regensburg, 93040 Regensburg, Germany.

1. Abstract.

Precision nickel printing screens are shown to be very useful as far infrared bandpass filters. For a range of such regularly perforated screens, transmission maxima have been observed to lie at frequencies between 58 cm^{-1} and 142 cm^{-1}. In general, the peak of transmission is measured to be over 0.9. It is found that this high transmission is little degraded by cascading several screens, but the overall filter Q value may be increased from about 2 to a value of about 6.

2. Introduction.

Considerable effort has been expended in the development of narrow bandpass filters for the far infrared (FIR) spectral region [1,2,3]. The term "narrow bandpass" is used here to describe filters with Q values of between 1 and 10, excluding Fabry-Perot interferometers. Schemes utilised to achieve high peak transmission coupled with good "out of band" attenuation include electroformed rectangular gratings, combinations of waveguide array high-pass filters with capacitive low-pass grids and regular arrays of cross shaped or annular apertures in thin metal films. These methods have some drawbacks, for example thin dielectric substrates may be required for filter elements and/or photolithographic and electrodeposition processes have to be perfected.

As an alternative type of bandpass filter, we propose the use of commercial precision printing screens. Consisting of freestanding electroformed nickel sheets with a regular array of circular holes, these are mechanically strong and readily available in large areas. When used as filters, peak transmissions close to unity have been measured with resonant frequencies between 58 cm^{-1} and 142 cm^{-1} depending on the mesh chosen. Furthermore, by cascading several screens, the resonance Q and out of band attenuation can be considerably improved, with little loss in peak transmission.

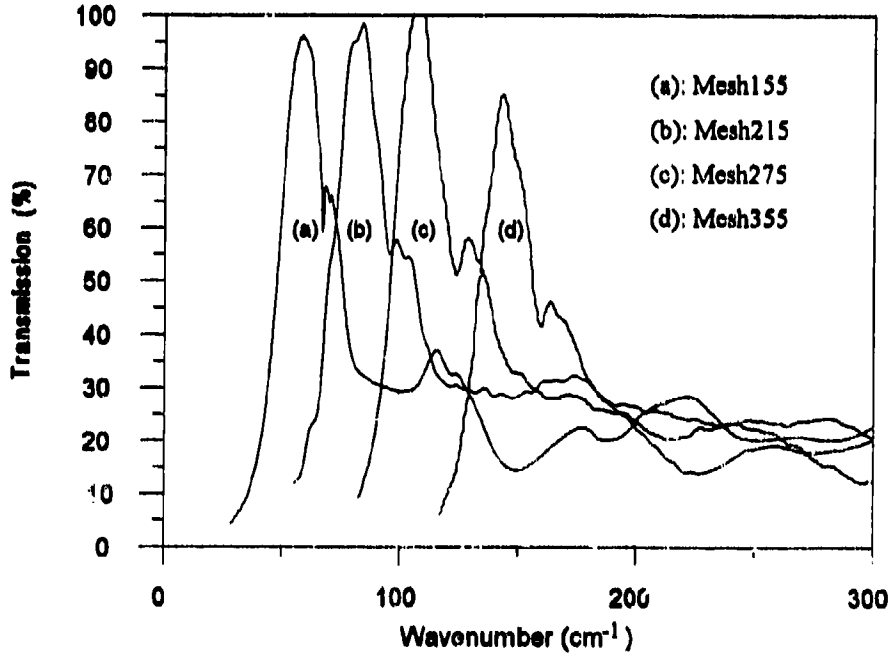

Fig 1. Measured transmission spectra of several HiMesh samples. Spectrometer resolution was 3 cm^{-1} with a measurement error of about 5%. Note the rapid fall in transmission at low frequencies, caused by the waveguide cut-off effect of the holes.

3. Experimental.

A series of screens with different hole diameters and spacing have been measured. In general the screens have a thickness of about 50 μm with a grating constant (g) ranging from 164 μm to 72 μm for Mesh155 to Mesh355 respectively. The corresponding minimum hole diameters vary from 111 μm to 37 μm. The apertures are arranged in an hexagonally close packed pattern, and each tapers from both ends towards the centre. This taper is such that the maximum diameter is approximately twice the minimum.

Transmission spectra, presented in Fig. 1, were measured in vacuum in a Fourier transform spectrometer with a weakly focused (f/3) beam. Measurement resolution was 3 cm^{-1}. The spectra are similar in form, with the transmission rising from a small value at low frequencies to a resonant peak of about 90%. This value is reached at a wavenumber approximately equal to the reciprocal of the grid constant. A small feature observable on the high frequency side of the resonance occurs at a frequency of about 1.2 times that of the transmission maximum [1]. The transmission then declines to a value of about 30% which is maintained up to the highest frequency measured. This value is expected to remain constant at yet higher frequencies, and to tend asymptotically to the fractional open area of the screens, approximately 30%.

4. Discussion and Conclusions.

Such spectra have characteristics of both waveguide filters and metal meshes. A resonant transmission close to unity, at a wavenumber ~ 1/g, is a common characteristic of thin meshes [1,4]. The decline in transmission for higher frequencies is due to the onset of diffraction. However, the below resonance transmission of these relatively thick screens, decreasing rapidly towards low frequencies, more closely resembles that of a waveguide filter [5] than of a thin mesh.

To study the effect of cascading several identical screens, pieces of Mesh275 were placed in series, separated by about 0.5 mm. As the number of screens increases from one to four, the transmission peak is considerably sharpened, with Q rising from 1 to 6. The transmission at the peak is relatively unaffected, remaining at about 85% for four screens, while that at high frequencies is severely attenuated, decreasing to about the noise level of the measurement (2%). It is worth remarking that the separations of the screens is not critical, in contrast to the exact spacings required for best performance from a series of thin cross aperture filters [3]. Furthermore, the attenuation at high frequencies is expected to be excellent, on purely geometrical grounds.

In conclusion, we have shown that metal screen printing meshes are very useful as FIR bandpass filters. They offer significant advantages over conventional filtering techniques, including high strength, the availability of large areas, low cost, high peak transmission and an easily controllable bandwidth (by the non critical cascading of several screens). It is believed that the excellent optical properties arise from a combination of the non negligible mesh thickness and the tapered hole sides.

5. Acknowledgements.

It is a pleasure to acknowledge the help of Dr. J. Magan for drawing these screens to our attention and to thank Stork Screens B. V., 5830 AB Boxmeer, Holland, for the very generous donation of HiMesh samples. P. G. H. and W. P. wish to thank the Bayerische Forschungsstiftung FORSUPRA for financial support.

6. References.

1: K. Sakai and T. Yoshida, "Single mesh narrow bandpass filters from the infrared to the submillimeter region", Infrared Phys. **18**, 137 (1978).
2: T. Timusk and P. L. Richards, "Near millimeter wave bandpass filters", Appl. Opt. **20**, 1355 (1981).
3: C. T. Cunningham, "Resonant grids and their use in the construction of submillimeter filters", Infrared Phys. **23**, 207 (1983)
4: J. M. Lamarre, N. Coron, R. Courtin, G. Dambier and M. Charra, "Metallic mesh properties and design of submillimeter filters", Int. J. Infrared and Millimeter Waves **2**, 273 (1981).
5: F. Keilmann, "Infrared high-pass filter with high contrast", Int. J. Infrared and Millimeter Waves **2**, 259 (1981).

Quasi-Optical Narrow-Band Notch Filters

G.G.Denisov, S.V.Kuzikov, and M.Yu.Shmelyov

Institute of Applied Physics, Russian Academy of Science,
46 Ulyanov Street, 603600 Nizhny Novgorod, Russia

A narrow frequency band (*20...600* MHz) at frequencies *50...200* GHz and high suppression (more than *40* dB) are the typical requirements for notch filters used in plasma diagnostic during experiments with fusion installations. A very narrow frequency bandwidth $\Delta f/f \approx 10^{-3}...10^{-4}$ in the short millimeter wavelength range implies using of quasi-optical high-quality ($Q \geq 10^4$) cavities as elementary cells that constitute a filter, and quasi-optical open transmission line as a primary waveguide. We considered two possible ways to produce such cavities (Fig. 1): 1) two-mirror cavity with a standing wave (a), 2) ring cavity with a traveling wave (b). For both cavities coupling is provided by a semi-transparent film or by diffraction grating. In the first scheme there is a reflected wave, so phase shift (mutual position of cavities) is important. The second scheme uses only a one-way wave and thus all cells are independent.

The second scheme was tested in the experiment at *140* GHz. The filter was combined of four cells coupled with the wave of an open mirror line. Each cell was made as a three-mirror quasi-optical cavity [1], with *5%* coupling and losses per round trip of wave (quality factor is about *7000*). A side of the equilateral triangle was *70* mm. The eigenmode of the transmission line was excited by a corrugated horn , which radiated HE_{11} wave. The filter had attenuation *30...40* dB within the frequency band *20...30* MHz and about *0.3* dB out of the band *50* MHz. Calculations showed that an increase in the number of cells can provide stronger damping of wave in the same narrow frequency band.

Reference:

1. G.G.Denisov and M.Yu.Shmelyov "Effective Power Input into Quasi-Optical Cavity with Traveling Wave," Int. J. of Infrared and Millimeter Waves, Vol.12, 10, pp. 1187-1194, October, 1991.

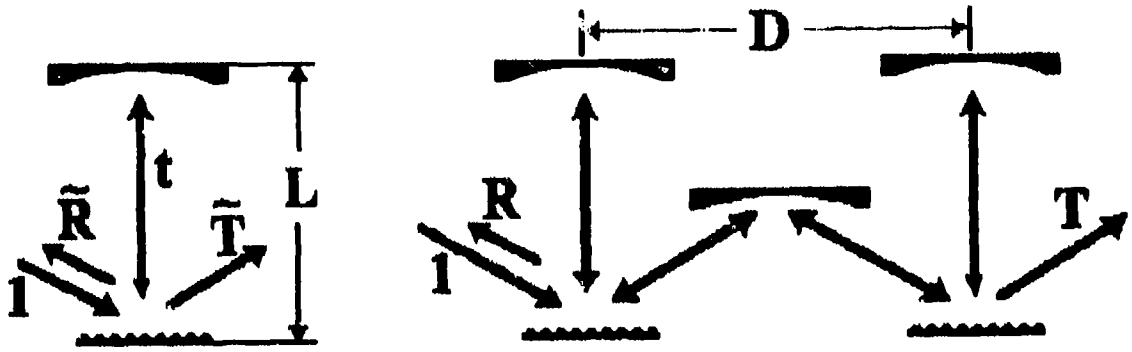

$$\tilde{T} = i \cdot \sqrt{1-t} \cdot \frac{1+\rho \cdot \exp(2ikL)}{1+(1-t)\cdot \rho \cdot \exp(2ikL)}; \qquad \tilde{R} = \frac{t \cdot \sqrt{\rho} \cdot \exp(ikL)}{1+(1-t)\cdot \rho \cdot \exp(2ikL)};$$

$$T = \frac{\tilde{T}_1 \cdot \tilde{T}_2 \cdot \exp(ikD)}{1-\tilde{R}_1 \cdot \tilde{R}_2 \cdot \exp(2ikD)}; \qquad R = \tilde{R}_1 + \frac{\tilde{T}_1 \cdot \tilde{T}_1 \cdot \tilde{R}_2 \cdot \exp(ikD)}{1-\tilde{R}_1 \cdot \tilde{R}_2 \cdot \exp(2ikD)}$$

t -coupling coefficient,
T̃ - transmission } for one
R̃ -reflection } cell

ρ - losses in cavity;
T - transmission } for two
R - reflection } cells

Figure 1a. Principle of filtration for cavities with standing wave.

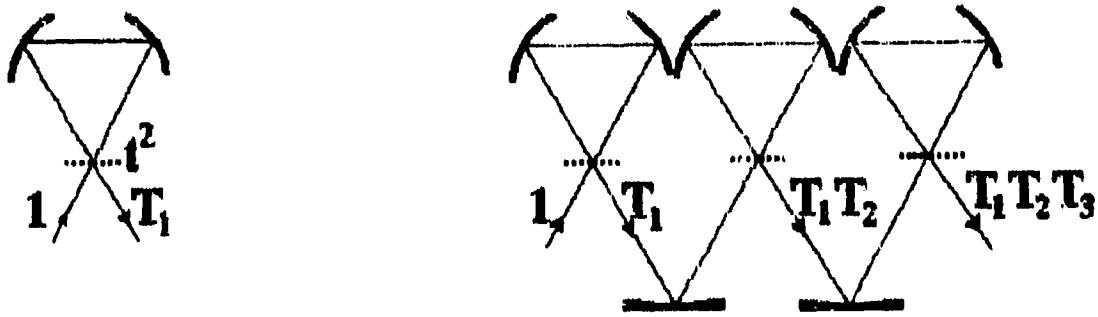

$$T_i = \sqrt{1-t^2} - \frac{t^2 \cdot \exp(ikL) \cdot \rho}{1-\sqrt{1-t^2}\cdot \rho \cdot \exp(ikL)}; \qquad T_N = \prod_{i=1}^{N} T_i$$

Figure 1b. Principle of filtration for cavities with traveling wave.

Design of Ridged Waveguide E-plane Bandpass Filters in Millimeter Wave Applications

D.Budimir, V.Postoyalko and J.R.Richardson

Microwave and Terahertz Technology Group,
Department of Electronic and Electrical Engineering,
University of Leeds, LEEDS LS2 9JT.

Abstract

This paper presents a numerical optimization based approach to the design of ridged waveguide E-plane bandpass filters. Equal ripple approach to optimization is adopted. The calculated insertion loss of X-band a five resonator conventional and ridged waveguide E-plane bandpass filters with and without ideal impedance inverters are presented.

Introduction

E-plane metal insert bandpass filters have found frequent use in many microwave and millimetre-wave applications. However, owing to the nonlinear relation between guide wavelength and frequency, and to the frequency dependency of the coupling elements, high edge steepness and attenuation requirements at the second stopband are often difficult to meet For many applications, such as for channel filters, when frequency selectivity and high stopband attenuation are considered to be important filtering properties, it may be highly desirable to improve the rejection quality. Several different solutions have been proposed to alleviate this problem. Although most of these solutions lead to a higher passband insertion loss, this at the expense of increased manufacturing complexity. In this paper a new possible solution for improvement in the upper stopband is presented. This improvement in the upper stopband associated with the superior electrical performance of ridged waveguide such as cutoff frequency reduction provides a convenient way to realize E-plane bandpass filters with improved stopband performance. The main features of the new structure are the use of conventional rectangular waveguide housing and the use of a metal insert which when mounted introduce ridges in the resonators, thereby not only maintaining the simplicity of the structure, but also obtaining good stopband attenuation properties. The structure is simple, compatible with the E-plane manufacturing process. The electromagnetic analysis is based on the multimodal mode-matching method, and theoretical amplitude-frequency characteristics are obtained from the ABCD matrices of the individual filter elements. Several different methods for the evaluation of eigenvalues in ridged waveguide have been employed. The present paper describes an application of Galerkin's method, developed by Montgomery. The transcendental equation of the eigenvalue of the nth mode in ridged waveguide was solved numerically. The initial lengths of the septa and resonators for the case of the conventional E-plane filters have been obtained by using the conventional method of synthesis in which the concept of impedance inverters is employed. However, for the case of these filters we cannot use the same method since the filter structure is not uniform (Fig.1b). A modified method of synthesis, which should include generalized impedance inverters [5] and impedance scaling of the impedance levels of the prototype filter, may help to alleviate this problem. The numerical results are presented for a five resonator E-plane filters without and with improved stopband performance. Finally the predicted filter performance showing improved stopband attenuation and reduced filter dimensions compared with waveguide E-plane metal insert bandpass filters is presented.

Numerical Example

To illustrate the application of this method to the design of E-plane filters with improved stopband performance the design of a five resonator E-plane bandpass filters with improved stopband performance is considered. Multimodal mode-matching is used in both the design and the calculation. The calculated insertion loss of X-band a five resonator conventional, ridged waveguide E-plane bandpass filters and ridged waveguide E-plane bandpass filter with ideal impedance inverters is shown in figure 2.

Conclusion

A Computer aided design method has been developed to synthesise E-plane bandpass filters with improved stopband performance. The predicted filter performance showing improved stopband performance and reduced filter dimensions compared with conventional E-plane bandpass filters.

Acknowledgement

The authors would like to acknowledge Prof. J.David Rhodes of Filtronic Components and the Department of Electronic and Electrical Engineering, University of Leeds, who provided expert advice throughout the course of the work.

References

[1] F.Arndt,"The Status of Rigorous Design of Millimeter Wave Low Insertion Loss Fin-Line and Metallic E-Plane Filters," *J.Instn.Electronics and Telecom.Engrs.*, vol.34, No.2, pp.107-119, 1988.

[2] Y.C.Shih,"*The Mode-Matching Method" in Numerical Techniques for Microwave and Millimeter-wave Passive Structures*,"pp.592-621, T.Itoh (ed.) New York: J.Wiley & Sons, 1989.

[3] A.Wexler, "Solution of Waveguide Discontinuities By Modal Analysis," *IEEE Trans.Microwave Theory & Tech.*, vol.MTT-15, pp.508-517, Sep.1967.

[4] J.P.Montgomery, "On Complete Eigenvalue Solution of Ridged Waveguide ," *IEEE Trans.Microwave Theory & Tech.*, vol.MTT-19, pp.547-555, June 1971.

[5] R.Levy, "The Generalized Design Technique for Practical Distributed Reciprocal Ladder Networks," *IEEE Trans.Microwave Theory & Tech.*, vol.MTT-21, pp.519-526, August 1973.

TABLE I
X-band five resonator E-plane band-pass filters with and without improved stopband performance

Waveguide WR16 (WR90)	Internal Dimensions (mm) 22.86 x 10.16		
Midband Frequency (GHz)	9.50		
Passband (GHz)	9.25 - 9.75		
Ripple Level (dB)	0.05		
Number of Resonators n	5		
Metal Insert Thickness t (mm)	0.100		
Septum Dimensions d(mm) and parameter of ideal impedance inverters (K)	d1=1.3334 K1=0.2953 d1=1.4294 d2=6.2502 K2=0.0866 d2=5.3322 d3=7.6076 K3=0.0812 d3=6.6760 d4=7.6076 K4=0.0924 d4=6.9946 d5=6.2502 K5=0.1320 d5=5.9988 d6=1.3334 K6=0.3956 d6=1.3086		
Resonator Dimensions l(mm)	l1=15.8258 l1=17.9619 l1=13.2680 l2=16.1814 l2=19.0730 l2=14.8399 l3=16.2054 l3=20.2713 l3=15.6547 l4=16.1814 l4=21.1981 l4=16.0273 l5=15.8258 l5=21.7935 l5=15.7190		
Ridged waveguide gaps W(mm)	W1=10.16 W2=10.16 W3=10.16 W4=10.16 W5=10.16	W1=9.00 W2=7.00 W3=5.00 W4=3.00 W5=1.00	W1=9.00 W2=7.00 W3=5.00 W4=3.00 W5=1.00
	Figure 2.	. . .	.. .. ..

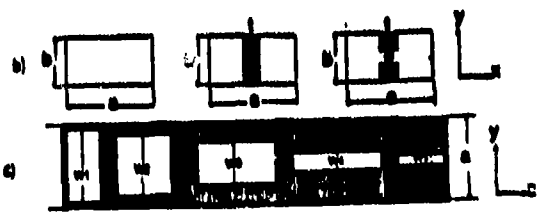

Figure 1. a) Configuration of E-plane filter with improved stopband performance
b) Cross-section dimensions
c) Longitudinal sections in the filter region

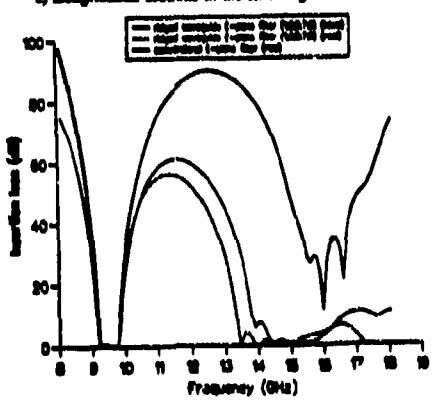

Figure 2. Comparison of the computed insertion loss of X-band a five resonator E-plane bandpass filters.

Filters and Wavefront dividing Beamsplitters for the near and mid Infrared produced by Micromachining Techniques.

J. Warren
National Synchrotron Light Source, Brookhaven National Laboratory, Upton NY 11973.

J. B. Heaney
NASA Goddard Space Flight Center, Greenbelt, Maryland 20771.

K. D. Möller
Department of Physics, New Jersey Institute of Technology, Newark NJ 07102

Introduction

Band pass filters for the far infrared have been produced by etching crosses into metal films on Mylar substrates[1,2]. Unsupported thin cross shaped filters for the far infrared have been produced by etching crosses into 4 microns thick nickel foils[3]. These authors studied the dependence of the wavelength of peak transmission, bandwidth, and percentage of peak transmission on the shape of the crosses. Very accurately shaped crosses in thick metals for the mid infrared have been produced using LIGA[4]. These filters showed a strong side peak and transmission in the 70% to 80% range. Theoretical calculations by Compton et al[5] for thin filters predict such a side peak, depending on the shape of the cross, and 100% transmission. To obtain maximum transmission for band pass filters, a tripod shape was used[6] instead of the cross. These filters showed 100% transmission and the side peak for a thickness of 10.5 microns. The side peak is getting smaller for thinner filters.

Band pass filters for the near and mid infrared.

The above mentioned investigations suggest that thin filters are more transmissive and have a much smaller side peak. 100% transmission may be obtained by using pattern of tripods which are much denser "packed" than the crosses. The width and slopes of the filters are determined by the periodicity constants and the shape and size of the crosses. Since there is much more known how the transmission curve depends on these parameters for crosses than for tripods, we decided to develop band pass filters for the short wavelength region by
a) using crosses in an arrangement as used before, and then
b) produce new pattern with densely packed crosses.

We developed the filters without using synchrotron radiation but with a process similar to LIGA. Masks have been produced with periodicity constants of (A) 5.5, (B) 16.4, (C) 16.7, and (D) 26.4 microns. Using masks (B) and (D), filters with the following values have been produced:

Table 1

	B	D_1	D_2
g	16.4	16.8	16.8
a/g	.08	.12	.08
b/g	.( )	.045	.065

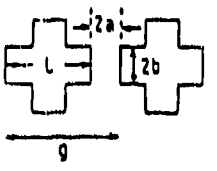

The filters were produced by first coating a chromium covered wafer with 1000A gold. Then, using positive resist, the cross pattern was produced on the gold coating, see Fig.1.

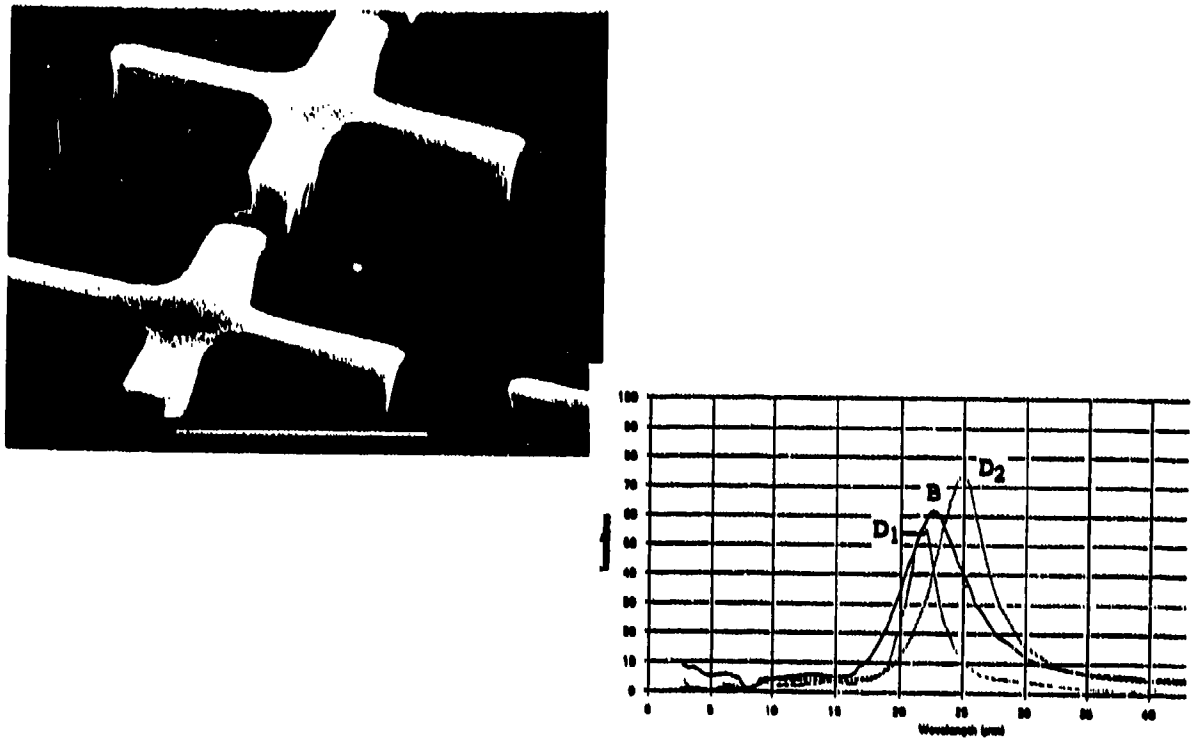

Fig.1 a. Cross made of photoresist. b. Transmission curves of filters of B, D_1 and D_2 of Table 1.

A 2-3 microns thick nickel film was formed around the crosses by using an electroforming process. The crosses of the photoresist were removed and the film taken off the wafer and mounted on a ring for support. At the end of the process the gold film was eliminated.
Micrographs of the actual crosses indicated that their shape and the corresponding transmission curve agree qualitatively with what would be predicted from the results of Ref.3. However, we found that the cross shape and size was not the same on both sides of the filter. The cross of Fig.1 shows clearly that the walls are not perpendicular to the plane of the cross and we think that this is the reason that the transmission curves are smooth and show no side peak. The "waveguide" of the cross is in our case distorted from a waveguide with parallel walls as has been produced with LIGA. This distortion seems to work for the advantage of a smooth curve without side peaks.

References:
1. R. Ulrich, Appl.Opt. 7, 1987 (1968)
2. V. P. Tomaselli, D. C. Edewaard, P. Gillen, and K. D. Moller, Appl.Opt.20, 1361 (1981)
3. S. T. Chase and R. D. Joseph, Appl.Opt.22, 1775 (1983)
4. R. Ruprecht, W. Bacher, P.Bley, M. Harmening, W. K. Schomburg, KfK-Nachr.Jahrg.23,118 (1991).
5. R. C. Compton, R. C. McPhedran, G. H. Derrick, and L. C. Botton, Infrared Phys.23, 239 (1983).
6. KfK Karlsruhe, IMT-Bericht Nr.110/16,Primar Bericht Nr. 16.02.01.P.05A, CPA-mo-3115-91.

APPLICATION OF HTSC-THIN FILMS IN MICROWAVE BANDPASS FILTERS

Dr.A.R. Jha, Technical Director,

JHA TECHNICAL CONSULTING SERVICES, CERRITOS, CA 90701 (USA)

ABSTRACT

This paper reveals unique performance capabilities of High-Temperature Superconducting Thin-Film(HTSCTFs) for possible applications in microwave bandpass filters(BPFs). Microwave filters fabricated with HTSCTFs have demonstrated lowest insertion loss, highest rejection, and sharpest skirt selectivity. Thin films of Yttrium Barium Copper Oxide(YBCO), Bismuth Strontium Calcium Copper Oxide(BSCCO) and Thallium Calcium Barium Copper Oxide(TCBCO) will be most attractive for filters.

INTRODUCTION

Recent research and development activities on HTSC microwave devices indicate that HTSCTF microstrip lines offer improved RF performance over conventional microstrip lines operating below 40 deg K. Furthermore, a HTSC filter using kinetic inductance tuning element offers superior alternative to a YIG filter, which suffers from high insertion loss and long tuning time. Implementation of both MMIC and HTSC technologies in a microwave filter will offer significant improvements in sensitivity, insertion loss, dynamic range, weight, and size. Values of surface resistance (Rs) for YBCO thin films on lanthanum aluminate (LaAlo3) substrate are computed as a function of temperature. Microwave filters employing conventional structures suffer from weight, size and insertion loss. A HTSC microwave filter will hardly have a loss of a fraction of a dB compared to filters using other structures.

FILM DEPOSITION TECHNIQUES AND PROCESSING REQUIREMENTS

HTSC film compounds and substrate materials require strict lattice match and compatibility with each other to achieve uniform film thickness, optimum surface geometry and stable structure. Epitaxial thin films of YBCO(123) compound have been grown successfully on several substrates such as SrTio3, MgO, YSZ and LaAlO3. Suitable deposition and processing techniques must be used to meet the structural characteristics, transport properties and surface quality for low insertion loss at MM-wave frequencies. Quality factors for various films and substrates at 10 GHz are calculated for various films and substrates. Sapphire has the highest unloaded Qs below 10 GHz. However, lanthanum aluminate provides the maximum unloaded Qs at MM-wave frequencies.

THIN FILM FABRICATION TECHNIQUES

Fabrication of HTSC films for microwave filters requires comprehensive knowledge regarding HTSC film compounds and low-loss substrates. Metal organic chemical vapor deposition(MOCVD) is widely employed to achieve high quality HTSC thin films. Three distinct film deposition and fabrication processes are available which are:(1) A two-step(growth/post anneal) process requiring oxygen anneal at 950-980 deg.C,(2) An in-situ (one step, no post growth anneal) process at 800-850 deg.C and (3) A plasma-enhanced,in-situ is possible still at lower temperature. High quality HTSC thin films can

be obtained only at lower growth temperatures.

PERFORMANCE CAPABILITIES OF FILTERS USING HTSC TECHNOLOGY

Minimum in-band insertion loss, high out-band rejection and sharp skirt selectivity are strictly dependent on unloaded Qs of HTSC films and substrates. Measured performance parameters of various BPFs at 77 deg.K using HTSC YBCO films on LaAlO3 substrates are compared with calculated data. The response of a HTSC, 4-pole, 4.8 GHz, BPF reveals a loss less than 1 dB over 2.5 % bandwidth. Computed values of insertion losses for narrowband HTSC filters are much lower over filters using conventional structures. The calculated insertion loss of a edge-coupled HTSC microstrip,5-pole, 15 GHz BPF at 80 deg.K using the LaAlO3 substrate is less than 0.75 dB over 3.5 % bandwidth.

Significant performance improvement is possible in a filter using TCBCO films on LaAlO3 and MgO substrates. The insertion loss will be much lower because of lower RF surface resistances associated with Thallium films. The measured insertion loss of a 3-pole, 10 GHz, BPF using Thallium films on LaAlO3 substrate is less than 0.3 dB at 77 deg.K, the lowest value reported so far. Our studies indicate that a filter fabricated with thin films of Thallium on Lanthanum Aluminate substrate will provide lowest insertion loss and sharp skirt selectivity even at MM-wave frequencies.

SUMMARY

HTSC microwave filters, including low pass, high pass, band reject and band pass filters, will be found most attractive for applications , where minimum insertion loss, lowest dispersion, minimum delay, and compact packaging are the principal requirements. HTSC filters have potential applications in low-noise receivers, high performance ECM systems, space sensors and satellite communication equipment, where weight, size and power consumption are the critical parameters. Further research is required in the areas of equilibrium thermodynamics, kinetics film growth temperature, oxygen pressure and surface control techniques to produce high quality HTSC films for MM-wave applications. High Q resonator filters offer lowest in-band insertion loss, highest out-band rejection, steepest skirt and maximum power handling capability.

ACKNOWLEDGEMENTS

The author wishes to thank Sukant Jain for computer analysis, Renu Agarwal for typing and Sanjay Jha for illustrations.

REFERENCES

(1)Dr. A.R.Jha,"Applications of HTSCs in MM-wave components and circuits", 15 th.International Conference on Infrared and Millimeter Waves, Conference Digest,pp. 163-165, 10-14 December 1990, Orlando, Florida.
(2)Dr. P.E Norris,"In-situ Superconducting YBCO Thin-Films by MOCVD: Present status and Prospects for Low Temperature Growth", EMCORE Corp. Summerset,NJ 08873.

Steerable scattering diagram of a finite set of magnetized ferrite cylinders

V. Kalesinskas, V. Shugurov, N. Milevsky, A. Puzakov

Vilnius University, Department of Physics
Vilnius, Universiteto 3, Lithuania

The main purpose of the research is to determine the steerability of scattering diagram in diffraction by several magnetized ferrite cylinders. We have shown the principal possibility of that in [1]. There are three feasible magnetization: 1) longitudinal, 2) azimuthal (of a metal cylinder with ferrite coat) and 3) transversal. We consider here only the first one easily done in practice.

Permeability of ferrite is being described by Polder's [2] tensor

$$\hat{\mu} = \mu_0 \begin{vmatrix} \mu & i\nu & 0 \\ -i\nu & \mu & 0 \\ 0 & 0 & \mu_{zz} \end{vmatrix}, \qquad (1)$$

where we've introduced the additional parameter $\mu_{zz} \neq 1$. The rectangular waveguide mode H_{10} is being imitated by two plane waves expanded in cylindrical partial waves as the geometry of the problem requires.

Electromagnetic interaction of cylinders can be taken into account using the formula

$$e^{im\varphi} Z_m(kr_1) = \sum_{n=-\infty}^{+\infty} J_n(kr_2)\, e^{in\varphi_2} Z_{m-n}(kr_{21})\, e^{i\varphi_{21}(m-n)} \qquad (2)$$

for the expansion of a cylinder wave of axis 1 in waves of axis 2 (Fig.1).

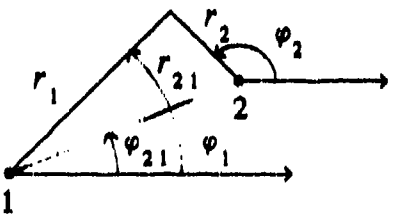

Fig.1

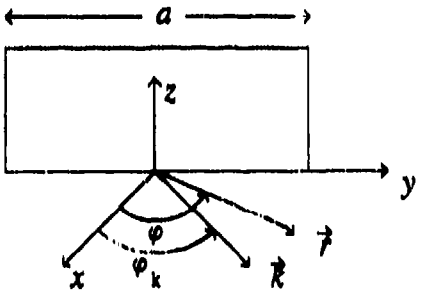

Fig.2

Generally, we solve the model problem exactly though practically we cut the infinite system of equations for unknown amplitudes of scattered field bringing this way some inaccuracy in.

Writing the incident H_{10} mode as the sum of cylindrical waves

$$E_z = \sum_{m=-\infty}^{+\infty} A_m J_m(kr) e^{im\varphi}$$

we get (Fig.2) amplitudes at the point (x_0,y_0) $A_m = (-i)^m e^{-ik_x x_0} \cos(k_y y_0 + m\varphi_k)$, $\mathrm{t}\varphi_k = k_y/k_x$.

The maximum amplitude and thus the strongest interaction of a cylinder and the incident wave is when

$$y_0 = (-m\varphi_k + p\pi)/k_y,\ p = 0,\pm1,\pm2,\ldots\ . \qquad (3)$$

Particularly when $m = \pm1$ we have from (3) the point of circular polarization of waveguide magnetic field.

Formula (3) states that every partial wave has its own optimal position for the cylinder.

But if $\varphi_k/\pi = p/q$, where p,q are integer, then there are not very many such positions. For example for $\varphi_k = \pi/3$ we have only three points with $y_0/a = 0,\pm 1/3$ and one can put within waveguide three cylinders of maximum radius $r_0 = a/6$.

In numerical calculations we've used following ferrite parameters: permeability $\mu_{zz} = 0.95$, permittivity $\varepsilon = 13$, saturation magnetization $M_0 = 3.742 \cdot 10^5$ A/m, wave length $\lambda = 3 \cdot 10^{-3}$ m. We satisfied condition (3) changing waveguid's width. The bias D.C. magnetic field was taken near to resonance and either equal for all cylinders (dashed lines) or changing in a linear fashion along y - axis (solid lines on Fig.3,4) the values beeing higher H_{rez}.

Fig.3 shows the dependence of scattered power on distance d between the two rows of the grid having 3 and 5 cylinders in the first and the second rows, intervals $l = 2r_0$, $r_0 = \lambda/12$, $H_0 = 2.696 \cdot 10^5$A/m, $a = \lambda$.

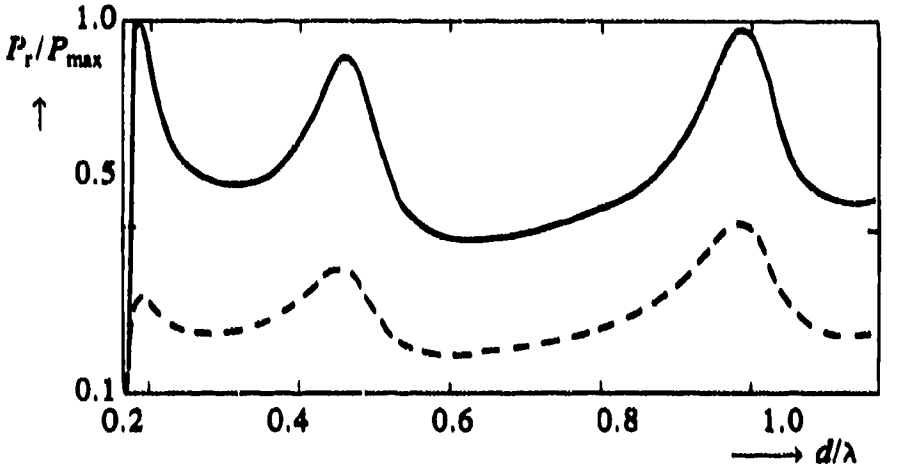

Fig.3

On Fig.4 we give scattering diagram of the same grid when $d = 0.643\ \lambda$.

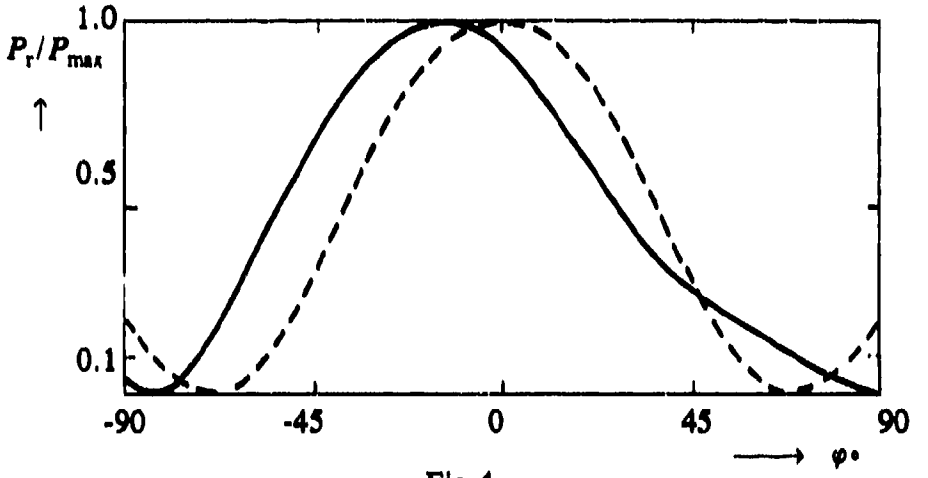

Fig.4

REFERENCES

1. Kalesinskas V., Shugurov V., Milevsky N., Puzakov A. "Plane EM wave diffraction by a finite set of magnetized ferrite cylinders". Proc. ISAP'92,pp.753-756, Sapporo, Japan, 1992.
2. Polder D. Philos.Mag, .Vol.40, No 300, P.99, 1949.

A NOVEL TYPE OF WAVEGUIDE-TO-COPLANAR WAVEGUIDE ADAPTER

Gong Ke Wang Ji

Department of Electronic Engineering
Tsinghua University
Beijing 100084, China

Abstract

A novel type of waveguide-to-coplanar waveguide adapter is proposed, which offers fairly good broadband performance of transition in Ka-band as revealed by experiment. It is believed that it is very useful in the system where MIMIC's are utilized with waveguide devices together.

1. Introduction

Utilizing the planar transmission lines, the MIMIC's have rapidly developed in recent years, on the one hand, it brings the advantages of high performance, good reliability and is compact in size. On the other hand, the traditional structure such as waveguide can not be totally replaced in many cases. Therefore, proper adaptation between waveguide and planar transmission lines is fatal for the application of MIMIC's in a millimeter wave system. The amphasis of this paper is laid on the transition between waveguide and coplanar waveguide, for the reasons of (1) the latter has become one of most widely used transmission lines for its outstanding feature of easy implementation of active elements and (2) such kind of transition has rarely been discussed in the present literature.

2. Design

A new type of waveguide-to-coplanar waveguide (CPW) adapter is proposed, Fig. 1 shows the structure of it. An electric probe on a dielectric substrate formed by an extension of the central strip of CPW is inserted vertically into the waveguide from a narrow square-shaped window in the middle of the broad wall of the waveguide. The substrate extends across the entire height of the waveguide for mechanical stability.

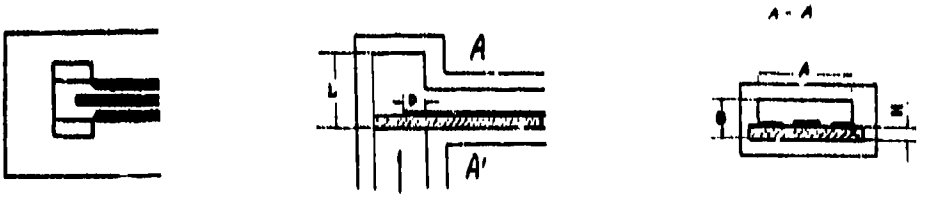

Fig. 1 The structure of the proposed waveguide-to-CPW adapter

A test configuration is outlined in Fig. 2. It consists of two adapters connected back to back by a 23mm long CPW. By optimizing the probe shape and adjusting the position of the sliding shorts, rather good transition characteristic can be obtained.

3. Experiment

The characteristic impedance of CPW is calculated by means of the method of line [1], then different size of probe has been carefully tested. Typical results are given in Fig.3. To be stressed is that the transmission loss measured is caused by two such adapters at two ends and a 25mm long CPW in between.

Fig. 2. The experimental setup

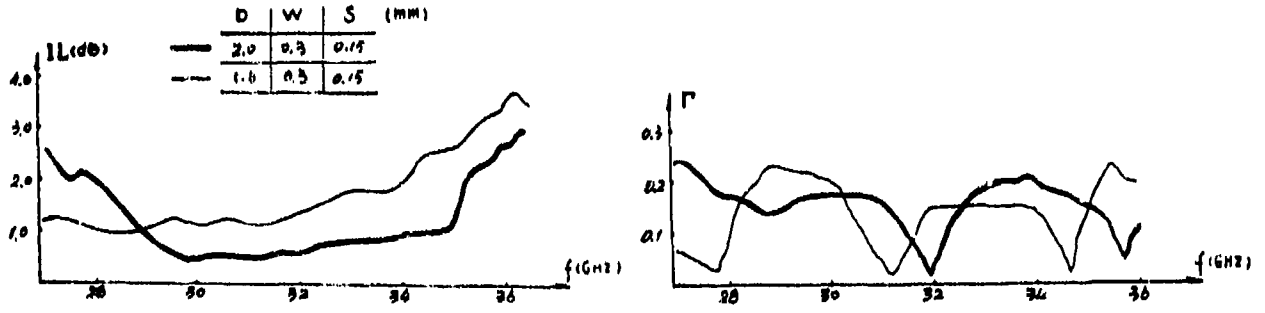

Fig. 3. Typical results of the measurement

It can easily be seen that using a 0.3x2.0 (WxD) rectangular probe, the insertion loss of the whole setup is less than 2dB (less than 1dB for single adapter) and the reflection is lower than 0.2 in a bandwidth over 8GHz in Ka-band.

4. Conclusion

The preliminary experiment shows that the proposed structure of waveguide-to-CPW adapter can offer fairly good broadband performance, so that is a promising approach for the application in millimeter wave systems.

SIMULTANEOUS CONSIDERATION OF CONDUCTOR THICKNESS AND SEMICONDUCTOR SUBSTRATE IN FINLINES

Humberto César Chaves Fernandes
Idalmir de Souza Queiroz Júnior
Eduardo Amorim Martins de Souza
Edvaldo Duarte Barbosa

Department of Electrical Engineering
Technological Center
Federal University of Rio Grande do Norte
P.O. Box 1583, Phone (084) 231 4254, Fax (084) 231 9048
Zip code 59072-970, Natal - RN, Brazil

ABSTRACT

The theory and numerical results to the effective dielectric constant and attenuation constant of bilateral finline structure, considering the conductor thickness and semiconductor substrate is presented. The full wave analysis of the Transverse Transmission line method in Fourier transform domain - FTD is used. The numerical results are computed with a program developed in Fortran77 language.

THEORY

The Transverse Transmission Line method has been used in the analysis of planar structures, particulary in study of finlines structures on lossless dielectric and semiconductor substrate [1]. In ref. [2], the effect of the conductor thickness only, had been considered.

The cross section of the bilateral finline with conductor thickness and semiconductor substrate is shown in fig.1. In this study, the simultaneous consideration of the conductor thickness and semiconductor substrate is presented to the structure shown in fig.1. From Maxwell equations, the electric and magnetic fields $\tilde{E}_{xi}$, $\tilde{E}_{zi}$, $\tilde{H}_{xi}$ and $\tilde{H}_{zi}$, as function of the transverse component $\tilde{E}_{yi}$ and $\tilde{H}_{yi}$, are obtained in Fourier Transform Domain, in each one of the dielectric regions (i=2, 3, 5). With the expressions of the electromagnetic fields, the boundary conditions are applied at the interfaces 'g' and 't', and the expressions of the current densities $\tilde{J}_{xt1}$, $\tilde{J}_{zt1}$, $\tilde{J}_{xt2}$ and $\tilde{J}_{zt2}$ are obtained as function of electric field in the interfaces $\tilde{E}_{xt1}$, $\tilde{E}_{zt1}$, $\tilde{E}_{xt2}$ and $\tilde{E}_{zt2}$. An inhomogeneous matrix equation is obtained : $\bar{Y}\bar{E} = \bar{J}$.

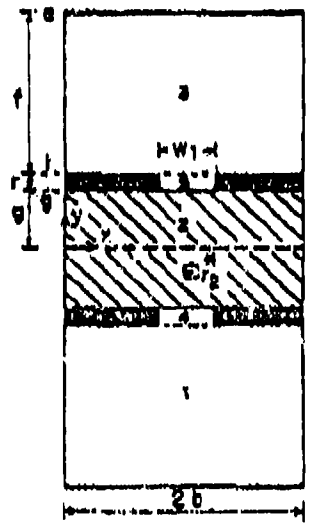

Fig.1 - Bilateral Finline cross section with conductor thickness and semiconductor substrate

The Y matrix representing the Green dyadic admittance function of the structure is obtained. Expanding the electric fields E_{xt1}, E_{zt1}, E_{xt2} and E_{zt2} in terms of basis functions, and using the Moment method, a homogeneous matrix equation is obtained. The characteriso equation is developed and the attenuation constant α, and the phase constant β are computed numerically. The effective dielectric constant is given by $\varepsilon_{ef} = (\beta / K_0)^2$, where Ko is the free space wavenumber.

RESULTS AND CONCLUSION

The Fig.2, shows the effective dielectric constant as function of frequency, with the thickness 't'. It can be noted that effective dielectric constant increases with the frequency. Keeping the frequency constant, ε_{ef} decreases when thickness is increased. The Fig.3 shows the attenuation constant as function of frequency. It can be noted that increasing the conductor thickness, α decreases to the same frequency. It is observed the agreement with the points obtained by theory in Ref. [1] when 't'=0, and the points obtained by theory in Ref.[3] when $\sigma_2 = 0$.

The semiconductor substrate used in region 2 is GaAs, with $\varepsilon_{r2} = 12.0$. The numerical results were computed using WR28 Waveguide, W1=0.15mm, 2g=0,254mm, $\varepsilon_{r3}=\varepsilon_{r5}=1.0$, $\sigma_3=\sigma_5=0$ and $\sigma_2=1$ S/m.

The developed program is very important because yields the propagation constant $\gamma = \alpha + j\beta$ of the bilateral finline, considering the influence of conductor thickness and semiconductor substrate together. This yields a full description of the bilateral finline.

This work is partially suported by CNPq and CAPES.

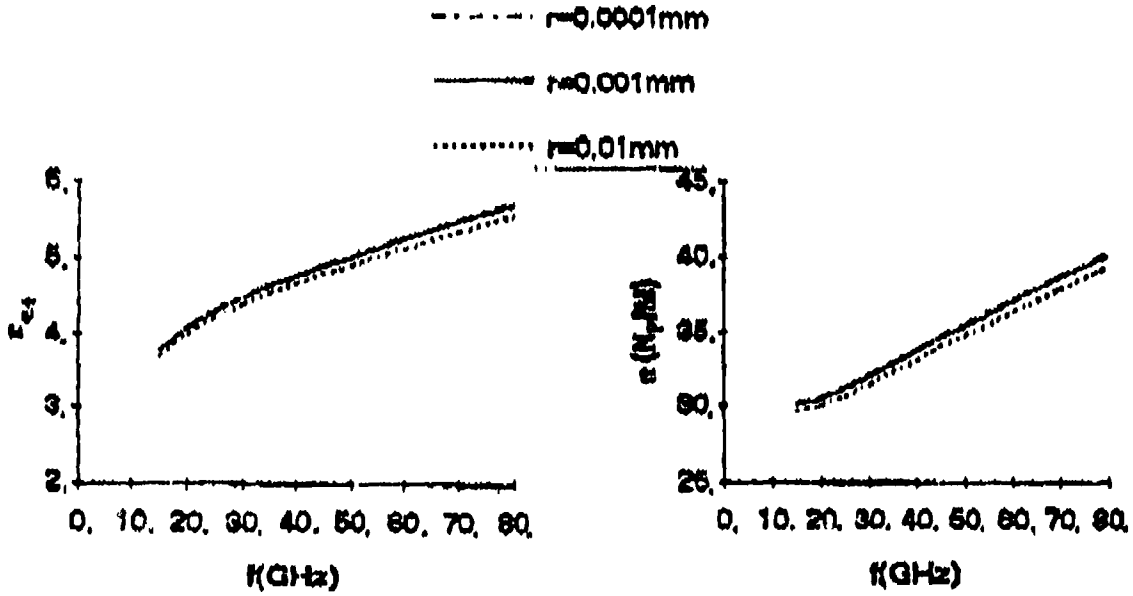

Fig.2 - Effective dielectric constant as function of frequency for the bilateral finline with semiconductor substrate andconductor thickness

Fig.3 - Attenuation constant as function of frequency for the bilateral finline with semiconductor substrate and conductor thickness.

[1] H.C.C. Fernandes, J.R.S. Oliveira and A.J.Giarola, "Dispersion in Finlines on semiconductor and the S-parameters of a step discontinuity", International Journal of Infrared and Milimeter Waves, Vol. 12, Nº 5, pp. 505-519, May 1991.

[2] H.C.C. Fernandes, E.A.M. Souza, E.D. Barbosa, and N.D. Freitas, "Characterization of Unilateral finline considering the conductor thickness", 17th International Conference on Infrared and Milimeter Waves, Conf. Proc. pp.480-481, Pasadena - CA, U.S.A., Dec. 1992..

[3] T. Kitazawa and R. Mittra, "Analysis of finline with finite Metallization thickness", IEEE, Trans. on Microwave Theory and Tech., Vol.. MTT-32, Nº 11, pp.1484-1487, Nov. 1989.

Characteristics of Microstrip Lines with Finite Metallization Thickness and Turning-up Edge for High Power Transmission

Ao Sheng Rong and Zhong Liang Sun
State Key Laboratory of Millimeter Waves
Department of Radio Engineering
Southeast University
Nanjing 210018, Jiangsu
People's Republic of China

Abstract

This paper presents a Quasi-TEM analysis of the microstrip lines with the finite metallisation thickness and turning-up edges. The characteristic impedance and effective dielectric constant are given as functions of the metallisation thickness and turning-up profile of the edges. At the extreme case where the metallisation thickness is assumed to be zero and the turning-up profile of the edges is of the circular arc, the calculated results are compared with the measured data available in literatures. This modified configuration of the microstrip lines exhibits great potential for high power transmission.

Spectrum dynamics of non-radiating modes of semi-open transmission lines based on planar waveguide joints

Alexander Yushchenko and Sergey Shibalkin
Microwave Devices Laboratory of Kharkov State University,
Freedom Square 4, 310077, Kharkov, UKRAINE

ABSTRACT

Study of the physical nature of existence of the natural[1] and quasi-natural[2] modes of $H_{p=0}$ type in H-plane waveguide joints suggests the idea of the possibility of creating joints-based transmission lines having the $E_{1\,1}$ working wave. A rigorous theoretical analysis of electrodynamic characteristics of the said modes was carried out with the help of Trefftz method. A rectangular region of orthogonal waveguides fields connection that has no special points inside the mode bases matching intervals was separated at the stage of determination of the problem geometry. Presented below are the results of the analysis of the spectrum dynamics of non-radiating H- and E- waves in transmission lines prospective for the millimeter wave band.

1. STUDIED STRUCTURES AND FIELD REPRESENTATION

Among the structures shown below only the groove guide[3] is capable of propagation of $H_{0\,1}$ wave without radiation; in semi-open (b)-(d) structures non-radiating conditions are ensured by $E_{1\,1}$ wave.

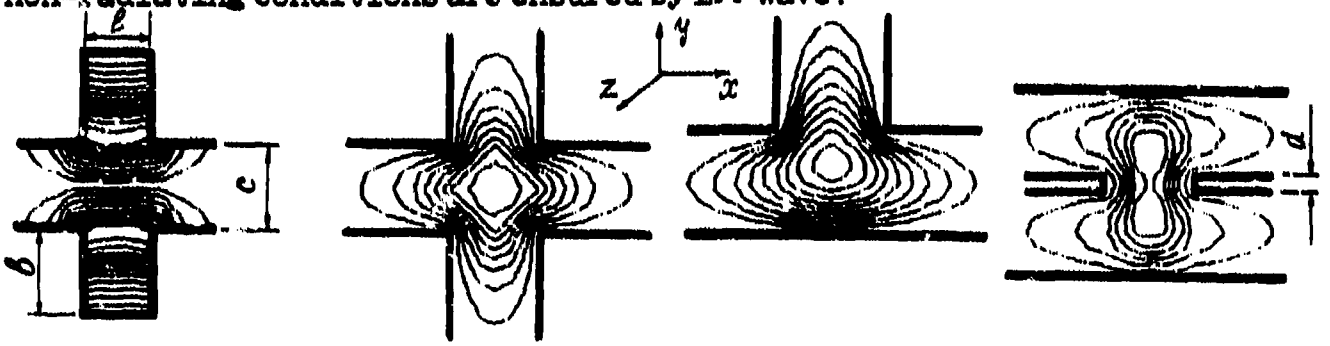

(a) $H_{0\,1}$ mode $|Hz|=Const$ (b) $E_{1\,1}$ mode $|Ez|=Const$ (c) $E_{1\,1}$ mode $|Ez|=Const$ (d) $E_{1\,1}$ mode $|Ez|=Const$

Accuracy of the electrodynamic modelling of wave processes carried out on the basis of Trefftz method depends on the accuracy of fulfilment of boundary conditions. In our approach an electric field representation in the connection region satisfies termwise all the boundary conditions, while the sought-for systems of linear algebraic equations (SLAE) of the second kind follow from matching the tangent magnetic components of the complete field. Therefore, the characteristic feature of the obtained SLAE is their high speed of convergence of numerical results to the main approximation.

To complete the above said, we supply representation of E_z component of the E- wave field (with odd indices) characteristic of the connection regions of the studied structures (a)-(d):

$$E_z=\left\{\sum_f B_f \cos\frac{f*\pi*y}{a}\,\frac{ch(\gamma_{f\,c}x)}{ch(\gamma_{f\,c}l/2)}+\sum_n A_n \cos\frac{n*\pi*x}{l}\,\frac{ch(\gamma_{n\,1}y)}{ch(\gamma_{n\,1}c/2)}\right\} e^{-i\Gamma z}.$$

where Bf, An are field amplitudes; $\gamma_{n(f)1(c)} = \sqrt{[n(f)\,\pi/l(c)]^2 - k^2 + \Gamma^2}$; Γ is propagation constant; n, f=1,3,5...

The groove guide (a) Hz (H-wave) component representation such as:

$$H_z = \left\{ -\sum_f B_f \sin\frac{f*\pi*y}{c}\,\frac{ch(\gamma_{f\,c}\,x)}{ch(\gamma_{f\,c}\,l/2)} - \sum_n A_n \cos\frac{n*\pi*x}{l}\,\frac{sh(\gamma_{n\,l}\,y)}{sh(\gamma_{n\,l}\,c/2)} \right\} e^{-i\Gamma z}.$$

ensures term-by-term matching of tangent Ex and Ey components on boundaries of the connection region; n=0,2,4..; f=1,3,5...

2. NON-RADIATING MODES SPECTRUM DYNAMICS

Figs. 1 - 3 show the results of the critical frequency calculation , and (a)-(d) - results of calculation of equal level lines of the Zth component of lower non-radiating modes. There should be noted the limiting values of calculated dependencies. Fig. 1 shows that when l tends to 0, the frequencies of the E- waves tend to the frequency of the planar waveguide [(a), (b) structure], and H-waves [(a) structure] remain close to the frequencies of H_{01} wave of the corresponding rectangular waveguides. When l are big, the frequencies of E - and H - waves tend to the frequency of the planar waveguide with dimensions $2b+c$. Fig. 2 shows that at small values of b, H - and E - waves tend to the frequency of the planar waveguide, while at big values of b the H - waves tend to H_{01} frequency of the rectangular waveguide, and E - waves - to that of the cross - shape waveguide (b). Fig. 3 shows that at increase of d waves E_{21} and E_{11} of (d) structure tend to the frequency of E_{11} wave of (c) structure, the dependencies themselves being typical for the connection frequencies of cophase and antiphase modes in the cut-off waveguide.

4. CONCLUSION

The presented field representation enabled to both obtain physically correct solutions for the critical frequencies of prospective transmission lines and calculate running attenuations .

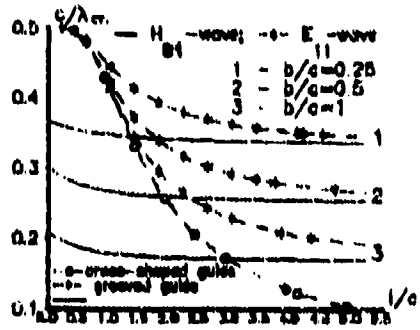

Fig.1

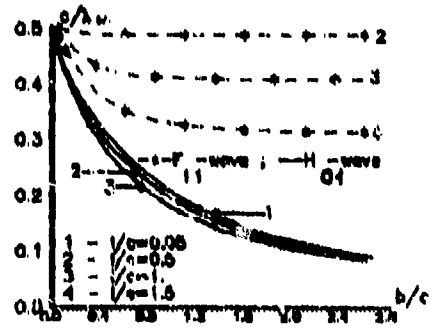

Fig.2

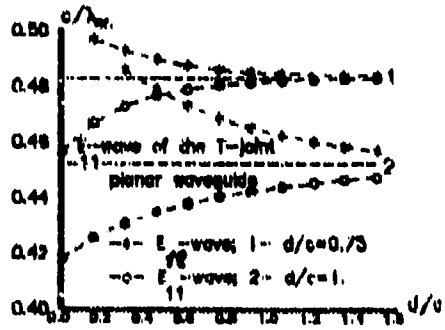

Fig.3

5. REFERENCES

1. V.A. Korobkin, V.V. Osintsev, "Natural modes of electromagnetic field of dielectric resonator in waveguide splitter", Radiotehnica i Elektronica, V.30, N.3, pp. 417-421, 1985.

2. V.A. Korobkin, S.F. Shibalkin A.G. Yushchenko "Coupled quasi-natural modes in waveguide junction", Radiot. i Electr., 1993, (To be published).

3. F.J.Tischer, "The groove guide. A low-loss waveguide for millimeter waves", IEEE Trans., Vol. MTT-11, pp.291-296, 1963.

TRANSVAR DIRECTIONAL COUPLER FOR MILLIMETER-WAVE APPLICATION

Yonghui Shu
Epsilon Lambda Electronics Corporation
427 Stevens Street, Geneva, IL 60134

Abstract

A millimeter-wave band coupler at 77.5 GHz with 6 dB coupling level has been developed. The coupler offered less than 2.0 dB insertion loss, ± 0.5 dB variation in coupling level and a typical isolation of 25 dB over approximately 10 GHz bandwidth. Other frequency band couplers with different coupling factor have been developed also. The advantages of this type of directional coupler are its large flexible coupling level selection (from 0 to 100 percent), simplicity in design, low cost and excellent producibility.

I. Introduction

Although there are various transmission media proposed thus far for microwave and millimeter-wave circuit application, conventional rectangular waveguide is still a major transmission line in most microwave and millimeter-wave systems due to the advantages of low loss, medium power handing capability, and convenience for incorporation of packaged solid state devices.

Transvar directional coupler[1] is a rectangular waveguide type coupler which can be designed to transfer variable amounts of power, 0 to 100 percent, from one waveguide to the other. The original Transvar coupler was proposed and realized at X-band. The coupling element of Transvar coupler is in the common narrow wall (H-plane) of the two waveguides. The advantages of this type of coupler are its flexible coupling level (0 to 100%), moderate operation bandwidth, conventional waveguide configuration, simplicity in design and excellent performance. By modern machinery techniques, such as computer controlled CNC milling machine, this type of coupler can be easily realized in low cost, good producibility and mass production for commercial application.

In this paper, the fundamental operation principles, the analysis formulas and design procedures of the Transvar coupler are given. As a design example, 10 couplers with frequency centered at 77.5 GHz and 6 dB coupling level were developed. The measured performance characteristics show low insertion loss, moderate bandwidth and good producibility which implies that this coupler is an ideal candidate for millimeter-wave low cost application.

II. Configuration and Fundamental Principle

The configuration of Transvar coupler is shown in Figure 1. The coupling element which consists of N-1 vertical grid wires is in the common narrow wall of the main and secondary waveguides.

The fundamental operation principle of the coupler can be described by the modes which satisfy the boundary conditions in the coupling region. Basically, there are two main modes, namely, symmetrical and asymmetrical . The asymmetrical mode is unaffected by the grid wires if the wire diameter is small enough compared to waveguide width while symmetrical mode, on the other hand, is inductively loaded by the grid wires, which results in a slower phase velocity. There is, therefore, a difference of the phase velocity of these two modes. A superposition of the two modes will produce an electric-field maximum where the two modes are in phase and a null where the two modes are out of phase. This can be expressed by following equation

$$\pi=(2\pi d/\lambda_{gs})-(2\pi d/\lambda_{ga}) \quad (1)$$

The above equation can be rewritten as

$$d=1/[(2d/\lambda_{gs})-(2d/\lambda_{ga})] \quad (2)$$

where λ_{gs} is the guide wavelength of the symmetrical mode
λ_{ga} is the guide wavelength of the asymmetrical mode
d is the distance between an electric field maximum and an adjacent null in one waveguide.

In the coupling region, assuming that the amplitude of the symmetrical and asymmetrical modes are the same and equal to half of the input electric field E_0, the resultant electric field in the main waveguide 1 can be expressed as the following

$$E_1=(E_0/2)(1+e^{j\alpha})=(E_0/2)(1+\cos\alpha+j\sin\alpha) \quad (3)$$

where α is the phase difference of the electric vectors of the two modes.

The amplitude of normalized resultant electric field in waveguide 1 and 2 can be expressed by

$$|E_1/E_0|=\cos\alpha/2=\cos(\pi L/2d) \quad (4)$$

$$|E_2/E_0|=\sin\alpha/2=\sin(\pi L/2d) \quad (5)$$

where L is the length of the aperture or coupling region.

Then the power in the two waveguides can be expressed by the following equations

$$P_1/P_0=\cos^2(\pi L/2d) \quad (6)$$

$$P_2/P_0=\sin^2(\pi L/2d) \quad (7)$$

From equations (6) and (7), if L is less than d, the coupler will partially couple the power from wave 1 to waveguide 2 and if L is equal to d, 3d, 5d and so on, the 100 % power coupling will happen. Therefore, any coupling level, from 0% to 100%, can be easily achieved by design the length of the coupling region.

III. Analysis Formulas and Synthesis Procedure

For coupler, the power coupling factor C is defined by equation

(7), which can be re-written as following

$$C=P_3/P_0=\sin^2[\pi(n+1)l/2d] \quad (8)$$

where $L=(n+1)l$, in which n is the number of the wires and l is the spacing between two adjacent wires.

As mentioned above, because the asymmetrical mode is unaffected by the presence of the grid wires, this mode, which is the TE_{20} mode in the composite of the coupling region, has a guide wavelength equal to that of the TE_{10} mode in the single guide. On the other hand, the guide wavelength of the symmetrical mode was expressed in [1], which is

$$\lambda_g=\lambda_0/\sin\theta \quad (9)$$

where θ is the angle of incidence of the electric field upon the wires in the coupling region. The angle θ can be obtained from following equation

$$\tan[(2\pi a\cos\theta)/\lambda_0]=[(-2l\cos\theta)/\lambda_0][\ln(l/2\pi r)+F(\theta,l/\lambda_0)] \quad (10)$$

or

$$(\tan p)/p=(-l/\pi a)[\ln(l/2\pi r)+F(\theta,l/\lambda_0)] \quad (11)$$

where r is the radius of the wire ($r\ll l$), F is a correction term given graphically by [2], a is the width of the waveguide channel and $p=(2\pi a\cos\theta)/\lambda_0$

By solving p and computing the angle of θ, the guide wavelength of the symmetrical mode can be obtained from (9).

From the above explanation and analysis equations, the synthesis procedure is developed as follows:

1) Select θ and l/λ_0, find $F'(\theta,l/\lambda_0)$ from the curves shown in [2] and calculate 2r from equation (10) as initial value;

2) Using selected θ and calculated 2r as start point, select real 2r and use equation (10) to find a θ which will force $F(\theta,l/\lambda_0)$ equal to $F'(\theta,l/\lambda_0)$;

3) Use θ found from step (2) and equation (9) to calculate λ_g;

4) Choose desired coupling factor C and use equation (2) and (9) to find the number of wires.

IV. Design Example and Performance

The design of 77.5 GHz Transvar directional couplers with 6 dB coupling level has been performed using the above procedure. Ten of these units with almost identical performance have been realized for transceiver subsystem application. The typical measured performance of the couplers is shown in Figure 2. The results show that the coupler offers less than 2.0 dB insertion loss, ± 0.5 dB variation in coupling and 25 dB of isolation over 10 GHz bandwidth. Due to the dynamic range limitation of the test equipment, the actual isolation of greater than 25 dB was checked using a different setup. The measured coupling level generally checks the designed performance. Several other Transvar couplers were developed and tested at millimeter-wave frequencies also. These results support the conclusion that the Transvar coupler can be used as a low loss, producible component for millimeter-wave subsystems.

V. Conclusions

Transvar directional couplers have been successfully designed and realized at millimeter-wave frequency. The fact of the simplicity in design, excellent performance and good producibility illustrates that Transvar directional coupler should have many applications in millimeter-wave commercial and military system.

Acknowledgement

The author would like to thank Dr. Peter Toulios for useful discussions and Ms. Xiaoxin Gu for technical support.

References

1) Kiyo Tomiyasu, Seymour B. Cohn, "The Transvar directional coupler," Proc. of IRE, Vol. 41, pp. 922-926, July, 1953.

2) G. G. Macfarlane, Surface impedance of an infinite parallel wire grid at oblique angles of incidence," Journal of Inst. Elec. Eng., vol.XCIII, Part III A, no. 10, pp. 1523-1527, 1946.

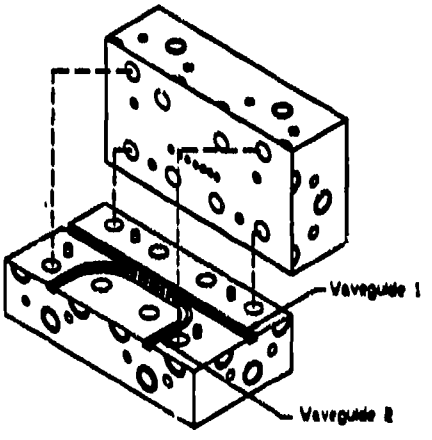

Figure 1. Configuration of Transvar Coupler at W-band

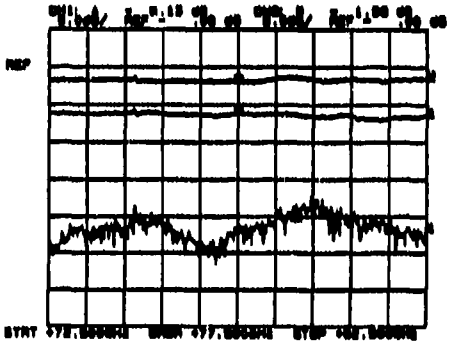

Figure 2. Typical Measured Performance of the Couplers

60 GHZ MICROSTRIP-LINE SP4T PIN DIODE SWITCH

Yonghui Shu
Epsilon Lambda Electronics Corporation
427 Stevens Street, Geneva, IL 60174

Abstract

A simple technique to determine the beam-lead PIN diode parameters at millimeter frequency has been developed. The obtained parameters were used in the computer-aided design of the novel 60 GHz microstrip single-pole four-throw (SP4T) switch. The switch offers less than 4.0 dB insertion loss (including about 1.0 dB waveguide to microstrip-line transition pair loss and circuit loss) and greater than 20 dB isolation in each path. Because of its planar configuration, the switch circuit is amenable to monolithic devices integration and the circuit configuration can be easily implemented to single pole multi-throw switch design.

I. Introduction

Semiconductor control devices have been used extensively in radars, radiometry, communication systems, and so on. In the millimeter-wave range, the PIN diode still holds its supremacy as a control device mainly because of its high switching speed, low control power requirement and high RF power handling capability. Microstrip PIN diode single-pole single-throw (SPST) and single-pole double-throw (SPDT) switches have been reported at millimeter frequency [1], [2]. Most of millimeter-wave PIN diode switches built so far were based on out-and-try method due to the difficulty of PIN diode parameters measurement in millimeter-wave frequencies. Additionally, there is demand for single-pole multi-throw switch such as in electronic scanning antenna application. In this paper, the PIN diode parameters supplied by manufacturer have been verified directly at 60 GHz by building a SPST switch according to computer simulation. Using the verified PIN diode parameters and developed SPDT switch computer simulation program, the SPDT switch, which was used subsequently as the key "element' in a SP4T switch design, has been designed and tested. The agreement of the simulation and measurement results of SPST and SPDT switches guaranteed the accuracy of the PIN diode parameters and the reliability of the circuit models and computer programs. Based on these information and knowledge, the SP4T switch network computer aided design program was developed and the microstrip SP4T switch was designed. The SP4T switch demonstrated an insertion loss of 3.8 dB (including the circuit loss) and a minimum isolation of 20.0 dB in each path over 6 GHz bandwidth centered at 60 GHz. The computer aided design did predict the performance of the switch. The switch circuit is amendable to monolithic implementation, can be used for single-pole multi-throw switch network design and should have many applications in millimeter-wave systems.

II. PIN diode Parameters Verification

The PIN diode switches used in microstrip configuration commonly employ beam-lead diodes. The parasitics of the diode are quite high at millimeter-wave frequencies and will give rise to poor circuit performance if not accounted for accurately in the circuit design. On the other hand, the main design issue of the single-pole multi-throw switch is to reduce the insertion loss of the circuit by using as few diodes as possible. Thus, it becomes more important to have reliable diode parameters and a computer model if the circuit only employs a single diode in each path to perform the switch function. Techniques for measuring PIN diode parameters in general have been described by White [3]. It is understandable that to measure the diode parameters accurately at millimeter-wave frequency by mounting the beam-lead diode in the circuit is very difficult. The alternative is to verify the manufacturer's parameters by building a simple single diode SPST switch according to computer simulating results. Reasonably accurate parameters can be obtained by comparing the theoretical prediction and measured results of the switch and making some appropriate adjustment of the diode parameters if necessary with the computer simulation.

Figure 1 shows the microstrip SPST circuit. The circuit consists of a Marconi DC2602 beam-lead PIN diode mounted on the main 50 Ω feedline, bias circuit and tuning stub. The diode is terminated by a 50 Ω tuning stub which is provided to tune out the diode parasitic and a lowpass filter which provides an RF open circuit while delivering DC power. The purpose of using the additional half-moon stub is to provide a better RF characteristic with wide bandwidth. The input and output of the circuit were connected to standard WR-15 waveguide through the step-ridge type microstrip to waveguide transitions (not shown in the figure). The insertion loss of the transition at this frequency was well defined, which is about 0.5 dB per pair. The PIN diode parameters used in the model were provided by the manufacturer. A computer program was developed and used to analyze and optimize the SPST switch performance. The length of the tuning stub and the parameters of the PIN diode were optimized with the reasonable boundary conditions for best insertion loss and isolation performance throughout the 55 to 65 GHz range. The optimized stub length and modified diode parameters were obtained.

Using the theoretical results, the SPST switch was fabricated on a 5 mil-thick RT-Duroid 5880 substrate and the beam-lead PIN diode was bonded on the circuit by using silver conductive Epoxy. The switch performance were tested through step-ridge type microstrip to waveguide transitions with an HP-8535 network analyzer. Overall, the theoretical and experimental results agree well which indicates that the modified PIN diode parameters are sufficiently accurate for this microstrip-line switch design application. This result has provided the foundation for the SPDT and SP4T switches design.

III. Microstrip SPDT and SP4T Switches

There are two possible approaches which can be used to realize a SP4T switch, i. e., one level four way power divider approach or

two level two way power divider approach. Due to the difficulty of the multi-port power divider design, the SP4T switch described in this paper was employing the two level SPDT approach. The benefits of using this approach are moderate bandwidth, simplicity of design, and ease to extend the design to multi-throw switch application. Ultimately, the design of the "key element"-- SPDT switch becomes the main task of the SP4T switch design.

Figure 2 shows the circuit configuration of the microstrip SPDT switch. The purpose of the quarter wavelength, low impedance transformers at the "T" junction is to provide better impedance matching over wider bandwidth. The functions of the rest of the circuits are similar to those of the SPST switch. In order to reduce the insertion loss of the switch, a single PIN diode has been implemented in each arm. Less than 1.0 dB insertion loss and about 16 dB of isolation throughout the 55 to 65 GHz range were obtained from the simulation program. Using the dimensions obtained from theoretical analysis, the microstrip-line SPDT switch was fabricated on the 5 mil-thick RT-Duroid 5880 substrate and the performance was measured through the transition with the network analyzer. About 2.0 dB insertion loss at zero bias condition and 20 dB isolation at 20 mA forward bias current condition were obtained. The slight higher insertion loss was mainly due to the loss of the transition pair and the microstrip circuit loss since they were not taken account in the model. Excluding the actual losses in the circuit, experimental result did check the theoretical prediction. Thus, the SPDT switch was well developed and to be used in SP4T switch design. The simulated and measured insertion loss and isolations of the SP4T switch are shown in Figure 3. A 3.8 dB insertion loss at zero bias condition and about 20.0 dB and 35 dB isolation at 20 mA forward bias current condition in different paths have been achieved. The higher measured insertion loss is including the transition loss and microstrip circuit loss. The actual loss due to the switch excluding the transition loss and extra circuit loss is about 2.5 dB which agrees very well with the theoretical results of 2.0 dB. Additional, the measured isolations agree extremely well with the theoretical prediction if the additional losses are subtracted.

The SP4T circuit proposed in this paper can be easily extended to single-pole eight-throw or multi-throw switch network design by cascading 3 level or multi-level SPDT switches by extrapolation of the results reported here.

IV. Conclusions

A simple technique and computer program have been developed to obtain beam-lead PIN diode parameters in millimeter-wave frequencies accurately. Based on this information, the CAD models for microstrip SPDT switch and SP4T switch network designs have been developed. The theoretical and experimental results agree very well, which indicates the computer model and design method used in this paper are very reliable and useful. The microstrip SP4T switch incorporating one pair of step-ridge microstrip to waveguide transition achieves 3.8 dB insertion loss and at least 20 dB isolation over 6 GHz bandwidth centered at 60 GHz. The circuit offers many advantages, such as planar configuration, ease of device integration, and low cost. The circuit is amendable to monolithic circuit integration, can be extended to multi-throw switch design and should have many applications in microwave and millimeter-wave systems.

Acknowledgments

The author would like to thank Dr. Peter Toulios and Mr. Robert Knox for useful discussions and Mr. Ahmed Khan for technical support. This work was supported by the Defense Advanced Research Projects Agency under contract No.DAAH01-90-C-0672.

References

[1] M. Dydyk, "Shielded Microstrip: Transmission Media for MM-wave Integrated Circuits," IEEE MTT-S Int. Microwave Symp. Digest, 1981, pp. 99-101.

[2] M. J. Sission, "Microstrip Devices for millimetric Frequency," IEEE MTT-S Int. Microwave Symp. Digest, 1982, pp. 212-214.

[3] J. F. White, Microwave semiconductor Engineering, Van Nostrand Reinhold, New York, 1982.

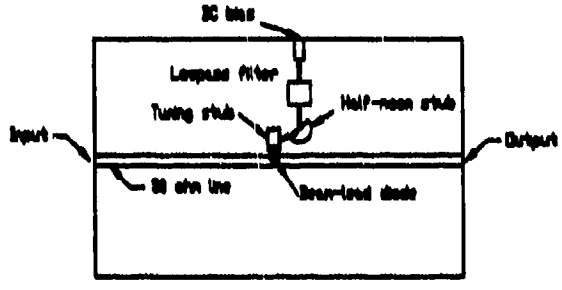

Figure 1. Configuration of Microstrip SPST Switch

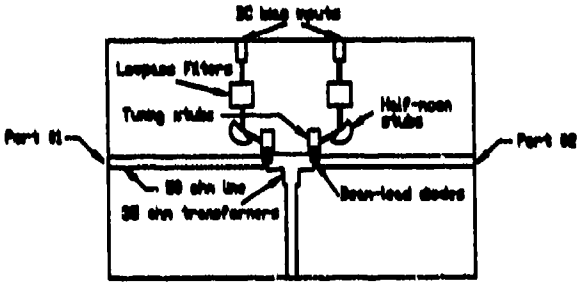

Figure 2. Configuration of Microstrip SPDT Switch

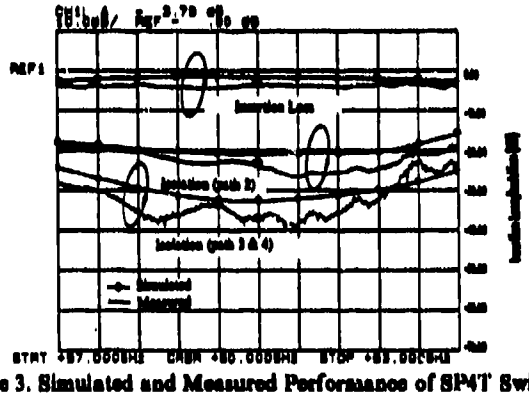

Figure 3. Simulated and Measured Performance of SP4T Switch

MODAL ANALYSIS OF MICROSTRIP AND FINLINE STEP DISCONTINUITIES FOR MICROWAVE AND MILLIMETER-WAVE INTEGRATED-CIRCUITS APPLICATIONS

Cam Nguyen and Khwaja M. Rahman
Department of Electrical Engineering
Texas A&M University
College Station, Texas 77843-3128

Abstract - Modal analysis of microstrip and finline step junctions, commonly seen in microwave and millimeter-wave integrated circuits, are derived. Numerical results of scattering parameters are presented in W-band (75 - 110 GHz). There is a good agreement between our calculated results and published data.

INTRODUCTION

Microstrip line has been used extensively for both microwave and millimeter-wave hybrid and monolithic integrated circuits (MIC's and MMIC's), whereas finline is normally employed for MIC's at millimeter wavelengths. In these circuits, step junctions are commonly seen and, thus, need to be accurately characterized.

In this paper, we describe a full-wave analysis of microstrip and finline step discontinuities using the mode-matching method [1]. Various results of scattering (S) parameters at microwave and millimeter-wave frequencies are presented and compared with existing data to confirm the analysis.

ANALYSIS AND RESULTS

To simplify the formulation, here we only present the analysis for single-step discontinuities. Figs. 1 and 2 show the cross sections and single-step discontinuities of microstrip line and finline, respectively. All the conductors are assumed perfectly conducting and infinitely thin. The dielectric substrates are assumed to be loss less. First, the hybrid modes on regions a and b of the plane of the discontinuity are determined using the spectral-domain approach [2]. Second, the transverse electric and magnetic fields on the two regions are matched across the discontinuity to produce the mode-matching equations. Third, the inner products of these equations with appropriate field components are taken, resulting in the following equations:

$$(1+\rho)\, I_{1m}^{ab} + \sum_{i=2}^{P} a_i I_{im}^{ab} = \sum_{j=1}^{Q} b_j I_{jm}^{bb}, \qquad m = 1, \cdots, Q$$

$$(1-\rho)\, I_{n1}^{aa} - \sum_{i=2}^{P} a_i I_{ni}^{aa} = \sum_{j=1}^{Q} b_j I_{nj}^{ab}, \qquad n = 1, \cdots, P$$

where ρ is the reflection coefficient corresponding to the incident fundamental mode; a_i and b_j are the mode coefficients; I's stand for the inner products, and P and Q represent the number of eigenmodes in regions a and b, respectively. Fourth, these equations are solved to determine ρ, a_i (i=2,3,..., P), and b_j (j=1,2,..., Q).

Various numerical results for microstrip and finline step discontinuities have been generated, and some were compared to existing data to confirm the analysis. Table 1 shows a good agreement between our results and those published for a microstrip single-step discontinuity at 2 GHz [3]. Fig. 3 shows the calculated S-parameters of a microstrip single-step discontinuity across the W-band (75 - 110 GHz).

CONCLUSIONS

Formulation for microstrip and finline step discontinuities has been presented. Various numerical results have been obtained. Good agreement between our calculated results and those published has also been found. The developed analysis should be useful for the analysis of microstrip and finline integrated circuits at microwave and millimeter-wave frequencies.

REFERENCES

[1] A. Wexler, "Solution of waveguide discontinuities by modal analysis," *IEEE Trans. Microwave Theory Tech.*, vol. MTT-15, pp. 508-517, Sept. 1967.

[2] T. Itoh and R. Mittra, "Spectral-domain approach for calculating the dispersion characteristics of microstrip lines," *IEEE Trans. Microwave Theory Tech.*, vol. MTT-21, pp. 496-499, July 1973.

[3] Q. Zu, K. J. Webb and R. Mittra, "Study of modal solution procedures for microstrip step discontinuities," *IEEE Trans. Microwave Theory Tech.*, vol. MTT-37, pp. 381-387, Feb. 1989.

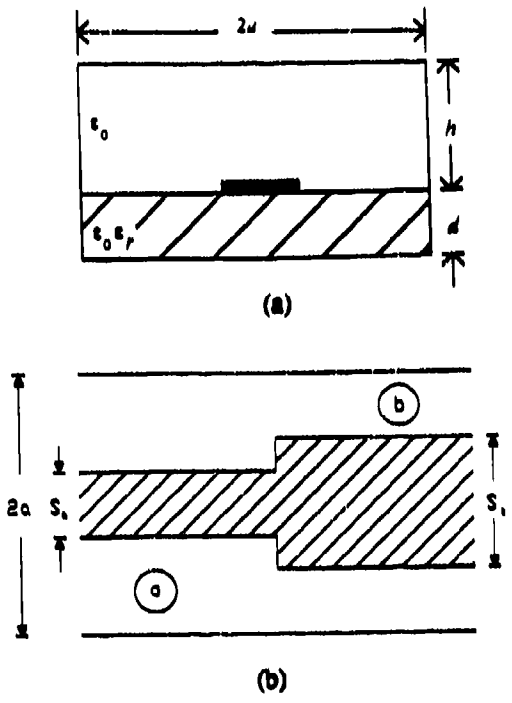

Fig. 1. Cross section (a) and a single-step discontinuity (b) of microstrip line.

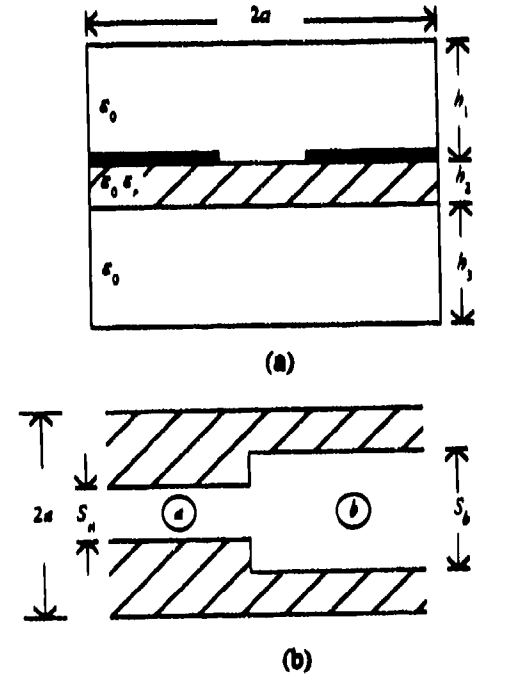

Fig. 2. Cross section (a) and a single-step discontinuity (b) of finline.

Table 1. Comparison of the magnitude of S_{11} for a single-step microstrip junction between our results and [3]. ε_r=2.32, h=15.8 mm, d=1.58 mm, a=17.233 mm, S_a=4.5 mm, S_b=15.65 mm, f=2 GHz.

S_{11} [3]		S_{11} (Our Result)	
Orthogonality not enforced	Orthogonality enforced	Orthogonality not enforced	Orthogonality enforced
0.3980	0.3946	0.3972	0.3972

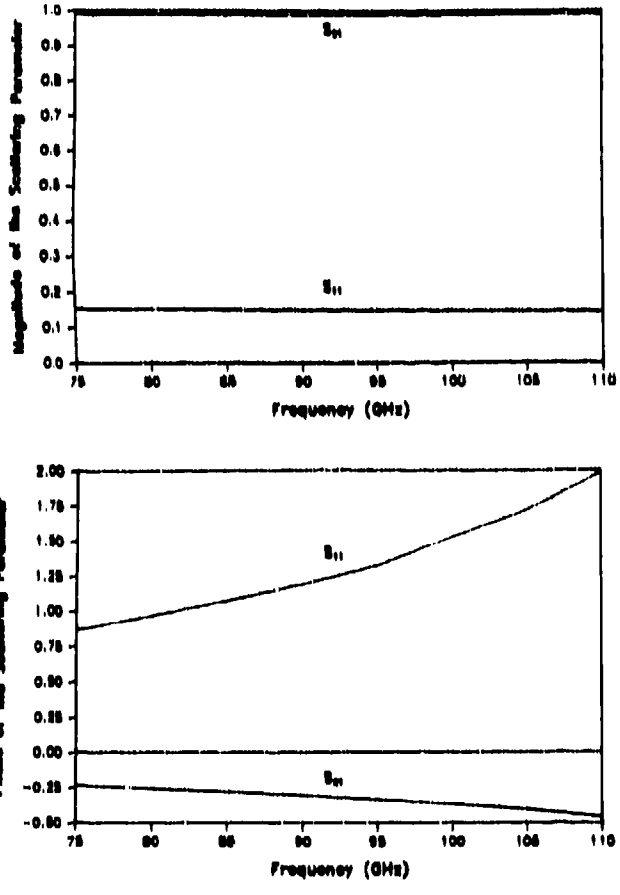

Fig. 3. Calculated S-parameters of a sigle-step microstrip discontinuity from 75 to 110 GHz. ε_r=2.2, h=1.143 mm, d=0.127 mm, a=0.635 mm, S_a=0.762 mm, S_b=0.508 mm.

RECENT DEVELOPMENT OF MICROSTRIP BAND-PASS FILTERS FOR MICROWAVE AND MILLIMETER-WAVE INTEGRATED CIRCUITS

Cam Nguyen
Department of Electrical engineering
Texas A&M University
College Station, Texas 77843-3128

Abstract - Microstrip band-pass filters recently developed for microwave and millimeter-wave integrated circuits are presented. The new half-wavelength coupled-line band-pass filters, employing symmetric and asymmetric broadside-coupled microstrip structures, exhibit about 1-dB insertion loss at 10 GHz. The novel spurline band-pass filters, using two and three parallel-coupled lines, have insertion losses of less than 1 and 1.3 dB, respectively, at 5 GHz. Experimental and theoretical results also agree well.

INTRODUCTION

Microwave band-pass filters play an important role in many microwave systems. Efforts have always been made in developing miniature microwave integrated circuit (MIC) and microwave monolithic integrated circuit (MMIC) band-pass filters to fulfill the increasing demand of systems with small size and weight.

In this paper, we report two new kinds of band-pass filters recently developed for MIC and MMIC applications. The first type is half-wavelength coupled-line band-pass filters employing symmetric and asymmetric broadside-coupled microstrip lines. These filters are suitable for wide bandwidths and tight couplings. Compared to the conventional microstrip and stripline coupled-line filters [1], they have wider bandwidths due to the inherently strong coupling achieved between the resonators and smaller size. The second type is spurline band-pass filters using two- and three-parallel-coupled-line spurline resonators. As compared to the conventional open-circuited shunt-stub band-pass filter [2], they have less radiation, susceptibility to nearby objects and dispersion and smaller size.

BROADSIDE-COUPLED MICROSTRIP FILTERS

Fig. 1 shows the new half-wavelength broadside-coupled band-pass filters, and Fig. 2 shows the cross sections of the shielded and open broadside-coupled microstrip lines employed in these filters. Several filters have been designed, built, and tested . Fig. 3 shows the measured and calculated results of one of the new filters in the X-band (8-12 GHz) which match almost exactly. As can be seen, about 1-dB insertion loss is achieved in the passband.

SPURLINE MICROSTRIP FILTERS

Fig. 4 shows photographs of the new spurline microstrip band-pass filters, each consisting of two spurline resonators. Their performances are given in Figs. 5 and 6. They exhibit less than 1- and 1.3-dB insertion losses in the pass bands around 5 GHz using two-conductor and three-conductor spurline resonators, respectively. Also, the calculated and measured results are in a good agreement.

CONCLUSIONS

Recent development of new microstrip broadside-coupled and spurline band-pass filters, suitable for MICs and MMICs, have been presented. The broadside-coupled filters possess wide bandwidths, compactness, and are based on microstrip technology. Measured results show insertion losses of about 1 dB at 10 GHz. The spurline microstrip filters have small size, radiation, sensitivity to nearby elements, and dispersion. These filters exhibit less than 1- and 1.3-dB pass-band losses at 5 GHz using two- and three-conductor spurline resonators, respectively.

ACKNOWLEDGMENT

This work was supported in part by the NASA Center for Space Power and by TRW Inc.

REFERENCES

1. S.B. Cohn, "Parallel-Coupled Transmission Line Resonator Filters," IRE *Trans. Microwave Theory Tech.*, Vol. MTT-6, pp. 223-231, Apr. 1958.

2. Matthaei, Young, and Jones, Microwave Filters, Impedance Matching Networks, and Coupling Structures. New York: McGraw-Hill, 1964.

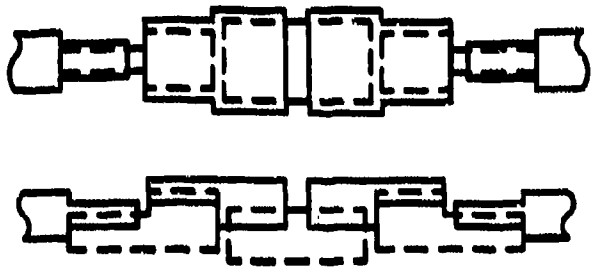

Fig. 1. New broadside-coupled bandpass filters. Top: —— and bottom: - - - -.

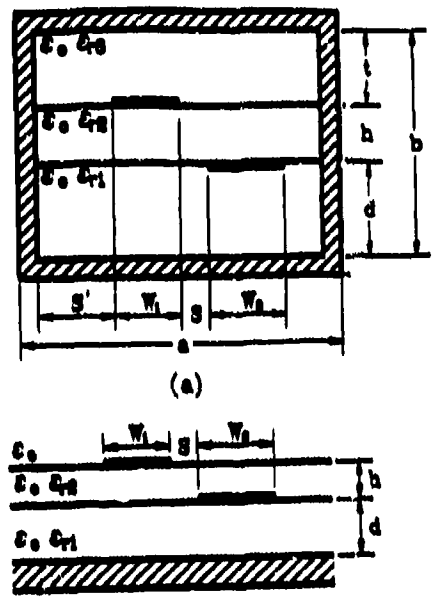

Fig. 2. Cross-section views of the broadside-coupled microstrip lines: (a) shielded and (b) open.

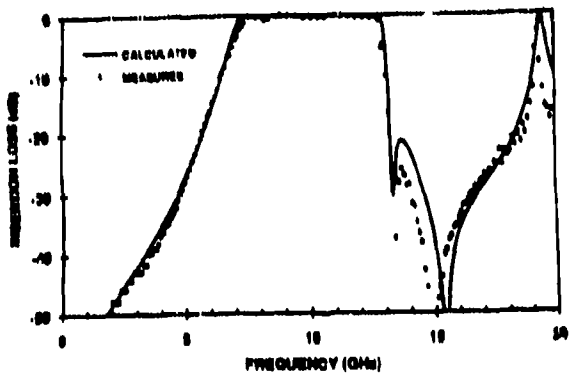

Fig. 3. Performance of a broadside-coupled microstrip bandpass filter.

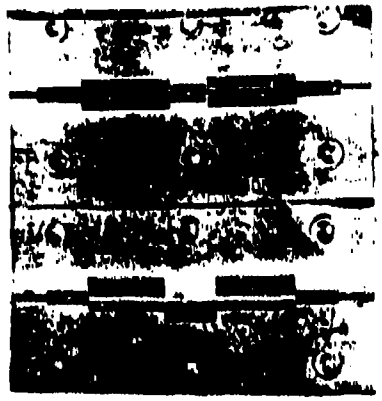

Fig. 4. Photographs of the spurline microstrip bandpass filters.

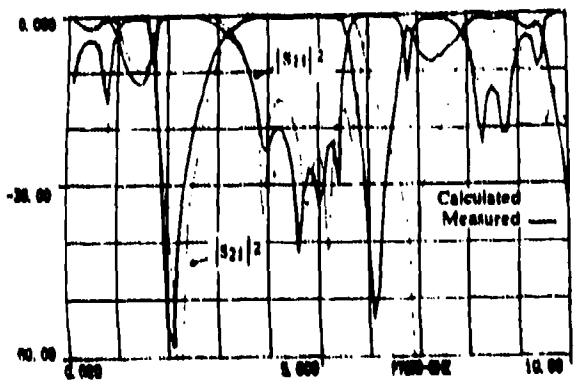

Fig. 5. Performances of the two-conductor spurline bandpass filter.

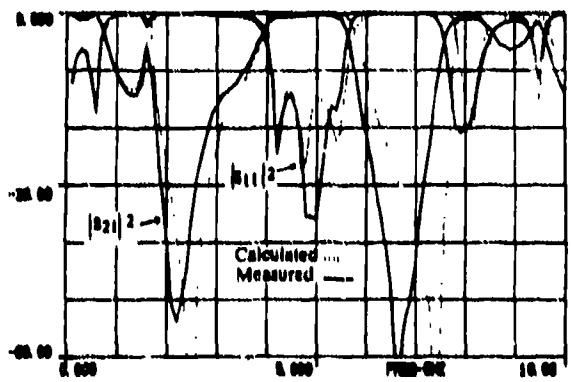

Fig. 6. Performances of the three-conductor spurline bandpass filter.

Millimeter waves and Quantum Medicine

Prof. Sergei P. Sit'ko, Ph.D.,
Director of the Interbranch Scientific Research Center on Physics of the Alive and Microwave Resonance Therapy,
Ukraine, 252033, Kiev, 61-b, Volodymirska St.

On the basis of multi-centered scientific studies carried out within the frames of the program "Physics of the Alive" and the experience of treatment of more than 196,000 patients the foundations of the "Quantum Medicine" have been layed. Its conceptual basis is provided by the idea that any living system is simultaneously a macroscopic quantum object and a maser (mm-range laser).

Infrared Spectra Of Urine From Cancerous Bladders

M.A.Moharram, A.Higazi* and A.A.Moharram*
Spectroscopy Department, Physics Division,
National Research Center, Cairo, Egypt.
*Faculty of Medecine, Cairo University

The infrared spectra of organic and inorganic constituents of urine from cancerous bladders of some patients were recorded. The spectra of the organic part of the samples were classified into five types according to the bulk constituents. Samples with type A spectra consisted mainly of proteins with only trace amounts of lipids. Their spectra were characterized mainly by the absorption bands of proteins at the frequencies 3330, 3075, 2960, 2850, 1650, 1530, 1450, 1400 and 1320 cm^{-1} in addition to a weak band at 1720 cm^{-1} due to the absorption of lipids. Samples with type B spectra were characterized by high amounts of proteins and low amounts of lipids and phosphate compounds. The presence of phosphate compounds was indicated by the absorption bands at the frequencies 1100 and 1030 cm^{-1}. Samples giving spectral type C were characterized by high urea contents as indicated by the presence of two strong bands at 1670 and 1630 cm^{-1}. Samples with the spectral type D consisted of urea and phosphate compounds whereas samples with the last spectral type E consisted mainly of calcium oxalates, uric acids and phosphate compounds. The presence of calcium oxalates was indicated by the presence of its diagnostic bands at the frequencies 1630 and 1330 cm^{-1} while the presence of uric acid was indicated by the bands at the frequencies 1360, 1130, 1020 and 880 cm^{-1}. On the other hand, the spectra of the organic part of urine from some normal bladders exhibited the characteristic bands of urea only.

Careful examination of the spectra of the inorganic part of urine revealed that some samples consisted mainly of hydroxyapatite. The absorption bands of hydroxyapatite appeared at the frequencies 568, 603, 985, 1037 and 1128 cm^{-1}. The spectra of the other samples showed the bands of basic phosphates at the frequencies 568, 620, 727, 890, 1035 and 1140 cm^{-1}. The spectra of the inorganic part of urine from a number of normal bladders displayed the bands of basic phosphates. The relationship between the types of urine constituents and the grade of the malignant tumors was discussed.

DRO-Autodyne Spectrometer for Investigation of Interaction of Millimeter Electromagnetic Waves with Biological Objects

G.P. Ermak, Ye.B. Senkevich

Institute of Radiophysics and Electronics
of the Ukrainian Academy of Sciences
12 Ac. Proskura st., 310085, Kharkov, the Ukraine

There exist the problems sending us in search of a simple, small in size and precision instrument to measure the parameters of the electromagnetic sygnal reflected from the object under investigation in the millimeter and submillimeter waves bands. Such a problem can be cracked by devising an apparatus operating as a transmitter and a receiver simultaneously. Such a transmitter-receiver system is called autodyne and allows to do away with a heterodyne, a mixer, a receiving aerial, and waveguide commutators.

The autodyne sensitivity depends on the level of the oscillator inherent noise and the frequency instability. Therefore autodynes devised on the base of BWT, magnetrons and klystrons give a bad fit for microwave spectroscopy.

In this report it is suggested a novel autodyne millimeter waves spectrometer devised on the base of the diffraction radiation oscillator (DRO). This DRO is a high-stability source of coherent electromagnetic oscillations in the frequency range from 30 to 300 GHz. Its noise level is in two orders lower than that inherent in other millimeter-wave oscillators. Besides, this DRO has the highest autodyne magnification coefficient.

The autodyne effect lies in the fact of the change of the working characteristics such as the resonator field amplitude, the oscillation frequency, the beam current under the action of the inherent coherent radiation reflected from the examined object. The amplitude and frequency increments are respectively

$$\Delta A = -(1/2)\Gamma A_0 \cos\delta;\ \Delta\omega = \Gamma\left[(\omega_0/2Q)\sin\delta - (1/2)K_a q\cos\delta\right] \quad (1)$$

where Γ and δ are respectively the modulus and phase of the reflection coefficient; A_0 and ω_0 are respectively the nondisturbed amplitude and frequency; K_a is the autodyne magnification coefficient; Q is the external Q-factor of the DRO-autodyne system; q is the oscillator non-isochronism.

The current increment at the interaction space boundary is

$$\Delta I(t) = -(1/2)\Gamma K_j I_0 \cos\delta \quad (2)$$

where K_j is the autodyne magnification coefficient of the current; I_0 is the nondisturbed current value.

DRO-autodynes are classified on the principle of detection of either external or internal sygnals and register respectively either sygnals (1) by a semiconductor detector or current increment (2) by internal electron detector. The internal electron detector is formed

by two electrodes. One of them is transparent for the electron beam and placed in the path of the beam at the outlet of the interaction space.

The operation of DRO-autodyne is as follows. The electromagnetic wave generated by DRO-autodyne is incident on the object under investigation. The reflected sygnal passes over the waveguide switch, phase shifter, directional coupler and comes back to the DRO-autodyne. The measurements of the frequency deviation and the amplitude modulation of DRO-autodyne sygnals are carried out by spectrum analyser and deviometer.

In the course of the experiment the measured sygnals reflected from the biological objects were compared with those from the matched load. The DRO-autodyne was set to the most sensitive range. The phase sensitivity of the DRO-autodyne spectrometer at 36 GHz was about 0.27 MHz/deg and the corresponding resolution for the spectral line width of 10 KHz was about 0.02 degree. Due to the slight electron transconductance (0.1 ÷ 0.2 MHz/V) of the DRO frequency tuning and high stability of the power supply the autodyne spectrometer operates stablely for a long time.

The effects of the interaction of the coherent electromagnetic waves with a natural neural network of the eyeball back retina of Rana temporaria and T-limphocites in the periferal human blood have been revealed [1] due to using 9 and 2 mm DRO-autodyne spectrometers.

The analysis of the experimental data shows that the level of the frequency modulation of the sygnal reflected from the biological objects much exceeds that of the amplitude while in measuring the matched load ΔA and $\Delta\omega$ are zero. The frequency and amplitude responces of the DRO-autodyne during its interaction with live objects are time-dependent nonmonotonic functions correlating with the objects functional activity.

Thus the DRO-autodyne provides the research of the structure of the sygnal reflected and reemitted by biological objects interacting with millimeter electromagnetic waves.

References

[1] G.P. Ermak, V.P. Shestopalov, "DRO-Autodyne Method of Investigation of the Biological Objects", Dokl. Akad. Nauk USSR, Vol. 315, No. 3, 1990 (in Russian).

Infrared spectroscopy detection of millimetre-wave effect upon biomolecules.

G.S.Litvinov,L.I.Berezhinsky,G.I.Dovbeshko,M.P.Lisitsa,L.I.Matseiko

Scientific Research Center "Vidhuk",
Volodymyrska 61-b, Kiev 252033, Ukraine.

ABSTRACT

It has been found out that milimetre-wave (MMW) radiation in the 37.5-78 GHz range affected spectral properties of aminoacids, nucleotides, proteins and nucleic acids in free and intracellular states. MMW radiation effect was detected by the infrared (IR) spectrum parameter changes such as intensity, halfwidth and shape of absorption and reflection bands. It was established that tuned MMW action upon intensity of IR reflection bands had sharp resonance with halfwidth of 40-60 MGHz, that corresponded to Q-quality of order 1000. For high ordered systems such as aminoacid single crystals MMW effect detection depended strongly on orientation of the mm-field electrical vector relative to symmetry axes of object.

2.INTRODUCTION

Recently biological effects of MMW radiation has been studied by using the living organisms as detectors. The existence of the MMW effect was established by the physiological parameter changes [1]. However, physiological parameters are stochastic and multifarious that lead to uncertainty in interpretation of MMW effect. In the paper the attempts to detect MMW effects by highly reproducible method of IR spectroscopy of biomolecules were described.

3.MATERIALS AND METHODS

Investigations of the MMW radiation effect upon α-glycine (Gly), β-alanine (Ala), DL-tryptophane (Trp), L-tyrosine (Tyr), L-histidine (His) aminoacids, adenosinemonophosphate (Amp) nucleotide and free and intracellular DNA were carried out by IR spectroscopy in the 400-3800 cm^{-1} range. MMW radiation was tuned in the range of 37.5-78 GHz. Incident power density of radiation varied from 1 to 30 mW/cm^2.

4.RESULTS AND DISCUSSION

Intensity changes up to 35% in IR absorption spectra of aminoacid and Amp films were registered (Table 1). Irradiation was affecting a great number of vibrational bands connected with different forms of vibrations and chemical bonds. Resonance character of MMW action was regarded as its distinctive feature. Maximum effects for different vibrations could be obtained at different MMW radiation frequencies. The MMW action appeared to be more pronounced for NH and deformational vibrations. Besides, depending on irradiation frequency one could obtain increase or decrease of IR bands peak intensities.

Table 1. Redistribution of peak intensities of IR bands of simple biomolecule films under MMW radiation

Trp		Tyr		Amp	
F = 37.50 GHz		F = 41.52 GHz		F = 41.67 GHz	
$\nu(cm^{-1})$	I	$\nu(cm^{-1})$	I	$\nu(cm^{-1})$	I
1317	1.35±0.10	1330	1.35±0.04	583	1.12±0.05
1346	1.30±0.08	1370	1.18±0.03	940	1.37±0.08
1360	1.31±0.05	1425	1.15±0.04	1125	1.35±0.10
1415	1.22±0.07	1450	1.04±0.04	1690	1.28±0.07
1460	1.31±0.05	1590	1.33±0.06		
1590	1.23±0.04				

ν - IR band wavenumber
I - peak intensity of IR band after MMW irradiation at F
F - frequency relative to the non-irradiative band

In IR reflection spectra of Gly, Ala, His single crystals band structure variations together with the intensity redistribution were found. The amplitude of changes approached 55% of initial intensity. The measured polarization dependencies of MMW effect for GLY, ALA and HIS monocrystals indicated that 1) it differed substantially for different vibration forms, 2) it depended on orientation of field electrical vector relative to symmetry axes of the crystal and 3) polarization indicatrices changed under MMW action.

Significant action of MMW radiation upon intensity, halfwidth and shape of the bands connected with the vibrations of phosphodiester bond atoms in free DNA was revealed. Changes in the IR spectra of E.coli clinical strains for the bands of DNA oscillations after the action of MMW radiation were found to be the same as for the free DNA dry films: the structure of the 1080 cm^{-1} band was changed, intensities of the O-P-O vibrational bands were redistributed. It was determined for Dunaliella viridis intracellular DNA that irradiation at the frequency of 37.51 GHz caused the 1080 cm^{-1} band narrowing by 25±1 cm^{-1} and its intensity increased by 27±5%. It should be emphasized that the effects observed were not connected, apparently, with the well-known influence of drying which caused the DNA B-A form transition and the following disordering [2]. On the basis of the data obtained it follows that the MMW irradiation resulted in the changes of the DNA IR parameters opposite to that observed with the reduction of film humidity. Thus, IR spectroscopy could be successfully used for detection of MMW effect upon biomolecules.

5. REFERENCES

1. H.Fröhlich, Biological coherence and response to external stimuli, Springer, Berlin, 1988.

2. M.Falk, A.G.Poole, C.G.Goymour,"Infrared study of the state of water in the hydration shell of DNA", Can. J. Chem., Vol.48, pp. 1536-1542, 1970.

Treatment of cardiovascular deceases by means of wide-band coherent signal of mm radio wave range

V.D.Yeremka, A.A.Kuznetsov, V.V.Smorodin, A.I.Fisun, A.M.Fursov, L.P.Himenko, P.L.Himenko

Institute of Radiophysics and Electronics of Ukrainian Academy of Sciences,
12, Acad.Proskura st., Kharkov, 310085, Ukraine

ABSTRACT

The results of study of therapeutic influence of mm waves having the frequency, periodically changing in the band from 50 to 80 GHz, on the patients with cardiovascular pathology are presented in the report. It was shown that their use allowed to return a number of physiological parameters of a man to normal and to improve peripherical and central haemodynamics.

1. INTRODUCTION

Lately the field of physical therapy, based on the use of electromagnetic waves with the frequency exceeding 30 GHz is sufficiently intensively developed. The mechanism of the influence of given spectrum region was not revealed. They suggest that a number of biological effects was connected with the change of cross-linking of aqueous phase of tissue, in particular nervous one.

2.WIDE-BAND EHF-THERAPEUTICS

The theoretical study shows the possibility to generate the oscillations of range from 100 GHz to 10 THz at the expense of coherent transitions in membrane canals between energy levels, that arise in electrical field of membrane potential. The frequencies of given range are typical for rotatory spectrum of macromolecule oscillations. Thus, not knowing real mechanism, all the same one can assert that biological tissues have sufficiently dense spectrum of natural oscillation frequency of the influence, especially received by subjective sensations [1,2] exists, seems doubtful. Monochromatic signal having the frequency, periodically changing in wide band will be more effective stimulus for biological system with dense spectrum[3].

Proceeding from above-stated conception the physical-therapeutic device, based on the use of backward wave tubes, that allows to provide the influence by oscillations having the frequency periodically changing in the band from 50 GHz to 80 GHz, the power of 0.1-10 mW and variation of type of polarization, was designed.

3. TREATMENT OF PATIENTS OF CARDIOLOGICAL PROFILE BY EHF-THERAPY METHOD

66 patients received the treatment. 52 of them suffered from acute infarctus myocardii or from unstable stenocardia, in the most of cases in combination with hypertension, 14 patients suffered from chronic form of heart ischemia. All patients had pronounced insufficiency of circulation of the blood. The treatment by the influence on the region of processes xiphodeus with the exposition of 15 min during 10 seances was carried out. Besides above-mentioned treatment all patients received traditional medicine treatment since their condition was estimated as from middle serious to extremely serious one. The indeces of central haemodynamics were studied by the method of integral rheography, by Tischenko-Estrin method, biological functions of miocardii was studied by means of electrical cardiography and central cardiodynamics - by ultrasonic scanning. In the result of this it was founded that the positive result was observed in 75% of cases. There was not any effect of treatment in 25%. There were no side-phenomena. Positive effect decreased or did not come totally at the presence of heart insufficiently and at the decreasing of contractive characteristics of myocardii in consequence of chronic coronarius disease and this tendency is proportional to decompensation degree. The positive effect was more strongly pronounced at the decompensation mainly stipulated by artery hypertensio.

4.CONCLUSION

On the base of analysis of received data (Fig.1) the decreasing (normalization) of specific peripheral resistance and increasing of blow-out fraction and degree of front/back size, that are correlated with the improvement of clinical state of a patient.

5.REFERENCES

1. E.A.Liberman, V.L.Eidus,"Proton SHF-oscillator", Biophysika, V.26, №6, PP.1109-1111, 1981.

2. E.A.Andreyev, M.U.Bely, S.P.Sit'ko, "The display of natural haracteristic frequenceies of human organism", DAN Ukrainy, Ser. B, N10, PP.60-63, 1984.

3. V.D.Yeremka, A.A.Kuznetsov, V.V.Smorodin, "The method of the influence on BAP in EHF-range and its apparatus equipment", 2-nd Crimean Conf. Digest, PP.214-219, Sevastopol, 1992.

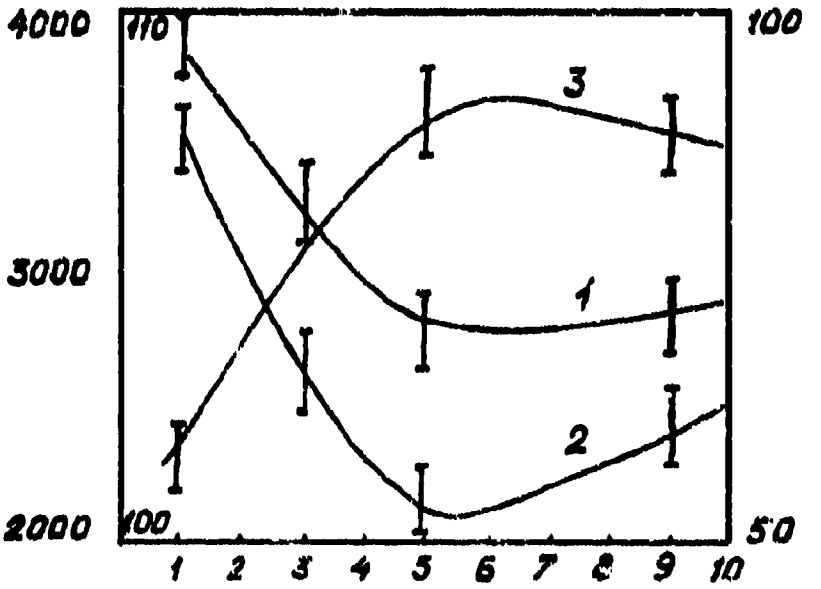

Fig.1. Dependence of specific perifery resistance (1), artery pressure (2) and stroke volume (3) on a number of performances

REARRANGEMENTS IN POLARIZED VIBRATIONAL SPECTRA OF GLYCINE-CONTAINING CRYSTALS UNDER MILLIMETER WAVE IRRADIATION EFFECT.

L.I.Bereshinsky, G.I.Dovbeshko, G.S.Litvinov, V.V.Obukhovsky,

Scientific Research Center "Vidhuk", Volodymyrska 61-b, Kiev 252033, Ukraine.

ABSTRACT

Rearrangements in polarized infrared reflection spectra of glycine-containing crystals - α-glycine and triglycinesulphate (TGS) were discovered in the area of 600-2000 cm^{-1} under millimeter wave irradiation applied with the power up to 5 mW/mm^2 within 37.5-53.5 GHz range. For NH_3 deformational vibration in both crystals measured polarization reflection indicatrices agreed with calculated indicatrices. Changes in polarization indicatrices under resonance millimeter wave effect were studied. Parameter values which characterize dielectric permeability tensors of α-gly and TGS and their changes under millimeter wave field were calculated on the basis of the experimental data.

2. INTRODUCTION.

In recent years the studies of mm-range electromagnetic radiation or extremely high frequency (EHF) effect upon the biological objects have received much attention. Among other things this interest is connected with the nontrivial biophysical and therapeutic effects observed under millimeter wave (MMW) action on the biosystems of different levels of complexity up to human organism [1-3]. At the present stage however the theoretical interpretation of these phenomena is a challenge, since the primary physical mechanisms of mm-range irradiation effect upon biologically active structures still remain unclear.

3. METHODS

In given experiments the monocrystal of the material under study in the form of a 1-2 mm thick plate with 5x8mm^2 cross-section was exposed to MMW radiation emitted along the normal to one of the planes. The generator Г4-141 (USSR) with the output power not over than 5 mW/mm^2 and smooth frequency tuning within the interval of 37-53.5 GHz was used as the irradiation source. EHF irradiation frequency was retuned with the accuracy of no less than ±5 MHz. During MMW action infrared (IR) reflection spectra in 600-4000 cm^{-1} range were detected from the opposite plane of monocrystalline plate. Measurements were taken by a double-beam diffraction spectrometer DS-402G (JASCO, Japan) with the use of reflection adapter wherein natural globar irradiation is incident on the reflection surface at an angle close to the normal. In front of the receiver a polarizer was set which could be tuned in the wide range of angles. Thus, IR reflection spectra intensity was measured as the dependence from polarizer rotation angle (φ) at fixed angle of

incidence and reflection of IR irradiation (~ 7°).

4.RESULTS AND DISCUSSION

It follows from the experimental data that in polarized IR reflection on spectra of α-Gly and TGS crystals MMW irradiation provokes essential intensity redistribution of bands, changes in their shape and structure. It may be noted that maximum rearrangements in the IR reflection spectrum bands of deformational NH_3^+ and CO_2^- vibrations were registered within the ranges of 1200-1600 cm^{-1} and 600-800 cm^{-1}, although quite noticeable changes were observed in the other spectrum ranges. Along with this the important feature of MMW effect is illustrated by strong, resonance-type (with 40-60 MHz halfwidth and Q-factor ~ 10^3) dependence of the effects on the incident irradiation frequency. Besides, there is a set of exstra hight frequencies in the vicinity of which the IR spectra rearrangements are induced by EHF field. For α-Gly and TGS, about 20 such resonances were detected within the range of 37-53.5 GHz. Versatile orientations of MMW field effects at different resonance frequencies are particularly remarkable: the external field frequency tuning may result either in the increase, or in the decrease of the intensity of the same IR band. Together with the abovementioned the fact that resonance frequencies induced by EHF field were different for different vibrations provided the basis for radical rearrangements of IR spectra under MMW irradiation action of different energies. Finally, the basic feature of the effects is offered by the dependence of the volume of changes on mutual orientation of polarizer, monocrystal and EHF field vectors. The dependence of MMW irradiation action on IR reflection intensity examined in polarized α-Gly and TGS spectra showed the intricate effect performed by simultaneous action of the external field and polarizer on the detected intensity of IR signal, and this action was different for different vibrational bands of the isolated crystal and for identical vibrations of different crystals. Parameter values which characterize dielectric permeability tensors of α-gly and TGS and their changes under MMW field were calculated on the basis of the experimental data. The comparison of the experimental data with indicatrix's theoretical form helps to find the relation of coefficients which determine the component values of dielectric permeability tensor and their changes under MMW field.

5.REFERENCES

1. H.Frohlich, "Biological effects of millimeter waves and related questions", Adv. Electron. Phys., Vol.53, pp.85-152, 1980.
2. S.I.Webb, A.D.Booth,"Absorption of microwaves by microorganisms", Nature, Vol.222, N5199, pp.1199-1200, 1969.
3. S.P.Sit'ko, E.A.Andreev, I.S.Dobronravova, "The whole as a result of self-organization", J.Biol.Phys., Vol.16, N1, pp.71-73, 1988.

The combined effect of high temperature and microwave fields on winter wheat seeds

V.G. Shakhbazov, A.A. Shmatko, Al.A. Shmatiko

Kharkov State University, Department of Genetics and Cytology
4 Nezavisimosti Square, Kharkov
Ukraine

Information about biological effect of electromagnetic radiation (EMR) on living organisms is known for a long time, but a systematic development of a problem began during the late 1940's by the group under guidance of an academician Devyatkov N.D. In particular, it was found that a millimeter band EMR can accelerate and decelerate a growth of microorganisms, increase an activity of synthesis by microorganisms of enzymes and change a complex of these enzymes with a predominance of a necessary component, to restore an ionic permiability of erythrocyte membranes broken by electric break-down, can accelerate a peroxide oxidation of lipids, weaken the effect of radiation and chemotherapeutic remedies on processes of medullary hemopoiesis of animals. It was determined a strong dependence of effects of radiation action on biological objects on a frequency of oscillations, i.e. a presence of acute resonances.

In selection of new sorts of cultured plants much attention is given to the evaluation of their steadiness degree to extreme conditions. So, in particular, an increase of a temperature can negatively influence on viability of seeds and sprouts of agricultural plants.

In this paper it was made an attempt to prevent this effect. We suggested a technique of combined effect of high temperature and low-intensity non-heat microwave radiation on seeds of cultured plants.

Seeds of a new sort of winter wheat were used as an object of investigation, they were subjected to the action at first of high temperature and then - that of low-power microwave field on different wavelengths in a millimeter band at different expositions of action.

50 pieces of wheat seeds were warmed up in a water thermostat during 20 minutes at a necessary temperature. After heat influence seeds in a special experimental dish were irradiated by a source of millimeter band during a certain time and then they were placed in a special-purpose thermostat for sprouting. On the 4th day after the experiment carrying out it was made an account of seed germination and increase of roots and stems according to a specific technique. Results were statistically processed. According to data obtained we have plotted histograms.

The figure 1 shows that in acting a high temperature (57° C) it takes place a lowering of seed germination indices by 40% in comparison with a control exposition. In case of combined effect of this

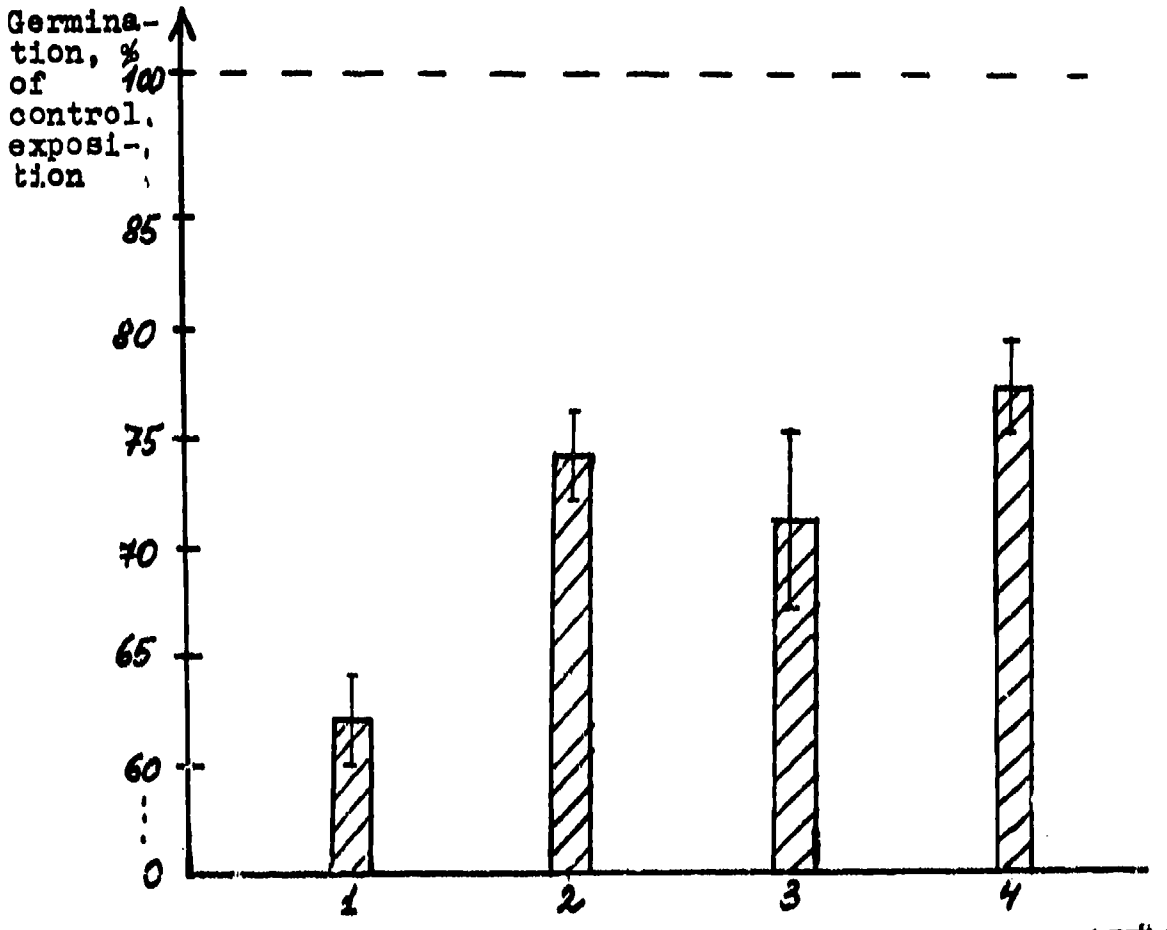

Fig. 1. The combined influence of high temperature (57° C) and microwave radiation on a germination of winter wheat seeds (1 - temperature, 2 - temperature + 1 min. of irradiation, 3 - temperature + 5 min. of irradiation, 4 - temperature + 10 min. of irradiation).

temperature and microwave radiation on seeds a pronounced stimulation in a seed germination index is observed (9-15% with respect to a temperature effect). As for indices of increase of roots and stems a great statistical spread is obtained, therefore it is difficult to speak about their increase or decrease. Similar effects were observed on other wavelengths.

Results obtained show that a microwave radiation partially renews seed germination indices after a high temperature action. This effect is observed when a certain small dose of microwave radiation is used that indicates on a resonance absorption mechanism of microwave radiation as well as on that of the inter-molecular interaction in a living organism.

The more detail check of effects obtained is of interest in connection with their possible use in the plant-growing and the agriculture.

PECULARITIES OF THE FAR INFRARED SPECTRA OF AMINOACIDS, BIOPOLYMERS AND CELLS

G.S.Litvinov, G.I.Dovbeshko.

Scientific Research Center "Vidhuk",
Volodymyrska 61-b, Kiev 252033, Ukraine.

ABSTRACT

Spectra of some aminoacid single crystals, proteins, DNA and cells of E.coli B bacteria were studied in the submillimeter region (10-400 cm^{-1}). Low-frequency vibrations were investigated by far infrared (FIR) absorption and Raman scattering (RS). The presence of a wide band in the 50-350 cm^{-1} interval is a characteristic feature of aminoacids of FIR absorption under study. On this absorption band about 10-30 relatively narrow bands (halfwidth - 2-10 cm^{-1}) were observed. In FIR and RS spectra of all aminoacids the observed number of low frequency bands exceeded the calculated one. In the FAR spectra not only of aminoacids but also of protein, DNA and cells broad background in the region of the 100-350 cm^{-1} was found. E.coli bacteria spectrum looked like the superposition of the constituent protein and DNA spectra.

2.INTRODUCTION

Existence of low-energy transition is the essential feature of the living matter. Unfortunately a few works [1] on low-frequency spectroscopy of biocbgects are now available. In the paper the low-frequency spectra of aminoacids and polycrystalline films of proteins, DNA and E.coli cells were investigated by RS and FIR spectroscopy in the submillimeter region.

3.METHODS

β-alanine (β-Ala) and DL-tryptophane (DL-Trp) single crystals were grown by slow evaporation from saturated aqueous solutions. RS spectra were recorded on the triple grating laser Raman spectrometer. The film samples for FIR spectroscopy were casted from highly purified water solutions on the transparent substrates (polyethylene). Far-infrared spectra were registered on the HITACHI FIS-3 grating spectrometer and Bruker FIR spectrometer.

4.RESULTS AND DISCUSSION

β-alanine.

The space group of β-Ala crystal is D_{2h}^{15} (Pbca), its unit cell contains 8 molecules and has the inversion center. So there are 45 grate vibrations, 15 of which are active in FIR absorption spectra. More than 40 bands were found in the FIR (20-370 cm^{-1}). Among them narrow enough bands (halfwidth up to 3 cm^{-1}) and much wider ones were found. If only narrow bands with the intensity no less than 5% can be assigned to the first order crystalline vibrations, then 15 bands may be found in the interval of 20-165cm^{-1}. However, this

coincidence does not mean that they all are of grating type, it is possible that there are intramolecular ones among them.

Table. Vibrational frequencies of protein, DNA and E.coli cells in the region of 40-350 cm^{-1}

Protein cm^{-1}	DNA cm^{-1}	E.coli cm^{-1}
330	330	330
280	276	282
-	-	276
257	256	257
236	236	237
-	-	228
216	210	210
190	202	190
175	-	175
158	165	160
140	135	134
-	-	127
-	-	120
90	95	90
77	78	77
75	72	72
50	48	47

DL-Tryptophane

Trp crystal belongs to $P2_1/c(C_{2h}^5)$ space group with 4 molecules per unit cell. In FIR spectra of Trp we observed 9 lattice modes in the interval of 50-196 cm^{-1}. The result is in a good agreement with the calculations. Despite the X-ray data and theory selection rules for β-ala and tryptophane crystals there were observed the forbidden dipole active vibrations of ungerade type in the Raman spectra and gerade vibrations in FIR spectra.

Proteins, DNA, E.coli B

DNA and protein FIR spectra in the 40-400 cm^{-1} range are very similar, differencies were noticed only in intensities of some bands and in the form of absorption in the 200-120 cm^{-1} region (Table). In the complex biological objects such as bacteria the low-frequency spectra are formed mainly as the result of the constituent macromolecule spectrum overlapping. Though four bands frequencies 276, 228, 127 and 120 cm^{-1} were not found in protein and DNA spectra. In a whole the spectral parameters of the investigated biological object vibrations are almost the same as for organic molecular crystals with saturated chemical bonds.

5.REFERENCES

1. "Coherent Excitations in Biology",ed.H.Frohlich, F.Kremer, Springer Verlag, New York, 1983.

The influence of microwave fields on electrokinetic properties of cellular nuclei of human buccal epithelium

V.G. Shakhbazov, Al.A. Shmatiko

Kharkov State University, Department of Genetics and Cytology
4 Nezavisimosti Square, Kharkov
Ukraine

The cellular nucleus as an organoid of storage and transfer of hereditary information is an interesting object for studying and attracts attention of researches from various fields of science.

In the early 1960s at the Department of Genetics and Cytology of the Kharkov State University it was developed a technique for study of cellular nuclei electrokinetic properties that made possible to widely investigate this index with using results in medicine, cattle-breeding, plant-growing, etc., though questions of theory in this field are not studied enough.

In this paper it was experimentally investigated the influence of low-power microwave radiation of millimeter band on electrokinetic properties (EKP) of cellular nuclei of human buccal epithelium. The microwave field action on bioelectrical properties of cells is of interest, so long as hitherto only statistical effects were investigated.

So, it was determined a connection of cellular nuclei EKP of plants, drosophile and a man with age of cells, genic activity, heterosis effect and physiological state of cells, as well as a dependence on extreme actions such as a high temperature, constant magnetic field, etc.

In this paper the buccal epithelium cells of a cheek internal surface of a man were chosen as an object of research, as they are the most convenient through their structure, as well as through easiness and painlessness of a sample taking. The buccal epithelium cellular nuclei EKP were investigated by a method of microelectrophoresis.

Prepared preparation from the buccal epithelium cells was subjected to the influence of low-power microwave field of millimeter band in dependence on irradiation time. The four expositions were considered as follows: 5, 15, 30 and 60 minutes. One exposition was a control one. After the effect of irradiation the preparation was placed in special chamber of a device for microelectrophoresis and with a help of a microscope the special electrophysical measurements were carried out. It was used the fact that cellular nuclei of buccal epithelium being in normal state displace in an electric field in the direction of the anode, i.e. have a negative surface charge. We visually counted up the percentage of electronegative nuclei displacing in an electric field before and after irradiation. Results were stat-

istically processed.

According to results obtained it was plotted the electronegative nuclei percentage (EN%) as a function of exposition time (Fig. 1).

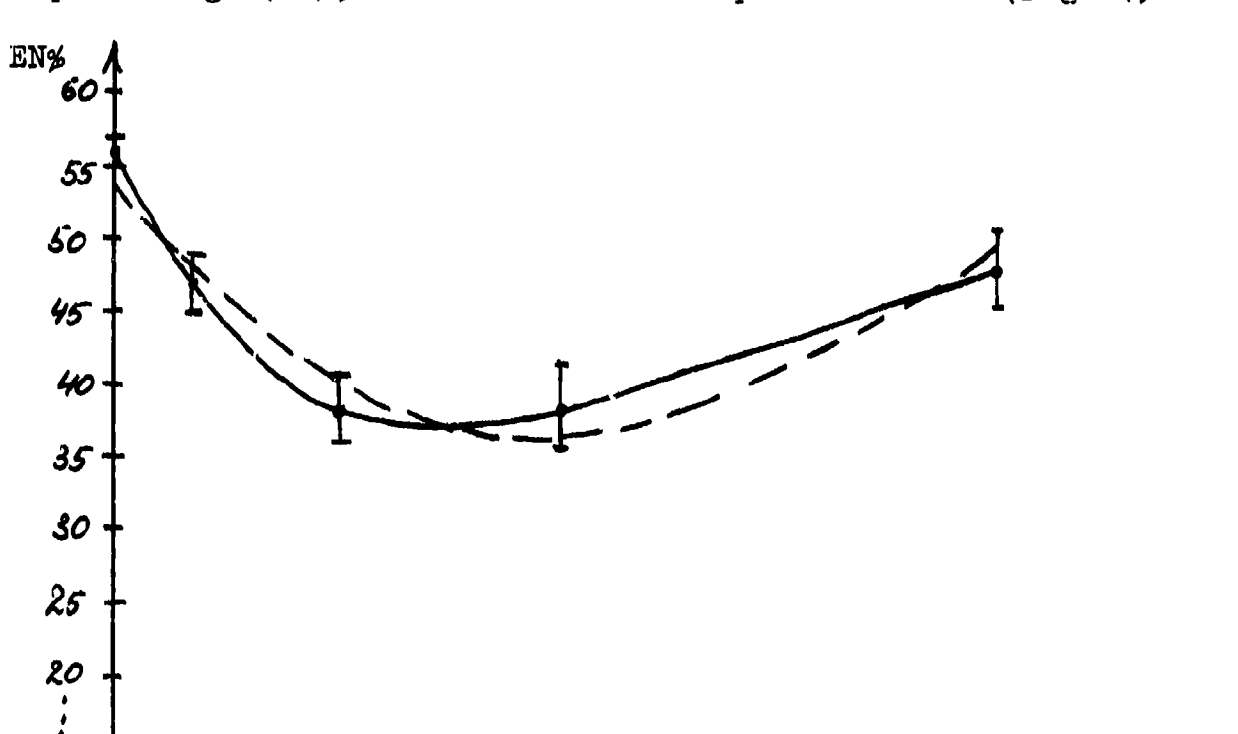

Fig. 1. Dynamics of changes of EN% index under the influence of microwave radiation (a regression curve is dotted).

From the figure one can see that during first 15 minutes after irradiation EN% decreases (a relative decrease accounts for 30.7%) and remains on a low level till 30 minutes of exposition. Through 60 minutes of the effect EN% rehabilitates itself to a considerable extent, though it doesn't reach the control level. By means of a regression equation it was plotted a theoretical curve values of which are well consistent with the facts (it is the 2-power parabola).

Thus, in this paper it is shown that a dependence of EN% index on expositions of microwave radiation has a parabolic nature. Microwave radiation of millimeter band at expositions of 5, 15 and 30 minutes leads to a significant lowering of electronegative nuclei content in the buccal epithelium cells. After 60 minute-irradiation it is observed a partial renewal of the EN% index, but its value doesn't reach a control one.

The more detail check of effects obtained is of interest in connection with their further possible use in the field of labour and sport hygiene, medicine, etc.

Optimum Operation of Gyrotwistrons

P.E. Latham and G.S. Nusinovich
Laboratory for Plasma Research
University of Maryland, College Park, MD 20742

Relativistic gyrotwistrons,[1] which can, in principle, achieve efficiencies in excess of 50%, are promising sources for driving particle accelerators. The optimum operating point for these devices represents a tradeoff between maximizing the available energy and minimizing the deleterious effects of velocity spread. The former increases with Doppler upshift and pitch ratio, while the effects of velocity spread are made worse by both of these quantities. To quantify these ideas, we start with the maximum single particle efficiency,[2]

$$\eta_{sp} = \frac{\gamma_0 + 1}{2\gamma_0} \frac{\bar{\alpha}^2}{1 + \bar{\alpha}^2} \frac{\omega}{s\Omega_c},$$

where γ_0 is the initial relativistic factor, $\bar{\alpha}$ is the average pitch ratio, ω is the operating frequency, Ω_c is the relativistic cyclotron frequency, and s is the cyclotron harmonic. The single particle efficiency, which is easily derived by noting that the Hamiltonian depends on a single phase and thus has two conserved quantities, has a simple physical interpretation: the available perpendicular energy increases with pitch ratio, and the available axial energy increases with increasing Doppler upshift (the $\omega/s\Omega_c$ term).

With no velocity spread, it is typically possible to achieve efficiencies on the order of 70% of the single particle efficiency. However, with velocity spread the picture changes dramatically. A good measure of the effect of velocity spread is the spread in phase which it induces, Δ_ψ. In Ref. 3, we derived the following expression for this quantity:

$$\Delta_\psi = \left[\frac{k_z c/\omega}{(1 - k_z \bar{v}_z/\omega)}\right]^{1/2} \frac{(s\Omega_c/\omega)^{s-1}(1 - s\Omega_c/\omega)}{\bar{\beta}_\perp^{(s-1)}(k_\perp c/\omega)^s} \frac{\bar{\alpha}^2}{\sqrt{\hat{I}}} \frac{\Delta\beta_{\perp 0}}{\beta_{\perp 0}}$$

where k_z and $k_\perp$ are the axial and perpendicular wavenumbers, respectively, $\bar{v}_z$ is the average axial velocity, $\bar{\beta}_\perp$ is the average perpendicular velocity normalized to the speed of light, c is the speed of light, $\Delta\beta_{\perp 0}/\beta_{\perp 0}$ is the perpendicular velocity spread (an adiabatic invariant), and $\hat{I}$ is the normalized current parameter, defined by

$$\hat{I} \equiv \frac{4eI_b}{m_e\gamma_0 c^3}\left[\frac{s^{(s-1)}}{(s-1)!2^s}\right]^2 \frac{J^2_{m\pm s}(k_\perp r_g)}{(\nu^2_{mn} - m^2)J^2_m(\nu_{mn})}$$

where I_b is the beam current, e and m_e are the electron charge and mass, respectively, r_g is the guiding center radius, and ν_{mn} is the nth root of the derivative of the Bessel function: $J'_m(\nu_{mn}) = 0$.

For large Doppler upshift, i.e. $k_z\bar{v}_z/\omega$ near one, the most important scaling in this expression is the term $(k_\perp c/\omega)^{-s}$, which indicates a rapid increase in Δ_ψ as k_z increases. This is consistent with the well known fact that large Doppler upshifted devices are sensitive to velocity spread. However, the sensitivity comes not so much from the $k_z v_z$ term in the resonance condition, but from the weak coupling that occurs when the perpendicular wavenumber becomes small. Note that a slow wave device would have significantly different scaling, as the coupling would not vanish at large k_z. For small k_z, the dominant terms are $\sqrt{k_z c/\omega}$ and $(1 - s\Omega_c/\omega)$. The former arizes

because the normalized current is inversely proportional to k_z, so the coupling increases as the axial wavenumber decreases. The latter term, which is proportional to $k_z v_z$ because of the resonance condition, reflects the fact that devices operating near cutoff are insensitive to velocity spread.

In Fig. 1 we plot level curves of both the single particle efficiency and Δ_ψ for the fundamental TE_{01} mode. The value $\Delta_\psi = 0.30$ used in this figure corresponds roughly to the parameters of the University of Maryland experiment[4] (voltage near 425 kV, current near 160 A, pitch ratio near 1, and perpendicular velocity spread near 6%.) At these parameters, numerical simulations indicate that we can achieve gyrotwistron efficiencies on the order of 35%.

The salient feature of these plots is that at a fixed pitch ratio, Δ_ψ increases rapidly as we move into the regime of high single particle efficiency; adjacent level curves of Δ_ψ increase by a factor of four. Consequently, to move from the level curve $\Delta_\psi = 0.30$ to $\Delta_\psi = 1.20$ and still extract a large fraction of the available energy, either the velocity spread would have to decrease by a factor of 4 or the current would have to increase by a factor of 16. Both of these are extremely difficult technologically. Thus, since the maximum pitch ratio is generally limited by instabilities and reflected particles, there are severe constraints on the achievable efficiency in a realistic gyrotwistron.

This work was supported by the U.S. Department of Energy.

1. G.S. Nusinovich and H. Li, "Theory of the Relativistic Gyrotwistron," *Phys. Fluids B*, **4**, 1058 (1992).

2. P.E. Latham and G.S. Nusinovich, "Modeling Relativistic Gyroklystron Amplifiers," Proceedings of the Workshop on Advanced Accelerator Concepts, Port Jefferson, NY, June, 1992.

3. P.E. Latham and G.S. Nusinovich, to be published in the proceedings of the 1993 Particle Accelerator Conference.

4. W. Lawson, B. Hogan, P.E. Latham, M.E. Read, V.L. Granatstein, M. Reiser, and C.D. Striffler, "Efficient Operation of a High Power X-Band Gyroklystron," *Phys. Rev. Lett.*, **67**, 520 (1991).

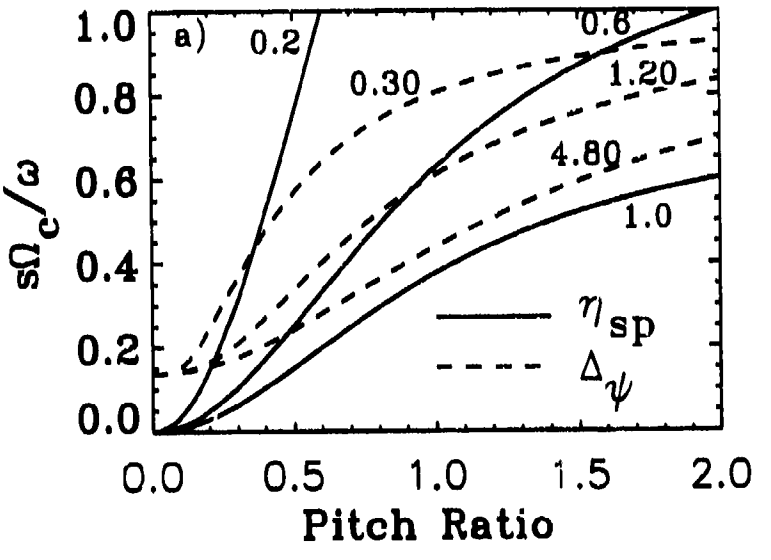

Fig. 1. Level curves of single particle efficiency (solid lines) and Δ_ψ (dashed lines).

Universally Scaled Equations For Gyrotron and CARM Amplifiers

B W J McNeil, G R M Robb and A D R Phelps

Department of Physics and Applied Physics
University of Strathclyde, Glasgow, G4 0NG, U.K.

We show that a set of five coupled equations describing steady state single TE_{pq} mode gyrotron/CARM evolution reduce to a universally scaled set of three equations identical in form to those of the steady state high gain Compton regime free electron laser (FEL). We do this using the approximation of slowly varying amplitude and phase over a cyclotron period and neglect space-charge effects. We also assume a thin annular beam concentric with a circular waveguide in the limit $k_\perp r_L << 1$, where $k_\perp$ is the perpendicular wavenumber and r_L is the Larmor radius.

Starting from the coupled Lorentz-Maxwell equations, the following equations can be derived using the above approximations :

$$\left.\begin{aligned} &\frac{d\phi_{jl}}{dz_1} = p_{jl} \qquad (1) \qquad \frac{dp_{jl}}{dz_1} = (p_{jl}-1)\frac{u_{\perp jl}}{u_{\|jl}^2}(A_1 e^{i\phi_{jl}} + c.c.) \qquad (2) \\ &\frac{du_{\perp jl}}{dz_1} = -\frac{1}{u_{\|jl}}(A_1 e^{i\phi_{jl}} + c.c.) \qquad (3) \qquad \frac{du_{\|jl}}{dz_1} = -\frac{u_{\perp jl}}{u_{\|jl}}(A_1 e^{i\phi_{jl}} + c.c.) \qquad (4) \end{aligned}\right\} \quad j = 1..N_e$$

$$\frac{dA_1}{dz_1} = \left\langle \frac{u_{\perp jl}}{u_{\|jl}} e^{-i\phi_{jl}} \right\rangle \qquad (5)$$

$$\phi_1 = (\omega - \frac{\omega_c}{\gamma})t - k_\| z - (p-1)\theta_0 \qquad z_1 = \frac{k_\perp^2}{k_\|} z \qquad u_{\perp 1} = \frac{1}{\sqrt{2}}\left(\frac{k_\| k_\perp^2}{k_{c0}^3}\frac{u_{\perp 0}^4}{u_{\|0}^3}\frac{1}{\sigma^3}\right)^{\frac{1}{4}} U_\perp \qquad u_{\|1} = \frac{1}{2}\left(\frac{k_\perp^2}{k_\| k_{c0}} u_{\|0}\frac{1}{\sigma^3}\right)^{\frac{1}{2}} U_\| \qquad A_1 = \frac{1}{\sqrt{2}}\left(\frac{k_\perp^6}{k_\| k_{c0}^5}\frac{1}{u_{\|0}}\frac{1}{\sigma^9}\right)^{\frac{1}{4}} A$$

$$U_\perp = \frac{\gamma v_\perp}{\gamma_0 v_{\perp 0}} \qquad U_\| = \frac{\gamma v_\|}{\gamma_0 v_{\|0}} \qquad u_{\perp 0} = \frac{\gamma_0 v_{\perp 0}}{c} \qquad u_{\|0} = \frac{\gamma_0 v_{\|0}}{c} \qquad \omega_c = \frac{eB_0}{m} \qquad k_{c0} = \frac{\omega_c}{c u_{\|0}}$$

$$D_{pq} = \frac{1}{J_p(\chi'_{pq})\sqrt{\pi(\chi'^2_{pq} - p^2)}} \qquad |A|^2 = \frac{U_w}{2\epsilon_0}\left(\frac{e}{4mc}\frac{k_\| k_{c0}}{k_\perp \omega} D_{pq} J_{p-1}(k_\perp R_0)\right)^2$$

$$\sigma = \left(\frac{1}{32}\frac{e}{mc}\mu_0 I_0 D_{pq}^2 J_{p-1}^2(k_\perp R_0)\right)^{\frac{1}{3}} \qquad \langle\ldots\rangle = \sum_{j=1}^{N_e}$$

and B_0 is the axial magnetic field, I_0 is the beam current, N_e is the number of electrons, U_w is the wave energy per unit length, (R_0,θ_0) are the constant guiding centre co-ordinates and A is a dimensionless complex field amplitude. All other variables have their usual meaning. These equations are similar in form to those used in earlier studies of various gyro-devices except for scaling (eg. [1]).

It can be seen from equations (2), (3) and (4) that there is a functional relationship between $p_1, u_{\perp 1}$ and $u_{\|1}$, so the number of equations can be reduced from five to just three:

$$\frac{d\phi_{jl}}{dz_1} = p_{jl} \qquad (6)$$

$$\frac{dp_{jl}}{dz_1} = \frac{2^{1/2}}{u_{\|0}^{(0)\,3/2}} \frac{(p_{jl}-1)^{5/2}}{(\delta_1-1)^{3/2}} \left(1-\frac{(p_{jl}-1)}{(\delta_1-1)}\left(1-\frac{u_{\perp jl}^{(0)\,2}}{2u_{\|0}^{(0)}}\right)\right)^{1/2} (A_1 e^{i\phi_{jl}} + c.c.) \qquad (7)$$

$$\frac{dA_1}{dz_1} = -\frac{2^{1/2}}{u_{\|0}^{(0)\,1/2}} \left\langle \frac{(p_{jl}-1)^{1/2}}{(\delta_1-1)^{1/2}} \left(1-\frac{(p_{jl}-1)}{(\delta_1-1)}\left(1-\frac{u_{\perp jl}^{(0)\,2}}{2u_{\|0}^{(0)}}\right)\right)^{1/2} e^{-i\phi_{jl}} \right\rangle \qquad (8)$$

$j = 1..N_e$

where $\delta_1 = p_1^{(0)}$ and $^{(0)}$ indicates values at $z_1 = 0$.

By further scaling and in the limit $|p_1|, |\delta_1| << 1$, equations (6)-(8) reduce to:

$$\frac{d\phi_{j2}}{dz_2} = p_{j2} \qquad \frac{dp_{j2}}{dz_2} = -(A_2 e^{i\phi_{j2}} + c.c.) \qquad \frac{dA_2}{dz_2} = \langle e^{-i\phi_{j2}} \rangle \qquad j = 1..N_e$$

where:

$$\phi_2 = \phi_1 \qquad z_2 = \frac{k_\perp^2}{k_\|} \rho z \qquad p_2 = \frac{p_1}{\rho} \qquad A_2 = 2\frac{k_\|}{k_{z0}} \frac{u_{\perp 0}}{u_{\|0}^2} \frac{A}{\rho^2} \qquad \rho = \left(4\frac{k_\|^2}{k_\perp^2}\frac{u_{\perp 0}^2}{u_{\|0}^3}\right)^{\frac{1}{3}} \sigma$$

These **universally scaled** equations are identical in form to those describing the high gain Compton FEL([2] and references therein). By universal scaling we mean that the solution depends only upon the initial conditions $p_2^{(0)}$ and $A_2^{(0)}$. As maximum values for A_2 and p_2 are ~ 1, the condition $|p_1|, |\delta_1| << 1$ implies $\rho << 1$, which can be satisfied over a wide range of parameter space. Using the analogy with FEL theory we call ρ the 'Fundamental Gyrotron/CARM Parameter'.

Linear stability analysis of the above equations for an initially unbunched, monoenergetic resonant ($\delta_2 = 0$) electron beam gives an intensity growth of $|A_2(z_2)|^2 = |A_2^{(0)}|^2 \exp(\sqrt{3} z_2)$ for $z_2 > 1$. Also, as $|A_2| \sim 1$ at saturation, this implies $|A_2|^2_{sat} \propto \rho^4 \propto I_0^{4/3}$.

Clearly, many of the results of Compton FEL theory now become applicable to gyrotrons and CARMs within the above assumptions and limits. We believe this to be a powerful statement, particularly with regard to effects not yet fully considered in the gyrotron/CARM literature e.g. superradiant effects, optical guiding and development of coherence. Work is currently underway to relax, or remove, the assumptions outlined above.

Acknowledgements

An SERC research Grant supported this research. AEA Technology and the SERC provided an SERC/CASE studentship for Mr GRM Robb.

References

[1] A.W. Fliflet. M.E. Read, K.R. Chu and R. Seeley, Int. J. Electronics, **53**, 505-521 (1982)

[2] R. Bonifacio, N. Piovella and B.W.J. McNeil, Phys. Rev. A, **44**, 3441-3444 (1991)

Experiments of 3rd and 10th cyclotron harmonic peniotron oscillators

K. Yokoo, T. Ishihara, H. Tadano, K. Sagae,
H. Shimawaki, N. Sato and S. Ono

Research Institute of Electrical Communication, Tohoku University
Sendai 980, Japan

ABSTRACT

Higher cyclotron harmonic peniotron oscillators with magnetron type cavities have been studied to achieve higher frequency electromagnetic wave for future applications. 3rd and 10th harmonic experimental tubes were designed and tested at 30GHz and 100GHz wave regions, respectively. The 3rd and 10th harmonic tubes generated successfully millimeter waves in the frequency range of 27-35GHz at 3rd, 4th and 5th cyclotron harmonics and in the range of 103-110GHz at 9 to 13th harmonics, respectively.

2. DESIGN PARAMETERS AND EXPERIMENTAL RESULTS

In the peniotron interaction, a high conversion efficiency is expected at higher cyclotron harmonics as well as the fundamental operation. The experimental test tubes were designed and fabricated as the 3rd and 10 th cyclotron harmonic peniotron oscillators using magnetron type waveguide resonators with 8 and 22 vanes, respectively.

The oscillation frequencies of the tubes were originally designed at 30GHz and 100GHz at respective modes of $TE_{4,1,1}$ and $TE_{11,1,1}$ in the magnetron waveguide cavities. Figures 1(a) and (b) show the cross-sectional view of the cavities and their dimensions for the 3rd and 10th harmonic experimental tubes, respectively.

Figure 2 and 3 show the simulation results of operational characteristics for the experimental tubes designed at the 3rd and 10th cyclotron harmonic operation, respectively. The electronic efficiencies of 70% at the 3rd harmonic and 40% at the 10th harmonic will be achieved at power level of nearly 10kW. The simulation results show that the high efficiency peniotron operation is capable at high cyclotron harmonics by using π mode magnetron type cavities.

Figure 4 and 5 show the oscillation frequencies observed in the 3rd and 10th harmonic tubes as a function of DC magnetic flux density, respectively. 3rd to 5th and 9th to 13th cyclotron harmonic oscillations were observed for the 3rd and 10th harmonic tubes, respectively. The 3rd and 5th harmonic oscillations in the 3rd harmonic tube correspond to the peniotron interaction at the respective axial modes of the $TE_{4,1}$ magnetron type waveguide resonator and the 4th harmonic oscillations correspond to the gyrotron interaction at the same modes. Similarly, the 10th and 12th oscillations in the 10th harmonic tube are considered as the peniotron interaction at $TE_{11,1}$ mode and the 11th oscillations are the gyrotron interaction at the same mode. On the other hand, the 9th and 13th oscillations may be the peniotron interaction at the $TE_{10,1}$ resonant mode in the magnetron type cavity.

In the Figure 4 and 5, broken and solid lines show the resonant conditions at higher cyclotron harmonic operations of the tubes between cycloiding electrons with a velocity ratio of 2 and the electromagnetic waves for the forward and the backward wave interaction modes at the experimental conditions. Most of the oscillations belong to the backward wave oscillations at the respective modes of the cavities, except at a few oscillations, due to a lower starting current in the backward wave interaction.

We demonstrated higher cyclotron harmonic peniotron and gyrotron operations and showed that a magnetron type waveguide resonator was attractive for generation of high frequency electromagnetic wave.

The work was supported by a Grant-Aid for Scientific Research from the Ministry of Education, Science and Culture in Japan.

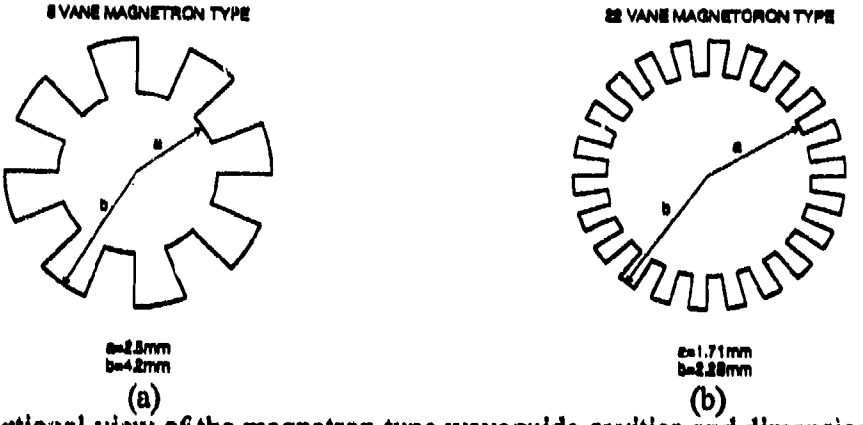

Figure 1. Cross-sectional view of the magnetron type waveguide cavities and dimensions for (a)3rd and (b)10th harmonic experimental tubes, respectively.

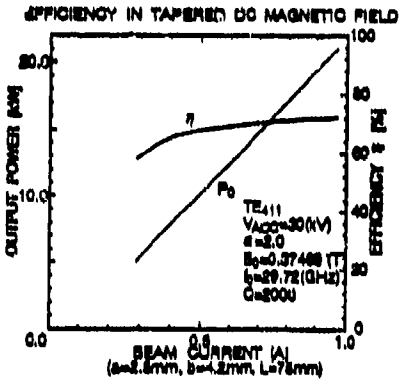

Figure 2. Simulation results of the optimum output power and the electronic efficiency in a tapered magnetic field intensity at the 3rd cyclotron harmonic operation as a function of the beam current.

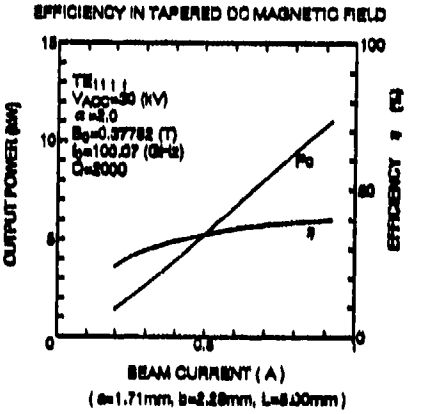

Figure 3. Simulation results of the optimum output power and the electronic efficiency in a tapered magnetic field intensity at the 10th cyclotron harmonic operation as a function of the beam current.

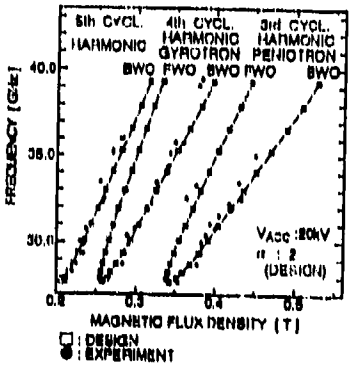

Figure 4. Oscillation frequencies observed in the 3rd harmonic experimental tube as a function of DC magnetic flux density.

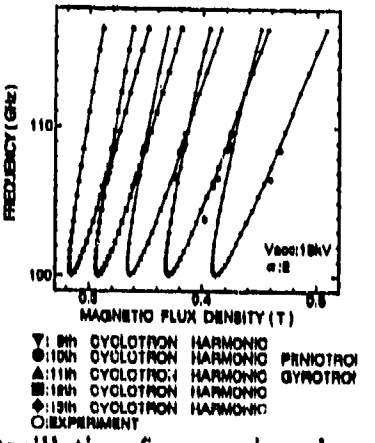

Figure 5. Oscillation frequencies observed in the 10th harmonic experimental tube as a function of DC magnetic flux density.

Relativistic peniomagnetron of mm and sub mm radio wave range

V.D.Yeremka, V.A.Zhurakhovskiy, L.P.Mospan

Institute of Radiophysics and Electronics of Ukrainian Academy of Sciences,
12, Acad.Proskura st., Kharkov, 310085, Ukraine

ABSTRACT

Two trends of application of gyroresonance, namely orbital acceleration of electrons by HF-field in order to receive mono-pipe beams with large reserve of rotational energy of particles and peniotron braking of mono-pipe beams at high harmonics of cyclotron frequency in order to generate and amplify mm and sub mm radio waves without use of super conductive magnetic systems, are considered.

1.INTRODUCTION

The operation of gyrodevice at high gyroharmonics in peniotron regime and supply of rotating electrons by relativistic energy by means of HF accelerator finds an outlook to design compact source of mm and sub mm radio waves. HF accelerator was proposed in the patent[1]. The theory of its operation and the results of experimental study were described in Ref.[2]. The typical characteristics of electron beam in such accelerator are current of 0.1-2.0 A, input kinetic energy of the particles of 0.5-1.0 MeV. Mono-pipe electron flow having relativistic energy of rotation and formed by the accelerator is used in relativistic peniomagnetron, operating at high gyroharmonic. The pumping of kinetic energy in the accelerator can be provided at the frequencies of 3 GHz, 10 GHz and 20 GHz and it is expedient to extract electron energy in the source in peniotron regime at the harmonics with the number from 10 to 30. The scheme of the gyrodevice having orbital accelerator in the first cascade and with peniomagnetron in the second one is shown in Fig.1.

2. THE RESULTS

Averaged equations of the motion of electron in orbital accelerator with rotating TE-wave were solved numerically in the typical range of values of the parameters U, $z=L/\lambda$, $V=\lambda/E_{st}$, $F=\Gamma/\omega$ (λ is the wavelength in vacuum, L - is resonator length, E_{st} is amplitude of electric field strength at inner wall of resonator, Γ-is non-relativistic electron gyrofrequency, ω-is circular frequency of HF field). The influence of above-mentioned factors on accelerator characteristics were disclosed during computer experiment. Fig.2 shows the current values of relativistic mass γ, orbit radius r, relativistic gyrofrequency Ω , number of turns N and longitudinal velocity β_z of electron versus axis coordinate $T=L/\omega$ inside the resonator. One can see that the value of relativistic mass-factor γ changes from 1.02 at the entrance of accelerator to 2.175 at the exit, that corresponds to the increasing of electron kinetic energy from 10 to 600 keV. The comparison of the data simulated by averaged equations with ones of Ref.[2], received by numerical integration of exact assumed equations, shows their good coincidence.

The conjugation of peniomagnetron accelerator section with orbital acceleration section reduces to the adjustment of magnetostatic field induction at the accelerator entrance to the level of exact gyroresonance. We cite the master data of the simulation of relativistic peniomagnetron-accelerator with mono-pipe electron flow. For beam $\gamma_l=2$, pitch-angle $\psi_l=75^0$, current is 5 A, initial radius is 4.6 mm, the number of turns is 42. For waveguide: mode is TE_{61}, $\beta_{ph}=1.8$, $\lambda=6$ mm, input power $Q_l=5$ kW, gain G>20dB, output power $Q_o=1.8$ MW. The regime is impulse one, gyroresonance order n=5, electron efficiency $\chi=70\%$, initial induction of profiled magnetostatic field $\beta_l=0.6$ T, final induction is 0.3 T. Fig.3 shows the dependences of parameters χ, ψ,G, N and magnetic field profile δ of relativistic peniomagnetron versus normalized length ζ of interaction space.

The length of device can be decreased by the increasing of the rate of transformation of particle energy into energy of the wave being amplified by means of the increasing of electron flow energy.

We present an example of judicious choice of calculated parameters of relativistic peniomagnetron operating at 10-th gyroharmonic in the regime of throughout gyroresonance. The beam has $\gamma_o=4$, $\psi=55^0$, initial diameter of 2.5

mm, the number of turns is 10. The waveguide has β_{ph}= 1.122, E_{st}=250 MW/m, mode is TE_{111}, wavelength is 0.5 mm, tube length is 10 cm, inner diameter is 4.51 mm. The regime is n=10, χ=60%, B_{z0}=4.33 T. The dependence of efficiency χ and field profile δ for 10 harmonics versus normalized length ζ of interaction space is shown in Fig.4.

3.CONCLUSION

The solution of averaged equations of magnetoguided motion of electrons in the field of rotating wave of TE_{111}-type coincides with numerical solution of the problem[2] in exact assumed definition.The ability of orbital accelerator to transform initially rectilinear electron beams having the voltage of 10-30 kV into rotating mono-pipe beams with the energy of transversal motion of particles of order of 0.5 meV, was demonstrated. It was demonstrated in monoenergetic approximation that relativistic peniomagnetron with profiled magnetic field retained electron efficiency of order of 40-60% at high order (n=5-10) of gyroresonance in mm and sub mm range. The influence of spreads and unhomogeneities on power characteristics of peniomagnetron was considered by us[3].

4. REFERENCES

1. J.Feinstein, H.R.Jory, "High frequency electron discharge device", USA Pat. N3457450, 1969.

2. D.B.McDermott, Furuno D.S., N.C.Luhmann, "Production of relativistic rotating electron beam by gyroresonant RF acceleration in a TE_{111} cavity", J. App. Phys., V.58, N12, PP.4501-4508, 1985.

3. V.D.Yeremka, V.A.Zhurakhovskiy, A.M.Kovalenko, "Autoresonance peniomagnetron with spreads and unhomohencities", in ICMWFT-90 Supplementary Conference Digest, PP.52-54, Beijing, China, 1990.

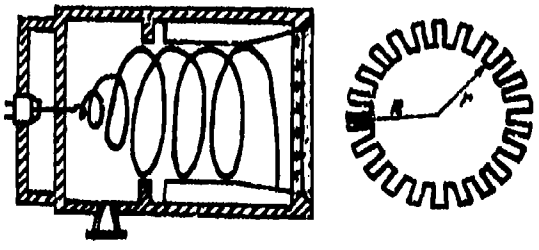

Fig.1. Scheme of relativistic peniomagnetron with orbital accelerator

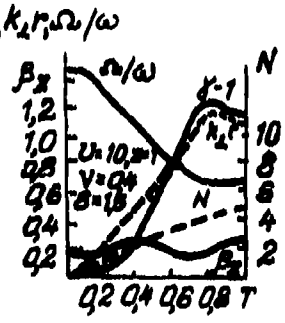

Fig2. Dependence of relativistic mass (γ), orbit radius (r), relativistic gyrofrequency (Ω), turns' number (N), longitudinal velocity (β_z) on axis coordinate (T)

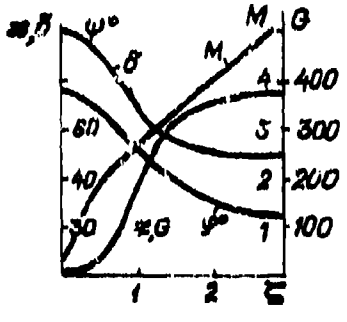

Fig.3. Dependence of electron efficiency (χ), normalized induction of magnetic field (δ), gain by power (G), electron turns' number (M) of relativistic peniomagnetron-amplifier on normalized length ζ of interaction space

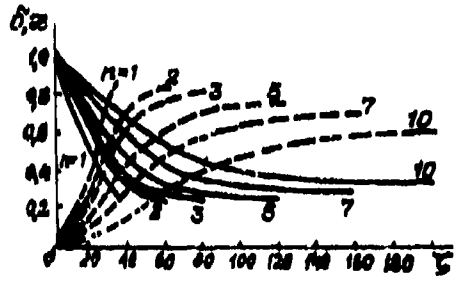

Fig.4. Dependence of normalized values of electron efficiency (χ) and magnetic field (δ) on normalized length of interaction space of relativistic peniomagnetron at gyroharmonic n=1 ÷ 10

TWO-STAGE 35 GHZ GYRO-PENIOTRON AMPLIFIER EXPERIMENT*

G.S. Park[§], C.M. Armstrong, A.K. Ganguly, R.H. Kyser[¶], and J.L. Hirshfield[§]
Naval Research Laboratory, Code 6840, Washington, DC 20375

ABSTRACT

A two-stage second harmonic $TE_{3,1}$ gyro-peniotron amplifier with a rising-sun slotted waveguide structure has been designed utilizing an axis-encircling beam. The unwanted $TE_{2,1}$ gyrotron BWO was suppressed by using a rising-sun interaction structure. 45% efficiency is predicted for a 70 kV, 3.5A beam with 5% velocity spread and 10% guiding center spread. Fabrication of couplers, rf circuits, 20dB attenuator, window, and electron gun are underway.

INTRODUCTION

Recent interest in high resolution radar has stimulated development of compact efficient high power millimeter wave amplifiers. Since the power levels of interest are beyond those available from conventional slow wave vacuum electronics technology, the development of advanced fast wave gyro-amplifiers is spurred on. However, the magnetic field required for gyro-amplifiers operating at the fundamental cyclotron frequency is too high at millimeter wave frequencies to make them practical for many system applications. Therefore the development of reduced-field harmonic gyro-amplifiers is required. A recent theoretical study of the gyro-peniotron[1] employing a slotted waveguide interaction structure with an axis encircling electron beam[2] has demonstrated the potential for efficient high power harmonic operation at reduced values of magnetic field and beam voltage.

STABILITY AND RISING-SUN STRUCTURE

The gyrotron BWO in the $TE_{2,1}$ mode is the most dangerous mode which can compete with the operating second harmonic $TE_{3,1}$ gyro-peniotron mode. The oscillation threshold interaction lengths of the $TE_{2,1}$ and $TE_{3,1}$ modes are calculated[3] to be 2 cm and 4 cm respectively for a 70 kV, 3.5A beam with a velocity ratio of 1.5 and the grazing B-field(6.7kG). Since the cutoff frequency of the $TE_{2,1}$ mode is close to that of $TE_{3,1}$ mode, a rising-sun structure is used to move the $TE_{2,1}$ mode cutoff frequency above the $TE_{3,1}$ mode, as shown in Fig.1. Fig.2 shows the stable operation of the $TE_{3,1}$ mode with s=2 beam mode by employing a rising-sun circuit.

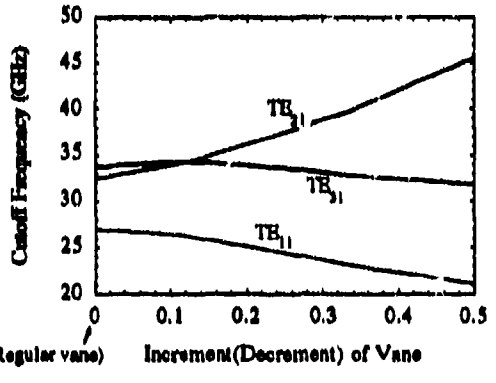

Fig.1. Evolution of cutoff frequency

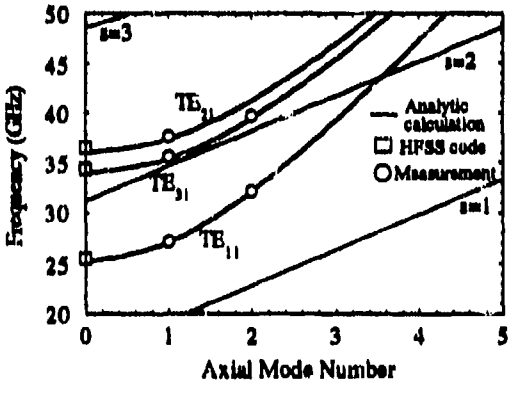

Fig.2. Dispersion of rising-sun structure and beam line

DESIGN STUDY AND EXPERIMENTAL SETUP

Since the $TE_{3,1}$ mode, or π-mode, in the rising-sun structure contains a sizable 2π-mode component, the saturation length of the rising-sun structure is observed to be longer than that of the regular (uniform) vane structure, as shown in Fig.3. The saturated efficiencies, however, are seen to be comparable for both circuit configurations. Nonlinear device calculations show 45% efficiency, 25dB gain for a 70kV, 3.5A beam with a 5% axial velocity spread and a 10% guiding center spread for both structures. An input power of 500W and beam velocity ratio of 1.4($=\alpha$) were used in the calculations. An electron gun for producing the high quality axis-encircling beam required is currently in fabrication. Gun code[2] results indicate 1% axial velocity spread and 3% guiding center spread for the above beam parameters. Fig.4 shows the schematic of the gyro-peniotron amplifier with the electron gun and magnet systems.

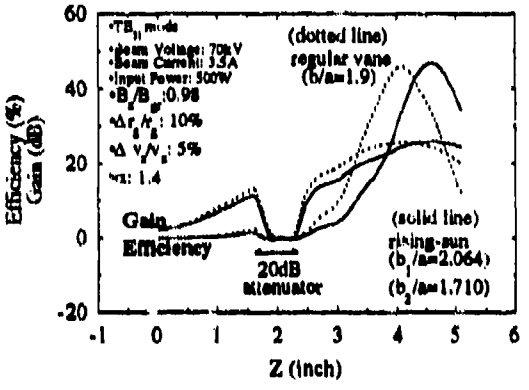

Fig.3. Axial evolution of simulated efficiency

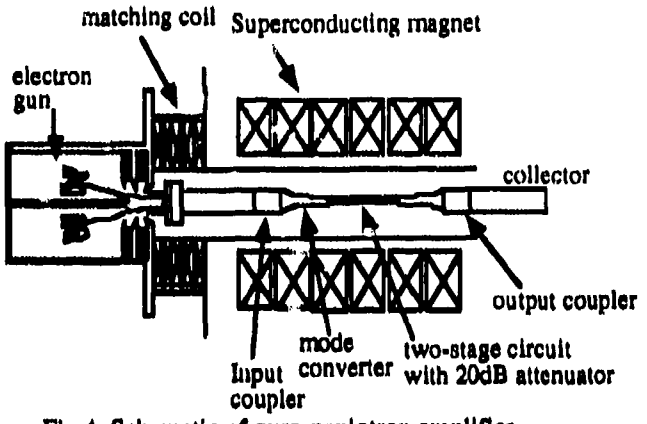

Fig.4. Schematic of gyro-peniotron amplifier

CIRCUIT DESIGN AND COLD TESTS

An X-band coupler and uniform vane mode converter previously[4] cold-tested has been modified for operation with a rising-sun structure. The modes of the Ka-band rising-sun structure have been identified experimentally as shown in Fig.2. A hybrid smooth guide linear polarized $TE_{3,1}$ coupler[5] (-0.2dB coupling and -25dB return loss: Fig.5) and a nonlinearly tapered transition waveguide for mode conversion from cylindrical $TE_{3,1}$ mode to rising-sun $TE_{3,1}$ mode (or π mode) have been designed using the HFSS code[6]. The simulated return loss of the 20dB attenuator is better than -20dB.

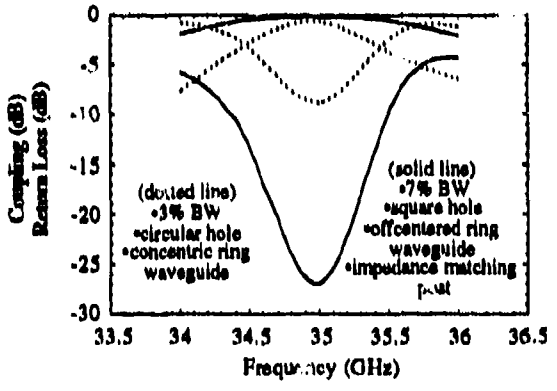

Fig.5. Simulated performance of the coupler

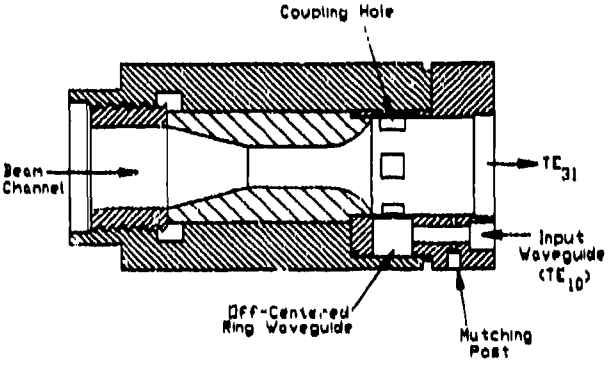

Fig.6. Drawing of the linearly polarized $TE_{3,1}$ coupler

REFERENCES

[1] A.K.Ganguly, S.Ahn, and S.Y.Park, Int. J. Electronics 65, 597 (1988).
[2] G.P.Scheitrum, et. al., Bulletin of IEEE Int. Conf. on Plasma science, 144 (1991)
[3] A.K.Ganguly, G.S.Park, and C.M.Armstrong, Phys. Fluids B 5, 1639 (1993)
[4] G.S.Park, et. al., Proc. 17th Int. Conf. Infrared and Millimeter Waves, 500 (1992)
[5] G.S.Park, C.M.Armstrong, R.H.Kyser, J.L.Hirshfield (to be published)
[6] High Frequency Structure Simulator, version A.02.01 Hewlett Packard Co. and Ansoft Co.
§ Omega-P, Inc., New Haven, CT 06520
¶ B-K Systems, Inc., Rockville, MD 20850

*Work is supported by ARPA/DSO and ONR.

Experimental Study of a Relativistic Peniotron

S. Musyoki,K.Sakamoto,A. Watanabe and M.Shiho
Japan Atomic Energy Research Institute,
Naka Fusion Research Establishment,
Naka-machi,Naka-gun, Ibaraki 311-01 Japan

K.Yokoo,N.Sato and S. Ono
Research Institute of Electrical Communication,
Tohoku University, Sendai 980, Japan

S.Kawasaki,M.Takahashi
Faculty of Science,Saitama University, 255
Shimookubo,Urawa-shi,Saitama-ken 388, Japan

H. Ishizuka
Fukuoka Institute of Technology,
Higashi-ku,Fukuoka, Japan

Introduction

The peniotron is an electron cyclotron resonance device in which RF radiation can be amplified by extracting the kinetic energy of a hollow rotating electron beam. The peniotron is unique among all electron tube devices because electron bunching is not essential in its operation mechanism and so each electron loses its kinetic energy independently. Therefore for an optimized device high electronic efficiency can be realized, especially in the auto-resonance mode, where electronic efficiency close to 100% has been predicted(1). The peniotron is suitable for high power generation because its wave guide circuit is simple. Operation at high cyclotron harmonics is also possible, resulting in generation of high frequencies in the millimeter and sub-millimeter wave regions at relatively low values of DC magnetic field. Although experimental work has been reported on efficient operation for peniotrons with low beam energies under 50 KeV(2),(3), performance at relativistic energies over 500 keV still remains experimentally unexplored. We have taken up this challenge and so we have set out to develop a relativistic peniotron in our laboratory, where an induction linac driven electron beam of 3 kA can be generated with energy of 1 MeV. We have completed the design of a prototype peniotron oscillator device and done some preliminary experiments where we obtained a strong RF radiation of 7 MW at 5 GHz.

Design and experiments

The peniotron interaction can be sustained in a circular waveguide structure if the RF angular frequency ,ω, and the electron cyclotron angular frequency,ω_c, are related by $\omega=(p-1)\omega_c+\beta v_z$, where p is the RF azimuthal harmonic, β, the RF wave phase propagation constant and v_z the electron longitudinal velocity. Therefore in a circular waveguide circularly polarized TE_{21} modes can be excited by electrons rotating at the fundamental cyclotron frequency. We have designed a peniotron oscillator, for operation at the fundamental cyclotron harmonic in a T_{211} mode circular waveguide cavity.The design parameters, shown in table 1, were chosen for the convenience of our laboratory, where the available beam energy is limited to 1 MeV and the guiding DC magnetic field cannot exceed 3 kG. According to the simulation results, shown in figure 1, with a beam current of 50 amperes RF power of 30 MW can be generated in the designed cavity at an optimum efficiency of 60%. Figure 2 shows the schematic diagram of the experimental device. In the experiment, electrons are extracted from a hollow cold velvet cathode using a 1 MeV ,4 stage induction LINAC. The electrons are then passed through a magnetic cusp, where they acquire rotational energy before entering the cavity, where they lose some of their kinetic

energy to the RF wave. A small fraction of the generated RF power is then tapped with a directional coupler for measurement and the rest is dissipated in a dummy load. Figure 3 shows the experimental results obtained by varying the DC magnetic guiding field. We observed a strong 5 GHz oscillation, which was well above the fundamental cyclotron frequency of 2.75 GHz. Therefore this oscillation corresponds to either higher cyclotron or longitudinal harmonics and more tests are necessary for its positive identification. Other clear oscillations were obtained at 2.75 GHz and 3.2 GHz, corresponding to second harmonic gyrotron interaction at the TE_{211} and TE_{212} modes in the cavity respectively. Strong mixed harmonic RF radiation , caused by mode competition, was also observed at other values of DC magnetic field as indicated in the figure. In order to excite the fundamental peniotron mode, we shall improve the shape of the cusp and introduce a mirror magnetic field for controlling the beam pitch angle to avoid excitation of high longitudinal modes.

References

1. Baird et al. IEDM, 1987, 913-916
2. Yokoo et. al Int. J. Electronics, 1989, vol. 67, no 3, 485-890
3. Musyoki et al. Int. J. Electronics, 1992, vol 72, no 5 and 6, 1067-1077
4. Rhee et al. The Physics of Fluids, 1974,vol 17, no 8, 1574-1581

operation mode	TE_{211}
cavity radius	55 mm
cavity length	200 mm
operation frequency	2.75 GHz
loaded Q	2000
beam energy	1 MeV
velocity ratio (v_t/v_z)	2
DC magnetic field	0.246 T

Table 1: Simulation parameters

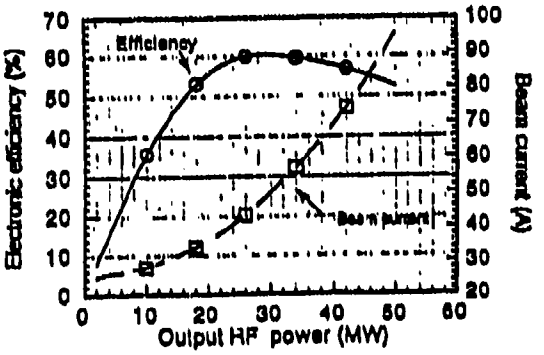

Fig 1: Simulation results

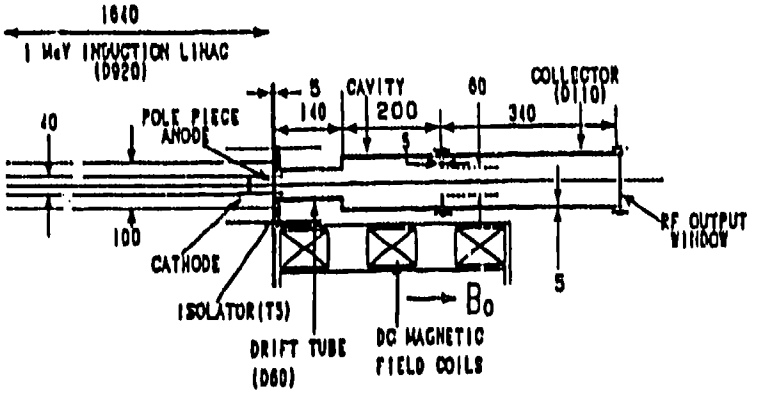

Fig 2: Schematic diagram of the relativistic peniotron

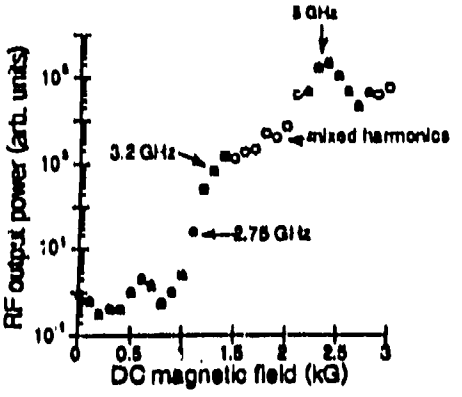

Fig 3: Experimental results

Peniomagnetron with quasioptical two-mirrors resonator

V.D.Yeremka

Institute of Radiophysics and Electroncs of Ukrainian Academy of Sciences
12, Acad.Proskura st., Kharkov, 310085, Ukraine

ABSTRACT

The peniomagnetron with two mirror open resonator is presented. Characteristic properties of the design and characteristics of electron-optical system of open resonator are described. It is shown that in nonrelativistic variant of the design the profiling of magnetostatic field by the law of exact cyclotron resonance provides the increasing of electron efficiency at high cyclotron harmonics. The application of open resonator and magnetron-type waveguide decreases mode competition.

1.INTRODUCTION

Lately the study of gyrodevices with peniotron mechanism of the interaction of electrons and waves are actively carried out. However, peniotron sources, operating at high gyroharmonics, have relatively small sizes and by the level of output power fill the "niche" between classical devices (TWT, magnetron, clynotron, orotron, echelettron) and gyrotrons. Gyromagnetron[1] and peniomagnetron[2] use cylindrical volumetric resonator, that limits mean value of output power at the shortening of wavelength. Besides, collector design with energy recuperation of worked-out electrons gets significantly complicated at the extraction of HF-power out of cylindrical resonator end of peniomagnetron. The application of two-mirror open resonator (OR) in peniomagnetron allows to increase output power at the shortening of wavelength and to increase the efficiency owing to recuperation and elimination of the influence of non-resonant components of standing wave field[3].

2.THE BASE DESIGN

The geometry of peniomagnetron with two-mirror OR, called by us "difratron", is presented in Fig.1. Interaction space 1 of electron and waves of form of waveguide with 22 ribs is coupled with two-mirror resonator by coupling openings 2. OR is formed by cylindrical mirror 3 and spherical mirror 4. The mirror 3 is supplied with the system 5 of extraction of the energy into load. Difratron has collector-recuperator. High-orbit electron flow 6 is injected of three-electrode electron gun (Fig.2), described in Ref.[4]. Beam current of 0.2-0.8 A and magnetic field in the space 1 of approximately 0.3 T. Vectors of magnetic field induction (B_k on the cathode and B in the interaction space) have opposite direction and their values satisfy the relationship $D^2 = 4{,}55 \cdot 10^{-11} \frac{U\,(W_1/W)}{B \cdot B_k}$ (where mean diameter D=5-10 mm, operating voltage U=6-20 kV, the ratio of rotational and full energies of electrons W_1/W=0.7-0.8.

3.OPERATING PRINCIPLE

Rotating H_{m1} mode is operating one. Effective operation of peniomagnetron with two-mirror OR at large order of gyroresonance $n=m\pm 1$ is possible only at large radii r of electron orbits, running into intensive field region. But the value r is defined by the gyroresonance condition[2]. The increasing of velocity v_t and decreasing of phase velocity v_{ph} of the wave facilitate the increasing of r. The technique of selection of H_{m1} wave was tested in gyromagnetron[2]. H_{m1}-wave field transforms into field of oscillation types of OR, diffracting on coupling slots. The change of output signal frequency can be carried out by the change of OR volume.

4. THE RESULTS

Averaged equations of magnetoguided motion of mono-pipe electron beam, rotating in the field of axially decelerated H_{m1}-wave were formed by analogy with the equations received in Ref.[2]. The system of equations was solved numerically. Fig.3 shows the dependencies of electron efficiency and normalized induction of magnetostatic field δ on dimensionless longitudinal coordinate ζ for different order of gyroresonance n. Growth rate of χ is inversely proportional to n. But it is still acceptable at n~10.

We cite calculated parameters of nonrelativistic difratron with axially decelerated wave and homogeneous and profiled magnetostatic field: γ_1=1.02, (initial electron energy is 10 keV), ψ_1=60%, β_{ph}= 0.383, n=0.0366nλ, n=10, λ=5 mm, m=11 ($H_{11,1}$-mode), χ=44%, $\delta \leq$ 1.44, N=6 turns. Calculated output power is 1.1 kW at beam current of 0.25 A. Cold measurements of sphere-cylindrical OR parameters show automatic compensation of phase unhomogeneity that present itself magnetron waveguide with coupling slots.

5.CONCLUSION

Difratron-peniomagnetron with two-mirror OR at nonrelativistic electron energies has a perspective to be an effective source of mm radio wave of kW-power level with electrical-mechanical frequency change and rarefied spectrum of high quality oscillations.

6.REFERENCES

1. Y.Y.Lau, L.R.Barnett, "A low magnetic field gyrotron-gyromagnetron", Int. J. El., V.53,№6, PP.693-698, 1982.
2. V.D.Yeremka, V.A.Zhurakhovskiy, V.P.Shestopalov "Peniomagnetron amplifier theory", in ICMWFT-90 Suppl. Conf. Dig., PP.48-51, Beijing, China, 1990.
3. V.D.Yeremka "Difratron", Pat. N1309824 (USSR), 1984.

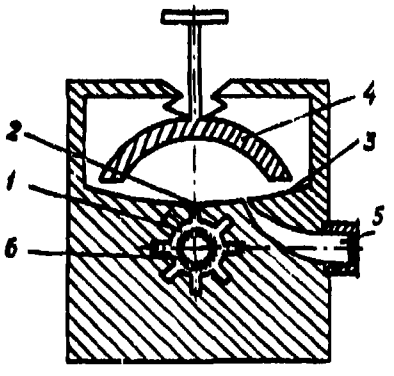

Fig.1. Diagrammatic representation of electrodynamic structure of difratron

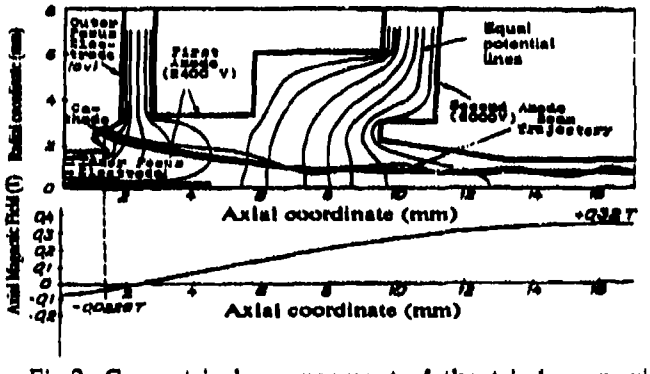

Fig.2. Geometrical arrangement of the triode gun with electron trajectories potential lines and axial magnetic field

Fig.3. Dependence of electron efficiency χ and profile δ of magnetostatic field induction on normalized length ζ of interaction space of peniomagnetron at high harmonics of cyclotron frequency

Theory of reflection-type gyro-TWT and gyro-BWO

Alexander P. Chetverikov

Saratov University, Physical Department,
Astrahanskaya, 83, Saratov 410071, Russia

ABSTRACT

The theory of a gyro-TWT-BWO based on a new approach is suggested. A substitution of a piece of the tapered waveguide by the conic one and a representation of the electromagnetic field in the waveguide as the superposition of a standing wave and travelling wave are used in the theoretical analysis. Regimes of the amplification and BWO-oscillation may be described by the theory.

As well known (see, for example, [1-2]), a tapering waveguide and tapering static magnetic field are used as a rule for a widening of a band of an amplification of the gyro-TWT or a band of a shift of a generation frequency of the gyro-BWO. In these wide-band devices the region of the interaction space is realized for a signal of each frequency ω from a wide band $\Delta\omega$, where an effective interaction between a helical electron beam and a TE e.m. wave takes place. An input signal is introduced into the interaction space either by means of the wide-band input arrangement or by means of the introduction of the signal through an output end of the waveguide and a following reflection from a critical section of the waveguide. We shall examine here both cases. In the gyro-BWO the generated signal is reflected from critical section and taken out through a collector end of the device too. The calculation of characteristics of devices are carried out often using the solution of the wave equation without a selection of a travelling and backward waves. But there is the problem of a correct formulating of boundary conditions in this case. In present work it is offered to express the field exited by an electron beam as

$$\vec{E} = \mathrm{Re}[(F_1(z)E_{01}(z) + F_2(z)E_{02}(z))\vec{\Psi}(r_\perp)]e^{i\omega t}, \qquad (1)$$

where $E_{01}(z)$ and $E_{02}(z)$ describe the standing and travelling waves, accordingly, and are defined as eigenfunctions of the conic waveguide since the limited tapering waveguide may be replaced by the conic waveguide for signals of acting frequencies in the theoretical analysis. In particular, they may be defined as solutions of the wave equation

$$\frac{d^2E_0}{dZ^2} + [q^2 - \frac{n^2 - 1/4}{Z^2}]E_0 = 0, \qquad (2)$$

following from the general wave equation under a condition of a slow change of the waveguide radius $R(z) \cong \theta z$ for $\theta \ll 1$. Here n is the integer part of the value $[(k_0R_0)/\theta + 1/4]^{1/2}$, $q = \omega/\omega_{cr}^0$, $Z = k_0z$, the index "0" marks values, corresponding to the input end of the waveguide. Assuming that the coordinate Z is counted out the apex of the cone it is convenient to express own functions as[3]

$$E_{01} = E_0\varphi_n(Z) = E_0\sqrt{q}\sqrt{\pi/2}\sqrt{qZ}J_n(qZ) \qquad (3)$$

$$E_{02} = E_0\phi_n(Z) = E_0\sqrt{q}\sqrt{\pi/2}\sqrt{qZ}N_n(qZ), \qquad (4)$$

where J_n and N_n are the Bessel function and Hankel function, accordingly, E_0 is an amplitude

of own mode. Then amplitudes of the field exited by the HF electron current j_ω may be represented as

$$F_1(Z) = \frac{1}{N}\int_{z}^{z_L}\int_{s_\perp} \vec{j}_\omega E_0 \vec{\Psi}\varphi_n dS_\perp dZ \qquad (5)$$

$$F_2(Z) = \frac{1}{N}\int_{z_0}^{z}\int_{s_\perp} \vec{j}_\omega E_0 \vec{\Psi}\varphi_n dS_\perp dZ + F_{in}\sigma(Z_{in}) \qquad (6)$$

In integrals (5)-(6) it is taken into account that the HF current j_ω exits on a certain side of the section corresponding to the coordinate Z_0 and by means $\sigma(Z_{in})$ it is described a non-reflection-type gyro-TWT. Boundary conditions for exited amplitudes are next. (1)For a generation regime $F_2(Z_0)=0$, $F_1(Z_L)=0$, $F_{in}=0$ and besides the value $F_2(Z_L)=F_0$ defines the output power, and a condition $F_0 \to 0$ gives a starting current (or a starting current of a parasitic self-excitation in a gyro-TWT). (2)For the reflection-type TWT $F_2(Z_0)=0$, $F_1(Z_L)=F_{1in}$, $\sigma=0$. (3)For the non-reflection-type gyro-TWT $F_2(Z_0)=0$, $F_1(Z_L)=0$ and $\sigma=0$ if $Z < Z_{in\omega}$ and $\sigma=1$, if $Z > Z_{in\omega}$, where $Z_{in\omega}$ is the section of input of the signal of the frequency ω.

The amplitude j_ω may be defined in a framework of models of a different level of complexity. For example, in a simple case when static magnetic field is changed according to $B(\zeta) = B_0(1 - \nu\zeta)$, the full system of equations of present theory of gyro-TWT-BWO with a tapering waveguide is

$$F_1 = -\int_{\zeta_{2\pi}}^{\zeta_L} \phi_n(X) I\, d\zeta, \qquad F_2 = -\int_{0}^{\zeta} \varphi_n(X) I d\zeta + \sigma(\zeta_{in\omega}) F_{in},$$

$$I = \frac{1}{2\pi}\int_0^{2\pi} \beta d\vartheta_0, \qquad \beta|_{\zeta=0} = e^{j\vartheta_0}, \qquad \vartheta_0 \in (0, 2\pi),$$

$$\frac{d\beta}{d\zeta} - j(1-V)\{-0.5\nu + [b - p\zeta - \mu[(1+\alpha^{-2}) - (1+\nu\zeta)](1+2\nu\zeta)|\beta|^2 +$$

$$(1+2V)\alpha^{-2}]]\} = (1-\nu\zeta-V)(F_1\varphi_n + F_2\phi_n),$$

$$\frac{dV}{d\zeta} = -0.5\alpha^2\nu|\beta|^2, \qquad V|_{\zeta=0} = 0,$$

where $\zeta = \varepsilon k_0(Z-Z_0)$, $\beta = [(r*\exp(j\vartheta))/r_0]\exp(jb\zeta)$, $b = (\omega-\omega_c)/\varepsilon k_0 v_{z0}$, $\mu = [\alpha^2(v_z/c)]/2\varepsilon$ is the nonizohronity parameter, ε is the parameter of an interaction (analogous to the Pierce parameter in the TWT theory), $X = n+\zeta/\varepsilon$, $q = q_c + (2\mu\varepsilon^2 b)/\alpha^2$, $q_c = \omega_c/\omega_{cr}^0$, $V = (v_z - v_{z0})/v_{z0}$, $p = (\nu\alpha^2\zeta)/(2\mu\varepsilon^2)$, $\alpha = v_{\perp 0}/v_{z0}$. In general case this system of equations must be solved by numerical methods.

REFERENCES

1.K.R.Chu, Y.Y.Lau, L.R.Barnett and V.L.Granatstein, "Theory of a wide-band distributed gyrotron TWA", *IEEE Trans. on Electron Devices*, vol.28, N7, pp.866-872, 1981.

2.Y.Y.Lau and K.R.Chu, "A proposed wide-band fast wave amplifier", *Int. J. of Infrared and Millimeter Waves*, vol.2, N3, pp.415-425, 1981.

3.L.A.Veinstein, "Electromagnetic waves", Soviet Radio, Moscow, 1988 (in Russian)

Comparative analysis of oscillations in backward wave oscillators

Alexander P. Chetverikov

Saratov University, Physical Department,
Astrahanskaya, 83, Saratov 410071, Russia

ABSTRACT

A comparative analysis of single-frequency, multi-frequency and chaotic oscillations in BWO's of different electrons-electromagnetic waves interaction mechanisms is presented. The conventional BWO with a nonrelativistic electron beam and relativistic BWO, gyro-BWO, BWO-peniotron, anomaly-Doppler-BWO are considered. The analysis is performed on the basis of author original theoretical results and known data from the literature.

As known, there are a number of microwave generators which are classified as "backward wave oscillators" (BWO's). They are based on the interaction of an e.m.wave and an electron beam with contrary group velocities. Oscillations arise in them due to an absolute instability and may be single-frequency or multi-frequency - periodic or chaotic but with a narrow frequency band. That is why electrodynamic processes in BWO's of different interaction mechanisms are like in spite of their various electrodynamic systems. In the theoretical analysis they are described by the equation of a simple wave for a slow time and space scale amplitude of the e.m. wave

$$\frac{\partial F}{\partial \tau} - \frac{\partial F}{\partial \zeta} = -I, \qquad (1)$$

because the relation $\omega \cong \omega_0 + (\partial\omega/\partial h)_{h0}(h - h_0)$ is right for each frequency from the narrow band out of the vicinity of cut-off frequencies of the waveguide system. Here ω_0 and h_0 are chosen under a condition of the exact synchronism between the e.m. wave $\vec{E}(z,r_\perp,t) = \mathrm{Re}[F(\tau,\zeta)\vec{\Psi}(r_\perp)\exp(j(\omega_0 t - h_0 z))]$ and the electrons wave (wave of a HF current) of the slow time and space scale amplitude $I(\tau,\zeta)$, which is defined specially for each type of BWO's, $\zeta = \varepsilon h_0 z$ and $\tau = c\omega_0 t(1 + v_0/|v_{gr}|)$ are slow axial coordinate and slow time in the coordinate system moving with the nonperturbed axial velocity of electrons v_0 , ε is a parameter of the interaction and is determined specially in each case also. In addition $F(\zeta_L) = 0$ and $F(\zeta,\tau=0) = F_0(\zeta)$, where F_0 is a function of an initial field distribution (L is the length of the interaction space).For the first time this model was studied by Ginzburg, Kuznetsov et al.[1] for a conventional BWO with nonrelativistic and relativistic beams, where I was defined by equations

$$I = \frac{1}{\pi}\int_0^{2\pi} e^{-ju}du_0, \quad \frac{\partial^2 u}{\partial\zeta^2} = -(1+2\gamma_0^2\varepsilon\frac{\partial u}{\partial\zeta})^{3/2}\mathrm{Re}(Fe^{ju}), \quad u|_{\zeta=0} = u_0, \quad u_0\in(0,2\pi) \qquad (2)$$

It was found by numerical simulation method that a regime of oscillations which arose when $\zeta_L > \zeta_{Lst}$ and was single-frequency under $\zeta_{Lst} < \zeta_L < \zeta_{Lsm}$ became complicated when ζ_L (ζ_L is proportional to $I_0^{1/3}$, if L =cons') was larger than a bifurcational value ζ_L: periodic and chaotic selfmodulation were settled. Also it was shown that complex oscillations were caused by an overbunching of electrons and a delaying feedback in a distributed system "an electron beam plus a backward e.m.wave". Analogous processes take place in other BWO with an inertia bunching - gyro-BWO[2] , where I is defined in a framework of a simple model by the equation

$$I = \frac{1}{2\pi}\int_0^{2\pi}\beta d\varphi_0, \quad \frac{\partial\beta}{\partial\zeta} + j\mu(1 - |\beta|^2)\beta = F, \quad \beta|_{\zeta=0} = e^{j\varphi_0}, \ \varphi_0\in(0,2\pi) \tag{3}$$

However, in this case characteristics of oscillations and the oscillation build-up process from "rising" until reaching "steady-state" are depended on also the parameter $\mu = v_0/(2c\varepsilon)$, defining a change of a cyclotron frequency ω_c electrons-oscillators (electrons, rotating in a static magnetic field) as a function of an energy.

There are BWO's with non-inertia mechanisms of bunching of electrons where nevertheless inertia properties of electrons-oscillators provide a possibility of a realization of complex oscillations. They are a BWO-peniotron where[3]

$$\frac{\partial I}{\partial\zeta} + j\mu p(1-\gamma)I = [p-(p+1)\gamma]\gamma^{p-1}F, \quad I|_{\zeta=0} = 0, \tag{4}$$

$$|I|^2 = (1-\gamma)\gamma^p \tag{5}$$

(p is a number of a cyclotron resonance), and an ultrarelativistic anomaly-Doppler BWO when[4]

$$\frac{\partial I}{\partial\zeta} + j\mu|I|^2 I = -(1 + |I|^2)(F + I^2F^*), \ I|_{\zeta=0} = 0. \tag{6}$$

The unique property of BWO-peniotron is a possibility of a generation of a high efficiency single-frequency oscillations when the parameter μ is small and multi-frequency ones under large μ. And vice versa single-frequency oscillations are not possible practically in ADBWO due to a strong dependence ω_c on an energy.

A comparative analysis of oscillations in these devices performed on the basis of results of Ref.[1-4] mainly shows that stages of the oscillations build up process from "rising" until reaching "steady state " are like and a difference is accounted by nonlinear properties of an electron beam. Thus a single linear mode with the most "smooth" space distribution and largest increment is stood out from an initial noise distribution during the linear stage of the build up process. Then the single-frequency steady state is a established if the disturbing of a phase correlation between HF field and current leading to an energy change direction does not take place in the interaction space. If the energy change process is occurred due to an overbunching of electrons as in devices with the inertia mechanism of the interaction (conventional BWO, gyro-BWO) or due to the change of own frequency of electrons-oscillators as in devices with the non-inertia mechanism (BWO-peniotron, ADBWO) then oscillations are multi-frequency including chaotic if the bifurcational parameter is sufficiently large. Studying of these processes permits to offer methods of the control of characteristics and besides methods connecting with electromagnetic processes may be universal.

REFERENCES

1.N.S.Ginzburg, S.P.Kuznetsov and T.N.Fedoseeva, "Theory of transients in relativistic back-wave tubes", *Sov. Radiophys. and Electron.*, vol.21, pp.728-739, 1979

2.A.Yu.Dmitriev, D.I.Trubetskov and A.P.Chetverikov, "Non-steady-state processes of the interaction of helical electron beam with backward wave in the waveguide", *Sov. Radiophys. and Electron.*, 1991 (in Rus. vol.34, pp.595-600)

3.A.P.Chetverikov, "Nonstationary theory and simulation of the backward wave peniotron oscillator", *J. of Infrared and Millimeter Waves*, vol.14, N2, 1993

4.S.P.Kuznetsov and A.P.Chetverikov, "Nonstationary nonlinear theory of the ultrarelativistic anomaly Dopler BWO", *Sov. Radiophys. and Electron.*, 1981 (in Rus. vol.24, N1, pp.109-117)

Infrared polarizers made of anodic alumina films

Mitsunori Saito, Tetsuo Kano, Takashi Seki, and Mitsunobu Miyagi

Tohoku University, Department of Electrical Communications
Sendai 980, Japan

ABSTRACT

Wire-grid type polarizers were fabricated by electroplating nickel or copper into the columnar pores of anodic alumina films. A film exhibited an extinction ratio larger than 30 dB in the wavelength range of 1–7 μm.

1. INTRODUCTION

Anodic oxidation is a well-known technique for forming an alumina (Al_2O_3) film on the surface of an aluminum plate. As Fig. 1 shows, an anodic alumina film contains columnar pores of ~100-Å diameter. By filling the pores with a guest material (metal, semiconductor, dielectric, etc.), the alumina films exhibit anisotropic optical properties.[1] In this work, we electroplated metals into the pores, and studied the optical-loss anisotropy in the infrared region.

2. SAMPLE PREPARATION[2]

An aluminum plate, 500-μm thickness and 10×15-mm^2 area, was anodized in a 15-wt% solution of sulfuric acid by a dc current of 0.5 mA/mm^2. An alumina film of 50–100-μm thickness was formed in 35–70 min. After the post-anodization treatment in a sulfosalicylic acid solution, we electroplated nickel into the pores by applying ac 15 V to the alumina/aluminum plate in an electrolyte of nickel sulfate. Nickel ions were first deposited at the bottoms of the pores, and then nickel columns grew gradually toward the surface of the film. The nickel columns grew to the height (thickness) of 50–70 μm in ~120 min. Copper was also deposited into the pores in a similar manner. For optical experiments, we sliced the film to the length of d≃10 μm and polished the side surfaces.

3. OPTICAL ATTENUATION

We observed alumina films by a transmission microscope. Illuminating light was polarized linearly in the direction horizontal (H) or vertical (V) to the nickel columns. Figure 2 shows the pictures of a nickel-implanted alumina film. The intensity of transmitted light depends strongly on the direction of polarization.

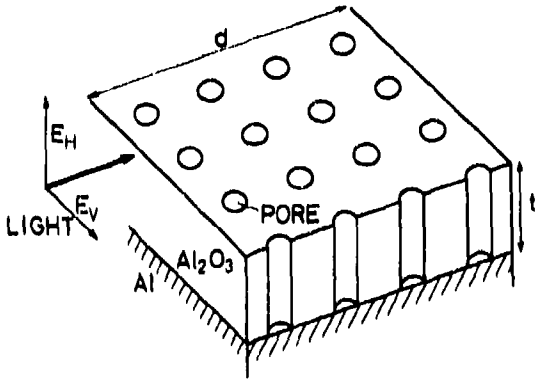

Fig. 1 Structural model of an anodic alumina film.

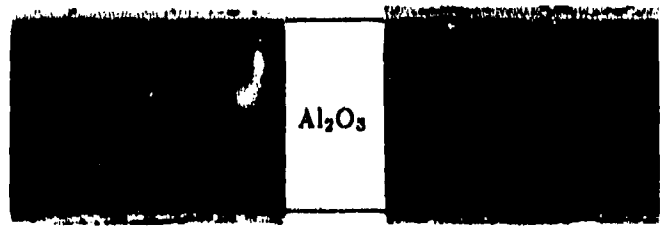

(a) Horizontal (b) Vertical

Fig. 2 Microscopic photographs of an anodic alumina film containing nickel columns. The film was illuminated from the back, and transmitted light was observed. Light was polarized linearly in the direction (a) horizontal or (b) vertical to the nickel columns. Film thickness is 50 μm.

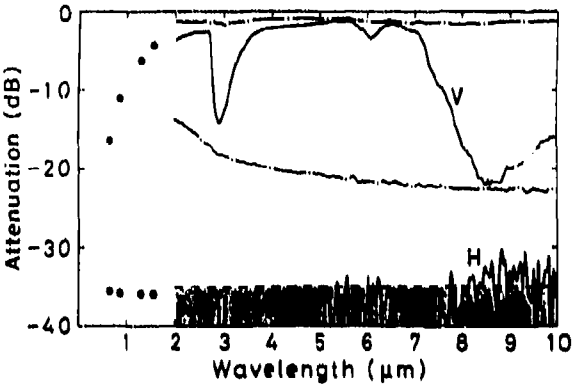

Fig. 3 Optical attenuation spectra of a nickel-implanted alumina film (circles and solid curves) and a wire-grid polarizer (dot-dash curves). The thickness of the alumina film is t=50 μm and the length is d=13 μm. The attenuations contain reflection losses at the entrance and exit surfaces of the polarizers. The detection limit is -35 dB at the wavelengths longer than 2 μm.

We measured the transmittances of alumina films by using a He-Ne laser (wavelength; 0.63 μm), LED's (0.85, 1.30, and 1.55 μm), and a microscopic FTIR spectrometer (Horiba, FT530). A light beam was focused to the spot size of ~10 μm and passed the film of 50-μm thickness. The polarization direction of the incident light was selected by a polarizer; i.e., a Glan-Thompson prism (extinction ratio; ~40 dB) at wavelengths below 2 μm and a wire-grid polarizer (Cambridge, IGP225) at longer wavelengths. To examine the performance of the wire-grid polarizer, we first evaluated the principal transmittances by using two wire-grid polarizers of the same type.[3] Dot-dash curves in Fig. 3 show the attenuations for two principal directions of polarizations. By using these data, we corrected the measured transmittances of alumina films. Circles and solid curves in Fig. 3 show the optical attenuation spectra of a nickel-implanted alumina film which were evaluated in this manner. Being limited by the sensitivity of the current measurement system, we could not evaluate the attenuation larger than 35 dB beyond 2-μm wavelength. The attenuation for H-polarization is larger than the detection limit. In the attenuation spectrum for V-polarization, the absorption bands are seen around 3- and 6-μm wavelengths, which are caused by water impurity in the alumina film. The extinction ratio is larger than 30 dB over the wavelength range of 1-7 μm. On the other hand, the extinction ratio of the conventional wire-grid polarizer (dot-dash curves) is ~20 dB or less.

4. DISCUSSION

In the electroplating process, the deposition rate decreases gradually with time and metal columns finally stop growing at some height; i.e., attainable column height is currently ~70 μm for nickel and ~20 μm for copper. We must improve the electroplating technique further to make polarizers of large aperture.

Concerning the extinction ratio, the nickel-implanted alumina film is superior to the conventional wire-grid polarizer. For practical uses, however, the insertion loss, i.e., the loss for V-polarization, must be reduced. Theoretical analysis predicts that copper columns yield a smaller insertion loss than nickel columns. We are currently evaluating the optical attenuations of copper-implanted films. For the reduction of the insertion loss, we are also studying the anodization in a phosphoric acid solution, by which we can form alumina films with smaller amount of impurities.[4]

5. CONCLUSION

Anodic alumina films exhibit a large anisotropy in transmittance when a metal is deposited in the pores. The films are useful as polarizers for the infrared region where efficient and inexpensive polarizers are not available.

6. REFERENCES

1. M. Saito and M. Miyagi, *J. Opt. Soc. Am. A*, **6**, 1895 (1989).
2. T. Seki, M. Saito, and M. Miyagi, *IEICE Trans.* **E74**, 3861 (1991).
3. J. P. Auton and M. C. Hutley, *Infrared Phys.* **12**, 95 (1972).
4. S. Nakamura, M. Saito, L. F. Huang, M. Miyagi, and K. Wada, *Jpn. J. Appl. Phys.* **31**, 3589 (1992).

REFLECTION TYPE ISOLATOR FOR SUBMILLIMETER WAVES

V.K. Kononenko, E.M. Kuleshov

Institute of Radiophysics and Electronics
Academy of Sciences of Ukraine
12 Acad. Proscura st., Kharkov, 310085, Ukraine

ABSTRACT

The properties of nonreciprocal attenuators with circular dichroic mirror based on the semiconductor-metal structure were analysed. Experimental data for the quasioptical isolator using n-InSb as a plasma medium are given.

1. INTRODUCTION

Nonreciprocal reflection type attenuators with the circular dichroic mirror (CDM) based on the various semiconductor structures are found a use for the isolation in a quasioptical circuits . The characteristics of such devices are defined by a type of employing CDM. The device considered here is a nonreciprocal attenuator, containing CDM based on the semiconductor-metal structure.

2. DESIGN OF DEVICE

Fig.1 illustrates the basic design of nonreciprocal attenuator for submillimeter wavelengths, taking into account the specific features of such waves transmission that is a broad wave beam using. Design consists of two principal assemblies: a duplex device and CDM. Duplex device including polarization divider and quarter-wave phase section realizes necessary transformations of the wave polarization and organizes entry and exit of the nonreciprocal attenuator. The polarization cells of the duplex device have been carried out on the base of the wire grids with diameter of the wire 8 μm and with the step 30 μm. CDM has been carried out on the basis of the n-InSb-metal structure. To achieve nonreciprocal operation, this structure was cooled to liquid nitrogen temperature and dc magnetic field was applied. Round hollow dielectric beamguide of 20 mm diameter was used as a quasioptical transmission line.

3. THEORETICAL RESULTS

Analysis of CDM properties and characteristics of nonreciprocal attenuator was accomplished in the plane wave and the ideal metal approximation. There were also used the conditions of wave reflection minimum from such structure determining maximum of reverse losses of nonreciprocal attenuator.

Fig.2 illustrates theoretical dependences of CDM parameters and characteristics of the nonreciprocal attenuator, calculated for values $\omega_p/\nu=6$ and $M=0$ (M - interference order). It can be seen, that there exist values ω_p/ω, in which the losses of wave reflection from CDM are acceptable for forward losses of the nonreciprocal attenuator. For example, the losses are less 1 dB for values $\omega_p/\omega \cong 1.1\text{-}1.3$ (helicon mode polarization) and $\omega_p/\omega \leq 0.75$ (antihelicon mode polarization). It should be noted, that opposite directions of the dc magnetic field correspond to orthogonal forms of the circular polarization on condition that spatial rotatory directory of wave field is retained invariable. It can be seen too, that two variant CDM on fixed frequency different in the choice of value: $\omega_p/\omega > 1$ or $\omega_p/\omega < 1$ are possible. The smaller forward losses are possible for

the second variant for lower dc magnetic field value, however in this case frequency bandwidth is narrower.

4. EXPERIMENTAL RESULTS

Fig.3 illustrates experimental results obtained for the submillimeter-wave isolator with CDM corresponding to the first variant ($\omega_p/\omega>1$) at the dc magnetic field 0.94 kG. The n-InSb plate had the following parameters: Hall electron concentration of about $4.7 \times 10^{}$ cm^{-3}, mobility of about $4.4 \times 10^{}$ cm^2/V·s, plate thickness 170 μm (M=0). The initial losses of beamguide elements were equal 1 dB.

The oscillation on frequency dependence of the reverse losses arises because of inhomogenity of dc magnetic field. This inhomogenity reached 3% within the circle limits, where according to calculations 90% EH_{11} mode power of beamguide are concentrated.

5. CONCLUSION

Quasioptical isolator providing insertion losses of ≤ 2.5 dB , a backward losses of 20-27 dB, VSWR < 1.2 in the wavelengths range of 0.98-1.00 mm at the magnetic field 0.94 kG has been built.

6. REFERENCES

1. V. K. Kononenko and E. M. Kuleshov, "Reflection-type isolator based on the structure dielectric-semiconductor", *Radiotechnics i Electronics*, Vol 30, N·7, pp. 1267-1277, 1985. [English translation in: *Radio Eng. Electron. Phys.* (USA)].

2. A. Ya. Usicov, ed. *Electronics and Radiophysics of millimeter and submillimeter Radio Waves*, Naukova dumka, Kiev, 1986.

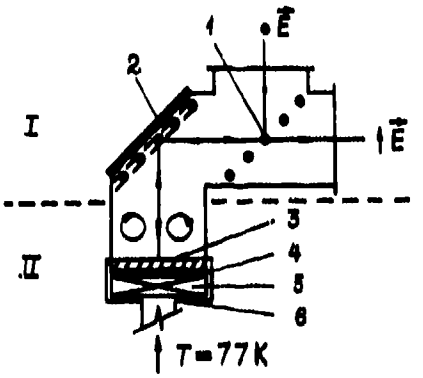

Fig.1.

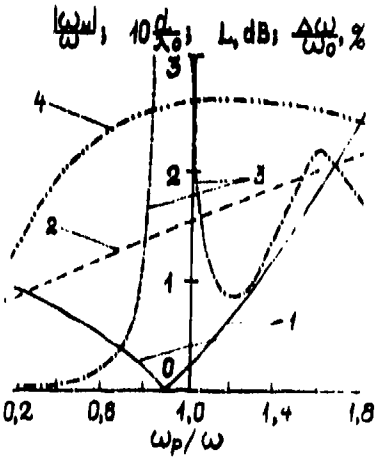

Fig.2.

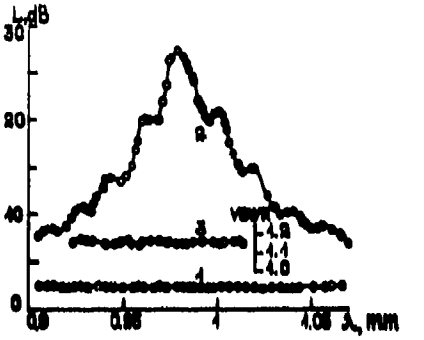

Fig.3.

Fig.1. Quasioptical isolator. I - duplex device; II - circular dichroic mirror. 1 - polarization divider; 2 - quarter-wave phase section; 3 - semiconductor plate; 4 - metal mirror; 5 - SmCo magnet; 6 - cooled holder.

Fig.2. Theoretical ω_p/ω dependences for: 1 - magnet field (ω_H/ω); 2 - thickness of the n-InSb plate ($10d/\lambda_0$); 3 - forward losses (L); 4 - relative bandwidth of reverse losses at the level of 20 dB ($\Delta\omega/\omega_0$).

Fig.3. Experimental frequency dependences of forward (curve 1), reverse (curve 2) losses and VSWR (curve 3) of the quasioptical isolator.

High performance quasi-optical Faraday rotators

G.M.Smith†, M.R.Webb*, J.C.G.Lesurf†

†St.Andrews University, Department of Physics and Astronomy, Fife, KY16 9SS, Scotland
*DSTO, SRL, Salisbury, Australia, formerly at St.Andrews

Abstract

The design, characterisation, manufacture and application of new, large area, quasi-optical Faraday rotators is discussed. When used as isolators these have given state of the art performance at W-band with isolations >60dB and insertion loss < 0.5dB at spot frequencies.

1. Introduction

Free-space isolators using ferrites with external magnets have been described before at 40GHz[1] and 285GHz [2] with respective isolations of 40dB and 18dB, and respective insertion losses of 0.1dB and 2dB. However they required large external magnets and had relatively small apertures. Free-space isolators using permanently magnetised ferrites were first examined by D.Martin and R.Wylde who surveyed a number of ferrites and produced an isolator with 17dB isolation at 115GHz [3]. This work was extended and improved upon by M.R.Webb [4] who produced isolators with isolations ~30dB at W-band. However, these isolators also had very small apertures which made it difficult to incorporate them into existing quasi-optical structures. This paper reports some new results, and considers some of the important design and manufacturing problems in the production of large area Faraday rotators of size 100mm x 100mm. Requiring no external magnetisation, these are extremely easy to use and incorporate into existing quasi-optical systems and have allowed a number of new quasi-optical techniques and systems to be utilised.

2. Design and Manufacture

The ferrite originally used by D.Martin, R.Wylde[3] and M.R. Webb[4] was Ferroxdure 330 (originally manufactured by Mullard in the U.K). This is an inexpensive, permanently magnetised hexagonal strontium ferrite, commonly used in motors, with a gyromagnetic resonance frequency of around 10GHz. It has a number of equivalents, manufactured by a number of other companies, known as Ceramic 8 or Ferrova 3 and is available in the form of relatively large sheets. These have been found to be equivalent magnetically to Ferroxdure 330, although a considerable variation in insertion loss has been noted on a batch to batch basis. When magnetised into saturation it has been found that the ferrite exhibits a rotation of 30 degrees/mm at W-band. For use as an isolator or circulator, which requires 45 degree rotation, the ferrite sheet is accurately ground to a thickness of 1.5mm, and then re-magnetised. (We use a magnet with a 1Tesla field).

The physical basis of Faraday rotation is that the spins of the ferrite material are aligned by a magnetic field, which interact with a propagating electro-magnetic beam causing different propagation rates (different complex refractive indices) for the two circular polarisation states. The net effect of this is to produce a rotation of a linearly polarised beam. At W-band the ferrite is operating well above resonance and the relative permeabilities for the two circular polarisation states are approximately given by $1 \pm \delta$ where δ is small and frequency dependent [5]. Using a Martin-Puplett polarising interferometer it is relatively simple to measure the reflection coefficient of a magnetised ferrite for each of the two circular polarisation states as a function of frequency. These have indicated that the refractive index of the ferrite at W-band is approximately given by $n(\lambda) = 5.32 \pm 0.83\lambda$ (where λ is measured in mm), although there has been some slight variation from batch to batch. (It should also be noted that the loss varies slightly with polarisation state).

Perfect rotation is essentially limited by multiple reflections within the ferrite, and is thus dependent on the matching of the ferrite to free-space. Because of its high refractive index, the isolation and return loss of the ferrite without matching is extremely poor. Ideally for minimum reflection at a given frequency, the matching layer should be quarter wavelength with a refractive index of approximately 2.3.

Two materials have been used in practice to match the ferrites. Fluorosint (manufactured by Polypenco) is an alloy of PTFE and mica, which is extremely low loss and very easy to machine, which has allowed quarter wavelength layers at 200GHz to be manufactured. It has a refractive index of 1.88 which although not ideal, is still relatively high compared to many other low loss materials. It is also possible to obtain artificial materials where the dielectric constant can be chosen by appropriate mixes of high dielectric constant and low dielectric constant materials. We have used a composite material with

a dielectric constant of 5.2, known as PT 5.2 (manufactured by GEC Plessey Semiconductors) This allows almost perfect matching, however, this material is extremely difficult to machine into the thin layers required for quarter wavelength matching at W-band and above (<350μm). In practice, three quarter wavelength matching has been employed which has given good performance but limited the bandwidth of the Faraday rotator. Both matching materials are glued onto the ferrite using a diluted epoxy resin mix. It is important that the glue is very thin and very even, otherwise air gaps can occur which can significantly degrade performance. The thickness of the glue should also be taken into account to determine the centre frequency, particularly for operation at high frequencies.

3. Results

When used as an isolator or circulator the ferrite is a 45 degree Faraday rotator positioned between two wire-grid polarisers angled at 45 degrees. At W-band with quarter wavelength Fluorosint matching, isolators have been constructed that have >20dB isolation from 75GHz to 105GHz with 30-40dB isolation at the centre of the band. Insertion loss is ~0.5dB at the centre the centre of the band rising slowly to 1.0dB at the band edges. The extra insertion loss is due to reflection losses due to non-perfect matching. The isolation is also limited by the matching.

With three quarter wavelength matching using PT5.2, isolation >40dB has been obtained at the centre of the band (5GHz bandwidth), although the isolation and insertion loss fall away rapidly out of band. In fact, we have obtained isolations in excess of 60dB at spot frequencies with insertion loss below 0.5dB. To obtain this level of performance care must be taken to terminate all unused ports, and ensure that isolation is not limited by the cross-polarisation component passed by the wire-grid polarisers which is typically of the order of -35dB. This is usually achieved by additional polarisers or using the extra cross-polarisation rejection provided by a corrugated feedhorn to waveguide transition (used in the measurements).

All these results have been successfully theoretically modelled, indicating that the isolation is simply a matter of appropriate matching. Details of the modelling and further experimental results will be given in a subsequent paper. Single pass resistive loss of the ferrite isolators described was estimated to be <0.3dB at W-band.

It has also been found that angling the ferrite slightly, with respect to the quasi-optical beam axis, can reduce standing waves (due to reflection from the ferrite) to negligible proportions, without significantly affecting the overall performance of the isolators.

4. Applications

These Faraday rotators are useful in any millimetre-wave system which requires high isolation where insertion loss is at a premium. Quasi-optical isolators and circulators have also been found to be extremely useful in coupling to high Q open resonator systems in reflection where they provide a highly sensitive frequency discriminator [6]. They have also been used in various oscillator stabilisation schemes [7], and have proved very useful in dual polarisation quasi-optical RADAR systems [8], and in systems which require analysis of the spatial frequency content of the beam[9]. They also have considerable potential for use at higher frequencies in the sub-millimeter wave band although their insertion loss and isolation at these frequencies has still to be established.

Acknowledgements - We would like to acknowledge the help and support of W. Dawber at A.R.E. and R.Yell and M.Sinclair at N.P.L. Malvern. We would also like to acknowledge G.Radley for his expertise in manufacturing the isolators.

5. REFERENCES

1) E.L.Moore, "A 300GHz quasi-optical Faraday rotation isolator," Int. Journal of Infrared and Millimeter Waves, Vol.10, pp. 1317-1325, Oct. 1989
2) G.F. Dionne, J.A.Weiss, G.A.Allen, W.D.Fitzgerald, "Quasi-optical Ferrite Rotator for Millimeter Waves," MTT Conf. Symp. Dig. pp.127-130, 1988
3) R.Wylde, Ph.D. Thesis, Chapter 4, Queen Mary College, 1985
4) M.R.Webb, "A mm-wave four port quasi-optical circulator," Int. Journal of Infrared and Millimeter Waves, Vol.12, pp.45-63 Jan. 1991
5) R.E.Collin, *Foundations for Microwave Engineering*, McGraw-Hill, pp. 286-299, 1966
6) G.M.Smith, J.C.G.Lesurf, "A Highly Sensitive Millimetre Wave Quasi-Optical FM Noise Measurement System," IEEE MTT Special Issue, December 1991
7) G.M.Smith, J.C.G.Lesurf, "Quasi-optical stabilisation of Millimeter Wave Sources," IEEE MTT Conf. Digest, Alburquerque, June 1992
8) M.Leeson, "The Application of Quasi-Optical Techniques to Millimetre Wave Radar ," PhD Thesis, St.Andrews University
9) M.R.Webb, "Millimetre Wave Quasi-Optical Signal Processing Systems," Ph.D. Thesis, St.Andrews University

MODULATION CHARACTERISTICS OF INJECTION HETEROLASERS COMPRISING CHARGE CARRIERS HEATED BY EXTERNAL MW ELECTRIC FIELD IN VIEW OF ELECTRON-ELECTRON AND ELECTRON-HOLE INTERACTIONS AS WELL AS HIGHER FIELD TRANSPORT

T.Yu.Bagaeva, I.I.Filatov, V.B.Gorfinkel,
S.A.Gurevich*, T.I.Solodkaya
Saratov Branch of IRE Russian Ac.Sci., Saratov, Russia
*A.F.Ioffe Institute of Russian Ac.Sci., Russia, St.Petersburg

A new method of effective modulation of heterolaser radiation was proposed in [1-2] consisting of charge carrier heating in an active laser area by the external microwave (MW) electric field. In the present paper the new results of theoretical and experimental study in the area of heterolaser radiation MW modulation and formation of picosecond optic pulses through the charge carrier heating in the active injection laser on the double heterostructure $n^+Al_xGa_{1-x}As$-$GaAs$-$p^+Al_xGa_{1-x}As$ with classic and quantum well in view of electron-electron and electron-hole interactions, as well as higher field transport are discussed.

To describe the effect of carrier heating of the steady-state and dynamic behaviour of the diode laser we used the model based on laser rate equations and the energy balance equations for electrons and holes in the active layer. Energy relaxation times were calculated by Monte Carlo technique.

In the steady-state case we calculated the dependence of laser threshold current on the heating electric field applied in direction parallel to active layer plane. The result is shown in the Fig.1. In the calculations we used the laser active region parameters as the length of 300 μm, width of 5 μm and the narrow-band layer thickness of 0.2 μm and 0.01 μm for the lasers with classic and quantum well respectively. The parameter for the solid curves plotted in Fig.1. is low-field electron mobility. The dashed curve corresponds to the case when the hole heating was not regarded and the hole temperature was assumed to be equal to the lattice one. The main result illustrated by Fig.1. is the sharp increase in the laser threshold current when applying the heating field of only a few kV/cm.

The modulation method under study enables to form picosecond optic pulses exhibiting high peak powers. In the active heterostructure layer a saturated optical gain is achieved because of current and optical pumping in the stationary state. With this, the temperature of charge carriers in active layer is maintained at the level which significantly exceeds the lattice temperature. As the heating action is ceased, the carrier temperature drops to that of the lattice during the time of the order of energy relaxation time. The optical gain grows abruptly and the recombination of stored electron-hole pairs proceeds as a short and powerful optic pulse.

It was shown that electron heating to temperatures corresponding to the intervalley electron transfer $\Gamma \leftrightarrow L$ allows for higher achievable peak pulse powers of a few tens of watts with durations of lower than 10ps in the above heterostructure where the conduction band gap is greater than the distance

between Γ and L valleys (0.3<x<0.4). Thereby, the optic pulse coding up to the frequency of 50 GHz can be realized.

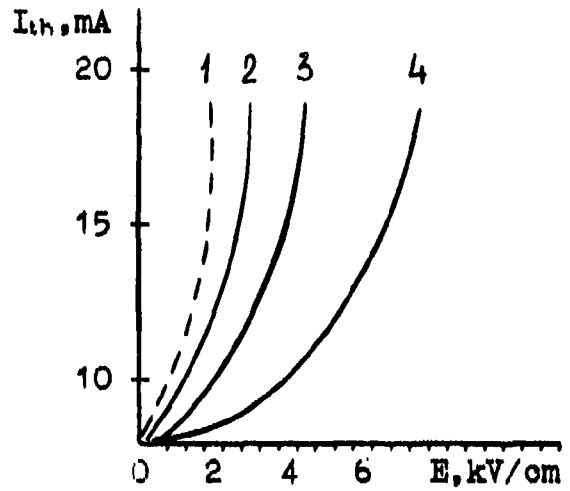

Fig.1.Low-field mobility: curves 1,2 - 8000 $cm^2/V \cdot s$; 3 - 4000$cm^2/V \cdot s$; 4 - 1200$cm^2/V \cdot s$.

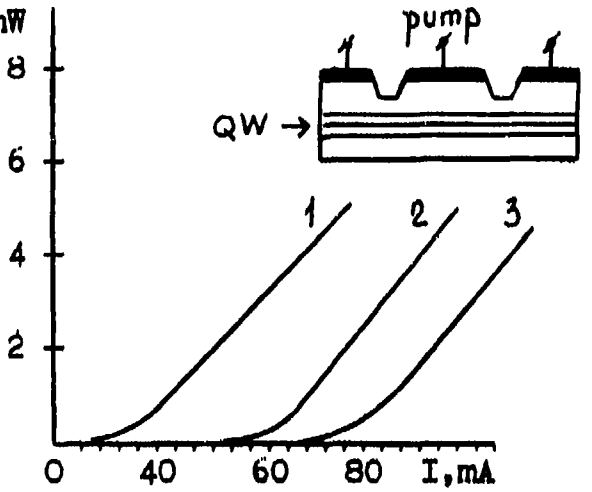

Fig.2.Heating current: curves 1 - 0; 2 - 80 mA;3 - 125 mA

The fabricated laser structure is shown schematically in the inset of Fig.2. It is essentially a common ridge-guide structure. For the laser preparation we used AlGaAs-GaAs separate-confinement heterostructure single quantum well wafer grown by MBE on p^+GaAs substrate. The thickness of quantum well active layer was 100 Å. The 6 μm ridge-guide mesa structure was formed by etching of two grooves each of 4 μm width. Then, the ohmic contacts were embedded onto the ridge top as well as on the surface of the structure outside of the grooves.The central contact pad has been used for the laser pumping, while the side one for plasma heating in the active layer.

The current-voltage characteristics measured on the side contacts were linear and with laser cavity length of 400 μm the resistance was about 100 Ohm at zero pumping current.Fig.2 shows the set of output power v.s. pumping current characteristics obtained at different currents applied to the side contacts. The significant increase of laser threshold manifests the influence of the applied current on the optical gain in the laser. Efficient near 100% modulation of the laser output has been obtained with 4GHz alternating voltage when the laser was driven at twice the threshold. In this experiment the pumping current was not practically influenced by 4 GHz signal. The results of these experiments demonstrate the effect of carrier heating produced by the voltage applied to the side contacts.

In summary we demonstrated that carrier heating in external electric field is very promissing for modulation of laser diode output up to the frequencies of 50 GHz. A new laser structure is designed to realize effective modulation by carrier heating.

References:

1.V.B.Gorfinkel, I.I.Filatov. Sov. Phys. semicond. 26, 3 (1992)
2.V.B.Gorfinkel, B.M. Gorbovitsky, I.I.Filatov. Int. J. of Infrared and MM Waves.no.6 (1991).

ABOUT USE OF THE INDUCED ANTIFERROMAGNETIC ORDERING EFFECT IN SHF DEVICES

Polupanov V.N.,Kiselev V.K.,Seleznev V.N.*

Institute of Radiophisics and Electronics
Academy of Sciences of Ukraine
12,Acad.Prosoura st.,Kharkov,310085,Ukraine
*State University of Simferopol',
4,Yaltinskaya st.,Simferopol',333036,Krimea,
Ukraine

ABSTRACT

The antiferromagnetic ordering effect in iron borate $FeBO_3$ by weak (to 0,1T) external field H was observed at the frequency 300 GHz at the room temperature. The losses on AFMR line, with width ~1%, increased or decreased depending on geometry H⊥k or H∥k respectively, but remained small and constant at the neithbouring frequencies. Such properties of monocrystals $FeBO_3$ enable to create nonreciprocal and modulation devices in the mm and submm ranges of radiowaves.

1. INTRODUCTION

The research of antiferromagnetic resonance (AFMR) in the weak-ferromagnetic crystal $FeBO_3$[1] showed this material to be prospective for using in the mm and submm radiowave devices. At present time perfect specimens of the monocrystal $FeBO_3$ are obtained in Simferopol' University. There were measurements made of the AFMR parameters at room temperature for clearing up the possibility of creating of SHF devices on the base such monocrystals.

The measuring instrument was developed by using devices based on quasioptic (QO) transmission line in the form of the round hollow dielectric beamguide (HDB) 20 mm diameter that was designed in IRE of Academy of Sciences of Ukraine. The specimen of the monocrystal of iron borate in the form of greenish semitransparent plate having size ~5x5x0,1 mm was placed in the metallic waveguide having the cross-section 0,2x3,6 mm that was matched with polymodal waveguide having the cross section 1,8x3,6 mm by means of wedge-shaped smooth transitions. The waveguide-to-beamguide transition (WBT) from 20 mm diameter to the cross-section 1,8x3,6mm implemented in the form of horn ensured the QO transmission line matching with the waveguide 1,8x3,6 mm. BWO was used as SHF generator that worked either in review mode, i.e. frequency sweeping regime, or in measuring mode, i.e. at fixed frequency. The waveguided sharpening detector was connected up to the QO transmission line by means of WBT.

2. SOME EXPERIMENTAL RESULTS

The signal attenuation was equal to -8 dB in the waveguide having the cross-section 1,8x3,6 mm and 50 mm length which included a narrower 10 mm lot of the cro ss-section 0,2x3,6 mm. Specimen is placed throuth the slots 0,2x10 mm in the narrow walls of the waveguide. In this case the attenuations increases by 4÷6 dB.

In fig.1 the signal level dependence is given on magnitude of the external ma gnetic field. It is seen that the specimen has ferric induction -1 Oe. The ori gin of this induction is still unclear.

Fig.2 shows the dependence of the variation of the level of the signal trans mitted $(E(H\|)-E(H\perp))/E(H\|)$, caused by magnetic field on the crystal temperature.

The resonant frequency retuning is 0,5÷1%/°C in the temperature range 5÷40 °C and the absorption line width $\Delta f/f_{res}$ is 4÷5% in accordance with our measurements. These characteristics allow to create devices such as modulators or rejection fil ters that are changable by temperature and controlled by magnetic field.

3.REFERENCE

L.V.Velikov, A.S.Prokhorov, E.G.Rudashevsky, V.N.Seleznev: "Antiferromagnetic reso nance in $FeBO_3$,JETP,vol.66,No.5,1974,pp.1847-1861(rus)

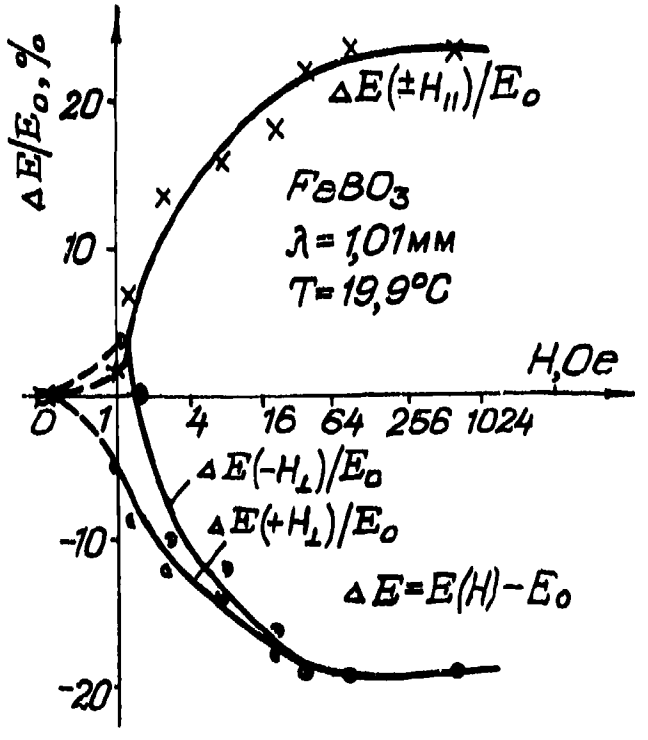

Fig. 1

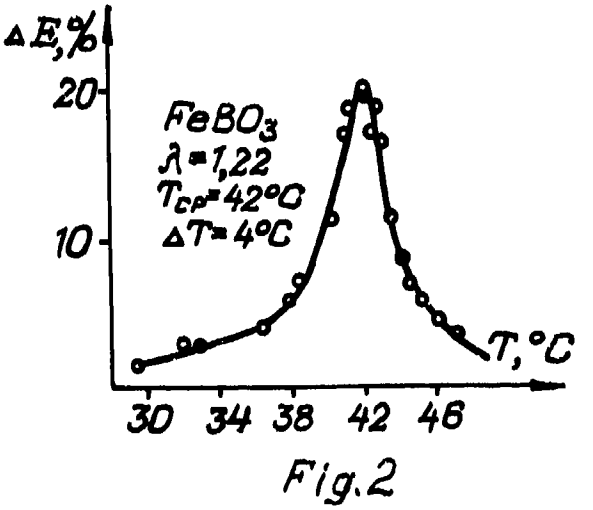

Fig.2

TRANSVERSE RESONANCES IN OVERSIZED WAVEGUIDES

D. Wagner, J. Pretterebner
Universität Stuttgart, Institut für Plasmaforschung,
70569 Stuttgart, Germany

M. Thumm
Kernforschungszentrum Karlsruhe, Institut für Technische Physik and
Universität Karlsruhe, Institut für Höchstfrequenztechnik und Elektronik,
76021 Karlsruhe, Germany

ABSTRACT

One possible way to achieve 100% reflection of a low order mode in an oversized waveguide is to use the principle of transverse resonances. In a short resonant section a high order waveguide mode close to cutoff is excited. If the coupling to the high order mode is equal to its losses and if the resonant phase condition is fulfilled a 100% reflection of the low order mode is possible.

INTRODUCTION

Short inner waveguide reflectors and notch filters can be realized by using the effect of transverse resonances [1]. A trapped mode is resonantly excited with the help of waveguide discontinuities. The quality factor of the trapped mode defines the bandwidth of the reflection. This type of waveguide element can be used as a short 100% reflector in a cyclotron autoresonance maser (CARM) resonator [2] or as a notch filter (diagnostics). Calculations and measurements on such a notch filter have been performed at 28 GHz and show a good agreement between theory and experiment.

SCATTERING MATRIX CODE

To analyze this effect we use a scattering matrix code which takes into account all forward and backward travelling modes as well as additional cutoff modes (evanescent modes)[2]. Using this method the change in the mode amplitude spectrum for a waveguide transition can be calculated accurately. Since the waveguide modes must satisfy the condition of power conservation, all the complex elements of the scattering matrix are bounded to the unit circle. This leads to a numerical stable description of the problem.

$$\begin{pmatrix} A_l \\ A_r \end{pmatrix} = \underline{S} \begin{pmatrix} B_l \\ B_r \end{pmatrix}$$

where A_l, A_r ... mode vector containing the incident and reflected modes in the left cross section
B_l, B_r ... mode vector containing the incident and reflected modes in the right cross section
S ... scattering matrix containing the coupling coefficients and propagation constants

EXAMPLES

As a first example we show this effect in a rectangular waveguide, where in the smaller cross section only one mode can propagate. We chose as an example a rectangular waveguide R320 at 28 GHz with a symmetrical step in the width (Fig.1). Fig.2 shows the calculated modal field distribution inside of the

waveguide at resonance, Fig.3 gives the power distribution in the waveguide, and Fig.4 presents the transmission curve over the frequency.
In the case of an oversized waveguide, i.e. if more than one mode can propagate in the smaller waveguide sections, the problem becomes more complicated. The excitation of spurious modes, different from the resonant higher order mode, which will occur in an arbitrary step has to be avoided. This can be achieved by using a nonlinear taper instead of a step and by using a partial mode converter in the resonance section.

SUMMARY

A transverse resonance allows to reflect waveguide modes frequency selectively. This is equivalent to a Fabry-Perot resonator where the transmittivity of the mirrors is defined by the coupling of the trapped higher order mode to the reflected low order input mode (distributed coupling).

REFERENCES

[1] P.E.Latham et.al., Int.J.Electronics, 1992, Vol.72, No.2, 273-304.
[2] C.K.Chong et.al., IEEE Transactions on Plasma Science, Vol.20, 393-402, 1992.
[3] D.Wagner, J.Pretterebner, Proc., 2nd Workshop on FEM-mmWaves, 1992, Rijnhuizen, Nieuwegein, The Netherlands.
[4] D.Wagner, J.Pretterebner, M.Thumm, Proc., 17th Int.Conf.on Infrared and Millimeter Waves, 1992, SPIE, Vol.1929, 114-115.

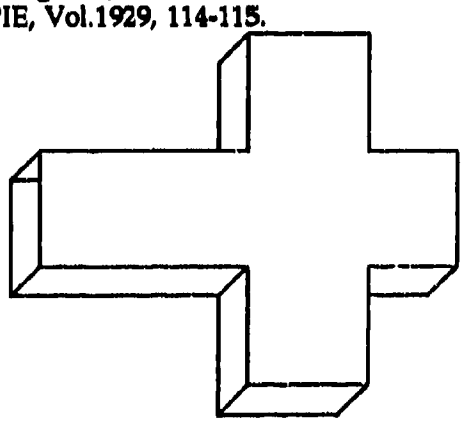

Fig1. Rectangular stepped waveguide.

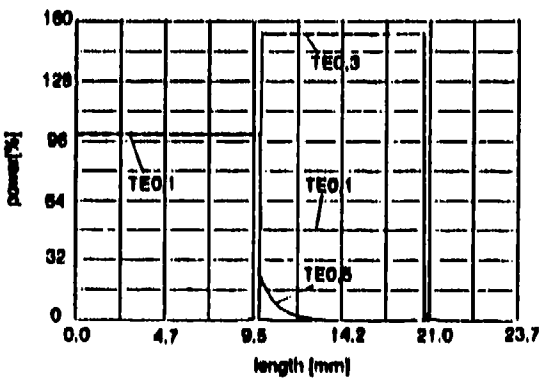

Fig2. Modal field distribution in the interior of the waveguide

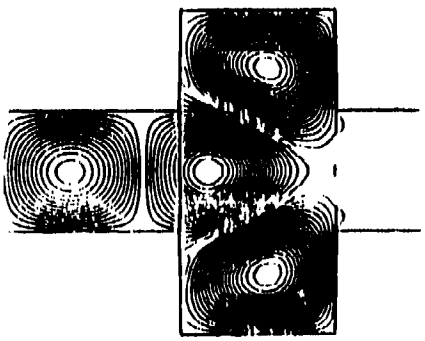

Fig3. Power distribution in the waveguide

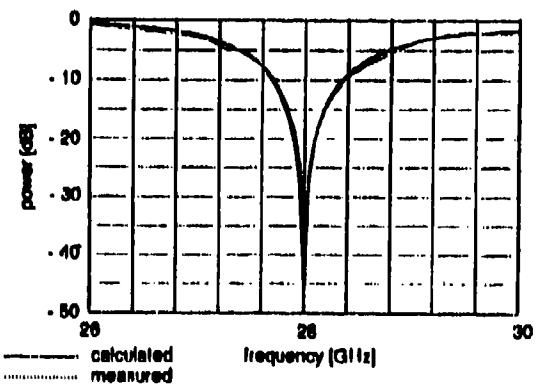

Fig4. Measured and calculated transmission curves

Wavefront divinding Ring-Interferometers for the Far Infrared.

K. D. Möller, K. Chin, and C. Qiu
Department of Physics, New Jersey Institute of Technology, Newark N.J. 07102

P. Bruelemans and P. Janssen
Department of Physics, Katholieke Universiteit Leuven, Belgium

A schematik of a lamella grating with four reflectors is given as

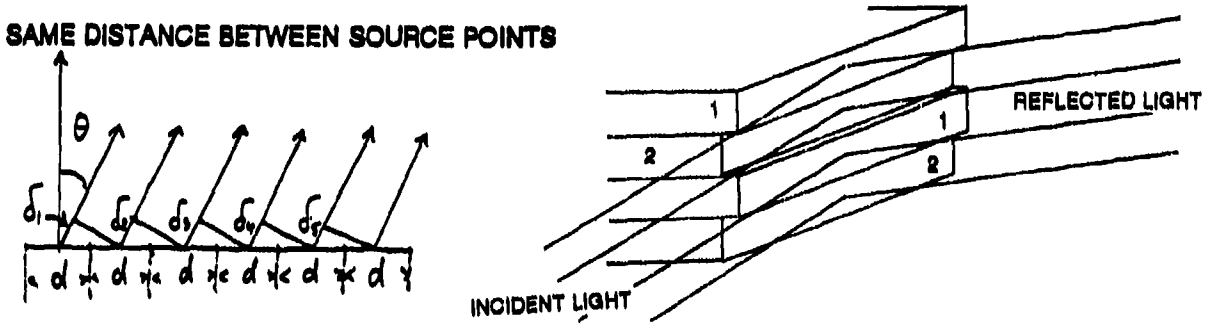

$\delta_1 = \delta_2 = \delta_3 = \delta_4 = \delta_5 = d \sin(\theta)$

The incoming wavefront is diffracted at the reflectors. One set of reflectors is displaced with respect to the other and light from the two sets is interfering with light from the other set. For monochromatic light, if the optical path difference between the two sets is such that we have constructive interference, all the light travels in the direction of reflection (zero order). If we have destructive interference, the light is diffracted into the first and higher orders and travel into a direction making an angle with the direction of reflection, but light is traveling in the direction of reflection. We can change the displacement between the two sets of reflectors at a sequence of intervals such that we have alternating light falling on the detector and not. The recorded intensity is the interferogram.

We now assume that we have as incident light a frequency band with highest frequency ν_g. To do this we may take a broad band source and use a low pass filter. The sample theorem of Fourier transform spectroscopy tells us that we have to choose the length l of the sampling intervall equal $1/2\nu_g$. The highest frequency used for calculation of the sample interval determines as well the minimum distance at which we have to place the detector in order not to detect first or higher order light. If non of the first order light arrives at the detector, we obtain optimum modulation of the interferogram. If a certain fraction of the first order light is as well detected, the modulation of the interferogram is reduced.

If we choose a position of the detector such that no light of the first order of the highest frequency will be detected, the lower frequencies will as well not arrive at the detector. Rectangular shaped reflectors diffract the first order to both sides of the zero order, square shaped reflectors diffract the first order into two dimensions.

A ring interferometer consists of two sets of interpenetrating rings, each ring having the same area. The incident light is reflected and diffracted and an optical path difference may be introduced by setting the two sets of reflecting rings at certain distances. For normal incident monochromatic light, for constructive interference, all the light is reflected backwards. For

destructive interference, the light is diffracted into various angles away from the normal, and we do not have a single direction for the "first" order.

DECREASING DISTANCE BETWEEN SOURCE POINTS

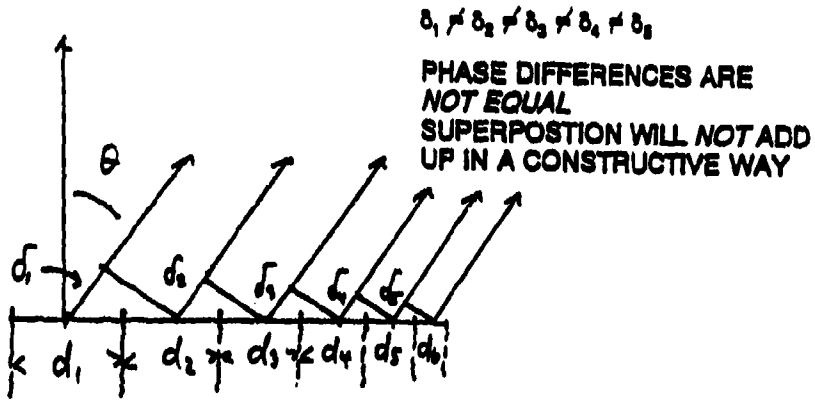

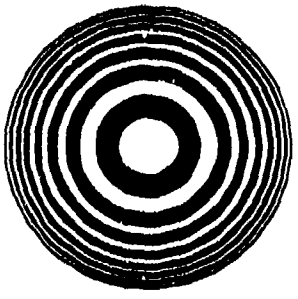

For a braod band input and destructive interference, the highest frequency is now distributed over an angle range, and similarly for all lower frequencies. If we may admit a certain fraction of the first order light on the detector, but still get an interferogram with sufficient modulation, we may use a much larger frequncy range than is possible with the lamellar grating.

Black body radiation is decreasing to longer wavelength in such a way that we have about a decrease of the intensity of 1/8 for each octave, that is, if the intensity at 200 cm^{-1} is 1 , it is at 100 cm^{-1} only .12. We may use entrance and exit apertures of diameters d to block off the first order of frequency ν. All higher frequencies will have an increasing amount of their first order falling onto the detector and will be less and less contained in the interferogram and the spectrum, that is the spectrum will decrease to higher frequencies. It will as well descrease to lower frequencies because the light will be less intense. Depending on d we may study a frequency range from the lower frequency ν_1 to the higher ν_2 , where ν_1 is determined by the amount of the intensity which may be detected with the aperture d, and ν_2 is determined by the amount of first order light not shielded off by the aperture d. We may do this procedure over a large wavelength range and need no low pass filters, making the ring interferometer a very flexible instrument for the choice of the wavelength range to be studied. However, using low pass filters, will make it possible to use a larger detector and increase the throughput.

A four ring interferometer has been successfully constructed at the Technische Universitat Aachen and 10 ring interferometers are under construction at NJIT and K.U.Leuven.

K. D. Moeller: Wavefront dividing interferometers, Infrared Physics, 32, 321 (1991).

High Resolution Far Infrared Fourier Spectrometer using a buffered ADC

A.K. Wan Abdullah, M. Roslan and W.A. Kamil*
School of Physics, Universiti Sains Malaysia, 11800 Penang, Malaysia
*School of Chemical Sciences, Universiti Sains Malaysia, 11800 Penang, Malaysia

ABSTRACT

A far infrared Michelson interferometer which includes a laser fringe sampling channel and a hydraulic piston to move one of the mirrors linearly has been developed. A maximum resolution of 0.08 cm^{-1} can be obtained with the present length of the piston. The buffered analogue-to-digital converter unit allows the interferogram points to be transferred in blocks to a storage device while the mirror is travelling. The instrument has been used to detect weak absorption bands due to water vapour believed to be either adsorbed onto or trapped in the film of chemically modified epoxidised natural rubber.

INSTRUMENTATION

The Fourier spectrometer that has been constructed uses an internal laser fringe sampling technique and a pneumatically driven hydraulic piston to move one of the mirrors mounted on a precision linear slide. The maximum stroke length of the present piston is 12.5 cm. This corresponds to an output spectral resolution of approximately 0.08 cm^{-1}. The laser sampling channel provides a precise and continuous calibration of the sampling position. By measuring the stability of the laser fringes with an accurate timebase the sampling interval has been determined with an uncertainty of about 5 nm. The moving mirror mechanism is basically identical to the one developed previously[1]. A Pfund focussing system at the output port allows samples as small as 3 mm in diameter to be studied by either transmission or reflection spectroscopy.

The data processing system that has been developed uses a commercially available[2] 12-bit buffered analogue-to-digital converter (ADC) unit. A high speed clock module enables the ADC to accumulate digitised signal first in the buffer and they can then be read later by the computer when it is convenient. By calling a unique secondary address of the ADC using high speed data collection software, the interferogram points can be transferred directly in blocks to a disc via IEEE bus lines while a scan is in progress. Each block consists of 12,000 integers with 2-byte format. The buffer size is 64 kbytes and the typical conversion time using the external trigger derived from the laser fringes is 40 μs. Since the speed of the scan is only about 500 laser fringes per second the conversion takes place safely. The infrared signal is sampled at every laser fringe so that a reference point used in co-adding a set of interferograms can be identified more precisely. The movement of data within the buffer follows the first-in-first-out protocol and thus assures the continuity of the interferogram. The flow of data and control signals in the system is shown schematically in figure 1. The TTL trigger pulse is used to control the piston either to move or to stop. In addition, a Pascal compiler[3] with a DOS extender for a 486-based personal computer is used which can store data in a very large number of arrays. Prior to Fourier transformation, the 2-byte integers are first converted into 4-byte format since the compiler only accepts 4-byte integers. Typically, an FFT of about 300,000 interferogram points (2^{19} points inclusive of zero smoothing) takes about 20 seconds.

DISCUSSIONS

Various proportions of *epoxidised natural rubber (ENR)* have been synthesized by methods that are well-documented in the literature[4], *i.e.* by oxidation of natural rubber with m-chloroperbenzoic acid. Dark brown, shining and uneven brittle solid films were obtained. The thin solid film of the chemically modified *ENR* was mounted at the focus of the beam position. The transmitted interferogram was recorded using a Golay detector with a CsI window. Figure 2 shows the spectrum of an *ENR* sample obtained after ratioing against a background

spectrum for an evacuated spectrometer. The spectrum gives a very broad and distinct band in the region of 335 cm^{-1} which corresponds to the bending of the carbon-carbon-chlorine bonds. It however did not show any notable bands from 430 to 480 cm^{-1}, thus indicating the absence of carbon-tin stretching. These early findings are preliminary and should be complimented with other spectroscopic techniques to ascertain the reaction products. Apparently this is the first time this reaction has been carried out. Weak absorption bands due to water vapour which may have been either adsorbed onto or trapped inside the polymer during the chemical reaction are clearly visible. The absorption lines were compared with the water vapour bands listed by Rao *et al* [5]. No shift has been observed in any of the lines thus indicating the polymer does not seem to alter the vibrational properties of the water vapour molecules.

The light from the He-Ne laser used in the sampling channel is not truly monochromatic. This limits the length of the interferogram that can be sampled. In the present setup, it is possible to increase the spectral resolution of the instrument by using a monomode laser and a piston with a longer travel.

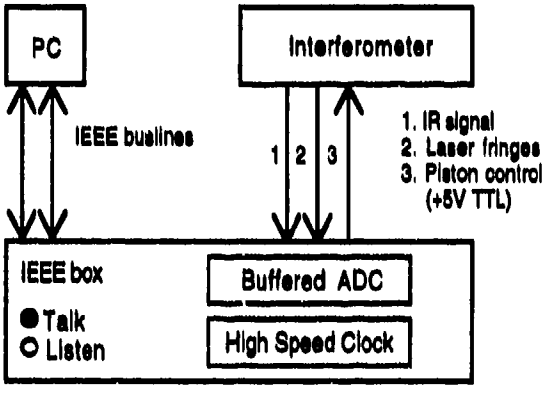

Figure 1: Block diagram showing the flow of data and signals between the interferometer, IEEE device box and the desktop computer.

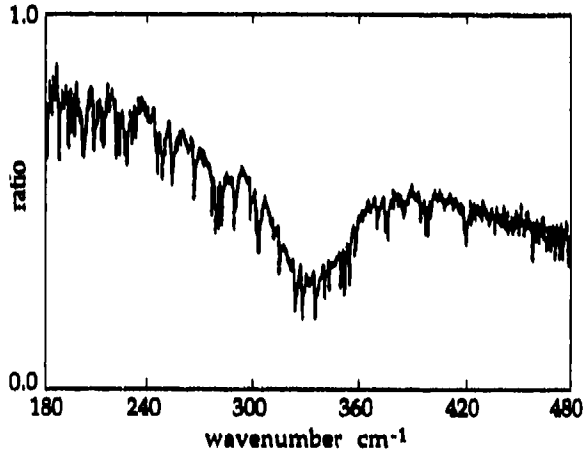

Figure 2: Spectrum of ENR sample ratioed against background spectrum for evacuated spectrometer with a resolution of about 0.1 cm^{-1}

ACKNOWLEDGEMENTS

The authors wish to thank the Government of Malaysia and Universiti Sains Malaysia for providing the *IRPA* R&D grant to carry out this work. The *NDP* Pascal compiler obtained through Dr. K. Shivanandan formerly at the Naval Research Lab., Washington DC and useful comments from Prof. T.J. Parker, University of Essex are gratefully acknowledged.

REFERENCES

1. A.K. Wan Abdullah and T.J. Parker, *"High Precision Dispersive Spectrometry for Transmission Studies in the Far Infrared"*, Infrared Phys., vol. 29, pp 799-803, 1989.
2. Biodata Ltd., 10 Stocks Street, Manchester M8 8QG, England.
3. Micro Way Inc., Research Park, Box 29, Kingston, Massachussets 02364, USA.
4. I.R. Gelling, *"Modification of Natural Rubber Latex with Peracetic Acid"*, Rubber Chem. Technol., vol. 58, pp 86-96, 1984.
5. K.N. Rao, C.J. Humphreys and D.H. Rank, *"Wavelength Standards in the Far Infrared"*, Academic Press, New York, (1966).

A high resolution, high speed data acquisition system based on an IBM-PC 486, for control of a Fourier Transform spectrometer

Z B Maricic+, L P Ellison+, B Gowland* and G A Gledhill+

+Department of Physics, *Computer Centre, Royal Holloway, University of London, Egham Hill, Egham, Surrey, TW20 0EX, UK

ABSTRACT

The mini-computer and control electronics of a Bruker 113v Fourier Transform spectrometer (FTS), capable of 0.03cm^{-1} resolution for frequencies up to 4000cm^{-1}, have been replaced by an inexpensive IBM-PC 486-based system. The original performance is exceeded. JCAMP-DX standard is used for data exchange. The system can be adapted to any FTS or similar time-domain instrument.

1. INTRODUCTION

We have replaced the data acquisition system and the control electronics of a Bruker 113v FTS with a "state-of-the-art" system based on an IBM-PC 486 computer. With relatively little modification, our system could be used to control other spectrometers or other instruments where high-speed, high-resolution data collection is required together with full instrumental control. The optical and mechanical components, even the fundamental design of many instruments have a much longer lifetime than the electronic control and data acquisition systems. This should make this report of interest to those operating instruments which are more than 5-years old. Our system uses modern LSI components, it has a high degree of sophistication, it is considerably reduced in size and more reliable than older systems.

2. DATA ACQUISITION SYSTEM AND CONTROL ELECTRONICS

Central to the design is a local instrument bus which is controlled by a microprocessor. All control and data collection is from a PC which is interfaced to the local bus by a RS232 link, communication being in standard ASCII strings. The operator can also control the instrumental settings from a switch box so that he can carry out operations such as alignment of the optics without running the full programme. A modular design is used for the electronics which controls settings of the interferometer (e.g. beam-splitter selection). Each module is a "euro-card" housed in a double height card frame with the power supply occupying the lower half. A detailed description of the electronics, which involves the use of both analogue and digital techniques, is beyond the scope of this report. The complete set-up is shown in Fig 1.

3. SOFTWARE

The package, which is transparent and easy to use, consists of a suite of modules used as a foundation for a high level language program (Pascal) which allows the capture, manipulation and storage of the data . The requirement of the program was to use a 16-bit ADC card capable of sampling at 400kHz and to be able to sample up to $\frac{1}{4}$ million data points: this meant that the input buffer would need to be $\frac{1}{2}$MB in size due to each data point being a 16-bit value. Also, it was required that successive additions of each scan would not be averaged. To do this, the storage buffer needed to hold the data points as 32-bit values, allowing a guaranteed maximum of 65537 scans to be added before the risk of overflow occurred. Thus the storage buffer needed to be 1MB in size for sampling the maximum number of data points; the total amount of memory required to provide the input and storage buffers is 1.5MB.

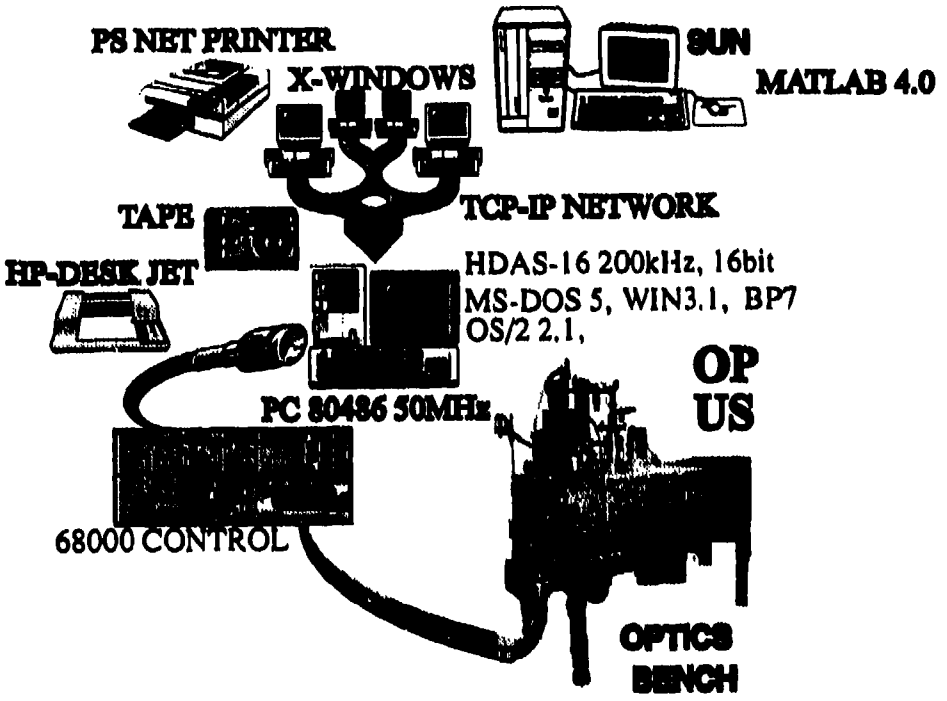

Fig1. The Bruker 113v with the new data acquisition system and control electronics.

With a high data acquisition rate, problems with information storage are encountered which require the fast and efficient manipulation of large blocks of memory. With MS-DOS the familiar problems of accessing large blocks of data arise. Using "conventional" memory (640kB) it is impossible to allocate sufficient space for high-speed data acquisition. Using the DOS Protected Mode Interface (DPMI) specification solves the problem but requires extensive familiarity with the protected addressing modes of the 286 and 386 microprocessors. It was necessary to make use of extensive machine language modules to use the properties of DPMI from within DOS.

Another problem encountered with the 80x86 family of processors is the "segmentation" approach to memory access. Access to the 64kB segments is enabled by the segment and offset registers. Manipulating these registers can introduce delays resulting in the loss of data at high acquisition speeds. It was decided that the use of DMA was unsuitable, so for data retrieval the technique of "pulling" a "data ready" flag from within a tight assembly language loop was used.

MS-Windows V3.1 was chosen as the operating environment due to its built-in DPMI capabilities. With the appropriate extensions, the allocation and manipulation of 32-bit memory blocks is allowed. This solves the problem of segmentation and allows for memory blocks of up to 16MB to be used.

Unfortunately Bruker do not provide an fast FT facility as part of their software package, preferring to carry out the FT using a separate transputer-processor. We elected to perform the FT using Matlab V4.0 on a separate SUN computer networked to our system (Very recently we have received Matlab V4.0 to run on the 486 which should lead to a considerable simplification). Spectral manipulation is carried out using the Bruker OPUS V1.4 software.

4. TESTING THE SYSTEM

A range of simulated test verified that data could be collected at the desired speed for full resolution of the ADC card. Absorbance spectra of gases recorded at 0.03cm^{-1} resolution show that the system performs to full specification over the spectral range 25 to 4000cm^{-1}.

Characterization of CH-Plasmas with CSR Based Microwave Spectrometers

F. Wolf, F. Neubert, T. Hessel, V.L. Vaks

Analytik & Meßtechnik GmbH Chemnitz,
Stollberger Str. 4a, D-09119 Chemnitz, Germany

In this paper the experimental analysis of plasmas suitable for thin film deposition using a high resolution mm-wave spectrometer is reported.

Low pressure plasma deposition techniques can be used to prepare thin solid films from various materials. One class of these materials is the class of diamond and diamond-like carbon films which may be used e.g. as surface coatings or as potential raw material for a 'diamond electronic'

However, the preparation of diamond films is difficult because there are many parameters to be controlled. Whether a thin carbon film is going to become diamond or amorphous carbon, depends mainly on the composition of the particle stream incident onto the top layer of the growing film as a result of chemical gas phase reactions near the substrate surface.

In the course of the years it appeared to be a problem to get direct information about the true composition of the 'active zone' of a plasma deposition system at a molecular level, e.g. that mass spectroscopy is not capable of detection of transient and short living species in real deposition systems. Although optical methods are sensitive, their application is limited because of strong interferences of signals of different species. When using laser absorption methods the problem of selectivity vanishes but the problem of frequency tuning over a wide range arises. Moreover, a plasma is a very harsh environment and so the number of suitable analytical methods is limited.

Therefore the method of choice should meet the following requirements:

- It should be highly sensitive because of the low concentration of species occuring in a plasma. (Absorption lines with absorption coefficients less than $10^{-8}cm^{-1}$ to $10^{-10}cm^{-1}$ should be detectable.)
- In order to guarantee a high selectivity it should have a high spectral resolution. (Of the order of the Doppler width of an absorption line, so that the line shape can be resolved.)
- The frequency should be tunable over a wide range to cover as many absorption lines as possible and thus absorption lines of different species.

One possible choice is microwave spectroscopy.

During the last years new substantially improved types of high resolution and high sensitive microwave spectrometers have become available. The spectrometer applied to our experiments uses the effect of coherent spontaneous radiation (CSR), which is re-emitted from the gas or plasma under investigation after its excitation by means of a microwave radiation impulse of finite duration. The frequency is synthesizer controlled and can be tuned to any frequency between 37GHz and 178GHz. The lowest detectable absorption coefficient is well less than $10^{-9}cm^{-1}$ (Valiid for standard conditions only: transmitter output power 10mW, length of the wave guide absorption cell 1m, integration time per frequency point 1s and gas pressure $10^{-2}Pa$.). The spectral resolution is of the order of Doppler broadening. The spectrometer dessign allows to track time dependent processes in the plasma with time constants of the order of $10\mu s$.

The CSR-spectrometer has been fitted to a vacuum deposition system. The path length through the plasma amounts to 50cm. The partial pressure of the two hydrocarbon gases in use was kept below 10^{-1}Pa. Although the mm-waves were not transmitted by a wave guide absorption cell but in free space between two gain horn antennas, the sensitiviy is hold at a reasonable high level. Two hydrocarbons (methanol, ethanol) have been used for the experiments. Table 1 and 2 show first results obtained from these experiments. Already identified radicals and their corresponding absoption lines are tabulated. Beside of these lines a couple of other but still not identified lines have been observed.

Table 1. Radicals detected in the ethanol plasma

Radical	Frequency (MHz)
CH_2	68380.9 69007.8 70678.6 70679.5 70680.7
C_3H	76199.2
CH_2O	72409.3 72838.1
CH_3OH	76509.7
C_2H_2O	60615.9 60617.3 60625.7
CH_3CHO	76866.4 76878.9 79099.2 79150.1
CH_3OCH_3	73465.5 73468.7 73472.6
$CHOOCH_3$	72681.4

Table 2. Radicals detected in the methanol plasma

Radical	Frequency (MHz)
CH_2	69007.8 70680.7
C_3H	76199.2
CH_2O	72409.3 72838.1
C_2H_2O	60625.7
CH_3CHO	76866.4

A Nb open resonator for millimeter wave surface resistance measurements of superconductive thin films

B.Komiyama and H.Shimakage

Communications Research Laboratory
Iwaoka Kobe 674, JAPAN

Abstract An open resonator with a Nb concave mirror has been developed for surface resistance measurements of high-Tc superconducting materials at 100 GHz band.Temperature of a superconducting sample can be varied from 4.2 K to at least 80 K with keeping temperature of the Nb mirror at 4.2 K. Frequency and temperature dependencies of Q were measured for a Nb thin film to check the resonator performance.

Introduction

Application of high-Tc superconductors (HTS's) to millimeter wave circuits appear to be very promising. For such application, surface resistance of materials becomes one of the most important parameters.

An open resonator technique has several advantages for millimeter wave surface resistance measurements, where a superconducting sample is used as a plane mirror of a semiconfocal type resonator [1]. Surface resistance can be calculated from quality factor Q of the resonator. With refinement of HTS thin film quality, improvement of measurement sensitivity of surface resistance is required. Surface resistance of the concave mirror of the resonator limits the sensitivity in this technique, if diffraction loss is negligible small.

We report here the development of a open resonator with a Nb concave mirror for surface resistance measurements of HTS thin films at 100 GHz band and describe preliminary experimental results.

Resonator Structure

The transmission type resonator fabricated is shown in Fig.1. The concave mirror was machined from a solid rod of Nb and polished after machining. The coupling of microwave power into and out of the resonator is done via two small holes [2]. The resonator is immersed in liquid helium after evacuating. A superconducting sample is mounted on a copper block which is connected to a bottom flange through a thin stainless steel tube to isolate the sample thermally from the resonator walls. Temperature of the sample is controlled by a heater and a Si sensor attached to the copper block. The diameter and radius of curvature of the Nb mirror are 46 mm and 80 mm, respectively. The distance between the concave and plane mirror is about 52 mm.

The surface resistance of the sample can be determined from the measurement of the resonator Q of the fundamental TEM_{oo} mode. The unloaded Q, Q_o is

$$Q_o = A/(R_{cc} + \alpha R_{ss}) \qquad (1)$$

where R_{cc} and R_{ss} are surface resistances of the Nb mirror and the sample, respectively and A and α are constants depending on the resonator size. Here, we neglect diffraction loss of the resonator.

Experiment

We have measured frequency and temperature dependencies of Q's to check the resonator performance using a Nb thin film . A 0 dBm W-band frequency multiplier was used to measure Q's [2]. The Nb film was deposited on a Si substrate by rf magnetron sputtering. Tc and thickness of the film were 8.0 K and 500 nm, respectively. Frequency dependencies of Q at 4.2 K and room temperature are shown in Fig.2. Oscillations are observed for both temperatures, which is probably caused by unexpected reflections inside the resonator. The diameter of the sample is 25 mm and the diffraction limited Q calculated is more than an order of magnitude higher than measured values. From the Q value at 89.4 GHz and 4.2 K in Fig.2, R_{cc}=49 mΩ is obtained by assuming $R_{cc}=R_{ss}$ in eq.(1), which is about an order of magnitude larger than the estimated value by f^2 law from typical

values at X-band for bulk Nb. Temperature depenency of Q measured at 89.4 GHz is shown in Fig.3. Rapid decrease in Q is observed around 8.0 K, which implies that the Si sensor indicate correct temperature of the sample. No transition of the Nb concave mirror was observed at least up to the sample temperature of 80 K.

Conclusion

The 100 GHz open resonator with the Nb concave mirror has been developed in order to measure surface impedance of HTS films with improved measurement sensitivity. It has been shown that surface resistances of samples can be measured over a broad range of temperatures. The expected decrease in R_{sa}, however, has not been obtained.

References

[1]J.S.Martens etal.,Appl.Phys.Lett.58,2543 (1991)
[2]B.Komiyama etal.,IEEE Trans.Microwave Theory Tech.39,1792 (1991)

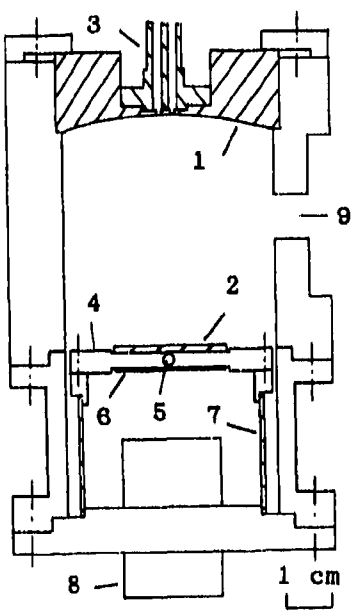

1.Nb concave mirror
2.Plane mirror
3.Wave guide
4.Cu block
5.Thermometer
7.Stainless steel tube
8.Feedthrough
9.Vacuum

Fig.1. Open resonator for surface resistance measurements of HTS films.

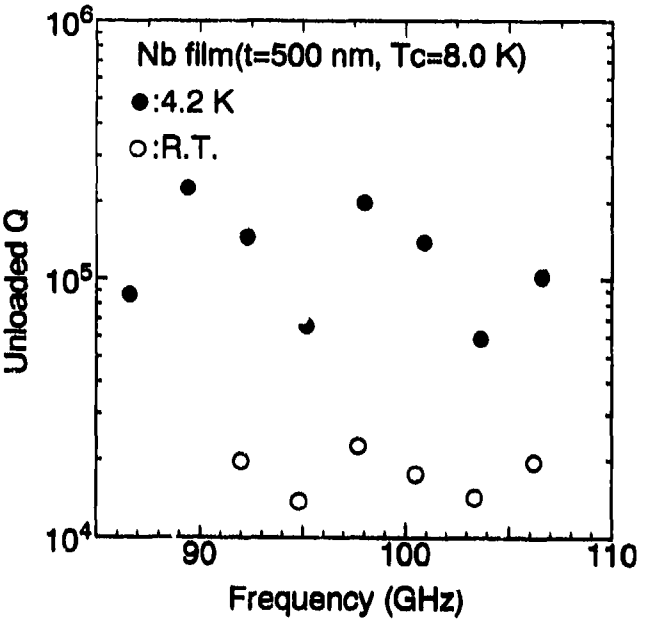

Fig.2. Frequency dependence of the unloaded Q for a Nb thin film at 4.2K and room temperature.

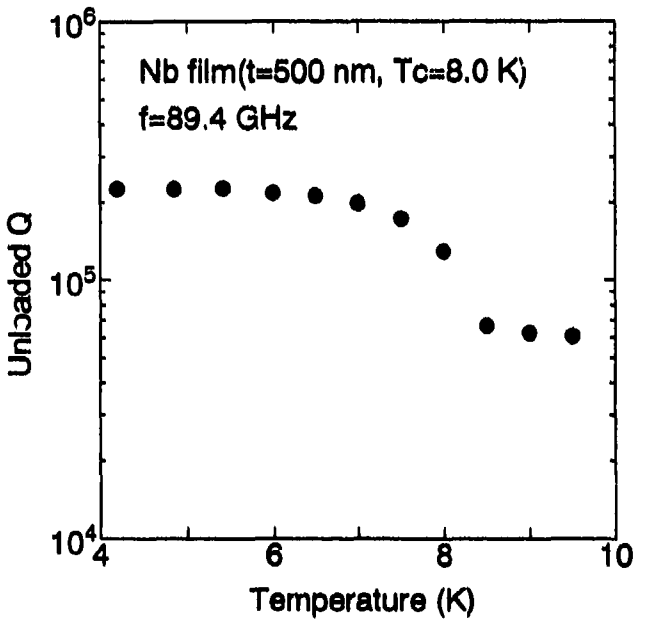

Fig.3. Temperature dependence of the unloaded Q for a Nb thin film at 89.4 GHz.

A New method for complex spectral measurements in millimeter and submillimeter frequency range

Latyshev A.B., Loukianov D.A., Semenov A.V.

General Physics Institute, Russian Academy of Science, 117942, Moscow, Russia

ABSTRACT

New method for measuring complex transmission or reflection coefficients has been proposed and demonstrated using a simple setup. High measurement quality was achieved: phase sensitivity ~ 0.005 rad., amplitude reproduceability ~1%, dynamic range to ~10^7 (previously 10^4), phase shift range 10^5. It is effective for BWO-Spectroscopy due to the absence of any mechanical adjustments during electronic frequency scan.

2. INTRODUCTION

This method is developed primarily for application in the BWO-Spectroscopy of millimeter and submillimeter frequency range [1], [2]., but in principle it may be useful for other applications. BWO-Spectroscopy is monochromatic spectroscopy with the Backward-Wave-Tube-Oscillator (BWO) as a source of radiation. The most attractive feature of the BWO is electronic frequency scanning.

The BWO-Spectroscopy has been greatly developed during last several decades mostly in Russia. The modern BWO-Specrometer is a computer controlled instrument with the possibility to get frequency dependences of complex transmission or reflection factors with high level of automation of measurement. The most popular measurement routine for such spectrometer consists in aquiring the whole complex spectrum by two non-equivalent steps: the measurment of amplitude and phase spectra of the object [2]. The quasioptical scheme of such spectrometer comprise a two-beam interferometer, but during amplitude spectra measurements it is not used, therefore the dynamic range of measurements is limited. The phase shifts are measured by so-called "compensation method"; it means, that some precise feedback electro-mechanic system compensates the necessary path difference in the interferometer during frequency scan. It makes the registration time of phase spectra longer then that for intensity, and reduces the accuracy of phase measurements and limits the range of phase to be measured.

There is another design of BWO-spectrometer, which enables whole complex spectra measurement without any precise mechanic displacement of quasioptic elements during frequency scan [3], [4], [5]. The process of getting of complex spectrum consists of two steps, each technically equivalent to the registration of amplitude spectrum. The usage of this method improves the main parameters of complex spectra: accuracy, time of work, simplicity etc.

The new method is the modification of [5], but with expanded dynamic range. That means the capability to measure the samples with very small transmission or reflection as well as samples with great variation of above factors during frequency scan. This effect is achieved primarily by inserting the modulator into the interferometer.

3. DEMONSTRATION

Hereafter the series of complex spectra, which demonstrate this method is shown. The potential of this method is even higher then demonstrated here because the spectrometer was not built specially, but only slightly modified for its implementation.

In Fig. 1 the complex transmission spectrum (in polar coordinates: amplitude and phase) of 10mkm thick mylar-film is shown. This spectrum demonstrates the phase sensitivity of the method. One can see, that this method easily registrates not only mean value of the phase shifts in mylar film (3 degr.), but also its monotonic slope of 0.5 degr. for frequency span of 20%. The RMS deviation of phase shift from the linear is aproximately 0.5 degr. The sensitivity achieved is 10 times better then that for [2], but not as good as for [3], [4] and is nearly same as for [5].

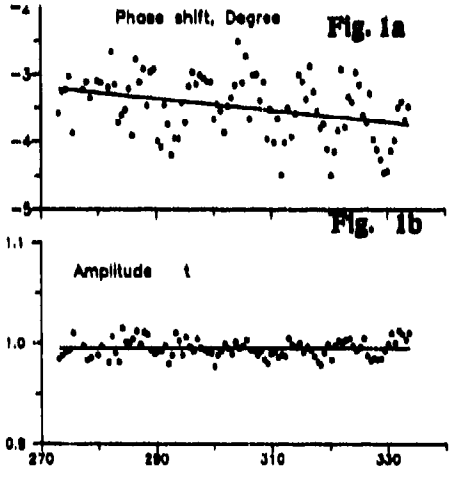

Fig. 1a

Fig. 1b

In Fig.2 and 3 the complex transmission of 28.5 mm thick glass plate is plotted. Fig.2 shows Cartesian real and imaginary parts of the complex transmission vs frequency. Nearly the same values were measured directly by this method. Fig. 3 shows the same spectrum in more usual polar coordinates. The goal of these plots is the demonstration both the expanded dynamic range (small transmission) and large phase shift measurement capability. The phase is changed over 2500 degr. (7 full turns) during frequency scan, yet not reaching any limit of the method. The principal restriction is only the monochromacity of the source (100,000 radian). The phase dependence is not limited to monotonic. The maximum measurable phase range in new method is 10^5 times better then in [2], 10^6 then methods [3], [4] and same as [5].

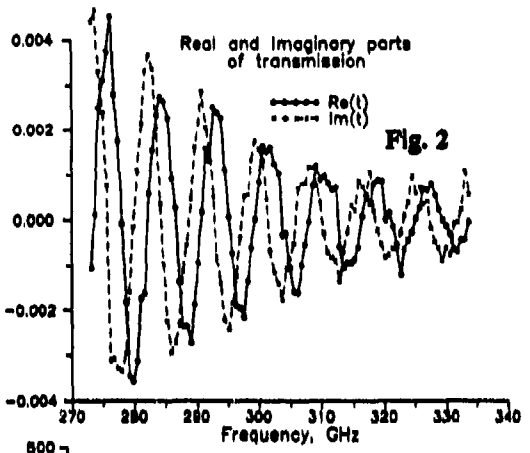

Fig. 2

Fig. 2-3 proves that this method is applicable for the transmission factors down to 10^{-7}, while [2], [3], [4], [5] failed to measure the transmission factors less then 10^{-4} with the same BWO and receivers (not cooled), so this sample is "opaque" for these methods. The real improvement is approximately 3 orders of transmission factor.

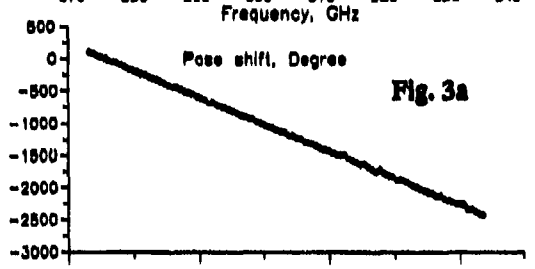

Fig. 3a

The capability to measure samples with large transmission contrast during single frequency scan is demonstrated by the transmission curves of Fabri-Perot resonator (Fig. 4). Resonator's two mirrors are 10 mkm thick metalised mylar films with power transmission of 0.0035 and 0.005. Thus power transmission contrast is greater then 100, yet not at the limit of this method. It is possible to measure the spectra even with the contrast of 10,000,000 (we have not such samples). This feature is 1000 times enhanced over [2], 100,000 times over [3] - [5]. The method [2] is capable to measure the spectra with contrast more than 100, but fails to measure a sample, shown on the Fig. 4.

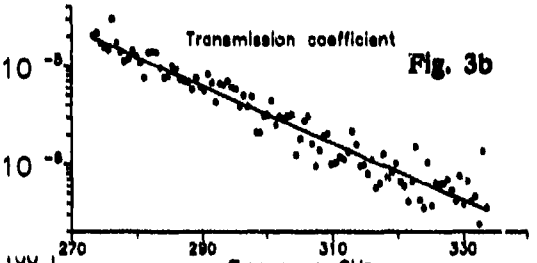

Fig. 3b

4. SUMMARY

The described method is unique not only for separate features (dynamic range, etc.) but also for the total combination. This method essentially exceeds the most popular compensation method [2] by all basic parameters. It can be successfully implemented in new spectrometers and other devices of millimeter-IR range.

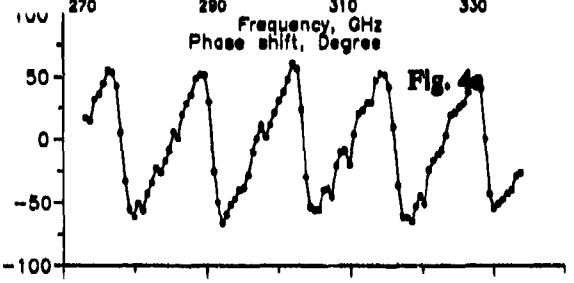

Fig. 4a

5. REFERENCES

1. N.A. Irisova "Metrica Submillimetrovyh Woln", Vestnik Academii Nauk SSSR, 1968, T. 10, ctr.63-70.(in Russian).

2. A.A.Volkov, Yo.G.Goncharov, G.V.Kozlov at al., "Dielectric Measurements in the Submillimeter Wave-length Region", Infrared Physics, 1985, Vol.25, N1/2, p.369-373.

3. A.B.Latyshev, D.A.Loukianov, I.M.Fedotova, "Method Izmereniya Phaso-chastotnyh Spectrov na Quasiopticheskom LOV-Spectrometre Millimetrovogo i Submillimetrovogo Diapazonov", Pribory I Tehnika Experimenta, 1990, N1, str.143-144. (in Russian).

4. E.A.Vinogradov, N.A.Irisova, A.B.Latyshev, D.A.Loukianov, "Sposob Opredeleniya Fazovogo Razbalansa Dvuhluchevogo Interferometra CWCh-IK Diapazonov", Patent USSR, N1237992, Cl. G 01 R 25/04.

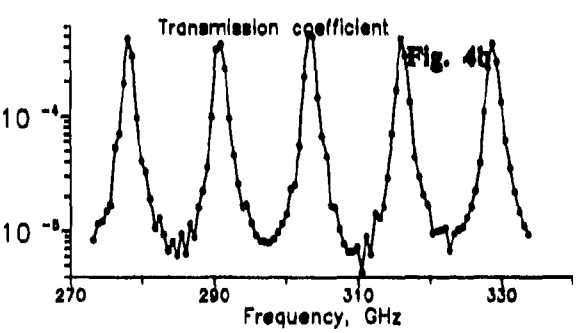

Fig. 4b

5.A.B.Latyshev, "Sposob Opredeleniya Fazovogo Razbalansa Dvuhluchevogo Interferometra", Patent USSR, N1575714, Cl. G 01 R 25/02.

High microwave pulse power measurement in a free space

Mindaugas Dagys, Žilvinas Kancleris, Rimas Simniškis

Semiconductor Physics Institute, Goštauto 11, Vilnius 2600, Lithuania

and

Mats Bäckström, Ulf Thibblin, Bo Wahlgren

SAAB Military Aircraft, Linköping S-581 88, Sweden

ABSTRACT

The unit consisted of a resistive head, horn antenna and matched load has been used to measure high microwave pulse power density in a free space. Experiments were carried out in S-, X- and Q-band at a frequency 2.75, 9.2 and 34.2 GHz, respectively. It was established that with a help of such unit microwave pulse power density up to a few hundreds of kW per m^2 can be measured.

1. INTRODUCTION

On the one hand, high frequency strong electromagnetic field becomes inalienable part of environment, since radiolocation and telecommunication systems are continuously growing up in the world. On the other hand, it was proposed to use microwaves (mw) as a directed energy weapons against electronic systems. Thus, in order to increase reliability of the electronic equipment used in the aircraft and satellites testing of this equipment for mw radiation has to be performed. For this purpose short high power mw pulses are usually used. Therefore for mw power control the problem of great importance is to develop sensors which will be able to measure high power mw pulses in a free space.

2. EXPERIMENTAL SETUP

To perform mw power density measurements in a free space we have developed resistive heads where a resistive sensor[1] was used as a sensitive element. The resistive sensor was mounted in the waveguide and was also connected into DC circuit together with a current source. When mw pulse reaches the sensor, electrons are heated[2] by mw electric field and the resistance of the sensor increases. Being appeared in DC circuit voltage pulse was amplified 5-6 times by properly shielded preamplifier. Maximum output signal was 10 V. Three power heads being able to detect mw pulse power up to 100 kW, 5 kW and 2 kW in S-, X- and Q-band waveguide, respectively, were designed. Voltage standing wave ratio was less than 1.2 for Q-band head and less than 1.1 at lower frequency bands. Horn antenna was employed to generate the electromagnetic field in a free space. Analogous horn antenna connected to the power head together with the matched load serves as mw power density detector. Mw pulse duration was 2 μs, repetition rate was 12.5 Hz and maximum available mw pulse power was 100 kW, 50 kW and 2 kW in S-, X- and Q-band at a frequency 2.75, 9.2 and 34.2 GHz. Horns with cross-sectional area 0.106, 0.0121 and $9.9 \cdot 10^{-4}$ m^2 were employed.

3. EXPERIMENTAL RESULTS

If a longitudinal axis of the horn antenna is supposed to be adjusted parallel to mw power flux, mw power getting into waveguide P will be obtained from simple geometrical consideration

$$P = W_p \eta S, \tag{1}$$

where W_p is a mw power flow density (Pountings vector) in a free space, η is the efficiency and S is a cross-sectional area of the horn antenna. We have measured mw pulse power P getting into waveguide when the receiving horn antenna is situated at some distance L from the transmitting one. Then assuming that the efficiency of the horn antenna $\eta = 1$ and making use of expression (1) the mw power density in a free space has been determined.

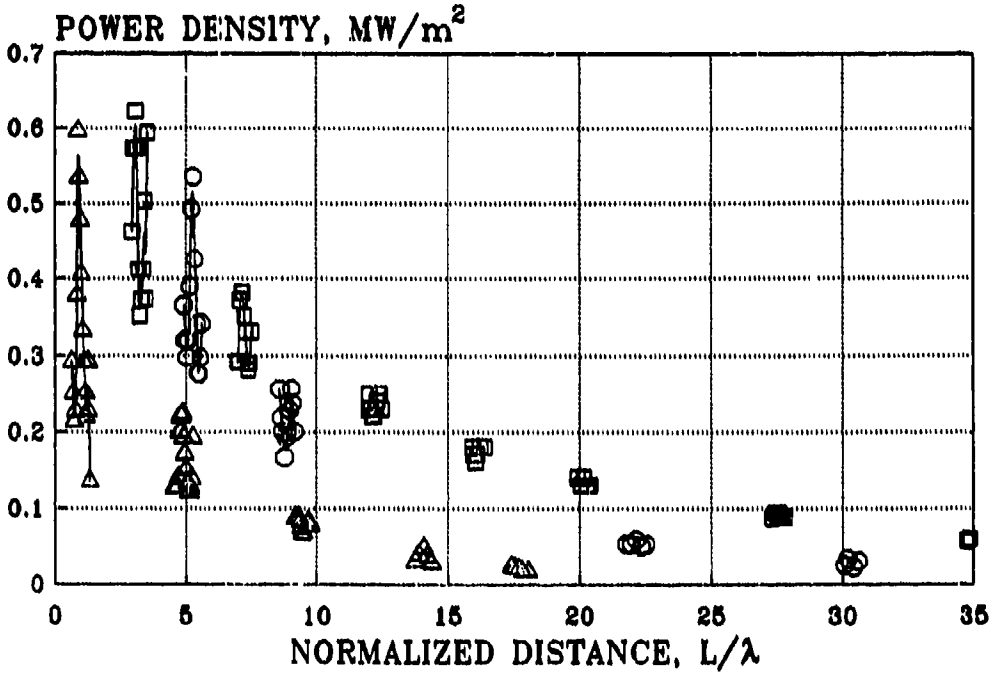

Fig. 1. Microwave pulse power density dependence on the normalized distance between horn antenna. Triangles, circles and squares correspond to S-, X- and Q-band, respectively.

Experimentally determined mw pulse power density dependencies on the distance normalized to wave length for all frequencies are shown in Fig. 1. It is seen that at a small distance ($L < 10\ \lambda$) standing wave between horn antennas is observed. As it could be expected, we get that at greater distance pulse power density decreases as L^2. There is no doubt that the efficiency of the horn antenna is lower than unity and this fact has to be taken into account if precise measurement of W_p is attempted. Switching off DC supply of the resistive sensor we had an opportunity to check up the value of parasitic signal. Our investigation showed that in the worst case the parasitic signal ranges less that 7% of useful one.

Concluding it has to be pointed out that high level pulse power density in a free space has been measured for the first time making use of resistive head connected to the horn antenna. Our investigation revealed that with a help of resistive heads mw pulse power density up to a few hundred of kW/m^2 can be measured.

4. REFERENCES

1. R. Baltuśis, M. Dagys, R. Simniškis, "Resistive sensors for high pulse power microwave measurement", Proceedings of 22nd European Microwave Conference, pp. 169-173, 1992.
2. E. M. Conwell, High field transport in semiconductors, Academic Press, New York and London, 1967.

The millimeter waves power transducer.

K.Repšas, R. Vaškevičius and V. Orševskis

Semiconductor Physics Institute, Goštauto 11, 2600 Vilnius, Lithuania

ABSTRACT

The transducer, based on the hot electrons termo e.m.f. in semiconductors, for CW and pulse microwave field or power indication and measurement is presented. This transducer have sensitivity 400÷600 mV/W in 4÷8 mm wave length range and can be used up to CW power about 10 W.

1. INTRODUCTION

In practice it is important to know microwave pulse form, electric field strength and pulse power. As an example can be the determination of these quantities, when a gas plasma is heated with high microwave power. The waves frequency is choosing the same as ion-cyclotron (20 MHz) or electron-cyclotron (2÷8 GHz) frequency.

Since the reflection of power from gas plasma is large, the wattmeter, witch is based on the Hall effect, usefully can be used for measuring of power, absorbed in plasma. Such a wattmeter we are constructed for electromagnetic wave with 18 m length together with scientists from Atomic energy institute of Russian Academy of Science. But the Hall effect can not be used for 2÷8 mm waves, because the wave length is very small. The employment of microwave detectors with p-n or Shottky junction often is impossible for high power since the reading of these detectors are instability and they are sensitive for impulse interference.

In this report is presented the transducer witch is based on volumetric effect of the hot electrons termo e.f.m. in the asymmetric doping silicon n^+-n-n^+ junction with different areas of n^+-n junctions.

2. THE PRINCIPLE OF ACTION, TECHNOLOGY AND A MEASURING TECHNIQUE.

The principle of the work of this transducer is based on the e.m.f., witch arise in above mentioned n^+-n-n^+ junction, when free charge carriers are heated in homogeneous isotropy semiconductor with high asymmetric inhomogeneous electric field[1], but the difference is that a inhomogeneous and asymmetric electric field was formed both asymmetric doping of semiconductor and his geometric form[2,3].

The transducer was prepared from the n^+-type silicon monocrystal with 10÷28 Ωcm specific resistivity. Plates with 1 mm thickness was cuted out in [111] plane. n^+ area on the one side of plate was formed by phosphor diffusion on 1 mm^2 plane and on another side -n^+ junction with 20 μm diameter. The difference of doping depth was formed by different time of heating. On n^+ areas (Cr + Pd) metals were coated by evaporation in vacuum and later on (V + Cu) - in argon atmosphere at T = 400°C. These planes were mounted in usual microwave detector frames and these were placed in waveguide detector sections. The metallic sonde was pressed to small n^+ area.

Transducers of 4 mm and 8 mm H type wave length were graduated with standard wattmeters in CW generation regime with error ± 6%.

3. RESULTS

In figure 1 are showed typical transducers output voltage dependencies for 8 mm wave length (curve 1) and 4 mm wave length (curve 2) from the power and in fig. 2 - dependencies of this output voltage from mw electric field (curve 1 - λ = 8 mm, 2 - λ = 4 mm). As shown in the figure 2 transducers have a right dependencies in the wide range of electric fields. In the table are presented main specifications of transducers.

Transducer type	Inside w/q size [mm]	Wave length [mm]	Sensitivity [V/W]	Max.CW power [W]	Output resist [kΩ]	Error of grad.
A	7,2 × 3,4	8	500	12	1	± 5
B	3,6 × 1,7	4	500	8	3	± 6

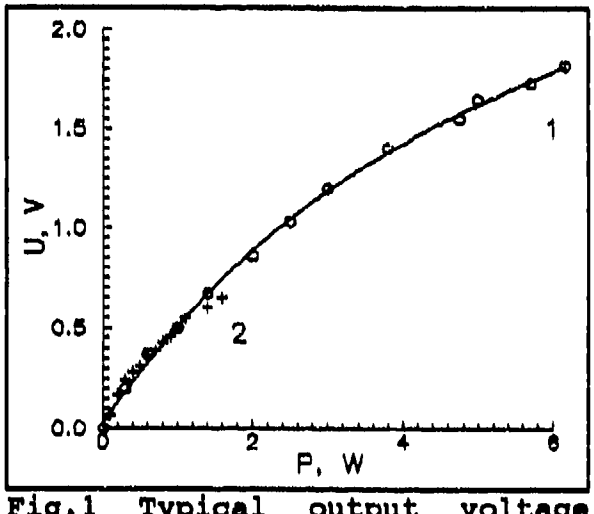

Fig.1 Typical output voltage dependence from the power.

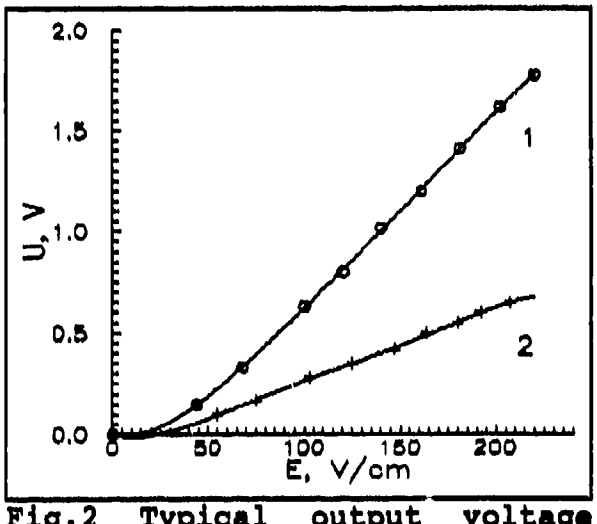

Fig.2 Typical output voltage dependence from mw electric field.

4. REFERENCES

1. S. Ašmontas, J. Požela, K. Repšas. The effect of e.m.f. and asymmetric of electric conductivity in homogeneous isotropic semiconductor. The discovery diploma Nr. 185. USSR, BI (Biuleten otkritij), 1977, No.39, p.1.

2. V. Blonskis, O. Vasilec, J. Požela, K. Repšas. Asymmetric n^+-n-n^+ structure in high mw electric field. Lietuvos fizikos rinkinys, 1981, Vol. XXI, No.6, p. 80-86.

3. S. Ašmontas, A. Olekas, J. Požela, R. Lapinskas. Voltamperic characteristics of point contacts with n^+ - n junction. Physics and technics of semiconductors (FTP), 1977, Vol. 11, No. 7, pp. 1289-1299.

Fourier transform infrared spectrometer using delta-sigma modulation for high dynamic-range spectrometry

Kei-ichiroh Minami and Satoshi Kawata
Department of Applied Physics, Osaka University, Suita, Osaka 565, Japan

Application of delta-sigma modulation (ΔΣ) to Fourier transform infrared (FT-IR) spectrometer is presented. This quantization features sampling of an interferogram at a rate higher than the Nyquist rate and a nonlinear feedback system with the 1-bit quantizer. The experimental results of IR absorption measurement demonstrate the practicality of the proposed method. The dynamic-range with this method can exceed over the limit of ordinary A/D converter.

INTRODUCTION

Use of a broadband source in absorption spectroscopy results in an interferogram with the large peak at the zero path-length difference and the trivial variation elsewhere. Although high dynamic-range is required for the A/D conversion of the interferogram [1], the dynamic-range of an ordinary A/D converter is limited by 16-20 bits. The gain-ranging is often used to virtually increase the dynamic-range while it improves by a few bits. Several alternative approaches have been proposed to overcome the dynamic-range limitation [2].

For carrying out high dynamic-range spectroscopy, we have proposed use of delta-sigma (ΔΣ) modulation to Fourier transform spectrometry [3]. In this method, the interferogram is oversampled at the rate that is much higher than the Nyquist sampling rate. After integrating the sampled interferogram the difference between the integrated result and the previous one is digitized to 1-bit binary sequence by a comparator within the nonlinear feedback loop [4]. This quantization is recently getting popular in the fields of acoustics/speech processing. We applied this ΔΣ modulation to FT-IR spectrometer and measured IR absorption spectra with the developed spectrometer.

FT-IR SPECTROMETER

We implemented a ΔΣ modulator, instead of ordinary A/D converter in a real FT-IR spectrometer for demonstrating the practicality of the proposed method. The spectrometer used was JEOL Model JIR-3510. We used a ΔΣ modulator of second order, CS-5316 of Crystal semiconductor, which has two feedback loops. The oversampling was performed with phase-lock-loop circuits by frequency multiplexing of the He-Ne fringe signal, which is used for monitoring the path-length difference of the interferometer. From the binary interferogram from the modulator, the spectrum is reconstruction with a FFT or a DFT for the significant spectral range.

Dynamic-range of the second-order modulator increases by 2.5 bits as doubling the sampling rate. For the sampling rate in our setup that was 64-times higher

than the Nyquist rate, the dynamic-range equivalent to ~13-bit A/D converter is anticipated for a spectral range of 0 - 4000 cm^{-1}.

EXPERIMENTAL RESULT and DISCUSSION

Figure 1(a) shows IR absorption spectrum of polystyrene film measured with the developed spectrometer. For comparison, the spectrum of the same sample measured with the same spectrometer but quantized with a 16-bit A/D converter is shown in Figure 1(b). Absorption peaks of the sample observed in Fig. 1(a) meet with those of Fig. 1(b), without occurrence of spurious peak.

The dynamic-range with this method can be enhanced by 1) increasing the sampling rate or 2) utilizing the modulator of higher order. In practical applications, the sampling rate is limited by stability of the interferometer and the He-Ne laser; if the sampling rate is too high, the spectrum is degraded by the sampling jitter. On the other hand, use of a high-order modulator is more promising to earn the dynamic-range exceeding over the limitation of the ordinary A/D converter; for example, a fourth-order modulator provides 23-bit dynamic-range at 128x oversampling.

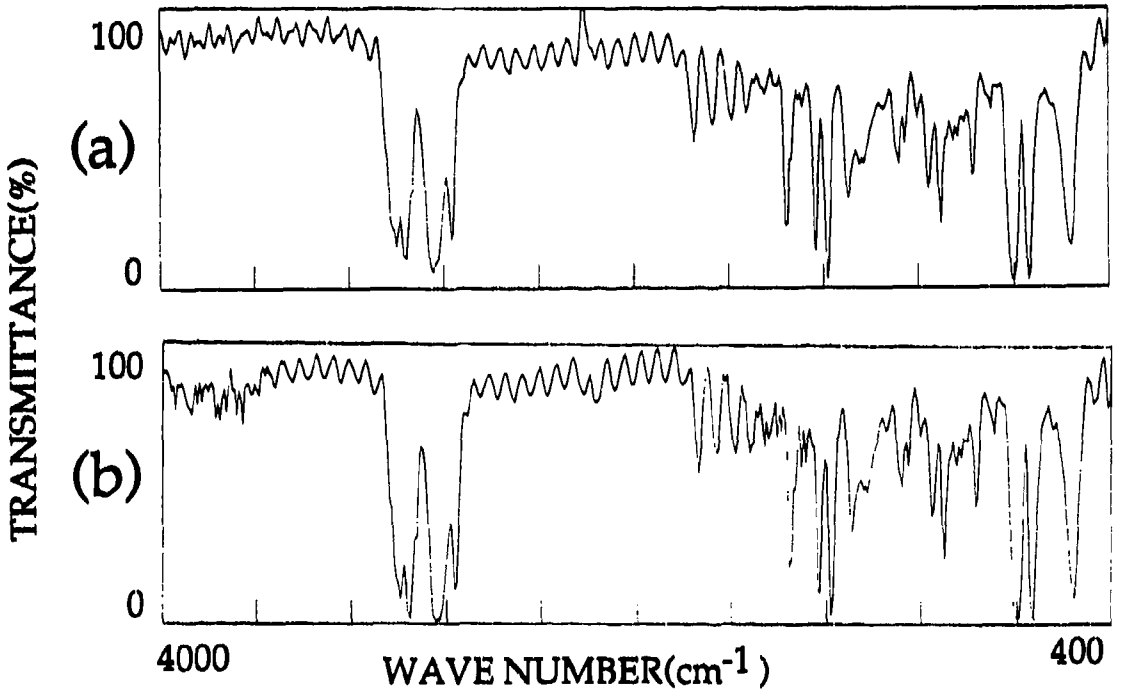

Fig.1. Absorption spectra of polystyrene reconstructed from interferograms quantized with (a) a ΔΣ modulator of second-order and (b) a 16-bit A/D converter

REFERENCES

1. P. R. Griffth et al., *Fourier Transform Infrared Spectrometry* (Wiley, 1986)
2. K. Minami et al, *Appl. Opt.*, **31**, 6322-6327 (1992)
3. K. Minami et al., "Dynamic range enhancement of FT-IR spectrum measurement using delta-sigma modulation," *Appl. Opt.* (in press)
4. H. Inose et al, *Proc. IEEE*, **51**, 1524-1535 (1963)

New FIR Laser Assignments in the ν_5, ν_7, and ν_8 Excited States of $^{13}CD_3OH$ Methanol

Li-Hong Xu and R.M. Lees

CEMAID and Physics Department, University of New Brunswick, Fredericton, N.B., Canada E3B 5A3

Abstract

High-resolution Fourier transform spectra of $^{13}CD_3OH$ methanol have been re-examined between 800 - 1350 cm^{-1}. In addition to further fundamental understanding of its complex torsion-vibration energy structure, several new FIR laser assignments have been made, which involve IR pump transitions to the ν_5, ν_7, and ν_8 CD_3-deformation, CO-stretching and CD_3-rocking states. The assignments have been used to confirm interesting perturbations in the energy level systems.

Introduction

FIR laser emission from optically pumped $^{13}CD_3OH$ has been an intense subject studied by several research groups around the world since the discovery of the strong 127 μm FIR laser line, the second most efficient known, pumped by the 10P(8) CO_2 laser line. More than 150 FIR laser lines have been reported to date for this species. However, only about 40 lines have been confidently assigned to specific energy states [1,2]. The difficulty in FIR laser assignments for $^{13}CD_3OH$ arises on the one hand from a lack of experimental information on precise frequency measurements, IR pump offsets and relative IR and FIR polarizations, and on the other from the crowded and complex nature of the spectra.

IR Spectra in the 800-1350 cm^{-1} Region

High-resolution spectra were obtained on a modified DA3.002 Bomem instrument at resolutions of 0.002 and 0.003 cm^{-1} from 800-1030 and 1000-1350 cm^{-1}, respectively, with the latter being at higher pressure and path length to enhance the weaker bands. In addition to possible hot bands, seven fundamentals lie in this region as shown in Table 1 from the latest force field calculation [3], and four of them have large transition strength and give strong spectra. We have been able to carry out extensive spectroscopic analyses for the ν_5, ν_7, and ν_8 bands [4,5]. The analysis of the ν_4 band is still in progress.

New FIR Laser Assignments

In this work, we present six further IR-pump/FIR-laser systems, listed in Table 2. System 1 involves the CD_3-deformation state, which has a larger rotational B-value than other known states. This results in interesting J-localized perturbations as the deformation levels cross through nearby states, and both the $(n\tau K)^v = (016)^{Def}$ and $(025)^{Def}$ states are perturbed as seen from the Δ_2 second differences in Table 3. However, the good agreement between the FIR laser wavenumbers from our loop technique and reported heterodyne measurements confirms our assignments of these IR series as given in Table 3.

In Systems 2, 3 and 4, the FIR laser transitions involve excited torsional levels of the CO-stretching state. Closed loops for these systems are valuable checks of the spectroscopy for these weak transitions, confirming the FIR laser assignments and also predicting more accurate wavenumbers and new lines. In Ref. 1, we tentatively proposed the 10P(42)+5MHz IR pump as P(121,14) to the CD_3-rocking state, based on observation of a few nearby n = 1 subbranches. However, all n = 1 series have now been assigned up to K = 6 for all torsional symmetries, and unfortunately no room is left for our original IR pump assignment as the CD_3-rock. An unknown state is required around 1265 cm^{-1}, about 23 cm^{-1} above the (030) CD_3-deformation state. The assignment scheme in Table 2 is supported by near-zero loop defects from closed loops including the observed FIR laser lines L_b and L_c themselves.

References

1. Li-Hong Xu, R.M. Lees, I. Mukhopadhyay and J.W.C. Johns, J. Mol. Spectrosc. **153**, 181-196 (1992).
2. Li-Hong Xu and R.M. Lees, Int. J. IR & MM Waves **14**, 569-587 (1993).
3. F.C. Cruz, A. Scalabrin, D. Pereira, P.A.M. Vazquez, Y. Hase and F. Strumia, J. Mol. Spectrosc. **156**, 22-38 (1992).
4. Li-Hong Xu, R.M. Lees, I. Mukhopadhyay, J.W.C. Johns and G. Moruzzi, J. Mol. Spectrosc. **157**, 447-466 (1993).
5. Li-Hong Xu, Ph.D. thesis, Univ. of New Brunswick, 1992.

Table 1. $^{13}CD_3OH$ Fundamental Wavenumbers (cm^{-1})

1	2	3	4	5	6
ν(OH)	ν(CD_3) asym	ν(CD_3) sym	δ(COH)	δ(CD_3) sym	δ(CD_3) asym
3686.1	2224.2	2048.0	1286.4	1108.5	1059.1
7	8	9	10	11	12
ν(CO)	ρ(CD_3)	ν(CD_3) asym	δ(CD_3) asym	ρ(CD_3)	τ(CD_3)
978.8	852.4	2198.7	1060.8	882.8	258.2

Table 2. Assignments of FIR Laser Lines in $^{13}CD_3OH$ Optically Pumped by a CO_2 Laser

System	CO_2 + Offset [ν in cm^{-1}]	IR Absorption [ν_{obs} in cm^{-1}]	$(n'\tau'K',J')v'$	→	FIR Laser Transition[a] $(n''\tau''K'',J'')v''$	Line Label[a]	ν_{obs}[b] [cm^{-1}]	Rel Pol	ν_{calc} [cm^{-1}]
#1	9R(52)	P(016,15)	$(016,14)^{Def}$	→	$(016,13)^{Def}$	L_a	18.4248*	[||]	18.4248
	1095.6636	1095.6623		→	$[(025,14)^{Def}]$	[L_b]		[⊥]	[13.1974]
				→	$(025,13)^{Def}$	L_c	31.4904*	[||]	31.4899
#2	10R(46)	R(117,8)	$(117,9)^{co}$	→	$[(117,8)^{co}]$	[L_a]		[||]	[11.4525]
	990.6169	990.6205		→	$[(126,9)^{co}]$	[L_b]		[⊥]	[52.0067]
				→	$(126,8)^{co}$	L_c	63.4199*	[||]	63.4196
#3	10R(24) - 10MHz	Q(234,5)	$(234,5)^{co}$	→	$[(234,4)^{co}]$	[L_a]		[⊥]	[6.3601]
	978.4720	978.4714		→	$[(113,5)^{co}]$	[L_b]		[||]	[155.7559]
				→	$(113,4)^{co}$	L_c	162.1218*	⊥	162.1214
#4	10P(34) - 119MHz	P(114,34)	$(114,33)^{co}$	→	$[(114,32)^{co}]$	[L_a]		[||]	[41.9268]
	930.9975	930.9944		→	$(123,33)^{co}$	L_b	66.83	⊥	67.0354
				→	$[(123,32)^{co}]$	[L_c]		[||]	[108.8970]
#5	10P(40) + 130MHz	P(030,39)	$(030,38)^{co}$	→	$(030,37)^{co}$	L_a	48.68	∥	Tentative
	924.9783	924.9775		→	$(311,38)^{o}$	L_b	49.91	⊥	Assignment
#6	10P(42) + 5MHz	P(130,14)	$(130,13)^{?}$	→	$(130,12)^{?}$	L_a	16.53	∥	16.5485
	922.9145	922.9144		→	$(121,13)^{R}$	L_b	67.4863*	⊥	67.4879
				→	$(121,12)^{R}$	L_c	84.0289*	∥	84.0284

[a] Transitions in brackets are predicted.

[b] Values with asterisks are converted from accurate frequency measurements, using 29979.2458 MHz/cm^{-1}.

Table 3. (nτK) = (025) and (016) Transitions in the CD_3-Deformation Band of $^{13}CD_3OH$

J	R(J)	Δ_1	Δ_2	Int.	J	R(J)	Δ_1	Δ_2	Int.
5	1119.49843	1.48166		0.8379	5				
6	1120.98009	1.50323	0.02157	0.8315	6	1120.75404	1.69514		0.8802
7	1122.48332	1.51698	0.01375	0.7934	7	1122.44918	1.71186	0.01672	0.5615
8	1124.00030	1.50690	-0.01008	0.7503	8	1124.16104	1.72475	0.01289	0.7640
9	1125.50720	1.38397	-0.12293	0.7416	9	1125.88579	1.73480	0.01005	0.7476
10	1126.89117	2.05647	0.67250	0.7968	10	1127.62059	1.74212	0.00732	0.7374
11	1128.94764	1.56425	-0.49222	0.7416	11	1129.36271	1.74676	0.00464	0.5662
12	1130.51189	1.61451	0.05026	0.7218	12	1131.10947	1.74863	0.00187	0.5497
13	1132.12640	1.64028	0.02577	0.7080	13	1132.85810	1.74643	-0.00220	0.7026
14	1133.76668	1.65890	0.01862	0.5256	14	1134.60453	1.73744	-0.00899	0.7247
15	1135.42558	1.67351	0.01461	0.6885	15	1136.34197	1.71534	-0.02210	0.7332
16	1137.09909	1.68620	0.01269	0.6612	16	1138.05731	1.66265	-0.05269	0.7343
17	1138.78529	1.69657	0.01037	0.7171	17	1139.71996	1.53954	-0.12311	0.7612
18	1140.48186	1.70504	0.00847	0.7327	18	1141.25950	1.31556	-0.22398	0.8167
19	1142.18690	1.70701	0.00197	0.7378	19	1142.57506			0.8798
20	1143.89391			0.7437	20				

ASSIGNMENT OF THE FIR AND IR ABSORPTION SPECTRA OF THE METHANOL ISOTOPIC SPECIES

Giovanni Moruzzi[1], Franco Strumia[1], Ronald. M. Lees[2], Li-Hong Xu[2], Brenda P. Winnewisser[3], Manfred Winnewisser[3] and Indranath Mukhopadhyay[4]

[1] *Dipartimento di Fisica dell'Università di Pisa*
Piazza Torricelli 2, I-56126 Pisa
[2] *Department of Physics, University of New Brunswick*
Fredericton, New Brunswick, Canada E3B 5A3
[3] *Physikalish-Chemisches Institut der Justus-Liebig-Universität Giessen*
Heinrich-Buff-Ring 58, D-W6300 Giessen
[4] *Government of India, Department of Atomic Energy*
Centre for Advanced Technology, Indore 452013, India

We are performing a systematic investigation of the infrared and far-infrared absorption spectrum of various isotopic species of methanol by high-resolution Fourier transform spectroscopy.

The entire spectra of CH_3OH and CD_3OH between 30 and 1250 cm^{-1} have been measured in several segments on the Bruker Fourier transform spectrometer of the Justus Liebig University of Giessen. Measurements for the isotopic species $CH_3^{18}OH$, $^{13}CH_3OH$, $^{13}CD_3OH$ and CH_2DOH are in progress on the same spectrometer.

Due to the large number of measured lines for each isotopic species (the order of magnitude is 100,000 lines between 30 and 1250 cm^{-1} for each species) we have developed computer software for the line assignment. We started our assignment work with an assignment program package based on a Taylor series expansion of the energy levels (Ref. 1 and references therein). This program performs extremely well as long as the investigated energy levels are not perturbed by nearby levels via Fermi resonances. When Fermi resonances are present, the sequence of levels sharing all the quantum numbers but J may not be well-behaved in the $J(J+1)$ energy expansion. Fermi resonances are quite common for the vibrationally excited levels of all the isotopic species of methanol, but relatively rare for the ground vibrational state of the normal species CH_3OH. Thus, we could use our "Taylor" assignment program for the assignment of the CH_3OH absorption spectrum without encountering particularly relevant problems. Up to now, we have assigned more than 36,000 lines of CH_3OH.

On the contrary, Fermi resonances are more frequent in CD_3OH because of the larger moment of inertia of CD_3 and of the smaller vibrational frequencies. This has led us to develop a new program, where the Taylor expansions are still used for predicting transitions involving new levels, but the energies of the levels involved in already assigned transitions are evaluated by the Rydberg-Ritz combination principle. That is, we evaluate the level energies E_i which minimize

$$\chi^2 = \sum_{i,j} \frac{(E_i - E_j - \nu_{ij})^2}{\epsilon_{ij}^2}, \qquad (1)$$

where E_i and E_j are the ith and jth energy level of the molecule, ν_{ij} is the experimental frequency of the corresponding transition, and ϵ_{ij}^2 the experimental accuracy. We have presented in previous works [1,2] our first results on the assignment of the CD_3OH spectrum and discussed the pertur-

bations and the forbidden $\Delta K = 2$ and $\Delta K = 3$ transitions which we have been able to assign for this species. We have assigned 20000 lines of CD_3OH up to now.

The assignment of the $^{13}CD_3OH$ has so far utilized a standard spreadsheat program [3]. About 20,000 lines comprising R, Q and P branches of about 250 ($n\tau K$) transitions have been assigned in the 14 - 240 cm^{-1} region and IR region, which had been measured on the modified Bomem DA3.002 Fourier transform instrument at the Herzberg Institute of Astrophysics in Ottawa at 0.002 cm^{-1} resolution. The analysis of the spectrum from Giessen utilizing the Taylor development program has just started.

More recently, we have started the assignment of the FIR absorption spectrum of CH_3OD. Also for this species we have found some important Fermi resonances within the vibrational ground state, which we have been able to follow along the level sequence with our new program. 3000 lines have been assigned up to now.

Simultaneously, we have also started to tackle the FIR absorption spectrum of the methyl-asymmetric species CH_2DOH. The Taylor expansions allow to follow many line series relatively well, and to assign the J and K values of the involved levels. But the complexity of the spectrum and the looser selection rules make more complete assignments a difficult task, at least for the moment.

---

[1] G. MORUZZI, R.M. LEES, L.H. XU, B.P. WINNEWISSER AND M. WINNEWISSER: in *12th International Conference on High Resolution Infrared and Microwave Spectroscopy*, Dobříš, September 7-11, 1992, page K2

[2] G. MORUZZI, R.M. LEES, L.H. XU, B.P. WINNEWISSER AND M. WINNEWISSER: in *17th International Conference on Infrared and Millimeter Waves*, Richard J. Temkin, Editor, Proc. SPIE 1929, page 238 (1992)

[3] L.H. XU, R.M. LEES, I. MUKHOPADHYAY, J.W.C. JOHNS AND G. MORUZZI: J. Mol. Spectrosc., **157**, 447 (1993)

Injection seeding of a pulsed far infrared molecular gas laser

H.P.M. Pellemans, J. Burghoorn,† T.O. Klaassen, W.Th. Wenckebach

Faculty of Applied Physics, Delft University of Technology, The Netherlands
†currently with the Max-Planck-Institut für festkörperforschung
Hochfeld-Magnetlabor, Grenoble, France

Abstract

The operating pressure of a FIR laser pumped by a Q-switched CO_2 laser can be increased by injection seeding it with a low-power, quasi-cw FIR laser. This increase in operating pressure is a result of an increased energy conversion efficiency. A five-level rate equation model of the laser gives the same general results as the experiments.

Introduction

The pressure-broadened gain width of a FIR laser pumped by a Q-switched low-pressure CO_2 laser is insufficient to sustain short (< 10 ns) pulses. We show that by increasing the pressure of the lasing gas the FIR cavity can be used as a regenerative amplifier for short seed pulses.

Experimental results

In our experiments we used two laser systems. Both consist of a FIR laser pumped by a CO_2 laser. The CO_2 laser of the first system is Q-switched. It delivers output pulses of up to 10 kW peak power and a FWHM width of 350 ns. The FIR laser has up to 10 W peak power, with the same pulsewidth. The second laser system is used in a quasi-cw mode and produces FIR pulses of 50 mW and pulse durations of 1 ms. Seeding radiation is coupled into the pulsed FIR laser through the outcoupling mirror by means of a beam splitter. In our experiments we used the 118.8 μm line of CH_3OH, pumped by the 9P(36) CO_2 line. The output of the pulsed FIR laser was measured with a Schottky diode, enabling time-resolved measurements of the pulses. In figure 1 FIR pulseshapes observed at two different pressures, both with and without seeding, are shown. The CO_2 pulse starts at $t = 0$.

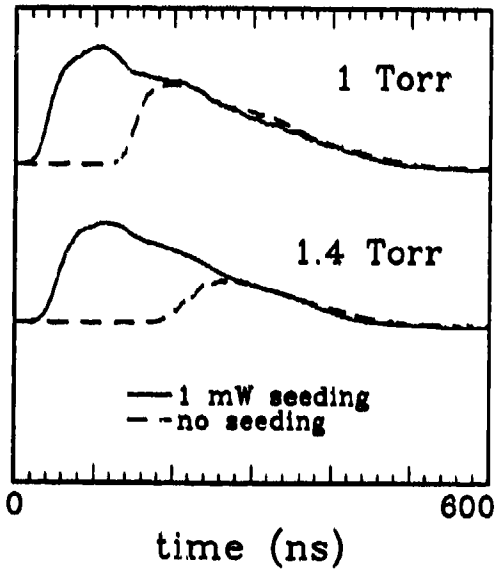

Figure 1: *FIR pulseshapes at different pressures with and without 1 mW of seeding.*

The amplitude of the pulses is larger in the seeded case and decreases less rapidly with pressure. The delay between the CO_2 pulse and the seeded pulse is shorter and increases less with pressure than the corresponding delay of the unseeded pulse.

The pulse amplitude as a function of the operating pressure is shown in figure 2. The increase in maximum amplitude is not very large, but the pressure range in which laser action is

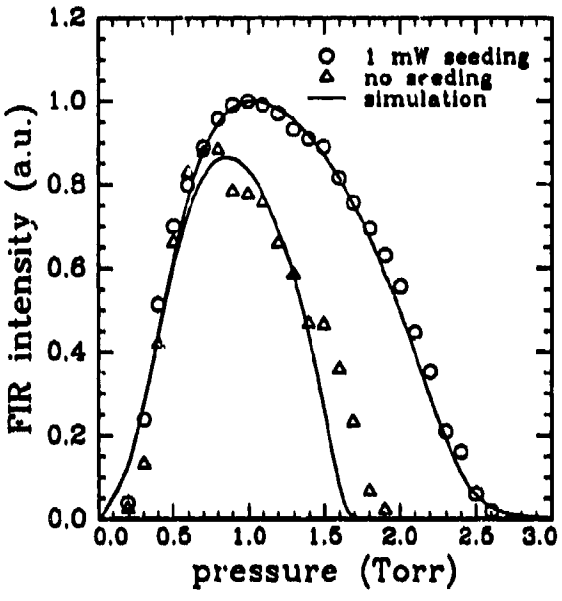

Figure 2: *observed pressure dependence of the FIR output with and without 1 mW of seeding. The simulation was fitted to the data of the seeded pulses.*

possible is extended by 40 %.

Measurements made of both the pulse amplitude and the delay between the FIR and the CO_2 pulses show a logarithmic dependency on the seeding power over at least four orders of magnitude. Extrapolation of the data to the value obtained without seeding results in a 'natural' seeding intensity which is in good agreement with the calculated value for the blackbody radiation density at 300 K ($\approx 10^{-13}$ Jm^{-3}).

Discussion

The data from our experiments were compared to numerical calculations. For these calculations we used a five-level rate equation model [1, 2]. In figure 1 the simulated curve for the pressure dependence is shown.

The logarithmic dependency of both pulse amplitude and pulse delay on the seeding intensity is reproduced by the model.

The effect of injection seeding can be understood using the results of the simulations. The main effect of increasing the pressure of the laser gas results from the increase of the fast ($\approx$ 70 $MHzTorr^{-1}$), pressure-dependent thermalization rate which counteracts the buildup of population inversion. At constant pump power therefore the small signal gain will decrease with increasing pressure, and it takes longer for the thermal background radiation to be amplified to such a level that the stimulated emission rate is comparable with the thermalization. As the pump pulse has a finite duration, the overall laser efficiency will decrease. If the pressure becomes too high, no significant laser action can develop anymore within the limited time span of the pump pulse. If we increase the level of the initial radiation density by injection seeding, a lower gain is sufficient to reach a significant FIR power level before the end of the pump pulse. Even a small amount of FIR power ($\approx$ 1 mW) is effective.

Conclusions

We have shown the feasibility of increasing the operating pressure – and thus the gain width – of a FIR cavity. When used as a regenerative amplifier, pumped with a CO_2 laser like the laser used in our experiments, operating pressures up to 10 Torr may be possible, resulting in a gain width of 230 MHz.

References

[1] J.O. Henningsen, H.G. Jensen, IEEE J. QE 11, no. 6, pp. 248-252 (1975)

[2] H.J.A. Bluyssen, R.E. Mackintosh, A.F. v. Etteger, P. Wyder, IEEE J. QE 11, no. 7, pp. 341-348 (1975)

Comparative Study of Gyrotrons Based on Thermionic and Cold Cathodes

AW Cross, SN Spark, K Ronald, ADR Phelps and W He

Department of Physics and Applied Physics
University of Strathclyde
Glasgow, G4 0NG, U.K.

A comparative investigation of the oscillating characteristics of a step-tunable (20 to 45GHz) gyrotron with the change in the electron beam source is reported. This was achieved by direct comparison between a gyrotron based on a two-electrode, cold cathode and a thermionic cathode configured within a magnetron injection gun.

It has previously been shown that a field-immersed, field emission cold cathode was able to emit large currents ≈800A with the application of both single and repetitive pulsed potentials of magnitude ≈-75kV. This system produced mm-waves in the frequency range 24 to 100GHz at power levels ≈6MW[1]. The pulse duration of the cold cathode gyrotron is normally limited by "gap closure" which is the process by which plasma from the cathode (and in certain cases from the anode) effectively "shorts out" the cathode-anode potential difference. The mildly relativistic electron beam terminates and a low voltage arc carries the current until the power supply is switched off. Gyrotrons depend inherently upon the interaction of an energetic electron beam with an applied magnetic field[2] and hence as soon as "gap closure" takes place the electromagnetic wave output ceases. With the use of a thermionic cathode continuous electron emission is possible. This allows the extension of the relativistic electron beam pulse duration beyond the 100ns to 500ns limit presently imposed by "gap closure". A high power (≈100kW), long pulse (≈50μs to 100μs) gyrotron has subsequently been developed utilising an electron beam forming system based on the three electrode configured thermionic cathode built by EEV Co fig(1). The operating parameters of both gyrotrons are compared in table 1.

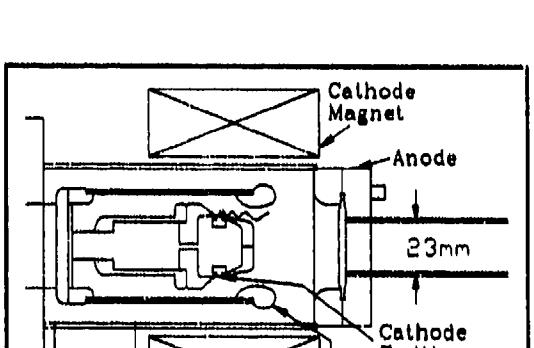

Figure 1. Scale drawing of MIG type thermionic cathode.

	Gyrotron: Cold Cathode	Gyrotron: Thermionic Cathode
I_{source}	800A	20A
V_{beam}	75kV	60kV
mm-Wave Power	6MW	100kW
Pulse Duration	100ns	50 to 100μs
Frequency Range	20 to 100GHz	20 to 45GHz

Table 1. Gyrotron operating parameters

Powering the thermionic cathode gyrotron with a (5μF, 723J) Marx bank, producing a cathode pulsed potential of magnitude -60kV, resulted in the generation of a 20A electron beam which had characteristic 1/e decay time of ≈100μs. This resulted in the generation of a 50μs and a 100μs duration mm-wave output pulse at a central intra-cavity B field value of 1.175T and 1.650T respectively. At central intra-cavity B fields of 1.175T and 1.650T, the cavity modes of oscillation were identified from the measured near-field radiation patterns with their corresponding critical starting currents required for mode

excitation measured as a function of B field. The TE_{02} mode, cut-off frequency ≈29.1GHz, was identified at an intra-cavity B field of 1.175T with a corresponding critical starting current of 1.5A, fig(2). The TE_{03} mode, cut-off frequency 42.2GHz, was identified at an intra-cavity B field of 1.650T with a measured starting current of 0.5A.

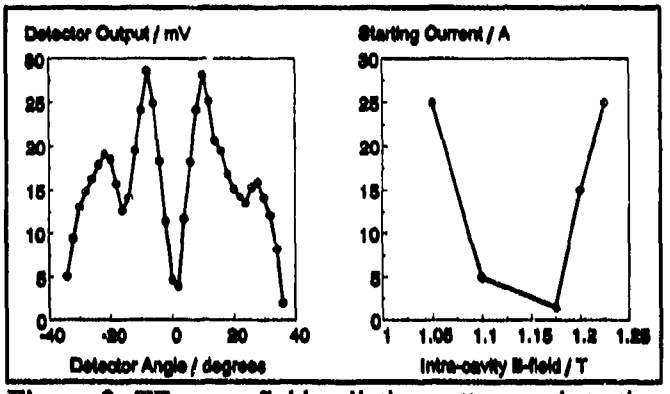

Figure 2. TE_{02} near field radiation pattern and starting current with respect to intra-cavity B-field.

A heterodyne diagnostic system was used to measure the frequency and bandwidth of both the TE_{02} and the TE_{03} modes. The TE_{02} mode was measured oscillating at a full-width, half-height bandwidth of 1.3MHz, at a centre frequency of (29.7±0.3)GHz fig(3). Similarly, the TE_{03} mode was found to be oscillating at four separate cavity resonant frequencies, with a centre frequency of (42.5±0.3)GHz. Each resonance had a measured bandwidth of ≈5MHz, with a frequency separation of ≈20MHz. This 20MHz frequency separation matches that of the longitudinal cavity modes.

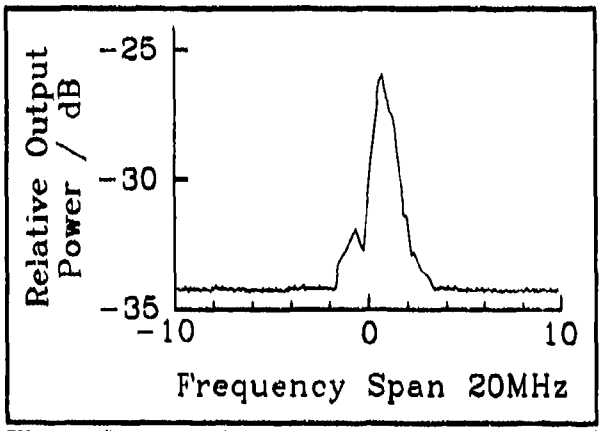

Figure 3. Heterodyne frequency measurement of TE_{02} mode, centre frequency 29.7GHz.

The gyrotron output power was measured using a broad band power meter. The energy content per pulse was determined via the absorption of the mm-waves in a calibrated thermocouple calorimeter, with the mm-wave pulse duration monitored using a Ka-band crystal detector. An energy content per mm-wave pulse of ≈12J, with a corresponding output power of ≈120kW was measured. A gyrotron operating efficiency of ≈10% was deduced. It can therefore be concluded that the change in the electron beam source from a field-immersed, field emission, cold cathode to a MIG type thermionic cathode did not significantly effect the gyrotron operating efficiency. As the thermionic cathode gyrotron and the cold cathode gyrotron were based on identical ill-defined, oxygen-free, high conductivity (OFHC) copper cavities, this suggests that in this experiment it is the interaction cavity and not the electron beam source which dominates gyrotron operating efficiency.

Acknowledgements

Support for this research was provided by DRA agreement 2065/61 and an SERC research grant. The authors thank the EEV company and the SERC for providing an SERC CASE studentship for Mr A W Cross. Helpful discussions with M. Esterson, H. P. Bohlen, D.M. Parkes and K. Trafford are gratefully acknowledged.

References

1. Spark S N, Cross A W and Phelps A D R, 1992, "Sub-μ-Second Diode Recovery Time and 330Hz PRF Measurements," *Proc. 17th Int. Conf. Infrared and Millimeter Waves*, SPIE **1929**, 466-467
2. Granatstein V L, Sprangle P, Parker R K, and Herndon M, 1975, "An Electron Synchrotron Maser Based on an Intense Relativistic Electron Beam," *J. of Appl. Phys.*, **48**, 2021-2027.

Results of Experiments on Parameters of Electron Guns for Gyrotrons

B. Piosczyk

Kernforschungszentrum Karlsruhe, ITP, Postfach 3640, D-7500 Karlsruhe 1

ABSTRACT

Measurements of the velocity distribution of gyrotron electron beams have been continued using the retarding field method. Improvements of the experimental equipment allows a larger range of scaling factors. Results for different electron guns built for 140 GHz gyrotrons will be presented and compared with numerical calculations.

1. INTRODUCTION

For a better understanding of the behaviour of gyrotrons and in order to be able to perform a reliable design of a gyrotron tube, it is very useful to know the real properties of the injected electron beam. Highly efficient operation requires a large average velocity ratio $\alpha=\beta_t/\beta_l$ with β_t and β_l the transverse and longitudinal velocity, respectively. A low velocity spread $\delta\beta_t$ is indispensable for being able to achieve a high value of α. In practice up to know only the method of retarding fields /1/ has proved to be useful for measuring the velocity distribution of helical electron beams as used in gyrotrons. There are two main disadvantages of this method: (1) A special experimental set-up is required. (2) The high power density of the electron beam requires, that the measurements have to be performed at scaled down parameters. Therefore some uncertainty remains concerning the validity of extrapolating the measured values towards the operating parameters.

2. EXPERIMENTAL ARRANGEMENT AND PERFORMANCE

The experimental arrangement is in principle as discribed in /2/. Some modifications have been made to allow measurements at a scaling factor k_s as low as about 4. This corresponds to operation at higher voltages and higher power densities compared to the measurements in /2/. The scaling factor k_s gives the value by which the voltages applied at the gun are reduced. To have unchanged electron trajectories the beam current and the magnetic field B(z) have to be scaled down by $(k_s)^{1.5}$ and $(k_s)^{0.5}$, respectively. The main part of the electron beam is stopped at a disc with a 2 mm slit. The part of the beam passing the slit enters the retarding field of a negatively biased electrode. The previously used cylindrically shaped electrode has been replaced by a gridded one. Because the motion within the retarding region is adiabatic, the retarding field acts only on the longitudinal momentum leaving the transverse momentum unaffected. Only electrons with an "longitudinal" energy $E_l>eU_{ret}$ are able to overcome the potential barrier and contribute to the current $I_c(U_{ret})$.

Measurements on electron guns designed for $TE_{0,3}$-gyrotrons at 140 GHz are in progress. Two guns, one with a non laminar and one with a laminar electron flow have been measured at scaling factors k_s between 5 and 20. The experimental procedure is as discribed in /2/. Out of the measured distribution of $I_c(U_{ret})$ the experimental values of α and $\delta\beta_t$ are evaluated according to:

$$\alpha_{exp} = \sqrt{(E_t/E_l)} \qquad \text{with} \quad E_l = eU_{ret}(0.5) \quad \text{and} \quad E_t = E_0 - E_l$$

$U_{ret}(50)$ is the value of the retarding field at which the current I_c is reduced to 50% of the value at $U_{ret}=0$ and E_0 is the total beam energy. Since in general $I_c(U_{ret})$ is not symmetric, it was decided to take the half value $U_{ret}(50)$ instead of the average calculated according to: $0.5*(U_{ret}(90)+U_{ret}(10))$ as done in /2/. $U_{ret}(90)$ and $U_{ret}(10)$ mean the values of U_{ret} at which I_c is reduced to 90% and 10%, respectively. Consequently, the relative transverse velocity spread is defined as:

$$\delta\beta_{t+} \approx 0.5(\Delta E_+/E_t) \qquad \delta\beta_{t-} \approx 0.5(\Delta E_-/E_t) \qquad \text{and} \qquad \delta\beta_t = 0.5[\,\delta\beta_{t+} + \delta\beta_{t-}]$$

with the energy spread $\Delta E_+=0.5e[U_{ret}(90) - U_{ret}(50)]$ and $\Delta E_-=0.5e[U_{ret}(50) - U_{ret}(10)]$. In case of a symmetric distribution both values are equal. However, with a non symmetric distribution $\delta\beta_{t+}$ determines the maximum achievable velocity ratio without reflected electrons.

3. RESULTS

The measured distributions $I_c(U_{ret})$ are found to be quite symmetric in the case of the gun with non laminar flow. However, $I_c(U_{ret})$ of the laminar flow gun have a tail with about 10% of the total beam with high axial energies. Typical measured distributions of $I_c(U_{ret})$ are shown in Fig. 1. The experimental dependence of $\delta\beta_t$ on the beam current at scaling factors of 5, 10 and 20 are given in Fig. 2. For the laminar gun $\delta\beta_{t+}$ is shown. The measurements have been done within a wide range of parameters. Both guns are designed for an electron current of 8 A at 70 kV. The spread $\delta\beta_t$ calculated with EGUN was found to be between about 4 and 10% depending on the operating parameters. It partly contributes to the observed spread $\delta\beta_t$ in Fig.2. Out of the results it follows that the measured $\delta\beta_t$ is within the accuracy (about±15%) independent of the scaling factor. This is a strong indication that the values of the beam parameters measured at scaled

down parameters can be extrapolated up to the gyrotron operating values and supports the validity of the necessary extrapolation of the measured beam parameters up to the gyrotron operating values.

4. CONCLUSION

Measurements of the beam parameters with the retarding field method at different scaling factors seem to prove the validity of extrapolation up to the gyrotron operating parameters. The electron gun with non laminar flow has a symmetric distribution $I_C(U_{ret})$ in contrast to the gun with laminar flow which has a distinct asymmetry of $I_C(U_{ret})$. The reason for the asymmetry - mechanical tolerances, type of electron flow or something else - is not yet clear. Up to about the design value of the electron current both guns have a similar velocity spread. Above about 10 A the laminar gun has a significantly lower velocity spread. This confirms the results of numerical calculations.

The author gratefully acknowledges the technical support of Dr.G.Dammertz and H.Budig.

/1/ E.G.Avdoshin, L.V.Nikolaev, I.N.Platonov, Sh.E.Tsimring, Radiofizika, Vol.16(4), 605-612 (1973)
A.N.Kuftin, V.K.Lygin, Sh.E.Tsimring, V.E.Zapevalov, Int.J.Electronics, Vol.72(5and6), p.1145(1992)
/2/ B.Piosczyk, 17th Int.Conf.Infrared and Millimeter Waves, Pasadena, 1992; SPIE Vol.1929, p.494-495

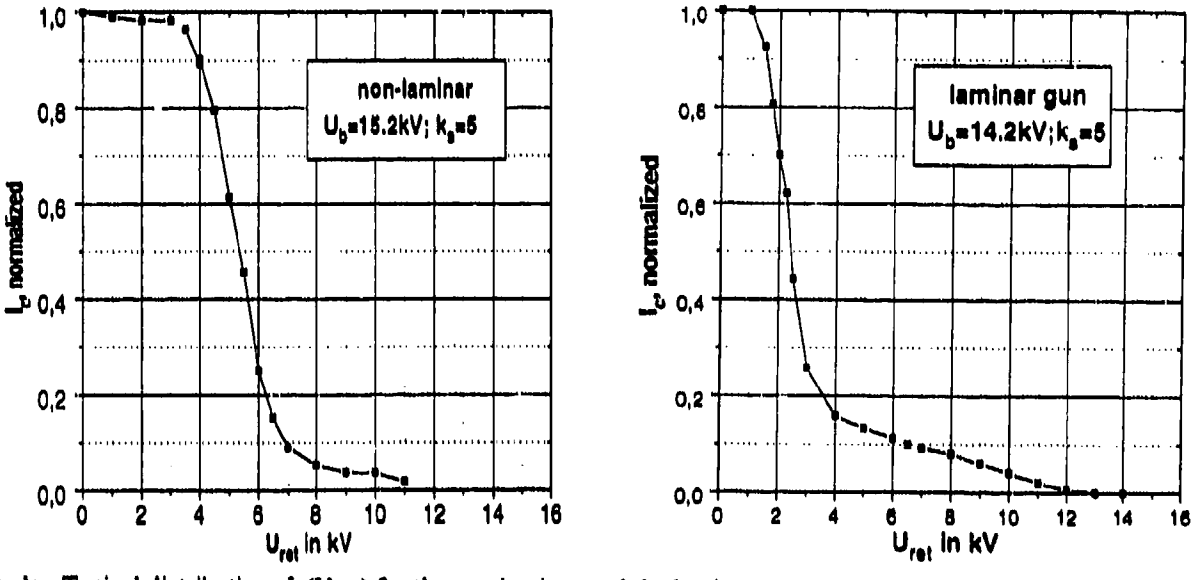

Fig. 1: Typical distributions $I_C(U_{ret})$ for the non laminar and the laminar gun

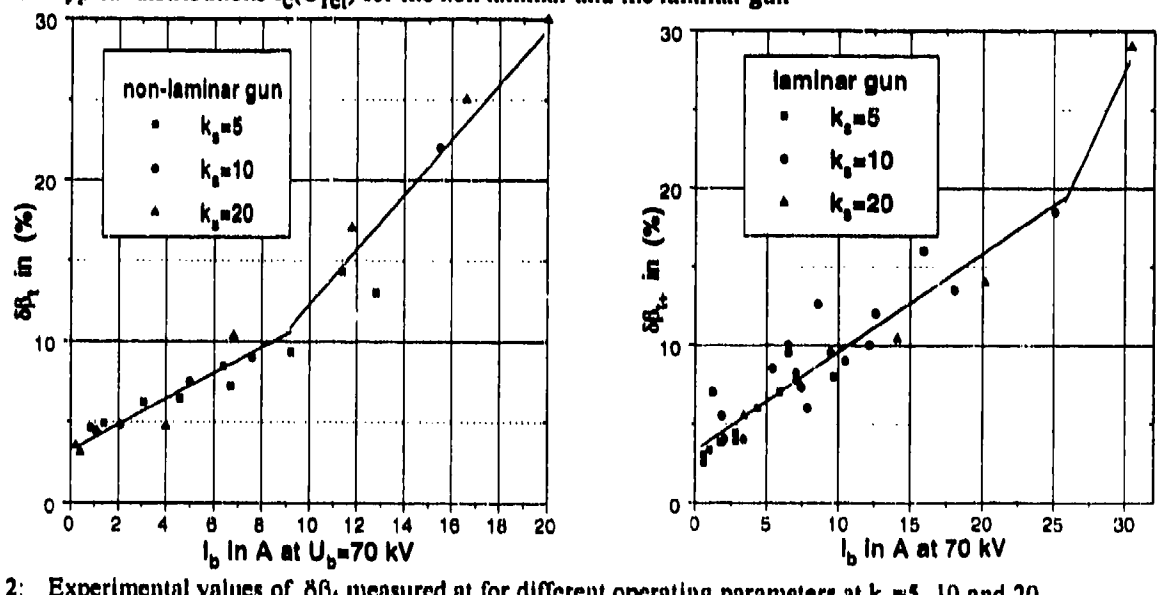

Fig. 2: Experimental values of $\delta\beta_t$ measured at for different operating parameters at k_s=5, 10 and 20.

Vacuum Microelectronic Array Gyrotron Cathode Experiments

M Garven, SN Spark, ADR Phelps and N Cade+

Department of Physics and Applied Physics
University of Strathclyde, Glasgow, G4 0NG, U.K.
+GEC-Marconi Ltd., Hirst Research Centre, East Lane
Wembley, Middlesex, HA9 7PP, U.K.

Field emitting cathodes, which are central to the new technology of vacuum microelectronics, are emerging as novel sources of electrons. Development of such cathodes is proceeding at many centres around the world, with applications in microwave devices and displays. Recent work, as part of a collaboration between the University of Strathclyde[1] and GEC-Marconi Ltd.[2], has involved the design and development of a field emission array (FEA) cathode for a vacuum diode millimetre-wave gyrotron. Initially this will be a low power, ~1kW mm-wave output, long pulse, ▶50μs, system. There are several advantages of using such cathodes as an electron beam source in gyrotrons including increased beam quality, low velocity spread and a well-defined and controllable spatial beam distribution. Further advantages lie in the ability to operate such cathodes gated, long pulse or DC. Treating the cathode and grid as a simple RC network predicts possible gating frequencies >1MHz. Previous cold cathode gyrotrons have been operated[4] at full power (~6MW mm-wave output) at a repetition frequency of 330Hz that was limited by the power supply. Utilising FEA's promises ultimate repetition frequencies three orders of magnitude beyond this, as the gating frequency is not related to the switching speed of the HT power supply.

FEAs fabricated at GEC consist of silicon emitters approximately 2μm high with approximately 10nm tip radii[3]. These are incorporated into a diode configuration, as shown in Figure 1, with silicon cathode tips and a metal grid separated by ~1.5μm SiO_2. The tips are fabricated from n-type Si (100) by a self-aligned technique which ensures that the apex of the silicon emitters is at the centre of the circular grid aperture. The grids are 0.5μm thick sputtered niobium and the diameter of the grid holes is typically 2μm.

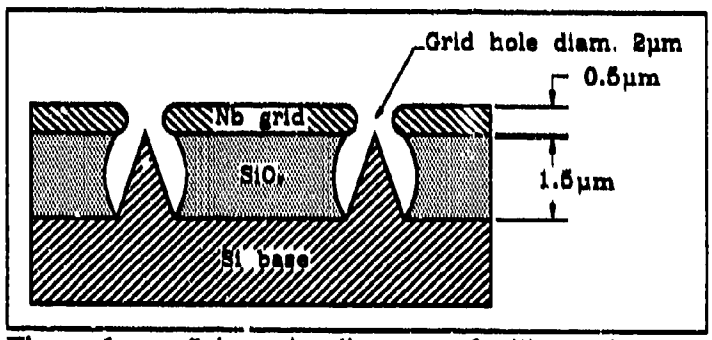

Figure 1. Schematic diagram of silicon tips and niobium grid.

Due to the sensitivity of these micron-dimensioned FEAs to contamination, ultra high vacuum (~10^{-10}mbar) test systems have been developed at both GEC and Strathclyde University. These systems allow I/V measurements, testing methods of vacuum recycling and vacuum conditioning experiments to be undertaken. Since the operating environment within the gyrotron is high vacuum (~10^{-9}mbar) rather than ultra high vacuum, it has been necessary to measure the emission characteristics of field emission arrays under such vacuum conditions.

In a working gyrotron cathode many of these FEAs will be operating simultaneously. Experiments were therefore undertaken to investigate the emission characteristics of multiple arrays. Figure 2 shows the I/V characteristics of combinations of three 100 tip arrays operated with each cathode held at the same potential. These arrays were chosen such that they had well matched I/V characteristics and in this case it was possible to achieve maximum currents of ~$0.8NI_a$ where N was the number of arrays and I_a the maximum emission current of any one array. These efficiency factors were obtained with each array having a common cathode potential. In a gyrotron cathode the efficiency factor is expected to be even higher as each array will be addressed individually.

Several important criteria must be met if these devices are to be used in a working gyrotron. Results show that FEAs are considerably more robust than expected in terms of vacuum changeover and can be easily transported without degradation of emission performance. Several chips have now undergone up to 10 vacuum recycles, with no measured degradation in the maximum emission current. FEA performance under differing vacua (10^{-10}→10^{-7}mbar) showed that the emission current was largely unaffected, implying that the resulting ion bombardment at these pressures was not great enough to produce large changes in emitter geometry. The arrays under test showed no sign of degradation after 68 hours continuous operation at 10^{-7}mbar argon. These performance characteristics satisfy the requirements of a working gyrotron.

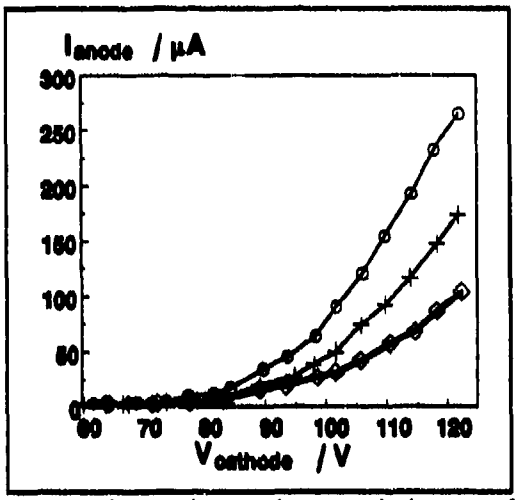

Figure 2. I/V characteristics of 1x100(□), 2x100 (+) and 3x100 (○) tip arrays.

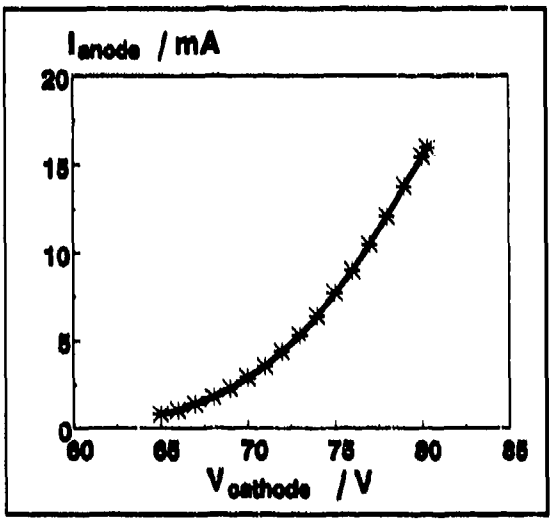

Figure 3. 16mA emission current from a 30,000 tip array.

Results from three types of devices (a) 100 tip (b) 1000 tip and (c) 8000 tip arrays, show an increase in emission current. Peak currents of (a) 8μA (b) 300μA and (c) 500μA per array respectively were measured. With ever-improving fabrication techniques and better understanding of the ideal FEA operating conditions, emission currents of ~16mA from 30,000 tips are now attainable, Figure 3.

Considering the required cathode parameters to build a working gyrotron namely, beam current ~100mA, gating voltage ~100V, accelerating potential ~80kV, emission area ~1.5cm^2, annular beam distribution, operating vacua ~10^{-8} mbar and a cathode lifetime of ≥100 hours - these devices in many instances already meet the required criteria. The operating currents needed may be obtained via modest extrapolation of both multiple chip and multiple array experiments. Recent high current results imply that a FEA gyrotron cathode incorporating 16 of these devices would give an emission current greater than 100mA as necessary for the operation of such a novel device.

Acknowledgements

Support for this research was provided by the DRA and an SERC/CASE award with GEC-Marconi Ltd. Helpful discussions with DM Parkes, K Trafford, B Kerr, J Lyons and DF Howell are gratefully acknowledged.

References

1 SN Spark, ADR Phelps and PR Winning, *Int.J.Infrared and Millimeter Waves*, 12, 885 (1991).
2 N Cade, *Vacuum Microelectronics 1989*, Inst.Phys.Conf.Ser., 99, 109 (1989).
3 RJ Harvey, RA Lee, AJ Miller and JK Wigmore, *IEEE Trans. Electron Devices*, 38, 2323 (1991).
4 SN Spark, AW Cross and ADR Phelps, *Proc. 17th Int.Conf.Infrared and Millimeter Waves*, SPIE 1929, 466 (1992).

High Speed Diagnostic Study of Pulsed, Cold Cathode, Gyrotrons

K Ronald, SN Spark, ADR Phelps and W He

Department of Physics and Applied Physics
University of Strathclyde
Glasgow, G4 0NG, U.K.

Results are reported of plasma formation in the diode of a pulsed cold-cathode gyrotron. Streak photography has been used to provide direct evidence of certain aspects of the plasma behaviour. When coupled to measurements of the simultaneous millimetre wave output of the gyrotron and the collapsing electrical impedance of the diode gap, these experiments demonstrate the rôle of the plasma in terminating the millimetre wave output pulse. Complementary experiments have used high speed framing photography to observe the spatial distribution of the cathode 'hot spots' as a function of the insulating magnetic field strength, during the low voltage arc discharge, subsequent to the termination of the gyrotron output. These diagnostic techniques have been applied to investigate the suitability of different cathode materials as plasma flare sources for high power gyrotron oscillators.

The cold-cathode gyrotron using a two-electrode field immersed diode has been regarded as a 'single shot' microwave source in contrast to the MIG configured devices using thermionic cathodes capable of very long pulse or D.C. operation. Interest in cold cathode gyrotrons has been spurred by recent experiments demonstrating the possibilities of operating these devices at high pulse repetition frequencies[1] ($\sim$300Hz) whilst maintaining high power outputs $\sim$6MW, and the inherent simplicity and robust nature of the plasma flare cathode, with beam currents $>$100A.

In the plasma flare gyrotron the maximum duration of the millimetre wave output pulse is limited by plasma disruption of the diode geometry. As the plasma expands outwards from the cathode so the required compression of the electron beam increases. The distortion of the beam results in inferior spatial coupling between the waveguide mode and electron beam. Ultimately the oscillations will terminate when the relativistic electron beam (which is essential to the gain mechanism) is grossly distorted.

It was the aim of these experiments to obtain a better understanding of the fundamental processes occurring at the cathode. Specific objectives were to establish if use of different cathode materials could significantly enhance either (a) the PRF performance of the gyrotron (where load matching of the diode, $\sim$200Ω with a stainless steel cathode, and the power supply are of great importance), (b) the reproducibility and stability of the millimetre wave output pulse, and (c) the maximum duration of the millimetre wave pulse.

The photographic observations of the cathode were made by placing a high speed camera at the output window of the gyrotron and focusing along inside the waveguide, thereby forgoing the necessity of potentially detrimental modifications to the gyrotron[2]. Streak photography of the cathode was achieved using a Hadland IMACON 500 camera operating typically at 50ns/mm giving a 2μs observation time. Using a series of calibrated optical time reference signals, the millimetre wave output of the gyrotron could be compared synchronously on the same timescale as the photographic observations. Such a result is shown in Figure 1.

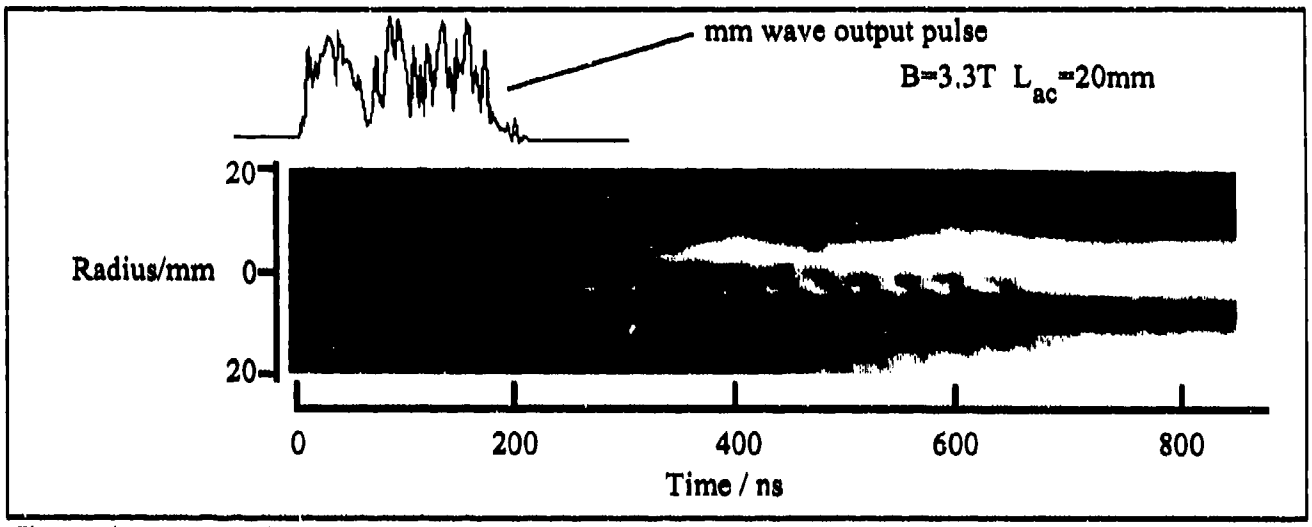

Figure 1. Streak photograph of plasma formation with simultaneous millimetre wave output pulse, plotted on the same horizontal time axis. Circles show spatial location of cathode (inner) and anode.

Framing photographic observation of the cathode was obtained using a Hadland IMACON 790 operating at 2×10^6 frames per second during the later low voltage arc discharge phase of each pulse. By adjusting the waveguide magnetic field and observing the effect upon the illumination of the cathode, the experiments revealed the spatial structure of the electron emission. Such a photograph is shown as Figure 2. The frames are separated by 500ns with 100ns exposure. The waveguide magnetic field was 3.3T. The results obtained from these experiments are consistent with the screening effect[3].

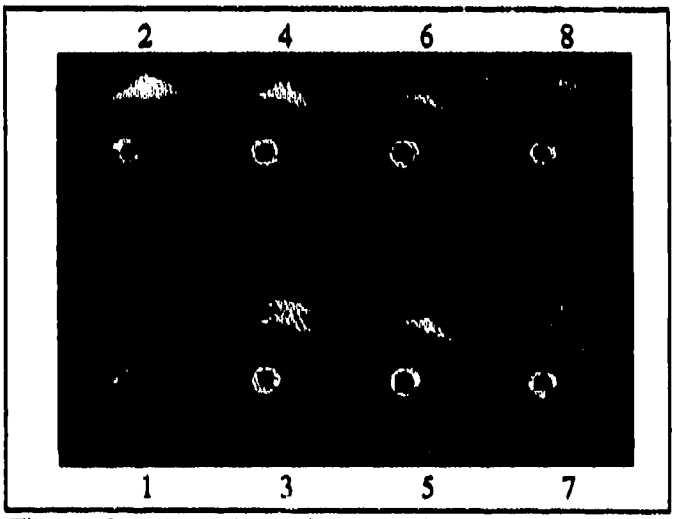

Figure 2. Framing photographs of the cathode. Framing sequence indicated by numbering of photographs.

Acknowledgements

The SERC and the MoD supported this research. DM Parkes, K Trafford and SJ MacGregor provided encouragement and stimulating discussions.

References

1. Spark SN, Cross AW and Phelps ADR, 1992, Proc. 17th Int. Conference on Infrared and Millimeter Waves, SPIE **1929**, 466-467.
2. Spark SN, Ronald K, Cross AW, He W and Phelps ADR, 1992, Proc. 17th Int. Conf. on Infrared and Millimeter Waves, SPIE **1929**, 322-323.
3. Mesyats GA, 1991, IEEE Trans. on Plasma Science, **19**, 683-689.

NON-ADIABATIC ELECTRON GUNS FOR GYROTRONS

J.J. Barroso, I.P. Spassovsky and C. Stellati
Instituto Nacional de Pesquisas Espaciais
12201-970 - São José dos Campos, SP - Brasil

Abstract

A non-adiabatic electron gun has been designed for a 35 GHz, 100 kW gyrotron. A 50 kV, 10 A laminar electron beam has been achieved with a perpendicular to parallel velocity ratio of 1.9 for a perpendicular velocity spread as low as 0.4% (optics and space charge). Extensive numerical parameter studies have been performed to investigate the constraints and performance of the gun.

Introduction

A critical element of the gyrotron is the electro-optical system, that must generate a high-quality helical beam with a sharply defined partition of electron energy between rotation and streaming energy along a magnetic field. The approaches for generating electron beams used in gyrotrons have fallen into two classes. In the first, the beam is created initially with a transverse velocity component. Most gyrotron devices are based on such a scheme that employs an electron gun called the magnetron injection gun, a crossed-field emitter that consists of a conical shaped cathode surrounded by a control electrode. In the second method [1], a rectilinear flowing beam is generated firstly and then is passed through a non-adiabatic modulation region where the beam experiences a transverse force that imparts to the particles rotational velocity.
In that paper, a non-adiabatic gun for a 35 GHz gyrotron [2] is presented. The gun operation is examined by use of a numerical simulation code [3] including the effects of space charge and self magnetic fields. Results indicate how the electron velocity ratio and the velocity spread are affected by variations in the modulation anode voltage and the magnetic field at the emitter.

Gun Geometry and Operation

The eletrode system along with electron trajectories is shown in Fig. 1, where the cathode structure comprises a right cylinder attached to a flat wall. The emitter surface consists of a concentric ring with a emission loading of 3.1 A/cm^2 for a 10 A beam. A stepped iris anode closing around the cathode provides a modulation region where the flowing beam experiences a sharp, non-adiabatic change of electrostatic field and much of the electron velocity is converted to orbital velocity round the guiding centers. Notice that this double-anode gun does not require ceramic structures, thus avoiding the use of ceramic-to-metal sealing techniques for its construction.

Results and Conclusion

Numerical simulations have been performed exploring the parametric dependence of the 10 A, 50 kV beam parameters (electron velocity ratio α_k, transverse velocity $\beta_{\perp,k}$) on the modulation anode voltage V_a and cathode magnetic field B_k. Transverse and axial velocities of twenty-one representative electrons were recorded at the final position in the beam tunnel z = 140mm, where most of the electric field acceleration is completed. The effects on α_k and $\beta_{\perp,k}$ of varying the control parameters V_a and B_k are shown in Figs. 2 and 3. Both the velocity ratio and the transverse velocity follow the scaling law $V_a^{1.7}/B_k^{2.2}$ as the axial velocity is quite insensitive to the control parameters variation, being restricted to the short interval $\beta_{\|,k} = (404 \pm 4)10^{-2}$ as $\alpha_k^2 \ll 1$ for all the cases examined here. It was also verified that the anode voltage has a lower bound $V_a >$ 18 kV posed by space-charge constraints, since below that voltage value the space-charge-limited current becomes less than the operating current of 10 A. The perpendicular velocity spread $\Delta\beta_{\perp,k}/\beta_{\perp,k}$, defined as the standard deviation normalized to the mean value, as function of V_a is displayed in Fig.4. As shown by the $B_k = 0.7$ kG curve, the velocity spread is remarkably small for voltage values around 25 kV. In particular, at $V_a = 26.5$ kV the corresponding beam parameters are $\alpha_k = 0.2$ and $\beta_{\perp,k} = 8.5 \times 10^{-2}$ with a relative velocity

spread of 0.4%. On compression by an increase in magnetic field to a value B_{cav} = 12.7 kG at the entrance to the cavity, these parameters result in α_{cav} = 1.9 and $\beta_{\perp,cav}$ = 0.36 according to the adiabatic equations $\beta_{\perp,cav} = \beta_{\perp,k}\sqrt{B_{cav}/B_k}$ and $(1+1/\alpha_{cav}^2)/(1+1/\alpha_k^2) = B_k/B_{cav}$.
In conclusion, a non-adiabatic electron gun able to generate a 10 A, 50 kV laminar beam, with a perpendicular velocity spread as low as 0.4% (optics and space charge) and an electron velocity ratio of 1.9, has been designed for a 35 GHz gyrotron. Presently, further parameters such as anode positioning and additional velocity spread effects due to the emitter surface roughness and cathode temperature are being investigated.

References

[1] B. Piosczyk, Thirteenth Int. Conf. Infrared and Millimeter Waves, Proc. SPIE, vol. 1039(1988), 422-423.
[2] J.J. Barroso, A. Montes, G.O. Ludwig and R.A. Correa, *Int. J. Infrared Millimeter Waves*, 11(2), 1990.
[3] W.B. Herrmannsfeldt, "Electron Trajectory Program", Stanford University, SLAC Report 226, Nov. 1979.

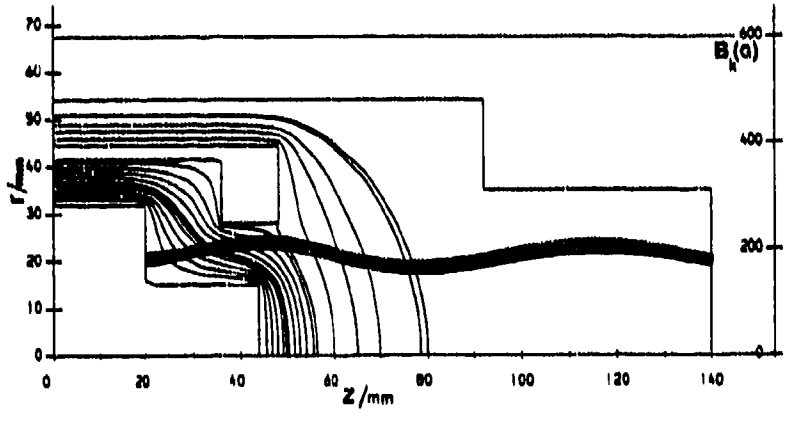

Fig. 1. Electrode system along with electron trajectories and equipotential lines. Modulation anode and beam tunnel voltages are, respectively, 20 kV and 50 kV.

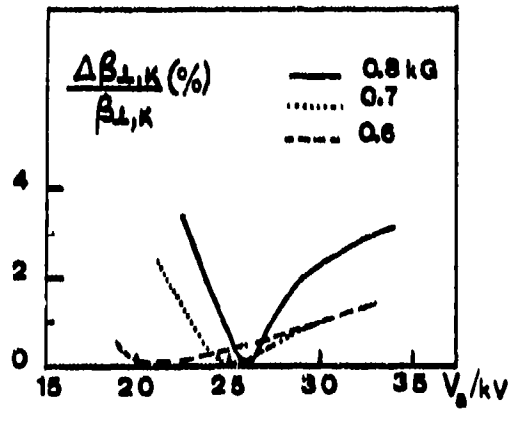

Fig.2. Perpendicular velocity spread as function of B_k and V_a.

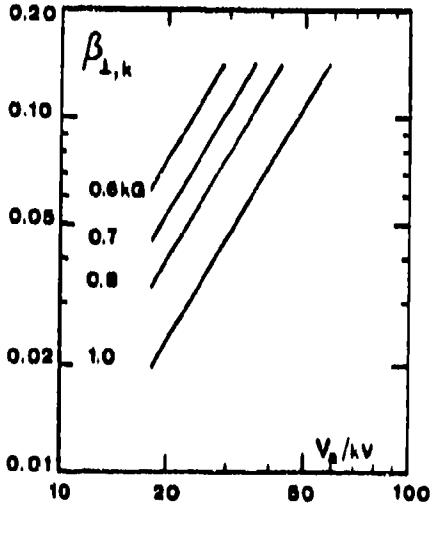

Fig. 3. Normalised trasnverse velocity as function of the cathode magnetic field (B_k) and the modulation anode voltage (V_a).

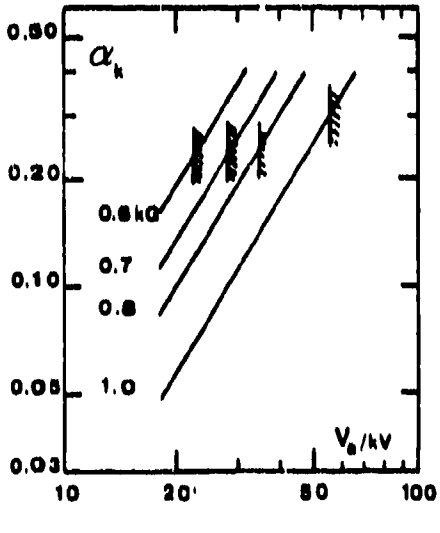

Fig. 4. Electron velocity ratio as function of V_a and B_k. Mirroring (for a cavity magnetic field B_{cav} = 12.7kG) is indicated by hatched segments.

Diocotron Instability in the Drift Tube of a Gyrotron

Rainer Schuldt
Nuclear Reserch Center Karlsruhe, HDI
W 7500 Karlsruhe 1 Germany

Abstract

A cold fluid model is used to investigate instabilities associated with a velocity shear due to the eigenfields of a relativistic electron beam [1] inside the beam tunnel of a gyrotron. Results are used to supplement the information provided by a stationary particle-in-cell code in order to simulate time dependent effects. General statements concerning the stability of such an electron beam system are possible.

General Introduction

In a gyrotron, an annular electron beam propagates in a waveguide with an applied magnetic field. The resonant interaction of the cyclotron rotation of the electrons with a waveguide mode feeds energy from the electrons to the wave [2]. A homogeneous electron beam is needed to obtain a good efficiency.
At KfK a particle in cell code (BFCPIC) [3] is used for simulating plasmas in technicial devices. It uses boundary fitted coordinates. Curved boundaries can be treated, but only stationary fields are calculated. Work on adapting this code for simulations of MIG guns is in progress [4]. Instead of calculating time dependant fields directly, we attempt to simulate some time dependant effects by adding an analytical model.

Analytical model and stationary state

We consider a metal tube with a hollow electron beam inside. The electron density $n_0(r)$ is input data. The stationary state consists of the following fields:

$$n_0(r)\,, \quad \phi_0(r)\,, \quad \vec{E}_0(r)\,, \quad \vec{B}_0(r)\,, \quad \vec{v}_0(r)\,, \quad \gamma_0(r) \tag{1}$$

and is determined by the equation of motion for a cold, relativistic electron fluid

$$\frac{1}{m_e}\frac{\mathrm{d}}{\mathrm{d}t}\vec{p} = \left[\partial_t + \left(\vec{v}\vec{\nabla}\right)\right]\gamma\vec{v} = \frac{-e}{m_0}\left[\vec{E} + \vec{v}\times\vec{B}\right], \tag{2}$$

the energy balance $(\gamma(r) - 1)\, m_e c^2 = e\,\phi(r)$ and Maxwell's equations $\vec{\nabla}\vec{E} = \frac{\rho}{\varepsilon_0}$,

$\vec{\nabla}\vec{B} = 0$, $\mathrm{curl}\,\vec{B} = \mu_0\vec{j} + \frac{1}{c^2}\partial_t\vec{E}$ and $\mathrm{curl}\,\vec{E} = -\partial_t\vec{B}$.

Stability analysis

In order to investigate the stability of the above described stationary state [5], we introduce perturbations of the following form

$$\vec{E}(r, \theta, t) = \vec{E}_0(r) + \delta\vec{E}(r)e^{i(\lambda\theta - \omega t)} \tag{4}$$

and similarly for $\delta\vec{B}(r)$, $\delta\vec{v}(r)$ and $\delta n(r)$ and plug them into the above described equations. After lengthy manipulations, we arrive at a 2×2 system of ordinary differential equations:

$$\begin{aligned} \zeta'(r; \omega, \lambda) &= A(r; \omega, \lambda)\,\zeta(r; \omega, \lambda) + B(r; \omega, \lambda)\,\xi(r; \omega, \lambda)\,, \\ \xi'(r; \omega, \lambda) &= C(r; \omega, \lambda)\,\zeta(r; \omega, \lambda) + D(r; \omega, \lambda)\,\xi(r; \omega, \lambda)\,. \end{aligned} \tag{5}$$

where $\zeta(r)$ is proportional to δE_θ and ξ is a combination of δE_r and δB_z. The boundary conditions are $\zeta(r)$ and $\xi(r)$ are nonsingular at $r = 0$ and $\zeta(r_{wall}) = 0$. For a given value of λ, this is only possible for special values $\omega = \omega(\lambda)$. It is well known, an instability can occur when $\mathrm{Im}\,\omega > 0$.

Results

The results of this analysis are the dispersion relation $\omega(\lambda)$ and the profile of the perturbation fields $\delta E_\theta(r)$, $\delta E_r(r)$ and $\delta B_z(r)$. The growth length L_{grow}, defined as $L_{grow} = \frac{v_{0z}}{\mathrm{Im}\,\omega}$ is the distance which the beam travels until the fields grow by the factor e.
One example for $\lambda = 1$ and typical gyrotron parameters $\phi_A = 75\mathrm{kV}$, $r_{wall} = 9\mathrm{mm}$, $r_{beam} = 3.5\mathrm{mm}$, $I_{beam} = 15\mathrm{A}$ this length $L_{grow} = 0.67\mathrm{m}$ when $B_{appl} = 1.28\mathrm{T}$ and $L_{grow} = 1.78\mathrm{m}$ when $B_{appl} = 4\mathrm{T}$.
These large values of L_{grow} indicate that the diocotron instability probably has only a slight effect on the quality of the electron beam. It is planned to investigate the effects of velocity spread and magnetic compression.

Literature

[1] O. Buneman, R. H. Levi, L. M. Linson, J. Appl. Phys. 37 3203 (1966).

[2] A. A. Andronov, V. A. Flyagin, A. V. Gaponov, A. L. Gol'denberg, M. I. Petelin, V. G. Usov, V. K. Yulpatov, Infrared Physics Vol. 18, 385 (1978).

[3] T. Westermann, Numerical Modelling of the Stationary Maxwell-Lorentz System in Technical Devices - A Review, to appear in Int. J. of Numerical Modelling, Electronic Networks, Devices and Fields (1993).

[4] E. Borie, T. Westermann, private communications.

[5] R. C. Davidson, Physics of Nonneutral Plasmas, Addison-Wesley (1990).

ELECTROSTATIC EFFECTS ON THE QUALITY OF GYROTRON BEAMS*

J.L. Vomvoridis, K. Hizanidis, I.G. Tigelis+ and D.I. Frantzeskakis+
Department of Electrical and Computer Engineering
National Technical University of Athens

1. Introduction

An explanation for the discrepency between the calculated and the measured performance of gyrotrons lies in the possible development of electrostatic waves in the electron beam before it enters the gyrotron cavity. From our research, aiming at assessing this possibility and proposing remedial action, we report here our results on the case of Langmuir waves, which may develop by their coupling to slow TM modes supported by the beam channel. Both the cases of quasi-uniform and of nonuniform guide magnetostatic field have been addressed analytically. In addition, computer simulations have been prepared, in which the trajectories of fast electrons are followed in the fields of slow TM waves in the beam channel. The results, which are in good agreement with the analytical ones, are not reported here, due to space limitations.

2. Quasi-uniform System

The phase of an electron relative to the Langmuir wave varies to zero order according to

$$\varphi^{(0)} = \varphi_0 + kz - \omega\int dz / v_z^{(0)}(z) \qquad (1)$$

where $v_z^{(0)}(z)$ describes the variation of the axial velocity under cyclotron motion in the magnetostatic field. There are situations, where a linear approximation,

$$\tilde{\varphi}^{(0)} = \varphi_0 + kz - \omega z / v_{z,eff} = \varphi_0 + \Delta_{eff}(\omega z / c) \qquad (2)$$

with an appropriate value for $v_{z,eff}$, gives errors φ-$\tilde{\varphi}$ less than $\pi/2$. Under such conditions, the system can be well approximated by a uniform system, with the magnetostatic field taken at the value B_{eff}, which correspond to $v_{z,eff}$. From the linear analysis, the starting current is obtained,

$$QI_{min} = \frac{\varepsilon_0 mc^2}{2e}\left(\frac{u_z^3}{1+u_\perp^2}\right)_{eff}\frac{S_{equiv}}{Z^2}\frac{1}{F_{qu}(\xi)} \quad ; \qquad F_{qu}(\xi) = [1-\cos\xi-0.5\xi\sin\xi]/\xi^3 \qquad (3)$$

with $\xi=\Delta_{eff}(\omega z/c)$. The nonlinear analysis has yielded the inverse of the dimensionless characteristic nonlinear length,

$$K = [u_\perp^2\varepsilon/(1+u_z^3)]^{1/2} \quad ; \qquad \varepsilon = eE/mc\omega \qquad (4)$$

and the nonlinear efficiency,

$$\eta_{nl} = p_1(\gamma_0-\gamma_c)/(\gamma_0-1)[1-\cos(p_2 K\omega z/c)] \quad ; \gamma_c = [(1+u_\perp^2)/(1-\omega^2/k^2c^2)]^{1/2} \qquad (5)$$

Here, γ_c is the value of γ at the vortex, while p_1 and p_2 are appropriate numerical coefficients of order 1, to be obtained by fitting from the numerical simulations. In addition, the temperature developed on the beam is obtained,

$$\delta\gamma = 2q[u^3\varepsilon/(1+u_\perp^2)]^{1/2} = q\tilde{\gamma} \qquad (6)$$

* Supported by the Commission of the European Communities, Directorate General XII, Fusion Programme.

+ *Department of Physics, University of Athens.*

where q is a coefficient of order 1, to be obtained numerically. Finally, these results have been related to the ratio I/I_{min}. The results for the saturation level (for p_1=0.5), for the temperature (for q=1) and the efficiency are shown in Figures 1-3.

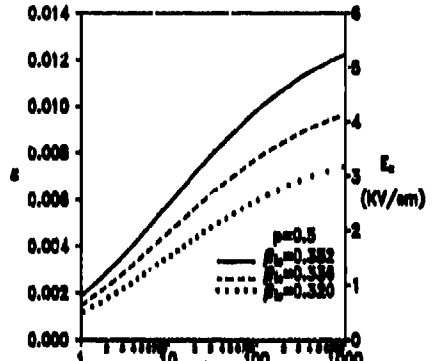

Figure 1

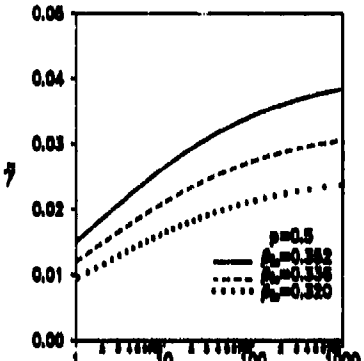

Figure 2

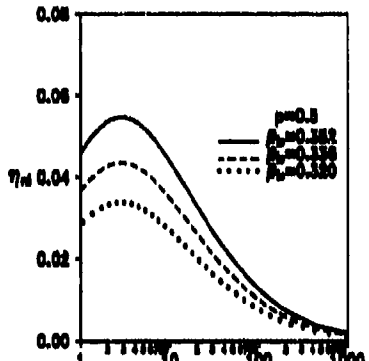

Figure 3

3. Nonuniform System

When the approximations in Sec.2 fail, i.e. when $\tilde{\varphi}$ is not within $\pi/2$ of the exact value of φ, then the slope dB/dz of the magnetostatic field is incorporated explicitly in the equations. In the small-signal regime, the quantity of relevance is found to be the ratio $A=\Delta_0/\pi\alpha$, where

$$\Delta_0 = kc/\omega - \gamma_0/u_{z0} \tag{7}$$

$$\alpha^2 = (\gamma_0 u_{\perp 0}^2/2\pi u_{z0}^3)(dB/dz)(c/\omega) \tag{8}$$

In this case, the starting current is still given by (3), except that the resonance function is now:

$$F_{nu} = \frac{[g(A)+g(A-x)][1-\cos(\pi x(A-x/2))]+[f(A)-f(A-x)]\sin(\pi x(A-x/2))}{2\pi x^3} \tag{9}$$

where f and g are the auxilliary functions for the Fresnel integrals and $x=\alpha\omega z/c$. The maximum of this function and the corresponding value x_{cr} are shown in Figure 4. It can be seen that a substantial reduction in $F_{nu,max}$ (i.e. a substantial increase in the value of I_{min}) occurs only when A<1, i.e. for very strong nonuniformity.

Similarly, the quantity of relevance in the high-signal regime is found to be the ratio $R=\pi\alpha^2/K^2$. Although the analysis has so far not been completed to reach quantitative results, the following interim conclusions have been obtained:

a) If $R<<1$ or $K(1-R^2)^{1/2}(\omega z/c)<2\pi$, then the situation is almost identical to that of the quasi-uniform system.

b) If $R \leq 1$ and $K(1-R^2)^{1/2}(\omega z/c)>>2\pi$, then a substantial separation of trapped and untrapped electrons occurs in phase-space, which corresponds to very large spreads in γ.

c) If R>1, no trapped electrons are present and the spread in γ appears to scale with the inverse square root of dB/dz.

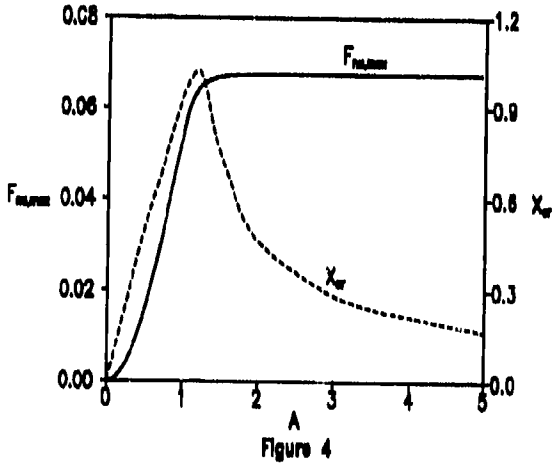

Figure 4

100Hz PRF CARM Experiment

SJ Cooke, SN Spark, W He and ADR Phelps

Department of Physics and Applied Physics
University of Strathclyde
Glasgow, G4 0NG, U.K.

Details are presented of the Strathclyde University Cyclotron Autoresonance Maser (CARM) experiment. The specification and device characteristics will be reported for CARM oscillation in the 12-20 GHz band. In contrast to previously reported CARM devices[1,2], pulse repetition frequencies (PRF) greater than 100 Hz have been employed. For applications to plasma heating and plasma diagnostics, where large average powers are required, pulse repetition rates of at least this order are necessary.

The CARM interaction promises to provide a means to achieve high power, high frequency radiation in the mm-wave region. Its advantages for this purpose arise from the large Doppler frequency upshift over gyrotron devices and the autoresonant nature of the interaction, leading to high efficiency and low magnetic field operation.

The characteristics of the CARM oscillator described are summarised in Table 1:

1. For this device, a highly relativistic electron beam is desired, since the interaction frequency is upshifted according to

$$\omega = \omega_c \gamma^2, \qquad \omega_c = \frac{eB}{\gamma m_e},$$

characteristic of a relativistic free electron device. For a given frequency of oscillation, this relaxes the requirement for a large B-field in cyclotron devices and extends the accessible frequency range.

2. To achieve high pulse rate operation in this experiment, a low cavity B-field was chosen for continuous operation. Nevertheless, with moderate Doppler upshift, this translates to mm-wave generation around 15 GHz.

3. The lowest cylindrical cavity mode ($TE_{1,1}$) was selected, being most accessible at low magnetic fields and least susceptible to parasitic excitation of lower frequency backward-wave and gyrotron interactions.

Accelerating potential	500-700 kV
Electron current	100 A
Relativistic factor, γ	2.0 - 2.4
Cavity magnetic field	0.3 - 0.38 T
Cyclotron frequency, ω_c	3 - 4 GHz
Doppler upshift factor	4 - 7
Operating frequency	12 - 20 GHz
Bandwidth	2-3 GHz
Power in $TE_{1,1}$ mode	5 MW
Pulse duration	100 ns
Pulse repetition frequency	100 - 300 Hz

Table 1: CARM specification details

Autoresonance, the compensation of the increase in cyclotron frequency (due to energy loss) by a reduction in the Doppler upshift, allows the interaction to remain close to resonance through a significant transfer of electron energy to the EM field. Theory predicts a possible conversion efficiency of up to 20-30%, though this has not yet been achieved.

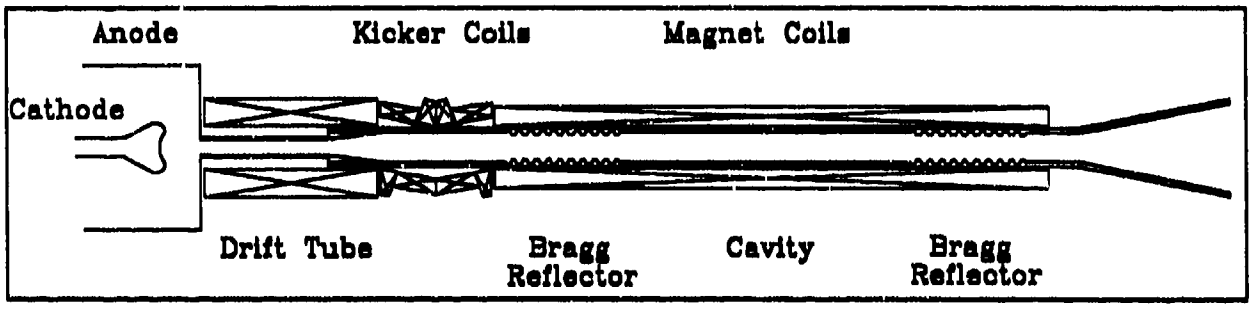

Figure 1: Schematic outline of CARM oscillator

The CARM oscillator design is depicted schematically in figure 1, and comprises four identifiable components:

1. Recent developments in cable pulser technology are employed to provide the -600kV pulsed cathode potential, at up to 100 Hz PRF or greater[3]. The electron source, an enhanced field emission, cold cathode, in a simple diode configuration as shown, may be operated in field-free or field-immersed modes. An anode aperture was chosen to maintain uniformity of the electron beam.

2. Within the drift region, the beam is transported axially, and adiabatically compressed to 6mm diameter. Currents of 100-200A may be transported through the drift region to obtain a low emissivity electron beam.

3. The kicker coils impart a transverse velocity to the beam, via resonant interaction with a spatially inhomogeneous, anadiabatic magnetic field configuration, to obtain the helical trajectory prerequisite for CARM interaction. The novel design depicted was developed to operate within the power limitations associated with continuous operation. This design exhibits good uniformity across the beam, and pitch-angle tunability over a wide range of beam energy and interaction conditions.

4. The interaction cavity is defined within a cylindrical OFHC copper waveguide, with Bragg reflectors providing high reflectance ends to give a large overall cavity Q-value. The Bragg section exhibit excellent beam transport characteristics, while providing selective feedback necessary to excite the convective CARM instability.

By modelling electron trajectories within each component, including space-charge effects, the beam parameters were optimised to give narrow velocity and energy distributions. Experimental data, from both electron beam and millimetre-wave diagnostics, will be compared with numerical predictions.

Acknowledgements

We would like to thank the SERC for support of this work. D.M.Parkes and K.Trafford provided encouragement and stimulating discussion.

References

1. V.L.Bratman, G.G.Denisov, M.M.Ofitserov, S.V.Samsonov, O.V.Arkhipov, V.I.Kazacha, A.K.Krasnykh, E.A.Perelstein and A.V.Zamrij, 1992, "Cyclotron autoresonance maser with high Doppler frequency up-conversion", *International Journal of Infrared and Millimeter Waves*, **13**, 1857-1873.

2. S.Alberti, B.G.Danly, G.Gulotta, E.Giguet, T.Kimura, W.L.Menninger, J.L.Rullier and R.J.Temkin, 1992, "High-power Cyclotron Autoresonance Maser (CARM) experiments", *Proc. 17th International Conference on Infrared and Millimeter Waves*, SPIE **1929**, 128-129.

3. S.N.Spark, A.W.Cross and A.D.R.Phelps, 1992, "Sub μ-second diode recovery time and 330Hz PRF measurements", *Proc. 17th International Conference on Infrared and Millimeter Waves*, SPIE **1929**, 466-467.

Effect of beam geometric deformation on the properties of ECRM

Yu Yongjian

University of Electronic Science and Technology
Department of Electronic Engineering
Chengdu, People's Republic of China

1. INTRODUCTION

Practical electron beams are subject to various kinds of errors relative to the ideal one. In particular, there would be eccentric errors due to the deviation between the symmetric axis of the beam and that of the waveguide; and geometric deformation errors caused by the non-axisymmetry of the beam cross-section. In order to quantitatively analyze the effect of these kinds of geometric deformation errors on practical gyrotron small-signal characteristics in a general sense, in this paper firstly is proposed the elliptical ring beam geometic deformation model and then is set up the kinetic theory that describes the interaction between the elliptical ring monoenergetic hollow beam and the TE^{+}_{mn} mode travilling wave. Finally, taking the TE^{+}_{01} mode fundamental cyclotron ECRM an example, is presented the quantitative relationship between the ECRM coupling coefficient and the geometric errors for elliptical ring beams with small eccectricity and small focus-waveguide axes deviation.

2. DERIVATION OF DISPERSIVE RELATION

Consider the ECRM configuration, shown in Fig. 1, of elliptical ring cross-section monoenergetic hollow beam. The waveguide is a circular cylinder. All electrons in the beam have equal longitudinal momentum and total energy, and the gyro-center of electron are distributed uniformly along the elliptical ring E; moreover, the symmetric axis of the waveguide does not coincide with the foci of E.

The equilibibrium distribution function for the elliptical ring cross-section 'cold' e-beam is given by

$$f_0 = \frac{N_e}{4\pi^2 R_0 \sqrt{1-\varepsilon^2} r_L}\delta\left(R_\theta - \frac{R_0(1-\varepsilon^2)}{1+\varepsilon\cos(\varphi_\theta - \varphi_0)}\right)$$

$$\delta(r_L - r_{L0})\delta(p_{//} - p_{//0}) \qquad (1)$$

where ε and R_0 is the eccentricity and half of the major-axis-length of E, respectively; the meaning of other symbols are identical with those appeared in [1]. Henceforth, the meaning of any symbol undeclared is identical with its counterpart in [1].

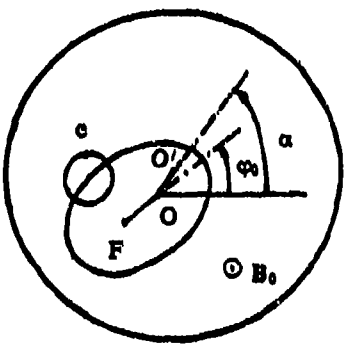

Fig. 1. Cross-sectional geometry of elliptical ring beam ECRM. ($\overline{OO'} = d$)

Adopting the method used in [1], one can obtain the ECRM dispersive relation for the elliptical ring cross-section beam; and it is seen that though, formally, the relation obtained is identical with that for the general ideal beam ECRM, their corresponding dispersive coefficients are quite different.

The ECRM coupling coefficient for elliptical ring beam is given by

$$H_{ml} = \frac{\sqrt{1-\varepsilon^2}}{2\pi}\int_{-\varphi_0}^{\pi-\varphi_0}\frac{d\varphi_\theta}{1+\varepsilon\cos\varphi_\theta}\left|\sum_{s=-\infty}^{\infty} J_{m-s}(\bar{d})J_{s-l}\left(\frac{k_c p}{1+\varepsilon\cos\varphi_\theta}\right)\exp\left[js(\alpha+\pi-\varphi_\theta-\varphi_0)\right]\right|^2 \cdot j_l'^2 \qquad (2)$$

where $p = R_0(1-\varepsilon^2)$, $\bar{d} = k_c d$, Eq. (2) indicates that H_{ml} is always greater than naught.

Due to the non-axisymmetry of the beam the expressions for Q_{ml} and U_{ml} are much more complicated than their counterparts in the ideal beam case.

3. FORMULAE SIMPLIFICATION

As far as discussing the effect of beam errors in engineering is concerned, only those cases with small beam errors are of great interest. Under practically operational conditions, i. e., $\varepsilon \ll 1$ and $d/R_0 \ll 1$, the general dispersive

coefficient expressions obtained above is simplified to

$$\bar{H}_{ml} = \sqrt{1-\varepsilon^2}\{X_1 + \varepsilon X_2 \cos\psi + \varepsilon^2[X_3 + 1/2 \cdot X_4 \cdot \cos(2\psi)]\} \tag{3}$$

in which $\bar{H}_{ml} = H_{ml}/j_l^2$, is referred to as the normalized coupling coefficient,

$$X_1 = \sum_{s=-\infty}^{\infty} J_{m-s}^2(\bar{d}) J_{s-l}^2(\bar{p}), X_2 = \sum_{s=-\infty}^{\infty} J_{m-s}(\bar{d}) J_{m+1-s}(\bar{d})\{J_{s-l}(\bar{p}) J_{s-1-l}(\bar{p}) + \bar{p}d[J_{s-l}(\bar{p}) J_{s-1-l}(\bar{p})]/d\bar{p}\},$$

$$X_3 = 1/2 \sum_{s=-\infty}^{\infty} J_{m-s}^2(\bar{d})[(1 + l^2 - \bar{p}^2 + s^2 - 2s) J_{s-l}^2(\bar{p}) + \bar{p}^2 J_{s-l}'^2(\bar{p}) + \bar{p} J_{s-l}(\bar{p}) J'_{s-l}(\bar{p})],$$

$$X_4 = \sum_{s=-\infty}^{\infty} J_{m-s}(\bar{d}) J_{m+2-s}(\bar{d})\{J_{s-l}(\bar{p}) J_{s-2-l}(\bar{p}) + \bar{p}d[J_{s-l}(\bar{p}) J_{s-2-l}(\bar{p})]/d\bar{p} + 1/2\bar{p}^2 d^2[J_{s-l}(\bar{p}) J_{s-2-l}(\bar{p})]/d\bar{p}^2\}$$

$\bar{d} = \chi'_{ms}(R_0/a_W)(d/R_0)$, $\bar{p} = \chi'_{ms}(R_0/a_W)(1-\varepsilon^2)$, $\psi = \alpha - \varphi_0$, is the supplementary angle to $\angle O'OF$, here being refeered to as the beam direction angle.

When estimating the effect of beam errors in engineering, to manifest dominant facts and save computational burden, it still can be approximated that

$$Q_{ml} \approx 2H_{ml}, U_{ml} \approx 0 \tag{4}$$

4. NUMERICAL CALCULATION AND DISCUSSION

The simplified formulae presented above can be applied to analyze the effect of some practical beam geometric deformation errors on the small—signal characteristics of the ECRM or gyrotron quantitatively. For a given $\beta_{\perp 0}$, the effect of the beam geometric deformation errors, which are measured by ε, d/R_0 and ψ in the case of elliptical ring beam, on ECRM is refected directly by the (normalized) coupling coefficient H_{ml} (or $\bar{H}_{ml}$).

Hereby, as an simple and useful example, we present quantitatively the relationship between ε, d/R_0 and ψ, and TE_{01}^{s} mode fundamental ECRM normalized coupling coefficient $\bar{H}_{01}$.

Viewing from Fig. 1, it is seen that the beam symmetric axis would approach the axis of the waveguide as ψ tends to 180^0. Particularly, in the cases that $d/R_0 = \varepsilon$, when $\psi = 180^0$, the two axes coincide with each other. Consequently, from Table 1, it is shown that beam geometric errors always result in the decrease in the TE_{01}^{s} mode fundamental ECRM coupling capacity, and the greater the errors, the more severe the reduction would be; and on the other hand, in the case of equal beam geometric deformations, the greater the deviation of the beam symmetric axis from that of the waveguide, the more severe the coupling capacity reduction would happen.

Tab. 1 Influences of ε and d/R_0 on $\bar{H}_{01}$, in cases of $\psi = 0^0$, 45^0, 90^0, 135^0, and 180^0.

$\bar{H}_{01}$ \ ε / d/R_0	0.0	0.1	0.2	0.3
0.0	0.3386	0.3346	0.3237	0.3084
0.1	0.3346	0.3230	0.3059	0.2874
		0.3252	0.3100	0.2925
		0.3307	0.3200	0.3051
		0.3362	0.3502	0.3181
		0.3385	0.3346	0.3236
0.2	0.3229	0.3047	0.2828	0.2624
		0.3089	0.2903	0.2717
		0.3192	0.3092	0.2955
		0.3299	0.3292	0.3209
		0.3344	0.3377	0.3320
0.3	0.3045	0.2811	0.2562	0.2353
		0.2868	0.2663	0.2478
		0.3012	0.2923	0.2804
		0.3162	0.3205	0.3166
		0.3226	0.3328	0.3327

5. CONCLUSIONS

In the paper the analytical expression describing the effect of elliptical ring beam geometric deformation errors on the small—signal characteristics of the TE_{mn}^{s} mode harmonic ECRM is derived, and also is established the quantitative relationship between the small beam geometric deformation errors and the coupling coefficient of the TE_{01}^{s} fundamental ECRM.

REFERENCES

[1] Yu Yongjian, "A Theorem in Relativistic Electronics", *Int. J. of IR& MM Waves*, Vol. 4, p. 588, Apr. 1990.

DESIGN AND PERFORMANCE OF 94-GHz HIGH POWER MULTICAVITY GYROKLYSTRON AMPLIFIER

I.I.Antakov, E.V.Zasypkin and E.V.Sokolov

Institute of Applied Physics, Russian Academy of Science
46 Uljanov St., 603600, Nizhny Novgorod, Russia

ABSTRACT

Four-cavity gyroklystron has been built and tested in pulse operation. At the TE_{04} cavity mode output power 65 kW, efficiency 26%, gain about 35 dB and bandwidth 0.3% were observed .Maximum efficiency 34% has been achieved with output power 57 kW.

2. DESIGN

A triode magnetron-injection-type gun was utilized to produce a hollow annular electron beam with a current of 3-5 A and a beam voltage V_0 of 55 kV. The Tsimring code [4] was used to optimize an electrode shapes. The simulation predicted a transverse velocity spread of 20% with velocity ratio $\alpha = v_\perp/v_\parallel =$ 1.73 when the anode voltage V_a is equal to 0,3 V_0. The nominal magnetic field in the interaction region was 3.7 T and the value of magnetic compression was 25. The cathode coil was used to control the beam's velocity ratio.

A schematic view of the RF circuit together with the longitudinal distribution of the constant magnetic field is shown in Fig.1.The circuit consists of four circular cavities operating in the TE_{04} mode at the fundamental cyclotron frequency.These cavities were separated by drift lengths ($L^{dr}_{1,2,3} \simeq 2\lambda$, where λ is the operating wavelength),which were cut off at the operating frequency for TE_{24} mode and other high-order modes. The optimal parameters of the cavities designed with the help of the nonlinear theory of the gyroklystron [2] were following :input cavity - $Q_1 = 150$, $L_1 = 1.3\lambda$, intermediate cavities - $Q_2 \simeq Q_3 \simeq 250$, $L_1 \simeq L_2 \simeq 1.5\lambda$, output cavity - $Q_4 = 300$, $L_4 \simeq 2\lambda$. The drive signal was introduced to the first cavity through a system of four slits in the wall of the cavity.The input RF power was supplied by a 100 μs, 100 W orotron which was mechanically tunable from 92.5 to 94.5 GHz. The gyroklystron was operated at a pulse repetition frequency of 5 Hz and a pulse duration of 100 μs.

3. EXPERIMENTAL RESULTS

Figure 2 plots measured dependencies of output power and efficiency on beam current. Beam and anode voltages, input power level were fixed and all other parameters - driving signal frequency, magnetic fields in the interaction region and cathode region - were adjusted to maximize the output power at each data point. The peak efficiency was 34% and the largest power

of about 65 kW occured at 4.5 A. Fig.3 shows the dependencies of output power and gain on input power. The peak saturated gain was about 33 dB and in the range of small input power levels gain achieved 40 dB. The dependence of output power on drive frequency at fixed beam and anode voltages, current, input power and optimal other parameters is illustrated in Fig.4. The optimal frequency f_0 = 93.16 GHz was close to the "cold" eighenfrequency of the output cavity. Half-power bandwidth determined, primarily, by the Q-factor of the fourth cavity was about 0.3% .

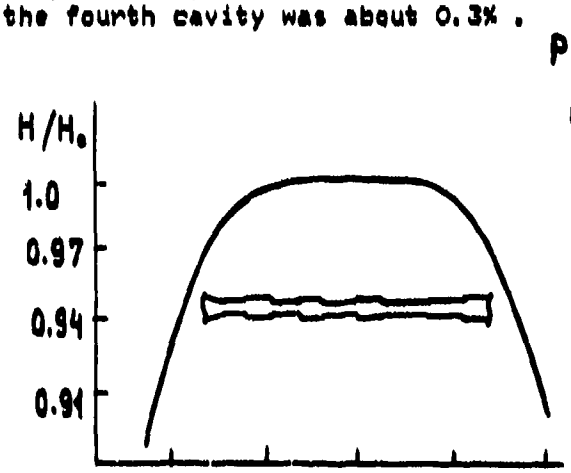

Fig.1. Sheматic view of the RF circuit and magnetic field

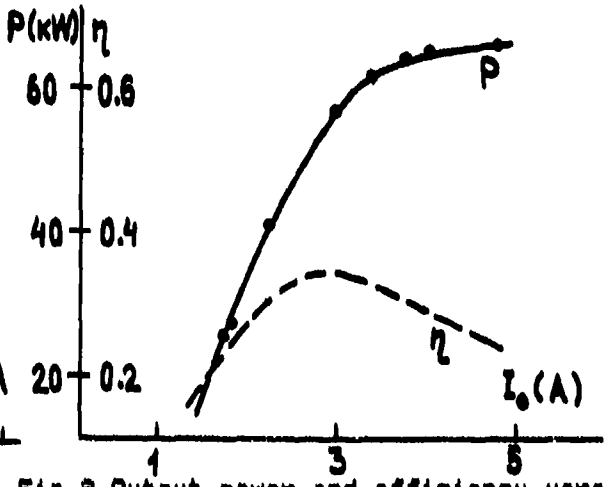

Fig.2. Output power and efficiency versus beam current (V_0= 55kV, V_a= 0.3V_0, f=f_0)

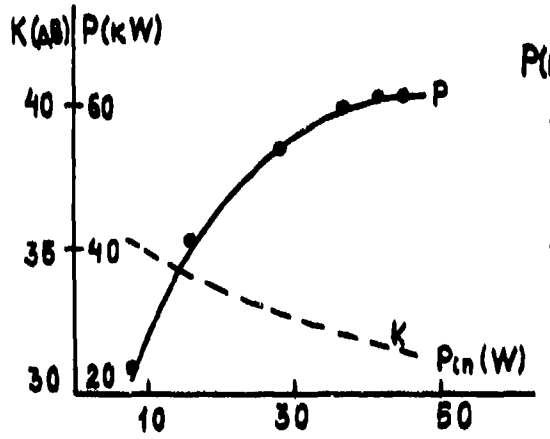

Fig.3. Output power and gain vs input power (V_0= 55kV, I_0= 3.4A)

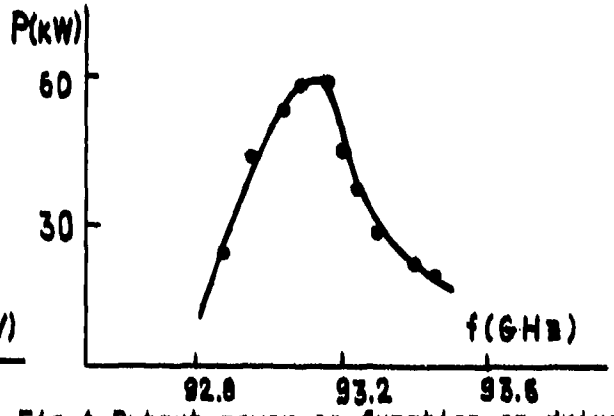

Fig.4. Output power as function on drive frequency (V_0= 55kV, I_0= 3.4A, P_{in}= 40W)

4. REFERENCES

1. V.K.Lygin, V.N.Manuilov, B.V.Rayski, Eh.E.Tsimring, " Theory of helical electron beams in gyrotrons," Int.Journal of Infrared and Millimeter Waves, Vol.14, N 4, 1993.

2. A.V.Gaponov, A.L.Goldenberg, V.K.Yulpatov, "Cyclotron resonance maser with two cavities (CRM - klystron)," Abstracts of the V th All-Union Conference on Microwave Electronics, Saratov University, p.20, 1966 (in Russian).

Analysis of a diode mounting structure of a subharmonically pumped millimeter-wave mixer

Stefan D. Vogel

University of Bern, Institute of Applied Physics
Microwave Department, CH-3012 Bern, Switzerland

ABSTRACT

A method of analysing a two-diode mounting structure of a millimeter-wave mixer, using commercially available high-frequency structure simulation software, is presented. The method yields an equivalent circuit representation suitable for subsequent mixer-simulation and can be transferred to analyse other mounting geometries.

1. INTRODUCTION

In 1979 Kerr[1] presented a method of analysing two-diode mixers like balanced or subharmonically pumped mixers. As a key part for a realistic mixer analysis one needs to know a suitable representation of the diodes' embedding circuit. Especially the parasitic circuit elements which are determined by the special diode mounting geometry are difficult to predict or to measure. However, they may have significant influence on the mixing performance, as Kerr[2] showed for example for the series inductance of mixer diodes.

In this paper a method is presented to analyse a two diodes mounting structure of a subharmonically pumped mixer using a commercial electromagnetic simulation product, the High Frequency Structure Simulator (HFSS) of the Hewlett-Packard Company. The electromagnetic behavior of the full three-dimensional mounting structure is simulated by HFSS under different states of the diode conductance. In a second step respective equivalent circuits are fitted simultaneously to meet the simulated performance.

2. STRUCTURE ANALYSIS

The configuration analysed exemplarily in this paper is schematically shown in Fig. 1. The two Schottky barrier notch front diodes are antiparallel shunt mounted on a suspended substrate stripline (SSS). This structure is used in a 142 GHz mixer scaled from a design described by Carlson et al.[3] For the embedding geometry the equivalent circuit representation shown in Fig. 2 seems to be reasonable. The whiskers contacting the anode of the diodes are expected to contribute series inductance L_1 and L_2 to the embedding circuit. The mounting pads together with the diodes themselves are expected to contribute some parallel capacitance C_1 and C_2. It is also reasonable to allow some magnetic coupling between the whiskers in form of a mutual inductance M and an electric coupling between the mounts represented by an additional capacitance C_3 as shown in Fig. 2.

HFSS is capable of calculating S-parameters of arbitrarily shaped multiport structures, where the ports have to be outer planes. The mounting structure is analysed as a discontinuity on the SSS where from structure to structure the conductances of the diodes are varied, e. g. any combination (a total of four) of short circuiting or open circuiting either diode is chosen. Three different whisker lengths are analysed ($l_{whisk.} = 78\,\mu m, 106\,\mu m, 134\,\mu m$), which cover the possible range in the present layout. Dielectric and conduction losses were neglected to reduce the calculation time required for the field simulations.

From the results of the field simulations of the structure as shown in Fig. 1 the impedances of the discontinuity in the respective states of conducting and nonconducting diodes are calculated. An optimisation algorithm of a commercial circuit simulation software product (MDS of Hewlett-Packard Company) is used to find the equivalent circuit parameters of Fig. 2 which meet the field simulation results. These optimisations are performed for different frequency ranges separately. 1st range (IF): 2 to 20 GHz, 2nd range (LO): 68 to 76 GHz, 3rd range (RF): 140 to 150 GHz.

3. RESULTS

The results of the optimizations are summarized in Tab. 1. Excellent agreement between the field simulations and the equivalent circuit performance could be achieved with reasonable equivalent circuit parameters. The mounting structure is found to be nearly symmetric with respect to the diodes. The equivalent circuit parameters are slightly dependent on the frequency-range. Especially at lower frequencies a significant magnetic coupling M between the whiskers has to be taken into account. At higher frequencies the electric coupling C_3 becomes significant.

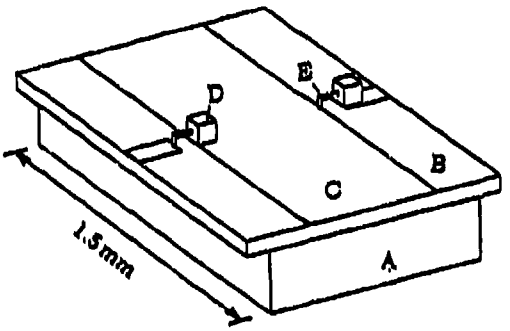

A: Air
B: Quarts
C: Metallisation
D: Notch Front Diode
E: Whisker

Figure 1: Two-diodes mounting structure, top cover of SSS removed.

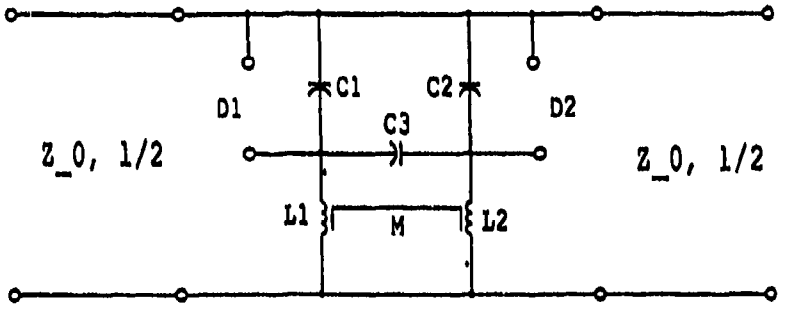

Figure 2: Equivalent circuit of two-diode mounting structure.

$l_{Whis.}/\mu m$	freq. range	L_1/pH	L_2/pH	C_1/fF	C_2/fF	M/pH	C_3/fF
78.	ZF	123.	122.	10.9	12.1	40.0	0.0
	LO	115.	113.	13.0	13.2	34.3	0.0
	RF	85.1	73.3	13.8	16.6	6.43	4.81
106.	ZF	130.	129.	11.0	11.1	40.2	0.0
	LO	123.	120.	12.6	13.0	35.0	0.0
	RF	90.3	96.3	30.9	8.22	14.8	9.63
134.	ZF	144.	143.	11.9	13.5	42.6	0.0
	LO	134.	132.	13.7	13.9	31.1	0.0
	RF	108.	99.7	14.2	14.7	10.5	2.52

Table 1: Equivalent circuit parameters determined by structure simulations.

4. REFERENCES

1. A. R. Kerr, "Noise and loss in balanced and subharmonically pumped mixers: Part I-Theory", *IEEE Trans. on MTT*, Vol. MTT-27, No. 12, pp. 938-943, Dec. 1979.

2. A. R. Kerr, "Noise and loss in balanced and subharmonically pumped mixers: Part II-Application", *IEEE Trans. on MTT*, Vol. MTT-27, No. 12, pp. 944-950, Dec. 1979.

3. E. R. Carlson, M. V. Schneider, T. F. McMaster, "Subharmonically pumped millimeter-wave mixers", *IEEE Trans. on MTT*, Vol. MTT-26, No. 10, pp. 706-715, Oct. 1978.

Terahertz Metal pipe Waveguides.

A.S.Treen and N.J.Cronin
School of Physics ,University of Bath,
Claverton Down, Bath, Avon. BA2 7AY.

Abstract

A novel photlithographic technique has been developed for the fabrication of fundamental mode metal pipe waveguide for operation at frequencies between 300GHz and ~2THz. The guides are formed on a semiconductor substrate and hence active devices such as Schottky or Resonant Tunnelling Diodes (RTD) may be incorporated within them.

Introduction

In recent years there has been a growth of interest in systems working in the millimetre to sub-millimetre region of the spectrum. A limitation to the number of uses that have so far been identified is the lack of a convenient, cost-effective waveguide media in which these systems may be designed . At present most devices working at frequencies in excess of 300GHz employ rectangular waveguide and devices are normally incorporated within this using the classic ' cats whisker' mount. In most cases this has proved quite successful due to the low parasitics associated with the whisker. The method does however have two major drawbacks. The first is that above ~400GHz the dimension of fundamental mode rectangular waveguide becomes so small that fabrication by conventional techniques such as milling or electroforming becomes increasingly difficult, time consuming and consequently costly. Secondly mounting active devices such as schottky or resonant tunnelling diodes using a whisker becomes difficult requiring considerable expertise and time to produce a contact whose reproducibility is at best questionable.
Above ~300GHz the width of fundamental mode waveguide (1mm) reduces to a size comparable to features commonly and accurately produced using photolithographic techniques. A novel method of manufacturing sub-millimetre waveguides using photolithography is thus presented and a method for incorporating an integrated active device is suggested.

Fabrication method

The process used to fabricate the waveguides is summarised in figure 1.
The base substrate, which is polished so that it is optically flat, is first coated with an evaporated layer of NiCr/Au as shown in fig 1a.
This metal layer forms the base wall of the final waveguide and must therefore be much thicker than the skin depth at the operating frequency in order to prevent excessive power loss.
A thick layer of photoresist is then applied to the substrate. The thickness of this layer determines the height of the final waveguide and must therefore be of the order of several tens of microns. This is appreciably thicker than a standard spun layer which has a maximum thickness of less than 10 microns. The maximum thickness produced thus far has been 80 microns. This corresponds to a quarter height guide for use at 300GHz or a full height guide at 1THz.
The guide is defined in the photoresist using standard photolithography techniques (figure 1c) to produce resist 'bars' (figure 1d) . These act as formers over which the top and side walls of the waveguide are produced.
This is achieved by again coating the substrate with an evaporated layer of NiCr/Au and then gold plating to a thickness of more than 15 microns. The plating is necessary so that the guide will not collapse when the resist former is removed. This is done by first opening the ends of the guide using selective wet etching and than dissolving the resist in an appropriate solvent. The thin resistive layer of NiCr may then be removed from the inside surface of the guide walls by wet etching. This leaves an air-filled, gold-walled, fundamental mode rectangular guide whose top and bottom walls are effectively featureless since they take on the surface finish of the substrate and the resist.

Waveguide Structures

The end of a guide made by the technique outlined above is shown in figure 2. The waveguide has dimensions of 400x50 microns. In this case the guide is 6mm long which corresponds to approximately ten guide wavelengths at 600GHz. This is not the greatest length that can be produced . The limit is only set by the area of uniform resist that can be produced and the size of the illuminating area on the mask aligner.

Aside from the ease with which such waveguides may be produced compared with more traditional machining techniques, another advantage lies in the ability to produce complicated waveguide circuits. The guide width and path may easily be varied to any 2D design which can be produced on a photomask. Figure 3 shows a test structure that has been produced . This is fabricated in quarter height 600GHz guide.

Perhaps the most useful property of waveguides produced by the above method is that they can be easily formed on the top of semiconductor substrates. This would allow active devices to be incorporated within the guide using a 'whisker-like' plated via hole from the base substrate to the top wall. This would produce the equivalent of a whiskered device mount, with similar parasitics, but which can be manufactured in comparatively large numbers.

The fabrication method also lends itself to producing either several separate systems on a single chip or several separate devices within a single waveguide. This may be of use in the production of mixer and RTD arrays respectively.

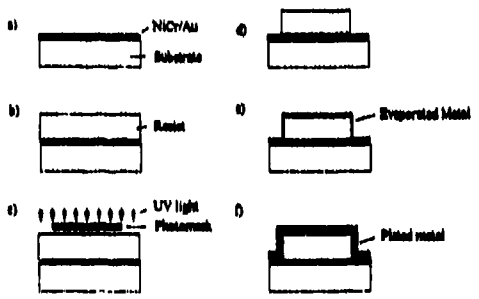

Figure 1 : Waveguide fabrication process.

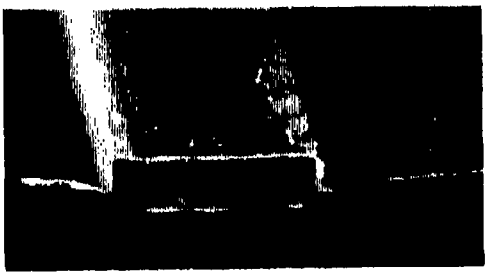

Figure 2 : End view of a waveguide (400 x 50 microns)

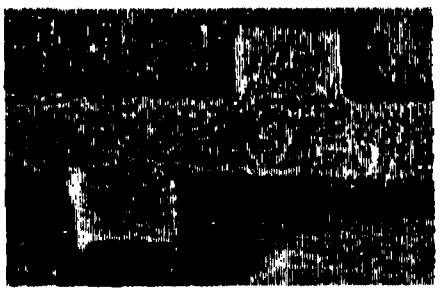

Figure 3 : Waveguide test structure.

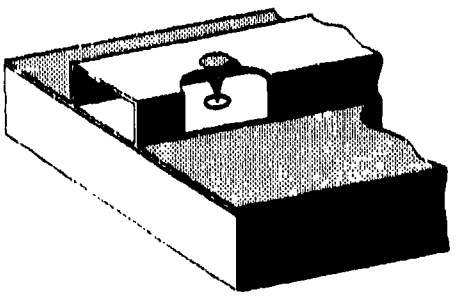

Figure 4 : Proposed whisker structure.

New Developments in Millimeter-Wave Beam Control Arrays

T. Liu, X-H. Qin, F. Wang, L. Sjogren, C.W. Domier, N.C. Luhmann, Jr.

Department of Electrical Engineering
University of California at Los Angeles
Los Angeles, California, U.S.A. 90024-1594

Abstract

Designs for a new generation of high performance quasi-optical millimeter-wave beam control arrays are presented. Through the use of low loss coplanar waveguide bias lines and improved processing techniques, wide bandwidth switching arrays and narrow bandwidth beam steering/focusing arrays are under development with predicted modulation rates in excess of 1 GHz.

Introduction

Monolithic, quasi-optical diode array beam controllers have now successfully demonstrated numerous beam control array functions, including beam steering, beam focusing, phase modulation and amplitude modulation [1,2]. Such arrays can provide high speed electronic scanning at millimeter-wave frequencies for use in millimeter-wave imaging systems, or may be employed as light weight, high speed Dicke-switch radiometers. The use of tens of thousands of varactor diodes gives the array a high power handling capability.

Beam Switching Arrays

Beam control arrays operated in transmission mode may be used to amplitude modulate a millimeter-wave beam. This is achieved by varying the dc bias placed upon each of the high frequency varactor diodes in the diode array, which in turn varies the array impedance and hence the array transmission. Although not designed for high speed switching, such an array has been successfully used to amplitude modulate a transmitted beam at 165 GHz with a measured modulation response thatis observed to be flat out to 50 MHz, with a 3 dB point of ~ 150 MHz [1].

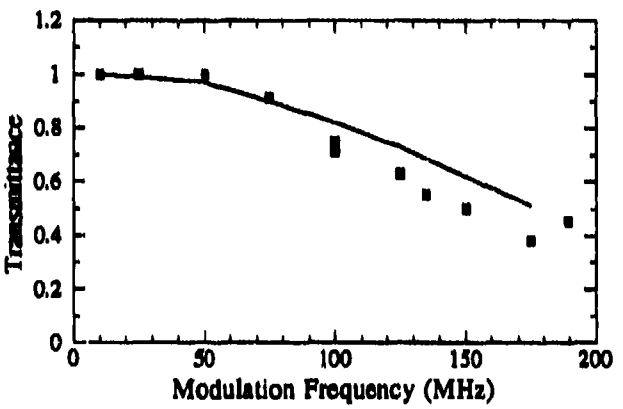

Figure 1. Experimental beam transmittance as a function of amplitude modulation frequency for the array of [1].

High bandwidth quasi-optical switching arrays capable of modulation rates in excess of 5 GHz are now under development, achieved by configuring the array as a series of low loss coplanar waveguide lines along which the control signals travel. Each control line is terminated by a 50 Ω resistor that has been fabricated monolithically. Simulation results for one such array show a contrast ratio (the ratio of the transmitted power when ON to the transmitted power when OFF) of at least 20 dB, with an average insertion loss of approximately 3 dB.

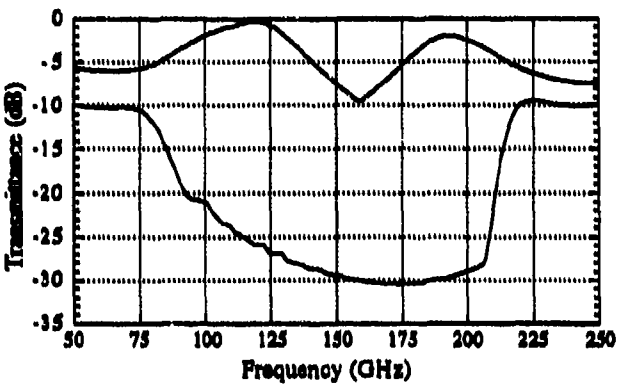

Figure 2. Minimum and maximum beam transmittance as a function of rf frequency for a high speed switching array.

Beam Steering/Focusing Arrays

Beam control arrays operated in reflection mode may be used to phase modulate a millimeter-wave beam. Such beam phase shifters, biased to provide a linear phase progression across one axis of the array, can provide electronic scanning for use in millimeter-wave imaging applications. Biasing the array to provide a quadratic phase progression across one axis of the array can likewise cause the array to act as an electronically controlled focal length mirror. Figure 3 shows that limited levels of beam steering (± 6°) and beam focusing/defocusing functions have now been demonstrated at 120 GHz [2]. It should also be noted that the same high switching speeds that were achieved for the amplitude modulation experiments are applicable here for beam steering and beam focusing/defocusing functions.

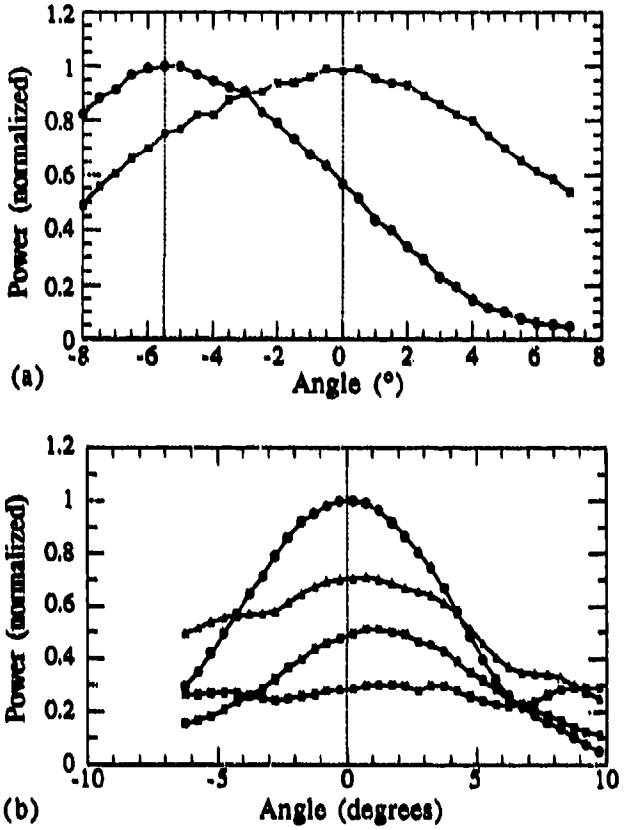

Figure 3. E-plane patterns at 120 GHz for (a) beam steering, and (b) beam focusing.

The limited angle steering and focusing/defocusing functions achieved by the array of Fig. 3 was achieved with an array with a useable phase range of ≈ 70°. This is nearly the best that can be achieved using a single grid reflection phase shfter array. By stacking two arrays together, however, it becomes possible to achieve a useable phase range in excess of 270°, which is the minimum useable phase range required [3] for successful beam steering/focusing/defocusing operation.

Computer simulations show that it should be possible to fabricate a two-grid reflection phase shifter, consisting of two identical beam control arrays stacked atop on another and backed by a perfectly reflecting mirror, with a 270° phase range with minimum power loss. For example, the high speed switching array design discussed earlier, designed solely for transmission control at very high frequencies (110-220 GHz bandwidth), is seen to work surprisingly well as a reflection mode phase shifter/beam steerer array. With suitably chosen wafer thicknesses, simulations show that this array could achieve a 270° phase range at 60 GHz with an average insertion loss of only 0.6 dB and a maximum insertion loss of only 1.1 dB.

Conclusions

Quasi-optical millimeter-wave beam control arrays have been shown to be an exciting new technology with applications in a variety of fields. At this point in time, we are just beginning to explore the vast range of configurations and control structures [4,5] that are possible using this technology, such as the use of monolithically integrated Schottky-barrier photodiodes to allow optical beam control rather than electrical beam control. In conjunction with a suitably modulated light source, this design should allow beam control on a picosecond time scale with a simple biasing arrangement and less susceptability to electromagnetic noise.

Acknowledgements

This work is supported by the Joint Services Electronics Program, the Department of Energy under contract DE-FG03-86-ER53225, and the Northrop Corp. under the University of California MICRO program.

References

[1] L.B. Sjogren, H-X.L. Liu, F. Wang, T. Liu, X-H. Qin, W. Wu, Esther Chung, C.W. Domier and N.C. Luhmann, Jr., "A Monolithic Diode Array Millimeter-Wave Beam Transmittance Controller," to be published in *IEEE Transactions on Microwave Theory and Techniques*, (1993).

[2] L.B. Sjogren, H-X.L. Liu, X-H. Qin, C.W. Domier and N.C. Luhmann, Jr., "Phased Array Operation of a Diode Grid Impedance Surface," to be published in *IEEE Transactions on Microwave Theory and Techniques*, (1993).

[3] P.F. Goldsmith, "Zone Plate Lens Antennas for Millimeter and Submillimeter Wavelengths," *Proceedings of the Third International Symposium on Space Terahertz Technology*, 345 (March 24-26, 1992).

[4] L.B. Sjogren, H-X.L. Liu, T. Liu, F. Wang, C.W. Domier and N.C. Luhmann, Jr., "Control Techniques for Millimeter-Wave Active Arrays," *International Journal of Infrared and Millimeter Waves*, 14, June 1993.

[5] L.B. Sjogren, H-X.L. Liu, X-H. Qin, C.W. Domier and N.C. Luhmann, Jr., "Electronic and Electromagnetic Devices for Millimeter-Wave Beam Control Arrays," *International Journal of Infrared and Millimeter Waves*, 14, June 1993.

Design of a Millimeter Wave Quasi-Optical Oscillator

J. Bae, M. Akaishi, Y. Aburakawa, and K. Mizuno

Research Institute of Electrical Communication, Tohoku University,
2-1-1 Katahira, Aoba-ku, Sendai 980, Japan

ABSTRACT

A Fabry-Perot resonator with a grooved mirror (Fig. 1) has been used for coherent power combining of active elements in the millimetre and submillimeter wave region. The elements are mounted on the mirror which acts as an impedance matching circuit as well as a heat sink, promising a high power operation of the elements. In this paper, equivalent circuits of the resonator with two-terminal (Gunn diodes) and three-terminal (HEMT's) elements are presented.

HEMT OSCILLATOR

Fig. 2 shows schematic drawing of the grooved mirror with HEMT array. For that configuration of the grooved mirror and for a TEM_{00} mode field distribution in the resonator, the equivalent circuit is considered as shown in Fig 3 when referring to Ref. 2. If an operating wavelength is much larger than a height d of the grooves, the lead inductance L_r and the parasitic capacitance C_r are considered as lumped elements, simply being calculated these values from a size of the metal leads. The fringing capacitance C_F can be also calculated by analyzing the field distributions at the surface of the grooved mirror [3]. The groove impedance is represented by $Z_G=Z_0 \times d/(2s)$, where s is the spacing between the HEMT's and Z_0 is the impedance of the free space. Z_m is the impedance corresponding to a coupling loss at the output mirror including the other cavity losses. Using the equivalent circuit, an oscillating frequency is determined by using S-parameters of a HEMT and the oscillation condition, $\Gamma_g\Gamma_l=1$.

In order to examine a validity of the equivalent circuit. an oscillating frequencies have been measured experimentally for a HEMT oscillator with 3x3 transistor array. The HEMT's used were type NE-32684A (NEC) which operates up to 18 GHz. The experimental results are shown in Fig. 4. The solid lines represent the calculated oscillating frequencies obtained from the equivalent circuit. Z_m has been adjusted to agree with the oscillation frequency range in the experiment. From Fig. 4, it is found that the equivalent circuit have well explained a variation of the oscillating frequency as a function of a cavity length in the HEMT oscillator.

GUNN DIODE OSCILLATOR

Fig. 5 shows an equivalent circuit of a Gunn diode oscillator. In order to design the Gunn diode oscillator, an admittance of the Gunn diode in oscillation must be determined for a diode RF voltage. An admittance of a waveguide cavity used to oscillate a Gunn diode has been measured in replacing the diode with an RF probe to a network analyzer. Fig. 6 shows the Gunn diode admittance in the range from 42 to 48 GHz. The Gunn diode used in this experiments is Alpha Industries, Inc. type DGB8466.

[1] K. Mizuno et al., Electron. Lett., vol. 24, pp. 792-793, 1988.
[2] Z. B. Popovic, Ph. D. Thesis, California Institute of Technology, 1990.
[3] H. Kondo et al., IEEE Trans. Microwave Theory Tech., vol. MTT-40, No. 5, pp. 857-863, 1992.
[4] J. Bae et al., IEEE Trans. Microwave Theory Tech., 1993 (to be published).

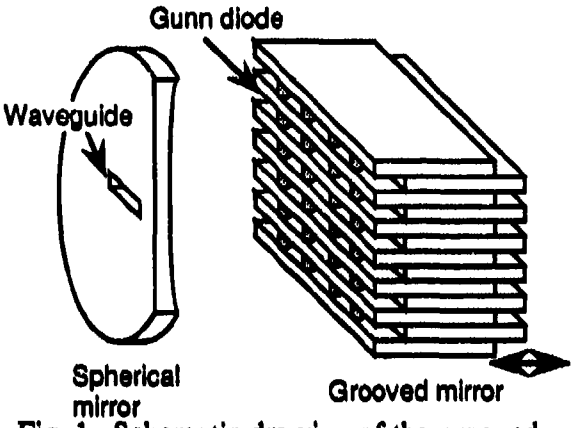

Fig. 1 Schematic drawing of the grooved mirror type Fabry-Perot oscillator.

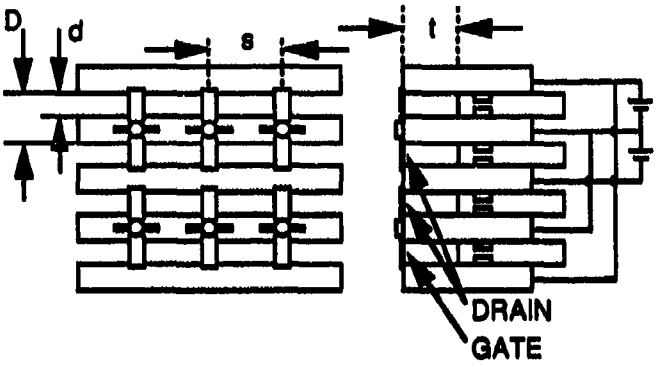

Fig. 2 Configuration of the grooved mirror with HEMT array.

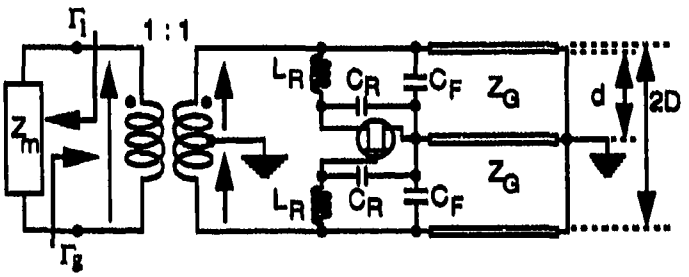

Fig. 3 Equivalent circuit of the HEMT oscillator.

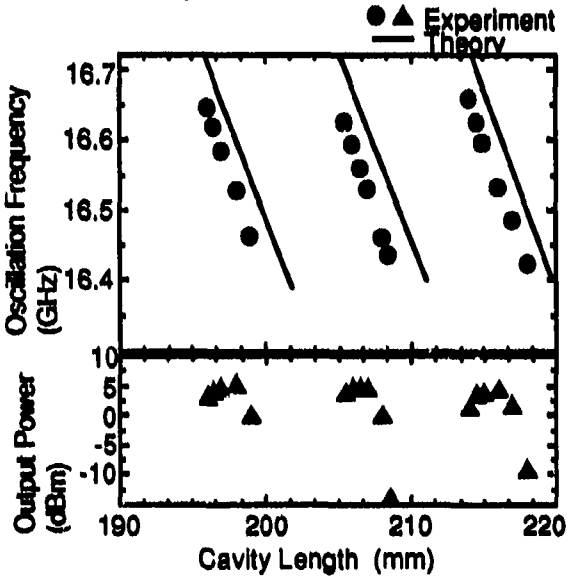

Fig. 4 Characteristics in the HEMT oscillator. The solid lines represent the predicted frequency changes from the equivalent circuit.

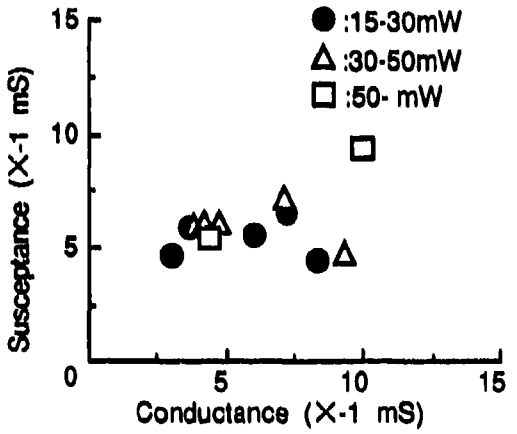

Fig. 6 Measured Gunn diode admittance for various output power.

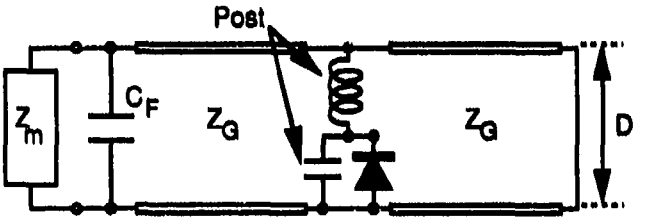

Fig. 5 Equivalent circuit of the Gunn diode oscillator.

LEAKY WAVE CORRUGATED DIELECTRIC ANTENNA FOR MILLIMETER WAVE APPLICATION.

S.C. Shrivastava and A.K.Tiwari
Maulana Azad College of Technology, Bhopal - 462 007
INDIA

Abstract

A dielectric corrugated leaky wave antenna has been developed. Metallic sidewalls have been encorporated so as to avoid radiation losses from the antenna parallel to ground plane and thus the minor lobes have been reduced. Optimization of the antenna has been done using computational methods.

Optimization of Coupling between HE_{11}-Waveguide Mode and Gaussian Beam

T. Graubner, W. Kasparek, H. Kumrić
Institut für Plasmaforschung, Universität Stuttgart
Pfaffenwaldring 31, D-7000 Stuttgart 80, Germany

INTRODUCTION

Megawatt microwave power transmission systems often use a combination of quasi optical mirror lines and overmoded corrugated circular waveguides. The optimum coupling between a free space Gaussian beam and a corrugated waveguide can be achieved by particular mode mixtures of HE_{11} and HE_{12} hybrid modes [1]. The wanted amount of the HE_{12} mode can be generated from the HE_{11} in a corrugated mode converter with periodic diameter variation or in a corrugated taper. In a previous publication [2] the design and first measurements on periodic mode converters have been presented. The promising detailed measurements (section A) of these rather long devices stimulated the development of very compact converters - i.e. nonlinear tapers. Their design is presented in section B.

A) MEASUREMENT RESULTS WITH PERIODIC HE_{11}-HE_{12} MODE CONVERTERS

HE_{12} content	1st sidelobe at E- / H-plane [dB]	X-pol. [dB]	beam-waist w_0/a E-plane/H-plane	theor. w_0/a
0 %	-28 / -26	-21	0.59 / 0.61	0.59
2.5 %	-32 / -28	-26	0.54 / 0.55	0.56
~9 %	-37 / -40	-30	0.49 / 0.50	0.50
~20 %	-40 / -38	-31	0.43 / 0.44	0.43

Table 1. Summary of far field measurements (w_0 is the eff. Gaussian beam waist radius)

The mode content of the particular HE_{11} - HE_{12} mixtures: a) 97.5%+2.5% , b) 91%+9% and c) 80%+20% produced by different optimized converters have been confirmed by k-spectrometer measurements [2]. Far field measurements yield pronounced reduction of sidelobes and cross polarisation as is shown in the example of Fig.1. Also confirmed is the calculated reduction of the beam width [1]. The results are summarized in Table 1.

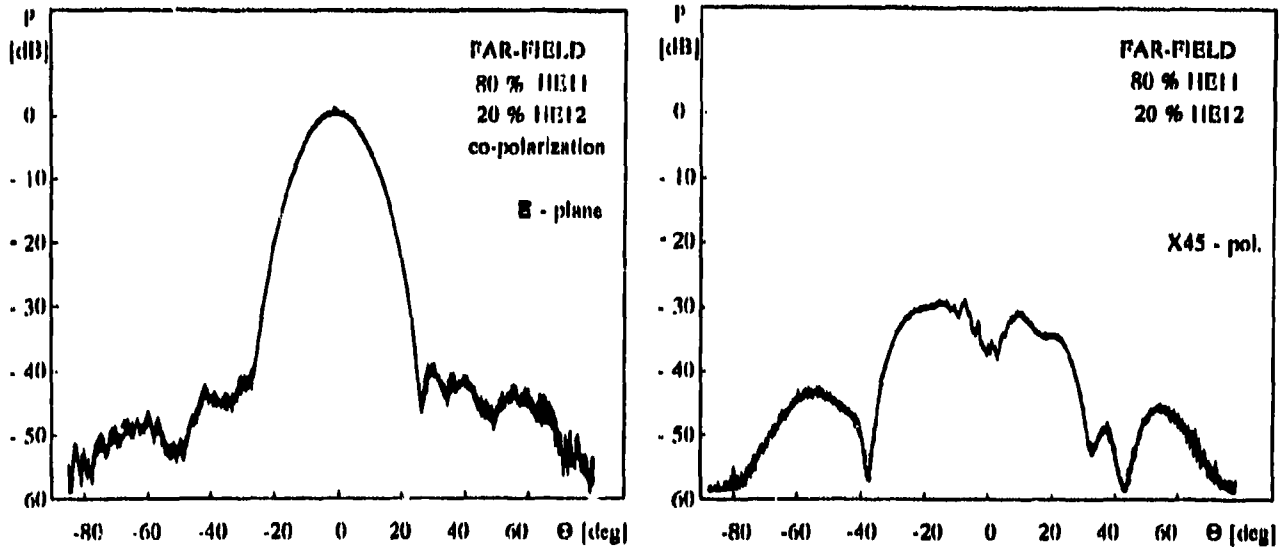

Figure 1. Measured far field 80% HE_{11} + 20% HE_{12} converter

Measurements of coupling between the waveguide and gaussian beam were performed with a resonator-technique: the plane mirror of a Fabry-Perot resonator is replaced by the mode converter with a back-short (Fig.2). The design

of the cavity is such that the beam waist is matched to the waveguide input and that no free-space modes are degenerate with the fundamental TEM_{00}. From the measured free spectral range ($\Delta\nu_F$) and the half width of the resonance line for the TEM_{00} mode ($\Delta\nu_L$) the finesse of the resonator ($F=\Delta\nu_F/\Delta\nu_L$) can be determined. The coupling efficiency η (Tab.2) is given by the formula :

$$\eta \approx 3 + \frac{\pi^2}{2F^2} - \sqrt{(1 + \frac{\pi^2}{2F^2})^2 - 1 - 2R}$$

where R is the reflectivity of the mirrors. The results are summarized in Table 2.

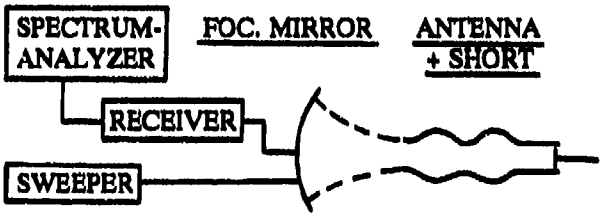

Fig.2. Experimental set up to determine the coupling efficiency

Number of beatwavelengths	η (meas.)	η (theor.)
0	0.982±.004	0.980
2	0.989±.006	0.998
3	0.986±.006	0.994

Table 2. Measured coupling efficiency for different mode converters

A clear improvement compared with the coupling of a pure HE_{11} mode is achieved, however lower than predicted. The reason for the discrepancy may be finite precision of the parts used and the alignment.

B) TAPER DESIGN

For high power applications where a large waveguide diameter is needed, periodic mode converters become very long. Therefore compact mode converting tapers have been designed with a taper profile of the type proposed by Vlasov and Shapiro [3]:
$a(z) = a_0 [1 + (z/\alpha\, k\, a_0^2)^2]$. The optimization of the taper was done at 140 GHz with different diameters and by varying of α in the formula. For example, with α=0.15 one obtains the mode composition as shown in Figure 3. The mode mixture at the output is 80% HE_{11} and 20% HE_{12}. Even for large waveguide diameters of 87.0 mm the length of a taper giving similar results is only 570 mm. Measurements with these mode converters are underway.

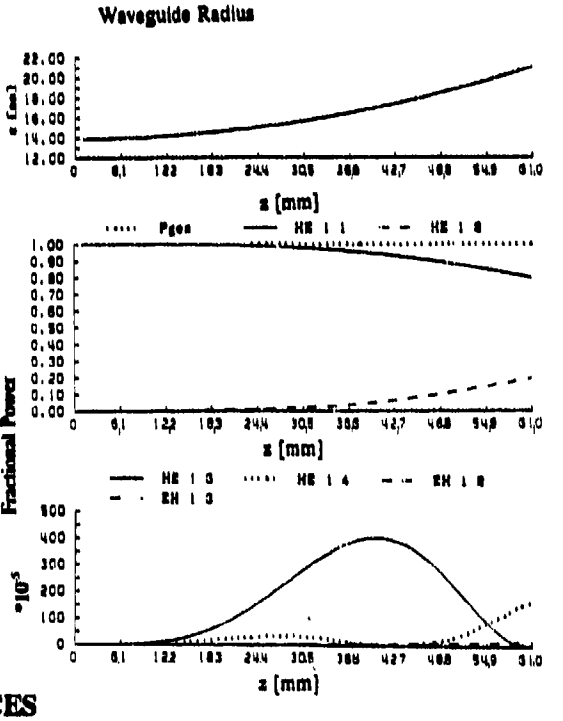

Figure 3. The mode composition as a function of the axial coordinate in an optimized taper

REFERENCES

1. Rebuffi, L., Gaussian Beam Matching to a Hybrid Mode Waveguide, Report MPI IPP Garching, 1991
2. Graubner T., Kasparek W., Kumrić H., Design and Measurements of HE_{11}+HE_{12} Mode Converters, in 17th Int.Conf. on Infrared and Millimeter Waves, R.J.Temkin, Editor, Proc. SPIE 1929, 106,(1992).
3. Shapiro M.A., Vlasov S.N., Study of Combined Transmission Line for High Power Wave Generated by a Gyrotron in the Millimetre Wavelength Range, Int. J. of Electronics, 72 (1992), 1127-1133.
4. Born, M. and Wolf, E., 1980, Fundamentals of Optics, Oxford: Pergamon Press.

SLOTLINE SURFACE-WAVE LEAKAGE AND SLOT ANTENNA PERFORMANCE

Christine LETROU*, Virgil POPESCU
Institut National des Télécommunications - DEC - 9 rue Charles Fourier - 91011 EVRY Cedex - FRANCE

Resonant slot antennas can be used in arrays to realize quasi-optical SIS mixers for submillimetric applications. Conclusions about surface-wave leakage of the slotline and its incidence on slot antenna radiation will be drawn from a transverse-resonance analysis of the slotline. This analysis is based on the use of mode-matching on the sides of the slot. Measurements on 30GHz models will be compared with theory.

Microstrip resonator using high-Tc superconducting thin film on sapphire substrates

O.D.Pustylnik, A.A.Dymnikov, I.V.Voinovsky, O.A.Khimenko

SRC "Fonon", 39, Pobedy Ave., KPI-3240, Kiev, Ukraine

V.F.Vratskikh

Institute for Thermophysics, Kutateladze 1, Novosibirsk 630090, Russia

ABSTRACT

We have measured very low microwave losses in Y-Ba-Cu-O fifth wave ring resonators. We deposited the Y-Ba-Cu-O film on (1012) non-buffered sapphire substrates and patterned microwave circuites. High-Tc microstrip resonators demonstrated best Q-factor greater then 800 at 31 GHz, corresponding to surface resistences less than 3,0 mohm. Indetical copper resonator showed Q's of 500 and surface resistance of 27 mohm. We show that the losses in the high loss samples can be accounted for by the presence of small fractions of c-axis-aligned grains highly misaligned in the plane of those films. Volume fraction of highly misagned c-axis-oriented grains as 3% lead to losses above 3 mohm.

1. INTRODUCTION

Epitaxial Y-Ba-Cu-O (123) films of high quality have been grown on substrates such as SrTiO, MgO, YSZ and LaAlO by various deposition techniques. It is known, however, that each of these substrates represent some kind of compromise [1]. From practical point of view, the substrate like sapphire is the most desirable material for 123 films because of the low microwave loss, high mechanical strength, high thermal conductivity, high Debye temperature, good surface chemistry and low cost. The lattice mismatch and reaction of Ba with sapphire are the main obstacles to epitaxial growth of 123 films on sapphire. Epitaxial Y-Ba-Cu-O films on sapphire with good critical and transport properties were demonstrated by Char et al[1], but the weak epitaxy and high surface resistance of the films have led to conclusion that it is necessary to use a buffer layer between the substrate and 123 film to improve the epitaxial match and to reducechemical reactions between substrate and film[2]. Here we report the substantial improvement of microwave properties of 123 films epitaxially grown on non-buffered sapphire by laser ablation technique.

2. FILM PREPARATION

Our deposition system will be described in details elsewhere. Briefly, 123 targets were ablated by many-mode Nd:YAG laser. The pulse energy was 300 mJ, the pulse duration 20 ns, the average beam energy density 4 J/cm^2. The distance of the target and the substrate was 6 cm and the screenwas placed between target and substrate in order to protect the film surfa-ce from droplets. At a pulse repetition rate of 10 Hz the average growth rate was 0,3 nm/s. The

oxygen pressure was 0,6 Torr and the substrate temperature, measured with accuracy 5°C, was 755-770°C. There latively high oxygen pressureis necessary to produce large clusters and to reduce in such way the chemical activity of Ba on the substrate surface. The elevated substrate temperature is required for surface mobility of large clusters. The films quality was sensitive both to substrate temperature and oxygen pressure.

3. SUBSTRATES

Among 1500 experiments required for optimisation of film growth conditions only 300 were carried out with the "fresh" substrates. In other cases 123 films were removed by etching and used again so that any substrate was utilized two or three times. In research aimed at optimisation of growth conditions, the assessment of the films quality was carried out by dc transport measurements. No difference in critical properties (Tc, Tc,Jc and R300/R100) for 1st, 2nd and 3rd deposition run with the same substrate was found. In opposite, our recent x-ray measurements reveal the strong dependence of volume percent of grains misaligned in a-b plane on substrate surface history and surface preparation procedure. The summarised volume percent of grains misaligned at various angles was varied from 0,5 to 5 % for different samples. For most samples, the distribution of misaligned at 45 grains was not uniform and varied from 0,1 % to 1,5 % . These observations indicates that the state of substrate surface in most cases was not perfect.

4. FILM CHARACTERIZATION

The x-ray diffraction pattern of our films contains only (00L) sharp peaks showing, that the film is highly oriented with the c-axis perpendicular to the substrate. The FWHM of the [005] rocking curve was in the range of 1.3-2.5° Some general parameters of samples, used for microwave measurements and device fabrication are represented in Tabel 1.

Tabel 1 General parameters of samples.

Sample	Tc (R=0), K	T, K	Jc, A/cm^2	R300/R100	Thickness, nm	Rs, mohm at 35 GHz
A	90	0.5	$> 10^6$ * at 77K	3	150	3.5 at 55K
B	89.3	0.5	$> 10^6$ * at 77K	3	150	10 at 55K
C	89	1.0	$> 3*10^5$ * at 77K	2.5	150	19 at 55K

* dc - transport measurements.

5. MICROWAVE MEASUREMENTS

The measurements of the temperature dependence of microwave surface resistance were carried out at 134 GHz using a method of a cylindrical copper host cavity. The cavities cavity excited in the TE_{011} mode. In detail this method was reported in work[3].Moreover, the temperature dependence of Rs was calculated from the measurements of the unloaded quality factor Qo of the cavity. Temperature variation between 10 and 150 K was provided by warming the cavity in vacuum in helium cryogenic system. The temperature was measured with a semiconductor resistor with an absolute accuracy of + 0.1 K. Fig.1 shows Rs vs T for our three films (sample A,B,C in Table 1) measured at 134 GHz.For comparison at the same figure by solid line is plottedthe temperature dependance of the surface resistance of the copper cavity walls. Thickness of films were about 150 nm. The low residual rezistance film A, taking into account that the film thickness was lower than penetration depth of magnetic field, shows that the film is of high quality.The calculated value of Rs at 31 GHz using quadratic frequency dependence of Rs is represented in Table 1.

6. DEVICE FABRICATION

The 123 film was patterned with photolithograhic technique and etched with dilute phosphoric acid. The film on sipphire was coated with 0.7 micron FP-383 positiv photoresist. The photoresist was then baked in 90 ^{o}C oven for 15 min and after wards was exposed 42 s using a 1:1 contact printer using UF lamp. Then 1:1 diluted developer was used to develop the photoresist for about 10 s in a < 100 ^{o}C over for 30 min stabilized the resist for optimized line width control during the 123 wet etch in a diluted solution phosphoric acid. After this etch, the photoresist was stripped in acetone. Fig.2 shows the temperuture dependence of the surface resistance of the film used for microstrip resonator fabrication, that was measured by resonator host cavity method before the lithography and the temperature dependence of microstrip resonator Q-factor of the patterned film.

7. MICROSTRIP RESONATOR MEASUREMENT

Ring resonators were designed at 31 GHz with a ring impedance of 50 ohm and excited in TM_{11} mode. The ring diametr was chosen for fifth hurmonic. The microstrip line width was 0,24 mm, the mean ring diameter was 2,52 mm for substrate thickness 0,245 mm. Coupling gaps provided insertion loss over 15 dB. Measurements of the transmission coefficient, made at temperature range 10-100 K, were used in standard way to determine unloaded quality factor Q. The substrate was placed inside a copper holder on the cooler of vacuum helium cryostat inside the vacuum chamber. The microstrip resonator was connected with the input/output transmition lines by a waveguide-to-microstrip transition. Fig.2 summarizes the Q data obtained from films A, B, C and includes the Q data of analog copper ring resonator as a comparision. Temperature dependence of Q data is in good agreement with temperature dependence of Rs data.However, Q-factor of the sample A is higher than all. It is explaned that the results presented here wereobtained for different substrate surface defect density (Na<Nb<Nc for sample A, B, C, respectively) .

8. CONCLUSION

We consider the obtained results as the base for further systematic experiments. Taking into account the nonuniformly of our samples, the poor quality of substrate preparation on present state, the spatial nonuniformity of laser beam, the facts that measured films were not thick enough, the absence of grains misoriented in a-b plane in some parts of the best films, we can conclude that further improvement of microwave properties of 123 films epitaxially grown on non-buffered sapphire is still possible.

Research is supported by the State Programm of Ukraine "The High Temperature Superconductivity"

9. REFERENCES

1. Char,K. et al, "Properties of epitaxial Y-Ba-Cu-O thin films sapphire", Appl. Phys.Lett., 56 , pp. 595-598, 1990.

2. Rowell,J.M., "Research advances and needs related to HTSC electronics", Supercond.Sci.Techol., 4 , pp. 51-58, 1991.

3. Kessler,J.R.and Gering,J.M., "Use of a Fabry-Perot resonator for the measurement of the surface resistance of high Tc superconductors at mm wave frequencies," Int.J. IR and MM waves, 11 , pp. 151-164, 1990.

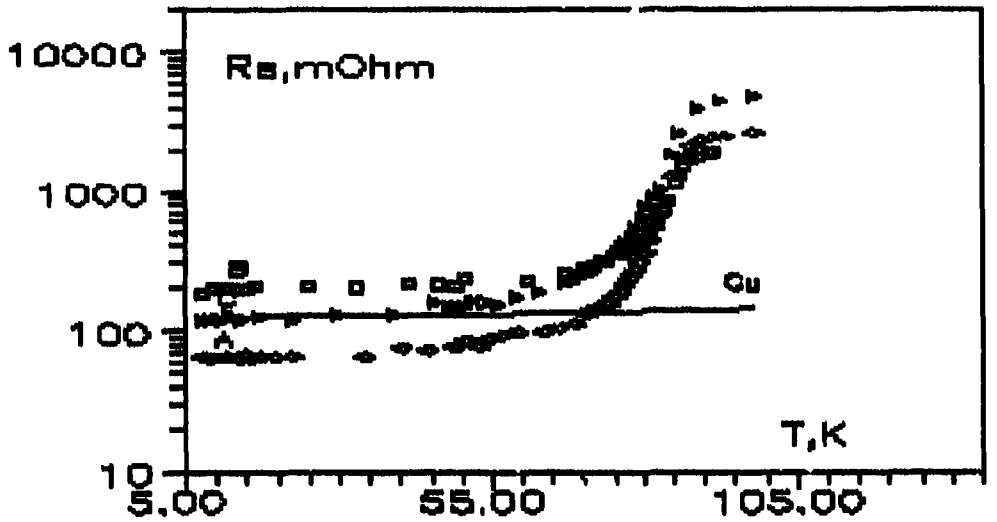

Fig. 1. The temperature depence of the surface resistance of samples.

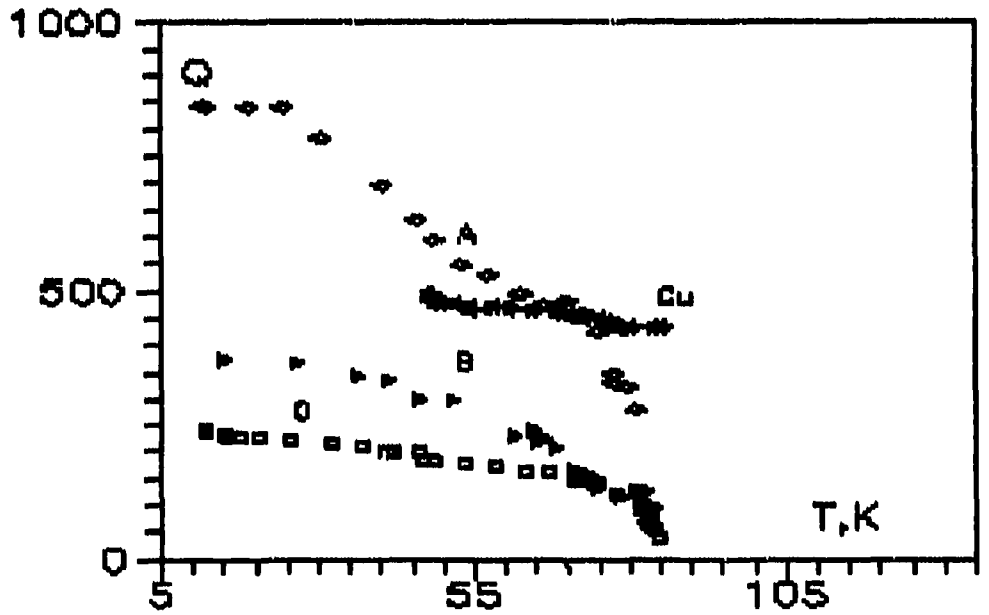

Fig. 2. The temperature depence of Q-factor of microstrip resonators.

Microwave Systems Based on the Effect of Image Multiplication in Oversized Waveguides

G.G.Denisov, D.A.Lukovnikov, and M.Yu.Shmelyov

Institute of Applied Physics, Russian Academy of Science, 46 Ulyanov Street, 603600 Nizhny Novgorod, Russia

A narrowly directed wavebeam injected into an oversized rectangular waveguide can be presented as a sum of eigenwaves. Each of them is transmitted to the remote cross-section, where they form an image of the initial wavebeam. There are certain distances, where the initial profile is repeated or split into a few beams with their amplitude profiles identical to the initial one [1]. Any initial profile is repeated at the distance $L=8a^2/\lambda$, where a is width of the waveguide, λ is wavelength. The symmetrical profile is repeated at $L_1=a^2/\lambda$, and split into n beams at $L_n=a^2/n\lambda$ (Fig. 1). Non-symmetrical input of a wavebeam results in splitting of the initial wavebeam into non-equal parts (Fig. 2). Similar effects can be formulated for linear-sectorial waveguides (Fig. 4).

If two identical wavebeams located at the position $a/4$ and $3a/4$ are inserted at the input, three wavebeams will be formed at the distance $L_2=a^2/2\lambda$ (Fig. 3a). Power of the central beam depends on the phase difference between the initial beams and varies from *0* to *100%* (Fig. 3b).

These effects of image multiplication in an oversized waveguide are suggested for use in various microwave elements and systems: tunable reflectors and attenuators, multi-window output systems, directional couplers, wavebeam scale transformers, resonators for free electron masers [2].

References:

1. L.A.Rivlin, V.S.Shil'dyaev, "Polyharmonic waveguides for coherent light," Izv. VUZov, Radiofizika, Vol. 11, 4, pp. 572-578, 1968 (in Russian).
   L.A.Rivlin, Laser Focus (1981) p.82.
2. Engineering Design of the FOM-Fusion-FEM, FOM-92, 2213/1, October, 1992.

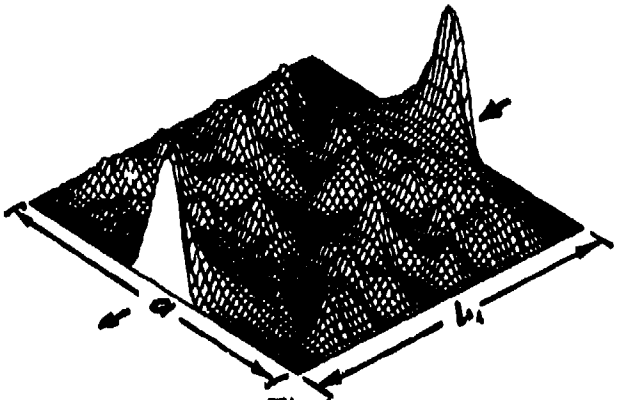

Fig.1.

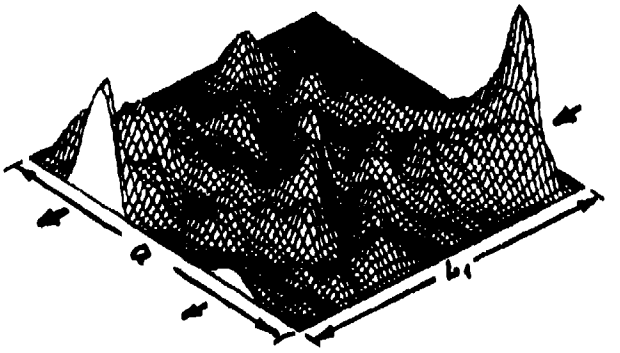

Fig.2.

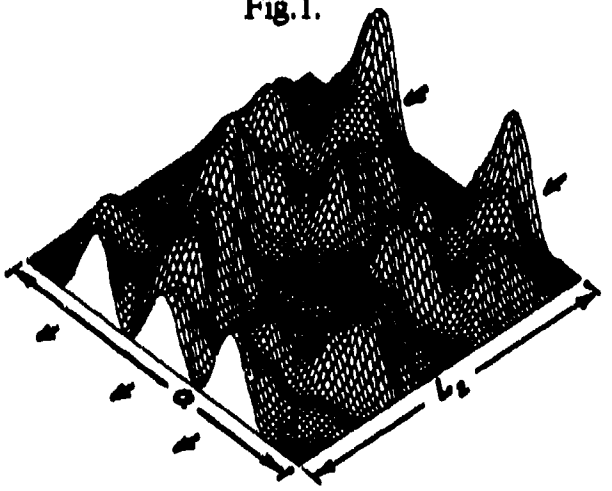

a)

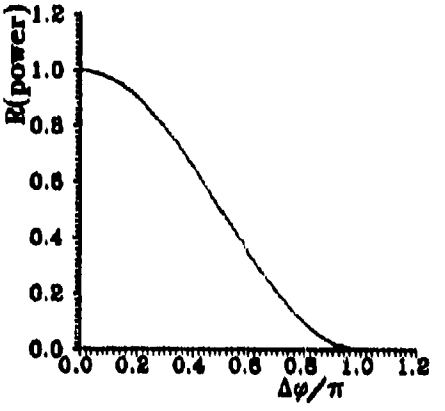

b)

Fig.3.

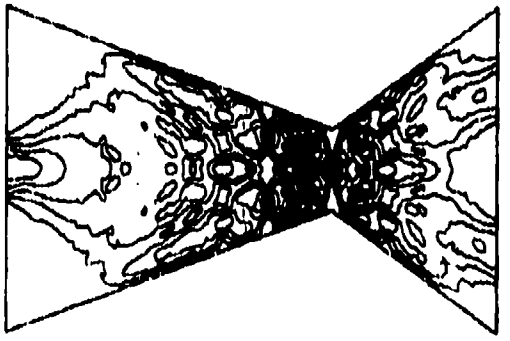

Fig.4.

Fig.1. Diffraction of symmetrically inserted wavebeam in a plane waveguide (field intensity).

Fig.2. Non-symmetrical input of wavebeam into a plane waveguide.

Fig.3. a)Interference picture of two identical wavebeams with phase difference (0.63π) in plane waveguide.

b)The fraction of the power in the central wavebeam, as a function of the phase difference between two initial beams.

Fig.4. Behaviour of symmetrically inserted wavebeam in a bisectorial waveguide (intensity levels).

Transmission-Reflection Measurements from 8 GHz to the THz

P. Goy, M. Gross, F. Beck*
AB Millimètre, 52 rue Lhomond, 75005 Paris, France, tel (33 1) 47 07 71 00, fax (33 1) 47 07 70 71
*Université de Lille 1, I.E.M.N., 59655 Villeneuve d'Ascq Cedex, France

Introduction

The Millimeter Vector Network Analyzer MVNA 8-350 has been developped by AB Millimètre since 1989. It was shown in operation up to ca. 400 GHz at the 14th Infrared & mmWaves Conference at Würzburg, Germany, in October 1989, and above 600 GHz at the 15th IR & mmW Conference at Orlando, Florida, in December 1990 (1) and at all subsequent IR & mmW Conferences (in 1991 at Lausanne, Switzerland (2), and in 1992 at Pasadena, California).

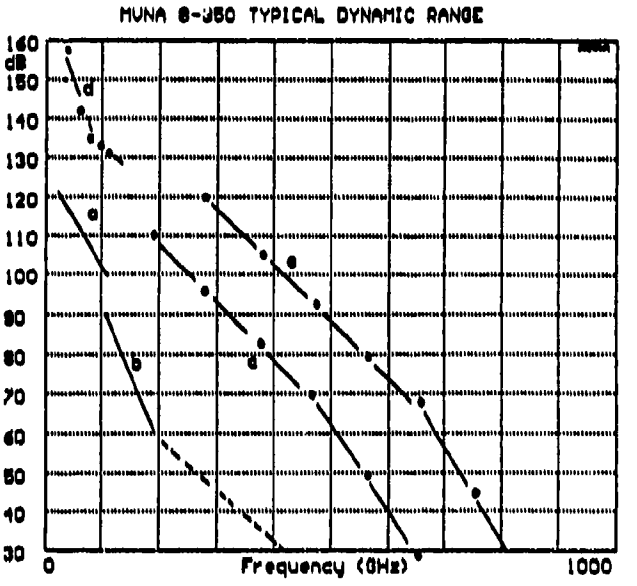

Figure 1

In the MVNA 8-350, the millimeter-submillimeter power is extracted from a Harmonic Generator HG by frequency multiplication of a source S_1, and the detection is performed in a Schottky diode Harmonic Mixer HM fed by a source S_2. The HM sends its beat frequency F_{IF} into an heterodyne Vector Receiver VR. A main oscillator defines the frequency difference between S_1 and S_2, so that their relative phase noise is cancelled. When using the same harmonic rank N on the source side and on the detection side, the phase noise of the beat at F_{IF} is also negligible, therefore the phase reference of the VR can be taken directly from the main oscillator (French Patent CNRS-ENS 1989, extended by AB Millimètre to Europe, Japan and the USA).

Depending on the desired dynamic range or frequency coverage (Fig.1), S_1 and S_2 are either centimeter sweepers feeding flat broadband (Fig.1a) or tunable (Fig.1b) millimeter heads HG and HM; S_1 can also be a millimeter Gunn oscillator followed (Fig.1c) or not (Fig.1d) by a multiplier HG. Finally, both S_1 and S_2 can be millimeter Gunn oscillators. In Fig.1e is shown the dynamic range of a system using two Gunn oscillators as S_1 and S_2, with the possibility of using all $3 \leq N \leq 8$ harmonics. More dedicated systems using two Gunn oscillators can reach the THz, although without the flexibility in the choice of N.

Transmission measurements

The calibration is obtained with HM directly linked to HG via an attenuator. The DUT is then inserted between HG and HM, and its S_{21} or S_{12} parameters are measured. Fig.2 shows, as an example of waveguide component test, the frequency response of a band-pass filter (by courtesy of Spacek Labs, Inc., Santa Barbara, CA). In a similar way, free space characterization of dielectric materials can be performed between horns. In Fig.3 are shown the absorption (squares, in dB) and the phase rotation (dots, in degrees) through a 9.78 mm

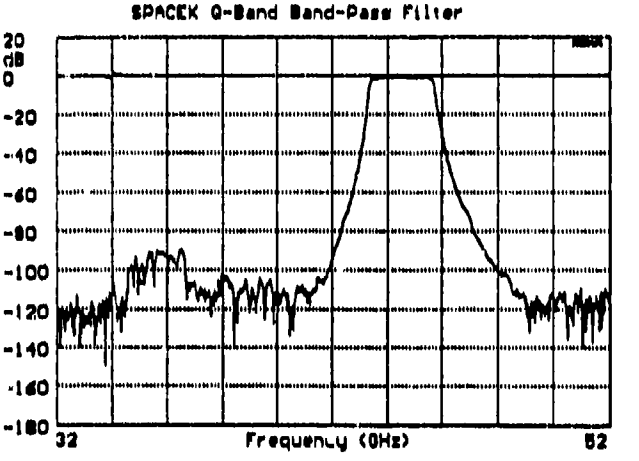

Figure 2

thick Altuglas sample. The upper solid lines correspond to the values of tan δ= 0.008 and ε' = 2.596 measured using an open cavity technique around 100 GHz. Above 200 GHz, losses increase more rapidly than frequency (tan δ is multiplied by about 4 at 760 GHz) and the real part of permittivity ε' decreases by a few percentage points. These effects have also been observed by far-infrared techniques (3).

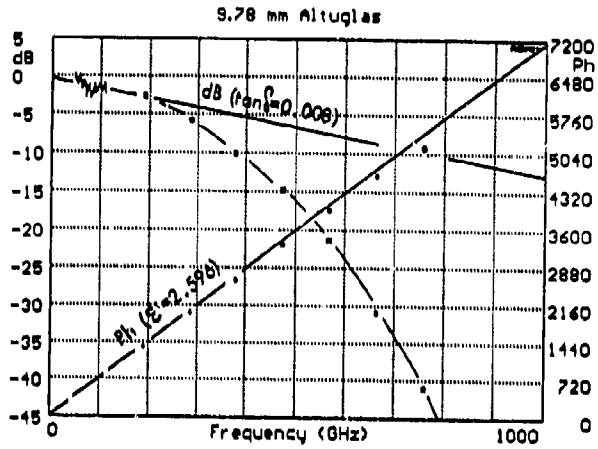

Figure 3

Reflection measurements

At frequencies where directional couplers are not easily available, reflection measurements can be performed in a quasi-optical structure: HG and HM are terminated by horn antennas facing the sample to characterize. The calibration is obtained by replacing the sample by a metal plate, supposed to be a perfect mirror. MVNA 8-350 has so observed a normal reflection of -50 dB at 475 GHz on a silicone-based anechoic (4).

When waveguide components have to be characterized in reflection (S_{11} and S_{22} parameters), HG and HM must be attached to a waveguide directional coupler DC. A calibration technique consists in terminating this DC by a short, a sliding short and a sliding matched load. Fig.4 shows an example of vector measurements with MVNA 8-350 on a 6 dB attenuator, observed by transmission (upper amplitude), and by reflection (lower amplitude). At the same scale are given amplitude measurements, at fixed frequencies, performed with three different millimeter vector analyzers, for a comparison (5). Dots are MVNA 8-350 one year before, squares are HP 8510, triangles are a six-port (5). The different angle measurements agree within ±4°.

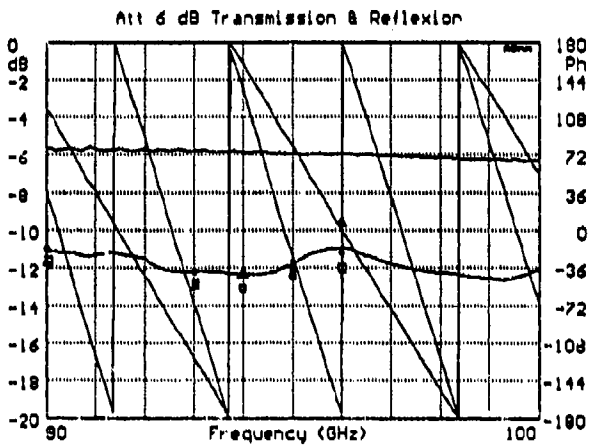

Figure 4

References

(1) P. Goy, M. Gross and J.M. Raimond, 15th Int. Conf. on IR and mm Waves, Orlando, Florida, Dec. 10-14, 1990, Proceedings R.J. Temkin Ed., p.172.

(2) P. Goy, J.M. Raimond and M. Gross, 16th Int. Conf. on IR and mm Waves, Lausanne, Switzerland, Aug. 26-30, 1991, Proceedings M.R. Siegrist, M.Q. Tran, T.M. Tran Ed., p.453.

(3) M.N. Afsar, IEEE Transactions on Instrumentation and Measurement, **IM-36 n°2**, 530 (1987).

(4) R.H. Giles, T.M. Horgan and J. Waldman, 17th Int. Conf. on IR and mm Waves, Pasadena, California, Dec. 14-17, 1992, Proceedings R.J. Temkin Ed., p.164.

(5) S. Abouchahine, B. Huyart, E. Bergeault and L. Jallet, Conf. on Precision Electromagnetic Measurements, June 9-12, 1992, p. 238.

An interferometer for near millimetre wave dielectric studies on solids at elevated temperatures

J.R.Birch and E.A.Nicol

Division of Electrical Science, National Physical Laboratory
Teddington, Middlesex TW11 OLW, UK

ABSTRACT

The construction and performance of a two-beam polarisation interferometer for use in dispersive Fourier transform spectroscopic measurements of the near millimetre wave dielectric properties of transparent solids at elevated temperatures are described.

1. INTRODUCTION

Quantitative measurements of the near millimetre wave properties of transparent solids at elevated temperatures are required in several areas of Terahertz Technology. Firstly, for the design of radomes on fast aircraft and missiles. Aerodynamic heating results in such radomes having operational temperatures that can be significantly above those of the local atmospheric environment. Second, for the design of output windows for high power electron tubes such as gyrotrons. Here, cw powers of 1 MW can be realised, and it is necessary to minimise the absorbed power in such windows in order to avoid thermal runaway window failures. Third, for the design of torus windows in fusion plasma research. These have to maintain the vacuum integrity of the torus while transmitting high input powers for rf heating and plasma diagnostics.

The present paper reports on the construction and performance of a two-beam interferometer used to study the temperature dependence of the near millimetre wave dielectric properties of transparent solids at temperatures from 300 to 1300 K.

2. EXPERIMENTAL

The interferometer was based on a two-beam polarisation configuration with tungsten wire grids as polarisers, analysers and beamdividers, as shown in figure 1. Collimated radiation from a mercury vapour arc lamp was incident at 45° on the first wire grid, wound from 10 μm diameter wire spaced 25 μm centre-to-centre. This acted as a polariser, creating orthogonally polarised beams in reflection and transmission. The reflected beam was lost to the experiment, while the transmitted beam propagated to the second grid. Its wires were oriented at 45° to the projected polarisation of the incident beam. Thus, two more orthogonally polarised beams were created, the reflected one entering the moving mirror arm of the interferometer, the transmitted one entering the fixed mirror arm. The moving mirror arm was bent through 90° by a plane mirror mounted on a vibration generator. This allowed phase modulation to be used in the measurements. The moving mirror was mounted on a stepper motor driven micrometer.

As measurements were to be made by dispersive Fourier transform spectroscopy[1], the fixed mirror arm contained the specimen furnace. This was electrically heated, approximately 350 mm long, 300 mm wide and 430 mm high[2]. It required 6.5 kW of heating to reach its maximum operating temperature of 1300 K. The specimen holder was made from a refractory material, and could be rotated through 90° under manual control so that it could be either in a vertical position with the radiation passing through

it, or horizontal and out of the beam. The fixed mirror was close to the furnace to reduce heating losses. It was made from stainless steel to avoid thermal degradation.

The two beams from the active arms of the interferometer recombine at the beamsplitter and propagate back to the original grid. This then acted as an analyser. The components of each beam that were parallel to the grid wires were reflected from it and focussed on the detector, a liquid helium cooled InSb hot electron bolometer. The orthogonal components were transmitted through the grid and lost to the experiment.

The interferometer was a rigid structure except for the furnace. This sat on the baseplate of the interferometer. This had three consequences. First, thermal expansion of the furnace was decoupled from the interferometer, avoiding phase errors. Second, as it was not a vacuum furnace, the interferometer was unevacuated and could only be used below about 60 cm^{-1} where the rotation spectrum of water vapour is less intense. Finally, in work of the nighest accuracy it would be necessary to correct for the atmospheric phase shift which is removed from the optical path when the specimen is in place[3]. The presentation will describe the instrument and its performance, illustrating this with the results of some measurements on materials of practical use.

3. REFERENCES

1. J.R.Birch and T.J.Parker, 'Infrared and Millimeter Waves, Vol.2, Ch.3', Ed. K.J.Button, Academic Press, New York 1979.

2. Supplied by Severn Furnaces, Brunel Way, Thornbury, Bristol, UK.

3. J.R.Birch, Infrared Physics 34,89-93,1993.

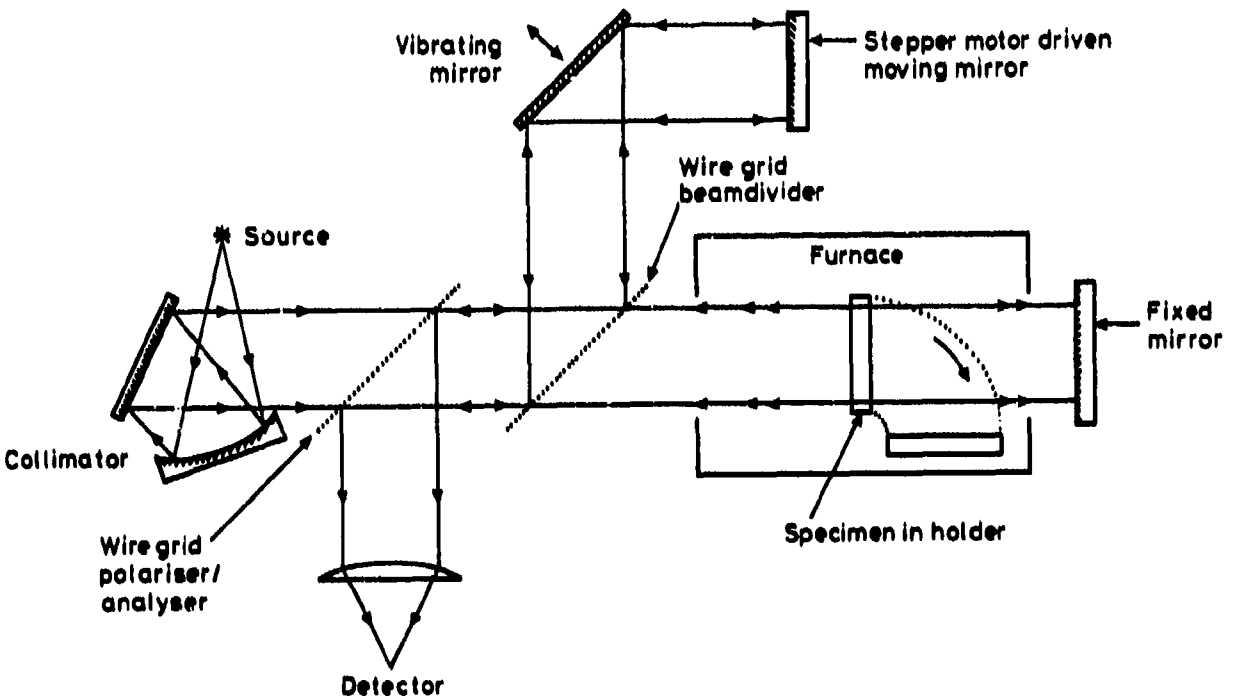

Figure 1. The interferometer for elevated temperature measurements.

Wavefront Dividing Interferometer With and Without Moving Parts.

K. D. Möller
Department of Physics, New Jersey Institute of Technology, Newark N.J. 07102
Fairleigh Dickinson University, Teaneck N.J. 07666.

1. Michelson interferometer with out moving parts using spatial superposition of amplitudes.

Interferometers without moving parts for Fourier transform spectroscopy use for the recombination process the spatial spread of the amplitudes of the two beams. At different points in space the two beams have different path differences, and by superposition, the interferogram is formed. There is a center with zero path difference and on both sides the absolute value of the path difference increases. The recombination process is schematically shown in Fig.1.

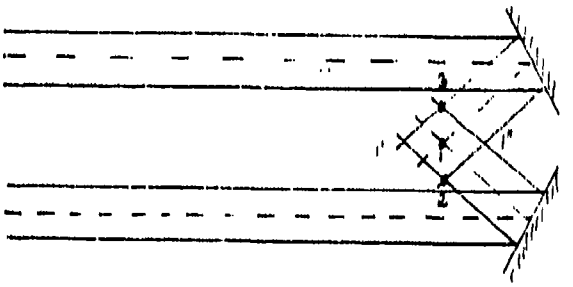

Fig.1. Recombination process by spreading the superposition of the two amplitudes over an interval in space, depending on the optical path difference of the rays in each beam. Point 1 is the center and points 1′, 1″ have zero optical path difference. Points 2 and 3 have the same optical path difference, but with opposite sign.

The sampling of the interferogram has to be done at points separated by multiples of equal length intervals. The sampling interval corresponds to $\lambda/2$ of the shortest wavelength contained in the spectrum to be studied. At each point a detector element has to be placed, but these detector elements record intensity proportional to their surface area. Making the detector area *a* small would result in a small signal but a good contrast of the recorded interferogram. Making the detector area *a* large, would reduce the modulation of the interferogram to a level that the quality of the spectrum is effected. A working size of the detector may record light corresponding to 1/10th of the sample interval, but then 90% of the light is lost.

2. Michelson interferometer without moving parts using wavefront division.

This big loss of the incident light will be avoided if we divide the incoming light into N equal cross-section parts, and proceed with each part through its own interferometer set-up for a certain optical path difference, and then superimpose the two beams of each of the N-parts on its own detector.

The incoming light is split into N parts, where N is the number of points we need for the interferogram and is therefore as well the number of detector elements in the array detector. Each part is split into two beams, each traveling to one of the two mirrors and reflected backwards to the beamsplitter. The mirrors are at different positions for each of the N-parts and consequently introduce different path differences for each of the N-parts. The two beams of each part are recombined by the beamsplitter and the amplitude of the two beams are superimposed and concentrated on one of the N detectors. The N path differences may be introduced by using for the two mirrors in the Michelson interferometer mirrors with steps as shown in Fig.2.

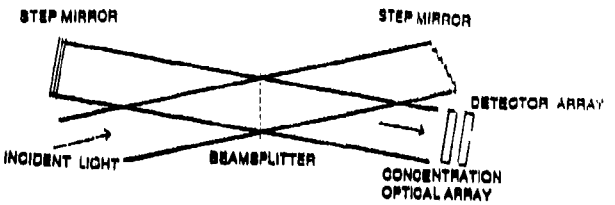

Fig.2. Profiles of the two Michelson mirrors, (a) having a sequence of small steps, (b) having a sequence of large steps.

The mirrors are positioned in such a way that the steps of one are horizontally, the steps of the other are vertically, as indicated in Fig.3.

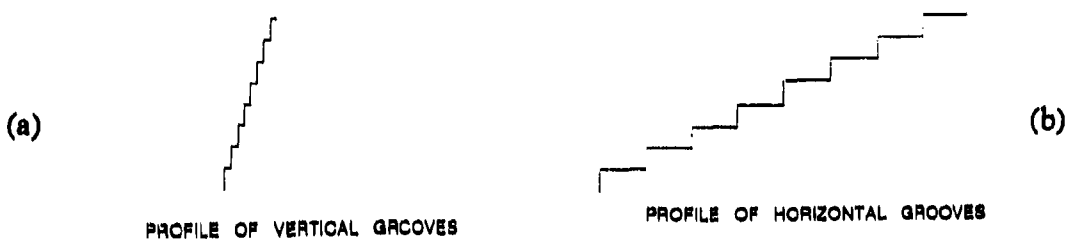

Fig.3. Michelson interferometer with two step mirrors, one with steps oriented horizontally, the other with steps vertically.

The N parts of the interferometer have now N different path differences and each produces one point of the interferogram at its detector. All of the incident light is used with this interferometer array and concentrated on the detector array. Since the interferogram points are instantly available, real time resolved spectroscopy may be performed.

Millimeter-wave band microwave signal spectrum measurement on the basis of the Hilbert transform of Josephson junction function response

S.Y.Larkin, S.E.Anischenko, V.V.Kamyshin

State Research Center "Fonon"
37, Pobedy Ave., KPI-3240, Kiev, 252056, Ukraine

ABSTRACT

Theory and the canonical algorithm of the Hilbert-spectroscopy of microwave signals on the basis of the AC Josephson effect is given. The microwave unit of the spectrum analyzer using the Josephson junction as a measuring sensor is described.

1. THEORY AND CANONICAL ALGORITHM OF HILBERT SPECTROSCOPY

Among known methods of microwave signal spectroscopy one could choose the method based on the use of the Josephson junction selectivity to the frequency of monochromatic oscillations exciting the junction[1]. In this case the selectivity of the Josephson junction to the external irradiation frequency ω is due to the availability of the own oscillations in the junction. Their frequency ω_j is actually determined by the bias voltage V impressed at the junction

$$\omega_j = 2eV/h \qquad (1)$$

The simple mechanism of the frequency control, the high frequency selection and the energy sensitivity of the Josephson junction bring about the natural desire of investigating the possibilities to use it for measuring energy spectra of the microwave signals[2]. It has been stated that the weighted difference function g(V) at the output of the Josephson junction and the energy spectrum of the signal $S(\omega)$ irradiating it (the latter being specifically interesting for the researcher) are bound by the Hilbert transform[1]:

$$g(V) = \frac{1}{\pi} \int_{-\infty}^{+\infty} \frac{S(\Omega)d\Omega}{\Omega - V} \qquad (2)$$

where g(V) is the weighted response of the junction including the involvement of the response intensity, the intensity of current behaviour and the operating mode of the junction; $\Omega = h\omega/2eV$ is the dimentionless frequency of the irradiating signal.

The above ratio uses the assumption that the transfer coefficient for the channaling path throughout the band of operating frequencies ($|K(\Omega)|^2 = 1$) is actually constant. The phenomenon alwais takes place if the microwave transmission-line system has been properly and correctly designed. From Eq.2 and with the involvement of the self-conjugation of the Hilbert transform, the

energy spectrum of the irradiating signal which to be experimentally estimated could be defined by the following equation

$$S(\Omega) = \frac{1}{\pi} \int_{-\infty}^{+\infty} \frac{g(V)dV}{V - \Omega} \qquad (3)$$

where the integral is presented by its main value and the original signal subject to transformation is formed out of the experimentally obtained and inverted basic and disturbed current-voltage characteristic[3] (CVC).

The Eq.(3) is the theoretical basis of the Hilbert-spectroscopy of microwave signals with solid spectrum and could be assuming that the assumptions made are true, a formula description of the algorithm for processing the experimental results providing the estimation of the energy spectrum on the basis of the Hilbert-spectroscopy.

As it comes from Eq.3 and the equations attending its derivation the canonical algorithm of Hilbert-spectroscopy prescribes the execution of seven successive steps:

Step 1. Input of the sequence of counts y2, representing CVC y2=f(x) of the junction disturbed by the irradiation of the external microwave signal.

Step 2. Input of the seguence of counts y1, representing the basic CVC y1=f(x) of the screened junction.

Step 3. Formation of the inverted sequence z2, representing the inverted CVC z2=g(y2) of the disturbed junction.

Step 4. Formation of the inverted sequence z1, representing the inverted basic CVC z1=g(y1).

Step 5. Formation of the colouring function wgh(x) equal to element-by-element product of the inverted basic CVC by the sequence of the counts of the independent variable y (the segment of the natural set of numbers).

Step 6. Formation of the difference function dz=z2-z1 and its colouring with the aim to yield the form dlt=dzx*wtgh suitable for transformation.

Step 7. Execution of the Hilbert transform of the colouring difference function with the size of the transformation core specified by the operator.

The final product of the transformation forms the equidistant sequence of counts of the estimated energy spectrum of the signal which irradiated the junction under the test determination of I-V values y2=f(x).

It should be mentioned that the synthesized canonical form of the Hilbert spectroscopy algorithm can be used both with non-coherent and monochromatic signals under the test conditions. In the last example the algorithm is realized by passing Step 5 and Step 6 which foresee the colouring of the difference function equalizing the non-uniformity of the Josephson junction sensitivity over the operating frequency band. The paper [3] illustrates that when investigating the spectrum of monochromatic irradiation $S(\Omega-\Omega_0)$,

consentrated in the narrow area $\delta \ll \Omega_0$ attributed to the central part Ω_0, one will have not to consider the change of the junction sensitivity under the change of the control bias voltage. Such junction allows to present the estimated spectrum in the following way

$$S(V-\Omega) \propto -\frac{1}{\pi}\int_{-\infty}^{+\infty} \frac{\Delta i(V,\Omega_0)}{\Omega_0-(V-\Omega)}\, d\Omega_0 \qquad (4)$$

where $\Delta i(V,\Omega_0)$ is the difference function characterizing the intensity of the junction response at the bias voltage variations and the fixed frequency of the external irradiation Ω_0. This expression shows that for estimating the spectrum it is sufficient to fulfill the Hilbert transform of the difference function $\Delta i(V,\Omega_0)$, without its preliminary colouring.

2. EXPERIMENTAL SET-UP

At the present moment the spectrum investigations of the laboratory sources are carried out using the prototype of the spectrum analyzer described by the authors of this paper in [3]. The present report presents the problems and the techniques of their technical solution occurred when creating the microwave module of the set-up.

Functionally, the microwave unit consists of a microwave transmission-line system channeling the external signal towards the cooled active component and the active component itself which is a Josephson junction and a matchind system.

There exist some basic problems which determine the design of a microwave unit. They are:

- wide band of the frequencies being investigated: from 50 to 250 GHz;
- high sensitivity: $.10^{-13}$ W/ $\sqrt{\text{Hz}}$;
- high frequency resolution: about 2 GHz;
- linearity of an amplitude-frequency characteristic (bandpass flatness not more than 2 dB);
- difficulty to match the high resistance of the waveguide with the low resistance of the active component over a wide band of frequencies.

According to the above the basic structural assemblies of the microwave unit were made in the way described below:

1. The microwave transmission-line system is made in the form of a superdimensional trough waveguide with an adapter from an input antenna. The developed microwave transmission-line system has the attenuation of not more than 0.6 dB per one metre at the length of 1.7 m, provides the operating frequency band from 25 to 400 GHz. The characteristics that follow can be attributed to the advantages of such choice. They are:

- monomode (self-filtering) operation;
- weak dispersion;
- stable wave polarization;

- simple connection of the section due to weak longitudinal current insensitive to the gaps in the cross-section;
- big cross size ensuring the technological effectiveness of Josephson junctions as active components placed in the transmission system.

2. The matching structure is made in the form of an integrally manufactured dipole antenna with a Josephson junction. The substrate matirial is Al_2O_3. The superconductive material used was of two kinds: the superpure niobiom (Josephson junction of low-temperature superconductor) or Y-Ba-Cu-O (Josephson junction of high-temperature superconductor). In the first case the junction is made in the form of a faced Josephson junction with the junction area of 0.4 mm^2. In the second case this is a weak link of narrowing type. The junction was formed by laser scribing at the grain boarders with the typical size of not more than 0.3 μm. At this the junction width appeared to be 0.5 μm. The signal losses matched with the input of the receiving structure were (3±1) dB over the frequency band from 60 to 150 GHz.

3. RESULTS

The set-up described above has allowed to perform the analysis of the complex line spectra over the frequencies from 40 to 250 GHz with the frequency resolution being not worse than 2 GHz and the sensitivity being not less than 10^{-13} $W/\sqrt{Hz}$.

4. ACKNOWLEDGMENTS

The authors are thankful to Dr.V.Makhov for supplying the Nb-Si-Nb Josephson junctions samples and to Dr.V.Chaykovsky for consulting on the canonical algorithm. This work is supported by the State Ukrainian Scientific Programme "The High Temperature Superconductivity".

5. REFERENCES

1. Yu.Ya.Divin, O.Yu.Polyanski, A.Ya.Schulman. Incoherent radiation spectroscopy by means of the Josephson effect, Sov.Tech.Phys.Lett.,1980, 6, 454-455.
2. S.E.Anischenko, S.Yu.Larkin, P.V.Khabayev. Microwave receiver system with quantum superconducting Josephson junction based on LTSC and H TSC, Int. Journal of Infr. and Mil. Waves, Vol. 14, No.3,1993,665-671.
3. S.Yu.Larkin, S.E.Anischenko, P.V.Khabayev. Using Josephson junctions for spectrum analyzing microwave signals of mm- and submm- wave bands. Pros. 17th Int. Conf.on Infr. and Mil. Waves, 1992, 439-440.

A New Method for Network Analyzer Calibration

A. Jöstingmeier[1], A. v. Borzyszkowski[2], G. Faby[1], M. Jenett[1], and K. Schünemann[1]

[1] Technische Universität Hamburg-Harburg
Arbeitsbereich Hochfrequenztechnik
Postfach 90 10 52, D-W-2100 Hamburg 90
Germany

[2] Universität Hamburg
Institut für Angewandte Mathematik
Edmund-Siemers-Allee 1, D-W-2000 Hamburg 13
Germany

Abstract

This paper presents an alternative method for network analyzer calibration which shows two advantages: It avoids de-embedding the device under test (dut) and it does not need any impedance standard. It is thus directly applicable to planar and integrated circuits at high frequencies.

Statement Of The Problem

In automated network analyzer measurements, two sources of error must be taken into account: imperfections in the equipment itself and non-ideal transitions to the dut. The latter point is of particular importance for modern planar circuit technologies as microstrip lines, coplanar waveguides, and fin-lines.

Such measurement errors must be eliminated by calibration procedures. In the most common error model, all measurement errors are assumed to be presented by an error 2-port in between measurement equipment (now assumed ideal) and dut. The scattering coefficients of the error 2-port are then defined by three complex quantities which can be determined by a number of well-established methods (e.g. [1]). Usually impedance standards (shorted, open, and matched load) are used which must be known precisely. On the other hand, there are also modern methods like TLR or TAN [2] which have the advantage of using partly unknown standards. All methods have in common that they need de-embedding what prevents their application to MICs where an important task is to characterize a well-defined subregion within a complex circuit. Moreover, they introduce additional errors which injure the measurement accuracy because the reference planes of the standards cannot always be reproduced with high accuracy, in particular in the millimeter-wave range. Furthermore standards are rather available in the most important circuit technologies.

The Calibration Method

We have developed a calibration method which does not need well-known impedance standards and which avoids any de-embedding. It only needs the presence of a uniform transmission line of about a quarter to half a wavelength in front of the dut, and a partially reflecting obstacle which can be moved along this line.

Fig. 1 shows the schematics of the calibration method for reflection measurements. Extending the method to 2-port measurements is straightforward. The reference plane is located in front of the dut which is separated from the measurement equipment by a quarter to half a wavelength long transmission line and an error 2-port. The imperfections in the equipment itself, non-ideal transitions and other 2-ports, are assumed to be represented by an error 2-port between the ideal measurement equipment and the transmission line. In order to keep the effect of errors which cannot be described by the error 2-port small, the calibration procedure needs a highly reflecting termination at the end of the transmission line. In many practical cases, this task cannot be fulfilled by the dut, whose input reflection coefficient should often be small. Therefore the first step of the calibration procedure is to introduce a highly reflecting obstacle, i.e. a screen, at the end of the transmission line and to measure the input reflection. In the second step, one introduces another obstacle which is movable, and measures the input reflection at (at least) five different positions of the obstacle. From step one and two, one can determine the parameters of the error 2-port. In the third step, one removes both the obstacle and the screen and measures the input reflections again. Inserting then the now known scattering parameters of the error 2-port, one can calculate the reflection coefficient of the dut.

Experimental Results

In order to verify the theory, we have performed some exemplary measurements within a microstrip circuitry. We have chosen a heterodyne receiver and an unknown impedance as dut whose reflection coefficient is to be determined in

X-band. The measurement set-up consists of a HP 8510 B network analyzer, a transition from coaxial to microstrip line, a microstrip line, the reverse transition from microstrip to coaxial line, and a coaxial termination. As obstacle and screen, we have used two small metal blocks (Fig. 2). The position of the movable obstacle can be adjusted by a micrometer screw. In order to avoid any irreproducible galvanic contact, the metal block corresponding to the obstacle has been isolated from the microstrip line by a thin nonconducting foil. The scattering of the obstacle can then be controlled by the thickness of the foil.

In order to check the validity of our calibration method, we have made measurements with two different error 2-ports. Figs. 3 and 4 show some results with a short as termination. The measurement set-up leading to the results shown in Fig. 3 differs from that for Fig. 4 by a 3 dB attenuator which has been inserted in front of the coaxial to microstrip transition. As expected, the transmission coefficient in Fig. 4 is 6 dB larger than the same quantity in Fig. 3. Thus the calibration is independent of the error 2-port.

Conclusions

A new method for network analyzer calibration which does not need impedance standards has been proposed. The dut has not to be de-embedded. Hence the method can also be applied to characterize an unknown 2-port embedded in a MIC. The validity of the method has been demonstrated by performing some measurements.

References

[1] *R. A. Soares, P. Gousien, P. Legand, and G. Follot, "A unified mathematical approach to two-port calibration techniques and some applications," IEEE Trans. Microwave Theory Tech., vol. MTT-37, pp. 1669–1674, 1989.*

[2] *H.-J. Eul and B. Schiek, "A generalized theory and new calibration procedures for network analyzer self-calibration," IEEE Trans. Microwave Theory Tech., vol. MTT-39, pp. 724–731, 1991.*

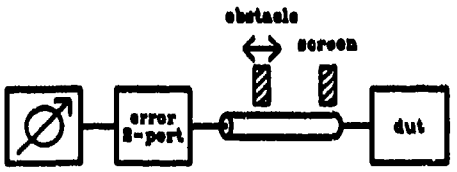

Figure 1: Block diagram for the reflection coefficient measurement set-up.

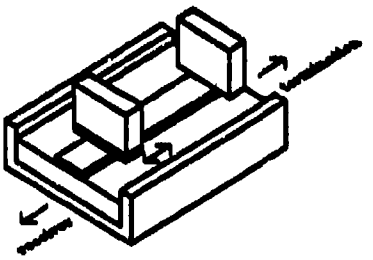

Figure 2: Realization of the measurement set-up in microstrip technique.

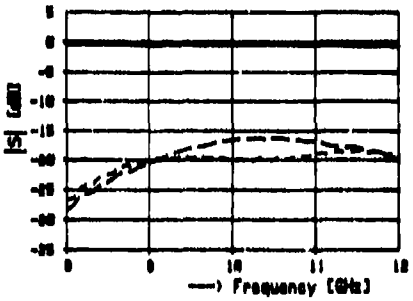

Figure 3: Scattering parameters of the error 2-port. Solid line: Transmission coefficient. Dashed lines: Reflection coefficients.

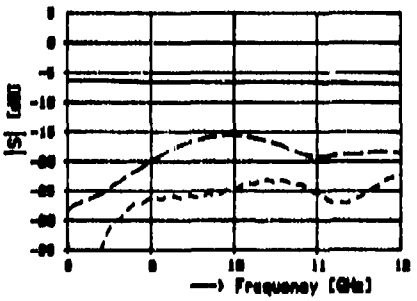

Figure 4: as Fig. 3 with an additional 3 dB attenuator in front of the coaxial to microstrip transition.

Far Infrared Spectroscopy of Phonons and Plasmons in Semiconductor Superlattices

T Dumelow, A A Hamilton, T J Parker, S R P Smith and D R Tilley.

Department of Physics, University of Essex, Colchester CO4 3SQ, UK.

The overall symmetry of both long and short period superlattices is uniaxial, with principal axes, z, parallel, and x and y, normal to the growth direction. Far infrared spectroscopy is a powerful technique for investigating both components, ε_{zz} and $\varepsilon_{xx} = \varepsilon_{yy}$, of the dielectric function of these structures. In this paper we shall review these techniques and present examples of how they can be used to characterise semiconductor superlattices. Because of the strong absorption due to the phonon modes in superlattices fabricated from compound semiconductors, transmission measurements require thinning of the substrate to a few microns in thickness. This is difficult to achieve, as well as being destructive, so in all our work reflection spectroscopy is used.

Using instruments which are heavily modified forms of the NPL modular cube interferometer, we have developed three variations of the technique of far infrared reflection spectroscopy which provide a range of information on the dielectric functions of these structures[1]. These techniques are: (a) polarised oblique incidence spectroscopy, which enables either ε_{xx} to be probed using s polarised radiation, or a combination of ε_{xx} and ε_{zz} to be probed using p polarised radiation, the exact combination depending upon the angle of incidence, (b) dispersive Fourier transform spectroscopy (DFTS), to measure the amplitude and phase reflection spectra directly, since the phase information sometimes aids the assignment of features in the spectrum, and (c) attenuated total reflection (ATR) spectroscopy, which is used to couple to non-radiative surface polaritons and guided waves. Silicon ATR prisms were used for this work, and measurements were made at internal angles of incidence which were a little larger than the critical angle for total internal reflection (~ 17°) in silicon.

In short period GaAs/AlAs superlattices the optical phonon branches in the two components do not overlap, and this causes confinement of optical phonon modes in each component. However, broadening of the interfaces occurs during the growth process, and this affects the degree of confinement, with the result that the frequencies of the confined modes are measurably different from those expected for perfect interfaces. Consequently measurements of the frequencies of confined optical phonons can be used as a sensitive probe of interface broadening[2]. Spectra showing confined modes are presented in Fig. 1.

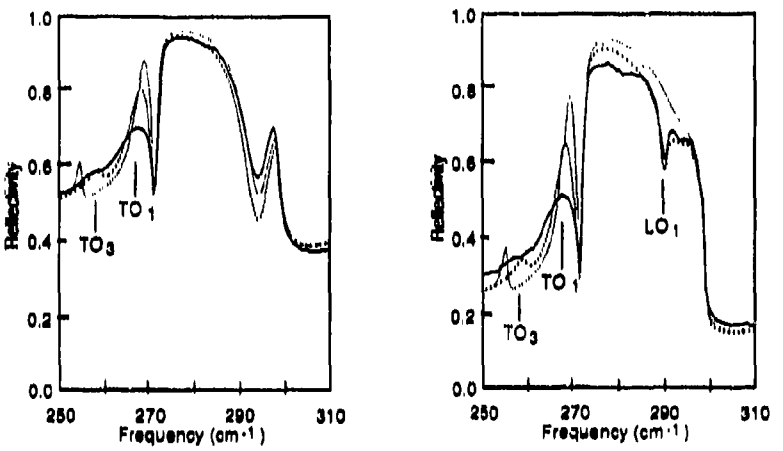

Fig. 1. Measured (solid lines) and theoretical (dotted curves: perfect interfaces, dashed curves: with interface broadening). The spectra show: on the left: s polarisation spectra for a $(GaAs)_4/(AlAs)_4$ superlattice, on the right: similar spectra for the same sample measured in p polarisation. The marked features correspond to experimental confined-mode frequencies. After Ref. 2.

The surface polaritons and guided waves propagating in this sample were studied by ATR, as shown in Fig. 2. Features due to surface modes and guided waves are clearly seen as dips in the reststrahl regions. Compare with Fig. 1.

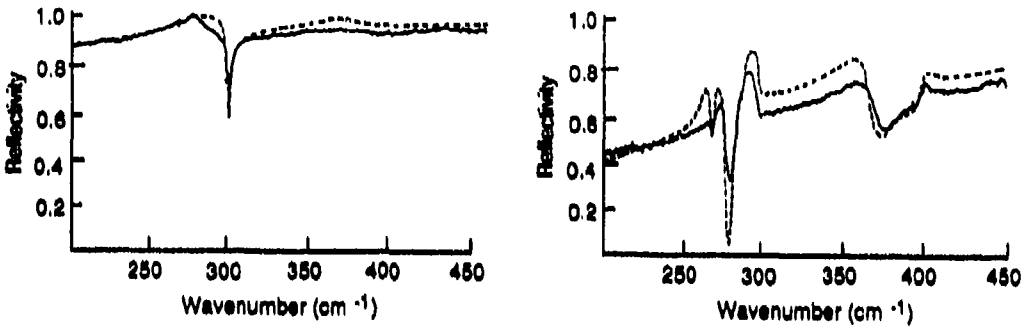

Fig. 2. Measured (solid lines) and calculated (dashed lines): room temperature ATR spectra of the same superlattice sample described in Fig. 1. On the left: s polarisation spectra, on the right: p polarisation spectra. After Ref. 3.

In the case of doped superlattices, a combination of p and s polarised oblique incidence measurements enables both the overall free electron concentration and the distribution of electrons between the wells and the barriers to be determined. In the case shown in Fig. 3, the sample consisted of a superlattice fabricated by δ-doping a GaAs crystal with 100 Si layers with a 2D density of the order of 10^{13} atoms per layer at 50 nm intervals. To account for the sharp feature at 296 cm^{-1} a thin depletion region at the surface was included in the theoretical model[4].

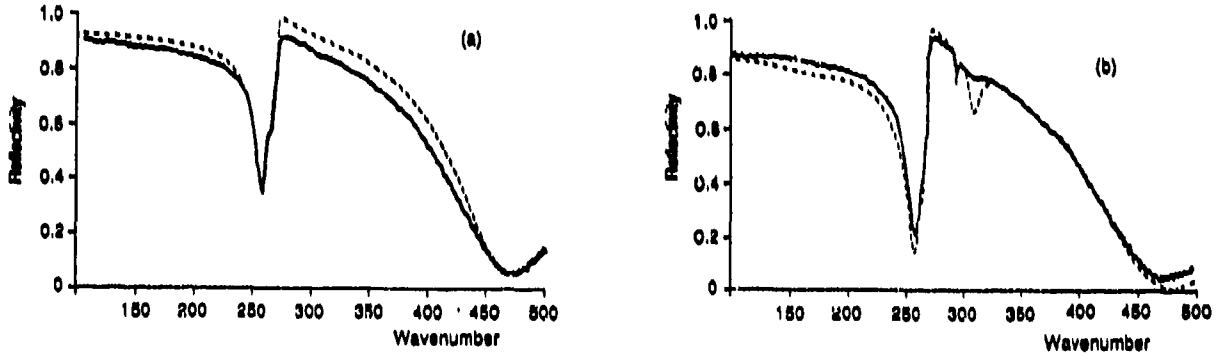

Fig. 3. (a) s polarised and (b) p polarised oblique incidence (45°) reflection spectra of a GaAs sample δ-doped with Si layers. After Ref. 4.

Acknowledgement.

We acknowledge financial support for this work from the UK Science and Engineering Research Council.

References.

1. T Dumelow, T J Parker, S R P Smith and D R Tilley, Surface Science Reports, 17, 151 (1993).
2. B Samson, T Dumelow, A A Hamilton, T J Parker, S R P Smith, D R Tilley, C T Foxon, D Hilton and K J Moore, Phys. Rev., B 46, 2375 (1992).
3. T Dumelow, A A Hamilton, T J Parker, D R Tilley, C T B Foxon, D Hilton and K J Moore, Int. J. Infrared and Mm. Waves, 11, 901 (1990).
4. T Dumelow, A A Hamilton, T J Parker, D R Tilley, B Samson, S R P Smith, R B Beall and J J Harris, Superlatt. and Microstruct., 4, 517 (1991).

FAR INFRARED OPTICS OF GaAs/AlAs SUPERLATTICES

A.A. Hamilton, T. Dumelow, T.J. Parker and D.R. Tilley

Department of Physics, University of Essex, Wivenhoe Park, Colchester, Essex CO4 3SQ, UK.

In the far infrared, superlattice dielectric functions can be well represented using an effective medium model, with the overall symmetry of the superlattice taking a uniaxial form. If only phonon effects are considered, superlattice dielectric tensors are usefully modelled in one of two ways, dependent on the thicknesses of the superlattice layers. Thus in long period superlattices the phonon resonances are determined by the bulk resonances of the constituent layers, whereas in short period superlattices the resonances are shifted from their bulk values due to phonon confinement.

Regardless of the model used in describing the uniaxial dielectric tensor, the in-plane component ε_{xx} will have different resonant frequencies from the out-of-plane component ε_{zz} (z is taken to be the growth direction). For propagation of radiation in the z direction, poles in ε_{xx} correspond to TO frequencies, and zeroes in ε_{zz} correspond to LO frequencies. We examine some consequences that are of importance in far infrared spectroscopy, with particular reference to oblique incidence reflectivity and attenuated total reflection measurements taken on short period GaAs/AlAs superlattices.

Of particular interest are the sharp dips that appear in the spectra obtained using these two techniques. In the case of a superlattice deposited on a substrate the main modes that lead to such features are as follows [1]:

1. Brewster Modes

We define Brewster modes as dips in the spectrum at discrete frequencies at which the dielectric function of the superlattice takes values corresponding to the Brewster condition, i.e. the incident angle is the Brewster angle for zero reflection. For propagation in the x-z plane using p-polarised radiation, they follow the dispersion relation

$$q_x^2 = \frac{\omega^2}{c^2} \frac{(\varepsilon_{xx} - \varepsilon_1)}{(\varepsilon_{xx}/\varepsilon_1 - \varepsilon_1/\varepsilon_{zz})}$$

where q_x is the in-plane component of the wavevector, and ε_1 is the dielectric constant of an isotropic medium in contact with the superlattice. Thus dips are observed in p-polarisation reflectivity from vacuum (of dielectric constant $\varepsilon_1 = 1$) at frequencies at which the above equation is satisfied. Although equivalent modes occur in reflectivity from bulk isotropic samples, such modes are usually fairly broad. However, in the case of a reflectivity from a superlattice, sharp Brewster modes occur at the LO phonon frequencies as a result of the uniaxial symmetry of the superlattice structure. Moreover, Brewster modes of this type are not appreciably affected by the presence of a substrate. These modes therefore act as an accurate measure of superlattice LO frequencies.

2. Surface Polaritons at the Vacuum/Superlattice Interface

Surface polaritons are modes localised at an interface between two media in p-polarisation. In the case considered here one of these media (the vacuum of dielectric constant $\varepsilon_1 = 1$) is isotropic whilst the other (the superlattice) is uniaxial. The E and H fields of a surface polariton decay exponentially away from the

interface (i.e. the out-of-plane component of the wavevector q_z is imaginary in both layers). For this to occur with ε_1 positive it is necessary that the in-plane component of the superlattice dielectric tensor ε_{xx} should be negative (although the out-of-plane component ε_{zz} may take either sign). In addition, the in-plane wavevector component q_x must exceed a value of $\varepsilon_1^{1/2}\,\omega/c$. In order to achieve this, the ATR setup is used. Here the light is incident through a silicon prism such that it strikes its base at an angle θ greater than the critical angle for total internal reflection. q_x is then given by

$$q_x = \varepsilon_p^{1/2}\,(\omega/c)\sin\theta$$

where ε_p is the dielectric constant of the prism material (silicon in this case). Since q_x remains continuous on either side of the prism base an evanescent wave decays from the prism/vacuum interface within the vacuum layer when θ exceeds the critical angle. This evanescent wave can couple to a surface polariton on the surface of a sample brought close to the prism base, so that a dip occurs in the spectrum at each surface polariton frequency. The exact value of this frequency is determined by the same dispersion relationship as is the Brewster mode, although it occurs within a different wavevector regime. This frequency depends on both the frequencies and the strengths of the oscillators contributing to the superlattice dielectric tensor.

3. Berreman Modes at the Superlattice/Substrate Interface

The Berreman effect has been known for a long time [2] - sharp dips in the p-polarisation reflectivity spectra occur at the LO frequencies of a thin film sample deposited on a metallic substrate. Here we describe the observed Berreman modes as surface polaritons localised at the sample/substrate interface. In contrast to the modes at the vacuum/sample interface, however, the full ATR geometry is not required for their observation. If the sample is a superlattice, Berreman modes occur in the same way as for isotropic samples, but only at LO frequencies at which ε_{xx} is positive. For short period GaAs/AlAs superlattices on GaAs substrates these modes occur at the appropriate LO frequencies occurring within the GaAs reststrahl region (in which the substrate dielectric function is negative). The effect on the overall p-polarisation reflectivity spectrum is that the strength of certain Brewster modes at LO frequencies appears to be enhanced.

4. Guided Wave Modes

For a surface polariton the field decays either side of an interface. In the case of a guided wave mode the field decays either side of a layer. Thus for a vacuum/superlattice/substrate system the field would decay in the vacuum and substrate layers. The guided wave mode would therefore be confined within the superlattice layer, in which q_z would be real. Guided wave modes of this type occur in both s- and p-polarisation and are observed in ATR within the substrate restatrahl region. In addition, surface modes at the vacuum/superlattice interface are actually perturbed by the presence of the other interface and, in this region, the p-polarised guided wave dispersion relation also applies to these modes.

All the above modes have been observed experimentally in short period GaAs/AlAs superlattices on GaAs substrates using the two techniques already mentioned. In these samples the superlattice dielectric tensor depends on both phonon confinement and interface roughness; the resulting mode frequencies provide useful probes for determining these parameters.

[1] T. Dumelow and D.R. Tilley, J. Opt. Soc. Amer. A10 (1993), 633-645.
[2] D.W. Berreman, Phys. Rev. 130 (1963), 2193-2198.

INVESTIGATION OF PHONONS AND PLASMONS IN ALLOYS AND SUPERLATTICES COMPOSED OF InAs AND InSb

S.K. Kang[1], T. Knight[2], Y.B. Li[2], A.G. Norman[2],
J.R. Birch[3], T. Dumelow[1], T.J. Parker[1], C.C. Phillips[2] and R.A. Stradling[2]

[1]Department of Physics, University of Essex, Colchester CO4 3SQ, UK.
[2]Blackett Laboratory, Imperial College, London SW7 2BZ, UK.
[3]National Physical Laboratory, Teddington, TW11 0LW, UK.

We report a series of far infrared measurements, using power reflectivity, dispersive Fourier transform spectroscopy, and attenuated total reflection spectroscopies, on the mixed crystal system $InAs_{1-x}Sb_x$. Two types of samples were studied; the first series of samples incorporated $InAs_{1-x}Sb_x$ as bulk epilayers on GaAs substrates, whereas the second series used the alloy as a superlattice component with InSb.

The phonon and plasmon response of the bulk alloy system was obtained from reflectivity measurements from the epilayer samples. In particular, the phonon TO frequencies applicable over a range of alloy compositions were measured, and the complete spectrum allowed the overall dielectric response of the alloys to be modelled, using a two oscillator fit. In practice plasmons played a significant role in the response but, by combining far infrared measurements of TO frequencies with Raman measurements of LO frequencies (at the depleted surface), it was easy to separate the phonon and plasmon contributions.

The other samples studied were doped superlattices of the type $InSb/InAs_{0.2}Sb_{0.8}$ having both wells (the $InAs_{0.2}Sb_{0.8}$ layers) and barriers (the InSb layers) of thickness 100 Å; the details of the doping levels are given in the table. The superlattices were grown on a $InAs_{0.1}Sb_{0.9}$ alloy buffer layer separating the superlattice from a GaAs substrate. The amplitude and phase spectra from DFTS measurements on one of these samples are shown in the figure.

The incorporation of the alloy into a superlattice structure has a number of effects on the far infrared spectrum, all of which assist in understanding the basic semiconductor physics.

1. Phonon Shifts due to Strain

The lattice constants of the two superlattice components are slightly different, so that the layers become strained. The superlattice layers grow to the lattice constant of the $InAs_{0.1}Sb_{0.9}$ buffer, so that the two layer types strain in opposite directions. This results in shifts in the phonon frequencies from their bulk values. This shift is only about 1 cm^{-1}, however, and is not easy to identify in these samples because of phonon-plasmon coupling.

2. Changes in Effective Mass

$InAs_{1-x}Sb_x$ bulk alloys undergo very large band bowing. As a result, for $x > 0.25$ the band gap of the mixed crystal is less than that of either InAs or InSb. For $InAs_{0.2}Sb_{0.8}$ the band gap is about 0.16 eV, corresponding to an effective mass of 0.0108. Due to this narrow gap the bands are extremely non-parabolic.

In the superlattice structures the band structure is affected both by strain and by confinement. Confinement effects are the more important in determining the electron effective masses in these samples. Confinement splits the conduction band into subbands, which are raised in energy. Thus the effective mass is

considerably enhanced. At the Fermi energy the effective mass is even larger due to band non-parabolicity.

The electron effective mass in each of these samples is experimentally determined by comparing the plasma frequency obtained from far infrared measurements with the carrier concentration obtained from Shubnikov de Haas measurements. The resulting values are compared with the results of a two band Kane calculation of the Fermi level effective mass in the table. It can be seen that both experiment and theory give values considerably larger than the bulk effective mass of 0·0108. We have not been able to resolve the expected carrier density dependence, however.

3. Changes in Electron Mobility

Electron mobility is of considerable importance in low dimensional structures. It is therefore of interest to compare the mobilities measured by transport measurements with those derived from the plasma damping seen in the far infrared. The table shows that the far infrared mobility values are roughly half those obtained from Hall measurements. The mobility appears unaffected by the position of the dopants (i.e. in the wells or in the barriers), but the more highly doped sample shows a lower mobility.

In summary, we have demonstrated a number of important effects which assist in understanding phonon and free carrier behaviour in $InAs_{1-x}Sb_x$ alloys and superlattices.

Sample	Doped Superlattice component	Nominal Doping (cm^{-2})	Free carriers (cm^{-2}) SdH	Plasma Frequency (cm^{-2})	Mobility μ ($cm^2\ V^{-1}s^{-1}$)		Effective mass	
					I.R.	Hall	I.R.	Theory
IC346	wells	$1x10^{12}$	$0.62x10^{12}$	310	6100	12000	0.0385	0.033
IC347	wells and barriers	$2x10^{12}$	$1.20x10^{12}$	430	3200	8000	0.0365	0.044
IC348	barriers	$1x10^{12}$	$0.60x10^{12}$	310	5000	11000	0.0372	0.033

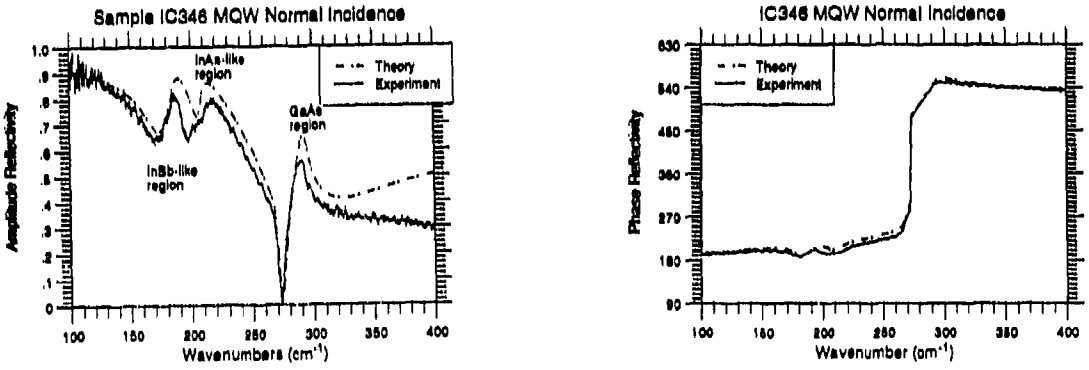

Typical DFTS amplitude and phase spectra.

Characterisation of hydrogenated silicon nitride films by low temperature FTIR spectroscopy

M. M. Pradhan and M. Arora

National Physical Laboratory, Dr. K. S. Krishnan Road
New Delhi-110012, India

ABSTRACT

Low temperature FTIR spectroscopy of hydrogenated silicon nitride films revealed many molecular species which are not observed at ambient temperature. The broad band at 700-1100 cm^{-1} splits into three bands at 744, 825 and 890 cm^{-1} at 50K. Similarly NH group gives strong absorption band at low temperature.

1. INTRODUCTION

Silicon nitride films grown on silicon substrate have been used in large number of applications by electronics industry. Many authors [1 - 5] have used infrared (IR) spectroscopy to observe the presence of different molecular groups present in these films. Different workers [4 - 7] have shown the temperature dependent broadening and frequency shift of IR bands due to interaction of inter and intra molecular vibrational and rotational levels. The purpose of this work is to use low temperature FTIR spectroscopy for the characterisation of hydrogenated silicon nitride films grown on silicon substrate.

2. MEASUREMENTS AND RESULTS

Hydrogenated silicon nitride films were grown on silicon wafer by PECVD technique using silane, ammonia and nitrogen in the ratio 1:2:4 and heating the wafer at 250°C. IR absorption measurements were done on a Digilab FTIR spectrophotometer Model 20E/V fitted with Air-Product cryostat.

Fig. 1 represents IR absorption measurements of a 200 nm thick film in the region 1100-680 cm^{-1} at 300K, 200K and 50K temperatures. This broad absorption band at 300K, splits into three bands at 744, 825 and 890 cm^{-1} in the measurements at 50K. The band at 825 cm^{-1} is assigned to Si-N bonds, the 744 cm^{-1} is assigned to nitrogen sites where Si-N bonds and local silicon network are distorted. The shoulder at 890 cm^{-1} in the measurements is attributed to the overtone of 424 cm^{-1} band due to Si-N breathing mode.

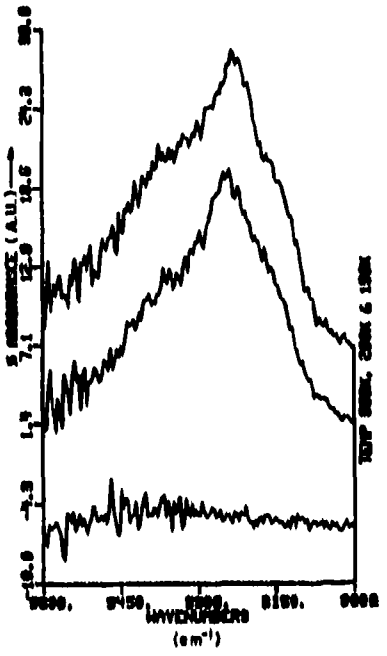

Fig. 2

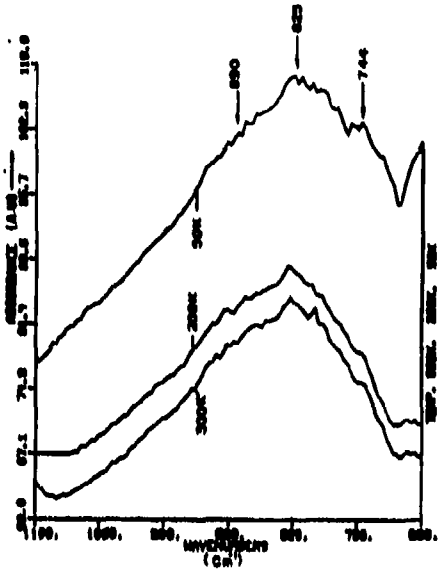

Fig. 1

Fig. 2 represents IR absorption spectra of a hydrogenated amorphous silicon nitride film 100 nm thick, grown by glow discharge CVD in an inductively coupled reactor using silane (80%) and ammonia (20%). The NH stretching vibration near 3300 cm^{-1} is not observable at 300K, but becomes strong band at 130K and shifts to 3230 cm^{-1}. The band at 3230 cm^{-1} is assigned as symmetric stretching, while the hump at 3260 cm^{-1} belongs to antisymmetric stretching modes of N-H group present in the film.

3. CONCLUSION

Characterisation of silicon nitride films by low temperature FTIR spectroscopy has not only identified the presence of NH group which is not observable at ambient temperature in thin films but as well revealed the presence of three bands in the broad band structure of 1100-700 cm^{-1}, which arise from different molecular groups.

4. REFERENCES

1. Z. Yin and F. W. Smith, Phys. Rev. B 42 (1990) 3666
2. E. Bustarret, m. Benosouda, M. C. Habrard, J. C. Bruyere, S. Poulin and S. C. Gujrathi, Phys. Rev. B 38 (1988) 8171
3. S. Narikawa, Y. Kojima and S. Ehara, Jpn. J. Appl. Phys. 24 (1985) L861
4. M. M. Pradhan & M. Arora, Optics Communs. 94 (1992) 428
5. M. M. Pradhan & M. Arora, Jpn. J. Appl. Phys. 31 Part 1 (1992) 176
6. J. M. Chen, L. M. Xei, G. R. Bai and Y. G. Zhao, Phys. Stat. Sol. b 153 (1989) 107
7. T. D. Kolomiitsova and D. N. Shchepkin, Opt. Spectrosc. (USSR)66 (1989) 603

Reflectance Study Of T.M.O. Glasses

A. Memon, M.N. Khan and S. Al-Dallal
Department of Physics, University of Bahrain

D.B. Tanner
Department of Physics, University of Florida, Gainesville

ABSTRACT

The frequency dependent optical and dielectric properties of binary semiconducting glasses in the system $(V_2O_5)_{60}$ $(TeO_2)_{40-x}$ $(PbO)_x$ were measured as a function of lead content. It was found that the optical phonon frequencies, and the reflectance minima in the oxide glasses appear to shift drastically towards the lower frequency as the PbO is partially substituted in these glasses. The activation energy calculated on the basis of effective dielectric constant appears to decrease upon the substitution of PbO.

1. INTRODUCTION

In V_2O_5 - TeO_2 glasses several studies on equilibrium, structure, switching mechanism, phase equilibrium and electrical conductivity has been reported [1-2]. However, there is no single measurement which has employed infrared reflectance to study the optical and dielectric properties of these compound and has correlated with the d.c conductivity measurement.

In the present work the extraction of the activation energy of the glass is based on the power reflection spectroscopy, which provides the values of frequency dependent dielectric response function when analysed by Kramer-Kronig (K-K) dispersion routines. The effective dielectric constant obtained by (K-K) is then used with Austin and Mott theory [3] to extract the values of activation energy and other physical parameters.

Two glass samples with the composition of 60% V_2O_5 - 40% TeO_2, and 60% V_2O_5 - 20% TeO_2 - 20% PbO were prepared by mixing the appropriate amount of research grade V_2O_5, TeO_2 and PbO. The details of the preparation method is described elsewhere [4]. The infrared measurements on the optically flat polished samples were performed at near normal incidence using IBM Brucker Interferometer which covers the 100 - 5000 cm^{-1} range whereas for NIR, UV and visible range carry 2300 spectro-photometer was utilized.

2. RESULTS AND DISCUSSIONS

Effect of substitution of PbO on the reflection spectra of V_2O_5 - TeO_2 system is investigated. Fig. 1 shows the infrared reflectance spectra of V_2O_5 - TeO_2 glass containing 20% of PbO. From this we observe that the reflectance of the glass increases as TeO_2 is partially replaced by PbO. Previous studies on V_2O_5 - TeO_2 system [4-5] have reported three infrared absorption bands at 1010, 860 and 680 cm^{-1}. Our reflectance spectra show a kink at 1000 cm^{-1}, a shoulder at 860 cm^{-1} and a peak at 680 cm^{-1}. These modes get weaker and shift to lower frequencies. The reflectance minimum which occurs at 1050 cm^{-1} is seen to be shifted by 25 cm^{-1} when 20% TeO_2 is replaced by 20% PbO. No localized mode due to PbO itself is observed. The shift of the vibrational frequencies to the lower frequencies indicates that some formation of Te-O-Pb bridges have taken place.

Fig. 2 represents the real part of the frequency dependent dielectric function computed from the reflectance data of Fig. 1 using K-K technique. From this we observe that above 3000 cm^{-1} there is no strong absorption mechanism. Therefore, at high frequencies $\varepsilon_1(\omega)$ attains a constant value ε_∞ which allows an estimate of the effective dielectric constant $\varepsilon_p = \varepsilon_\infty = n^2$.

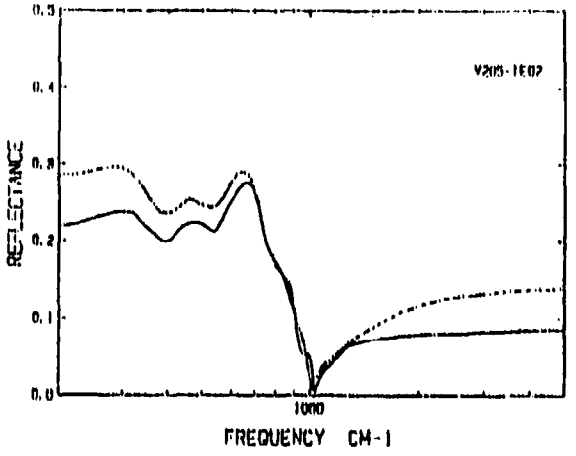

Fig. 1 Reflectance spectra for 60 V_2O_5 - 40 TeO_2 (_) and 60 V_2O_5 - 20 TeO_2 - 20 PbO (...)

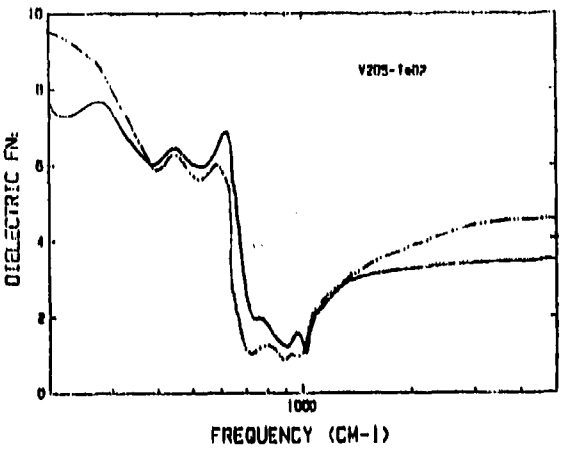

Fig. 2 The frequency dependent real part of dielectric function for 60 V_2O_5 - 40 TeO_2 (_) and 60 V_2O_5 - 20 TeO_2 - 20 PbO (...)

The theoretical approach for the activation energy in the semiconducting oxide glasses is discussed in ref [3]. The calculation of physical parameters is discussed elsewhere [4]. Using the physical parameters and measured value of ε_p one can estimate the polaron hopping energy (W_H) from relations $W_H = e^2/4\varepsilon_p \left(\frac{1}{r_p} - \frac{1}{R}\right)$ and the activation energy as $W = W_H + W_D/2$ where W_D is the disorder energy for the vandate system[6] caclulated from $W_D = Ke^2/\varepsilon_o R$. Here ε_o is the static dielectric constant, and K is a constant of the order of 0.3. W_D is calculated using the estimated value of the $\varepsilon_o$as obtained from K-K analysis. Using this value of W_D and the measured values of ε_p the activation energy calculated for our glasses are listed in table I. Our measured values of W, W_H and W_D agrees with those found in the literature.

Table I

Measured values of dielectric constant, refractive index n and activation energy of Vanadium Tellurite glasses.

Composition	ε_o	ε_p	n	W_D (eV)	W_H (eV)	W (eV)
60 V_2O_5 - 40 TeO_2	12	3.8	1.94	0.094	0.33	0.377
60 V_2O_5 - 20 TeO_2 - 20 PbO	15	4.66	2.16	0.074	0.29	0.327

These measurements suggest that the dielectric response function of the glass increases on lead substitution and hence, the dispersion and refractive index of the glass increases. As a result the conductivity of the glass increases and the activation energy decreases.

3. REFERENCES

1. C.H. Chung and J.D. Mackenzie, J. of Noncrystalline Solid Vol 32, PP 351-370, 1980.
2. V.K. Dhawan and A. Mansingh, J. of Noncyrstalline Solid Vol. 51, PP 87-103, 1982.
3. I.G. Austin and N.F. Mott, Adv. Phys, Vol. 18, PP 41, 1969.
4. A. Memon, M.N. Khan, K.E. Rajab and D.B. Tanner, J. of Materials Sc. 25, PP 511-513, 1990.
5. H. Hirashima, T. Kawaguchi, F. Tanaka and E. Tarura, The Physics of non-crystalline solids edited by Pye, Lacourse and Stevens, PP 266-270, Taylor and Francis, London, 1992.
6. A. Miller and E. Abrahams, Phys Rev 120 P 745, 1969.

THEORY OF MULTIPHONON ABSORPTION IN CRYSTALS AT IR AND MM RANGES

B.M. Garin
Institute of Radio Engineering and Electronics of the Russian Academy of Sciences, Vvedensky square 1, Fryazino, Moscow region 141120, Russia

ABSTRACT

A general quantum theory of absorption due to the excitation of phonons in optically anisotropic dielectric crystals have been considered. Expressions for the imaginary part of the dielectric susceptibility tensor for the processes with an arbitrary number of phonons are given.

INTRODUCTION

At the bands between the frequencies of fundamental crystal lattice modes at IR range and at the lower and higher frequencies only the multiphonon absorption (MPA) may contribute to the lattice absorption in ideal crystals [1-5]. The MPA are caused either by "mechanical" anharmonicity (MA) or by "optical" anharmonicity (OA) [1,4](see lower).

Theoretical investigations of MPA was limited as a rule by considerations of two-phonon processes [1]. But the theoretical results and experimental data are available [2-5] about possibilities of essential contribution or predomination of the MPA processes with the number of participating phonons $n \geqslant 3$. At the known theoretical works dedicated to the MPA with $n \geqslant 3$ [2,3] only particular kinds of such processes or models applicable at limited frequency regions (for example at the near IR range [3]) have been considered. Expressions for MPA with arbitrary n, which are applicable at the whole frequency region $\omega \gg \tau^{-1}$ (where τ is the phonons life time) including usually IR and MM ranges, have been considered in [4]. At the present work the generalization of this expressions to optically anisotropic crystals have been considered.

EXPRESSIONS FOR THE MPA

Let us consider the expansions of electric dipole moment of crystal M^i and lattice potential energy U in powers of atoms displacements from its equilibrium positions:

$$M^i = \sum_n M^i_n = \sum_n \frac{1}{n!} O^{ij_1 \dots j_n}_{n\nu_1 \dots \nu_n} x^{j_1}_{\nu_1} \cdots x^{j_n}_{\nu_n} ; \quad U = \sum_n \frac{1}{n!} \Phi_{n\nu_1 \dots \nu_n} x^{j_1 \dots j_n}_{\nu_1} \cdots x^{j_n}_{\nu_n} , \qquad (1)$$

where i is the index of Cartesian component; $n=1,2,\dots$; x^j_ν is the jth component of displacement of the atom with index $\nu=(l,\beta)$, l is the index of primitive unit cell of crystal lattice, β is the index of atom in the cell; $O^{ij_1 \dots j_n}_{n\nu_1 \dots \nu_n}$ and $\Phi^{j_1 \dots j_n}_{n\nu_1 \dots \nu_n}$ are coefficients of the expansions (1). O_n at $n \geqslant 2$ and Φ_n at $n \geqslant 3$ are parameters of OA and MA respectively. The harmonic macroscopic electric field in crystal E^i of frequency ω have been assumed and nonstationary quantum mechanical perturbation theory in the first order [4] have been used.

Let us consider for example the n-phonon absorption due to the OA. The perturbation operator is $-(M^i_n E^i_{loc})$, where E^i_{loc} is the local elec-

tric field, $E^i_{loc}=L^{ij}E^j$. L^{ij} are the Lorentz's coefficients. For the contribution of such processes to the imaginary part of the dielectric permittivity tensor it may be obtained:

$$\varepsilon''_{nij}=B_n \mathrm{sh}\left(\frac{\hbar\omega}{2kT}\right)\sum_{\mu}\int_{\sigma_n^{(\mu)}} d\sigma \frac{(\mathrm{grad}\,\tilde{\omega}_\mu)^{-1}L^{ii'}L^{jj'}\mathrm{Re}[H_t^{ni'}(k)H_t^{nj'*}(k)]}{\prod_{r=1}^{n-1}\omega_{t_r}(k_r)\mathrm{sh}[\hbar\omega_{t_r}(k_r)/2kT]\}\tilde{\omega}_{t_n}\mathrm{sh}(\hbar\tilde{\omega}_{t_n}/2kT)}, \quad (2)$$

where $B_n=(2\pi^2/\Omega)(h\Omega/32\pi^3)^{n-1}$, Ω is the volume of unit cell; $\hbar$ and k are the Planck's and Boltzmann's constants; T is the absolute temperature ; $\mu=(t,s,K)$ is the index of kind of n-phonon process with the phonons belonging to the set of lattice vibrations branches $t=(t_1,\ldots,t_n)$; index s_r $(r=1,\ldots,n)$ in the set $s=(s_1,\ldots,s_n)$ have the magnitudes +1 and -1 respectively in the cases of absorption and excitation of phonon of branch t_r in process μ; in addition, s obey to the requirement: $\omega_\mu(k)=\sum_r s_r\omega_{t_r}(k_r)>0$, where $\omega_{t_r}(k_r)$ is the frequency of phonon (t_r,k_r) with wave vector k_r; $\sigma_n^{(\mu)}=\sigma_n^{(\mu)}(\omega)$ is surface in space $k=(k_1,\ldots,k_n)$, defined by the next system of equations (conservation laws) [4]:

$$\sum_{r=1}^{n}k_r-K=0 \quad (3); \qquad \omega_\mu(k)-\omega=0 \quad (4)$$

where K are vectors of the reciprocal lattice; the sign ~ means that the vector k_n is expressed through the vectors $k_1,\ldots,k_{n-1}$ by means of (3); grad $\tilde{\omega}_\mu$ is the gradient in the space $(k_1,\ldots,k_{n-1})$;

$$H_t^{ni}(k)=\sigma_{n\tilde{\nu}_1\ldots\tilde{\nu}_{n-1}\beta_n}^{ij_1\ldots j_n} b_{t_1k_1}^{\beta_1 j_1}\ldots b_{t_nk_n}^{\beta_n j_n}\exp\left[i\sum_{r=1}^{n-1}k_r(r_r-r_n)\right],$$

where r_r is the radius-vector of the cell l_r; $\tilde{\nu}_q=(\tilde{l}_q,\beta_q)$, $\tilde{l}_q=l_q-l_n$; $b_{t_1k_1}^{\beta j}$ (that is obeying to the requirement: $M_\beta b_{t_1k_1}^{\beta j*}b_{t_1k_1}^{\beta j}=\delta_{t_1t_1}$) is the jth component of polarization vector of atom β in the complex normal vibration (t_1,k_1); M_β is the mass of atom β.

The analogous expressions have been obtained for the MPA processes concerned with the MA.

REFERENCES

[1] M. Lax, E. Burstein, Phys. Rev. 97, 39 (1955); V.S. Vinogradov, Sov. Phys. Solid State 4, 519 (1962); V.L. Gurevich, ibid., 21, 1993 (1979); B.M. Garin, A.V. Galdetskii, Opt. Spectrosk. (USSR) 50, 540 (1981).

[2] R. Stolen, K. Dransfeld, Phys. Rev. A139, 1295 (1965); B.Ya. Balagurov, V.T. Vaks, B.I. Shklovskii, Fiz. Tverd. Tela (USSR) 4, 89 (1970) (In Russian); M. Sparks, Phys. Rev. B10, 2581 (1974).

[3] B. Bendow, Solid State Phys., 33, 249 (1978).

[4] A.V. Galdetskii, B.M. Garin, Preprint No.17(320), IRE of the USSR Academy of Sciences, Moscow, 1981 (in Russian).

[5] E. Amrhein, H. Heil, J. Phys. Chem. Sol. 32, 1925 (1971).

A FEL study of Relaxation between bound Donor States in Si:P

K.K.Geerinck, J.E.Dijkstra, J.N.Hovenier
T.O.Klaassen, W.Th.Wenckebach
Faculty of Applied Physics, University of Technology Delft, The Netherlands

A.F.G van der Meer, P.W. van Amersfoort
FOM Institute for Plasma Physics Rijnhuizen, Nieuwegein, The Netherlands

The present paper concerns a study of the life time T_1 of the excited $2p_0$ level of shallow donor phosphorus in silicon at low temperatures ($T \approx 18$ K) and in the absence of an external magnetic field. The experiments are performed usin g the free electron laser (FEL) FELIX of the FOM institute for plasma physics Rijnhuizen. As discussed below T_1 is determined from the behaviour of the $1s \rightarrow 2p_0$ transition at 275 cm^{-1} upon saturation with this laser.

The pulse structure of FELIX as used in our experiments (It emits macropulses with a width $\tau_M = 5\mu$s, each consisting of a train of micropulses with a width $\tau_m = 12$ ps separated by $\tau_r = 1$ ns) plays a vital role in this study. In a standard cw saturation experiment the steady state saturated absorption is given by

$$\alpha = \alpha_0 \frac{1}{1 + 4\omega_R^2 T_1 T_2}, \tag{1}$$

where α_0 is the unsaturated absorption, T_2 is the dephasing time and

$$\omega_R = \langle 1s | \frac{exE_0}{2\hbar} | 2p_0 \rangle \tag{2}$$

is the Rabi frequency. Here, $|1s\rangle$ and $|2p_0\rangle$ the $1s$ and $2p_0$ states, E_0 the amplitude of the electric component of the optical field, which is supposed to be polarized in the x-direction. Finally, e is the elementary charge and $\hbar$ Planck's constant. Thus, cw saturation experiments yield the product T_1T_2 only.

Using FELIX, the situation is comletely different. Eq. (1) is based on Fermi's golden rule which is only valid when the pulse width is much longer than T_2. However, in our case the inhomogeneous width of the transition is of the order of $1/\tau_m$, so we may confidently assume the micropulse length $\tau_m \ll T_2$. Then, we are in the coherent regime and during the micropulse the transition rate and hence the absorption shows an oscilating behaviour. As a result, after a single micropul se

$$\alpha(\tau_m) = \alpha(0) \cos \omega_R t \approx \frac{1}{2}\omega_R^2 \tau_m^2 . \tag{3}$$

We analyse our results assuming $\tau_m \ll T_2 \ll \tau_r \ll T_1 \ll \tau_M$. As discussed above, the first inequality is very plausible. Afterwards, we check whether our results are consistent

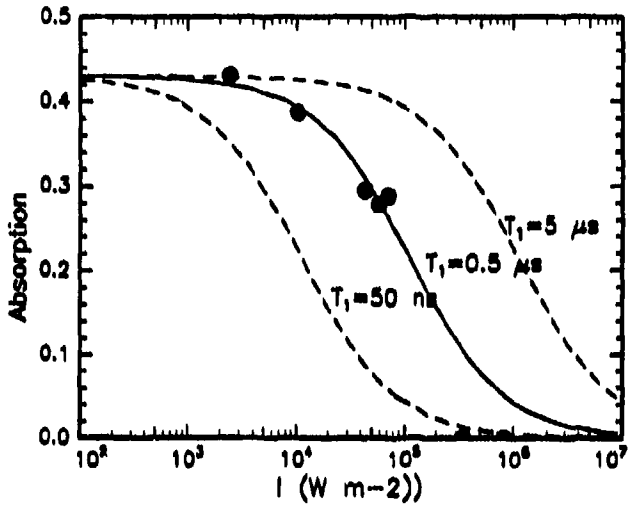

Figure 1: *Peak absorption peak percentage as a function of average power per macropuls of incident FIR radiation.* λ_{peak}=275 cm^{-1}.

the next two inequalities. Then, during the macropu lse a steady state absorption

$$\alpha = \alpha_0 \frac{1}{1 + 4\overline{\omega_R^2}\tau_m T_1} \tag{4}$$

where

$$\overline{\omega_R^2} = \omega_R^2 \frac{\tau_m}{\tau_r} \tag{5}$$

defines the average Rabi frequency during the macropulse. It is calculated from the average power during that macropulse. It is seen that now T_1 may be directly obtained from the experiment, contrary to the case of cw saturation.

The experiments are performed on a sample of 5 Ωcm Si:P with a thickness of 0.4 mm which is mounted under Brewster's angle. are shown in fig. 1. It is checked that the $1s \rightarrow 2p_0$ transition does not overlap with a water vapour abs orption line of the air in the set up. At different calibrated laser powers frequency scans were made through the absorption lines and the peak absorption is determined by fitting the observed absorption to a Gaussian line shape. The resulting data are shown in fig. 1. They are fitted to eq. 4 using $\langle 1s \,|\, x \,|\, 2p_0 \rangle = 1.50 \times 10^{-9}$ nm. As result we find $T_1 = 0.5\mu s$. The results fit well within the restrictions assumed above. In future we plan to extend our work with cw saturation experiments, so we are able to extract T_2 as well. Apart from providing a unique new way to determine T_2, it also allows to check whether really $T_2 \ll \tau_r$ as assumed above.

FT-FIR magneto-spectroscopy on resonant bound polarons in n-GaAs

A.J. van der Sluijs, K.K. Geerinck, T.O. Klaassen, W.Th. Wenckebach

Faculty of Applied Physics, Delft University of Technology, The Netherlands

Abstract

Resonant polaron effects on donor metastable states in n-GaAs in external magnetic field have been studied using a FT-FIR spectrometer in the 100 - 350 cm^{-1} region. Pinning effects are observed near both the ($1s_0$ + 1 LO-phonon) and the ($2p_{-1}$ + 1 LO-phonon) energies. The results are compared with theory.

Introduction

The electron-optical phonon interaction in polar materials generally has three effects on the electron Landau levels. The first effect is a magnetic field independent energy shift $-\alpha\hbar\omega_{LO}$. The second is an enhancement of the electron effective mass by a factor $(1 + \frac{\alpha}{6})$. The third, resonant, effect occurs when $E_N - E_{N=0} \approx \hbar\omega_{LO}$ and consists of a splitting of the energy levels and a pinning of the lower energy level to the optical phonon energy. The effects on donor excited states are expected to be similar to those on Landau levels. Until now, experimental results are only known for the $2p_{+1}$ state [1, 2].

We report an investigation of the resonant effects on the donor metastable states $(N, m, \nu) = (3, 1, 0)$ and $(4, 1, 0)$. Relating all energies to the donor groundstate $1s_0$, resonant effects occur when the (N, m, ν) energy approaches either the optical phonon energy or the energy of the $2p_{-1}$ plus one phonon state.

Experiments

In photoconductivity experiments on a high purity n-GaAs sample, transitions from the $1s_0$ ground state to the $(3, 1, 0)$ and $(4, 1, 0)$ metastable states are studied as a function of magnetic field at T=4.2 K. All spectra are obtained using a BOMEM FT-FIR spectrometer, together with a telescopic light transport system to couple FIR radiation into a liquid helium cryostat. The sample was mounted in the centre of a superconducting magnet, providing fields up to 9T.

As shown in figure 1, just above the LO-phonon energy the upper branches of the split levels are observed. The lower branches are unobservable because of the strong reststrahlen reflection between approximately 270 cm^{-1} and 296 cm^{-1}. The dashed-dotted lines represent the unperturbed $(3, 1, 0)$ and $(4, 1, 0)$ energy levels, including a, field dependent, correction for band non-parabolicity. The next resonance occurs when $E(N, m, \nu) \approx E(2p_{-1}) + \hbar\omega_{LO}$. Since this phonon level lies clear from the reststrahlen band, the pinning of the lower polaron branches to the ($2p_{-1}$ + 1 LO-phonon) energy can be observed. The upper branches were not observed because of system limitations.

Discussion

Lacking information on the eigenfunctions of metastable states, an analytic approach of the resonant effects is not possible. Therefore we use a very simple model to describe the pinning effects, including only the resonant levels. Starting from the experimentally determined

unperturbed energies, which are the eigenvalues of the unperturbed Hamiltonian, off-diagonal matrix elements representing the electron-phonon coupling are included. The level anticrossing effects are found by diagonalizing the resulting matrix. The following unperturbed levels are used: The LO-phonon energy is 296.4cm^{-1}, the (3,1,0) and (4,1,0) energies follow from the low field data, including a correction for band non-parabolicity, and the $2p_{-1}$ energy is also known experimentally. The matrix elements of the electron-phonon coupling are in this approach parameters that are varied to obtain a best fit to the experimental data. Treating the (3,1,0) and (4,1,0) energy levels independently, the curves shown in figure 2 are obtained.

We find that the electron-phonon coupling for the (3,1,0) state is a factor 1.05 stronger than that for the (4,1,0) state. Larsen concludes that the effects on donor states are similar to those on Landau levels [1]. Comparing our results to those of Pfeffer et al. who calculated a factor 1.2 for the ratio of the coupling strenghts of the N=3 and N=4 Landau levels [3], we conclude that our results are qualitatively consistent with theirs.

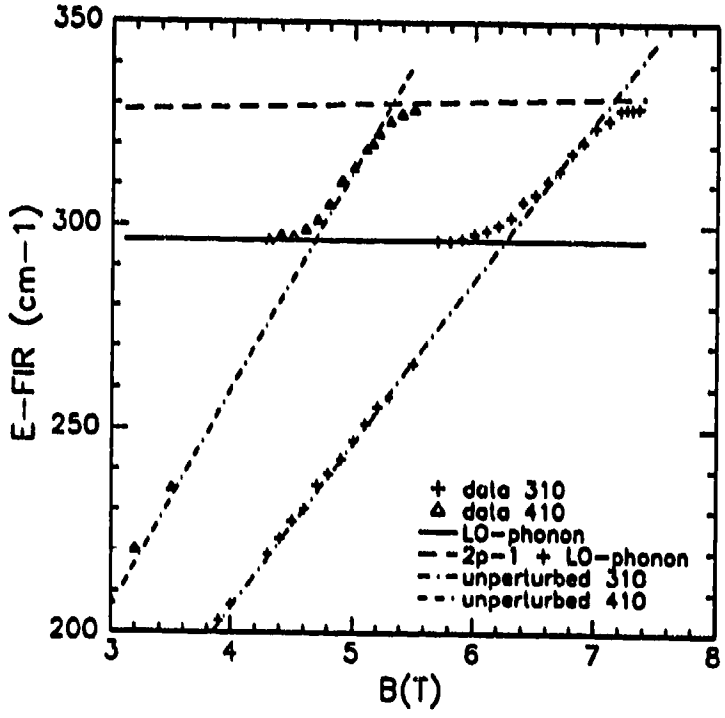

Figure 1: *experimental field dependance of transition energies*

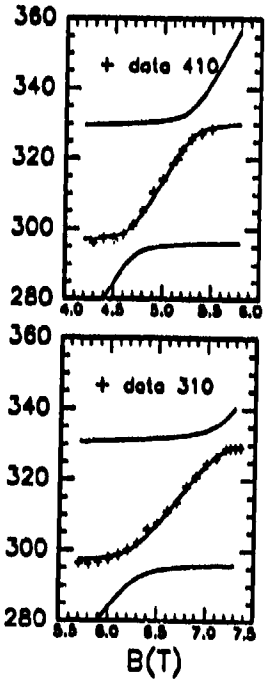

Figure 2: *theoretical calculation of pinning behaviour*

References

[1] D.M. Larsen in *Polarons in ionic crystals and polar semiconductors, ed J.T. Devreese, (North-Holland, 1972) 237*

[2] H. Sigg, H.J.A. Bluyssen and P. Wyder, Solid State Comm. 48, (1983) 897

[3] P. Pfeffer and W. Zawadzki, Solid State Comm. 57, (1986) 647

High frequency, megawatt gyrotron experiments at MIT

K.E. Kreischer, M. Blank, W.C. Guss,
S.K. Lee, and R.J. Temkin

MIT Plasma Fusion Center
Cambridge, MA 01219 USA

ABSTRACT

Results from megawatt gyrotron experiments operating between 110 and 140 GHz will be presented. The beam velocity spread has been measured using a retarding potential diagnostic. The measured perpendicular velocity spread was typically between ±10% and ±15% for velocity ratios between 1.5 and 2.0. The spread was larger at higher beam currents. Good agreement was also obtained between two separate measurements of the velocity ratio. A new experiment at 110 GHz is now being assembled. This device will operate in the $TE_{22,6,1}$ mode and will have an internal converter to produce a Gaussian output beam.

1. 140 GHz EXPERIMENTS

High frequency gyrotrons suitable for ECRH are presently being investigated at MIT. Our recent goal has been to increase the efficiency to levels predicted by theory (40-50%). In order to reach that goal, we have investigated a variety of cavity shapes, identified weak, parasitic modes that can degrade the efficiency[1], and measured the beam quality. The best results to date has been achieved with a two-section cavity, which consists of two cylindrical sections of slightly different radii. Care must be taken in the first section to reduce the diffractive Q of higher order axial modes that can compete with the desired mode. Recent experiments have produced powers up to 1.33 MW at 140 GHz in the $TE_{15,2,1}$ mode. This represents an efficiency of 40%, with 42% being achieved at the 1 MW power level. Mode maps indicate that high power can be achieved with the two-section cavity over a wide range of operating space. Power and efficiency measurements are in agreement with predictions based on self-consistent non-linear theory using the measured beam velocity ratios (α).

One of our concerns in these experiments has been the need, as we increase the beam current, to reduce the velocity ratio to achieve the highest output power. In order to determine whether this is an indication of higher velocity spreads at higher current, we have measured the parallel electron velocity distribution using a retarding potential diagnostic. This diagnostic consists of a slotted plate that allows about 5% of the beam to be transmitted through a cylinder to a collector. This cylinder is biased to high negative voltage, and the collected current is measured as a function of this voltage, giving the distribution function. The measurements are made at one-fourth the normal cathode voltage in order to avoid breakdown. The beam current and magnetic field are also reduced in such a manner as to preserve the beam radius and thickness. Data was taken for both dynamic and static bias voltages. For the dynamic voltage case, the repelling voltage was swept during the 3 μsec gyrotron pulse to give the distribution function in a single shot. In the static bias case, the repelling voltage was constant during each shot, and adjusted in steps over a series of shots. Both methods produced similar results. The perpendicular velocity spread was calculated assuming a mono-energetic beam. It was found that the spread was relatively constant for $\alpha \geq 0.7$ and increased with the beam current. Results are shown in Fig. 1. Note that data is given in terms of the reduced beam currents, which must be multiplied by a factor of eight to scale up to high voltage operation. In Fig. 2 a comparision is made of the average beam α as measured by a capacitive probe[2] before the cavity and α inferred from the distribution function. Both approaches are in good agreement for $1 < \alpha < 1.8$. Above this range the capacitive probe gives somewhat higher values of α.

2. 110 GHz GYROTRON DESIGN

In our next set of experiments a 110 GHz gyrotron with an internal converter will be tested. The $TE_{22,6,1}$ mode was chosen in order to have ohmic wall losses well below 1 kW/cm^2. Previous MIT experiments[3] at 267 GHz indicate that this should be a good operating mode. The 267 GHz experiments involved the $TE_{22,5,1}$ mode, and produced a maximum output power of 537 kW at 80 kV and 35 A for an efficiency of 19%. At 15 A, the efficiency increased to 27%. The $TE_{22,5,1}$ could be excited over a wide range of parameters, suggesting that mode competition was not a major limiting factor. Good results have also been obtained in Russia with this class of modes[4].

A tube design has been completed that contains an efficient, internal rippled-wall converter[5] that will be used to produce a Gaussian beam and separate the radiation from the electron beam. It is hoped that this arrangement will reduce the deleterious effects of window reflections, and provide better pumping conductance within the vacuum tube. The first cavity to be tested will be a standard, tapered cavity with the following parameters: 4° input linear taper, a nonlinear uptaper at the output to the converter that operates at 6% above cutoff, and an axial rf profile with a width L/λ of 6.5. The transition from the input taper to the straight section will be rounded in order to minimze mode conversion that could cause power leakage back towards the gun. The large input angle and relatively short interaction length were selected in order to avoid multimoding that could limit the efficiency[6]. The diffractive Q is 850, and the peak ohmic losses are 0.8 kW/cm^2 at 1 MW. We have modelled the cavity using self-consistent theory and assuming a beam with an α of 1.6 and perpendicular spread of ±10%. The simulations indicate 1.2 MW is possible with a 77 kV, 34 A beam for an efficiency of 46%. The mode converter operates close to cutoff in order to reduce the converter length to about 14 cm and provide clearance for the electron beam. One concern we have had with operation near cutoff was the possibility of beam-rf interaction outside the cavity. However, simulations indicate that the interaction does end early in the nonlinear uptaper, primarily due to the dropoff in the magnetic field. In the upcoming experiments we will be measuring the efficiency of the cavity and internal converter, and couple the output Gaussian beam into corrugated transmission line.

This work is supported by U.S. DOE contract DE-FC02-93-ER-54186.

3. REFERENCES

1. W.C. Guss, M.A. Basten, K.E.Kreischer, and R.J. Temkin, "Sideband mode competition in a gyrotron oscillator," *Phys. Rev. Lett.* Vol. 69, pp. 3727-3730, 1992.

2. W.C. Guss, T.L. Grimm, K.E. Kreischer, J.T. Polevoy, and R.J. Temkin, "Velocity ratio measurements of a gyrotron electron beam," *J. Applied Phys.*, Vol. 69, pp. 3789-95, 1991.

3. K.E. Kreischer, T.L. Grimm, W.C.Guss, and R.J. Temkin, "The operation of a megawatt gyrotron in the submillimeter wave region," IEDM Technical Digest, IEEE Cat. No. 89CH2637-7, pp. 751-4, 1989.

4. V.I. Kurbatov, S.A. Malygin, and E.O. Vasilyev, "Commercial gyrotrons for thermonuclear investigations," Strong Microwaves in Plasmas, Inst. of Applied Phys., Nizhny Novgorod, pp. 765-772, 1991.

5. M. Blank, K.E.Kreischer, and R.J. Temkin, "A quasi-optical mode converter for gyrotrons operating in high order modes," in these proceedings.

6. S.Y. Cai, T.M. Antonsen, Jr., G. Saraph, and B. Levush, "Multifrequency theory of high power gyrotron oscillators," *Int. J. Electronics*, Vol. 72, pp. 759-777, 1992.

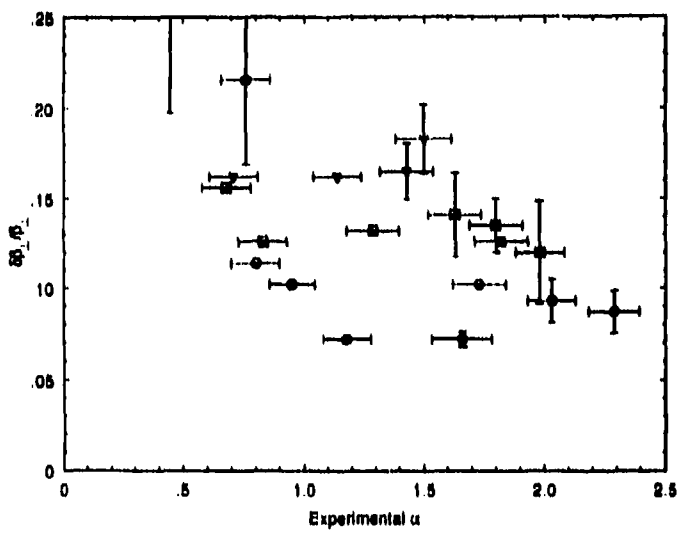

Figure 1. Measured velocity spread versus the beam velocity ratio for beam currents of 1.9 A (circles), 3.6 A (squares), and 5.0 A (triangles).

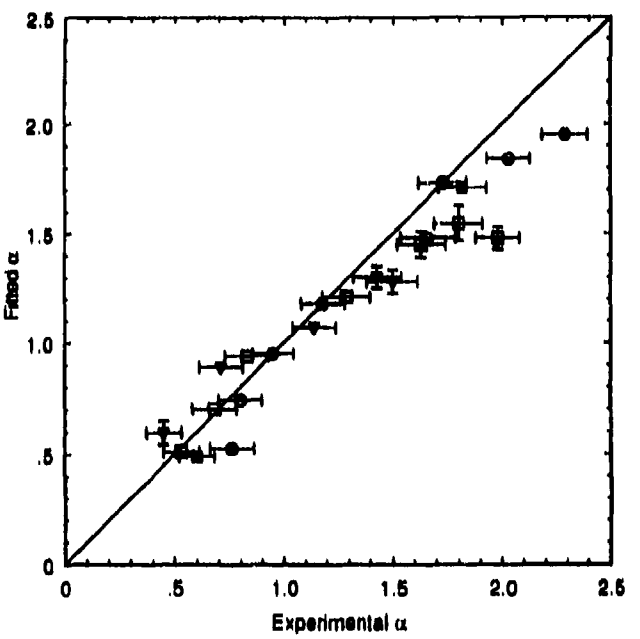

Figure 2. Comparison of the beam velocity ratio measured by the retarding potential diagnostic (vertical axis) and the capacitive probe (horizontal axis).

Design considerations for a 1 MW CW gyrotron with an internal converter

K. Felch, T.S. Chu, H. Huey, H. Jory, J. Neilson, and R. Schumacher

Varian Associates, Inc.
811 Hansen Way, Palo Alto, CA 94304 USA

J.A. Lorbeck and R.J. Vernon

University of Wisconsin - Madison
Dept. of Electrical and Computer Engineering
1415 Johnson Drive, Madison, WI 53706 USA

ABSTRACT

Varian is carrying out the development of high-power, CW gyrotrons at frequencies ranging from 100-140 GHz. Recent experiments, carried out at a frequency of 110 GHz, resulted in the generation of output powers of 500 kW for 2.5-second pulses and 1 MW for 1 ms pulse durations.[1] The output mode of this tube was a whispering-gallery mode, based on the $TE_{22,2}$ mode employed in the interaction cavity. Current design activity is aimed at producing a 1 MW CW gyrotron at the same frequency, but with a gaussian output mode structure. This type of output mode is desirable for low-loss transmission in a corrugated waveguide or mirror transmission line. In addition to the change in output coupling, the cavity mode will be changed to the $TE_{22,6}$ mode. The higher order cavity mode is consistent with higher power or higher frequency requirements that will be addressed in subsequent development activities.

1. INTRODUCTION

Electron cyclotron resonance heating (ECRH) requirements for planned magnetic fusion experiments such as the International Thermonuclear Experimental Reactor (ITER) will require millimeter-wave sources capable of output powers of at least 1 MW CW at frequencies in the range, 100-200 GHz. Recent megawatt-level development work at Varian resulted in a gyrotron design that was tested to output powers of 1 MW for short pulses (~1 ms) and 500 kW for 2.5-s pulses at a frequency of 110 GHz.[1] The output mode of this tube was a whispering-gallery mode, based on the $TE_{22,2}$ mode employed in the interaction cavity. Present design efforts are centered around the introduction of a mode converter, inside the tube, that transforms the waveguide output mode from the cavity to a gaussian beam, before the output power exits the tube. Other design activities are related to the thermal management problems that arise in operating under full CW conditions at output powers of 1 MW. The present development plan involves the construction of two tubes, each with several test iterations, with the ultimate goal of achieving 1 MW CW with a gaussian-like output mode.

Much of the design of the first experimental tube will be similar to the one employing the $TE_{22,2}$ cavity mode, discussed above. The electron gun, collector and output window will be of nearly identical design, and the cavity will utilize the same $TE_{22,n}$ class of modes. The major change will be in the output coupling portion of the tube. Below we summarize the design of the major elements of the first experimental tube with a gaussian or gaussian-like output mode.

2. DESIGN OF GYROTRON WITH INTERNAL CONVERTER

2.1 Electron gun

The first experimental tube, with a gaussian-like output mode, will make use of the same electron gun design employed on the earlier $TE_{22,2}$-mode design. The decision to utilize a cavity interaction employing the same $TE_{22,n}$ class of modes at the same frequency, means that the desired electron beam parameters are essentially identical to that in the earlier design. This electron gun is a double-anode, magnetron-injection gun, that operates at a beam voltage of 80 kV and a nominal beam current of 35 A. In the cavity, the average radius of the hollow beam corresponds to the innermost radial maximum of the cavity electric field. Computer simulations of the electron gun predict a perpendicular velocity spread of ±4% for a perpendicular-to-parallel velocity ratio (α) of 2.0. In operation, it was found that the achievable value of α was somewhat lower at full operating current (limited by mirroring electrons), so the tube design will be optimized for a value of $\alpha = 1.5$.

2.2 Cavity

The decision has been made to use a $TE_{22,6,1}$ mode in the cavity. As with the $TE_{22,2,1}$ cavity, the electron beam will be situated on the innermost electric field maximum of the cavity mode. The increase in cavity size from the $TE_{22,2,1}$ mode will make cavity-wall-loading problems much less severe and thus enable use of a significantly higher-Q cavity design. The higher Q should serve to stabilize operation in the desired mode more effectively than in the lower Q design employed with the $TE_{22,2,1}$ mode, and thereby lead to higher efficiency operation . Initial designs being considered have a Q of about 1000 with peak wall-loading values of less than 1 kW/cm^2 for ideal copper cavity walls. Use of the $TE_{22,6,1}$ mode is consistent with higher power or higher frequency requirements that will be the subject of subsequent development activities.

2.3 Output coupler

An internal converter, after the interaction cavity, will serve to transform the $TE_{22,6}$ mode produced in the cavity to a gaussian-like beam that will exit the tube perpendicular to the tube axis. The converter design is similar to the one described by Denisov et al.[2] and consists of a section of waveguide with small perturbations to transform the output waveguide mode into a gaussian-like geometry, followed by a system of mirrors that provide further shaping of the output into a microwave beam, with the desired gaussian-mode parameters, and direct the resultant power to the output window. Initial designs have calculated efficiencies of greater than 95% in transforming the $TE_{22,6}$ output mode from the cavity into a gaussian mode.

2.4 Collector

The electron beam collector will be quite similar to the one used in the earlier tube with the $TE_{22,2}$ mode that employed radial extraction of the spent electron beam.[1] The electron beam will be collected after the microwave power has been transmitted through the output window. The diameter of the collector in the first tube will remain at 24 inches. Some changes in the magnetic environment have been made since there is no longer the need to direct the electron beam though a narrow slot in the output waveguide.

2.5 Output window

The output window for the first experimental tube with an internal converter will be quite similar to the 4-inch diameter, double-disk, sapphire design employed on the earlier $TE_{22,2}$-mode tube.[1] Face-cooling of the two sapphire discs is provided by a low-loss dielectric fluid. It will have the capability to transmit between 200-700 kW CW, depending on the exact parameters of the gaussian mode that results from the internal coupler system. For full 1 MW CW operation, alternate geometries and cooling methods are currently being studied.

3. SUMMARY

The demonstration of a full 1 MW CW tube with a gaussian output mode will provide an important tool for use in upcoming fusion experiments. The use of a gaussian output mode (as opposed to a waveguide output mode) should result in the most effective overall system design for such experiments. The first experimental tube in our effort to develop a gyrotron with these parameters will be an important step in achieving the ambitious goals.

4. ACKNOWLEDGMENTS

The 1 MW gyrotron oscillator is being developed under contract with Lawrence Livermore National Laboratory, operated by the University of California for the U. S. Department of Energy, under Prime Contract W-7405-eng-48.

5. REFERENCES

1. K. Felch, T.S. Chu, J. Feinstein, H. Huey, H. Jory, J. Neilson, and R. Schumacher, "Long-Pulse Operation of a Gyrotron with Beam/RF Separation," in Seventeenth International Conference on Infrared and Millimeter Waves, Richard J. Temkin, Editor, Proc. SPIE 1929, pp. 184-185, December 1992.

2. G.G. Denisov, A.N. Kuftin, V.I. Malygin, N.P. Venediktov, D.V. Vinogradov, and V.E. Zapevalov, "110 GHz Gyrotron with a Built-In High-Efficiency Converter," Int. J. Electronics, Vol. 72, Nos. 5 and 6, pp. 1079-1091, May-June 1992.

0.5 MW/140 GHz $TE_{10,4}$ Gyrotron with Built-in Highly Efficient Quasioptical Converter

E. Borie, G. Dammertz, G. Gantenbein, M. Kuntze,
A. Möbius, H.-U. Nickel[1], B. Piosczyk, M. Thumm[1]

Kernforschungszentrum Karlsruhe GmbH, ITP, Postfach 3640, 76021 Karlsruhe, Germany
[1] also: Universität Karlsruhe, Institut für Höchstfrequenztechnik und Elektronik

1. INTRODUCTION

KfK is continuing the development of 140 GHz high power gyrotrons for electron cyclotron wave (ECW) applications. Experiments with a $TE_{10,4}$ mode gyrotron have been performed using an axial rf output coupling. The achieved maximum output power of this version amounted to 0.7 MW in the design mode with a mode purity of about 99 % and an electronic efficiency of 26 %. Since these experiments have been performed using the superconducting magnet system designed for the previous $TE_{0,3}$ mode tube the pulse length was limited to 5 ms. With a more appropriate magnet system with increased bore hole diameter which allows the use of a built-in quasioptical converter a pulse length of up to 300 ms with 0.5 MW rf power is expected.

In the following we will present some experimental results with respect to frequency step-tuning of the $TE_{10,4}$ mode gyrotron and describe the radial output coupling system.

2. FREQUENCY STEP-TUNING

One of the main advantages of ECW heating of fusion plasmas is the well localised energy deposition of the microwave beam. By tuning the frequency of the generator it is possible to heat and to stabilize well defined areas of the plasma without the need for a steerable launching mirror. This will require a tunable mm-wave source.

In gyrotrons the frequency can be varied by changing the operating mode. It has been shown that frequency step-tuning of gyrotrons operating in high order modes is possible[1,2]. Different modes may be excited by (fast) tuning of the beam voltage or (slow) variation of the magnetic field. Azimuthal neighbouring modes seem to be suitable for frequency step-tuning in a gyrotron as their radial structure is very similar to that of the main mode. Subject to this condition the coupling of the electron beam and the rf wave in a gyrotron resonator is comparable for these modes. This behaviour is shown in Fig. 1 for the $TE_{10,4}$ mode and its neighbours. Although the frequency spacing of approximately 7.4 GHz of these modes is probably too large to fulfill the requirements for fusion plasma applications, investigations with respect to single mode operation and output power can be performed.

By increasing and decreasing the magnetic field (~5.3 %) we optimized the tube to oscillate in the $TE_{11,4}$ (147.4 GHz) and $TE_{9,4}$ (132.6 GHz) mode, respectively. In the $TE_{9,4}$ mode we achieved 420 kW rf power at 25 A (to be compared with $TE_{10,4}$: 600 kW). We observed strong mode competition with the modes $TE_{8,4}$ (124,96 GHz) and $TE_{11,3}$ (126.24 GHz). It is assumed that this effect is supported by a high amount of reflection of these modes at the window (up to 35 %) which is tuned to 140.0 GHz. Taking realistic beam properties and window reflections into account the measured peak output power of the $TE_{9,4}$ mode is in reasonable agreement with numerical calculations.

Fig. 2 shows the oscillating area of the $TE_{11,4}$ mode in the U_{mod}-U_{beam} plane. Several frequencies spaced by approximately 60 MHz have been observed for the $TE_{11,4}$ mode, corresponding to different longitudinal modes of the long-line cavity formed by the gyrotron resonator and the (reflecting) window. The maximum output power in this mode was 300 kW.

3. BUILT-IN QUASIOPTICAL CONVERTER

The built-in highly efficient quasioptical converter and a focusing matching mirror system (three reflectors) has been manufactured according to design criteria given by Pretterebner et al. (1992)[3]. Low power tests are in progress. After assembling and conditioning of the tube with the radial outcoupling scheme first high power experiments will start.

4. CONCLUSIONS

We have seen that it is possible to operate the $TE_{10,4}$ mode gyrotron in the azimuthal neighbouring modes, thus giving the possibility to change the frequency of the rf output. One limiting factor is the broadband characteristic of the single disc window used in the experiments. Strong reflections at the window which propagate back to the interaction region may increase the problem of mode competition in the step-tuning experiments. To avoid these complications KfK is developing broadband mm-wave windows.

5. ACKNOWLEDGEMENTS

This work was performed under the auspices of the Projekt Kernfusion at the KfK and was supported by the European Community as part of the European Fusion Technology Program.

6. REFERENCES

1. Kreischer, K.E. und Temkin, R.J., 1987, Single-mode operation of a high-power, step-tunable gyrotron. Physical Review Letters, 59, 547-550.
2. Kurbatov, V.I., Malygin, S.A., Vasilyev, E.G., 1991, Commercial gyrotrons for thermonuclear investigations. Strong Microwaves in Plasmas, Proceedings of the International workshop, Volume 2, A.G. Litvak, Editor, 765-772.
3. Pretterebner, J., Möbius, A., Thumm, M., 1992, Improvement of quasi-optical mode converters by launching an appropriate mixture of modes, in Seventeenth Int. Conf. on Infrared and Millimeter Waves, R.J. Temkin, Editor, Proc. SPIE 1929, 40-41.

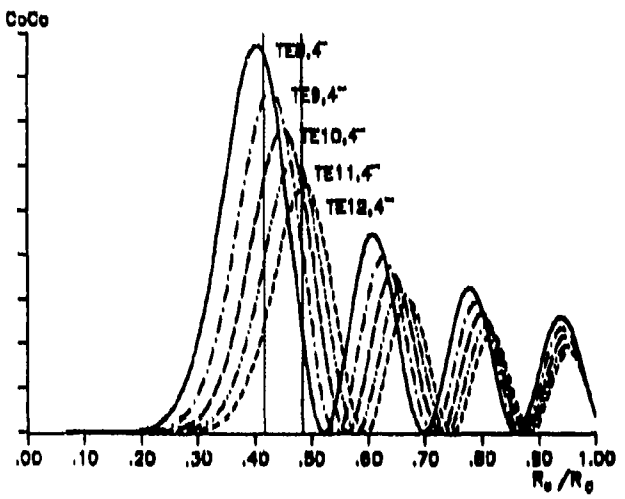

Fig. 1: Coupling coefficient for beam-wave interaction.

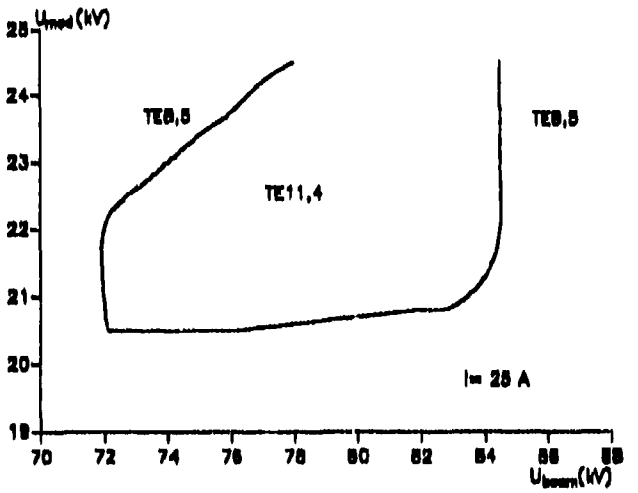

Fig. 2: Oscillating area of the $TE_{11,4}$ mode.

DESIGN OF A 3 MEGAWATT, 140 GHZ GYROTRON BASED ON A $TE_{21,13}$ COAXIAL CAVITY

M.E. Read, G.S. Nusinovich, O. Dumbrajs, H.Q. Dinh, D. Opie and G. Bird
Physical Sciences, Inc, Alexandria, VA 22314 USA
K. Kreischer and M. Blank
Massachusetts Institute of Technology, Cambridge, MA 02139

Introduction

For electron cyclotron heating to be economically attractive for large scale tokamaks, such as ITER, the unit power source, the gyrotron, should be above 1 MW cw. At frequencies of interest, ~140 GHz, mode competition makes the realization of such high power devices quite difficult. Reduction of the number of modes that compete by use of a coaxial insert in the cavity has been found to be effective. We report here on the design of a 3 MW, 140 GHz gyrotron based on the $TE_{23,16}$ mode, including brief discussions of the cavity, electron gun and output mode converter.

Cavity

The $TE_{21,13}$ mode was chosen because it has a ratio of the radial to azimuthal eigenumbers similar to the $TE_{23,16}$, which was found in a previous study of a 280 GHz gyrotron to have high efficiency, and has an acceptable ohmic heating in the outer wall. For small radii, the heating of the inner conductor is a sharply increasing function of increasing radius. This gives an upper bound for the inner conductor radius. Limiting the ohmic heating to 700 W/cm^2 fixed the inner conductor radius to 6 mm. To determine the efficiency, a code modeling the non-linear interaction of a beam with several modes present simultaneously was used. Results with and without spread in velocity in the beam were obtained. The axial profile of the RF field was taken as the eigenfunction of the cavity without the beam, *i.e.*, the solution was not self consistent. This has been found to be a good approximation in cavities with similar Q's, but lower order modes. The average radius of the beam was 8.13 mm, on the first peak of the co-rotating mode. Detailed studies were made with a beam voltage of 95 kV and a current of 70 A. In order to model the start-up phase of the operation, which has been found in previous studies to be critical, the simulation was started at a voltage of 50 kV, at which the beam velocity ratio, α, was predicted to be 0.69, and the start currents of all but a few modes, quite high. Those that had start currents less than the beam current were included in the initial simulation run. Results of the simulation, starting at 65 kV, are shown in Figure 2. The mode at 65 kV is $TE_{23,13}$, followed by the $TE_{22,13}$ at 70 kV- 80 kV, with $TE_{21,13}$ starting at 85 kV. Several other modes started at voltage changes, but were suppressed. The $TE_{21,13}$ mode is stable until 97 kV. The final efficiency was 45%. This was roughly the same as that found within the previous study of the $TE_{23,16}$ mode where a Gaussian axial profile of the RF field was used. For the study of the $TE_{21,13}$ mode, the profile calculated for the actual (cold) cavity was used.

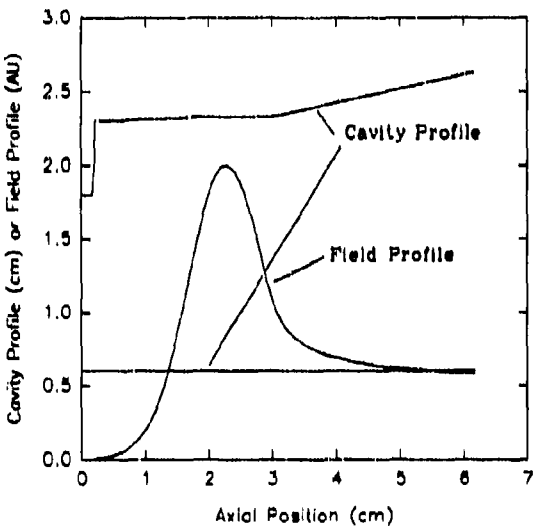

Figure 1. Axial profile of the RF fields in the $TE_{21,13}$ cavity.

Electron Gun

The electron gun is an inverted magnetron injection gun (MIG), as shown in Figure 3. The inner anode is at ground potential, allowing the support of the inner conductor at both the gun and output end of the gyrotron. The outer anode is also at ground; thus this is

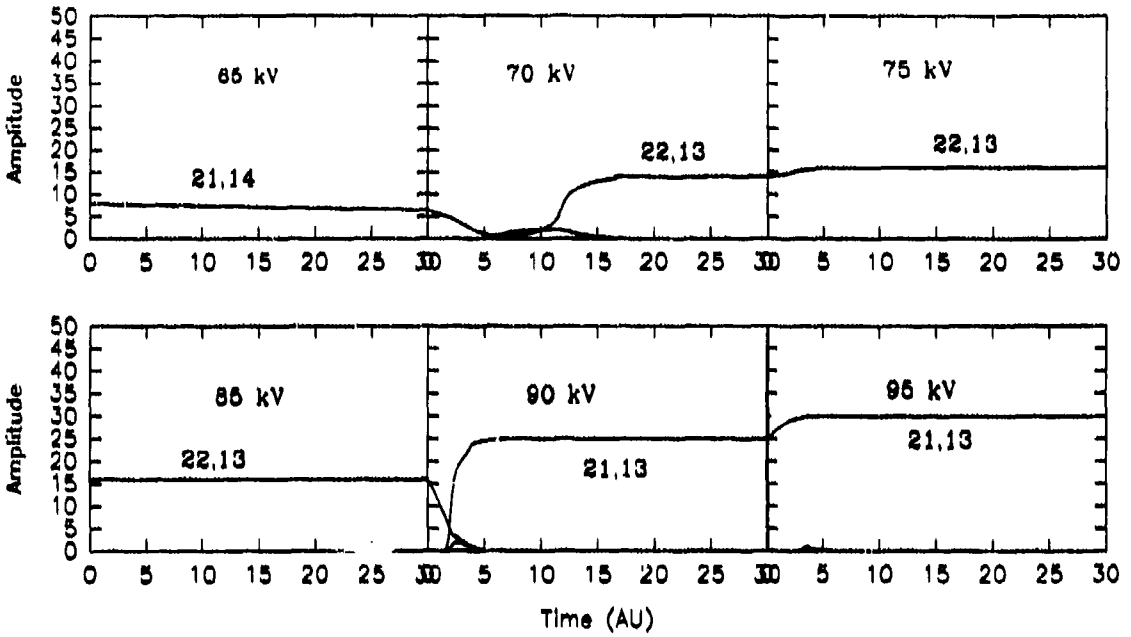

Figure 2. Results of the multimode simulation, showing scaled amplitudes of different modes versus time for several beam voltages.

effectively a single anode gun. The cathode radius was 4.73 cm, the current density 5.5 A/cm^2, and the compression ratio, 32:1. Simulation of the gun was done using EGUN by Hermannsfeldt. With a final beam α of 1.4, the rms spread in perpendicular velocities was 4%, including contributions from surface roughness. This appears satisfactory, given the fact that the simulation code with a velocity spread of 8% showed a decrease of only 3% in the efficiency.

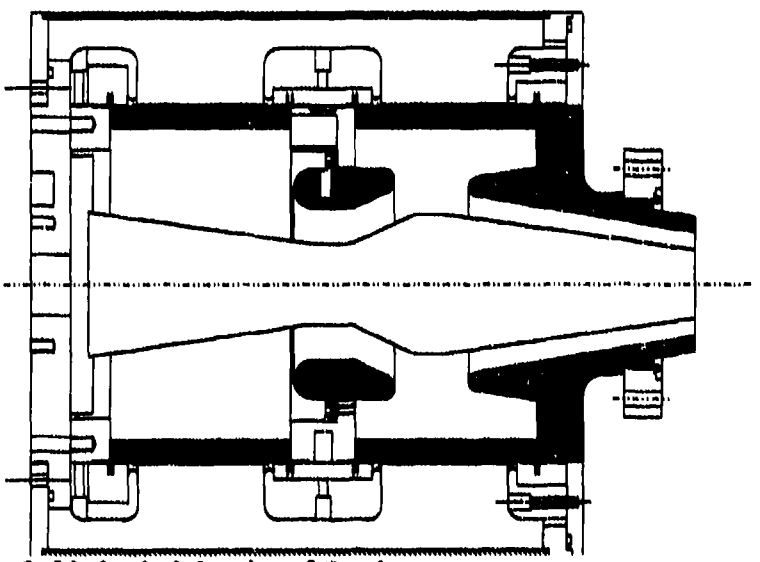

Figure 3. Mechanical drawing of the electron gun.

Mode Converter

A quasi-optical mode converter has been designed to convert the $TE_{21,13}$ waveguide mode to a Gaussian mode in free space. The converter consists of a rippled wall waveguide section followed by a step-cut launching aperture and several focussing reflectors. The rippled wall waveguide, which is designed using coupled mode theory, bunches the $TE_{21,13}$ radiation into Gaussian bundles. Because a Gaussian beam is launched from the step-cut aperture, the reflectors are designed using Gaussian optics. Diffraction theory shows that the conversion efficiency is greater than 90%.

95 GHz Harmonic Gyroklystron

G.P. Scheitrum, T. Bemis, T.A. Hargreaves, L. Higgins

Litton Systems, Electron Devices Division
San Carlos, California 94070

ABSTRACT

The harmonic gyroklystron[1] (HGK) is capable of generating kilowatts of average power at millimeter wavelengths. Operating the device at a harmonic ($n > 1$) of the cyclotron frequency reduces the required magnetic field to levels attainable by normal solenoids. Size and weight of the device are reduced with a normal solenoid. An advanced centerpost (ACP) gun is used to generate the hollow axis-encircling beam. Computer simulations predict very low velocity and guiding center spreads in the beam. A 95 GHz fourth harmonic HGK design simulation predicts 30% overall efficiency and >2kW average power. The electron gun will be tested in a beamstick in which the rf circuit is replaced by segmented capacitive probes.

1. Background

The HGK, shown in Fig. 1, consists of an electron gun and magnetic focusing system, several coaxial magnetron cavities and a depressed collector. A magnetic field reversal or cusp causes the annular electron beam to orbit its axis at the cyclotron frequency, $\omega_c = (eB_z)/(\gamma m_o)$. The operating frequency of the HGK is a harmonic of the cyclotron frequency, $\omega_o = n\,\omega_c$. The rotating beam enters the input coaxial magnetron cavity. A typical cavity is shown in Fig. 2. The outer coaxial cavity is coupled to the vaned inner cavity by a set of n slots which run parallel to the beam axis. The coaxial cavity operates in the TE_{01} coaxial mode and the inner cavity, with $2n$ vanes, operates in the π mode. The azimuthal electric field in the input cavity modulates the beam and produces n rodlike bunches which travel down the beam tunnel. The drift regions between cavities are cut off to the fundamental TE_{11} mode. Intermediate cavities further modulate the bunches and the output cavity transfers the azimuthal beam energy to the RF field. RF signals are coupled to the cavities using rectangular waveguide joined to the outer diameter of the coaxial cavity. The depressed collector recovers a significant fraction of the spent beam energy.

2. Electron Gun and Magnetic Circuit

The electron gun cross section is shown in Figure 1. The gun is enclosed in an iron shell so that the conical section cathode is in a magnetic field free region. All the flux enclosed by the cathode is carried by the iron centerpost. Given the desired angular velocity ω_2, velocity ratio α and beam radius r_b, Busch's theorem is used to calculate the required magnetic flux φ_1 enclosed by the cathode.

$$\omega_2 = (\varphi_2 - \varphi_1)e/2\pi r_2^2 m$$

Given α, r_2 and ω_2 the required beam voltage can be determined from

$$V_k = \frac{\gamma m_o r_2^2 \omega_2^2}{2e}\left(1 + \frac{1}{\alpha^2}\right)$$

where e and m_o are the electronic charge and mass, γ is the relativistic factor, subscript 1 refers to the cathode and subscript 2 to some arbitrary plane downstream of the magnetic field reversal.

3. Coaxial Magnetron Cavities

Using coaxial magnetron cavities for the interaction greatly simplifies the mode competition and RF coupling problems usually associated with gyroamplifiers. The coaxial magnetron was developed by Feinstein[2] to reduce mode competition in magnetrons. Thus the solutions found for magnetrons can be directly applied to the HGK cavities. The RF power is coupled in and out of the cavities through an iris in the outer cylinder of the coaxial cavity into the TE_{10} mode in a rectangular waveguide. This separates the RF output from the spent electron beam and enables the use of a depressed collector.

4. Modeling HGK Performance

Both a small signal code and a large signal code have been developed for simulating the performance of the HGK. The small signal code is based on Symons' equivalent circuit model[3] of the gyroklystron. A beam coupling factor and a transconductance are calculated from Zhurakhovskii and Rapoport's equations of motion. These are used to calculate the small signal gain and start oscillation current for the HGK. The large signal code is a modified version of Ganguly's 3-D nonlinear code[4] for the gyropeniotron. The code was modified to solve for a multicavity HGK with variable length cavities and drift tubes. The large signal code predicts electronic efficiencies of 35% and 20% for third and fourth harmonic operation. Overall efficiencies of 51% and 36% are predicted using a single stage depressed collector.

5. Experimental Device

Currently a beamstick is being assembled for the 95 GHz HGK. The beamstick will be used to verify the performance of the hollow beam for both third and fourth harmonic operation. Operating the solenoid at 11 kG will dissipate about 7 kW versus 3.5 kW for the 8.5 kG needed for the fourth harmonic. This makes fourth harmonic operation attractive despite the penalty in electronic efficiency. Two capacitive probes will be used in the beamstick to measure it at either end of the beam tunnel. Each probe is split into four quadrants to determine beam position in the beamstick. After the beam performance is measured the beamstick will be retrofitted with a tunable 95 GHz oscillator cavity. This will be used to determine start oscillation currents, bandwidth and electronic efficiency for the interaction.

6. References

1. G. P. Scheitrum, "The Harmonic Gyroklystron", PhD Thesis, Stanford University, 1991.
2. J. Feinstein and R. J. Collier, "The circular electric mode magnetron," in *Crossed Field Microwave Devices*, (E. Okress, ed.), Academic Press, 1961.
3. R. S. Symons and H. R. Jory, "Cyclotron Resonance Devices", Advances in Electronics and Electron Physics, Vol. 55, Academic Press, NY 1981.
4. A.K. Ganguly, S. Ahn and S.Y. Park, "Three Dimensional Nonlinear Theory of the Gyropeniotron Amplifier", Int. Journal of Electronics, Vol. 65, No. 3, 1988.

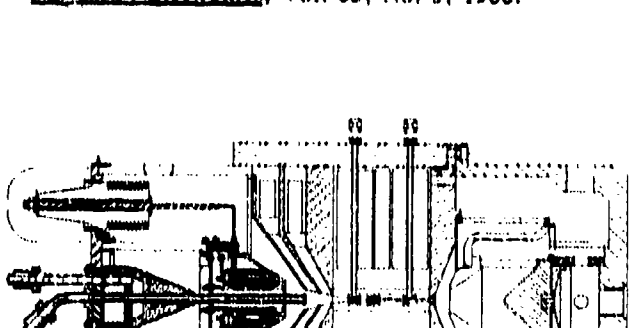

Figure 1 Four cavity harmonic gyroklystron

Figure 2 Cross section of coaxial magnetron cavity

Design of a 100 MW, 17 GHz Second Harmonic Gyroklystron Experiment

P.E. Latham, W. Lawson, J. Calame, V. Specht,
M.K.E. Lee, Q. Qian, M. Rimlinger, and B. Hogan
Laboratory for Plasma Research
University of Maryland, College Park, MD 20742

In an effort to expand the frontiers of high-energy physics, electron-positron colliders with center-of-mass energies approaching 1 TeV (and beyond) are being planned.[1] These machines will require efficient, reliable, pulsed microwave amplifiers with peak power levels exceeding the state-of-the-art. The current linear collider standard is the 100 GeV Stanford Linear Collider,[2] for which a 1 μs, 150 MW, S-Band klystron was developed.[3] It is anticipated that comparable power levels will be required in 10-20 GHz devices. Because klystron peak power scales (optimistically) with the output wavelength squared, considerable enhancement is required.

At the University of Maryland, we have been pursuing amplifiers based on the cyclotron resonance instability.[4] Because the cyclotron frequency associated with the external magnetic field acs as a mode selector, overmoded structures can be used, and gyroklystrons scale much more favorably with frequency than klystrons: the peak power is proportional to the wavelength rather than its square. Here we present the design of a 100 MW, 17 GHz second harmonic gyroklystron operating in a coaxial configuration. We first describe the electron gun, then give the circuit design along with its nonlinear efficiency.

A single-anode magnetron injection gun (MIG) was determined to be feasible and was selected because of its simpler configuration and wider current range[5] (compared to a double-anode MIG). The key gun parameters are summarized in Table 1. The magnetic compression is fairly low and the cathode loading is modest. The total current and cathode radius, however, are well above state-of-the-art. Table 2 indicates the nominal beam parameters at the end of the simulated region, which corresponds to the center of the input cavity. The axial velocity spread, which is given for a current of 600 A, is from ballistic considerations only; spread contributions from thermal and surface roughness considerations should be much smaller. The nominal current is less than 28% of the space-charge limit. The electric field on the anode is quite small and the peak cathode field has a reasonable safety margin. The average field on the emitter strip is near 52 kV/cm and varies less than 8% along the strip length.

Using the simulated gun results given in Table 2, we designed a two-cavity gyroklystron circuit operating at the second harmonic. Because we were after the highest possible power, we designed for 800 A; at that value of the current the axial velocity spread is 10%. The parameters of the circuit which yielded the highest efficiency is shown in Table 3. Note that the output cavity is made up of two sections; the lengths and radii of these sections are chosen so that the backward propagating TE_{01} mode, which is not cutoff in the drift section, vanishes due to destructive interference. However, the TE_{01} mode does not vanish in the forward direction, so the output mode is a mix of TE_{01} and TE_{01}, with about 80% of the power in the TE_{01} mode. The overall efficiency of this design was 25%, which yields an output power of 100 MW. The main reason for the relatively low efficiency is that the third harmonic also interacted with the beam, and since the operating frequency is below the third harmonic frequency, this interaction tends to accelerate rather than decelerate electrons. Future work will concentrate on eliminating this effect, either by increasing the length of the interaction or operating in the gyrotwistron configuration.

Table 1: The electrode specifications.

Cathode radius (cm)	9.58
Emitter strip length (cm)	1.67
Cathode-anode gap (cm)	12.64
Cathode half-angle	36° - 44°
Magnetic compression ratio	9.9
Cathode loading (A/cm^2)	5.95

Table 2: The simulated MIG performance.

Axial velocity spread (%)	6.70
Guiding center radius (cm)	3.07
Guiding center spread (cm)	0.27
Space-charge limiting current (A)	2,190
Electric fields (kV/cm)	
peak cathode	91.0
peak anode	29.3
emitter strip (aug)	51.6
emitter strip (variation)	3.9

1. B. Richter, "Physics and technology challenges of the next-generation linear colliders," presented at the 1991 Particle Accelerator Conference, San Francisco, CA, May 1991.
2. N. Phinney, "The Stanford Linear Collider," presented at the 1992 Linear Accelerator Conference, Ottawa, August, 1992.
3. T.G. Lee, G.T. Konrad, Y. Okazaki, M. Watanabe, and H. Yonezawa, IEEE Trans. Plasma Sci. **PS-13**, 545 (1985).
4. R.S. Symons and H.R. Jory, *Advances in Electronics and Electron Physics*, vol. 55 (New York: Academic Press, 1981), pp. 1.75.
5. W. Lawson and V. Specht, IEEE Trans. Electron. Dev. (in press).

Table 3: Circuit Design. All lengths in cm.

Input cavity; Q=350	
inner/outer radius/length	2.000/4.206/2.000
Drift section	
inner/outer radius	2.350/3.850
Output cavity; Q=730	
first section inner/outer radius/length	2.234/3.920/0.978
second section inner/outer radius/length	1.914/4.205/0.922
lip inner/outer radius/length	2.358/3.798/0.422
output section inner/outer radius	2.356/4.415

High power operation of a K-band second harmonic gyroklystron

W. Lawson, H. W. Matthews, M. K. E. Lee, B. Hogan, J. P. Calame, and J. Cheng

Electrical Engineering Department and Laboratory For Plasma Research
University of Maryland, College Park, MD 20742 USA

At the University of Maryland, we have been performing a sequence of experiments to determine the suitability of gyroklystrons for linear collider applications. Initial experiments with six different two-cavity[1] and four three-cavity[2] fundamental mode gyroklystrons have produced about 27 MW of power in 1 μs pulses at 9.87 GHz with 32% efficiency and gains near 40 dB. A program to modify the final two-cavity circuit for amplification studies at the second harmonic is well underway.[3] In this paper we summarize test results of the first four configurations.

The second harmonic tubes are derived from the fundamental devices by making a few changes to the test bed and microwave circuit. The main test bed changes include replacing the non-linear waveguide tapers and reworking the microwave diagnostics. The primary circuit modification is to replace the TE_{011}, 9.87 GHz output cavity with one that resonates in the TE_{021} mode at 19.7 GHz. The drift tube is also modified as described below. A schematic of the third harmonic circuit is shown in Fig. 1. The circuit is realized by stacking a series of metal and ceramic washers inside a vacuum housing. The main input cavity section has a length of 1.73 cm and a radius of 2.81 cm. The measured resonant frequency and quality factor are 9.844 $\pm$ 0.01 GHz and 380 $\pm$ 40, respectively. A thin carbon-impregnated Aluminum-Silicate (CIAS) ring located against the downstream end wall is used to load the cavity. The output cavity is machined from OFHC copper on a CNC lathe. The measured cold cavity resonant frequency and Q are 19.712 $\pm$ 0.02 GHz and 346 $\pm$ 25, respectively. The main cavity section has a length of 0.605 cm and a radius of 1.73 cm. The radius is selected to avoid fundamental amplification in the TE_{01} mode. Adiabatic wall transitions are used to minimize mode conversion to the TE_{01} at the second harmonic. The length is chosen to minimize the microwave signal flowing upstream toward the electron gun. The overall length of the cavity, including the integral output taper, is 9.42 cm. Theory predicts the mode to be 99.4 % pure and the power flowing upstream to be more than 38 dB down from the output power. A small-signal code predicts that the output cavity is stable at the desired operating point.

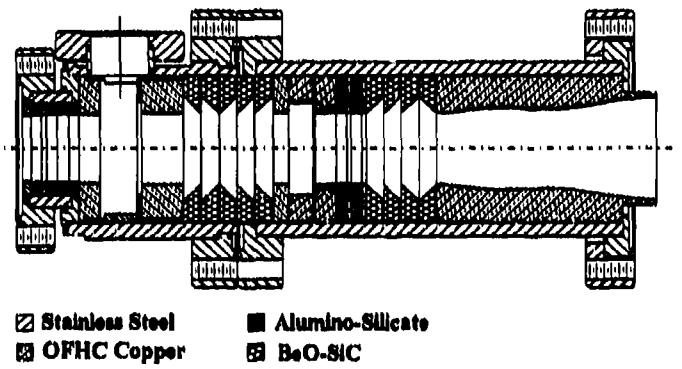

Fig. 1. The two-cavity second harmonic circuit (H3).

The preliminary drift tube is made mostly from CIAS rings. The main drift tube (between cavities) consists of nine tapered non-porous ceramic rings (80% BeO - 20% SiC) surrounding a band-stop filter which is designed to prevent any 19.75 GHz, TE_{01} mode signal from propagating to the input cavity and electron gun. The maximum rejection is over 45 dB at 19.72 GHz and remains above 20 dB for more than 275 MHz. Attenuation in the TE_{11} mode (which is the most troublesome in fundamental mode tubes) is greater than 15 dB from 6.0 GHz to 11.5 GHz. The total drift tube length is 12.28 cm and the minimum radius is 1.5 cm.

The output cavity of the first tube was longer and closer to cutoff than the one shown in Fig. 1. It also had a larger Q (~650) and the adjacent output waveguide radius was considerably smaller. This tube was plagued by fundamental mode oscillations that prevented amplification. The second tube's output cavity was intermediate both in dimensions and Q to the first and third tubes. This circuit produced a peak power near 12 MW with an efficiency near 15%. The third tube produced powers above 21 MW near 19.76 GHz with an efficiency of about 21%. Performance was limited by low frequency oscillations that were postulated to be derived in part from the drift tube's resonant trap. The replacement of this trap with the standard BeO-SiC rings resulted in the only difference between the third and fourth tubes.

The maximum power point in tube H4 is found when the beam voltage and current are 451 kV and 240 A, respectively. The drive signal is optimal at a frequency of 9.881 GHz and a power level near 60 kW. The optimum magnetic field is about 5.25 kG at the input cavity center and about 3% higher at the output cavity center. The peak power point is characterized by a strong interaction in the input cavity which is quite sensitive to the magnetic field. The time dependence of the output power, unfolded from the detector diode, is shown for this point in Fig. 2. The corresponding voltage pulse is also indicated. The peak power of nearly 30 MW corresponds to an efficiency near 27% and a gain over 26 dB. The narrow pulse width is due primarily to the time variation in α that results from a compensation problem with the resistive divider.

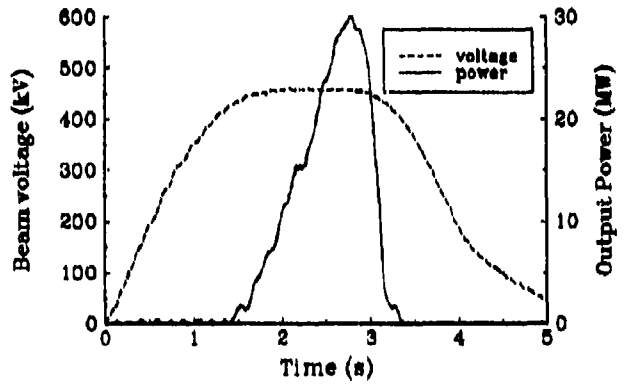

Fig. 2. The time evolution of the amplified signal in tube H4.

The far field mode pattern when the antenna is oriented to pick up the azimuthal electric field is indicated in Fig. 3. A least squares data fit indicates a signal which is 0.7 % TE_{01} and 99.3 % TE_{02}. This is close to the cold cavity estimate discussed earlier. As to be expected with circular electric modes, a sweep of the far field pattern when the antenna is rotated by 90° picks up virtually no power.

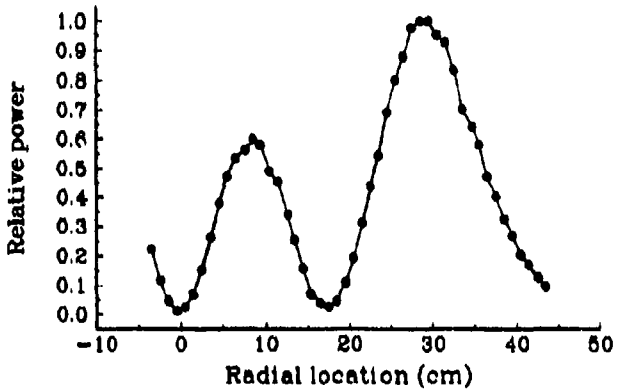

Fig. 3. The radial mode pattern of the anechoic chamber signal.

REFERENCES

1. W. Lawson, *et al.*, "Performance characteristics of a high-power X-band two-cavity gyroklystron," *IEEE Trans. Plasma Sci.* vol. 20, pp. 216-223 (1992).

2. S. G. Tantawi, *et al.*, "High-power X-band amplification from an overmoded three-cavity gyroklystron with a tunable penultimate cavity," *IEEE Trans. Plasma Sci.* vol. 20, pp. 205-215 (1992).

3. W. Lawson, *et al.*, "High-power operation of a K-band second harmonic gyroklystron," Submitted to *Phys. Rev. Lett.*, April 1993.

WIDEBAND GYRO-TWT AMPLIFIER EXPERIMENTS

J. J. Choi*, G. S. Park¶, S. Y. Park¶, C. M. Armstrong, A. K. Ganguly,
R. H. Kyser§, and M. L. Barsanti
Naval Research Laboratory, Code 6840, Washington, D.C. 20375

INTRODUCTION

Research on broadband, multi-kilowatt millimeter wave gyro-TWT amplifiers operating at low beam power (< 300 kW) is attractive for applications such as electronic warfare, radar, and communications. In order to achieve wideband rf amplification in gyro-devices, the waveguide is either tapered along the axial distance or loaded with disks or dielectric. Two Ka-band gyro-TWT amplifiers are considered; (1) a tapered rectangular waveguide and (2) a dielectric loaded rectangular waveguide. A frequency multiplied harmonic interaction in tapered waveguide is also investigated for W-band rf amplification.

TWO-STAGE TAPERED GYRO-TWT AMPLIFIER

Previous experiments on the single-stage Ka-band tapered gyro-TWT at NRL[1] have demonstrated high power (~5 kW), millimeter wave amplification with an instantaneous bandwidth > 30%. It was found that gain in the single stage amplifier was limited by reflection-type oscillations caused by the rf mismatch in the vacuum window. Separation of the input section from the output section will stabilize such oscillations.

A two-stage Ka-band gyro-TWT has been assembled and experiments are currently underway. Preliminary experimental results show that there is some beam interception in the multihole directional coupler due to insufficient magnetic compression of the small orbit beam (33 kV, 1 A) produced by the MIG. An improved input coupler is designed for better beam clearance and wider coupling bandwidth. A 3-D electromagnetic code (HFSS)[2] predicts a coupling value of -0.4 dB and a bandwidth of 60 % (22 GHz - 40 GHz).

Numerical results obtained from a slow-time scale non-linear code[3] predict a two-stage gain of ~ 30 dB, an electronic efficiency of 20 - 30 %, and an instantaneous bandwidth of 10 - 15 % for $\Delta v_z/v_z = 2$ %. In contrast to the single-stage gyro-TWT, the bandwidth is expected to be very sensitive to axial velocity spread.

RIDGED SLOW WAVE CYCLOTRON AMPLIFIER

A dielectric loaded rectangular waveguide can provide a constant group velocity over a wide frequency range. Figure 1 shows a cross-section view of the ridged circuit loaded with two dielectric slabs. A high quality axis-encircling beam[4] (60 kV, 5 A, $\alpha = 1$) couples with the slow wave. The dielectric height is less than that in the beam tunnel to insure that the fundamental beam line does not intersect any undesired higher order hybrid modes in the operating frequency range. The ridged circuit has some advantages over a regular rectangular shape. First, the dielectric slabs can be protected from beam interception. Secondly, the peak electric field is shifted from inside the dielectric to near the ridges in the beam tunnel. Thus the interaction coupling is expected to be improved.

Large signal calculations of the two-stage ridged SWCA predict a saturated efficiency of ~ 17 %, a gain of ~ 28 dB, and an instantaneous bandwidth of ~ 20 % (29 - 36 GHz) for input power = 150 W, B = 7 kG, and $\Delta v_z/v_z = 2$ %. The results from the slow time-scale non-linear code agree with MAGIC[5] simulations for a cold beam.

A broadband rf window has been designed by the use of the HFSS code. It consists of three sections of 1/4 wavelength BeO. As shown in Figure 2, the return loss is better than - 15 dB in the frequency range of 23.5 - 37.2 GHz (bandwidth = 46 %).

FREQUENCY MULTIPLIED HARMONIC GYRO-TWT AMPLIFIER

The operation of a "frequency multiplier" broadband harmonic gyro-TWT amplifier configuration is also under investigation. Figure 3 depicts the schematic of the amplifier, and the axial profiles of the non-linear tapered magnetic field (9 - 13 kG) and the circuit cutoff frequency. A Ka-band frequency drive signal is injected in the tapered fundamental input section to modulate the axis-encircling beam (50 kV, 2 A), as in the two-stage tapered gyro-TWT. However, in the tapered output section, the waveguide width is designed so that the waveguide mode is in phase synchronism with the third harmonic beam cyclotron mode. As a result, amplified radiation in the tapered output section is extracted at frequencies increased by the harmonic number. The operating waveguide mode is the lowest order mode, TE_{10}, in both the input and output sections of the amplifier.

---

*SAIC, McLean, VA 22102
¶Omega-P, Inc., New Haven, CT 06520
§B-K Systems, Inc., Rockville, MD 20850

A self-consistent slow-time scale non-linear code has been used to simulate the amplifier performance. The calculated efficiency and output power are shown in Figure 4 as a function of frequency for various axial velocity spreads of the electron beam. The efficiency drops slowly as the beam velocity spread increases but the instantaneous bandwidth shrinks more rapidly. Simulations also show that the amplifier operation is insensitive to the guiding center spread. At $\Delta v_z/v_z = 2$ %, the saturated efficiency and gain are ~ 12 % and ~ 30 dB. The bandwidth is predicted to be ~ 10 % with output frequency in the range of 90 - 100 GHz. A drive signal of ~ 10 W in the 30 - 33 GHz frequency range is sufficient to saturate the output power in the frequency range of 90 - 100 GHz.

CONCLUSION

Experiments on the Ka-band two-stage tapered gyro-TWT amplifier are underway with the improved input directional coupler. The ridged SWCA has been designed to conduct Ka-band experiments operating at a low magnetic field. The frequency multiplied harmonic gyro-TWT has been investigated to produce W-band radiation with ~ 10 % instantaneous bandwidth. Both the SWCA and the harmonic gyro-TWT require an axis-encircling beam with low velocity spread.

ACKNOWLEDGMENTS

This work is supported by the Office of Naval Research.

REFERENCES

[1]G.S. Park, et. al., IEDM Technical Digest, p. 779-781, 1991
[2]HP High Frequency Structure Simulator, Version A.02.01, Hewlett Packard Co. and Ansoft Co.
[3]A. K. Ganguly, et. al., Int. J. Electronics, 53(6), p. 641-658, 1982
[4]G. P. Scheitrum, et. al., IEEE Int. Conf. on Plasma Science, 1991
[5]B. Goplen, et. al., MAGIC User's Manual (MRC), Newington, VA, 1989

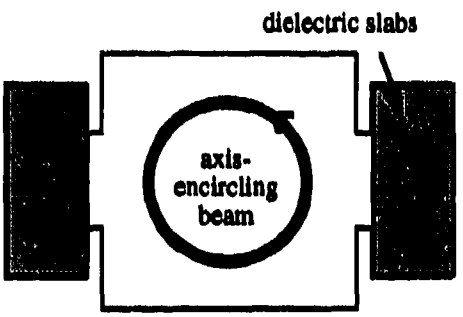

Figure 1. Cross section view of the ridged slow wave circuit.

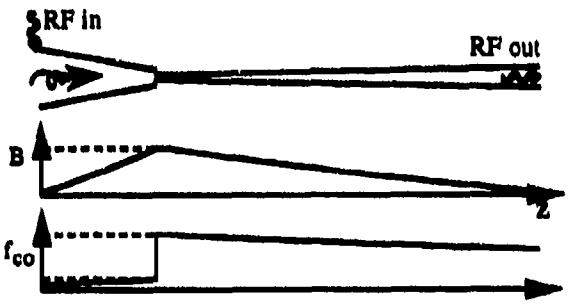

Figure 3. Schematic of the broadband frequency multiplied harmonic gyro-amplifier with magnetic field and cutoff frequency axial profiles.

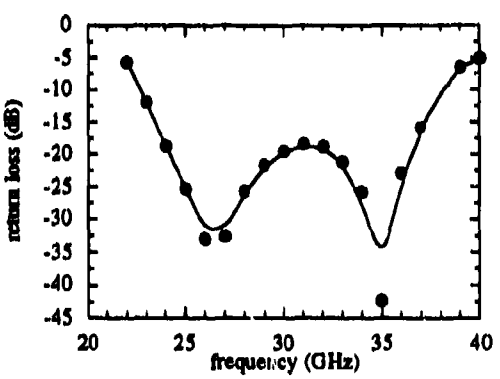

Figure 2. Return loss of the BeO window.

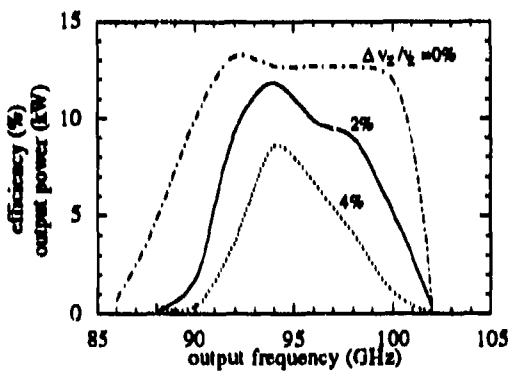

Figure 4. Efficiency and output power versus output frequency for various velocity spreads.

Gyro-TWT Amplifiers at UCLA

K. C. Leou, Q. S. Wang, C. K. Chong, A. J. Balkcum, S. N. Fochs, E. S. Garland,
J. Pretterebner[a], A. T. Lin[b], D. B. McDermott, F. Hartemann, and N. C. Luhmann, Jr.
Department of Electrical Engineering, University of California, Los Angeles, Ca 90024

Abstract

The status of three unique gyro-TWT amplifiers under development at UCLA will be presented. They include 1) a slotted third-harmonic gyro-TWT, 2) a wideband dielectric- loaded gyro-TWT, and 3) an extremely high power second-harmonic gyro-TWT.

(1) Slotted Third-Harmonic Gyro-TWT

Varian's 95 GHz, 70 kV, 5 A, $\alpha = 1.3$, three-section six-vane π-mode third-harmonic gyro-TWT [1], which is predicted by a nonlinear self-consistent simulation code [2] to yield a peak output power of 90 kW with 26% efficiency, a saturated gain of 61 dB and 3% constant-drive bandwidth, will be tested in a scaled experiment at 10.3 GHz using the axis-encircling electron beams produced by a gyroresonant rf accelerator [3]. The entire slotted circuit, including the 0 dB axial phase-velocity couplers, has been fabricated by electric discharge wire machining. The new rf accelerator has produced 3 A, 70 kV axis-encircling beams and will soon yield 5 A beams. A broadband two-period beat-wave TE_{31}/TE_{11} output mode converter shown in Fig. 1 was measured. As shown in Fig. 2, its center-frequency is shifted by strong coupling effects. Until an improved converter has been built, the amplifier will use an input coupler for its output.

(2) Dielectric-Loaded Wideband Gyro-TWT

The bandwidth of a gyro-TWT can be widened by using a dielectric-loaded waveguide to reduce the circuit's dispersion [4]. A 100 kV, 5 A wideband gyro-TWT [5], which is predicted from a nonlinear simulation code to generate an output power of 80 kW with 15% efficiency, a saturated gain of 30 dB, and a constant-drive bandwidth of 20%, has been designed for 10 GHz and has undergone its initial hot-tests. The single-anode MIG was built at NTHU to generate the $\alpha = 0.6$ beam with $\Delta v_z/v_z = 2\%$. The rectangular interaction waveguide has been loaded with thin MaCor slabs along both narrow walls [6]. The E-plane-bend 0 dB input and output couplers shown in Fig. 3 were measured and yielded excellent agreement with HFSS as seen in Fig. 4. The insertion loss is less than 0.1 dB over the entire 20% bandwidth.

With unoptimized alignment, the amplifier's preliminary results are 20 kW peak power, 25 dB saturated gain and 5% constant-drive bandwidth. Although the single-section amplifier is absolutely stable, oscillation near the cutoff frequency could be induced by increasing the magnetic field by 15%.

(3) High-Power Second-Harmonic Gyro-TWT

Harmonic gyro-TWT's not only require a substantially weaker magnetic field and offer nearly the same high efficiency as fundamental gyro-TWT's, but also have the potential to stably generate significantly higher levels of power [7] because the threshold beam current level for oscillation is raised significantly due to the relatively weaker harmonic interaction. A high power, single-stage second-harmonic linearly-polarized TE_{21} gyro-TWT, which is predicted by a self-consistent nonlinear simulation code to produce an output power of 400 kW with an efficiency of 20%, saturated gain of 33 dB and constant-drive bandwidth of 6%, has been designed for 16.1 GHz and is currently under construction. A single-anode 100 kV, 20 A MIG is being built at NTHU to generate the beam with $\alpha = 1$ and $\Delta v_z/v_z = 8\%$. The single-stage amplifier is predicted to be stable because the dominant TE_{11} and TE_{31} gyro-BWO modes have been suppressed as a result of axially slicing the cylindrical waveguide with two cuts separated in azimuth by 90°. The similar effect from a single slice on the TE_{11} mode is shown in Fig. 5. A slice transverse to the average rf electric field yields a loss of ≈ 3.7 dB $/\lambda$ (Fig. 5(a)), whereas a cut parallel to this field produces negligible effect (Fig. 5(b)).

Each of these three gyro-TWT amplifiers use a wideband 6 - 18 GHz, 1 kW pulsed Varian helix TWT amplifier as their input signal source. All three use couplers designed with HP's HFSS electromagnetic code.

The authors are grateful to Prof. K. R. Chu and Prof. C. S. Kou of the National Tsing Hua University for their substantial assistance. This work was supported by ARO under Contract DAAH04-93-G-0084, AFOSR under Grants 91-0382 and F49620-92-J-0175, Rome Laboratory (ATRI) under Contract F30602-91-C-0020 and Varian under Subcontract 109BAR05943.

(a) IMT GmbH, Heinrich-Baumann-Strasse 49, D-7000 Stuttgart 1, Germany

(b) Department of Physics, University of California, Los Angeles, CA 90024

[1] C. K. Chong, et al., *IEEE Plasma Sci.* 20, 176 (1992).
[2] A. K. Ganguly, et al., *Int. J. Elec.* 65, 597 (1988).
[3] D. B. McDermott, et al., *J. Ap. Ph.* 58, 4501 (1985).
[4] H. Guo, et al., *Phys. Rev. Lett.* 49, 730 (1982).
[5] K. C. Leou, et al., *IEEE Plasma Sci.* 20, 188 (1992).
[6] A. K. Ganguly, et al., *Int. J. Elec.* 53, 641 (1983).
[7] Q. S. Wang, et al., *IEEE Plasma Sci.* 20, 163 (1992).

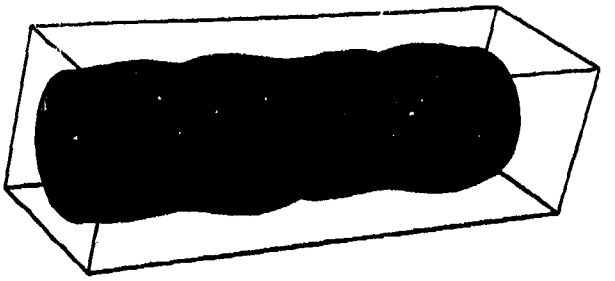

Figure 1: Schematic of two-period TE_{31}/TE_{11} beat-wave mode converter.

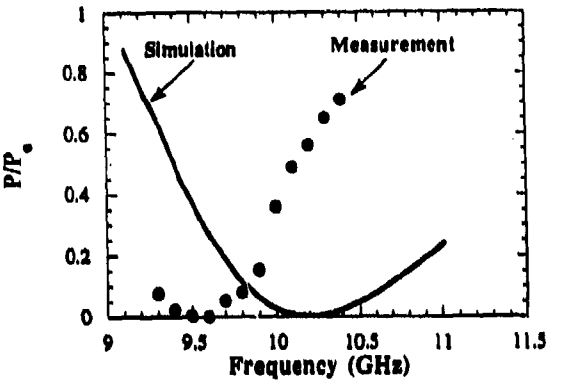

Figure 2: Dependence of conversion efficiency on frequency in TE_{31}/TE_{11} converter from measurement and linear theory.

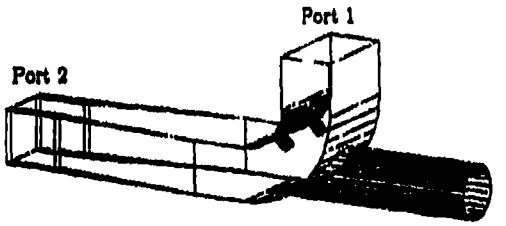

Figure 3: Schematic of broadband E-plane-bend input/output coupler with tuning screws and cutoff beam tunnel.

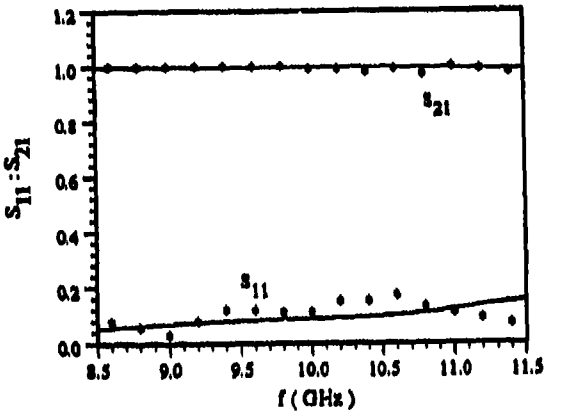

Figure 4: Dependence of S_{11} and S_{12} on frequency for E-plane-bend coupler from measurement (symbols) and HFSS code (solid lines).

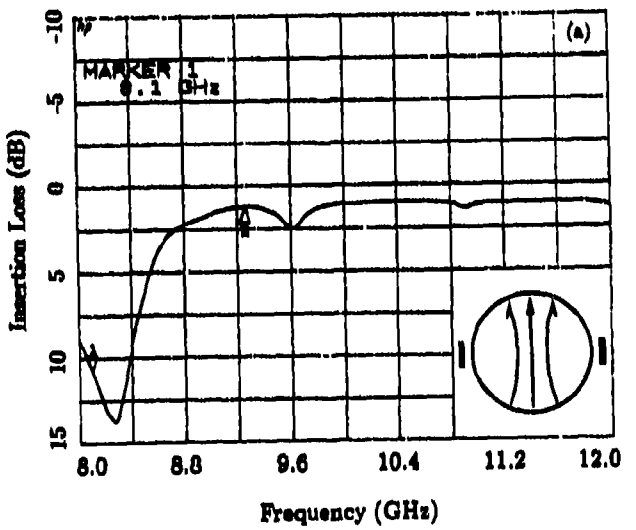

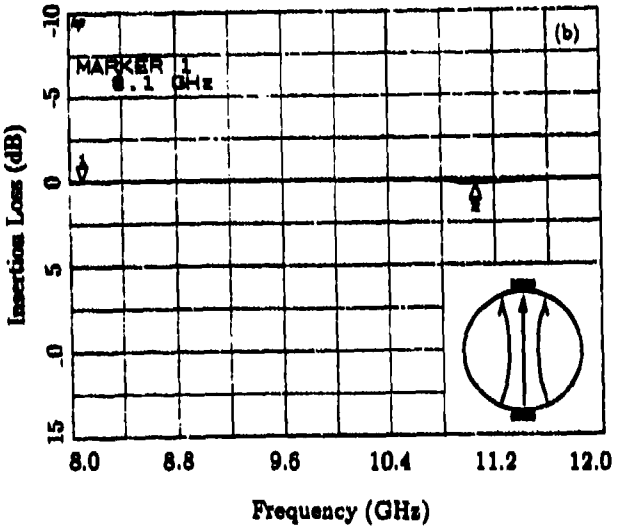

Figure 5: Dependence of insertion loss on frequency for TE_{11} mode in tube with slice (a) orthogonal and (b) parallel to average rf electric field.

Development of medium power, submillimeter wave gyrotrons

T.Idehara, T.Tatsukawa, I.Ogawa, Y.Shimizu, S.Makino and K.Ichikawa

Department of Applied Physics, Faculty of Engineering,
Fukui University, Fukui 910, Japan

Developmental study of high frequency, step tunable gyrotrons using 12 T superconducting magnet is described. Single mode operations at the second harmonic resonance have generated submillimeter wave outputs up to 638 GHz. The typical power is several hundred watts.

1 Introduction

Medium power, submillimeter wave gyrotrons have many advantages which other conventional sources do not possess, for example, frequency tunability and high power output. In recent years, single mode operation in gyrotrons using a high magnetic field at the second harmonic of the electron cyclotron frequency has produced submillimeter wave output approaching 800 GHz.[1)-3)] In our recent paper[4)], we showed that single mode operation at the third harmonic can occur in our submillimeter wave gyrotron. In the near future, we expect that such a gyrotron will cover the whole submillimeter wave range by using high harmonics and higher magnetic fields. In this paper, the achievement of 638 GHz (corresponding to a wavelength of 472 μm) by operating at the second harmonic, at the high magnetic field of 12T, is described.

2 Experimental setup

Fig.1 shows a schematic drawing of the whole gyrotron device. The magnet produces a high magnetic field up to 12T. The superconducting magnet consists of two coils, an inner coil made of Nb_3Sn wire, and an outer coil of NbTi wire. The gyrotron is demountable and is essentially a vacuum chamber set in the room temperature bore of the cryostat. The diameter of the bore is 70 mm and the inner diameter of the vacuum chamber is 38 mm. Inside the chamber there are three parts; a guiding tube for the electron beam, a cylindrical resonant cavity and a collector for the electron beam which also acts as the output waveguide. The diameter and the length of the cavity are 3.8 mm and 10 mm, respectively.

At the bottom of the vacuum chamber there is a magnetron injection gun, and at the top there is a ceramic vacuum window. A vacuum valve installed between the gun and the guiding tube allows the resonant cavity and other pieces to be changed while keeping a high vacuum in the electron gun. Conventional magnet coils or gun coils around the electron gun allow the field intensity in the region of the gun to be varied independently of that in the region of the cavity.

3 Results

The frequency can be varied from 160 GHz to 630 GHz, by changing the intensity of the magnetic field. The behaviour of the gyrotron tube has been tested for each cavity mode by setting the field intensity at the optimum value. Wavelengths are measured by transmitting the output power through a waveguide system with three corner bends to a Fabry-Perot interferometer. Output powers are measured by setting a water load on the top of the window and observing the rate at which the water temperature rises. Our gyrotron is pulsed so the duty factor, whose typical value is $5 \cdot 10^{-3}$, must be taken into account to calculate the power in each pulse.

Fig.2 shows a number of typical frequency measurements using the Fabry-Perot interferometer. When the field intensity is changed many instances of single mode operation are obserbed. The figure corresponds to operation at the second

harmonic. The measured frequencies are indicated on the figure.

In only one case, when the field intensity is just below 12T, is there operation at both the fundamental and the second harmonic. The TE_{721} cavity mode (fundamental) and the TE_{042} cavity mode (second harmonic) are excited at the same time. The frequency corresponding to this second harmonic is 636 GHz, which is the maximum frequency attained by our gyrotron and, we believe, may be a record for a gyrotron. For other single mode operations, measured frequencies are noted near the corresponding interferometer patterns.

In Fig.3, All of the frequencies observed until now are plotted as function of a magnetic field intensity. Operations at the third harmonic have been observed together with those at the fundamental and the second harmonic.

4 Conclusion

In summary, we have a step tunable, millimeter to submillimeter wave gyrotron covering a wide frequency range, whose output power is typically several hundred watts. In almost all cases the operation is in a single mode. It is an excellent source with many advantages over conventional sources which are all lower power, fixed frequency devices.

Acknowledgments

The authors wish to thank Dr. G.F.Brand of University of Sydney for valuable discussions. The work was partially supported by a Grant in Ais from the Ministry of Education, Science and Culture of Japan.

References

1) S.E.Spira, K.E.Kreischer and R.J.Temkin, IEEE Trans. on Plasma Sci. 18 (1990) 334.
2) K.D.Hong, G.F.Brand, P.W.Fekete and T.Idehara, Int. J. Infrared and Millimeter Waves 13 (1992) 215.
3) T.Idehara, T.Tatsukawa, I.Ogawa, H.Tanabe, T.Mori, S.Wada, G.F.Brand and M.H.Brennan, Phys. Fluids B4 (1992) 267.
4) T.Idehara, T.Tatsukawa, I.Ogawa, S.Wada, K.Yoshizue, F.Inoue and G.F.Brand, Phys. Fluids B4 (1992) 769.

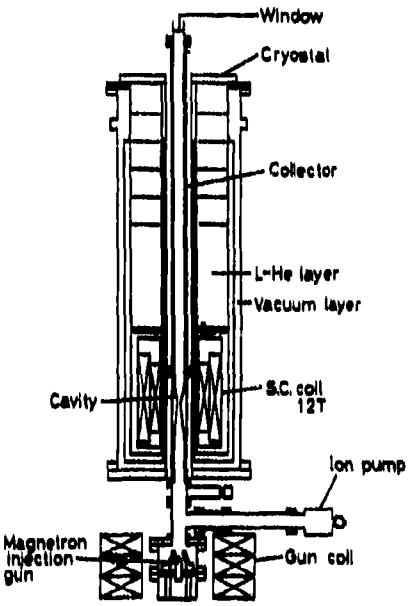

Fig.1 Set up of submillimeter wave gyrotron

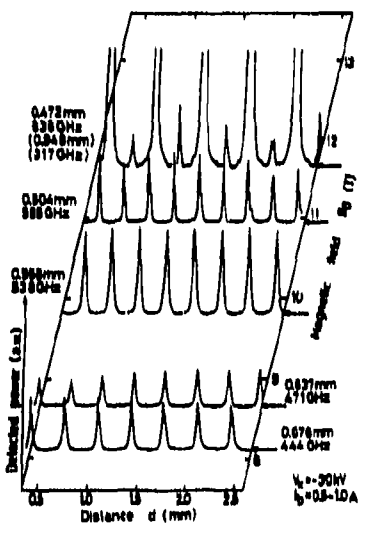

Fig.2 Output of a Fabry-Perot Interferometer

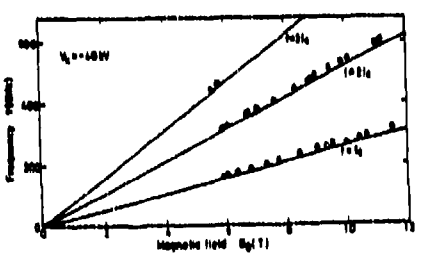

Fig.3 Measured frequencies vs field intensity B

HARMONIC CONVERTERS FOR MEGAWATT-LEVEL 140 GHz RADIATION*

A. K. Ganguly
Code 6841, Naval Research Laboratory, Washington, DC 20375

J. L. Hirshfield
Omega-P, Inc., 2008 Yale Station, New Haven, CT 06520; and
Physics Department, Yale University, New Haven, CT 06511

ABSTRACT - Linear and non-linear analysis of the power flow from spatiotemporally modulated gyrating electron beams into the fields of TE_{mn} modes of a cylindrical waveguide has been applied to megawatt-level sources at 140 GHz for plasma heating hand control. Results are given for a 5-th harmonic smooth-wall converter driven at 28 GHz, and for a 13-th harmonic ridge-wall converter driven at 10.8 GHz.

INTRODUCTION - Linear and non-linear theory and simulations [1] were developed for the coupling to modes in a cylindrical waveguide of a spatiotemporally modulated helical rotating electron beam prepared using cyclotron autoresonance acceleration [2]. Under "grazing" conditions, where the axial beam velocity equals the group velocity of the desired waveguide mode, efficient power transfer to the TE_{m1} mode can occur, with only negligible power flow into other TE modes, or into any TM mode. Here m, the mode's azimuthal eigenvalue, is also the ratio of the converter's output frequency to the beam's temporal rotation frequency. One can scale prior results obtained for a smooth-wall TE_{51} mode 94 GHz device to 140 GHz, to find the parameters given in Table I below.

output frequency	140 GHz
drive frequency	28 GHz
beam voltage	150 kV
beam current	6.7 A
velocity ratio α	2.0
waveguide radius	0.228 cm
waveguide length	27.0 cm
magnetic field	11.9 - 9.76 kG
output power	705 kW

Table I. Parameters for a conceptual 5-th harmonic 140 GHz converter.

HIGH HARMONIC CONVERSION - The 140 GHz device described above could be driven by a 28 GHz, 1 MW gyrotron pulsed oscillator [3], or (at lower power) by a 220 kW cw gyrotron oscillator [4]. It is possible that a megawatt-level 28 GHz cw driver could now be built. Nonetheless, the achievement of megawatt or multimegawatt cw gyrotron oscillators might be easier at longer wavelengths. Indeed, it has been reported that a 1 MW, 8 GHz long-pulse device has been built [5]. This has prompted examination of the harmonic conversion mechanism at higher harmonics, where an X-band driver could be used. Preliminary simulations for 13-th harmonic conversion using a 10.77 GHz, 1 MW driver have shown that 800 kW output at 140 GHz would be obtained from a 2 MW, 2 A beam in the $TE_{13,1}$ mode, but that competition from the $TE_{12,1}$ mode at 129.2 GHz would be severe. Evidently, additional means to supress competing modes must be developed to allow successful 13-th harmonic operation.

COMBATING MODE COMPETITION - Two strategies have been considered to combat mode competition for a 13-th harmonic converter. The first strategy is to operate with a beam whose velocity ratio α is such that, under grazing conditions, all lower TE_{m1}

modes are cutoff. This occurs [1] if $(1 - \beta_z^2)^{1/2} > (1 - m^{-1})(f_m/f_{m-1})$, where f_m and f_{m-1} are cutoff frequencies for the TE_{m1} design mode and for the TE_{m-1} mode. For m = 13, this reduces to $\beta_z < 0.1225$ which, for a 250 kV beam, gives $\alpha > 5.97$. Whether a beam with such a high α-value can be introduced stably into an output waveguide is an open question. This uncertainty has prompted a second strategy, based on an experimental finding [6] that radiation from an intense relativistic axis-encircling beam in a cylindrical overmoded waveguide emerged over a broad band in many modes; but with 12 shallow axial slots machined in the waveguide periphery, essentially all of the radiation was observed in a narrow band in the $TE_{12,1}$ mode. This result can be interpreted as due to selective coupling between the beam and the $TE_{12,1}$-like mode of the ridged waveguide, since competing modes would have smaller coupling impedences to the beam. A study of beam coupling to 13-ridged cylindrical waveguides has been initiated. Vacuum modes have been analyzed from theory used for 6- and 10- vane peniotrons [7]. It was found that the optimal ratio of outer-to-inner vane radius depends upon the beam parameters, so as to provide the largest possible latitude for optimizing conversion efficiency. The efficacy of this strategy for obtaining high conversion efficiency and combating mode competition is shown in Fig. 1a, where 13-th harmonic conversion efficiency is seen to reach 40% at 140 GHz (the parameters are given in the Figure). Power at the 12-th harmonic, which was the most serious competitor for the smooth-wall example, is too small to show on the scale of Fig. 1a. Fig. 1b shows the required guide field profile.

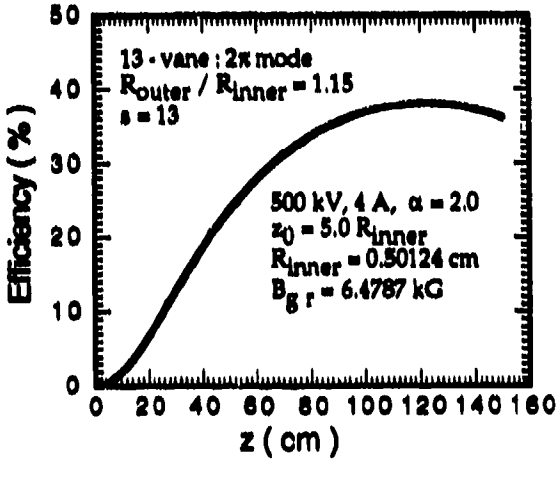

Fig. 1a. Efficiency *vs* axial distance. $B = B_{gr}$ for $z < z_o$; tapered for $z > z_o$.

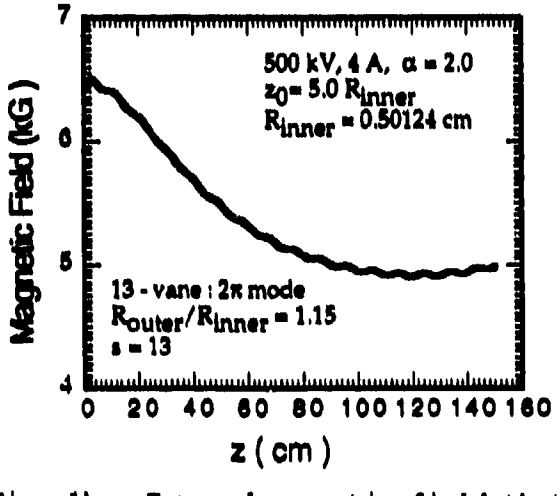

Fig. 1b. Tapered magnetic field that preserves phase matching in Fig. 1a.

*Work supported by Naval Research Laboratory, Office of Naval Research, and Department of Energy.

[1] A. K. Ganguly and J. L. Hirshfield, Phys. Rev. Lett. 70, 291 (1993); Phys. Rev. E, June 1993.
[2] C. Chen, Phys. Rev. A 46, 6654 (1992).
[3] A. A. Andronov *et al*, Infrared Physics 18, 385 (1978).
[4] R. S. Symons and H. R. Jory, "Cyclotron Resonances Devices", in *Advances in Electronics and Electron Devices*, v. 55, 1 (Academic, New York, 1981).
[5] G. Mourier (private communication).
[6] W. W. Destler *et al*, Appl. Phys. Lett. 38, 570 (1981).
[7] A. K. Ganguly *et al*, IEEE Trans.Electron Devices 38, 2229 (1991).

Impedance matching of microstrip line circuits by optically tunable stubs

Hitoshi Shimasaki and Makoto Tsutsumi

Kyoto Institute of Technology
Matsugasaki, Sakyo-ku, Kyoto 606, Japan

ABSTRACT

This paper treats a tunable stub of a microstrip line which can change the input and output impedances of the line by laser light. Transmission characteristics controlled by optical means through the stub are demonstrated both theoretically and experimentally.

2. INTRODUCTION

Recently there has been increasing interest in applications of lightwave technology to control, generation and measurement of microwaves[1]. One method for the control of microwaves makes use of optical injection of electron-hole pairs by illuminating a semiconductor waveguide with above-bandgap radiation.

We have already reported an optically-controlled microstrip line, in which one end of the strip is open terminated and illuminated with the laser light thereby changing the input impedance of the line[2]. We propose here an optically-tunable stub as an application of the open-ended microstrip line.

Stub lines are widely used for impedance matching of microstrip line circuits. However their tuning after the fabrication is generally difficult. Even if the precise design of the fabrication is taken into account, it is necessary to tune the matching element. Thus the open-ended microstrip line reported previously is developed to a tuning stub as shown in Fig.1, and the optical tunability of this line is discussed.

3. THEORY

Illumination to near the open end of the stub induces electron-hole pairs in the semiconductor substrate. The induced carriers are able to change only the resistance part of the terminal impedance. But by connecting the stub line to a proper position on the main line, the reactance of the line at the connecting point also can be changed due to the impedance transformation corresponding to the proper length of the stub. Therefore the impedances measured from the input and output ports are changed and can be optically matched to those of other elements of the next stage in the circuits.

We have calculated the terminal impedance of the illuminated open-end assuming the exponential distribution of the induced carriers [2]. According to the conventional transmission line analysis, the scattering parameters of the line are numerically estimated with respect to the impedance variation of the stub.

We suppose the following structural parameters in the calculation. The thickness of the substrate is 0.4mm. The strip widths of the main and the stub lines are 0.5, 0.7mm, respectively. The main line is 18.8mm long. The stub is positioning at a distance 6.6mm apart from the input port and its length is 5.6mm.

Figure 2 shows the transmission characteristics for the frequency range from 1 to 13GHz. It can be seen that the transmitted power and phase shift of waves is varied by the induced carriers.

The reflection characteristics and the input impedance are also calculated and it is confirmed that they can be controlled by the illumination.

4. EXPERIMENT

We made a prototype device using a silicon substrate. The dimensions are the same as those in the calculation. The end of the stub is illuminated with a laser light of 830 nm wavelength up to 32mW.

The measured transmission characteristics are shown in Fig.3. The experimental result agrees with the calculated one.

The change of the S parameters in the figures indicates the impedance variations of the input and output ports by optical means.

5. CONCLUSION

We have proposed a microstrip line with a tunable stub. The impedance of the stub can be changed with a laser light for optical injection of carriers in the silicon substrate.

The optically-tunable stub proposed here is simple and made easy. We have the more degree of freedom for tuning by multi-stubs and lasers.

The authors would like to thank Mr.Nakai for his assistance in the experiment.

6. REFERENCES

1.Special issue on applications of lightwave technology to microwave devices, circuits and systems, IEEE Trans. Microwave Theory & Tech., **MTT-38**, 5, May 1990.

2.H.Shimasaki and M.Tsutsumi, "Reflection characteristics of optically-controlled microwave through an open-ended microstrip line," IEICE Trans. on Electronics, **E76-C**, 2, pp.301-304, Feb. 1993.

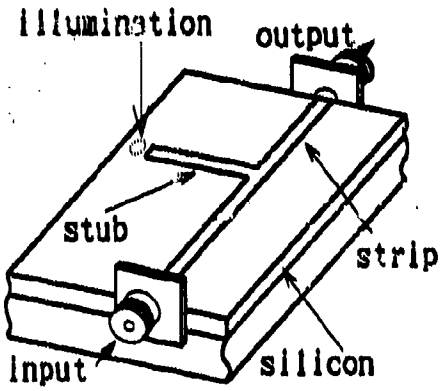

Fig.1 Microstrip line with an optically-tunable stub.

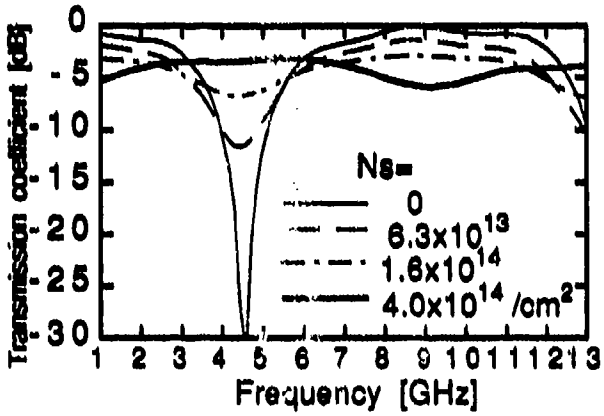

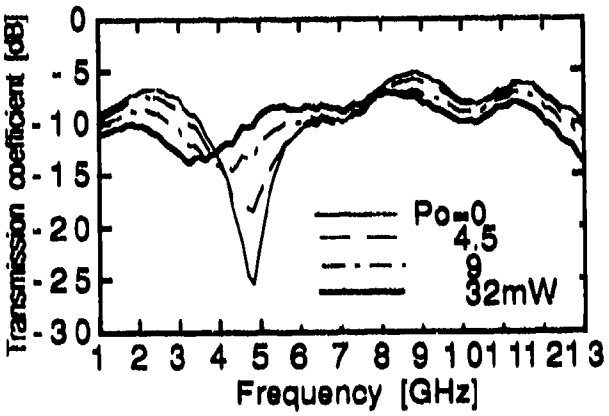

Fig.3 Measured transmission characteristics. P_o is the illuminating optical power.

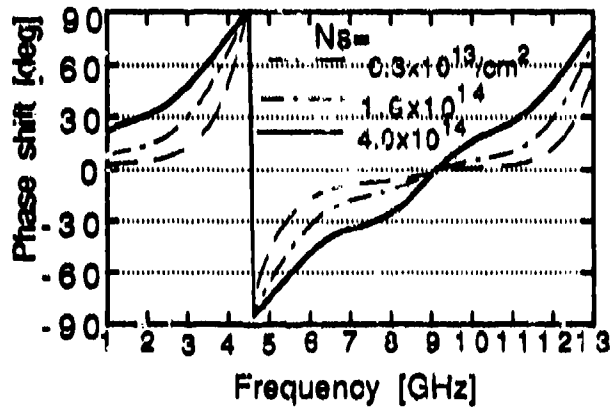

Fig.2 Theoretical transmission characteristics. Ns is the carrier density per unit area.

Optical control of millimeter waves in the silicon waveguides

Makoto Tsutsumi
Kyoto Institute of Technology
Matsugasaki, Kyoto, Japan

Yutaka Satomura
Osaka Institute of Technology
Omiya, Osaka, Japan

ABSTRACT

The optical control of millimeter waves in the silicon image and H-guides were investigated. The optical control of the dispersion characteristics of those guides were confirmed both theoretically and experimentally using the Xenon arc lamp. To increase the sensitivity of the optical control of the image line filter, the Mach-Zehnder interferometer type filter was demonstrated experimentally. To obtain the switching behaviour of the radiation beam from the H-guide leaky wave antenna, the Bragg type antenna cascaded with the optical switching element was also demonstrated experimentally.

2.INTRODUCTION

There is now considerable interest focussed on the field of optical control of microwave and millimeter devices, circuits and systems, such as phased array antennas, optical probings and high speed optical fiber links.[1] This paper discusses the optical control of the millimeter wave in the image line and H-guide using the high resistivity silicon substrate and by means of the optically induced plasma. The image line filter of the Mach-Zehnder interferometer type and the optical switching of the radiation beam from the H-guide leaky wave antenna are experimentally demonstrated.

3.THE IMAGE LINE

The dispersion relation of the image line was derived using the effective dielectric constant method. The phase and the attenuation characteristics of the line were estimated numerically for various values of the plasma densities.

The experiment was carried out at the Q-band. The waveguides used in the experiment were made of high resistivity silicon having resistivity of 5000 Ω-cm. When the optical energy of 2.2 W from the Xenon arc lamp was applied to the image line, attenuation in the transmitted signal of more than 20 dB was observed with the strong frequency dependence. To enhance the sensitivity of the optical control, Mach-Zehnder interferometer type waveguide using the image line was proposed with one of the waveguide arms periodically corrugated as shown in Fig.1. If the phase of the corrugated arm differs by 180^0 from that of the other arm without corrugation, the two signals interfere and a sharp notch feature will appear.

Experiments on the optical control of a interferometer with 14 cells periodically corrugated on one of the arms were carried out at the Q-band, and the result are shown in Fig.2. When optical power of about 90 mW was illuminated to the corrugated arm, the sharp notch feature was significantly reduced to about 15 dB around 41 GHz.

4.THE H-GUIDE

Optical control of the H-guide geometry consisted of a dielectric slab attached to the silicon slab at a side of it. The dispersion relation of the LSE (TE_{11}^z) mode was estimated numerically as a function of the plasma densities. The frequency dependence on the wave attenuation of TE_{11}^z mode by the plasma was increased for the lower frequency.

The H-guide was carefully designed using both the teflon and the the silicon slabs of 90mm length. The 20 dB change of amplitude of the millimeter waves in the H-guide was observed by illuminating

the Xenon arc lamp. The optical switching of radiation beam from the H-guide leaky wave antenna was examined, which was designed by the metal grating and the switching element in the cascade form. The switching element consisted of a silicon slab as shown in Fig.3.

If optical response of the switching element is chosen to be the Bragg frequency of the leaky wave antenna, the radiation frequency pattern of the leaky wave will be significantly controlled by the optical means. Fig.4 shows a typical response of the leaky wave with and without illumination by Xenon arc lamp of 200 mW optical power. The radiation beam was switched 15 dB by the light.

5.CONCLUSIONS

We have investigated the optical control of the millimeter waves in the image line and the H-guide. The optical control of the dispersion characteristics were confirmed theoretically and ex ,erimentally for both the waveguides.

To increase the sensitivity of the optical control of the image line filter, the Mach-Zehnder interferometer type filter was demonstrated experimentally. Optical switching of the radiation beam from the H-guide leaky wave antenna was also examined. These devices may be useful to find new signal processing devices for the millimeter wave frequency.

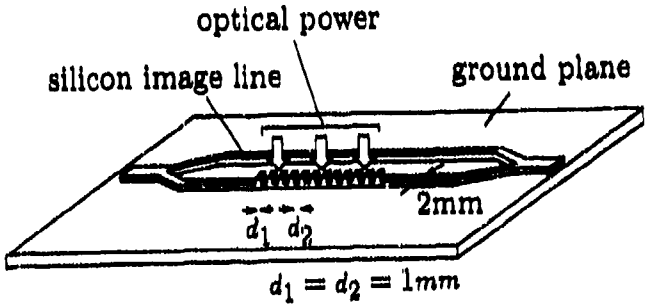

Fig.1 Geometry of the problem of the Mach-Zehnder interferometer.

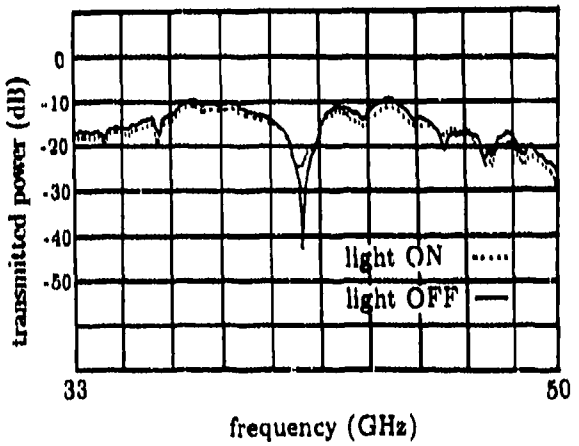

Fig.2 Filter response of the interferometer.

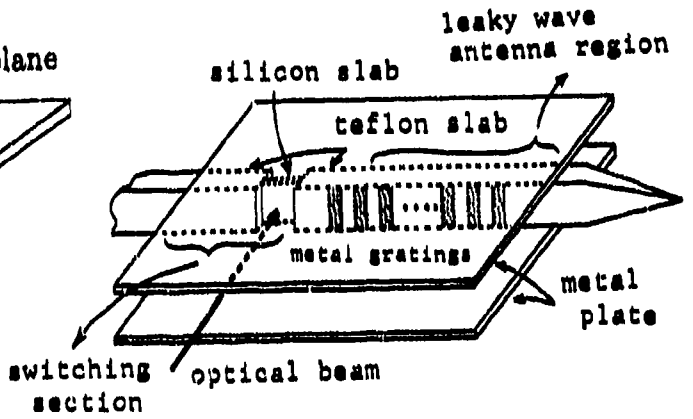

Fig.3 Geometry of the H-guide leaky wave antenna.

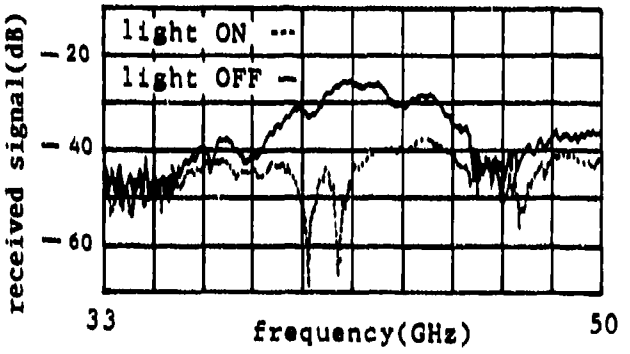

Fig.4 Optical response of the radiation beam from the H-guide antenna.

6.REFERENCE

1. Special issue on applications of lightwave technology to microwave devices, circuits and system, IEEE Trans. Microwave Theory Tech., vol. 38, May 1990.

Quasi-optical switching for mm-wave cavity dumping

G.M.Smith, J.C.G.Lesurf, Y.Cui, M.H.Dunn

St.Andrews University, Department of Physics and Astronomy, Fife KY169SS, Scotland

Abstract

A thin silicon wafer when illuminated by a Q-switched frequency doubled Nd-YAG laser is used as a very fast ultra-low loss, quasi-optical photo-conductive switch to cavity dump a millimetre-wave open resonator. Initial experiments indicate that it should be possible to provide short pulses at millimetre-wave frequencies with power gains of several hundred.

1. Introduction

It has been demonstrated that, with beam-splitter coupling, the finesse of a matched open cavity at 94GHz can exceed 1500 and be limited only by the resistive losses in the copper mirrors (0.08%)[1]. For a matched cavity this means that the circulating power within the cavity is about 500 times the incident power density. It would be of interest if this power level could be 'cavity dumped', to create short high power pulses. This requires a switch to be fast compared to the round trip time of the cavity, but that doesn't substantially degrade the losses and the circulating power within the cavity. This requires a switch to operate on nano-second or sub nano-second time scales, but with an insertion loss well below 0.1% (0.004dB).

Such a switch has been demonstrated using a very thin sheet of high resistivity silicon placed at 45 degrees in a high Q open resonator as illustrated in Figure 1. In normal operation, the silicon acts as a dielectric sheet and can have extremely low loss. However, the silicon can be switched by illuminating the sheet with a fast rising laser pulse whose photon energy is above the bandgap of silicon. This creates an almost instantaneous electron-hole plasma layer that can have metallic properties at high enough carrier densities [2] and reflect nearly all the microwave power out of one arm of the cavity.

High purity silicon (resistivity > 10k Ωcm) has extremely low loss at millimetre and sub-millimetre wave frequencies with power absorption <0.02 cm^{-1} at 100GHz [3] and no more than 0.05cm^{-1} between 100GHz and 2THz [3]. Thus the silicon's resistive loss can be very low compared to the resistive loss in the end mirrors. In addition, the loss due to reflection from the sheet can be cancelled by positioning a third mirror in a Michelson interferometer arrangement as illustrated in Figure 1. Thus the circulating power within the cavity can remain extremely high. Experimental measurement of the cavity Q and coupling parameter has shown that a 130μm silicon wafer (3 inch diameter) contributed no more than 0.05% extra loss in the cavity. In this particular experiment, diffraction losses around the wafer may also have contributed significantly to this figure.

Simple theoretical considerations and initial experiments have indicated that energy levels of a few mJ must be absorbed by the silicon in a few nano-seconds for efficient quasi-optical switching over reasonable areas. This requirement indicates the use of a Q-switched Nd:YAG system, at energy levels which are compatible with diode-pumped technology [4]. In addition, frequency doubling of Nd:YAG is usually preferred because the high conversion efficiencies and small absorption depth in silicon allow more photons to be absorbed in thin silicon sheets. (This is because the absorption depth for green light at 0.53μm is only 1.25μm compared to an absorption depth of 1.4mm for infra-red at 1.06μm at 94GHz [5]).

2. Experiments

Figure 2 illustrates the optics that have been used in initial experiments to demonstrate the feasibility of cavity dumping at 94GHz where the silicon switch was also used as the input beam-splitter. Despite the silicon having a net reflectivity of around 40%, it is still possible to completely match power into the 3-mirror system by adjusting the backshort mirror [1]. To demonstrate efficient switching the millimeter-wave spot size at the silicon was focused to<5mm and the long arm of the cavity was made approximately 1.0m giving a round-trip time of 6nano-seconds. This meant that the diameter of the mirror in the long arm of the cavity needed to be very large (1.0m). A low loss quasi-optical Faraday rotator was used as a circulator and provide isolation from the source which would otherwise be load-pulled by the external cavity. The source was a Gunn oscillator phase locked to an EIP counter to ensure that the input frequency of the Gunn oscillator remains at cavity resonance. A Q-switched, frequency doubled, flash-lamp pumped Nd:YAG laser capable of delivering 6mJ of green light in 10ns was used in the experiments. It was estimated that the laser provided at least 1mJ of green light within the first three nano-seconds and the illuminated area at the silicon was approximately 5cm^2. However, the maximum

finesse obtained with the cavity shown in Figure 2 was 100 which meant that the circulating power was only around 30 times the incident power. This is partly due to imperfections in the large diameter mirror and partly due to the large reflectivity of the silicon beam-splitter. Figure 3 shows a typical cavity dumped pulse when this cavity was switched, where the time-base is 50ns/division. Pulse duration was typically 8ns, with a power gain of the of the order of 10. Measurement of the output power was made using a single ended Schottky barrier mixer diode and a fast sampling oscilloscope (HP54111D).

These results clearly demonstrate the principle and feasibility of fast switching and cavity dumping. However, substantial performance improvements are expected at higher laser pulse energies (or shorter pulse duration's) for faster and more efficient switching. Doubling the input laser energy is expected to double the rf power output. Large improvements in the level of circulating power in the long arm of the cavity should also significantly increase the power output, and are expected for thinner silicon wafers and operation in the type of circuit illustrated in Figure 1. Cavity dumped systems with power gains of several hundred at W-band would appear to be very feasible and are expected to be demonstrated in the near future.

Acknowledgements - It is a pleasure to acknowledge useful discussions with Dr. A.Harvey, Dr. M.Padgett, Dr.P.Hirst, Prof. A.Maitland and Prof. J.W.Allen. We would also like to thank J.Terry and D.Withers for help with the laser system and M.Whyte and G.Radley for much of the mechanical construction.

4. REFERENCES

1) G.M. Smith, J.C.G.Lesurf, "A Highly Sensitive Millimetre Wave Quasi-optical FM Noise Measurement System", IEEE MTT Special Issue, December 1991
2) D.H.Auston, "Picosecond optoelectronic switching and gating in silicon", Applied Physics Letters, Vol.26, No.3, February, 1975
3) D. Grischowsky et al. "Far-Infrared Time Domain Spectroscopy with TeraHz Beams of Dielectrics and Semi-Conductors", JOSA-B, Oct. 1990
4) I.A. McIntyre, D.M.Giorgi, D.E.Hargis, O.S.F.Zucker, "Optical Requirements for Light Activated Switches", SPIE Proceedings, 'Optically Activated Switching', Boston, November, 1990
5) C.Lee, P.S.Mak, A.P.DeFonzo, "Optical Control of Millimeter-Wave Propagation in Dielectric Waveguides", IEEE Journal of Quantum Electronics, Vol. QE-16, No.3, March 1980

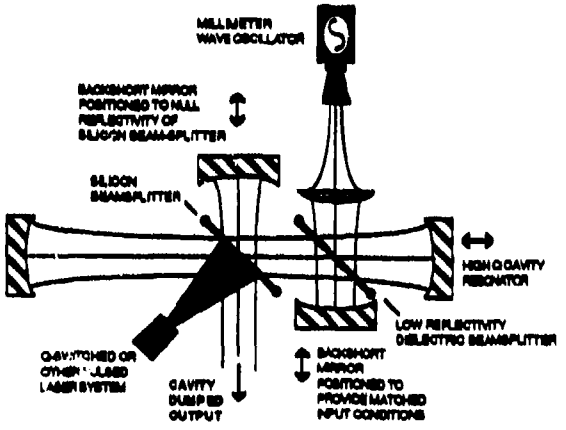

Fig.1 Diagram illustrating principle of quasi-optical cavity dumping. When the silicon beam-splitter is illuminated by a laser pulse it changes from a low loss dielectric to a highly reflective plasma and dumps power from one arm of the cavity.

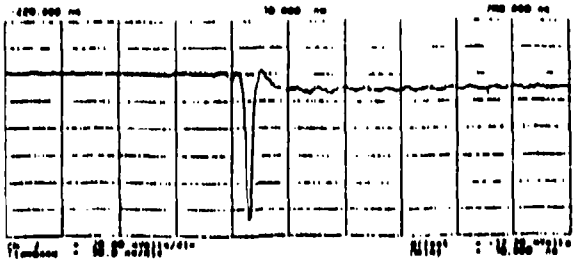

Fig. 3 Trace indicating a typical cavity dumped output

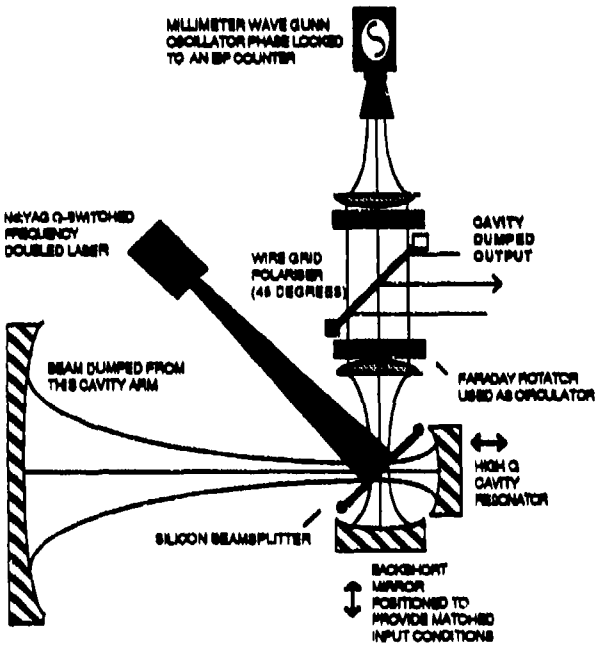

Fig 2. Diagram illustrating schematically the optics used to demonstrate quasi-optical cavity dumping

Phase Shift and Loss Mechanism of Optically Excited E-plane Electron-Hole Plasma

Ao Sheng Rong and Zhong Liang Sun
State Key Laboratory of Millimeter Waves
Department of Radio Engineering, Southeast University
Nanjing 210018, Jiangsu
People's Republic of China

Abstract

This paper describes the phase shift and loss mechanism of the optically excited E-plane electron-hole plasma. For GaAs as the inserted semiconductor, it is shown that an optically sensitive regime occurs, where the phase shift is highly influenced by the illumination and the peak of the optically induced loss exists. The regime is changed by the distribution profile of the excess carriers. It is observed that at the high injection light power level, the optically excited plasma behaves as the metallic strip does. The field distributions at the optically excited plasma section are also demonstrated, which support the field-displacement effects of the plasma.

Formulation

Fig.1 shows the configuration under investigation. The semiconductor is longitudinally inserted in a rectangular waveguide and at the section $0<z<w$, is laterally illuminated by laser radiation. The injected photons generate free carriers or electron-hole plasma over a thin layer directly under the surface. The free carriers are assumed to be uniform on the plane $(o<y<b, 0<z<w)$, but inhomogeneously distribute inside semiconductor along x direction due to the diffusion effect and the exponential absorption of the photon energy. For more subtle information to be required, the diffusion of free carriers along z direction will be involved. For simplicity, the effects of optical injection hole are not addressed in this paper although the hole is inevitable in practical applications. When the end discontinuity effect is taken into account, the problem of interest concentrates on calculating the scattering parameters of the optically excited E-plane plasma.

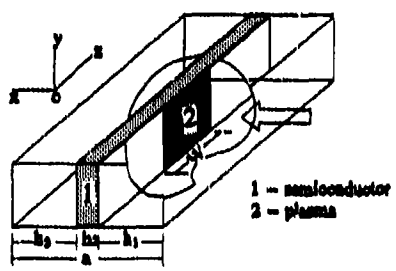

Fig.1

The model above suggests that the electric fields in Fig.1 has only y-component independent of y variable.

Suppose an incident field $E_y^{in}(x,z)$ of the dominant mode, the existence of the plasma excites the scattered field $E_y^s(x,z)$. It can be expressed in terms of the total electric field $E_y(x,z)$ as

$$E_y(x,z) = E_y^i(x,z) + E_y^s(x,z) \tag{1}$$

By definition, the scattering parameters of the plasma are determined by

$$S_{11} = \frac{E_y^s(h_1,-\lambda_g)}{E_y^i(h_1,0)}, \qquad S_{21} = \frac{E_y(h_1,L+\lambda_g)}{E_y^i(h_1,0)} \tag{2}$$

The difference between the phase angles for S_{21}^d and S_{21}^p without and with illumination gives the phase shift of the plasma $\Delta\phi$, i.e.,

$$\Delta\phi = \angle S_{21} + 2\pi + \beta L \tag{3}$$

The optically induced loss α can be derived from S_{11} and S_{21}:

$$\alpha = 1 - |S_{11}|^2 - |S_{21}|^2 \quad (4)$$

Eqn.(1) is the Fredholm's integral equation of 2nd kind, the kernel of which is a slowly convergent and is rapidly oscillating for large wave number. The direct implementation of eqn.(1) will be accompanied by the poor numerical efficiency. The great improvement on the numerical efficiency is achieved by using asymptotic extraction technique.

Numerical results and discussion

The formulation described above has been used to compute extensively the phase shift and the attenuation characteristics of the optically excited E-plane electron-hole plasma, where the inserted semiconductor is assumed to be GaAs. Its material and property parameters have been summarized in [1]. Fig.2 and 3 illustrate the curves for the phase shift and the optically induced loss, where the waveguide dimensions are axb=2.54x1.27mm^2, $h_1=h_3=1.17$mm.For GaAs, the thickness $h_2=0.2$mm and the permittivity without illumination $\epsilon_{rd}=13.1$. The plasma length is maintained at w=1mm. The millimeter wave signal is generated by a source f=94GHz. It is noted that an optically sensitive regime occurs where the phase shift is highly affected by the illumination and the peak of the optically induced loss exists. It also is observed that the regime is changed by the diffusion length of the excess carriers. The dependency of α on N_{p0} indicates that under the intense illumination, the large attenuation of millimeter wave signal passing the plasma is mainly attributed to the reflection from the input end of the plasma rather than the energy dissipation. Insight into the change of the field configuration at the optically excited plasma section reveals that the plasma has the field-displacement characteristics. At the high density of the excess carriers, the field is nearly excluded, or shortly circuited by the plasma. The millimeter wave signal passes the plasma as if it entered a cut-off waveguide.

References

[1] A.M.Vaucher,C.D.Striffler and C.H.Lee, "Theory of optically controlled millimeter wave phase shifters", IEEE Trans. on MTT, vol.MTT-31, pp.209-216,1983

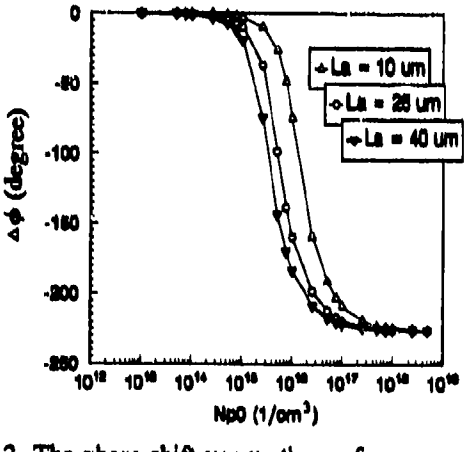

Fig.2 The phase shift versus the surface excess carrier density with the diffusion length as a parameter

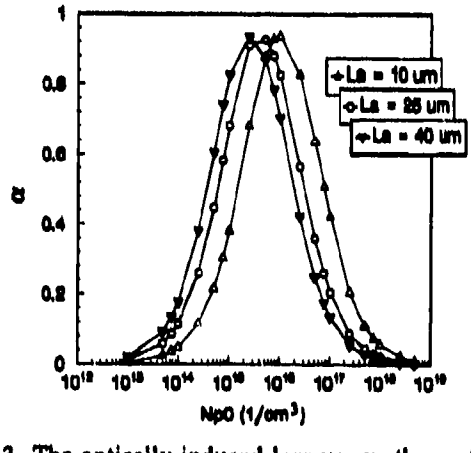

Fig.3 The optically induced loss versus the surface excess carrier density with the diffusion length as a parameter

MULTIMODE ANALYSIS OF SUBMILLIMETRE-WAVE OPTICAL SYSTEMS

S. Withington, Cavendish Laboratory, Cambridge, U.K.

J.A. Murphy, St. Patrick's College, Maynooth, Ireland.

We have developed a software package called PROFILE for designing millimetre- and submillimetre-wave optical systems. The software is based on the principles of multimode Gaussian optics. It is run in an interactive mode, where one simply moves forwards or backwards through an optical system adding in components as the occur. At any stage, it is possible to inspect the basic parameters of the beam, look at the power distribution across any cut, or store the beam away for future use. Simple Gaussians, corrugated horns, Potter horns, diagonal horns, conical horns, or previously saved images can be used to illuminate a system comprising free-space paths, thin lenses, dielectric slabs with curved surfaces, ellipsoidal mirrors, and truncating apertures. When placing an aperture, the software first works out the amount of loss that will be incurred if the aperture is put in place; the user is then given the option of using the component or not. If the aperture is placed, the new beam will diffract away from the aperture towards the next component. In the case of an ellipsoidal mirror, all of the parameters required to manufacture the mirror are calculated. During a session, a log file is kept, which at the end becomes a complete record of the system being studied.

PROFILE uses the techniques of multimode Gaussian optics; that is to say the fields across the effective aperture of the illuminating source are broken down into diffracting free-space modes. Once the mode coefficients are known, the beam can be followed through a system simply by propagating three parameters: the Gaussian radius, which characterises the scale size of the beam; the radius of curvature, which characterises the phase front of each mode; and the phase slippage, which characterises the form of the beam. In our software, we use Associated Laguerre modes throughout because they are based on a cylindrical co-ordinate system and have a number advantages when applied to general problems. One advantage is that the image can be rotated easily about the direction of propagation. Another advantage is that the scattering matrix describing the way in which power is scattered between modes at diffracting apertures can be calculated through recursion relationships alone, and there is no need to numerically evaluate overlap integrals. Systems containing multiple diffracting apertures are particularly interesting to study.

The above software has appears to be an excellent way of designing complicated millimetre and submillimetre-wave optical systems. If one were to do it in a classical way, it would be necessary to perform numerous diffraction integrals, and one would not get the flexibility or physical insight provided by the Gaussian-mode approach. Once a system has been designed, it is of course possible to get a more precise understanding of its performance by using rigorous classical techniques.

In addition to enhancing PROFILE, we are working on a number of supplementary problems. We have already developed a technique for calculating the scattering matrices of thin, shaped off-axis mirrors. The surfaces of the mirrors can have standard analytical forms, or they can be described numerically. Unfortunately, the technique uses Hermite modes, and so, at present, it is not compatible with the above software. A second problem is that we would like to know the mode content of sources other than simple horns. To this end, we are working on a phase-retrieval method for experimentally determining the complex mode coefficients of submillimetre-wave beams from intensity measurements alone.

The implications of partially-coherent signal beams on the performance of interferometric spectrometers in the 30–800 GHz range.

J W Bowen

Department of Physics, Queen Mary and Westfield College, University of London

1. INTRODUCTION

In the 30–800 GHz range interferometric spectrometers are commonly employed in the spectral characterisation of materials and components. However the multi-octave beams propagating through such spectrometers are not only diffractively spreading but have a degree of coherence which changes with frequency resulting in an instrument resolution function that changes with frequency. I will describe how it is now possible to treat partially-coherent signal beams using Gauss-Hermite beam-mode analysis and will present numerical models, based on this technique, of the instrument resolution function of a typical spectrometer.

2. PARTIALLY-COHERENT BEAMS AND DIFFRACTIVE PROPAGATION

If we are to avoid the use of impractically large optical components in the 30–800 GHz range signal beams will typically be less than one hundred wavelengths across and diffractive spreading will be a feature of propagation. To facilitate the design of optical systems it is convenient to decompose such (paraxial) beams into a superposition of orthonormal "beam-modes" the relative amplitudes of which are completely determined by knowledge of the field in any beam cross-section. The field of each beam-mode changes as it propagates in a well defined manner and the total beam field at any "down-beam" distance may be calculated by coherently summing the beam-mode fields over that cross-section. The Gauss-Hermite (GH) functions are particularly well suited for the decomposition of the field and the propagating GH beam-modes that they give rise to have become familiar in the analysis of *coherent* "quasi-optical" beams and their propagation through systems of lenses and mirrors.

Wolf[1] has shown that a *partially-coherent* beam can be decomposed into a superposition of mutually uncorrelated but spatially completely coherent orthonormal beam-modes. The forms of these modes and their relative statistical weights are dependent on the second-order statistical correlations of the field. The lower the degree of coherence the greater the number of modes in the superposition. For a paraxial partially-coherent beam of arbitrary form, we can decompose each of *these* beam-modes into a superposition of GH beam-modes each of which will propagate through an optical system as in the coherent case. The resultant intensity distribution in the beam at any down-beam cross-section can be found by summing the *complex amplitudes* of the GH beam-modes to find the power carried by each mutually uncorrelated coherent beam-mode and then summing these *power* contributions.

For a special case of partial-coherence, the two-dimensional Gaussian-Schell model (GS) source, for which the intensity distribution function and correlation function take the form of two-dimensional Gaussian functions over a given beam cross-section, the beam can be decomposed *directly* into a superposition of mutually uncorrelated GH beam-modes. If the intensity distribution function and correlation function widths are known the number of modes required to describe the beam well, their relative weights, their common beam-waist width parameter, the width parameters describing the intensity and correlation functions at all down-beam cross-sections and the far-field spread angle of the beam may all be determined.

A common situation is that of the beam from an incoherent source (eg. a mercury arc lamp) incident on the input optics of a quasi-optical system. If the acceptance angle of the optical system (defined by aperture stops) is smaller than the spread angle of the beam launched by the source it will determine the degree of coherence of the beam accepted by the optical system. Modelling the source as a GS source with the system input optics in its far-field and relating the acceptance angle to the far-field spread angle and the intensity distribution width to the source output aperture the modal composition of the accepted beam may be determined.

3. SPECTROMETER INSTRUMENT RESOLUTION FUNCTION

The basic principle of the two-beam interferometric spectrometer is to divide the beam launched by a source into two equal amplitude beams into one of which a variable phase delay is introduced by varying the path length. The beams are recombined and focussed onto a detector and the variation in the resultant power caused by the changing interference between the two beams as the path difference alters is detected and recorded. This record is known as the interferogram and is the squared modulus of the autocorrelation function of the time-dependent field of the input beam. Hence, Fourier transformation of the interferogram yields the power spectrum of the source.

In practice it is, of course, only ever possible to record the interferogram over a limited range of path difference and this results in convolving the power spectrum with a factor known as the instrument resolution function (IRF) which imposes a limit to the attainable resolution. If the interfering beams were perfectly collimated the IRF would be a sinc function (resulting from multiplying the interferogram by the truncating top hat function). The lack of perfect collimation resulting from diffractively spreading partially-coherent beams broadens this limiting IRF.

If the modal composition of the beam accepted by the spectrometer is determined by approximating the source as a GS source, the interferogram for a single frequency component may be constructed numerically by adding *coherently*, in the recombination plane, the fields as a function of path difference of each pair of constituent GH beam-modes of the same mode number (beam-modes of differing mode number do not interfere because they are mutually uncorrelated) and then adding *incoherently* the correctly weighted resultant powers. Because the beams are diffractively spreading the depth of modulation for a given beam-mode will reduce as the path difference is increased, apodizing the interferogram and reducing the resolving power. This effect is more pronounced the higher the mode number and therefore for beams with a higher proportion of high order beam-modes (ie. a lower degree of coherence) the resolving power will be reduced. The IRF can be obtained by Fourier transformation of a truncated version of the model interferogram.

The process used to calculate the signal frequency in Fourier transform spectrometry assumes that the collimated beams travelling through the interferometer are plane-waves. The apparent measured frequency will, however, be modified by a phase-slippage relative to a plane-wave which is both mode dependent and varies non-linearly with path difference. Hence the measured frequency will be shifted away from its true value and a monochromatic input will be spread into a range of frequencies further reducing the resolving power.

4. NUMERICAL RESULTS

The numerical results presented here are for a typical spectrometer designed for the 30–800 GHz range with a mercury arc lamp source. Fig. 1 shows the computed IRF at 60, 100, 300 and 800 GHz. At 60 GHz the accepted beam is almost completely coherent with 97% of the total power carried in the first 10 modes. As the frequency is increased the beam becomes less coherent with 98 modes needed to successfully model the beam at 800 GHz. The IRF for a perfectly collimated beam would have its first zeroes at ±1.5 GHz from the central peak. It is clear that the partially coherent beam has little effect on the resolution at 60 and 100 GHz. At 300 and 800 GHz, however, the IRF is broadened towards the lower frequencies with a degradation in resolution by factors of 2 and 4.5 respectively. At 800 GHz the apparent measured frequency is lower than the true value by 2.5 GHz. At lower frequencies this frequency error is smaller and in all cases is less than the spectral resolution at that frequency.

5. REFERENCES

1. E. Wolf, "New theory of partial coherence in the space-frequency domain. Part II: Steady-state fields and higher-order correlations", *J. Opt. Soc. Am.*, vol. 3, no. 1, pp. 76–85, 1986.

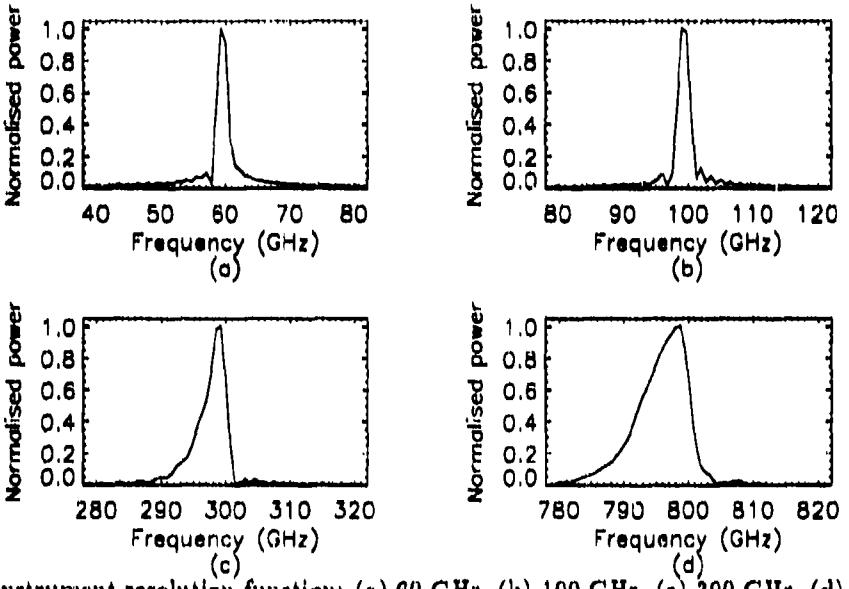

Fig. 1. Computed instrument resolution function: (a) 60 GHz, (b) 100 GHz, (c) 300 GHz, (d) 800 GHz.

NONLINEAR TRANSMISSION LINES USING MULTIPLE BARRIER VARACTOR DEVICES

W-M. Zhang, H. Shi, C.W. Domier, N.C. Luhmann, Jr.

Department of Electrical Engineering
University of California at Los Angeles
Los Angeles, California, U.S.A. 90024-1594

Abstract

To improve the power handling ability of Nonlinear Transmission Lines (NLTLs), multiple barrier varactor devices are utilized. NLTLs have been designed and fabricated on GaAs wafers with a variety of stacked multi-barrier structures.

Introduction

With the advent of modern MBE technology, stacked multi-barrier varactors have become extremely promising devices for high speed and high power applications. Two such devices, the Multi-Quantum-Barrier Varactor (MQBV) and the Schottky-Quantum-Barrier Varactor (SQBV), offer improved performance as compared to standard Schottky varactor diodes in harmonic generation applications. The MQBV is a stacked quantum barrier varactor, while the SQBV is comprised of a Schottky barrier on top of an MQBV structure [1,2]. The epitaxial stacking structure, together with the zero built-in voltage of the quantum barrier, make both devices have a higher cut-off frequency and an improved breakdown voltage compared to Schottky varactors. By using a back-to-back layout configuration, MQBV and SQBV varactors have symmetric C-V curves; hence, these two devices have strong nonlinearities for both positive and negative voltages.

Schottky diodes have been generally employed as nonlinear elements in nonlinear transmission line application for picosecond waveform generation [3,4]. In this work, we utilize multiple barrier varactor devices as nonlinear elements to increase the power handling capability of Nonlinear Transmission Lines (NLTLs).

Approach

Our NLTLs consist of high impedance coplanar waveguides loaded with stacked multi-barrier varactors. As a proof-of-principle, the NLTLs were designed to generate short pulses with <7ps rise time, which match the limit of our current testing system. However, simulations indicate that short pulses with <1ps rise time can be generated with MQBV and SQMV structures, using parameters consistant with our monolithic array fabrication experience. In current work, the impedance of each coplanar waveguide is chosen as 90Ω, with a large signal impedance of 50Ω. Each NLTL consists of 30 sections. The spacing between diodes is 300μm, and the diode area is $180\mu m^2$. To reduce the series resistance, the interdigital layout for the diodes was employed , as shown in Fig.1. The finger width is 4μm, and the gaps between the fingers is 3μm.

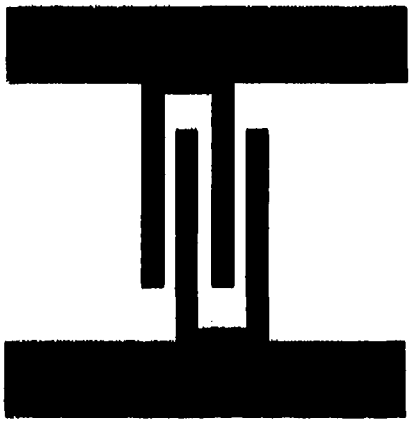

Fig. 1 Single Diode Layout

We employed a three-mask fabrication procedure. NLTLs were fabricated on GaAs wafers with MQBV and SQBV Structures. To further improve the NLTL performance, we have also investigated the use of stacked superlattice barrier structures. The cross sectional view of Stacked Superlattice Varactors is shown in Fig. 2.

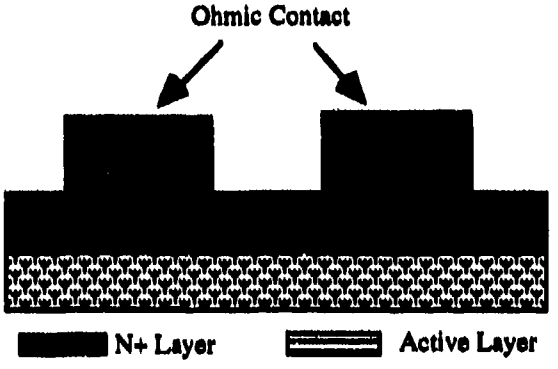

Fig. 2 Cross Sectional View of Stacked Superlattice Varactors

The measured ohmic contact resistivity of single devices is $2.85 \times 10^{-7} \Omega cm^2$. A GaAs/AlAs superlattice barrier was employed instead of a AlGaAs barrier to reduce the leakage current associated with GaAs based barrier varactors [5-7]. The doping profile of the stacked superlattice barrier varactor in shown in Figs. 3 and 4.

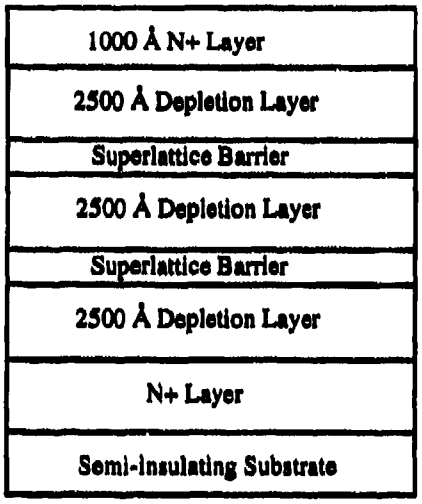

Fig. 3. Doping Profile of Stacked Superlattice Barrier Varactors

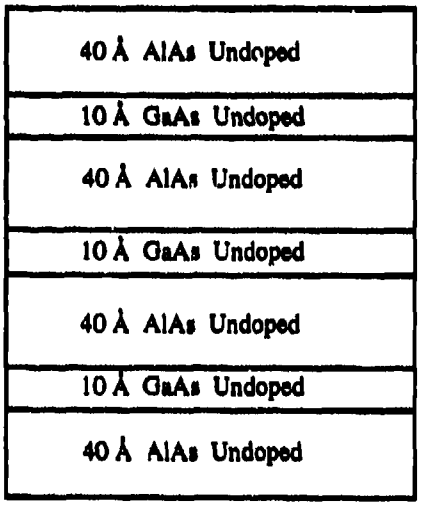

Fig. 4 Profile of the Superlattice Barrier

Each NLTL is tested using the testing setup shown in Fig. 5. The output of a 90ps FWHM impulse generator is introduced to the NLTL using 65 GHz bandwidth probes manufactured by Cascade Microtech. The output is likewise connected to a Tektronix 11802 Digital Sampling Oscilloscope equipped with a 50 GHz sampling head.

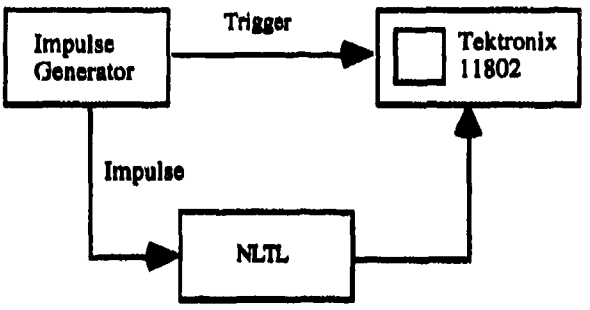

Fig. 5 Testing System for Short Pulse Generation

Acknowledgments

This project is supported by the Joint Services Electronics Program, and the Department of Energy under contract DE-FG03-86-ER53225.

References

[1] H-X. Liu, L. B. Sjogren, N. C. Luhmann, Jr., D. B. Rutledge, *International Journal of Infrared and Millimeter Wves*, Vol. 13, 251, (1992).

[2] H-X. Liu, X-H. Qin, L. B. Sjogren, W. Wu, E. Cheung, C. W. Domier, and N. C. Luhmann, Jr., *Third International Symmpostium on Space Terahertz Technology*, p. 595-599, (1992)

[3] M. Rodwell, M. Kamegawa, Ruai Yu, M. Case, E. Carman, K. Giboney, *IEEE Trans. on Microwave theory and Techniques*, Vol. 39, 1194, (1991)

[4] M. Case, Eric Carman, Ruai Yu, and M. Rodwell, *IEEE Trans. on Electron Devices*, Vol. 39, 2668, (1992)

[5] C. Raman, J. P. Sun, W. L. Chen, G. Munns, J. East, G. Haddad, *Third International Symposium on Space Terahertz Technology*, 146 (1992)

[6] W-M. Zhang, H. Shi, C. W. Domier, N. C. Luhmann, Jr., *the 17th International Conference on Infrared and Millimeter Waves*, Dec. (1992)

[7] H. Shi, W-M. Zhang, C. W. Domier, N. C. Luhmann, Jr., submitted to *IEEE Transactions on Microwave Theory and Techniques*. (1993)

MM-Wave spatial interferometry as a passive alternative to radar.

J. C. G. Lesurf & M. R. Robertson

Physics & Astronomy Dept. University of St. Andrews, Fife KY16 9SS, Scotland

1. Abstract.

Information regarding the bearing and range of an emitting (or absorbing) object may be obtained using suitable quasi-optical circuits to perform spatial interferometry. These circuits can also be used to recover spectral information. The system considered here may be used to detect and locate either narrowband or broadband thermal targets which may be placed in a semi-transparent medium such as the atmosphere. Unlike conventional thermal imaging the technique may be employed to detect and range a target whose temperature is the same as that of its background and surroundings.

2. The Spatial Interferometer.

By the use of appropriate spatial interferometry techniques we may measure the phasefront shape radiated by an emitting object. This measurement then permits us to deduce the range and bearing of the object under observation. The mm/sub-mm wavelength range is particularly suitable for spatial phase interferometry of this kind. Longer wavelengths would tend to lead to a reduction in linear positional resolution for a given phase accuracy. Attempts to use visible & near-visible wavelengths would lead to relatively severe problems arising from atmospheric fluctuations and phase ambiguities due to signal path lengths varying by many wavelengths.

Various quasi-optical circuits[1] may be employed to perform mm/sub-mm spatial interferometry. Circuits of this general type have been chosen for this application due to the high levels of measurement performance they can provide in the mm/sub-mm range.[2,3,4] Here we will consider a three-port system whose functional circuit is shown in figure 1. The meanings of the symbols used in this diagram are as defined in reference 1. The three ports are assumed to be placed along the x-axis of the co-ordinate system and the assumed source or 'target' is at a nominal range, Z_t, as indicated in figure 2.

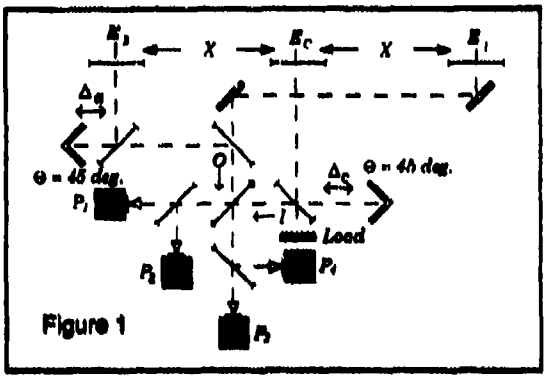

Figure 1

It should be noted that this arrangement is a simple example of the class of N-port spatial interferometers. In general, more than three ports are required to determine the three-dimensional location of an observed 'target' object. Here, however, we will assume that the instrument's field of view is narrowly confined to a specific line of sight. Hence we may set $\Delta_a = 0$ and concentrate upon the recovery of range information.

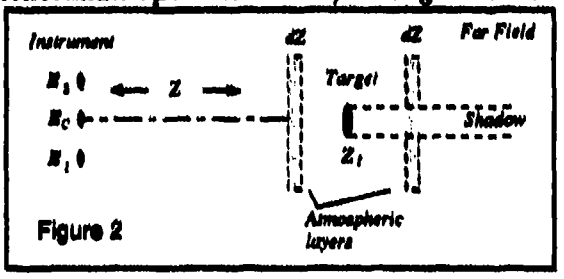

Figure 2

3. Observing extended thermal sources.

The $\frac{(P_2 - P_3)}{P_1}$ interferogram produced by keeping $\Delta_a = 0$ and altering Δ_c whilst observing the combination of an atmospheric distribution and a specific target illustrated in figure 2 may be written as

$$M_{12} = \int_0^\infty \left[\int_0^{Z_t} dI + I_t + \int_{Z_t}^\infty (1 - \eta\kappa)\, dI \right] df \quad (1)$$

where

$$dI = T_a \beta \Gamma\{Z\} \operatorname{Exp}\{-\beta Z\}\, dZ \quad (2)$$

$$I_t = T_t \eta\kappa \operatorname{Exp}\{-\beta Z_t\} \quad (3)$$

$$\Gamma\{Z\} = \alpha N \operatorname{Cos}\left\{ \frac{2\pi}{\lambda} \left(\sqrt{Z^2 + X^2} - Z - \Delta_c \right) \right\} \quad (4)$$

Here T_a & T_t are the nominal physical temperatures of the atmosphere and target respectively, β is the atmosphere's attenuation coefficient, α is the responsivity of the detection system, η is the effective fraction of the antenna pattern occupied by the target and κ is the target's optical thickness. The factor N represents the efficiency with which the optical system is able to convert input power into interferometric

modulation. This depends upon the system's antenna pattern and the port spacing, X. For an ideally coupled system using fundamental mode Gaussian beams it may be shown to have the value $N = \mathrm{Exp}\{-X^2/(2\omega_o^2)\}$, where ω_o is the waist radius of the beams.

The change in the observed interferogram produced by the target will be

$$D_{12} = \int_0^\infty \left[I_t - \eta\kappa \int_{Z_t}^\infty dl \right] df \qquad (5)$$

Conventional spectroscopic interferometers such as a Martin-Puplett ideally produce an interferogram symmetric about zero path difference which may be Cosine Fourier Transformed to obtain the source spectrum. Spatial interferometers of the kind considered here generally produce an asymmetric interferogram whose asymmetry depends upon the spatial distribution of the observed sources and any absorbing layers located between the instrument and more distant sources. As a consequence we may both Sine and Cosine Transform the interferogram to obtain a frequency dependent equivalent vector temperature which contains a combination of spectral and spatial information. The interferograms produced will depend upon the nature of the atmospheric distribution, the target, the system design, and the properties of the chosen detectors. The general properties of the system can be illustrated by considering a simple situation which produces the results shown in figures 3 & 4.

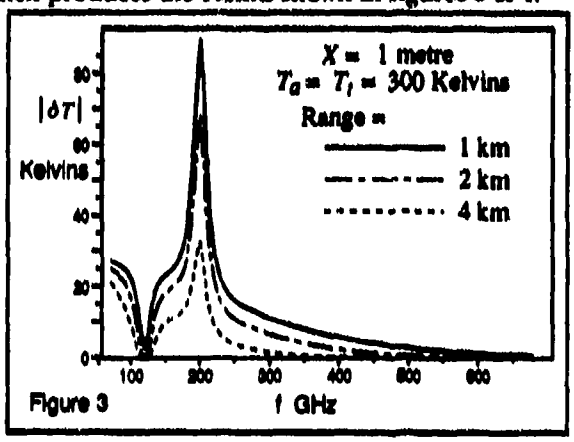

Figure 3

Here the effect of a target is considered by performing symmetric (Cosine) and anti-symmetric (Sine) transforms upon D_{12}. The graphs plotted show the modulus, $|\delta T|$ of the observed change and its nominal symmetry offset displacement $\Delta_\phi = \phi\lambda/2\pi$ where ϕ is the vector phase of δT.

For the sake of example a simple model of the atmosphere is assumed which combines an attenuation coefficient which rises with signal frequency with a single 10 dB/km absorption line at 120GHz. The target is assumed to have a general $\eta\kappa = 0{\cdot}1$ with a line of peak $\eta\kappa = 0{\cdot}5$ at 200GHz and a temperature equal to that of the surrounding atmosphere. Such a target would be difficult to detect using conventional thermal methods which require a temperature differential.

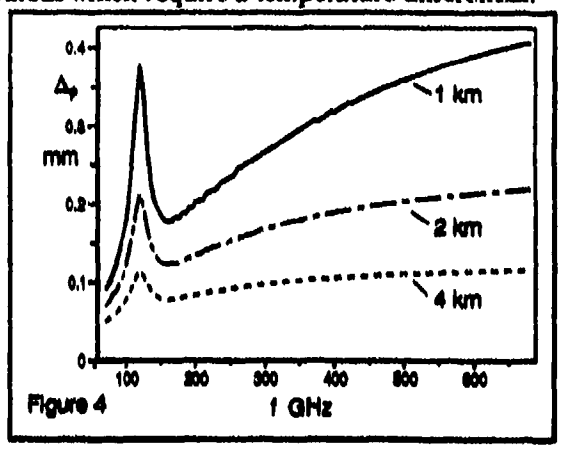

Figure 4

These assumptions allow us to illustrate the effects of atmospheric and target spectral features upon the recovered information. D_{12} is computed for three Z_t values to illustrate the effect of the target range From figure 3 it can be seen that both the atmospheric line and the target line clearly affect the modulus plots. Figure 4 shows that Δ_ϕ also depends upon the target range and the atmospheric attenuation, but is largely unaffected by the target's line feature. Since the effects of the uniform atmospheric distribution may be deduced from I_{12} and $|\delta T|$ this implies that — provided $\eta\kappa$ is large enough to produce a noticeable change in the observed interferogram — we may extract information about the target range from Δ_ϕ.

4. References

1 J. C. G. Lesurf, "MM-Wave optics, devices, and systems." Institute of Physics Press, Bristol 1990

2 A. R. Harvey & J. C. G. Lesurf, "A mm-wave single-mode quasi-optical complex reflectometer operating as a nulling bridge." Conf. Dig. T2.8 pp199-200 15th Int. Conf. I.R. & MM waves, Orlando, 10-14th Dec. 1990, SPIE Vol. 1514

3 G. M. Smith & J. C. G. Lesurf, "A highly sensitive mm-wave quasi-optical FM noise measurement system." I.E.E.E. MTT-39(12) 2229-36 (1991)

4 J. Brune, "A flexible quasi-optical system for polarimetric sub-mm reflectometry." I.E.E.E. MTT-40(12) 2321-4 (1992)

A special 3-mirror quasi-optical power combining system *

Xie weikai Liu shenggang
University of Electronic sience and Technolgh of China
Chengdu, Sichuan 610054, P. R. China

Abstract

A special quasi-optical power combining system of millimeter wave has been proposed and developed in this paper. It can be classified into two categorise, power combiner of a Multiple oscillators and power combiner of a multiple devices oscillation. The combining condition, the input and output coupling factor and combining coefficient are treated, based field theary of guided-wave and an eigenfunction appproach for active microwave circuit respectivilly. The validity of the descriptions given for this combining has already been experimetally verified.

1. Intruduction

By the principle of operation, this power combining system can be classified in two structures,

1) The combiner of a Multiple oscillators, The output powers from a number of oscillators that are summed in the quasi-optical cavity to produce a higher output power.

2) The combiner of a Multiple devices oscillation, a number of devices that contributed to the output power in the quasi-optical cavity.

2. Power combiner of a Multiple oscillators

The power coming from N-way different sources are coupled throngh the N-holes in the cylindrical mirror M_3 into the cavity respectively. And the combined power in the cavity is output through the horn in the mirror M_2 to the load.

3. Combiner of a Multiple devices oscillation

A multiple solid-state device (Gunn and Impatt), were mounted axisimmetrically at the center of the cylintrical mirror M_3, are coupled to the electric field inside the cavity by means of coaxial probers. The output window on the mirror M_2 center was readjusted to obtain the sum of the power from all devices. DC bias is applied using thin wires connected to the probes inside the cavity.

4. Experiments

1) Experiments of combiner of a Multiple oscillators. The attenuations in each power source branch are spearately adjusted to get the same power in each waveguide branch. When all branches inject simultaueously into the cavity, phase shifters are adjusted in each branch until the maximum combined power output is obtained.

2) Experiment of combiner of a Multiple devices oscillation. Gunn diodes (WT56) was mounted at one end of a coaxial transformer with a proper length, and the other end of the transformer was extended into the cavity as a probe. The length of each probe are adjusted until the maximum combined power output is obtained.

5. Conclusion

1) A special 3-mirror quasi-optical power combining system proposed in this paper is a new class of resonance cavity type power combiners. Owing to good mode separation abilily, axisymmetrical field prodile and high Q-Value, the proposed power combiners have attractive advantages in shor millimeter and submillimeter waves.

2) The 3-mirror quasi-optical power combiner apilied the combining approach of a multiple oscillators is important for the purpose of combining oscillators, such as magnetrons, klystrons and gyrotrons. It seems that this power combiner can be used for high-power system such as electron plasma heating and free electron laser.

3) The 3-mirror quasi-optical power combiner apilied the combining approach of a Multiple devices oscillation is avialable especially for the purpose of combining solid-state sources such as Gunn and Impatt diodes. This power combiner can offer an attranctive approach to overcame limitations of conventional waveguide power combiners in power output efficiency and number of sources that may be combined in the millimter-wave region.

References

[1] Wandinger L, Nalibandian V. millimeter wave power combiner using Quasi-optical Techniques. IEEE Trans on MTT, 31(2). 189-193. 1983.

[2] Mink J. W. Quasi-optical power combining of solid-state Millimeter-wave sources. IEEE Trans on MTT, 34 (2). 273-279. 1986.

[3] Liu Shenggang, Lin Chongwen, Xie Wenkai, Wang Changbiao. A special 3-mirror axisymmetric quasi-optical resonance system, scientia sinica(SeriesA). 24(9). 979-993. 1986.

---

* The project sapported by Natual Science Foundation of China

Optimization Calculation of 3-mirror axisymmetric quasi-optical power combining*

Xie Wenkai, Cheng Zhixun, Liu Senggang
University of Electronic Science and Technology of China
Chengdu, Sichuan 610054, P.R. China

Abstract

Very efficient power combining of solid-state Millimeter wave sources may be obtained through 3-mirror quasi-optical resonators and source arrays. The location and configuration of the source array are determined by CAD(Combuter-aided design) technique. The results above enables one to obtain efficient transfor of power to the lowest order "Gaussion wave beam" within 3-mirror quasi-optical resonator.

1. Introduction

Acoording to character of field profil of this axisymmetric quasi-optical cavity, a new approach of power combining of a Multiple devices oscillation has proposed in the paper. The location and canfiguration of source array are determined by CAD(Combuter-aided design) technique.

2. Power Combining Configuration

Multiple source array are plased with uniform spacing nerar the periphery on the axis center of the M_3-mirror. Each array may have single or multiple device which applied short post diode mouded strcutrue or integrated-circuit fabrication techniques.

3. Theory

By means of the scalar potential treatment, the function U_i defined as the eigen mode in the open cavity, Satisfies the following equation

$$\triangle U_i + k^2 U_i = 0 \tag{1}$$

We can obtain an ortho-normal spectrum of wave-beam modes for the 3-mirror quasi-optical resonator.

$$a_{mn} = \frac{1}{2}\sum_p I_p \triangle s_p \overline{M}^p_{mn}(x_p, y_p, z_p) \qquad P_{mn} = a_{mn}a_{mn}$$

$$P_0 = a_{mn}a_{mn} \qquad FP_0 = \frac{a_{00}a_{00}}{\sum_{mn} a_{mn}a_{mn}} \tag{2}$$

4. Computed Results

The theory developed above enables one to determine the number of current elements and the current source locations required to obtain efficient transfor of power to the lowest order "Gaussian wave beam" within the resonator.

(1) The power of fundamental mode

Results shows the fundamental mode power as a function of the source spacing $\triangle x$ for different number of sources at the same generatrix on M_3 mirror.

(2) The fractional power of fundamental mode

The fractional power coupled into the fundamental mode for three different array configuratons coutaning 3、5、7 elements at the same generatrix on the mirror M_3 is obtained.

5. Experiments and conclusions

We utilized four source line-array which axisymmetricliy plased with uniform spacing near the periphery on the axis center of the M_3 mirror. Each array has single Gunn device which applied short post diode mouded structour. The operation of the combiners is stable and neither spurious oscillations nor jump phenomena are observed during the experiment.

With the computer calculating results, the curves of fundamenteal mode combining power and fractional power to active souces number、location and configuration are drawn. It is show that very effiient power combining of solid-state millimenter wave sources may be obtained through 3-mirror quasi-optical resonatar and sources array.

Refrence

1. J. W. Mink, Quasi-optical power combining of solidstate Millimetre-wave sources, IEEE Trans on Microwave Theory and Tech., Vol. MTT-34, No. 2, Feb, 1986.
2. Liu shenggang, Xie wenkai, Liang Zheng, and Klaus. Jugen Grimpe, 3-mirror quasi-optical powor combining of millimentre-wave sources, Int. J. Electronices, Vol. 65. 3. 717-724, 1988.

---

* The projet supported by Natual Science Foundation of China

Advances in measurements with an all-electronic terahertz spectroscopy system

Daniel W. Van Der Weide,† Jeffrey S. Bostak, Bertram A. Auld, and David M. Bloom
Edward L. Ginzton Laboratory, Stanford University, Stanford, CA 94305
†Currently with Max-Planck-Institut für Festkörperforschung, Heisenburgstr. 1, D-7000 Stuttgart 80, Germany

ABSTRACT

We have developed electronic circuits that generate and detect subpicosecond shock-waves. We have used these circuits with integrated antennas in a system capable of free space spectroscopy with greater than 10 dB foreground to background radiation from 6.4 GHz to 1 THz. This system was used to characterize a submillimeter wave filter. In particular, 250-375 GHz measurements are demonstrated with 2 dB accuracy over a 20 dB dynamic range.

INTRODUCTION

In the study and application of picosecond electromagnetic pulse propagation, generation and detection of these pulses is usually done with ultrashort optical pulses driving photoconductive switches which are used both as transient generators and samplers. These systems have been applied to problems in THz spectroscopy. Fourier analysis of the detected pulses, with and without a test sample in the beam path, yields the magnitude and phase of the transmission of the sample as a function of frequency.

In contrast to this hybrid optical/electronic approach, we have developed an all-electronic system using monolithic nonlinear transmission lines (NLTLs) as voltage step generators for both generating picosecond pulses and driving monolithically integrated diode samplers for detection of these pulses.[1] Advantages of this approach lie in its relative simplicity and robustness, as well as its ~100x greater pulse repetition rate. The system can also be used at cryogenic temperatures where enhanced performance is possible. Recently, similar all-electronic systems have been applied to THz spectroscopy, but have been limited to frequencies below 250 GHz.[2] We have used our system to perform spectroscopic measurements from 250 to 375 GHz with 2 dB correspondence to manufacturer's data over a 20 dB dynamic range. We have also demonstrated measurements up to 1 THz.

NONLINEAR TRANSMISSION LINES

Nonlinear transmission lines are synthetic structures of series inductors (approximated by sections of high-impedance transmission line) with varactor diodes periodically placed as shunt elements. On this structure a voltage shock-wave develops from a sinusoidal input because the propagation velocity varies with the nonlinear capacitance-voltage relationship of the diodes, $v_p = 1/\sqrt{LC_{tot}(V)}$, where L is the inductance and $C_{tot}(V)$ the sum of the varactor and parasitic capacitance of the line, all per unit length. Limitations of the NLTL arise from its periodic cutoff frequency, $\omega_{per} = 2/\sqrt{LC_{tot}(V)}$, waveguide dispersion, interconnect metallization losses, and diode resistive losses.

APPLICATIONS TO A FREE SPACE TRANSMISSION SYSTEM

We have applied the ultrafast pulse generating capability of the NLTL to drive antennas and a sampler in a coherent, all-electronic free-space signal generation system. We used integrated magnetic dipole (slot) antennas measuring 5 μm wide and 190 μm long, resonant at ~330 GHz. We also used high resistivity silicon hyper-hemispheres to collect and focus the quasi-optical beam. The distance between the system generator and detector is 48 cm.

To perform a free space spectroscopic measurement, a submillimeter wave filter under test is placed in the THz beam. By taking the ratio of the detected signal spectrum with and without the filter in place, the transmission of the filter as a function of frequency can be obtained. Because the system detects voltage, not power, both the magnitude and phase of the transmission can theoretically be obtained.

In this experiment, the filter under test was a multiple bandpass filter. Because the filter had a diameter of 2 cm, it was placed close to the generator, where the beam diameter is smallest. The manufacturer[3] had used a backward-wave oscillator spectrometer to characterize the magnitude of the filter transmission magnitude from 235 to 390 GHz. Passbands were measured by the manufacturer to be centered around 279 and 348 GHz.

A comparison of this measurement to ours is shown in Figure 1. Our data corresponds within 2 dB over a 20 dB dynamic range from -7 to -27 dB transmittance. Below -27 dB transmittance, our system was not capable of reproducing the

manufacturer's data due primarily to the limited broadband power output of our system. A straightforward way to improve this is to use broadband antennas, currently under development. The magnetic dipoles currently used are resonant antennas. These have a radiation resistance which is a strong function of frequency. A second way to improve the dynamic range of the system would be to reduce the effects of phase noise on the measurement by using better synthesizers. Alternatively, the intermediate frequency could be increased so that the downconverted harmonics are spaced further apart in frequency and are less susceptible to the phase noise of adjacent harmonics.

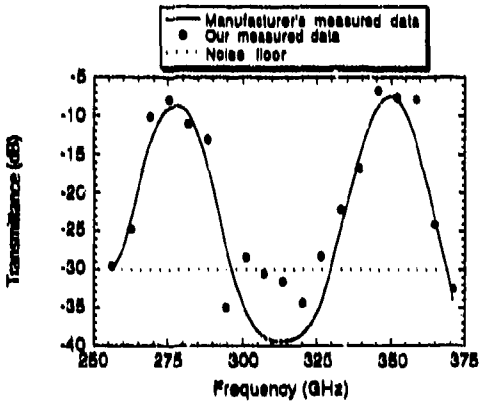

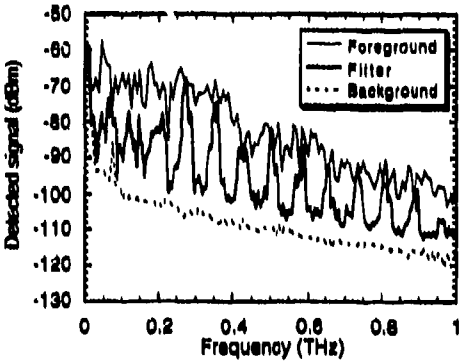

Figures 1 and 2. Manufacturer's transmission data and measured transmission data for a submillimeter-wave filter.

Figure 2 shows data from a measurement that spans the frequency range from 6.4 GHz to 1 THz. Here we plot separately the foreground (detected signal with no filter in place), the radiation with the filter in place, and the background (detected signal with beam blocked). The dark trace, which represents the filter measurement, shows clearly visible transmission peaks out to 1 THz. This periodic repetition of the signal peaks verifies that the filter is indeed an etalon, and not a simple bandpass filter. If signal-to-noise ratio is calculated as the ratio of foreground signal to background signal, the signal-to-noise is seen to be at least 20 dB over the entire frequency range from 6.4 GHz to 1 THz. A more conservative estimate, which accounts for the effects of phase noise between the two synthesizers, is the ratio of detected passband to stopband in the "filter" signal. This gives at least 10 dB over the entire frequency range.

CONCLUSION

We have developed an all-electronic system capable of free space spectroscopy with greater than 20 dB signal to noise from 6.4 to 375 GHz and greater than 10 dB signal to noise over the full range from 6.4 GHz to 1 THz. An improved antenna design and microwave source should result in even better performance, making this system a compact, useful spectroscopic tool.

ACKNOWLEDGMENTS

This work was supported by the Joint Services Electronics Program under Contract No. N00014-92-J-1050. J. S. Bostak acknowledges a Joint Services Electronics Program fellowship. The authors wish to thank J. Martin and P. Prather for circuit assembly. They also acknowledge discussions with M. Rodwell, E. Özbay, and M. Kauffman.

REFERENCES

1 D.W. Van Der Weide, J.S. Bostak, B.A. Auld, D.M. Bloom, "All-electronic generation of 880 fs, 3.5 V shockwaves and their application to a 3 THz free-space signal generation system, Appl. Phys. Lett. 62, 22-24, (1993).

2 Y. Konishi M. Kamegawa, M. Case, R. Yu, M. J. W. Rodwell, and R. A. York, "Picosecond electrical spectroscopy using monolithic GaAs circuits," Appl. Phys. Lett., 61, 2829-2831 (1992).

3 Center for Submillimeter Radiophysics, Saint Petersburg, Russia, via F. Kielmann, Max-Planck-Institut für Festkörperforschung, Stuttgart, Germany.

Some Recent Applications of the Free Electron Laser (CLIO and FELIX) in Semiconductor Nonlinear Optics

C R Pidgeon,
Department of Physics, Heriot Watt University, Edinburgh.

A brief review is given of some recent rf-linac pumped free electron laser experiments on two-photon absorption (TPA) in semiconductors, conducted in collaboration with the CLIO group at Orsay, and saturation subband spectroscopy in GaAs quantum structures with the Delft and FELIX groups at the FOM-Institute for Plasmaphysics Rijnhuizen.

TPA in the narrow gap semiconductors InAs and InSb has been measured for the first time over a broad spectral range - from one-photon to two-photon threshold (E_G to $E_G/2$) - utilizing the mid-infrared tunability of CLIO. Previously [1] an assumption had to be made concerning the lifetime of the excited carriers in order to interpret the results within the time structure of the exciting FEL. We have now made a direct measurement of the lifetime of two-photon-induced free holes in InAs using an excite-probe technique. The lifetime was determined by measuring the transmission of an adjustable delayed weak picosecond probe pulse following an intense picosecond pump pulse from CLIO. Results show good agreement with the exponential behaviour expected, and lifetimes of between 2.5ns and 10ns were measured consistent with Auger scattering. Strong power limiting was observed at wavelengths between E_G and $E_G/2$, which yielded the two-photon absorption coefficient over the entire range by fitting a simple theoretical model. The results are consistent with a model for the two-photon transition probability incorporating the nonparabolic band structure for narrow gap semiconductors.

FELIX has been used to measure the nonlinear intersubband absorption in GaAs/AlGaAs multiple quantum wells. The GaAs wells are 270 angstroms wide, leading to a subband separation of 18 meV. At this photon energy the FEL is the only tunable high-intensity radiation source available. The samples were prepared with a metallic grating on the top surface, which enables coupling of the radiation to the subband transition in a normal incidence geometry. Complete bleaching of the absorption is achieved at an intensity $I = 100kW/cm^2$. The intensity-dependent absorption is fitted with a homogeneously broadened two-level system, leading to a saturation intensity of $I_s = 10kW/cm^2$, and a population lifetime, T_1, of 1ps. This is shorter than the pulse length of the laser micro-pulse (10ps), which justifies the steady-state analysis.

In the strong saturation regime ($I \sim 1MW/cm^2$) the Rabi frequency is already larger than the inverse coherent time, T_2. This opens up the possibility of observing coherent nonlinear effects in future experiments.

[1] H-W and CLIO, Optical Materials 2, 89 (1993).

Quasi-optical devices for submillimeter techinique

V.B.Anzin, G.A.Komandin, G.V.Kozlov,
S.P.Lebedev, A.N.Lipatov, A.A.Volkov
Institute for General Physics, Russian Academy of Sciences,
Vavilov str., 38, 117942 Moscow, Russia

The devices considered in this report may be usable in laser and spectroscopic techiniques of submillimeter and FIR frequency range.

1 Polarizing two-beam interferometers

Polarizing two-beam interferometers are used in two modes — a) interferogram mode $I = I_0 \cos^2 \frac{2\pi\Delta}{\lambda}$ and b) antiinterferogram mode $I = I_0 \sin^2 \frac{2\pi\Delta}{\lambda}$, where Δ is an optical path difference. These interferometers allow to create effective filters for odd and/or even harmonics supression. Supression level in a single interferometer depends on polaroids quality and in optimal case is larger than 30 dB.

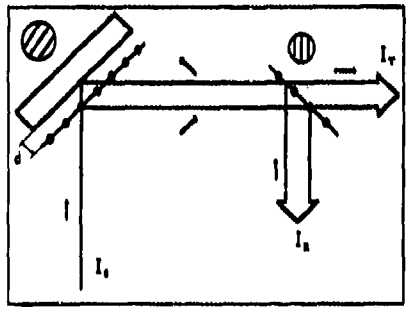

Fig.1 Compact polarizing interferometer. Arrows show beam polarization. Hatched circles represent wire grids directions.

To increase the supression level one can connect several interferometers consequently (see Fig.2). The scheme of the interferometer with wire grid beamsplitter mounted just before the mirror is the most compact [1].

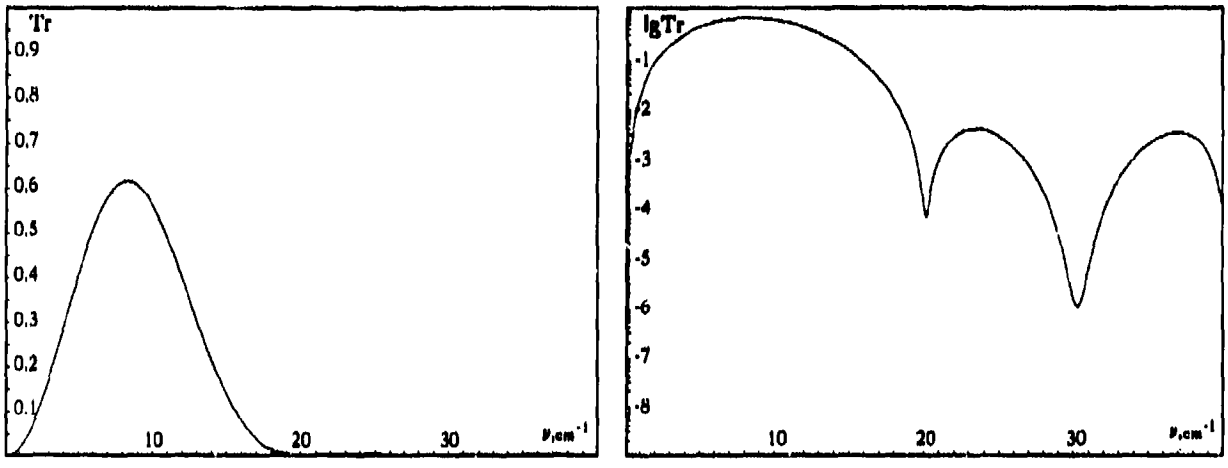

Fig.2 Calculated transmissivity of 3-interferometer filter for the 2-nd and the 3-rd harmonics supression. Parameters are: $\Delta_1 = \Delta_3 = 0.166cm$, $\Delta_2 = 0.05cm$.

2 Fabry-Perot interferometer (FPI)

The possibilities of developing the tunable duplex and triplex filters are investigated in [2]. Authors investigated FPI filters with partially crossed polarizing mirrors of different types. Also possibilities of using dielectric FPI and systems on their base as non-tunable filters have been considered.

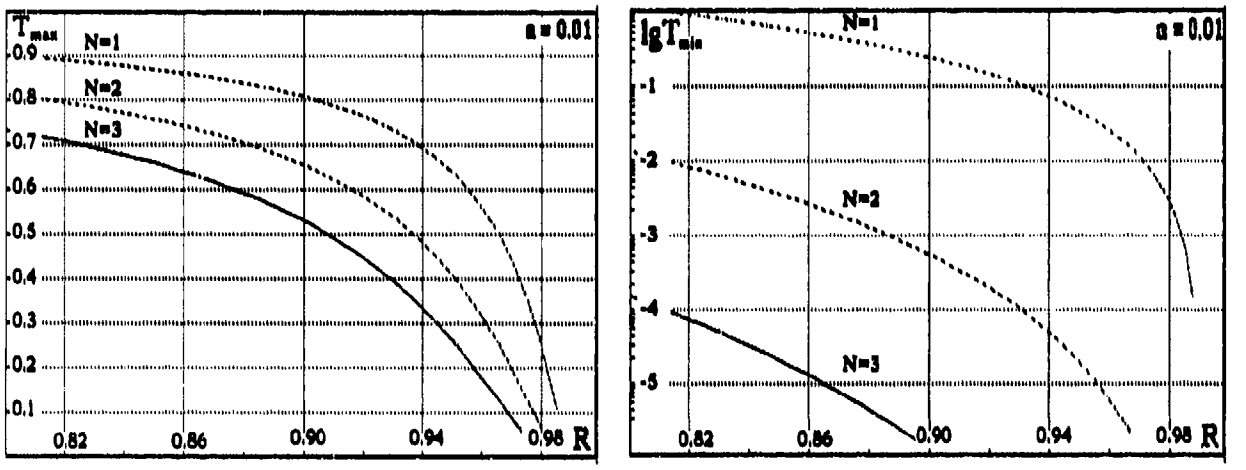

Fig.3 Calculated maximal and minimal transmissivities of FPI depending on mirror reflection. Absorption coefficient of mirrors is 0.01.

References

[1] G.V.Kozlov *Pribori i Tehnika experimenta*, 1970, N6, p147-148

[2] O.Tudisco *Int. Journ. IR and MM waves*, 1988, v.9, N1, p41-53

Bias pulse modulator for a high power K-band (26-40GHz.) IMPATT oscillator

P.G.Frayne and C.Nicholls

Royal Holloway College, London University, Department of Physics
Egham, Surrey TW20 OEX, United Kingdom

ABSTRACT

A pulse modulator , for driving K_a band IMPATT diodes is described , which enables chirp control and optimization of oscillator performance via current pulse shaping .Peak powers in excess of 20Watts have been achieved , with a pulse duration of 250ns and 0.1% duty cycle.

1.OVERVIEW OF DESIGN CONCEPT

The development of a pulse modulator for a K_a band IMPATT oscillator is described without detailed reference to the waveguide test cavity that constitutes the modulator load .In practice the development of both components is closely interrelated .Essential considerations for satisfactory overall source design are:

(a).Electrically rugged modulator design to withstand high peak currents.
(b).Good impulse power match between driver and cavity to ensure single mode operation.
(c).Fast current rise for rapid thermal stabilization of diode.
(d).Electronic compensation for thermally induced chirp.
(e).Current limit protection for the costly IMPATT diode and short circuit protection for the modulator.

A power MOSFET device rather than a bipolar transistor was used as the IMPATT driver for the following reasons:

(a).Robust, high power, high speed switching capability.
(b).No thermal runaway problems.
(c).Low cost in comparison to an equivalent bipolar device.

A transient voltage suppressor diode type P6KE39A, supplied by SGS-Thompson Microelectronics, was used as a dummy load for the initial testing of the modulator .The R.F. system performance analysis was then evaluated with DC1152 and DX1298 IMPATT diodes, manufactured at G.E.C. Plessey, Lincoln Laboratory.

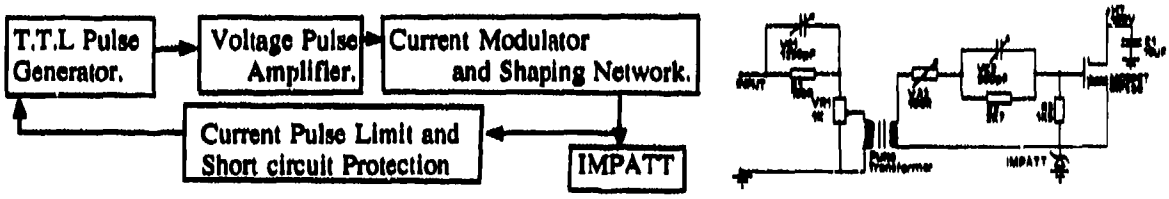

Fig.1.The IMPATT pulser system and output current modulator circuit.

2.T.T.L. PULSE GENERATOR

The NE555 timer chip was used to set a 4KHz repetition frequency.The pulse duration was established by triggering a 74HCT123 monostable , selected because of its high speed operation .An emitter follower stage was then used to match the T.T.L. output to the pulse amplifier.

3.VOLTAGE PULSE AMPLIFIER

A cascode transistor pair was used in the input stage of the amplifier and power MOSFETs in subsequent stages to effect the required voltage translation . Transition times of 10-15ns were maintained by operating the MOSFETs in their non-linear switching mode .The output voltage pulse from the circuit was continuously variable over the range 0-150V.

4.CURRENT MODULATOR

Voltage-to-current conversion was achieved using an IRF530 power MOSFET. Selection criteria for the device were :low $r_{DS}(ON)$ <3Ω, low Ciss <800pF, high $V_{(BR)DSS}$ ≥ 100V and pulsed current capability ≥ 20A .The common drain configuration was used to eliminate Miller effect capacitance .This arrangement resulted in a floating source potential which necessitated the use of a D.C. isolating transformer for the provision of gate-to-source drive.The transformer was constructed from a Siemens B64290K615X830 SIFERRIT, broadband, high permeability, toroidal core bifilar wound with 18 turns of 25s.w.g. enamelled copper wire.Variation in pulse top gradient was achieved by a parallel RC network between gate and transformer secondary and amplitude control by VR1 in the primary circuit, (see fig.1).

Transition times of 12A/50ns and pulse top gradient variation from 0A/200ns to 8A/200ns have been attained with this circuit topology.

5.PROTECTION CIRCUITRY

Conditions of the diode short circuit and drive currents that exceed a presetable limit are detected by comparators which disable the pulse generator until the system is reset .Open circuit protection of the modulator is unnecessary because of the high breakdown voltage of the output MOSFET.

6.OSCILLATOR PERFORMANCE

Typical oscillator R.F. and current pulse profiles are illustrated by the photograph in fig.2. These were obtained with the following modulator and source conditions : 8A/50ns rise time, 12A/25ns fall time, 12A peak current, 4A/200ns pulse top gradient, 34Watts peak R.F. power, 32.7GHz centre frequency, 50MHz chirp bandwidth.The importance of the current pulse profile adjustability in chirp compensation is highlighted in fig.3, in which typical experimental data has been displayed on representative current pulse curves.

Fig.2 Oscillator R.F. and current profiles.

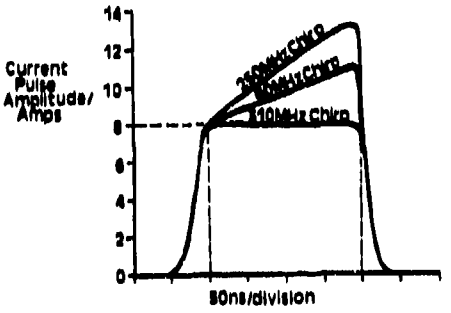

Fig.3 Illustration of typical chirp compensation data.

7.ACKNOWLEDGEMENTS

This research was supported by R.S.R.E. Malvern .The authors wish to thank Mervyn Hobden, G.E.C. Plessey Semiconductors and Leon Ellison, Royal Holloway College, for their helpful discussions throughout the course of the work.

Microwave Spectrometers for the Investigation of fast Processes in the Time Domain

Brailovsky A.B., Khodos V.V., Vaks V.L., Panin A.N., Pripolzin S.J., Wolf F.

Analytik & Meßtechnik GmbH Chemnitz,
Stollberger Str. 4a, D-09119 Chemnitz, Germany

By means of microwave gas spectroscopy it is possible to obtain information about many properties of the molecules under investigation as there are information about chemical composition of molecules (including exchange of isotopes), structural (geometric) parameters of molecules, their electrical and magnetic properties but also information about intra- and intermolecular interactions.

Over the last decades the significant improvement of non-stationary microwave spectroscopy had an increasingly strong impact on the realisation of a new type of spectrometers with a sensitivity near the theoretical limit and a resolution of the order of the Doppler width of a absorption line [1]. However, the disadvantage of these spectrometers is, that they are not fast enough to track high speed processes which occur for instance in chemical gas phase reactions.

Therefore it had become necessary to develop a method capable to obtain chemical and physical parameters from the observed matter in very short time intervals. The influence of the measuring process should be kept as small as possible in order to cause no distortions of the molecules undergoing reactions of interest.

The new developed microwave Fourier-transform spectrometer applies a broad band excitation signal to the gas and subsequently the spectrum of the re-emitted spontaneous radiation is analysed. The fast registration unit allows to detect simultaneous the signals in a frequency range 2 to 3 times as large as the width of an absorption line. This gives the opportunity of observing the kinetics of fast processes. The high sampling rate and the large information content (curve shape of an absorption line) obtained from each single shot, permits of investigation of the time dependency of the concentration of transition and final products of fast chemical reactions. It is possible to conduct in-situ experiments in low pressure environments without mentionable distortion of observed processes.

List of some important parameters of the microwave FT-spectrometer:

- Frequency range (using interchangeable MW-generator blocks): 37.7--178.1GHz
- Lowest detectable absorption coefficient (Path length in the absorption cell 1 meter): $10^{-7}cm^{-1}$
- Desired time for one signal caption process: $10^{-5}s$
- Pressure range: 10^{-1}. . . 10Pa

Literature:

[1] V.L. Vaks, 10th Colloquium on High Resolution Molecular Spectroscopy, Dijon, 14-18 Sept. (1987).

A Frequency-stabilised microwave generator for investigations of absorption lines of water

Vaks V.L., Pripolsin S.J.

Analytik & Meßtechnik GmbH Chemnitz,
Stollberger Str. 4a, D-09119 Chemnitz, Germany

Backward Wave Oscillators (BWO) are frequently used as sources of mm- and sub-mm-wavelength radiation in microwave spectroscopy. They can easily be tuned to any frequency in a broad frequency band. However, an oscillator without any stabilisation unit has a relatively broad spectrum and the long term stability is bad as well.

Up to now there have been three main methods to improve the stability of the frequency:

- Application of a highly stable low noise frequency generator,
- Using a PLL, multiplexers and mixers to lock the EHF generator to a highly stable NF generator,
- Stabilisation and synchronisation of the EHF source using an external resonator.

The first method is difficult and the result is not as good as one would expect. The second method results in an excellent stabilisation, however one has to deal with a very complex system. The third method is based on external resonators and so the long term stability can not be guaranteed.

The matter of this paper is a system suitable to frequency stabilisation. It realises the generation of a signal at a fixed frequency which is given by a strong absorption line (e.g. a line from H_2O). The frequency stabilisation around the centre frequency is realised (capture range).

The fixed frequency stabilisation is performed by means of a reference gas absorption cell which already contains the gas of interest. The BWO is low frequency modulated so that it emits a broad band signal. The resulting output signal of the BWO is divided by a directional coupler. A small part of the radiation is taken away and subsequently guided into the reference cell. (The second part is available for an external application). After detecting and processing, this signal contains the deviation of the absorption line so that the centre frequency of the peak is accessible. Via correction filters and amplifiers a correction signal for the BWO is generated.

The whole microwave source consists of four main components: BWO, voltage supply, stabilisation system and reference gas absorption cell. The gas cell is a tube made of quartz with Brewster windows. If the gas is long term stable, the reference cell can be used for several years.

The resulting long term instability is of the order of 10^{-9} (Explicitly measured for a base frequency of 133.0GHz: registration time: 3h, the frequency drift for these 3h was less than 250Hz). The lowest detectable absorption coefficient under these conditions was $10^{-9}cm^{-1}$. The measurements have been conducted under laboratory conditions.

A similar device has been developed for the 380,1973GHz absorption line of water. For technical reasons the parameters were not explicitly measured.

The developed generators can be applied as highly stable superheterodyn receivers in radiometry, as reference generators for meteorology and as radiation source in microwave spectroscopy.

Quasi-optical method for moisture measurements of gases

A.A.Vertiy and S.P.Gavrilov

Institute of Radiophysics and Electronics,
Academy of Sciences of Ukraine,
12 Acad.Proskura st., Kharkov
310085 Ukraine
Phone (0572) 448-467
Fax (0572) 441-105

ABSTRACT

In this paper we suggest to use quasi-optical resonator with dielectric inclusion for moisture measurements of gases. This method employes the electromagnetic frequency in the range of 35 to 150 GHz. The main idea of the approach is a registration of moment of dew point or phase transitions on cooling dielectric element of the resonator using the changes of resonator characteristics. The results of moisture measurements of air at atmospheric pressure using a barrel-shaped resonator with a dielectric bar are given. It is shown that such electrodynamical structures allow to registrate the dew point and phase transitions as "water-ice" and "ice-water" at cooling dielectric bar by Peltier element. The experiments were carried out at frequencies f≈136 GHz.

2.INVESTIGATION RESULTS

Moisture is one of the most important technological gas parameters to be controlled. The known methods are based on application of waves of optical or radiofrequency range. Radiofrequency methods are usually used in moisture measurements of solid and friable materials and their sensitivity is not sufficient. Optical moisture measuring devices are rather complex and expensive and they can not employ under real production conditions. So the important scientific and engineering problem is a development of new methods allowing to perform a control of gas moisture measurement under complex production conditions. The prospective methods for these purpose are the quasi-optical ones employing the electromagnetic frequencies in the range of 35 to 150 GHz.

For successful application of these methods it is necessary to develop experimental and theoretical approaches for studing of electrodynamical processes in quasi-optical devices.

In the present paper we suggest to use a quasi-optical resonator with a spherical cuvette as a moisture sensor. The main idea of this approach is a registration of the moment of dew point on the quasi-optical elements of the resonator. Taking into account that the frequencies chosen (35-150GHz) are sufficiently sensitive to medium moisture changing and a quality factor of the resonator is rather high a high sensitivity of the moisture measuring device is just what to be expected. Such quasi-optical dew point method may be used for analyzing of gas components if dew points of components are observed when gas

mixture temperature is changing. In the case of nature gas the method may allow to measure moisture and hydrocarbon composition. For this purpose the following scientific problems are to be solved:

1. Calculation of spherical characteristics of quasi-optical resonator perturbed by dew.
2. Development of quasi-optical methods of measurement of electromagnetic fields and spectrums of the quasi-optical resonators.
3. Creation of experimental model of "resonance quasi-optical dew point spectrometer" (RQDPS) for moisture and component structures of gas mixture.
4. Creation of microprocessor device and a system of quasi-optical signal processing.

We have investigated experimentally the quasi-optical the resonant cell for air moisture measurements at atmospheric pressure and room temperature ($t \simeq 21^{\circ}$ C). The resonant cell is designed on the base of quasi-optical barrel-shaped resonator. Inside the resonator a dielectric bar (sapphire) is located coaxially and it is cooling by Peltier element. The resonator's diameter is $d \simeq 9\lambda_0$ ($\lambda_0 \simeq 2,2$mm) and the bar's one is $d \simeq \lambda_0/2$, correspongly. The resonator is connected with a waveguiding line by slots in its side surface. The transfer constant T of the resonator is measured in dependonce on the dielectric bar temperature t. Condensation of water steams on the bar surface and phase transitions "water-ice" and "ice-water" (when heating) are studied at the rate of bar temperature changing by

t/sec 0,35 /sec.

When water steams condensating the transfer constant T is decreasing monotonically by $\Delta T \simeq 12$ %. In the transient area ($t \simeq 0^{\circ}$C) T increases fast (during $\Delta t \simeq 0,5^{\circ}$C) by $\Delta T = 7\%$, and with grouth of ice thickness it decreases slowly. The Fig.1 shows measured dependences of transfer coefficient T of the resonator on temperature t of dielectric bar. Dashed line corresponds to phase transition "water-ice".

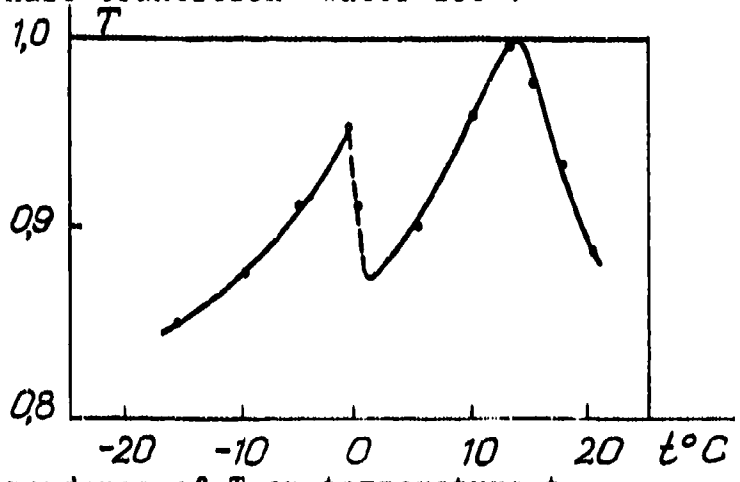

Fig.1.Dependence of T on temperature t.

3.CONCLUSION

Thus, the results obtained will be the base for creating of new class of quasi-optical spectrometers (dew point spectrometers) and they will find the application in echology, medicine, industry etc.

METHOD AND MEASUREMENT COMPLETE SET FOR NON-DESTRUCTIVE LOCAL PARAMETER MICROWAVE MEASUREMENTS OF MATERIALS

Dr.sc.ZVYAGINTSEV A.A., Dr.sc. STRIZHACHENKO A.V.
University, Freedom Sq.,4,310077,Kharkov,Ukraine

Modern methods of measurement allow to determine with a high degree of exactness dielectrics electric parameters. However, the overwhelming majority of existing measuring instruments made on the basis of those methods are actually destructive measuring means, allowing to measure only integral characteristics of materials. Modern technological process demands a basically new approach to this problems: manufacturing new high Q and highly expensive materials (leucosapphires, artificial rubins, a number of ferrite marks, etc.) and also goods on their basis (stripline bases and microwave integral schemes, dielectric waveguides and resonators, etc.) supposes materials characteristics measurements without ruining them. From this point of view nondestructive methods of measurement possess obvious advantages. Nevertheless, the existing non-destructive measuring means mostly have a not very high exactness of measurement of dielectric permittivity, magnetic permeability and material losses and also have low sensitivity to their changes. On the basis of our analysis, an automated complex, allowing to measure samples measbility with high degree of exactness, effectively and without destruction them, has been constructed. An original part of the complex is a measuring devise on the basis of a waveguide junction of cylindrical and radial waveguides. The necessary condition of natural modes presence in such a structure is cut-off of all junction-forming waveguides at resonant frequencies. In such a case an electromagnetic field of resonating modes appears to be concentrated in the region of waveguide junction and its characteristics (resonant frequency, Q-factor) are determined by the region sizes and the parameters of that volume of the sample being tested, which is to be found in the above-mentioned region. The coupling of a measuring resonator with the plumbing of the automatic VSWR and attenuation meter (a measuring complex block-diagram is shown in Fig.1) is achieved by waveguide-to-coaxial adapters ending in excitation elements and a waveguide channels selector. A test sample of flat form and arbitrary configuration in the perimeter (a substrate, a disk, etc.) is fixed on a frame with divisions on it. The frame is moved on the guides. so that the sample part successively get into each resonant region.

After a measuring section is made, there is no need in special turning of any kind. The integration of a frequency meter and personal computer, allowing to introduce data from the frequency meter directly in the process of measurements, allows to essentially improve the effectiveness of measurements. The measuring complex includes PC AT 286/287, due to which the

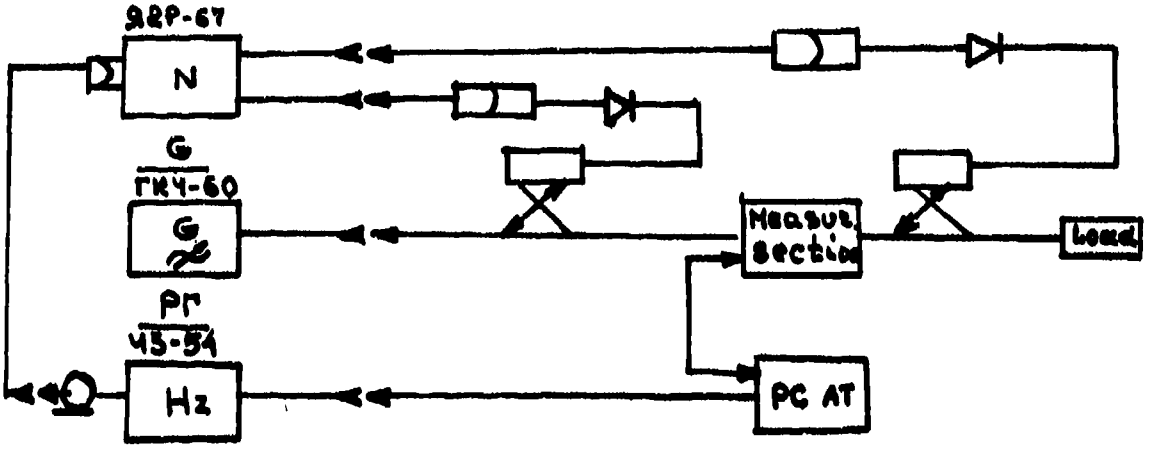

average time of one ε , μ and tgδ measurement with the error of not more than 0.5% (ε,μ) and 3% (tgδ), is 5-10 sec. The symmetrical H_{011} mode and non-symmetrical HE_{111} (the indices indicate to the number of field variations with respect to the cylindrical coordinates φ, r, z, correspondingly) one, " non-radiating " for the given device (as shown in this work) have been chosen as the measuring section modes of operation.

CONCLUSION

1. In empty cylindrical waveguide junctions there is an exceptionally rare spectrum of natural modes: out of the axially-symmetrical H-type modes the H_{01} and H_{02} modes are natural; the only possible mode in the class of non-symmetrical ones is the mode of HE type. The spectrum of natural modes is essentially widened when the structure is killed with some substance.

2. The technique of materials electromagnetic characteristics measurements has been suggested. The technique, which is simple and of non-destructive character, allows to:

- measure dielectrics and magnetodielectrics local parameters;
- determine the directions of ellipsoid axis of dielectric permittivity of uniaxis anisotropic crystals;
- control properties anisotropy of materials dielectric permittivity.

3. On the basis of theoretical and experimental analysis a device design for dielectrics and ferrites local parameters non-destructive measurement has been developed. The device is characterized by:

a) for symmetrical modes:
- high sensitivity to ε, μ (700-800 MHz/unit $\varepsilon\mu$ changes);
- small error in measurements of dielectrics permittivity and magnetic permeability in a wide range of $\varepsilon\mu$ (0.5 %) changing;

b) for non-symmetrical mode (HE_{111}):
- high sensitivity to test material electric properties anisotropy;
- the ability to defect local non-uniformities.

FREQUENCY STABILIZED MILLIMETER WAVE PULSED IMPATT OSCILLATORS IN AUTO-OSCILLATED AND INJECTION-LOCKED MODES (DESIGNING AND INVESTIGATION)

A.V. Gorbachev, L.V. Kasatkin, V.V. Novozhilov, M.I. Poigina

Research Institute " ORION ", Kiev, Ukraine, p.o. 252057

The schemes and constractions of millimeter wave frequency stabilized pulsed IMPATT oscillators in auto-oscillation and injection-locked modes are determined. The methods of current and varactor compensation of the thermal frequency unstabilities, the methods of stabilisation of the diode's p-n junction temperature, the directions for the use of stabilising resonators are considered theoretically and experimentally. As a result of the use of above mentioned methods there were designed frequency stabilized pulsed oscillators of 32-37 GHz, operating over the ambient temperature from -50 to +50 C with pulse power 5 , 10 , 20 W and frequency chirp 1-3 MHz in auto-oscillation mode and phase chirp during the pulse less than 10-15 in injection-locked mode. There is achieved injection-locked bandwidth over 10-15 percent at 13 dB gane in pulsed IMPATT oscillators.

SOLID-STATE 8-mm WAVE TRANCEIVER WITH PULSE-TO-PULSE SWITCHING OF OPERATING FREQUENCIES (INVESTIGATION AND DESIGNING)

A.V. Gorbachev, L.V. Kasatkin, V.A.Sackov,
I.N.Homenko, I.V. Zverghovsky

Research Institute " ORION " , Kiev, Ukraine, p.o. 252057

The decisive questions of designing the solid-state millimeter wave tranceiver are discussed. The tranceiver designe has become possible on the basis of R & D studies of high-power pulsed IMPATT diodes working in EHF band, systems of summing the IMPATT outputs and development of methods allowing a considerable widening of the band of injection-locked oscillators, high stability of their performances over a wide temperature range and within the SHF-signal pulse. The main parameters of the designed tranceiver are following: frequency range 34 36 GHz; output pulse power 30 W; pulse width 50 200nsec; duty cycle 0.5 % ; 8 switching frequencies at 800 MHz bandwidth with 50 100 nsec switching time; receiver sensitivity from -90 to -100 dBm; weight 2.5kg; volume 2,000 cub cm. The tranceiver can operate over environmental temperature range from -50 to +50 C. It includes microwave block and bias and control block. The microwave block consists of the Gunn VCO, PIN upconverter, three stage injection-locked pulsed IMPATT amplifier, 3 GHz pulsed and 3.08 GHz CW transistor oscillators with dielectric resonators, high-speed PIN switches, two balanced mixers and two IF amplifiers. There are two modifications of the tranceiver architecture - for coherent and noncoherent radars.

Surface layers and far infrared spectra of high-Tc superconductors

Xavier Gerbaux, Armand Hadni and Masato Tazawa (*)
Laboratoire Infrarouge Lointain, L.M.C.P.I., U.R.A. - C.N.R.S. n° 809
B.P. 239, F-54506 Vandœuvre-lès-Nancy Cedex - France.
(*) GIRI, Nagoya, 1, Hirate cho, Nagoya 462 - Japan.

It is possible to increase significantly the acuracy of Far IR (FIR) transmission spectra of High-Tc superconductors by depositing a very thin oriented film (e.g. t = 300 Å), of either YBaCuO or GdBaCuO on a very thin MgO plate (e.g. t_0 = 90 μm). Such very thin films of superconductors are very fragile and FIR transmission either at 300 K or 10 K increases dramatically after a few weeks. A phenomenological model is however possible to explain all spectra at different temperatures from 300 to 10 K if we consider a thin layer of insulating barium cuprate (e.g. $GdBaCuO_6$) due to a progressive loss of oxygen.

More precisely, a very thin film of GdBaCuO (t = 300 Å), deposited on an MgO plate (t_0 = 90 μm) has given a somewhat higher precision in the FIR spectra observed at T = 300 K, 185 K, 86 K, and 10 K, for a transition temperature Tc = 88 K, than in any other previous measurement. For that sample, and within the accuracy of the measurements, plasma frequency $\nu_p = \frac{1}{2\pi c}\left(\frac{Ne^2}{m\varepsilon_0\varepsilon_R}\right)^{\frac{1}{2}}$, is a constant, ν_p = 4500 cm^{-1}; ν_c is a linear function of temperature for T > Tc (ν_c = 1.6T + 55 cm^{-1}). For T < Tc, a T^4 law as been used to get the number of quasiparticles in the superconductive phase, and the spectrum at T = 86 K with the additional assumption of a collision frequency saturating around 50 cm^{-1}. We have also to introduce 3 Mid-IR active oscillators at room temperature, and to keep them in the superconductive phase, with a definite increase in their strengths.

That phenomenological model contains eleven parameters only since we have shown the possibility to use simply one plasma frequency at all temperatures and to adjust only one collision frequency (the one at very low temperatures). Moreover to explain transmission around ν = 10 cm^{-1} we have to adjust one parameter (dc resistivity ρ_0), and in the spectral range 10 - 50 cm^{-1}, we keep the ρ_0 value and we have to choose one plasma frequency. Finally in the 50 - 200 cm^{-1} range we use these two parameters and we have to fit the Lorentz oscillators (frequency, strength and damping).

We shall discuss some important points:

- The T^4 law,
- The collision frequency variations in the superconductive phase,
- The gap problem,
- The Mid IR oscillators and their considerable strengths.

REFERENCES

1. P.G. Quincey, P.B. Whibberley and J.R. Birch, Conf. Digest of the 14th Int. Conf. on Infrared and Millimeter Waves, pp. 519 - 20 (1989).
2. X. Gerbaux, M. Tazawa, A. Hadni, J. Hubsch and A. Kitade, Infrared Phys, 31, pp. 517-526 (1991).
3. X. Gerbaux, A. Hadni, M. Tazawa, J. C. Villégier, and H. Marin Cudraz, Int. J. Infrared Millimeter Waves, 12, pp. 1105 - 1109 (1991).
4. A. Hadni, X. Gerbaux and J.C. Villégier, Phys. Stat. Sol. B 175,409 - 420 (1993).
5. Bonn et al (Preprint 1992).
6. K.F. Renk, J. Schützmann, A. Prückl, W.Ose, B. Roas and B. Saemann Ishenko, in "*Electronic Properties of High-Tc Superconductors*", pp. 275 - 279, Springer-Verlag Berlin (1990).
7. F. Gao, G.L. Carr, C.D. Porter and D.B. Tanner, Phys. Rev. B 43, pp. 10383 - 10389 (1990).
8. A. Hadni and X. Gerbaux, Infrared Phys. (1993).
9. Da - Wei Zhang, Thesis, UCLA (1992).
10. P. Richards, preprint.

Measurements of the Far Infra Red Laser Transmission of $Y_1Ba_2Cu_3O_{7-\delta}$ Thin Films

T.P.O'Brien, M.L.McConnell, P.G.Huggard, G.Schneider, W.J.Blau

Physics Department, Trinity College Dublin, Ireland

The properties of HTSC materials in the millimeter and the submillimeter region are of great technological interest at present. The absorptive losses are of particular importance for potential applications, and the nature of these losses can shed light on some of the as yet unresolved issues pertaining to the mechanisms of superconductivity in these materials. We report measurements of the transmission of the Far Infra Red radiation through thin films of $Y_1Ba_2Cu_3O_{7-\delta}$ at a range of frequencies from 13.5cm^{-1} to 250cm^{-1}. The films were produced using the *in-situ* laser ablation/deposition technique onto MgO substrates and ranged in thickness from 100 to 250nm.

The chopped, continuous wave FIR radiation was generated using an optically pumped low pressure gas laser operating on methanol, formic acid, methyl flouride or dimethyl flouride. The maximum CO_2 laser pump power was approximately 50 Watts CW when operating on the 9P36 transition, and FIR power from 5 to 120 mW was generated depending on the laser line.

For the transmission measurements, the superconducting sample was mounted in a closed cycle He fridge, with two FIR windows. The temperature was controllable from 12 K up to room temperature with an accuracy of 0.2 K. The transmitted radiation was measured using a Golay Cell Detector with a responsivity of 10^3V/W. A Mylar beam splitter provided a reference signal which was measured using a pyroelectric detector. The transmissivity of the optical train was determined at each frequency without any sample in the fridge, and was found to be independent of the fridge temperature to within the accuracy of the measurement. Absolute transmission data (for the film and substrate) obtained at room temperature without the fridge could therefore be used to scale the relative transmission measurements made as a function of temperature with the sample mounted in the fridge. The temperature dependent data was obtained in the form of the ratio of the power transmitted through the beam splitter, fridge, and the sample to the power reflected to the reference detector. It was found that the ratio of the reflectance to transimttance was sensitive to the precise cavity length of the pump laser. Thus the cavity length was adjusted to maximise the FIR power before each transmittance ratio was measured.

For all the frequencies measured the transmisson of the superconductor-substrate samples was found to drop as the temperature was reduced towards T_c. At low frequencies a sharp reduction in the transmission was observed at T_c, followed by a levelling off at temperatures below $T_c/2$. At frequencies above 120 cm^{-1} the size of the step at T_c decreased with frequency. The onset of strong absorbtion in the MgO substrate at approximately 100 cm^{-1} makes quantative interpretation of the data difficult at frequencies above 100cm^{-1}.

A computer simulation using a frequency and temperature dielectric function for MgO (as determined by T.R. Yang et al.), a Drude type conductivity for the normal state of the superconductor and a two fluid model for the superconducting state was used to model the optical properties of the sample. The conductivity of the superconducting films were thereby obtained at millimeter and submillimeter wavelengths. A temperature dependent Drude relaxation rate was required to fit the normal state data at all frquencies, with the relaxation rate inversely proportional to the temperature. When the dependence of the penetration depth on film thickness is taken into account, the two fluid model can fit the observed optical properties at frequencies up to 200 cm^{-1}. A two fluid temperature dependence for the penetration depth produces the best fit to the data at all frequencies. No evidence is seen for quasiparticle excitation, or pairbreaking over the range of frequencies studied.

Far infrared ellipsometric study of HTSC gap in ab- and c-oriented epitaxial YBaCuO films

A.B.Sushkov* and E.A.Tishchenko

P.L.Kapitsa Institute for Physical Problems, Russian Academy of Science,
Kosygina str. 2, 117973 Moscow, Russia

*Institute of Spectroscopy, Russian Academy of Science,
142092 Troitsk, Moscow region, Russia

1. INTRODUCTION

To test different models of HTSC and to study mechanism of this phenomenon comparison of the measured complex dielectric function $\varepsilon(\omega,T)$ and of the computed one is very useful. In the case of anisotropic substance, such as $YBa_2Cu_3O_7$, $\varepsilon(\omega,T)$ is tensor with different $\varepsilon_a, \varepsilon_b, \varepsilon_c$ components. However, the structure of oriented YBaCuO films permits to determine ε_c and only averaged ε_{ab} value. To carry out ellipsometric measurements on small samples in far IR the light beam should be focused onto the sample surface. Earlier we find an original decision of the *direct* problem of convergent beam ellipsometry[1] (CBE). This report is devoted to the *inverse* problem of CBE for the following reflecting system: 1-axis anisotropic film on isotropic substrate. By this technique we have obtained temperature dependencies (4 — 300 K) of ε_{ab} and ε_c at fixed laser frequencies 84, 120, 357 cm^{-1}.

2. ELLIPSOMETRIC SCHEME AND PARAMETERS

We use PSA-scheme or $PW_1W_2SW_3W_4A$ if sample is in cryostat. The expression for detected signal $I_D(A)$, where A is analyser angle, was found in[1].Two ellipsometric parameters of the polarisation ellipse azimuth χ and ellipticity γ both averaged over the aperture in output plane of CB ellipsometer can be as measured, as computed:

$$\chi = A_{min} \tag{1}$$

$$\tan^2(\gamma) = I_D(A_{min})/I_D(A_{min} \pm \pi/2) \tag{2}$$

Working without compensator we lose information about the sign of ellipticity γ.

3. CRYOSTAT WINDOWS

Windows must be *thin*. It means that convergent beams, reflected inside window plate, all must have the same focal point. Because of this reason, due to its transparency in visible and far IR and also due to its low temperature properties we use 50 mkm mylar as material both for warm and cold windows. Two characteristic features of mylar are essential for us: anisotropy of the optical constants[2] and a short time of work at low temperature. These features determine the account of the windows effects. Anisotropic windows can give larger values of ellipticity γ_i^c than good reflecting sample can do. This effect put down an upper level of measured optical constants of the sample, that can be dramatic point for a study of SC transitions. We decide to minimise windows effects by compensating orientation. We have two rotations in our disposal: around x-axis on 90° and around $z(or\ y)$-axis on 180° (Fig. 1).

4. INVERSE PROBLEM

Solving inverse problem, we find such values of parameters of the reflecting system, that error function F has a minimum value[3]:

$$F = \sum_{i=1}^{M} \left\{ (\chi_i^m - \chi_i^c)^2 + (\gamma_i^m - \gamma_i^c)^2 \right\}, \tag{3}$$

where M is the number of measurements (e.g. the number of incidence angles), χ_i^m and γ_i^m denotes angles from the ith measurement, χ_i^c and γ_i^c are the computed values.

Let the film being growthed to have two of principal axis lying in the plane of the film (Fig. 2). Our approach to the decision of the inverse problem in the case of anisotropic reflecting system is based upon that fact, that Fresnel reflection coefficients very weakly depend on N_y, N_z, if XZ-plain is the incidence one. Because, carrying out measurements in Fig. 2 orientation we practically measure N_z value.

Fig. 1. Compensating orientation of mylar windows

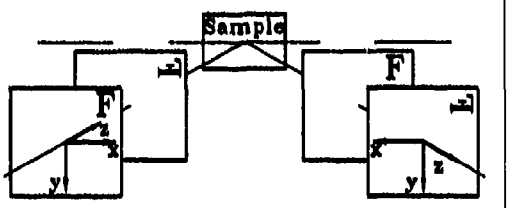

Fig. 2.

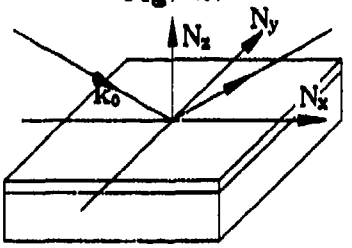

Fig. 3.

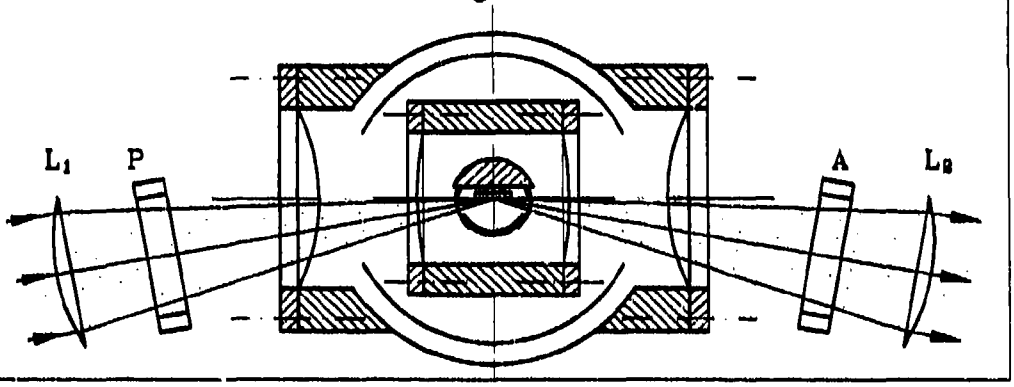

5. EXPERIMENT

Horisontal crossection of experimental setup, excluding H_2O-laser and helium-cooled detector, is in Fig. 3. Sample is in cryoagent's atmosphere. Black polyethylene, surrounding the sample, filtrates short wavelength irradiation. The following measurement routine is used. By Multi-Angle-of-Incidence ellipsometry the thickness of the film is measured. In cryostat without windows for c-oriented film ($N_a = N_c$) χ^m and γ^m are measured. Mylar windows are mounted. χ^m and γ^m are measured again and complex transmission coefficient of windows is known. Temperature dependence of χ^m and γ^m is measured. The film is rotated on 90° for N_{ab} now to be N_a. All this steps are repeated for this ab-orientation. Combined treatment in iterative process, which converges in one step, gives $\varepsilon_{ab}(\omega_0, T)$ and $\varepsilon_c(\omega_0, T)$.

The results obtained will be discussed together with the computed ones by authors of work[4] in frames of the strong electron-phonon interaction.

6. REFERENCES

1. A.B.Sushkov and E.A.Tishchenko, "Far-infrared ellipsometry of convergent beam: theory and experiment", 16 Int. Conf. on IR&MMW, Lausanne, 1991, SPIE v.1576, pp.310-311.

2. D.R.Smith and E.V.Loewestein, "Optical constants of far infrared materials.3:plastics", Appl. Opt., v.14, No.6, 1335(1975).

3. R.M.Assam and N.M.Bashara, "Ellipsometry and Polarised Light", N.-H., A., 1977.

4. S.V.Shulga, O.V.Dolgov and E.G.Maksimov, "Electronic states and optical spectra of HTSC with electron-phonon coupling", Physica C, v.178, pp.266-274, 1991.

Submillimeter wave ESR of copper-oxides

Hitoshi Ohta and Mitsuhiro Motokawa

Department of Physics, Faculty of Science, Kobe University, Rokkodai, Nada, Kobe 657, Japan

Since the discovery of high T_c superconductors the magnetism of various copper-oxides has attracted much interest. Especially the magnetism of strong spin correlation systems in various CuO_4 networks is of great interest because it is well known that the superconductivity is occuring in the CuO_2 plane of the high T_c superconductors. Here we will show some of our works done on copper-oxides by submillimeter wave ESR. Our submillimeter wave ESR can provide the frequency region of 90~3100 GHz and the pulse magnetic field up to 30T. The details of our experimental methods can be found in ref. 1 and 2.

The isolated CuO_4 units stack along c-axis in Bi_2CuO_4 instead of the layered structure in the superconducting copper-oxides. At first this system was inferred to be one-dimensional ferromagnetic compound with easy axis along the c-axis. But from the analysis of our antiferromagnetic resonance (AFMR) of single crystal Bi_2CuO_4 for H//c (Fig. 1) and $H_{\perp}c$, it turned out to be easy-plane type three-dimensional antiferromagnet and the ferromagnetic array of moments which couple by an antiferromagnetic interaction along the c-axis is stabilized by the strong interchain antiferromagnetic interactions.[2] Using a far-infrared Fourier transform spectrometer the zero field AFMR mode was also observed at 13 cm^{-1} which was consistent with our analysis of AFMR. The electron paramagnetic resonance (EPR) was also observed and the g-values were determined to be $g_{//}$=2.26 and $g_{\perp}$=2.04. The line width was determined to be 0.37T which was quantitatively explained by the dipole and anisotropic exchange interactions.

$SrCuO_2$ and Sr_2CuO_3 have very interesting structures and strange magnetic properties. $SrCuO_2$ has two one-dimensional 180° Cu-O-Cu interaction chains along the c-axis which are coupled together by 90° Cu-O-Cu interaction. On the other hand Sr_2CuO_3 has essentially the K_2NiF_4 structure with an one-dimensional 180° Cu-O-Cu interaction due to the corner-linked CuO_4 planar chains along the b-direction. This chain is identical with the one-dimensional $Cu(I)O_4$ planar chains in high T_c superconductor $YBa_2Cu_3O_7$. The strange part of $SrCuO_2$ and Sr_2CuO_3 is that their magnetic susceptibility is very small (about 10^{-4} emu/mol) and they don't show EPR signal for wide temperature range as if they don't have any magnetic moment.[3] The lack of EPR signal is related to the fact that $YBa_2Cu_3O_7$ also does not show EPR signal. But $SrCuO_2$ and Sr_2CuO_3 start to show EPR signals when they are exposed in H_2O atmosphere. The example in the case of Sr_2CuO_3 is shown in Fig. 2. The effect of H_2O should have some connection with the fact that $YBa_2Cu_3O_y$ starts to show EPR signal when y≠7.[3] But the origin of the very small magnetic susceptibility and the lack of EPR signal in $SrCuO_2$ and Sr_2CuO_3 is still an open question.

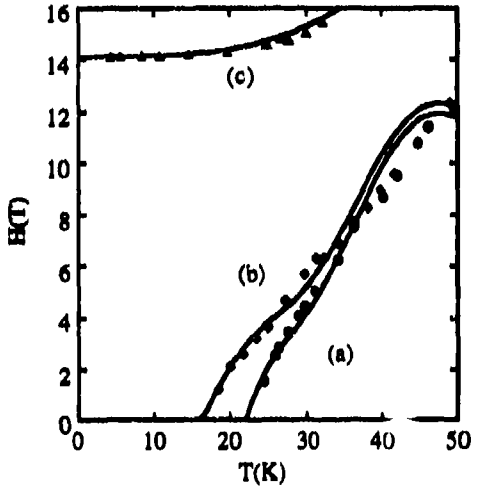

Fig. 1 Temperature dependence of resonance field of Bi_2CuO_4 for H//c-axis at (a) 370.4, (b) 383.3 and (c) 584.9 GHz.

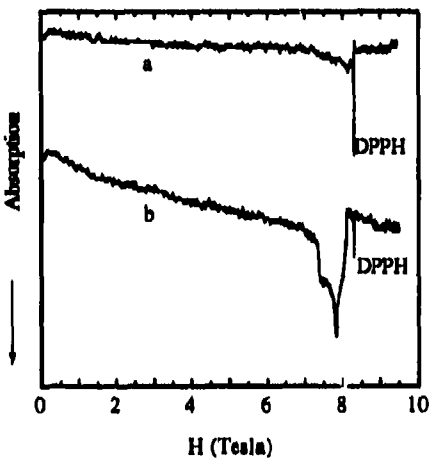

Fig.2 EPR spectra of (a) freshly prepared Sr_2CuO_3 and (b) Sr_2CuO_3 exposed to H_2O observed by using 232.3 GHz line at 86 K.

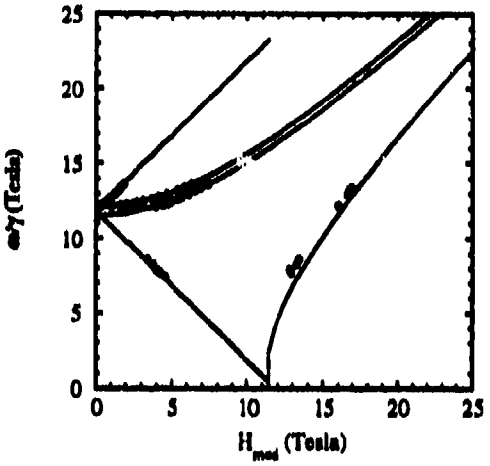

Fig. 3 Frequency-field diagram of observed resonance lines (open circle) for Li_2CuO_2 powder at 1.9K and calculated one (solid lines) by mean field theory.

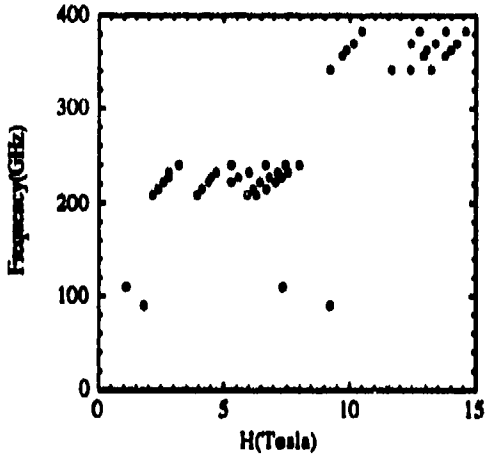

Fig. 4 Frequency-field diagram of observed resonance lines (open circle) for $Y_2Cu_2O_5$ powder at 1.9K.

In Li_2CuO_2 the CuO_4 units form one-dimensional chains along the b-axis sharing the edge with other ones. At firstt Li_2CuO_2 was supposed to be one-dimensional system with ferromagnetic exchange interaction along the chain because of the existence of 90° interaction via oxygen in the chain. But our AFMR measurements below T_N=9.3K and their analysis as shown in Fig. 3 clearly show that this system is three-dimensional antiferromagnet with almost uniaxial anisotropy.[4] The exchange interaction inside the chain turned out to be antiferromagnetic and the ferromagnetic alignment of the magnetic moments along the chain seems to be forced by the strong interchain antiferromagnetic exchange interactions. We also found that the easy axis was perpendicular to the CuO_4 plane which was similar to CuO but was different from most copper oxides with easy plane type anisotropy. The CuO_4 planes also share the edges in CuO as in Li_2CuO_2. Therefore the origin of the easy axis in the case of Li_2CuO_2 and CuO is an interesting problem to be solved.

$Y_2Cu_2O_5$ is known as an impurity phase found in $YBa_2Cu_3O_7$ at the early stage of the investigation of high T_c superconductors. In this system the pairs of edge-shared CuO_4 units are linked in turn by corners of these units. The most interesting magnetic property of $Y_2Cu_2O_5$ is that it shows two successive metamagnetic transitions at 3T and 5T below T_N=13K when the field is applied parallel to the b-axis.[5] As the anisotropy is usually smaller than the exchange interactions in copper compounds, it is very strange to observe metamagnetic transitions in $Y_2Cu_2O_5$. But if we assume strong ferromagnetic exchange interaction in the two edge-shared CuO_4 units to produce dimers with S=1, two metamagnetic transitions can be interpreted by the model used in the case of $NiCl_22H_2O$[6]. We have performed submillimeter wave ESR of $Y_2Cu_2O_5$ as shown in Fig. 4. The ESR modes seem to be changed around 3T and 5T. We have to check if the magnetic resonances observed in $Y_2Cu_2O_5$ can be interpreted by the same model. The g-values of $Y_2Cu_2O_5$ were determined to be 2.29, 2.08 and 2.03 at 86K by our submillimeter wave ESR.

REFERENCES

1. M. Motokawa, H. Ohta and N. Makita, "Submillimeter EPR of Co:Rb_2MgF_4 and anomalous g-values," Int. J. Infrared & MMW, Vol. 12, No. 2, pp. 149-155, 1991.

2. H. Ohta, K. Yoshida, T. Matsuya, T. Nanba, M. Motokawa, K. Yamada, Y. Endoh and S. Hosoya, "EPR and AFMR of Bi_2CuO_4 in submillimeter wave region," J. Phys. Soc. Jpn., Vol. 61, No. 8, pp. 2921-2929, 1992.

3. H. Ohta, N. Yamauchi, M. Motokawa, M. Azuma and M. Takano, "Submillimeter wave ESR of $SrCuO_2$ and Sr_2CuO_3," J. Phys. Soc. Jpn., Vol. 61, No. 9, pp. 3370-3376, 1992.

4. H. Ohta, N. Yamauchi, T. Nanba, M. Motokawa, S. Kawamata and K. Okuda, "EPR and AFMR of Li_2CuO_2 in Submillimeter wave region," J. Phys. Soc. Jpn., Vol. 62, No. 2, pp.785-792, 1993.

5. S-W. Cheong, J. D. Thompson, Z. Fisk, K. A. Kubat-Martin and E. Garcia, "Field-Induced transitions in $Y_2Cu_2O_5$," Phys. Rev. B, Vol. 38, No. 10, pp.7013-7015, 1988.

6. M. Motokawa, "Magnetism of $NiCl_22H_2O$," Proceedings of the 12th International Conference on Low Temperature Physics, pp. 703-704, 1970.

Millimeter waves scanning - new methods and possibilities investigating the high temperature superconductors

M.N.Kotov[1], V.F.Masterov[2], A.V.Prichodko[1], O.V.Smertin[1]

[1]*Microwave Laboratory, Semiconductor Physics Institute*
11 A.Gostauto str., Vilnius 2600, LITHUANIA
[2]*Experimental Physics Department, State Technical University*
29 Politechnitcheskaja str., St Petersburg, RUSSIA

Various experimental techniques are in use at present time to investigate electromagnetic properties of high temperature superconductors (HTS). Usually, integral measurements of a surface impedance or related characteristics are being made. Non-resonance methods are based on the measurements of electromagnetic wave transition through the HTS sample. This technique requires very sensitive equipment unless the samples are very thin, approximately, no more than 100 nm. Resonance methods are more precise but technologically sophisticated and expensive. Specific difficulties occur when measurements are to be made in a millimeter wave (MMW) band due to small dimensions of resonators and samples. In the present work two new experimental methods of investigating the HTS in the MMW band have been proposed. The scheme of the first one is presented in Fig.1 [1]. Powder of $YBa_2Cu_3O_7$ ceramics was put into a capsule and contained by blocks made of glass carbon with buffed surface; a certain pressure was applied to the blocks to make the structure conductive. A circuit shown in the Fig.1 was employed to measure low-frequency voltage-current characteristics (VCCh) of the HTS powder and a dielectric aerial was used to measure the rectification of microwave signal by the HTS. A scanning device was used to control the position of the aerial with respect to the sample. The investigations of low-frequency VCCh have shown that with the temperatures of the sample below the critical temperature T_c, the critical current region appeared on the curve. With the temperatures above T_c no critical current region was observed.

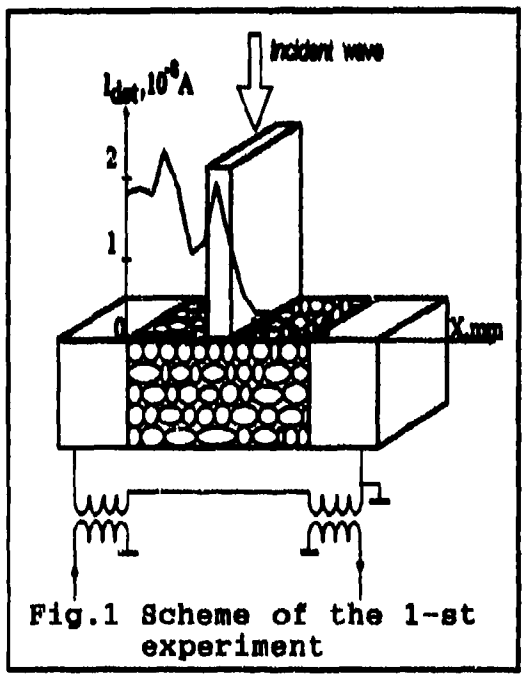

Fig.1 Scheme of the 1-st experiment

The results of the measurements of the dependence of microwave signal (f=29.04 GHz, P_0=1.8 mW) rectification on the position of the aerial are presented in the same Fig. These results as well as the measured stepped dependence of rectificated current on the incident power make us suppose that the Josephson effect took place.

The scheme of the second experiment is presented in Fig.2 [2,3]. The method is based on the experimentally tested fact: the amplitude profile of an open dielectric resonator (ODR) loaded with a HTS sample is sensitive enough with respect to the change of electromagnetic properties of the load. We have carried out the measurements in a 2-mm band using

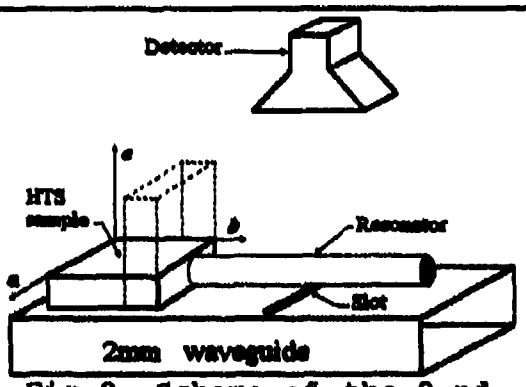

Fig.2 Scheme of the 2-nd experiment

bulk $YBa_2Cu_3O_7$ ceramics as well as single-phase and multiphase $Bi_2Sr_2CaCu_2O_8$ single-crystals. By using the method, we have observed the isotropic effect of the Josephson harmonic generation in bulk ceramic samples as well as anisotropic one in multiphase single-crystals. The experiments have shown the nonlinear dependence of the amplitude of the Josephson harmonics on the incident power. Fig.3 presents such a dependence measured at 77K with a multiphase single-crystal orientated as shown in Fig.2 by solid lines. It should be emphasized that with perpendicular orientation of the sample or with the temperature above T_c, no steps have been observed. Fig.4 presents the temperature dependence of the detected signal for two orientations of the sample. Sharp resonance peaks have been observed at temperatures close to T_c. These peaks seem to be of the same origin as those of the conductivity observed at 60GHz [4].

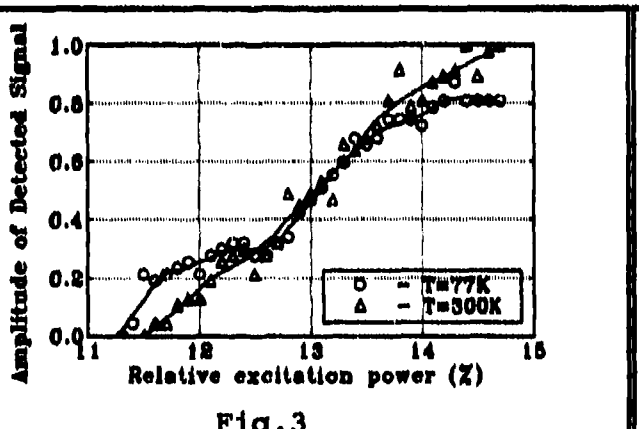

Fig.3

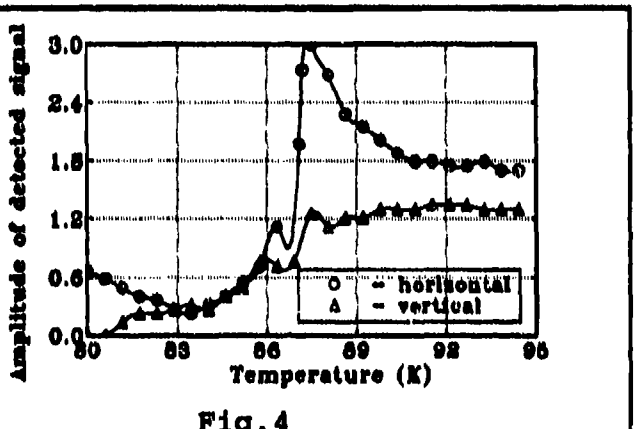

Fig.4

References

1. V.Masterov, A.Prichodko, G.Selmistraitis, A.Chursinov, "Investigation of Josephson effect in weakly-coupled high-temperature superconductors using MW scanner", Int.J. of Infrared and Mm Waves, vol.14, No.3, 1993.
2. M.N.Kotov, V.F.Masterov, A.V.Prichodko and O.V.Smertin, "Simple method for investigating electromagnetic properties of high-T_c superconductors at 2-mm wavelengths", Int.J. of Infrared and Millimeter Waves. vol.14, No.5, 1993.
3. M.N.Kotov, V.F.Masterov, A.V.Prichodko and O.V.Smertin, "Simple method for investigating electromagnetic properties of high-T_c superconductors at 2-mm wavelengths", Int.J. of Infrared and Millimeter Waves. vol.14, No.5, 1993.
4. K.Holczer, L.Forro, L.Mihaly, and G.Gruner, "Observation of conductivity coherence peak in superconducting $Bi_2Sr_2CaCu_2O_8$ single crystals", Phys.Rev.Lett. vol.67, No.1, pp.152-155, 1991.

Local and non-destructive diagnostics of high-T_C superconductor layers by millimeter waves

A. Laurinavičius, F. Anisimovas, A. Deksnys, V. Lisauskas, and B. Vengalis

Semiconductor Physics Institute, Goštauto 11, 2600 Vilnius, Lithuania

ABSTRACT

For the first time millimeter waves are used for non-destructive diagnostics of superconducting layers and their quality control. The quality of the whole layer depending on T_C and ΔT_C is determined by local transmission of millimeter waves.

1. INTRODUCTION

Since the discovery of the high-T_C superconductors, both microwaves and millimeter waves were used for the determination of their surface impedance[1]. The main reason for this interest is good prospects for the application of these materials in microwave and electronic devices. For this purpose it is also very important to know how superconductive properties are distributed in the layer area. Such data would make it possible to receive information about layer homogeneity and its quality.

In the present paper the possibility of millimeter wave application for non-destructive diagnostics of superconductor layers and their quality control is shown for the first time.

2. EXPERIMENT

The main idea of the experiment was local excitation of millimeter waves in superconductor layer and the measurement of their transmission dependence on temperature in different places of the sample. The schematic diagram of experimental set-up is shown in Fig.1. A superconducting layer deposited onto dielectric substrate was placed between special dielectric wavequide probes that provided local excitation and reception of the millimeter waves. The measured sample could be moved in regard to exciting and receiving probes in the x-y plane. Earlier such method was used for semiconductor plate homogeneity control[2]. Spatial resolving power of this method was about 0.5 mm^2.

All measurements were carried out at eighth millimeter wavelengths. Y-Ba-Cu-O and Bi-Sr-Ca-Cu-O superconductor layers deposited onto MgO (100) substrates were used for the experiment. Laser ablation, magnetron sputtering and conventional thermal evaporation methods for the preparation of superconducting layers were used. Measuring samples area was about 1 cm^2. The thickness of superconducting layers was less then 1 mkm.

3.RESULTS AND DISCUSSION

An example of measurement results for Bi-Sr-Ca-Cu-O (2212) superconducting layer is shown in fig.2. Curves presented in this figure show sharp decrease of the transmitted signal in the region of transition from normal to superconducting state associated with the millimeter wave penetration depth decrease. Measurement results presented in Fig.2 clearly demonstrate the difference for T_C and ΔT_C in separate places of the investigated sample. The greatest difference for T_C and ΔT_C, as seen from Fig.2, is about 1K and 2K, respectively. This fact shows inhomogeneous distribution of superconductive properties in the layer area.

4. CONCLUSIONS

Results presented in the paper show that millimeter waves can be successfully used for the contactless determination of such superconductor parameters as T_C and ΔT_C as well as for their distribution in the layer area. The proposed method can be used for the development of superconductor layer technology as well as for the physical research.

5. REFERENCES.

1. G. Müller, N. Klein, A. Brust, H. Chaloupka, M. Hein, S. Orbach, H. Piel, and D. Reschke. Survey of Microwave Surface Impedance Data of High-T_c Superconductors - Evidence for Nonpairing Charge Carriers. J. Superconductivity, Vol.3, No. 3, pp. 235-242, 1990.

2. A. Laurinavičius, P. Malakauskas, and K. Požela.Semiconductor Nondestructive Testing by Helicon Waves. Intern. J. Infrared and Millimeter waves, Vol. 8, No. 5, pp. 573-582, 1987.

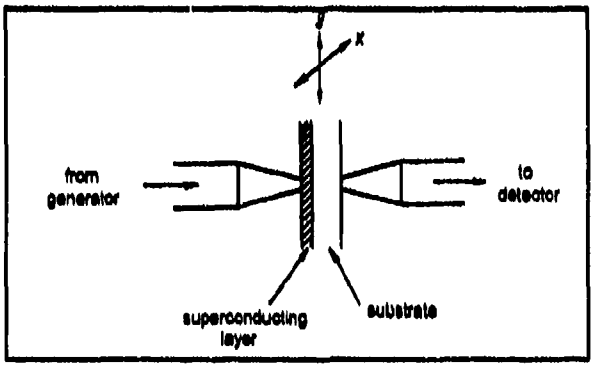

Fig.1. Schematic diagram of the experimental set-up.

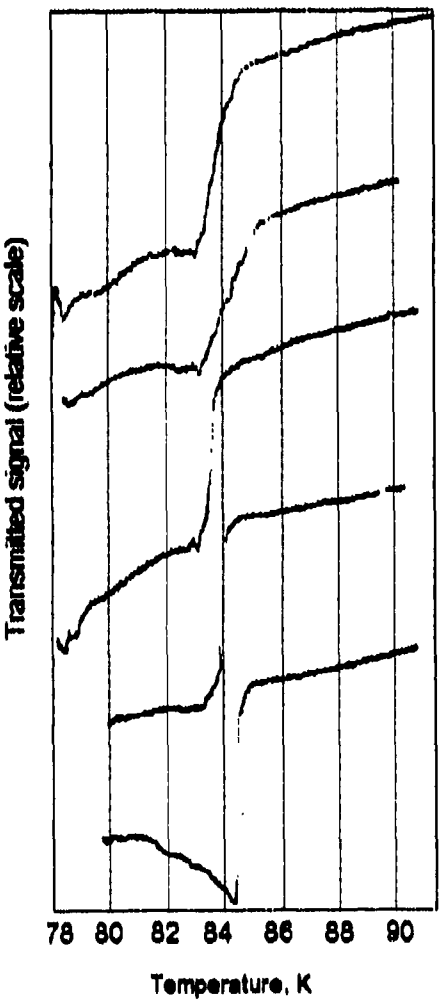

Fig.2. Transmitted signal dependences on temperature in different places of Bi-Sr-Ca-Cu-O (2212) superconducting layer prepared using conventional thermal evaporation method. Curves are shifted along the ordinate to avoid blending.

COLLECTIVE MM-WAVE SCATTERING TO MEASURE FAST ION AND ALPHA-PARTICLE DISTRIBUTIONS IN JET

J.A. Hoekzema, A.E. Costley, T.P. Hughes, J.A. Fessey, N.P. Hammond,
H. Oosterbeek, P. Roberts, A.L. Stevens, P.E. Stott, W. Suverkropp

JET Joint Undertaking, Abingdon, Oxfordshire, OX14 3EA, UK.

1. INTRODUCTION

The fast ion and alpha-particle diagnostic is based on collective Thomson scattering of high power 140 GHz radiation. The main aim of the system will be the determination of the spatially resolved velocity distribution of fast ion populations in JET plasmas, by measuring the frequency spectrum of scattered radiation. A spatial profile of the velocity distribution, with resolution <10 cm, can be determined by scanning the scattering volume (the overlap of the antenna patterns of the launch and receive antennas) over the plasma, using steerable launch and receive mirrors. The diagnostic will be used to measure fast ion populations produced by the heating systems, and will be particularly important in the tritium phase of JET when, by a measurement of the velocity distribution of alpha particles created by fusion reactions, the efficiency of alpha particle heating can be established. It is expected that their velocity distribution can be determined between 0.5 MeV (limited because at low frequency shift the spectrum is dominated by the thermal ion feature) and their birth energy (3.5 MeV) with a typical time resolution of 0.1 s. The principal components of the diagnostic are shown schematically in figure 1. They are: a high power long pulse gyrotron and associated equipment, a heterodyne receiver system and transmission lines. The RF transmission and the receiver system are described in accompanying papers[1,2]. The physics principles of the diagnostic are described elsewhere[e.g. 3,4].

2. TECHNICAL SYSTEMS

2.1 Gyrotron

The source of radiation is a gyrotron which can be operated at up to 300 kW RF average during long pulses (5 s.). The gyrotron operates in a whispering gallery mode ($TE_{15,2}$). A high spectral purity: ratio of noise power to total RF power $P_N/P_0 < 10^{-18}$/Hz, has been verified. High spectral purity is necessary because injected radiation at different frequencies, which is received as stray light, can not be discriminated from the scattering signal. The gyrotron will be operated at ~80 kV, up to 20 A beam current. At higher current it can produce up to 1 MW RF in short pulses.

2.2 Modulation

To discriminate the scattering signal (with equivalent blackbody temperature of a few eV) from the background radiation (few hundred eV, mainly electron cyclotron emission), the gyrotron RF power will be modulated between peak and zero power during a pulse (modulation between two non-zero power levels is also possible). The modulation frequency is high (>10 kHz) to avoid significant modulation of the background radiation due to absorption of the injected radiation in the plasma after reflection from the wall. RF modulation will be accomplished by modulating the anode voltage using a special purpose anode modulator. Special care will be taken to obtain a reproducible RF modulation waveform: the filament supply will be operated at the same frequency and phase locked to the modulation frequency to eliminate a non-reproducible effect of the magnetic field associated with the filament current, an intelligent boost control of the filament supply will be used and the anode voltage will have high stability.

2.3 Protection

In addition to the normal fail to safe protection features of a gyrotron system, there are protection features specific to this particular application. The system is protected (i.e. by switch-off) against operation at the wrong frequency, necessary because a high level of stray light could damage the sensitive detectors if the frequency is outside the range where the detectors are protected by a narrow band notch filter. Several protection features, including a protection against excessive power at the detector, are associated with the possibility of direct sight (or indirect via reflection) of the injected beam by the receiver antenna. It is also possible to protect against operation without plasma (which, after reflection is the dump for the injected power). Since, at least initially, the torus window is inertially cooled and has a long thermal time constant, the window temperature (IR measurement) is also incorporated in the protection system.

2.4 Control

A control system to control the parameters of gyrotron operation as well as the scattering parameters (angle of injection, polarisation) and settings of the receiver system, has been implemented local to the gyrotron. The different subsystems; Gyrotron Systems, Cooling, Transmission and Detection, each have their own PLC, linked to a PC. The HV Power Supplies are CAMAC interfaced to a separate computer. Rotation of mirrors (polarisers, in-vessel mirrors) is done by stepper motors, except for the steerable receive mirror, where two servo motors are used to obtain maximum speed of response for feedback of the mirror orientation during the pulse. This feedback is important at higher densities to maintain an overlap of injected and detected beams when refraction of the beams in the plasma is significant. Extension of the control to the JET diagnostic control room is in progress. A link to the mainframe IBM will make it possible to set up the optimum scattering parameters on the basis of numerical computations (e.g. ray tracing).

3. STATUS

During the last JET operational period the receiver system was used for passive measurements of the background radiation[5]. These measurements confirmed expectations with respect to the background radiation level ,which is important since statistical fluctuations on the background radiation are the main source of noise for the measurement. Transmission systems have been tested at low power, at which they perform satisfactorily. Presently, a prototype gyrotron, on loan from the US DoE, is being commissioned, while a commercial gyrotron is now scheduled for delivery in early '94. New in-vessel components are being installed to make the diagnostic compatible with the new divertor geometry of JET. First plasma measurements are expected to be done after JET operation is resumed in '94. There is a formal and important collaboration with the US DoE on this diagnostic, involving equipment and personnel from MIT and LLNL.

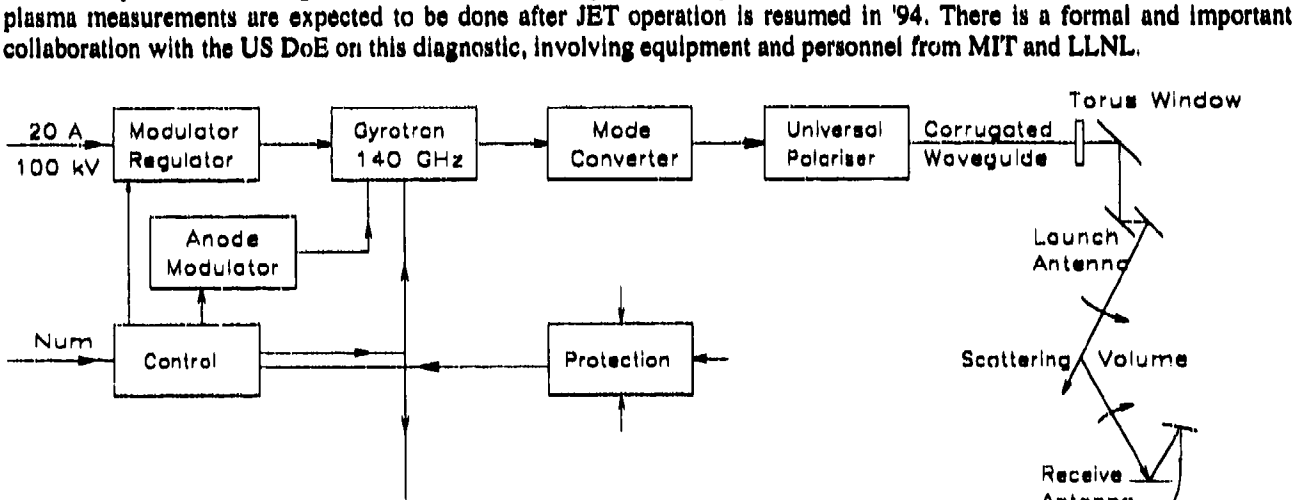

Figure 1: Schematic overview of the diagnostic system

4. REFERENCES

1. J.A. Hoekzema et.al., "mm-wave transmission in the fast ion and alpha-particle diagnostic at JET", this conference.
2. J.A. Fessey et.al., "The receiver system of the fast ion and alpha-particle diagnostic at JET", this conference.
3. A.E. Costley et.al., "A Thomson scattering diagnostic to measure fast ion and alpha particle distributions in JET", Report JET R(88)08 (1988).
4. H. Bindslev, "Dielectric effects on Thomson scattering in a relativistic magnetised plasma", Plasma Phys. and Contr. Fusion, Vol 33, pp 1775-1804 (1991).
5. J. Machuzak et.al., "Receiver calibration of the JET fast ion and alpha particle diagnostic", Rev. Sci. Instr., Vol 63, pp 4648-4650 (1992).

State of the art of gyrotron investigation in Russia

V.A.Flyagin, A.L.Goldenberg, V.E.Zapevalov

Institute of Applied Physics of Russian Academy of Sciences,
46, Uljanova str., 603600, Nizhny Novgorod, Russia.

ABSTRACT

Parameters of modern family of ECRH 0.5 MW gyrotrons are described. Some outlines of strategy of elaboration of new family of ECRH gyrotrons with 1 MW output are given.

INTRODUCTION

For ECRH systems at fusion plasma installations, the family of 0.5 MW gyrotrons with near - 1 s pulse duration at frequency range from 53 up to 160 GHz is created (see table 1). These gyrotrons satisfy the most part of modern fusion devices. For future ones, RF output power 1 MW and pulse duration 10 s or CW regime are regarded as obligatory. Problems of development of the new family of ECRH gyrotron can be classified in following 4 groups.

1. Creation of intense electron helical beam with low velocity spread and rather large share of gyration energy and transportation of the beam to resonant cavity;

2. Selective excitation of an operating mode with high efficiency in highly oversized gyrotron cavity;

3. Spatial separation of electron beam from RF radiation and high-efficiency conversion of the operating mode into wave beam which is convenient for its emission from gyrotron and further transportation to load;

4. Effective thermal drain from thermal loaded gyrotron's parts (cavity, collector, internal mirrors and output window).

Generally the accomplishment of the 1 MW long pulse gyrotrons will require larger dimensions of all their main parts and higher operating modes.

1.ELECTRON FLOW

For computation and optimization of gyrotron's electron gun, the adiabatic theory[1], trajectory analysis[2] and experimental methods[3] are used. In the latest time, the more attention is paid to theoretical and experimental determination of the velocity distribution functions of electrons in gyrotrons. Some experimental distribution functions in a 140 GHz/0.5 MW tube given in Fig. 1 show explicit changes in their width and form at various beam currents. These changes can influence the beam's stability and gyrotron's efficiency.

The stability of an electron beam actually defines the maximum electron beam current. There can be various mechanisms of instabilities, particularly associated with potential depression in beams[4]. At typical parameters of gyrotrons, thresholds of such instabilities can be overcome at currents near 50 A, which are necessary for 1 MW tubes. The deformation of the electron velocity distribution function can be a signal of some instabilities in electron beams.

2. SELECTION OF OPERATING MODE

The calculation of oscillations in a gyrotron cavity is carried out using the non-linear theory of multimode gyrotron[5]. In principle it is possible to attain 1 MW level at frequencies up to 110 GHz with modes which are proved to be stabilized by rather ordinary means of electron and electrodynamic selection[6]. Now new experiments are planned to check the stability of operating modes at 1 MW gyrotrons at frequencies up to 150 GHz.

3. SEPARATION OF ELECTRON BEAM FROM RF RADIATION

In ECRH gyrotrons an electron beam is separated from RF radiation by means of an quasi-optical mode converter. Internal mirrors transform the radiations into a narrowly directed wave beam escaping a gyrotron through its output window transversely to the tube's axis. This provides relatively high resistance of such gyrotron against reflections in an external transmission line and protects a window against bombardment by stray electrons, ions and neutrals especially during internal breakdowns.

Measurements of the spatial structure and frequency spectrum of the output radiation allow to estimate the mode contents and to design first elements of an external transmission line. Results of measurements of the structure of the output wave beam of an industrial 110 GHz gyrotron are given in Fig.2. The analysis of it shows that with attained accuracy of measurements about 2 %, in the gyrotron the single $TE_{15,4}$ mode was excited.

4. THERMAL REGIMES

Two kinds of cooling systems are used in long pulse gyrotrons, depending on the ratio of thermal time constant τ_T to pulse duration τ. If $\tau_T/\tau < 1$ the heat capacity of material can be used, while relatively non-intense flow of coolant removes just mean thermal load; if $\tau_T/\tau \geq 1$ rather intense flow of coolant removing the maximum thermal load must be used. For metal parts τ_T can be close to 1 s, for windows τ_T is usually from 10 to 100 s.

4.1. Collector

Designing a collector, the acceptable thermal load and stability of operation to external magnetic fields are to be taken into

consideration. Now in ECRH gyrotrons with over 0.5 s - pulses, scanning of an electron beam along the collector surface by a special coil with alternating magnetic field is usually used.

4.2. Cavity

Thermal load is one of main factors defining an operating mode of gyrotron's cavity. At pulses near 0.5 s duration and cooling based on the heat capacity of cavity's walls, the maximum load reaches 1.5 kW/cm^2. At longer pulses and CW regime an intense flow of coolant is used, and the maximum thermal load in a cavity can be up to 2 ... 2.5 kW/cm^2.

4.3. Mirrors

In 1 MW gyrotrons with pulses longer than 3 ... 5 s, the RF ohmic losses can essentially heat up the mirrors. This leads to necessity of their cooling.

4.4. Window

Usually maximum transmitting power of an output window limits output power of ECRH gyrotrons. Now the main version of an output window for 1 MW CW gyrotrons at frequencies up to 150 GHz is the single-disk sapphire window cooled down to and below the L N_2 temperature.

CONCLUSION

Modern ECRH gyrotrons can not attain the goal of 1 MW multisecond or CW output. For this, new investigations and developments are needed. The most serious problems seem to be associated with stability of electron beams and transmitting power of output windows.

REFERENCES

1. A.L.Goldenberg and M.I.Petelin, "Formation of helical electron beam in the adiabatic gun," Izvestiya Vysshikh Uchebnykh Zavedenii. Radiofizika, Vol.16, pp.141-149, 1973.

2. A.L.Goldenberg et al., "Adiabatic Theory and Trajectory Analysis of Gyrotron Electron Gun," Gyrotrons (Gorky, Institute of Applied Physics, Akad.Nauk SSSR), pp.86-106, 1981.

3. A.N.Kuftin et al., "Numerical simulation and experimental study of magnetron-injection guns for powerful short-wave gyrotrons," Int.J.Electronics, Vol.72, NN 5 and 6, pp.1145-1151, 1992.

4. Sh.E.Tsimring, "Limiting current of the helical electron beam," Radiotechnika et Electronika, Vol.35, N 6, pp.1284-1288, 1990.

5. G.S.Nusinovich, "Mode Interaction in Gyrotrons," Int. J. Electronics, Vol.51, p.457, 1981.

6. A.V.Gaponov et al., "Powerful Millimeter-Wave Gyrotrons," Int. J. Electronics, Vol.51, N 4, p.227, 1981.

Table 1.
Experimental and industrial ECRH gyrotrons.

N°	frequency GHz	output MW	efficiency %	cavity wall losses kW/cm²	pulse duration s	output mode
1	83	0.5	37	1.2	1.5	Gaus
2	82	1.0	50	2.5	10^{-4}	high
		1.5	36	~4	10^{-4}	
3	100	0.5	50	1.3	10^{-4}	high
		1.0	40	2.6	10^{-4}	
4	110	1.0	44	3.1	10^{-4}	Gaus
		0.5	35	1.5	0.5	
5	140	0.8	38	2.5	10^{-4}	high
6	140	0.5	36	1.5	0.5	
		0.5	36	2.6	0.3	
		0.6	34		2	
7	167	0.5	30	3...4	0.7	Gaus

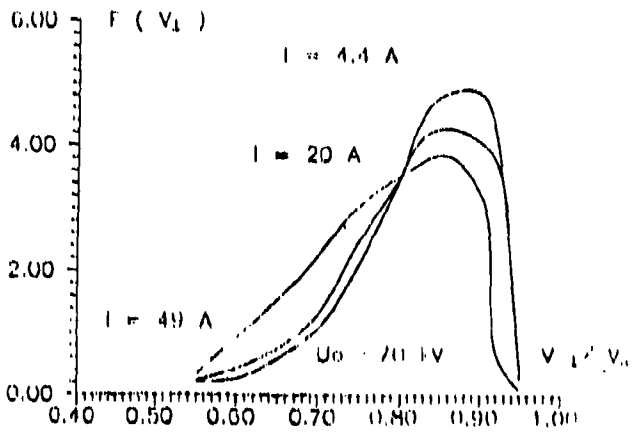

Fig.1. Distribution function of gyrotron velocities in electron beam of 140 GHz gyrotron at various beam currents I.

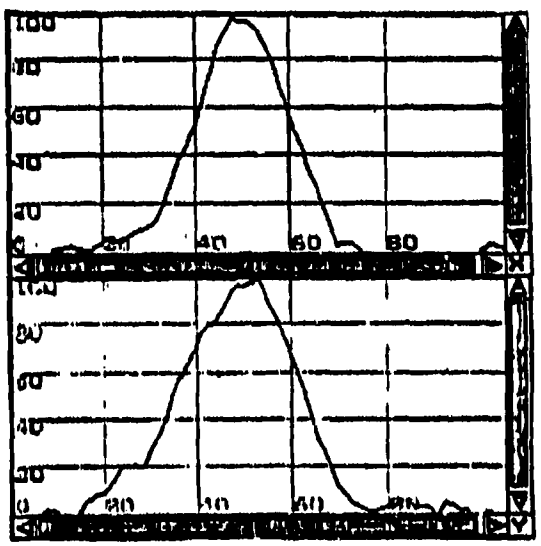

Fig.2. Wave beam structure at output window of 140 GHz gyrotron.
x - horizontal axis,
y - vertical axis.

The transmission lines and antennas of the Tore Supra ECRH system

F.M.A. Smits, G. Berger-by, G. Bon Mardion, J.-J. Capitain,
D. Chatain, J.-J. Cordier, J.P. Crenn, L. Doceul, M. Pain, G.-F. Tonon
A. Dubrovin*, P. Garin*, J.M. Krieg*

Association CEA-Euratom sur la Fusion Contrôlée, CEN Cadarache
F-13108 Saint Paul-lez-Durance CEDEX, France
*Thomson Tubes Electroniques
2, Rue Latécoère, 78141 Vélizy-Villacoublay, France

ABSTRACT

Technical aspects of the installation of the ECRH transmission lines and antennas on Tore Supra are outlined. Six corrugated circular transmission lines will transport each 500 kW in HE_{11} mode at 110 or 118 GHz. Special attention is given to vacuum operation, CW operation, cooling, alignment and support structures, and mode purity measurements.

1. INTRODUCTION

On the Tore Supra tokamak, plasma heating and current drive experiments are planned with high power waves (2 MW in the plasma) in the electron cyclotron frequency range (ECRH) [1]. Tore Supra is dedicated to long plasma pulse operation (210 s), which must be met by the ECRH system. The system must be relevant for ITER. This leads to a high unit source-power and closed transmission lines. The use of cryogenic windows and small wave guide cross-sections requires the lines to be evacuated. A 110 GHz, 350 kW, TE64 prototype gyrotron and HE11 transmission line will be used to study the problems related with vacuum and CW operation. The final generator will consist of a series of six gyrotrons at 118 GHz delivering 500 kW each in HE11 mode or in Gaussian Beam using an internal vlasov converter. These gyrotrons will have cryogenic windows. Reliable simultaneous operation of the whole system will be studied. For current drive experiments, the antenna must allow to direct the power at any radial position in the plasma, and to launch horizontally under angles up to ±30° with respect to perpendicular injection.

2. TRANSMISSION LINES

The transmission line of the prototype consists of a vertical mode conversion section and a horizontal and a vertical HE11 mode section connected by two mitre bends. The power will be dissipated in a load which allows 500 kW CW. The series transmission lines will consist of a polariser at the gyrotron output to produce the polarisation required for launching obliquely into the plasma [2], and a HE11 mode section including four mitre bends to connect the gyrotrons to the antenna.

The diameter of the mode conversion section is 20 mm to reduce its length. Before and after the conversion section, the diameter is tapered to 63.5 mm. The TE64 gyrotron output is consecutively converted to TE04, TE01, TE11 and HE11-mode. Low power antenna pattern measurements have been performed showing a mode purity of 98% for the TE01-TE04-TE64 section (Fig. 1), and a mode purity of approximately 99% for the TE01-TE11-HE11 conversion chain (Fig. 2). Conservatively estimating the ohmic losses in tapers and converters as 16%, total losses in the conversion section are about 19%. The power loss being of the order of 80 kW, active cooling of the converter is required for CW operation. Special mounting techniques are foreseen to protect the gyrotron window for the converter section weight.

The HE11 mode section consists of 2 m long pieces of corrugated aluminium guide with 63.5 mm diameter.

It includes components as bellows, pump sections, mitre bends, vacuum valves and a DC-break, each having almost negligible ohmic losses and low mode conversion losses. To measure the influence of misalignment on the mode purity, a displacement of 2 mm was introduced between two straight sections. Although no interpretation software is available to simulate the resulting antenna pattern, it can be said that the mode content was changed in an important way. The support distance, 2 m, is very different from the beat wavelengths of the HE11 mode with most important other modes. This limits mode conversion, therefore gravity sag between supports (below .2 mm) is not important. Alignment techniques using a theodolite are under development and reach 0.1 mm / m accuracy. Alignment will start from the antenna and end at the gyrotron. Therefore, the gyrotron will be moveable. In the case this fails, a technique has been developed to connect two arbitrarily directed transmission lines using two 90° mitre bends.

3. ANTENNAS

An outline of the antennas has been given in [1]. The launch direction of three assemblies of two beams will be independently variable in horizontal and vertical direction for optimum flexibility. An important difficulty in the design is the cooling of the mirrors. The best solution found suffers from a local plastic deformation due to thermal stress, but stresses stay below the rupture stress (Fig. 3). For technical ease, the antenna will be connected rigidly to the torus port. To avoid alignment problems due to movements of the torus port (of the order of one mm), the transmission lines will be supported by one single beam of 10 m long between the torus and the wall. In this way the misalignment is distributed over 10 m of transmission line.

4. ACKNOWLEDGEMENTS

Alignment calculations of J. Doane and H. Kumric are gratefully acknowledged. The first author was supported by the Commission of the European Communities and EURATOM under grant nr. B/FUS*–91 3005.

5. REFERENCES

[1] M. Pain et al., "Technical aspects of the 110 GHz experiment on Tore Supra", to be published in *Proc. of 17th Symposium on Fusion Technology*, Rome, 1992.

[2] F.M.A. Smits, "Elliptical polarisation for oblique EC-wave launch", *Proc. of 8th joint workshop on ECE and ECRH*, Vol. II, pp. 549-559, Gut Ising, 1992.

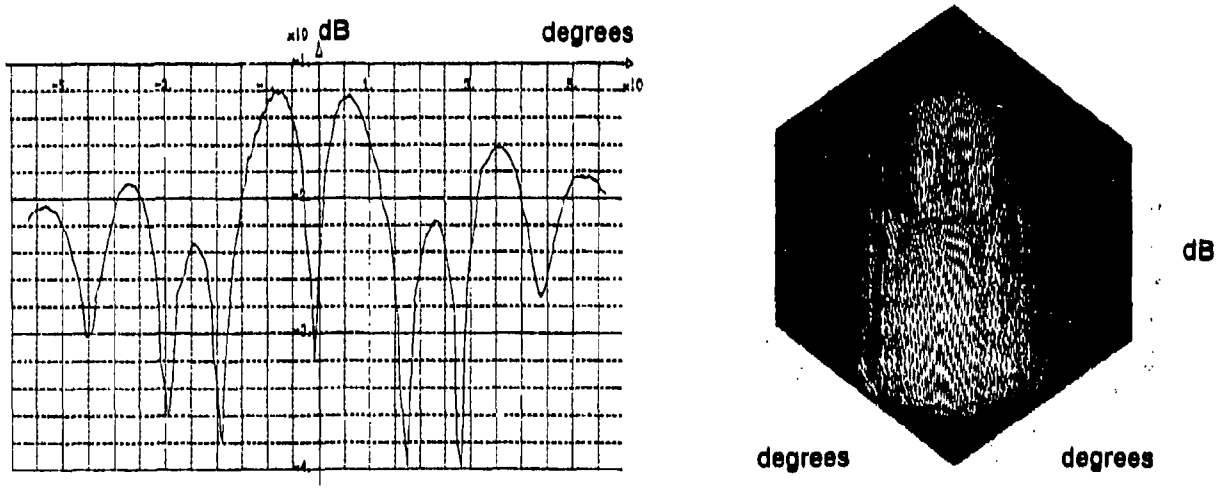

Fig. 1. The antenna pattern of the rotating TE64 mode (**E**-polarisation perp. to the radial coordinate **r**)

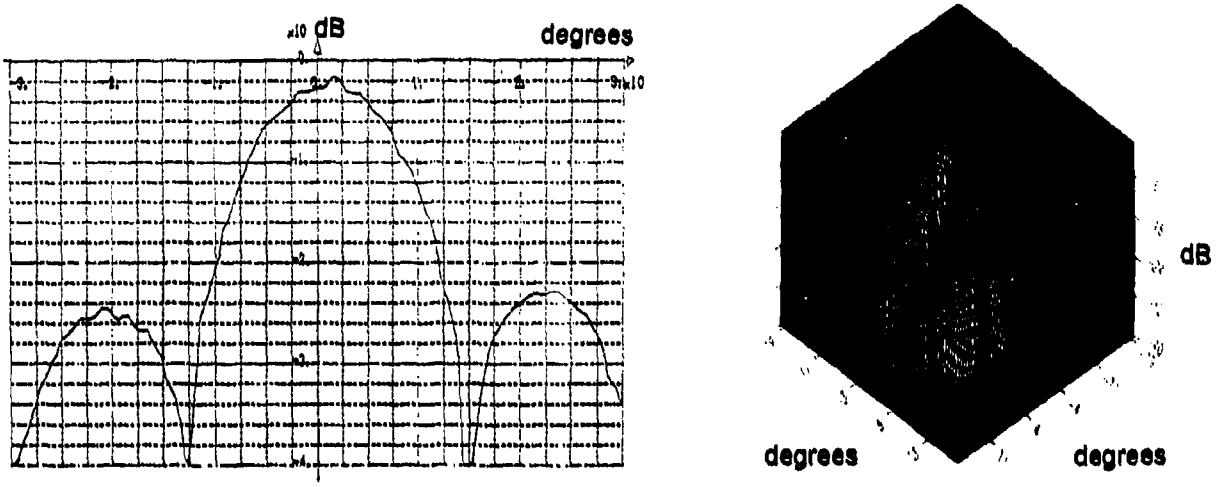

Fig. 2. The HE11 mode antenna pattern (2D-plot: E-plane scan, $\mathbf{E} \parallel \mathbf{r}$) , (3D-plot: $\mathbf{E} \perp \mathbf{r}$)

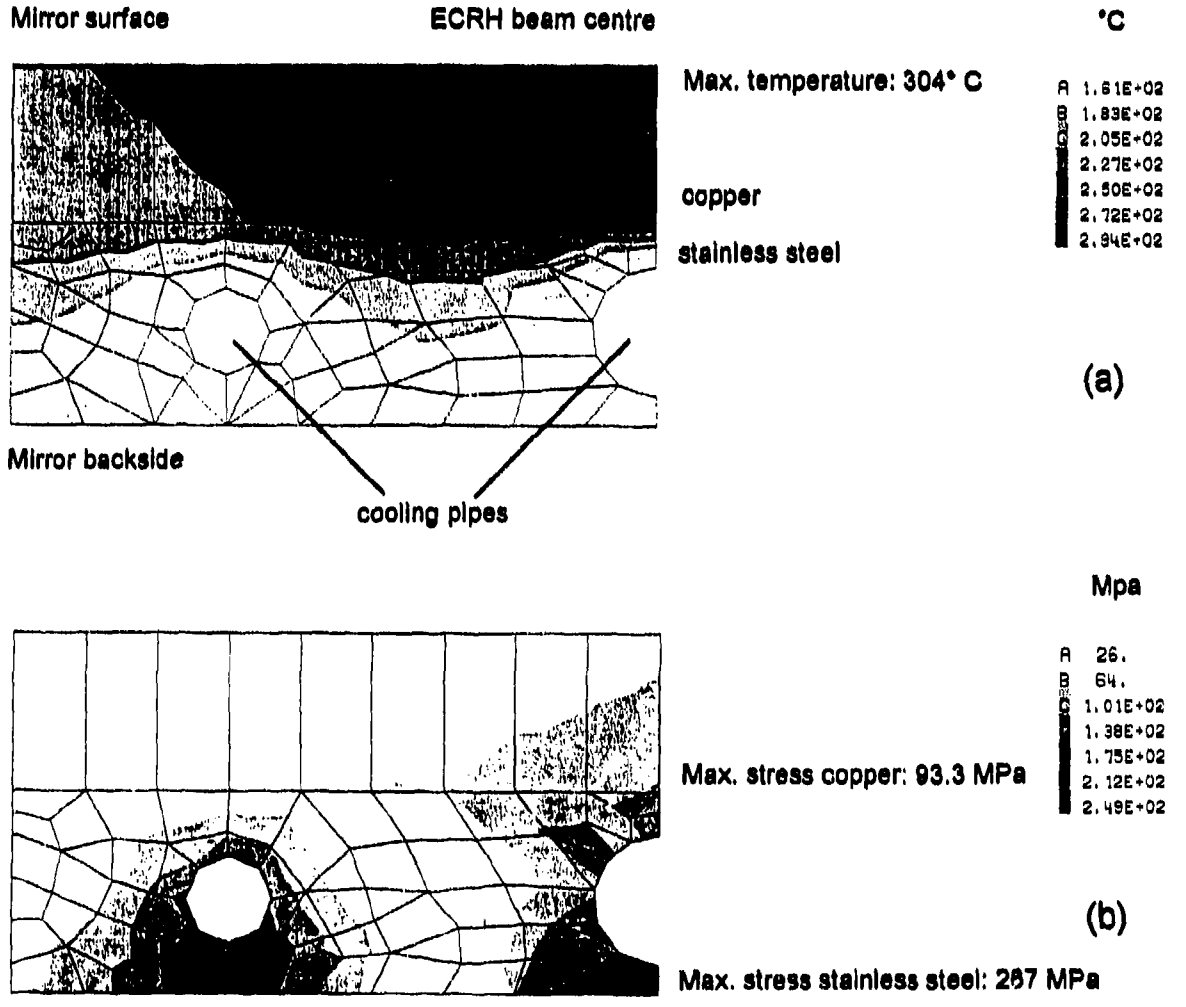

Fig. 3. (a) The temperature chart and (b) the mechanical stress chart of one half of the antenna mirror

MM-WAVE TRANSMISSION IN THE FAST ION AND ALPHA-PARTICLE DIAGNOSTIC AT JET

J.A. Hoekzema, N.P. Hammond
JET Joint Undertaking, Abingdon, Oxfordshire, OX14 3EA, UK

A combination of quasi-optical and in-waveguide propagation is used for transmission of high power 140 GHz gyrotron radiation to the plasma and low power scattered radiation to the detection system in the JET fast ion and alpha-particle diagnostic[1]. The systems have wide band (110-180 GHz) transmission characteristics. Several components are described in more detail in reference 2.

1. HIGH POWER TRANSMISSION

1.1 Quasi-optical converter and polariser

The $TE_{15,2}$ mode generated by the gyrotron is converted to a Gaussian beam using a quasi-optical mode converter. A high efficiency converter, using deformations of the feed waveguide, is in preparation to replace the existing standard converter. The feed waveguide of the converter has an internal diameter of 88.9 mm, equal to the gyrotron output waveguide. This requires large dimensions (the total height of the converter is 4 m.) but avoids a downtaper and consequent reflection of spurious high order modes and should give high power (MW) handling capability at atmospheric pressure. The converter is mounted inside an airtight and radiation tight box (PVC with Al cladding) and stray radiation is mainly absorbed by water in low velocity cooling channels. The required polarisation of the radiation is also produced quasi-optically. The polarisation at the plasma should be such that coupling is to the O-mode or the X-mode. Since injection will generally be angled in the toroidal direction, both modes require elliptical polarisation. The linear polarisation at the output of the mode converter is converted to the required elliptical polarisation by means of a universal polariser. This consists of a rooftop mirror facing a corrugated mirror. Rotation of the polariser as a whole rotates the polarisation while rotation of the corrugated mirror creates the required amount of ellipticity. The polariser is also mounted inside an airtight box. An arc detector, looking at the corrugated mirror, will be incorporated.

1.2 Waveguide transmission

After the polariser, the radiation is coupled at the beam waist into 88.9 mm ID corrugated waveguide, using the excellent coupling of a Gaussian beam to the $HE_{1,1}$ mode. Alternatively, a movable mirror at the entrance of the waveguide can couple radiation from a low power klystron into the waveguide. The low power source is used for alignment of the in-vessel components. The waveguide run is 60 m. long and includes 7 mitre bends. The relatively large diameter of the waveguide will allow high power transmission at atmospheric pressure. In fact the whole transmission system will be at a slight under pressure, equal to the pressure inside the torus hall. Precise alignment of the waveguide (radius of curvature > 3 km) is crucial to avoid mode conversion. Alignment is achieved by precise machining of the 2 m. long waveguide sections and supporting them by constant spring supports which are adjusted individually to counterbalance the weight of the sections. Alignment is then determined by the quality of machining of waveguide and flange connections and the waveguide can move to eliminate the effect of moving support structures (e.g. due to thermal effects). Expansion joints are included and allow fixed positions of the waveguide at both ends and at the torus hall penetration. Most of the waveguide is made of electroformed copper with NiP coating but more resistive sections (plasma sprayed stainless steel) are included after

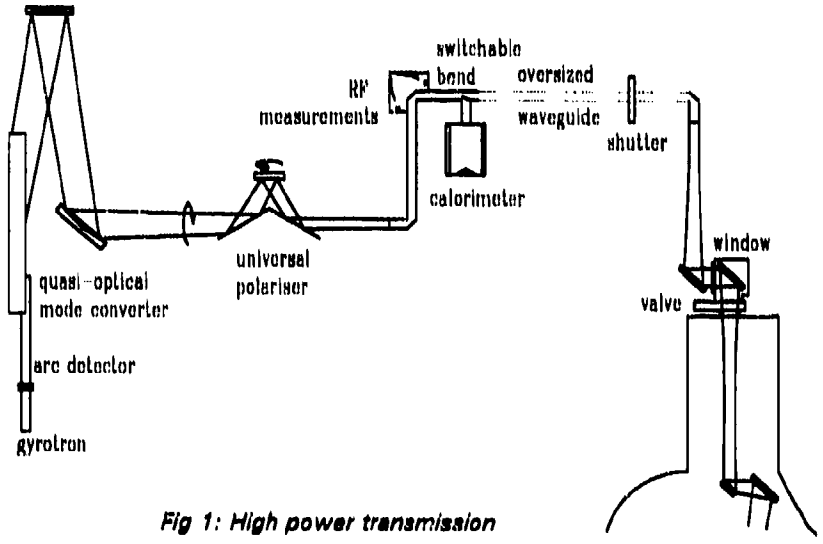

Fig 1: High power transmission

each bend. The increased resistivity has negligible effect on transmission of the $HE_{1,1}$ mode, but gives some attenuation of high order modes. Forward and reflected power measurements are done by coupling some radiation through an array of small (cut-off) holes in one of the mitre bends. By switching a mitre bend the radiation can be re-routed to a silicon oil cooled calorimeter. A mechanical shutter is included in the line for safety reasons.

1.3 Quasi-optical launch

Near the torus the transmission switches back to quasi-optical transmission. The Gaussian beam, launched from the waveguide is allowed to expand to reduce the power density at the torus window. Initially this will be an inertially cooled waterfree fused silica disk with 180 mm clear view. This material has been selected because of the low loss, low expansion, relatively low refractive index and limited temperature dependence of this index. It will allow transmission at the full pulse length (<5 s.) but will have to be operated at an elevated temperature (a few hundred °C) to achieve sufficient radiative cooling between pulses. The quasi -optical system includes 4 slightly elliptical mirrors. The use of pairs of parallel mirrors compensates for the movement of the torus (due to thermal and magnetic effects) which can amount to a few cm. The last mirror is rotatable in two directions. The focused Gaussian beam reaches a waist of 30 mm in the centre of the torus.

2. LOW POWER TRANSMISSION

The scattered radiation is collected by a receive antenna, consisting of two mirrors; a flat mirror which can be rotated in two independent directions and an elliptical mirror which focuses a Gaussian beam (with 30 mm waist in the centre of the torus) into a 10 mm ID corrugated waveguide. This small diameter is chosen to allow bending the waveguide around the divertor structures in the torus. Four additional corrugated waveguides, with ID 7.5 mm are bundled with the main receive waveguide. These slave waveguides collect Gaussian beams slightly displaced from the main beam and larger beam diameter to be used for feedback purposes[3]. The waveguide bundle is supported by an Inconel structure which is sufficiently flexible to allow the movement of the antenna end of the waveguide, mounted on the torus wall, with the torus while at the other end the waveguides are supported off the transformer limbs. The main receive waveguide is tapered up to 31.75 mm, before going through a mitre bend and double disk crystal quartz window assembly. The corrugated waveguide is continued to the detection area (40 m.) where the radiation is launched into a quasi optical polariser to select the correct mode and polarisation. The polariser uses two mirrors with rotatable wire grids which act as quarter and half lambda plates. The slave waveguides end before the vacuum window and radiation is transmitted through the windows quasi-optically. Outside the vacuum, polarisers (again using mirrors with wire grids) select the required polarisation and coupling into fundamental waveguide selects the correct mode. After a converter-taper the radiation is transmitted to the slave detection systems in the $TE_{1,1}$ mode in 27.8 mm smooth waveguide.

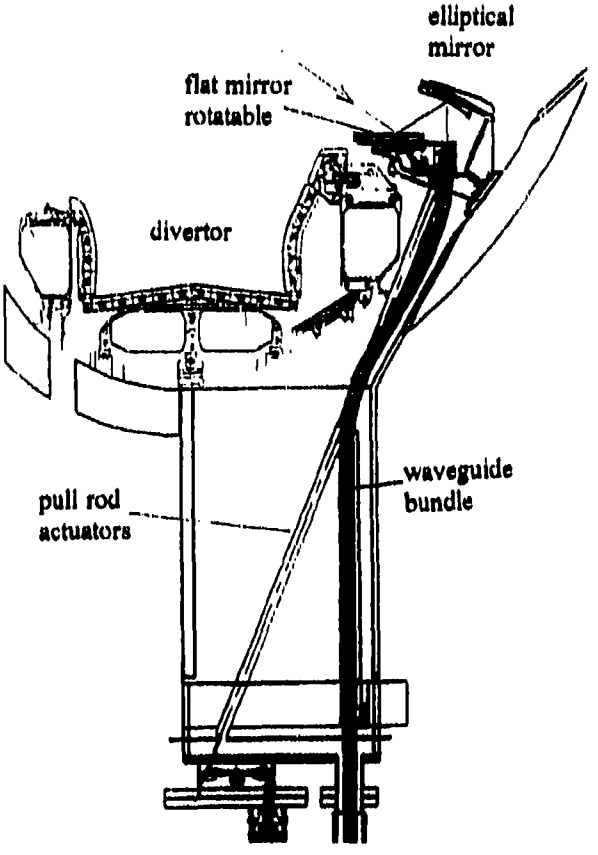

Fig 2: In-vessel components, receive side

3. REFERENCES

1. J.A. Hoekzema et.al., "Collective mm-wave scattering to measure fast ion and alpha particle distributions in JET", this conference.

2. M. Thumm et.al., "Feasibility study on a high power (1 MW) mm-wave (140 GHz) transmission system for diagnostics of fusion alpha-particles in JET by collective mm-wave scattering", Report IPF Stuttgart (1988).

3. J.A. Fessey et.al., "The receiver system of the fast ion and alpha-particle diagnostic", this conference.

Optimization of an Overmoded Smooth-Wall Circular Waveguide Section for Carrying Strong MM-Wave Power in ECRH Experiments

F. Billè *, G. Granucci **, L. Manià *, A. Simonetto **, G. Viciguerra *

(*) DEEI - Università di Trieste - Via A. Valerio 10 - 34127 TRIESTE - Italy
(**) Istituto di Fisica del Plasma - Assoc. EURATOM-ENEA-CNR, Via Bassini 15 -20133 MILANO - Italy

1. Abstract

In this paper we explore the possibility of using sections of overmoded smooth-wall circular waveguide instead of an overall corrugated waveguide transmission line to carry strong mm-wave power in ECRH experiments. To this end we carry out an exact analysis of the transitions from corrugated to smooth-wall waveguide and optimize the length and size of the smooth-wall waveguide to achieve minimum losses. The whole structure is described by a generalized scattering matrix whose elements are obtained using the exact quasi-TE and quasi-TM uncoupled modes in the lossy smooth-wall waveguide.

2. Introduction

The hybrid HE_{11} mode propagating in a corrugated circular waveguide is very suitable for carrying high microwave power in ECRH experiments. The HE_{11} mode propagates with very low losses and with constant linear polarization. On the other hand, in the realization of a long transmission line with corrugated waveguides a few mechanical problems can arise and, in any case, costs are high. It seems therefore justified to investigate the possibility of introducing a few sections made of smooth-wall waveguide in the transmission line.

3. Preliminary considerations.

The hybrid HE_{11} mode is essentialy a combination of the TE_{11} and TM_{11} modes, the ratio between them depending on the corrugation depth. Hence, one expects that connecting the corrugated and the smooth-wall waveguides directly will result mainly in the excitation of the TE_{11} and TM_{11} modes in the smooth-wall waveguide. Morover, if the length of the smooth-wall waveguide is roughly equal to the beat-wavelength λ_B between the two modes, in the corrugated waveguide the modes will again merge into the HE_{11} mode. At the transition the power reflection should be small, in particular if the corrugated waveguide is highly overmoded, as in the case considered here. Namely, we refer to a system operating at 140 GHz, with standard corrugated circular waveguide having an inner radius a = 44.45 mm ($\approx 20\,\lambda$) and a corrugation depth of $\lambda/8$.

4. Global analysis of the structure.

With reference to fig. 1, it is evident that losses are due to:
a) reflection at the two transitions P_1P_1' and P_2P_2';
b) power transfer to unwanted modes at the two transitions P_1P_1' and P_2P_2';
c) attenuation in the smooth-wall waveguide.
The two transitions are modeled by means of generalized scattering matrices S_1 and S_2 (fig. 2), derived with a mode-matching technique. An exact analysis is performed for the lossy waveguide: the wave equation is solved taking into account the conductivity of the waveguide walls and imposing the exact boundary conditions at the interface between the inner region and the metallic wall. This procedure allows us to expand the e. m. field in a set of orthogonal (and therefore uncoupled) quasi-TE and quasi-TM modes, characterized by complex propagation constants. This set of modes is equivalent to a set of uncoupled lines, connecting the network S_1 and S_2; the whole structure is then equivalent to a scattering matrix S, corresponding to the cascade of: S_1 - the uncoupled line set - S_2. (fig. 3).

5. Results.

A set of results are given in fig.s 4 to 9. Fig. 4, 5 and 6 refer to a smooth-wall waveguide length L equal to λ_B. They illustrate the behaviour of the return loss, of the HE_{11} power transfer, and of the power transfer to unwanted modes, respectively, versus the smooth-wall waveguide radius b. As shown, the return losses are

always very small. The optimum value of b for the maximum power transfer is somewhat smaller than a. Moreover, the analysis has confirmed that the optimum value for the length of the smooth-wall waveguide coincides with λ_g, that is 6.63 m for our system. Actually, as shown in fig.s 7, 8 and 9, this value yields the maximum HE_{11} power transfer and the minimum values both of the return losses and of the power transferred to the unwanted modes. The minimum overall losses amount to 4% and are almost entirely ohmic losses.

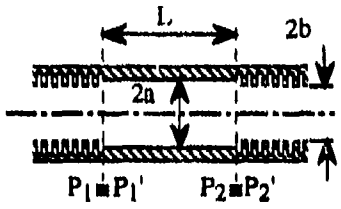

Fig. 1

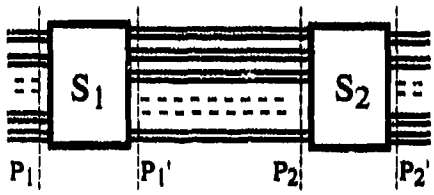

Fig. 2

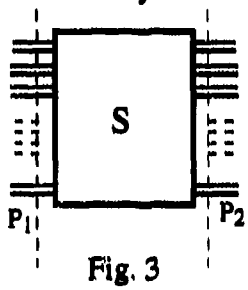

Fig. 3

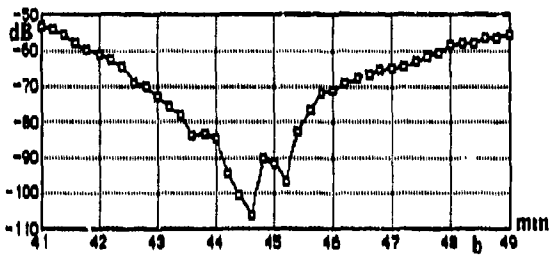

Fig. 4 - Return losses vs. the smooth-wall waveguide radius b

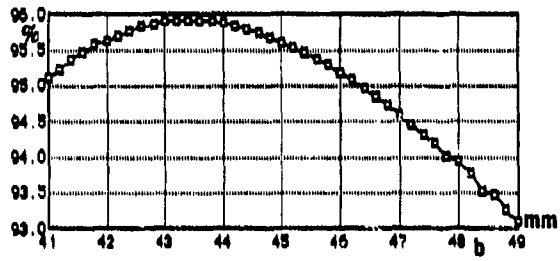

Fig. 5 - Overall HE_{11} power transfer vs. b

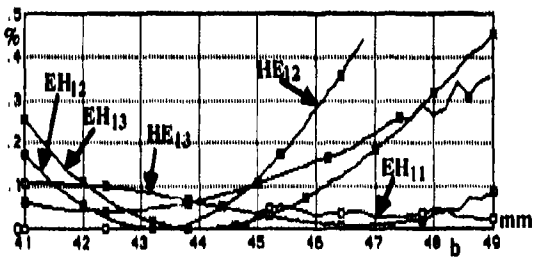

Fig. 6 - Power transfer to unwanted modes vs. b

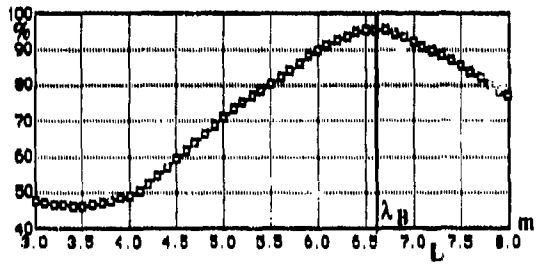

Fig. 7 - HE_{11} power transfer of the smooth-wall waveguide length vs. L

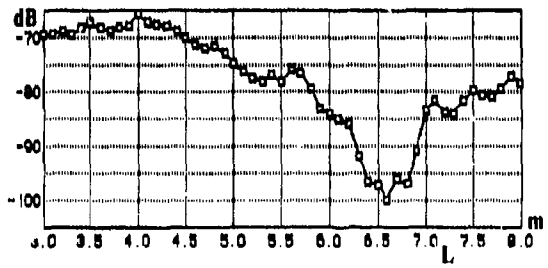

Fig. 8 - Return losses vs. L

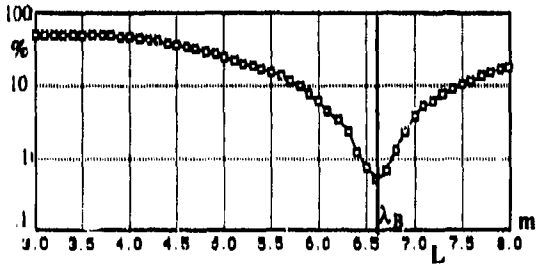

Fig. 9 - Power transfer to unwanted modes vs. L

Radiation Patterns and Optimization of Beam Excitation of Highly Overmoded Corrugated Rectangular Waveguides

Bradley C. Brown, Jeffrey A. Lorbeck, and Ronald J. Vernon
Department of Electrical and Computer Engineering
The University of Wisconsin- Madison
Madison, Wisconsin 53706

Abstract

It may be helpful to use a rectangular geometry for the output window in high power gyrotrons. Coupling through the window might be to an overmoded corrugated rectangular waveguide on the other side. The radiation patterns of such waveguides and the efficiency of coupling to them is discussed in this paper.

Introduction

If high efficiency coupling from a high power gyrotron to a corrugated waveguide is to be achieved, then the radiation patterns of the corrugated guide must be determined. By reciprocity, this will allow us to determine how a beam will couple into the guide from free space. Because the expressions for the radiation patterns are complicated, it is desirable to have approximations for them. Calculations show that the radiation pattern of the HE_{11} mode in a rectangular guide may be closely approximated by a Gaussian beam. Therefore, it should be possible to efficiently inject a Gaussian beam into the corrugated waveguide and excite the HE_{11} mode.

Design Techniques and Theoretical Results

To determine the radiation pattern of the waveguide, the fields inside the guide are needed. These may be found by the method of potentials [1]. For the HE_{11} mode, with the polarization shown in Fig.1, E_x and H_y are the dominant field components and have the greatest influence on the radiation patterns.

Using the geometry of Fig.1 and the expressions for the HE_{11} fields inside the guide, the radiation pattern of the waveguide can be calculated using the Stratton-Chu equations [2]. The plots, shown in Fig. 2, show side lobe levels of -23dB in the E and H planes and a narrow main lobe. It can also be seen that the 3 to 1 ratio of guide dimensions produces a 1 to 3 beam width in the E and H planes. The power in the main lobe is 98.70% of the power carried in the HE_{11} mode inside the guide. This determines an upper limit on the coupling efficiency which may be achieved. Also, the total radiated power found using the Stratton-Chu equations is 99.87% of the power inside the guide.

Using the radiation patterns obtained from the Stratton-Chu equations, it is possible to fit a Gaussian beam to the radiation pattern in the far field [3]. By minimizing the total error in power density, it is possible to determine a best fit to the radiation pattern. To a good approximation, the radiation pattern is separable in the x and y directions, thus the x and y fits may be obtained independently. A typical match is shown in Fig. 4, for which the total error in the power distribution is 1.7%. It has been found that this best match is achieved when the waist size of the Gaussian beam at the guide entrance is 0.63(d/2), where d is the dimension of the guide in the desired direction.

Acknowledgements

This work was supported by the U.S. Department of Energy under contract number DE-FG02-85ER52122.

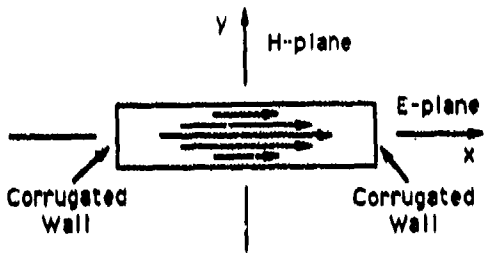

Fig. 1. 6" by 2" corrugated waveguide showing HE_{11} field pattern.

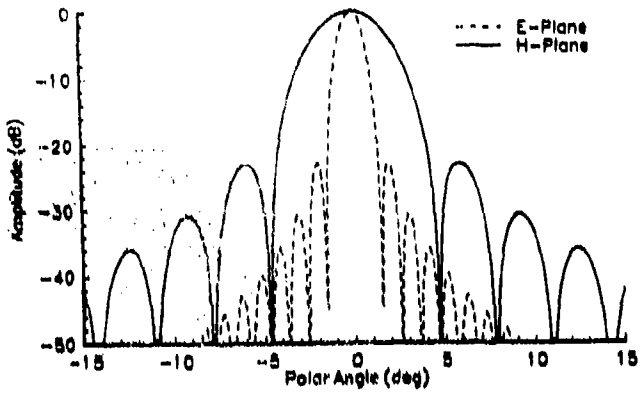

Fig. 2. E-plane and H-plane radiation pattern of HE_{11} mode in corrugated guide.

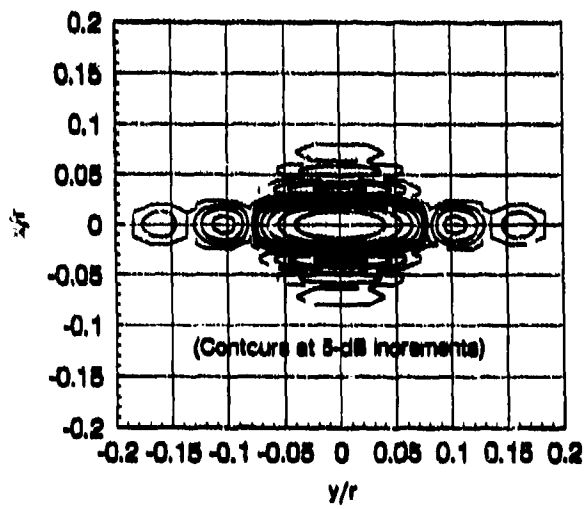

Fig. 3. Contour plot of HE_{11} radiation pattern. $x/r = \sin\theta\cos\phi$, $y/r = \sin\theta\sin\phi$.

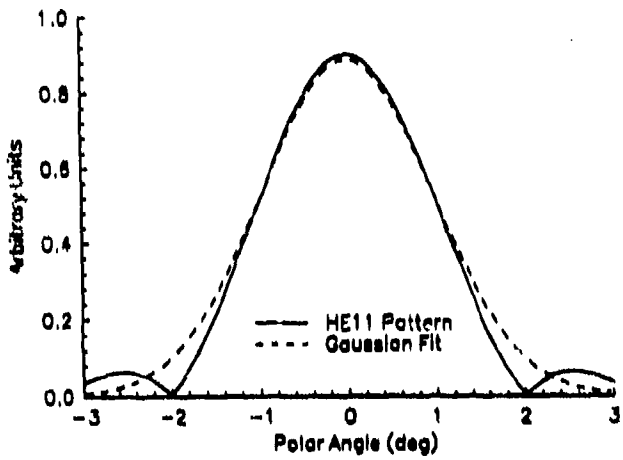

Fig. 4. Gaussian beam fit to HE_{11} pattern in the far field.

References

[1] G. H. Bryant, "Propagation in Corrugated Waveguides," Proc. IEE, Vol. 116, No.2, February 1969.

[2] Jin Au Kong, Electromagnetic Wave Theory, pp. 358-381, John Wiley & Sons, New York, 1986.

[3] L. Rebuffi and J. P. Crenn, "Radiation Patterns of the HE_{11} Mode and Gaussian Approximations," Int. J. Infrared and Millimeter Waves, Vol. 10, No. 3, pp. 291-311, March 1989.

Conditioning Optics for Astigmatic Gaussian Beams at 140 GHz, 0.5 MW

A. Bruschi , S.Cirant , G.Granucci ,A.Simonetto , G.Solari

Istituto di Fisica del Plasma, EURATOM/ENEA/CNR Association - Milano - Italy

ABSTRACT

A Quasi Optical system has been designed to couple the power coming from a Gyrotron with astigmatic gaussian beam output, into an oversized corrugated waveguide (HE11 mode). The fraction of the power injected in the transmission line can be controlled by means of a wire grid beam splitter. Polarization control is provided by two rotating corrugated mirrors of electrical depth $\lambda/4$ and $\lambda/8$ respectively.

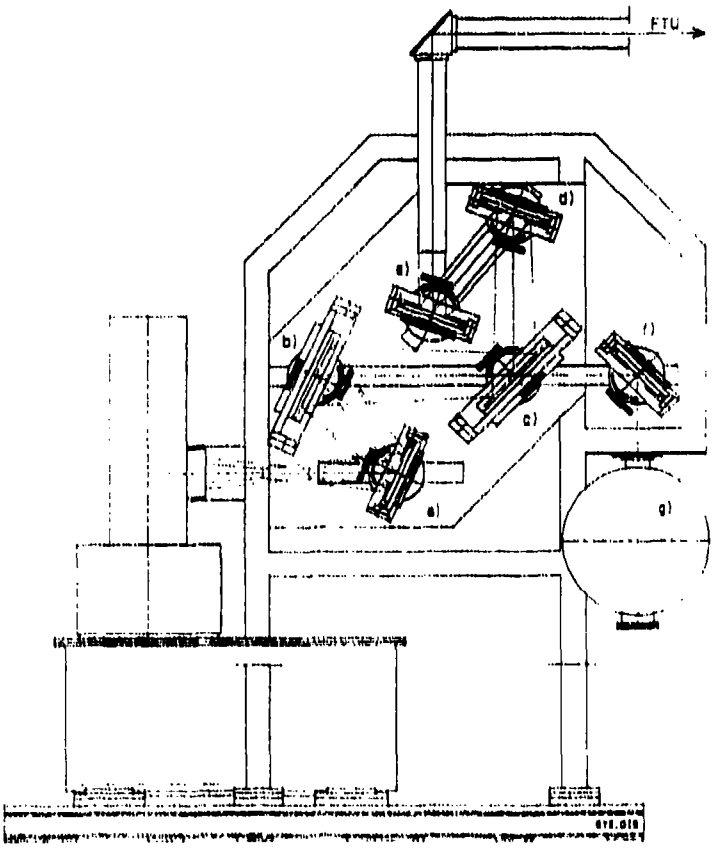

*Fig.1- System outline. a,b) beam shaping mirrors ; c) beam splitter ; d,e) universal polarizer ; f) converging mirror ; g) matched load . The beams in the picture have 4*w transverse dimension.*

1. DESIGN GUIDELINES

Presently available 140 GHz gyrotrons with quasi optical output need shaping optics to symmetrize the astigmatic beam emerging from the window. That can be done reducing first the divergence of the beam in the plane where it has the major spread, by the mirror a) of fig.1), so to equalize the beam radii at a given position; then placing there a second mirror to perform the phase matching with the gaussian beam which maximizes the power transfer (98%) to the HE11 mode of the waveguide. At present only the fundamental

g.b. mode has been considered. Any power in higher order modes that may be present at the gyrotron output will be reduced more than the power in the fundamental mode due to higher diffraction losses on the finite size mirrors. The surfaces of the mirrors a,b) are computed point by point equating the local phase of the incident beam to the local phase of the desired one. This procedure cancels the phase aberration introduced by the "thin lens" approximation in the classical design of q.o. mirrors. The machining of surfaces described with a matrix of points is sometimes more difficult than the machining of the correspondent zero order analytical solution (ellipsoid or hyperboloid); anyway, if the given incident or reflected gaussian beam has no well established phase center in the zone where the mirror is placed, the entity of the correction may be not negligible.

To design the beam splitter c) of fig.1 a code has been written to solve the boundary problem for a plane wave incident on a perfectly conducting wire grid of infinite extent [1]. Both TE and TM polarization with respect to the direction of the wires, at arbitrary incident angle θ, have been considered. For a given diameter of the wires and provided that the spacing b of the grid satisfies $b < \lambda/(1+\sin\theta)$ the behaviour of this structure can be described, at sufficient distance from the grid, by the complex amplitudes of a reflected plane wave and of a transmitted plane wave only.

It has been found possible to achieve high power reflectivity (>99.5%) of the component of incident E field parallel to wires, while reaching total transmission of the perpendicular component at the given angle of incidence, with relatively thick wires (diameter of the order of $\lambda/4$). Measurements on a prototype have confirmed this expectations. The losses in the case of finite conductivity of the wires material have been estimated using current density on the wire surface computed in the case of perfect conductor. To remove the heat generated during high power operation, capillaries (i.d.=0.35 mm) cooled with forced water must replace the wires.

The changing of the polarization of the beam to the desired one is performed by a couple of flat corrugated mirrors operating at an angle of incidence of 20 deg. The corrugations are semicircles emerging from a plane. The radius and the period of the corrugations have been determined using the same code described above; the correct boundary condition imposed by the corrugated surface is obtained exciting the wire grid with two plane waves in counter-phase and anti symmetric with respect to the plane of the grid. Once a geometry which determines the correct phase difference between the reflection coefficients for TE and TM polarization has been found, the low sensitivity of this parameter with respect to variations of the angle of incidence has been checked. It has been found that, due to the small angular range of the plane wave spectrum of the gaussian beam in object (waist =14 λ), poor mode conversion should arise. The same consideration holds as the wire grid is concerned. All the optics have their dimension transversal to the beam near to four times the local radius of the beam. All the mirror mountings can be moved along slides fixed on a common flat base, which can be shifted up and down with respect to the framework. The position of the framework with respect to the gyrotron is adjustable too. A two-direction angular adjustment is provided for every mirror to match the axis of the waveguide with an acceptable angular error (0.5 mrad).

The beam transmitted across the beam splitter is directed by the mirror f) of fig.1 into the calorimetric matched load [2] g). It is made of an hollow copper sphere (600 mm i.d.) internally coated with a lossy ceramic. The incoming beam has its waist (= 8 mm) placed at the entry hole of the sphere; a diverging mirror placed in the bottom of the sphere has been designed to distribute uniformly the first pass incident power density on the inner surface. An external forced water circuit provides for cooling and permits calorimetric measurement.

2. REFERENCES

[1] L. Argenti et al.,"Polarization Sensitive Reflectors Made by Grids of Thick Wires ", *Conf.Digest. 17th Int.Conf.Infrared and Millimeter Waves*, SPIE Vol.1929, pp.425-426 , Pasadena, California, 1992.

[2] L. Argenti et al., "A Proposal for a Calorimetric Load at 140 GHz for High Power HE11 Transmission Lines", this digest.

A Proposal for a Calorimetric Load at 140 GHz for High Power HE11 Transmission Lines

L. Argenti, A. Bruschi , S.Cirant , G.Solari

Istituto di Fisica del Plasma, EURATOM/ENEA/CNR Association - Milano - Italy

ABSTRACT

Power measurements in mm-wave systems for ECRH are essential during hot tests of Gyrotrons and transmission lines. A matched load made of a hollow copper sphere internally coated with a thin layer of absorbing ceramic is proposed. The collimated beam radiating into the sphere from the waveguide is defocussed by an internal scatterer made of good conductor. An appropriate external water circuit provides for cooling and permits calorimetric measurement.

1. DESIGN GUIDELINES

The optic theory of integrating sphere [1] states that the throughput T, defined as the ratio of the exiting power to that entering the sphere, is given by:

$$T = R^{*}A_e / (1-R^{*}(1-A_t) \qquad (1)$$

where R is the power reflectivity of the inner surface, A_e is the ratio of the exit port area to the sphere surface and A_t is the ratio of the summation of all the port areas to that of the sphere surface.
According to this formula a low throughput (-22 dB, diffused radiation) can be reached with relatively high values of the reflectivity (55%), for appropriate dimensions of the sphere (600 mm i.d.; input hole diameter=88.9mm). A diverging mirror (a) of fig.1) avoids direct reflection of the energy back into the entry hole and spreads uniformly on the walls the impinging gaussian beam. A phase scrambling reflector has been tested as an alternative, less sensitive to the amplitude distribution of the beam to be dumped.
Despite the different range of wavelength at which this devices find common application, measurements taken at 140 GHz on a stainless-steel sphere of 168 mm i.d. gave results (fig.2) of the same order of magnitude of that predicted by the above formula, although weak resonances were observed with a frequency step of the order of 10 MHz . Measurements were taken at holes drilled at different position both covering the inner surface of the sphere with moderately absorbing material (neoprene, 3 and 6 mm thickness) and without any additional absorber.

2. DIELECTRIC CONSTANTS MEASUREMENT

The dielectric constants of the candidate absorber materials for the inner coating were estimated from power reflection measurements on metal-backed samples of different thickness, launching a converging polarized gaussian beam at 140 GHz and using a Thomas -Keating terahertz absolute power meter.
The power reflection coefficients for the polarizations parallel and perpendicular to the plane of incidence were measured at different angles of incidence. For each material, the results for both polarizations for two samples of different thickness were best-fitted using the real and imaginary parts of the dielectric constant as the fitting parameters.
A converging polarized gaussian beam at 140 GHz was made to impinge on each of the samples, and the reflected power was measured using a Thomas-Keating terahertz absolute power meter [2].
The reflection at the metal-backed sample was modelled taking fully into account the losses of the dielectric material. The model used is based on plane wave reflection and transmission [3], improved by taking into

account, via a multi-beam interference process, the walkoff effects due to the finite transverse dimension of the gaussian beam.
It was found that the desired power reflectivity range (70%-40%) can be obtained by choosing the appropriate thickness (0.2 - 0.6 mm) of commercially available aluminium oxide - titanium dioxide blend, deposited by plasma spray technique on metal substrate.

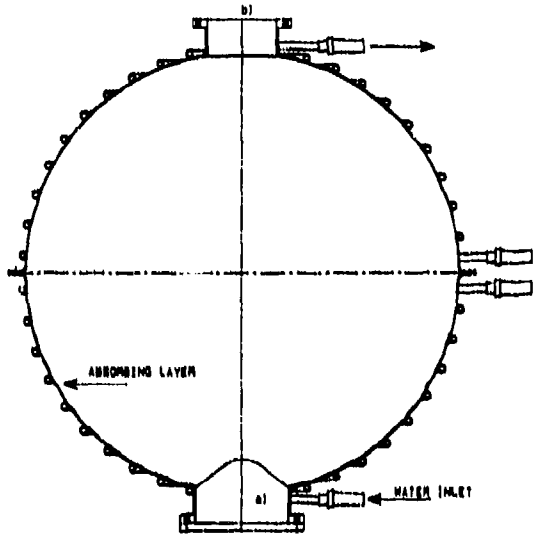

Fig.1- Calorimetric load (i.d.=600 mm) for gaussian beam like radiation a) diverging mirror or phase scrambling surface; b) input flange.

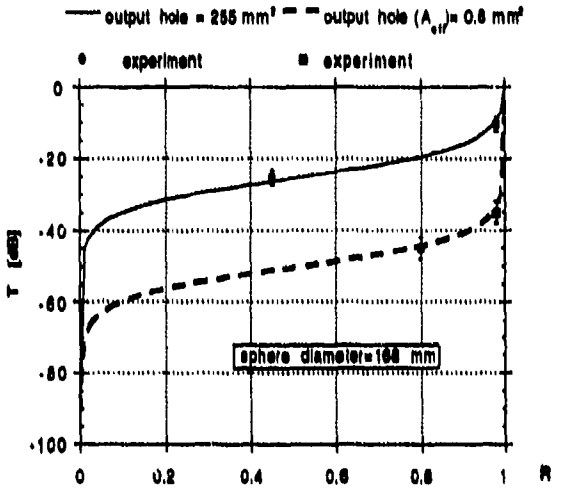

Fig. 2 -Throughput (T) vs. reflectivity (R) for different inner coatings and exit port areas. Error bars account for measurements at different positions and for cavity resonances effects.

3. COOLING SYSTEM

The present system is designed for a 500kW, half a second gyrotron. The corresponding mean thermal load at the walls is 45 W/cm^2, which is 2-3 times lower than that used in industrial application on similar water cooled substrates. Heat diffusion through the thin ceramic layer to the highly conducting substrate limits the peak temperature in the coating.Taking into account the total thermal capacity of the structure (12.5KJ/°C), the mean temperature increase induced by a single shot is of 20 °C. The power from the trapped μwave beam is dissipated as heat to a coolant flow. Using a high accuracy measuring turbine and two precision temperature measuring sensors, absorbed power can be calculated from the flow rate and the temperature differential of the coolant . To allow CW operation a more effective heat removal system must be studied with flow rates of about 6 l/min per 10 KW absorbed power.

4. REFERENCES

[1] D.J.Lovell "Theory and applications of integrating sphere technology", Laser Focus,Vol.20, n.5, pp.86-96(1984)

[2] D.H.Martin,G.W.Paulson and R.J.Wylde "Absolute power measurements for millimeter and submillimeter waves", 16th International Conference on Infrared and Millimeter Waves, M.R.Siegrist, M.Q.Tran, M.T.Tran Editors, SPIE Vol. 1576,210(1991)

[3] C.A. Balanis, "Advanced Engineering Electromagnetics", J.Wiley & S., New York, pp.210-214 (1989)

DIFFRACTION RADIATION OSCILLATORS FOR HIGH-TEMPERATURE PLASMA DIAGNOSTICS AND SPECTROSCOPY

V.P.Shestopalov, B.K.Skrynnik, I.D.Revin, G.P.Ermak

Institute of Radiophysics and Electronics of the Ukrainian Academy of Sciences, 12Acad. Proskura st., 310085 Kharkov, Ukraine

A variety of modifications of microwave oscillators with high frequency stability have been developed in the Institute of Radiophysics and electronics of Academy of Sciences of Ukraine for high-temperature plasma diagnostics and spectroscopy. One of them is named diffraction radiation oscillator (DRO). An operating principle of these oscillators is based on the diffraction radiation effect (Smith-Purcell) arising when an electron beam skims the surface of metallic diffraction grating placed on one open resonator's mirror. They have a low level of frequency noises near the carrirer. For example, this level amounts to -96 dB/Hz at 10 KHz separation from the carrier. Oscillators are retuned in a wide frequency range (20-30%) by displacement of the open resonator's mirror. Main characteristics of the DRO at cathode current 0.1-0.12 A and cathode voltage 2-3 kV are given in the Table.

Two-millimeter range DROs were used in the diagnostic equipment of cooperative scattering of microwave radiation on plasma density fluctuations on the Stellarator L-2.

For the diagnostic equipment there has being developed a homodyne analyzer of asymmetric spectra and module of assembled DROs for heterodyne systems of the reception and observation of scattered radiation spectra in a real time scale on the base of DRO. DROs are synchronizated by a phase lock loop.

For the plasma reflectometry in the conditions of high levels of neutron and γ-radiation an autodyne receiver-transmitter with the electron signal detection has been developed on the base of DRO. DRO-autodyne is an electron-vacuum device combining functions of generator, amplifier, heterodyne and mixer, it is designed for simultaneous radiation and reception of electromagnetic signals of the millimeter wavelength range.

The signal detection is realized by an inner electron detector which consist of two electrods, one of which is transparent for electrons, and the other is a collector. The detector current is recorded in the supply circuit of the collector.

Advantages of the DRO-autodyne are as follows: transmission and reception of signals along one waveguide, absence of semiconductor elements, a possibility of detuning relative to radiation of the SHF-plasma pumping generators, high reliability of electron detector.

DROs were used for making highresolution spectrometer of shortwave part of millimeter wave range. To acheive the high resolution of spectrometer DRO is phase locked by reference oscillator. Spectrometer is designed for investigation of inverse

characteristics of active substance of traveling wave maser in millimeter wave range, spectral characteristics of nucleus polarization targets by EPR with purpose of search for new substances and methods to obtain the high extent of nucleaus polarization.

TABLE

Device's type	Range mm	Output power,W	Electron frequency tuning,MHz	Tuning transconductance MHz/V	MHz/mA
DRO-1	0.8-1.1	0.5-0.1	25	0.5-0.7	0.1-0.7
DRO-1.5	1.1-1.8	0.1-1.8	25	0.5-0.7	0.1-0.6
DRO-2	1.7-2.6	0.3-2.6	30	0.4-0.6	0.1-0.5
DRO-3	2.5-3.9	0.6-5.0	35	0.3-0.5	0.1-0.3
DRO-4-5	3.8-6.0	1.4-10	40	0.2-0.4	0.1-0.4
DRO-6-8	5.9-8.0	3.0-30	60	0.1-0.3	0.1-0.3

Telescope Design Study for the NASA Stratospheric Observatory for Infrared Astronomy (SOFIA)

George W. Sutton
Kent Pflibsen
Kaman Aerospace Corporation
Optical Development Center
Tucson, AZ 85706

H.M. Martin
Steward Observatory Mirror Laboratory
University of Arizona
Tucson, Arizona

Hans Kärcher
MAN GHH
Gustavsburg, Germany

ABSTRACT

A conceptual design study was performed for the proposed "SOFIA" project, which is a 2.5+ meter primary telescope to be mounted in an open port on the side of a Boeing 747 aircraft, aft of the wing. Among the requirements are pointing stability of 0.14" per axis and a blur circle of 1.5" for the telescope in the visible portion of the spectrum. The wavelength band is from 0.3 μm to 1600 μm. The telescope is to be a Nasmyth type so that the instrument package extends into the pressurized cabin for easy access to the experimenter. The designs studied included a centered bearing telescope, a dumbbell configuration similar to the Kuiper Airborne Observatory, and an off-axis configuration with no obscuration. Both attached and unattached Nasmyth tubes were considered. The latter requires an articulated tertiary, so scan noise was calculated. A nonlinear tracking model was used to determine the closed loop pointing stability. Observable star magnitudes were calculated. A survey of primary mirrors was performed, with the spin-cast borosilicate honeycomb sandwich mirror having the best overall qualities. The remaining major issues were identified, including fabricating the air bearing and a laboratory demonstration of the pointing stability in the presence of the aircraft vibration spectra.

PRIMARY MIRROR

The thermal response and figure maintenance of the primary mirror are primary considerations. A survey was taken of both meniscus and honeycomb sandwich mirrors fabricated by various techniques including frit bonding, machining from a solid blank, and spin casting. All except the last can be made from very low expansion glass, such as Zerodur™. An important requirement of the primary mirror is rapid cool down. The recovery temperature in the telescope cavity will be about 240°K. Thermal equilibration of the reflective surface of the telescope is important to minimize the infrared background noise. The telescope cavity will be precooled prior to aircraft takeoff, but this cannot be achieved from all airfields. The honeycomb sandwich mirror with forced ventillation will achieve a time constant of about 40 minutes, which is adequate. A diagram of the forced ventillation is shown in fig. 1, and a top view of the honeycomb sandwich mirror is shown in fig. .2. The thin meniscus, with a thickness of 6 to 10 cm, requires 2 hours which is a major penalty for some observations. While Zerodur™ has a very low expansion coefficient at room temperature, it is much higher at low temperatures. Another consideration is thermal distortion after cool down. For the borosilicate to be adquate, the properties must be uniform. If the properties vary with spatial frequency f, then the maximum peak-to-valley figure error is given by $2^{1/2}\alpha\Delta T/f^2h$, where h is the mirror thickness. ΔT is the total temperature change of the mirror, and α is the coefficient of thermal expansion. For a p-v of 0.1 μm, the requirement is that $\alpha<8E\text{-}9K^{-1}$. The borosilicate glasses can achieve $2E\text{-}9K^{-1}$. Rapid heating could occur during an emergency descent. There is a temperature rate restriction of 94°K/hr on the borosilicate glass to prevent stresses from exceeding 100 psi. This can be mitigated by bleeding dry cold nitrogen into the cavity (to prevent condensation) if the cavity door can be closed. A novel method of checking the figure of entire telescope was conceived which utilizes a pentaprism. The mirror would be supported with a wiffle-tree arrangement using passive hydraulic rolling diaphragm cylinders

TELESCOPE CONFIGURATION

The KAO telescope configuration is a Cassegrain on a dumbell. Initial analyses of this configuration for SOFIA indicated aircraft translational vibration would cause excesstive bending of the Nasmyth tube which made the pointing stability marginal. We initially examined a design with the air bearing in a cage enclosing the entire telescope, see fig. 3, which would obviate this problem. In addition, it minimizes the torques caused by aerodynamic steady and unsteady forces. Howerver, there was insufficient clearance between the two bulkheads to make this concept practical. There were also difficulties involved in removing the primary mirror for servicing. We also examined an off-axis configuration which avoids IR emitting structure in the field of view, and could have a cold stop and cold down beam mirrors. This part of the design study was not completed. However, we were able to redesign the dumbell configuration to increase its stiffness and shorten the length of the Nasmyth tube, see figure 4. This was analyzed for tracking stability, which is marginal only if the unsteady wind torque is 20% of the steady torque. Much lower unsteady torques may be achieved with the use of the aft fairing on the cavity. Note the excellent design of the torquers and the active vibration isolation system shown in fig. 4. The structural material chosen is carbon reinforced plastic because of its high modulus and low expansion coefficient.

OPTICAL PERFORMANCE

The height of the aircraft cavity permitted a full f/1.6 telescope, and the shortened Nasmyth tube a back f/# of f/12. A full optical performance analysis was performed using ZEMAX. All tolerances could be achieved easily. It is planned to have active laser metrology of the secondary decenter and tilt, which we have designed for other systems. A concern was the elastic compliance of the rolling diaphragm hydraulic supports for the primary mirror will change the primary to secondary spacing due to aircraft vibration. A two-degree of freedom analysis showed that for the vibration spectrum, the spacing would not exceed the tolerance if the damping of both the hydraulic supports and telescope vibration isolation system was about 1/2 that of critical damping. A detailed analysis of scan noise was conducted. It was found that a scanning secondary caused a factor of 10 reduction in scan noise compared to an active tertiary. The effect of dust on scan noise was included; our analysis should that the dust noise is a factor of 5 greater than those of the thermal (1°K) inhomogeneity noise and is acceptable for a tracking error PSD amplitude < 0.3 μr/√Hz. The telescope is inertially stabilized; a guide star magnitude of 18 should give a S/N of 10 for the guide star loop bandwidth of 2 Hz.

ACKNOWLEDGEMENTS

Dr. Bobby Ulich made many invaluable suggestions during the course of the study. The optical analysis was performed by Mr. Skip Radau; the scan noise by Mr. Tony Gleckler, and the pointing stability model was developed by Dr. Kent Pfilbsen. The study was funded by NASA Ames Research Center and monitored by Mr. Jerry Hirata and Dr. Ed Erickson.

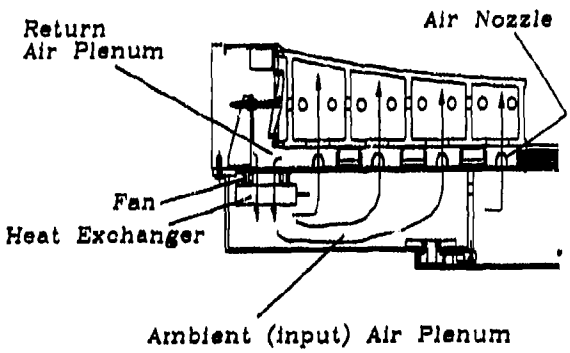

Fig. 1. Side view of part of the ventillation system. It includes multiple fans and heat exhangers and plastic nozzles 25 mm in diameter directed toward each honeycomb cell.

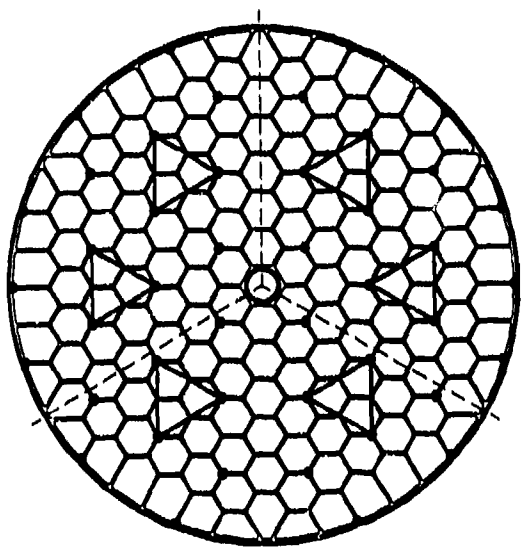

Fig. 2. SOFIA honeycomb sandwich 2.5m f/1.6 mirror showing support points.

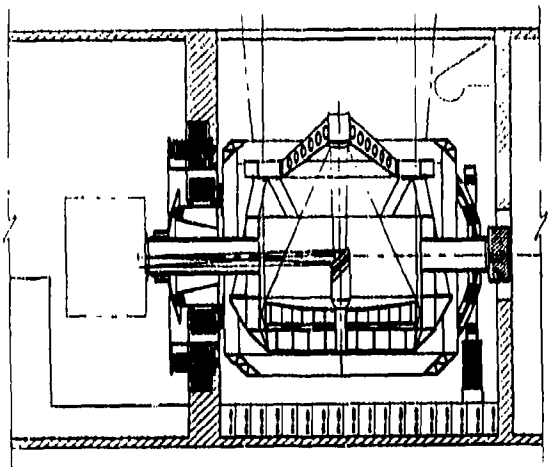

Fig. 3. Centered confiruation of SOFIA telescope

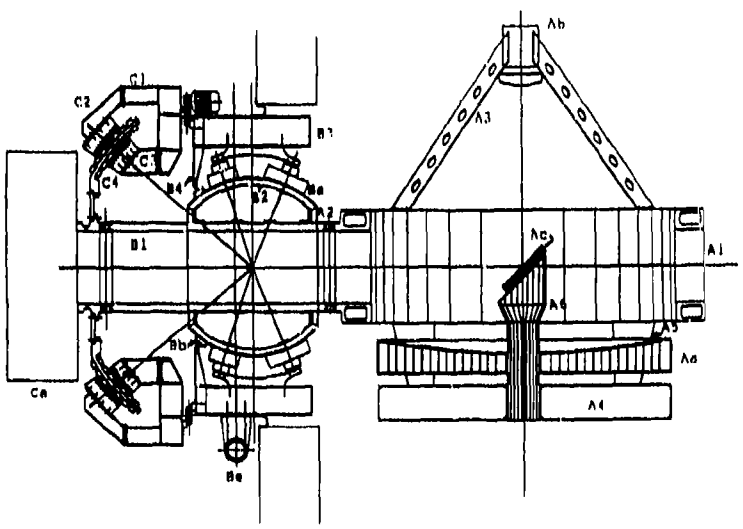

Fig. 4. Improved dumbbell configuration for SOFIA.

A 380 GHz SIS Heterodyne Spectrometer for "PRONAOS" (balloon borne experiment for submillimeter radioastronomy)

G. Beaudin, A. Deschamps*, P. Encrenaz**, P. Febvre*, P. Feautrier**, C. Gac*, M. Gheudin*, B. Léridon*, R. Maoli*, D. Michet*, J.C. Pernot**, C. Robert*, C. Rosolen*, G. Ruffié*, P. Vola**

** Observatoire de Paris-Meudon, 5 place Jules Janssen - 92195 Meudon - FRANCE*
tel : 33 1 45 07 79 13 - fax : 33 1 45 07 78 93
*** Ecole Normale Supérieure, Laboratoire de Radioastronomie, 24 rue Lhomond - 75005 Paris - FRANCE*
tel : 33 1 44 32 32 92 - fax : 33 1 43 36 72 04

Abstract :
To prepare the space programs on astrophysics, the development of a balloon-borne observatory (PRONAOS) , including a 2 metre telescope associated with a submillimetre heterodyne spectrometer for radioastronomy, has been supported by the french space agency (CNES).
The receiver includes a SIS mixer using Nb/AlOx/Nb tunnel junctions operating at 4K, a 6 GHz IF low-noise cooled preamplifier, a LO quasi-optically injected with a phase locked Gunn oscillator and two cascaded frequency multipliers. Noise temperature as low as 300 K has been obtained ; less than 200 K is expected. An Acousto-Optical Spectrometer (AOS) is used for high resolution ($\nu/\Delta\nu \approx 10^6$) spectral analysis. This instrument will be used to simultaneously detect the 368 GHz O_2 and the 380 GHz H_2O lines in the interstellar medium. Observations in this part of the spectrum requires low atmospheric water vapor and oxygen molecule emission, so that the telescope will fly under a 1 000 000m^3 balloon at an altitude of ≈ 37 km.

1- INTRODUCTION

Observations from a stratospheric balloon are unobstructed by the atmosphere which is opaque at submillimetre and far-infrared wavelengths from the ground . For this reason, a submillimeter balloon-borne observatory (PRONAOS) is being developed under the responsibility of the (CNES) to prepare the future space programme in radioastronomy.
PRONAOS is intended to provide a facility for long duration flights (20-40 h) of an altitude of 37 km. It consists of a stabilized gondola supporting a 2m diameter telescope, associated alternately with an infrared multiband photometer or a submillimeter heterodyne high resolution spectrometer.
The two meters segmented telescope is made by MA'TRA-Espace with a light weight primary mirror witch is a cassegrain telescope with a focal ratio F/20. This telescope is pointed (accuracy of 15 arc seconds) with a three axis system.
The focal plane instruments are :
. A spectrophotometre (S.P.M.) using He_3 cooled bolometers, dichoïcs filters, on the field 180 µm - 1.2 mm (4 bandes)
. An heterodyne spectrometer receiver (S.M.H.) with high resolution $\nu/\Delta\nu \approx 10^6$ will operate, in the first generation, to detect simultaneously the 368 GHz (O_2) and the 380 GHz (H_2O) lines, with a next goal of operating up to 500 GHz.

2 - SUBMILLIMETRE HETERODYNE RECEIVER (SMH)

A block diagram of our submillimeter wave heterodyne spectrometer is shown in the figure. Rotation for a flat mirror set allows the calibration of the receiver by commuting the incoming beam from the telescope between a hot and a cold load. Due to the short wavelengths, a quasi-optical free space propagation is adopted. A Mach-Zehnder diplexer is used for the 374 GHz local oscillator signal injection into the mixer.
Receivers using SIS tunnel junctions have shown better sensitivities than Schottky diode receivers operated at millimeter and submillimeter wavelengths. Theoretically, sensitivities approaching the quantum limit can be achieved.The Nb/Al-Al_2O_3/Al SIS junctions with small areas and sharp I-V curves have been successfully fabricated, dc measured and integrated in the mixer (1). The smallest area achievable with our process is about 0.9 µm² whith high current densities (≥ 10 kA/cm²). Arrays of 2 junctions with this area, have been made.
The 380 GHz SIS mixer was designed from B. Ellison (RAL) with an integrated IF matching circuit and two integrated superconducting coils ; it has been tested over a 40 GHz LO bandwidth (2). The best

receiver noise temperature (300 K DSB) has been measured with an array of a couple of junctions in series having an effective surface of 0.47 μm^2. The lower mixer noise temperature is around 100 K at the LO frequency ≈ 374 GHz.

The 374 GHz LO source has been made with a fundamental InP Gunn Oscillator at 93.5 GHz followed by two cascaded GaAs varactor doublers (3). This subsystem provides enough power (>10μW) to drive the SIS mixer .

The intermediate frequency (IF) is chosed at 5.85 GHz to allow the simultaneous detection of the O_2 line in the lower band at 368 GHz and the H_2O line in the upper band at 380 GHz. The IF output feeds a specially designed cooled low-noise HEMT amplifier with a gain of 30 dB (4). The signal is then amplified at room-temperature , down converted at 2 GHz and coupled to the acousto-optical spectrometer (AOS) subsystem. The resolution of 800 kHz is available on 800 MHz bandwidth (1000 channels ; ≈ 2000 pixels).

Data acquisition and controls : an in-board computer can control the receiver (house keeping) and compact the datas to send them to the ground station. The transmission flow from the instrument is about 15 kbps.

Cryogenics : the constraints and requirements for the cryogenic system are : 3.5 K operating temperature with a 40 hours lifetime. The baseline design is a liquid Helium dewar with a 40 K stage screen for the IF cooled amplifier.

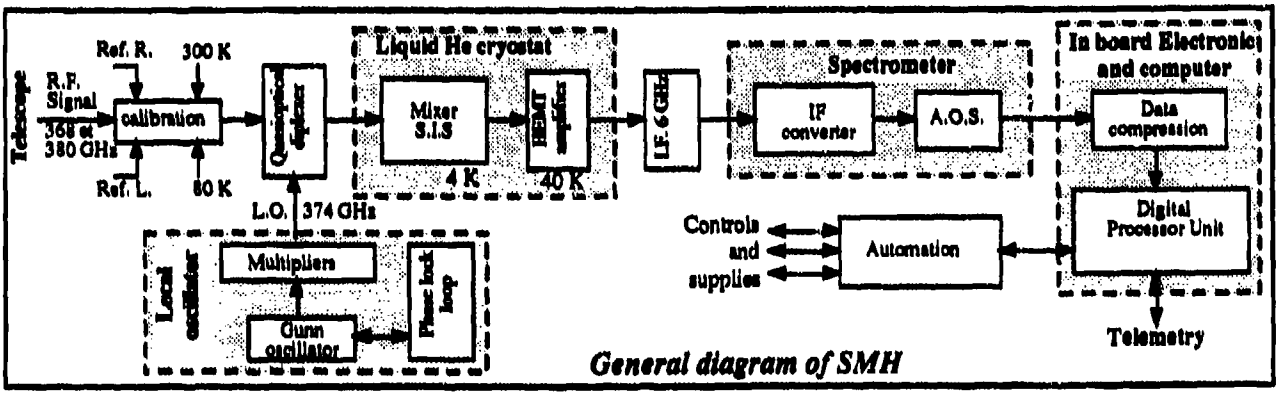

General diagram of SMH

3 - CONCLUSION

The PRONAOS submillimetre SIS receiver (5) is under development at Meudon observatory. The balloon lauch from Fort Sumner (USA) is schedule on may 1995 to detect the O_2 and H_2O molecules in the interstellar medium in our galaxy.

This instrument is the first steep for the future space submillimeter heterodyne receivers (generation 2000's) in which Meudon observatory is involved : submm Explorer (SMIM) with Caltech JPL, NASA (USA), FIRST (far infrared space telescope) with ESA ...

Acknowledgements : The studies have been financed and supported by the French Space Agency (CNES), with the technical advices of CESR, Bordeaux observatory .

REFERENCES

(1) *Feautrier P., Hanus M., Febvre P. : Nb/Al-AlO$_x$/Nb junctions for a 380 GHz SIS receiver ; Supercond. Sci. Technol. 5 (1992), 564-568., May 1992.*

(2) *Feautrier P., Febvre P., Hanus M., Maoli R., Léridon B., Robert C., Ruffié G., Pernot J.C., Beaudin G., Encrenaz P. : A 380 GHz SIS receiver using high quality and high current densities Nb/AlO$_x$/Nb junctions, Conference IRMM Caltech, Los Angeles, december 92.*

(3) *Febvre P., Feautrier P. & al :"A 380 GHz SIS receiver using Nb/AlO$_x$/Nb junctions for a radioastronomical balloon-borne experiment : Pronaos", Terahertz Technology, Proceedings, University of Michigan, USA, april 92.*

(4) *Robert C., Gheudin M. : "A 6 GHz HEMT low-noise cooled amplifier for a radioastronomical submillimeter heterodyne receiver", 15th International Conference on Infrared and Millimeter waves, conference digest, Orlando, dec 90.*

(5) *Beaudin G., Deschamps A., Encrenaz P., Feautrier P., Febvre P., Gac C., Gheudin M., Léridon B., Maoli R., Michet D., Pernot J.C., Robert C., Rosolen C., Ruffié G., Vola P. : "PRONAOS", a balloon borne experiment for submillimeter radioastronomy with a 380 GHz Heterodyne Spectrometer ; Conférence SPIE LASE 93, Los Angeles, january 93.*

A Cost Effective Total Power Radiometer Package for Atmospheric Research

B.N.Lyons, W.M.Kelly, D.R.Vizard and U.S. Lidholm

Farran Technology Limited,
Ballincollig, Cork, Ireland.

1.INTRODUCTION

Millimeter wave radiometers are being increasingly used for plasma diagnostics and remote sensing applications. To date however the widespread use of such systems, particularly for applications requiring frequency coverage above 100 GHz, have been inhibited by the lack of availability of an appropriately specified commercial package. This paper outlines the design and construction of such a radiometer package and gives details of results obtained to date.

2.SYSTEM OVERVIEW

The radiometer has 7 channels, one each at 20.6 GHz, 31.5 GHz and 150 GHz, and 4 channels at 183.3 GHz. It is contained within a weatherproof enclosure and temperature stabilised to better than 0.002 deg.C/min. The radiometer operates in a total power mode with frequent calibration using internal hot and cold loads. The cold load uses liquid nitrogen to achieve a low temperature reference and has a minimum operating time of 3 hours. A front-end quasi-optical system defines the beamwidths and splits the incoming radiation into 3 bands at 20/30 GHz, 150 GHz and 183 GHz. The frequency splitting is accomplished using 2 dichroic plate filters[1] as illustrated in the schematic in Figure 1. The optical design was developed using simple Gaussian beam techniques[2] and refined using modal analysis. Subharmonic mixers were chosen for the 150 and 183 GHz receivers as these have significant cost and layout advantages over the conventional single-ended approach. The mixers are located on the optics plate to minimise front-end losses. The 20/30 GHz band is split in a waveguide diplexer and downconverted using balanced mixers. The mixers are mounted on the rear of the optics plate and linked by waveguide to the feed.

The detected output from each channel is fed to a video processor which integrates and amplifies the signals prior to digitisation and subtracts an offset approximately equal to the noise contribution of the radiometer. This maximises the resolution of the retrieval system in the range of interest 0-330K. The offset is corrected during each calibration cycle. The processor is also fitted with a nulling circuit which periodically corrects for level changes due to temperature drifts. The processed video is digitised using a 14 bit DAC.

The system software runs on an IBM compatible PC. The PC is linked to the radiometer using an RS232-C serial interface. The radiometer has a dedicated controller which responds to commands from the PC and supervises the operation of the radiometer hardware. The PC displays the retrieved scene temperatures in real time and logs the scene temperatures and raw data to disk for subsequent analysis.

Results to date indicate a retrieval precision of better than 0.35K RMS in channels 1-6 and 1K RMS in channel 7 with an integration time of 1 second.

3.CONCLUSIONS

A low cost compact total power radiometer package suitable for a range of applications has been developed. The radiometer has integrated hot and cold loads to facilitate frequent calibration. Data acquisition is performed on a standard PC.

4.REFERENCES

1. T.E. O'Ciardha, W.M.Kelly and B.N. Lyons, "Modal Modelling of Millimetre/Submillimetre Wavelength Filters", Proceedings of European Microwave Conf., pp. 474-479, London, 1989.
2. P.F. Goldsmith, "Quasi-Optical Techniques at Millimeter and Submillimeter Wavelengths", Infrared and Millimeter Waves, K.J. Button editor, Vol.6, chapter 5, Academic Press, New York, 1982.

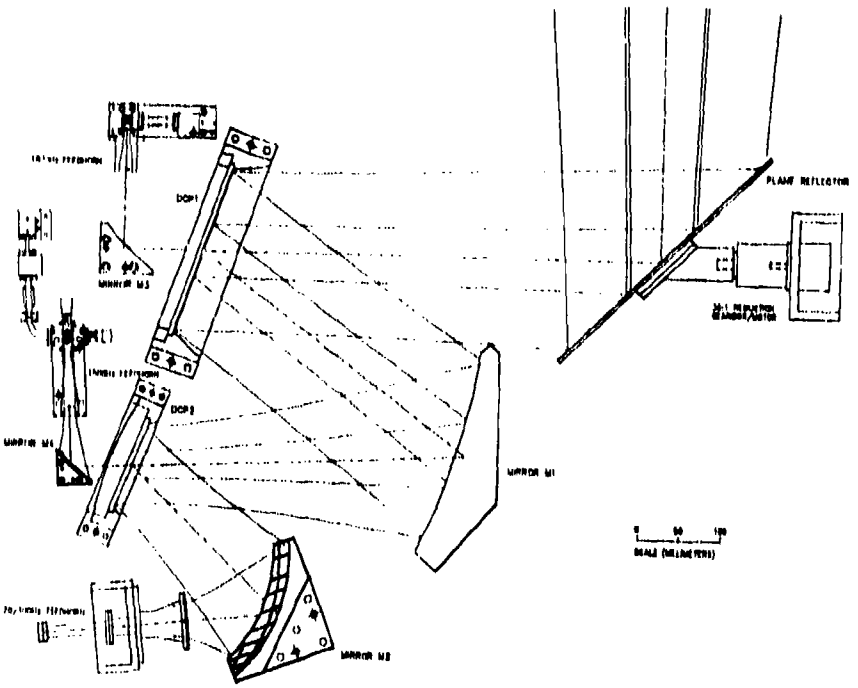

Figure 1: Optical Layout for 7 Channel Radiometer.

IR DETECTORS FOR SPACEBORNE APPLICATIONS

Y V Munro and D Hickman

Matra Marconi Space UK LTD
Anchorage Road, Portsmouth

The aim of the present paper is to discuss the application of IR detectors and focal plane concepts to spaceborne remote sensing in terms of performance requirements and current technology. Critical aspects such as detector characterisation, material selection, pre and post detection processing, interconnection methodologies will be reviewed in the context of a number of space programmes. Additionally, the strong interdependence of the detector configuration, overall radiometer design and platform operational conditions is identified and shown to be a major constraint on the configuration of space-based instruments.

The role of spaceborne remote sensing was firmly established in 1972 with the launch of Landsat-1 carrying a multi-spectral scanner designed to provide images in several visible and reflective IR bands (0.5-0.6, 0.6-0.7, 0.7-0.8 and 0.8-1.1μm). The Landsat series of spacecraft have produced Earth resources data with applications as diverse as mineral and petroleum exploration, forestry and land use. Subsequent satellite missions have continued and extended the role of IR remote sensing. In addition, satellite generated IR imagery provides data for oceanographic and atmospheric studies, meteorology and surveillance. The number of applications is continuously growing.

Different missions tend to have marked differences in the range of their objectives and it therefore follows that the corresponding detector system is application specific. For example, measurements are generally required in a particular waveband which then defines the range of usable detector technologies. In the assessment of choice of detector type, a major consideration is performance. Parameters which must be optimised include the time constant, signal to noise ratio, sensitivity, spectral response, uniformity of response and operating temperature. In addition, minimization of the number of interconnections with post focal plane assembly should be a design aim as well as optimisation of the thermal interface between the detectors and post focal plane electronics.

Earth observation systems can be based on either single or multiple element detector configurations. To produce an image with a single detector element, some form of mechanical scanning is required. An example of such a system is the current Meteosat programme which utilises a scanning mirror in the N-S direction, the rotation of the satellite giving the E-W scan. If the Meteosat programme were to adopt a staring array approach, an array of 2500 x 2500 elements would be required to image the Earth disc at the current 5 km resolution. IR staring arrays with 256 x 256 elements are currently available, larger arrays will be possible as technology evolves.

Multiple element or staring arrays require little or no mechanical scanning which may be an important advantage in terms of reliability and vibration control. Also the image cells are observed in parallel rather than sequentially as for scanned images. This throughput advantage can allow either a more rapid image update or a reduced optic aperture. The disadvantages of staring arrays include manufacturing difficulties, complex electronic processing and focal plane cooling. Using a large array also requires that aberrations (such as Petzval curvature) are minimised across the image plane. There are significant system difficulties associated with the use of staring arrays at geosynchronous altitudes. In order to ensure good geometrical image quality and reproducibility, the platform must be very stable and employ a sophisticated attitude control sub-system. In addition, the instrument will be subject to solar flux for a significant period of the year which will impact on instrument thermal control.

Earth resources satellites can use small detector arrays in conjunction with small angular swath width scans to

produce ground coverage with a low repeat frequency. The Landsat Multi-Spectral Scanner provides 185 km swath width imagery with a repeat frequency of 18 days using an array of six detectors per band. High resolution applications, for example for vegetation di crimination studies, may lead to use of larger arrays to maintain coverage rate.

In general, scanning systems have been preferred for Earth observation, particularly in geosynchronous orbits, as in the case of Meteosat. Currently, however, there is a trend towards utilising payloads with larger arrays which will increase individual instrument coverage rate and minimise the number of platforms needed for high repeat frequency applications. The SPOT HRV instrument uses an array of 6000 detectors in push-broom mode to provide high resolution images. The instrument can be repointed to allow reimaging frequencies of up to 11 times in 26 days.

To meet the needs of satellite-based remote sensing systems, radiometers are required to operate over wide spectral bands including visible and IR. A number of detectors, which encompass this spectral band, are described here in the context of current or proposed space programmes. These include semiconductor P-N junctions which operate over the visible to near IR band. Silicon-based photodiodes have been used on a number of programmes including ATSR, Meteosat, SPOT HRV and IRS. Another type of detector used in the near IR is InGaAs which is currently proposed for Meteosat Second Generation and HRVIR, the enhanced SPOT 4 instrument. CMT based detectors are also another extensively used detector type. These can be used in either a photovoltaic or photoconductive mode although the latter is generally preferred for longer wavelengths (as used on the Meteosat Transitional Programme). Operation at wavelengths above 20μm generally requires the use of thermal detectors (bolometer or pyroelectric) as used on the Nimbus meteorological satellites and which have been considered for the GERB radiation instrument. However, new detectors such as SiGa are now available.

In addition to fulfilling operational requirements, detectors must undergo a flight qualification programme to ensure their capability of surviving the acoustic and vibration levels associated with launch. Uncooled detectors and electronics must undergo thermal cycling over a temperature range exceeding operational limits. Other requirements exist, many of which are application specific. For example, on station detectors will require a window to provide protection against degradation by satellite thruster efflux and micro meteorite impact. Additionally, the satellite will be in a radiation environment (defined primarily by orbital altitude) and, as such, the detector design must be shown to be capable of maintaining required performance throughout its lifetime.

Limitations on mass, power and accommodation will place restrictions on the size of cooled arrays. In addition, focal plane vibration due to mechanical coolers is undesirable. Therefore, detector technology which allows operation at the maximum temperature compatible with performance requirements should be selected. However, the advent of low vibration, long life cryocoolers will allow larger arrays to be accommodated than have been previously been possible.

As the scale of detector arrays increases so will the demand on readout circuitry. Hybrid technology allows the detector and readout circuitry to be optimised separately. However, this creates problems with the interconnection of the two, namely thermal expansion mismatch and charge injection efficiency which requires a higher detector impedance to match the electrical characteristics of the multiplexer input. CMOS or NMOS technology will allow multiplexing circuits to be made which are smaller and lighter and with a lower power consumption than is possible using CCDs. MOS technology can support on-plane signal processing which will allow greater functional flexibility and reduce the requirement on electronics subsystems.

In summary, remote sensing programmes have demonstrated the advantages of satellite based Earth observation systems. The ever increasing demands on instrument performance have been partially met through improvements in detector arrays, readout techniques and cooling technology. However, many applications are now restricted by the instrument optics, platform and space environment rather than those restrictions imposed by detector technology. Although a detector element and telescope may readily produce a ground resolution of a few metres, the pointing stability required (typically subarcsecond) cannot be easily afforded by the platform.

Quasi-optical triplexing feed for spacecraft radiometer.

R J Martin and W J Hall,
BAe Space Systems, Bristol, UK.

1. INTRODUCTION

A sounding radiometer called AMSU-B has been developed for the UK Met Office. It is designed to measure altitude profiles of atmospheric water vapour over a ± 50° swath from low Earth orbit. Upwelling radiation is collected by a common aperture dual reflector with a rotating 90° offset main dish. A quasi-optical (QO) triplexing feed then successively separates the input into frequency bands at 89 GHz, 150 GHz, and 183.3 GHz by means of dichroic filters, and conveys it to the appropriate receivers via chains of off-axis mirrors [1]. We present here predicted and measured performance, and describe the design method required to meet the following constraints for all three channels: beam efficiency ≥ 95%, half-power beamwidth 1.1° ± 10%, and temperature measurement accuracy of 1.0 K. The bandwidths are 3 GHz for the two low frequency channels, and 16 GHz for the 183 GHz channel.

2. DESIGN AND PERFORMANCE

We have developed a powerful and versatile method for designing quasi-optical (QO) systems that retains the intuitive aspects associated with simple, quantifiable rules, and adds to that the accuracy and detail of a full numerical analysis. It is based on the iterative use of a number of complementary routines described below. The QO front-end for the AMSU-B radiometer was produced using this scheme.

2.1 Gaussian Beam-mode analysis

GB analysis has been used for many years to describe QO *propagation* for both circularly symmetric and elliptical or astigmatic beams [2-4]. To apply the approach successfully to systems, the form of the beam emergent from any component within the system, such as reflectors, lenses, and dichroic filters, must be readily predictable in terms of modifications to the incident Gaussian distribution. Similarly, the radiation pattern of any antenna used to couple an active device to the QO system must also be well-described.

Any additional application-specific requirements must also be catered for. For example, rotation of the copolar E-vector on reflection from an arbitrarily oriented surface in 3-D may be important. Volume, mass, and cross-polar constraints may also be present. When they have all been accounted for, a framework of simple, easy to visualise, and perhaps more importantly, quantifiable rules emerges. It is this which is used to generate and compare quickly alternative designs [5].

2.2 The Physical Optics suite

While the GB method is excellent for generating preliminary designs, it will not provide detailed performance figures. The PO suite, on the other hand, is well suited to the numerically intensive task of evaluating a multi-element antenna system in sufficient depth to allow the design to be optimised. It provides detailed information on the form of the fields at a chosen output interface based on the predicted (or measured) fields at the input interface. Included in the information are the levels and locations of sidelobes and cross-polar peaks, the orientation of the co-polar E-vector, the beam efficiency, and the shape of the beam far from boresight. The routines cater for shaped reflectors with arbitrary perimeters, allowing both mechanical tolerances, and the effects of truncations and surface finishes, to be explored.

For AMSU-B, the PO routines used a suite of mode-matching algorithms to generate the outputs from the feedhorns (see below), and propagated these through all the optics and on into the far-field of the dual-reflector antenna. The match between prediction and measurement for the 89 and 183 GHz channels with the main dish rotated away from nadir by 49° is shown in Figures 1 and 2 respectively. The 89 GHz channel contains 7 elements including two drilled-plate dichroic filters and a linear taper corrugated scalar feedhorn. The 8 elements in the 183 GHz channel include one drilled-plate filter, and a scalar feed horn with a profiled inner taper. In neither case was measured data substituted for predicted data at any location within the system.

2.3 CATIA

CATIA is a commercial 3-D CAD package. Its uses here are two-fold, firstly to check for obscurations, volume infringements etc., and secondly to generate suitable designs for the component mounts. Since both tasks are being carried out on the same model it is easy to see how they interact. The view in Figure 3 was generated on CATIA, and shows representational beams travelling through AMSU-B. It illustrates volume and component re-use. The compactness of the design becomes apparent in the view reproduced in Figure 4, which shows the same system with the components now attached to their brackets. The beams, and a common mounting shelf, have been omitted for clarity.

2.4 Modal-matching software

As mentioned above, suitable predictive models must be found that describe the behaviour of various quasi-optical components. This must be done for both the GB and PO analyses.

Cascaded mode-matching routines are available for several types of feedhorn. Figure 5 shows the agreement obtained between prediction and measurement for the AMSU-B corrugated 183 GHz scalar horn. The profiled inner taper (inset) is designed to provide a plane phasefront which remains co-located with the horn aperture over the full 16 GHz bandwidth. The deep nulls between the main beam and the first sidelobes are characteristic of this. Analyses of the sort carried out by Wylde [6] provide the Gaussian parameters, while the output from the modal analysis is suitable for immediate use by the PO suite.

Dichroic filters are modelled using Floquet modes weighted by the spectrum of plane waves of the incident Gaussian beam to represent the effects of diffractive-spreading. Once again the outputs from such models can be converted to forms that are appropriate as inputs for both the GB and PO routines.

3. SUMMARY

A powerful and versatile iterative approach has been presented which provides quasi-optical designers with the accuracy of numerically intensive Physical Optics while retaining the advantages of a framework of simple, quantifiable rules amenable to the generation, easy visualisation, and fast turn-around comparison, of alternative designs for complex and demanding systems. In the process, the effects of individual components are revealed, and mechanical tolerances can be explored.

4. ACKNOWLEDGEMENTS

We should like to acknowledge the kind permission of the UK Met. Office to use material pertaining to AMSU-B. We should also like to thank Dr. R Cahill for provision of the feedhorn pattern.

5. REFERENCES

1. R J Martin and W J Hall, "Quasi-Optical Triplexing Feed for AMSU-B Radiometer", *Proc. 8th International Conference on Antennas and Propagation*, 1993

2. H Kogelnik and T Li, "Laser Beams and Resonators", *Proc. IEEE*, Vol.54, pp.1312-1329, 1966

3. P F Goldsmith, "Quasi-Optical Techniques at Millimetre and Submillimetre Wavelengths", *Infrared and Millimetre Waves*, ed. K J Button, Chap.5, Vol.6, Academic Press, New York, 1982

4. J C G Lesurf, *Millimetre Wave Optics, Devices and Systems*, Adam Hilger, Bristol, 1990

5. R J Martin and W J Hall, "Three-dimensional Design of Quasi-Optical Systems at BAe Space Systems", *SPIE Proc. Symp. Aerospace and Remote Sensing*, 1993

6. R J Wylde, "Millimetre Wave Gaussian Beam Mode Optics and Corrugated Feedhorns", *Proc. IEE*, Vol.54, Pt.H, p.258, 1984

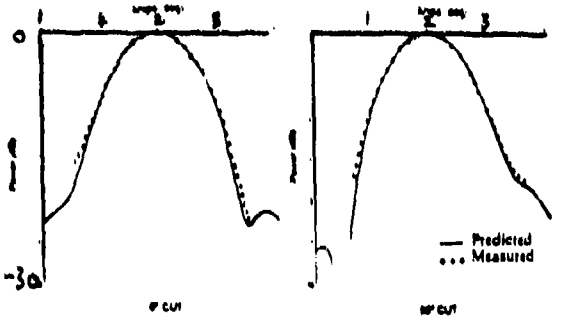

Figure 1

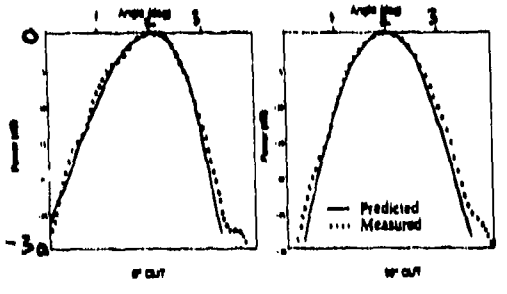

Figure 2

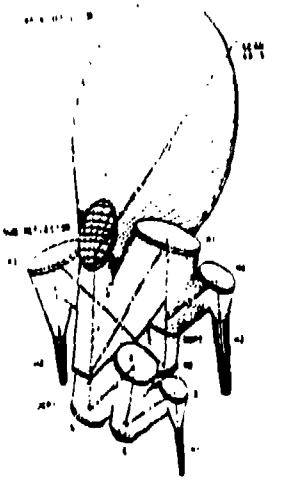

Figure 3

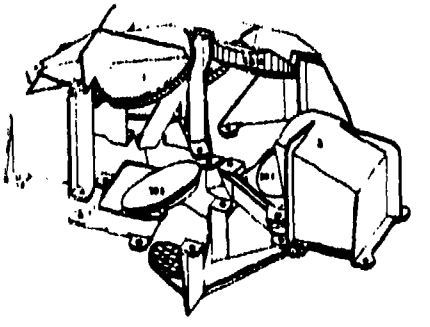

Figure 4

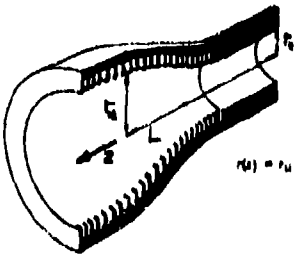

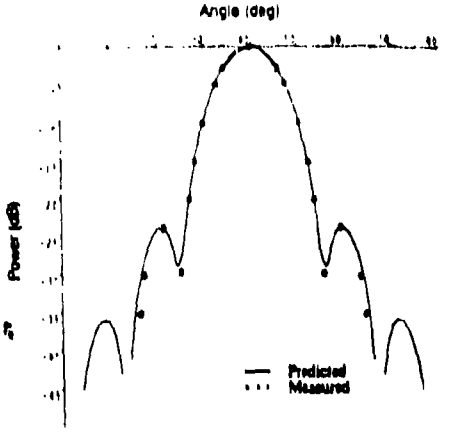

Figure 5

THE ISO LONG-WAVELENGTH SPECTROMETER

P E Clegg

Queen Mary and Westfield College

ABSTRACT

The Long-Wavelength Spectrometer (LWS), to be launched in the ESA's *Infrared Space Observatory*, covers the wavelength range 45-180 μm at both moderate (~200) and high (~10^4) spectral resolving power. This paper describes how the scientific requirements were translated into a space-qualified design.

REFLECTOR AND MIRROR SYSTEMS FOR SUBMILLIMETER AND INFRARED TELESCOPES - AN OVERVIEW OF TECHNOLOGY AND COSTS

by Hans J Kärcher, MAN GHH, Germany

Infrared and submillimeter astronomy has advanced dramatically in the last 10 years. Technically this advance is dependent not only upon the improvement of the instrumentation and the telescopes themselves but also upon their location on the earth's surface or in space. The key mechanical component of the telescope, which determines its observational performance, is the main mirror or reflector. In the past the technology for reflectors of radiotelescopes developed completely independent from the technology for mirrors of optical telescopes. William Herschel manufactured the first really large optical mirror in 1789 in polished bronze and Lovell, together with Husband & Co, built the first really large radiotelescope in 1956 from riveted steel. Due to the different demands on size and accuracy, up to now optical and radiotelescopes have used different technologies, but the mechanical principles on which the design of the mirrors or reflectors is based are very similar. As infrared and submillimeter astronomy is bridging the gap between optical and radio astronomy, the mirrors and reflectors for infrared and submillimeter telescopes are bridging the gap in technologies between optical mirrors and radiotelescope reflectors.

1. Technologies for Mirrors and Reflectors

Since about 100 years ago professional optical telescopes have been built as reflectors with a large main mirror made of polished glass. The mirrors are rather thick. The largest telescopes of this type are the 50-year old 5 m Mt Palomar and the Caucasian 6 m Bolshoi telescope. For larger diameters the weight, performance and costs of this type of telescope become prohibitive. In the last 10 years a lot of projects have been undertaken for larger optical telescopes, which are therefore using new mirror concepts such as the thin meniscus concept, segmented mirrors or lightweight honeycomb designs. Up to now no concept prevails, however the first two need active optics.

Large radio reflectors have been built for 40 years with steel trusswork and a surface made from wire mesh or welded steel plates. The design of the reflector trusswork differs depending upon the different methods of load transmission to the telescope mount, eg 2-point supports, 4-point supports, central hub concepts, homologous "umbrella type" systems etc. With the increase of frequencies and accuracies, the reflector surface has changed to aluminium panels. These are manufactured by milling or stretch-forming and stiffened at the rear by ribs or a honeycomb sandwich. For millimetre and submillimeter applications the use of carbon fibre reinforced plastics prevails for the surface panels as well as the trusswork struts. Concepts for active control of the reflector surface are also under consideration.

2. Structural Principles and Related Accuracies

The accuracy of an optical mirror must be in the order of nanometres and of a radio reflector in the order of microns – a factor of a thousand! However, the main influences which disturb the reflecting surfaces are the same, except the differences in the manufacturing process, ie gravity, temperature and wind.

To suppress the influence of gravity deformations for both applications an adequately distributed support of the reflector rear is necessary. This can be achieved by controlling the forces rather than the deformations. For optical mirrors this is done by load spreading systems which disconnect the mirror from the telescope mount via an additional structural element, the mirror cell. For radio reflectors no additional cell-like structural element is used, the distributed connection to the mount is achieved internally in the trusswork by so called homologous design.

Regarding temperature and wind, the influences of the outside environment at the telescope site, three levels of countermeasures are applied:–

I passive compensation by adequate structural layout and materials,
II protection against the environment by enclosures, domes or shields,
III active compensation.

Optimum performance and minimum costs are achieved by an appropriate combination of all three measures.

3. Trends, Tendencies and Costs

The gap between submillimeter and infrared is one of the last windows in the electromagnetic spectrum to be opened. The telescope reflectors needed are in accuracy ranges from 15 microns to 150 nanometers with reflector diameters from 2.5 m to 15 m. To avoid atmospheric blockage, the telescopes are located on high mountains, balloons, aeroplanes or in space. For these special demands traditional radio telescope layouts are too inaccurate, traditional optical layouts are too expensive and both are too heavy. Very lightweight features should be used, which are not naturally in the mind of a classic telescope designer. Submillimeter and infrared telescopes present a field where carbon fibre composites can display their full advantages in high stiffness, minimal thermal expansion and low weight. Replica techniques can be used to achieve cost effectiveness and formerly unbelieved accuracies for the reflector surface and careful design of the backing structure and its connections to the telescope mount lead to low cost and high accuracy large submillimeter and infrared reflectors of optimum operational performance.

4. Conclusion

In the paper the basic principles of mirror and reflector design are described and compared and the latest state of the art technologies are explained. Trends and tendencies in the progress of infrared and submillimeter telescopes are analysed and the influence on cost and availability are described.

A HORIZONTAL ATMOSPHERIC TEMPERATURE SOUNDER BASED ON THE 60 GHz OXYGEN ABSORPTIONS

R. W. McMillan
Georgia Institute of Technology
Georgia Tech Research Institute
Atlanta, Georgia 30332, USA

ABSTRACT

Implementation of a multichannel radiometer, operating on the family of oxygen absorptions near 60 GHz, potentially useful for horizontal temperature sounding, is discussed. Application of this instrument to the detection of atmospheric hazards such as wind shear and clear air turbulence is considered.

1. Introduction

The group of molecular oxygen absorptions lying near 60 GHz in the millimeter-wave portion of the electromagnetic spectrum provides the basis for vertical temperature sounding of the atmosphere from satellites or aircraft based on weighting functions for different frequency channels. This paper describes a radiometer operating near 60 GHz which will be able to sense temperatures on a horizontal path using a similar weighting function approach, although the weighting functions for horizontal sensing are exponential instead of sharply peaked.

The instrument described in this paper is a millimeter wave (MMW) radiometer which has several channels positioned on the skirts of the group of oxygen absorptions centered near 60 GHz. Based on the frequency of each channel, the absorption in the band which it senses will vary, and therefore the temperature measured in that channel will be different from that measured in the other channels. These temperature differences provide the basis for detection of an atmospheric anomaly as well as its range, if a simple model of the atmosphere is assumed.

2. Theory of Operation

The radiometer equation gives the temperature measured by a radiometer for arbitrary positions and orientations of the radiometer relative to the atmosphere. Integration of this equation for a vertically stratified homogeneous atmosphere in which the radiometer views the atmosphere horizontally gives multiple equations depending on the number of vertical strata chosen. Solution of these equations gives the individual temperatures of the strata as well as their ranges if a few basic assumptions are made. The differences in temperature of adjacent strata are a measure of the severity of the atmospheric perturbation.

3. Application to Detection of Atmospheric Hazards

Most atmospheric hazards are characterized by a change in temperature. In particular, wind shear events are usually downdrafts which cause the air in the wind shear plume to be colder than ambient.

The multichannel radiometer described in this paper could be used to detect such an event based on this temperature difference. The simplest type of wind shear event is one in which the atmosphere in front of the plume is clear while that in the plume may be opaque due to rain or heavy clouds. In this case, a simple two-channel radiometer should be able to measure both the range to the event and its temperature. For the case of a dry wind shear, in which the air is clear both in the plume and in front and back of it, a four-channel radiometer would be required for adequate characterization since there are three regions of homogeneous temperature in front of the radiometer. Additional channels, added in multiples of 2, provide temperature data on increasingly more complex atmospheric structures, although the accuracies of these soundings will vary strongly with radiometer performance, size of the features, and their temperature differences from ambient.

It is possible that this radiometer could also be used to detect wingtip vortices caused by the passage of large aircraft. This phenomenon is responsible for the spacing of aircraft takeoffs and landings at major airports, since air traffic controllers must wait until the vortices from an aircraft dissipate before allowing another to follow the same path. A channel could be added to the radiometer with a small time constant such that it could sense remotely the spectrum of temperature fluctuations in a volume of air after the passage of an aircraft. Vortices will cause the temperature spectrum to change, specifically they will cause the high frequency portion of the spectrum to increase in power. This change could be sensed by a simple high-pass filter and used to alert ground controllers.

4. Approach

MMW receivers which cover the entire 50-75 Ghz waveguide band with a noise figure of better than 10 dB double sideband are available. The radiometer discussed herein would use a 60 GHz local oscillator and would have symmetrical high transmission channel sidebands at 49-51 and 69-71 GHz and intermediate transmission sidebands at 52-54 and 66-68 GHz. With a 10 dB double sideband noise figure, the radiometer would have a minimum detectable temperature of about 0.13 degree for 2 GHz channel bandwidths and a 0.5 second integration time. Channels used for remote sensing of temperature spectra would have a minimum detectable temperature of 0.31 degrees for an integration time of 100 milliseconds. It is likely that this 10 dB noise figure could be improved with an accompanying improvement in performance.

5. Conclusions

Atmospheric hazards characterized by temperature differences from ambient may be detected by a radiometer operating on the 60 GHz oxygen transitions. Hazards of particular interest and concern to the aviation community are wind shear, clear-air turbulence, and wake vortices. With recent improvements in componentry, a sensitive MMW radiometer whose outputs can be used to determine both the range to the hazard and its temperature difference can be constructed.

A submillimeter-wave sensor for trace gas studies in the middle atmosphere

H. Nett, S. Crewell, K. Künzi

University of Bremen, FB 1, Institute of Remote Sensing,
P.O. Box 330440, 2800 Bremen 33, FRG

ABSTRACT

A low-noise 625-650 GHz receiver has been developed for trace gas measurements in the stratosphere. The instrument is designed for single-sideband operation allowing the detection of a variety of weak emission lines in both receiver sidebands. During several measurement campaigns over northern Europe, in the winters 1991/92 and 1992/93, the radiometer was operated on board the research aircraft FALCON. We report on receiver performance and present recent results of the flight experiments.

1. INTRODUCTION

The concern about the potential loss of stratospheric ozone, first observed over Antarctica in the mid 1980's, has initiated large efforts to develop novel experimental methods to study middle atmospheric chemistry. Among the different techniques in use heterodyne spectroscopy in the submillimeter-wave frequency range ($\upsilon > 300$ GHz) has proven to be of particular advantage allowing the detection of numerous species of interest within a narrow frequency interval [1]. The goal of the research program SUMAS (Submillimeter-wave Atmospheric Sounder) [2] was to develop a heterodyne receiver for operation in the 650 GHz frequency range covering a number of strong emission features of stratospheric trace gases, e.g. O_3, ClO and HCl, the latter playing a key part in the catalytic cycles of ozone depletion. This instrument is flown on board the research aircraft FALCON, operated by the German Air and Space Research Organization (DLR), at flight altitudes of 10-12 km.

An improved front end (SMS, Submillimeter Sounder) was developed in the frame of an international research program funded by ESTEC [3]. Both receivers were flown successfully on several missions as part of the European Arctic Stratospheric Ozone Experiment (EASOE) in 1991/92, and in a subsequent campaign in February 1993. Emission line measurements of ^{35}ClO (649.4 GHz), $H^{35}Cl$ (625.9 GHz) and O_3 (647.8 GHz) were made during these campaigns.

2. LOW-NOISE 625-650 GHz RECEIVER

The SUMAS/SMS receiver front ends are characterized by a single-ended Schottky-diode mixer pumped by a solid-state local oscillator (l.o.) source. The l.o. consists of an InP Gunn oscillator followed by a cascaded diode multiplier (doubler and tripler) [4]. Frequency stability of $\delta\nu/\nu \approx 10^{-8}$ is achieved by means of a phase-lock loop. In the radio frequency (r.f.) section low-loss propagation of signal and l.o. radiation is realized by a quasi-optical coupling scheme [5]. Two cascaded Martin-Puplett type interferometers are used as single-sideband (ssb) filter and diplexer. Micrometer tuning allows accurate setting of the ssb filter's internal pathlength difference during flight operation. The filter can thus be set for operation in either the upper or the lower receiver sideband or for double sideband operation. Relative sideband suppression > 20 dB across the receiver's total instantaneous bandwidth of 1.2 GHz could be experimentally verified.

During spectroscopic measurements a periodic total-power calibration is performed using a rotating mirror at the receiver optics input and two absorbers, one at ambient temperature and one at 77 K. A high-density polyethylene (HDPE) window is integrated in the side wall of the pressurized aircraft cabin, allowing observation angles in the range +10° to +15° (elevation). Table 1 lists performance data of the SUMAS/SMS front ends.

The i.f. signal is pre-amplified in a cooled (77 K) HEMT stage. Additional amplifiers, bandpass filters and a second mixing stage match the signal to the input of the back end that consists of a 28-channel filterbank (bandwidth 1.2 GHz, 10×80 MHz, 8×40 MHz, 10×8 MHz) in parallel to an 850 MHz bandwidth acousto-optical spectrometer (AOS). The AOS, covering the central fraction of the receiver passband, provides an effective resolution of approx. 1.5 MHz.

3. RESULTS

In Figure 1 two filter bank spectra of the ClO (649.448 GHz) line, measured during a flight between Kiruna (Sweden) and Stockholm and between Stockholm and Munich at a flight altitude of 11,700 m is shown. For comparison a synthetic line spectrum based on a disturbed chemistry ClO profile [6] has been plotted. The measued spectra indicate a strong variability in ClO along the flight tracks and large ClO amounts, particularly at altitudes below 30 km, over south Sweden (Flight No. 1).

4. CONCLUSIONS

The concept of a compact, low-noise submillimeter-wave receiver has been described. The radiometer was designed for operation on board a high-flying research aircraft allowing spectroscopic measurements of middle atmospheric minor trace gases that are key species in ozone chemistry. Recent measurements performed over northern Europe will provide accurate data on concentrations of stratospheric chlorine monoxide being a sensitive indicator for a disturbed ozone chemistry.

Table 1. Performance of SUMAS/SMS front ends.

	SUMAS	ESTEC-SMS
Spectral Lines	$H^{35}Cl$ (625.917 GHz), O_3 (647.840 GHz)	^{35}ClO (649.448 GHz)
Mixer Element	quasi-optical Schottky mixer (uncooled)	waveguide mixer (cooled, 77 K)
I.F. Pre-Amplifier	HEMT, ν_0 = 11.08 GHz (cooled, 77 K)	HEMT, ν_0 = 10 GHz
Receiver Noise Temperature (single-sideband, B = 1.2 GHz)	8,700 K, ($H^{35}Cl$, lower sideband) 9,600 K (O_3, upper sideband)	3,400 K (upper sideband)

5. ACKNOWLEDGEMENTS

The flight experiments were funded by the German Bundesministerium für Forschung und Technologie (BMFT Grant No. 01LO9223). We thank the DLR Flugabteilung/Oberpfaffenhofen and Paul Hartogh, MPAe/Lindau, for their support during the flight campaigns. We thank the Max-Planck-Institut für Radioastronomie for providing the acousto-optical spectrometer.

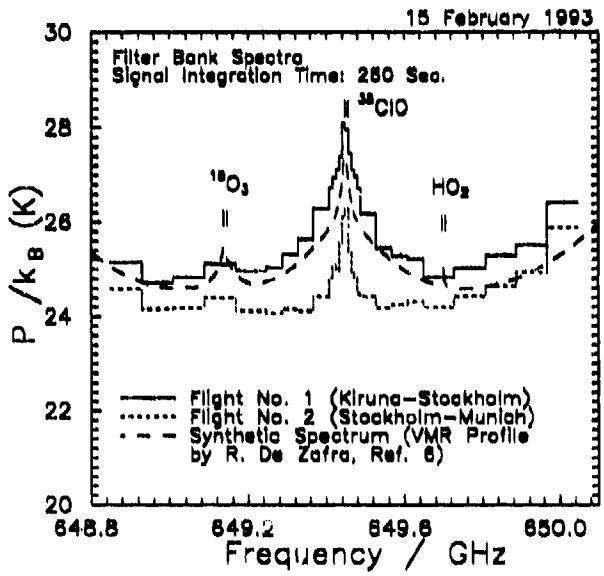

Figure 1. ^{35}ClO (649.45 GHz) emission line.

6. REFERENCES

[1] J.W. Waters, "Submillimeter-Wavelength Heterodyne Spectroscopy and Remote Sensing of the Upper Atmosphere", *Proceedings of the IEEE*, Vol. 80, No. 11, 1992, pp. 1679-1701.

[2] Research grant provided by the Land Bremen, project no. FV026.

[3] ESTEC Contract No. *8742/90/NL/PB(SC)*. This contract involves several companies (Deutsche Aerospace GmbH, Radiometer-physics GmbH, Germany) and research institutes (Univ. of Bern, Switzerland, Univ. of Bremen, Germany, Chalmers University, Sweden, Univ. of Florence, Italy and the Space Research Organization, The Netherlands).

[4] Manufactured by RPG-Radiometer physics GmbH, Germany.

[5] H. Nett, S.Crewell, P. Hartogh, K. Künzi, "Detection of Stratospheric Minor Constituents using an Airborne Submillimeter-Wave Sensor", *Int. Symposium on Environmental Sensing*, Berlin, FRG, June 1992, Proceedings, SPIE Vol. No. 1715, pp. 468-475.

[6] R. L. DeZafra, M. Jaramillo, J. Barrett, L. K. Emmons, P. M. Solomon, A. Parrish, "New Observations of a Large Concentration of ClO in the Lower Springtime Stratosphere over Antarctica and Its Implications for Ozone-Depleting Chemistry", *J. Geophys. Res.*, **94**, 1989, pp. 11423-11428.

Ground-based millimeter-wave monitoring of stratospheric ozone at altitudes above 20 km

A. A. Krasil'nikov, Yu. Yu. Kulikov, L. I. Fedoseev

Institute of Applied Physics of the Russian Academy of Sciences
46 Ul'janov Str., Nizhny Novgorod, 603600

ABSTRACT

Millimeter waves give a unique possibility for ozone monitoring at any weather. The equipment, technique and preliminary results of the annual series of ozone observations (February 1992 – March 1993) above Nizhny Novgorod (56.3° N) are described. The comparision with Keating – Young model is given.

1. EQUIPMENT. CALIBRATION. OZONE VERTICAL DISTRIBUTION RETRIEVAL

Thermal ozone emission was measured in the rotational transition $6_{0,6} - 6_{1,5}$ (resonance frequency 110.836 GHz) by the heterodyne total power spectral radiometer. Its single sideband equivalent noise temperature equals 3000 K. Ten 3 MHz-channels and four 9 MHz-channels covered 110 MHz-analysis band.

The zenith emission was compared with the emission of a "black body" at ambient temperature and a "black body" at liquid nitrogen temperature. The ozone spectrum was corrected taking into account the tropospheric attenuation obtained from continuum measurement.

The retrieval of the vertical ozone density distribution $N(z)$ was based on choosing the parameters of the analytical expression for $N(z)$ and on the season-average temperature and pressure profiles[1].

2. RESULTS OF OBSERVATION

Commensurable seasonal and sporadic components of annual variation X ($z \geq 22$ km) " total ozone content at the altitudes above 22 km are detected (Fig. 1). The maximum month-average X ($z \geq 22$ km) is observed in May, the

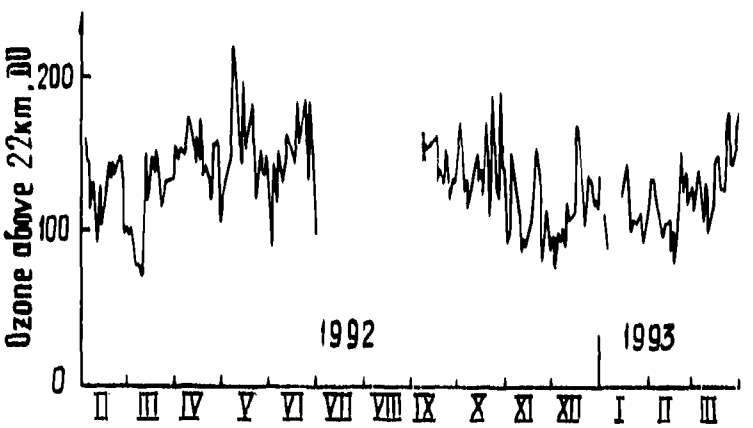

Fig. 1. Variability of the ozone content at the altitude above 22 km (Nizhny Novgorod, 56.3° N)

minimum one – in November. When the altitude z increases, the maximum of the ozone density N (z) displaces to the middle of summer (Fig. 2) and the minimum – to December.

The greatest sporadic variations took place in March 1992, the smallest – in September. In winter X ($z \geq 22$ km) frequently became close to the value typical of Antarctic ozone hole[2].

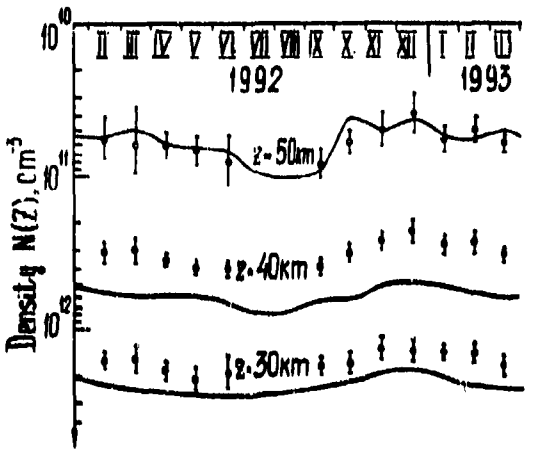

Fig. 2. Month-averaged ozone density at altitudes 30 km, 40 km and 50 km in comparison with Keating – Young model (solid lines)

On February 22,1993 occured the sudden rise of N ($z \geq 22$ km) which coincided with the stratospheric warming. The ozone concetration near $z = 25$ km increased by 70%, near $z = 50$ km " by 15% only.

The comparison of the obtained data and Keating – Young model[3] for 55° N (solid lines in Fig. 2) shows rather good coincidence for the altitude $z = 50$ km and the discrepancy for other altitudes up to 1.5 – 2.5 times at $z = 40$ km. The similar discrepancy was already mentioned[2].

The influence of the solar proton events on ozone did not reveal itself on the background of the sporadic component.

3. REFERENCES

1. J. J. Barnett and M. Corney "Middle atmosphere reference model derived from satellite data", *Hardbook for MAP*, Vol.16, pp. 47–85, 1985.

2. A. F. Andriyanov, O. N. Borisov et al. "Millimeter sounding of stratospheric ozone in high altitudes", *Preprint N 326*, Institute of Applied Physics of the Russian Academy of Sciences, Nizhny Novgorod, 1992.

3. G. M. Keating and D. F. Young "Interim reference ozone models for middle atmosphere", *Hardbook for MAP*, Vol. 16, pp. 205–229, 1985.

FAR INFRARED SPIN RESONANCE IN II-VI D.M.S

J.L MARTIN*, M.GOIRAN*, Z.GOLACKI**, J.LEOTIN* and S.ASKENAZY*

*Service des Champs Magnetiques Intenses, INSA
Complexe scientifique de Rangueil, 31077 Toulouse-Cedex (France)
**Institute of Physics,
Polish Academy of Sciences, 32/46 Al. Lotnikow, 02668 Warsaw (Poland)

Abstract

Exchange interactions in dilute magnetic semiconductors (D.M.S.) $Zn_{1-x}Co_xS$, $Zn_{1-x}Mn_xSe$ and $Cd_{1-x}Mn_xSe$ are studied by E. P.R. in the F.I.R. region with high magnetic field up to 40 Tesla. For x ≈ 5%, transmission spectra exhibit very sharp satellite lines on both sides of the single magnetic ion resonance. We assigne these structures to be relevant of the exchange interaction in magnetic ions pairs. A calculation of pairs energy levels, including Dzialoshinsky Morya (D.M.) effects, and symetrical exchange terms of the interaction tensor, allows to extract from the measurements the values of D.M. constant. Moreover, in the case of cobalt, the occurrence of an absorption peak at half field is well interpreted by taking into account the symetric anisotropic terms.

The D.M.S. that we have studied are wide gap compounds and thus very good candidates for E.P.R. measurements by transmission [1]. The most general form of the exchange interaction is:

$$\mathcal{H}_{exch.} = -2 \sum_{<i,j>} \vec{S}_i J_{i,j} \vec{S}_j \qquad (1)$$

where $\sum_{<i,j>}$ is the sum over all magnetic ions pairs and $J_{i,j}$ is a third order effective spin coupling tensor.

The fast decreasing of $J_{i,j}$ contants with the distance between magnetic ions allows to neglect long range exchange interactions. Thus, we use the J_1 cluster model in which the probability for having a next nearest neighbour pair is maximum for $x \approx 5\%$. We have used sample with a wide concentration range ($0.5\% < x < 15\%$) and we focus here on the results concerning the 5% concentration samples.

The sources of the magnetospectrometer are a F.I.R. cavity optically pumped by a CO_2 laser and a Gunn diode emitting 96 GHz radiation. The pulsed magnetic field was set parallel to <110> axis for Zinc Blende structure compounds and parallel to <001> axis for Wurtzite structure compounds.

As illustration, figure 1 shows transmission spectra for $Zn_{1-x}Co_xS$. The satellite lines have a maximum intensity for $x \approx 5\%$ as well as the half field peak. We reject the hypothesis of interference phenomena for two different reasons: the half width of the peaks varies with temperature (figure 2) and the satellite lines occurs independently of the sample geometry.

The developpement of equation 1 leads to the Hamiltonian:

$$\mathcal{H} = \mathcal{H}_0 + \mathcal{H}_1 + \mathcal{H}_2 + \mathcal{H}_3 \quad (2)$$

$$\mathcal{H}_0 = g\mu B(S_{1z} + S_{2z}) - 2J.\vec{S}_1.\vec{S}_2 \quad (3)$$

$$\mathcal{H}_1 = -2[D_e(3S_{1z}S_{2z} - \vec{S}_1.\vec{S}_2) + E_e(S_{1x}S_{2x} - S_{1y}S_{2y})] \quad (4)$$

$$\mathcal{H}_2 = -2\vec{d}_{12}.(\vec{S}_1 \wedge \vec{S}_2) \quad (5)$$

$$\mathcal{H}_3 = -2\vec{S}_1\vec{b}_{12}\vec{S}_2 \quad (6)$$

J is the isotropic exchange constant. In D.M.S., J is negative (antiferromagnetic). D_e and E_e are functions of diagonal terms of the interaction tensor, $\vec{d}_{12}$ is expressed with antisymmetric terms: it is the D.M. interaction. The terms of the symetric tensor $\vec{b}_{12}$ explain the half field resonance in $Zn_{0,95}Co_{0,05}S$.
The basic states on which the hamiltonian $\mathcal{H}$ is developped are $|S, M_S>$ with $\vec{S} = \vec{S}_1 + \vec{S}_2$ and $M_S = S_z$. At the second order of the pertubation theory the state $|0,0>$ and $|1,-1>$ are coupled through the D.M. interaction. When $|d| \ll -g\mu B_{-1,0} - 2J + 3.7(-2D_e)$, the transition energies are given by:

$$\Delta\mathcal{E}_a = E(1,0) - E(1,-1) \approx g\mu B_{-1,0} - 11.1(-2D_e) - \frac{1.2^2(2|d|)^2}{-g\mu B_{-1,0} - 2J + 3.7(-2D_e)}$$

$$\Delta\mathcal{E}_b = E(1,1) - E(1,0) \approx g\mu B_{0,1} + 11.1(-2D_e)$$

where $B_{i,j}$ is the resonant field for $M_S = i \rightarrow M_S = j$ transition.
The magnetic field distances between satellite lines and the single ion resonant field B_0 are:

$$g\mu(B_0 - B_{0,1}) \approx 11.1(-2D_e) \quad (7)$$

$$g\mu(B_0 - B_{-1,0}) \approx -11.1(-2D_e) - \frac{1.2^2(2|d|)^2}{-g\mu B_0 - 2J - 7.4(-2D_e)} \quad (8)$$

A fitting of the experimental results gives the values (figure 3):

$$D_e \approx 0.014K \quad \text{in ZnMnSe}$$

$$D_e \approx 0.009K \quad \text{in CdMnSe}$$

$$|d| \approx 0.18K \quad \text{in ZnMnSe}$$

$$|d| \approx 0.11K \quad \text{in CdMnSe}$$

These values are in relatively good agreement with theoritical predictions by Larson et al. [2] and magnetization results [3].

References

[1] L.M. Claessen, A. Wittlin and P.Wyder, Phys. Rev. B 41, 451 (1990)

[2] B.E. Larson and H. Ehrenreich, Phys. Rev. B 39, 1747 (1989)

[3] V. Bindilatti, T.Q. Vu, Y. Shapira, C.C. Agosta, E.J. McNiff,Jr., R. Kershaw, K. Dwight and A. Wold, Phys. Rev. B 45, 5328 (1992)

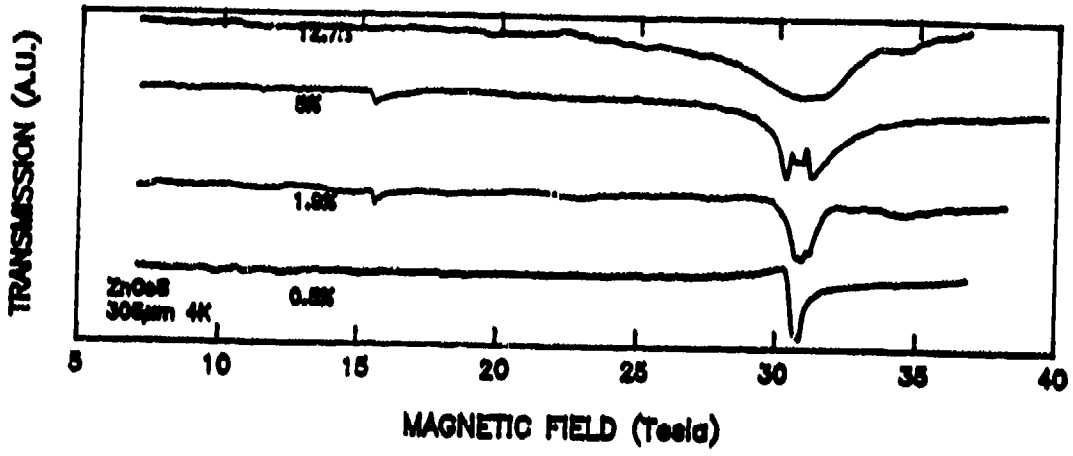

Figure 1: Transmission of ZnCoS for different concentrations at λ= 305μm

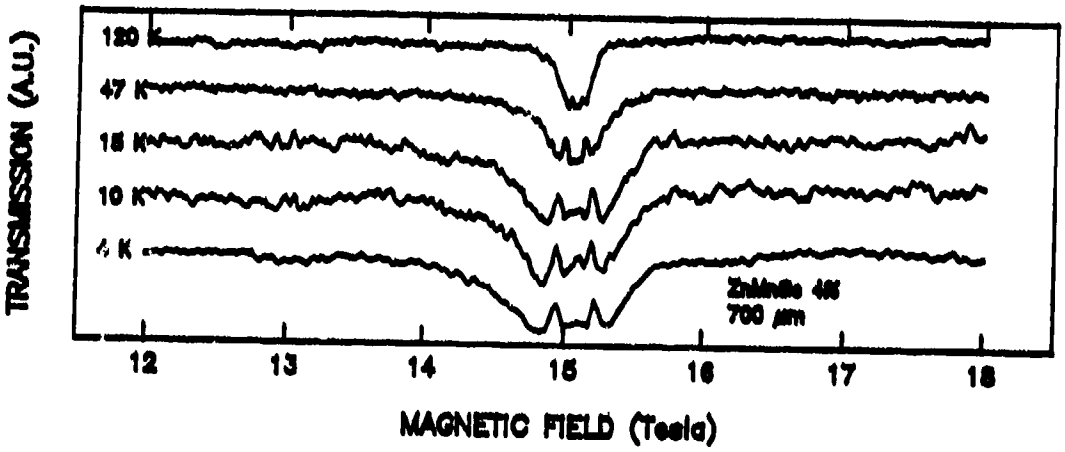

Figure 2: Variation of the satellite line intensity in ZnMnSe with temperature

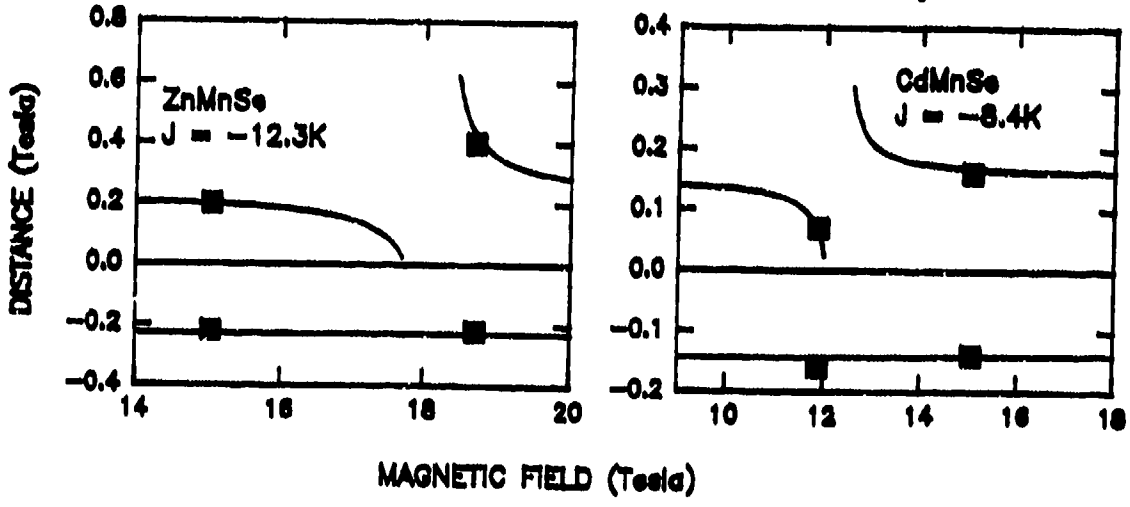

Figure 3: Distance in magnetic field between satellite lines and the single ion line

SUBMILLIMETER SPECTROSCOPY OF THE ELECTRON EXCITATIONS IN RARE-EARTH ORTHOFERRITES

G.V. Kozlov, S.P.Lebedev, A.A.Mukhin , , A.S. Prokhorov, A.A.Egoyan
Institute of General Physics of Russia Acad. Sci., 38 Vavilov St., 117942 Moscow, Russia

We have investigated the high-frequency magnetic and dielectric properties of the orthoferrites $RFeO_3$ (R = Tm, Er) possesing various spin-reorientation phase transitions (SRPT). It is known that in $TmFeO_3$ and $ErFeO_3$ the SRPTs occur in the *ac*-plane via two second-order phase transitions $\Gamma_4(G_x) \rightarrow \Gamma_{24}(G_xG_z) \rightarrow \Gamma_2(G_z)$ [1,2] , where G is the antiferromagnetism vector of the Fe-subsystem.

The $RFeO_3$ single crystals were grown by float zoning with radiative heating. Submillimeter (SBMM) transmission spectra of the *a*-, *b*-, *c*-cut plane-parallel plates of the orthoferrites were measured by the backward wave oscillator spectrometer «*Epsilon*» [3] in the frequency range ν = 100 - 1000 GHz (3 - 33 cm^{-1}) at temperatures 4.2 - 600K.

In all the orthoferrites studied we revealed two narrow antiferromagnetic resonance (AFMR) modes of the Fe-subsystem (quasiferromagnetic (F) and quasiantiferromagnetic (AF) modes) and several wide absorpsion lines identified as the rare-earth modes which are caused by electronic transitions inside the Tm^{3+}, Er^{3+} ion ground multiplets.

The transmission spectra were fitted according to the well-known formulae for a plane parallel layer. To describe a dispersion of the magnetic permeability and the dielectric permittivity we have used the harmonic oscillator model

$$\mu_\kappa(\nu) = 1 + \Sigma_\alpha \Delta\mu_\kappa^{(\alpha)} \nu_\alpha^2 / (\nu_\alpha^2 - \nu^2 + i\nu\Delta\nu_\alpha),$$
$$\varepsilon_\kappa(\nu) = \varepsilon_\kappa^\infty + \Sigma_\alpha \Delta\varepsilon_\kappa^{(\alpha)} \nu_\alpha^2 / (\nu_\alpha^2 - \nu^2 + i\nu\Delta\nu_\alpha),$$

where ν_α and $\Delta\nu_\alpha$ are the α-mode resonance frequency and linewidth, $\Delta\mu_\kappa^{(\alpha)}$, $\Delta\varepsilon_\kappa^{(\alpha)}$ - mode contributions into the static magnetic permeability and the dielectric permittivity, respectively, α=x,y,z. As the result, there were obtained the temperature dependences of the mode parameters.

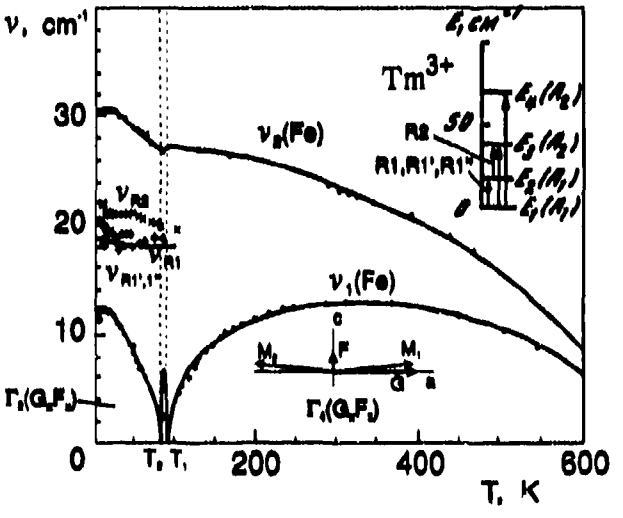

Fig.1. The temperature dependences of the AFMR- and R-mode frequencies in $TmFeO_3$: points - experiment, solid lines - theory. In the inset - the lower part of the ground Tm^{3+} multiplet spectrum in $TmFeO_3$.

$TmFeO_3$. The SRPT is characterized by a softening of the F-mode frequency ν_1(Fe) on both bondaries of the spin reorientation (Fig.1). A strong enhancement of the soft F-mode contributions $\Delta\mu_x^{(1)}$ ($T \to T_1$) and $\Delta\mu_z^{(1)}$ ($T \to T_2$) was also observed which result from a divergence of the Fe-subsystem rotation susceptibility.

For T<100K we observed broad absoption lines ($\Delta\nu/\nu \approx 1$): R_1(h∥c, e∥b), R'_1(h∥a, e∥b), R''_1(h∥b, e∥a), R_2(h∥b, e∥c) which were assigned to the R-modes. These modes correspond to the certain electronic transitions inside the Tm^{3+} ground multiplet split by a crystal field (Fig.1). According to the selection rules for the electronic transitions we have identified R_1-mode as magnetodipolar one and other R-modes as electrodipolar ones (see also [4]). An increase (up to 30%) of the quasistatic dielectric permittivity along *c*-axis in $TmFeO_3$ was observed at low T, resulted from an appreciable contribution of the electrodipolar R- modes in Tm^{3+}.

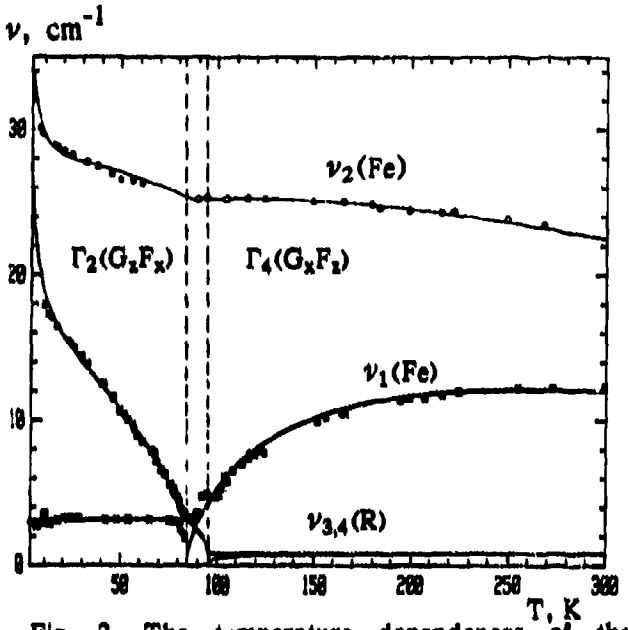

Fig. 2 .The temperature dependences of the resonance frequencies in $ErFeO_3$: points– experiment, solid lines – theory.

$ErFeO_3$. Along with the already known AFMR modes [5] we have revealed the R-modes ($\nu_{3,4}$(R)) indentified as the magnetodipolar electronic transitions inside the ground Er^{3+} Kramers doublet split by the exchange field of the Fe-subsystem. The main feature of the temperature dependences of the corresponding resonance frequencies is the softening of the F-mode frequency ν_1(Fe) at the smooth spin-reorientation (Fig. 2) . However, this softening occurs only at the lower SRPT's boundary $T_2 = 87$ K. The value of the F-mode gap at $T = T_2$ is closed to the Er^{3+} ground doublet splitting ($\approx 3cm^{-1}$) in the Γ_2 phase . An interaction of the F and R modes was observed near T_2, preventing from the full softening of the F-mode frequency ν_1(Fe).

We have developed a theory describing dynamic properties of the orthoferrites with various rare-earth ions. The theory is based on a general linear response of the R-subsystem to a high-frequency external magnetic (electric) field and anisotropic exchange fields of the Fe-subsystem. Some results of our calculations for the resonance mode behavior are shown in Fig. 1,2.

1. R. L. White, J. Appl. Phys. 40 ,1061 (1968) .
2. K. P. Belov, A. K. Zvezdin, A. M. Kadomtseva, R. Z. Levitin, "Orientational phase transitions in the rare-earth magnets " (Nauka, Moscow, 1979), in Russian.
3. A.A. Volkov, Yu.G. Goncharov, G.V. Kozlov, et al., Infrared Phys.25, 369 (1985).
4. A.A.Mukhin, A.Yu.Pronin, A.S.Prokhorov, et al., Phys. Letters A, 153, 499 (1991).
5. N. Koshisuka, S. Ushioda, Phys.Rev.B,22, 5394 (1980).

Progress in German High Field Magneto Spectroscopy using IR, FIR, and mm Waves: a Quantum Transition from the Hochmagnetfeldanlage in Braunschweig to the HUMBOLDT High Magnetic Field Center in Berlin

by

Michael von Ortenberg and coworkers

HUMBOLDT Universität zu Berlin and Technische Universität
Braunschweig, Germany

The paper covers the concept of the newly established HUMBOLDT High Magnetic Field Center and discusses the results of the following experiments in detail:

* optically induced magnetization in Cd(Mn)Te using spin-flip resonance in finite magnetic fields

* the HALDANE gap: angular and temperature dependence of the magnetic resonance in NENP

* application of the strip-line technique in magnetooptics of narrow gap semimagnetic semiconductors

* single coil experiments up to 160 Tesla on semiconductors using IR radiation.

These results demonstrate again the tremendous efficiency of high magnetic fields in conjunction with optical radiation of the IR, FIR, and mm range for the investigation of electronic energy levels in solids and justify the concept and establishment of the new HUMBOLDT High Magnetic Field Center.

Origin of satellite structures of high field EPR in $Cd_{1-x}Mn_xTe$

G. Eilers[1] , M. von Ortenberg, R. Galazka+

Institut für Halbleiterphysik und Optik,Technische Universität Braunschweig, 3300 Braunschweig, Germany; +Polish Academy of Science, Institute of Physics, Warsaw, Poland

ABSTRACT

The electron paramagnetic resonance (EPR) of Mn^{2+} in $Cd_{1-x}Mn_xTe$ ($0.01 < x < 0.65$) was examined at low temperatures and high magnetic fields. A far infrared laser was used as a radiation source. The structure of the resonance was strongly influenced by electromagnetic propagation effects. By variation of the sample thickness it was clearly shown that the satellite structures besides the main EPR peak are solely due to interference effects.

1. INTRODUCTION

$Cd_{1-x}Mn_xTe$ belongs to the group of semimagnetic semiconductors (SMSC). $Cd_{1-x}Mn_xTe$ exhibits a zincblende structure within a wide compositional range up to $x = 0.77$. The wide range of composition exhibiting spin concentrations between $10^{18}cm^{-3}$ and $10^{23}cm^{-3}$ makes this material especially attractive for fundamental studies of the spin-spin interactions, because one can examine the magnetic properties as a function of the concentration of the magnetic ions. One fundamental problem is to understand the processes underlying the interaction between the Mn^{2+} spins. In this respect, the formation of clusters of Mn^{2+} ions is important. Assuming a random distribution of Mn^{2+} on cation sites of the zincblende crystal, the fraction of Mn^{2+} nearest neighbor pairs, the simplest cluster-type, has a maximum of about 25% at a concentration $x = 0.05$. High magnetic fields can impose new physical conditions on the spin system of the pairs. At low temperatures and high magnetic fields the Zeeman splitting can be larger than the thermal energy k_BT and the internal exchange splittings. In $Cd_{1-x}Mn_xTe$ this leads to level crossings resulting in a steplike behavior of the magnetization[1].

2. RESULTS AND DISCUSSION

In this work the electron paramagnetic resonance is studied on the semimagnetic semiconductor $Cd_{1-x}Mn_xTe$ for various Mn concentrations x at low temperatures and high magnetic fields up to 18 T. We are especially interested in the effect of exchange coupled pairs, which are responsible for the magnetization steps, on the paramagnetic resonance. Claessen et al.[2] reported "satellite" structures besides the main $g = 2$, EPR peak at high magnetic fields and low Mn concentrations. Our investigations are aimed to get a better understanding of the origin of these resonances especially at concentrations around $x = 0.05$, where the number of the exchange coupled nearest neighbor pairs is the largest. It was shown that the structure of the resonance is strongly influenced by electromagnetic propagation effects. These effects are especially pronounced for the narrow and strong resonance at low Mn concentrations. Calculations of the transmission through a plane parallel slab including multiple reflections at the sample interfaces and employing a simple Bloch model for the resonance, were used to simulate the structures of the resonance observed in the experiment (see figure 1,2). By variations of the sample thickness it was clearly shown that the "satellite" resonances are solely due to interference effects. No additional structures owing to transitions originating from the exchange coupled Mn^{2+} pairs as they were claimed by Claessen et al.[2] could be found. The positions of all additional structures besides the main EPR were dependent on temperature as well as the sample thickness (figure 1). Accordingly they can not be due to transitions in the energy level system of the exchange coupled pairs. In the spectra obtained in this study there was no evidence for an influence of the ground state change of the Mn^{2+} pair clusters on the paramagnetic resonance. However, the line shape of the resonance was distorted by the presence of interference effects even for the thinnest samples prepared and we can therefore not rule out an effect of the ground state changes on the resonance.

[1] Present adress: Department of Material Science and Engineering, Nagoya University, Furo-cho, Chikusa-ku, Nagoya 464-01, Japan

The examination of the magnetic resonance at high concentrations showed the same features as they were reported by Wittlin et al.[3]. As the concentration of the Mn^{2+} ions is increased the resonance broadens and, for concentrations in the spin glass phase (i.e. $x > 0.20$ at $2\,K$), a shift of the resonance position was observed at low temperatures. Following the theoretical analysis of Larson and Ehrenreich[4] about the broadening mechanism of the paramagnetic resonance in $Cd_{1-x}Mn_xTe$, the broadening of the resonance can be explained by the anisotropic antiferromagnetic exchange interaction between the ions. This exchange interaction also accounts for the internal fields responsible for the shifts of the resonance positions in the spin glass phase. The application of FIR laser magnetospectroscopy could be shown to be advantageous for the examination of the broad resonances. In high magnetic fields the studies of the paramagnetic resonance in the spin glass phase could be extended to lower temperatures which was not possible using standard EPR techniques at low radiation frequencies. This was already stated before by Wittlin et al.[3]. Because of the influence of interference effects it was not possible to extract reliable information about microscopic parameters from the spectra. This problem may be solved by preparing samples thin enough to be able to neglect the influence of interference effects on the line shape. In that case the line width can be extracted directly from the spectra and related to the results of theoretical calculations of this parameter as they were done for example by Larson and Ehrenreich.

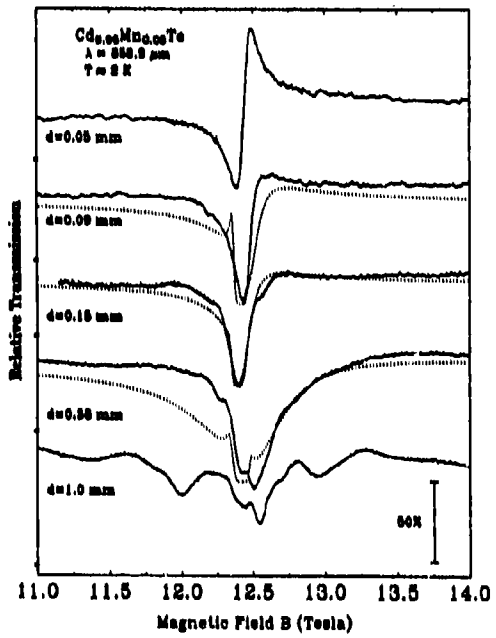

Figure 1: Thickness dependence of the resonance shape at low temperature (Mn concentration $x = 0.05$). The dashed lines represent simulation calculations.

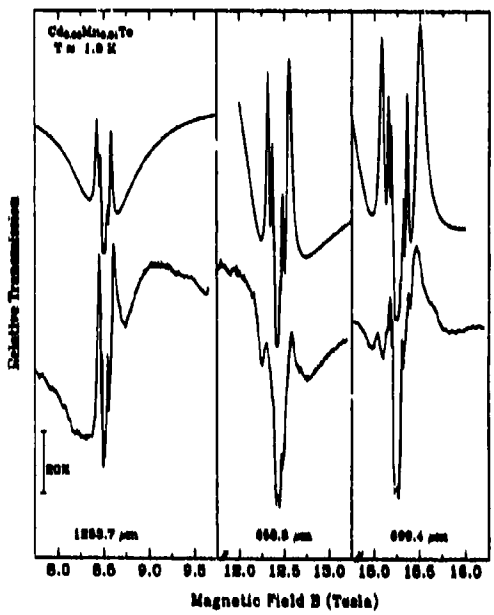

Figure 2: Low temperature transmission spectra of a sample with a concentration $x = 0.01$ and a sample thickness $d \approx 1.2\,mm$. The upper traces represent simulation calculations of the resonance.

3. REFERENCES

[1] S. Foner, Y. Shapira, D. Heiman, P. Becla, R. Kershaw, K. Dwight, and A. Wold. Magnetization steps in dilute magnetic semiconductors to 55T: Mn^{++} pair saturation in $Cd_{1-x}Mn_xTe$ and steps in $Zn_{1-x}Mn_xSe$,$Zn_{1-x}Mn_xTe$ and $Cd_{1-x}Mn_xSe$. *Phys. Rev. B*, Vol.39:11793, 1989.

[2] L. M. Claessen, A. Wittlin, and P. Wyder. High-magnetic-field EPR in $Cd_{1-x}Mn_xTe$. *Phys. Rev. B*, Vol.41:451, 1990.

[3] A. Wittlin, L. M. Claessen, and P. Wyder. High-field magnetic resonances in $Cd_{1-x}Mn_xTe$ at far-infrared energies. *Phys. Rev. B*, Vol.37:2258, 1988.

[4] B. E. Larson and H. Ehrenreich. Anisotropic superexchange and spin resonance in diluted magnetic semiconductors. *Phys. Rev. B*, Vol.39:1747, 1989.

Infrared reflectivity of semiconductor magnetoplasmas

F. Elmzughi and D.R. Tilley

University of Essex, Department of Physics
Wivenhoe Park, Colchester, CO4 3SQ U.K.

The simple expression $\varepsilon = 1 - \omega_p^2/\omega^2$ for the frequency dependence of a plasma dielectric function predicts a reflectivity $R = 1$ for $\omega < \omega_p$, decreasing sharply from unity as ω increases above the plasma frequency ω_p. Since $\omega_p^2 = ne^2/\varepsilon_0 m_e$, infrared reflectivity of semiconductors can be used as a characterisation technique to determine the ratio n/m_e, where n is the carrier density and m_e the effective mass. However, in a sample containing minority carriers (density p and effective mass m_h, say) this technique loses its power since then $\omega_p^2 = ne^2/\varepsilon_0 m_e + pe^2/\varepsilon_0 m_h$. It has been pointed out[1] that if a magnetic field is applied the parameters of both types of carrier can be determined, essentially because the Lorentz force acts differently on electrons and holes. The dielectric tensor in the presence of a field takes a gyrotropic form quoted explicitly elsewhere[1].

Calculated curves for normal-incidence reflectivity[1] indicate that all four of the parameters n, m_e, p and m_h and in addition the relaxation time τ_e and τ_h can be determined from the spectra, but experimental studies have not yet appeared. For practical applications two extensions of the previous calculations are needed. First, in a practical instrument[2] the magnetic field is vertical, the plane of incidence horizontal and it is convenient to use an angle of incidence of 45°. The simplest samples of interest are likely to include an epilayer on a substrate as well as the surface of a bulk sample. We therefore present here the formal results and some illustrations for oblique-incidence reflectivity in these two cases.

The notation is shown in Fig.1 In s polarisation the optical E field is transverse to the plane of incidence, therefore along the magnetic field, and only the non-resonant component ε_∞ is probed. The interesting case is therefore p polarisation and application of standard methods gives an expression for the power reflectivity R off a bulk sample in which a crucial part is played by the Voigt permittivity $\varepsilon_v = \varepsilon_1 - \varepsilon_2^2/\varepsilon_1$.

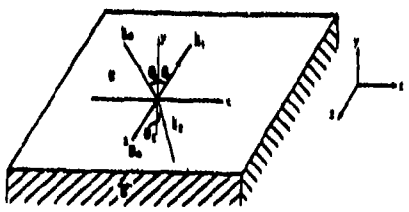

Fig.1 Notation for calculations.

The frequency dependence of ε_v is illustrated in Fig.2 for doped CdTe in several different magnetic fields. The optic phonon response is included by means of the usual expression[3] with TO frequency $\omega_T/2\pi = 118$ cm^{-1}, LO frequency $\omega_L/2\pi = 139$ cm^{-1} and damping parameter $\Gamma/2\pi = 6$ cm^{-1}. The carrier parameters are those used previously[1]. For small frequency $\mathrm{Re}(\varepsilon_v)$ is negative, as with any plasma. The resonance around ω_T in ε_v is due to the phonons, perturbed by plasma effects, while the resonance above 300 cm^{-1} is due to the plasma response. $\mathrm{Im}(\varepsilon_v)$ has a series of resonant peaks.

The corresponding oblique-incidence reflectivity ($\theta_0 = 45°$) off a bulk sample may be calculated from (2) and is shown in Fig.3. In normal incidence and in the absence of damping, $R = 1$ when $\mathrm{Re}(\varepsilon_v) < 0$, $R < 1$ when $\mathrm{Re}(\varepsilon_v) > 0$ and $R = 0$ when $\mathrm{Re}(\varepsilon_v) = \varepsilon = 1$, the dielectric constant in the medium of incidence. This general correlation between R and $\mathrm{Re}(\varepsilon_v)$ is seen to persist in the relation between Figs. 2a and 3, although the details might merit further discussion.

The expression for the reflectivity off a film of thickness d on a substrate is quite complicated. Typical calculated reflectivity curves are shown in Fig.4. Comparison with Fig.3 shows that the same general features are present although the general level is lower because there is some transmission into the substrate. Fig.4 also illustrates the phenomenon of non-reciprocity[4], that is, R changes when the magnetic field is reversed . This also holds for reflection off a bulk sample, although it was not illustrated in Fig.4.

REFERENCES

1. B.L. Johnson, R.E. Camley and D.R. Tilley, *Phys.Rev.B* 44 8839 (1991).
2. D. Brown, T. Dumelow and T.J. Parker, *these Proceedings.*
3. T. Dumelow, T.J. Parker, S.R.P. Smith and D.R. Tilley, *Surface Science Reports* 17 151 (1993).
4. R.E. Camley, *Surface Science Reports* 7 103 (1987).

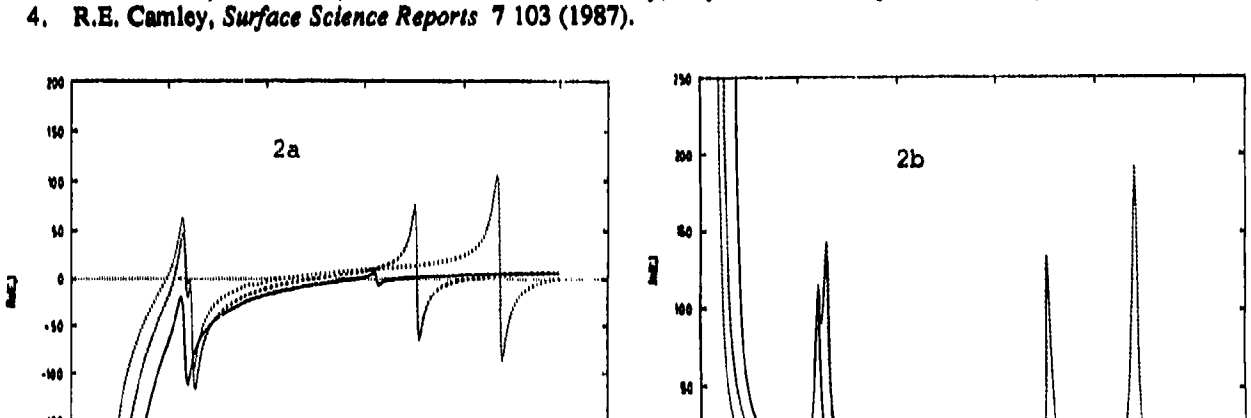

Fig.2 Voigt permittivity for CdTe doped with two species of carrier. (2a) Re(ε_v), (2b) Im(ε_v).
Fields are ——————— 1T, - - - - - - - - - - 4T, ... 7T.

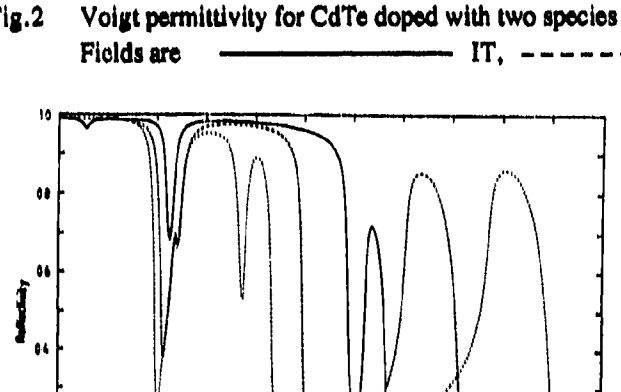

Fig.3 Reflectivity in p polarisastion, 45^0 angle of incidence in air, off CdTe in geometry of 1 with ε_v given by Fig.2
Fields as in Fig.2

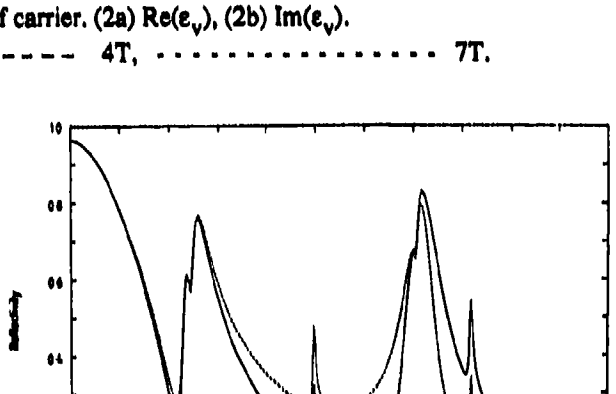

Fig.4 As Fig.3, but for a 100 μm film on a substrate.

Fields are ——————— +4T.- - - - - - - -4T

Infrared reflectivity calculations for rare-earth metals

K. Abraha and D.R. Tilley

University of Essex, Department of Physics

Wivenhoe Park, Colchester, CO4 3SQ U.K.

The development of high resolution Fourier transform infrared spectrometers capable of making measurements in high magnetic fields and over an extended temperature range[1] opens up the possibility of studies of a wide range of magnetic materials. The far-infrared reflectivity depends on both the dielectric permittivity and the magnetic permeability, the latter containing information about the magnetic excitations. The permeability, which normally takes a gyromagnetic form, has poles at magnetic resonance frequencies. In order for these to be accessible to far infrared instruments it is necessary for the exchange coupling to enter the restoring force, otherwise the frequency is too low. Thus simple ferromagnets are excluded but any system with some form of antiferromagnetic coupling is a potential candidate for far infrared studies. Recent work[1] on the simple uniaxial antiferromagnet FeF_2 shows very sharp resonance lines which can be followed over a range of temperatures and magnetic fields.

One intriguing possibility is the study of the magnetic structure of the rare-earth metals and superlattices. Due to the competition between first and second neighbour exchange, some rare earth metals have a helical or conical ordered spin structure over some temperature range. The metals are hexagonal close-packed and in the helical and cone states all the spins within one close packed plane are aligned, in the former case in-plane and in the latter case at an angle out of the plane. The direction of the projection of the spin on the plane rotates by an angle ϕ from one close-packed plane to the next. Examples of the helical state are Dy between 85 K and 179 K and Tb between 221 K and 230 K. The cone state is found in Ho and Er for $T < 20$ K. In rare-earth superlattices a variety of specific orderings is found, for example, the phase of the spiral is "transmitted" across a non-magnetic (Y) spacer layer[2].

The magnetic permeability for the spiral and cone states has been found previously[3] and applied to a calculation of the surface magnetostatic (Damon-Eshbach) mode. This is carried out in the limit $c \to \infty$ in which Maxwell's equations decouple into an electrostatic and a magnetostatic part. Damon-Eshbach type modes have been extensively investigated in metallic surfaces and films during the last 15 years[4]. Here we consider the FIR reflectivity. The calculation is more or less standard, involving solution of Maxwell's equations with standard boundary conditions.

Since the rare earths are metallic, the reflectivity is expected to be near unity because of the relatively high conductivity. The standard result when only conductivity is involved is that the reflectivity decreases slowly from unity as the frequency increases. With the inclusion of the permeability, reflectivity dips should appear at the magnetic resonance frequencies. The feasibility of experimental detection depends crucially on the sharpness and depth of the dips.

We are not aware of any data on the optical parameters of the rare earth metals in the far infrared. We have therefore taken published values of the rf conductivity s and extrapolated to give a pure imaginary FIR dielectric function $\varepsilon = i\sigma/\varepsilon_0\omega$. This is large, of order $|\varepsilon| \sim 10^4$, and correspondingly the reflectivity R is very close to unity. For the magnetic parameters, fairly good estimates of the resonance frequency and pole strength can be made[3] but the linewidth is unknown.

Typical calculated spectra, for two different values of linewidth, are shown in Figure 1. The magnetic features might be experimentally detectable, preferably with the use of a technique like infrared reflection absorption spectroscopy (IRRAS) to remove the high background. An alternative experimental technique is attenuated total reflection (ATR), which has proved a useful technique in the investigation of semiconductor superlattices, for example[5]. We have calculated ATR spectra for a Si coupling prism and 45^{o} angle of incidence. For an optimised coupling gap the ATR dips related to the permeability tensor are much more pronounced than the reflectivity dips of Fig.1. It appears that they should be resolvable with current experimental techniques.

In conclusion, we suggest that determination of the FIR optical parameters of the rare-earth metals is desirable, since nothing is known at present. On the basis of the estimates we are able to make detection of the magnetic features in reflection is challenging but may be possible. On the other hand, ATR should give much more accessible spectra. If this prediction is experimentally verified then a wide range of metallic magnetic systems should be open to study by FIR spectroscopy.

REFERENCES

1 D. Brown, T. Dumelow and T. J. Parker, *these Proceedings*.

2. C. F. Majkrzak et al, "Magnetic rare-earth superlattices" *Advances in Physics* 40 99-189 (1991).

3. N. S. Almeida and D. R. Tilley, "Susceptibility and surface magnetostatic modes for the spiral and cone states of rare-earth magnets" *Phys.Rev. B* 43 11145-53 (1991)

4. M. G. Cottam and D. R. Tilley, "Introduction to surface and superlattice excitations" *Cambridge University Press* 1989

5. T. Dumelow, T.J. Parker, S.R.P. Smith and D.R. Tilley, "Far infrared spectroscopy of phonons and plasmons in semiconductor superlattices" *Surface Science Reports* 17 151-212 (1993).

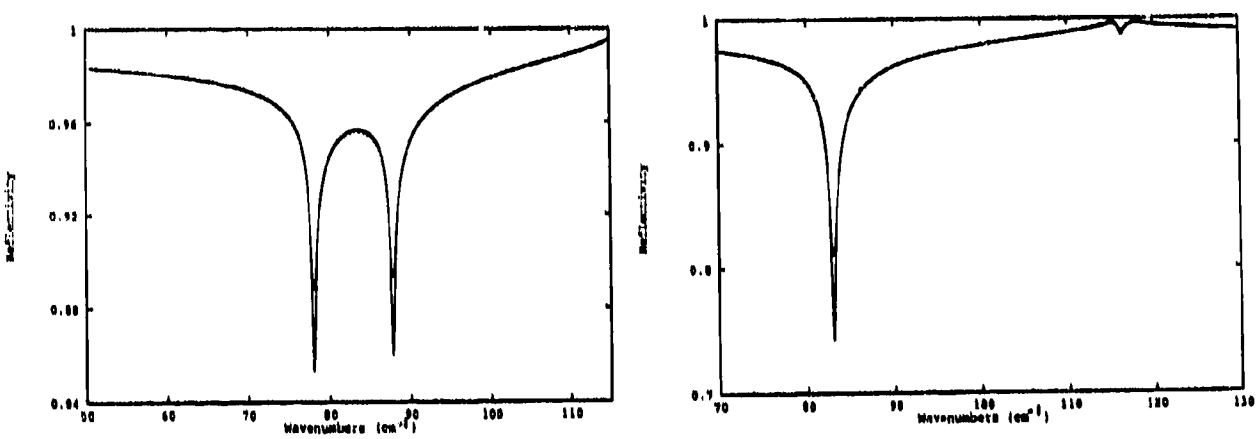

(a) (b)

Fig.1 Calculated oblique incidence (45^{o}) s-polarisation reflectivity off Ho for two different values of magnon damping Γ. ——————— $\Gamma = 0.2\ cm^{-1}$, - - - - - - - - $\Gamma = 0.4\ cm^{-1}$.

(a) Cone axis normal to surface, (b) Cone axis in surface and normal to plane of incidence

High resolution FTS studies of magnetic compounds

M.N.Popova

Institut of Spectroscopy, Russian Academy of Sciences, 142092 Troitsk, Moscow region, Russia

ABSTRACT

We show that high resolution Fourier-transform infrared spectroscopy offers new possibilities in the study of magnetic ordering in rare earth containing solids. Review of the results on the magnetic compounds related to high-T_c superconductors and on quasi-one-dimensional rare earth nickelates is presented.

1.INTRODUCTION

In this report, the work of the author's group since 1988 is summarised. We have carried out the spectral studies of $R_2Cu_2O_5$,[1,2] R_2BaCuO_5 (here, R stands for rare earth or yttrium)[3-7] and R_2BaNiO_5 (R=Lu,Yb)[8] magnetic cuprates and nickelates which are related to the high-T_c superconductors of 123 type. It is interesting to study these compounds also in connection with the problem of low-dimensional magnetism. There are Cu-O planes in the structure of $R_2Cu_2O_5$, with in-plane Cu-Cu distances considerably smaller than intra-plane ones. The so called "green phases" R_2BaCuO_5 and "brown phase" Nd_2BaCuO_5 of R-Ba-Cu-O superconducting ceramics contain isolated Cu^{2+} ions not interconnected by direct bonds through oxygen. Various Cu-O-O-Cu or Cu-O-R-O-Cu superexchange paths, low-dimensional in particular, may dominate in these compounds depending on the particular R^{3+} ion. R_2BaNiO_5 with R=Lu, Yb are isostructural to the green phases, while the other members of this family (also studied by us[9]) have completely different structure containing isolated -Ni-O-Ni- chains.

2.EXPERIMENTAL

Polycrystalline samples of the mentioned compounds, pure or with 1 at.% of erbium or dysprosium introduced as spectral probes, were prepared from oxides by solid state reaction in air. The powder samples were carefully ground, mixed with ethanol and put on the sapphire platelet directly before the window of InSb detector. The whole assembly was inside an optical cryostat, either in liquid helium or in cold helium vapor. Near IR diffuse transmittance spectra due to *f–f* optical transitions in the intrinsic R^{3+} ion or Er^{3+} probe were measured at 2÷120K with a spectral resolution up to 0.2 cm^{-1} employing BOMEM DA3.002 Fourier-transform spectrometer.

3.DETECTION OF MAGNETIC PHASE TRANSITIONS

High resolution spectrum of R^{3+} Kramers ion in a crystal is extremely sensitive to the changes of local magnetic field at the place of this ion. This gives a possibility to register unambiguously magnetic phase transitions, even those not detectable by other methods, and, in some cases, to determine their nature. We have found for the first time a magnetic ordering in Y_2BaCuO_5,[3] Lu_2BaCuO_5,[6] Nd_2BaCuO_5,[7] R_2BaNiO_5 with R = Lu, Nd, Sm, Eu, Dy, Ho, Er, Tm. [5,9]. Spin reorientation transitions not known before have been detected in Y_2BaCuO_5,[3,5] Dy_2BaCuO_5,[4] Lu_2BaCuO_5 and Yb_2BaCuO_5.[6]

On the other hand, our spectral method permits to verify the interpretation of magnetic susceptibility (χ) and specific heat (c) measurements. Thus, we have shown that the maxima in c(T) and χ(T) curves for Er_2BaCuO_5 and in χ(T) curve for Er_2BaNiO_5 which had been attributed to the phase transitions within the erbium magnetic subsystem were, in fact, caused by the population changes within the ground Er^{3+} Kramers doublet split by an exchange interaction with an ordered d–subsystem.[5,6]

4.COEXISTENCE OF TWO DIFFERENT MAGNETIC PHASES

In the region of first order spin reorientation phase transition two magnetic phases coexist, usually, in a small interval of temperatures. The spectrum there is a superposition of two different spectra with temperature dependent relative intensities. We have found that in Y_2BaCuO_5 and Lu_2BaCuO_5 two different magnetic phases coexist down to the lowest measuring temperature of 2K.[5,6] Evidently, various links Cu-O-O-Cu compete with each other in these compounds.

5.SPECTRA OF Er PROBE AND MAGNETIC STRUCTURE OF d-SUBSYSTEM

We proposed the method of Er^{3+} probe in a series of isostructural f-d compounds to select the right magnetic structure of an ordered d-subsystem from several structures that fitted neutron scattering data equally well.[3,6] This method has been tested on $R_2Cu_2O_5$ cuprates[2] where reliable neutron scattering data exist and applied to some of the R_2BaCuO_5 compounds.[6] The analogous work on R_2BaNiO_5 chain nickelates is in progress now.

6.SHORT RANGE ORDER AT $T>T_c$

For $T>T_c$ the splittings of spectral lines ($\Delta\nu$) do not vanish - a "tail" is observed due to short range order. We have compared the curves $\Delta\nu(T/T_N)$ for two $R_2Cu_2O_5$ compounds with identical structure of copper magnetic moments $\vec{\mu}_{Cu}$ (ferromagnetically ordered $\vec{a}\vec{b}$ planes coupled antiferromagnetically one with another, $\vec{\mu}_{Cu}$ aligned along the $\vec{b}$ axis) but with strongly different T_N temperatures, namely, for $Er_2Cu_2O_5$ (T_N = 28K) and $Y_{1.98}Er_{0.02}Cu_2O_5$ (T_N = 14K). Both curves have a point of inflection at $T=T_N$, but the "tail" is about two times longer for the second one. This fact can be naturally explained if we assume that magnetic correlations within isolated CuO planes take place below the same temperature in both compounds, while $Er_2Cu_2O_5$ where these planes interact through magnetic Er^{3+} ions orders three-dimensionally at two times higher temperature than $Y_2Cu_2O_5$ with nonmagnetic Y^{3+} ions.

Various manifestations of low-dimensional magnetic correlations have been observed in the spectra of erbium probe in Ho_2BaCuO_5 and Er_2BaCuO_5,[5] Yb_2BaNiO_5 and Lu_2BaNiO_5.[8] Probably, the most interesting phenomenon is connected with different temperature behavior of the spectra from two different structural positions, Er1 and Er2 in these compounds. While the spectral lines of Er1 are markedly split only below T_N, those of Er2 remain split up to $T = 1.6\ T_N$ and demonstrate a long tail of residual splitting at higher temperatures. We suppose that the Er2 ions are inside dominant magnetic chains and experience the establishment of short range order within a chain at $T \gg T_c$ while Er1 ions interconnect the chains and announce the 3D-ordering at T_c.

7.ACKNOWLEDGEMENTS

The author would like to emphasise the decisive contribution of her colleagues I.V.Paukov, Yu.A.Hadjiiskii and G.G.Chepurko. The synthesis of the samples by B.V.Mill and Ja.Zoubkova from Moscow State University is greatly acknowledged.

8.REFERENCES

1. G.G.Chepurko, I.V.Paukov, M.N.Popova and Ja.Zoubkova, "Spectral studies of magnetic cuprates $R_2Cu_2O_5$ (R = Tb, Er, Tm, Lu, Y)", *Sol. State Comm.*, Vol.79, No.7, pp.569-572, 1991.

2. M.N.Popova and I.V.Paukov, "Spectral studies of magnetic cuprates $R_2Cu_2O_5$ (R = Yb, Ho, Dy)", *Phys. Lett. A*, Vol.159, No.3, pp.187-192, 1991.

3. N.I.Agladse, M.N.Popova, E.P.Khlybov and G.G.Chepurko, "Magnetic order in Y_2BaCuO_5", *Soviet Physics. JETP Lett.*, Vol.48, No.1, pp.45-47, 1988.

4. M.N.Popova and G.G.Chepurko, "Splitting of low-temperature magnetic transition in Dy_2BaCuO_5", *Soviet Physics. JETP Lett.*, Vol.52. No.10, pp.562-566, 1990.

5. M.N.Popova and I.V.Paukov, "Spectroscopy of magnetic cuprates R_2BaCuO_5", *Proceedings of the 2nd International School on Excited States of Transition Elements, Poland, Sept.1991*, ed. W.Strek, W.Ryba-Romanowski, J.Legendziewicz, B.Jeshowska-Trzebiatowska, pp.211-220, World Scientific, 1992.

6. I.V.Paukov, M.N.Popova and B.V.Mill, "Spectral studies of magnetic ordering in the cuprates R_2BaCuO_5 (R = Sm, Eu, Tm, Yb, Lu), *Phys. Lett. A*, Vol.169, No.4, pp.301-307, 1992.

7. I.V.Paukov, M.N.Popova and B.V.Mill, "Magnetic phase transition and short range order in Nd_2BaCuO_5", *Phys. Lett. A*, Vol.157, No.4,5, pp.306-308, 1991.

8. Yu.A.Hadjiiskii, R.Z.Levitin, B.V.Mill, I.V.Paukov, M.N.Popova and V.V.Snegirev, "Spectral and magnetic studies of nickelates Lu_2BaNiO_5 and Yb_2BaNiO_5", *Sol. State Comm.*, Vol.85, No.9, pp.743-748, 1993.

9. G.G.Chepurko, Z.A.Kasei, D.A.Kudrjavtsev, R.Z.Levitin, B.V.Mill, M.N.Popova and V.V.Snegirev, "Magnetic and spectral studies of Er_2BaNiO_5 and other rare earth nickelates", *Phys. Lett. A*, Vol.157, No.1, pp.81-84, 1991.

Far infrared studies of magnetic systems.

T Dumelow, D E Brown and T J Parker

Department of Physics, University of Essex, Wivenhoe Park,
Colchester, CO4 3SQ, UK.

The overall aim of this research programme is to use far infrared spectroscopy to investigate non-reciprocal behaviour[1] of coupled bulk and surface polaritons under an applied magnetic field in a selection of bulk and low dimensional antiferromagnetic media. The materials of interest include bulk antiferromagnets like FeF_2, thin films of metallic Cr, and rare earth elements such as Ho, together with superlattices fabricated from alternate layers of these and other, non-magnetic, materials.

An NPL far infrared cube interferometer[2] has been modified for this work by adding a hydraulically controlled moving mirror arm with a scan length of 1 m and a single mode He-Ne laser to monitor the optical path difference so that measurements can be made with a nominal resolution limit of 10^{-2} cm^{-1}. The specimen is located between the poles of a 7 T magnet.

The interferometer is shown schematically in Fig.1, and the main modifications are as follows: The moving mirror is mounted on a high precision slide and scanned continuously at a constant speed. The He-Ne laser beam passes along the optical axis of the instrument. In the fixed arm of the interferometer the end mirror is vibrated to provide phase modulation for the infrared beam. The laser beam, however, is reflected from a small fixed mirror to an adjustable side mirror so that the laser fringes are modulated (at 500 Hz) only by the motion of the moving mirror. The "fixed" mirror is vibrated at 167 Hz and the infrared beam is detected using a lock-in amplifier system. Consequently, the advantages of phase sensitive detection for the infrared beam and laser sampling control are achieved simultaneously, since the modulation (at ~ 1 Hz) of the infrared radiation by the slow scan of the moving mirror is rejected by the lock-in amplifier.

The output beam from the beam divider is focussed on to a sample located between the poles of a 7 T magnet in a liquid He cryostat, and the beam reflected from the sample is subsequently focussed on to a liquid He cooled Si bolometer operating at 4.2 K. A Spectromag magnet and cryostat from Oxford Instruments, with the field vertical, are used for this work and, for the present measurements, the plane of incidence is horizontal. The output from the interferometer is strongly s-polarised in the vertical plane due to the Fresnel reflectivity of the mylar beam divider, which is convenient for s-polarised measurements on the specimen. It is not possible, however, to obtain acceptable signal-to-noise ratios in a reasonable time using the direct p-polarised component from the beam divider, so, to enable measurements to be carried out in p-polarisation without re-orienting the sample and cryostat, a roof top mirror and a wire grid polariser are used to rotate the plane of polarisation of the beam by 90° between the interferometer and the cryostat.

For our initial investigation we have studied the antiferromagnetic resonance in FeF_2, since the Neel temperature (79 K) and antiferromagnetic resonance frequency (near 50 cm^{-1}) in this crystal are both easily accessible with this instrument. Far infrared reflection spectra measured at 45° angle of incidence at 4.2 K and with a resolution of 0.1 cm^{-1} are shown in Fig. 2. These measurements were made in s-polarisation, with the magnetic field and crystal c axis axis normal to the plane of incidence. The middle spectrum shows the antiferromagnetic resonance in the absence of a magnetic field, and the two other spectra show the Zeeman splittings which occur at magnetic fields of ± 3 T. The vertical scale is correct for the lowest curve, but the curves for 0 and +3 T have been offset to separate the three sets of data. The expected non-reciprocal behaviour is strikingly clear from the difference in the asymmetry of the spectra measured with the two field directions. A more extensive study of the magnetic field dependence of magnons in FeF_2 has been carried out using this beam geometry, including measurements in both s and p-polarisation with the crystal c axis horizontal, vertical, and at intermediate angles, and a report is in preparation on this work[5].

There is also considerable interest in non-reciprocal behaviour of surface polaritons in these materials. Since the excitations of interest are non-radiative, techniques such as attenuated total reflection (ATR) spectroscopy will be needed to advance the wave vector of the incident beam to couple with the surface polaritons. These modes are expected to be observed as dips in the reflectivity in the antiferromagnetic resonance peak, and theoretical work on the ATR spectra of antiferromagnets[3,4] has shown that a resolution of the order of 10^{-2} cm^{-1} will be required. This resolution is within the mechanical design specification of this instrument, but further software developments of a relatively straightforward nature are still required to handle the large data arrays.

Our previous experience with ATR on semiconductors at higher frequencies[6] indicates that the construction of an ATR stage for this work should also be comparatively straightforward. Usually the key engineering problem in ATR, particularly at higher frequencies and low temperatures, is the accurate setting of the small gap which is required between the prism and the specimen for satisfactory coupling. However, calculations of ATR spectra for FeF_2 by Almeida and Tilley[4] indicate that satisfactory coupling should occur with comparatively large gaps, of the order of several hundred microns.

ACKNOWLEDGEMENT.

The authors wish to acknowledge financial support for this work from the UK Science and Engineering Research Council under Grant No. GR/G/54139, and DEB wishes to thank SERC for the award of a Research Studentship.

REFERENCES.

1. R E Camley, Surface Science Reports, 7, 103 (1987).
2. G W Chantry, Long-wave Optics I and II (Academic Press, London, 1984).
3. R E Camley and D L Mills, Phys. Rev. 26B, 1280 (1982).
4. N S Almeida and D R Tilley, Solid State Commun. 73, 23 (1990).
5. T Dumelow, D E Brown, T J Parker, Kamsul Abraha and D R Tilley, to be published.
6. T Dumelow, T J Parker, S R P Smith and D R Tilley, Surface Science Reports, 17 , 151 (1993).

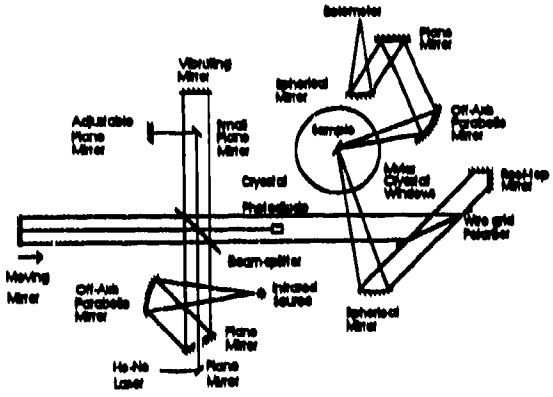

Figure 1. Schematic diagram of the Michelson interferometer set up for P-polarised experiments.

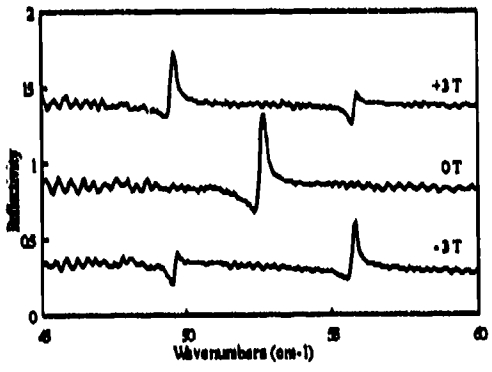

Figure 2. Far infrared spectrum showing the Zeeman splitting and non-reciprocal behaviour of the antiferromagnetic resonance in FeF_2.

FIR-study of $TbPO_4$

P. Janssen and P. Bruelemans
K.U. Leuven
Laboratory for Low Temperatures and High Magnetic Fields
Celestijnenlaan 200D
B-3001 Leuven

ABSTRACT:

The transmission of a $TbPO_4$-crystal is measured in magnetic fields up to 12 Tesla at wavelengths ranging from 100 to 2000 μm and temperatures around 2K. Strong absorptions are seen with the field along the tetragonal axis.

Time-resolved far infra-red magnetospectroscopy of ultra-high mobility n-GaAs layers and GaAs/AlGaAs multi quantum wells.

R E M de Bekker[+], J M Chamberlain[*], M B Stanaway[*], P Wyder[+],
C R Stanley[#] and M Henini[*].
[+] MPI/HML, Boite Postale 166X, F-38042 Grenoble Cedex, France.
[*] Physics Department, Nottingham University,
Nottingham, NG7 2RD, England.
[#]Department of Electronic & Electrical Engineering,
Glasgow University , Glasgow G12 8QQ, Scotland.

ABSTRACT

The time-resolved (TR) FIR photoconductivity of exceptionally high mobility n-GaAs ($\mu \approx 250{,}000$ cm^{2}V^{-1}s^{-1}) samples has been measured at 1.8K and in magnetic fields up to 8T using short (5ns) FIR pulses. The photoconductive decay time-constant (τ) is determined at zero magnetic field and at several non-zero fields with FIR laser energies resonant with the 1s-2p$_+$ impurity transition. Comparisons are made with previous measurements on MQWs and a simple Golden Rule theory.

1.INTRODUCTION

Time-resolved (TR) magnetospectroscopy in the FIR was first reported by Chamberlain et al [1,2], who used long (50-100ns) pulses to investigate the shallow donor recombination dynamics of n-InP. Subsequently, de Bekker et al [3,4] used a cavity-dumped, optically-pumped FIR laser with additional pulse-slicing to generate 5ns FIR pulses and study the TR decay of the FIR photoconductivity of GaAs/AlGaAs multi-quantum wells (MQWs). Very recently, Burghoorn[5] has described improvements of this technique which lead to pulses as short as 1ns. The recombination of an ionised electron to a shallow donor in a III-V semiconductor involves (i) the capture of free electrons by ionised donors into an excited bound state, followed by (ii) a cascading relaxation to the ground state accompanied by phonon emission. The characteristic time-scale of (i) and (ii) is of order tens of nanoseconds. For recombination under conditions of resonant 1s-2p$_+$ excitation, an additional initial transfer (iii) of electrons from the 2p$_+$ state into the N=0 landau level occurs in under one nanosecond. In this paper, we report measurements of τ (the photoconductivity decay time following pulsed FIR excitation) in exceptionally high mobility n-GaAs epitaxial layers in magnetic fields up to 8T. Previous measurements[6] of τ for n-InP in a magnetic field, using less-well defined pulses, had indicated that τ decreases with field. It was argued that the mechanism for this decrease is the increased phonon emission efficiency occurring as the electron wavefunction shrinks in the applied magnetic field. A similar argument was applied to explain the observed decrease in τ for the FIR photoconductive response of GaAs/AlGaAs multiquantum wells (MQWs), where the wavefunctions of the in-well donors are already squeezed by the quasi-two dimensional geometry. The present measurements present further evidence for this mechanism in another semiconductor material of exceptional purity, using more precisely-defined pulses than previously used for n-InP[6]. The differences in τ found at zero magnetic field are related to the number of acceptors in the samples[2], and the changes noted in τ in a magnetic field are discussed using a simple Golden Rule argument[6].

2. EXPERIMENTAL DETAILS

Full experimental details of the optical and electronic arrangements used have been given elsewhere[4]. Particular attention was paid in the design of the system electronics and the sample processing to ensure that the measurements represented the true photoconductive decay of the intrinsic photoconductivity. Two very high mobility[7] epitaxial n-GaAs samples (#1 and #2; μ(77K)= 220x and 180x10^3 cm^{2}V^{-1}s^{-1} respectively, and N_D-N_A=2.8x and 5.0x10^{13} cm^{-3} respectively) were studied, together with a more highly-compensated n-GaAs sample (#3; μ(77K)=47x10^3 cm^{2}V^{-1}s^{-1}, N_D-N_A=3X10^{14} cm^{-3}). In addition, a GaAs/AlGaAs MQW (#4; for electrical and dimensional details see reference (4)) was also investigated.

3.RESULTS.

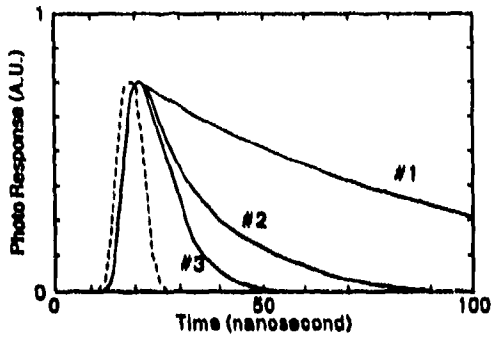

Figure 1

Figure 1 shows the TR photoresponse at 4.2K and zero magnetic field of samples #1,#2 and #3 to 5ns laser pulses with $\lambda = 90.9\mu m$ and power approximately 5W at the sample. The delay between stimulus (dotted line) and response arises from the shape of the laser pulse. It is assumed that the mobility of the warm electron gas does not change significantly during the decay, so that the conductivity signal measures the decay of carrier population, n(t). It is argued elsewhere[2] that, during the decay, a rate-equation model implies $n(t) \approx n_0 \exp(t/\tau)$, where n_0 is the initial population, $\tau = (1/CN_A)$ and C is a recombination constant. The values of τ obtained in this way are 150, 23 and 8 ns respectively. This demonstrates clearly the N_A dependence on τ. A comparison of experimental and calculated τ values may be made using the calculated values[2] of C; this consistently yields higher values of τ, which may be evidence that the electron gas mobility change should not be neglected, as has been suggested recently by Burghoorn[5]. By comparison, the MQW sample (#4) shows a photoconductive response[4] which effectively follows the excitation pulse, from which a value of $\tau < 2$ns has been deduced. The mechanism for this reduction in τ is discussed fully elsewhere[4].

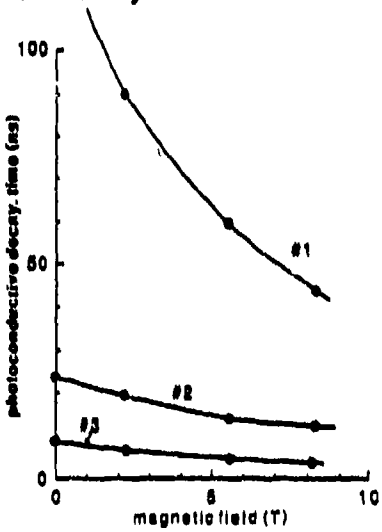

Figure 2

Figure 2 shows the results of several such measurements of τ made at FIR energies and magnetic fields resonant with the $1s\text{-}2p_+$ transition. For the epitaxial n-GaAs layers, a clear decrease in τ is noted as B increases; for the GaAs/AlGaAs MQW sample (#4), τ is so small[4] that any further decrease in field is unmeasurable. It has been previously shown[6] that application of the Fermi Golden Rule to the processes (i) and (ii) noted in the Introduction leads to a rate expression of the form:

$$\Gamma = Aq^2 \exp(-2a^2q^2) \qquad (1)$$

where the parameter A contains both material constants and a weighted average over all the individual recombination transitions involved; q is a phonon wave-vector and a is a parameter describing the size of the impurity wave-function. Clearly Γ is a maximum when $2(a^2q^2) = 1$; since Γ is dominated by the prefactor Aq^2, a change in effective Bohr radius (a) from 10nm (in the case of bulk n-GaAs) to 5.5nm (in the case of the MQW[4]) explains the substantial decrease in τ noted for the MQW in comparison with the bulk. Similarly, for the bulk samples (#1,#2 and #3) in a magnetic field, the squeezed Bohr radius, a, at a field of 10T is approximately 6.7nm[6], so that for each sample τ is diminished by a factor of $(6.7/10)^2$ ie a reduction of around 2.2 as noted in Figure 2. Further features of Figure 2, together with details of temperature- and intensity-dependence effect, will be published elsewhere.

4.REFERENCES

1. J M Chamberlain *et al*, "Impact excitation and bottleneck effects in the time-resolved FIR photoresponse of n-InP", *Phys. Rev.*,**B35**(5), 2391-2398, Feb.1987.

2. G L J A Rikken *et al*, "Time-resolved recombination dynamics of photoionized hydrogenic impurities", *Phys. Rev.*,**B38**(6), 4156-4164, August 1988.

3. R E M de Bekker *et al*, "Generation of very short FIR pulses by cavity dumping in a molecular gas laser", *J.Appl.Phys.*,**68**(7), 3729-3731, October 1990.

4. R E M de Bekker *et al*, "Subnanosecond far infrared photoconductivity from a GaAs/AlGaAs multiquantum well", *J.Appl.Phys.*,**68**(4), 1913-1915, August 1990.

5. J Burghoorn, "Time resolved FIR spectroscopy", *Ph.D. Thesis (unpublished)*, University of Delft, 1992.

6. G L J A Rikken *et al*, "Time resolved FIR magnetospectroscopy of hydrogenlike impurities in III-V semiconductors", *Phys. Rev.*,**B38**(3), 2002-2011, July 1988.

7. C R Stanley *et al*, "Electrical characterization of molecular beam epitaxial GaAs with peak electron mobilities up to $\approx 4\times10^5$ $cm^2V^{-1}s^{-1}$", *Appl.Phys.Lett.*,**58**(5), 478-480, February 1991.

Infra-red cyclotron resonance of 'crossed' band gap superlattices at magnetic fields of upto 150T

D.J. Barnes*#, R.J. Nicholas+, R.J. Warburton+, N.J. Mason+, P.J. Walker+ and N. Miura*

* Institute of Solid State Physics, Roppongi 7-22-1, Tokyo 106, Japan.
+ Physics Dept., Clarendon Laboratory, Parks Road, Oxford OX1 3PU, U.K.

Type II structures such as InAs/GaSb have the peculiar property that the valence band of the GaSb lies at a lower energy than the conduction band of the InAs[1]. This crossed (or negative) band gap configuration results in the intrinsic generation of high density gases of electrons and holes on either side of the interface. In a superlattice, the formation of subbands due to wavefunction overlap allow the band gap overlap to be reduced, and ultimately made positive, by the reduction of the periodicity[2]. This transition from a semimetal to a semiconductor can also be generated magnetically[3]. The action of a perpendicular magnetic field is to produce Landau levels which fan upwards in energy from the electrons and downwards in energy from the holes. If the superlattice has a negative band gap at zero magnetic field, then the gap will decrease and then uncross as the magnetic field increases. For a superlattice whose band gap is Eg=-0.07eV, the lowest Landau levels have been calculated to uncross at about 37T.

This paper presents an investigation of the effect of the layer periodicity and magnetic field on the band gap of InAs/GaSb and InAs/GaInSb superlattices. The cyclotron resonance (CR) of these samples has been studied using CO_2 and CO lasers which produce wavelengths of around 10μm and 5μm respectively. Pulsed magnetic fields of upto 150T with a duration of 5μsec were generated using a destructive, single-turn coil magnet and the transmitted radiation measured using a fast-response HgCdTe detector[4].

Due to the difference in the effective masses (m*) of the electron and holes and the cyclotron energies used, only the electron resonances were observed. As the absorption of the CR is proportional to the total electron concentration of the superlattice, the dramatic depopulation of the superlattice can be directly seen with decreasing period and increasing magnetic field. As an example, the CR of 1252(100) is shown in figure 1, depopulation occuring at about 50T. CR was studied in a wide variety of superlattices, including those grown on the piezoelectrically active (111)A substrate plane[5] and also those grown with 10% In in the GaSb[6], both of which act to enhance the band gap overlap (the growth characteristics of the samples are shown in table 1). The trends of the results are illustrated in figure 2, where the electron concentration is plotted as a function of magnetic field.

Clearly, as the thickness of the layers is reduced and the band gap overlap decreased, the overall electron concentrations and the magnetic field required to cause depopulation are both decreased. At a thickness of 500Å InAs on the (111) plane the transition lies above 120T, whereas by 100Å of InAs on the (100) plane the transition has been reduced to 45T and at 60Å the superlattice is already depopulated at zero magnetic field. The effect of the addiation of In into the GaSb layer is not as strong as previously thought as there is little difference between 1265(111) (500Å InAs) and 1249(111) (300Å InAs).

Despite the unusually high energies involved (<230meV) and the strong non-parabolicity of InAs,.the effective mass is accurately described by simple non-parabolicity of bulk InAs ($m^*=m_{InAs}^*(1+2.66E/E_{g(InAs)})$), incorporating the effect of the superlattice simply as an increase in energy above the band gap edge[7]. The influence of the GaSb layers does however become more noticable at short periodicities when the electrons are delocalised throughout the superlattice and m* becomes a function of both the mass in the InAs and in the GaSb (m*=0.023 and 0.042 respectively). This effect is shown in figure 3 for the InAs/GaSb superlattices.

In conclusion, we present direct evidence for the semimetal to semiconductor transition in type II superlattices caused by the formation of periodicity dependent subbands and also by the uncrossing of the electron and hole Landau levels at high magnetic fields.

Figure 1: InAs/GaSb 1252(100) Cyclotron Resonance

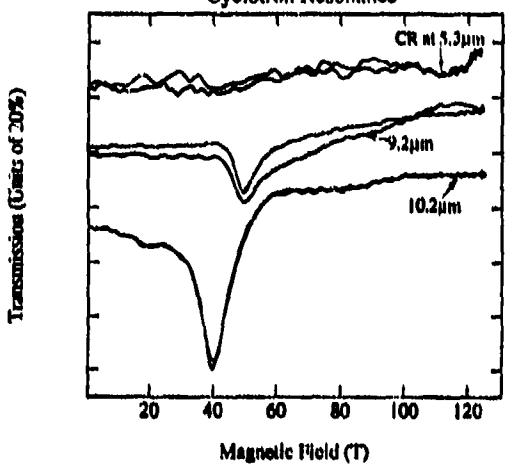

Figure 2: InAs/Ga(In)Sb Superlattices Electron density as a function of magnetic field

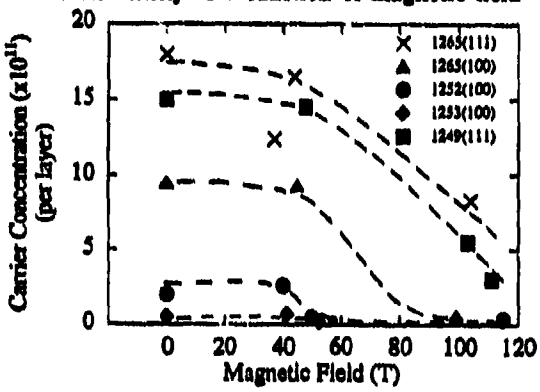

Figure 3: InAs/GaSb Superlattices m* as a function of InAs layer thickness

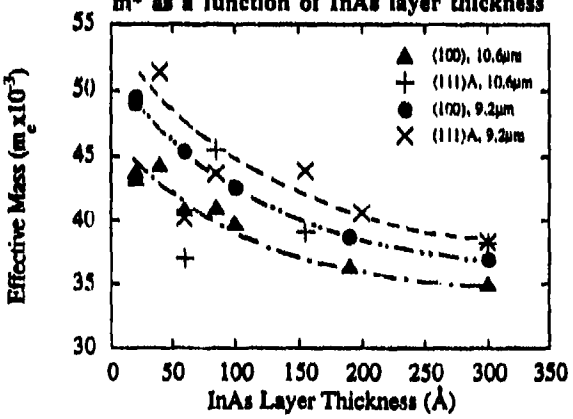

Table 1: Sample Details

	Number of Periods	InAs(Å)	GaSb(Å)	GaInSb(Å)
1265(111)A	20	500	-	100
1265(100)	20	500	-	100
1252(100)	100	100	50	-
1253(100)	100	60	30	-
1249(111)A	20	190	80	-

(1) H. Sakaki, L. Chang, R. Ludeke, C. Chang, G. Sai-Halasz, and L. Esaki *Appl. Phys. Lett.* 31 211 (1977)

(2) L. Esaki and L.L: Chang *J. Magn. Magn. Mater.* 11 208 (1979)

(3) N.J. Kawai, L.L: Chang, G.A. Sai-Halasz, C.-A. Chang, and L. Esaki *Appl. Phys. Lett.* 36 (1980)

(4) S.P. Najda, S. Takeyama and N. Miura *Phys. Rev.* B40 6189 (1989)

(5) D.L. Smith *Sol. State Comm.* 57 919 (1986)

(6) S. Haywood, E. Chidley, R. Mallard, N. Mason, R. Nicholas, P. Walker and R. Warburton *Appl. Phys. Lett.* 54 922 (1989)

(7) Y. Guldner, J.P. Vieren, P. Voisin, M. Voos, L.L. Chang and L. Esaki *Phys. Rev. Lett.* 45 1719 (1980)

Present address; Physics Dept., Geschwister-Scholl-Platz 1, University of Munich, 8000 Munich 22, Germany